Astronomical Society of the Pacific Conference Series Volume 73

AIRBORNE ASTRONOMY SYMPOSIUM ON THE GALACTIC ECOSYSTEM: FROM GAS TO STARS TO DUST

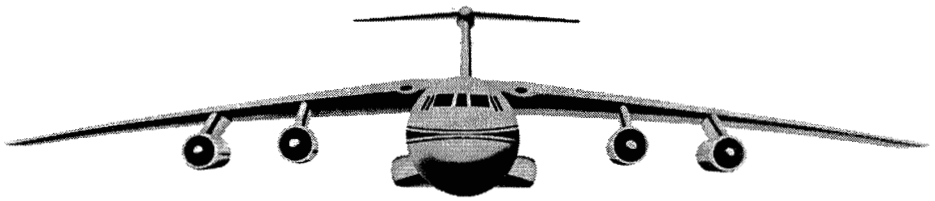

Edited by
Michael R. Haas, Jacqueline A. Davidson, and Edwin F. Erickson

AIRBORNE ASTRONOMY SYMPOSIUM ON THE BALACTIC ECOSYSTEM: FROM GAS TO STARS TO DUST

A SERIES OF BOOKS ON RECENT DEVELOPMENTS IN ASTRONOMY AND ASTROPHYSICS

Printed by BookCrafters, Inc.

First published 1995

Library of Congress Catalog Card Number: 95-75017
ISBN 0-937707-92-9

D. Harold McNamara, Managing Editor of Conference Series
408 ESC Brigham Young University
Provo, UT 84602
801-378-2298

A SERIES OF BOOKS ON RECENT DEVELOPMENTS IN ASTRONOMY AND ASTROPHYSICS

Vol. 1-Progress and Opportunities in Southern Hemisphere Optical Astronomy: The CTIO 25th Anniversary Symposium
ed. V. M. Blanco and M. M. Phillips ISBN 0-937707-18-X

Vol. 2-Proceedings of a Workshop on Optical Surveys for Quasars
ed. P. S. Osmer, A. C. Porter, R. F. Green, and C. B. Foltz ISBN 0-937707-19-8

Vol. 3-Fiber Optics in Astronomy
ed. S. C. Barden ISBN 0-937707-20-1

Vol. 4-The Extragalactic Distance Scale: Proceedings of the ASP 100th Anniversary Symposium
ed. S. van den Bergh and C. J. Pritchet ISBN 0-937707-21-X

Vol. 5-The Minnesota Lectures on Clusters of Galaxies and Large-Scale Structure
ed. J. M. Dickey ISBN 0-937707-22-8

Vol. 6-Synthesis Imaging in Radio Astronomy: A Collection of Lectures from the Third NRAO Synthesis Imaging Summer School
ed. R. A. Perley, F. R. Schwab, and A. H. Bridle ISBN 0-937707-23-6

Vol. 7-Properties of Hot Luminous Stars: Boulder-Munich Workshop
ed. C. D. Garmany ISBN 0-937707-24-4

Vol. 8-CCDs in Astronomy
ed. G. H. Jacoby ISBN 0-937707-25-2

Vol. 9-Cool Stars, Stellar Systems, and the Sun. Sixth Cambridge Workshop
ed. G. Wallerstein ISBN 0-937707-27-9

Vol. 10-The Evolution of the Universe of Galaxies. The Edwin Hubble Centennial Symposium
ed. R. G. Kron ISBN 0-937707-28-7

Vol. 11-Confrontation Between Stellar Pulsation and Evolution
ed. C. Cacciari and G. Clementini ISBN 0-937707-30-9

Vol. 12-The Evolution of the Interstellar Medium
ed. L. Blitz ISBN 0-937707-31-7

Vol. 13-The Formation and Evolution of Star Clusters
ed. K. Janes ISBN 0-937707-32-5

Vol. 14-Astrophysics with Infrared Arrays
ed. R. Elston ISBN 0-937707-33-3

Vol. 15-Large-Scale Structures and Peculiar Motions in the Universe
ed. D. W. Latham and L. A. N. da Costa ISBN 0-937707-34-1

Vol. 16-Atoms, Ions and Molecules: New Results in Spectral Line Astrophysics
ed. A. D. Haschick and P. T. P. Ho ISBN 0-937707-35-X

Vol. 17-Light Pollution, Radio Interference, and Space Debris
ed. D. L. Crawford ISBN 0-937707-36-8

Vol. 18-The Interpretation of Modern Synthesis Observations of Spiral Galaxies
ed. N. Duric and P. C. Crane ISBN 0-937707-37-6

Vol. 19-Radio Interferometry: Theory, Techniques, and Application, IAU Colloquium 131
ed. T. J. Cornwell and R. A. Perley ISBN 0-937707-38-4

Vol. 20-Frontiers of Stellar Evolution, celebrating the 50th Anniversary of McDonald Observatory
ed. D. L. Lambert ISBN 0-937707-39-2

Vol. 21-The Space Distribution of Quasars
ed. D. Crampton ISBN 0-937707-40-6

Vol. 22-Nonisotropic and Variable Outflows from Stars
ed. L. Drissen, C. Leitherer, and A. Nota ISBN 0-937707-41-4

Vol. 23-Astronomical CCD Observing and Reduction Techniques
ed. S. B. Howell ISBN 0-937707-42-4

Vol. 24-Cosmology and Large-Scale Structure in the Universe
ed. R. R. de Carvalho ISBN 0-937707-43-0

Vol. 25-Astronomical Data Analysis Software and Systems I
ed. D. M. Worrall, C. Biemesderfer, and J. Barnes ISBN 0-937707-44-9

Vol. 26-Cool Stars, Stellar Systems, and the Sun, Seventh Cambridge Workshop
ed. M. S. Giampapa and J. A. Bookbinder ISBN 0-937707-45-7

Vol. 27-The Solar Cycle
ed. K. L. Harvey ISBN 0-937707-46-5

Vol. 28-Automated Telescopes for Photometry and Imaging
ed. S. J. Adelman, R. J. Dukes, Jr., and C. J. Adelman ISBN 0-937707-47-3

Vol. 29-Workshop on Cataclysmic Variable Stars
ed. N. Vogt ISBN 0-937707-48-1

Vol. 30-Variable Stars and Galaxies, in honor of M. S. Feast on his retirement
ed. B. Warner ISBN 0-937707-49-X

Vol. 31-Relationships Between Active Galactic Nuclei and Starburst Galaxies
ed. A. V. Filippenko ISBN 0-937707-50-3

Vol. 32-Complementary Approaches to Double and Multiple Star Research, IAU Collouquium 135
ed. H. A. McAlister and W. I. Hartkopf ISBN 0-937707-51-1

Vol. 33-Research Amateur Astronomy
ed. S. J. Edberg ISBN 0-937707-52-X

Vol. 34-Robotic Telescopes in the 1990s
ed. A. V. Filippenko ISBN 0-937707-53-8

Vol. 35-Massive Stars: Their Lives in the Interstellar Medium
ed. J. P. Cassinelli and E. B. Churchwell ISBN 0-937707-54-6

Vol. 36-Planets and Pulsars
ed. J. A. Phillips, S. E. Thorsett, and S. R. Kulkarni ISBN 0-937707-55-4

Vol. 37-Fiber Optics in Astronomy II
ed. P. M. Gray ISBN 0-937707-56-2

Vol. 38-New Frontiers in Binary Star Research
ed. K. C. Leung and I. S. Nha ISBN 0-937707-57-0

Vol. 39-The Minnesota Lectures on the Structure and Dynamics of the Milky Way
ed. Roberta M. Humphreys ISBN 0-937707-58-9

Vol. 40-Inside the Stars, IAU Colloquium 137
ed. Werner W. Weiss and Annie Baglin ISBN 0-937707-59-7

Vol. 41-Astronomical Infrared Spectroscopy: Future Observational Directions
ed. Sun Kwok ISBN 0-937707-60-0

Vol. 42-GONG 1992: Seismic Investigation of the Sun and Stars
ed. Timothy M. Brown ISBN 0-937707-61-9

Vol. 43-Sky Surveys: Protostars to Protogalaxies
ed. B. T. Soifer ISBN 0-937707-62-7

Vol. 44-Peculiar Versus Normal Phenomena in A-Type and Related Stars
ed. M. M. Dworetsky, F. Castelli, and R. Faraggiana ISBN 0-937707-63-5

Vol. 45-Luminous High-Latitude Stars
ed. D. D. Sasselov ISBN 0-937707-64-3

Vol. 46-The Magnetic and Velocity Fields of Solar Active Regions, IAU Colloquium 141
ed. H. Zirin, G. Ai, and H. Wang ISBN 0-937707-65-1

Vol. 47-Third Decinnial US-USSR Conference on SETI
ed. G. Seth Shostak ISBN 0-937707-66-X

Vol. 48-The Globular Cluster-Galaxy Connection
ed. Graeme H. Smith and Jean P. Brodie ISBN 0-937707-67-8

Vol. 49-Galaxy Evolution: The Milky Way Perspective
ed. Steven R. Majewski ISBN 0-937707-68-6

Vol. 50-Structure and Dynamics of Globular Clusters
ed. S. G. Djorgovski and G. Meylan ISBN 0-937707-69-4

Vol. 51-Observational Cosmology
ed. G. Chincarini, A. Iovino, T. Maccacaro, and D. Maccagni ISBN 0-937707-70-8

Vol. 52-Astronomical Data Analysis Software and Systems II
ed. R. J. Hanisch, J. V. Brissenden, and Jeannette Barnes ISBN 0-937707-71-6

Vol. 53-Blue Stragglers
ed. Rex A. Saffer ISBN 0-937707-72-4

Vol. 54-The First Stromlo Symposium: The Physics of Active Galaxies
ed. Geoffrey V. Bicknell, Michael A. Dopita, and Peter J. Quinn ISBN 0-937707-73-2

Vol. 55-Optical Astronomy from the Earth and Moon
ed. Diane M. Pyper and Ronald J. Angione ISBN 0-937707-74-0

Vol. 56-Interacting Binary Stars
ed. Allen W. Shafter ISBN 0-937707-75-9

Vol. 57-Stellar and Circumstellar Astrophysics
ed. George Wallerstein and Alberto Noriega-Crespo ISBN 0-937707-76-7

Vol. 58-The First Symposium on the Infrared Cirrus and Diffuse Interstellar Clouds
ed. Roc M. Cutri and William B. Latter ISBN 0-937707-77-5

Vol. 59-Astronomy with Millimeter and Submillimeter Wave Interferometry
ed. M. Ishiguro and Wm. J. Welch ISBN 0-937707-78-3

Vol. 60-The MK Process at 50 Years: A Powerful Tool for Astrophysical Insight
ed. C. J. Corbally, R. O. Gray, and R. F. Garrison ISBN 0-937707-79-1

Vol. 61-Astronomical Data Analysis Software and Systems III
ed. Dennis R. Crabtree, R. J. Hanisch, and Jeannette Barnes ISBN 0-937707-80-5

Vol. 62-The Nature and Evolutionary Status of Herbig Ae / Be Stars
ed. P. S. Thé, M. R. Pérez, and E. P. J. van den Heuvel ISBN 0-937707-81-3

Vol. 63-Seventy-Five Years of Hirayama Asteroid Families: The role of Collisions in the Solar System History
ed. R. Binzel, Y. Kozai, and T. Hirayama ISBN 0-937707-82-1

Vol. 64-Cool Stars, Stellar Systems, and the Sun, Eighth Cambridge Workshop
ed. Jean-Pierre Caillault ISBN 0-937707-83-X

Vol. 65-Clouds, Cores, and Low Mass Stars
ed. Dan P. Clemens and Richard Barvainis ISBN 0-937707-84-8

Vol. 66- Physics of the Gaseous and Stellar Disks of the Galaxy
ed. Ivan R. King ISBN 0-937707-85-6

Vol. 67-Unveiling Large-Scale Structures Behind the Milky Way
ed. C. Balkowski and R. C. Kraan-Korteweg ISBN 0-937707-86-4

Vol. 68-Solar Active Region Evolution: Comparing Models with Observations
ed. K. S. Balasubramaniam and George W. Simon ISBN 0-937707-87-2

Vol. 69-Reverberation Mapping of the Broad-Line Region in Active Galactic Nuclei
ed. P. M. Gondhalekar, K. Horne, and B. M. Peterson ISBN 0-937707-88-0

Vol. 70-Groups of Galaxies
ed. Otto G. Richter and Kirk Borne ISBN 0-937707-89-9

Vol. 71-Tridimensional Optical Spectroscopic Methods in Astrophysics
ed. G. Comte and M. Marcelin ISBN 0-937707-90-2

Vol. 72-Millisecond Pulsars—A Decade of Surprise, ed. A. A. Fruchter
M. Tavani, and D. C. Backer ISBN 0-937707-91-0

Vol. 73-Airborne Astronomy Symposium on the Galactic Ecosystem: From Gas to Stars to Dust
ed. M. R. Haas, J. A. Davidson, and E. F. Erickson ISBN 0-937707-92-9

Inquiries concerning these volumes should be directed to the:
Astronomical Society of the Pacific
CONFERENCE SERIES
390 Ashton Avenue
San Francisco, CA 94112-1722
415-337-1100
e-mail asp @ stars.sfsu.edu

ASTRONOMICAL SOCIETY OF THE PACIFIC
CONFERENCE SERIES

Volume 73

AIRBORNE ASTRONOMY SYMPOSIUM ON THE GALACTIC ECOSYSTEM: FROM GAS TO STARS TO DUST

5-8 July 1994
NASA-Ames Research Center

Edited by
Michael R. Haas, Jacqueline A. Davidson, and Edwin F. Erickson

As in all complex scientific endeavors,
airborne astronomy depends heavily
on the skills and hard work of many people.
These proceedings are dedicated, with deep gratitude,
to the individuals who have contributed
to the development, operation, and administration
of NASA's Airborne Astronomy Program.

TABLE OF CONTENTS

Preface

This symposium was organized to review the science related to NASA's Airborne Astronomy Program on the occasion of the twentieth anniversary of the Kuiper Airborne Observatory (KAO). The sponsoring organizations were NASA and the SETI Institute. The Science Organizing Committee insisted on identifying a theme for the symposium, which was no easy task considering that KAO observers work over a range of 5000 in wavelength (0.3 – 1600 μm), and that the science program is subject to annual restructuring in the peer review process. The theme selected, "The Galactic Ecosystem: From Gas to Stars to Dust," was considered to capture the underlying commonality of much of the research discussed.

The introductory talk was given by Martin Harwit (NASM), who talked about the scientific discovery potential afforded by new technology and described, with some nostalgia, his experiences in the early days of the airborne program. He also showed a collection of photographs from the KAO archives, some of which are reproduced in this volume, as are some photographs from the symposium and recent KAO activities. The remainder of the symposium consisted of plenary oral sessions. Each of these began with an overview by an expert in the field, followed by talks on particular topics in that area, with most emphasizing KAO research. In addition, over 70 poster papers were on display for the three days of the symposium. A fine overview of the airborne program and its contributions to science, education, and technology is given in the paper by Hal Larson (University of Arizona) on page 591.

The symposium attracted 247 registered participants, including over 160 scientists, and 212 different authors contributed to the 123 articles which comprise this volume. The organization of the symposium was conducted largely via electronic mail over the Internet. Over 2500 electronic messages were exchanged regarding the symposium; ultimately only three abstracts were submitted solely in hardcopy form. We have included electronic mail addresses for as many of the participants as possible to facilitate communications among members of the community.

The Local Organizing Committee attempted to create an ambience of celebration in honor of the KAO anniversary. This atmosphere was aided materially by much appreciated donations from our Corporate Sponsors who are listed on page xxiii. The poster papers were displayed and the refreshments were served in a circus tent on the lawn near the Ames Administration Building, close to the Main Auditorium where the talks were given. Both the oral and poster sessions were attended by many of the KAO staff and other interested Ames employees, as well as by K–12 teachers who have become involved with the KAO through educational outreach programs. The symposium dinner was held at a golf course restaurant with delightful talks by Hans Mark (University of Texas at Austin), who revealed how the KAO was started, and by Dale Cruikshank (NASA/Ames), who described professional and personal vignettes of Gerard P. Kuiper.

This was the second decade Airborne Astronomy Symposium. The previous one, held in July of 1984, celebrated the first ten years of KAO operations, and was organized following a suggestion by Harley Thronson, Jr. (University of Wyoming). That meeting was attended by about 75 astronomers, over half of whom also attended this symposium. The proceedings of that meeting† are extremely interesting in retrospect, both as a benchmark of the accomplishments up to that time, and as a view to the future decade which is now behind us. Nancy Boggess (then the NASA Program Scientist) said in the *Foreword* to that volume, "This first decade has been exciting and challenging, but it is clear ... that we have not yet reached the ultimate capability of the KAO". This insight was correct – at that time thermal infrared instruments had one or few detectors, and were typically not close to achieving background-limited performance; techniques of far-infrared polarimetry were just being developed; the sensitivity of heterodyne receivers was a factor of 100 from the quantum noise limit; and the telescope was guided by analog electronic cameras mounted on mechanical stages for offsetting. As a comparison of the papers in this volume and the previous one† will attest, remarkable improvements in these and other areas over the past decade have greatly extended the limits of our perception on the KAO, enabling much of the exciting science reported here.

The present symposium also featured a discussion of future missions (Session 9), which naturally included some emphasis on the next generation airborne platform, the Stratospheric Observatory for Infrared Astronomy (SOFIA). Again, remarks at the 1984 meeting are apposite: In a concluding talk about the possibility of a three meter class airborne telescope, Eric Becklin (UCLA) described the scientific need for it, and – among other recommendations – suggested that its approval could be aided by phasing out the KAO at the beginning of development to reduce cost, to utilize the KAO staff, and to fortify science community resolve. This is the approach currently planned for the development of SOFIA, if it is approved. However, as pointed out by Charlie Telesco (MSFC) at the conclusion of this year's meeting, there are numerous important observations which would be made from the KAO if it were to remain operational during such a development period. Hopefully, such concerns will soon be forgotten and, in less than a decade, we will be discussing results obtained from SOFIA and reminiscing about the pioneering work done "in the good old days" on the KAO, much of which is reported here.

We are extremely grateful to the other members of the Local Organizing Committee and to the many volunteers who helped to make the symposium a success. In particular, we thank Sara Acevedo and Juliet Wiersema for their remarkable organization and attention to detail, and Jeff Ota for his excellent design work on the symposium poster and the cover art for this volume.

Michael R. Haas
Jacqueline A. Davidson
Edwin F. Erickson

---

†Proceedings of the Airborne Astronomy Symposium, 1984, NASA Conference Publication 2353, eds. H. A. Thronson, Jr., & E. F. Erickson

Airborne Astronomy Symposium
on the Galactic Ecosystem: From Gas to Stars to Dust
NASA-Ames Research Center
Moffett Field, California
1994 July 5 – 8

Supporting Instititutions

National Aeronautics and Space Administration
SETI Institute

Corporate Sponsors

Contraves Incorporated, Pittsburg, PA
E-Systems, Greenville, TX
Hughes Aircraft Company, El Segundo, CA
Sterling Software, Palo Alto, CA

Scientific Organizing Committee

Harriet L. Dinerstein
University of Texas

Reinhard Genzel
Max Planck Institute, Garching

Roger H. Hildebrand
University of Chicago

Daniel T. Jaffe
University of Texas

Charles M. Telesco
NASA-Marshall Space Flight Center

Charles H. Townes
University of California, Berkeley

James L. Elliot
MIT and Lowell Observatory

Terry L. Herter
Cornell University

David J. Hollenbach
NASA-Ames Research Center

Gary J. Melnick
Center for Astrophysics

Alexander G. G. M. Tielens
NASA-Ames Research Center

Michael W. Werner
Jet Propulsion Laboratory

Local Organizing Committee
NASA-Ames Research Center and SETI Institute

Jacqueline A. Davidson *(Co-Chair)*

Edna K. DeVore

Carlton M. Gillespie, Jr.

Dora S. Willoughby

Diane H. Wooden

Edwin F. Erickson *(Co-Chair)*

Edward W. Dunham

Michael R. Haas

Fred C. Witteborn

Registered Symposium Participants

Sara Acevedo	sara_acevedo@qmgate.arc.nasa.gov	SETI Institute
Kaiser Adeni	adeni@cave.arc.nasa.gov	NSI Technology
Andrew Afflerbach	affl@singha.astro.wisc.edu	Univ. Wisconsin
Michael Ahern	mahern@quest.arc.nasa.gov	Corte Madera School
Leni Alday	leni_alday@qmgate.arc.nasa.gov	Sterling Software
Lex Alday	lex@cave.arc.nasa.gov	Sterling Software
Lou Allamandola	allamand@ssa1.arc.nasa.gov	NASA/Ames
Arthur L. Altshiller	altshill@quest.arc.nasa.gov	Van Nuys High School
Jacob W. M. Baars	baars@tucsmt.as.arizona.edu	Univ. Arizona
Emma L. O. Bakes	bakes@minos.princeton.edu	Princeton
Betty Baldwin	baldwin@ssa1.arc.nasa.gov	NASA/Ames
James Baltz	baltz@cygnus.arc.nasa.gov	SETI Institute
Aaron Barnes	barnes@windee.arc.nasa.gov	NASA/Ames
Eric Becklin	becklin@bonnie.astro.ucla.edu	UCLA
Jim Bell	jimbo@anarchy.arc.nasa.gov	Univ. Washington
Chris Bero	chris@cave.arc.nasa.gov	Sterling Software
Albert Betz	betz@spot.colorado.edu	Univ. Colorado
Michael D. Bicay	mbicay@hq.nasa.gov	NASA Headquarters
Gordon Bjoraker	y9glb@lepvax.gsfc.nasa.gov	NASA/GSFC
Rita Boreiko	boreiko@spot.colorado.edu	Univ. Colorado
Jack Boyd	jack_boyd@qmgate.arc.nasa.gov	Allied Signal
Jesse Bregman	bregman@ssa1.arc.nasa.gov	NASA/Ames
Geoffrey Briggs	geoff_briggs@qmgate.arc.nasa.gov	NASA/Ames
Shari L. Brooks	brooks@anarchy.arc.nasa.gov	Synernet
Walter F. Brooks	walt_brooks@qmgate.arc.nasa.gov	NASA/Ames
Michael Burton	mgb@newt.phys.unsw.edu.au	Univ. New South Wales
Harold M. Butner	butner@dtm.ciw.edu	Carnegie Institution
Bob Cameron		ERA Aviation
Murray F. Campbell	mfcampbe@colby.edu	Colby College
Amy Carlow	carlow@cave.arc.nasa.gov	NSI Technology
Lawrence J. Caroff	lcaroff@gm.ossa.hq.nasa.gov	NASA Headquarters
Kin-Wing Chan	chan@stars.gsfc.nasa.gov	NASA/GSFC
Steven Charnley	charnley@galileo.arc.nasa.gov	UC Berkeley
Jean E. Chiar	chiar@charon.phys.rpi.edu	Rensselaer Polytechnic
Jim Cockrell	jcockrell@ames.arc.nasa.gov	NSI Technology
Martin Cohen	cohen@bkyast.berkeley.edu	UC Berkeley
Dave Cole	dmc@oddjob.uchicago.edu	Univ. Chicago
Sean W. J. Colgan	colgan@cygnus.arc.nasa.gov	SETI Institute
Cecilia Colomé	cc@astro.as.utexas.edu	Univ. Texas
Angela S. Cotera	cotera@cygnus.arc.nasa.gov	Stanford
Sylvia Cox	sylvia_cox@qmgate.arc.nasa.gov	NASA/Ames
Dale Cruikshank	cruikshank@ssa1.arc.nasa.gov	NASA/Ames
Steve Culp	steve@cave.arc.nasa.gov	Sterling Software
Jacqueline Davidson	davidson@cma.arc.nasa.gov	SETI Institute
Paul A. DeLeon	deleon@cave.arc.nasa.gov	NSI Technology
Edna K. DeVore	edna_devore@setigate.seti-inst.edu	SETI Institute
James Di Francesco	jamesd@astro.as.utexas.edu	Univ. Texas

Harriet Dinerstein	harriet@astro.as.utexas.edu	Univ. Texas
Carsten Dominik	dominik@cosmic.arc.nasa.gov	NASA/Ames
Jessie Dotson	dotson@yerkes.uchicago.edu	Univ. Chicago
Charles Darren Dowell	cdd@oddjob.uchicago.edu	Univ. Chicago
Frank Drake	fdrake@helios.ucsc.edu	SETI Institute
Edward W. Dunham	ted@chandon.arc.nasa.gov	NASA/Ames
Palmer Dyal	palmer_dyal@qmgate.arc.nasa.gov	NASA/Ames
Martha Eckert	marty@cea.berkeley.edu	UC Berkeley
Allen L. Edwards		Argo Systems
Jim Elliot	jim@astron.mit.edu	MIT/Lowell Obs.
Richard A. Ely		Chrysler Technologies
Sandra Engel	sengel@eis.calstate.edu	Bret Harte School
Edwin F. Erickson	erickson@cygnus.arc.nasa.gov	NASA/Ames
Dan Evans	evans@nsipo.arc.nasa.gov	Sterling Software
Neal J. Evans	nje@astro.as.utexas.edu	Univ. Texas
Diane Farrar	diane_farrar@qmgate.arc.nasa.gov	NASA/Ames
Andrea Ferrara	ferrara@arcetri.astro.it	OAArcetri
Debra Fischer	fischer@helios.ucsc.edu	UC Santa Cruz
Marina Fomenkova	marifo@max.arc.nasa.gov	NASA/Ames
Mino Freund	mino@max.arc.nasa.gov	SETI Institute
Norbert Geis	geis@isi5.ssl.berkeley.edu	UC Berkeley
Reinhard Genzel	genzel@mpe.mpe-garching.mpg.de	MPE/FRG
Richard Gerber	gerber@pokey.arc.nasa.gov	NASA/Ames
Carl Gillespie, Jr.	carlg@cave.arc.nasa.gov	NASA/Ames
Bill Glaccum	glaccum@stars.gsfc.nasa.gov	Applied Research Corp.
John H. Goebel	goebel@fil.arc.nasa.gov	NASA/Ames
Alyssa Goodman	goodman@cfa.harvard.edu	Harvard
David Goorvitch	goorvitch@cma.arc.nasa.gov	NASA/Ames
Albert D. Grauer	algrauer@ualr.edu	Univ. Arkansas
John Graybeal	john@cave.arc.nasa.gov	Sterling Software
Martin Greenfield		Hughes Aircraft
Anthony Gross	argross@ames.arc.nasa.gov	NASA/Ames
George Gull	gull@astrosun.tn.cornell.edu	Cornell
Michael R. Haas	haas@cygnus.arc.nasa.gov	NASA/Ames
David Harker	harker@lick.ucsc.edu	UC Santa Cruz
Doyal A. Harper	al@oddjob.uchicago.edu	Univ. Chicago
Andrew Harrison	aph@roe.ac.uk	Univ. Edinburgh
Paul Harvey	pmh@astro.as.utexas.edu	Univ. Texas
Martin Harwit	mharwit@wright.nasm.edu	NASM
Martin Hasha	martin_hasha@qmgate.arc.nasa.gov	Sterling Software
Barbara Hastings	barbara_hastings @qmgate.arc.nasa.gov	NASA/Ames
Louis C. Haughney		NASA/Ames (retired)
George Hawkins	ghawkins@sunlight.llnl.gov	Lawrence Livermore
Isabel Hawkins	eureka@netcom.com	Eureka Scientific
Neil Heather	heather@barsoom.arc.nasa.gov	Synernet
Karen Heere	heere@ssa1.arc.nasa.gov	Sterling Software
George Helou	gxh@ipac.caltech.edu	IPAC/Caltech
Terry Herter	herter@astrosun.tn.cornell.edu	Cornell
Roger Hildebrand	roger@oddjob.uchicago.edu	Univ. Chicago
Jerry Hirata	jerry_hirata@qmgate.arc.nasa.gov	NASA/Ames
Peter Höflich	pah@cfa141.harvard.edu	CfA/Harvard

David Hollenbach	hollenbach@gal.arc.nasa.gov	NASA/Ames
Ben Horita		NASA/Ames (retired)
Wendy Horton	wendy_horton@seti-inst.edu	SETI Institute
John Howe	jhowe@astro.umd.edu	Univ. Maryland
Scott Hubbard	scott_hubbard@qmgate.arc.nasa.gov	NASA/Ames
Donald M. Hunten	dhunten@titan.lpl.arizona.edu	Univ. Arizona
John Hurthere	jhurthere@scuacc.scu.edu	Santa Clara
Bruce Ives		Rep. Eshoo's Office
James Jackson	jackson@fish.bu.edu	Boston University
Dan Jaffe	dtj@bubba.as.utexas.edu	Univ. Texas
Paul Jaminet	jaminet@cfa.harvard.edu	SAO
Petrus Jenniskens	peter@max.arc.nasa.gov	NASA/Ames
Michael Jura	jura@bonnie.astro.ucla.edu	UCLA
Kay Justtanont	kj@prometheus.arc.nasa.gov	NASA/Ames
William Kahn		E-Systems
Mike Kaplan	mskaplan@gm.ossa.hq.nasa.gov	NASA Headquarters
Jocelyn Keene	jbk@tacos.caltech.edu	Caltech
John Keller	jokelle@eis.calstate.edu	Los Altos High School
Bruce Kelly		NASA/Ames (retired)
Gillian Knapp	gk@astro.princeton.edu	Princeton
David Koch	koch@icthus.arc.nasa.gov	NASA/Ames
Chris Koresko	koresko@zoe.as.utexas.edu	Univ. Texas
Tom Kosic		Hughes Aircraft
Richard Kozlowski	kozlow@ssa1.arc.nasa.gov	Susquehanna Univ.
Kathleen E. Kraemer	kraemer@fish.bu.edu	Boston University
Monika Kress	kress@prometheus.arc.nasa.gov	Rensselaer Polytechnic
Mark Kritz	mkritz@asrc.albany.edu	ASRC/SUNY
Wilfried Krone-Schmidt		Hughes Aircraft
Nans Kunz	nans_kunz@qmgate.arc.nasa.gov	NASA/Ames
Stephen Langhoff	langhoff@pegasus.arc.nasa.gov	NASA/Ames
Harri Latvakoski	harri@tristan.tn.cornell.edu	Cornell
Curt Laughlin	cdl@cave.arc.nasa.gov	NASA/Ames
David Lee	lee@cygnus.arc.nasa.gov	SETI Institute
Dan Lester	dfl@astro.as.utexas.edu	Univ. Texas
Darek Lis	dcl@tacos.caltech.edu	Caltech
Robert Loewenstein	rfl@oddjob.uchicago.edu	Univ. Chicago
Steven Lord	lord@heaven.ipac.caltech.edu	IPAC/Caltech
Nanyao Lu	lu@ipac.caltech.edu	IPAC/Caltech
Dana Lynch	dana_lynch@qmgate.arc.nasa.gov	NASA/Ames
David Lynch	dave_lynch@qmail2.aero.org	Aerospace Corporation
Beverly Lynds	blynds@unidata.ucar.edu	Unidata/UCAR
Suzanne Madden	madden@cygnus.arc.nasa.gov	NASA/Ames
Thomas E. Maiello	thomas_maiello@qmgate.arc.nasa.gov	NASA/Ames
Larry A. Manning	larry_manning@qmgate.arc.nasa.gov	NASA/Ames
Hans Mark		Univ. Texas
Michael Marlaire	michael_marlaire @qmgate.arc.nasa.gov	NASA/Ames
Elaine Mathias	mathias@cave.arc.nasa.gov	NSI Technology
Craig R. McCreight	craig_mccreight@qmgate.arc.nasa.gov	NASA/Ames
John S. McDonald	jmcd@mintaka.sdsu.edu	SDSU
Nancy McKown	nancy@cave.arc.nasa.gov	Sterling Software
Thomas McMahon	mcmahon@hale.yerkes.uchicago.edu	Univ. Chicago

Gary J. Melnick	melnick@cfa.harvard.edu	CfA
Ramsey K. Melugin	ramsey_melugin@qmgate.arc.nasa.gov	NASA/Ames
Lawrence N. Mertz		Lockheed Res. (retired)
Allan W. Meyer	meyeraw@ames.arc.nasa.gov	NSI Technology
John Mihalov	mihalov@windee.arc.nasa.gov	NASA/Ames
Richard H. Miller	rhm@oddjob.uchicago.edu	Univ. Chicago
Walt Miller	wmiller@cave.arc.nasa.gov	NSI Technology
Bob Monk		NSI Technology
Felicia Moraida	moraida@cygnus.arc.nasa.gov	NASA/Ames
Mark Morris	morris@osprey.astro.ucla.edu	UCLA
David Morrison	david_morrison@qmgate.arc.nasa.gov	NASA/Ames
Lee G. Mundy	lgm@astro.umd.edu	Univ. Maryland
Ken K. Munechika	ken_munechika@qmgate.arc.nasa.gov	NASA/Ames
Giles Novak	g-novak@nwu.edu	Northwestern
Goetz Oertel	goertel@stsci.edu	AURA
Donald M. Oishi		NASA/Ames (retired)
Cathy Olkin	colkin@astron.mit.edu	MIT
Kristin Orabona	kristin_orabona@qmgate.arc.nasa.gov	Sterling Software
Donald Osterbrock	don@lick.ucsc.edu	UC Santa Cruz
Hallie Patterson	hallie@nsipo.arc.nasa.gov	Sterling Software
Steve Patterson	spatter@cave.arc.nasa.gov	NASA/Ames
Yvonne Pendleton	pendleton@galileo.arc.nasa.gov	NASA/Ames
Robert Pernic	pernic@yerkes.uchicago.edu	Univ. Chicago
Tom G. Phillips	phillips@tacos.caltech.edu	Caltech
Bruce E. Pirger	pirger@astrosun.tn.cornell.edu	Cornell
Albrecht Poglitsch	alpog@mpe-garching.mpg.de	MPE/FRG
Robert A. Provencal	bob@copper.cchem.berkeley.edu	UC Berkeley
David Rank	rank@helios.ucsc.edu	UC Santa Cruz
Milo D. Reisner		NASA/Ames (retired)
Michael Religioso	religios@cygnus.arc.nasa.gov	NASA/Ames
Mike Robinson	mike@cave.arc.nasa.gov	Sterling Software
Bernadette Rodgers	rodgers@astro.washington.edu	Univ. Washington
Tom Roellig	roellig@ssa1.arc.nasa.gov	NASA/Ames
Hans Peter Röser	hans-peter.roeser@dlr.de	MPIfR/FRG
Stefan Rosner	stefan@asrc.albany.edu	ASRC/SUNY
Ted Roush	roush@barsoom.arc.nasa.gov	San Francisco State
Robert Rubin	rubin@cygnus.arc.nasa.gov	Orion Enterprises
Ray Russell	russell@dirac2.span.nasa.gov	Aerospace Corporation
Farid Salama	salama@ssa1.arc.nasa.gov	UC Berkeley
Rainer Sandau	sandau@hardy.ws.ba.dlr.de	DLR-ISST/FRG
Scott A. Sandford	sandford@ssa1.arc.nasa.gov	NASA/Ames
Anneila L. Sargent	afs@mmstar.caltech.edu	Caltech
Peter Schilke	schilke@medoc.caltech.edu	Caltech
David Schleuning	david@oddjob.uchicago.edu	Univ. Chicago
Angie Schultz	schultz@ssa1.arc.nasa.gov	NASA/Ames
Dave Scimeca	scimeca@ssa1.arc.nasa.gov	NASA/Ames
J. Michael Shull	mshull@casa.colorado.edu	Univ. Colorado
Jan Simpson	simpson@cygnus.arc.nasa.gov	UC Berkeley
Brad Sitton	sitton@anarchy.arc.nasa.gov	Synernet
Christopher J. Skinner	skinner@tristan.llnl.gov	Lawrence Livermore
Gregory C. Sloan	sloan@ssa1.arc.nasa.gov	NASA/Ames
Beverly Smith	beverly@zoe.as.utexas.edu	Univ. Texas

Bruce Smith	smith@humbabe.arc.nasa.gov	NASA/Ames
Randy Smith	randy_smith@qmgate.arc.nasa.gov	Sterling Software
Carl Sorenson	carl@cave.arc.nasa.gov	Sterling Software
Gordon Stacey	stacey@astrosun.tn.cornell.edu	Cornell
Bruce Stanton		Hughes Aircraft
Tom Steiman-Cameron	tomsc@boombox.arc.nasa.gov	UC Santa Cruz
Monica Kane Stewart	monica@nsipo.arc.nasa.gov	Sterling Software
Susan Stolovy	stolovy@astrosun.tn.cornell.edu	Cornell
Robert Strane		Contraves
Vladimir Strelnitski	vstrelni@coral.nmt.edu	New Mexico Tech
Stephen E. Strom	sstrom@donald.phast.umass.edu	Univ. Massachusetts
Pam Stryker	pstryker@tenet.edu	Barton Creek School
Charles M. Telesco	telesco@ssl.msfc.nasa.gov	NASA/MSFC
Pasquale Temi	temi@lick.ucsc.edu	UC Santa Cruz
Domenic J. Tenerelli		Lockheed Missiles
Lou Testaguzza		Contraves
Gary W. Thorley	gary_thorley@qmgate.arc.nasa.gov	NASA/Ames
Harley Thronson, Jr.	thronson@uwyo.edu	Univ. Wyoming
Alexander Tielens	tielens@prometheus.arc.nasa.gov	NASA/Ames
Marvin Toles		Hughes Danbury
Charles Townes	cht@sunspot.ssl.berkeley.edu	UC Berkeley
John Tsai	jcht@cloud9.arc.nasa.gov	NASA/Ames
Deanne Tucker	deanne_tucker@qmgate.arc.nasa.gov	NASA/Ames
Barry D. Turney	bear@cave.arc.nasa.gov	NSI Technology
Alan Van Orden	alan@cluster.cchem.berkeley.edu	UC Berkeley
Janice Varney	janice_varney@qmgate.arc.nasa.gov	NASA/Ames
Peter Wannier	wannier@jplsp.jpl.nasa.gov	JPL
Michael Werner	mww@ipac.caltech.edu	JPL
Wendy Whiting	wendy@cave.arc.nasa.gov	NASA/Ames
Juliet Wiersema	juliet_wiersema@qmgate.arc.nasa.gov	SETI Institute
Suzanne C. Williams	suwilli@eis.calstate.edu	Graham Middle School
Dora S. Willoughby	willough@cygnus.arc.nasa.gov	SETI Institute
Chris Wiltsee	christopher_wiltsee @qmgate.arc.nasa.gov	NASA/Ames
Caesar (Jesse) Wirth	wirth@hale.yerkes.uchicago.edu	Univ. Chicago
Fred C. Witteborn	wittebor@ssa1.arc.nasa.gov	NASA/Ames
Grace A. Wolf-Chase	wolf@ssa1.arc.nasa.gov	NASA/Ames
Mark Wolfire	wolfire@cygnus.arc.nasa.gov	UC Berkeley
Diane Wooden	wooden@ssa1.arc.nasa.gov	NASA/Ames
Brian Wright	brian@cave.arc.nasa.gov	Sterling Software
Wei-Hong Yang		Northwestern Polytech
Bob Yee	robert_yee@qmgate.arc.nasa.gov	NASA/Ames
Anne Youngblood		Lockheed Aircraft
Rolaine C. Young Owl	rolaine@astro.uiuc.edu	Univ. Illinois
Lunming Yuen	yuen@ssa1.arc.nasa.gov	Orion TechnoScience
Jonas Zmuidzinas	jonas@tacos.caltech.edu	Caltech
Robert Zoller		Lockheed Aircraft

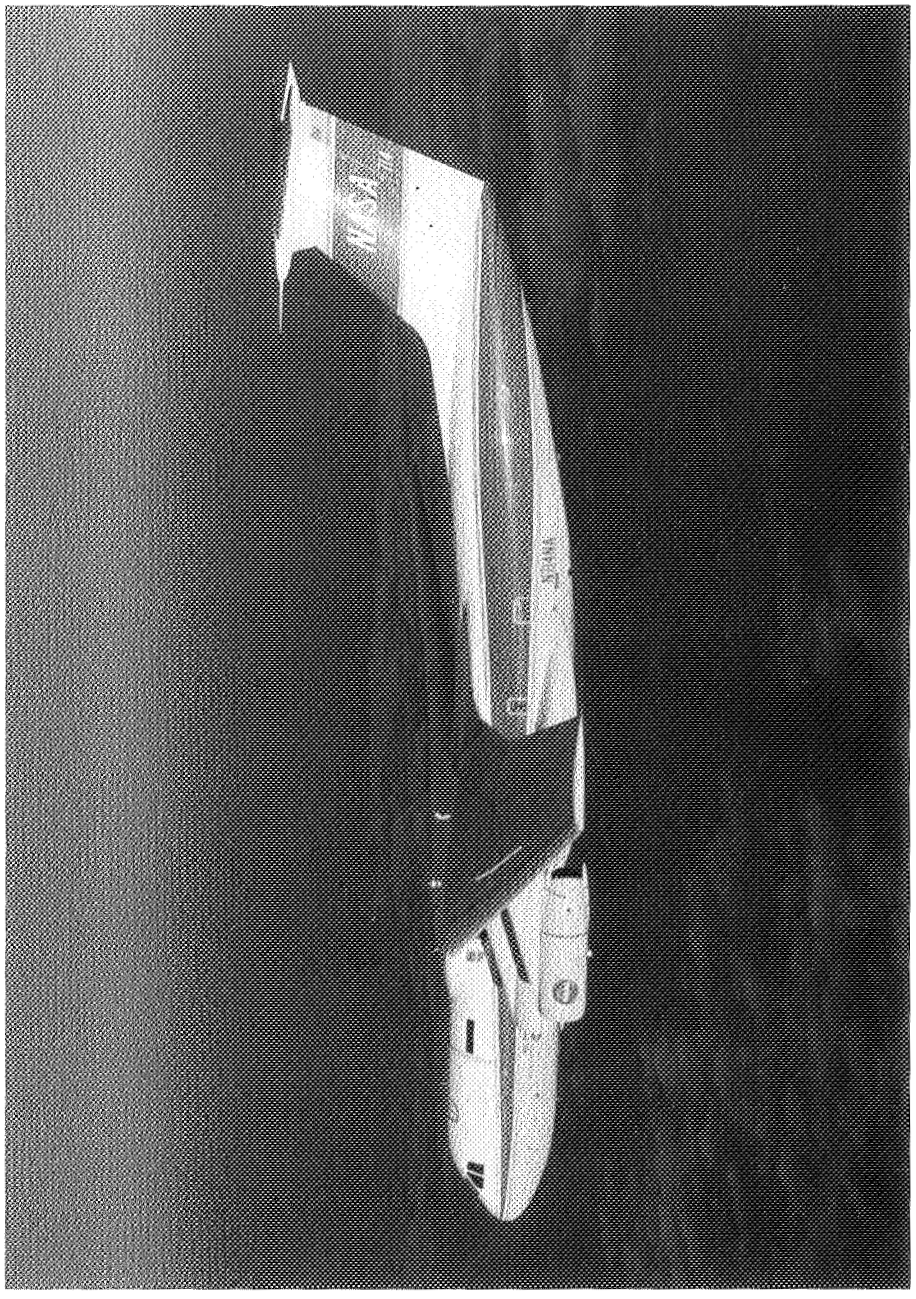

The Kuiper Airborne Observatory (1974)

WELCOMING REMARKS

KEN MUNECHIKA, Director
NASA/Ames Research Center, MS 200-1, Moffett Field, CA 94035-1000

Good morning and welcome to NASA/Ames. Although the KAO has been here a lot longer than I have, it has become apparent to me that it is one of our outstanding Space Science programs, both at this Center and in the Agency at large. What makes the program so successful? A fundamental scientific need? Yes. The physical capability to get the data? Yes. But beyond these required ingredients, it takes many motivated, talented people.

This is an unusual moment in the history of Airborne Astronomy, in that a large fraction of these people are here today. I would like to congratulate you, the scientists who have utilized so well the capabilities of the KAO, to obtain such a wide range of important scientific results, a number of which will be described at this meeting. I'm aware in addition that many of you have developed important advances in focal plane instruments, detectors, and observing techniques to enable the exciting measurements made from our aircraft.

Also, I have a strong interest in education, and so am particularly impressed by the educational accomplishments of the airborne program. I'm referring of course to the numerous Ph.D. dissertations which have been earned, and many young scientists who have been trained in collaboration with the science teams. In addition I'm thinking of the K-12 teacher education program, which brings the excitement of scientific discovery in a direct and highly leveraged way into the classroom.

The scientific, technological, and educational achievements of airborne astronomy have had and continue to have a significant impact on the planning and implementation of infrared space missions, such as IRAS, COBE, SWAS, ISO, and SIRTF. I understand that numerous participants in these missions have extensive experience in the airborne program.

In addition to my congratulations to you, however, I want to thank the staff here at Ames for their dedicated service. I am proud that the synergy of our resources has created the world's only airborne astronomy program. It is a fine example of our aeronautical, engineering, technological, scientific, and operational people working together to achieve a unique capability.

It is fitting that I should end my remarks by talking about the future of airborne astronomy. As you know, the National Academy of Sciences has selected SOFIA as one of its highest priorities for astronomy in this decade. We at Ames have committed significant resources to the predevelopment studies of SOFIA, and are prepared take on a significant part of the development effort. It is my hope that this will begin soon, and I look forward to supporting its operation here at Ames throughout the first quarter of the next century.

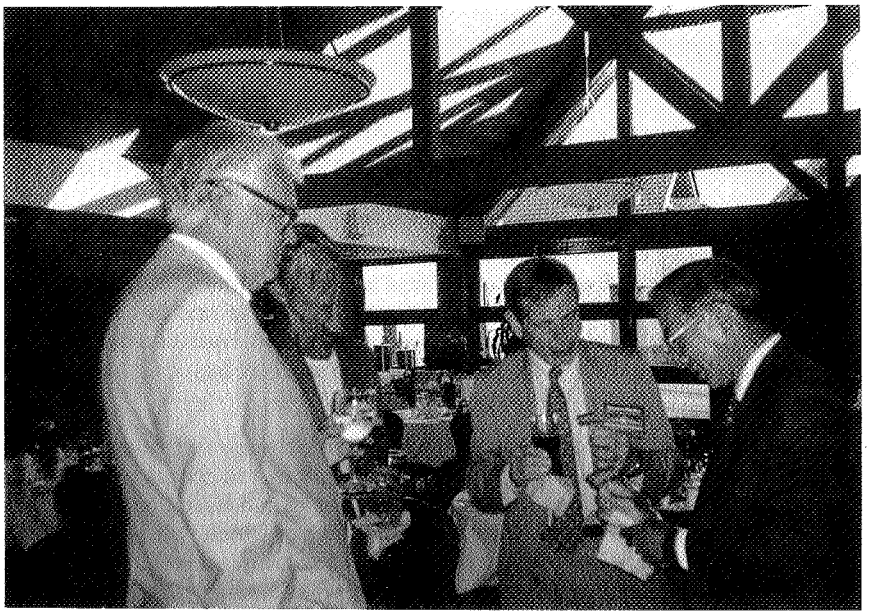

Hans Mark, Marianne and Martin Harwit, Ken Munechika

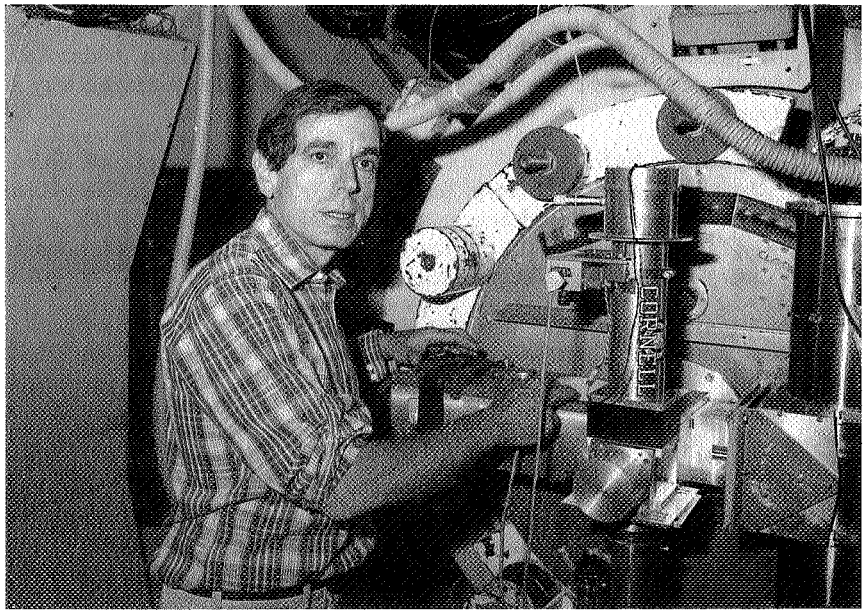

Martin Harwit (1981)

Session One

The Interstellar Medium

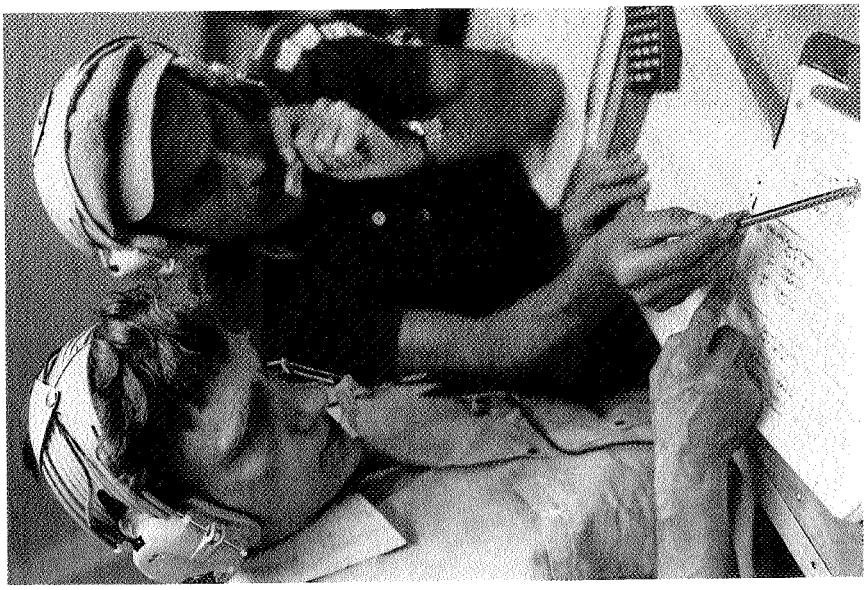

Pat Thaddeus, Joe Waters (1977)

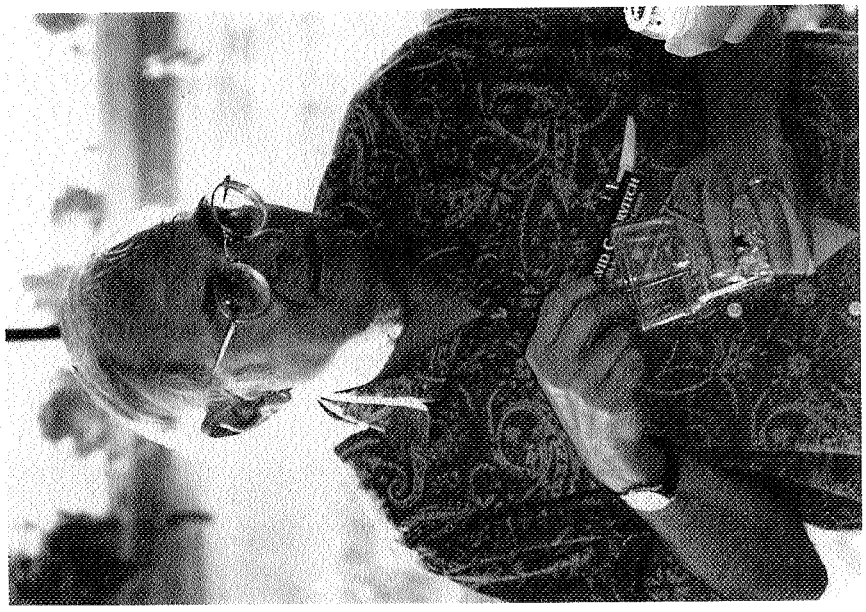

Dave Goorvitch

Airborne Astronomy Symposium on the Galactic Ecosystem
ASP Conference Series, Vol. 73, 1995
M.R. Haas, J.A. Davidson, and E.F. Erickson (eds.)

The Interstellar Medium

A.G.G.M. Tielens
MS 245-3, Space Science Division, NASA Ames Research Center, CA 94035-1000

1. Introduction

The Interstellar Medium (ISM) forms an integral part of the lifecycle of stars and the galaxy. Stars are formed by gravitational contraction of interstellar clouds. Over their life, stars return much of their mass to the ISM through winds and supernova explosions, resulting in a slow enrichment in heavy elements. The composition and structure of the ISM is determined by a complex interplay of microscopic and macroscopic processes. The energy balance of the interstellar medium is dominated by stellar photons and the injection of kinetic energy through winds and supernova explosions. The former probably dominates the heat balance of the gas while the turbulence generated by the latter supports the ISM against galactic gravity. The bubbles blown by stars can also influence the large scale structure of the ISM through, for example, the formation of chimneys and fountains. Cosmic rays, X–rays, and ionizing photons influence the ionization state of the interstellar gas. Shielding by dust and gas leads to the formation of largely neutral and molecular phases of the ISM. As a result of these processes, the interstellar medium contains a variety of components or phases. These include diffuse and molecular clouds as well as intercloud media. Section 2 reviews our knowledge of the components of the ISM with an emphasis on interstellar ecology.

Understanding the origin and evolution of the ISM is a key problem within astrophysics. The KAO has made many important contributions to studies of the interstellar medium both on the macro and on the micro scale. Obviously far-IR studies of protostellar regions have been of great importance in understanding the star formation process. Those are discussed in chapter 3 of this volume. The chemical evolution of the galaxy is discussed in chapter 5 of this volume. The study of shocks is also a KAO subject of great interest. This is also related in chapter 5. In this overview, I will concentrate on two breakthroughs in the last decade in which KAO observations have played a major role: (a) The importance of large Polycyclic Aromatic Hydrocarbon (PAH) molecules for the ISM (section 3) and (b) The study of Photodissociation Regions (PDRs) as an analog for the diffuse ISM at large (section 4). Appropriately, the micro and macro problem are intricately interwoven in these problems. Finally, section 5 reviews the origin of the [CII] emission observed by COBE.

2. The Ecology of the Interstellar Medium

2.1. Dust and gas budget

Ecologically speaking, the ISM is a disaster area. Stars in various stages of their lives indiscriminantly pollute their environment with gas, dust, and metals. Table 1 summarizes various mass injection rates into the ISM (Tielens 1989). Low mass stars ($<8M_\odot$) predominantly contribute during the Asymptotic Giant Branch (AGB) phase. In this short–lived phase ($\simeq 10^5$ yr), $\simeq$ 0.5-7 $M_\odot$ is ejected in the form of a cool dusty wind. In contrast, high mass stars have winds during most of their lives. In terms of total mass (ie., H) returned to the ISM, low mass stars dominate the budget and, within that class, 1–3 $M_\odot$ stars rule because of lifetime and number considerations. The contribution by massive stars – mainly Wolf Rayets – is about an order of magnitude less (van der Hucht et al. 1987). The budget for heavy elements is more complicated. Intermediate mass elements such as ^{16}O and ^{28}Si are injected predominantly through type II supernovae, as are the p- and r-process elements (proton/rapid neutron capture on seed elements). Type Ia supernovae may dominate the Fe–group element production. ^{14}N and the s-process elements (slow neutron capture) originate in AGB stars. Some elements, ie., ^{12}C, have important contributions from low mass stars (ie., C–rich giants) and from high mass stars (ie., WC phase).

At present, the ISM is in a steady state where stellar mass injection is approximately balanced by star formation at a rate of $1M_\odot$ averaged over the galaxy. Hence, the present ISM is circulated into stars in $\simeq 6 \times 10^9$ yr. Due to the constant injection of enriched material, the ISM and stars newly formed from it are slowly enriched in their metalicity (cf., Rana 1991; Pagel 1987; Audouze and Tinsley 1976). The rate of this enrichment depends among other things on the star formation rate. Hence, the increasing rate of star formation towards the galactic center leads to a gradient in metalicity. For our galaxy, this gradient is -0.07 dex per kpc but the dispersion is large (Rana 1991; Pagel 1987). Because different stars dominate the budgets of different elements, the rate of this enrichment as well as the slope of the gradient, depend on the element considered. Metalicity may actually indirectly influence these variations through the initial mass function (IMF) of newly formed stars (cf., Pagel 1987; Audouze and Tinsley 1976). Likely, opacity (dust) and ambipolar diffusion (ionization) in molecular clouds, which are coupled to the metalicity, may have a strong influence on the star formation rate as well as the IMF. This galactic elemental differentiation is counteracted by mixing and by infall of primordial (ie., low Z) material. Mixing takes predominantly place through the halo. Supernova explosions blow material into the halo on highly non–circular orbits and, after dissipation, this material rains down again on the disk. The value given for the mass "recycled" in the ISM (Table 1) follows from analysis of HI in non–circular orbits ($|v_{lsr}| > 90$ km/s; Wakker 1990) and of observed CIV fluxes (Martin and Bowyer 1990). Since the HI scale height of the (lower) halo is $\sim$0.5 kpc, mixing in the radial direction will occur on that scale length as well. In galactic fountain models, mixing occurs on $\sim$3 kpc length scales (Houck and Bregman 1990). Typically, the mixing rate is ten times higher than the star formation or the mass injection rate. Hence, on average, a parcel of gas is "mixed" ten times over its interstellar lifetime, increasing the total mixing length by about a factor

of three. A small fraction of the gas raining in on the disk may be intergalactic (< 0.01) or LMC (< 0.1) material and has low metalicity.

Table 1. Interstellar Gas and Dust Budgets[a]

Source	$\dot{M}_H$[b]	$\dot{M}_c$[c]	$\dot{M}_{sil}$[d]
C–rich giants	5 (-4)	2 (-6)	–
O–rich giants	5 (-4)	–	3 (-6)
Novae	6 (-6)	3 (-7)	3 (-8)
SN type Ia	–	3 (-7)[e]	2 (-6)[e]
OB stars	3 (-5)	–	–
Red supergiants	2 (-5)	–	2 (-7)
WC 8-10	1 (-4)[f]	6 (-8)	–
SN type II	1 (-4)	2 (-6)[e]	1 (-5)[e]
Recycle[g]	5 (-3)	?	?
Star formation	–1 (-3)	?	?

[a]Mass injection rates in units of $M_\odot$ $kpc^{-2}yr^{-1}$ (Tielens 1989).
[b]Total gas mass injection rate.
[c]Carbon dust injection rate.
[d]Silicate and metal dust injection rate.
[e]If dust condenses at all. See text.
[f]H–mass injection by all Wolf Rayet stars. WC stars are actually H–deficient and do not contribute at all.
[g]Mixing through the halo.

Besides gas, stars also inject dust into the ISM (Table 1). The chemistry involved depends very much on the physical conditions in the ejecta, including the elemental composition (eg., C/O abundance ratio). Carbon soot is predominantly formed in the ejecta of C–rich AGB stars. While WC stars contribute to the gaseous C budget, they are inefficient dust producers (van der Hucht et al. 1987). Observations of SN 1987A have shown that type II supernovae produce dust but the dust composition as well as the efficiency of of the condensation process is not known (Wooden et al. 1993). Type II supernovae might form carbon dust in their He burning shells, if internal mixing of the ejecta is unimportant. In that case, Mg–rich silicates and FeNi metal grains will form in the ejecta from the O–burning shell and the FeNi core, respectively. However, if mixing is important, only FeMg silicates are expected to condense. Whether type Ia SN condense dust in their ejecta is unknown. If so, FeNi grains would be formed and they might dominate the metal grain budget. In total dust volume, their contribution is in any case less than for type II SN or AGB stars. O-rich AGB stars are known to inject silicates but their injection rate might be overshadowed by that of type II SN. Finally, star formation is a sink for interstellar dust. However, protostellar outflows might enrich the ISM in dust if they entrain disk material. In that case, high temperature condensates (ie., inner disk) such as metals and/or silicates grains might be injected.

In this discussion, star dust has been divided into C–soot and minerals (silicates and metals). However, this division is only global and on the microscopic

level each stellar source produces dust with its own unique characteristics (eg., C/H or Fe/Mg ratio, isotopic composition, as well as sizes and structure). For example, due to the difference in C/H ratio, C–dust formed in C–rich giants is expected to be different in structure and characteristics from that produced by WC stars (PAH–like versus fullerene–like; Tielens 1989; Cherchneff and Tielens 1994). Even within a stellar class, dust characteristics will vary. This is illustrated rather directly by some O-rich giants which produce mainly aluminum oxide dust rather than silicates (Onaka et al. 1989).

As for elemental abundances, a gradient in star dust abundance and star dust characteristics is expected in the ISM. Such dust variations have been observed between the local ISM and the Galactic center region (Roche and Aitken 1985; Pendleton et al. 1994) but are likely a general galactic characteristic. Like the gas, stardust will also be mixed by SN explosions on a time scale of 10^9 yr. However, shocks also lead to grain destruction through sputtering and grain–grain collisions. Hence, a typical volume of interstellar gas contains a much smaller fraction of its condensibles in the form of stardust than originally injected by stars. For example, a 100 km/s shock leads to 10 and 20% destruction of the graphite and silicate dust volume, respectively (Jones et al. 1994). Calculated life times are 4 and 2×10^8 yr and hence, without local interstellar sources, the average interstellar stardust fraction is $\sim$ 0.1 of that originally injected. Since the observed dust fraction is much larger then this limiting fraction – for some elements in excess of 0.9 – the conclusion is inescapable; there has to be an efficient dust reformation process in the ISM. Likely, this involves ice mantle growth through accretion in molecular clouds followed by FUV photolysis into an organic or carbonaceous material (Tielens and Allamandola 1987). The composition of this newly accreted material will depend on the local interstellar physical conditions (ie., elemental abundances, FUV field, cosmic ray dose) and hence will also vary with galactic position. Moreover, this interstellar medium dust is probably less refractory and hence has an expected lifetime even shorter than stardust.

2.2. Phases of the ISM

Various phases are present in the ISM, each characterized by its own physical conditions (ie., density, temperature, and degree of ionization; Table 2). A very tenuous, hot phase may fill a large fraction of the interstellar volume. Most of the mass is however, in cool and dense clouds, either Spitzer–type HI clouds or in molecular clouds. There are also two types of intercloud media which differ in their degree of ionization. The origin and interrelationship of these clouds, and their energy and ionization sources are among some of the most fundamental questions in the field. Theoretical studies in the sixties and seventies (Field et al. 1969; McKee and Ostriker 1977) have given great insight in their answers. Quite generally, a new stable phase reflects the onset of a new cooling mechanism or the decline of a heating source (cf., Shull 1987). Hence, cold HI clouds and the warm intercloud medium result from the increased importance of [CII] cooling at higher densities and Lyα and [OI] 6300Å cooling at higher temperatures, respectively. The hot phase reflects the recent input of supernova energy. Molecular clouds fall outside this classification scheme since their existence reflects the importance of self–gravity.

Table 2. Characteristics of the Phases of the ISM[a]

Phase	n_o[b]	T[c]	ϕ_v[d]	M[e]
Hot intercloud	0.003	10^6	50	–
Warm Neutral Medium	0.5	8000	40	1.4
Warm Ionized Medium	0.3	8000	10	1
Diffuse clouds	50	80	2	2.2
Molecular clouds	>300	10	1	3.5
HII regions	1–10^5	10^4	–	0.1

[a]Taken from Kulkarni and Heiles (1987), Savage (1987), and Reynolds (1993).
[b]Gas density in units of cm^{-3}.
[c]Gas temperature in units of K.
[d]Volume filling factor in %.
[e]Total mass in 10^9 $M_\odot$.

Understanding the structure of the ISM requires thus an understanding of its heating and cooling sources. Unfortunately, very little is presently known empirically about these processes. Cooling of diffuse clouds is thought to be dominated by [CII] 158 μm line emission and there are observational determinations of the cooling rate for a few sight lines from UV measurements of the population of the upper level of this fine–structure transition (Pottasch et al. 1979; Gry et al. 1992). Direct measurements of the [CII] emission of the general ISM have been made by the Lear Jet, balloons, rockets, and satellites (COBE; Stacey et al. 1985; Shibai et al. 1991; Bock et al. 1993; Wright et al. 1991; Bennett et al. 1994). These are reviewed in section 5. The warm neutral intercloud medium is cooled by Ly α and [OI] 6300 Å with possibly a large contribution from the [OI] 63 μm fine–structure line if the temperature of this phase is 6000 K or less. None of these lines is easily observed and hence the cooling rate is unknown.

The cooling of diffuse clouds has to be balanced by a heating process. Interestingly, various astrophysically relevant energy densities have comparable values (Table 3). The heating rate depends however on how well they couple to the gas. Cosmic ray heating, originally proposed to be the dominant heating source (Field et al. 1969), is now known (a.o. through studies of molecular abundances) to fall short by a considerable factor. Hydro(magnetic) waves driven by turbulence may be an important energy source for the intercloud medium (Ferriere et al. 1988) but they are inefficient heaters of diffuse clouds (cf., Cowie 1987). However, likely, FUV photons play a dominant role in the heating of the interstellar gas (Watson 1972; de Jong 1977). While photons with $h\nu < 13.6$eV do not couple directly to the gas, they can cause ejection of photoelectrons from dust grains which then heat the gas. Increasingly sophisticated theoretical models have been developed for the photoelectric effect on dust grains and the latest are in good agreement with the observed cooling rates for diffuse clouds (see §3).

In view of the various observed gradients in ISM constituents, galactic variations in the structure of the ISM can be expected. Theoretical studies show

that the general phase characteristics of the ISM scale with the ambient radiation field/cosmic ray field; ie., enhanced radiation fields require enhanced interstellar pressures for phase stability between warm and cold phases (Wolfire et al. 1994). The increased star formation rate towards the inner galaxy leads to an enhanced FUV radiation field. At the molecular ring, the average interstellar radiation field is about a factor of 4 larger than at the solar circle (Mathis et al. 1983). The gas pressure in the molecular ring is likewise much higher. Small scale variations will also exist, particularly in the neighborhood of OB associations. For example, in the local ISM, the region associated with the Orion OB associations experiences a higher FUV field and seems to have slightly lower O abundance than the sun. Of course, in the environment of an OB association, self–gravity and supernovae energy input likely dominate the local structure.

Table 3. Energy Balance.

Source	Diffuse Clouds		Dense Cloud Cores	
	Energy density [eV cm^{-3}]	Heating rate [erg s^{-1} H–atom^{-1}]	Energy density [eV cm^{-3}]	Heating rate [erg s^{-1} H–atom^{-1}]
Thermal	0.5	−5 (−26)[a]	20	−8 (−28)[a]
UV	0.5	5 (−26)	4 (-6)	4 (−31)
Cosmic Ray	0.8	4 (−28)	0.8	4 (−28)
Magnetic Field	0.2	2 (−27)	5	2 (−27)
Turbulence	0.3	1 (−27)	5	1 (−27)
Gas–grain	–	–	3	3 (−29)
Gravity	–	–	25	3 (−28)

[a]Energy loss rate.

2.3. The ISM and star formation

The structure and phases in the ISM are intimately linked to the present and past star formation rate. Low mass stars and, hence, the past star formation rate dominate the total mass balance of interstellar gas. Likewise, they dominate the injection of C–soot, an important opacity source, and possibly PAH molecules, the dominant heating agent of interstellar gas (cf., section 3). High mass stars (ie., the present star formation rate) dominate the mechanical energy injection into the ISM and thus the turbulent pressure which supports clouds against galactic gravity as well as the thermal pressure through the formation of the hot phase (McKee and Ostriker 1977). Massive stars also dominate the FUV photon energy budget and the cosmic ray flux which are important heating, ionization, and dissociation sources of the interstellar gas. Massive stars are also an important source of intermediate mass elements which play an important role in interstellar dust. Eventually, it is of course the dust opacity which allows molecule formation and survival. The enhanced cooling by molecules is crucial in the onset of gravitational instability of molecular clouds.

Clearly, therefore, there is a complex feedback between star formation and the ISM. And it is this feedback that determines the structure, composition,

chemical evolution, and observational characteristics of the interstellar medium in the Milky Way and in other galaxies. If we want to understand this interaction, we have to understand the fundamental physical processes that link interstellar gas to the mechanical and FUV photon energy inputs from stars. Our understanding of the latter process has increased considerably in recent years. PAH molecules are now thought to form the key link between the interstellar gas and stellar FUV photons (section 3). Likewise, studies of bright PDRs have lead to a better understanding of the interaction of FUV photons with interstellar gas (section 4). The KAO has played a crucial role in both of these recent developments.

3. Interstellar PAHs

The near and mid–IR spectra of many sources are dominated by strong emission features at 3.3, 6.2, 7.7, and 11.3 μm. At this symposium it is good to recall that initially the features in ground–based accessible windows (ie., at 3.3 and 11.3 μm) were not assigned correctly. The most promising candidates at that time were considered to be carbonate grains for the 11.3 μm feature and the molecule HeH^+ for the 3.3 μm feature. It was only when the full IR spectrum became available, in particular with the discovery of the 6.2 and 7.7 μm features in follow up KAO studies, that it was realized that these emission features are unquestionably carried by aromatic hydrocarbon materials (Duley and Williams 1981; Leger and Puget 1984; Allamandola et al. 1985). To outsiders confusion might still be rampant with a multitude of proposed acronyms for the carriers, including PAHs (Leger and Puget 1984; Allamandola et al. 1985), HAC (Duley 1989), QCC (Sakata & Wada 1989), and coal (Papoular et al. 1991). However, all these materials have in common the presence of aromatic hydrocarbon structures and, indeed, any match with the interstellar features results from the presence of such aromatic hydrocarbon structures (Allamandola et al. 1989).

Now, the spectroscopic evidence provides only information on the material present, not on its size (ie., grains versus molecules). The identification with molecular–sized carriers results from the discovery that these IR features are strong even far from exciting stars where dust grains attain radiative equilibrium temperatures much too low to explain emission around 3 μm (Sellgren et al. 1983). The inescapable conclusion is that the IR emission features are due to an IR fluorescence process in molecules/micrograins. Because of its very limited heat capacity, a small species will be temporarily highly excited upon absorption of an FUV photon. This species will then cool down rapidly ($\simeq$ 1 s) through emission in the vibrational modes in the near IR; ie., the IR emission features. It will stay at a very low temperature until the absorption of a new FUV photon, typically after an hour. The initial temperature reached by a small species depends on its size (ie., number of vibrational modes over which the energy can be divided) and the energy of the photon absorbed. From the observed emission temperature, a size of $\simeq$ 50 C–atoms is derived for the carrier of the interstellar IR emission features; ie., a large Polycyclic Aromatic Hydrocarbon molecule.

The KAO observations also revealed the presence of broad emission plateaus underneath the 6.2 and 7.7 μm features (Cohen et al. 1986; 1989; Bregman et al. 1989). These features are likely also carried by aromatic materials. A

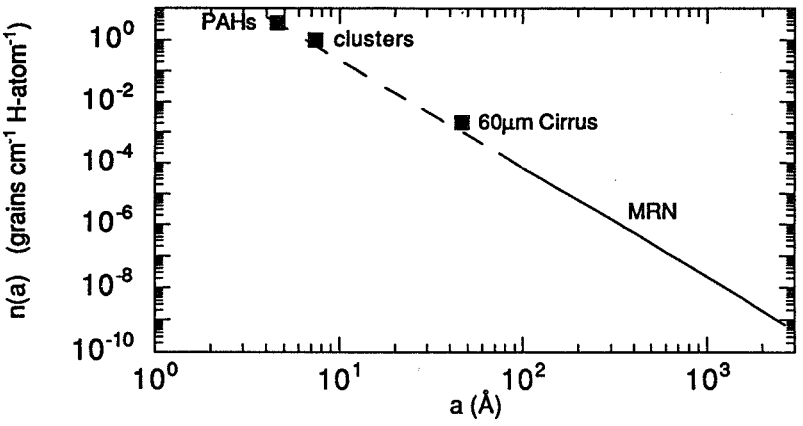

Figure 1. The grain size distribution derived from infrared observations (Tielens 1990). The points labeled PAHs, clusters and 60 μm correspond to the carriers of the IR emission features, the underlying plateaus, and the 60 μm cirrus. The curve labeled MRN is the interstellar grain size distribution derived from visual to FUV extinction measurements (Mathis et al. 1977).

similar analysis to that of the IR emission features shows that they are carried by somewhat larger ($\simeq$ 300 C–atoms) aromatic species (PAH clusters). IRAS discovered that emission at 12 and 25 μm is widespread in the ISM (the IR cirrus). Again this is due to IR fluorescence of UV pumped species and derived sizes are $\simeq$ 200 and 3000 C–atoms for 12 and 25 μm, respectively. While there is no spectroscopic information for the cirrus emission, likely, the carrier is related to the carrier of the IR emission features; ie., small PAHs and clusters of PAHs. Even the 60 μm cirrus has a fluctuating component ($\simeq$ 50 %). The required temperature ($\sim$ 60 K) corresponds to a carrier size of 50 Å ($N_c \simeq 5 \times 10^4$ C–atoms; Puget et al. 1985; Draine & Anderson 1985; Tielens 1990).

The abundances of these different species can be rather directly derived from the observed strength of the IR emission. All the absorbed FUV photon energy is eventually emitted in these features. Hence, the observed strength of these features relative to the FIR dust continuum is directly proportional to the ratio of the FUV absorption cross section of its carrier relative to that of the dust. For small species, the FUV absorption cross section is proportional to the total number of C–atoms involved (eg., Rayleigh limit). For aromatic materials it is also little dependent on the particular species involved ($\simeq 7 \times 10^{-18}$ cm^2 (C–atom)$^{-1}$). The results are shown in Figure 1 (Tielens 1990). Thus, these IR observations reveal that the interstellar grain size distribution extends smoothly into the molecular domain and is well represented by $n(a)da = 6.9{\times}10^{-26}\, a^{-3.5}da$ or $n(N_c)dN_c = 1.24{\times}10^{-6}\, N_c^{-11/6}dN_c$ grains per H–atom (Figure 1; Tielens 1990). This single grain size distribution may indicate a physical connection between small and large grains. Possibly, small PAHs are the left over condensation nuclei in the dust formation process around C–giants (Allamandola et al.

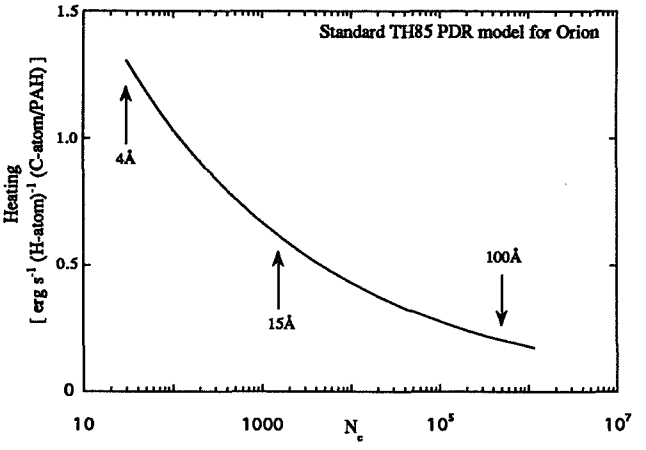

Figure 2. The contribution to the photoelectric heating of interstellar gas by grains of different sizes (Bakes and Tielens 1994). The results of these calculations are presented in such a way that equal areas under the curve correspond to equal contributions to the heating. Species with $\simeq$ 50 C–atoms are the carriers of the IR emission features at 3.3, 6.2, 7.7, and 11.3 μm. The plateaus underneath these features and the 12 μm cirrus are carried by somewhat larger species ($\simeq$ 200 C–atoms). The 25 and 60 μm cirrus correspond to species with 5×10^4 and 5×10^5 C–atoms, respectively.

1985; Latter 1991). Alternatively, PAHs could be the shattering fragments produced by grain–grain collisions in interstellar shocks (Jones and Tielens 1994). Detailed models for the IR emission of interstellar grains, including PAHs, have been developed by Draine and Anderson (1985), Desert et al. (1990), Siebenmorgen et al. (1992a,b), Schutte et al. (1993), and Natta et al. (1993).

The presence of a large populations of molecules has important ramifications for other aspects of the ISM besides its IR spectral appearance. These include the charge balance in atomic and molecular clouds (Lepp and Dalgarno 1988), the Diffuse Interstellar Bands (Crawford et al. 1985), and interstellar chemistry, including the formation of H_2 (Lepp et al. 1988; Tielens 1993). Of particular importance is the contribution of these species to the photoelectric heating of the interstellar gas (d'Hendecourt & Leger 1987). It has long been realized that the photoelectric heating will be dominated by the smallest grains present in the ISM (Watson 1972). FUV photons absorbed by a grain will create energetic electrons. These electrons may diffuse in the grain, reach the surface, overcome the work function of the grain and any Coulomb barrier if the grain is charged, and be injected into the gas phase with excess kinetic energy. Now, the collision length scale for low energy electrons in solids is $\simeq$ 10 Å and hence photoelectrons created inside large grains rarely reach the surface. Thus, small grain are more efficient heating agents of the gas than large grains. This is illustrated in Figure 2 which shows the contribution to the photoelectric heating as a function of grain size (Bakes and Tielens 1994). About half the gas heating is due to grains with sizes less than 15 Å ($N_c \simeq$ 1500 C–atoms). The other half originates in grains

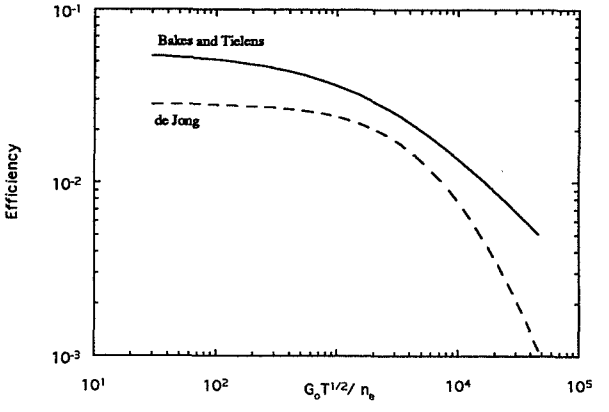

Figure 3. The photoelectric heating efficiency (Bakes and Tielens 1994) as a function of the parameter γ ($=G_oT^{0.5}/n_e$) which is proportional to the ionization over the recombination rate. Neutral grains are to the left while grains are positively charged to the right. The curve labeled de Jong is an earlier, semi–empirical estimate of the photoelectric heating efficiency.

with sizes between 15 and 100 Å ($1500 < N_c < 5 \times 10^5$ C–atom). Grains larger than 100 Å contribute negligibly to the photoelectric heating of the interstellar gas.

The contribution to the photoelectric heating of the gas by a grain depends on its charge. A higher charge implies a higher Coulomb barrier (ie., higher ionization potential) that has to be overcome. Thus, a smaller fraction of the electrons "dislodged" in the grain will escape. Moreover, those that do escape will carry away less kinetic energy (de Jong 1977). Figure 3 shows the results of a theoretical calculation of the photoelectric heating efficiency as a function of the parameter, γ ($=G_oT^{0.5}/n_e$), which is proportional to the ionization rate over the recombination rate of a grain. Thus, grains are predominantly neutral when γ is small and the photoelectric heating has the highest efficiency. When γ increases, the grains will charge up and the photoelectric efficiency will drop.

4. PhotoDissociation Regions

Photodissociation regions are regions where FUV ($h\nu < 13.6$ eV) photons dominate the heating and/or cooling of the gas. PDRs are associated with HII regions, reflection nebulae, bright rim clouds, galactic nuclei, Active Galactic Nuclei, and planetary nebulae. All of the HI mass of the galaxy is, of course, in regions dominated by FUV photons. As discussed in section 2, FUV photons dominate not only the composition but, through the gas heating, also the structure (cloud/intercloud) of the HI gas. Penetrating FUV photons from the interstellar radiation field also dominate the chemical composition and heating of molecular clouds for $A_v < 4$ magn. Thus, most of the molecular mass is in

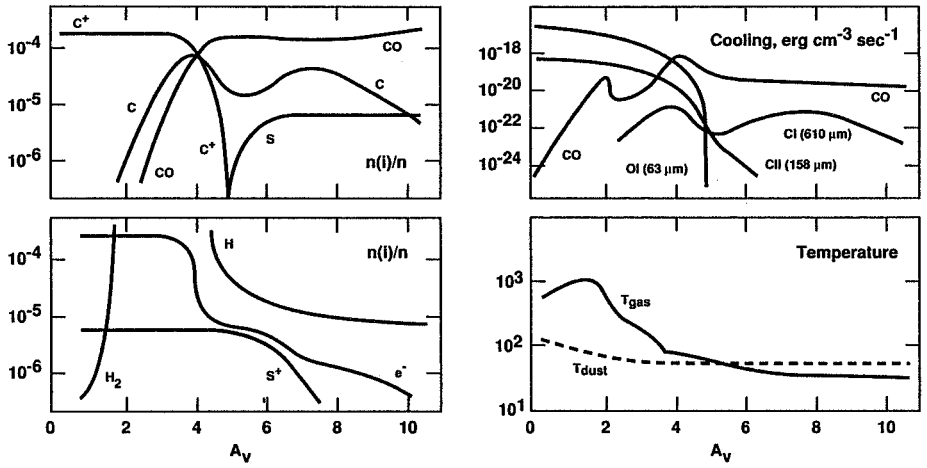

Figure 4. Calculated structure of the PDR in Orion (Tielens and Hollenbach 1985). The illuminating source is to the left. Left: Abundances relative to total hydrogen as a function of visual extinction into the PDR. Right: Cooling in the various gas lines and gas and dust temperatures in the PDR as a function of A_V.

the PDRs as well. Several reviews of PDR observations and theory have appeared over the years (Genzel et al. 1989; Hollenbach 1990; van Dishoeck 1992; Hollenbach and Tielens 1994).

4.1. PDR models

Detailed theoretical models have been developed for the interaction of FUV photons with atomic and molecular gas and dust (cf., Tielens and Hollenbach 1985; van Dishoeck and Black 1986; 1988; Sternberg and Dalgarno 1989; Burton et al. 1990; Hollenbach et al. 1991; Meixner and Tielens 1993). Generally, these models consider a plane parallel slab illuminated from one side by an intense FUV field (Figure 4). The penetrating FUV photons create an atomic surface layer. At a depth corresponding to $A_v \simeq 2$, the transition from atomic H to molecular H_2 occurs while at $A_v \simeq 4$ the carbon balance shifts from C^+ to C and CO (Figure 4). Except for the O locked up in CO, essentially all the oxygen is in atomic form until very deep in the cloud $A_v \sim 8$. Besides the chemical composition, the FUV photons also control the energy balance of the gas through the photoelectric effect (cf., Section 3). Typically, about 0.5% of the FUV energy is converted into gas heating this way. The rest is emitted as far–IR dust continuum radiation. The gas in the surface layer is then much warmer ($\simeq$ 500 K) than the dust (30–75 K). Somewhat deeper in ($A_v > 4$, penetrating red and near–infrared photons keep the dust warm and gas–grain collisions couple the gas to slightly below the dust temperature. Cosmic ray heating is never very important. Even in dark molecular cloud cores, where little radiation penetrates, heating of the gas is probably dominated by decay of turbulence rather than cosmic rays. In PDRs, the gas cools through the far–IR

fine–structure lines of mainly [OI] 63 μm and [CII] 158 μm at the surface and the rotational lines of CO deeper in (Figure 4).

4.2. PDR observations

PDRs are bright in the far–IR dust continuum, in the PAH emission features, the far–IR fine–structure lines of [OI] and [CII], and the rotational lines of CO. Besides these dominant cooling processes, PDRs are also the source of (fluorescent or collisionally excited) rovibrational transitions of H_2 in the near–IR, the atomic fine–structure lines of [CI] at 609 and 370 μm and [SiII] at 34 μm, and the recombination lines of CI in the radio (eg., C90α) and the far red (eg., 9850 and 8727 Å). In view of the dominance of IR emission in the cooling of PDRs, it is not surprising that the KAO and its predecessor, the Lear Jet, have played key roles in observational studies of PDRs. Indeed, for compact, high surface brightness PDRs associated, for example, with HII regions or galactic nuclei, the KAO provides the best available platform. Particularly in mapping of such regions, in continuum or in lines, the KAO is unsurpassed. The KAO can take full advantage of the rapid advance in (far) IR detector technology and, hence, the KAO (or its successor, SOFIA) will keep this edge into the distant future. The striking 37 μm image of the Orion nebula presented at this meeting (Stacey et al. 1994) exemplifies this point.

These observations can be used to determine the physical conditions in the emitting gas. The far–IR fine–structure lines are particularly useful in that respect since the critical densities of the CII and OI lines ($3 \times 10^3 - 3 \times 10^5$ cm^{-3}) and excitation energies (100–300 K) span the range present in many PDRs. The [CII] 158 μm line, which is optically thin, can be used to determine the total mass of emitting gas. Of course, these analyses require assumed abundances (or abundance ratios) which for C at least is somewhat uncertain. Often densities are inferred from the ratio of the total cooling rate (ie., the [OI]+[CII] intensity) to the far-IR dust continuum. This ratio is equal to the photoelectric heating efficiency which depends on the local density through the charging of the grains (cf., section 3). Of course, this analysis requires a good understanding of the photoelectric heating process itself and hence is also uncertain. The temperature and column density can also be determined directly from the lowest, pure rotational lines of H_2 which have very low critical densities. To date, that has only been done for the Orion Bar (Parmar et al. 1991). This indicator requires an assumed ortho to para ratio. For the higher H_2 levels, a ratio of three is expected, but the lowest level may originate in cooler gas characterized by a lower o/p ratio (Burton et al. 1992). The intensity distribution of the rotational CO levels also provides density and temperature information, albeit for the molecular component in the PDR ($A_v > 4$ magn.). Generally, the J=7-6 transition is quite strong in PDRs implying densities of 10^5 cm^{-3} and temperatures of 150 K. The presence of CO J=14–13 emission in some sources indicates even higher densities and temperatures (10^7 cm^{-3}; 500 K).

4.3. The Orion Bar

Observational studies of bright PDRs provide a unique opportunity to test theoretical models for the photoelectric heating of interstellar gas. FUV photons will clearly dominate the heating balance of such regions. Moreover, their high

surface brightness makes them an easy target for present day infrared arrays both from the KAO as well as from the ground. Among the lines to be targeted are the [OI] 63 μm, [CII] 158 μm, and [SiII] 34 μm fine–structure lines which dominate the cooling of the gas. Together with FIR 30–100 μm dust continuum studies and mid–IR studies of the PAH emission features, this will allow a direct determination of the heating efficiency of the gas relative to the total dust emission as well as to the PAH emission (cf., §3). The fine–structure lines will also give a handle on the density of the gas and the column density of C^+. The electron density can then be derived from the far red carbon recombination lines at 9850 and 8727 Å. The intensity of the incident FUV field can be determined from the FIR continuum. The gas temperature and column density is directly measured by the H_2 rotational lines. Hence, all the ingredients for a detailed test of photoelectric heating models are in hand. A first attempt at such a study has been made for the Orion Bar.

The Orion Bar is one of the best studied PDRs in the sky. The ionizing star Θ^1C Ori has carved out a bowl–shaped HII region on the facing side of the Orion molecular cloud. The Orion Bar is the limb brightened edge of this bowl where an ionization front is eating its way into the surrounding cloud. The sharp transition from H^+ to H^0, apparent in the [OI] 6300 and [SII] 6731 Å lines, is displaced to the Southeast from the fully ionized Bar present in radio (free–free) emission. The penetration of FUV photons into the surrounding cloud can be followed by selecting various molecular tracers with different photochemical stability (Tielens et al. 1993). Observational studies of the PAH emission features, H_2 1–0 S(1) line and CO J=1–0 line reveal a spatial structure in good agreement with that predicted by PDR models; ie., linear H_2 and CO emission structures parallel but displaced into the molecular cloud with respect to the PAH emission and the optical forbidden lines. The penetration of FUV photons is governed by dust extinction. From the observed separation between these different tracers and assuming standard dust–to–gas conversion factors, a total H density can be derived (5×10^4 cm^{-3}). This density agrees well with that derived from the intensities of the [OI] and [CII] fine–structure lines observed by the KAO (Tielens et al. 1993). The temperature of 500 K indicated by PDR models is also in good agreement with that observed in the H_2 rotational lines (Parmar et al. 1991). Higher density regions are also present as indicated by high level CO observations and a "thermalized" H_2 v=1–0 ratio (Burton et al. 1990). Such clumps are also apparent in the maps of the various PDR tracers (Tauber et al. 1994; Bregman et al. 1994; van der Werf et al. 1994). The observed heating efficiency is 5×10^{-3} (Tielens et al. 1993). The electron density derived from the CI 9850Å and [CII] 158 μm lines is 60 cm^{-3}. With a G_o of 5×10^4 (derived from the FIR continuum; Tielens et al. 1993) and a gas temperature of 500 K (Parmar et al. 1991), γ is calculated to be $\simeq 2\times10^4$ and the theoretical efficiency is 9×10^{-3} (Figure 3); well within experimental errors. Further studies of this kind may result in a semi–empirical determination of the heating efficiency of interstellar gas by FUV photons.

The properties of the various interstellar gas components associated with the Orion HII region are summarized in Table 4. The atomic and molecular components of PDRs each contain about 100 $M_\odot$. For comparison, the ex-

tended molecular ridge contains about twice that amount of gas[1]. The observations show pronounced clumping of the emitting gas. First, the [CII] and [CI] emission is extended on tens of arc minute scale. All this gas is photoionized, photodissociated and (photo)heated by θ^1C Ori. This emission scale size is much larger than expected for a homogeneous region at the density indicated by the line ratios. Clearly, the gas is organized in filamentary and clumpy structures which allow the illumination by FUV photons at very large distances from the star. It is well–known that on a parsec scale, the Orion molecular cloud consists of a highly non–uniform complex of filaments and clumps (Bally et al. 1987). Second, maps in ^{13}CO and H_2 in the Orion Bar region show direct evidence for clumping with a surface filling factor of 0.1. In deriving the physical conditions in these clumps (Table 4), we assume that these clumps are responsible for the observed high level CO and "thermal" H_2 emission. Likewise, CII recombination line studies indicate clumpy, high density ($\sim 10^5 - 10^6$ cm^{-3}) regions over a large area of the Orion PDR (Natta et al. 1994). The inferred thermal pressures for these clumps ($10^9 - 10^{10}$ K cm^{-3}) are well in excess of that sustainable by the interclump medium (or the HII region pressure). Likely, these clumps are therefore confined by self–gravity and either are on their way to forming stars or already contain an embedded protostar. Hence, they may be the PDR counterparts of the small partially ionized (Bok) globules (PIGs) and stellar "proplyds" observed in the HII region (Churchwell et al. 1987; O'Dell et al. 1993). These objects may thus well be widespread in the Orion molecular cloud. Further studies (ie., searches for embedded protostars) could be very interesting.

Table 4. Physical Conditions in Orion.

Component	n [cm^{-3}]	T [K]	M [M$_\odot$]	N_H [10^{22} cm^{-2}]	Lines
Atomic	10^5	500	75	1	OI, CII
Molecular[a]	10^5	120	125	1.7	CO J<7
Clumps	$10^5 - 10^7$	(500)	1.5[b]	0.03[c]	CO>7
Extended Ridge	10^5	70	400	5	CO, CS, HCN

[a]Warm molecular gas associated with the PDR.
[b]Mass of one clump.
[c]Column density of warm molecular gas.

5. The CII Emission from the Galaxy

The FIRAS instrument on COBE has surveyed the galaxy in the far-IR dust continuum and various interesting lines (Wright et al. 1991; Bennett et al. 1994). The large beam ($\simeq 7°$) makes COBE sensitive to extended low surface brightness emission associated with interstellar dust and gas. Still, some structure

[1]Here, C^+ in the PDR and CO in the molecular cloud are assumed to be the dominant gaseous carbon reservoir and all mass estimates are based upon the same gas phase elemental C–abundance of 3×10^{-4}.

is apparent including the Orion molecular cloud and the molecular ring. The [CII] 158 and [NII] 205 μm lines are particularly interesting. The [CII] line is the dominant cooling line of the interstellar gas with an observed luminosity of 5×10^7 $L_\odot$ or L(CII)/L(far-IR)$\simeq 3 \times 10^{-3}$ averaged over the galaxy. A similar CII/FIR ratio is obtained from cross cuts through the inner galaxy (6×10^{-3}; Shibai et al. 1991). The origin of the galactic [CII] emission is of great interest. Three interstellar components have been proposed as possible "carriers": the galactic HI, PDRs on molecular cloud surfaces, and the WIM.

5.1. Diffuse HI clouds

Because of their temperatures and densities, diffuse HI clouds will radiate most of their cooling through the [CII] 158 μm line (cf., Dalgarno and McCray 1972). For a few lines of sight the expected [CII] line emission has been measured in an indirect way; ie., through FUV measurements of the population of the upper level of this fine-structure transition (Pottasch et al. 1979). These observations yielded an emissivity per H-atom of about 10^{-25} erg/s. A recent study measured a somewhat lower cooling rate of 3×10^{-26} erg/s/H-atom (Gry et al. 1992). The earlier study concentrated on lines of sight characterized by relatively high FUV radiation fields and hence high cooling rates (cf., section 3). The latter study was predominantly towards stars with relatively low average densities and, consequently, a large admixture of warm neutral medium. The WNM cools largely through Lyman α and [OI] 6300 Å emission and is an inefficient [CII] 158 μm emitter. Allowing for these systematic effects, an average cooling rate of 5×10^{-26} erg/s/H-atom is derived for diffuse HI clouds (Bakes and Tielens 1994; Wolfire et al. 1994). With a total galactic HI mass of 3.5×10^9 $M_\odot$ with about half in diffuse HI clouds, a total galactic [CII] luminosity of $\simeq 3 \times 10^7$ $L_\odot$ is derived, which is somewhat less than observed by COBE.

5.2. PDRs on molecular cloud surfaces

Airborne studies towards the molecular ring show a good correlation between the [CII] emission and the CO emission but not the HI emission (Stacey et al. 1985; Shibai et al. 1991). This has lead to the suggestion that the galactic [CII] emission is associated with PDRs on molecular cloud surfaces created by nearby OB associations and/or the ambient interstellar radiation field. Indeed, the Orion molecular cloud can be easily recognized upon the COBE [CII] map. Theoretically, we expect that HI clouds (as well as molecular clouds) have the maximum possible efficiency of converting FUV radiation into [CII] 158 μm emission (ie., small γ; cf., section 3). Hence, in this interpretation, the observed CII/CO correlation implies that molecular clouds intercept much of the total available FUV radiation field. Now, this conclusion is mainly based upon analysis of a few lines of sight associated with molecular clouds exhibiting massive star formation (ie., W43, NGC 6334; Shibai et al. 1991). Studies of individual OB association/molecular cloud regions in the solar neighborhood have shown that a considerable fraction of the stellar luminosity is reradiated by the dust in the molecular cloud during the early phases of evolution (the embedded and blister phases of HII regions; ~30% of an O star's lifetime; Leisawitz and Hauser 1988; Cox et al. 1990). However, this is not true for the galaxy as a whole. IRAS studies concluded that only about 20% of the galactic IR emission is starlight

reprocessed by molecular clouds. Much of the remainder (70%) originates in HI gas (Sodroski et al. 1989; Bloemen et al. 1990). In the later phases, much of the OB association's light escapes from the local environment. Moreover, in the solar neighborhood, half the O stars are field stars. Hence, on the whole, PDRs on molecular cloud surfaces are not expected to be the dominant source of the galactic CII emission.

5.3. The Warm Ionized Medium

COBE also measured the emission in the [NII] 205 μm line. The ionization potential of neutral N is slightly above that of H and hence this emission has to originate in largely ionized H^+ zones; the Warm Ionized Medium (WIM). Low density HII regions can also be important sources of [CII] emission (Shibai et al. 1991; Heiles 1994) and, indeed, the observed [NII] emission correlates well – but not linearly – with the [CII] emission ($I_{NII} \simeq 10 \times I_{CII}^{1.5}$; Bennett et al. 1994). At the low densities of such regions, N^+ and C^+ are the dominant ionization stages of these elements and, assuming a C elemental depletion twice that of N, the [CII]/[NII] intensity ratio is 9 (Heiles 1994). Thus, the WIM can dominate the observed [CII] emission at the higher intensities (eg., for $I_{CII} \simeq 10^{-4}$ erg/cm^2/s/sr) but not at lower intensities. The good correlation between [CII] emission and the free–free radio emission in a cross cut through the galactic plane across the molecular ring (Shibai et al. 1991) has been cited as additional support for an WIM origin of the galactic [CII] emission (Heiles 1994). However, as for the CII/CO correlation, this correlation may merely reflect enhanced emissivity in regions of massive star formation.

5.4. Discussion

Hence, there are three plausible origins for the observed galactic [CII] 158 μm emission observed with COBE: diffuse HI clouds, PDR surfaces of molecular clouds, and the WIM. The contribution of each of these components depends on the location in the galaxy as well as the scale size of the observations. In the local ISM, diffuse HI clouds dominate the [CII] emission with typical intensities of $1 - 10 \times 10^{-6}$ erg/cm^2/s/sr. Locally, molecular clouds contribute little to the total [CII] emission. Nevertheless, local molecular cloud complexes, such as Orion which are undergoing massive star formation, are quite apparent in the COBE [CII] map. Per H–nuclei, the [CII] emission from the WIM is as important (Wolfire et al. 1994), but locally the mass of HII is only 1/3 of that of HI (Reynolds 1993). Indeed, for a typical Hα intensity from the local WIM of $1 - 4 \times 10^{-7}$ cosec$|b|$ erg/cm^2/s (Reynolds 1993), the expected [CII] emission is $0.8 - 3 \times 10^{-7}$ erg/cm^2/s/sr. Towards the inner galaxy, the ISM pressure increases and hence the density in the WIM increases as well (from $\simeq$0.3 to 3 cm^{-3}). The contribution from the WIM becomes then comparatively more important. Indeed, judging from the [NII] observations, the WIM may contribute substantially to the [CII] emission from the inner galaxy (and hence the total CII luminosity). On a galactic scale, dust in molecular clouds contributes only $\simeq$ 20% of the total FIR emission. Likely, the contribution to the galactic CII emission from PDRs on molecular cloud surfaces is equally small. Further studies of the interrelationship of the CII and NII emission on a much smaller scale size than possible with COBE may well be instrumental in settling these points.

Table 5. Energy Sources.

Source	Luminosity [$L_\odot$]
Observations	
..... [CII] 158 μm	5 (7)
..... FIR	1.7 (10)
Stellar Luminosities	
..... All stars	4 (10)
..... OBA	8 (9)
Mechanical Energy	
..... SN	2 (8)
..... WR	6 (6)
..... OBA	2 (6)

As already emphasized in §2, the understanding of the heating of interstellar gas is the key to understanding the ISM. The observed CII emission is a lower limit to the total heating rate of the galaxy. Table 5 compares the observations to the various energy sources of the interstellar gas. The mechanical energy input by SN is calculated assuming a SN rate of 2×10^{-2} yr^{-1} and an energy per SN of 10^{51} erg. The mechanical energy input by Wolf Rayet and OB stars is taken from van der Hucht et al. (1987). Since a large fraction of the mechanical energy will be dissipated by strong shocks and such shocks are inefficient [CII] emitters, it is clear that the heating of the interstellar gas has to result from tapping into the stellar FUV energy reservoir (cf., §2). Now, the efficiency of the photo electric effect (L(CII)/L(FIR)) inferred from the COBE observations is only $\simeq$ 0.003. The CII observations of local diffuse clouds in the UV imply much higher efficiencies (0.05). The low efficiency derived from the IR observations may reflect the heating of interstellar dust by visible (and far–red) rather than FUV photons. Long wavelength photons are not very efficient in heating the gas through the photoelectric effect (Spaans et al. 1994). Assuming that only stellar photons from OBA stars are efficient heating agents and that typically only 50% of those photons are in the FUV increases the estimated yield to only $\simeq$0.01, still considerably less than the value derived for local HI clouds. Possibly, we are missing an important cooling agent of the diffuse interstellar medium (ie., [OI]). Alternatively, a substantial proportion of the FUV stellar flux is absorbed in the Warm Neutral Medium (WNM) which is an inefficient [CII] emitter. In particular, a non–negligible fraction of these photons may escape into the galactic halo. At least 15% of the ionizing stellar flux from OB stars has to escape into the halo to explain the WIM (Reynolds 1993) and, likely, the escaping FUV flux is much larger than that. Because of the larger scale height, this FUV flux will wind up heating the WNM rather than diffuse clouds. FIR emission by dust in the WNM phase is, thus, likely the cause of the rapid drop in the efficiency (I(CII)/I(FIR)) with galactic latitude observed by COBE (Bennett et al. 1994). At this point in time, it seems fair to conclude that the origin of the

galactic [CII] emission as well as the heating of the diffuse interstellar gas is not (yet) completely understood. Further studies, in particular, of the atomic fine-structure line emission along a few well-defined lines of sight (eg., ζ Oph, ζ Per, o Per, α Vir) are in reach with ISO and could lead to a direct determination of the heating efficiency of the interstellar gas as a function of the physical conditions.

References

Allamandola, L.J., Tielens, A.G.G.M. & Barker, J.R. 1985, ApJ, 290, 25

Allamandola, L.J., Tielens, A.G.G.M. & Barker, J.R. 1989, ApJS, 71, 733

Audouze, J. & Tinsley, B.M. 1976, ARA&A, 14, 43

Bakes, E.L.O. & Tielens, A.G.G.M. 1994, ApJ, 427, 822

Bally, J., Langer, W.D., Stark, A.A. & Wilson, R.W. 1987, ApJ, 312, 45

Bennett, C.L., et al. 1994, ApJ, 434, 587

Bloemen, J.B.G.M., Deul, E.R. & Thaddeus, P. 1990, A&A, 233, 437

Bock, J.J., et al. 1993, ApJ410, 115

Bregman J., et al. 1989, ApJ, 344, 791

Bregman, J., Larson, K., Rank, D. & Temi, P., 1994, ApJ, 423, 326

Burton, M., Hollenbach, D.J. & Tielens, A.G.G.M. 1990, ApJ, 365, 620

Burton, M., Hollenbach, D.J. & Tielens, A.G.G.M. 1992, ApJ, 399,

Cherchneff, I. & Tielens, A.G.G.M. 1994, in Wolf Rayet Stars, K. van der Hucht, Dordrecht: Kluwer, in press

Cohen, M., et al. 1986, ApJ, 302, 737

Cohen, M., et al. 1989, ApJ, 341, 246

Cowie, L.L. 1987, in Interstellar Processes, D.J. Hollenbach & H. Thronson, Dordrecht: Reidel, 245

Cox, P., Derhaveng, L. & Leene, A. 1990, A&A, 230, 181

Crawford, M.K., Tielens, A.G.G.M. & Allamandola, L.J., 1985 ApJ, 293, 45

Churchwell, E., Felli, M., Wood, D.O.S., & Massi, M., 1987, ApJ, 321, 516

Dalgarno, A. & McCray, R.A. 1972, ARA&A, 10, 375

d'Hendecourt, L.B. & Leger, A. 1987, A&A, 180, L9

de Jong, T. 1977, A&A, 55, 137

Desert, F.X., Boulanger, F., and Puget, J.L. 1990, A&A, 237, 215

Draine, B.D. & Anderson, N. 1985, ApJ, 292, 494

Duley, W.W. & Williams, D.A. 1981, MNRAS, 196, 269

Duley, W.W. 1989, in Interstellar Dust, L.J. Allamandola & A.G.G.M. Tielens, Dordrecht: Kluwer, 141

Ferriere, K.M., Zweibel, E.G. & Shull, J.M. 1988, ApJ, 332, 984

Field, G.B., Goldsmith, D., & Habing, H.J. 1969, ApJ, 15, L49

Genzel, R., Harris, A.I. & Stutzki, J. 1989, in Infrared Spectroscopy in Astronomy, ESA SP 290, 115

Gry, C., Lequeux, J. & Boulanger, F., 1992, A&A, 266, 457

Heiles, C., 1994, ApJ, in press

Hollenbach, D.J. 1990, in The Evolution of the Interstellar Medium, L. Blitz, ASP: SF, 167

Hollenbach, D.J., Takahashi, T. & Tielens, A.G.G.M. 1991, ApJ, 377, 192

Hollenbach, D.J. & Tielens, A.G.G.M., 1994, in Physics and Chemistry of Interstellar Molecular Clouds, G. Winnewisser, in press

Houck, J.C. & Bregman, J.N, 1990, ApJ, 352, 506

Jones, A.P. & Tielens, A.G.G.M. 1994, in The Cold Universe, Th. Montmerle, C.J. Lada, I.F. Mirabel, J. Trân Trânh Van, Montpellier: Editions Frontieres, 35

Jones, A.P., Tielens, A.G.G.M., Hollenbach, D.J., & McKee 1994, ApJ, 433, 797

Kulkarni, S.R. & Heiles 1987, in Interstellar Processes, D.J. Hollenbach & H. Thronson, Dordrecht: Reidel, 87

Latter, W. 1991, ApJ, 377, 187

Leger, A. & Puget, J.L. 1984, A&A, 137, L5

Leisawitz, D. & Hauser, M.G. 1988, ApJ, 332, 954

Lepp, S. & Dalgarno, A. 1988, ApJ, 324, 553

Lepp, S. & Dalgarno, A., van Dishoeck, E.W. & Black J.H. 1988, ApJ, 329, 418

Martin, C. & Bowyer, S. 1990, ApJ, 350, 242

Mathis, J.S., Rumpl, W. & Nordsieck, K.H. 1977, ApJ, 217, 105

Mathis, J.S., Mezger, P.G. & Panagia, N. 1983, A&A, 128, 212

McKee, C.F. & Ostriker, J.P. 1977, ApJ, 218, 148

Meixner, M.M. & Tielens, A.G.G.M. 1993, ApJ, 405, 216

Natta, A., Prusti, T., & Krugel, E. 1993, A&A, 275, 527

Natta, A., Walmsley, C.F. & Tielens, A.G.G.M. 1994, ApJ, 428, 209

O'Dell, C.R., Wen, Z. & Hu, X. 1993, ApJ, 410, 696

Onaka, T. de Jong, T., & Willems, F., 1989, A&A, 218, 169

Pagel, B.E.J. 1987, in The Galaxy, G. Gilmore & B. Cardswell, Dordrecht: Reidel 341

Papoular, R., Reynaud, C. & Nenner, I., 1991, A&A, 247, 215

Parmar, S.P., Lacy, J.H. & Achterman, J. 1991, ApJ, 372, L25 563

Pendleton, Y., Sandford, S., Allamandola, L.J., Tielens, A.G.G.M., & Sellgren, K. 1994, ApJ, in press

Pottasch, S.R., Wesselius, P.R. & van Duinen, R.J. 1979, A&A, 74, L15

Puget, J.L., Leger, A. & Boulanger, F. 1985, A&A, 142, L19

Rana, N.C, 1991, ARA&A, 29, 129

Reynolds, R.J. 1993, in Massive Stars: Their lives in the ISM, J. Cassinelli & E. Churchwell, PASP: SF, 338

Roche, P. & Aiken, D.A. 1985, MNRAS, 215, 425

Sakata, A. & Wada, S. 1989, in Interstellar Dust, L.J. Allamandola & A.G.G.M. Tielens, Dordrecht: Kluwer, 191

Savage, B.D. 1987, in Interstellar Processes, D.J. Hollenbach & H. Thronson, Dordrecht: Reidel, 123

Schutte, W., Tielens, A.G.G.M. & Allamandola, L.J. 1993, ApJ, 415, 397

Sellgren, K.S., Werner, M.W. & Dinerstein, H.L., 1983, ApJ, 217, 149

Shibai, H., et al. 1991, ApJ, 374, 522

Shull, J.M. 1987, in Interstellar Processes, D.J. Hollenbach & H. Thronson, Dordrecht: Reidel, 225

Siebenmorgen, R. & Krugel, E. 1992a, A&A, 259, 614

Siebenmorgen, R., Krugel, E. & Mathis, J.S. 1992b, A&A, 266, 501

Sodroski, T.J., Dwek, E., Hauser, M.G. & Kerr, F.J. 1989, ApJ, 336, 762

Spaans, M., Tielens, A.G.G.M., van Dishoeck, E.F. & Bakes, E.L.O., 1994, ApJ, in press

Stacey, G.J., Viscuso, P.J., Fuller, C.F. & Kurtz, N.T. 1985, ApJ, 289, 803

Stacey, G.J., et al. 1994, in Proc of the Airborne Astronomy Symposium, M.R. Haas, J.A. Davidson & Erickson, E.F., ASP: SF, paper 3.1

Sternberg, A. & Dalgarno, A., 1989, ApJ, 338, 197

Tauber, J., Tielens, A.G.G.M., Meixner, M.M. & Goldsmith, P. 1994, ApJ, 422, 136

Tielens, A.G.G.M. 1989, in Carbon in the Galaxy, J. Tarter, NASA SP 3061, 59

Tielens, A.G.G.M, 1990, in Submillimetre Astronomy, G.D. Watts & A.S. Webster, Dordrecht, Kluwer, 13

Tielens, A.G.G.M. 1993, in Dust and Chemistry in Astronomy, T. J. Millar & D.A. Williams, The Institute of Physics Publ Co: Bristol, 103

Tielens, A.G.G.M. & Hollenbach. D.J., 1985, ApJ, 291, 722

Tielens, A.G.G.M. & Allamandola, L.J. 1987, in Interstellar Processes, D.J. Hollenbach & H. Thronson, Dordrecht: Reidel, 397

Tielens, A.G.G.M., et al. 1993, Science, 262, 86

van der Hucht , K.A., Williams, P.M., & The, P.S. 1987, QJRAS, 28, 254

van der Werf, P., et al. 1994, in preparation

van Dishoeck E.F., 1992, in Infrared Astronomy with ISO, Th. Encrenaz & M. Kessler, Nova: NY, 283

van Dishoeck E.F. & Black, J.S. 1986, ApJS, 62, 109

van Dishoeck E.F. & Black, J.S. 1988, ApJ, 334, 711

Watson, W.D. 1972, ApJ, 176, 103

Wakker, B., 1990, Ph. D. Thesis, Groningen

Wolfire, M., McKee, C.F., Hollenbach, D.J., Tielens, A.G.G.M. 1994, ApJ, in press

Wooden, D., et al., 1993, ApJS, 88, 477

Wright, E.L., 1991, ApJ, 381, 200

Airborne Astronomy Symposium on the Galactic Ecosystem
ASP Conference Series, Vol. 73, 1995
M.R. Haas, J.A. Davidson, and E.F. Erickson (eds.)

AIRBORNE AND LABORATORY STUDIES OF INTERSTELLAR PAHS

L. J. ALLAMANDOLA, S. A. SANDFORD, D.M. HUDGINS, AND F.C. WITTEBORN
NASA Ames Research Center, MS 245-6, Moffett Field, CA 94035-1000

ABSTRACT A brief history of the observations which have led to the hypothesis that polycyclic aromatic hydrocarbons (PAHs) are the carriers of the widespread interstellar emission features near 3050, 1615, "1300", and 890 cm^{-1} (3.29, 6.2, "7.7", and 11.2 μm) is presented. The central role of airborne spectroscopy is stressed. The principal reason for the assignment to PAHs was the resemblance of the interstellar emission spectrum to the laboratory absorption spectra of PAHs and PAH-like materials. Since precious little information was available on the properties of PAHs in the forms that are thought to exist under interstellar conditions -isolated and ionized in the emission zones, with the smallest PAHs being dehydrogenated- there was a need for a spectral data base on PAHs taken in these states. Here, the relevant infrared spectroscopic properties of PAHs will be reviewed. These laboratory spectra show that relative band intensities are severely altered and that band frequencies shift. It is shown that these new data alleviate several of the spectroscopic criticisms previously leveled at the hypothesis.

INTRODUCTION

An intriguing and exciting chapter of modern astrophysics was opened by Gillett, Forrest, and Merrill (1973) with their discovery of an unexpected, broad infrared emission feature in the spectrum of the planetary nebulae NGC 7027 and BD+30°3639. Gillett et al. pointed out that this broad feature, which peaked near 885 cm^{-1} (11.3 μm), was most likely associated with dust and that identification of the carrier could give important insight into dust formation processes and evolution from the late type star through planetary nebulae phases. This feature could not be associated with graphite grains nor was it in the spectra of late type stars such as M supergiants, or M and C Mira variables, long thought to produce graphitic carbon and to be the predecessors of planetary nebulae. This implied that "...if the dust in planetary nebulae is a remnant of an earlier stage of evolution, then the forerunners of planetary nebulae are not found among the above-mentioned stellar types. On the other hand, if the forerunner of a planetary nebula is to be found among the above stellar types, then the dust around planetaries is not a remnant of its earlier evolution phase." Thus, the identification of this band carried with it some very important implications.

Gillett et al. showed that there was a remarkable similarity between the interstellar emission feature and an absorption band common to the spectra of carbonate minerals. There was excellent agreement in the position and profile of

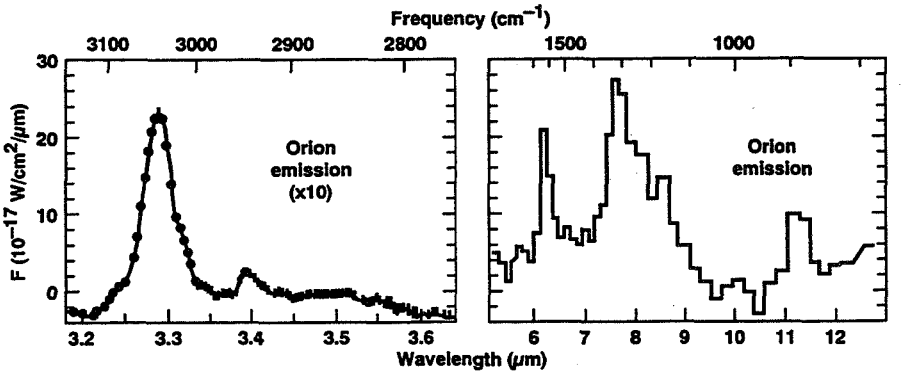

Figure 1. The infrared emission spectrum from position 4 of the ionization ridge in the Orion Nebula. Figure reproduced from Bregman et al. (1989).

the interstellar feature with the 885 cm^{-1} absorption band in $MgCO_3$. Since carbonates also produce a strong band near 1450 cm^{-1} (6.9 μm), assignment of the new interstellar feature required searching for an emission band near 1450 cm^{-1}. Gillett et al. pointed out that although "...this spectral range cannot be examined from the ground due to H_2O absorption in the Earth's atmosphere...observations from aircraft or balloons should be possible."

During the next five years airborne observations did indeed become possible and the pioneering airborne spectroscopic work of Gillett, Joyce, Puetter, Russell, Soifer, and Willner in the 2000-1250 cm^{-1} (5-8 μm) region demonstrated that carbonates could not account for the new feature. Instead of a strong, broad band at 1450 cm^{-1}, they found two very intense features at 1615 and about 1300 cm^{-1} (6.2 and 7.7 μm) (e.g., Russell, Soifer, and Willner 1977; Willner et al. 1977).

During this same period it also became clear that these bands were part of a family of infrared emission features which were emitted by a large number of very different types of astronomical objects. Aitken (1981) and Willner (1984) have reviewed the ground breaking observations which showed that the group of prominent features peaking near 3050, 1615, "1300", and 890 cm^{-1} (3.28, 6.2, "7.7", and 11.2 μm) were always closely correlated. An example of this emission spectrum is shown in Figure 1. The bands are broad, with a FWHH on the order of 30-50 cm^{-1}, the "1310" cm^{-1} feature being an exception. It is considerably broader, most likely because it is a composite of several overlapping bands. The peak frequencies do not seem to vary by more than a few wavenumbers from object to object, again excepting the "1310" cm^{-1} feature, which varies by as much as 50 cm^{-1} .

As the list of astronomical objects which emit these features grew, it became clear that the emission came from regions where ultraviolet radiation was impinging on areas in which dust was known to be present. Surprisingly, the age and history of the dust seemed to be unimportant, with objects as diverse as H II regions, reflection nebulae, planetary nebulae, and galaxies emitting similar spectra. The intensities of the bands emitted from other galaxies were found to be far greater than what would be expected from the individual objects which comprised the galaxies, such as planetary nebulae and H II regions. The implication was that a substantial fraction of this extragalactic emission came from regions which were not associated with individual stars, but from the interstellar

medium itself (Phillips, Aitken, and Roche 1984). Subsequent observations of our galaxy by the Infrared Astronomical Satellite (IRAS) suggest that this is also the case in the Milky Way (Low et al. 1984; Giard et al. 1988).

Understanding the source of this unexpected, yet widespread, phenomenon became an important problem in astrophysics. As the number and variety of objects found to emit the features increased, identifying the carrier and determining the emission mechanism became the key challenges. A number of models have been proposed to account for both aspects of the problem. A review of many of the models proposed up to 1984 can be found in Allamandola (1984). The idea, now gaining wide acceptance, that aromatic material may be the carrier of the features began with the suggestion made by Duley and Williams (1981) that they arise from vibrations of chemical groups attached to the aromatic moieties which make up small (<0.01 micron-100 Å radius) amorphous carbon particles. Subsequently, Leger and Puget (1984) and Allamandola, Tielens, and Barker (1985) proposed that individual polycyclic aromatic hydrocarbon molecules (PAHs-5-10 Å) were the band carriers. PAHs are extremely stable, planar molecules with a chicken-wire structure (see Figure 2 for examples). Carbon atoms form the internal, hexagonal network; hydrogen atoms lie on the periphery. Thorough reviews of the PAH hypothesis can be found elsewhere (Allamandola, Tielens, and Barker 1989, and Puget and Leger 1989).

The principal reason for the assignment to PAHs was the suggestive, but not perfect, resemblance of the interstellar emission spectrum with the infrared absorption spectra of PAHs in KBr pellets and the infrared and Raman spectra of chars and soots which are comprised of mixtures of PAHs (Figures 2 and 3). The comparable intensity of the 3050 cm^{-1} feature to those at lower frequencies, and the close association with ultraviolet radiation, led Allamandola and Norman (1978) and Allamandola, Greenberg, and Norman (1979) to propose that the emission was due to the infrared fluorescence from molecule-sized emitters excited by the absorption of ultraviolet and visible photons. Although the carrier initially proposed (molecules, frozen on 10K dust grains) was incorrect, this excitation-emission mechanism is now generally accepted because of observations of reflection nebulae made by Sellgren (1984) who showed that the ultraviolet and visible photon fluxes present were unable to sufficiently excite species larger than about 10 Å to emit in the 3000 cm^{-1} region at the intensities observed. Energy deposited in a particular molecular structural unit of a larger particle or cluster is thought to become thermalized on timescales on the order of 10^{-11}-10^{-13} seconds, many orders of magnitude shorter than the 10^{-3} -10^{-2} second timescale appropriate for the emission of IR photons. Emission from molecular units in a particle would require unusually weak intermolecular coupling and has yet to be demonstrated. This question is presently not settled, however, as the proponents of particulate materials being responsible for the interstellar emission features such as HAC (Jones, Williams, and Duley 1990), QCC (Sakata et al. 1990) and certain types of coals (Papoular et al. 1993) continue to espouse their viewpoints.

It is our view that both free, individual PAH molecules *and* particles comprised of PAH building blocks are responsible for the overall interstellar emission spectrum. The suggestion that free molecules produce the emission features and the particles produce the underlying continuum at the lower frequencies (Allamandola, Tielens, and Barker 1987) was supported by the early experimental work of Blanco, Bussoletti, and Colangeli (1988) and Flickinger and Wdowiak (1990). It is likely that the molecular-sized PAHs which produce the features are the small end of the distribution of aromatic-rich interstellar materials (Allamandola, Tielens, and Barker 1989; Tielens 1989), and that specific features of the interstellar emission spectrum are produced by different portions of that

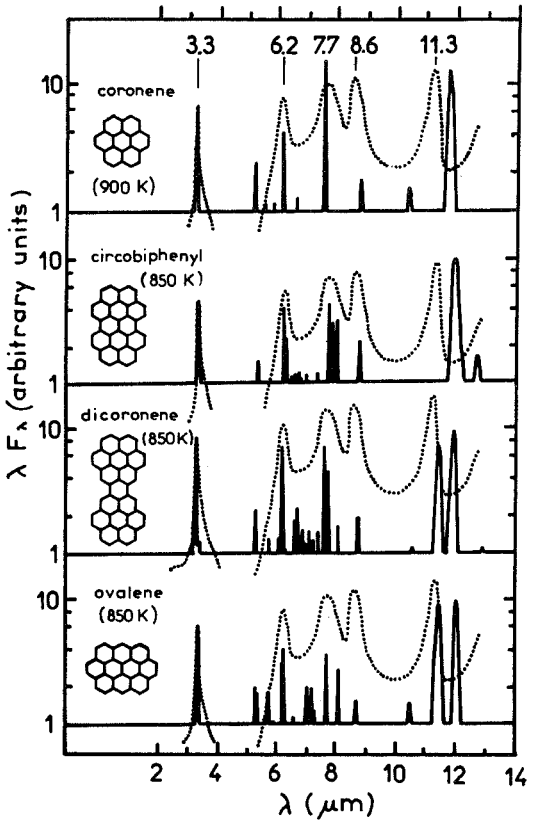

Figure 2. Emission spectra of several compact PAHs *calculated* from laboratory absorption spectra measured at room temperature in KBr compared to the observed spectrum of the reflection nebula NGC 2023 (dots). Figure reproduced from Leger and d'Hendecourt (1987).

distribution (Schutte, Tielens, and Allamandola 1993).

The discovery of a previously unrecognized and surprisingly ubiquitous component of the interstellar medium has important implications for our understanding of many interstellar processes. Current estimates are that between 1 and 10% of all of the carbon in the galaxy is in PAHs comprised of roughly 15 to 500 carbon atoms. The PAHs responsible for the IR features are thought to be more abundant than all of the other known interstellar, gaseous, polyatomic molecules combined. Their proposed ubiquity and high abundance has serious ramifications for other spectral regions. They may well contribute to the strong ultraviolet interstellar extinction between 100 - 200 nm, the weak, diffuse, visible absorption bands (van der Zwet and Allamandola 1985; Leger and d'Hendecourt 1985; Crawford, Tielens, and Allamandola 1985), and the far-IR Cirrus (Allamandola, Tielens, and Barker 1985; Puget, Leger, and Boulanger 1985). Similarly their influence on many physical processes may be profound (Omont

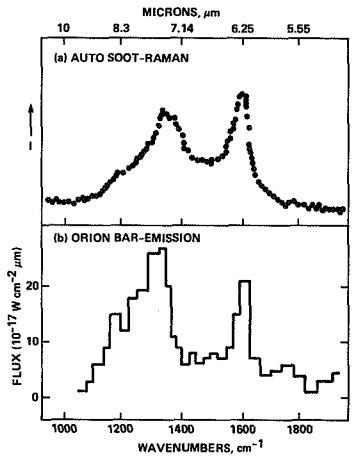

Figure 3. Comparison of the 2000-1000 cm^{-1} (5 to 8 μm) Raman spectrum of auto soot (a form of amorphous carbon) with the emission from Orion. Figure reproduced from Allamandola, Tielens, and Barker (1985)

1986). They may be responsible for maintaining interstellar cloud temperature (d'Hendecourt and Leger 1987), and moderating interstellar cloud chemistry (Lepp and Dalgarno 1988). PAHs may comprise much of the carbon in meteorites (Wdowiak, Flickinger, and Cronin 1988), and contribute to the deuterium enrichment found in interplanetary dust particles and meteorites (Allamandola, Sandford, and Wopenka 1987).

In view of the previous paragraph, it is important to realize that until about 1990, precious little information was available on the properties of PAHs in the forms that are thought to exist under interstellar conditions i.e., as isolated molecules in the gas phase, ionized in the emission zones, with the smallest members of the family (<~20 carbon atoms) being dehydrogenated. Most of the relevant data available on the physics and chemistry of PAHs had been applied to the problem by this time and new laboratory studies of PAHs under conditions relevant to astrophysics were required to raise this area from one in which the PAH hypothesis was used to explain observational results to a level where it could be exploited to make predictions and give further insight into the evolution of interstellar carbonaceous materials.

During the past decade experimentalists around the world have responded to this need, and data has become available on many properties of PAHs which are of direct application to astrophysics. These are difficult experiments as PAHs are refractory materials, and maintaining a population of individual, non-interacting molecules for study is not straightforward. As if this isn't bad enough, ionized or dehydrogenated species are very reactive and short-lived, providing further experimental challenges. These data, which started to become available about five years ago, cover a wide range of physical and chemical properties. In this article the infrared spectroscopic properties of PAHs under relevant interstellar conditions will be reviewed. The discussion will focus on those points which specifically address the criticisms leveled at the hypothesis in the past.

INFRARED PROPERTIES OF ISOLATED, IONIZED PAHS

Comparisons between the interstellar emission spectra and the absorption spectra of PAHs in KBr pellets show important differences which are used by some to draw conclusions about the nature of interstellar PAHs and by others to raise doubts as to the validity of the PAH hypothesis. While the overall similarities between the interstellar emission spectra and the available laboratory spectra of neutral, non-isolated PAHs are very suggestive, there are many differences in detail. These differences are not surprising since most of the available laboratory spectra are of neutral PAHs in solution or salt pellets, whereas if PAHs are indeed responsible for the interstellar emission, they would be positively charged and isolated in the emission zones. The laboratory media are not only highly perturbing, but in many cases the PAHs are not isolated, but clustered. In this situation the transitions are shifted, sometimes severely, and relative intensities are altered (Witteborn et al. 1989). Thus, it was felt plausible that the differences between the interstellar and laboratory spectra were artifacts of the laboratory techniques used.

Comparisons between the interstellar spectra and the previous laboratory spectra of PAHs showed the following important differences. First, the position and profile of the 3050 cm^{-1} (3.28 μm) interstellar band was never adequately reproduced. Second, the interstellar 1610 cm^{-1} (6.2 μm) and "1300" cm^{-1} ("7.7" μm) features are much more intense than the interstellar 890 cm^{-1} (11.2 μm) band, behavior which is just the opposite of that for the spectra of PAHs in KBr pellets and in solution, where the bands in the 900 -700 cm^{-1} (11-14 μm) region are typically five to eight times stronger (Figure 2). Third, the dominance of the 890 cm^{-1} (11.2 μm) interstellar feature in the 900-700 cm^{-1} (11-14 μm) range appeared to require extremely high degrees of dehydrogenation, a situation which seemed unreasonable to many. These important criticisms are addressed below.

3050 cm^{-1} (3.28 μm) Emission from Isolated PAHs

Initial comparisons between the interstellar 3050 cm^{-1} (3.28 μm) feature and the corresponding band of PAHs in KBr show mismatches in detail, a point considered to be a weakness of the gas phase PAH hypothesis. Recent, more appropriate, spectroscopic studies have addressed this issue. Elegant UV pumped, IR emission experiments on gas phase PAHs have been carried out by Cherchneff and Barker (1989), Shan, Suto, and Lee (1991), Brenner and Barker (1992), Schlemmer et al. (1994) and Williams and Leone (1994). The results of these experiments, in conjunction with absorption studies of PAHs in the gaseous state at various temperatures by Flickinger, Wdowiak, and Gomez (1991), Colangelli, Mennella, and Bussoletti (1992), Kurtz (1992), Joblin et al. (1995), and Wdowiak (1994), show that: (i) the emission peak frequency of the aromatic CH stretch in gas phase PAHs shifts as a function of internal energy content and matches that of the interstellar band at 3050 cm^{-1} at reasonable levels of excitation, (ii) the band-width increases with energy and matches that of the interstellar band at similarly appropriate internal energies, and (iii) the plateau which underlies the interstellar feature, and extends out to about 2740 cm^{-1} (3.65 μm), is reproduced as well. This plateau arises from anharmonically shifted $\Delta v = -1$ transitions originating in the v=1, 2, and 3 states overlapping with combinations and overtones of lower energy CC stretching vibrations.

The experiments just discussed, which were carried out on neutral PAHs, are inherently very difficult and it will probably be some time before this type of data becomes available for charged PAHs. Nonetheless, these results should be applicable to cationic PAHs, the form thought to be dominant in the emission zones, since removal of an electron from the pi-electron system should have little

effect on the CH stretch which is an in-plane motion involving atoms bound only by s-electrons.

Relative Band Intensities of Ionized PAHs

The second issue, that of the relative intensity mismatch between the interstellar bands and the laboratory spectra of PAHs in KBr or solvents, has recently been addressed in detail by laboratory studies of the IR spectroscopic properties of PAH cations. As shown in Figure 1, the interstellar 1610 cm^{-1} (6.2 μm) feature and broad emission envelope centered near 1300 cm^{-1} (7.7 μm), which are attributed to CC stretching and CH in-plane-bending vibrations, are *much* more intense than the interstellar feature near 890 cm^{-1} (11.2 μm) which is attributed to the CH out-of-plane bending mode. As illustrated by Figure 2, this behavior is just opposite that of PAHs in KBr pellets and in solvents where the bands due to the out-of-plane CH bending vibrations are often 5 to 8 times greater than the average band strength in the CC stretch and CH in-plane-bending region between about 1650 and 1100 cm^{-1} (6 and 9 μm). The relative intensities of the interstellar features have been taken by some as evidence that if interstellar PAHs are indeed responsible for the features, they must be severely dehydrogenated in spite of the fact that atomic hydrogen is on the order of 10,000 times more abundant than PAHs in most of the emission zones.

This difficulty is removed if the PAHs in space are largely ionized. Results on the infrared spectroscopic properties of fifteen PAH cations from the Ames Astrochemistry Laboratory and the Chemistry Department at the University of Florida have shown the following: (i) the intensity of the bands in the 1650 -1100 cm^{-1} range, the CC stretching and CH in-plane bending region of PAH cations, are typically 2 to 5 times greater than that of the CH out-of-plane bending modes which fall between 900 and 550 cm^{-1}, (ii) the CH out-of-plane bending mode of the cations is typically 5-20 times weaker than the out-of-plane bending mode of the neutrals, and (iii) the bands in the CC stretching and CH in-plane bending region are generally an order of magnitude stronger than that for the corresponding transitions in neutral PAHs (See Hudgins and Allamandola 1994, and Vala et al. 1994 for references). This experimental work, which confirms the behavior predicted theoretically by Defrees et al. (1993) and Pauzat et al. (1992), resolves one of the more troubling aspects of the interstellar PAH model.

In addition to this intensity reversal, it is important to stress that the strongest bands of all PAH cations studied to date fall within the envelope produced by the most intense interstellar features, those at 1610 cm^{-1} (6.2 μm) and 1300 cm^{-1} (7.7 μm); and that the bands in the CH out-of-plane region fall under the profile of the interstellar 890 cm^{-1} (11.2 μm) feature and pedestal. This is illustrated by Figure 4 which compares the 2000-770 cm^{-1} (5-13 μm) emission spectrum from the ionization ridge in Orion to a schematized version of the absorption spectrum expected from a mixture of PAH cations comprised of the most stable, small PAHs up to coronene ($C_{24}H_{12}$). While the absorption band frequencies of the PAH cations studied to date and plotted in Figure 4 do not reproduce the precise profile of the interstellar features, these first results are quite promising. Since PAH geometry influences the spectrum, and the more stable PAHs used to produce Figure 4 tend to have compact geometries, the regions in which there are PAH bands lacking will probably be filled in as the spectra of less compact PAH cations become available. There should also be a 5-10 cm^{-1} redshift between the peak frequencies plotted for most of the bands in Figure 4, which are for matrix-isolated PAH cations at 12°K, and the emission frequencies for these same PAHs (Colangeli, Mennella, and Bussoletti, 1992; Joblin et al. 1995). The

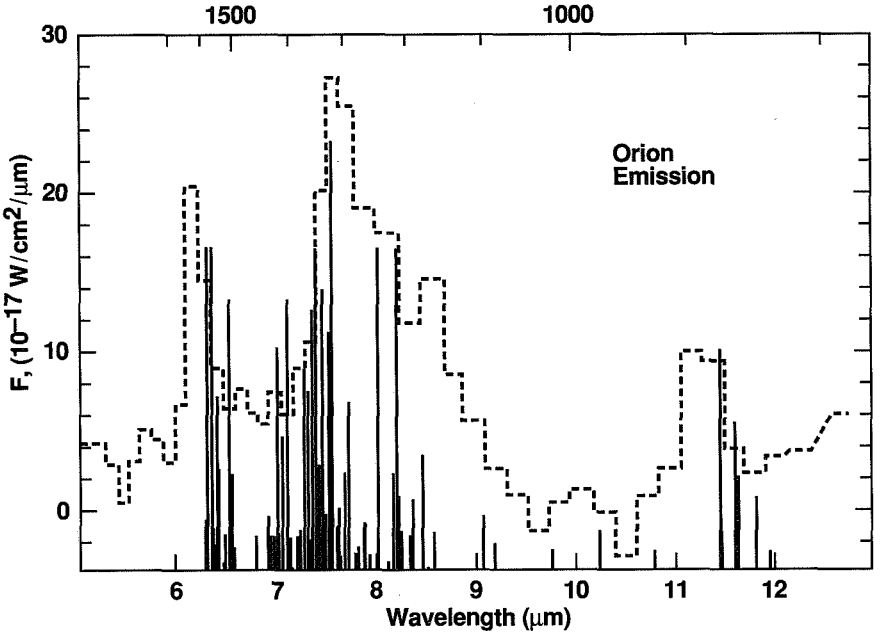

Figure 4. Schematic absorption spectrum (sticks) of a mixture of the PAH cations naphthalene, phenanthrene, pyrene, benzo[e]pyrene, benzo[ghi]perylene, and coronene with the 2000-770 cm^{-1} (5-13 μm) spectrum from the Orion nebula. (Orion-Bregman et al. 1988, PAH Hudgins and Allamandola 1995)

intensity contributions from the different molecules plotted in Figure 4 have been arbitrarily grouped into three categories, with the strongest bands for a particular molecule given a very strong, strong, or moderate weight. The rest of the band strengths for each molecule follow accordingly. Once a library of PAH cation spectra becomes available, such comparisons with interstellar spectra will shed light on the types of PAHs present in different objects.

Dominance of the 890 cm^{-1} (11.2 μm) Feature in the1000-666 cm^{-1} range

The third serious spectroscopic criticism concerns the dominance of the 890 cm^{-1} (11.2 μm) feature in the 1000-666 cm^{-1} (10-15 μm) range. Within the framework of the interstellar PAH model, features in this region are attributed to CH out-of-plane bending modes. Specifically, bands near 890 cm^{-1} (11.2 μm) are assigned to the out-of-plane bending vibration of non-adjacent peripheral H atoms. Bands at slightly lower frequencies are due to doubly and triply adjacent H atoms. Perusal of compact PAH geometries (the most stable, and thus most likely forms of interstellar PAHs) shows that many would have triply adjacent as well as doubly and non-adjacent peripheral H atoms. While the interstellar emission spectra show a broad plateau over this region, with substructure assigned to these different types of hydrogen (Cohen, Tielens, and Allamandola 1985; Witteborn et al. 1989; Roche, Aitken, and Smith 1989), the dominance of the 890 cm^{-1} interstellar band has been taken to indicate that non-adjacent H's are the most common, in spite of the fact that this seems highly unlikely given a reasonable mixture of PAHs.

Hudgins and Sandford (1995a,b) provides part of the solution to this puzzle. They show that the infrared cross sections for the out-of-plane bending modes are quite different for non-adjacent, doubly, and triply adjacent peripheral H atoms for individual PAH molecules. Individual non-adjacent H atoms absorb between 2 to 5 times more strongly than individual doubly adjacent H atoms, which in turn are 2 to 3 times as intense as individual triply adjacent H atoms. Thus, on first principles, if the interstellar mix had equal numbers of non-adjacent, doubly, and triply adjacent H atoms, one would expect relative intensities of the 890 cm^{-1} (11.2 μm) band to the interstellar subfeatures near 840 cm^{-1} (11.9 μm) and 787 cm^{-1} (12.7 μm) of about 12 to 3 to 1. This follows the general trend of the interstellar intensities observed in this region.

In conclusion, the availability of spectroscopic data on PAHs taken under astrophysically relevant conditions has alleviated the most significant weaknesses of the interstellar PAH hypothesis. The IR evidence for a mixture of isolated, ionized PAHs being responsible for the unidentified interstellar emission features associated with high excitation objects appears compelling. The next challanges are to increase the data base on the properties of PAHs under relevant interstellar conditions, to obtain higher resolution and higher signal-to-noise astronomical spectra, and to identify specific PAH species and PAH molecular classes associated with different types of astronomical objects.

ACKNOWLEDGEMENTS

We gratefully acknowledge the expert technical and experimental support of Robert Walker. Without his high standards and dedication to the Astrochemistry Laboratory most of the experimental work reported here would not have been possible. This work was fully supported by NASA's Laboratory Astrophysics and Long Term Space Astrophysics programs, under grants # 188-44-57-01 and # 399-20-01-05. The 2000-1250 cm^{-1} (5-8 μm) spectrum of Orion was obtained on the Kuiper Airborne Observatory.

REFERENCES

Aitken, D.K.1981, in Infrared Astronomy, eds C.G. Wynn-Williams and D.P. Cruikshank (D. Reidel, Dordrecht), 207

Allamandola, L.J.1984, in Galactic and Extragalactic Infrared Spectroscopy, eds M.F. Kessler and J.P. Phillips, (D. Reidel, Dordrecht), 5

Allamandola, L.J., Greenberg, J.M., and Norman, C.A.1979, AAp 77, 66

Allamandola, L.J., and Norman, C.A.1978, AAp. 66, 129

Allamandola, L.J., Sandford, S.A., and Wopenka, B. 1987, Science 237, 56

Allamandola, L.J., Tielens, A.G.G.M., and Barker, J.R. 1985, ApJL, 290, L25

Allamandola, L.J., Tielens, A.G.G.M., and Barker, J.R. 1987, in Polycyclic Aromatic Hydrocarbons and Astrophysics, eds, A. Leger, L.B. d'Hendecourt, and N. Boccara (D. Reidel, Dordrecht), 255

Allamandola, L.J., Tielens, A.G.G.M., and Barker, J.R. 1989, ApJS, 71, 733

Blanco, A., Bussoletti, E. and Colangeli, L. 1988, ApJ. 334, 875

Bregman, J.D., Allamandola, L.J., Tielens, A.G.G.M., Geballe, T.R., and Witteborn, F.C. 1989, Ap.J. 344,791

Brenner, J. D., and Barker, J. R. 1992, ApJL, L39

Cherchneff, I., and Barker, J.R. 1989, ApJL, 341, L21

Cohen, M., Tielens, A.G.G.M., and Allamandola, L.J. 1985, ApJ 299, L93

Colangeli, L., Mennella, V., and Bussoletti, E. 1992, ApJ 385, 577

Crawford, M.K., Tielens, A.G.G.M., and Allamandola, L.J. 1985, ApJ 293, L45

DeFrees, D.J., Miller, M.D., Talbi, D., Pauzat, F., and Ellinger, Y. 1993, ApJ, 408, 530.

Duley, W.W., and Williams, D.A. 1981, MNRAS, 196, 269
Flickinger, G. C., and Wdowiak, T.J., 1990, ApJL, L71
Flickinger, G.C., Wdowiak ,T.J., and Gomez ,P.L. 1991, ApJ, 380, L43
Giard, M., Pajot F., Lamarre, J.M., Serra, G., Caux, E., Gispert, R., Leger, A., Rouan, D., 1988, AAp, 201, L1
Gillett, F.C., Forrest, W.J., and Merrill, K.M. 1973, Ap J 183, 87
d'Hendecourt, L.B. and Leger, A. 1987, AAp, 180, L9
Hudgins, D.M.and Allamandola, L.J. 1994, J. Phys. Chem., in press
Hudgins, D.M.and Sandford, S.A. 1995a, J. Phys. Chem., in preparation
Hudgins, D.M.and Sandford, S.A. 1995b, ApJ, in preparation
Joblin, C., Boissel, P., Leger, A., d'Hendecourt ,L.B., and Defourneau, D. 1995, AAp, in press
Jones, A.P., Duley, W.W., and Williams, D.A. 1990, QJRAS, 31, 567
Kurtz, J. 1992, AAp, 255, L1
Leger, A. and d'Hendecourt, L.B.1985, AAp, 146, 81
Leger, A. and d'Hendecourt, L.B. 1987, in Polycyclic Aromatic Hydrocarbons and Astrophysics, editors: Leger, A, d'Hendecourt, L.B. and Boccara, N. (D. Reidel, Dordrecht), 223
Leger, A. and Puget, J.L. 1984, AAp, 137, L5
Lepp, S. and Dalgarno, A. 1988, ApJ, 324, 553
Low, F.J. et al. 1984, ApJL, 278, L19
Omont, A. 1986, AAp, 164, 159
Papoular, R., Ellis, K., Guillois, O., Reynaud, C., and Nenner, I. 1993, J. Chem.Soc. Faraday Trans. 89, 2289
Pauzat, F., Talbi, D., D.J., Miller, M.D., DeFrees, D.J.and Ellinger, Y. 1992, J. Phys. Chem.,96, 7882.
Phillips, M.M., Aitken, D.K. and Roche, P.F. 1984, MNRAS, 207, 25
Puget, J.L. and Leger A. 1989, ARAA 27, 161
Puget, J.L., Leger, A. and Boulanger, F. 1985, AAp, 142, L19
Roche P., Aitken D.K., and Smith,C.H., 1989, MNRAS 236, 485
Russell, R.W., Soifer, B.T., and Willner, S.P. 1977, ApJ 217, L149
Sakata, A., Wada, S., Onaka, T. and Tokunaga, A.T. 1990, Ap. J. 353, 543
Schlemmer, S., Cook, D.J., Harrison, J.A., Wurfel, B., Chapman, W., and Saykally, R.J. 1994, Science 265, 1686
Schutte, W., Tielens, A.G.G.M., and Allamandola, L.J. 1993, ApJ, 415, 397
Sellgren, K. 1984, Ap. J. 277, 627
Shan J., Suto M., and Lee, L.C. 1991, Ap J 383, 459
Tielens, A.G.G.M., 1989, in Submillimeter Wave Astronomy, ed. E.D Watt & D.S. Webster (Dordrecht: Reidel), 273
Vala, M., Szczepanski, Pauzat, F., Parisel, O., Talbi, D., and Ellinger, Y. 1994, J.Phys Chem., in press
van der Zwet, G.P. and Allamandola, L.J. 1985, AAp 146, 76
Wdowiak, T.J. 1994, private communication
Wdowiak, T.J., Flickinger, G.C. and Cronin, J.R. 1988, ApJL, 328, L75
Williams, R. M., and Leone, S. R. 1994, in The Diffuse Interstellar Bands: Contributed Papers, ed. A.G.G.M. Tielens, NASA CP 10144, 59
Willner, S.P. 1984, Galactic and Extragalactic Infrared Spectroscopy, eds M.F. Kessler, and J.P. Phillips (D. Reidel, Dordrecht), 37
Willner, S.P., Soifer, B.T., Russell, R.W., Joyce, R.R., and Gillett, F.C. 1977, ApJ 217, L121
Witteborn, F.C., Sandford, S.A., Bregman, J.D., Allamandola, L.J., Cohen, M., Wooden, D.H., and Graps, A.L. 1989, ApJ 341, 270

Airborne Astronomy Symposium on the Galactic Ecosystem
ASP Conference Series, Vol. 73, 1995
M.R. Haas, J.A. Davidson, and E.F. Erickson (eds.)

SUBMILLIMETER SPECTROSCOPY OF INTERSTELLAR HYDRIDES

J. ZMUIDZINAS, G. A. BLAKE†, J. CARLSTROM, J. KEENE, D. MILLER, P. SCHILKE, N. G. UGRAS
Division of Physics, Mathematics, and Astronomy, and †Division of Geological and Planetary Sciences, California Institute of Technology, 320-47, Pasadena, CA 91125

ABSTRACT We discuss airborne observations of rotational transitions of various hydride molecules in the interstellar medium, including $H_2{}^{18}O$ and HCl. The detection of these transitions is now feasible with a new, sensitive submillimeter receiver which has been developed for the NASA Kuiper Airborne Observatory (KAO) over the past several years.

INTRODUCTION

Atmospheric water vapor is responsible for the generally poor atmospheric transmission in the submillimeter band (300-3000 GHz). In particular, even for observatories located on dry high-altitude sites such as Mauna Kea, the atmosphere is essentially opaque between 500-600 GHz and 700-800 GHz because of the very strong water lines at 547 GHz and 752 GHz. In addition, ground-based submillimeter observations are impossible above 900 GHz. Nonetheless, these portions of the spectrum are very interesting astronomically because they contain many fundamental rotational transitions of hydride molecules, such as CH at 532 and 536 GHz, $H_2{}^{18}O$ at 547 and 745 GHz, NH_3 at 572 GHz, HCl at 626 GHz, CH_2 at 945 GHz, and H_3O^+ at 985 GHz. Observations of these molecules are important for testing our understanding of the chemistry of molecular clouds, since the hydrides are the initial products of the ion-molecule reaction network which is thought to be responsible for the synthesis of more the more complex molecules commonly observed at radio and millimeter wavelengths.

In addition, hydrides may play a crucial role in the energetics of molecular clouds, particularly at the high densities found in star-forming cores, because their large rotational level spacings and large dipole moments make them very effective coolants. In fact, it is possible that cooling due to hydrides, especially H_2O, plays a decisive role in establishing the rate at which molecular clouds collapse, and thus ultimately controls the efficiency of star formation.

The Kuiper Airborne Observatory (KAO) is the only platform at present which allows observations of the transitions listed above (with perhaps the

exception of HCl, which can be observed from Mauna Kea in extremely good weather). Although some of these molecules can also be observed through transitions at radio wavelengths, airborne observations of the fundamental rotational transitions can often give essential information regarding the abundance and excitation of these species.

In this paper, we discuss studies of interstellar $H_2{}^{18}O$ and HCl we have been pursuing over the past two years. We have also detected the CH transitions at 532 and 536 GHz in Orion, W51, M17, and other sources, but these observations will not be discussed in this paper due to the limited space. The observations which we present were obtained with a new submillimeter heterodyne receiver developed for the KAO, which at present operates over the 500-750 GHz band, which is described in a paper elsewhere in this volume (Zmuidzinas *et al.* 1994b).

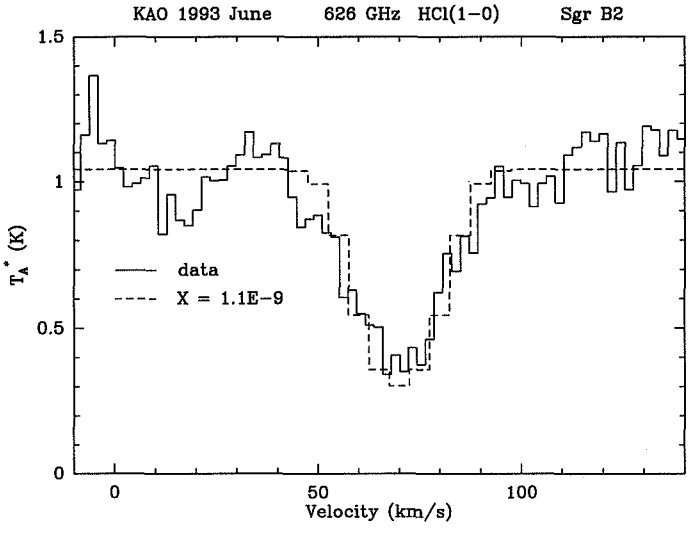

Figure 1. Solid line: detection of the 626 GHz HCl line in absorption toward Sgr B2. Dashed line: spectrum predicted by our radiative transfer model for a fractional abundance of $HCl/H_2 = 1.1 \times 10^{-9}$.

HCl IN ABSORPTION IN SGR B2

The abundance of atomic chlorine in diffuse interstellar clouds has been studied using ultraviolet absorption lines by Jura & York (1978), Harris & Bromage (1984), and Harris, Gry, and Bromage (1984). These studies have shown that the depletion of chlorine (on dust grains) in diffuse clouds is not severe, with

abundances at most a factor of 2-3 below the solar value of Cl/H $\approx 2 \times 10^{-7}$ (Anders & Grevesse 1989), although there is some indication that the depletion increases with density. It would be very interesting to study the depletion in denser regions; however, ultraviolet studies of dense clouds are obviously impossible. The submillimeter rotational transitions of HCl may be a useful probe of the chlorine depletion in dense molecular clouds, since gas-phase chemical models predict that a substantial fraction (> 10%) of chlorine will be in the form of HCl (Jura 1974; Dalgarno *et al.* 1974; Blake, Anicich, & Huntress 1986; Schilke, Phillips, & Wang 1994).

The 626 GHz $J = 1 \rightarrow 0$ line was first detected in OMC-1 from the KAO by Blake, Keene, and Phillips (1985). The observed emission line ($T_A^* \approx 0.7\ K$) was interpreted to give $HCl/H_2 \sim 0.5 - 5.0 \times 10^{-8}$, which corresponds to a probable range of chlorine depletion of 3-30 (below solar). The lower end of this range could be consistent with the chlorine depletion in diffuse clouds, but Neufeld and Green (1994) have recently reanalyzed this data using improved collisional excitation rates and a more detailed radiative transfer model, and argue that in fact the abundance may be only 2×10^{-9}. Hence, it is likely that chlorine is either heavily depleted or the fraction of chlorine in HCl is much smaller than the predictions of the chemical models.

During a June 1993 KAO deployment to Hickam AFB in Honolulu, HI, we detected the 626 GHz line in absorption against the submillimeter continuum from the Sgr B2 (N) and (M) dust cores (Figure 1). It is not entirely surprising that the line is in absorption, given the fact that this is a ground-state transition which has a very large critical density of $n_{cr} = 4 \times 10^7 \mathrm{cm}^{-3}$. Furthermore, Sgr B2 has an extended envelope of moderate density, relatively cool molecular gas which could produce the absorption. However, Sgr B2 is also known to have very massive, dense, and hot cores, which might have been expected to produce an emission line instead.

To clarify the situation, we created a detailed radiative transfer model. The model assumes a spherical cloud whose density and temperature (dust and gas) vary with radius as

$$n(r) = 2.2 \times 10^3 \ + \ 8.6 \times 10^4 \left(\frac{r}{1\ \mathrm{pc}}\right)^{-2} \ \mathrm{cm}^{-3}$$

and

$$T(r) = 40 \left(\frac{r}{1\mathrm{pc}}\right)^{-0.5} \ \mathrm{K}\ .$$

This simple cloud model is based on the work of Lis, Goldsmith and collaborators, and is consistent with a map of $C^{18}O(1-0)$ (Lis & Goldsmith 1989) and with a large variety of dust continuum observations ranging from 4″ OVRO interferometer measurements at $\lambda = 1.3$ mm to the continuum intensity we observe in our 2′ KAO beam at $\lambda = 479\ \mu$m (Zmuidzinas *et al.* 1994a). Our radiative transfer program subdivides this model cloud into 200 radial shells, and self-consistently solves for the level populations and radiation intensities in each shell using an accelerated lambda-iteration method (Rybicki & Hummer 1991). This model treats collisional and radiative excitation of the molecular levels up to $J = 11$, and includes emission and absorption of radiation by both molecules and dust.

The model is successful in predicting our observed absorption line (Figure 1). The abundance needed to obtain the measured line to continuum ratio is $HCl/H_2 \approx 1.1 \times 10^{-9}$; hence, it appears that the chlorine is depleted by a factor of 50-180 below the solar abundance, if in fact HCl represents 10-30% of the gas-phase chlorine as predicted by the chemical models. This conclusion is fairly robust, since the same HCl fractional abundance can be obtained by comparing an HCl column density of 1.6×10^{14} cm^{-2} derived from the integrated optical depth (determined from the line to continuum ratio), to an H_2 column density of 1.5×10^{23} cm^{-2} for the absorbing envelope (determined from the $C^{18}O$ map of Lis & Goldsmith 1989). The radiative transfer model verifies that the assumptions inherent in this simple calculation are correct, and that the absorption line is indeed formed in the cool, presumably quiescent outer layers of the cloud, corresponding to $r > 5$ pc, $n \sim 6 \times 10^3$ cm^{-3}, and $T_{\rm dust} \sim 20$ K. An interesting prediction of our model is that dust continuum radiation dominates the excitation of the rotational levels of HCl throughout the cloud; this is quite plausible since Sgr B2 is a very bright continuum source and since the critical density of the 626 GHz transition is very large, $n_{cr} = 4 \times 10^7$ cm^{-3}.

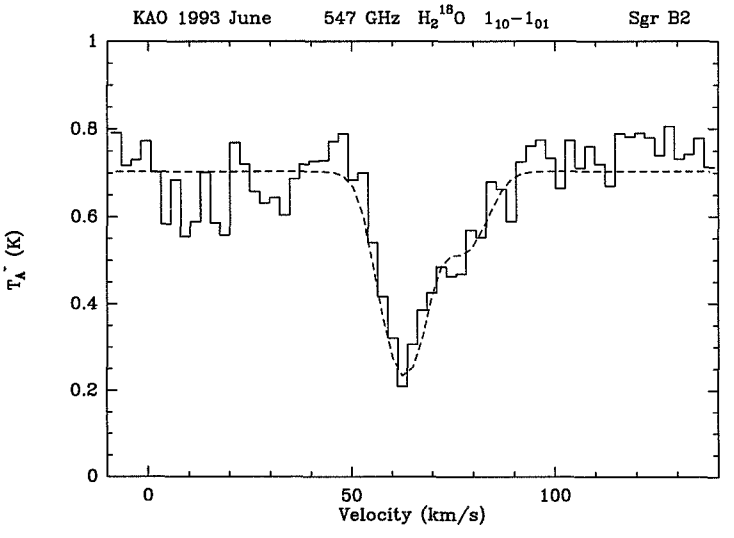

Figure 2. The 547 GHz $H_2{}^{18}O$ transition detected in absorption in Sgr B2. The dashed line is the prediction of a simple model consisting of a background continuum source ($T_A^* \approx 0.7$ *K*) and a foreground cloud with two velocity components. The *minimum* $H_2{}^{18}O$ column density capable of producing this absorption is about 1.1×10^{14} cm^{-2}.

AIRBORNE STUDIES OF OXYGEN-18 WATER

Oxygen is the third most abundant element, and yet surprisingly little is understood about the chemistry of oxygen in molecular clouds. Potentially abundant oxygen-bearing species include O, O_2, and H_2O, but ground-based observations of these species are obviously difficult. Although the 22 GHz H_2O masers are very well known, the energy levels of the $6_{16} \rightarrow 5_{23}$ transition lie about 640 K above the ground state. In fact, this is why the 22 GHz transition is observable from the ground, and partially explains why the masers are thought to arise from very dense and hot clumps of gas rather than the more ordinary regions of molecular clouds. If it is abundant, water may also be the major coolant of dense star-forming regions, since the water molecule has a strong asymmetric rotor spectrum with transitions throughout the submillimeter and far-infrared.

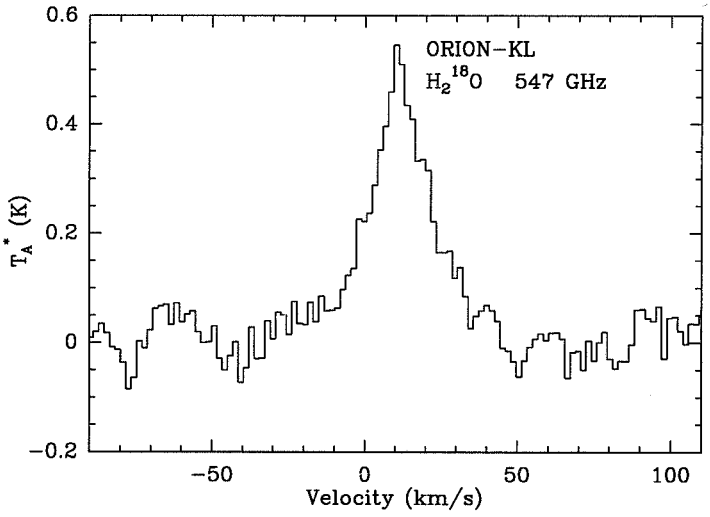

Figure 3. Detection of the $1_{10} - 1_{01}$ 547 GHz ground-state transition of ortho-$H_2{}^{18}O$ in Orion-KL.

To probe the abundance of water in a more general way, one must observe lower lying transitions which are more likely to be populated under the typical conditions found in interstellar clouds. However, absorption by atmospheric H_2O precludes this approach, unless one takes advantage of the fact that the lines of $H_2{}^{18}O$ are slightly shifted in frequency due to the somewhat larger moments of inertia. However, the isotopic ratio is $^{16}O/^{18}O \approx 500$, so the $H_2{}^{18}O$ lines are weak. Nonetheless, we have recently detected the 547 GHz ground-state transition and the 745 GHz transition ($E_{\rm lower} \approx 100\ K$) in Orion-KL using our SIS receiver on

the KAO. We have also detected the 547 GHz line in absorption toward Sgr B2. Using the Caltech Submillimeter Observatory (CSO), we have followed up the airborne observations with detections of the 391 GHz transition ($E_{\rm lower} \approx 300\ K$) in Orion-KL, Sgr B2, and several other sources as well.

The 547 GHz $H_2{}^{18}O$ absorption line in Sgr B2 is shown in Figure 2. This detection can be analyzed in the same manner as the HCl absorption line, since the critical densities and A-coefficients of these two ground-state transitions are similar. The integrated optical depth determined from the line to continuum ratio implies a minimum $H_2{}^{18}O$ column density of 1.1×10^{14} cm^{-2}. As in the case of HCl, we suspect that this is the actual column density in the low excitation molecular envelope that we are sampling. Thus, we arrive at a fractional abundance of $H_2{}^{18}O/H_2 \approx 7 \times 10^{-10}$, again taking the relevant H_2 column density to be 1.5×10^{23} cm^{-2} for the absorbing envelope. Since the isotopic ratio near the center of the galaxy is thought to be $^{16}O/^{18}O \approx 250$, we obtain $H_2O/H_2 \approx 1.7 \times 10^{-7}$. This value is low, but within the range predicted by current chemical models.

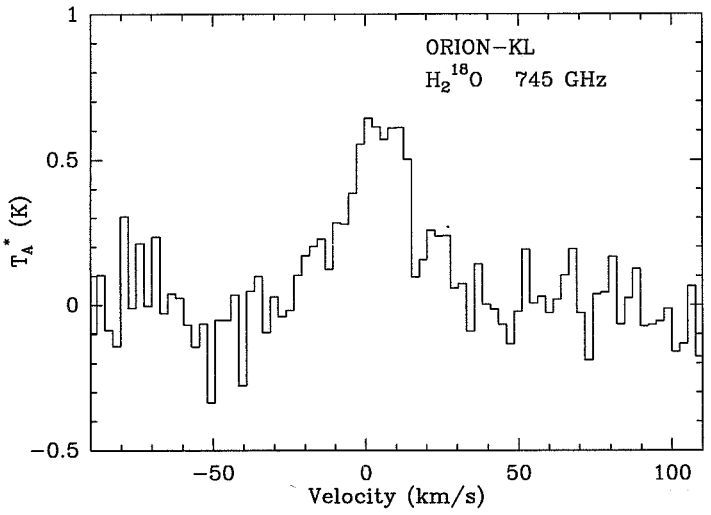

Figure 4. Detection of the $2_{11} - 2_{02}$ 745 GHz transition of para-$H_2{}^{18}O$ in Orion-KL. The energy of the lower level in this transition is about 100 K.

$H_2{}^{18}O$ may have previously been detected in Orion-KL through the 203 GHz and 321 GHz transitions using ground-based telescopes. However, these observations are badly confused by strong nearby SO_2 lines which hampers their interpretation. As Figures 3 and 4 show, we have unambigously detected the 547 and 745 GHz lines from the KAO. In addition, we have obtained a solid

detection of the 391 GHz line from the CSO. All of these $H_2{}^{18}O$ observations of Orion-KL are summarized in the table below.

$H_2{}^{18}O$ LINES DETECTED IN OMC-1

Telescope	ν (GHz)	Line	$E_{\rm lower}$ (K)	$\theta_{\rm beam}$ (arcsec)	T_A^* (K)
NRAO [a]	203	$3_{13} \rightarrow 2_{20}$	194	30	0.9
CSO [b]	322	$5_{15} \rightarrow 4_{22}$	452	20	0.6
CSO [c]	391	$4_{14} \rightarrow 3_{21}$	303	17	2.5
KAO [c]	547	$1_{10} \rightarrow 1_{01}$	0	150	0.55
KAO [c]	745	$2_{11} \rightarrow 2_{02}$	101	110	0.65

[a] Jacq *et al.* 1988; blended with SO_2 $12_{0,12} \rightarrow 11_{1,11}$.
[b] Menten *et al.* 1990; blended with SO_2 $34_{4,30} \rightarrow 33_{5,29}$.
[c] Zmuidzinas *et al.* 1994.

We have attempted a simple rotation diagram analysis of these lines, which yields H_2O abundances in the 10^{-7} range, but the large variation in beamwidths makes the results fairly sensitive to the assumed source size. In addition, the 547 GHz line appears to be weaker than what one would extrapolate from the higher-lying transitions, and furthermore, the line profile of the 547 GHz transition does not seem to be consistent with either the 745 or 391 GHz profiles. Thus, we speculate that there may be foreground lower excitation gas which partially absorbs the 547 GHz radiation and distorts the line shape. We hope to learn more about the spatial distribution of $H_2{}^{18}O$ by mapping the 391 GHz transition at the CSO, and perhaps by mapping the 203 GHz transition with the OVRO interferometer. This could give us the source size and therefore reduce the ambiguity in the rotation diagram analysis. In addition, these maps might tell us whether the "hot core" or "low-velocity outflow" component is primarily responsible for the $H_2{}^{18}O$ emission, and therefore whether evaporation from radiatively heated dust grains or shock chemistry is leading to a substantial enhancement of the $H_2{}^{18}O$ abundance. We have some hint of the answer from the linewidths of the $H_2{}^{18}O$ transitions that we observe, which seem to be more consistent with the "low-velocity outflow" source than with the "hot core", but the inconsistency in the observed line profiles points to several emission (or absorption) components.

ACKNOWLEDGEMENTS

We are deeply grateful to the staff of the Kuiper Airborne Observatory for their invaluable assistance with this new project, and commend their enthusiasm and dedication to airborne astronomy. We also thank T. Phillips, D. Neufeld, W. Langer, and G. Melnick for illuminating discussions. We are also indebted to A. Betz and R. Boreiko for the loan of their AOS. This work was supported by a grant from the NASA Airborne Astronomy program (NAG2-744). SIS mixer development at Caltech is supported by NASA grant NAGW-107, NASA/JPI, and a NSF PYI grant to J. Zmuidzinas.

REFERENCES

Anders, E., & Grevesse, N. 1989, Geochim. Cosmochim. Acta, 53, 197

Blake, G. A., Keene, J., & Phillips, T. G. 1985, ApJ, 295, 501

Blake, G. A., Anicich, V. G., & Huntress, W. T. 1986, ApJ, 300, 415

Dalgarno, A., de Jong, T., Oppenheimer, M., & Black, J. H. 1974, ApJL, 192, L37

Harris, A. W., & Bromage, G. E. 1984, MNRAS, 208, 941

Harris, A. W., Gry, C., & Bromage, G. E. 1984, ApJ, 284, 157

Jacq, T., Jewell, P. R., Henkel, C., Walmsley, C. M., & Baudry, A. 1988, A&A, 199, L5.

Jura, M.1974, ApJL, 190, L33

Jura, M., & York, D. G. 1978, ApJ, 219, 861

Lis, D. C., & Goldsmith, P. 1989, ApJ, 337, 704

Menten, K. M., Melnick, G. J., Phillips, T. G., & Neufeld, D. A. 1990, ApJL, 363, L27.

Neufeld, D. A., & Green, S. 1994, ApJ, in press.

Rybicki, G. B., & Hummer, D. G. 1991, A&A, 245, 171

Schilke, P., Phillips, T. G., & Wang, N. 1994, in prep.

Zmuidzinas, J., Blake, G. A., Carlstrom J., Keene, J., Miller, D., & Schilke, P. 1994a, in prep.

Zmuidzinas, J., Carlstrom, J., Miller, D., & Ugras, N. G. 1994b, in Proc of the Airborne Astronomy Symp on the Galactic Ecosystem: From Gas to Stars to Dust, ed. M. R. Haas, J. A. Davidson, & E. F. Erickson (San Francisco: ASP), paper 710.

Airborne Astronomy Symposium on the Galactic Ecosystem
ASP Conference Series, Vol. 73, 1995
M.R. Haas, J.A. Davidson, and E.F. Erickson (eds.)

FIR Line Profiles as Probes of Warm Gas Dynamics

A. L. Betz and R. T. Boreiko
Center for Astrophysics & Space Astronomy, University of Colorado, Boulder, CO 80309

Abstract. Measurements of the shapes, velocities, and intensities of FIR lines all help to probe the dynamics, physical associations, and excitation conditions of warm gas in molecular clouds. With this in mind, we have observed the J=9-8, 12-11, 14-13, and 16-15 lines of ^{12}CO and the 158 micron line of C II in a number of positions in 4 selected clouds. The data were obtained with a laser heterodyne spectrometer aboard NASA's Kuiper Airborne Observatory. Line measurements at 0.6 km/s resolution allow us to resolve the profiles completely, and thereby to distinguish between UV- and shock-heating mechanisms for the high-excitation gas. For CO, the high-J linewidths lie in the range of 4-20 km/s (FWHM), similar to those observed for low-J (J<4) transitions in these sources. This correspondence suggests that the hotter gas (T = 200-600 K) is dynamically linked to the quiescent gas component, perhaps by association with the UV-heated peripheries of the numerous cloud clumps. Much of the C II emission is thought to emanate from these cloud peripheries, but the line profiles generally do not match those seen in CO. None of the observed sources show any evidence in high-J ^{12}CO emission for shock-excitation (i.e., linewidths > 30 km/s).

1. Introduction

The uniqueness of the CO molecule as a probe of molecular clouds is well recognized. CO is abundant and durable, and the relatively low permanent dipole moment of 0.1 D keeps the critical density for collisional excitation within bounds possible in dense clouds, at least for the lower levels (J<10). A large number of levels are energetically accessible under typical molecular cloud conditions. Studies in the millimeter transitions of CO have given valuable information on the dynamics and structure of cool material throughout molecular clouds. In particular, observations of the (usually) optically thick J=1-0 and J=2-1 transitions of ^{12}CO have established the conditions on the cloud peripheries. Similarly, the high-J CO lines (which have more stringent excitation requirements) are important for selectively probing regions of higher density and temperature.

In many cases, however, the interpretation of line intensities is complicated by a variety of systematic effects which make a straightforward LTE analysis impossible. Obvious examples are beam dilution (the telescope is too small) and subthermal excitation (the source is too diffuse). Because we cannot generally eliminate these problems, we resort to modeling of the data, often in more

detail than is justified by the number of available measurements. In spite of the uncertainty associated with interpreting intensities, we can extract quantitative information from the observed velocities and line widths if we have adequate spectral resolution. It is especially useful to compare high J (J>10) and low J (J<4) line profiles to establish the dynamical relationships between hot and cold gas. The required resolution is 3 parts in 10^6 km s^{-1}, easily achievable with heterodyne spectroscopy.

We observed the J=12-11, 14-13, and 16-15 transitions of ^{12}CO in M17, W3, DR21, and W51, all of which have previously been observed in the ^{12}CO and ^{13}CO J=9-8 transitions (Boreiko & Betz 1991) and for which numerous lower J observations are available. For comparison, high resolution observations of C II in M17 and DR21 are presented by Boreiko, Betz & Zmuidzinas (1990).

2. Observations

The observations were done on the Kuiper Airborne Observatory in 1991 August and 1992 September using a far-infrared laser heterodyne spectrometer (Betz & Boreiko 1993). Radiation from the telescope is combined with a local oscillator (LO) signal from a far-infrared molecular laser pumped by a CO_2 laser. The beams are focused on a liquid nitrogen-cooled GaAs Schottky diode mixer which has a wide IF bandwidth of 24 GHz. The difference frequency between the LO and signal radiation is amplified by a cooled HEMT amplifier and then is converted in an RF mixer to a base band. The back end consists of a 1000 channel acousto-optic spectrometer with 1 GHz bandwidth and 3.2 MHz spectral resolution. System temperatures increase approximately linearly from 7500 K to 10200 K over the observed range of 1350 to 1850 GHz. Examples of observed spectra for M17 and W3 are shown in Figures 1 and 2.

3. Discussion

A lower limit to the excitation temperature can be derived from the line peak intensity ratios under the unlikely condition of LTE. In this case, the minimum excitation temperature for the 4 sources observed is about 150-250 K. Figure 3 clearly illustrates for two of the sources (DR21 and W3 IRS5) the necessity of modeling to obtain a more probable estimate for the conditions within the molecular cloud. For example, for DR21, a temperature as low as the 170 K used for the illustrative curve leads to higher mid- and low-J emission than is observed. By contrast, for W3 IRS5, there is no discrepancy with lower J emission, but that from the highest transition observed is too low compared with the expectation from 250 K gas in LTE. The most likely solution is that the excitation temperature significantly exceeds the minimum values listed here, and that the upper levels are subthermally populated. Critical densities for the transitions increase with J, leading to the additional complication that beam filling factors are likely to decrease for the higher transitions. More detailed analysis of the data taking these complications into account is underway.

The observed linewidths are all narrow, ranging from 4 to 12 km s^{-1} for the four sources, and identical for all three transitions. Thus we can reasonably preclude shock excitation as a source for the observed emission, and infer that

UV excitation of the quiescent gas component is the likely excitation mechanism. In addition, for all sources the line widths are smaller than those observed with similar beam sizes (about 50″) in the J=2-1 and J=1-0 transitions of ^{12}CO or in the 158 μm C II line. This suggests a smaller velocity dispersion for the dense gas producing the high-J CO emission compared with the more widespread and diffuse material that gives rise to low-J CO and C II radiation. The V_{lsr} centroid values, however, are identical for the high-J CO, low-J CO, and C II lines. Thus, there is a dynamical association between the hot gas seen in high-J CO data, the photodissociated gas traced by C II, and the cooler "quiescent" gas component of low-J emission.

This work was supported by NASA Grants NAG2-254 and NAG2-753.

References

Betz, A. L., & Boreiko, R. T. 1993, ASP Conf. Series, 41, 349
Boreiko, R. T., & Betz, A. L. 1991, ApJ, 369, 382
Boreiko, R. T., Betz, A. L., & Zmuidzinas, J. 1990, ApJ, 353, 181

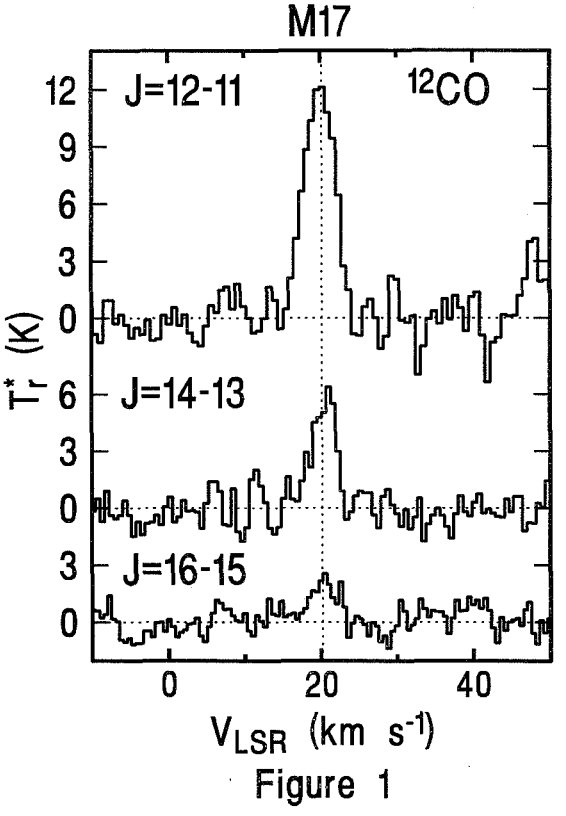

Figure 1

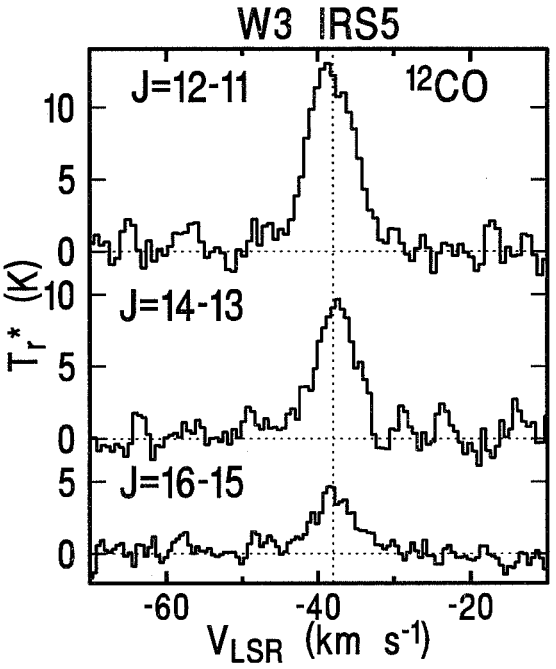

Figure 2

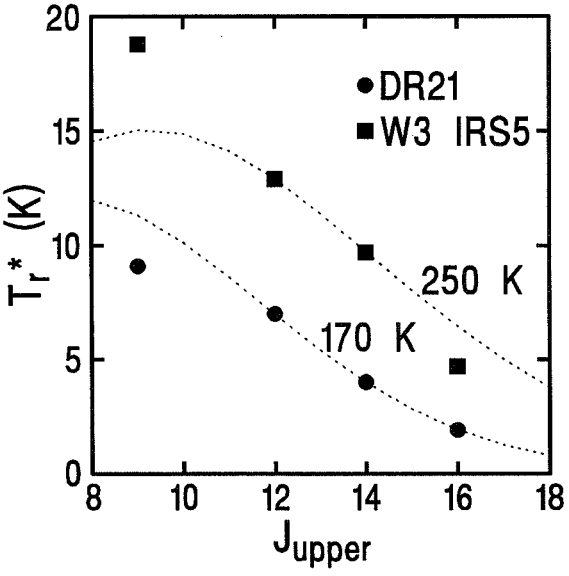

Figure 3

Airborne Astronomy Symposium on the Galactic Ecosystem
ASP Conference Series, Vol. 73, 1995
M.R. Haas, J.A. Davidson, and E.F. Erickson (eds.)

The Future of Magnetic Field Mapping in The Interstellar Medium

Alyssa A. Goodman
Harvard University Department of Astronomy,
60 Garden Street, Cambridge, MA 02138

Abstract. This paper explains why far-infrared and sub-mm polarimetry should be used instead of background starlight polarimetry in order to map the magnetic field in the dense ($>10^3 cm^{-3}$) regions of the interstellar medium. Results indicating the inadequacy of background starlight polarimetry, as well as the promise of far-infrared polarimetry, are discussed.

1. Introduction

Our physical picture of the interstellar medium (ISM) will remain critically incomplete until we can include a three-dimensional view of the magnetic field. Over the past four decades, polarimetry of background starlight has been the primary tool for deciphering the magnetic field structure in our Galaxy's neutral ISM. Recently, airborne far-infrared and ground-based mm- and sub-mm polarimetry have been added to this toolbox, and this paper illustrates why these newer techniques are the future of magnetic field mapping in the ISM.

2. Understanding Polarization of Background Starlight

As starlight travels through the ISM, it occasionally encounters a dust grain of a size comparable to its own wavelength. When this happens, if the grain is asymmetric, the light becomes weakly linearly polarized along the direction of the grain's shortest axis, as projected onto the plane of the sky. In 1951, Davis and Greenstein (DG) explained that the observed polarization of background starlight is likely to be due to a population of such asymmetric dust grains which have been systematically aligned by interstellar magnetic fields. This explanation, with a few refinements (e.g. see Purcell 1979), is still accepted today.

With the DG theory as justification, several researchers have used background starlight polarimetry in attempts to map out the magnetic field in the ISM by using the polarization direction to represent the line-of-sight-averaged plane-of-the-sky field direction. Often, spectacular results are achieved with this technique, such as the Mathewson and Ford (1970) polarization map of the local ISM which shows that the magnetic field follows the plane of the Galaxy rather closely, except for excursions out of the plane to wrap around the local bubbles so evident in H I maps (e.g. Heiles and Jenkins 1976). There is, however, a danger in considering this technique to be generally applicable: not every dust grain is equally good at polarizing light. If one looks along lines of sight where a disproportionate number of grains are especially

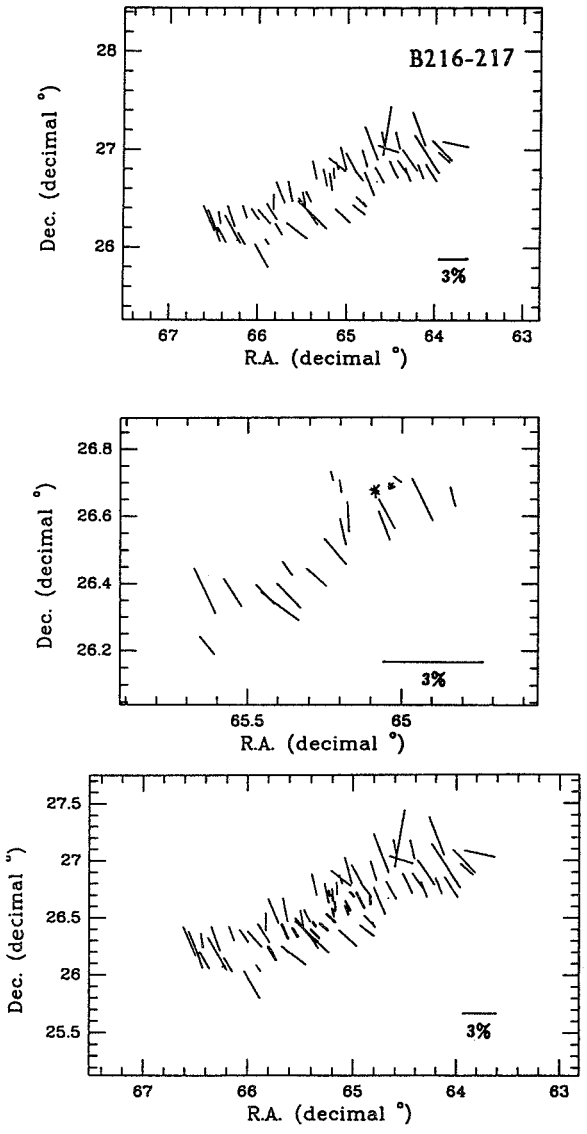

Figure 1a: *Top panel:* Optical (~6500 Å) polarization map of the B216-217 dark cloud (Heyer et al. 1987). *Middle panel:* Near-infrared (2.2 micron) polarization map of the B216-217 dark cloud (Goodman et al. 1992). *Bottom panel:* Superposition of optical and infrared polarimetry based on the data shown in the two panels above.

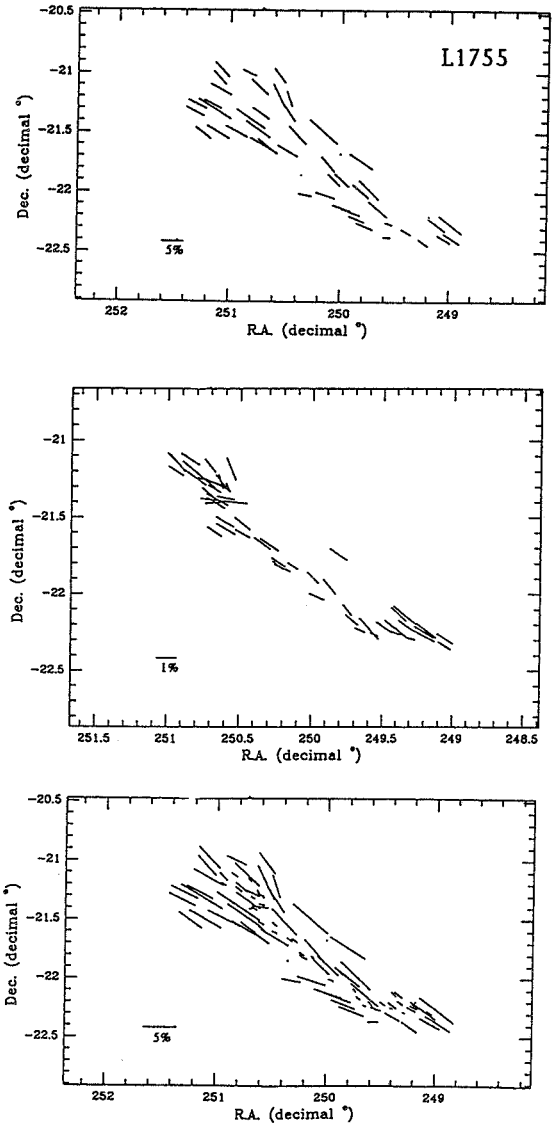

Figure 1b: *Top panel:* Optical (6500 Å) polarization map of the L1755 dark cloud (Goodman et al. 1990). *Middle panel:* Near-infrared (2.2 micron) polarization map of the L1755 dark cloud (Goodman et al. 1994). *Bottom panel:* Superposition of optical and infrared polarimetry based on the data shown in the two panels above.

good or bad at polarizing light, then the polarization observed is no longer a fair representation of the "average" plane-of-the-sky field direction along the line of sight.

Recently, there has been a great deal of interest in magnetic fields in the dense ($>10^3 cm^{-3}$) ISM (Heiles et al. 1991), and especially in star-forming clouds. These dense (a.k.a. "dark") clouds are visually opaque, so polarization of *visual* starlight can only be measured around their periphery. However, even in the periphery of a nearby dark cloud the extinction is high enough so that the vast majority of the grains along the line of sight are associated with the cloud. Thus, the presumption was that a polarization map of a dark cloud would reveal the field associated with the cloud (e.g. Vrba, Strom and Strom 1976). The top panels in Figures 1a and 1b show optical background-starlight polarization maps of the elongated dark clouds B216-217 and L1755, respectively. In B216-217, the field would appear to be perpendicular to the long axis of the cloud, and in L1755, parallel. However, larger scale optical polarimetry shows that these "systematic" field-cloud orientations may be accidental, in that other elongated clouds near B216-217 and L1755 show the same field direction, but different orientation (Goodman et al. 1990).

In an attempt to see if the field structure "inside" these dark clouds was different than around their peripheries, we measured the polarization of background starlight at *near-infrared* wavelengths, through up to ~10 magnitudes of extinction, in the "dark" interiors of B216-217 and L1755 (Goodman et al. 1992, 1994). The results of these observations are shown in the middle panels of Figures 1a and 1b. It is evident (see lower panels of Fig. 1a and 1b) that the optical and near-IR polarimetry are *tracing the same field,* despite the fact that the near-IR lines of sight pass through much denser gas. Thus, we are led to two choices: **1)** the magnetic field structure is not influenced at all by the presence of the density enhancements represented by the dark clouds; or **2)** *background starlight polarimetry is not revealing the true field in the dark clouds.* Possibility #1 is physically quite unlikely, and the relationship between polarization and extinction indicates that possibility #2 is very likely.

Figure 2 shows that the percentage of polarization appears to be independent of extinction in B216-217 and L1755 (middle panel), and rises only very slowly with extinction in other (rounder) dark clouds (lower panel). In other words, one can add more and more dust to a dark cloud, producing higher and higher extinction, without influencing the polarization. *If every grain producing extinction were also producing polarization, one would clearly expect a rise in polarization with extinction.* Field tangling can reduce the slope of this rise, but even a model assuming equipartition between a tangled and straight field (the solid line in Fig. 2) predicts a slope much larger than what is observed (Jones, Klebe & Dickey 1992).

The results in Figures 1a, 1b, and 2 can be reconciled in a scenario like the one shown schematically in Figure 3. It is well known that there is a wide array of grain types in the ISM, many of which contribute significantly to extinction of background starlight. Yet, only "special" grains which are aligned, asymmetric, of a certain composition, and of a size not too dissimilar from the wavelength of the incident light will produce polarization of background starlight. These special *polarizing* grains form a subset of the grains producing *extinction*. If a particular region (e.g. a dark cloud) is deficient in such efficiently polarizing grains, then the

field in that region is effectively "invisible" to background starlight polarimetry. We suspect that this polarization-efficiency-weighting, caused by variations in grain properties, is critical in interpreting background starlight polarization maps, especially of the dense interstellar medium. In dense clouds, the gas is overwhelmingly molecular, and many molecule-forming reactions take place on the surface of grains.

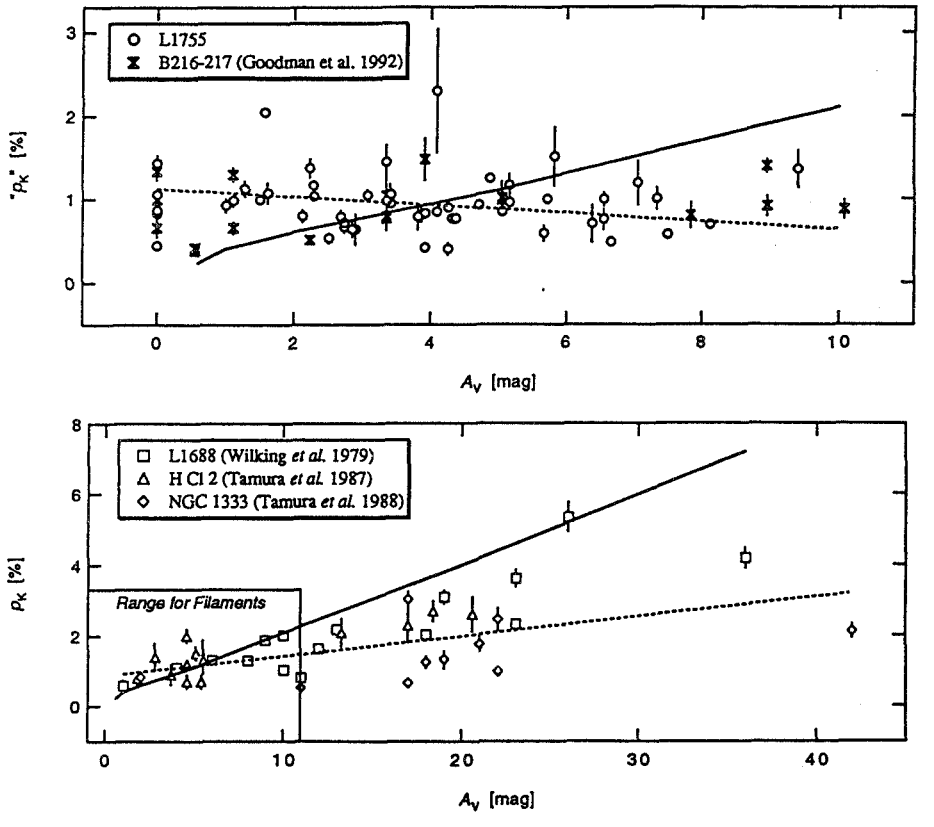

Figure 2: Observed relationships between polarization and extinction in dark clouds. *Top panel:* Data for filamentary dark clouds, B216-217 and L1755 (Goodman et al. 1992; 1994). *Bottom panel:* Data for L1688 (Wilking et al. 1979), HCl 2 (Tamura et al. 1987), and NCG 1333 (Tamura et al. 1988), dark clouds which are closer to round, in projection, than L1755 and B216-217, and produce higher extinction. The box in the lower panel shows how small the range of polarization-extinction space covered by the "filamentary" clouds in the top panel is in comparison with the range for "round" clouds. Both panels show *K*-band polarization on the *y*-axis; some points measured at *J* or *H* have been converted to *K*. *Dashed lines* in each panel show error-weighted least-squares linear fits to the data points. *Solid lines* show the predictions of the Jones, Klebe & Dickey 1992 model, assuming equal non-uniform and uniform magnetic field energy.

It is not at all unreasonable to expect grains in dense regions to have a very different distribution of shape, size, and/or composition than their counterparts in the lower-density ISM.

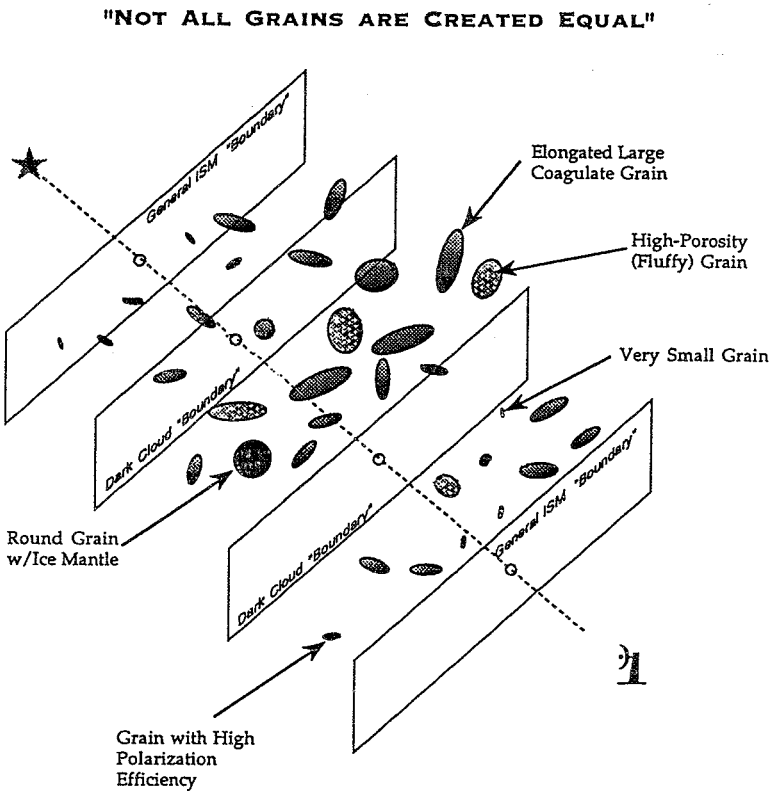

Figure 3: Schematic diagram of grains in the interstellar medium along a line of sight through a dark cloud to a background star. Many different grain types are present, only some of which produce the polarization of the background starlight observed. Meanwhile, those "polarizing" grains *plus many others* produce the extinction associated with the dark cloud.

3. The Future: Mapping Magnetic Fields using Polarized Dust Emission

Luckily, the same aligned grains in the dense ISM which are not very good at polarizing background starlight *can be* very good at producing polarized thermal emission. In order to efficiently polarize background starlight, grains must meet very tight specifications on their size and composition; but the requirements are different--and less restrictive--for a grain to efficiently produce polarized thermal emission. So, it is possible to map the magnetic field in regions where background starlight polarimetry is insensitive to the field by using thermal emission polarimetry.

It is extraordinarily difficult to measure the polarization of thermal emission from dust, but keep in mind that this polarization gives the most accurate view of the magnetic field in the dense ISM that we have ever had. The Hildebrand et al. and Davidson et al. articles in this volume describe the very successful pioneering use of this technique , and I refer the reader there for more detail.

In conclusion, I present the best example to date of the difference in the information provided by background starlight polarimetry and dust emission polarimetry. In M17, which is 2.2 kpc from the Sun, polarization of background starlight has been observed in the optical (Schulz et al. 1981) and in the near-infrared (Goodman, Jones, and Myers 1994). Both the optical and the near-infrared polarimetry reveal a very confusing plane-of-the-sky field structure (given by the polarization direction), probably caused by at least two independent field distributions along the long line of sight to M17 (see Figure 4). Dotson (1994; see also Hildebrand et al.) has used the STOKES polarimeter on the KAO to measure the polarization of 100-micron emission from M17. The plane-of-the-sky magnetic field

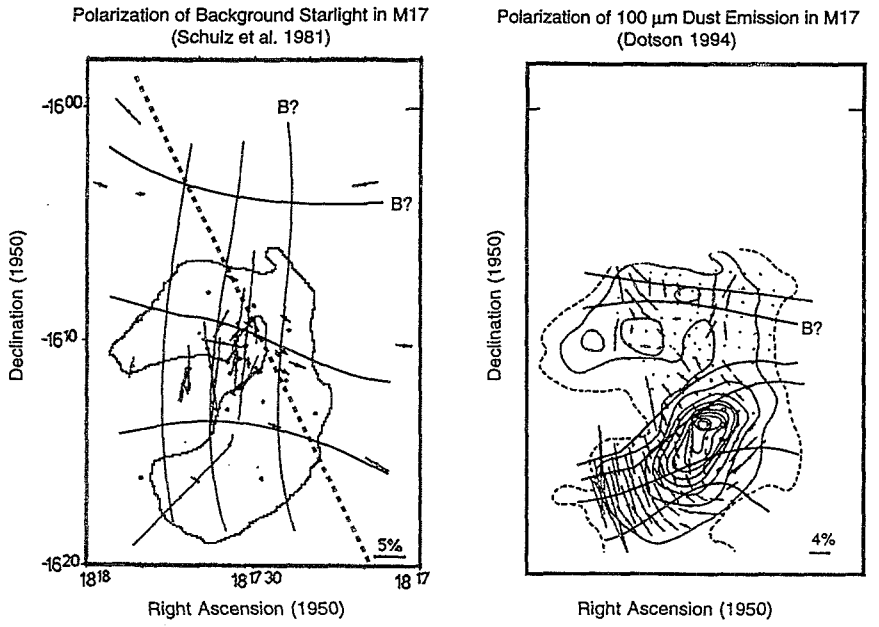

Figure 4: Polarimetry in M17. The *left panel* shows a map of the polarization of background starlight (Schulz et al. 1981), which implies at least two independent plane-of-the-sky field orientations along the line-of-sight. The dashed line in this panel is parallel to the Galactic plane, and neither implied field direction appears to be along it. The *right panel* shows a recent KAO-STOKES 100 micron polarization map of M17 (from Dotson 1994, see also Hildebrand et al. 1994). The pattern of polarization is very systematic and implies a smooth field, at a position angle unlike either of those implied by background starlight polarimetry.

structure derived from the 100-micron polarimetry (normal to the direction of polarization) is very systematic and smooth, and *completely different* from any field apparent in the background starlight polarimetry (see Figure 4). In comparing these two maps, I believe it is clear that the background starlight polarimetry is telling us about all of the fields *along the line of sight to M17,* but not "in" M17, while the emission polarimetry is revealing a field much more *closely associated with M17.*

Dust emission polarimetry apparently has the ability to actually isolate dense regions along the line of sight, and thus to measure magnetic fields in those dense regions. Since thermal dust emission from the dense ISM is strongest at far-IR and sub-mm wavelengths, it must be observed either from outside the atmosphere, or very high sights on Earth. Although, it is clearly the premier instrument of the day, the STOKES 100-micron system on the KAO is only sensitive enough to observe the very brightest star-forming regions in our Galaxy. So, in an effort to map out the magnetic field in more typical regions of the dense ISM, my collaborators and I have recently proposed an extensive program of 100-micron polarization mapping for the ISO satellite. In the not-too-distant future, polarimetry of thermal dust emission--from ISO and its successors, from the KAO and its successors, and from single-dish and interferometric mm- and sub-mm observatories--should reveal a much-needed clear view of the nature of the magnetic field in the dense ISM.

References

Davidson, J.A., Dowell, C.D., Schleuning, D., Dotson, J., and Hildebrand, R.H. 1994, this volume.

Davis, L., Jr. & Greenstein, J.L. 1951, ApJ, 114, 206

Dotson 1994, Ph.D. Thesis, University of Chicago, in prep.

Goodman, A.A., Bastien, P., Myers, P.C. & Ménard, F. 1990, ApJ, 359, 363

Goodman, A.A., Jones, T.J., Lada, E.A. & Myers, P.C. 1992, ApJ, 399, 108

Goodman, A.A., Jones, T.J., Lada, E.A. & Myers, P.C. 1994, ApJ, in prep.

Goodman, A.A., Jones, T.J., and Myers, P.C., 1994, ApJ, in prep.

Heiles, C., Goodman, A.A., McKee, C.F. & Zweibel, E.G. 1991, in Fragmentation of Molecular Clouds and Star Formation, ed. E. Falgarone et. al. (Dordrecht: Kluwer), p. 43

Heiles, C. & Jenkins, E.B. 1976, A&A, 46, 333

Heyer, M.H., Snell, R.L., Schloerb, F.P., Vrba, F.J., and Strom, S.E. 1987, Ap. J., 321, 855

Hildebrand, R.H., Davidson, J.A., Dotson, J.L, Dowell, C.D., Novak, G., Platt, S.R., and Schleuning, D. 1994, this volume.

Jones, T.J., Klebe, D. & Dickey, J.M. 1992, ApJ, 389, 602

Mathewson, D.S. & Ford 1970, V.L. 1970, Mem Roy Astr Soc, 74, 139

Purcell, E.M. 1979, ApJ, 231, 404

Schulz, A., Lenzen, R., Schmidt, T. & Proetel, K. 1981, A&A, 95, 94

Tamura, M., Nagata, T., Sato, S. & Tanaka, M. 1987, MNRAS, 224, 413

Tamura, M., Yamashita, T., Sato, S., Nagata, T. & Gatley, I. 1988, MNRAS, 231, 445

Vrba, F.J., Strom, S.E. & Strom, K.M. 1976, AJ, 81, 958

Wilking, B.A., Lebofsky, M.J., Rieke, G.H. & Kemp, J.C. 1979, AJ, 84, 199

Airborne Astronomy Symposium on the Galactic Ecosystem
ASP Conference Series, Vol. 73, 1995
M.R. Haas, J.A. Davidson, and E.F. Erickson (eds.)

THE STRUCTURE OF H II REGIONS AND THE VARIATIONS IN THEIR PROPERTIES WITH GALACTOCENTRIC DISTANCE

JANET P. SIMPSON,
Univ. of Calif. Berkeley; NASA/Ames Research Center, MS 245-6, Moffett Field, CA 94035-1000

SEAN W. J. COLGAN,
SETI Institute; NASA/Ames Research Center, MS 245-6, Moffett Field, CA 94035-1000

ROBERT H. RUBIN,
Orion Enterprises; NASA/Ames Research Center, MS 245-6, Moffett Field, CA 94035-1000

EDWIN F. ERICKSON, and MICHAEL R. HAAS
NASA/Ames Research Center, MS 245-6, Moffett Field, CA 94035-1000

ABSTRACT We summarize some of our KAO observations of far-infrared ionic fine-structure lines from Galactic H II regions, and discuss their interpretation.

INTRODUCTION

An H II region consists of the ionized gas surrounding a newly formed, massive (and therefore hot) star or cluster of massive stars. The ionized gas comes from the star's natal molecular cloud, and the ionization structure, or stratification, of the gas surrounding the star and found in the vicinity of the cloud tells us about the young stars and the processes of massive star formation. To adequately determine this ionization structure, one must map the region surrounding the stars in lines of different excitations. As an example, using the Cryogenic Grating Spectrometer (Erickson et al. 1985) we have mapped the [O III] 52 and 88 μm, the [N III] 57 μm, and the [Ne III] 36 μm lines in the Orion Nebula (Simpson et al. 1986). These lines were used to determine the electron density, the abundances, and the spectral energy distribution of the radiation from the exciting stars of the Trapezium. Further modeling (Rubin et al. 1991) demonstrates that the H II region is indeed an ionized blister on the near side of the natal molecular cloud.

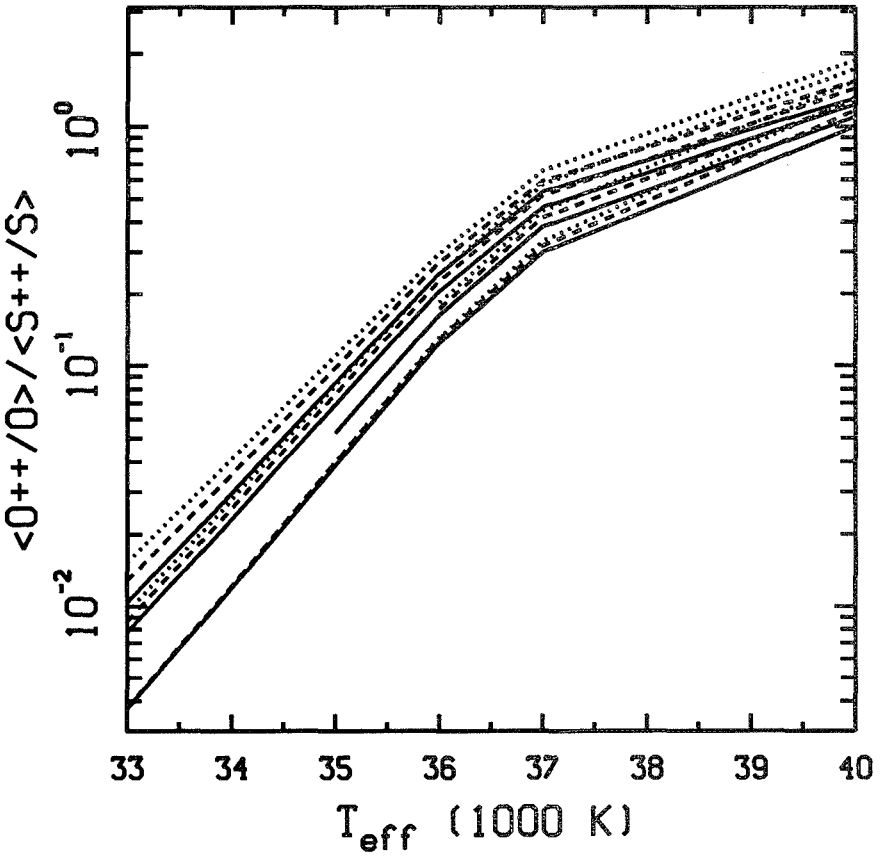

Figure 1. The ionic fraction ratio $<O^{++}/O>$ / $<S^{++}/S>$ for models of H II regions.

RECENT STUDIES

Because far infrared photons from distant H II regions can penetrate the interstellar dust, we can observe H II regions over the entire Galaxy to study its structure and evolution. We (Simpson et al. 1995) have observed the [S III] lines at 18 and 33 μm, and the [O III], [N III], and [Ne III] lines in 17 H II regions with galactocentric radii R_G ranging from 0.01 to 10.2 kpc. Electron densities were estimated from the [S III] and [O III] line ratios (see Rubin et al., this meeting). From the line intensities, we calculated the ratios of the ionic abundances. Figure 1 shows that the ratio of the ionic fractions $<O^{++}/O>$ and $<S^{++}/S>$ calculated by Rubin (1985) for a large parameter space of H II region models is a strong function of the effective temperatures T_{eff} of the exciting stars. From our observed O^{++}/S^{++} ratios, we estimated the ionic fractions, and using Figure 1, we estimated T_{eff} for each H II region. This analysis shows that all the observed H II regions in the inner Galaxy are of significantly

lower excitation than many of the H II regions in the intermediate and outer Galaxy, even though they were selected for high excitation from their He^+ radio recombination lines. Possible explanations include both variations in stellar spectral type and variations in Galactic abundances.

Other galaxies have been shown to contain gradients of abundances decreasing with increasing distance from the center. Such gradients have also been seen in non-airborne observations of our own Galaxy (e.g., Shaver et al. 1983). Our FIR observations of the abundances also show that our Galaxy exhibits gradients of N/H, O/H, Ne/H, and S/H with galactocentric radius. Furthermore, the data for our Galaxy are better fitted by at least 2 steps: inner, intermediate, and possibly outer regions of more constant abundance. This is shown in Figure 2, where we plot the N/O abundance ratio vs. R_G. The dotted lines, illustrating the steps, have higher statistical significance than the solid line.

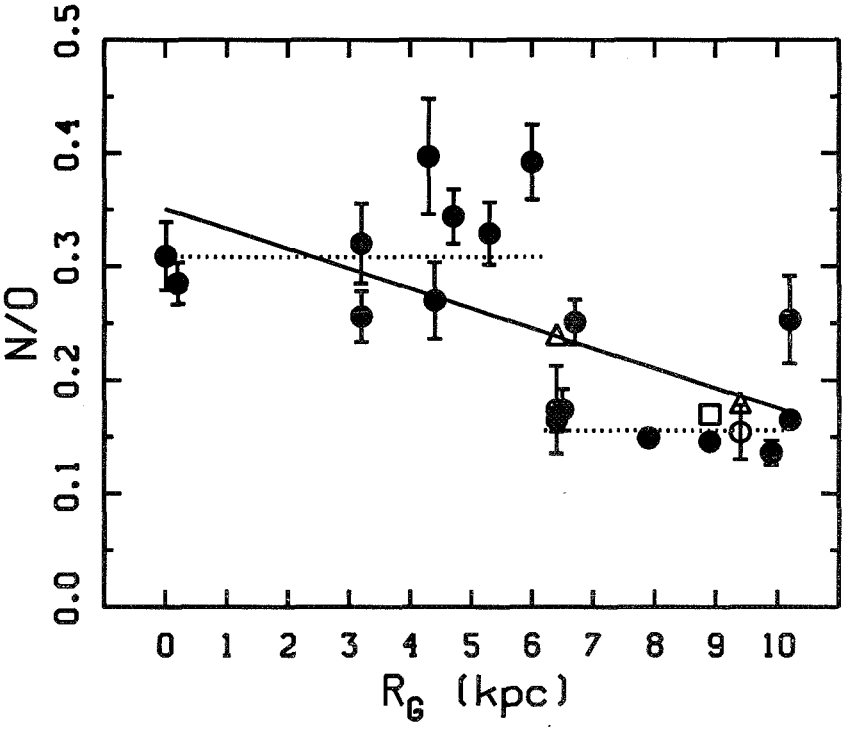

Figure 2. N/O vs. R_G for Galactic H II regions (Simpson et al. 1995), including the Orion Nebula (open square) from Rubin et al. (1991). The open triangles are G45.13+0.14 and K3–50, which were modeled by Colgan et al. (1991); the open circles are our reanalysis of their data.

FUTURE WORK

The Orion Nebula at 0.5 kpc from the sun can be easily mapped with the 0.75′ beam of the 0.9m KAO telescope at 88 μm. Such mapping is necessary for detailed studies of the abundances in the H II region and studies of the relationship of the H II region with its parent cloud. However, most H II regions are at much larger distances, and thus cannot be mapped with the relatively large beam of the KAO (Simpson et al. 1995). A large airborne telescope such as SOFIA would be of enormous use in studies of the structure of H II regions and the abundances of galaxies.

REFERENCES

Colgan, S.W.J., Simpson, J.P., Rubin, R.H., Erickson, E.F., Haas, M.R., & Wolf, J. 1991, ApJ, 366, 172

Erickson, E.F., Houck, J.R., Harwit, M.O., Rank, D.M., Haas, M.R., Hollenbach, D.J., Simpson, J.P., & Augason, G.C. 1985, Infrared Physics, 25, 513.

Rubin, R.H. 1985, ApJS, 57, 349

Rubin, R.H., Simpson, J.P., Erickson, E.F., Haas, M.R., Lord, S.D., & Colgan, S.W.J. 1994, in Proc of the Airborne Astronomy Symp on the Galactic Ecosystem: From Gas to Stars to Dust, ed. M.R. Haas, J.A. Davidson, & E.F. Erickson (San Francisco: ASP), paper 114

Rubin, R.H., Simpson, J.P., Haas, M.R., & Erickson, E.F. 1991, ApJ, 374, 564

Shaver, P.A., McGee, R.X., Newton, L.M., Danks, A.C., & Pottasch, S.R. 1983, MNRAS, 204, 53

Simpson, J.P., Colgan, S.W.J., Rubin, R.H., Erickson, E.F., & Haas, M.R. 1995, ApJ, submitted

Simpson, J.P., Rubin, R.H., Erickson, E.F., & Haas, M.R. 1986, ApJ, 311, 895

Mike Haas, Bob Rubin, Sean Colgan, Patricia Carral,
Ed Erickson, Sabina DeLara, Jan Simpson, Jim Baltz (1990)

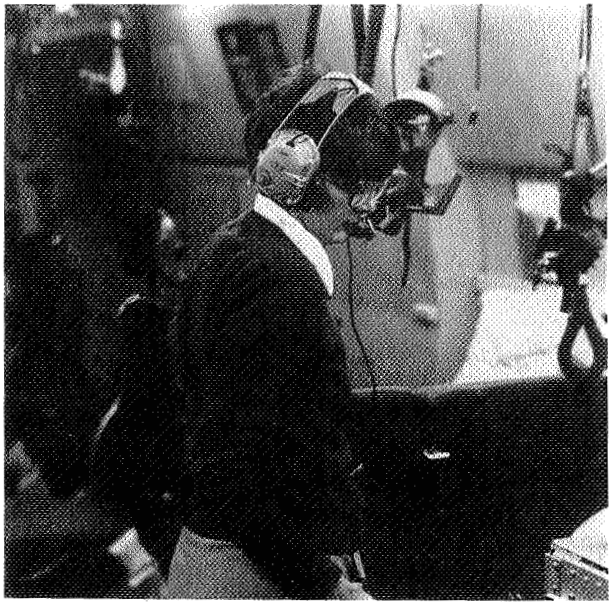

Jan Simpson (1975)

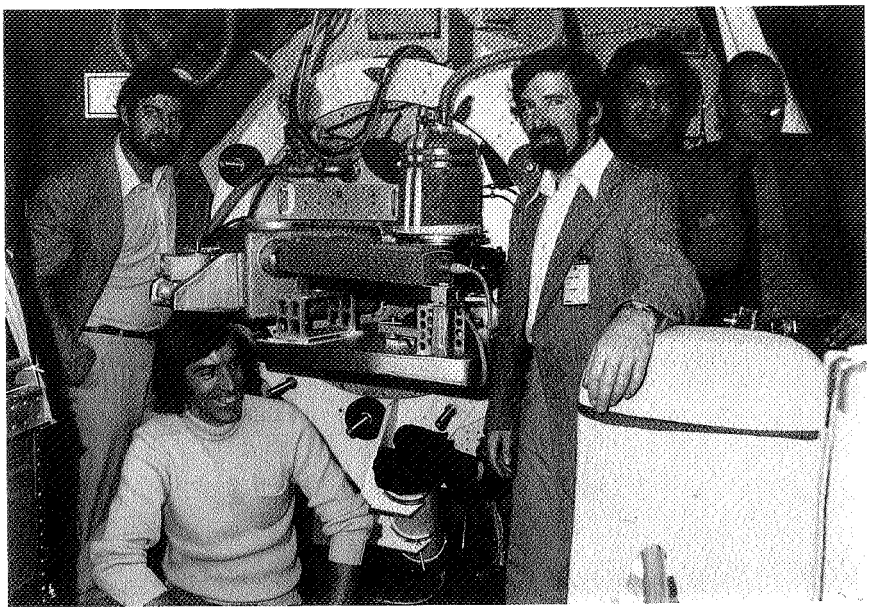

Alan Moorwood, Jean-Paul Baluteau, John Beckman
Ezio Busoletti, Michel Anderegg (1975)

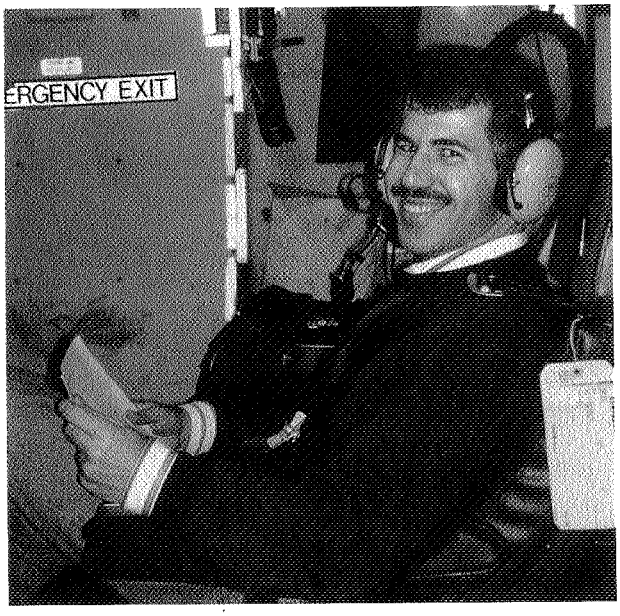

Humberto Campins

Airborne Astronomy Symposium on the Galactic Ecosystem
ASP Conference Series, Vol. 73, 1995
M.R. Haas, J.A. Davidson, and E.F. Erickson (eds.)

OBSERVATIONAL ASPECTS OF POLYCYCLIC AROMATIC HYDROCARBON CHARGING IN THE INTERSTELLAR MEDIUM

E.L.O. BAKES
Peyton Hall, Princeton University, Princeton, NJ 08544-1001

A.G.G.M. TIELENS
NASA/Ames Research Center, MS 245-3, Moffett Field, CA 94035-1000

ABSTRACT We have investigated the charging processes which affect small carbonaceous dust grains and polycyclic aromatic hydrocarbons (PAHs). Because of their high abundance, interstellar PAH molecules can dominate the charge balance of the interstellar medium (ISM), which controls the heating and cooling of interstellar gas and interstellar chemistry. We present the results of our model, which compare well with observations and suggest further applications to both laboratory measurements and data obtainable from the KAO.

INTRODUCTION

PAHs form an important component of the ISM because they dominate the energy balance of the gas by the photoelectric effect. The absorption of a FUV photon may lead to the photoelectric ejection of an energetic electron into the surrounding gas. The electron will impart energy to the gas particles via inelastic collisions before recombining with the PAH. The efficiency of PAHs in charge exchange with the gas creates not only a highly efficient heating mechanism, but also provides a large surface area for a complex chemical network involving both neutral and charged PAHs. Because we have accurately quantified the charging effects, we can use our model to determine how the PAH charge will differ depending on the interstellar conditions. We can also run simulations to determine the effects on the chemistry occurring with PAHs. These can be compared with observations or used to predict the abundances of various species in a particular Galactic environment.

RESULTS

We have developed a model of grain charging by balancing the photoelectric ejection of electrons with the collisional recombination (Bakes & Tielens 1994). We have used this model to calculate the charge distribution for different grain sizes and evaluated the photoelectric heating rate as a function of the physical

conditions. The total heating rate Γ_{pe} for very small graphitic grains and PAHs is given by

$$\Gamma_{pe} = 10^{-24}\,\varepsilon\,G_o\,n_H \qquad erg\ s^{-1}\ cm^{-3}$$

where for gas temperatures up to 10^4 K, ε is given by

$$\varepsilon = \frac{4.87 \times 10^{-2}}{[1 + 4 \times 10^{-3}(G_o T^{1/2}/n_e)^{0.73}]} + \frac{3.65 \times 10^{-2}(T/10^4)^{0.7}}{[1 + 2 \times 10^{-4}(G_o T^{1/2}/n_e)]}$$

such that G_o is the UV radiation field strength in Habings, n_H is the hydrogen nucleus density, n_e is the electron density and T is the gas temperature.

The heating rate derived from UV absorption studies of the level populations of the dominant cooling line [CII] 158 μm by Pottasch, Wesselius & van Duinen (1979) for the line of sight towards ζ Per is observed to be 10^{-25} erg s^{-1} (H atom)$^{-1}$. Using an incident intensity of the UV field $G_o = 5$ determined for this diffuse cloud by van Dishoeck & Black (1986), we calculate a net heating rate of 1.5×10^{-25} erg s^{-1} (H atom)$^{-1}$, in good agreement with the observations.

We have calculated the charging for interstellar PAHs in conditions appropriate for ζ Per using recent experimentally determined PAH–electron recombination rates from Abouelaziz et al (1993). This rate is much slower than the rate of Draine & Sutin (1987) extrapolated into the molecular domain, hence the PAHs are more positively charged than previously thought. The PAH charge distribution at the surface of this cloud is shown in Figure 1 for pentacene ($C_{22}H_{14}$), coronene ($C_{24}H_{12}$) and a larger PAH comprised of a 100 carbon atom disk.

Coronene has a low electron affinity and hence, a low electron sticking coefficient ($s_e = 10^{-3}$) when neutral. Consequently, it will be mainly neutral with a significant fraction positively charged. In contrast, pentacene has a high electron affinity ($s_e = 1$) and has an almost equal chance of being either negatively charged or neutral with a smaller positive fraction. Larger disk shaped and spherical grains will be predominantly neutral.

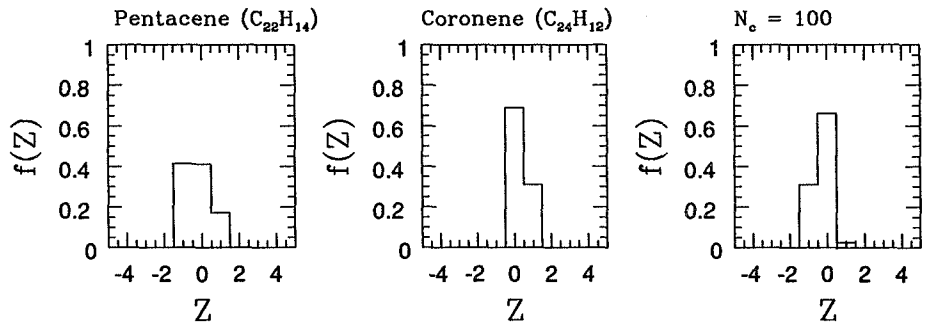

Fig. 1. PAH charge distributions evaluated for typical conditions in the diffuse ISM corresponding to electron density $n_e = 7.5 \times 10^{-3}$ cm^{-3}, gas temperature T=100K and G_o=1.

Figure 2 shows the charge distribution for pentacene and coronene as a function of depth through the diffuse cloud ζ Per. As electron density increases and FUV flux decreases, these particles become increasingly neutral or negatively charged.

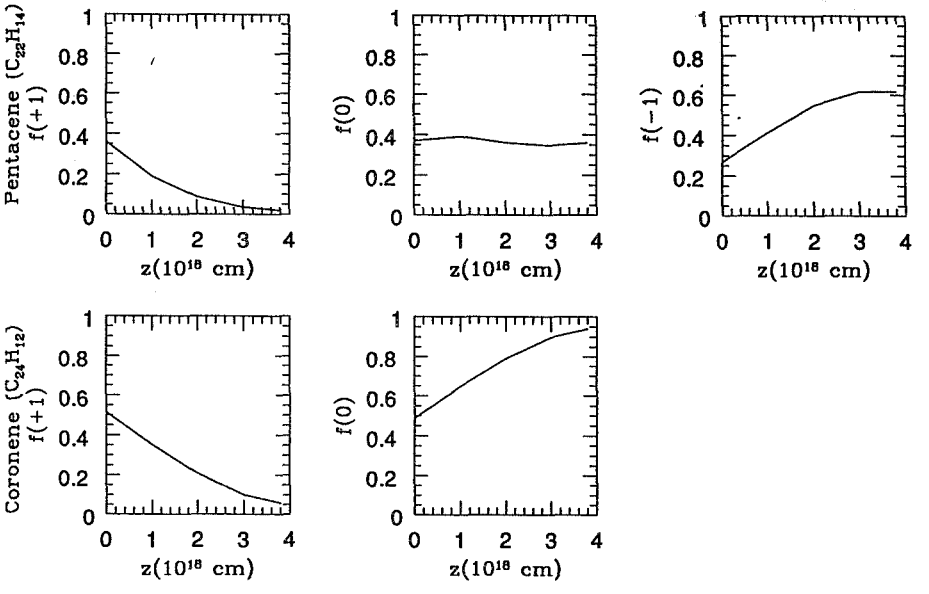

Fig. 2. The charge variation f(Z) for PAHs with depth z for the diffuse cloud model F from van Dishoeck and Black (1986).

The chemistry of the diffuse interstellar medium will involve PAHs of neutral and singly positive and negative charge, forming a rich and complex network of reactions. For a warm, dense photodissociation region (PDR), PAHs may be neutral, positively and negatively charged. We have included a population of PAHs comprised of 50 carbon atoms (similar to Lepp and Dalgarno 1988) into the Tielens and Hollenbach (1985, hereafter TH85) PDR model to determine the effects on the abundance of atoms and molecules with depth into the PDR. We present a few of the preliminary results here. A detailed study will be presented in forthcoming publications (Bakes & Tielens, in preparation). The inclusion of PAH particles makes a significant difference to the atomic and molecular abundances in the PDR. In particular, because neutral PAHs are efficient electron scavengers, cation reaction with PAH^- becomes the dominant recombination channel. This significantly increases the abundance of neutrals, as illustrated in Figure 3 for the metals iron (Fe) and magnesium (Mg). By observing the distribution of PAHs throughout our Galaxy, we can pinpoint regions where PAH chemistry occurs and use this model to quantify the abundance of neutrals such as carbon and sulfur.

C-2

CONCLUSIONS

We conclude that our PAH charging model produces heating efficiencies which are in good agreement with that derived from observations of the diffuse interstellar clouds. Our results also agree well with the FIRAS observations on COBE (Bakes & Tielens 1994). It has also allowed us to investigate the effect of including a population of 50 carbon atom PAHs in the TH85 PDR and conclude they significantly modify the abundance of neutral particles through their superior charge transfer efficiency.

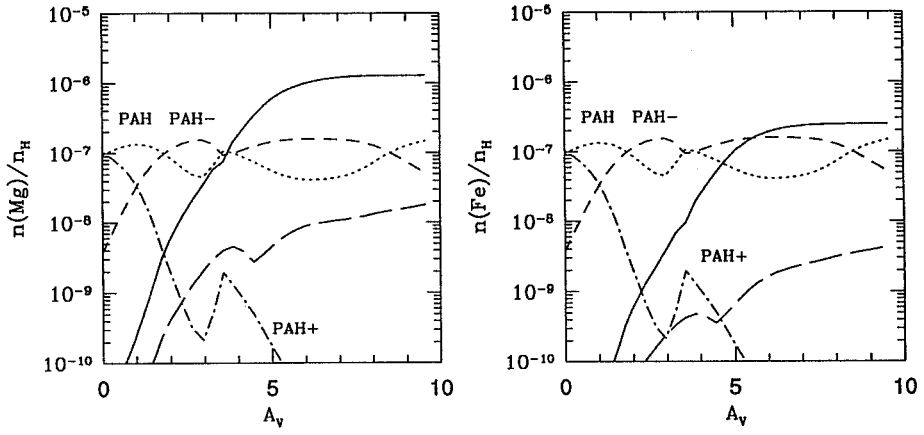

Fig. 3. The presence of PAHs in the TH85 PDR model results in a significant alteration in abundance of neutrals in the PDR compared to the original model due to the efficiency of the PAH^- ion in charge transfer. We plot visual extinction A_v against abundance, where the long dashed line represents the neutral metal abundance for a PDR with no PAHs, whilst the solid line is for a PDR with PAH chemistry included.

REFERENCES

Abouelaziz, H., Gomet, J.C., Pasquerault, D. & Rowe, B.R. 1993, J.Chem.Phys., 99, 237

Bakes, E.L.O. & Tielens, A.G.G.M. 1994, ApJ, 427, 822

Draine, B.T. & Sutin, B. 1987, ApJ, 320, 803

Lepp, S. & Dalgarno, A. 1988, ApJ, 335, 769

Pottasch, S. R., Wesselius, P. R. & van Duinen, R. J. 1979, A&A, 74, L15

Tielens, A. G. G. M. & Hollenbach, D. J. 1985, ApJ, 291, 722 (TH85)

van Dishoeck, E.F. & Black, J.H. 1986, ApJS, 62, 109

Airborne Astronomy Symposium on the Galactic Ecosystem
ASP Conference Series, Vol. 73, 1995
M.R. Haas, J.A. Davidson, and E.F. Erickson (eds.)

SPECTRAL IMAGING OF THE ORION BAR AT 6.2 AND 7.8 MICRONS

Jesse Bregman and David Harker
MS 245-6, NASA Ames Research Center, Moffett Field, CA 94035-1000

David Rank and Pasquale Temi
UCO and UCSC, Santa Cruz, CA 95064

ABSTRACT We have obtained images of the Orion Bar region through narrow-band filters at 6.2 and 7.8 μm to determine whether the emission observed at these wavelengths arises from C-C modes in polycyclic aromatic hydrocarbons (PAHs). Morphologically, the distribution of the emissions are similar, but appear different in detail. Quantitative comparisons of these band intensities with previous data at 8.4 and 11.3 μm indicates that they are indeed consistent with emission from fluorescently excited PAH molecules.

INTRODUCTION

The set of narrow emission bands and broad underlying plateaus which dominate the mid-infrared spectrum of planetary nebulae, HII regions, galactic nuclei, reflection nebulae, and WC stars are generally attributed to material containing only carbon and hydrogen atoms. Several forms of this material have been suggested, but they all are dominated by aromatic carbon structures. The narrow bands are most likely due to emission from polycyclic aromatic hydrocarbons (PAHs), while the broad plateaus arise from larger amorphous carbon particles or PAH clusters. If the narrow features are due to PAHs, then PAHs contain about 1% of the interstellar carbon, making them the most abundant molecules after H_2 and CO. Thus, deciphering the physics of these molecules and their spectra could lead to an understanding of some of the organic chemistry of the interstellar medium.

OBSERVATIONS

The Ames/Lick mid-IR camera was used to image the Orion Bar region at 6.2 and 7.8 μm (PAH features) and 6.8 μm (continuum). The camera uses a 128x128 Si:Ga Amber Engineering array. A filter wheel holding a 4-8 μm CVF and 4 fixed filters determines the wavelength of the image. The 6.2 and

6.8 μm images were obtained through the $\lambda/\delta\lambda$=1.8% CVF while the 7.8 μm image was obtained through a $\lambda/\delta\lambda$=2.5% wide fixed filter. The Bar was chopped 4 arcmin in azimuth at a frequency of 1/3 Hz. Each integration consisted of the difference of 20 on-source and off-source frames. The scale was 1.6 arcsec/pixel. Telescope motion produced FWHM images of point sources of about 4 pixels. Guiding was relative to Θ^2Ori. The telescope was operated in its rotation freeze mode where field rotation is compensated by rotation of the line-of-sight axis. This method held the rotation constant for about 6 integrations. Derotation of the frames for coaddition was done after the flight during image processing.

DISCUSSION

C-C Modes

Previously, Bregman et al. (1994) had shown that the spatial distribution of the emission bands observable from the ground (3.3, 11.3 μm, and a point at 8.4 μm on the long wavelength wing of the 7.7 μm band) could be described by a quantitative model of PAH emission calculated by Schutte et al. (1993). In the PAH model, the 3.3 and 11.3 μm bands are due to C-H modes while the 6.2 and 7.8 μm bands are due to C-C modes. Thus, airborne observations were required to observe the C-C modes and find out if they also fitted the PAH model.

Since the 6.2 and 7.8 μm bands are close in wavelength (and therefore in excitation energy) and are supposed to be due to the same modes in the same molecules, to first order they should have the same spatial distribution. Inspection of the images shows that they are similar, but there are differences in the details of their intensity distribution. We also wanted to confirm that the 8.4 μm image we previously obtained was a good indicator of emission from the C-C modes of PAHs. To do these tests quantitatively, we used the technique we developed in our previous work. In Figures 1a, 1b, and 1c we have plotted the intensity of the bands attributed to C-C modes relative to each other. We use averages of rows of pixels parallel to the front of the Bar and extending from the northern side (next to the HII region) to the southern side (next to the molecular cloud) of the Bar, since in this direction the molecules within the Bar experience a large variation of UV flux and, hence, show a large variation in intensity. On each figure, the solid line is the trend expected if the band intensities are proportional. All the data points should lie along this line if the spatial distribution of the bands are the same. Also plotted are the direction and magnitude of deviations from this line predicted by the PAH model of Schutte et al. (1993). Their standard model has been normalized to the observed intensity of the mid-Bar pixels.

The 7.8 and 6.2 μm data (Fig. 1a) do not correlate 1:1. The points along the front and back of the Bar deviate from the 1:1 trend line in a direction consistent with either a distribution of larger molecules than in the middle of the Bar or with lower UV flux. We observed similar trends in our previous data, with the points along the front of the Bar showing emission characteristic of larger PAHs and the points along the back of the Bar

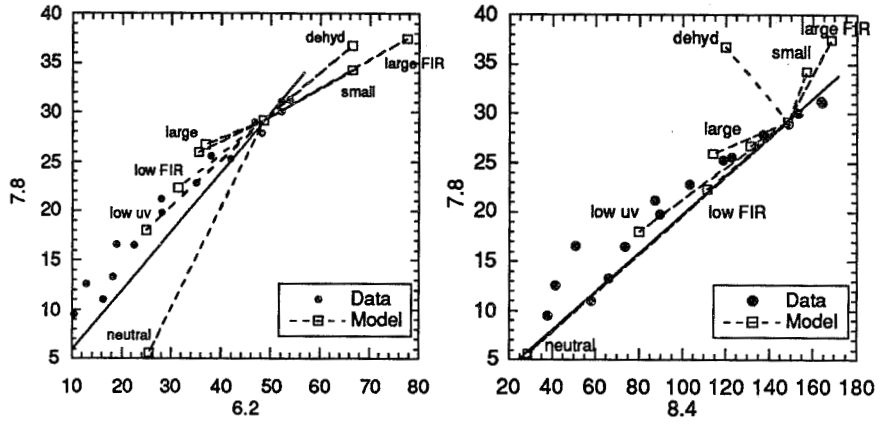

Figure 1 a (left) and Figure 1b (right) show the correlation between the C-C mode band intensities as measured at 6.2, 7.8, and 8.4 microns.

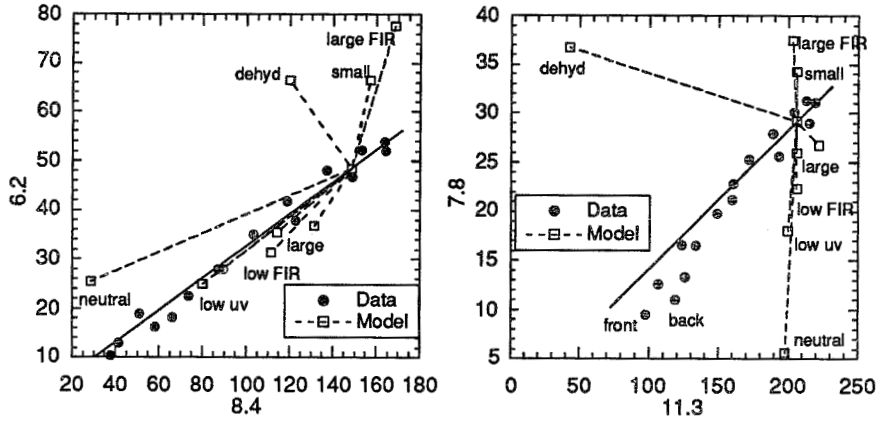

Figure 1c (left) shows the excellent correlation between the C-C mode band intensities as measured at 6.2 and 8.4 μm. Figure 2 (right) shows the correlation between the band intensities of the C-C mode measured at 7.8 μm and the 11.3 μm C-H mode.

consistent with emission expected from lower UV flux regions. The model predicts similar behavior for the 7.8 vs. 8.4 μm data even though the data appear to sample the same emission band. Fig. 1b shows that the 7.8 vs. 8.4 μm data follows the model predictions. The 6.2 and 8.4 μm data (Fig. 1c) are highly correlated, showing almost no deviation from the 1:1 trend line. The model variables which might have accounted for the previous plots (low UV and larger PAHs) move the data points nearly parallel to the 1:1 trend line and thus have little effect in this plot. We thus conclude that the distribution of emission from the C-C mode in PAHs is well represented by the 8.4 μm image. These correlations are also strong support for the identification of PAHs as the source of the emission bands.

C-H Modes

The C-C vs C-H mode plots are good tests of dehydrogenation of the molecules. It is possible that the UV field in some objects is intense enough that the some of the hydrogen atoms will be removed from the PAH molecules. Figure 2 shows the comparison of the 7.8 μm C-C mode with the 11.3 μm C-H mode. The data deviates from the 1:1 trend line, but not in the direction expected if dehydrogenation is significant. The data are instead consistent with the previous plots, where molecule size variations or attenuation of the UV field are adequate to explain the results.

CONCLUSIONS

1. The 6.2 and 8.4 μm data correlate extremely well, in good agreement with predictions of the PAH fluorescence model of Schutte et al. (1993).
2. The other data are consistent with our previous findings (Bregman et al. 1994) that there are variations in the PAH size distribution within the Bar and that the the front of the Bar has a larger size distribution while the back of the Bar shows the effects of a lower UV intensity.
3. As in our previous results, there is no evidence for dehydrogenation of the PAH molecules.

REFERENCES

Bregman, J.D., Larson, K., Rank, D., and Temi, P. 1994, Ap. J., 423, 326.
Schutte, W.A., Tielens, A.G.G.M., and Allamandola, L.J. 1993, Ap. J., 415, 397.

Airborne Astronomy Symposium on the Galactic Ecosystem
ASP Conference Series, Vol. 73, 1995
M.R. Haas, J.A. Davidson, and E.F. Erickson (eds.)

A SEARCH FOR THE C_3 CARBON CLUSTER IN THE INTERSTELLAR MEDIUM

A. VAN ORDEN, J.D. CRUZAN, R.A. PROVENCAL, T.F. GIESEN, AND R.J. SAYKALLY
Department of Chemistry, University of California, Berkeley, CA 94720

R.T. BOREIKO AND A.L. BETZ
Center for Astrophysics and Space Astronomy, University of Colorado, Boulder, CO 80309

ABSTRACT We have searched for rovibrational emission and absorption transitions arising from the 63 cm^{-1} ν_2 (π_u) bending vibration of the C_3 carbon cluster in the interstellar medium using the Betz/Boreiko heterodyne receiver on board the Kuiper Airborne Observatory. The Q(4) line at 1896.707 GHz was searched for in the IRc2 Orion/M42 and the W3 sources, and the R(2) transition at 1968.594 GHz was searched for in Sgr B2. No emission lines were observed in any source. However, a weak absorption was detected in Sgr B2 with a LSR velocity of 63.7±0.6 km s^{-1} and a FWHM linewidth of 7.9±0.8 km s^{-1}. This absorption is tentatively identified as the R(2) transition of the C_3 bending mode.

INTRODUCTION

A vital component of the NASA Astrophysics and Exobiology programs is to establish the form and distribution of carbon in the galaxy. The purpose of this goal is to address such diverse subjects as the fundamental physics and chemistry of circumstellar shells, interstellar clouds, and planetary atmospheres, as well as the role of interstellar carbonaceous material in the early evolution of life and the possibility of life elsewhere in the Universe. Several abundant forms of carbon are well studied in the interstellar medium, including CO, CI, and CII. In addition, a host of trace carbon-containing molecules, including the linear carbon chains HC_nN, (n=1, 3, 5, 7, 9, 11), C_nH (n=1-6), C_nN (n=1-3), C_nO (n=1, 3), and C_nS (n=1-3) have been observed (Herbst 1990). Much of the interstellar dust is thought to be composed of carbonaceous material, including polycyclic aromatic hydrocarbons (PAH's). There is strong evidence to support the ubiquitous presence of pure (C_n) carbon clusters in the interstellar medium. Optical emission from C_2 and C_3 was detected in comet tails (Weltner and Van Zee 1989), and mid-infrared absorption from C_3 (Hinkle *et al.*

1988) and C_5 (Bernath *et al.* 1989) has been observed in the circumstellar dust surrounding the carbon star IRC+10216. The absence of a permanent dipole moment for these molecules precludes their detection in the cold interstellar medium by submillimeter astronomy. However, the linear forms of these clusters are known to possess low-frequency bending modes in the far-infrared region of the spectrum. We have proposed that these low-frequency bending modes may serve as the chromophores for detection of pure carbon clusters in the ISM by far-IR astronomy.

Over the last few years, the Saykally group has developed the technique of tunable far-infrared laser spectroscopy of jet-cooled clusters produced by laser vaporization (Figure 1), which is being used to perform precise measurements of the far-infrared bending frequencies of pure carbon clusters (Saykally 1993). The 63 cm^{-1} ν_2 (π_u) bending mode of C_3 has been characterized using this technique (Schmuttenmaer *et al.* 1990). Recently, the laboratory measurements of this C_3 bending mode were used to design a search for C_3 in the interstellar medium using the Betz/Boreiko heterodyne receiver (Betz and Zmuidzinas 1984) on board the KAO. A search for the Q(4) transition at 1896.707 GHz in the IRc2 Orion/M42 and W3 sources was performed during a KAO flight from the NASA Ames Research Center on January 28, 1994. The R(2) transition at 1968.594 GHz was searched for in the Sgr B2 source during the 1994 KAO Southern Skies Expedition #5 in New Zealand. No emission lines arising from these transitions were detected in any source. However, a weak absorption signal, which we have tentatively identified as the R(2) transition of C_3, was observed in Sgr B2. We are currently searching for the far-infrared bending frequencies of C_6-C_9 in the laboratory using the tunable far-infrared laser spectrometer. The bending transitions of these clusters are predicted to be lower in frequency than that of C_3, which may increase the probability of detecting emission lines from these larger clusters.

RESULTS AND DISCUSSION

The transition dipole of the ν_2 bending mode of C_3 has been calculated to be 0.437 D (Jensen *et al.* 1991). From this we obtain an A-coefficient of about 7×10^{-2} s^{-1} for the dipole transition in the ν_2 fundamental rovibrational band centered at 63.1 cm^{-1}. The critical density necessary to thermalize the ν_2=1 level is thus estimated to be 2×10^8 cm^{-3}, assuming the temperature of the H_2 gas to be about 50 to 100 K. Such densities are observed only near the cores of dense molecular clouds. Therefore, emission signals arising from de-excitation of the ν_2 mode should only be detectable in these regions. From the Betz/Boreiko receiver sensitivity, we have estimated that the minimum total column density required to detect these emissions is 3×10^{14} cm^{-2} for 100 K gas.

These constraints are relaxed somewhat when a source of continuum radiation at far-IR wavelengths is present, permitting molecular absorption lines to be observed. Such is the case in the HII star-forming region near the core of Sgr B2. Figure 2

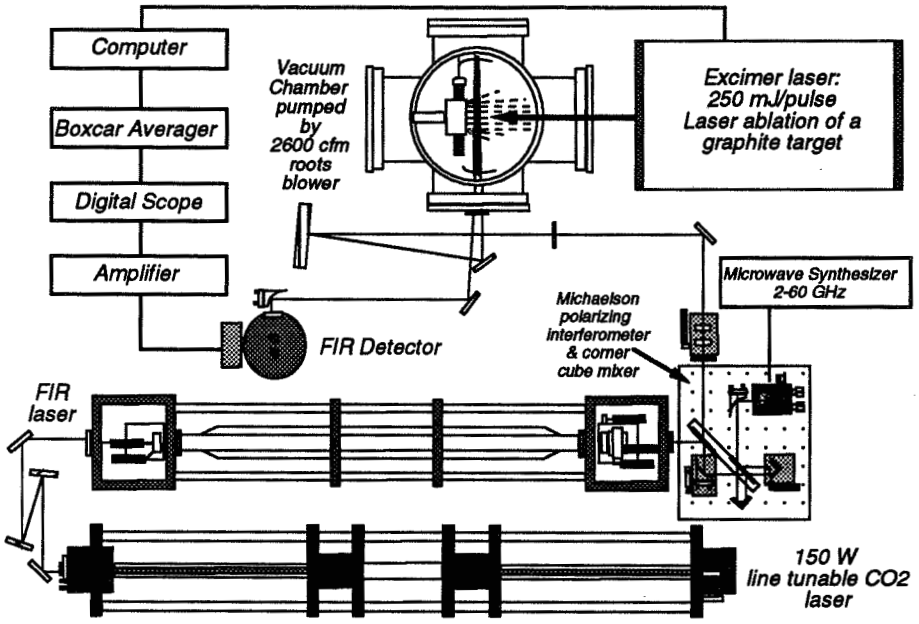

Fig. 1. Schematic of the Berkeley tunable far-infrared spectrometer used in the laboratory determination of the ν_2 bending mode of C_3. Tunable far-IR laser light is used to probe a supersonic expansion of vaporized graphite.

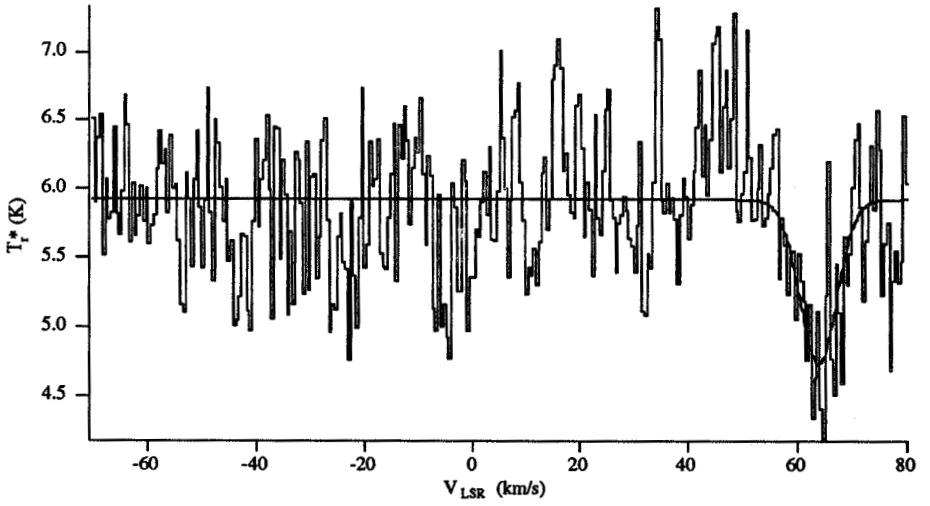

Fig. 2. Sgr B2 spectrum at the frequency of the R(2) transition of the C_3 bending mode. The smooth curve is a Gaussian profile fit to the data giving a peak amplitude of -1.2(2)K at 63.7(6) km/s and a FWHM linewidth of 7.9(8) km/s. The uncertainty per channel is 0.6 K after 84 min of integration. The numbers in parenthesis are uncertainties in the last digit.

displays the Sgr B2 spectrum that we observed at the wavelength of the R(2) line of the C_3 bending mode. Generally, detection of at least two transitions at the same LSR velocity is required to confirm the existence of a new molecule in an astrophysical source. Therefore, our assignment of the absorption line at 63.7±0.6 km s^{-1} to C_3 is only tentative. However, the LSR velocity is characteristic of absorption lines from molecules in the gas near the core of Sgr B2 (Greaves *et al.* 1992) and is also consistent with other carbon chain molecules observed in this source (Turner 1971, Avery *et al.* 1976). A complete analysis of the Sgr B2 data is currently in progress and will be presented in a future paper.

It is curious that a C_3 absorption was not detected in the IRc2 region of Orion, since this is also a source of continuum far-IR radiation and since other carbon chain molecules have been detected in this region (Genzel and Stutzki 1989).

ACKNOWLEDGMENTS

This work was supported by the NASA Astrophysics, Exobiology, and Airborne Astronomy Programs. AVO wishes to thank the NASA Graduate Student Researchers Program for a graduate fellowship.

REFERENCES

Avery, L.W., Broten, N.W., MacLeod, J.M., Oka, T., and Kroto, H.W. 1976, Ap.J., 205, L173.

Bernath, P.F., Hinkle, K.H., and Keady, J.J. 1989, Science, 244, 562.

Betz, A. and Zmuidzinas, J. 1984, in Proceedings of the Airborne Astronomy Symposium, NASA Conference Publication 2353, p. 320.

Genzel, R. and Stutzki, J. 1989, Annu. Rev. Astron. Astrophys., 27, 41.

Greaves, J.S., White, G.L., Okishi, M., Hasegawa, T., and Sunada, K. 1992, Astron. Astrophys., 260, 381.

Herbst, E. 1990, Angew. Chem. Int. Ed. Engl., 29, 595.

Hinkle, K.H., Keady, J.J., and Bernath, P.F. 1988, Science, 241, 1319.

Jensen, P., McMichael-Rohlfing, C., and Almlöf, J. 1991, J. Molec. Spectrosc., 150, 137.

Saykally, R.J. 1993 in Astronomical Infrared Spectroscopy: Future Observational Directions, ed. S. Kwok, ASP Conference Series, Vol. 41, p. 233.

Schmuttenmaer, C.A., Cohen, R.C., Pugliano, N., Heath, J.R., Cooksy, A.L., Busarow, K.L., and Saykally, R.J. 1990, Science, 249, 897.

Turner, B.E. 1971, Ap. J., 163, L35.

Weltner, W. and Van Zee Jr., R.J. 1989, Chem. Rev., 89, 1713.

Airborne Astronomy Symposium on the Galactic Ecosystem
ASP Conference Series, Vol. 73, 1995
M.R. Haas, J.A. Davidson, and E.F. Erickson (eds.)

Physical and Chemical Evolution of Reduced Organic Matter in the ISM

Peter Jenniskens and David F. Blake

NASA/Ames Research Center, MS 239-4, Moffett Field, CA 94035

Abstract. A mechanism is described that can cause a high yield of reduced organic matter from the recombination of the radicals in UV-photolysed ice mantles of interstellar grains.

1. Introduction

Icy mantles on interstellar grains have been a topic of study in airborne astronomy. Recent laboratory analog studies of the yield of organic residue from UV photolysed ices have shown that this mechanism (Greenberg *et al.* 1972, Hagen *et al.* 1979, d'Hendecourt *et al.* 1986) can be the most significant source of complex reduced organic matter in the interstellar medium (Jenniskens *et al.* 1994). However, the total yield is a function of the occurrence of heating events that evaporate the ice, i.e. T > 130 K, and the mechanism for such events is debated. Recently, we proposed that the recombination of radicals in the ice does not need high temperature excursions and, instead, occurs during a structural transformation of water ice at temperatures in the range 38 – 68 K (Jenniskens & Blake 1994).

2. Observation

The observation upon which this thesis is based was made during the study of the structural changes of pure water ice by means of electron diffraction. A thin layer of ice was frozen on a transparent amorphous carbon substrate, in situ in an electron microscope, by vapor deposition at 15 K. During a warmup at 1 K/min, a structural transition was observed from one form of amorphous water ice to another in the temperature regime of 38 – 68 K. The position of the first diffraction maximum changed gradually from about k = 1.87 $Å^{-1}$ to 1.72 $Å^{-1}$ over this temperature interval (Jenniskens & Blake 1994).

The change in the diffraction pattern coincides with a change of the structure of water ice from one amorphous form into another. At low temperatures, water vapor freezes into a high-density form, with a significant amount of interstitial water in the ice network (Narten *et al.* 1976). At higher temperatures, the interstitial water is expelled from the cages by a reconfiguration of the lattice and transforms into a low-density form.

The temperature range for this reconstruction, as found in our experiments, coincides with the diffusion of radicals observed in the studies of UV photolysed

layers of water ice contaminated with impurities (Schutte 1988). These studies use infrared absorption to measure the presence of the radicals.

3. Discussion

This structural transformation of the water ice network can play an important role in the physical and chemical evolution of reduced organic matter in the interstellar medium. Small heating events that raise the grain temperature to some 60 K are sufficient to allow periodic recombinations of radicals, induced by the structural transformation of the high-density amorphous form to the low-density amorphous form. When the ice is in the low-density form and is subsequently cooled to a temperature in the stability regime of the high-density form, irradiation by UV photons can transform the network back into the high-density form. This phenomenon has been observed during electron-beam irradiation (Heide 1984, 1985) and is analogous to UV photon destruction of the cubic lattice at low temperatures (Kouchi & Koruda 1990). In the process, new radicals are formed. A second heating event can recombine these radicals and, as a result, increase the yield of organic residue. The cycle can continue as long as traces of small carbon bearing molecules (CO, CO_2) are present.

The rather sudden onset of structural change during a heating event allows the ice to accumulate a high radical concentration in the periods that it remains at low temperature. A high radical concentration prior to the heating event enhances the average molecular weight of the recombination products, which increases the yield of organic residue (Jenniskens *et al.* 1994). The larger molecules are less likely to sublimate, before additional processing by UV photons creates the final complex organic residue of large molecular weight.

Acknowledgments. We are indebted to G. Palmer, who is responsible for a number of important modifications to the electron microscope, and A. Breon, who automated the reduction process of large batches of diffraction patterns.

References

Greenberg, J. M., Yencha, A. J., Corbett, J. W., & Frisch, H. L. 1972, Mem. Soc. R. Sci. Liege 6e serie, tome III, 425

Hagen, W., Allamandola, L. J., & Greenberg, J. M. 1979, Ap&SS, 65, 215

Heide, H. G. 1984, Ultramicroscopy, 14, 271

Heide, H. G., & Zeitler, E. 1985, Ultramicroscopy, 16, 151

d'Hendecourt, L. B., Allamandola, L. J., Grim, R. J. A., & Greenberg, J. M. 1986, A&A, 158, 119

Jenniskens, P., & Blake, D. F. 1994, Science, 265, 753

Kouchi, A., & Koruda, T. 1990, Nature, 344, 134

Narten, A. H., Venkatesh, C. G., & Rice, S. A. 1976, J. Chem. Phys., 64, 1106

Schutte, W. A. 1988, *The Evolution of Interstellar Organic Grain Mantles*, Thesis, University of Leiden, Leiden, The Netherlands

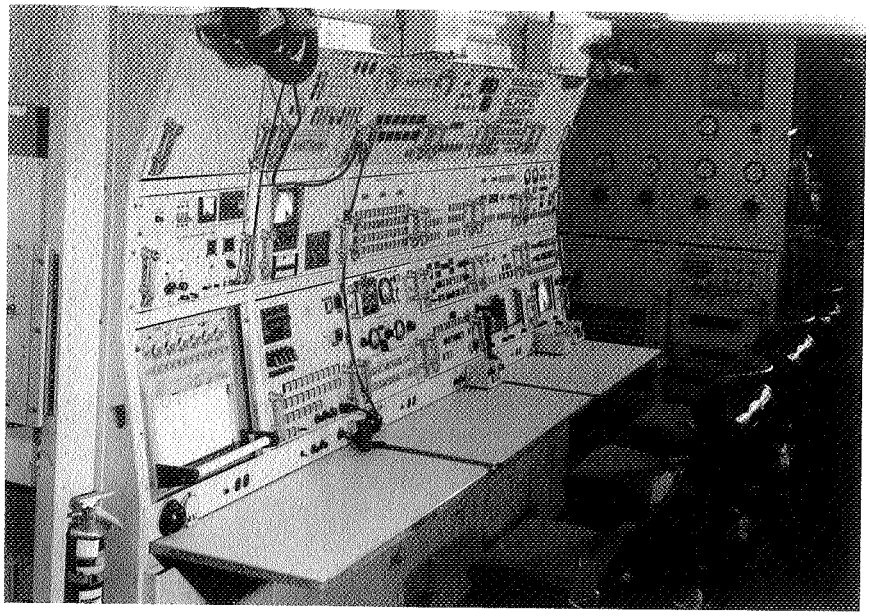

Main Console (1975)

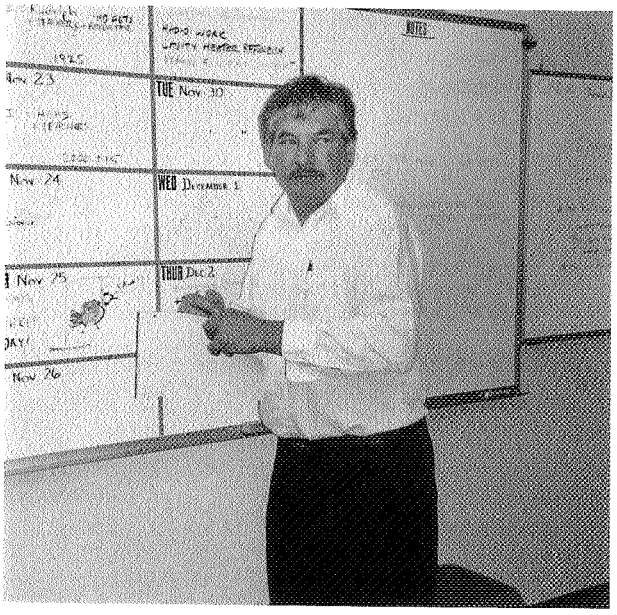

Jim McClenahan

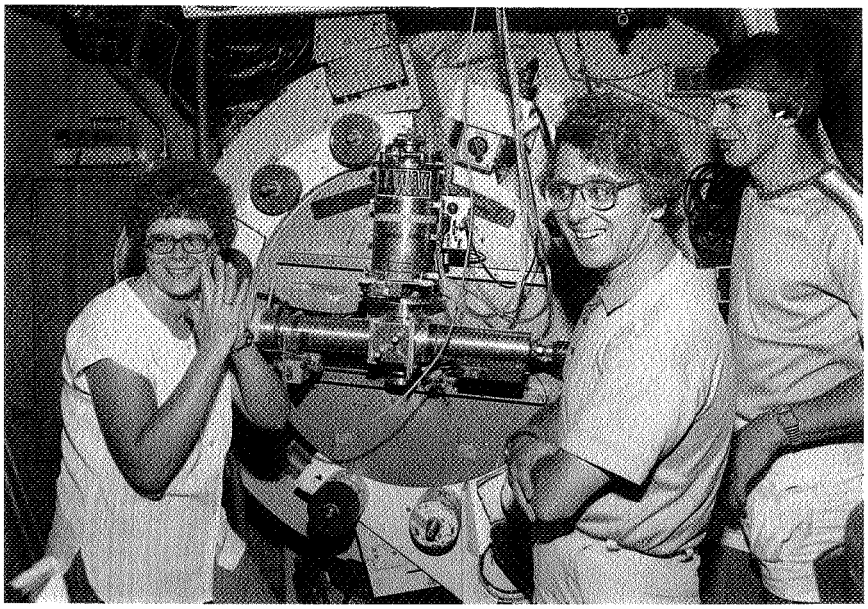

Judy Pipher, Larry Helfer, Terry Herter (1979)

Gary Morris, Tom Kalaskey

Airborne Astronomy Symposium on the Galactic Ecosystem
ASP Conference Series, Vol. 73, 1995
M.R. Haas, J.A. Davidson, and E.F. Erickson (eds.)

Ices in the Taurus Dark Cloud Environment

J.E. Chiar & D.C.B. Whittet
Dept. of Physics, Rensselaer Polytechnic Institute, Troy, NY 12180

A.J. Adamson
Dept. of Physics and Astronomy, University of Central Lancashire, Preston PRI 2HE, UK

T.H. Kerr
Dept. of Chemistry, University of Nottingham, University Park, Nottingham NG7 2RD, UK

1. Introduction

The chemical evolution of star forming regions and the role of dust grains as sites for molecule formation and mantle growth are topics of much current interest (e.g. Whittet 1993). Both theoretical models and observational evidence suggest the existence of at least two phases of mantle growth in molecular clouds, leading to the occurrence of distinct H_2O-rich and CO-rich ice phases (d'Hendecourt et al. 1985; Tielens et al. 1991).

The solid CO feature at 4.67 μm provides a spectroscopic signature of dust in the coldest regimes of dense molecular clouds. The CO feature consists of two overlapping components: a narrow component centered at 4.674 μm and a broad shallower component centered at 4.681 μm. The broad component is generally identified with CO in a matrix dominated by H_2O. The narrow component is produced by pure CO, CO in a non-polar matrix (such as CO:CO_2 or CO:O_2), or CO in a highly dilute polar matrix (e.g. Kerr et al. 1993, Chiar et al. 1994). Mixtures that provide a good fit to the CO profile can give indirect evidence for molecules that are not directly observable.

The long-wavelength wing of the water-ice feature (between 3.2 and 3.6 μm) contains the C-H stretching vibrations in carbon-bearing molecules. Smith et al. (1989) attribute the long-wavelength wing toward *protostars* to unspecified hydrocarbons. Higher resolution observations of a 3.54 μm substructure in protostars by Allamandola et al. (1992) were compared to laboratory data; a good fit with methanol was obtained, confirming earlier work by Grim et al. (1991) and showing that the methanol in these objects is intimately mixed with water on the grain mantles rather than being present in pure form. A weaker absorption at 3.47 μm was attributed to stretching vibrations of tertiary C-H bonds in aliphatic hydrocarbons; these are probably associated with a refractory component of the grains rather than volatile grain material. However, Smith et al. (1993) obtained low-resolution data in the 3 μm region for *field stars* behind the Taurus cloud and conclude that the long-wavelength wing cannot be the result of a highly refractory hydrocarbon residue.

Field stars provide an important means for probing undisturbed regions of molecular clouds where icy mantles are most likely to form. Combining observations of field stars with those of protostars provides a comparison of the extent of grain processing in protostellar environments. The Taurus dark cloud provides an ideal environment for the formation of icy mantles as it is free from shocks and bright internal sources of ultraviolet (UV) radiation. Earlier low-resolution observations of the Taurus cloud done by Whittet et al. (1989) showed that about 30% of the available CO is depleted on to the grains.

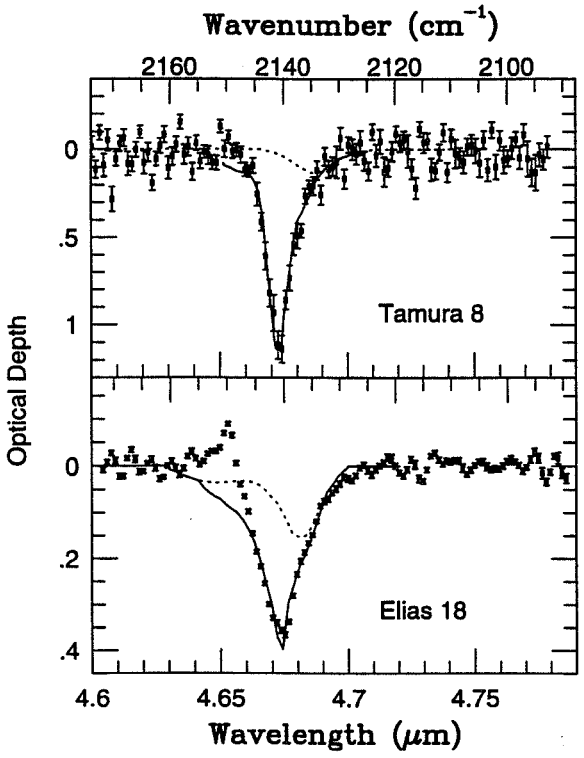

Figure 1. CO spectra of (top) Tamura 8: the narrow and broad (dashed line) features are fit with CO:H_2O (10:1, 10 K) and CO:H_2O (3:4, 100 K), respectively, and (bottom) Elias 18: the narrow and broad features are fit with CO_2:CO (20:1, 10 K) and H_2O:CO (20:1, 10K). The combination of the broad and narrow components is shown by the solid line.

2. Observations

Observations were carried out in 1993 November using cooled grating spectrometer CGS 4 on the United Kingdom Infrared Telescope (UKIRT) at Mauna Kea Observatory in Hawaii. Standard chopping/nodding techniques were used and

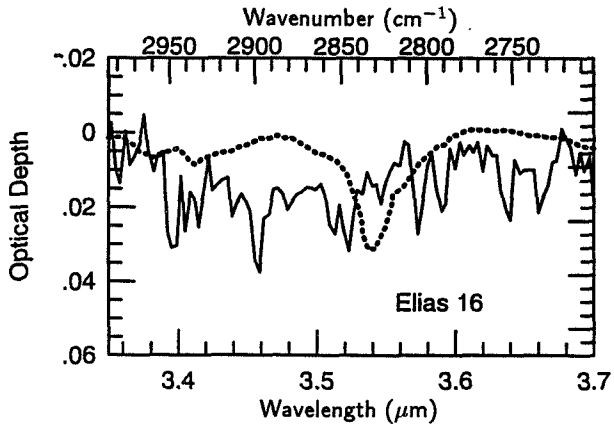

Figure 2. 3 μm spectrum for Elias 16 (solid line) relative to a local continuum, overlaid with CH_3OH spectrum from Allamandola et al. (dashed line). Wavelengths shortward of 3.35 μm are heavily affected by atmospheric methane absorption.

a variety of standard stars were observed to permit cancellation of any photospheric features. We discuss some preliminary results of these observations in these proceedings.

3. The CO spectra

Our high resolution ($R \sim 1200$) data for the Taurus dark cloud allows us to fit laboratory mixtures to the narrow and broad components of the solid CO feature using the fitting procedure discussed by Kerr et al. (1993). The laboratory data used are from Sandford et al. (1988), Schmitt et al. (1989), and Tielens et al. (1991). Figure 1 shows the spectra of the field star Tamura8 and embedded object Elias 18. The spectrum of Tamura 8 is well matched with a mixture of CO:H_2O (10:1) with a small contribution of CO:H_2O (3:4) at 100 K. The spectrum of Elias 18 is notably broader and best matched with a mixture of CO_2:CO (20:1) with a small contribution of H_2O:CO (20:1) at 10 K. This preliminary analysis of the Elias 18 spectrum strongly suggests evidence for the presence of carbon dioxide in the grain mantles around this object. In this case, the embedded object may be supplying sufficient UV radiation necessary to overcome the activation energy barrier for the creation of CO_2.

4. 3 μm spectra

Figure 2 shows the low-resolution ($R \sim 550$) CGS 4 spectrum of the Taurus field star Elias 16, compared to the methanol absorption feature which would be expected at this A_V if the ration $\tau_{3.54}/A_V$ were the same as in NGC7538 IRS9 (Allamandola et al. 1992). The feature is clearly not detected; we estimate an upper limit of 0.01 on the optical depth of any feature of this width at this wave-

length. Using the mean width and absorption strength given by Allamandola et al., methanol column density $< 1.0 \times 10^{17}\,\mathrm{cm}^{-2}$ is required to produce this upper limit on the 3.54 μm band. By contrast, the solid CO column towards Elias 16 is $6.7 \times 10^{17}\,\mathrm{cm}^{-2}$ (Whittet et al. 1989). CO outnumbers CH_3OH in this line of sight by a factor in excess of 6; by comparison, in the heavily embedded sources W33A and NGC7538 IRS9, this ratio is 0.1 and 1.05 respectively, and methanol is the second most abundant mantle volatile after H_2O. It would appear that the simple hydrocarbons from which more complex refractory material may be photolyzed are rather underabundant in Taurus.

5. $5 - 8\,\mu$m spectra

Observations of the $5 - 8\,\mu$m region are essential for studying the presence of alcohols and hydrocarbons in the grains. This spectral region includes resonances for the C-H, N-H, and O-H bending and deformation modes and is unhampered by other stronger absorption features. Specifically, observations of the $6.8\,\mu$m C-H deformation mode will help to characterize the organic component of the mantles. At present, Kuiper Airborne Observatory (KAO) data exist in this spectral region for protostars but data for field stars using the KAO have not appeared in the published literature. It would be interesting to see if more complex molecules such as ammonia and hydrocarbons exist in the lines of sight towards Taurus.

References

Allamandola, L.J., Sandford, S.A., Tielens, A.G.G.M., & Herbst, T. 1992, ApJ, 399, 134

Chiar, J.E., Adamson, A.J., Kerr, T.H., & Whittet, D.C.B. 1994, ApJ, 426, 240

d'Hendecourt, L.B., Allamandola, L.J., & Greenberg, J.M. 1985, A&A, 152, 130

Grim, R.J.A., Bass, F., Geballe, T.R., Greenberg, J.M., & Schutte, W. 1991, A&A, 243, 473

Kerr, T.H., Adamson, A.J., & Whittet, D.C.B. 1993, MNRAS, 262, 1047

Sandford, S.A., Allamandola, L.J., Tielens, A.G.G.M., & Valero, G.J. 1988, ApJ, 329, 498

Schmitt, B., Greenberg, J.M., & Grim, R.J.A. 1989, ApJ, 340, L33

Smith, R.G., Sellgren, K., & Brooke, T.Y. 1993, MNRAS, 263, 749

Smith, R.G., Sellgren, K., & Tokunaga, A.T. 1989, ApJ, 344, 413

Tielens, A.G.G.M., Tokunaga, A.T., Geballe, T.R., & Baas, F. 1991, ApJ, 381, 181

Whittet, D.C.B. 1993, in Dust & Chemistry in Astronomy, ed. T.J. Millar & D.A. Williams (Bristol: Institute of Physics Publishing), 9

Whittet, D.C.B., Adamson, A.J., Duley, W.W., Geballe, T.R., & McFadzean, A.D. 1989, MNRAS, 241, 707

Airborne Astronomy Symposium on the Galactic Ecosystem
ASP Conference Series, Vol. 73, 1995
M.R. Haas, J.A. Davidson, and E.F. Erickson (eds.)

P-4

Carbon in Photon Dominated Regions: CII/CI/CO Observations of NGC 2024

D.T. Jaffe and R. Plume

Department of Astronomy, University of Texas, Austin TX 78712

Abstract. We present observations of the large–scale distribution of the major forms of carbon, neutral and singly ionized atomic carbon and carbon monoxide, in the NGC 2024/Orion B cloud. The overall extent and morphology of the different types of emission are similar, consistent with a picture in which the atomic carbon lies on the UV–illuminated surfaces of molecular clumps throughout the cloud. However, emission from ionized carbon extends considerably farther to the west than the CO emission. Integrated over the region mapped in the 158 μm [C II] line, about half of the gas–phase carbon is in a form other than CO.

1. Introduction

Over more than a decade, the Kuiper Airborne Observatory has played a major role in uncovering the characteristics of interstellar C^+ emission. In photon dominated regions (PDRs) on the surfaces of molecular clouds, far–UV photons control the energetics, chemistry, and ionization state of the mostly neutral gas. Initial observations of the 158 μm [C II] $^2P_{3/2} \rightarrow ^2P_{1/2}$ line in star formation regions in our Galaxy and in other galaxies showed that PDRs could account for the bulk of the large–scale emission in the C^+ line (Crawford et al. 1985; Stacey et al. 1991); although a significant contribution from extended low density HII regions cannot be ruled out (Shibai et al. 1991). Detailed observations of several individual PDRs have demonstrated that the large scale [C II] emission in these sources arises in a highly clumpy medium, with a far–UV extinction length scale 10–100 times longer in the interclump gas than in the clumps themselves (Stutzki et al. 1988; Howe et al. 1991).

The extended nature of the [C II] emission has made it difficult to study the structure of PDR's. In systems which employ spatial chopping, reference beam contamination from extended [C II] emission can compromise observations of the [C II] intensity distribution (Russell et al. 1981). One can mitigate the effects of reference beam contamination, in some cases, by careful bootstrapping of the observations from more distant reference points (Stacey et al. 1993). We have recently completed a large–scale map of the [C II] distribution toward the L1630 (Orion B) molecular cloud with the MPE/UCB imaging Fabry–Perot spectrometer (Poglitsch et al. 1991). In this new work, we made use of a frequency–switching technique to allow coverage of a $\sim 30' \times 40'$ area without problems of reference beam contamination (Jaffe et al. 1994).

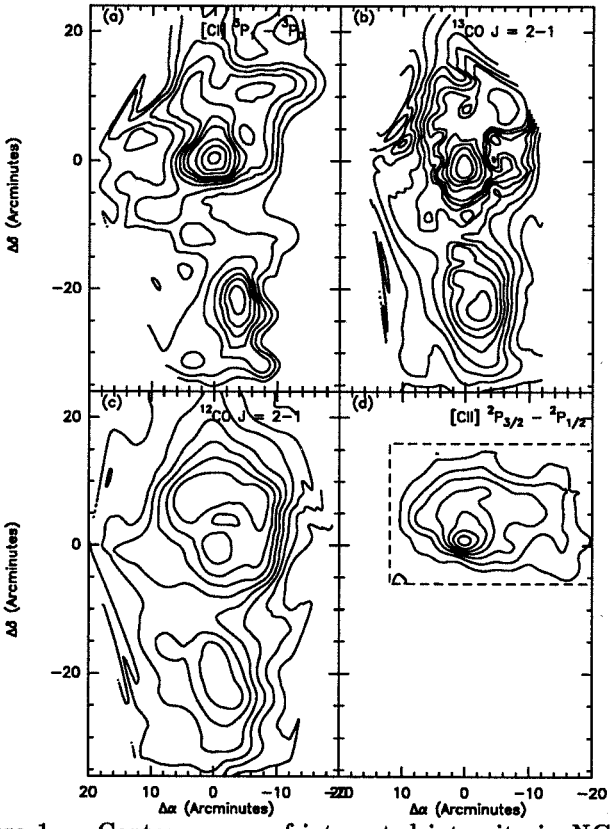

Figure 1. Contour maps of integrated intensity in NGC 2024. All maps have a 3′ resolution. (a) [C I] $^3P_1 \rightarrow {}^3P_0$. Contour levels are 5 to 20 K kms^{-1} in steps of 2.5 K kms^{-1} and 25 to 35 K kms^{-1} in steps of 5 K kms^{-1}. (b) ^{13}CO J = 2→1. Contour levels are 5 to 40 K kms^{-1} in steps of 5 K kms^{-1} and 40 to 80 K kms^{-1} in steps of 10 K kms^{-1}. (c) ^{12}CO J = 2→1. Contour levels are 20 to 160 K kms^{-1} in steps of 20 K kms^{-1}. (d) [C II] $^2P_{3/2} \rightarrow {}^2P_{1/2}$. Contour levels are $2.6 \times 10^{-4}$to 1.85×10^{-3} erg s^{-1} cm^{-2} sr^{-1} in steps of 2.6x10^{-4} erg s^{-1} cm^{-2} sr^{-1}. The dashed box indicates the region for which we have included data.

Between the C^+ zone and the region where CO is the dominant carrier of gas–phase carbon, there is a narrow zone at the molecular cloud surface where neutral atomic carbon is the most abundant carbon bearing species. [C I] emission should be widely distributed in regions with extended [C II] emission, since the lowest transition in the ground–state triplet of [C I] is more easily excited than [C II], and neutral carbon can be produced in regions with weaker UV fields than those necessary to produce large amounts of C^+ (e.g. van Dishoeck & Black 1988; Tielens & Hollenbach 1985). In addition, the strength of the 609 μm [C I] $^3P_1 \rightarrow {}^3P_0$ transition is far less dependent on physical conditions, such as the strength of the local interstellar radiation field, than the strength of the [C II] line. Observations of this [C I] line were pioneered with the KAO more than a decade ago (Phillips et al. 1980; Phillips & Huggins 1981).

We have recently constructed a re–imaging system for the Caltech Submillimeter Observatory on Mauna Kea which permits us to make large–scale observations of the 609 μm [C I] line, and the 1.3mm ^{12}CO and ^{13}CO J = 2→1 transitions with a 3′ beam (Plume, Jaffe & Keene 1994; Plume & Jaffe 1995). We have used this instrument to map these lines across the portion of the L1630/Orion B cloud covered by Jaffe et al. (1994). The maps show that the distribution of [C I], [C II] and ^{13}CO J = 2→1 emission are similar in extent (Figure 1). The main exception occurs in the West, near ζ Ori, where [C II] is more extended than the other transitions. The spectral line profiles of the ^{13}CO and [C I] lines are also remarkably similar. Typical column densities (assuming $\tau << 1$) in a 3′ beam are : $N(CI) \approx 1.1 \times 10^{17}$ cm^{-2}, $N(CII) \approx 8 \times 10^{17}$ cm^{-2}, and $N(^{13}CO) \approx 8.5 \times 10^{15}$ cm^{-2}. The morphological similarities between the emission line maps, the magnitude of the observed column densities, and the similarities in the emission line profiles, argue for a picture in which the [C I] emission arises from PDRs on the surfaces of molecular clumps. Plume, Jaffe & Keene (1994) reached the same conclusion from their observations of S140. Over the region mapped in [C II], there are $\sim 1.4 \times 10^{55}$ C^0 atoms, $\sim 5 \times 10^{55}$ C^+ atoms, and $\sim 1.2 \times 10^{54}$ ^{13}CO molecules. Assuming that $[^{12}CO/^{13}CO] = 50$, the relative amount of material in each of the three main carbon phases (C^+:C^0:CO) is given by the ratio 40:10:50. Therefore, the CO region accounts for only about 50% of the total gas–phase carbon in the region. The ^{13}CO observations imply a typical $A_v \sim 5$. Therefore, regions with only a slightly smaller A_v and similar UV fields and particle densities, can have substantial amounts of molecular (H in H_2) gas with essentially no detectable ^{13}CO emission.

The results from L1630 show that, on large scales, emission from the ground state fine–structure lines of [C I] and [C II] are morphologically similar to ^{13}CO. The ^{12}CO distribution is similar in overall extent but does not display the same amount of small–scale variations as seen in the other species. A likely explanation is that ^{13}CO locates clumps, as do the [C II] and [C I] lines which trace the surfaces of clumps and are generally optically thin. In regions with large UV fields, such as near ζ Ori, the [C II] emission more closely resembles that of ^{12}CO. In these moderate density, high UV field regions, much of the ^{13}CO may be destroyed by isotope selective photodissociation (van Dishoeck & Black 1988; Jaffe et al. 1994), and ^{12}CO opacities may be lower than usual. In addition, the lower column densities in these regions may result in a much higher surface area to volume ratio for the clumps, than elsewhere in the cloud.

Acknowledgments. This work was supported by NASA grant NAG2-402 to the University of Texas and by a David and Lucile Packard Foundation fellowship. We thank our many collaborators on the KAO and at the CSO who have helped in this effort.

References

Crawford, M.K., Genzel, R., Townes, C.H., & Watson, D.M. 1985, ApJ, 291,755.

Howe, J.E., Jaffe, D.T., Genzel, R., & Stacey, G.J. 1991, ApJ, 373, 158.

Jaffe, D.T., Zhou, S., Howe, J.E., Herrmann, F., Madden, S.C., Poglitsch, A., van der Werf, P.P., & Stacey, G.J. 1994, ApJ, 436, in press.

Phillips, T.G., Huggins, P.J., Kuiper, T.B.H., & Miller, R.E. 1980, ApJ, 238, L103.

Phillips, T.G. & Huggins, P.J. 1981, ApJ, 251,533.

Plume, R. & Jaffe, D.T. 1995, PASP, submitted.

Plume, R., Jaffe, D.T., & Keene, J. 1994, ApJ, 425,L49.

Poglitsch, A., Beeman, J.W., Geis, N., Genzel, R., Haggerty, M., Haller, E.E., Jackson, J., Rumitz, M., Stacey, G.J., & Townes, C.H.,1991, Int. J. Infrared Millimeter Waves, 12, 859.

Russell, R.W., Melnick, G., Smyers, S.D., Kurtz, N.T., Gosnell, T.R., Harwit, M., & Werner, M.W. 1981,ApJ, 250, L35.

Shibai, H., et al. 1991, ApJ, 374, 522.

Stacey, G.J., Geis, N., Genzel, R., Lugten, J.B., Poglitsch, A., Sternberg, A., & Townes, C.H. 1991, ApJ, 373, 423.

Stacey, G.J., Jaffe, D.T., Geis, N., Genzel, R., Harris, A.I., Poglitsch, A., Stutzki, J., & Townes, C.H. 1993, ApJ, 404, 219.

Stutzki, J., Stacey, G.J., Genzel, R., Harris, A.I., Jaffe, D.T., & Lugten, J.B. 1988, ApJ, 332, 379.

Tielens, A.G.G.M., & Hollenbach, D. 1985, ApJ, 291, 747.

van Dishoeck, E.F., & Black, J.H. 1988, ApJ, 334, 771.

Airborne Astronomy Symposium on the Galactic Ecosystem
ASP Conference Series, Vol. 73, 1995
M.R. Haas, J.A. Davidson, and E.F. Erickson (eds.)

Molecular, Atomic, and Ionized Gas in the NGC 6334 Star Forming Region

K. E. Kraemer, J. M. Jackson and T. A. D. Paglione

Astronomy Department, Boston University, Boston, MA 02215

A. P. Lane

Harvard-Smithsonian Center for Astrophysics, Cambridge, MA 02138

Abstract. NGC 6334 is a nearby (1.7 kpc, Neckel 1978) giant molecular cloud which contains at least 7 distinct sites of massive star formation. Using the Far-infrared Imaging Fabry-Perot Interferometer (FIFI) on the Kuiper Airborne Observatory, we have imaged this region in the FIR fine structure lines of O^0 and C^+. The line intensity ratios are compared with the predicted line ratios from the PDR models of Wolfire, Tielens and Hollenbach (1990) (hereafter WTH) to determine the gas density and UV field strength. The [O I] 63 μm/ 145 μm intensity ratio is at least a factor of 10 lower than predicted. We suggest that self-absorption by cooler foreground material suppresses the [O I] 63 μm line. We have also mapped CO $J = 2 \rightarrow 1$ emission with the Caltech Submillimeter Observatory (CSO). In general, we find an *anticorrelation* of [C II] and CO emission. Particularly striking is a [C II] peak which is not associated with any CO, FIR or radio continuum source. Consequently, there is no *local* source of hard UV radiation. Either (1) the [C II] peak is illuminated by a cluster of embedded B stars, which radiate enough soft UV photons to ionize carbon, or (2) the [C II] peak is illuminated by a distant O star.

1. Introduction

NGC 6334 is a nearby (1.7 kpc, Neckel 1978) giant molecular cloud which contains at least 7 distinct sites of massive star formation. Because multiple sites exist in the same cloud, global effects, such as elemental abundances or global magnetic fields, will not contribute to the differences between the stars. Only local effects such as age, mass, and UV field vary from site to site. This allows a cleaner comparison of the young stars and their effects on the cloud than if they were forming in different clouds. Important species such as O^0 and C^+, which are the dominant coolants of the ISM via their atomic fine structure lines in the FIR, abound in the PDRs around OB stars such as those in NGC 6334. Because NGC 6334 is nearby and has multiple sites of massive star formation, the differences in the properties of the PDR gases due to local effects such as different UV fields strengths can be easily examined using the KAO.

Source	OI 145 / CII 158	OI 63 / OI 145	CII 158 / OI 63
V	—	—	2.619
A	0.669	0.611	2.447
C	0.373	1.846	1.451
D	0.238	1.776	2.370
E	0.181	2.785	1.989

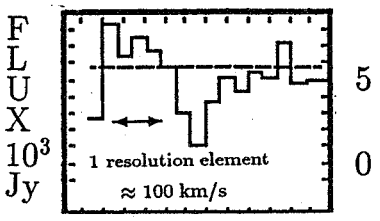

Figure 1. Measured FIR intensity ratios (table). Possible [O I] 63 μm absorption spectrum toward source V (right).

2. Observations

The [O I] 145 μm and [C II] 158 μm lines were observed with the Far-infrared Imaging Fabry-Perot Interferometer (FIFI) on the KAO in 1992 April on a flight series from New Zealand. The [O I] 63 μm line was observed with FIFI on a flight from Hawaii in 1992 August. The CO (J=2→1) line was observed with the CSO 10-m telescope. The 12 μm dust image and color temperature map are IRAS HIRES images.

3. Results

3.1. Line Intensity Ratios.

Line intensity ratios were determined toward five of the sources (Figure 1). By comparing these ratios with the PDR models of WTH, we can, in principle, determine the gas density and the incident UV field. However, the [O I] 63/ 145 μm ratio is at least a factor of 10 lower than the models predict. The [C II] 158 μm/[O I] 63 μm ratio is also an order of magnitude higher than Orion ([C II] 158 μm/[O I] 63 μm$\sim$ 0.09, Stacey et al. 1993) and the Galactic Center ([C II] 158 μm/[O I] 63 μm$\sim$ 0.06, WTH), but are comparable to the ratios measured toward DR 21 ([C II] 158 μm/[O I] 63 μm$\sim$ 1.3, Lane et al. 1990) and M17SW ([C II] 158 μm/[O I] 63 μm$\sim$ 1.4, Stutzki et al. 1988). We suggest that cooler foreground material suppresses the 63 μm line by self-absorption. A spectrum toward source V shows a possible absorption detection in the [O I] 63 μm line (Figure 2, right).

3.2. Gas Distribution.

The distributions of the FIR lines are compared to that of the CO (J=2 → 1) emission (Figure 2a). The [O I] 145 μm (Figure 2c) generally follows the CO distribution, but the [C II] (Figure 2d) does not. In fact, there is an *anticorrelation* between the [C II] and CO emission. The [C II] intensity peak, east of source II, coincides with a hole in the CO emission. Even more interesting is the [C II]

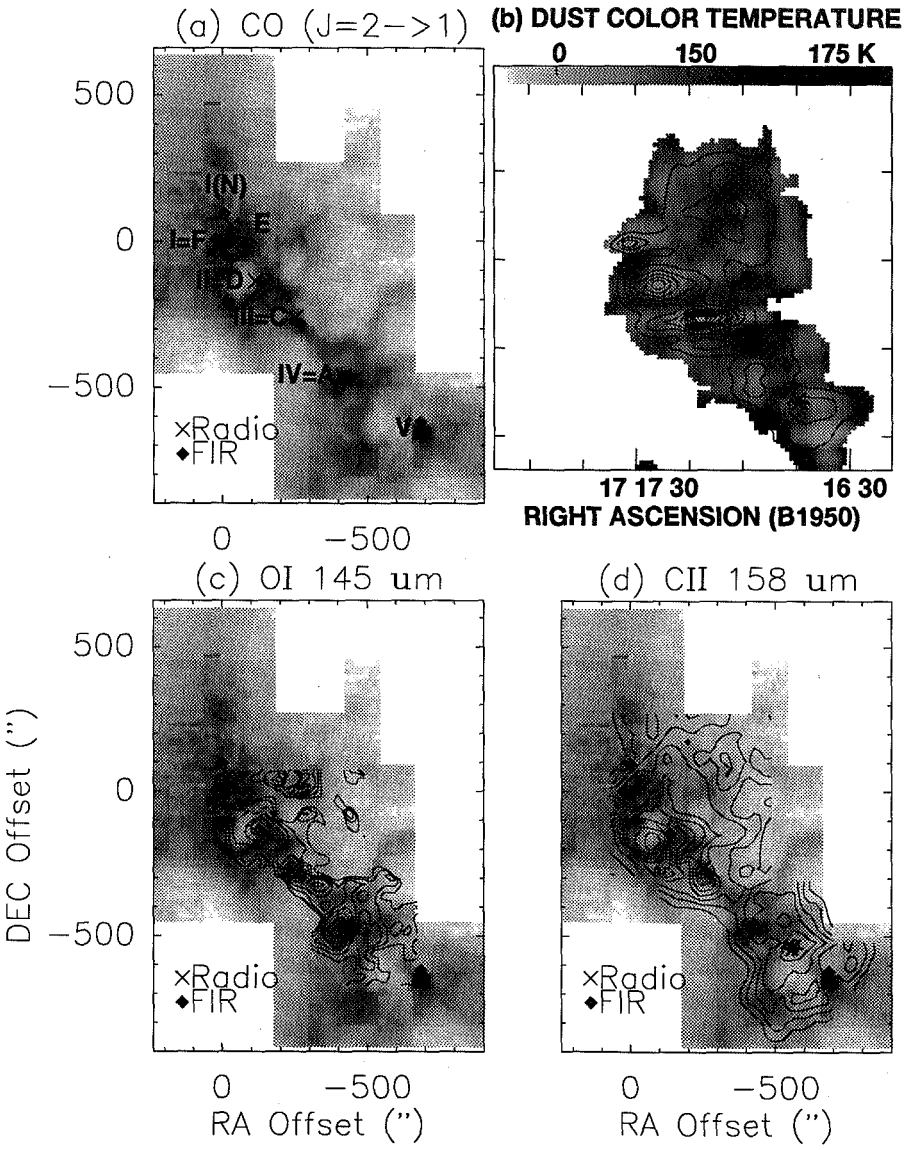

Figure 2. (a) Distributions of CO J=2 → 1 emission (greyscale), peak intensity 616 K-km s^{-1}; (b) 12 μm IRAS emission (contours), peak intensity 4.26 kMJy $ster^{-1}$ and dust color temperature (greyscale); (c) [O I] 146 μm emission (contours), peak intensity 4.49×10^{-14} W m^{-2}; (d) [CII] 158 μm emission (contours), peak intensity 1.43×10^{-13} W m^{-2}. Alphabetical labels correspond to the radio sources (Rodriguez, Canto and Moran 1982). Roman numerals correspond to the FIR sources (McBreen et al. 1979). The map (0,0) position is source F, $\alpha = 17^h17^m32^s.3$, $\delta = -35°44'04''$.

peak which lies between sources IV and V (marked with an asterisk), which also corresponds to a hole in the CO. This peak is not associated with any radio or FIR continuum source; thus there is no *local* source of hard UV radiation. At least two possible explanations for this isolated peak exist: (1) The [C II] peak is illuminated by a cluster of embedded B stars, which radiate enough soft UV photons to ionize carbon but not enough hard UV photons to ionize hydrogen. Straw and Hyland (1989) detected a number of IR sources at this position with blue J-K colors which might be the embedded B stars. (2) Alternatively, the gas may be illuminated by a distant O star. The radiation from source IV or V may penetrate the cloud until it encounters and photoionizes the gas at the [C II] peak. The position of this [C II] peak also corresponds to an emission peak in the 12 μm IRAS data (Figure 2b). This continuum peak is not present at the higher IRAS wavelengths.

4. Summary

We have imaged the NGC 6334 star forming region in the FIR fine structure lines [O I] 63 μm, [O I] 145 μm and [C II] 158 μm with the KAO, and the CO J=2 $\rightarrow$ 1 rotational transition. We find that the [O I] 63/ 145 μm ratio is at least a factor of 10 lower than the models predict (WTH). This may be caused by self-absorption of the 63 μm emission by cooler foreground oxygen. A comparison of the FIR gas distribution with that of the CO shows that the [O I] 145 μm distribution corresponds well to the CO, but there is an *anticorrelation* between the [C II] 158 μm and CO emission. There is a [C II] emission peak, between sources IV and V, which seems to have no local source of hard UV photons. It may be illuminated by a cluster of B stars, or by a distant O star.

References

Lane, A.P., Haas, M.R., Hollenbach, D.J. and Erickson, E.F. 1990, ApJ **361**, 132

McBreen, B., Fazio, G.G., Stier, M., & Wright, E.L. 1979, ApJ **333**, L183

Neckel, J. 1978, A&A **69**, 51

Rodriguez, L.F., Cantó, J., & Moran, J.M. 1982, ApJ **255**, 103

Stacey, G.J., Jaffe, D.T., Geis, N., Genzel, R., Harris, A.I., Poglitsch, A., Stutzki, J, and Townes, C.H. 1993, ApJ **404**, 219

Straw, S.M. and Hyland, A.R. 1989, ApJ **340**, 318

Stutzki, J., Stacey, G.J., Genzel, R., Harris, A.I., Jaffe, D.T. and Lugten, J.B. 1988, ApJ **332**, 379

Wolfire, M.G., Tielens, A.G.G.M. and Hollenbach, D. 1990, ApJ **358**, 116

Airborne Astronomy Symposium on the Galactic Ecosystem
ASP Conference Series, Vol. 73, 1995
M.R. Haas, J.A. Davidson, and E.F. Erickson (eds.)

HCN and HCO^+ Images of the Photodissociation Region in the Orion Bar

Rolaine C. Young Owl and Margaret Meixner

Department of Astronomy, University of Illinois, Urbana, IL 61801

A. G. G. M. Tielens

NASA/Ames Research Center, MS 245-3, Space Sciences Division, Moffett Field, CA 94035

Jan A. Tauber

European Space Agency, Astrophysics Division, ESTEC, Keplerlaan 1, 2201 AZ Noordwijk, The Netherlands

Abstract. We present preliminary millimeter-wavelength images of the photodissociation region (PDR) in the Orion Bar, observed with the Berkeley- Illinois-Maryland array (BIMA). These new BIMA observations have attained 5″ resolution in the J=1-0 emission lines of HCO^+ (formyl ion) and HCN (hydrogen cyanide). The results are compared with previous observations of the J=1-0 transition lines of ^{13}CO. We find that the HCO^+ and HCN have different spatial distributions. HCN appears to lie primarily inside dense clumps of gas, which are defined by areas of intense ^{13}CO emission. However, the HCO^+ emission appears to be only loosely associated with the surfaces of the gas clumps. We suggest that HCO^+ abundance is enhanced by the presence of vibrationally excited H_2 on the surfaces of dense clumps, and that the HCN abundance is attenuated by photodestruction outside the cores of dense clumps of gas.

1. Background

A photodissociation region (PDR) is the intermediate, neutral atomic zone situated between the ionized region surrounding young O or B stars and the molecular cloud in which the stars are embedded. The standard PDR model (Tielens and Hollenbach, 1985) is a semi-infinite homogeneous slab of warm (200–1000 K), dense (10^3 – 10^6 cm $^{-3}$) gas illuminated by a strong UV field (10^3 – 10^6 times the average interstellar field). The model predicts the stratification of the slab into several layers. The warm (greater than 300 K) surface layer consists of mainly atomic hydrogen and oxygen, and singly ionized carbon. At a depth where A_v ~2 mag, molecular hydrogen can exist, giving rise to emission lines from fluorescent vibrational excitation. Deeper into the cloud (at A_v~ 4), the temperature drops to 50K, and C^+ undergoes electron recombination to form neutral carbon, which then quickly combines with oxygen, forming CO.

The chemical processes occurring in PDRs are governed by the UV radiation flux from the young stars, and are dominated by UV-driven photodestruction and ionization of molecules. The positions, spatial distributions, and intensities of radio emission from several different molecular tracers reveal the local physical conditions and the dominant chemical processes occuring in each part of the region. In particular, by comparing HCO^+, a product of oxygen chemistry in the molecular cloud, with its nitrogen-bearing analog HCN, it may be possible to define the physical conditions under which different pathways involving oxygen or nitrogen chemistry dominate.

This paper describes a study of HCO^+ and HCN images of the Orion Bar. Located in the central portion of the nearest giant molecular cloud, the Orion Bar is the archetype of a bright PDR. It is a region of moderately dense gas ($\sim 5 \times 10^4$ cm^{-3}) illuminated by a UV field which is a factor of $\sim 5.0 \times 10^4$ larger than the average interstellar radiation field. It also has an edge-on orientation to the observer, which makes it easy to see the sharp transition from ionized region to neutral gas, then to molecular gas, as a function of the line-of-sight column density to the UV source.

2. Observations/Results

Images of the Orion Bar in the rovibrational transition lines of HCN and HCO^+, at 88.63 and 89.18 GHz, respectively, were obtained at a spatial resolution of 5″ with the six-element millimeter array (BIMA) at Hat Creek Radio Astronomy Observatory. Figure 1 shows each of these images overlaid onto a previously obtained ^{13}CO J=1–0 image which delineates the positions of dense clumps of gas (Tauber et al. 1994). For both maps, the velocity is 10–11 km s^{-1}, and the lowest contour level shown is 1σ with intervals of 1σ between contours (σ= 0.363 Jy bm^{-1} for HCO^+, and 0.355 Jy bm^{-1} for HCN). Three important features of these images are noted: (1) Intense HCO^+ emission is not very well confined to dense gas clumps, but seems to arise primarily from the interclump region or on the surfaces of clumps. (2) Very intense HCN emission coincides very well with the clumps, implying that the HCN emission arises primarily from the cores of dense gas clumps. (3) The HCO^+ and HCN emissions are not spatially coincident, suggesting that the chemical pathways producing HCO^+ and HCN in PDRs require very different physical conditions or the presence/absence of certain chemical species.

Figure 2 is a plot of the relative intensities of HCO^+, HCN, and H_2 emission from the Orion Bar as a function of position along a crosscut line centered at the highest emission value of the HCN image (+44″ offset RA, +17″ offset DEC), with a direction angle of 135° east of North. This direction is perpendicular to the bar, and radial to the direction of the UV source. The H_2 emission is in the near-infrared (2.12 microns), and is due to the S(1) 1–0 transition of vibrationally excited molecular hydrogen. The shapes and positions of the emission peaks indicate that HCO^+ is enhanced at the surface of the PDR, whereas HCN is attenuated there. This result supports predictions by Tauber et al.(1994), who have extended the standard PDR model from a homogenous to a two-component PDR model (cf., Meixner & Tielens, 1993). The two-component PDR model is a moderately dense (10^4 cm^{-3}) homogeneous medium embedded with very dense

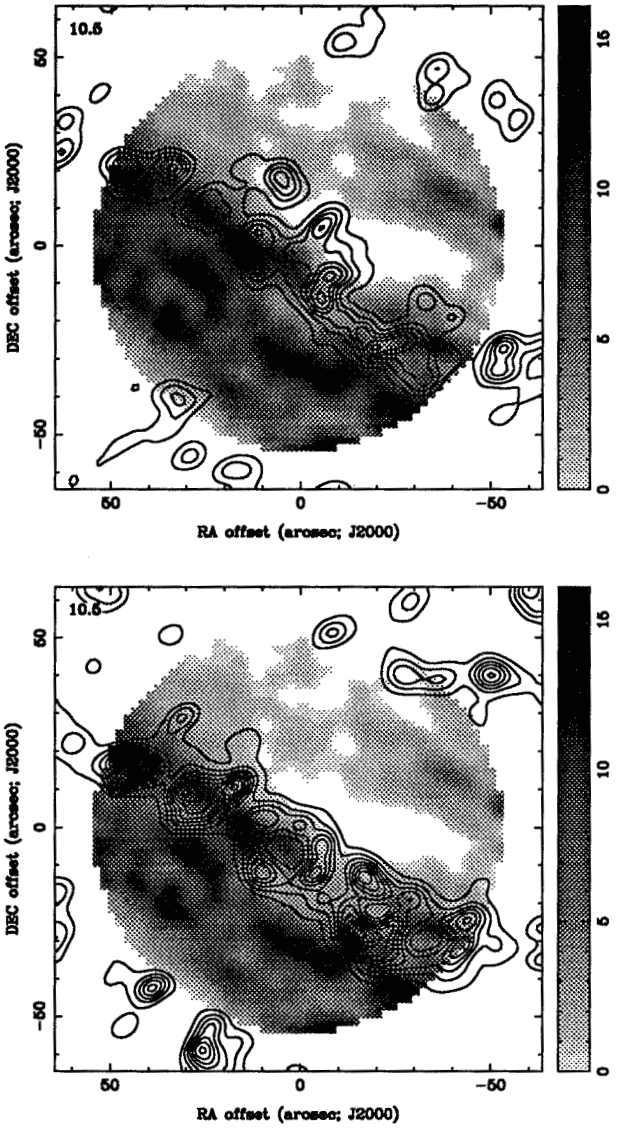

Figure 1. The top map is a small-scale (5 ″) HCO^+ contour map of the Orion Bar, overlaid on a greyscale ^{13}CO image of the Orion Bar. The bottom map is a similar overlay of HCN (contours) on ^{13}CO.

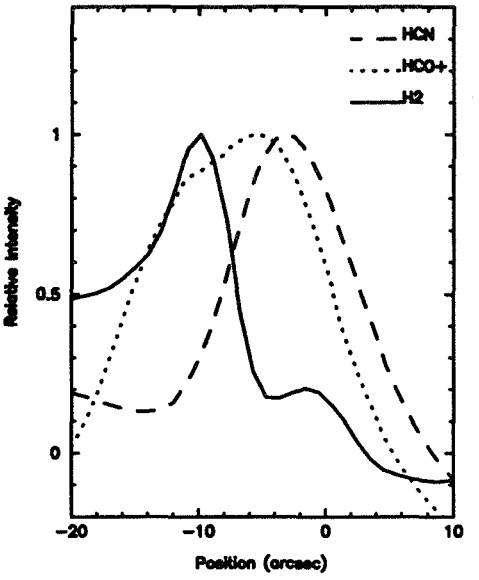

Figure 2. Relative intensity crosscuts through a dense gas clump in the Orion Bar. The position is positive into the molecular cloud and negative toward the UV source.

(10^7 cm^{-3}) clumps of gas. The interclump medium is treated as one homogeneous PDR, while the dense clumps are treated as separate PDRs. Abundance profiles calculated from the two-component model predicts that HCO^+ emission should be greatly enhanced on the surfaces of dense clumps nearest the interface between the molecular and ionized regions. The HCO^+ enhancement is expected because of the increased abundance of vibrationally excited molecular hydrogen, which facilitates a main formation pathway for HCO^+. On the other hand, the HCN emission is expected to be attenuated at the surface of dense clumps due to photodestruction of HCN by UV photons. Assuming that the intensity distribution is dominated by abundance, and not excitation, the HCO^+ emission is shown to be enhanced by the increased abundance of H_2*, and HCN emission is attenuated by increased UV flux at the surface of the PDR.

Our work provides motivation for and demonstrates the necessity of incorporating nitrogen chemistry into the existing PDR model, which has previously treated oxygen and carbon chemistry in detail.

References

Meixner, M. & Tielens, A. G. G. M. 1993, ApJ, 405, 216–228

Tauber, J., Tielens, A. G. G. M., Meixner, M., & Goldsmith, P. F. 1994, ApJ, 422, 136–152

Tielens, A. G. G. M. & Hollenbach, D. 1985, ApJ, 291, 722–746

Airborne Astronomy Symposium on the Galactic Ecosystem
ASP Conference Series, Vol. 73, 1995
M.R. Haas, J.A. Davidson, and E.F. Erickson (eds.)

Atomic Far-IR Fine-Structure Line Mapping of L1630, M17, and W3: Comparison of [O I] and [C II] Distributions

J. E. Howe

University of Maryland, Department of Astronomy, College Park, MD 20742-2421

D. T. Jaffe

University of Texas, Department of Astronomy, R. L. Moore Hall, Austin, TX 78712

S. Zhou

University of Illinois, Department of Astronomy, 1002 West Green Street, Urbana, IL 61801

Abstract. We mapped the distribution of atomic far-IR line emission from [O I] and [C II] over parsec scales in the Galactic star-forming regions L1630, M17, and W3 using the MPE Far-Infrared Fabry-Perot Imaging spectrometer (FIFI) on board the NASA Kuiper Airborne Observatory. The lines mapped include [O I] 63 μm, [O I] 146 μm, and [C II] 158 μm. Comparison of the intensities and ratios of these lines with models of photodissociation regions (e.g., Tielens & Hollenbach 1985, ApJ, 344, 770) allows us to derive temperatures and densities of the primarily neutral atomic gas layers lying on the surfaces of UV-illuminated molecular gas. In general, the [C II] line arises ubiquitously throughout the molecular clouds while the [O I] lines are mainly confined to warm, dense gas ($T > 100$ K, $n > 10^4$ cm^{-3}) near the sites of O and B stars. The distribution of [C II] in the star-forming clouds implies that the [C II] emission arises on the surfaces of molecular clumps throughout the clouds, rather than only at the boundary layer between molecular gas and H II regions.

In L1630, we mapped the [C II] emission over a 35′ × 45′ region encompassing the NGC 2024 H II region, the reflection nebula NGC 2023, and the Horsehead Nebula (Jaffe *et al.* 1994, ApJ, in press; Zhou *et al.* 1993, ApJ, 419, 190). Emission over a 1.5 × 2.5 pc region encompassing the H II region NGC 2024 indicates the amount of ionized atomic carbon is equal to the amount of carbon in CO. A 10′ × 3′ map of the [O I] 63 μm line in NGC 2024 shows that the [O I] 63 μm/[C II] line intensity ratio varies from about 7 at the cloud core to less than 2 in the region 5′ (0.6 pc) to the west. This drop off is consistent with a constant gas density in the core region of about 5×10^4 cm^{-3}, but a decrease in the UV intensity by more than a factor of 50. In M17, the [O I] 63 μm emission is concentrated on the UV-illuminated eastern edges of dense clumps traced by emission from

CS (Wang *et al.* 1994, ApJ, in press). In W3, we mapped the [O I] 146 μm and [C II] 158 μm distribution in a $6' \times 6'$ (4×4 pc) region of the W3 Main molecular cloud. Both the [O I] and [C II] lines are emitted throughout the cloud, attesting to the penetration of UV photons into the molecular gas. The [O I] 146 μm/[C II] intensity ratio varies from 0.1 at the cloud edge to about 1 near the W3(B) H II region, indicating gas densities from 10^4 to 10^6 cm^{-3}. Although the [O I] emission is primarily confined to the cloud core region, the [C II] emission also arises south of the molecular core where the molecular gas is almost completely photodissociated by young O and B stars.

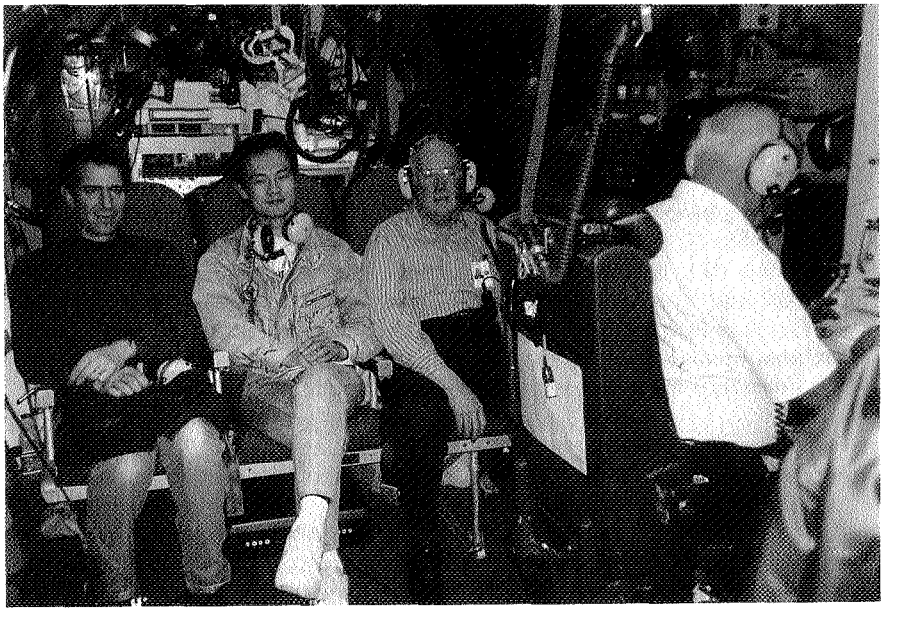

Dan Jaffe, Shudong Zhou, Charlie Townes, Carl Gillespie

Airborne Astronomy Symposium on the Galactic Ecosystem
ASP Conference Series, Vol. 73, 1995
M.R. Haas, J.A. Davidson, and E.F. Erickson (eds.)

RADIO EMISSION FROM SPINNING GRAINS

A. Ferrara

Osservatorio Astrofisico di Arcetri, 50125 Firenze, Italy

R.-J. Dettmar

Space Telescope Science Institute, Baltimore, MD 21218, USA

Abstract. We present a study of the radio emission from rotating, charged dust grains immersed in the ionized gas constituting the thick, Hα-emitting disk of many spiral galaxies.

1. Introduction

Grains are found to have substantial radio emission peaked at a cutoff frequency in the range 10-100 GHz, depending on the grain size distribution and on the efficiency of the radiative damping of the grain rotation. To obtain the radiation spectrum one has to determine: (a) *radiation field*, $\mathcal{F}_\nu$; (b) *grain charge*, Z; (c) *grain rms rotational velocity*, $\langle\omega\rangle$.

(a) Radiation Field

For the UV radiation field at high galactic latitudes, the one relevant for the present calculation, we use the compilation given by Reynolds (1990):

$$\mathcal{F}_\nu = \mathcal{F}_{\nu_L}\epsilon_{Ry}^{-4} \qquad 8 < \epsilon_{Ry} < 300 \text{ Ry}, \tag{1}$$

where $\mathcal{F}_{\nu_L} = 10^4$ phot cm^{-2} s^{-1} sr^{-1} eV^{-1} is the flux at the Lyman limit and ϵ_{Ry} is the photon energy expressed in *Ry*.

(b) Grain Charge

The detailed balance equation we have used to determine the grain charge Z is

$$n_p\left\{\left(\frac{8kT}{\pi m_p}\right)^{1/2}\left[\tilde{J}_{\nu_p,\tau_p}(a,Z,T)s_p+\delta_p(a,Z,T)\right]+\tilde{J}_{pe}(a,\mathcal{F}_\nu)\right\}=$$

$$n_e\left\{\left(\frac{8kT}{\pi m_e}\right)^{1/2}\left[\tilde{J}_{\nu_e,\tau_e}(a,Z,T)s_e-\delta_e(a,Z,T)\right]\right\}, \tag{2}$$

where the indices p and e stand for protons and electrons, respectively; $\tilde{J}_{\nu,\tau}$ are the collisional charging rates; δ are the secondary emission rates; $\tilde{J}_{pe}$ is the photoelectric charging rate; and s is the sticking probability. $\tilde{J}_{\nu,\tau}$ are taken from Draine & Sutin (1987); $\tilde{J}_{pe}$ is taken from Draine (1978); and δ and s are taken

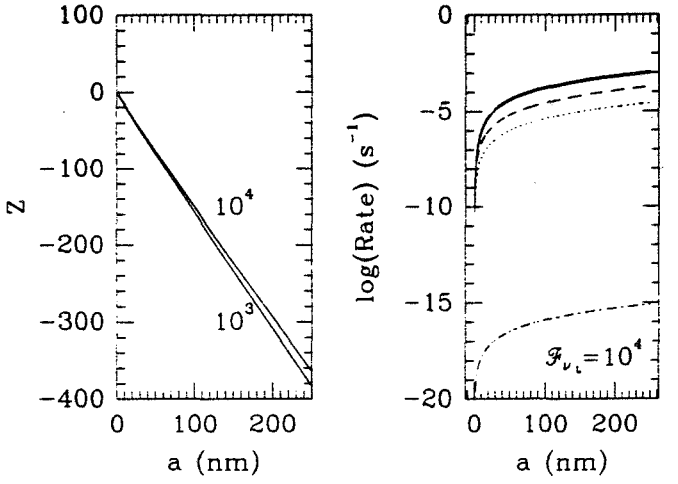

Figure 1. Numerical solutions of the detailed balance equation. **Left:** grain charge as a function of a for different values of $\mathcal{F}_{\nu_L}$, as shown by the numbers; **right:** rates for the various charging processes for the standard case $\mathcal{F}_{\nu_L} = 10^4$; *long-dashed line-* electron collisions; *solid-* proton collisions; *short-dashed* - photoelectric effect; *dotted-* proton secondary emissions; *dot-dashed-* electron secondary emission.

from Draine & Salpeter (1979). Eq. (2) must be solved together with the field emission condition (Draine & Sutin 1987) that limits the value of the charge:

$$-1 - 0.7\left(\frac{a}{\mathrm{nm}}\right)^2 < Z < 1 + 21\left(\frac{a}{\mathrm{nm}}\right)^2. \tag{3}$$

The solution of eq. (2)-(3), along with the charging rates, are shown in Fig. 1. A linear relation between Z and a approximates very accurately the numerical solutions found (Fig. 1):

$$Z(a) = -2.504\frac{kT}{e^2}a = -1.49 \times 10^7 T_4 a = -\eta a, \tag{4}$$

where $T_4 = T/10^4$. Eq. (4) is also a restatement of the classical result obtained by Spitzer (1941) and is indicative of the relative unimportance of the radiation field in determining the grain charge.

(c) Rotational Velocity

Once the effective temperature T_{eff} characterizing the Brownian motion is known, the rms rotational velocity $\langle\omega\rangle$ can be obtained straightforwardly from

$$\frac{1}{2}I\omega^2 = \frac{3}{2}kT_{eff}, \tag{5}$$

where I is the rotational inertia. If the only processes exciting rotation are atom-grain collisions and atom evaporation from the grain surface, then T_{eff} would be exactly the arithmetic mean of T and T_d, where T_d is the dust temperature. Non-thermal contributions from photoelectric emission, photon absorption/emission,

and H_2 molecule formation are shown to contribute less than 3% to $\langle\omega\rangle$ for the adopted parameters. Assuming spherical grains, the radius-rotation velocity relation is

$$a = 5.94 \times 10^{-4} T_{eff}^{1/5} \omega^{-\gamma} = 3.26 \times 10^{-3} T_4^{1/5} \omega^{-\gamma} = \beta \omega^{-\gamma}, \ \gamma = 2/5. \quad (6)$$

2. Predicted spectrum

The volume emissivity ϵ_ν^d from the rotating, charged grains can be easily calculated once the dust size distribution is specified. We will assume for the latter a power law of the form

$$\frac{dn}{da} = A_i n_H a^{-q} \quad \text{for } a_0 \leq a \leq a_1, \quad (7)$$

where n_H is the hydrogen density, which reduces to the standard MRN distribution if $q \sim 3.5$; in this case, the coefficient A_i is obtained by normalizing the distribution to the dust-to-gas ratio $\sigma = 0.01$. Using eqs. (4), (6), (7) we obtain

$$\epsilon_\nu^d d\omega = \frac{1}{3} \frac{e^2 \eta}{c^3} \gamma \beta^{4-q} A_i n_H \omega^{3-4\gamma+\gamma q} d\omega, \qquad \text{for } \left(\frac{a_1}{\beta}\right)^{-\frac{1}{\gamma}} \leq \omega \leq \left(\frac{a_0}{\beta}\right)^{-\frac{1}{\gamma}}. \quad (8)$$

Eq. (8) contains all the physics introduced in the calculation so far; its implications are discussed below.

3. Observational Implications

• *The wavelength range of the emission falls in a spectral band that can be easily observed.* In fact, if we use $a_1 = 0.25\,\mu$m and $a_0 = 3$ Å, the emission is expected in the frequency range

$$3.1 \times 10^4 \leq \nu \leq 6.2 \times 10^{11} = \nu_c \quad \text{Hz}.$$

In the absence of radiative damping (see below), small grains contribute to the 100 GHz band and the position of the high frequency cutoff ν_c turns out to be a powerful tracer of the smallest sizes in the dust distribution; Fig. 2 (left panel) shows the dependence of ν_c on a_0 for different temperatures. Note that ν_c depends very weakly on the model parameters (see eq. 6) and also on the temperature T. This can be used to infer the minimum grain size of the distribution.

• *Is it really observable?* The detection of the predicted radio emission would be the major consequence of this paper; to evaluate this possibility we compare the emissivity per H nucleus given by eq. (8) with the free-free emissivity, ϵ_ν^{ff}, of the ionized gas surrounding the dust. The comparison between the two fluxes is shown in the right panel of Fig. 2.

• *The dust emission spectral index α depends only on the size distribution index q*, since γ is fixed and determined by the microphysics (eq. 8); for a MRN

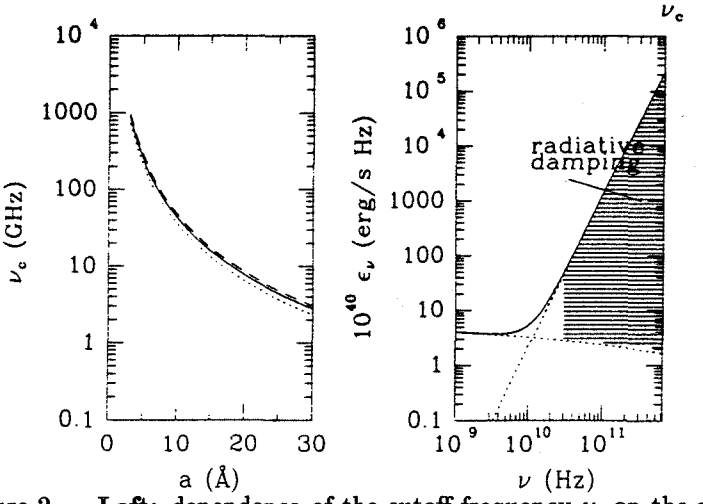

Figure 2. **Left:** dependence of the cutoff frequency ν_c on the minimum size of the grain distribution, a_0, for different temperatures: *solid-* $T_e = 10^4$ K; *dotted-* $T_e = 7000$ K; *dashed-* $T_e = 1.2 \times 10^4$ K. **Right:** comparison between the free-free emissivity (*flat dotted line*) from a gas with $T_e = 10^4$ K and $n_e = 0.1$ cm^{-3} and dust emissivity (*steep dotted line*) per H nucleus; the *solid* line is the sum of the two. The dashed region denotes the range of frequency in which the spectrum may be modified by radiative damping (see text). In the upper right corner the cutoff frequency ν_c is shown.

distribution $\alpha = 2.8$. This should reduce the possibility of confusion with the flat free-free spectrum and Fig. 2 clearly demonstrates that the emission can in principle be detected. The MRN distribution can therefore be tested directly.

• *A Caveat:* since the grains are charged and rotating, radiative damping due to dipole emission may slow down the rotation rate. For a grain with an electric dipole moment $d \simeq \xi Zea$ ($\xi \sim 0.01$), the radiative damping time becomes equal to the collisional damping time for

$$a_d = 10^{-7} \left(\frac{\xi U}{V}\right)^{2/5} \left(\frac{n_e}{0.1\mathrm{cm}^{-3}}\right)^{-1/5} \left(\frac{\delta}{3.3\mathrm{g\ cm}^{-3}}\right)^{-1/5} \left(\frac{T}{10^4\mathrm{K}}\right)^{1/10} \text{cm.} \quad (9)$$

Hence, rotation of very small grains ($a \lesssim 10$ Å) will be affected by radiative damping (see Fig. 2).

References

Draine, B. T. 1978, ApJS, 36, 595
Draine, B. T. & Salpeter, E. E. 1979, ApJ, 231, 77
Draine, B. T. & Sutin B. 1987, ApJ, 320, 803
Reynolds, R. J. 1990, The Galactic and Extragalactic Background Radiation, eds. S. Bowyer & C. Leinert, (Dordrecht:Kluwer), 165
Spitzer, L. 1941, ApJ, 93, 369

Airborne Astronomy Symposium on the Galactic Ecosystem
ASP Conference Series, Vol. 73, 1995
M.R. Haas, J.A. Davidson, and E.F. Erickson (eds.)

FAR-INFRARED POLARIMETRY

R.H. HILDEBRAND
Department of Physics, Department of Astronomy and Astrophysics, and Enrico Fermi Institute, The University of Chicago, Chicago, IL 60637

J.L. DOTSON, C.D. DOWELL, S.R. PLATT, and D. SCHLEUNING
Department of Astronomy and Astrophysics, Yerkes Observatory, and Enrico Fermi Institute, The University of Chicago, Chicago, IL 60637

J.A. DAVIDSON
SETI Institute, Ames Research Center, MS 245-6, Moffett Field, CA 94035-1000

G. NOVAK
Department of Physics and Astronomy, Northwestern University, Evanston, IL 60208-3112

ABSTRACT Airborne observations with the The University of Chicago polarimeter, Stokes (Platt et al. 1991), have produced maps of far-infrared polarization over large areas in molecular clouds. Subsequent papers will discuss the implications of the results concerning the magnetic fields of individual objects. Our purpose here is to show a broad sample of the results and to point out certain general characteristics of the polarized emission.

INTRODUCTION

The polarization of the far-infrared emission from molecular clouds has provided the most detailed observational data now available on the configuration of magnetic fields in dense cloud cores.

We now have results for eleven sources: M17, Orion (M42), W3, the arched filaments north of Sgr A, S106, W51, NGC 2024, Sgr B2, DR21, NGC 7538, and the dust ring at Sgr A. Figures 1–8 show maps of the polarization in the first eight of these sources. The results for the dust ring at Sgr A have been published elsewhere (Hildebrand et al. 1993; Hildebrand and Davidson 1994). The vectors show the direction and degree of polarization of the 100 μm emission at each point. All the vectors represent measurements of at least 3σ. Open circles denote measurements at less than 3σ where the 2σ upper limit is below 1%. Except at the peak of Sgr B2 the sources have measured optical depths less than 1. We assume that the polarization of the flux from any volume element along the line of sight is perpendicular to the local magnetic field.

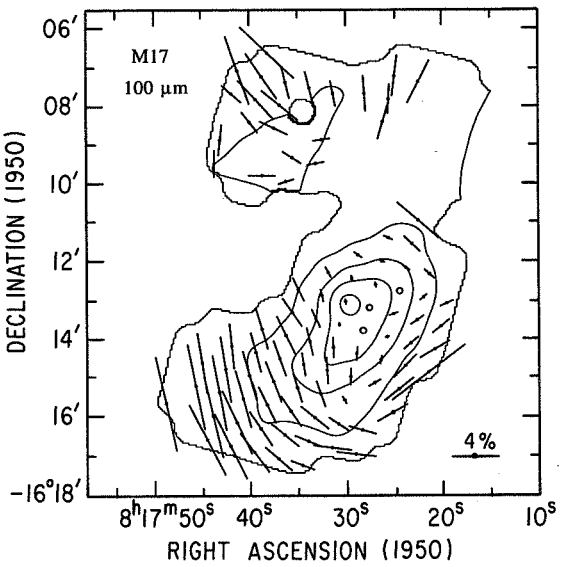

Fig. 1. Far-IR polarization of M17. The flux density contours have been derived by adding the signals for the two orthogonal components of polarization. The lowest contour represents 10 times the photometric noise and follows the edge of the mapped area. The hole in the northern bar represents a small region for which we have no data.

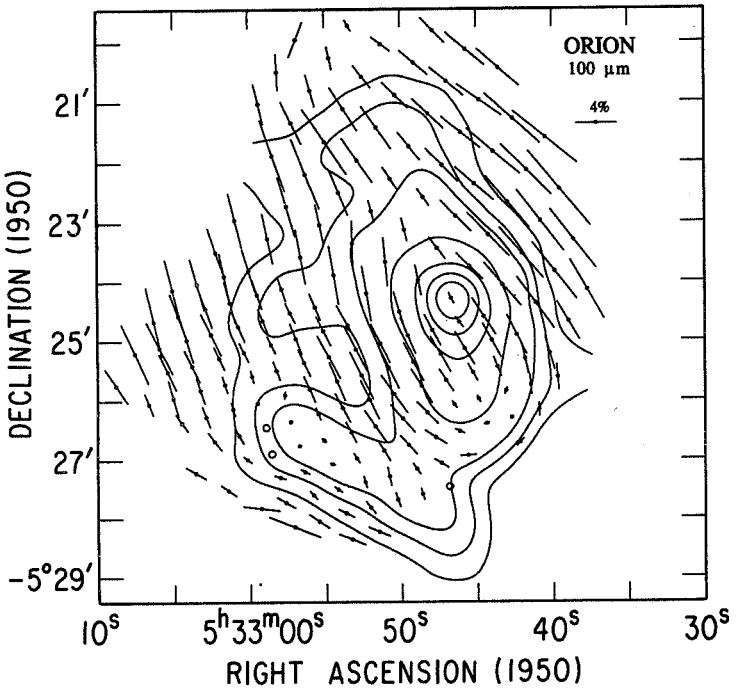

Fig. 2. Far-IR polarization of Orion (M42). (See discussion by Davidson et al. 1994.) The flux density contours have been derived from the polarimetric signals (Platt et al. 1994; see also Harper et al. 1994). Low flux points in the SW quadrant have been deleted because of possible contamination from the NE reference beam. The southern half of the map has been oversampled.

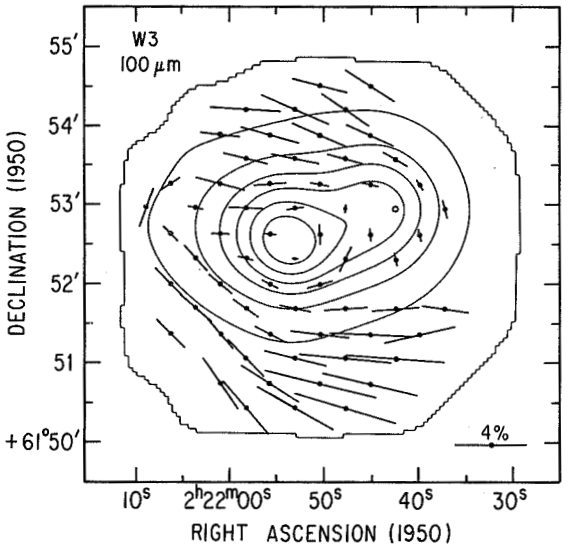

Fig. 3. Far-IR polarization of W3. The flux density contours have been derived from the polarimetric signals.

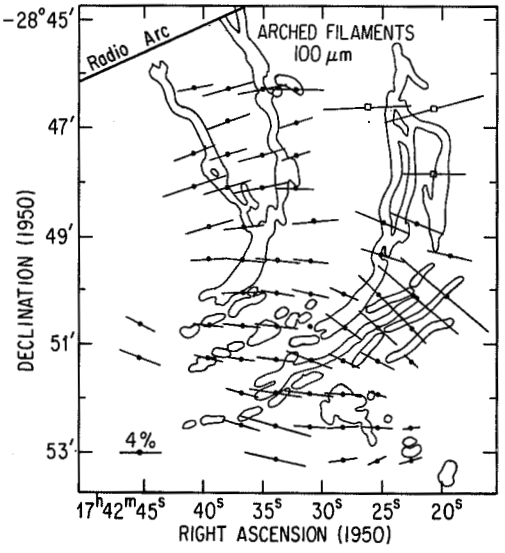

Fig. 4. Far-IR polarization of the Arched Filaments near the Galactic Center. (See discussion by Morris, Davidson, and Werner 1994.) In the northwest, where the flux density is low, each of the three vectors with central squares represents the combined signals from the four immediately surrounding points.

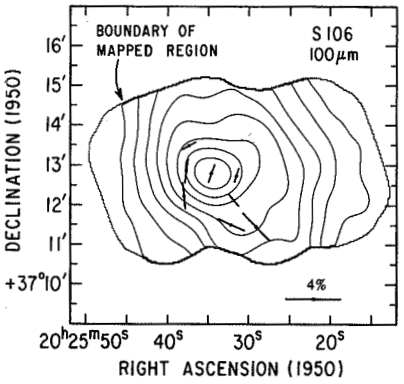

Fig. 5. Far-IR polarization of S106. The flux density map is by Harper et al. (1994).

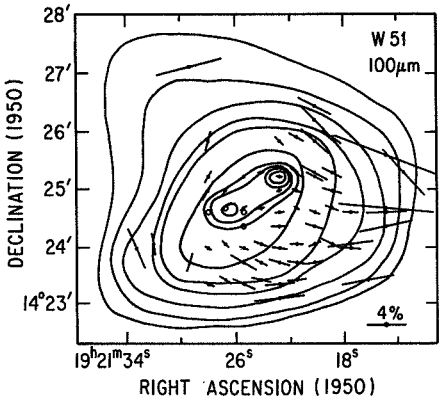

Fig. 6. Far-IR polarization of W51. The flux density map is by Harvey et al. (1986).

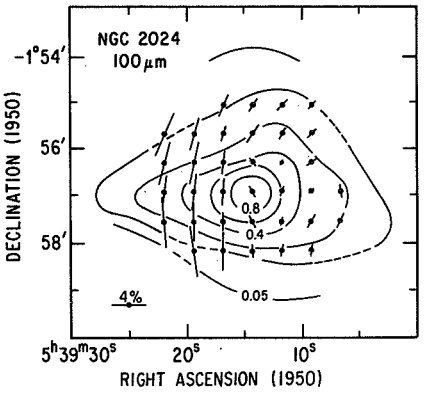

Fig. 7. Far-IR polarization of NGC 2024 from one hour of observations. The flux density map is by Thronson et al. (1984).

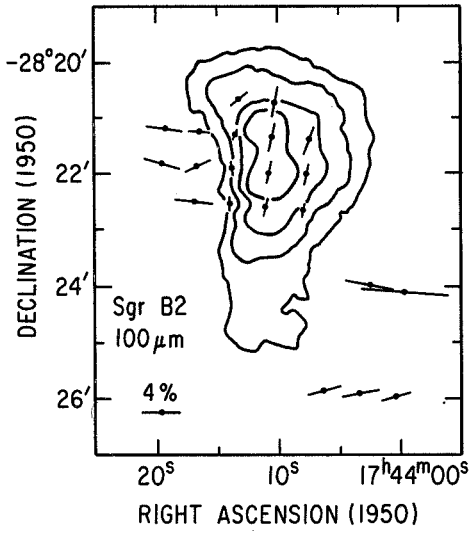

Fig. 8. Far-IR polarization of Sgr B2. (See discussion by Novak et al. 1994.) The flux density map (1300 μm) is by Lis, Carlstrom, and Keene (1991).

GENERAL PROPERTIES

The eleven objects we have observed are bright, extended, and conveniently located for observations during our scheduled flights. The results for this sample show the following characteristics:

Ubiquity

Measureable polarization appears in every one of the eleven clouds.

Degree

The observed degrees of polarization fall in the range 0 to 10% with a median value of ~2.2%. The distribution as given by the raw data is shown in Figure 9.

Dependence on optical depth

The maximum polarization decreases with increasing optical depth more rapidly than would be expected on the basis of opacity alone (Fig. 10; also see discussion by Goodman 1994). It is not yet clear whether the decrease is due to changes in the intrinsic properties of the grains in dense cores, to unfavorable conditions for grain alignment, to changes in the inclination of the magnetic field, or to unpolarized emission from clumps of much higher optical depth than the beam-averaged values. The degree of polarization is insensitive to temperature in the range 30–70 K.

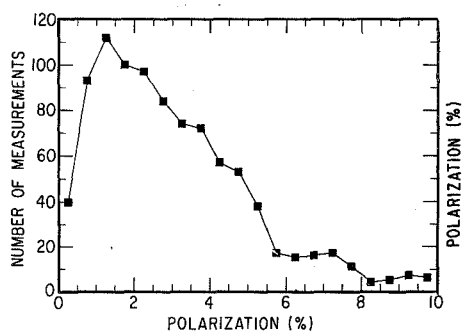

Fig. 9. Distribution in degrees of polarization for a sample of 985 measurements including measurements of low signal to noise. For the measurements shown in the figure (P < 10%) the median error in polarization is 0.53%. The remaining 67 measurements (P > 10%) have a median error of 17% and are consistent with noise. The high noise points are in regions of low flux density. The median error for the vectors shown in Figures 1–8 (all ≥ 3σ) is 0.32%.

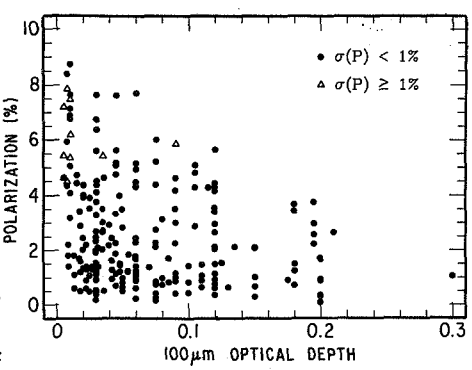

Fig. 10. Polarization vs optical depth for clouds in which data on optical depth are available. In most cases fractional errors in optical depth are much greater than the fractional errors in polarization.

Smoothness

The magnetic field varies smoothly over regions much larger than the separation of the beams. In most cases the position angles of the polarization are correlated over the entire extent of a cloud (Fig. 11). A comparison of optical and far-infrared polarization shows that the field direction in the dense core of Orion is the same as that in the nearby diffuse cloud, Lynds 1641 (Fig. 12).

The polarization does not always reflect small scale features in flux density maps of the same angular resolution. In Orion, for example (Fig. 2), a

change in polarization does appear in the bar at the southeast but not in the small finger of emission east of the intensity peak.

Fig. 11. Correlation function for position angles in M17 and Orion. The graphs show the average differences in position angle vs separation, ΔL, for all pairs of points where $\langle \Delta\phi \rangle_L$ is an average over all points separated by a distance L. The increasing scatter of the points at large L is due in part to the decreasing number of pairs averaged to find $\langle \Delta\phi \rangle$. For a random distribution the mean difference would be 45° for all values of L.

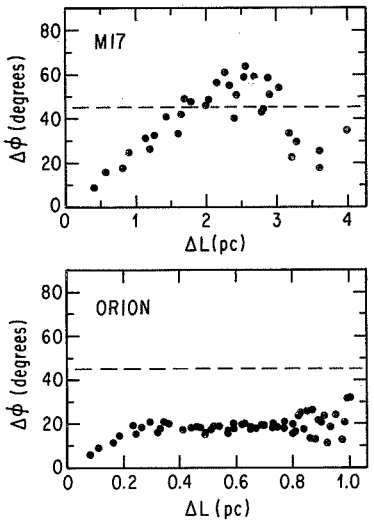

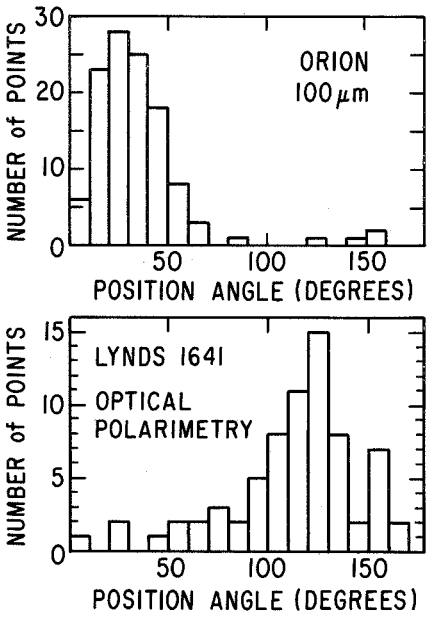

Fig. 12. Comparison of the angular distribution of the polarization in Orion, with the distribution in the nearby diffuse cloud Lynds 1641. The distribution in Orion is that for 100 μm emission (Fig. 2). The distribution in Lynds 1641 is that for optical absorption (Vrba et al. 1988). The optical data have been cut to accept only measurements with $P > 1\%$ and have been corrected for a local ISM polarization of 0.25% at 40°. The mean difference, ~90°, between the angles measured in emission and in absorption shows that the field direction is the same in the two clouds.

ACKNOWLEDGEMENTS

We are grateful to the crew of the Kuiper Airborne Observatory for their support during our flights and to J. Jewell, T. McMahon, D. Pernic, R. Pernic, and J. Wirth for their assistance in the flight preparations and observations. This work has been supported by NASA grant NSG 2057. J.L.D. acknowledges support from NASA Graduate Student Researchers Grant NGT-50894.

REFERENCES

Davidson, J.A., Dowell, C.D., Schleuning, D., Dotson, J.L., & Hildebrand, R.H. 1994, in *Proc of the Airborne Astronomy Symp on the Galactic Ecosystem: From Gas to Stars to Dust*, ed. M.R. Haas, J.A. Davidson, & E.F. Erickson (San Francisco: ASP), paper 3.2

Goodman A.A. 1994, in *Proc of the Airborne Astronomy Symp on the Galactic Ecosystem: From Gas to Stars to Dust*, ed. M.R. Haas, J.A. Davidson, & E.F. Erickson (San Francisco: ASP), paper 1.4

Harper, D.A., Cole, D.M., McMahon, T., Loewenstein, R.F., & Dowell, C.D. 1994, in *Proc of the Airborne Astronomy Symp on the Galactic Ecosystem: From Gas to Stars to Dust*, ed. M.R. Haas, J.A. Davidson, & E.F. Erickson (San Francisco: ASP), paper 301

Harvey, P.M., Joy, M., Lester, D.F., & Wilking, B.A. 1986, *ApJ*, **300**, 737

Hildebrand, R.H., Davidson, J.A., Dotson, J., Figer, D.F., Novak, G., Platt, S.R., & Tao, L. 1993, *ApJ*, **417**, 565

Hildebrand, R.H. & Davidson, J.A. 1994, in *The Nuclei of Normal Galaxies: Lessons from the Galactic Center*, ed. R. Genzel (Dordrecht: Kluwer)

Lis, D.C., Carlstrom, J.E., & Keene, J. 1991, *ApJ*, **380**,429

Morris, M., Davidson, J.A., & Werner, M.W. 1994, in *Proc of the Airborne Astronomy Symp on the Galactic Ecosystem: From Gas to Stars to Dust*, ed. M.R. Haas, J.A. Davidson, & E.F. Erickson (San Francisco: ASP), paper 6.3

Novak, G., Platt, S.R., Goldsmith, P.F., Hildebrand, R.H., & Dowell, C.D. 1994, In preparation

Platt, S.R., Dotson, J.L., Dowell, C.D., Hildebrand, R.H., Novak, G., & Schleuning, D. 1994, in *Proc of the Airborne Astronomy Symp on the Galactic Ecosystem: From Gas to Stars to Dust*, ed. M.R. Haas, J.A. Davidson, & E.F. Erickson (San Francisco: ASP), paper 707

Platt, S.R., Hildebrand, R.H., Pernic, R.J., Davidson, J.A., & Novak, G. 1991, *PASP*, **103**, 1193

Thronson, H.A., Jr., Lada, C.J., Schwartz, P.R., Smith, H.A., Smith, J., Glaccum, W., Harper, D.A., & Loewenstein, R.F. 1984, *ApJ*, **280**, 154

Vrba, F.J., Strom, S.E., Strom, K.M. 1988, *AJ*, **96**, 680

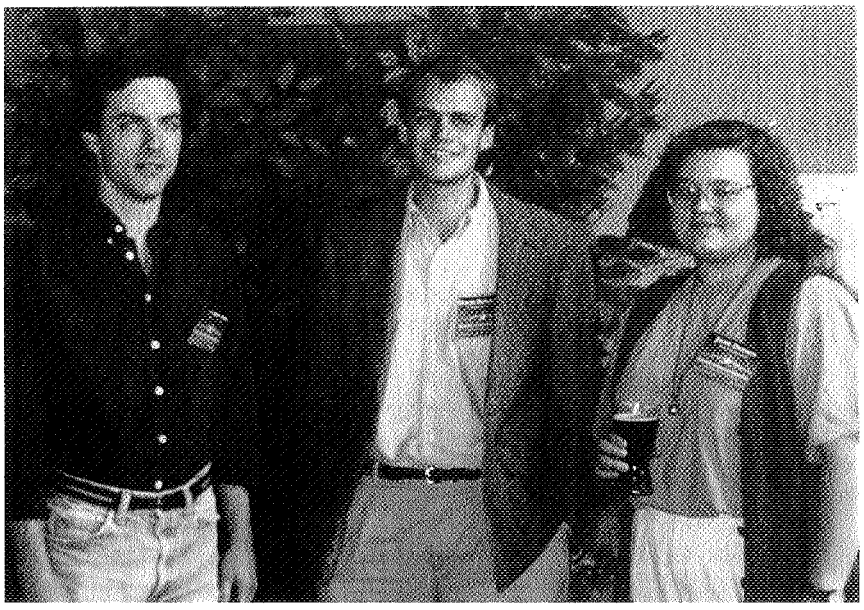

Darren Dowell, David Schleuning, Jesse Dotson

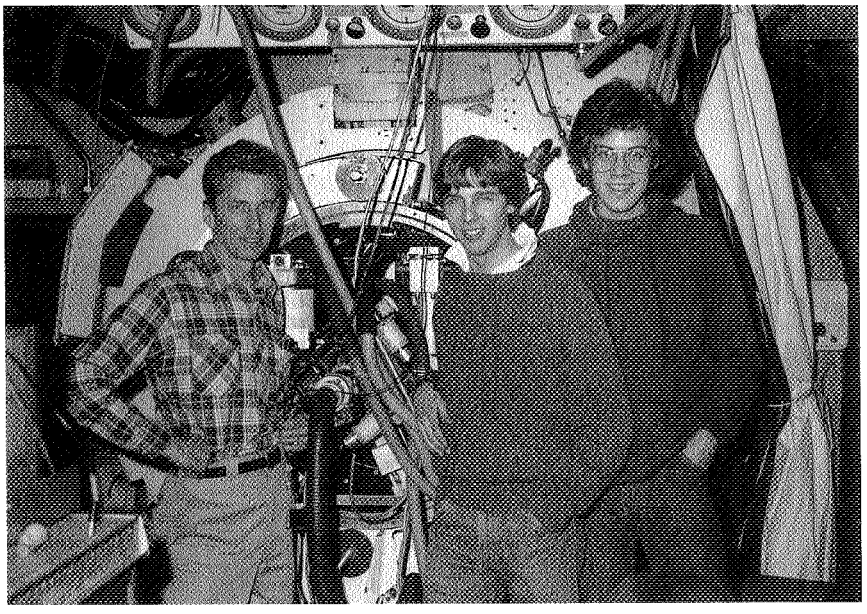

Roger Hildebrand, Mark Dragavon, Giles Novak (1983)

Airborne Astronomy Symposium on the Galactic Ecosystem
ASP Conference Series, Vol. 73, 1995
M.R. Haas, J.A. Davidson, and E.F. Erickson (eds.)

ARGON AND NEON IN GALACTIC NEBULAE

J. P. Simpson[1,2], J. D. Bregman[1], H. L. Dinerstein[3], D. F. Lester[3], D. M. Rank[4], F. C. Witteborn[1], and D. H. Wooden[1]

[1]*NASA/Ames, MS245-6, Moffett Field, CA 94035-1000*
[2]*University of California, Berkeley*
[3]*Dept. of Astronomy, University of Texas, Austin, TX 78712-1083*
[4]*Board of Studies in Astronomy and Astrophysics, Univ. of Calif, Santa Cruz, CA 95064*

ABSTRACT KAO observations of the 6.98 μm line of [Ar II], and KAO and ground-based observations of the 8.99 μm line of [Ar III] and the 12.8 μm line of [Ne II] are presented for a number of Galactic H II regions and planetary nebulae.

INTRODUCTION

The abundances of the elements tell us about the history of star formation and the recycling of the interstellar medium through stars, and they provide observational constraints on the nucleosynthesis of the elements. Argon and neon are excellent choices for such a study of abundances because: (1) With 18 and 10 protons, respectively, they have different enough masses that they are synthesized in sufficiently different types of stars to tell us about nucleosynthesis and any variations in the initial mass function. (2) Both neon and argon have lines in the infrared for the ionization states that are dominant in H II regions. This means that they can be observed in sources in the Galactic Center (which has ~30 mag of visible extinction). Moreover, one can determine the total abundances by summing the abundances of the two ionic states without the need for large ionization correction factors (as are necessary for N and O; Simpson et al. 1995). (3) Both have their strongest lines in the mid-IR (6 to 16 μm), where the lines have no sensitivity to electron temperature (unlike optical forbidden lines) and very little sensitivity to electron density (unlike far-IR forbidden lines).

OBSERVATIONS

In order to study the abundances of argon and neon, we measured the 6.98 μm line of [Ar II], the 8.99 μm line of [Ar III], and the 12.8 μm line of [Ne II] in 13 Galactic H II regions and the low excitation planetary nebulae IC 418 and BD+30 3639. So that our abundances could be estimated with respect to hydrogen, we also measured the 7.46 μm Pfund α line of hydrogen (see e.g., Lester et al. 1981), or took radio fluxes from the astronomical literature. We used the KAO for the [Ar II] line and Pfund α, which fall in terrestrial water absorption features, and the NASA/Steward Observatory 60" telescope on Mt. Lemmon for the [Ar III] and [Ne II] lines, which lie in the 10 μm window. In 1981 and 1982, we used the Lick Observatory Grating Spectrometer (LickGS) (Bregman 1975), which has a resolution of about 200, and since then, we have used the NASA/Ames Faint Object Grating Spectrometer (FOGS) (Witteborn & Bregman 1984; Witteborn et al. 1989), which has 24 detectors and a resolution of about 100. Chopper throws were typically 1.5'.

The spectra were calibrated by dividing by the spectrum of a standard star and then multiplying by the assumed flux for the standard star. Standard star fluxes are given in Walker and Cohen (1992) and in papers in preparation. The 12.8 μm line measured in G333.6-0.2 is an exception because the calibration star, σ Lib, was too faint for good signal/noise. This very bright line was calibrated against the continuum (which was in turn flat fielded by dividing by a black-body); we assumed a continuum flux by extrapolating from 11 μm following the shape of the IRAS LRS spectrum. The data are listed in Table 1 for H II regions where only the peak position was measured, in Table 2 for H II regions which were mapped in a 5 point cross, and in Table 3 for planetary nebulae.

The line fluxes were corrected for extinction using the method described by Simpson & Rubin (1990) and Simpson et al. (1995), which uses the 10 μm silicate absorption measured from the IRAS LRS spectra or other mid-IR spectra. We assumed an uncertainty of 20% in the silicate feature optical depths. This can be a very large effect for the 8.99 μm [Ar III] line.

ABUNDANCE RATIOS

We estimated the abundances of Ar^+/H^+, Ar^{++}/H^+, and Ne^+/H^+ by ratioing the observed fluxes (corrected for extinction) to the radio free-free continuum fluxes. For those sources where argon was observed but not neon, we took [Ne II] line fluxes from the literature (Gillett et al. 1975; Willner et al. 1979; Aitken & Roche 1982; Lacy et al. 1982). Although most sources in this study are low excitation and have very little Ne^{++}, a few are not - for these sources, we took the Ne^{++}/H^+ ratios from Simpson et al. (1995). The collisional excitation cross-sections for Ar^+ are from Mendoza (1983), for Ar^{++} from Johnson &

Kingston (1990), for Ne^+ from Bayes et al. (1985), and for Ne^{++} from Butler & Mendoza (1984).

Our calculated abundances are the sums $Ar/H = Ar^+/H^+ + Ar^{++}/H^+$, and $Ne/H = Ne^+/H^+ + Ne^{++}/H^+$. The Ar/Ne ratios are plotted in Figure 1 vs. the Galactocentric radius R_G. A fit to the Ar/Ne data has a slope given by $d(\log Ar/Ne)/dR = +0.12 \pm 0.04$ dex kpc^{-1} and is plotted on the figure. Since argon is probably made in more massive stars than neon, a difference in gradients, if real, could indicate that the initial mass function is steeper in the outer Galaxy than in the inner Galaxy. We note that other observations in the literature (e.g., Pipher et al. 1984), and also other unpublished data, produce a flat slope for Ar/Ne vs. R_G.

For the planetaries, IC 418 has an Ar/Ne ratio similar to that of the H II regions, but BD+30 3639 has a large overabundance of argon.

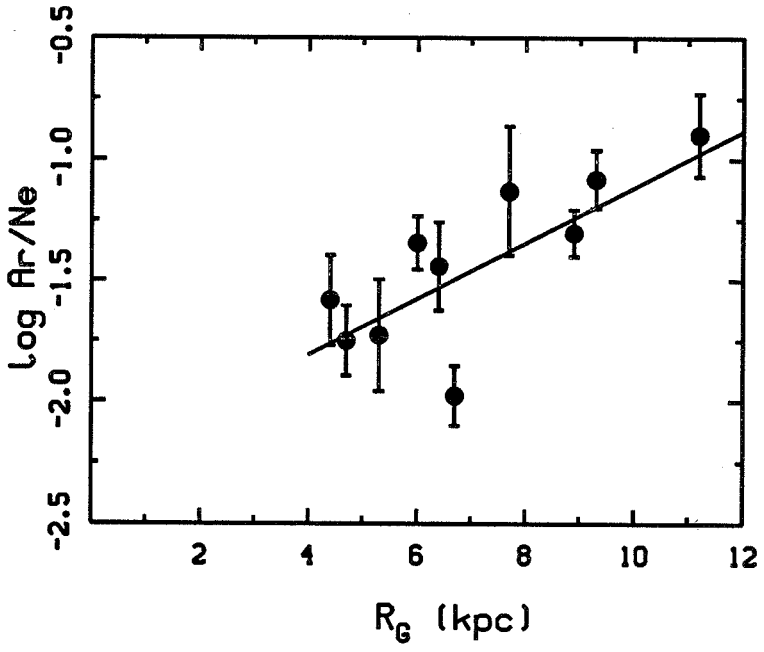

Fig. 1. The abundance ratio Ar/Ne vs. R_G for Galactic H II regions.

TABLE I Observed Fluxes - H II Regions

Source	R_G kpc	Line	Date	Telescope	Beam	Spectrometer	Cal. Star	Flux $\times 10^{-18}$ W cm^{-2}
Sgr A IRS3	0.0	[Ar II]	5/85	KAO	21"	FOGS	α Boo	28.1 ± 3.8
G29.9-0.0	4.4	[Ar II]	7/81	KAO	10x20"	LickGS	α Boo	8.3 ± 2.5
		Pfund α	7/81	KAO	10x20"	LickGS	α Boo	10.0 ± 2.8
		[Ar II]	7/82	KAO	20"	LickGS	μ Cep	8.6 ± 2.6
W43N	4.7	[Ar III]	5/82	60"	15"	LickGS	α Boo	1.1 ± 0.4
		[Ne II]	5/82	60"	15"	LickGS	α Boo	10 ± 3
G333.6-0.2[a]	6.0	[Ar II]	4/87	KAO	21"	FOGS	α Hya	51.0 ± 1.6
		[Ar III]	4/87	KAO	21"	FOGS	σ Lib	24.2 ± 2.2
		[Ne II]	4/87	KAO	21"	FOGS	σ Lib	338 ± 50
G45.13+0.14	6.4	[Ar III]	5/82	60"	15"	LickGS	α Boo	6.8 ± 1.1
		[Ne II]	5/82	60"	15"	LickGS	α Boo	56 ± 14
		[Ar II]	7/82	KAO	21"	LickGS	μ Cep	4.5 ± 2.1
W51d IRS2	6.7	[Ar II]	7/81	KAO	10x20"	LickGS	α Boo	4.8 ± 2.0
		Pfund α	7/81	KAO	10x20"	LickGS	α Boo	5.0 ± 1.8
		[Ar III]	9/81	60"	14"	LickGS	α Boo	18.5 ± 1.4
W51e IRS1	6.7	Pfund α	7/81	KAO	10x20	LickGS	α Boo	7.7 ± 4.2
		[Ar III]	5/82	60"	15"	LickGS	α Boo	3.2 ± 1.2
S88B	7.7	[Ar III]	5/82	60"	15"	LickGS	α Boo	1.0 ± 0.4
		[Ne II]	5/82	60"	15"	LickGS	α Her	11 ± 3
		[Ar II]	7/82	KAO	20"	LickGS	μ Cep	2.2 ± 1.0
W3 IRS1	10.3	[Ar II]	7/82	KAO	20"	LickGS	μ Cep	2.2 ± 1.2
M1-78[b]	11.2	[Ar II]	7/84	KAO	20"	FOGS	β And	2.0 ± 0.7

[a] Spectrum plotted in Cohen et al. (1989).

[b] Spectrum plotted in Cohen et al. (1986).

TABLE II Observed Fluxes - H II Regions with Maps - Spectrometer: LickGS

Source	RA	Dec	R_G kpc	Line	Date	Telescope	Beam	Cal. Star	Flux $\times 10^{-18}$ W cm^{-2}
G25.4-0.2SE			5.3	[Ar III]	5/82	60"	15"	α Boo	3.1 ± 1.0
				[Ne II]	5/82	60"	15"	α Her	25 ± 3
				[S IV]	5/82	60"	15"	α Boo	2.3 ± 0.6
C	18 35 32.7	-6 50 42		[Ne II]	5/82	60"	15"	α Her	22.2 ± 3.1
N	18 35 32.7	-6 50 32		[Ne II]	5/82	60"	15"	α Her	13.2 ± 3.7
E	18 35 33.3	-6 50 42		[Ne II]	5/82	60"	15"	α Her	6.4 ± 3.5
S	18 35 32.7	-6 50 52		[Ne II]	5/82	60"	15"	α Her	10.4 ± 2.0
W	18 35 32.1	-6 50 42		[Ne II]	5/82	60"	15"	α Her	12.6 ± 3.0
				[Ar II]	7/82	KAO	20"	μ Cep	2.3 ± 1.1
Orion Nebula Radio Peak			8.9						
C	5 32 48.0	-5 25 18		[Ar III]	12/81	60"	10"	α Ori	7.0 ± 3.6
N	5 32 48.0	-5 25 08		[Ar III]	12/81	60"	10"	α Ori	6.2 ± 3.3
E	5 32 48.7	-5 25 18		[Ar III]	12/81	60"	10"	α Ori	6.4 ± 2.6
S	5 32 48.0	-5 25 28		[Ar III]	12/81	60"	10"	α Ori	9.1 ± 3.6
W	5 32 47.3	-5 25 18		[Ar III]	12/81	60"	10"	α Ori	9.1 ± 2.9
C	5 32 48.0	-5 25 18		[Ne II]	12/81	60"	10"	α Tau	9.2 ± 1.1
N	5 32 48.0	-5 25 08		[Ne II]	12/81	60"	10"	α Tau	12.0 ± 1.2
E	5 32 48.7	-5 25 18		[Ne II]	12/81	60"	10"	α Tau	7.8 ± 1.7
S	5 32 48.0	-5 25 28		[Ne II]	12/81	60"	10"	α Tau	10.2 ± 1.6
W	5 32 47.3	-5 25 18		[Ne II]	12/81	60"	10"	α Tau	11.5 ± 2.5
Mon R2 IRS1			9.3	[Ar II]	1/82	KAO	21"	α Tau	4.6 ± 1.4
C	6 5 20.0	-6 22 37		[Ar III]	12/81	60"	10"	β Gem	8.6 ± 1.8
C	6 5 20.0	-6 22 37		[Ne II]	12/81	60"	10"	β Peg	17 ± 3
N	6 5 20.0	-6 22 27		[Ne II]	12/81	60"	10"	β Peg	6 ± 3
E	6 5 20.7	-6 22 37		[Ne II]	12/81	60"	10"	β Peg	34 ± 3
S	6 5 20.0	-6 22 47		[Ne II]	12/81	60"	10"	β Peg	15 ± 12
W	6 5 19.3	-6 22 37		[Ne II]	12/81	60"	10"	β Peg	19 ± 3

TABLE III Observed Fluxes - Planetary Nebulae

Source	Line	Date	Telescope	Beam	Spectrometer	Cal. Star	Flux $\times 10^{-18}$ W cm^{-2}
IC 418	[Ar III]	12/81	60"	10"	LickGS	α Tau	3.3 ± 0.4
	[Ar II]	1/84	KAO	14"	FOGS	β And	2.8 ± 1.0
	[Ar III]	1/84	60"	6"	FOGS	α Tau	1.4 ± 1.0
	[Ar II]	1/85	KAO	20"	FOGS	α Leo	3.5 ± 0.5
BD +30 3639	[Ar II]	7/81	KAO	10x20"	LickGS	α Boo	12.6 ± 1.4
	[Ne II]	5/82	60"	15"	LickGS	α Boo	44.5 ± 5.7
	[Ar II]	7/84	KAO	20"	FOGS	β And	9.8 ± 0.8
	[Ar II]	9/87	KAO	20"	FOGS	β And	8.9 ± 0.7
	[Ne II][a]	10/87	60"	12"	FOGS	α Her	30.7 ± 1.9

[a] Spectrum plotted in Witteborn et al. (1989).

REFERENCES

Aitken, D. K., & Roche, P. F. 1982, MNRAS, 200, 217
Bayes, F. A., Saraph, H. E., & Seaton, M. J. 1985, MNRAS, 215, 85P
Bregman, J. D. 1975, Ph.D. Thesis, University of California, Santa Cruz
Butler, K., & Mendoza, C. 1984, MNRAS, 208, 17P
Cohen, M., Allamandola, L., Tielens, A. G. G. M., Bregman, J., Simpson, J. P., Witteborn, F. C., Wooden, D., & Rank, D. 1986, ApJ, 302, 737
Cohen, M., Tielens, A. G. G. M., Bregman, J., Witteborn, F. C., Rank, D. M., Allamandola, L. J., Wooden, D. H., & de Muizon, M. 1989, ApJ, 341, 246
Gillett, F. C., Forrest, W. J., Merrill, K. M., Capps, R. W., & Soifer, B. T. 1975, ApJ, 200, 609
Johnson, C. T., & Kingston, A. E. 1990, JPhysB:At.Mol.Opt.Phys., 23, 3393
Lacy, J. H., Beck, S. C., & Geballe, T. R. 1982, ApJ, 255, 510
Lester, D. F., Bregman, J. D., Witteborn, F. C., Rank, D. M., & Dinerstein, H. L. 1981, ApJ, 248, 524
Mendoza, C. 1983, in IAU Symp 103, Planetary Nebulae ed. D. R. Flower (Dordrecht: Reidel), p. 143
Pipher, J. L., Helfer, H. L., Herter, T., Briotta, D. A. Jr., Houck, J. R., Willner, S. P., & Jones, B. 1984, ApJ, 285, 174
Simpson, J. P., Colgan, S. W. J., Rubin, R. H., Erickson, E. F., & Haas, M. R. 1995, ApJ, submitted
Simpson, J. P., & Rubin, R. H. 1990, ApJ, 354,165
Walker, R. G., & Cohen, M. 1992, NASA CR-177604
Willner, S. P., Jones, B., Puetter, R. C., Russell, R. W., & Soifer, B. T. 1979, ApJ, 234, 496
Witteborn, F. C., & Bregman, J. D. 1984, Proc. SPIE, 509, 123
Witteborn, F. C., Sandford, S. A., Bregman, J. D., Allamandola, L. J., Cohen, M., Wooden, D. H., & Graps, A. L. 1989, ApJ, 341, 270

Airborne Astronomy Symposium on the Galactic Ecosystem
ASP Conference Series, Vol. 73, 1995
M.R. Haas, J.A. Davidson, and E.F. Erickson (eds.)

Compact H II Regions – Deriving Galactic Abundances and Local Properties

A. Afflerbach and E. Churchwell

Department of Astronomy, University of Wisconsin, Madison, WI 53706

M. W. Werner

Jet Propulsion Laboratory, Pasadena, CA 91109

Abstract. Far-infrared fine-structure lines of compact H II regions can provide reliable abundances throughout the Galactic plane. We present here our most recent results, which, once analyzed, will help to constrain models of the abundance gradient in our galaxy.

1. Introduction

Compact H II regions are among the brightest objects in the far-infrared sky. They are manifestations of newly-formed or still-forming O and B stars, so their composition traces the present composition of the local interstellar medium. They can be observed throughout the galactic plane at infrared and radio wavelengths. KAO observations of a well-selected sample of regions in the O III (51.8 and 88.3 μm), the N III (57.3 μm), and the S III (18.7 μm) fine structure lines can provide abundances as a function of position in the plane, less dependent on extinction and nebular temperature than optical wavelength observations. Ionization corrections are also minimized by selection of high excitation nebulae.

Abundances and their distribution within the Galaxy provide a record of Galactic evolution. The observed metallicity (O/H and S/H) constrains the amount of nuclear processing of interstellar material by stars, as well as the mixing of halo and disk gas via a "fountain mechanism" and/or infall of extragalactic gas. Observed metallicity may indicate whether infalling metal-poor gas is preferentially deposited in the outer or inner disk, thus indicating the initial angular momentum of the gas. The observed N/O is a measure of the ratio of secondary to primary nuclear processing. The distribution of this ratio can help determine the local IMF.

Several abundance studies using FIR fine-structure lines have been reported, most recently Simpson et al. (1994) and references therein. Along with studies at optical wavelengths, these studies show clear gradients in O/H, N/H, and S/H, but there are still questions about the exact form of the gradients. For instance, Simpson et al. (1992) find that N/O could vary as -0.017 ± 0.005 per kpc in the range 0 to 13 kpc, or equally well be described as an enhanced gradient of N/O of -0.30 per kpc at $R_g \leq 7$ kpc with a constant value of 0.18 $\pm$ 0.014 for $R_g \geq 7$ kpc.

2. The Sample

We choose 36 objects ranging in galactocentric distance from 0 to 16 kpc with good coverage of the galactic plane. The sampled regions have:

1. high excitation ($T_{eff} \geq$ 40,000 K) to minimize ionization corrections,
2. radio continuum fluxes $\geq$ 0.5 Jy to ensure that the lines are observable,
3. projected diameters $\leq$ 40" to fit the nebulae into the KAO beam, and
4. sizes generally $\leq$ 1 pc to simplify modeling.

The twelve regions presented in Table 1 were chosen because of their availability for a June flight from Moffett Field. The radio flux is the free-free flux within the KAO beam at a frequency where the radiation is optically thin. The source diameter is the FWHM from compact array observations, which sample flux with large spatial dimension.

Table 1. Sources Observed

Source	α (1950) hh mm ss.s	δ (1950) ° ′ ″	Radio Flux (Jy)	Diameter (")
G24.47+0.49	18 31 26.7	-07 20 24	4.2[a]	46[a]
G25.38-0.18	18 35 33.6	-06 50 34	10.6[a]	46[a]
G25.4-0.14	18 35 26.8	-06 48 38	4.4[a]	9[a]
G32.80+0.19	18 47 56.8	-00 05 35	3.1[a]	11[a]
G34.26+0.15	18 50 46.2	01 11 13	4.0[b]	8[c]
G37.87-0.40	18 59 24.7	04 08 26	3.1[d]	10[c]
G61.47+0.10	19 44 43.5	25 05 22	5.2[a]	21[a]
G75.84+0.40	20 19 47.3	37 21 26	8.6[a]	28[a]
DR21C	20 37 14.1	42 08 54	13.0[e]	24[e]
WB191 (S138)	22 30 52.6	58 12 48	0.7[f]	5[g]
WB212 (S146)	22 47 30.7	59 38 56	2.5[f]	22[f]
WB228 (S152)	22 56 36.4	58 30 46	1.4[f]	15[f]

[a]Garay et al., 1993; [b]Wood & Churchwell, 1989; [c]Zoonematkermani et al., 1990; [d]Kurtz et al., 1994; [e]Roelfsema et al., 1989; [f]Fich, 1986; and [g]Kurtz et al., 1995.

3. Observations

Observations took place on the nights of June 9 and 13, 1994, using NASA's Kuiper Airborne Observatory (KAO). Data were taken with the facility Cryogenic Grating Spectrograph (Erickson et al. 1994). Guiding and boresight errors were 5". The chopper throw was ~4′. Spectral resolving power for the 88, 57, 52, and 19 μm observations was 3920, 3503, 4470, and 4034; the FWHM aperture sizes were 36.4", 39.6", 40.1", and 43.2". Wavelength, atmosphere, and diffraction corrections were applied to all spectra. The data have not been corrected for interstellar extinction. From observations of Saturn in the H_2O (85.4

μm) line, we derived a water column of 7 to 8 μm. Observations took place at altitudes of 37,000 to 41,000 feet.

The absolute flux calibration was obtained by dividing each spectrum by a calibration spectrum of Saturn observed on the same flight. The brightness temperature for the disk of Saturn (Hanel et al. 1983; Bézard, Gautier, and Marten 1986) was combined with the ring spectrum (Haas et al. 1982) using the technique of Matthews & Erickson (1977).

Line and continuum fluxes were determined from a moment analysis of the profiles (see Tables 2 and 3). Quoted one-sigma uncertainties are the statistical rms errors plus 8% added in quadrature to account for error in flux calibration, differences in beam coupling for the unknown source, and systematic uncertainties.

Table 2. Line Fluxes

Source	Line Flux (10^{-18} W cm^{-2})			
	SIII (18.7μm)	OIII (51.8μm)	NIII (57.3μm)	OIII (88.3μm)
G24.47	52.9±4.6	52.2±4.3	33.6±2.8	22.3±1.8
G25.38	106.6±8.9	120.3±9.7	48.4±4.0	38.9±3.1
G25.4	12.3±1.2	17.2±1.5	11.0±1.1	6.1±0.6
G32.80	3.3±0.7	15.6±1.6	3.6±0.7	3.6±0.4
G34.26	13.0±1.8	15.8±1.8	8.5±1.1	4.8±0.6
G37.87	6.3±1.0	31.5±2.6	6.7±0.7	9.5±0.8
G61.47	7.6±2.1	16.2±1.6	1.8±0.9	2.6±0.4
G75.84	66.3±5.6	118.2±9.5	20.8±1.8	27.0±2.2
DR21C	2.8±1.6	12.3±1.2	5.8±0.8	4.1±0.4
WB191	2.5±0.8	2.2±0.3	0.7±0.2	1.1±0.1
WB212	21.4±3.6	36.4±3.3	7.9±1.1	16.9±1.4
WB228	16.0±1.6	6.6±0.8		4.0±0.6

4. Discussion

Abundances will be derived using the measured line intensities in conjunction with the statistical equilibrium code of Mathis (1985), which permits iterative solutions for a clumped medium of two or more densities. With the detailed structure and density provided by radio continuum and recombination lines, there should be adequate constraints to derive accurate abundances.

Acknowledgments. This project will make use of KAO observations to be published by Simpson et al. (1994), Rudolph et al. (1995), and others. We acknowledge invaluable assistance from Mike Haas, Alex Rudolph, Janet Simpson, David Lee, and the staff of the KAO. A.A. is a NASA Graduate Student Researcher and acknowledges support from NGT-51132. This project is funded by NASA grant NAG 2-859. Portions of this research were carried out at the Jet Propulsion Laboratory, California Institute of Technology, under contract with the National Aeronautics and Space Administration.

Table 3. Continuum Fluxes

Source	Continuum Flux (Jy)			
	18.7μm	51.8μm	57.3μm	88.3μm
G24.47	405±80	1750±160	1900±180	2200±200
G25.38	1250±140	4600±400	4525±380	4080±340
G25.4	0±100	3340±280	3760±320	4900±400
G32.80	35±35	2775±250	3300±290	3800±310
G34.26	40±65	5600±475	8240±680	14260±1150
G37.87	70±45	2070±200	2830±240	3570±290
G61.47	380±100	6130±500	5200±520	7730±630
G75.84	305±70	4360±380	4300±355	4010±340
DR21C	225±65	5650±465	7715±630	11185±900
WB191	60±50	760±100	890±80	900±75
WB212	295±155	910±180	670±130	650±100
WB228	165±70	910±140		700±90

References

Bézard, B., Gautier, D., & Marten, A. 1986, A&A, 161, 387

Erickson, E. F., Haas, M. R., Colgan, S. W. J., Simpson, J. P., & Rubin. R. H. 1994, in Proc of the Airborne Astronomy Symp on the Galactic Ecosystem: From Gas to Stars to Dust, ed. M. R. Haas, J. A. Davidson, & E. F. Erickson, (San Francisco: ASP), paper 702

Fich, M. 1986, AJ, 92, 787

Garay, G., Rodriguez, L, F., Moran, J. M., & Churchwell, E. 1993, ApJ, 418, 368

Haas, M. R., Erickson, E. F., McKibbin, D. D., Goorvitch, D., & Caroff, L. J. 1982, Icarus, 51, 476

Hanel, R. A., Conrath, B. J., Kunde, V. G., Pearl, J. C., & Pirraglia, J. A. 1983, Icarus, 53, 262

Kurtz, S., & Churchwell, E. 1995, ApJS, in prep.

Kurtz, S., Churchwell, E., & Wood, D. O. S. 1994, ApJS, 91, 659

Mathis, J. 1985, ApJ, 291, 247

Matthews, S., & Erickson, E. F. 1977, NASA TM, X-73, 204

Roelfsema, P. R., Goss, W. M., & Geballe, T. R. 1989, A&A, 222, 274

Rudolph, A. L., Simpson, J. P., Haas, M. R., Erickson, E. F., Fich, M., Churchwell, E., & Afflerbach A. 1995, ApJ, in prep.

Simpson, J. P., Colgan, S. W. J., Erickson, E. F., Haas, M. R., & Rubin, R. H. 1992, BAAS, 24, 1131

———. 1994, ApJ, in prep.

Wood, D. O. S., & Churchwell, E. 1989, ApJS, 69, 831

Zoonematkermani, S., Helfand, D. J., Becker, R. H., White, R. L., & Perley, R. A. 1990, ApJS, 74, 181

Airborne Astronomy Symposium on the Galactic Ecosystem
ASP Conference Series, Vol. 73, 1995
M.R. Haas, J.A. Davidson, and E.F. Erickson (eds.)

Density Determination from Far-Infrared Lines

Robert H. Rubin[1,2], Janet P. Simpson[1,3], Edwin F. Erickson[1], Michael R. Haas[1], Steven D. Lord[4], and Sean W. J. Colgan[1,5]

[1]*NASA-Ames Research Center, MS 245-6, Moffett Field, CA 94035-1000*
[2]*Orion Enterprises, 2135 Woodleaf Way, Mountain View, CA 94040*
[3]*Astronomy Department, University of California at Berkeley, Berkeley, CA 94720*
[4]*IPAC, California Institute of Technology, 770 S. Wilson Ave., Pasadena, CA 91125*
[5]*SETI Institute, 2035 Landings Drive, Mountain View, CA 94043*

Abstract. We demonstrate that when there are gas density variations within a nebula, various line ratios used to determine electron density (N_e) can give different results. When there are non-constant density conditions, it is shown that by using one (average) N_e, significant, systematic biases may occur in the derived chemical abundance ratios. The abundance ratio of a heavy element (when a collisionally excited line is used) to ionized hydrogen may be subject to a large underestimate in the presence of density fluctuations. The more N_e-diagnostic observations made, the more reliable will be the deciphering of the actual N_e variation throughout a nebula.

Introduction

Measurement of the two $\Delta J = 1$ FIR fine-structure transitions for species with a ^3P ground state provides a diagnostic for N_e. For example, the flux ratios [O III] 52/88 μm, [S III] 19/33 μm, and [N II] 122/205 μm provide N_e[O III], N_e[S III], and N_e[N II], respectively, as shown in Figure 1 (Rubin *et al.* 1994). The [N II] (122, 205 μm) lines provide a new tool to examine low density, low ionization gas. For conditions prevalent in many H II regions, these lines readily show the effect of collisional deexcitation because their critical densities ($N_{crit} \sim 40$ and ~ 260 cm^{-3}, at $T_e = 8000$ K, for the 205 and 122 μm lines respectively) are much lower than for most lines used in nebular analyses. The 205/122 intensity ratio provides an excellent diagnostic of N_e at low density ($1\ \mathrm{cm}^{-3} \lesssim \mathrm{N_e} \lesssim 10^3\ \mathrm{cm}^{-3}$).

Two additional line ratios, [Ne III] 36/15 μm and [Ar III] 22/9 μm, will be useful once suitable space platforms (e.g., ISO and SIRTF) become available. These ratios are displayed in Figure 2. Note that [Ne III] 36/15 μm and [Ar III] 22/9 μm are sensitive indicators of higher density material than those ratios in Figure 1. Both the [Ne III] and [Ar III] ratios are similar in that they are most discriminant in the range $4.0 \lesssim \log N_e \lesssim 5.4$. For all of these species, within a certain density range, the line flux ratio is an excellent probe of N_e that is insensitive to electron temperature, T_e (e.g., see Rubin 1989).

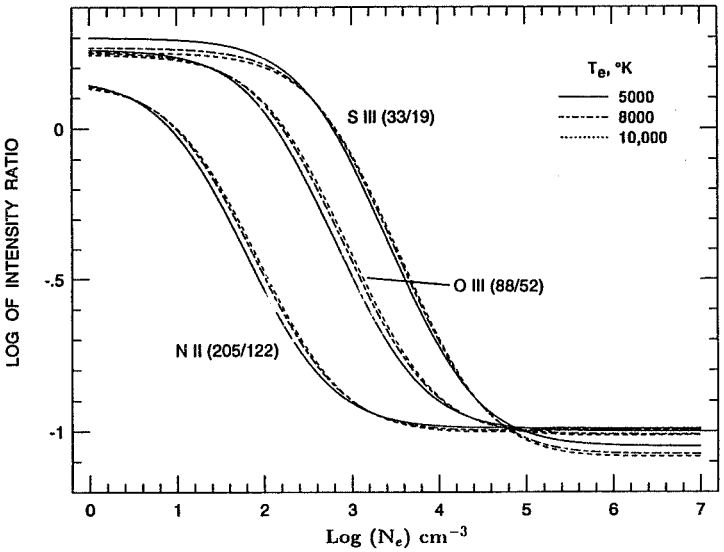

Figure 1. This shows three excellent indicators of N_e – the intensity ratio of [N II] 205 μm/122 μm, [O III] 88 μm/52 μm, and [S III] 33 μm/19 μm vs. N_e (cm^{-3}) for T_e of 5000, 8000, and 10,000 K. The [N II] ratio is most sensitive at the lowest N_e, and [S III] at the highest N_e. All six lines have been observed with the KAO.

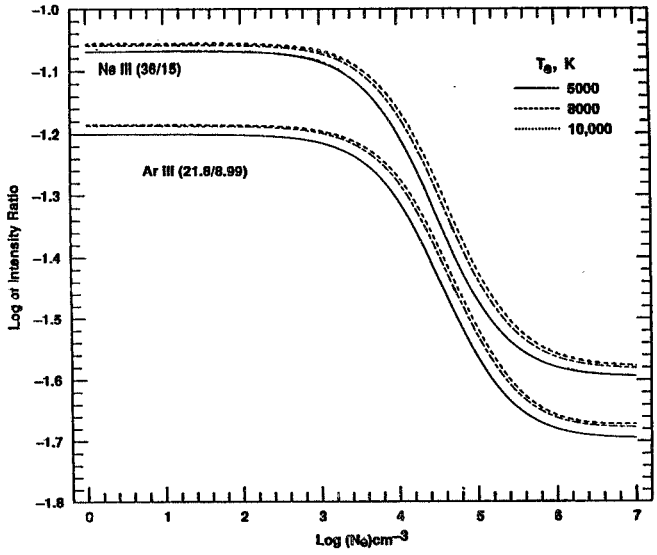

Figure 2. Similar to Figure 1 for two other excellent indicators of N_e – the intensity ratio of [Ne III] 36 μm/15 μm, and [Ar III] 21.8 μm/8.99 μm. These ratios will be useful once suitable space platforms become available. These ratios are sensitive indicators of higher density material than those ratios in Figure 1.

We may order these N_e-diagnostics along with several from optical/UV line ratios as to where they are most useful. Maximum sensitivity occurs roughly half way between the low and high-density asymptotic limits. We rank the various line pair methods from the lowest to highest N_e, with approximate log N_e of maximum sensitivity in parenthesis: N_e[N II] (1.85), N_e[O III] (2.95), N_e[S II](6731/6716 Å) (3.10), N_e[O II](3729/3726 Å) (3.15), N_e[S III] (3.4), N_e[Ar IV](4711/4740 Å) (4.4), N_e[Ne III] (4.7), N_e[Ar III] (4.7), and N_eC III](1906/1909 Å) (5.8).

The values of N_e determined from the various N_e indicators above will depend on density variations in the zone where the lines originate. The various line pairs probe a range of excitations via the different ionic species. There is also a dependency on T_e variations for UV/optical lines, which is much less important for the FIR line ratios. We conducted numerical tests to examine the effects of a non-uniform density on the empirical determinations of N_e and the consequences of using this value to obtain elemental abundance ratios. T_e variations and ionization stratification have been neglected in order to focus on the effects of density variations.

From our model-generated line intensities, we use the ratio of the density sensitive line pair of interest to infer N_e. This value of N_e is then used to derive the ratio of the volume emissivity, $\jmath$, for a line of another species to $\jmath$ of either of the density indicator lines.

Electron Density and Abundance Ratios Inferred from Models

We consider several test cases. In Case I, there are two components with masses M_1 and M_2 with N_e of 10 and 10^6 cm^{-3}, respectively, $M_1/M_2 = 250$, and $T_e = 8000$ K. Let us define the term BIAS as,

$$[N(X)/N(Y)]_{Inferred} = BIAS \times [N(X)/N(Y)]_{Input} , \quad (1)$$

where X and Y represent two ionic species. The input ratio is that used in our calculations. In Table 1 we present the three lines used for each species ratio, the average log N_e, and the BIAS inferred for the selected ions. We include ions that have the density sensitive line pairs listed above. These ions are placed in the denominator and are ordered by increasing inferred log N_e values. The other species considered in the ratios are chosen so that significant overlap in the volumes both species occupy would be possible. Some of the abundance ratios have been used in analyses of observations, while others are rather arbitrarily formed to illustrate the points of this paper. For Case I, log $(N_e)_{rms} = 2.30$.

For Case II, a spherical model with a continuous density distribution and $T_e = 8000$ K is considered. N_e is obtained by linearly interpolating between N_e (r = 0) = 10^5cm^{-3}, N_e (r = ℓ) = 10^4 cm^{-3}, N_e (r = 2ℓ) = 10^3 cm^{-3}, and N_e (r = 3ℓ) = 10^2 cm^{-3}, where ℓ is a scale factor. The analysis is performed on the integrated fluxes generated from the model; results are in Table 1. Cases I and II were chosen in order that all abundance ratios are affected. They may not be that extreme in view of the recent finding from [Fe II] lines that in at least some parts of the Orion Nebula H II region, there is a high density component with $N_e \sim 10^6$ cm^{-3} (Bautista, Pradhan, & Osterbrock 1994).

For Case III, we consider a narrower range in density. Again, this is a two component model with mass M_1 and M_2 and N_e of 10^3 and 10^4 cm^{-3}, $M_1/M_2 = 3$

TABLE 1

AVERAGE DENSITIES AND INFERRED BIAS

SPECIES	LINE RATIO	CASE I		CASE II		CASE III	
		log N_e	BIAS	log N_e	BIAS	log N_e	BIAS
Ne^{+}/N^{+}	122/205 12.8/122	1.07	111.	3.50	6.06	3.12	2.42
N^{++}/O^{++}	52/88 57/52	2.25	0.914	3.82	0.991	3.24	0.986
N^{+}/S^{+}	0.6731/0.6716 0.6584/0.6716+31	3.43	5.86	4.057	1.53	3.47	1.29
N^{++}/S^{++}	18.7/33.5 57/18.7	3.45	1.36	4.064	1.03	3.48	1.06
N^{+}/O^{+}	0.3729/0.3726 0.6584/0.3727	3.49	5.36	4.07	1.48	3.49	1.26
N^{++}/Ne^{++}	15/36 57/15	5.55	4.10	4.48	1.39	3.85	1.64
S^{+3}/Ar^{+3}	0.4711/0.4740 10.5/0.4711+40	5.71	0.940	4.49	0.966	3.84	0.989
N^{++}/Ar^{++}	8.99/21.8 57/8.99	5.82	4.39	4.54	1.51	3.87	1.71
N^{++}/C^{++}	0.1906/0.1909 57/0.1906+09	5.99	4.67	4.61	1.70	3.89	1.79

and T_e = 8000 K. With less density variation, the BIAS values are less than for Cases I and II; log $(N_e)_{rms}$ = 3.31.

Table 2 presents the analogous information to that in Table 1 for ratios involving H^{+}, where Hβ is used for determining abundances relative to hydrogen.

TABLE 2

BIAS WHEN USING HYDROGEN

Species	Case I	Case II	Case III
H^{+}/N^{+}	378.	6.66	2.46
H^{+}/O^{++}	231.	3.33	1.96
H^{+}/S^{+}	78.9	2.04	1.37
H^{+}/S^{++}	81.8	2.03	1.36
H^{+}/O^{+}	71.8	1.97	1.33
H^{+}/Ne^{++}	23.7	1.09	1.008
H^{+}/Ar^{+3}	1.60	1.04	1.003
H^{+}/Ar^{++}	1.36	1.03	1.002
H^{+}/C^{++}	1.00	1.00	1.00

The biases in Tables 1 and 2 are generally significant and indicate the importance of density variations in abundance determinations.

References

Bautista, M. A., Pradhan, A. K., & Osterbrock, D. E. 1994, ApJL, 432, L135

Rubin, R. H. 1989, ApJS, 69, 897

Rubin, R. H., Simpson, J. P., Lord, S. D., Colgan, S. W. J., Erickson, E. F., & Haas, M. R. 1994, ApJ, 420, 772

omit

Session Two

The Life Cycle of the Interstellar Medium in Other Galaxies

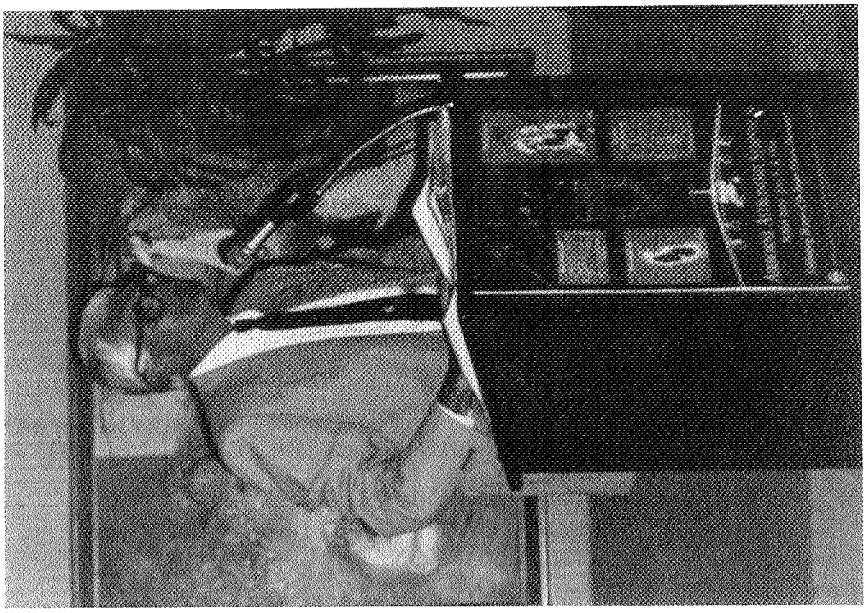

Hans Mark

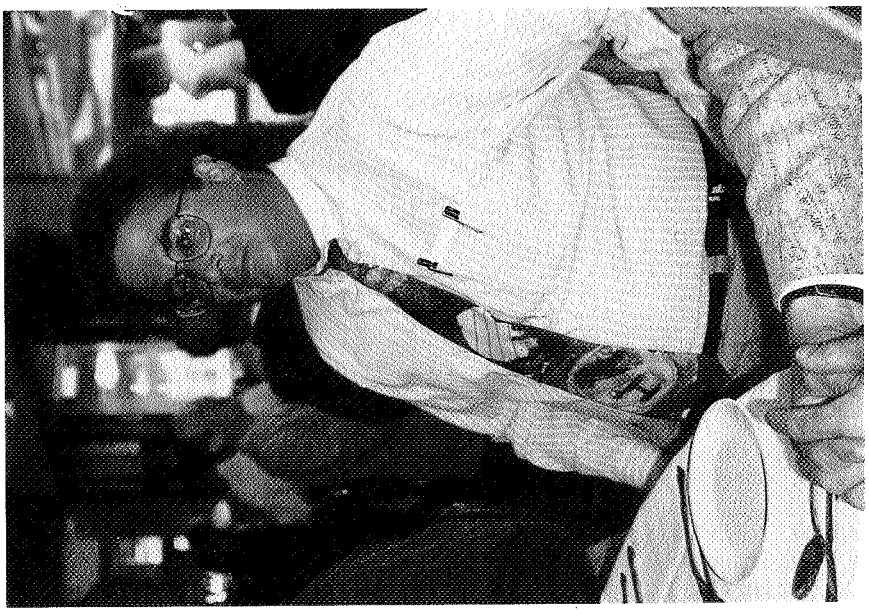

Mike Kaplan

Airborne Astronomy Symposium on the Galactic Ecosystem
ASP Conference Series, Vol. 73, 1995
M.R. Haas, J.A. Davidson, and E.F. Erickson (eds.)

THE LIFE CYCLE OF THE INTERSTELLAR MEDIUM IN OTHER GALAXIES

G. R. KNAPP
Princeton University Observatory, Princeton, NJ 08544

ABSTRACT Gas in spiral galaxies cycles between the diffuse and dense phases as clouds collapse, form stars and are dispersed back into the ISM. Far infrared observations of continuum emission from interstellar dust and line emission from interstellar gas have revealed a wealth of information on the state of the ISM in galaxies of different morphological types. The analysis of these observations gives us information about the processes of star formation and about the evolution of the ISM. Star formation rates vary widely from galaxy to galaxy, with the rates in starburst galaxies being 10 - 100 times those in quiescent spiral galaxies. Far infrared spectroscopy of star-forming galaxies shows that the interstellar pressure increases with star formation rate. The structure of the interstellar medium in starburst galaxies is quite different from that of quiescent galaxies - much of the mass and volume are in HII regions and photodissociation regions.
The size distribution of dust grains seems to depend on environment; small grains are abundant in the diffuse interstellar medium but not in dense molecular star forming regions. Quiescent spiral and elliptical galaxies contain a significant population of small grains, but starburst galaxies do not. Dwarf irregular galaxies also seem to contain few small grains; this may be the result of the higher UV flux in these galaxies. The star-forming regions in dwarf irregulars also have a higher ratio of atomic to molecular gas than do those in the Galaxy. These results show that the ISM in galaxies of different morphological types reaches different equilibria, resulting in different modes of star formation and global galaxy evolution.

1. INTRODUCTION

As the overarching theme of this conference shows, we have begun in the last several decades to develop a feeling (this new-age word is more accurate than is 'understanding') for the intricate interplay among the stars, gas and dynamics which results in the forms and properties of galaxies, and which determines their evolution. Above all else, these processes act to ensure that the global properties of a galaxy change but slowly with time unless something fairly drastic, such as a collision between two galaxies, occurs.

As in the terrestrial ecology to which galaxies are often compared, the processes which determine the large-scale properties of a galaxy often occur on quite small scales and yet, via feedback mechanisms and the overall equilibrium enforced by a galaxy's global gravitational field, act to maintain the large-scale balance. Much of this equilibrium is mediated by processes taking place in the interstellar medium, and the Kuiper Airborne Observatory has made many

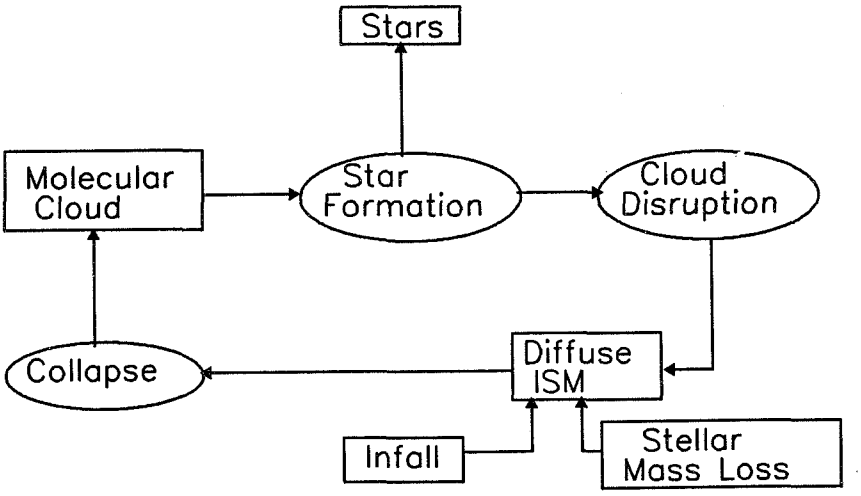

Figure 1. Flow chart for gas between the diffuse and dense phases of the ISM. "Processes" are enclosed in elliptical bubbles.

fundamental contributions to our understanding of how the ISM "works".

Figure 1 shows a very oversimplified diagram of the flow of the ISM between the two phases which, at least in the Galaxy, contain most of the mass: the diffuse and dense neutral gas. The gas in the diffuse ISM is largely in atomic form; that in the dense ISM is molecular. Mass leaves the ISM by star formation which takes place entirely, to the best of our knowledge, in the dense molecular gas. Gas is added to the ISM by stellar mass loss and by infall.

What is actually observed is another matter (cf. Figure 2). We observe radiation from the diffuse and dense ISM which is the result of the heating, ionization and general stirring-up of the gas by starlight, cosmic rays and by many types of stellar wind. Observations of this radiation are used to understand the temperature and density structure of the ISM, which in turn tells us about the interaction between stars and the interstellar gas.

Much of the radiation from the ISM (and from the entire galaxy) emerges at wavelengths between something like 50μm and 500μm, encompassing the far infrared and submillimeter regions of the spectrum. The lion's share of observational data at these wavelengths has been contributed by the IRAS, KAO and (more recently) COBE missions. Both KAO and IRAS have contributed immensely to observational work on the continuum emission from warm interstellar dust; KAO has provided almost all of the far infrared spectroscopy of the gas.

This review discusses far infrared observations of galaxies of different morphological type. This approach is taken because different types may represent different equilibria of the interstellar medium. The review also focuses almost entirely on observational evidence from the wavelength régime longer than about 10μm. The next chapter very briefly reviews far infrared probes

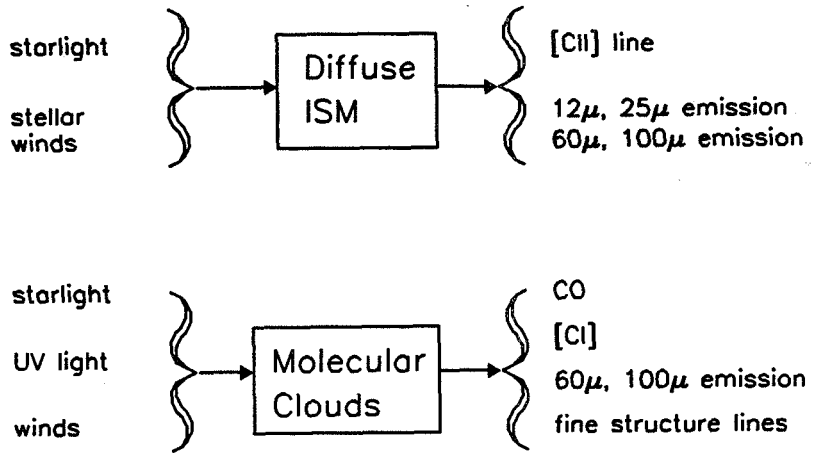

Figure 2. Schematic diagram showing the energy input and output in (a) the diffuse and (b) the dense ISM.

of the ISM. Subsequent chapters deal with what we have learned from KAO observations about quiescent spirals, elliptical galaxies, interacting systems, active galactic nuclei, starburst galaxies and dwarf galaxies. The review closes with some speculation about future possibilities.

2. FAR INFRARED OBSERVATIONS OF THE ISM

Dust grains in the diffuse ISM in galaxies are heated by starlight to (equilibrium) temperatures of $\sim$ 20 K and in star-forming molecular clouds to temperatures of 50 - 100 K; they therefore radiate continuum emission in the far infrared region of the spectrum. Figure 3 shows a schematic continuum spectrum of a galaxy. The stars in this model have a spherical distribution like that of an elliptical galaxy; the starlight spectrum is described by a 4000 K black body. Distributed in this galaxy is an optically thin dusty ISM of constant density to a radius five times the effective radius of the galaxy. The dust contains two grain sizes, "small" grains, which are transiently heated by the absorption of single photons, and "large" grains which are in thermal equilibrium. The grains are half graphite and half silicate by number; the optical constants of Draine & Lee (1984) are used.

Figure 3 illustrates several important points. First, about half of the total luminosity of the galaxy is re-emitted at wavelengths longer than about 50μm. Second, at very long wavelengths, the photon energy is low enough that $h\nu <$ kT for all of the dust; in this case the spectrum is $S_\nu \sim \nu^{2+\beta}$, where β is the grain emissivity index. Thus if the spectrum is observed at long enough wavelengths β can be measured regardless of the temperature or density distribution of the dust. Third, the small grains, which produce the "warm dust" component, can be transiently heated by relatively cool stars and emit significant flux even

in relatively low-energy radiation fields. Fourth, small silicate grains should produce significant emission in the 9.7μm silicate feature, and its presence or absence tells us about the chemical composition of the small grains.

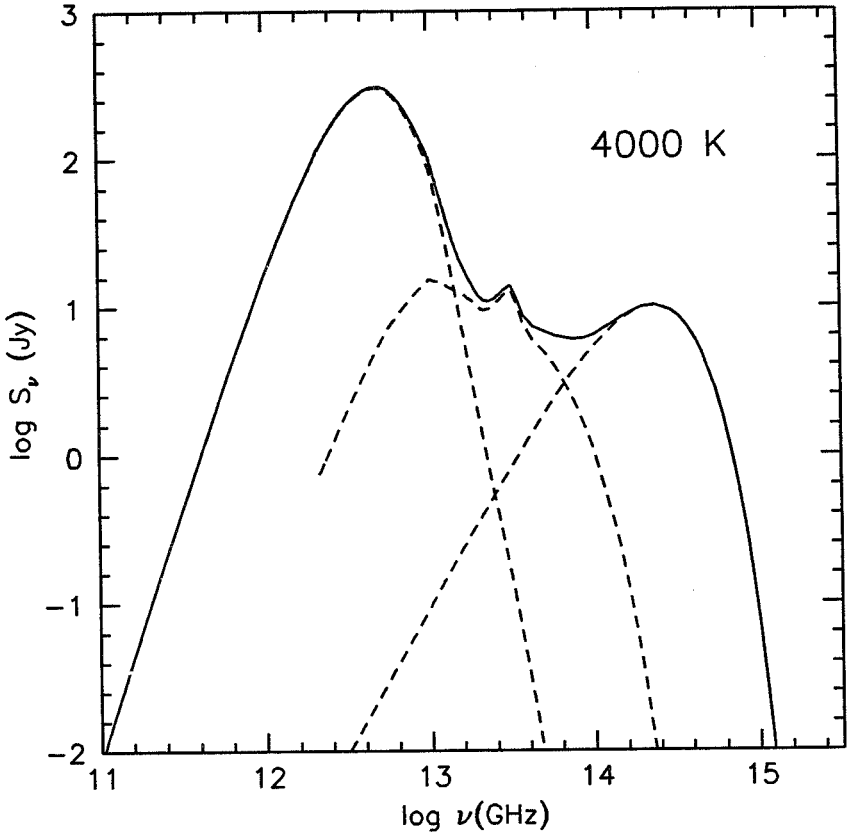

Figure 3. Schematic continuum spectrum for a dusty galaxy. The total spectrum is shown by the solid line. The three components shown by dashed lines are, from left to right: emission from large grains; emission from small grains; stellar continuum. See text for details.

Continuum observations in the far infrared region of the spectrum of a galaxy, together with observations at shorter infrared and optical wavelengths, give: (1) the total luminosity: if the galaxy is undergoing strong current star formation, the star formation rate can be estimated from this luminosity; (2) the total mass of dust and an estimate of the total interstellar mass; (3) the long wavelength dust emissivity index, which is determined by the structure of the grains; (4) an estimate of the numbers of small and large grains and hence of the dust grain size spectrum; (5) information on the chemical composition of the dust; and (6) the dust temperature or temperature distribution, which is related to the relative distributions of the dust and stars.

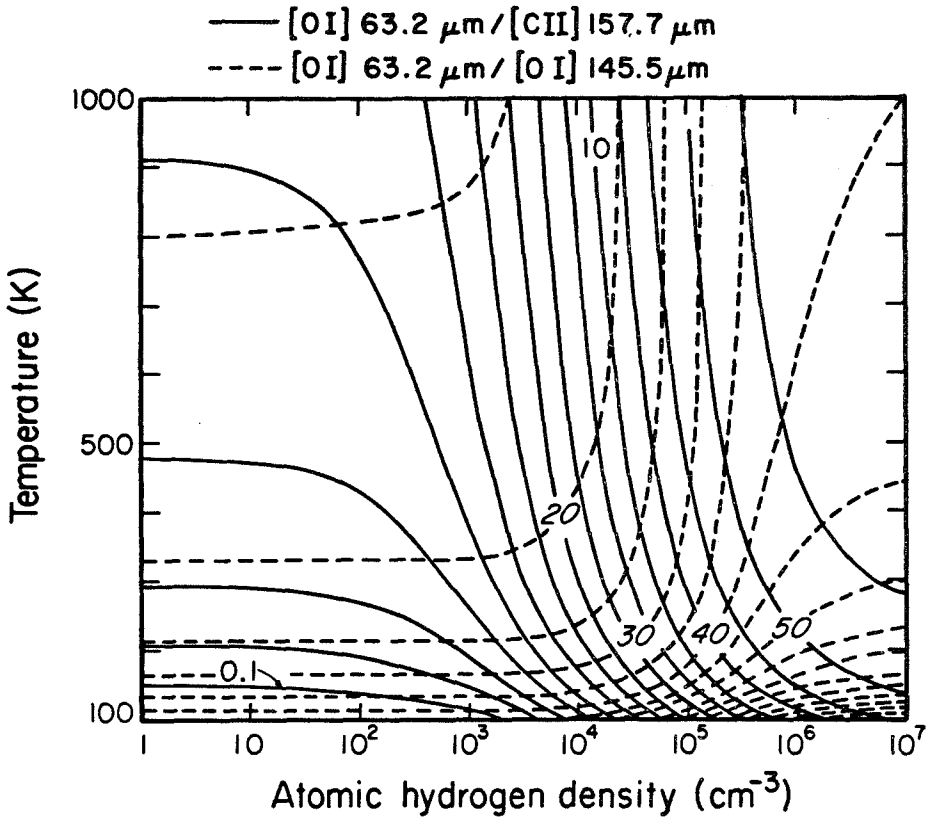

Figure 4. The line intensity ratios [OI]63μm/[CII]158μm (solid lines, upright numbers) and [OI]63μm/[OI]146μm (broken contours, slanted numbers) plotted as functions of the atomic hydrogen density and temperature. The contour intervals are logarithmic for the [OI]63μm/[CII]158μm ratio and linear for the [OI]63μm/[OI]146μm ratio. The C^+/O° abundance is 0.5. (From Watson 1984. Reprinted by permission of Kluwer Academic Publishers).

IRAS provided an enormous data base for the study of the emission from interstellar dust. These observations become much more powerful if the emission can be mapped, and the KAO has provided long-wavelength maps of a large number of galaxies. The KAO's second major contribution has been to provide flux densities at wavelengths longer than 100μm; as Figure 3 shows the flux density from cool dust in the ISM often peaks at wavelengths longer than 100μm, the longest wavelength observed by IRAS, and KAO observations allow the dust temperature and total luminosity to be measured much more reliably.

Infrared spectral lines measured by the KAO have provided a wealth of important data. These are fine structure lines emitted by neutral and ionized species like O, N, C, Ar, Ne, Si, Fe and S between wavelengths of about 50μm

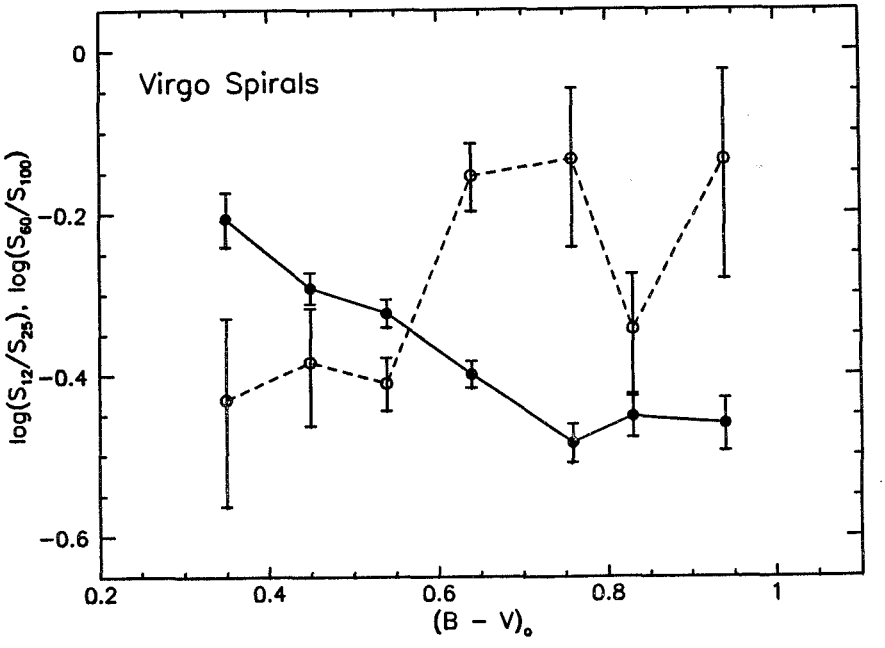

Figure 5. Mean value of S_{60}/S_{100} (filled symbols, solid line) and S_{12}/S_{25} (open symbols, dashed line) versus corrected $(B - V)_o$ color for spiral galaxies in the Virgo cluster. The infrared data are from Helou et al. (1988) and the optical colors from de Vaucouleurs et al. (1991).

and 200μm. Like their optical counterparts, these lines are collisionally excited and their strengths are sensitive to temperature and density, but they have the enormous advantage of being emitted at wavelengths which are little affected by interstellar extinction. They can thus be used to study the ISM throughout the Galactic disk and to measure conditions inside heavily obscured starburst regions. Lines of various ionization levels of the above species can be used to probe the hardness of the radiation field; observations of these lines are a good probe of the spectrum of the radiation from the nuclear source in active nuclei, for example.

Theoretical models of emission in these lines, including the dependence of various line ratios on density, temperature, radiation field etc. have been presented by Watson (1984) for predominantly neutral media, by Rubin et al. (1994a,b) for HII regions, and by Voit (1992) and Spinoglio & Malkan (1992) for AGNs. The lines predominantly observed from the neutral medium are the [CII]158μm line (the "cooling line" for the atomic ISM), the [OI]63μm line, and the [SiII]35μm line. These are also observed from photodissociation regions (PDRs). The critical densities required to collisionally thermalize the [OI] and [CII] lines are very different: $n_{crit} = 10^5 - 10^6$ cm^{-3} for [OI]63μm and 3000 cm^{-3} for [CII]158μm. The ratio of these lines measures the pressure in the atomic ISM, as shown in Figure 4, taken from Watson (1984). Finally, the abundance of Si

derived from the [SiII]35μm line gives an estimate of heavy element depletion.

The [OIII]52μm and 88μm and the [SIII]33μm lines are used to derive HII region properties and estimates of the star formation rate. Together with 21 cm line observations of HI and millimeter wavelength observations of the rotational lines of CO, these lines provide a powerful set of probes of the structure of the interstellar medium in galaxies.

3. QUIESCENT SPIRALS

IRAS provided global flux densities at 12μm, 25μm, 60μm and 100μm for a large number of spiral galaxies. The infrared colors derived from these flux densities show a number of global trends. Figure 5 shows the mean 12/25 and 60/100 flux density ratios versus color, $(B-V)_o$, for a sample of spiral galaxies in the Virgo cluster. The IRAS data are total flux densities given by Helou et al. (1988) and the optical colors are from de Vaucouleurs et al. (1992). The 60/100 flux density ratio roughly measures the temperature of the large grains, and Figure 5 shows that this temperature is systematically higher for bluer galaxies, which presumably have higher star formation rates. The 12/25 ratio, on the other hand, increases with increasing (B - V), though the data are much noisier. Figure 6 shows the 60/100 ratio versus the 12/25 ratio for Virgo spirals; this diagram, originally plotted by Helou (1986), has been interpreted as a "mixing" diagram, with the relative contribution from star forming regions and the diffuse ISM proportional to the global star formation rate.

To ascertain in detail the source of the infrared emission we need to map its distribution and compare it with other constituents of the galaxy. Only a few galaxies are large enough in angular size to be sufficiently resolved by IRAS. Rice (1993) presents maps of several large galaxies made by deconvolving the IRAS data. In the galaxy of largest angular size, M31, both the molecular and atomic gas lie in a ring at a radius of about 10 kpc while the inner regions of the disk have little ISM. The emission at all IRAS wavelengths also arises from this ring. Strong emission is also seen from the bulge of M31; since there is no strong AGN and little evidence of star formation, this is likely to be due to dust heated by the bulge stars, whose volume density is much higher than that in the disk.

Stark et al. (1989) mapped four of the largest spiral galaxies in the Virgo cluster with the Yerkes bolometer array at 160μm and 360μm, and found that the long wavelength emission is extended on the scale of the optical disk. Roughly 50% of the total luminosity from these spiral galaxies is emitted at wavelengths longer than 50μm.

Smith et al. (1991, 1994) have carried out an ingenious set of observations of the large nearby ring galaxy NGC 4736. This galaxy has a large bulge and a disk with a large inner hole, and the emission from the galaxy at various wavelengths can straightforwardly be associated with the disk or bulge. The red starlight (measured at 6500 Å) is emitted from the bulge, while the galaxy's Hα emission is from the disk, where star formation is taking place. The 50μm and 100μm emission, on the other hand, comes from *both* the bulge and the disk (cf. Figure 7). This observation, like the IRAS observation of M31, shows that the far-infrared flux measures not just the star formation rate but is emitted by several different regions of the galaxy. As Figure 3 shows, the densely distributed

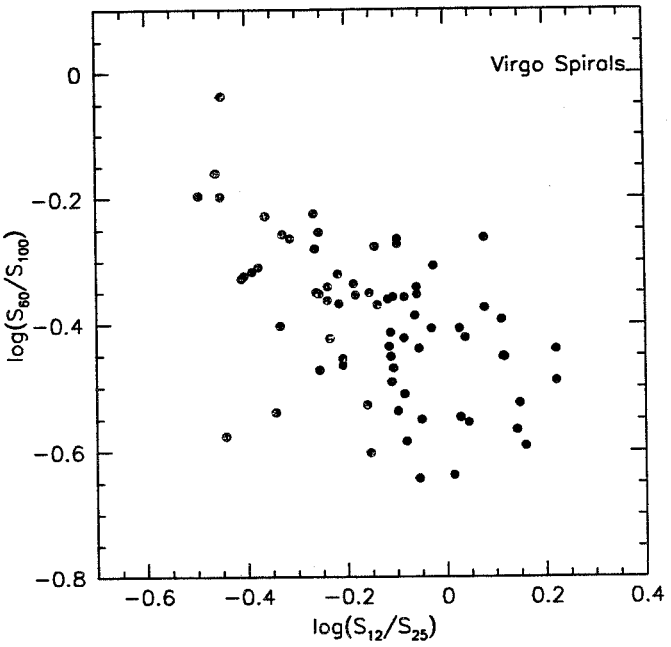

Figure 6. Ratio of S_{60}/S_{100} versus S_{12}/S_{25} for Virgo cluster galaxies from the data of Helou et al. (1988).

bulge stars can heat interstellar dust to respectable temperatures, even though they are cool.

Probably the most quiescent spiral galaxy observed in detail to date is NGC 4565. This large edge-on galaxy has very weak distributed radio emission from the disk, indicating a low current rate of star formation (Rupen 1991). Engargiola & Harper (1992) have taken advantage of the edge-on orientation, which gives the highest surface brightness for optically thin emission, and have mapped it at 100μm, 160μm, and 200μm using the KAO with spatial resolutions of 45″ – 56″. The long-wavelength dust emission is fairly coextensive with the optical disk.

The HI and CO emission from this galaxy have also been mapped at high spatial resolution, ~ 20″ (Rupen 1991; Sofue & Nakai 1994). The integrated CO emission along the major axis is fairly constant in average intensity, with peaks which may coincide with spiral arms. The integrated 21 cm emission has a minimum towards the center of the galaxy. This resembles the distribution of 100μm emission (Engargiola & Harper 1992). The far infrared emission in this galaxy, then, seems to be distributed more like the atomic than the molecular gas.

NGC 6946 is a nearby spiral galaxy with a much higher star formation rate than NGC 4565, as shown by the strength of the radio continuum emission, the Hα emission and so on. The extended 60μm, 100μm and 160μm emission can be decomposed into bulge and disk components, with the bulge emission being

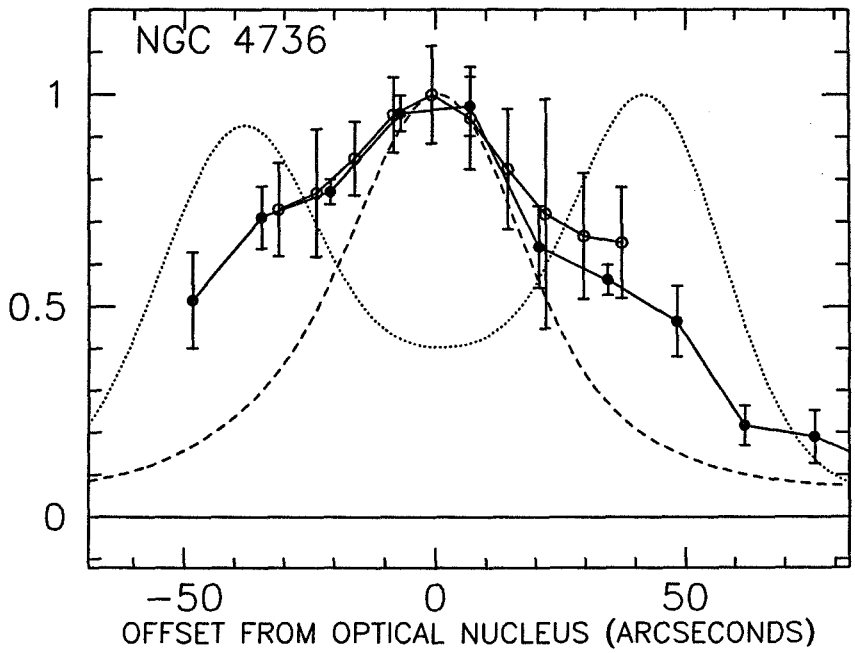

Figure 7. Normalized intensity distribution in right ascension of emission from various components of the ring galaxy NGC 4736. Solid line, filled symbols: 100μm continuum. Solid line, open symbols: 50μm continuum. Dotted line: Hα. Dashed line: 6500Å continuum (from Smith et al. 1994).

considerably hotter than the disk emission (Engargiola 1991). Localized peaks of emission can also be seen associated with the HII region complexes in the disk.

These mapping observations show that the far infrared emission from spiral galaxies is due to at least three components: (1) dust in the bulge, where the dust is hotter than that in the disk. This phenomenon is seen in galaxies with (NGC 6946) and without (M31, NGC 4736) nuclear star formation or active nuclei. In the latter case, the emission can be explained by the relatively higher radiation density in bulges due to the high stellar density. (2) diffuse emission distributed more or less like the blue light: and (3) hot spots in the disk associated with regions of intense star formation.

Comparison of these maps with HI and CO maps shows that in really quiescent galaxies like NGC 4565 the far infrared emission is more closely associated with the atomic hydrogen, while in more actively star-forming galaxies like NGC 6946 the far infrared emission is more closely associated with the molecular gas. For apparently similar galaxies (similar HI content, diameter, circular velocity etc.) the fraction of the energy emerging at $\lambda \geq 50\mu$m varies from 20-30% to more than 60% and the global star formation rates differ by an order of magnitude. These observations show that the far infrared luminosity is not a direct indicator of the star formation rate unless it is high enough that emission from star-forming regions dominates that from the rest of the galaxy. Given that

the shorter wavelength emission (in the IRAS 12μm and 25μm bands) seems to arise from the diffuse ISM (cf. Figures 5 and 6) it may be possible to correct the longer wavelength emission for the contribution from the diffuse medium and to evaluate the contribution from star forming regions.

The gas to dust ratio derived from comparisons between the far infrared emission and HI and CO observations is a few hundred, higher than the Galactic value but probably the result of generally overestimating the dust temperature in the diffuse ISM. These numbers are additionally uncertain because we do not know the long-wavelength dust emissivity values very well; to measure these empirically we need observations at much longer wavelengths, 1 mm and longer.

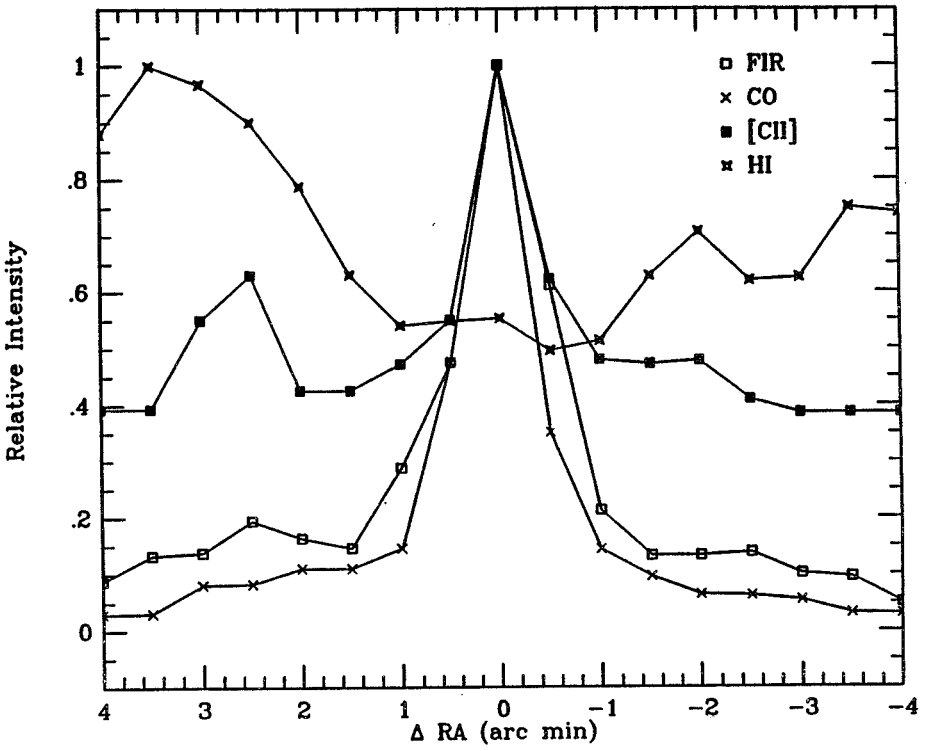

Figure 8. Normalized intensity distribution versus right ascension for emission from various components of the ISM of NGC 6946. Stars: HI. Filled circles: [CII]158μm. Open squares: far-infrared continuum. Filled squares: CO. From Madden et al. (1993).

Far-infrared spectral line emission from spiral galaxies gives a similar picture. Figure 8 shows the radial distributions of CO(1–0), far-infrared continuum (Engargiola 1991), HI, and [CII]158μm emission (Madden et al. 1993) in NGC 6946, which, as discussed above, has a fairly high current star formation rate. The far infrared emission and the molecular emission are strongly centrally peaked and have similar radial distributions, showing that the far infrared

emission is predominantly due to star formation, while the HI surface density is roughly constant with radius. The [CII] emission is associated with the molecular star forming regions (the nucleus, the spiral arms and the HII regions) and the extended atomic medium. It is therefore likely to be emitted both from the diffuse medium and the photodissociation regions associated with star forming molecular clouds. The total luminosity of the [CII] line is $\sim$ 1% of the total far-infrared emission.

Similar results are found for other spiral galaxies with fairly high current rates of star formation (cf. Lord et al. 1994). For example, the central region of IC 342 contains molecular gas which is hotter than typically found in galactic disks, while the ratio of the [OI]63μm line intensity to that of the [CII]158μm intensity shows that the neutral ISM has a pressure about ten times the value in the Galactic disk (Eckard et al. 1990). These properties of the ISM are likely to be both a result of, and a cause of, enhanced star formation in this galaxy, as we shall see when discussing the conditions in starburst galaxies in Section 7.

4. ELLIPTICAL GALAXIES

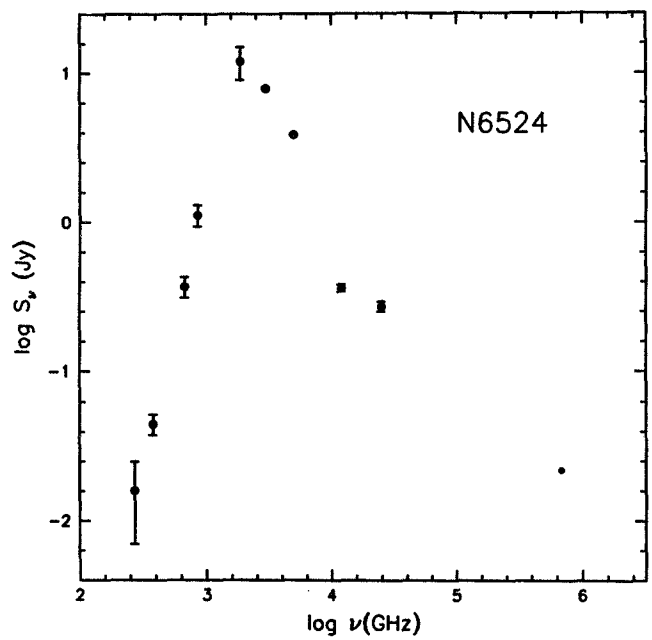

Figure 9. Continuum spectrum of NGC 6524 observed at the JCMT (1 mm - 350μm), with the KAO (160μm), by IRAS and in the optical B band.

Although these galaxies have traditionally been defined as devoid of ISM, recent surveys for hot and cold gas have shown that small amounts of ISM are the rule, rather than the exception, in these galaxies (e.g. Roberts et al. 1991). The KAO

has now contributed observations of the cold ISM in several elliptical galaxies. High spatial resolution observations at 100μm of NGC 5128 (Centaurus A) by Joy et al. (1988) show, as expected, that much of the emission comes from the dense polar dust lane. However, the observations also show that the 100μm emission is extended perpendicular to the dust lane, along the major axis of the galaxy. This emission may well be from dust associated with the shell structure seen at optical wavelengths, heated by the ambient starlight, and shows a similar distribution to that seen in HI (Schimanovich et al. 1994) and in CO (Quillen et al. 1992; Rydbeck et al. 1993) emission. Finally, a large fraction of the emission comes from an unresolved region at the center of the galaxy, perhaps due to dust heated by the powerful active nucleus of this galaxy (see Section 6 below).

The far infrared emission from two other elliptical galaxies has been observed with the Yerkes bolometer array (Lees et al. 1994). The continuum spectrum of NGC 6524 is shown in Figure 9. These observations show that the dust is fairly cool, and is therefore likely to be in an extended distribution: that the ISM contains a significant amount of dust in small grains: that the long-wavelength dust emissivity index β is about 1.5, and that the gas-to-dust ratio is about 150 by mass. The dust in elliptical galaxies thus appears to be similar to that in spiral galaxies. If this conclusion is confirmed by observations of other elliptical galaxies, it implies that the evolution of the ISM in ellipticals is similar to that in spirals; the difference is that the amounts of ISM are much smaller due to efficient early star formation in ellipticals (but see Tsai & Mathews 1994).

5. INTERACTING GALAXIES

A small fraction of galaxies are in pairs in which the galaxies are interacting strongly enough to cause severe tidal distortions of their structure; some at least of these pairs are probably in the process of merging. These systems are interesting because the interaction generally results in enhanced star formation or in enhanced activity in the central regions of the galaxies, and reproduces at least in part the conditions in the early Universe when galaxies were forming and transforming much of their gaseous matter into stars at a high rate. In the present-day Universe, the interaction of a spiral galaxy and an elliptical galaxy probably leads to activity in the nucleus of the elliptical galaxy fueled by gas from the spiral, while the merger of spirals is thought to lead to a starburst and, perhaps, to the formation of an elliptical galaxy. Indeed, interacting galaxies are generally found to be strong sources in the IRAS sky survey. Observations of AGNs are discussed in a little more detail below (Section 6) while those of starburst galaxies are discussed in Section 7.

The KAO has mapped the far-infrared continuum emission from several interacting systems including NGC 4485/90 (Thronson et al. 1989), NGC 4038/39, the 'Antennae' (Harper et al. 1994) and NGC 7464/65 (Harper et al. 1994). These observations show that the far infrared emission is closely spatially related to dense molecular gas and Hα emission. The luminosities derived from these observations give local star formation rates at least ten times those in quiescent galaxies. The high resolution available from these maps also shows that the regions of enhanced star formation lie between the main optical bodies of the interacting galaxies.

6. ACTIVE GALACTIC NUCLEI

The emitting regions involved with AGNs are small on the scale of a galaxy, and infrared observations, particularly at long wavelengths, do not generally have sufficient spatial resolution to detect the AGN directly; rather, they provide information about the physical conditions in the ISM in the inner kpc or so of the galaxy containing the AGN. In several cases, high spatial resolution maps at far-infrared wavelengths have shown that a significant fraction of the total far-infrared emission from dusty galaxies is emitted from a small region at the center of the galaxy. The observation of Centaurus A by Joy et al. (1988) has been discussed above in Section 4. Scans across the large (24′ diameter) spiral galaxy NGC 4945 show that fully half of the 100μm emission from this post-starburst galaxy is from a nuclear source no larger than 12″ × 9″ (Rice et al. 1988; Brock et al. 1988). The nearby spiral galaxy M51 also has a strong far-infrared nuclear point source. A possible explanation is that the emission arises from dust heated by a heavily obscured active nucleus.

Many quasars and radio galaxies are also observed to be relatively strong far-infrared sources (Neugebauer et al. 1986). The infrared beams are large enough that when observing these relatively distant objects emission from the entire galaxy is observed. The far infrared flux from these objects has three possible origins: (1) objects like BL Lac have smooth, featureless continuum spectra from long radio through X-ray wavelengths, and the far-IR radiation, like the radiation at all wavelengths, is completely dominated by non-thermal radiation from the central engine: (2) many radio galaxies like 3C120 show a strong IR bump, well in excess of the extrapolated radio emission, between wavelengths of about 1 mm and 50μm. This is almost certainly due to large amounts of interstellar dust in the galaxy: (3) radio galaxies like 3C274 (M87) which contain hot (X-ray emitting) gas and very little cold gas show excess emission at shorter infrared wavelengths ($\lambda \leq 10$ μm) which may be due to hot dust in the vicinity of the powerful central nucleus.

7. STARBURST GALAXIES

One of the major discoveries by IRAS was the detection of ultraluminous ($L \sim 10^{13}$ $L_\odot$) starburst galaxies, which emit most of their radiation at wavelengths between 50 and 200 μm. The luminosity of these galaxies is dominated by the output of hot young stars and the star formation rates are often tens to hundreds of times those in quiescent spiral galaxies (e.g. Soifer et al. 1987). High angular resolution observations of starburst galaxies such as M82 (Joy et al. 1987) and NGC 1068 (Lester et al. 1987) clearly show the association of continuum emission peaks with large clusters of hot stars.

The continuum spectra of starburst galaxies have the characteristic shape of a modified black body: see, for example, the continuum spectrum of II Zw 40 published by Joy and Lester (1988) and that of M82 (Figure 10). This spectral shape resembles that of an HII region (cf. Figure 10) and differs from that of a quiescent spiral galaxy in two respects. First, the color of the longer wavelength emission shows that the large grains are hotter than are those in spiral galaxies: $S_{60}/S_{100} \sim 1$ for starburst galaxies and ~ 0.3 - 0.5 in spirals. Second, there is little or no excess at 12μm and 25 μm over that of the modified black body,

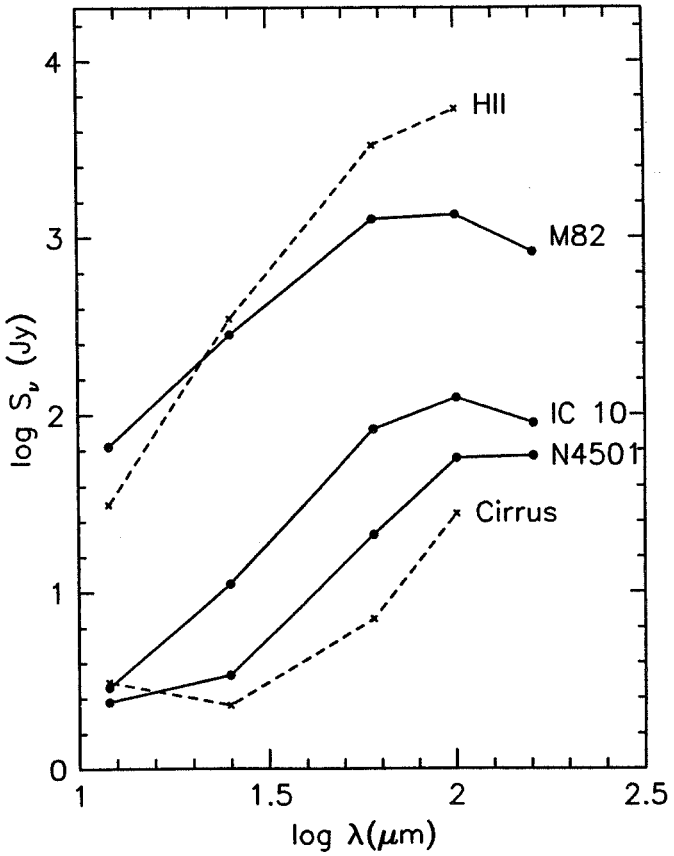

Figure 10. Continuum spectra of M82 (a starburst galaxy), NGC 4501 (a quiescent spiral galaxy), and IC 10 (a dwarf irregular galaxy). For comparison, the spectrum of a typical compact HII region and of a cirrus cloud are plotted (see text). The data at 12μm, 25μm, 60μm and 100μm are from IRAS, and the data at 160 μm from KAO observations.

showing that the small grain population is much lower in abundance in starburst galaxies than it is in quiescent spirals.

Starburst galaxies are of high enough luminosity that they should be readily detectable (if they exist) at very large redshifts by telescopes we hope to have in the near future, such as the Millimeter Array (MMA) and SIRTF. The flux observed near about 1 mm is from the Rayleigh-Jeans part of the spectrum in galaxies at redshifts as high as $\sim$ 15; indeed, galaxies of the same luminosity will produce about the same observed millimeter-wavelength flux density over this entire redshift range. This is because the steeply-rising spectrum ($S_\nu \sim \nu^{3-4}$ in the Rayleigh-Jeans limit) offsets the effects of distance and redshift. SIRTF, on the other hand, observes the Wien spectral region at $z \geq 1$ and so the SIRTF/MMA spectral index will provide an estimate of the redshift, allowing

the distribution and luminosity function of these objects to be measured to $z \sim 5$ (Werner & Eisenhardt 1994).

Far infrared spectroscopy has led to major advances in knowledge about the physics of starburst galaxies. These systems have roughly the same [CII]/CO ratio as do giant molecular clouds in the Galaxy, with a value about 3 times higher than the global value observed in quiescent spirals (Wolfire et al. 1989; Stacey et al. 1991). Starburst galaxies thus look very like enormous star-forming giant molecular clouds, both in terms of their continuum and line spectra. These properties appear to be independent of the luminosity of the starburst (Stacey et al. 1991; Carral et al. 1994). The exception to this appears to be NGC 6240, whose [CII]/CO ratio is similar to that in more quiescent spirals; Stacey et al. (1991) suggest that this may be an old starburst galaxy. They also show by comparison with star-forming molecular clouds in the Galaxy that much of the [CII] emission arises from PDRs, which account for something like 40% of the total gas mass in starburst galaxies.

Observations of [CII], [OI], [OIII] and [SiII] lines in the nearby starburst galaxies M82 and NGC 253 show that the gas pressure is more than ten times that in the local Galactic neighborhood and that the HII regions fill a substantial fraction of the volume (Carral et al. 1994). Further, the Si abundance is about solar, showing that this species is not depleted in the gas phase and that dust grains are destroyed in the environments of starburst galaxies. The ISM in a starburst galaxy is thus in quite a different state from that in the disks of more quiescent spiral galaxies (Carral et al. 1994). In the Galaxy the volume is occupied by collisionally ionized coronal gas and diffuse HI, with only a small fraction of the volume in molecular clouds and HII regions: most of the mass is in the atomic and molecular phases. In starburst galaxies, on the other hand, most of the volume seems to be occupied by ionized gas (the 10^6 K coronal gas and 10^4 K HII regions), while the molecular gas remaining from the starburst is in warm tattered filaments embedded in extended PDRs.

8. DWARF GALAXIES

Gas-rich dwarf irregular galaxies have low luminosities and no well-defined shape. Unlike spiral galaxies, in which star formation is localized in the disk and occurs fairly steadily, star formation in dwarf galaxies occurs at more or less random locations. Maps of the 100μm emission in IC 10, for example, show that star formation is concentrated in the inner regions of the galaxy. The inferred star formation rate is only $\sim 0.1 - 0.2\ M_\odot\ yr^{-1}$, a factor of 20 - 50 times smaller than the global rate in the Galaxy but with about the same ratio of star formation rate to total gas content as seen in the Galaxy. These observations strongly imply that star formation requires a threshold density (Thronson et al. 1990).

The continuum spectrum of IC 10 is also plotted in Figure 10, which shows the continuum spectra of the starburst galaxy M82 and the quiescent spiral NGC 4501. The IRAS spectra of the R CrA cloud, which is a typical dense cirrus cloud, and the compact HII region AFGL 4101 are plotted for comparison (the data are from Leene 1986 and Crawford and Rowan-Robinson 1986 respectively). These data show that the continuum spectrum of IC 10 resembles that of the starburst galaxy M82 rather than that of the quiescent spiral NGC 4501 (cf. also the spectrum of the active dwarf galaxy NGC 1569 compared with that of the spiral

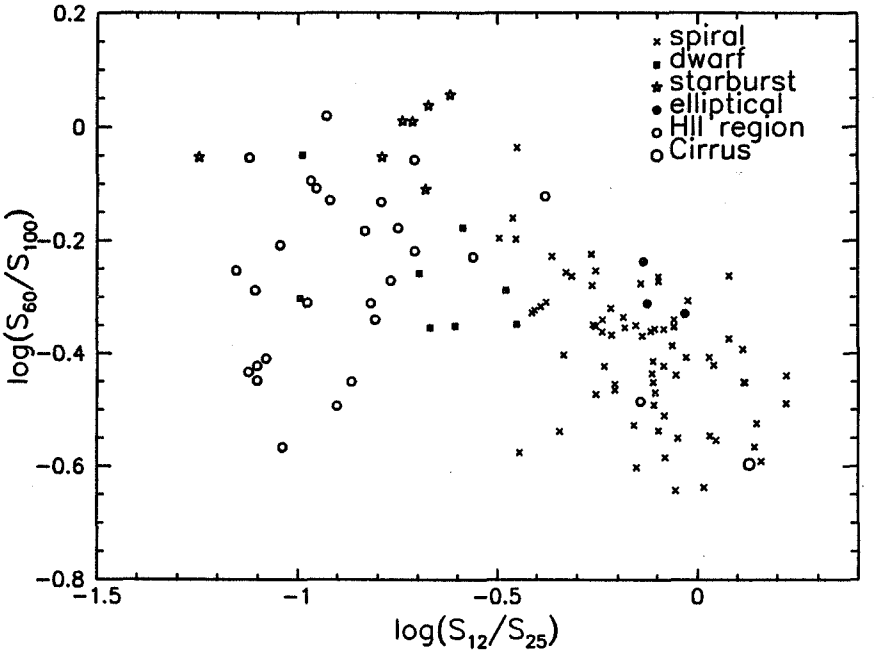

Figure 11. Color-color plot from IRAS data for Galactic HII regions and cirrus, compared with the global colors of galaxies of different types.

galaxy NGC 3593 by Hunter et al. 1989).

This is further illustrated in Figure 11 which shows a plot of S_{60}/S_{100} versus S_{12}/S_{25} for various samples of galaxies: (1) the Virgo cluster spirals from Helou et al. (1988) whose data were used to derive the average properties of quiescent spirals shown in Figure 6 and discussed above in Section 3: (2) the three elliptical galaxies observed to date by KAO. While these points lie along the spiral galaxy locus, the value of S_{60}/S_{100} is higher than average, due to greater starlight density in these systems: (3) compact HII regions; the data are from Crawford and Rowan-Robinson (1986): (4) the "cirrus" point from Leene (1986): (5) dwarf galaxies: and (6) starburst galaxies. Figure 11 shows a very clear distinction between dwarf and spiral galaxies; dwarfs have roughly the same 12/25 colors as do starburst galaxies and molecular clouds but are generally cooler. In all cases the total flux densities, derived by integrating the emission over the area of the galaxy, are used (Rice et al. 1988; Helou et al. 1988).

As noted above, the general trend illustrated in Figures 6 and 11 is due to different contributions by diffuse and dense gas, and can be reproduced by models of dust heated by radiation fields of different intensities, with the dust size distribution changed also; cf. Désert (1986). Figure 11 suggests that dwarf galaxies, like starburst galaxies, are deficient in small grains relative to spirals (cf. also the study of the nearby dwarf system NGC 6822 by Gallagher et al. 1991). This conclusion needs to be tested by more sensitive observations; there is a possible selection effect operating in the sense that dwarf galaxies bright enough

to be detected by IRAS and KAO are likely to have a relatively high level of star formation. However, it agrees with the finding that the 2200 Å bump, which is though to be produced by small carbon grains, is fairly weak in the LMC (e.g. Fitzpatrick and Massa 1990).

CO line observations of dwarf irregular galaxies have usually shown that the relative strength of the CO line is lower than in spiral galaxies (e.g. Rubio et al. 1991). Either the relative amount of molecular gas in irregulars is low, or the CO emission is relatively weak because of metallicity effects. Observations of the [CII] line in the LMC show that the [CII]/CO ratio is much larger than in other galaxies (Stacey et al. 1991; Mochizuki et al. 1994; Poglitsch et al. 1994), and that the [CII] line emission shows a closer spatial correspondence to far infrared than to CO emission (Jones et al. 1986; Boreiko and Betz 1991). Hence star-forming regions in this dwarf galaxy have more HI and less CO than do those in the Galaxy. These observations suggest that a much larger fraction of the gas in star-forming cloud complexes in a dwarf galaxy is in atomic form compared to such regions in the Galaxy. This might well be a function of the lower metallicities in dwarf galaxies, since their clouds have lower dust contents and have less shielding against radiation from interstellar UV. The apparent paucity of small grains might also be due to strong UV radiation, which can destroy small grains.

9. THE NEXT 20 YEARS?

Far infrared observations have yielded a wealth of information on the physical state and equilibrium of the ISM in galaxies of many different types. In particular, observations of the conditions in dwarf and starburst galaxies tell us a great deal about star formation in interstellar environments like those present in the early history of 'normal' spiral galaxies. We have learned that nearby galaxies with active nuclei contain large amounts of ISM, and that much of the luminosity in such galaxies comes from a small region in the center of the galaxy. We have learned that star formation is in a sense a 'local' phenomenon; the properties of starbursts of different luminosities are similar in most respects except for luminosity.

What of the future? ISO, SOFIA and SIRTF bring greater sensitivity, spatial resolution and wavelength coverage; some of the investigations they might allow us to make are:

1. High resolution observations with KAO have shown that much of the radiation from galaxies with AGNs comes from the inner few hundred parsecs. Observations with the new facilities can localize the emission, measure spectra of the surrounding ISM and hence the spectrum of the nuclear source.
2. How does star formation proceed in different environments, and how does it depend on metallicity, total gas content, gas density amd the dynamical 'hotness' or 'coldness' of the galaxy? Observations of dwarfs, spirals, and ellipticals are beginning to allow this sort of comparative study, and the new instruments will provide the sensitivity needed for observations of a good-sized sample of elliptical and dwarf galaxies.
3. How do grain properties (composition, size distribution, etc.) vary from galaxy to galaxy and from place to place in a galaxy? If we can track the formation and destruction history of grains in the ISM we will have gone a long

way towards understanding the evolution of the ISM.

4. How do starburst galaxies evolve? What happens after the burst is over? Can we identify post starburst galaxies? Why do bursts stop? Does the galaxy run out of gas, or does the pressure get too high or too low?

5. Can the effect of the furious star formation activity in starbursts on the composition of the ISM be seen? Can we observe rapid enrichment, and spatial variations in the composition?

6. Powerful new millimeter-wavelength synthesis instruments are likely to detect very large numbers of faint continuum sources if all or most big galaxies go through an Arp 220-like stage of intense star formation early in their evolution. These weak sources should also be detectable by SIRTF and will show a very wide range of IR - to - millimeter wave color index, with strong dependence on redshift. Observations by these two future telescopes will tell us about the luminosity function and the redshift distribution of galaxies in the process of formation.

ACKNOWLEDGEMENTS

I am very grateful to the scientific and local organizing committees for their invitation to this most educational, stimulating and enjoyable conference and for financial support; many thanks to Jackie Davidson in particular for a very good time, both scientific and social. I also thank NASA's ADP program for research support via grant NAG5-2376.

REFERENCES

Boreiko, R. L. & Betz, A. L. 1991, ApJL, 380, L27

Brock, D., Joy, M. H., Lester, D. F., Harvey, P. A. & Ellis, H. B. 1988, ApJ, 329, 208

Carral, P., Hollenbach, D. J., Lord, S. D., Colgan, S. W. J., Haas, M. R., Rubin, R. H. & Erickson, E. F. 1994, ApJ, 423, 223

Crawford, J., & Rowan-Robinson, M. 1986, MNRAS, 221, 923

Désert, F. X. 1986, in 'Light on Dark Matter', ed. F. P. Israel, D. Reidel Co., p213

Draine, B. T. & Lee, H. -M. 1984, ApJ, 285, 89

Eckard, A., Downes, D., Genzel, R., Harris, A. I., Jaffe, D. T. & Wild, W. 1990, ApJ, 348, 434

Engargiola, G. 1991, ApJS, 76, 875

Engargiola, G. & Harper, D. A. 1992, ApJ, 394, 104

Fitzpatrick, E. L. & Massa, D. 1990, ApJS, 72, 163

Gallagher, J. S., Hunter, D. A., Gillett, F. C. & Rice, W. L. 1991, ApJ, 371, 142

Harper, D. A., Lees, J. F. & Cole, D. 1994, in preparation.

Helou, G. 1986, ApJL, 311, L33

Helou, G., Khan, I. R., Malek, L. & Boehmer, L. 1988, ApJS, 68, 151

Hunter, D. A., Thronson, H. A., Casey, S. & Harper, D. A. 1989, ApJ, 341, 697

Jones, T. J., Hyland, A. R., Straw, S., Harvey, P. M., Wilking, B. A., Joy, M., Gatley, I. & Thomas, J. A. 1986, MNRAS, 219, 603

Joy, M. & Lester, D. F. 1988, ApJ, 331, 145

Joy, M., Lester, D. F. & Harvey, P. M. 1987, ApJ, 319, 314

Joy, M., Lester, D. F., Harvey, P. M. & Ellis, H. B. 1988, ApJ, 326, 662

Leene, A. 1986, A&A154, 295

Lees, J. F., Harper, D. A., Rupen, M. P. & Knapp, G. R. 1994, BAAS, 25, 1355

Lester, D. F., Joy, M., Harvey, P. M., Ellis, H. B. & Parmer, P. S. 1987, ApJ, 321, 755

Lord, S. D., Hollenbach, D. J., Colgan, S. W. J., Haas, M. R., Rubin, R. H., Steiman-Cameron, T. Y., Carral, P., Maloney, P. & Erickson, E. F. 1994, in Proc. of the Airborne Astronomy Symp. on the Galactic Ecosystem: From Gas to Stars to Dust, ed. M. R. Haas, J. A. Davidson & E. F. Erickson, (San Francisco: ASP), paper 2.2

Madden, S. C., Geis, N., Genzel, R., Herman, F., Jackson, J., Poglitsch, A., Stacey, G. J. & Townes, C. H. 1993, ApJ, 407, 579

Mochizuki, K., Nakagawa, T., Doi, Y., Yui, Y. Y., Okuda, H., Shibai, H., Yui, M., Nishimura, T. & Low, F. J. 1994, ApJL, 430, L37

Neugebauer, G., Miley, G. K., Soifer, B. T. & Clegg, P. E. 1986, ApJ, 308, 815

Poglitsch, A., Geis, N., Herrman, F., Johannson, L. E. B., Krabbe, A., Madden, S. C., Stacey, G. J. & Townes, C. H. 1994, in Proc. of the Airborne Astronomy Symp. on the Galactic Ecosystem: From Gas to Stars to Dust, ed. M. R. Haas, J. A. Davidson & E. F. Erickson, (San Francisco: ASP), paper 2.1

Quillen, A. C., de Zeeuw, P. T., Phinney, E. S. & Phillips, T. G. 1992, ApJ, 391, 121

Rice, W. 1993, AJ, 105, 67

Rice, W., Lonsdale, C. J., Soifer, B. T., Neugebauer, G., Kopan, E. L., Lloyd, L. A., de Jong, T. & Habing, H. J. 1988, ApJS, 68, 91

Roberts, M. S., Hogg, D. E., Bregman, J. N., Forman, W. D. & Jones, C. 1991, ApJS, 75, 751

Rubio, M., Garay, G., Montani, J. & Thaddeus, P. 1991, ApJ, 368, 173

Rubin, R. H., Simpson, J. P., Lord, S. D., Colgan, S. W. J., Erickson, E. F. & Haas, M. R. 1994a, ApJ, 420, 772

Rubin, R. H., Simpson, J. P., Erickson, E. F., Haas, M. R., Lord, S. D. & Colgan, S. W. J. 1994b, in Proc. of the Airborne Astronomy Symp. on the Galactic Ecosystem: From Gas to Stars to Dust, ed. M. R. Haas, J. A. Davidson & E. F. Erickson, (San Francisco: ASP), paper 114

Rupen, M. P. 1991, AJ, 102, 48

Rydbeck, G., Wiklind, T., Cameron, M., Wild, W., Eckard, A., Genzel, R. & Rothermal, H. 1993, A&A, 270, L13

Schimanovich, D., van Gorkom, J. H., van der Hulst, J. M. & Kasow, S. 1994, ApJL, 423, L101

Soifer, B. T., Houck, J. R. & Neugebauer, G. 1987, ARAA, 25, 187

Smith, B. J., Harvey, P. M., Colom, C., Zhang, C. Y. & Difrancesco, J. 1994, ApJ, 425, 91

Smith, B. J., Lester, D. F., Harvey, P. M. & Pogge, R. 1991, ApJ, 373, 66

Sofue, Y. & Nakai, N. 1994, PASJ, 46, 147

Spinoglio, L. & Malkan, M. 1992, ApJ, 399, 504

Stacey, G. J., Geis, N., Genzel, R., Lugten, J. B., Poglitsch, A., Sternberg, A. & Townes, C. H. 1991, ApJ, 373, 423

Stark, A. A., Davidson, J. A., Harper, D. A., Pernic, R., Loewenstein, R., Platt, S., Engargiola, G. & Casey, S. 1989, ApJ, 337, 650

Thronson, H. A., Hunter, D. A., Casey, S. & Harper, D. A. 1990, ApJ, 355, 94

Thronson, H. A., Hunter, D. A., Casey, S., Latter, W. B. & Harper, D. A. 1989, ApJ, 339, 803

Tsai, J. C. & Mathews, W. G. 1994, in Proc. of the Airborne Astronomy Symp. on the Galactic Ecosystem: From Gas to Stars to Dust, ed. M. R. Haas, J. A. Davidson & E. F. Erickson, (San Francisco: ASP), paper 201

de Vaucouleurs, G., de Vaucouleurs, A., Corwin, H. G., Buta, R. J., Paturel, G. & Fouqué, P. 1991, 'Third Reference Catalogue of Bright Galaxies', Springer-Verlag

Voit, G. M. 1992, ApJ, 399, 495

Watson, D. M. 1984, in 'Galactic and Extragalactic Infrared Spectroscopy' ed. M. F. Kessler & J. P. Phillips, D. Reidel Co., p 195.

Werner, M. W. & Eisenhardt, P. 1994, in Proc. of the Airborne Astronomy Symp. on the Galactic Ecosystem: From Gas to Stars to Dust, ed. M. R. Haas, J. A. Davidson & E. F. Erickson, (San Francisco: ASP), paper 2.4

Wolfire, M. G., Hollenbach, D. J. & Tielens, A. G. G. M. 1989, ApJ, 344, 770

Airborne Astronomy Symposium on the Galactic Ecosystem
ASP Conference Series, Vol. 73, 1995
M.R. Haas, J.A. Davidson, and E.F. Erickson (eds.)

A Multi-Wavelength Study of 30 Doradus: The Interstellar Medium in a Low-Metallicity Galaxy

A. Poglitsch, R. Genzel, F. Herrmann, A. Krabbe, and S. C. Madden[1]
Max-Planck-Institut für extraterrestrische Physik, Garching, Germany

N. Geis, G. J. Stacey[2], and C. H. Townes
University of California, Berkeley, California 94720

L. E. B. Johannson
Onsala Space Observatory, Onsala, Sweden

Abstract. We report maps of the 158 μm [CII] line, the 63 μm and 146 μm [OI] lines, the 2.2 μm Brγ line, and the 2.6 mm CO $(1-0)$ line toward the 30 Doradus complex in the Large Magellanic Cloud. The maps of all tracers emphasize the shell-like structure of the 30 Doradus region which is seen edge-on. The fact that the molecular gas as traced by CO $(1-0)$ and the photodissociated gas as traced by [CII] are co-extensive over tens of parsecs can only be explained by a highly fragmented structure of the interstellar medium which allows UV radiation to penetrate deep into the molecular cloud. Clumpiness is also the key to understanding the extremely high [CII]/CO line intensity ratios.

1. Introduction

The 30 Doradus region in the Large Magellanic Cloud is the most luminous and massive star forming region in the Local Group (Kennicutt 1984); there is no comparable giant HII region in our Galaxy. At a distance of ~50 kpc it is still close enough to allow a detailed, spatially resolved investigation even in the far-infrared. Furthermore, with its low metallicity, it could provide a model case for star formation in the earlier universe.

2. Observations

Observations of the 157.7409 μm [CII] line, the 145.5255 μm [OI] line and the 63.1837 μm [OI] line were carried out on three flight series with the Kuiper Airborne Observatory (KAO) from Christchurch, New Zealand, in March / April

[1]Present address: NASA Ames Research Center, Moffet Field, California

[2]Present address: Cornell University, Ithaca, New York

1991, in March / April 1992, and in March 1993. Full descriptions of our instrument, the MPE/UCB Far-infrared Imaging Fabry-Perot Interferometer (FIFI), are given in Poglitsch et al. (1991) and Geis et al. (1994). The beam sizes are 55″ (FWHM) at 150 μm and 22″ (FWHM) at 63 μm.

[CII] data were taken at 11 different, partly overlapping, partly interleaving array positions, resulting in a $7' \times 7'$ mapped area most of which was fully sampled (1/2 beam spacing). The center velocity was at $v_{LSR} = 250$ km s^{-1}, the bandwidth was 75 km s^{-1} (FWHM). Two frames centered at $(+40'', +100'')$ and $(-60'', -20'')$ from R136, respectively, were taken in the 146 μm [OI] line by scanning a range of 340 km s^{-1} centered at $v_{LSR} = 250$ km s^{-1}, with a 70 km s^{-1} resolution (FWHM). The 63 μm [OI] data were taken toward 5 different positions around $(+40'', +100'')$ with respect to R136, with a 65 km s^{-1} bandwidth (FWHM). We mapped an area of $3' \times 3'$. The central $1' \times 1'$ was sampled at 0.7 beam spacing and the rest of the map with full beam spacing.

The CO(1→0) observations were carried out at the Swedish-ESO Submillimeter Telescope (SEST). This radio telescope is located at La Silla (Chile) and has a 43″ (FWHM) beam size at the CO(1→0) wavelength. The 2.1655 μm HI Brγ line was observed from the 2.2 m ESO-MPIA telescope at La Silla with our imaging NIR-spectrometer FAST in January 1990. The instrument is described in detail in Krabbe et al. (1993). The spectrometer employs a 62×58 pixel InSb direct read-out array from Santa Barbara Research Corporation. The focal plane scale is 0.8″/pixel. We observed the Brγ line toward 27 positions, with a resulting mapped area of approximately $3' \times 3'$ around R136.

3. Results

3.1. Brγ

The Brγ image of the 30Dor region is shown in Fig. 1. The Brγ emission forms a shell-like structure around the ionizing cluster with R136 at its center. The peak integrated line intensity is 7.0×10^{-4} erg s^{-1}cm^{-2}sr^{-1}, and the total flux from the mapped area is 5.0×10^{-10} erg s^{-1}cm^{-2}. At an assumed distance of 50 kpc (Feast 1991), this corresponds to a luminosity of 3.74×10^3 $L_\odot$ in the Brγ line.

Assuming case B recombination in a "standard" HII region and neglecting extinction, we can derive the (minimum) rate of Lyman continuum (Lyc) photons required to ionize the mapped region. The lower limit on the Lyc photon rate required to produce the observed Brγ luminosity is then estimated to be 1.1×10^{51} s^{-1}. This number may be compared with the result of $\sim4.5\times10^{51}$ s^{-1} Lyc photons from a spectroscopic analysis of the stars in the 30Dor cluster over a region of $\sim 3'$ diameter (Walborn 1991). In a similar way the Brγ line intensity, $I_{Br\gamma}$, can be translated into a Lyc intensity, I_{Lyc}. Averaged over a $15'' \times 15''$ region around the peak position north of R136 we have a Brγ intensity of 3.5×10^{-4} erg s^{-1}cm^{-2}sr^{-1}, from which we derive a Lyc intensity of 0.7 erg s^{-1}cm^{-2}sr^{-1}.

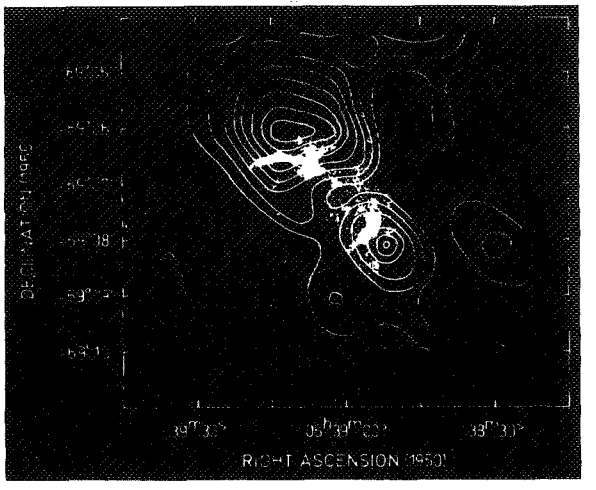

Figure 1. Brγ image of 30Dor. Superposed in white: contour map of the CO(1–0) integrated line intensity, contour interval 1 K km/s.

3.2. CO(1→0)

The map of the integrated CO(1→0) line intensity is shown in Fig. 1 as white contour lines superposed on the Brγ image. Taking into account the different angular resolutions, the CO and Brγ maps show similar shell-like structures, with two peaks to the north-east and south-west of R136, respectively. These peaks, while being close to the brightest filaments in the Brγ map, are consistently offset toward larger radial distances from R136. The CO(1→0) line is commonly used as a tracer of (cold) molecular gas in both Galactic and extragalactic sources. The conversion factor $X = N_{H_2}/I_{CO}$, however, depends on the detailed physical parameters and on the metallicity of the ISM and is a subject of discussion. Cohen et al. (1988) have done a large-scale CO(1→0) survey of the LMC. They find that the CO luminosity, L_{CO}, as a function of velocity spread, Δv, is similar to the Galactic relation, only a factor of about 6 lower. Using the virial argument, one can then conclude that the H_2/CO conversion factor should be a factor of six higher than the canonical conversion factor $X = 2.3\times10^{20}$ cm^{-2} / K km s^{-1} (Strong et al. 1988). With this modified conversion factor, we derive a H_2 column density $N(H_2)=1.2\times10^{22}$ cm^{-2} toward the NE peak, and the total molecular mass within the mapped area is 9×10^4 $M_\odot$.

3.3. [CII]

The map of the integrated [CII] line intensity is shown in Fig. 2 superposed on our CO(1→0) map. There is a very strong spatial correlation between the two maps: both CO and [CII] peaks are perfectly aligned with each other, and the ratios of the SW peak to the NE peak integrated line intensities are almost identical. We find a maximum line intensity of 1×10^{-3} erg s^{-1}cm^{-2}sr^{-1} toward the NE peak; the total luminosity of the [CII] line within the mapped area is 6.5×10^4 $L_\odot$. Both maps also show a protrusion toward the NW. The [CII]

C-3.

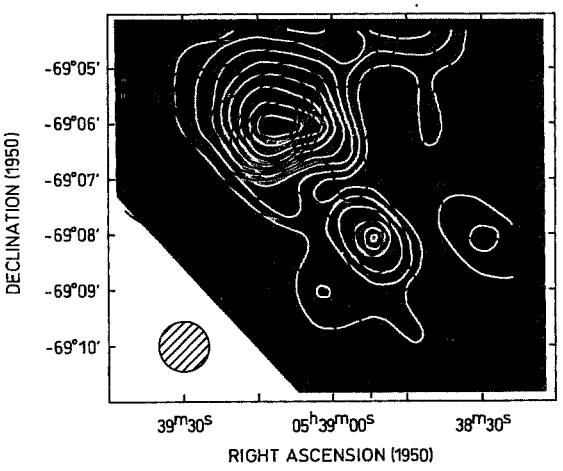

Figure 2. Contour map of the [CII] integrated line intensity (black) superposed on the CO(1–0) map (white). Contour interval: 10^{-4} erg $s^{-1}cm^{-2}sr^{-1}$

emission is expected to arise from interface layers between the fully ionized gas and the molecular gas. The [CII] emission from such photodissociation regions (PDRs) can be expected to be optically thin (Stacey et al. 1991b). In this case the integrated line intensity, $I_{[CII]}$, is a direct measure of the hydrogen column density, N_H, contained in the PDR (Crawford et al. 1985). If we assume that the carbon abundance in the LMC is a factor of 3.6 smaller than in the Galaxy (Dufour 1984), we derive a minimum column density of hydrogen nuclei $N_H = 7.5\times10^{21}$ cm^{-2}, more than half the column density of the molecular gas derived above from CO(1→0). Integrated over the mapped area we find a minimum hydrogen mass of 3.7×10^4 $M_\odot$ contained in a PDR environment. Unless the N_H/I_{CO} conversion factor that we have used still underestimates the amount of hydrogen greatly, we can conclude that the PDR extends over most of the interstellar gas. The apparent coexistence of molecular and photodissociated gas over distances ~30 pc demonstrates a deep penetration of the UV radiation into the molecular cloud, indicating that the ISM must be highly clumped.

3.4. [OI] 146 μm

The emission spectrum of the [OI] 146 μm line was only strong enough for quantitative evaluation toward the NE peak in the [CII] emission. In order to determine the line intensity and the continuum level we fitted the observed spectrum with a model line shape plus a baseline. The continuum level agrees well with the the results of Werner et al. (1978). The derived integrated intensity in the [OI] line is $8.4\pm0.6\times10^{-5}$ erg $s^{-1}cm^{-2}sr^{-1}$.

3.5. [OI] 63 μm

The map of the [OI] 63 μm integrated line intensity is shown in Fig. 3 superposed on the [CII] map. The spatial resolution in the inner square, centered on the NE

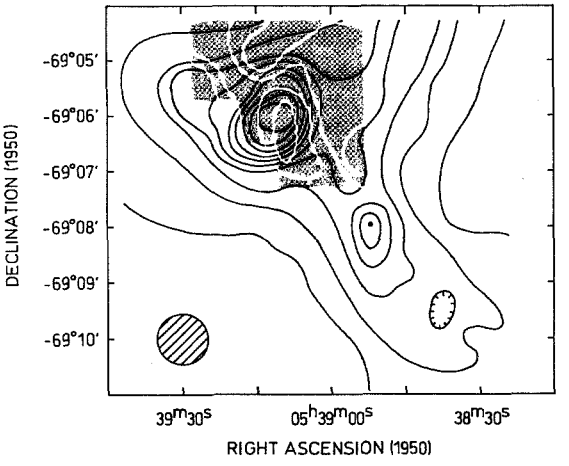

Figure 3. Contour map of the 63 μm [OI] integrated line intensity (white) superposed on the [CII] map (black). Contour interval: 1.5×10^{-4} erg $s^{-1}cm^{-2}sr^{-1}$

CO(1→0) peak is 21″; in the outer parts of the map we convolved the data to a 40″ beam size in order to obtain a uniform noise level over the full map. We find a peak integrated line intensity $6.1\pm0.8\times10^{-4}$ erg $s^{-1}cm^{-2}sr^{-1}$. Besides the main peak, we find emission extended in the NE/SW direction and a tongue of emission toward the NW which appears to be the beginning of the protrusion seen in the CO(1→0) and [CII] maps.

4. Comparison of different tracers and physical parameters

4.1. Source morphology

The maps of the different tracers emphasize the shell-like structure of the 30Dor region and an edge-on perspective. The tracers of the ionized gas (Hα, Brγ) peak at the smallest projected radii from the central source R136. The FIR continuum (Werner et al. 1978), which traces the FUV at wavelengths longward of the Lyc, peaks at slightly greater radii. The other tracers that are excited by the FUV ([CII], [OI]) show an interesting peculiarity: The peaks in the [CII] emission and the 63 μm [OI] emission show a small, but significant offset. While the 63 μm [OI] line is perfectly correlated with the FIR peak, the [CII] emission peaks at a somewhat larger radius yet, possibly reflecting a gradient in the FUV field and in the temperature. The thermal dust emission in the FIR is a linear function of the FUV intensity, whereas the [CII] line intensity saturates at higher FUV intensities. The [CII] peak will therefore represent mainly a peak in column density of photodissociated gas. This conclusion is also supported by the perfect correlation of the [CII] map with the CO(1→0) map, which also mainly traces the column density of molecular gas. The fact that the molecular and the photodissociated gas appear coextensive over tens of parsecs may be an indicator

of a highly clumped state of the ISM. The 63 μm [OI] line, on the other hand, requires a higher excitation temperature than the [CII] line and it is expected to be optically thick at typical PDR column densities. Both conditions, therefore, favor high temperatures over high column densities. This could explain why the [OI] line peaks at a smaller radial distance from the source of excitation.

4.2. Brγ / Hα / Hβ line intensities

We compare our Brγ data with the Hα and Hβ photometry results of Caplan & Deharveng (1986) and their analysis in terms of reddening and extinction. They found an Hα line flux of 4.0×10^{-9} erg s^{-1}cm^{-2} and a ratio Hα/Hβ = 4.57. They derive extinctions A_β=2.1 and A_α=1.6 by referring their Hα and Hβ intensities to the 6 cm (thermal) radio continuum measured in the same area. These values are higher than expected from the color excess $E_{\beta-\alpha} = 0.51$ for the case of absorption by a uniform interstellar medium. Caplan & Deharveng discuss the higher extinction (or reduced reddening) in terms of several models (clumped ISM, scattering slab close to the source).

However, both Hα, Hβ and our Brγ measurement are in perfect agreement with "normal" reddening by a homogeneous ISM, indicating a possible error with the separation of the thermal and non-thermal radio continuum in the earlier analysis. We then derive an extinction $A_\gamma \sim 0.1$ corresponding to a correction factor of 1.1 for the Brγ intensity and hence for the derived Lyc luminosity.

4.3. Brγ / FIR continuum

Interstellar dust is the main absorption medium for the far-ultraviolet continuum and the visible light that can emerge from HII regions. The absorbed energy is reradiated in the far-infrared (FIR); the FIR continuum is therefore a direct measure for the FUV radiation field. Lyc radiation is only a minor heating source for the bulk of the dust because of its strong absorption by hydrogen and helium.

From the census of the stars composing the 30Dor cluster (Walborn 1991), we estimate that we can use the spectral distribution of an O5.5 star as typical for the radiation field. In this case 54% of the total stellar luminosity is emitted as Lyc, with an average photon energy of 23.5 eV, the rest mainly as FUV radiation (Panagia 1973). From the Brγ intensity averaged over the FIR beam, $I_{Br\gamma} = 3.5\times10^{-4}$ erg s^{-1}cm^{-2}sr^{-1}, we derive a Lyc intensity I_{Lyc}=1.0 erg s^{-1}cm^{-2}sr^{-1}. For an O5.5 spectral distribution, the corresponding FUV intensity emerging from the HII region is then 0.85 erg s^{-1}cm^{-2}sr^{-1} or 4300 χ_0, where χ_0 is the local interstellar UV field. The distance from R136 to the main FIR peak, r_{FIR}, is $\sim$ 1.1 to 1.2 $r_{Br\gamma}$, where $r_{Br\gamma}$ is the radius of the brightest Brγ filament. Thus the FUV intensity, as determined by purely geometrical dilution, is estimated to be I_{FUV} = 3100 to 3600 χ_0. This number agrees with the integrated FIR continuum of Werner et al. (1978), who find I_{FUV} = 3500 χ_0. This further supports the lower value for the Brγ extinction that we derived from Hα, Hβ and Brγ as compared to the higher value that would follow from the analysis by Caplan & Deharveng (1986).

4.4. [CII] / [OI] / CO / FIR

The most complete data set in the FIR tracers is available toward the NE peak in the [CII] and CO emission; this position will therefore be analyzed further. We only present the main results of this analysis; the details will be given elsewhere (Poglitsch et al. 1994). Assuming that the [CII] line and both [OI] lines arise from the same component of the ISM, one can use the relative and absolute intensities of these lines to derive a representative temperature, T, hydrogen density, n_H, and column density, N, of the emitting gas. We assumed a relative abundance ratio of oxygen to carbon of $X_O/X_C = 2$.

We derive a range of temperatures T = 200 to 100 K for densities n = 10^3 to 10^4 cm^{-3}. This agrees well with the physical parameters found in Galactic PDRs. Similarly, the ratio of the [CII] line intensity to the FIR continuum, $Y_{[CII]} = I_{[CII]}/I_{FIR} = 1.4\times10^{-3}$ toward the NE peak, is in a range typical for Galactic star formation regions and nuclei of starburst galaxies (Stacey et al. 1991a).

The ratio $Y_{CO} = I_{[CII]}/I_{CO} = 6.9\times10^4$, however, is almost an order of magnitude higher than in Galactic star formation regions or external galactic nuclei. One-dimensional, semi-infinite PDR models cannot explain this result (Wolfire, Hollenbach & Tielens 1989).

A possible explanation could be a different geometry, leading to different beam filling factors for different tracers of the ISM. This situation could exist in an inhomogeneous medium with most of the gas being contained in denser clumps which are embedded in a low-density medium. We assume that both the FIR, [CII] and CO(1→0) emission arise from these clumps. Depending on the clump size distribution, the illumination (omnidirectional / unilateral), and the metallicity, a certain fraction of the volume will be contained in PDRs. For comparison with the one-dimensional, semi-infinite model (Wolfire et al. 1989), one can define a relative beam filling factor Φ_{PDR}/Φ_0 as the ratio of the power emitted from the clump to the power emitted from the semi-infinite medium over a surface area equal to the projected surface area of the clump.

Similarly, for the CO(1→0) line, one can define a relative beam filling factor Φ_{CO}/Φ_0, as the ratio of the projected surface area of the CO bearing part of the clump to the (total) projected surface area of the clump. Knowledge of the physical conditions in the PDR allows one to predict the ratio Y_{CO} expected for the one-dimensional case. Assuming that, except for the geometry / beam-filling factor, the physical parameters remain unchanged as compared to the one-dimensional model, we find a ratio $\Phi_{CO}/\Phi_{PDR} = Y_{CO}^{(meas)}/Y_{CO}^{(pred)} \sim 0.1$ for the 30Dor NE peak.

4.5. Determination of clump size

For the physical conditions that we find, PDR models predict a C^+ column density of 2×10^{18} cm^{-2} in a PDR front. For a relative carbon abundance of 1/3.6 of the solar value, this is equivalent to a hydrogen (nuclei) column density of 2.4×10^{22} cm^{-2}. Since the hydrogen molecule is strongly self-shielding, a major fraction of the hydrogen is expected to be in molecular form (Maloney & Black 1988). The total column density of hydrogen, $N_H + N_{H_2}$, can therefore be estimated to be $N_{tot} \sim 1.4 \times 10^{22}$ cm^{-2}. With the beam filling factor ratio Φ_{CO}/Φ_{PDR} from above and the simplifying assumption that the clumps all have

the same size and the same [CII] emitting column density N_{tot} in their PDRs, one can derive their diameter (Poglitsch et al. 1994). For a nominal density of n = 6800 cm^{-3}, the clump diameter is D = 0.8 pc with a hydrogen mass of M = 87 $M_\odot$. Clump sizes on that scale are directly observed in our Galaxy; our observations show that the ISM in the low-metallicity environment of an irregular galaxy is structured / fragmented in a similar way.

It should be pointed out, however, that this number may only be understood as a characteristic size scale; a much more realistic assumption would be a distribution of clump sizes. In the smaller clumps the CO would be completely photodissociated, whereas the larger clumps would contribute the observed (beam-averaged) CO line intensity.

References

Caplan, J. & Deharveng, L. 1986, A&A, 155, 297

Cohen, R.S., Dame, T.M., Garay, G., Montani, J., Rubio, M., & Thaddeus, P. 1988, ApJ, 331, 95

Crawford, M.K., Genzel, R., Townes, C.H., & Watson, D.M. 1985, ApJ, 291, 755

Dufour, R.J. 1984, in IAU Symp. 108, Structure and Evolution of the Magellanic Clouds, eds. S. van den Bergh & K.S. de Boer, (Dordrecht: Kluwer) p. 353

Feast, W.M. 1991, in IAU Symp. 148, The Magellanic Clouds, eds. R. Haynes & D. Milne, (Dordrecht: Kluwer) p. 1

Geis, N., Genzel, R., Haggerty, M., Herrmann, F., Jackson, J., Madden, S.C., Nikola, T., Poglitsch, A., Rumitz, M., Stacey, G.J., Timmermann, R., & Townes, C.H. 1994, in Proc. of the Airborne Astronomy Symp. on the Galactic Ecosystem: From Gas to Stars to Dust, eds. M.R. Haas, J.A. Davidson, & E.F. Erickson, (San Francisco: ASP) paper 708

Kennicutt, R.C. 1984, ApJ, 287, 116

Krabbe, A., Rotaciuc, V., Storey, J.W.V., Cameron, M., Blietz, M., Drapatz, S., Hofmann, R., Sämann, G., & Genzel, R. 1993, PASP, 105, 1472

Maloney, P. & Black, J.H. 1988, ApJ, 325, 389

Panagia, N. 1973, ApJ, 78, 929

Poglitsch, A., Beeman, J.W., Geis, N., Genzel, R., Haggerty, M., Haller, E.E., Jackson, J., Rumitz, M., Stacey, G.J., & Townes, C.H. 1991, Int. J. IR Millimeter Waves, 12, 895

Poglitsch, A. et al. 1994, in preparation

Stacey, G.J., Geis, N., Genzel, R., Lugten, J.B., Poglitsch, A., Sternberg, A., & Townes, C.H. 1991a, ApJ, 373, 423

Stacey, G.J., Townes, C.H., Poglitsch, A., Madden, S.C., Jackson, J., Herrmann, F., Genzel, R., & Geis, N. 1991b, ApJ, 382, L37

Strong, A.W., Bloemen, J.B.G.M., Dame, T.M., Grenier, I.A., Hermsen, W., Lebrun, F., Nyman, L.A., Pollok, A.M.T., & Thaddeus, P. 1988, A&A, 207, 1

Walborn, N.R. 1991 in IAU Symp. 148, The Magellanic Clouds, eds. R. Haynes & D. Milne, (Dordrecht: Kluwer) p. 145

Werner, M.W., Becklin, E.E., Gatley, I., Ellis, M.J., Hyland, A.R., Robinson, G., & Thomas, J.A. 1978, MNRAS, 184, 365

Wolfire, M., Hollenbach, D., & Tielens, A.G.G.M. 1989, ApJ, 344, 770

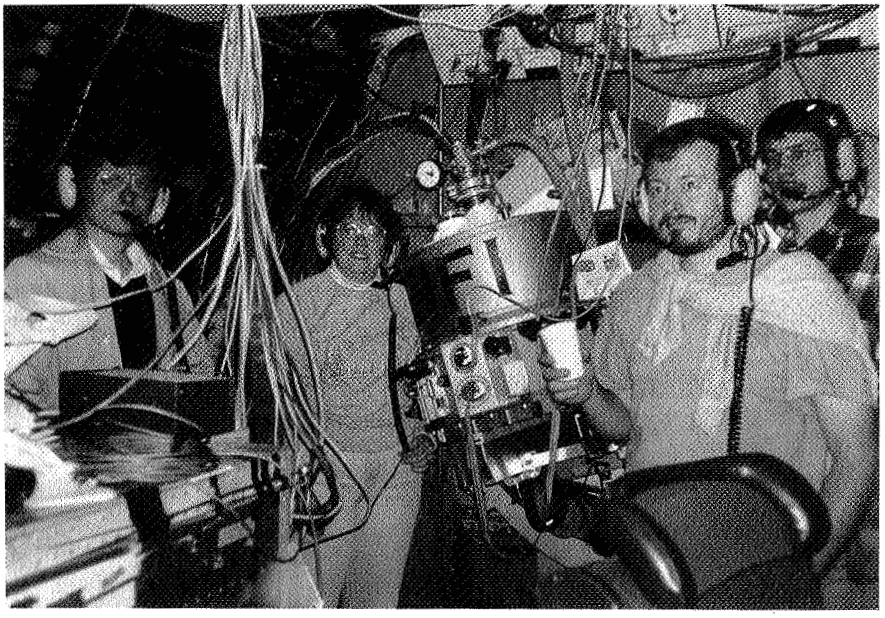

Albrecht Poglitsch, Edna DeVore, Norbert Geis, Thomas Nikola

Diane Wooden

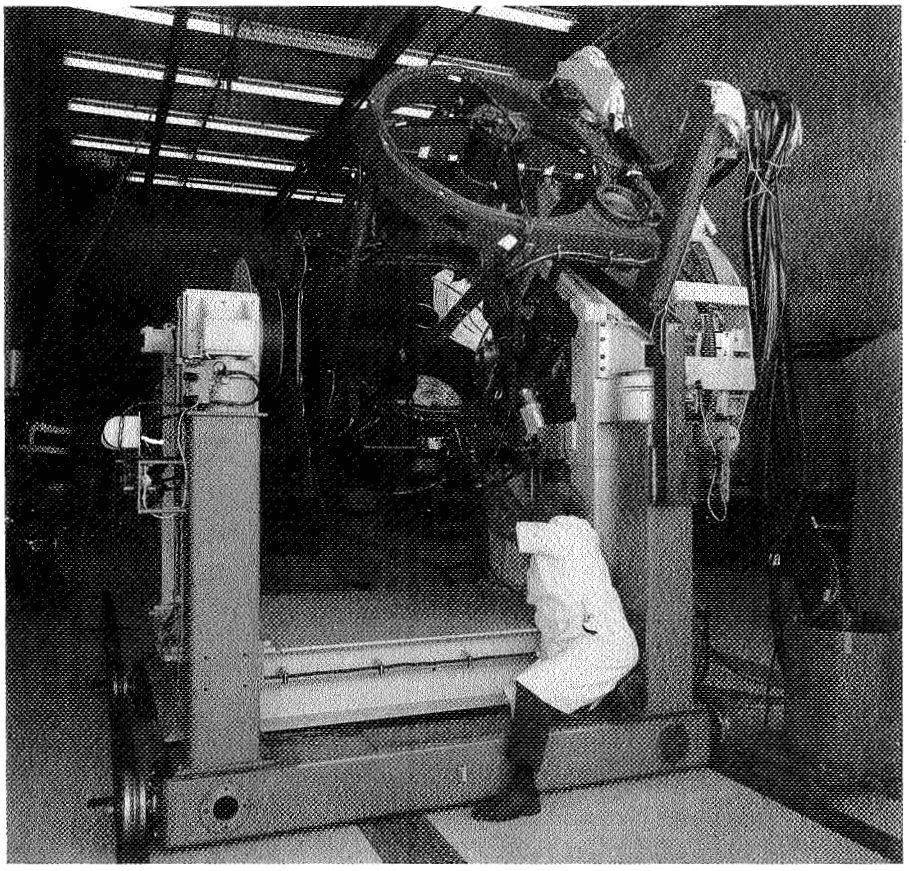

The KAO Telescope before installation, Bob Krouse (1972)

Airborne Astronomy Symposium on the Galactic Ecosystem
ASP Conference Series, Vol. 73, 1995
M.R. Haas, J.A. Davidson, and E.F. Erickson (eds.)

A Far-Infrared Spectral Line Survey of 23 Infrared-Bright Galaxy Nuclei

Steven D. Lord[1], David J. Hollenbach[2], Sean W. J. Colgan[3,4], Michael R. Haas[3], Robert H. Rubin[3,5], Suzanne C. Madden[3], Thomas Y. Steiman-Cameron[2,6], Patricia Carral[7], Philip R. Maloney[8], Edwin F. Erickson[3]

[1]*MS 100-22, IPAC/Caltech, Pasadena, CA 91125*
[2]*MS 245-3, NASA-Ames Research Center, Moffett Field, CA 94035-1000*
[3]*MS 245-6, NASA-Ames Research Center, Moffett Field, CA 94035-1000*
[4]*SETI Institute, 2035 Landings Drive, Mountain View, CA 94043*
[5]*Orion Enterprises, 2135 Woodleaf Way, Mountain View, CA 94040*
[6]*University of California, Berkeley, CA 94720*
[7]*Universidad de Guanajuato, Guanajuato, Mexico*
[8]*JILA, University of Colorado, Boulder, CO 80309-0440*

Abstract. We present results from a KAO survey of fine-structure lines observed in 23 infrared-luminous galaxies. One or more of the following lines was observed and/or detected in each galaxy: [S III] 19, 33 μm, [Ne V] 24 μm, [O IV] 26 μm, [Fe II] 26 μm, [Si II] 35 μm, [O III] 52, 88 μm, [O I] 63, 146 μm, [N III] 57 μm, [N II] 122, 205 μm, [C II] 158 μm. The galaxies span a wide range of morphologies (irregular to grand design), have varying metallicities, and include mergers, AGNs, and starburst systems. The observations were made beginning in 1988 using the facility Cryogenic Grating Spectrometer onboard the KAO at a typical resolution of ~60–140 km/s and with a 30–44″ beam. We interpret the [C II] and [O I] fluxes, along with previous measurements of the IR continuum fluxes, in the context of photodissociation region (PDR) models (Tielens & Hollenbach 1985; Wolfire et al. 1990). With these models, we obtain estimates of the typical interstellar UV fields incident on the line emitting regions (10^2–10^4 times the local interstellar radiation field) and the total masses (10^7–10^8 $M_\odot$), densities (10^3–10^4 cm^{-3}), and temperatures (100–250 K) of the warm atomic gas. The [O III] (52/88) and [S III] (33/19) line flux ratios constrain the range of electron densities and pressures found within the ionized regions. The [O III] and [S III] lines also provide estimates of the effective temperature of the ionizing stars and elemental abundances within the ionized regions of these galactic nuclei. Our measurements imply typical gas pressures of nT~ 5×10^6 cm^{-3}K and typical upper mass cutoffs of 25–35 $M_\odot$. The low-metallicity systems show high [C II]/CO and [O I]/CO flux ratios, 3–5 times the Milky Way value, indicating that they contain a larger fraction of photodissociated gas relative to the molecular material.

1. Introduction

The determination of physical parameters in the interstellar medium of galactic nuclei is made possible through far-infrared (FIR) spectroscopy. Observations at other wavelengths alone cannot adequately probe these heavily-obscured regions: optical lines are usually so heavily reddened that large extinction corrections make interpretation difficult; radio continuum observations of the ionized gas are often contaminated by a significant nonthermal component; and millimeter observations of molecular emission probe only the relatively cold gas component. However, FIR fine-structure lines are relatively unaffected by extinction and insensitive to the electron temperature, T_e. In combination with the diagnostics at other wavelengths, FIR lines enable us to accurately determine the physical state (composition, density, temperature) of the neutral and ionized gas components. Furthermore, we can indirectly infer sources of excitation, be they thermal (stellar) radiation, shocks, or illumination by a nonthermal (AGN) UV field. We have undertaken a survey of 23 IR-bright galaxies using FIR spectroscopy to characterize these components of the ISM in the nuclear regions.

2. Photodissociation Regions

Photodissociation Regions (PDRs) consist of neutral gas illuminated by 6–13.6 eV photons. PDRs are often the interfaces between H II regions and their parent molecular clouds (Tielens & Hollenbach 1985). In PDRs, the ratio of the ([O I]+[C II]) intensities (the prime gas coolants) to the FIR continuum luminosity (the grain cooling) provides a measure of the heating efficiency of the grains by UV-photoejected electrons. Since the cooling efficiency decreases with increasing positive charge on the grains, the efficiency depends on the ratio of the incident FUV flux, G_0, and the gas density, n. This efficiency is expected to be between 0.1% and 1.0% when the dominant excitation source is a thermal UV spectrum from massive stars. A complementary probe is the [C II]/[O I] ratio, which depends of n and T_a, the temperature of the atomic gas. T_a is specified if n and G_0 are known, so the two ratios taken together (as prescribed by Wolfire et al. (1990) give n, T_a, and the UV field. Also, by assuming a C/H ratio, the [C II] 158 μm luminosity gives us a measure of the total atomic gas mass.

Our theoretical models assume that the galaxy nuclei are populated with an ensemble of molecular clouds surrounded by a warm atomic PDR layer. In this context we use the derived UV flux, atomic gas density and mass, together with the molecular mass estimated from CO J=1-0 observations, to obtain several additional cloud properties (Wolfire et al. 1990; Carral et al. 1994): the number of clouds N within our aperture, their average radius r_{cl} and temperature T_a, and their volume ϕ_v and area ϕ_a filling factors.

3. Low Metallicity Systems

As part of our program, we are conducting a study of metal-poor and dwarf galaxies. CO J=1-0 has been detected in only a handful of such systems and the relative paucity of CO emission has been interpreted as a low molecular gas column or else the effects of selective destruction of CO. Maloney & Black

(1988) modeled individual metal-poor clouds and found that low metallicity can strongly lower the CO-to-H_2 ratio. Clouds with low abundances have less dust to attenuate UV radiation and so have reduced CO cores surrounded by larger than normal photodissociation regions. In our study we measure the emission from the dissociation products C^+ and O^o directly. Elevated [C II]/CO and [O I]/CO ratios in low metal systems serve to verify and constrain the models. We have observed three such systems in this program, NGC 4449, NGC1569, and IC 10.

4. Ionized Regions

The ionized component of the ISM in starburst galaxies is assumed to consist of a number of identical, ensemble-averaged H II regions. Our H II region models are presented in detail in Rubin (1985), Rubin et al. (1994), and Carral et al. (1994). The electron density is derived in these regions from the ratio of two [O III] lines, two [S III] lines, or two [N II] lines. The H II region pressure follows assuming T_e=8000 K. In most cases the average pressure of the H II regions is found to be similar to the average pressure of the PDRs. Likewise, the line profiles from the ionized and PDR species are typically found to be similar. When such correspondence is noted, it suggests that the H II regions and PDRs coexist in pressure equilibrium, with the H II regions perhaps forming photoevaporating blisters on neutral cloud surfaces.

In our studies, the volume filling factor and the ionized mass come from knowledge of the density and the volume emission measure, the latter derived from the thermal radio continuum or hydrogen recombination emission. The characteristic effective temperature T_{eff} of the UV source is determined from the [S III]/[O III] ratio (assuming a solar elemental S/O abundance ratio) and/or from the abundance-independent [N II]/[N III] ratio, although one or more of these last two lines are often too weak to measure. The sulfur and oxygen abundances are derived from the ratios of [S III] and [O III] to the radio continuum or hydrogen recombination line emission. Unlike oxygen, sulfur is largely doubly ionized over a broad range of T_{eff}, so that its derived abundance is insensitive to T_{eff}. An estimate of the number of exciting stars is made by comparing the total ionizing luminosity of the nucleus with the ionizing luminosity of a single star at the derived T_{eff}. For these studies, we use the model stellar atmospheres (with $\log q = 4$) of Kurucz (1979).

5. Active Galactic Nuclei

Direct measurements of AGNs indicate that the central engines emit a very hard spectrum in the UV to X-ray, with a significant fraction of photons more energetic than 54.4 eV (as distinguished from O stars which have negligible flux beyond the He^+ ionization edge). In their narrow line regions, AGNs excite highly ionized species such as O^{+3} and Ne^{+4}. Transitions such as [O IV] 26 μm and [Ne V] 24 μm in the FIR are now included as part of detailed AGN photoionization codes (e.g., Spinoglio & Malkan 1992). Our recent efforts have included a study of several AGNs and Seyferts, including the Seyfert 1 galaxy

NGC 4151, looking for these distinctive AGN "signpost" transitions.

6. Sample Selection

The galaxy sample was selected primarily on the basis of central FIR intensity. The IRAS Cataloged Galaxies and Quasars (Lonsdale et al. 1989) were searched and the brightest IR galaxy nuclei were identified. The search yielded a candidate list of 59 sources with F(60 μm)>20 Jy, with 20 of these sources having F(60 μm)>50 Jy. All but two of the galaxies in our sample of 23 are chosen from the candidate list with 15 of these surpassing the 50 Jy level. Thus we have observed 3/4 of the brightest (at 60 μm) 20 galaxy nuclei in the sky. It is worthwhile to note that while the [O I] 63 μm transition is an important diagnostic line for our program, it is totally absorbed by telluric water vapor in about half of the sources: those galaxies with systemic velocities between 400 and 1400 km/s. Our multi-wavelength survey of galaxy nuclei complements other FIR spectroscopic studies (e.g., Stacey et al. 1991; Madden et al. 1994) which concentrate on mapping the extended [C II] 158 μm component in galaxies.

Our sample includes small subgroupings of different morphological types. These groups have been the subject of separate studies within our program: starbursts (e.g., M82, NGC 253, Arp 299); late-stage mergers (e.g., NGC 2146, Cen A, NGC 3256); AGNs (e.g., NGC 4151, NGC 1068, Cen A); "normal" galaxies (e.g., IC 342, NGC 6946, M83); and metal-poor irregulars (e.g., IC 10, NGC 4449). There is clearly significant overlap between the subgroups. Table 1 lists the sample, giving a morphological type taken from the Hubble Atlas or the RC3 and a comment regarding a salient attribute of each galaxy. Galaxies such as NGC 1068 and those with concentrated FIR nuclei usually show evidence of both starburst and AGN activity, with both components conceivably contributing characteristic FIR lines. We have geared our recent observations toward studying the AGN/starburst connection.

7. Observations

The observations were made starting in January 1988 using the facility Cryogenic Grating Spectrometer (CGS) on the 91.4 cm telescope of the KAO. The CGS instrument is discussed in detail by Erickson et al. (1985). The velocity resolution of the observations ranges typically between 60 and 140 km/s depending on the particular instrument configuration used. For a few lines, a low resolution grating (constructed for SN1987A observations) was used, yielding unresolved lines for our program objects. Guiding was accomplished using either nearby bright stars or direct guiding on the galaxy image, with resulting errors typically less than 5″. The beamsize (30″ to 44″ FWHM) was selected so as to include the bright near-infrared emission centers of each galaxy. For Arp 220 and NGC 2146, the Doppler-broadened line is wider than the total spectral bandpass of the CGS, so more than one echelle position (passband) was used to observe the entire line and nearby continuum.

Table 1. FIR Line Survey of Galaxy Nuclei

Galaxy	Type, Comment	Lines Detected	Upper Limits
IC 10	Ibm, Low Metal	[O I], [C II]	—
NGC 253	Sc,Starburst	[Si II], [O III] 52, 88, [C II]	[S III] 33, [N III]
Maffei II	Sbc,Mild Starburst	[O I]	[Si II]
NGC 1068	Sb,AGN, Starburst	[S III] 19, [Si II],	[Ne V], [O IV]
		[O III] 52, 88, [N II] 205	—
IC 342	SAB(rc)cd,Starburst	[Si II], [O I]	[O III] 88
NGC 1569	Im, Low Metal	[O I], [C II]×2	—
NGC 2146	SB(s)ab,Merger	[S III] 33, [Si II],	—
		[O III] 52, 88, [C II]	—
M82	Irr,Starburst	[Fe II], [S III] 33×5, [Si II]×3,	[Fe III], [Ne V],
		[O I]×3, [N II] 122, 205, [C II]	[S I], [O IV]
NGC 3256	SB(s)m,Merger	[Si II], [O I], [O III] 88, [C II]×4	[Si II], [O III] 52
Arp 299	Interacting	[Si II], [O III] 52, 88, [O I]	[S III] 33, [N III]
NGC 4151	Seyfert 1	[Ne V]	[O IV], [O III] 88
NGC 4449	Irr I, Low Metal	[C II]×2	—
NGC 4945	SA(s)d,AGN?	[O III] 88, [C II]×3, [N II] 205	[Si II]
Cent A	E0+Sb,AGN,Starburst	[Si II], [C II]×4	[S III] 19
M51	Sc,AGN, Interacting	—	[S III] 19, [Ne V]
M83	SBb,Mild Starburst	[S III] 19, 33, [Si II],	[S III] 33
		[O III] 52, 88, [C II]	—
Circinus	SB(s)cd,Starburst	[Si II], [O III] 88, [C II]×3	[O III] 52, [O I] 146
Arp220	Irr,AGN, Starburst?	—	[O III] 52, [O I]
Arp 293	Interacting	[O I]	—
NGC 6240	Irr,Shocks	[O I], [C II]	—
NGC 6946	Scd,Starburst	[Si II], [O I]	—
NGC 7469	SAB(rs)a,Seyfert	[O III] 52	—
NGC 7552	SB(s)a,IR-Luminous	[C II]	[O I]

Raw galaxy spectra were corrected for absorption by atmospheric water vapor, responsivity differences between the different detectors, and the wavelength dependence of the instrument's filter and grating efficiencies. Absolute flux calibration was accomplished through observations of the spectrum of a bright calibrator, such as Jupiter. Results of our observations and further details of the data reduction and analysis are given for NGC 253 and NGC 3256 in Carral et al. (1994) and for M82 in Lord et al. (1995b). Results (as well as spectra) for the entire survey will appear in Lord et al. (1995a).

8. Results and Conclusions

In Table 1 we list the detections and nondetections for our sample. Where there is ambiguity about which line was observed, the wavelength in μm is given. Multi-point observations are designated as "×3", etc. This list includes eight [O I] 63 μm detections, nine [Si II] 35 μm detections (each of comparable strength to [C II] and [O I] in these galaxies) and the first detection of [Fe II] 26 μm beyond the Milky Way system (M82). The [N II] 205 μm detections in NGC 1068 and M82 were made in collaboration with S. Petuchowski (Petuchowski et al. 1994).

We have modeled many of these galaxies to obtain average physical parameters of the ISM in the central $\sim 40''$, with results for selected sources given in Table 2.

Table 2. Derived Astrophysical Quantities[a]

Galaxy	n (cm^{-3})	T_a (K)	G_0	M_a ($M_\odot$)	ϕ_a	ϕ_v	N	r_{cl} (pc)	n_e (cm^{-3})
NGC 253	6×10^3	250	5×10^4	10^7	0.8	5×10^{-3}	2×10^4	0.8	430
Maffei 2	6×10^3	240	10^3	9×10^6	0.05	4×10^{-3}	6	36	–
IC 342	10^4	100	10^2	2×10^7	2	10^{-4}	10^8	0.1	–
Arp 299	3×10^3	200	10^3	6×10^8	0.1	10^{-6}	6×10^8	0.2	600
M82	10^4	210	10^3	3×10^7	0.4	7×10^{-3}	10^6	0.3	190
NGC 3256	2×10^4	150	3×10^3	3×10^7	–	3×10^{-4}	4×10^5	1.8	–
NGC 6946	10^4	200	10^3	1×10^7	0.1	3×10^{-5}	10^6	1.0	–

[a] Global parameters for gas clouds in a $\sim 1'$ beam. n is gas density, T_a is the temperature of warm atomic component, G_0 is the incident FUV flux in units of the average Milky Way interstellar radiation field, M_a is the mass of the warm atomic gas, ϕ_a is the area filling factor of the warm atomic component, ϕ_v is the volume filling factor of neutral clouds, N is the number of clouds, r_{cl} is the radius of a typical cloud, and n_e is the electron density in the ionized component.

We see that the regions are in general populated by small ($r_{cl} \sim 0.1$–1.0 pc), warm ($T_a \sim 200$ K), dense ($n \sim 10^3$–10^4) cm^{-3} cloud "building blocks," each illuminated by a UV field 10^2–10^4 times the average Milky Way field. We find that clouds exist in pressure equilibrium with the ionized gas, with typical PDR and H II region pressures of $\sim 5 \times 10^6$ $cm^{-3}K$. We have also derived T_{eff} estimates for the galaxies M82, M83, NGC 2146, and NGC 1068 and, assuming an ensemble of star-centered H II regions, find values in the range 35,000–37,000 K, which corresponds to an O6-O8 ZAMS star. This stellar type ($M \sim 25$–35 $M_\odot$; Van Buren 1983) may represent the upper limit to the IMF in these galaxies, assuming that the most massive stars dominate the excitation and have not yet evolved off the main sequence.

For M82, the brightest IR galaxy, we have used the [O III], [N II] line pairs, the [N II]/[N III] ratio, and the assumption of Orion-like elemental abundances to model the central H II regions. Figure 1 shows the observed line fluxes with 1σ error bars, and the model fluxes. The agreement is seen to be generally good, with a few exceptions. The observed [C II] flux is much greater than the H II region model value due to a large PDR contribution expected from starburst nuclei (Carral et al. 1994). The [Si II] flux may have a PDR contribution as well, but may also be largely due to gas-phase enrichment of silicon in H II regions and PDRs, caused by the partial destruction of silicate grains by fast supernovae-driven shocks (Lord et al. 1995a). At the short wavelengths, large extinction corrections were required, and such corrections may contribute to the lack of agreement for the [Ne II] line.

We have measured [O I] 63 μm in nine sources and in Figure 2 we show the correlation between the [O I] and total FIR flux in the central $\sim 40''$ regions.

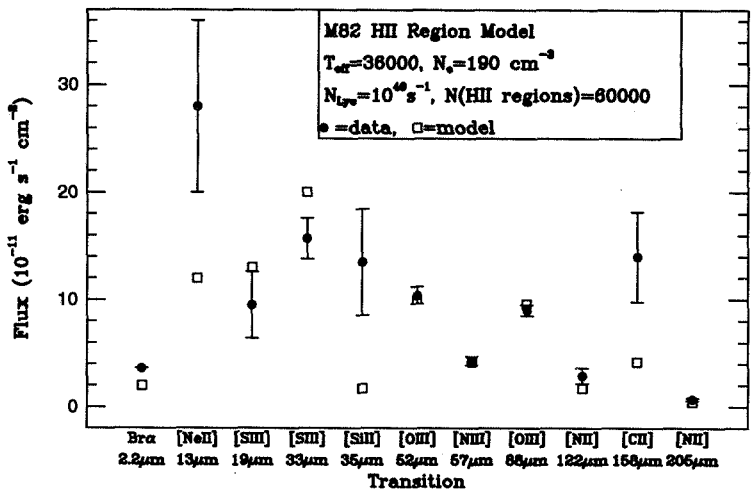

Figure 1. Observations of FIR transitions in M82 are shown along with the model predictions of Rubin (1985), for an ensemble of 6×10^4 H II regions. This number was selected to match the Lyman continuum output determined from the thermal radio emission (Carlstrom 1988).

We see [O I] emission accounting for a fraction of a percent of the total FIR emission; a result that holds for [C II] as well. Exceptions to this are seen in the excess [O I] emission from NGC 6240, which may originate from shocks or X-ray heated gas, and the strong upper limit placed on the [O I] emission for Arp 220, suggesting excitation from an AGN.

As part of our AGN study, we have observed several systems looking for the [O IV] 26 μm and [Ne V] 24 μm transitions. Preliminary analysis of our NGC 4151 data indicates a tentative [Ne V] detection which, if confirmed, will be modeled in conjunction with mid-IR observations and photoionization models (e.g., Spinoglio & Malkan 1992).

Finally, our study of metal-poor irregulars has yielded new evidence for the deep UV penetration and photodissociation of CO in the envelopes of low-metallicity molecular clouds. For NGC 4449 (Z=1/3 $Z_\odot$), NGC 1569 (Z=1/6 $Z_\odot$) and IC 10 (Z=1/6 $Z_\odot$), we find [C II]/CO emission ratios of 17×10^3, 37×10^3, and 10×10^3 which are larger than typical Milky Way values: e.g., [C II]/CO for Orion KL is 6×10^3. However, the lack of direct correlation between metallicity and CO destruction in these systems has been noted, and further studies will be aimed at identifying the additional controlling parameters.

References

Carlstrom, J.E. 1988, Ph. D. thesis, University of California, Berkeley

Carral, P., Hollenbach, D.J., Lord, S.D., Colgan, S.W.J., Haas, M.R., Rubin, R.H., & Erickson, E.F. 1994, ApJ, 423, 223

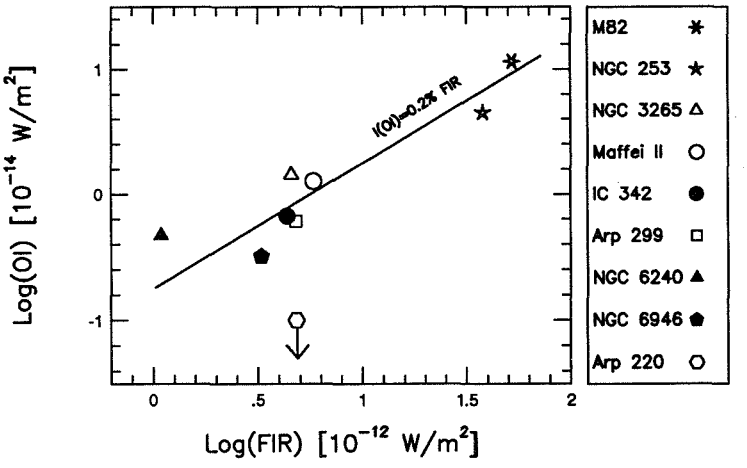

Figure 2. The correlation of [O I] 63 μm emission with total FIR emission in the central 40″ in nine IR-bright galaxies.

Erickson, E.F., Houck, J.R., Harwit, M., Rank, D.M., Haas, M.R., Hollenbach, D.J., Simpson, J.P., Augason, G.C., & McKibben, D.D. 1985, IRPhy, 25, 513

Kurucz, R.L. 1979, ApJS, 40, 1

Lonsdale, C.J. et al. 1989, Cataloged Galaxies and Quasars Observed in the IRAS Survey, version 2, IPAC, Caltech

Lord, S.D., Hollenbach, D.J., Colgan, S.W.J., Haas, M.R., Rubin, R.H., Madden, S.C., Steiman-Cameron, T.Y., Carral, P., Maloney, P.R., Erickson, E.F. 1995a, in preparation.

Lord, S.D., Hollenbach, D.J., Haas, M.R., Rubin, R.H., Colgan, S.W.J., Erickson, E.F. 1995b, in preparation.

Madden, S.C., Geis, N., Genzel, R., Herrmann, F., Poglitsch, A., Stacey, G.J., & Townes, C.H. 1994, Infrared Phys. Technol., 35, 311

Maloney, P.R. & Black, J.H. 1988, ApJ, 325, 389

Petuchowski, S.J., Bennett, C.L., Haas, M.R., Erickson, E.F., Lord, S.D., Rubin, R.H., Colgan, S.W.J. & Hollenbach, D.J., 1994, ApJ 427, L17

Rubin, R.H. 1985, ApJS, 57, 349

Rubin, R.H., Simpson, J.P., Lord, S.D., Colgan, S.W.J., Erickson, E.F., & Haas, M.R. 1994, ApJ, 420, 772

Spinoglio, L. & Malkan, M.A. 1992, ApJ, 399, 504

Stacey, G.J., Geis, N., Genzel, R., Lugten, J.B., Poglitsch, A., Sternberg, A., & Townes, C.H. 1991, ApJ, 373, 423

Tielens, A.G.G.M. & Hollenbach, D.J. 1985, ApJ, 291, 722

Van Buren, D. 1983, PhD Dissertation, University of California at Berkeley

Wolfire, M., Tielens, A.G.G.M. & Hollenbach D.J. 1990, ApJ, 358, 116

Airborne Astronomy Symposium on the Galactic Ecosystem
ASP Conference Series, Vol. 73, 1995
M.R. Haas, J.A. Davidson, and E.F. Erickson (eds.)

P-10

THE EXTENT OF FAR-IR EMISSION IN LUMINOUS GALAXIES

DAN F. LESTER
Astronomy Department, University of Texas, Austin TX 78712

ABSTRACT The size of far-infrared emission in luminous IR galaxies is an important parameter in studies of its source. The KAO is the largest aperture that can be brought to bear on the continuum emission of these galaxies at their far-infrared spectral peak. It therefore offers the best opportunity for probing the extent of this emission on the smallest possible scales. In this paper, I give a retrospective on efforts at the University of Texas, over the last decade, to use the KAO to understand the distribution of far-infrared continuum emission in luminous IR galaxies.

1. LARGE WAVELENGTHS, SMALL SCOPES, AND LUMINOUS GALAXIES

The source of power in luminous galaxies is one of the more critical questions of the last few decades, a question that has been spurred by the IRAS discovery that such luminous galaxies are a substantial component of the universe. Whether luminous galaxies are so because of violent star formation, an active nucleus, dissipation of kinetic energy in a collision, or simply a lot of quiescent starlight is not well understood, though there is evidence for all of these contributors as we look at a range of different sources.

At least partly because of their identification by IRAS, these galaxies put out most of their luminosity in the far-IR (~100 μm), a part of the spectrum that is not visible from ground-based telescopes. While the spatial distribution of this emission, and correlation of it with the distribution of other spectral and continuum diagnostic features at other wavelengths, is a key requirement for understanding its source, the spatial resolution that we have to work with in this part of the spectrum is poor. We are in a regime where the wavelengths are long, and the telescopes are small. Far-IR observers are at a disadvantage compared with observers at shorter wavelengths, whose work is largely seeing limited, and those at longer wavelengths, whose interferometrically-coupled telescopes can yield data with resolution approaching that achievable optically.

While IRAS mapped the far-IR sky at high sensitivity, the spatial resolution was lacking for many applications. The 2'x4' survey beams at 100 μm are suitable for resolving the far-IR continuum only in nearby galaxies. While substantial and focused effort has gone into extracting the maximum amount of spatial information from this extraordinary archive (see the reviews of this excellent work in the 1993 IPAC Workshop on Science with High Spatial Resolution Far-Infrared Data, eds S. Terebey and J. Mazzarella 1993), even after heroic effort on data for individual sources, spatial information on scales < 1' is generally not available.

With a diffraction-spot diameter of about 20" at 100 μm, and a pointing and tracking accuracy at the few arcsecond level that is required to take advantage of

it, the Kuiper Observatory offers the highest spatial resolution in the far-IR. The performance of the oscillating secondary is, in fact, the limit on the spatial dynamic range that is imposed by the facility. Present array formats subtending fields of view of several arcminutes are easily accommodated by this chopper, however. It is only within the last decade, as the need for large-aperture, total flux measurements in the far-IR have been satisfied by the IRAS database, has the spatial resolution of the KAO in the far-IR been pushed to the limit.

For almost a decade, capitalization of the high spatial resolution obtainable with the KAO has been the focus of activity of the Texas group and our collaborators. While a large number of people have worked hard to squeeze high spatial frequencies out of this telescope, I would like to mention, in particular, the extragalactic work by Marshall Joy (now at NASA MSFC), and Beverly Smith, whose work on NGC 2146 is detailed elsewhere in these proceedings. In this retrospective, I have made liberal benefit of text from my similarly oriented review at the June 1993 IPAC Workshop (Lester 1994).

2. IN PURSUIT OF HIGH RESOLUTION FAR-IR DATA ON GALAXIES

The achievements of the Texas group in high spatial resolution studies of galaxies were encouraged by large advances in focal plane instrumentation. Each new generation of instrument fostered development of new techniques for pointing, flux calibrating, and derivation of the point source response function. It is this evolutionary development of methodology and instrumentation that is a hallmark of airborne astronomy.

Starting in 1985, the Texas team, under the direction of Paul Harvey, made the first attempts to push the far-IR spatial resolution of the KAO to its ultimate limits. This required development of instrumentation with diffraction-limited detectors, and techniques for careful pointing. The first instrument to be used in this way was a three spatial channel (0.8K bolometer) photometer, configured with diffraction-limited slits instead of large apertures. While the orientation of these slits on the sky was fixed in elevation and azimuth, careful flight planning allowed the slits to be scanned across astronomical sources at interesting angles.

It is important to understand that, while two dimensional spatial resolution is important, many of the most important questions in far-IR continuum photometry hinge not so much on the detailed profile of an astronomical source, but simply on whether a large fraction of the luminosity of the source is from a component that is resolved at all. This question can easily be addressed with slit scans. For example, the optical depth (and hence dust column density) in a galactic cloud, can be derived by comparison of its color temperature and brightness temperature. The latter requires an estimated size. The source of far-IR luminosity in galaxies with active nuclei remains a crucial problem and, for the more nearby galaxies, this problem can be reduced to whether the far-IR is point-like on the scale of the galaxy. This understanding provoked a lot of work with one dimensional slit scans by the Texas group in the years that followed.

A novel guiding strategy was used to precisely scan the astronomical sources across the detector array. Motion of the photometer relative to the telescope is not permitted because of changing thermal offsets. The telescope itself had to be precisely moved across the sources. The low frequency end of the telescope stabilization loop is achieved, on the KAO, by video tracking on a star in the field. We move the telescope by precisely moving the camera, which is fiber coupled to the focal plane. As the camera feed moves across the focal plane in one direction, the tracking system moves the telescope in reflection. In this way, the telescope

can be scanned precisely and reproducibly in a way that is independent of the (rather poor) isoplaneticity of the video tracker camera.

The success of high spatial resolution observations with diffraction-limited slits led to new generations of instruments with diffraction-limited detector arrays. The current Texas instrument employs a 2x10 He-3 cooled bolometer array. Each detector in the array is sized λ/D x $\lambda/2D$, with the short axis of the detector aligned along the long axis of the array. Magnifying optics are used to make the array match the diffraction spot at either 50 and 100 μm. The array can be scanned over bright sources, to give 2-D data, or guided at a fixed location to give one dimensional profiles of faint sources (see below for NGC 4736 and NGC 1275).

A critical need for pushing the limits of spatial resolution on the KAO is the knowledge and stability of, the point source profile of the system. While at shorter wavelengths nature provides point sources in just about every field (background stars), and at longer wavelengths compact radio sources fit the bill, in the far-IR there are few bright objects that can be assumed, a priori, to be unresolved on a scale of a few arcseconds ($<<\lambda/D$ in the 50, 100 μm bandpasses of the KAO photometer). As shown by Hawkins (see 1993 IPAC Workshop) using the KAO and IRAS, even red giants and supergiants can have far-IR structure on scales larger than this. The sky is filled with sources that are intrinsically fuzzy in the far-IR. Much more so than in the optical, for which point sources abound.

Solar system bodies are the only ones that are bright enough, and verifiably point like at our resolution. We have used the outer Galilean satellites (Ganymede and Callisto, sizes ~1"), Uranus (~4"), and the brighter asteroids (Ceres and Vesta, sizes ~0.5") for this purpose. These objects are bright enough that, in most cases, the point source profile is not the limiting factor in the deconvolution. Other bona fide point-like sources are much fainter, and restricting ourselves to these five objects has sometimes resulted in serious constraints on workable flight plans.

Fortunately, the instrumental stability of the point source profile is very good. This was verified early in our work, by looking at these sources several times in the course of a flight. In practice, the PSP stability is limited mainly by the stability of the oscillating secondary mirror, which is moving the image by as much as 10 arcminutes at more than 20 Hz. A new oscillating secondary mirror system, installed in 1989, was an important factor in our ability to do this work.

3. INDIVIDUAL SOURCES

In the following, I recall some of the high points of high spatial resolution far-IR studies of galaxies on the KAO. While this review concentrates on diffraction-limited studies by the Texas group, it should be clear to the reader that all of the work ever done on the KAO including, in particular, that done in beamsizes of order 1' by the Yerkes team is, by comparison to data from IRAS or balloon, very high spatial resolution also.

Because of their relatively low flux levels, galaxies present a special challenge to high resolution studies in the far-IR. The easiest are those that are brightest, and that strongly selects nearby objects with high luminosity. Thus, with the modest aperture of the KAO, it is star forming regions and or active galaxies that have received the most attention. In addition to those objects that are discussed below, diffraction-limited scans of M 82 (Joy, Lester, and Harvey 1987), the prototypical Seyfert 2 galaxy NGC 1068 (Lester et al. 1987), NGC 4945 (Brock et al 1988), Arp 299 (Joy, et al. 1989), and NGC 2146 (Smith et al., these Proceedings) have been made by the Texas group.

a) M51

The limits of spatial resolution in the far-IR on the KAO were first probed, in galaxies, in M51. Scans across this nearby spiral galaxy constituted a first proof of the potential of our techniques on a relatively low surface brightness source. Figure 1 (Lester, Harvey, and Joy 1986) shows co-added scans across the nucleus of M51 superimposed on a point source profile from identical scans across Vesta. The source is clearly resolved into double peaks, with separation 25" (120 pc). In the context of a slit profile, this is most simply interpreted as ring of far-IR emission with that diameter. Two deconvolution algorithms (Richardson-Lucy, and MEM) were applied to the data, and these increased the contrast in the structure that was already evident in the raw data.

This structure corresponds well with that seen in CO interferometer studies, with spiral arms wrapping around the nucleus terminating in a nearly complete ring of this size. This structure also very nearly envelops the older nuclear bulge of the galaxy, as delineated well by near-IR continuum images (Thronson and Greenhouse 1988). The association of this far-IR structure with star formation around the nucleus is supported by the optical images of Worden (1974).

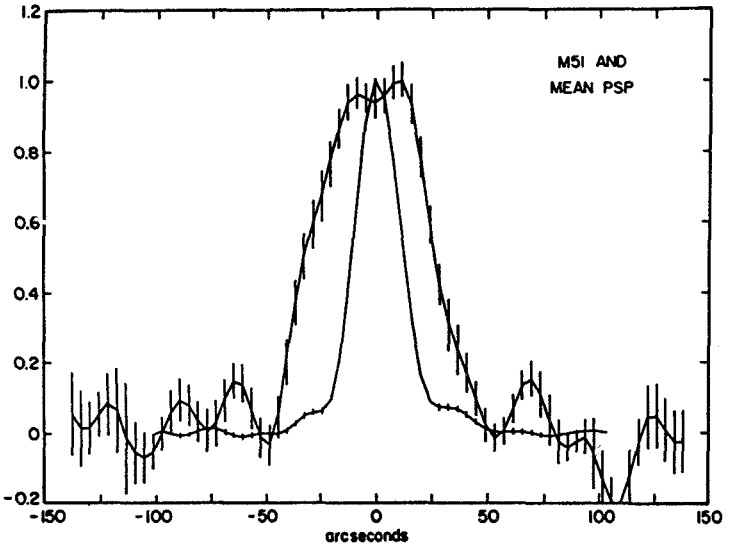

Figure 1: Co-added KAO slit scans at 100 μm across the nucleus of M51 are shown against a point source profile from observations of Vesta. The source is clearly resolved into two components.

It is worth noting at this point that, while M51 has been considered a test case for IRAS deconvolution techniques, that work pertains to a much larger scale. While the KAO observations do not have the S/N to easily detect the large scale emission (spiral arms, relationship to the companion) that is so accessible in the IRAS data, the structure that is seen in the KAO data is almost an order of

magnitude smaller (25" versus several arcminutes) than that available in the raw IRAS images, and a factor of several smaller than seen in the best IRAS deconvolutions. This latter work is comparable to the large beam KAO maps of Smith (1982).

b) NGC 5128 (Cen A)

Ground based studies in the mid-IR have shown that the star formation in this galaxy is strongly concentrated in the dust lane that bisects it. Presumably this giant elliptical has swallowed whole a disk galaxy, and the gas attached to this disk galaxy is now involved in a strong starburst. High resolution scans of NGC 5128 in the far-IR were made from the KAO during its 1986 deployment to New Zealand. Scans at both 50 and 100 μm, perpendicular and parallel to the dust lane were obtained. The resulting profiles give a wealth of information (Joy et al. 1988). The 100 μm profiles are shown in Figure 2, where they are compared (with common scale and orientation) to an optical photograph.

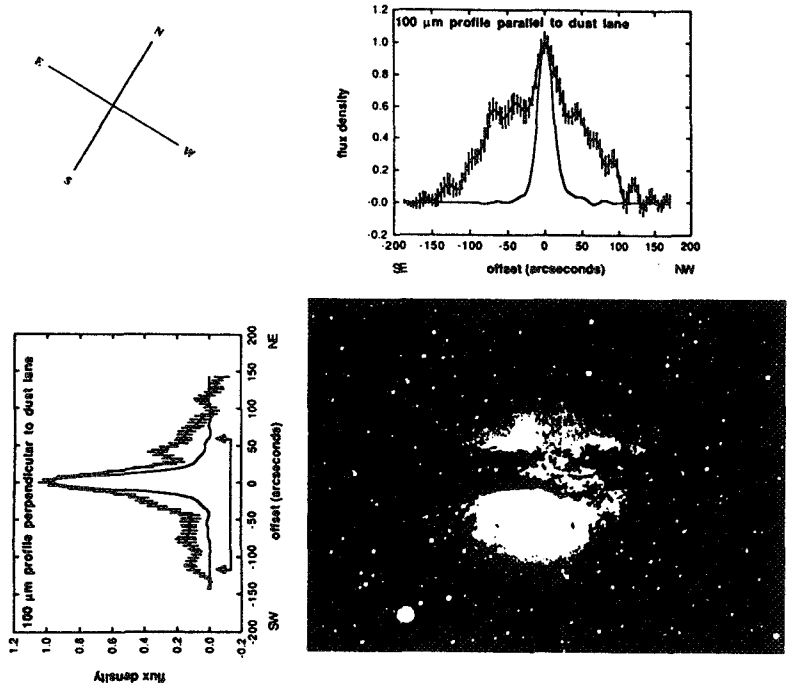

Figure 2: Slit scans at 100 μm parallel and perpendicular to the dust lane in NGC 5128 are scaled and oriented for comparison with an optical photograph. Comparing the data with that of point source profiles (solid line) three separate emission components are clearly visible -- extended emission from the starburst disk along the plane, extended emission at large z distances, and emission from an unresolved point source coincident with the nonthermal nucleus. The slit length is approximately 40".

The profile perpendicular to the disk (left side of figure) clearly shows that most of the far-IR emission is concentrated to the dark lane. From the mid IR work of Telesco (1978), this is not unexpected. The extent of the far-IR emission to high z, well away from the dust lane was not expected, and suggests that dust at high latitudes contributes substantially to the luminosity of this galaxy. This dust is not heated by the central source, but by star formation in situ, or perhaps by the interstellar radiation field of a quiescent bulge population. The slit scan along the dust lane shows that the star formation is fairly uniform along the disk, to the outermost optical isophote of the bulge, but shows a marked unresolved peak that is coincident with the nuclear radio source. The extended equatorial emission has a profile that is well fit by a uniform disk model, and poorly fit by a thin ring. Thus the star formation in the disk of NGC 5128 is not restricted to those bits of peripheral pieces that we can see optically, but probably covers the disk.

c) Arp 220

Arp 220 (IC 4553) has been characterized as an "ultraluminous" galaxy, that radiates almost all of its $10^{12} L_{sun}$ in the far-IR. There is a rich literature on this galaxy, which shows evidence for a buried AGN. The optical extent of its disk, which is highly distorted, is more than 30", corresponding to 10 kpc. KAO observations by Joy et al. (1986) showed conclusively, however, that the far-IR emitting region was a factor of four smaller than this, and most likely is produced in the nucleus. Using several deconvolution techniques, it was established that the 100 μm size of Arp 220 was less than 7.5". Using this size to compare the color temperature to the brightness temperature, a far-IR optical depth in excess of 0.05 was derived. This corresponds to a visual extinction of 25-50 magnitudes, which is consistent with the fact that high nuclear velocity dispersion that is evident in the near-IR is not seen in the visible (DePoy, Becklin, and Geballe 1987).

d) NGC 4735

This galaxy shows a compact, high surface brightness bulge that, while relatively blue, shows no sign of ongoing star formation. The bulge is surrounded by a ring of ionized and molecular gas with a radius of about 50" (1.6 kpc), that is clearly dominated by star formation. The far-IR profile across the galaxy shows striking differences compared with both the red starlight and the ionized gas. This comparison is shown in Figure 3 (Smith et al. 1991).

In this face-on ringed galaxy, the morphological distinction between bulge stars (F-band profile) and star formation (Hα profile) is evident. Integrated-light studies of the far-IR emission from galaxies in the IRAS survey show that, while far-IR emission is dominated by star formation in many galaxies, in quiescent galaxies the far-IR emission comes from thermalization of diffuse starlight by interstellar grains. Our high resolution profiles of NGC 4736 show both mechanisms at work in different parts of the same galaxy. Note that the 100 μm profile in this galaxy resembles neither the quiescent bulge light or the star formation in the ring closely. Unlike the H-alpha profile, the 100 μm profile is peaked in the center. The far-IR emission from the inner parts of NGC 4736 is thus dominated by diffuse starlight. The elevation in the shoulders of the 100 μm profile at the Hα ring radius shows that this emission is from star formation.

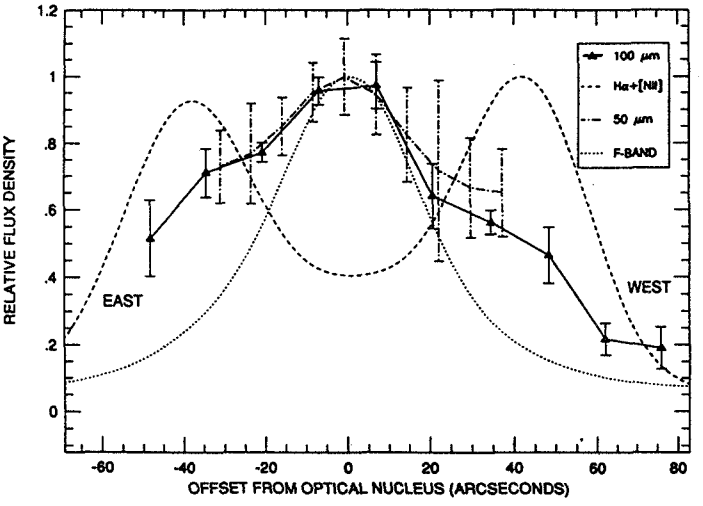

Figure 3: Profiles of the ringed galaxy NGC 4736. The far-IR emission follows the profile of diffuse starlight in the inner regions, yet shows enhancement at the radius of the starburst ring. Two mechanisms for production of far-IR emission in galaxies are thus clearly spatially resolved for the first time in a single galaxy.

e) NGC 1275 (Per A)

One of the more recent results in this program is the discovery that the far-IR luminosity in NGC 1275 is extended thermal emission (Lester et al. 1995) surrounding what is one of the brightest nonthermal nuclei in the radio sky (Perseus A). The spectral energy distribution of NGC 1275 hints at a thermal peak superimposed on a nonthermal continuum. The giveaway was the photometric comparison of contemporary far-IR continuum emission with that seen by IRAS in 1983. During this intervening period, the nonthermal millimeter radio source had declined in intensity by a factor of almost ten. KAO observations showed, however, that the far-IR continuum emission did not decrease, and therefore was produced by a physically distinct source. Careful comparison with point source profiles revealed (see Figure 4), that the source was extended on a scale of about ten kiloparsecs.

The source of this emission is not well understood. While a starburst is a convenient explanation for such an extended thermal emitting region, the optical spectrum of this region is more LINER-like, representing gas that is thought to be associated with a cooling flow around this galaxy. Kinetic heating of grains by the hot gas that gives rise to this cooling flow is energetically feasible. While the lifetime of grains in this hot gas is short, and argues against an equilibrium situation, there is evidence for a recent collision in this cluster giant elliptical that may have dumped large quantities of dust into the hot gas. If the dust in NGC 1275 is, in fact, being heated by the hot gas, then this dust heating, rather than thermal brehmsstrahlung, is the dominant coolant for this gas, and cooling flow mass inflow estimates based on the X-ray emission are probably underestimates.

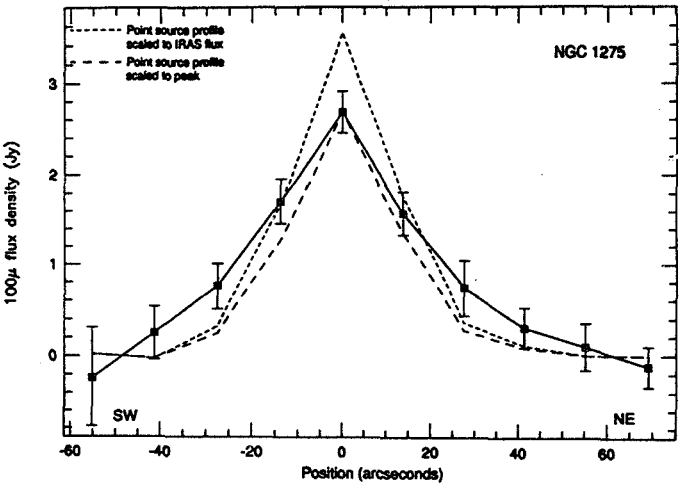

Figure 4: The spatial profile of NGC 1275 at 100 μm is compared with that of a point source profile normalized to the peak, (dashed) and normalized to the total flux (dotted). The size of the emitting region appears to be on a scale of ~30".

4. THE FUTURE OF HIGH RESOLUTION FAR-IR STUDIES OF GALAXIES

Work in the last ten years has shown clearly that image restoration work from an airborne platform is highly profitable. Modest aperture diffraction limited space telescopes (ISO, SIRTF, Edison) of the future will provide enormous increases in sensitivity and, to a great extent, these increases in sensitivity can be harnessed to provide, through image restoration, enhancements in spatial information (c.f. IPAC Workshop 1993). The fact remains, however, that for reasonably bright sources (and it should be noted that most of the sources that define IR astronomy are, even in this post-IRAS era, bright sources), the biggest gain in spatial resolution comes with the largest aperture.

The Stratospheric Observatory for Infrared Astronomy (SOFIA) will answer to this challenge, and the KAO has shown us the way. With an aperture of 2.5 m, SOFIA will provide a factor of three increase in spatial resolution over the KAO, as well as more than a factor of a hundred in single-point-source sensitivity. For a plethora of the brightest far-IR galaxies, SOFIA will provide several times higher spatial resolution than any other space facility. The accessibility of an airborne platform will, as it has for the KAO, encourage new technology that is not yet robust enough for space missions. Thus, SOFIA will always be equipped with instruments that push the edge of technology. The hands-on instrumentation expertise that SOFIA will develop will be precisely that which, with a little foresight, we will need for the long-term future of high spatial resolution far-IR measurements, with large apertures in earth orbit or on the moon.

ACKNOWLEDGMENTS

I appreciate the opportunity originally provided by organizers of the 1993 IPAC Workshop on Science With High Spatial Resolution Far-Infrared Data, in encouraging parts of this review, as well as the organizers of this Airborne Astronomy Symposium. High spatial resolution far-IR work at the University of Texas has been an exceptional team effort. I wish to thank Marshall Joy, Bev Smith, Benton Ellis, Cheng-yue Zhang, Chris Koresko, grad students Parvinder Parmar, Cecilia Colomé and James DiFrancesco, Niall Gaffney, and Eric Zink as well as undergraduates Greg Doppmann and David Brock for their efforts and scientific enthusiasm over the years. Thanks are also due to the Texas technical staff and many KAO guest investigators. Finally, special thanks are given to Paul Harvey, whose instrumental wisdom made it possible, and to the staff and crew of the KAO, who made it all happen. This research was supported through NASA through Airborne Astronomy Grants NAG 2-67 and NAG 2-748.

REFERENCES

Brock, D., Joy, M., Lester, D.F., Harvey, P.M., & Ellis, H.B. Jr. 1988 ApJ 329, 208
DePoy, D. , Becklin, E.E., & Geballe, T.G. 1987 ApJ Lett. 316, L63
Joy, M., Lester, D.F., & Harvey, P.M. 1987 ApJ 319, 314
Joy, M., Lester, D.F., Harvey, P.M., & Ellis, H.B. Jr. 1988 ApJ 326, 662
Joy, M., Lester, D.F., Harvey, P.M., & Frueh, M. 1986 ApJ 307, 110
Joy, M., Lester, D.F., Harvey, P.M., Telesco, C.M., Decher, R. Rickard, L., & Bushouse, H. 1989 ApJ 339, 100
Lester, D.F., Harvey, P.M., & Joy, M. 1986 ApJ 304, 623.
Lester, D.F., Joy, M., Harvey, P.M., Ellis, H.B. Jr, & Parmar, P. 1987 ApJ 321, 755.
Lester, D.F. 1994, in "Science With High Spatial Resolution Far-Infrared Data", eds. S. Terebey and J. Mazzarella,) Pasadena: Jet Propulsion Laboratory), p. 33.
Lester, D.F., Zink, E., Doppmann, G., Gaffney, N., Harvey, P., Smith, B., & Malkan, M. 1995 ApJ, in press
Thronson, H., and Greenhouse, M. 1988 ApJ 327, 671
Smith, B.J., Harvey, P.M., Colomé, C., Zhang, C.Y., DiFrancesco, J., & Pogge, R.W. 1991 ApJ 373, 66
Smith, J. 1982 ApJ 261, 463
Telesco, C.M. 1978 ApJ Letters 226, L125
Worden, P. 1974 Pub. A.S.P. 86, 92

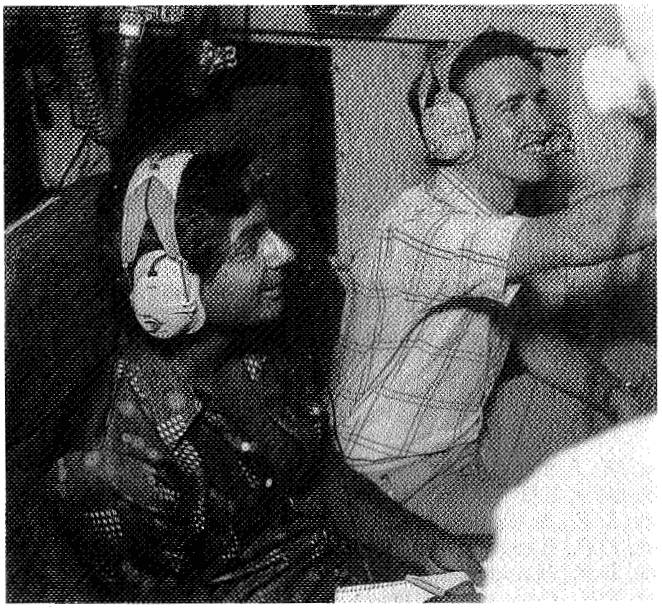

Parvinder Parmar, Dan Lester (1986)

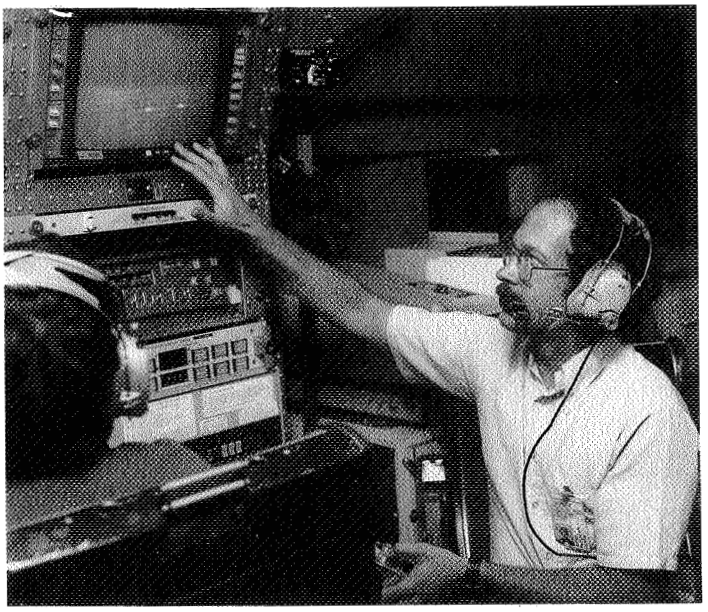

Paul Harvey (1986)

Airborne Astronomy Symposium on the Galactic Ecosystem
ASP Conference Series, Vol. 73, 1995
M.R. Haas, J.A. Davidson, and E.F. Erickson (eds.)

Infrared Studies of Galaxies from Space

M. W. Werner and P. R. M. Eisenhardt
MS 169-327, Jet Propulsion Laboratory, California Institute of Technology, Pasadena, CA 91109

Abstract. The Kuiper Airborne Observatory has been a powerful instrument for the study of nearby galaxies, and SOFIA could probe still further into the local Universe. However, a comprehensive program of extragalactic exploration in the infrared - and in particular a study of galaxies at cosmological redshifts - requires the high sensitivity and complete wavelength coverage which is achievable only with a cryogenic telescope in space. This program was begun by IRAS and will be continued by the upcoming ISO (Infrared Space Observatory), WIRE (Wide field Infrared Explorer) and SIRTF (Space Infrared Telescope Facility) missions. This paper previews a set of extragalactic investigations which could be carried out by these missions.

1. Overview

Future infrared space missions can make major steps in extragalactic exploration from $z \sim 0.5$ to $z > 5$ - beyond the most distant quasars currently known. Over this redshift range one can study not only the properties - luminosity, mass, excitation conditions, etc. - of individual objects, but also the evolution of classes of objects ranging from normal galaxies to the hyperluminous systems recently discovered in the IRAS data base. Here we discuss several scientific investigations which can produce such major steps. These investigations have been proposed for three upcoming infrared space missions - the European Space Agency's Infrared Space Observatory (ISO) mission (Kessler 1993) - now on schedule for launch in the Fall of 1995; the Wide Field Infrared Explorer (WIRE), which is being considered for development phase funding in NASA's Small Explorer program (Schember and Hacking 1993) and the Space Infrared Telescope Facility (SIRTF), which is in the final definition phase as NASA's observatory-class mission for infrared astronomy (Werner and Simmons 1994). Although these missions differ in scope, instrumentation, and orbit, they have in common the use of cooled optics to exploit the low background of space.

2. The Scientific Investigations

2.1. Near/mid-IR surveys for normal galaxies to $z > 3$

Measurements of starlight from stars in distant galaxies probe the formation and early evolution of the galaxies and trace the distribution of luminous matter

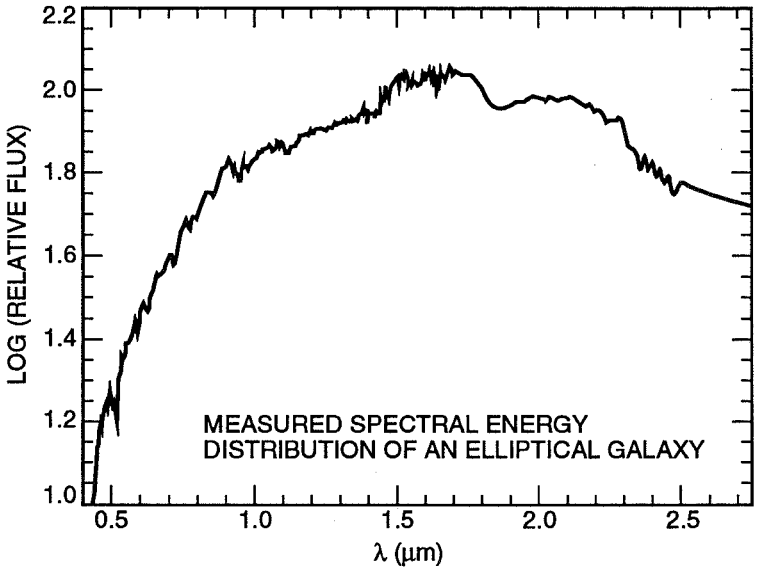

Figure 1. The rest frame visible-near IR energy distribution of an elliptical galaxy, showing the H^- emission feature at 1.6 μm and the CO bandhead at 2.3 μm. Data provided by M. Rieke (private communication).

in the early Universe. Observations of nearby galaxies between 1 and 2.5 μm (Figure 1) reveal several spectral features - the 2.3 μm CO bandhead and the 1.6 μm emission peak due to the minimum in H^- opacity - which are present because most of the near IR radiation from a galaxy arises from cool stars which have these features in their spectra. These features are thus relatively immune to changes in star formation rate and dust content, and are expected to appear shortly after a galaxy forms and to persist throughout its lifetime (see e.g. Franceschini *et al.* 1991).

As an energy distribution such as that shown in Figure 1 is redshifted to longer wavelengths, the measured colors of a galaxy vary in a predictable fashion as the spectral features move through the measurement passbands (see e.g. Figure 3 of Eisenhardt and Lebofsky 1987). This variation allows the use of the observed IR colors to determine a photometric redshift. This can be done more reliably using rest frame near IR starlight than from observations at visible or ultraviolet wavelengths, which are influenced more strongly by extinction or by the presence of a small number of hot stars. For similar reasons, selection in the rest frame near IR provides a more uniform sample of galaxies above a given stellar mass than do rest frame optical or UV samples.

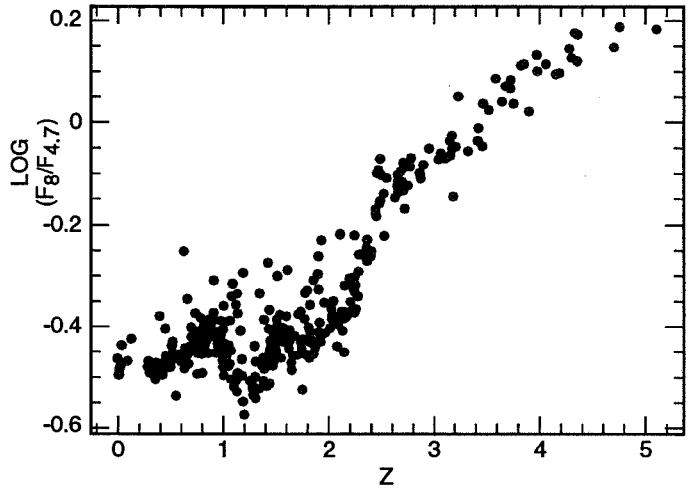

Figure 2. Relationship between 8/4.7 μm flux ratio and galaxy redshift, as determined from the simulations of Wright *et al.* (1994).

An experiment based on this principle has been simulated by Wright, Eisenhardt, and Fazio (1994), using instrumental parameters appropriate for SIRTF, which will carry InSb and Si:As arrays with imaging fields of view 5x5 arcmin in extent. They assume a galaxy population normalized to current epoch observations and extending back to z=10 with luminosity and color evolution given by Bruzual (1983) models. A simulation was made of a single $5 \times 5'$ field of view at 3, 4.7, 6.2, and 8 μm, with a total integration time of 1.6 days. The image quality and detector performance assumed were consistent with what is expected for SIRTF, and the simulated data were analyzed with standard image processing techniques. Approximately 350 galaxies were detected, including virtually all those in the simulation more massive and luminous than the present day characteristic mass and luminosity M^* and L^* (Schechter 1976), and with $z < 5$. By comparing the "observed" colors of the detected galaxies in the simulated images with their known redshifts, it was possible to demonstrate the usefulness of these colors as redshift indicators.

In Figure 2, for example, we show the 8.0/4.7 μm flux ratio vs. redshift for this sample of galaxies. Although this ratio is relatively independent of z for $z < 2$, it varies systematically with z for larger redshifts, increasing by about a factor of 4 between $z \sim 2$ and $z \sim 5$. Analogous results are obtained from the other flux ratios determined in the simulation. This shows not only that a mission such as SIRTF can detect normal galaxies at cosmological redshifts, but also that multiband imaging data can be used to estimate the galaxy redshifts and thus to explore a series of problems ranging from the geometry of space-time and the presence of large scale structure in the early Universe to the evolution of the stellar populations in galaxies.

2.2. Evolution of the Starburst Galaxy Population

Future studies of galaxies at wavelengths of 10 μm and beyond will be heavily based on the results from IRAS, which inaugurated the infrared exploration of the extragalactic sky from space. Indeed IRAS is a "gift that keeps on giving", because the newest catalogs - the Faint Source Survey and the Faint Source Data Base - reduce the 60 μm detection limit from the 560 mJy of the Point Source Catalog to about 200 mJy. As a result, the faint source data base contains five times more high galactic latitude 60 μm sources (presumably almost entirely galaxies) than were contained in the original Point Source Catalog. Searches based on these new catalogs have led to the discovery of the Hyperluminous Galaxies described in section 2.4. below.

One of the major results apparent from even the earliest analyses of the Point Source Catalog is that interacting galaxies are brighter at IR wavelengths than are their non-interacting cousins (Bushouse, Lamb, and Werner 1988). The IR luminosities of these otherwise fairly ordinary galaxies range up to $10^{11}L_{\odot}$. Based, for example, on visible wavelength spectroscopy, it has been established that the extra IR luminosity is traceable to bursts of star formation triggered by the galaxy-galaxy interactions. This scenario can be tested by tracing the co-moving density of these starburst galaxies as a function of redshift. At earlier epochs, when the galaxies were closer together, the higher frequency of interaction ought to have produced a larger fraction of IR-luminous systems. In addition, comparison of the evolution of the infrared galaxy population with that which has been determined for quasars can test the conjecture that extremely close and violent interactions - those which lead to IR luminosities in excess of $10^{12}L_{\odot}$ - trigger the formation of quasars.

The WIRE mission is designed specifically to test these ideas by determining the evolution of the starburst galaxy population out to $z \sim 0.5$. WIRE will carry a 30-cm diameter telescope feeding two 128 x 128 Si:As arrays, which view the same $\sim 32 \times 32$ arcmin field of view simultaneously at 12 and 25 μm through the use of a dichroic. The telescope and detectors will be cooled by solid hydrogen, leading to a lightweight system which can be inserted into low Earth orbit by a Pegasus launch vehicle and still achieve a 4 month lifetime. WIRE's principal scientific program will be to survey 20 square degrees to the confusion limit at 25 μm (approximately 1mJy 1σ) and detect 20,000 starburst galaxies with a median redshift of ~ 0.5. Addition of the companion 12 μm survey allows - statistically - sorting in redshift and luminosity because the 25 μm/12 μm flux ratio increases with increasing overall luminosity. Comparing the number counts vs. flux will distinguish among various models for the evolution of this population, as shown in Hacking and Soifer (1991) and Schember and Hacking (1993), and the WIRE data base will be an invaluable source of targets for the diagnostic investigations described below.

2.3. Energy Generation in Infrared Luminous Galaxies

The luminosity of IR-luminous galaxies correlates positively with the infrared-to-visual luminosity ratio. Many of the Ultraluminous Galaxies (ULGs) - those with IR luminosities in excess of $10^{12}L_{\odot}$ - emit upwards of 99% of that luminosity in the IR (Soifer 1993). At this luminosity level, either extreme starburst activity or an embedded quasar might be the fundamental energy source, and

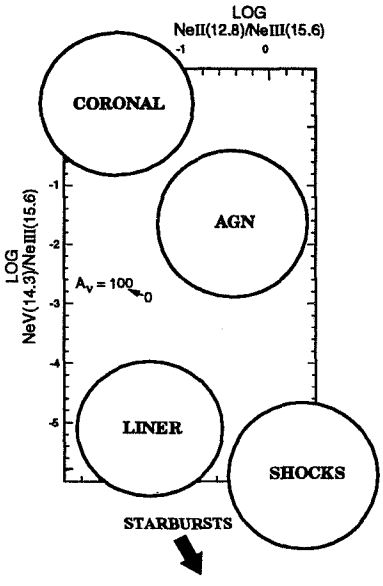

Figure 3. The regions in the (NeII/NeIII, NeV/NeIII) infrared line ratio plane corresponding to different possible ionization and energy sources are shown.

either possibility would have interesting consequences. Because the observed IR radiation is thermal emission from dust which has been heated by the primary power sources, continuum IR observations alone cannot distinguish among these and other possibilities.

For less heavily dust-enshrouded sources, optical emission line spectroscopy provides a means of distinguishing between thermal and non-thermal ionizing spectra, which would be associated with starburst or quasar energy sources, respectively. For sources which emit > 99% of their total luminosity in the IR, however, any optical emission produced in the immediate vicinity of the central energy sources is likely to be very highly extincted, and the optical emission observed from these galaxies may arise in their less interesting outer regions. Infrared emission lines can emerge from the enshrouding dust, however, so that IR spectroscopy is potentially capable of providing the diagnostic information needed to identify the character of the energy sources.

Voit (1992) has drawn attention to a particular set of emission lines which are uniquely useful for this type of diagnostic spectroscopy. These are lines of three different ionization states of neon: NeII at 12.8 μm, NeIII at 15.6 μm, and NeV at 14.3 μm. The ionization energies to produce these three ions are, respectively, 22, 63, and 97 eV. Thus, as shown in Figure 3, the relative intensities of these three emission lines are highly indicative of the character of the ionizing source. This triad of neon lines has other important characteristics: since they arise from different ionization states of an element which is particularly unlikely to be depleted onto interstellar grains, their ratios should not be

influenced by differential variations of the gas phase neon abundances within a source. Of particular importance in the present context is the fact that the lines lie close together in wavelength and in a spectral interval where extinction by dust is weak and spectrally smooth. Thus the line ratios are only imperceptibly influenced by differential extinction even if the region is observed through 100 magnitudes of overlying visual extinction.

Because the NeIII (15.6 μm) and NeV (14.3 μm) wavelengths are totally blocked by CO_2 in the Earth's atmosphere, application of this diagnostic to nearby galaxies - even to very bright ones - requires observations from space. Observations of this type on known infrared galaxies will be carried out with the Short Wavelength Spectrometer on ISO. Similar investigations on more distant, fainter galaxies will be carried out by SIRTF, using targets selected from the WIRE survey and from SIRTF's own deep surveys. SIRTF's spectrometers will be instrumented with 128×128 Si:As and Si:Sb arrays which will be sensitive at least to 40 μm. Use of these arrays in echelle spectrographs which cover several spectral orders simultaneously will provide simultaneous observation - through the same entrance slit - of all three lines in galaxies out to redshifts $z > 1.5$.

2.4. The Most Luminous Galaxies

Exploration of the IRAS Faint Source Survey and Data Base has led to the discovery of the most luminous known galaxies. The most notorious (and luminous) of these objects, FSC10214+4724 (Rowan-Robinson *et al.* 1991) appeared in the Faint Source Catalog as a 60 μm only source with 60 μm flux = 190mJy. Follow up observations led to the identification of this 60 μm source with an optically faint galaxy at redshift $z = 2.286$, giving FSC10214 a luminosity of $\sim 5 \times 10^{14} L_{\odot}$. Two other galaxies having luminosities within an order of magnitude of FSC10214 have also been identified - PSC09104+4109 (Kleinmann *et al.* 1988) and FSC15307+3252 (Cutri *et al.* 1994) - and the latter authors introduced the label Hyperluminous Galaxies (HLGs) to identify this class of objects. The nature of the processes which produce these gargantuan luminosities is unclear. At $10^{14} L_{\odot}$, a galaxy with $10^{11} M_{\odot}$ consumes its nuclear fuel in $< 10^8$ yrs, which has led to the suggestion that objects of this type are protogalaxies undergoing the initial burst of star formation which is thought to accompany their initial collapse. This star formation hypothesis is consistent with the enormous quantity of interstellar gas and dust discovered in FSC10214. On the other hand, the fact that the luminosities of these objects lie in a range previously occupied only by the most luminous quasars suggests that a hidden quasar may be the energy source (see e.g., Elston *et al.* 1994).

SIRTF can further our understanding of this intriguing phenomenon by detailed studies of individual objects - for example, using the spectroscopic probes mentioned previously - and by additional surveys aimed at uncovering additional examples. SIRTF's imaging arrays will survey large areas of sky to 60 μm flux levels far below the IRAS FSC limit. For example, SIRTF can survey about 50 square degrees to a limiting 60 μm flux of 1mJy (5σ) in about 100 days. This survey would include about 10^5 galaxies. Sorting through this cosmic haystack in search of the 3000 ULGs and 100 HLGs it is expected to include (the numbers will be greater if strong cosmic evolution occurs) poses an interesting challenge. One possible approach to this search is to use the fact that the shape of the rest

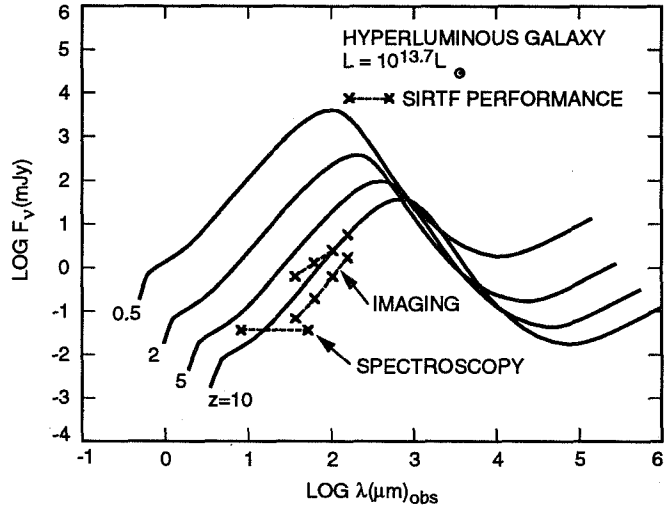

Figure 4. The capability of SIRTF for imaging and spectroscopy of Hyperluminous Galaxies as a function of redshift are shown. The imaging performance is given as 1σ uncertainty in 10 and 1000 seconds of observation, while for spectroscopy, we show the 1σ uncertainty in 3600 seconds.

frame energy distribution of the three HLG's mentioned above is the same to better than a factor of two, as shown in Figure 3 of Cutri *et al.* (1994). The similarities of these energy distributions allows one to concoct a color-based criterion to select candidate ULG's from the survey data base. SIRTF's instrumentation is being designed to permit imaging at several wavelengths simultaneously. In addition, SIRTF's surveys would be coordinated with other large scale surveys, such as WIRE and the Sloan Digital Sky Survey, to create a multispectral data base which would facilitate the selection process.

Figure 4 shows that SIRTF can obtain high quality imaging and follow up spectral data on ultraluminous objects as distant as $z > 5$, beyond the most distant quasars currently identified. This program would define the luminosity function of $L > 10^{12} L_{\odot}$ systems from $z = 0$ to $z > 2$, determine the energy generation processes which power these tremendous luminosities, and delineate their variation (if any) with redshift. For faint distant objects with high infrared-to-visual ratios, SIRTF's spectroscopy may be the only means of determining redshifts. This may be possible even for HLGs with $z \sim 10$ (assuming that there are any), for which the 3.28 μm "PAH" emission feature is shifted beyond 35 μm. SIRTF surveys would probe the evolutionary connection between ultraluminous objects and quasars and explore the possibility that these objects are in fact protogalaxies. Finally, SIRTF can go beyond the horizon of our present understanding and determine whether ULG's exist at $z > 5$ and whether there are objects with properties even more extreme than those identified to date.

3. Summary and Conclusions

Just as the success of the KAO has paved the way for larger airborne telescopes such as SOFIA, the successes of IRAS and COBE have set the stage for the next steps in infrared astronomy from space. This paper has highlighted a few areas of extragalactic astronomy in which future cooled space telescopes - particularly when instrumented with large format IR detector arrays - can make major contributions. The scientific prospects for such facilities are virtually unlimited, and we hope that the examples put forward here will stimulate even more exciting ideas in the readers' minds.

Acknowledgments. This work was carried out at the Jet Propulsion Laboratory, California Institute of Technology, under contract to the National Aeronautics and Space Administration.

References

Bruzual, G. 1983, ApJ 273, 105.

Bushouse, H.A., Lamb, S., and Werner, M.W. 1988, ApJ 335, 74.

Cutri, R.M., Huchra, J.P., Low, F.J., Brown, R.L., and Vanden Bout, P.A. 1994, ApJ, 424, L65.

Eisenhardt, P.R.M., and Lebofsky, M.J. 1987, ApJ 316, 70.

Elston, R., McCarthy, P., Eisenhardt, P., Dickinson, M., Spinrad, H., Jannuzi, B., and Maloney, P. 1994, AJ 107, 910.

Franceschini, A., Toffolatti, L., Mazzei, P., Danese, L., and De Zotti, G. 1991, A&AS 89, 285.

Hacking, P.B., and Soifer, B.T. 1991, ApJ, 367, L49.

Kessler, M.F. 1993, Proc. SPIE 2019, 2.

Kleinmann, S.G., Hamilton, D., Keel, W.C., Wynn-Williams, C.G., Eales, S.A., Becklin, E.E., and Kuntz, K.D. 1988, ApJ, 328, 161.

Rowan-Robinson, M., *et al.* 1991, Nature 351, 719.

Schechter, P. 1976, ApJ, 203, 297.

Schember, H., and Hacking, P.B. 1993, Proc. SPIE 2019, 395.

Soifer, B.T. 1993, ASP Conf. Series, 43, 101.

Voit, M. 1992, ApJ, 399, 495.

Werner, M.W., and Simmons, L.L. 1994, To be Published in Proceedings of Saclay Conference on Future Infrared Space Missions.

Wright, E.L., Eisenhardt, P., and Fazio, G.G. 1994, BAAS 26, 893.

Airborne Astronomy Symposium on the Galactic Ecosystem
ASP Conference Series, Vol. 73, 1995
M.R. Haas, J.A. Davidson, and E.F. Erickson (eds.)

Interstellar Grains in Elliptical Galaxies

John C. Tsai
NASA Ames Research Center, Mail Stop 245-3, Moffett Field, CA 94035-1000

William G. Mathews
University of California Observatories/Lick Observatory, Board of Studies in Astronomy and Astrophysics, University of California, Santa Cruz, CA 95064

Abstract. We consider the evolution and heating of dust embedded in the hot interstellar medium of isolated elliptical galaxies. We first construct a new set of galaxy models spanning a decade in luminosity which we use to study the evolution of dust as it is ejected by stellar sources, merges and flows with the interstellar gas, and is sputtered away due to the presence of the hot gas. We find that although grains can flow a considerable distance from the parent star in some cases before being sputtering away, the grain size distribution at a given location is accurately determined by assuming *in situ* sputtering of dust grains as they are ejected by the parent star. We find that dust heating is dominated by absorption of ambient starlight. Heating due to collisions with energetic electrons in the hot gas and absorption of thermal X-rays is smaller by orders of magnitude. We also find that for the largest galaxy considered ($L_B \sim 10^{11} L_\odot$) the energy lost from the hot gas due to electronic collisions with the dust is about an order of magnitude less than that lost due to thermal emission in X-rays. The gas in smaller galaxies loses even less of its energy via heating of grains. In deriving this result, we find that the inclusion of grain sputtering is a crucial ingredient of the calculation. The presence of dust grains is therefore energetically unimportant for elliptical galaxy cooling flow models.

1. Introduction

Elliptical galaxies, long thought to be simple ensembles of non-interacting stars, are now known to be more complicated multicomponent systems. In addition to both hot ($\sim 10^7$ K) and cold (~ 100 K) interstellar media, $\sim 50\%$ of ellipticals are known to contain sizeable quantities ($\sim 10^7 - 10^8 M_\odot$) of dust based on IRAS observations (e.g., Knapp et al. 1989) and on optical observations of dust lanes, patches, and disks (e.g., Sadler & Gerhard 1985).

The determination of the quantity and distribution of dust in ellipticals is important for many reasons. For example, the distribution of the dust potentially gives information on its origin, whether it be from mergers with dust rich

dwarf or spiral galaxies, as has often been suggested (e.g., Forbes 1991), or from internal sources like red giant winds or planetary nebulae. This ultimately sheds light on the formation and evolution of the elliptical itself.

Past work has provided many insights into the nature of the dust in ellipticals. However, most of this work has been focused on the dust associated with the cool ISM in the centers of galaxies. More extended dust was usually ignored because it was expected to both be too cold to emit at observed wavelengths and too sparse to account for much of the total emission (e.g., Jura 1986). The hot ISM was also thought to be an effective agent for rapidly sputtering any dust which might be produced in these regions. It is not clear, however, that emission from distributed dust should be so readily dismissed. The limited spatial resolution of IRAS does not allow the distinction between emission from central dust and extended dust. Evolved stars are also known to give off dust in sizeable quantities. This dust will be sputtered by the hot gas as the stellar winds merge with the ISM, however, a detailed calculation of the amount of dust remaining in the ISM has not been undertaken.

In this contribution, we consider the distributed dust arising only from stellar sources. This source of dust is always present regardless of the role played by mergers in the evolution of elliptical galaxies. We are thus considering a lower limit to the amount of dust that could be present. This is not a limitation of our modeling. Rather, if we find that additional dust is required to match observations, we would have uncovered independent evidence that mergers are important in the life history of ellipticals. We therefore adopt the following view of dust evolution. Red giants expel dusty gas into the $\sim 10^7$K ISM. The ejecta merges with the ISM in $\sim 10^4 - 10^5$ yrs, so fast that very little grain destruction can occur before the dust is immersed in the hot ISM. Once in the ISM, the grains are sputtered and are advected along with the galactic cooling flow. The conditions in the cooling flow are well known both from successful hydrodynamical simulations (e.g., Loewenstein & Mathews 1987) and from X-ray observations (e.g., Trinchieri, Fabbiano, & Canizares 1986). The mass loss rate from an ageing stellar population is also well known (Mathews 1989) as are the optical–IR (Bruzual 1985) and ultraviolet (UV) spectra (e.g. Ferguson et al. 1991) of ellipticals. This complete knowledge of the conditions in the ISM allows an accurate determination of the amount, composition, and distribution of dust in the ISM once these parameters are specified for the initial stellar ejecta. Detailed comparison of theoretical results with IR observations can then be used to determine the dust parameters in the stellar ejecta (work in preparation).

2. Galaxy Models, Cooling Flows, and Grains in the Hot ISM

We adopt a King type model for the stellar distribution of the galaxy and a related distribution for the density of hot gas,

$$\rho_*(\xi) = \rho_{*o}(1+\xi^2)^{-\frac{3}{2}}, \quad \rho_g(\xi) = \rho_o(1+\xi^2)^{-\frac{3}{4}}; \quad \xi \equiv r/r_c \qquad (1)$$

where r_c is the core radius and both profiles are truncated at outer radius r_t or $\xi_t = r_t/r_c$. Using the fundamental plane relation for ellipticals (e.g. Djorgovski & Davis 1987), a mass to light relation, a core radius to light relation (Lauer 1989), and the core relation for isothermal spheres, we get a one parameter

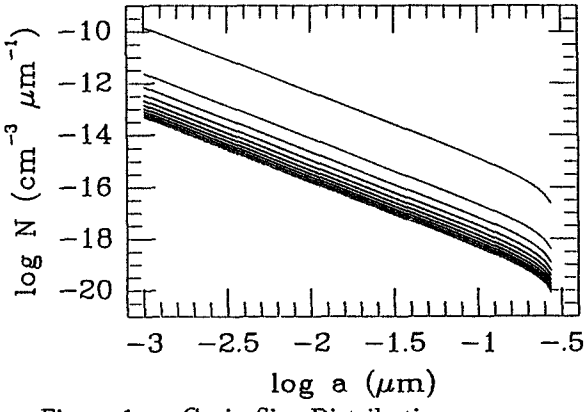

Figure 1. Grain Size Distributions

family of galaxy models given in Table 1. The gas density ρ_g is specified by

Table 1. Properties of the Galaxy Models.

Model	$L_B(10^{10}L_\odot)$	r_c(kpc)	r_t(kpc)	ρ_{*o}(g cm^{-3})	ρ_o(cm^{-3})	$\langle T_*\rangle(10^7$K)
a	10.6	0.774	123.	3.37×10^{-21}	0.145	0.922
b	3.31	0.192	76.4	3.86×10^{-20}	0.303	0.468
c	0.976	4.44×10^{-2}	44.4	5.18×10^{-19}	0.879	0.252

X–ray observations, the stellar temperature $\langle T_*\rangle$ (listed in Table 1) is derived by solving the equation of stellar hydrodynamics with a reasonable dark matter halo distribution. The temperature of the gas is assumed to be the same as $\langle T_*\rangle$. Flow velocities can be derived by solving the continuity equation for the hot ISM (see Tsai & Mathews 1994).

The grain content of the hot ISM is determined given the properties of the gas by solving the grain flow equation,

$$\frac{\partial N(r,a)}{\partial t}+\frac{\partial}{\partial a}\left[N(r,a)\frac{da}{dt}\right]+\vec{\nabla}\cdot[N(r,a)\,\vec{u}]=S(a,r) \qquad (2)$$

where N is the grain size distribution, a is the grainsize, $\dot{a}$ is the sputtering rate of grains in the hot gas, and S is the source of dust. We assume $S\propto a^{-3.5}$ and assume a minimum grainsize of 0.001μ and a maximum size of 0.3μ. Resulting grain size distributions for galaxy model a are shown in Figure 1. The topmost curve corresponds to the size distribution at the core radius r_c and the lower curves give the size distribution at larger radii in the galaxy. These results are the same as would be derived if *in situ* sputtering had been assumed.

3. Heating of Grains

Heating of the grains by ambient starlight can be computed using

$$H_* = \int \left(\frac{4\pi J_\nu}{c}\right) cQ_\nu \pi a^2 d\nu \tag{3}$$

where J_ν is the mean intensity of ambient starlight, Q_ν is the dust absorption efficiency and the integration is over optical and ultraviolet frequencies. Heating by hot electrons is computed using

$$H_e = \pi a^2 \left(\frac{\rho_g}{m_p}\right) \int_0^\infty E f(E) v(E) \zeta(E) dE \tag{4}$$

where E is the energy of the impinging particle, $v(E)$ is its velocity, and ρ_g is the gas density. The energy distribution of the electrons is Maxwellian, $f(E) = 2\pi^{-1/2}(kT)^{-3/2} E^{1/2} \exp(-E/kT)$, where T is the gas temperature and k is Boltzmann's constant. ζ gives the fraction of the energy of an incident electron that gets absorbed by the grain and is given by (Dwek & Werner 1981). Heating by thermal X–rays is also computed using eq. (3) above, but where J_ν is replaced by the mean intensity of thermal X–rays.

We find that H_* dominates that of the other sources by over an order of magnitude in all the galaxy models considered and for both silicate and graphite grains. We also compute the total rate of energy loss from the hot gas due to electronic heating by using the heating rate per grain of eq. (4). This mode of energy loss is about an order of magnitude less important than the rate of energy loss by emission of thermal X–rays. The presence of dust is therefore energetically unimportant for the theory of cooling flows. These results do not depend on the assumed grainsize distribution.

References

Bruzual, A. 1985, Rev. Mexicana Astr. Ap., 10, 55

Djorgovski, S., & Davis, M., 1987, ApJ, 313, 59

Dwek, E., & Werner, M. W. 1981, ApJ, 248, 138

Forbes, D. A. 1991, MNRAS, 249, 779

Ferguson, H. C. et al. 1991, ApJ, 382, L69

Jura, M. 1986, ApJ, 306, 483

Knapp, G. R., Guhathakurta, P., Kim, D. W., & Jura, M. 1989, ApJS, 70, 329

Lauer, T. R. 1989 in Dynamics of Dense Stellar Systems, ed. D. Merritt, (Cambridge: Cambridge University Press), 3

Loewenstein, M. & Mathews, W. G., 1987, ApJ, 319, 614

Mathews, W. G., 1989, AJ, 97, 42 Galaxies, ed. C. Chiosi, & A. Renzini, (Dordrecht: Reidel), 135

Sadler, E. M., & Gerhard, O. E. 1985, MNRAS, 214, 177

Trinchieri, G., Fabbiano, G., & Canizares, C. R., 1986, ApJ, 310, 637

Tsai, J. C. & Mathews, W. G. 1994, ApJ, submitted

Airborne Astronomy Symposium on the Galactic Ecosystem
ASP Conference Series, Vol. 73, 1995
M.R. Haas, J.A. Davidson, and E.F. Erickson (eds.)

Extragalactic Diffuse [CII] Emission

S. C. Madden

NASA Ames Research Center, MS 245-6, Moffett Field, CA 94035-1000

N. Geis and C. H. Townes

Department of Physics, University of California, Berkeley, CA 94720

R. Genzel, F. Herrmann, A. Poglitsch

Max-Planck Institut für Extraterrestrische Physik, D-85748, Garching, Germany

G. J. Stacey

Department of Astronomy, Cornell Univ., Ithaca, NY, 14853-6801

Abstract. The 158 μm [CII] line has been mapped in the galaxies Centaurus A, M83, NGC 6946, and NGC 891. The emission exists over very large scales, peaking in the nuclei and extending beyond the spiral arms and molecular disks. While most of the [CII] emission from the nuclei and spiral arms originates in photodissociated gas, the diffuse atomic gas can account for much of the [CII] emission in the extended regions.

1. Introduction

One of the most important cooling lines observed from the interstellar medium is the 158 μm $C^+ {}^2P_{3/2} - {}^2P_{1/2}$ fine structure line. This transition originates 91 K above the ground state and has a critical density of about 4000 cm^{-3} in neutral hydrogen gas. Since CI has an ionization potential of 11.3 eV, and carbon is one of the most abundant elements in the ISM, C^+ can be present in various phases of the ISM. It has been extensively observed in photodissociation regions (PDRs) associated with the surfaces of molecular clouds exposed to FUV radiation from embedded stars both in our Galaxy (Crawford *et al.* 1985, Howe *et al.* 1991; Shibai *et al.* 1991) and in the nuclei of external galaxies (Crawford *et al.* 1985; Stacey *et al.* 1991; Lord *et al.* 1994). More recently, it has been shown that C^+ line emission can also originate from the diffuse ISM as seen in the extended emission in the spiral galaxy, NGC 6946 (Madden *et al.* 1993) and in our Galaxy (Bennett *et al.* 1993; Bock *et al.* 1993).

We have been conducting a study of the distribution of C^+ emission over large scales in external galaxies using FIFI (Far-infrared Imaging Fabry-Perot Interferometer; Poglitsch *et al.* 1990, 1991; Stacey *et al.* 1993) from NASA's Kuiper Airborne Observatory (KAO). Here we present a summary of maps of

the 158 μm [CII] line emission in M83 (Geis *et al.* 1994), NGC 6946 (Madden *et al.* 1993), Centaurus A (Figure 1) and NGC 891 (Figure 2) (Stacey *et al.* 1994). Surveys of the nuclei of galaxies (Stacey *et al.* 1991; Lord *et al.* 1994) focus mainly on the photodissociated gas. Now it is possible to study the spatial distribution and physical properties of the far-infrared line emission in external galaxies not only in nuclei, but throughout and beyond galactic disks.

2. Interpretation of The Extended [CII] Emission

We find that the [CII] line luminosity represents 0.3 to 1% of the total FIR luminosity of these galaxies. In all of these galaxies, the [CII] emission peaks strongly toward the nuclei. The spatial coincidence with CO, FIR continuum and star formation regions suggests that PDRs are an origin of the [CII] emission in the nuclei. However, we find [CII] emission beyond the extent of the spiral arms as traced by the CO (1–0) line (see Madden *et al.* 1994). In most cases, the CO detections are quite weak or non-existent in the outer regions, resulting in an enhanced [CII]/CO intensity ratio - greater than that expected from PDRs.

The HI is more often correlated with the [CII] toward the outer regions of the galaxies. Since the [CII] in the extended component is associated with relatively large masses (on the order of at least 10^8 $M_\odot$, in some cases), we consider the excitation of [CII] from the atomic medium. We consider at first the various possibilities of the diffuse medium: the cold neutral medium (CNM) with temperatures ranging from 40 to 400 K, a warm neutral medium (WNM) of about 4000 to 8000 K and a warm ionized medium (WIM) of 8000 K (Kulkarni & Heiles 1987). The relative importance of these different processes depends on the fractional ionization, X_e. In our Galaxy, for example, X_e is thought to be $\sim 6 \times 10^{-4}$ in the CNM and $\sim 3 \times 10^{-2}$ in the WNM (Kulkarni & Heiles 1988).

If we assume that the atomic clouds in these galaxies have about the same range of kinetic temperatures as in the CNM in our Galaxy, we find a wide range of densities, but the pressures are better constrained, having values between 6×10^3 to 1×10^4 cm^{-3} K. This is consistent with the value of 8000 cm^{-3} K derived for the diffuse local interstellar medium of our Galaxy from ultraviolet C^0 measurements (Pottasch, Wesselius & van Duinen 1979).

If the [CII] intensity originates from a WNM, the excitation is dominated by electron impacts assuming the fractional ionization is greater than or about equal to 0.03, the value estimated for the WNM in our Galaxy (Kulkarni & Heiles 1988). The WNM probably does not explain a significant fraction of the observed [CII] intensity, unless the filling factor is quite small (< 0.1) (Madden *et al.* 1993)

The [CII] emission can also originate from the fully ionized interstellar medium. We can use the thermal component of the radio continuum observed in these galaxies to estimate the contribution to the [CII] emission from the ionized gas. If we assume 1) a solar fractional abundance of carbon, 2) all of the carbon is in the form of C^+ in these regions and 3) that the electron density is $<< n_{crit}$, we find that 30 to 50% of the [CII] emission in the extended regions can originate in the diffuse HII regions.

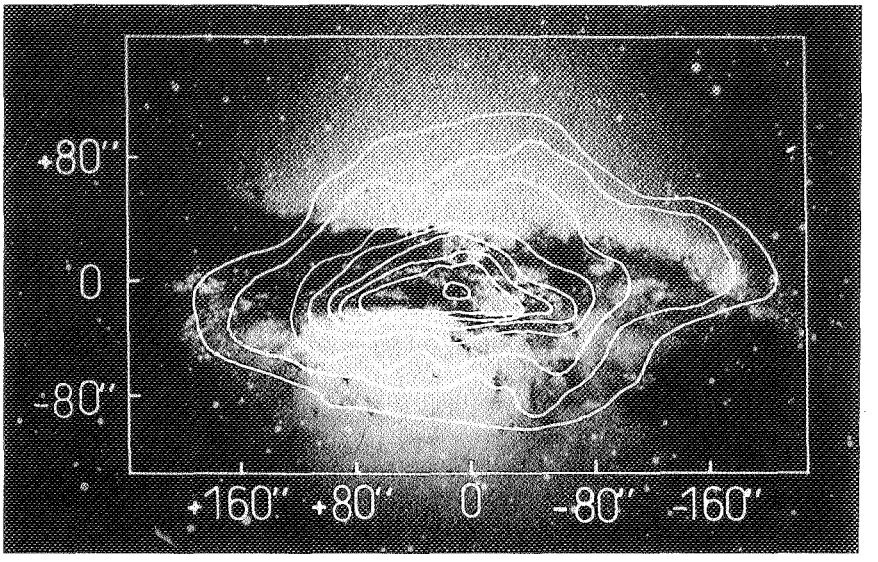

Figure 1. [CII] contours overlaid on an optical image of Centaurus A. The peak [CII] intensity is 2.8×10^{-4} erg s^{-1} cm^{-2} sr^{-1} and the lowest contour is 2.0×10^{-5} erg s^{-1} cm^{-2} sr^{-1}.

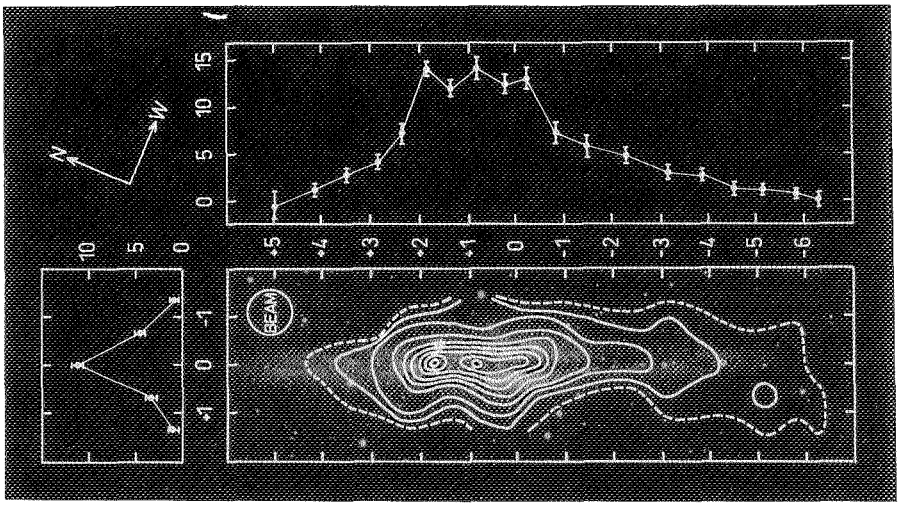

Figure 2. Integrated [CII] line intensity contours of NGC 891 shown on an optical image. The relative [CII] intensities are shown as cuts along the plane of the galaxy (top) and along the z axis perpendicular to the plane (left). The peak [CII] intensity is 1.4×10^{-4} erg s^{-1} cm^{-2} sr^{-1}.

3. Conclusion

From large scale maps of the 158 micron line in M83, NGC 6946, NGC 891 and Centaurus A, we find that the [CII] emission is not only concentrated in the PDR regions in the nucleus and spiral arms, but extends beyond the spiral arms/molecular disk originating in the atomic medium. The [CII] emission can arise from cold (T~100 K), neutral hydrogen clouds. Low density HII regions could also account for 30 to 50% of the [CII] emission.

References

Bennett, C. L. & Hinshaw, G. 1993, in Back to The Galaxy, ed. A. Holt & F. Verter, (AIP: NY), 257

Bock, J. J. *et al.* 1993, in Back to The Galaxy, ed. A. Holt & F. Verter, (AIP: NY), 299

Crawford, M. K., Genzel, R., Townes, C. H. & Watson, D. M. 1985, ApJ, 291, 755

Geis, N. *et al.* 1994, in preparation

Howe, J. E., Jaffe, D. T., Genzel, R. & Stacey, G. J. 1991, ApJ, 377, 192

Kulkarni, S. & Heiles, C. 1987, in Interstellar Processes, ed. D. J. Hollenbach & H. A. Thronson, (Reidel: Dordrecht), 87

Kulkarni, S. & Heiles, C. 1988, Galactic and Extragalactic Radio Astronomy, ed. G. Verschuur & K. Kellerman, (Springer-Verlag), 95

Lord, S. D. *et al.* 1994, in Proc. of the Airborne Astronomy Symp on the Galactic Ecosystem: From Gas to Stars to Dust, ed. M. R. Haas, J. A. Davidson & E. F. Erickson, (San Francisco: ASP), paper 2.2

Madden, S. C. *et al.* 1993, ApJ, 407, 579

Madden, S. C. *et al.* 1994, IR Phys. & Tech., 35, 311

Poglitsch, A. *et al.* 1990, in Proceedings of the 29th Lige International Astrophysics, ed. B. H. Kaldeich, ESA SP-314

Poglitsch, A. *et al.* 1991, Int. J. of IR. & MM. Waves, 12, 859

Pottasch, S. R., Wesselius, P. R. & van Duinen, R. J. 1979, A&A, 74, L15

Shibai, H. *et al.* 1991, ApJ, 374, 522

Stacey, G. J. *et al.* 1991, ApJ, 373, 423

Stacey, G. J. *et al.* 1993, Int. J. of IR & MM Waves, 13, 1689

Stacey, G. J. *et al.* 1994, in preparation

Airborne Astronomy Symposium on the Galactic Ecosystem
ASP Conference Series, Vol. 73, 1995
M.R. Haas, J.A. Davidson, and E.F. Erickson (eds.)

Too Much Carbon in NGC253

Andrew Harrison and Peter Brand
University of Edinburgh, Blackford Hill, Edinburgh EH9 3HJ

Phil Puxley and Adrian Russell
Royal Observatory, Blackford Hill, Edinburgh EH9 3HJ

Abstract. We have observed C^0 across the nucleus of the starburst galaxy NGC253. C^0 is very bright and we find $N(C^0)/N(CO)$ is between 1.5 and 2.3 across the nucleus. Existing PDR models cannot explain the observed C^0 intensity. The size of the observed region seems to rule out "simultaneous very early time chemistry" across the nucleus. Chemical models in which C^0/CO is enhanced deep in molecular clouds by large fluxes of cosmic rays also struggle to explain our observations. The most plausible explanation for the observed C^0 is that the C/O elemental ratio is enhanced in NGC253.

1. Introduction

NGC253 is a nearby, highly inclined spiral galaxy, and along with M82 has become an archetypal starburst (e.g., Carral *et al.* 1994). We have mapped the

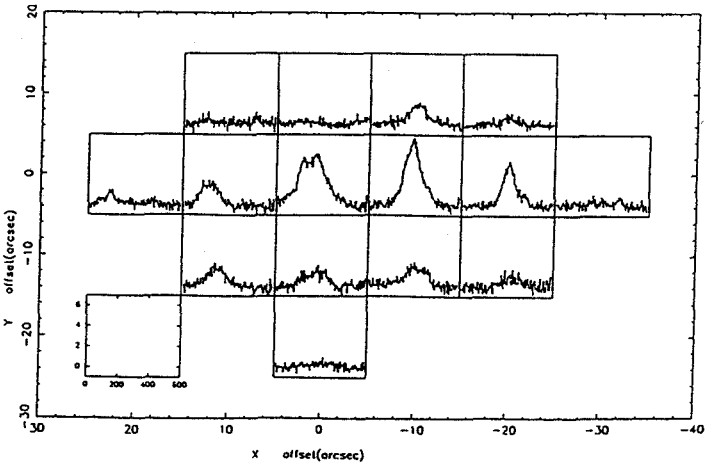

Figure 1. Rotated R.A.-Dec map at P.A. 53.1° of the 15 [CII] spectra observed towards the nuclear region of NGC253, shown on a T_R scale. The map centre (0,0) is at $\alpha(1950)=0^h45^m0.58^s$, $\delta(1950)=-25°33'38''$.

central 500 pc of NGC253 in the $^3P_1 \rightarrow ^3P_0$ line of neutral carbon [CI]. Theoretical models of photon dominated regions (PDRs) predict that the majority of [CI] should arise from a thin layer of gas at the edges of the clouds, typically at a few A_v (Hollenbach *et al.* 1991).

2. C^0/CO Ratio in NGC253

C^0 shows a similar distribution to the CO bar (Canzian *et al.* 1988) and shows that the C^0 and CO are tracing the same gas (*i.e.*, the atomic gas is well mixed with the molecular gas). Across the $40'' \times 10''$ bar we find $N(C^0)=5.8 \times 10^{18}$ cm^{-2}. Assuming $^{12}C/^{13}C \sim 40$ (Henkel *et al.* 1993), the $^{13}CO(3\text{-}2)$ observation of Wall *et al.* (1991) gives $N(C^0)/N(CO)=1.54$ across the central $15''$. Assuming $^{18}O/^{16}O \sim 200$ (Henkel *et al.* 1993), the $C^{18}O$ $(2\rightarrow1)$ observation made by Sage *et al.* (1991) with a $13''$ beam gives $N(C^0)/N(CO)=2.4$. Henkel *et al.* (1993) argue that chemical fractionation and selective photodissociation are small effects in NGC253.

3. Existing PDR Models Cannot Explain C^0 in NGC253

Carral *et al.* (1994) modelled the nucleus of NGC253 in terms of a population of $n=10^4$ cm^{-3}, $G_0=10^4$ PDRs filling the beam with a factor of order unity. The intensity of atomic carbon in such a PDR is predicted by Hollenbach *et al.* (1991) to be $\sim 2 \times 10^{-6}$ erg cm^{-2} s^{-1} sr^{-1}. However, we find across the $40'' \times 10''$ bar, $< I_{CI} > \sim 5 \times 10^{-5}$ erg cm^{-2} s^{-1} sr^{-1}, a factor ~ 30 greater than predicted.

It is possible to make [CI]/[CII] and [OI]/[CII] consistent with a PDR origin for [CI] in two ways, either by reducing the density of the PDR gas or by lowering the UV field. Both ways result in much less [OI] and [CII] being produced, but have little effect on the [CI]. However, [OI] drops off much more dramatically than the [CII]. Since shocks result in [OI]/[CII]>1 (Hollenbach & McKee 1989), by having an ensemble of PDRs and shocks, with large filling factors, ~30, we can make I[CII]/I[CI] and I[OI]/I[CII] consistent with observations and the PDR models of Hollenbach *et al.* (1991). Unfortunately, changing either the density or the UV field of the PDR result in conflicts with the PDR model predictions and other observations.

Reducing the UV field results in large pressure differentials between different components of the ISM, too much CO $(1\rightarrow0)$ emission and requires that the UV flux from OB stars only plays a minor role in heating the dust (Telesco & Harper 1980). Reducing the density of the PDRs results in the production of more H^0 than is observed, as well as producing large pressure differentials between different components of the gas. There is also little observational evidence for such a major component of diffuse gas. It is only at low densities or at low UV fields that I[OI] and I[CII] are low enough to make the O^0, C^+ and C^0 consistent with each other. Hence intermediate densities and UV fields are also ruled out. The C^0 emission we have detected is inconsistent with the models of Hollenbach *et al.* (1991), so we have to look for a non-PDR origin for the C^0 emission in NGC253.

4. The Diffuse Gas Only Plays a Minor Role in Producing C^0 in NGC253

In the Galactic cold diffuse ISM the gas is mainly atomic and $C^0/CO > 1$ for $A_v < 1$ (Keene 1990). Thus a possible explanation for our observed C^0/CO value is to postulate a population of cold diffuse clouds in the starburst nucleus which gives rise to most of the C^0 emission. A difficulty with this picture is that the ISM in NGC253 is at high pressure ($\sim 5 \times 10^6$ K cm^{-3} (Carral *et al.* 1994) and thus, if we have to postulate the existence of diffuse clouds of n $\sim$ 40 cm^{-3}, these clouds must be unreasonably hot ($\sim 10^5$ K where both hydrogen and carbon will be readily ionised).

The observed Lyman continuum photon luminosity is 2×10^{53} s^{-1} in NGC253 (Beck & Beckwith 1984) and the effective temperature of the ionising stars is $\sim$ 35,000 K (Carral *et al.* 1994). If we postulate a component of diffuse gas (n = 10^2 cm^{-3}) at T$\sim$ 5000 K and we require that only 10% of the carbon ionising photons actually ionise carbon, n_{c^0}/n_{c^+} is less than 0.1. Assuming a C/H abundance ratio of 3.3×10^{-4} (Keene 1990), $N_{H^0} = 1.3 \times 10^{22}$ cm^{-3} (Combes *et al.* 1977), and n_{C^0}/n_{C^+} $\sim$0.1, N(C^0)=4.3×10^{17} cm^{-2}, which is a factor of 10 smaller than the [CI] observation. Thus, diffuse gas may provide, at the most, a 10% contribution to the [CI] emission. Furthermore, Wall *et al.* (1991) argue that towards the nucleus virtually all the CO arises from dense (n $\sim 10^{4-5}$ cm^{-3}) molecular gas.

5. Enhanced Cosmic Ray Fluxes Cannot Explain C^0 in NGC253

Schilke *et al.* (1993) and White *et al.* (1994) explained the large C^0 abundance in M82 in terms of chemical models, outlined by Flower *et al.* (1994), in which a high cosmic ray flux (300 times the local value) produces large amounts of carbon deep in clouds. $C^0/CO \sim 1.5$ in NGC253, a factor of $\sim$ 2 greater than M82.

Since the far-IR luminosities from the central $\sim$ 400 pc of the two galaxies are comparable (M82: $3 \times 10^{10} L_\odot$; NGC253: $1.5 \times 10^{10} L_\odot$, Telesco & Harper 1980) then, if they have similar IMFs, the star-formation, and hence supernova, rates will be comparable. Jackson *et al.* (1994) argue that the molecular gas in NGC253 is an order of magnitude more dense than the molecular gas in M82. It seems very unlikely that the expected CR flux (200-300 times the local solar neighbourhood value) in NGC253 impinging on dense gas (10^5 cm^{-3}) can perturb the chemistry enough to account for C^0/CO being >1. Also, because the gas is denser in NGC253 than in M82, the models of Flower *et al.* (1994) predict that C^0/CO should be greater in M82 than NGC253, contrary to what is observed.

C^0/CO is $\sim$ 1.3 - 2.9 toward the C-shocked gas of IC443(C2) (White 1994). The SN remnants in NGC253 are within $\sim$ 100 pc of the nucleus (Ulvestad & Antonucci 1994). Localised SNRs would be expected to cause a local change in C^0/CO, but we find that C^0/CO is fairly uniform across a region $\sim$ 500 pc, far larger than would be expected if SNRs are causing the C^0 to be enhanced.

6. Chemical and Elemental Explanations

Time-dependent chemical models (Leung *et al.* 1984) show that at early times, *i.e.* $<10^5$ yrs, large amounts of neutral C^0 exist and yield a C^0/CO ratio greater than unity. Another explanation for the observed [CI] in NGC253 is that the elemental abundances are not identical in NGC253 and M82, with C/O enhanced in NGC253, possibly due to a different stellar mass and star formation history (Henkel & Mauersberger 1993). It is very hard to distinguish between early-time chemistry and a high C/O elemental ratio, as both models produce similiar chemical abundances (e.g., molecules that are carbon-rich). However, in order for the C^0/CO ratio in NGC253 to be explained by early time chemistry, we must be seeing a snapshot of NGC253 when the chemistry has been perturbed almost simultaneously (to within 10^5 years) across the whole of the nuclear region (500 pc), which seems unrealistic. Hence, the only plausible explanation we are left with to explain our observations of C^0 in NGC253 is to invoke an enhanced C/O elemental ratio in the starburst region.

References

Beck, S.C., & Beckwith, S.V. 1984, MNRAS, 207, 671

Canzian, B., Mundy, L.G., & Scoville, N.Z. 1988, ApJ, 333, 157

Carral, P., Hollenbach, D.J., Lord, S.D., Colgan, S.W.J, Haas, M.R., Rubin, R.H., & Erickson, E.F. 1994, ApJ, 423, 223

Combes, F., Gottesman, S.T., & Weliachew, L. 1977, A&A, 59, 181

Flower, D.R., Le Bourlot, J., Pineau des Forêts, G., & Roueff, E. 1994, A&A, 282, 225

Henkel, C., & Mauersberger, R. 1993, A&A, 274, 730

Henkel, C., Mauersberger, R., Wiklind, T., Hüttemeister, S., Lemme, C., & Millar, T.J. 1993, A&A, 268, L17

Hollenbach, D.J., & McKee, C.F. 1989, ApJ, 342, 306

Hollenbach, D.J., Takahashi, T., & Tielens, A.G.G.M. 1991, ApJ, 377, 192

Jackson, J.M., Paglione, T.A.D., Carlstrom, J.E., & Nguyen-Q-Rieu 1994, Boston preprint

Keene, J., 1990, in *Carbon In The Galaxy: Studies From Earth & Space*, eds. Tarter, J.C., Chang, S., & Defrees, D.J. (NASA CP-3061), 181

Leung, C.M., Herbst, E., & Heubner, W.F. 1984, ApJS, 56, 231

Sage, L.J., Mauersberger, R., & Henkel, C. 1991, A&A, 249, 31

Schilke, P., Carlstrom, J.E., Keene, J., & Philips, T.G. 1993, ApJ, 417, L67

Telesco, C.M., & Harper, D.A. 1980, ApJ, 235, 392

Ulvestad, J.S., & Antonucci, R.R. 1994, ApJ, 424, L29

Wall, W.F., Jaffe, D.T., Israel, F.P., & Bash, F.N. 1991, ApJ, 380, 384

White, G.J. 1994, QMWC preprint

White, G.J., Ellison, B., Claude, S., Dent, W.R.F., & Matheson, D.N. 1994, A&A, 284, L23

Airborne Astronomy Symposium on the Galactic Ecosystem
ASP Conference Series, Vol. 73, 1995
M.R. Haas, J.A. Davidson, and E.F. Erickson (eds.)

The Far-Infrared Distribution in the 'Dusty Hand' Galaxy NGC 2146

Beverly J. Smith, P. M. Harvey, and D. F. Lester

Astronomy Department, University of Texas, Austin TX 78712

Abstract. Our high spatial resolution 50 and 100 μm observations of the peculiar galaxy NGC 2146 show that the FIR emission arises in a $21'' \times \leq 16''$ (1.5 kpc $\times \leq$1.1 kpc) region (FWHM) elongated along the major axis. This size limit is similar to that of the radio continuum, the ^{12}CO (1 – 0), and the Hα. From an investigation of the energetics in this galaxy, we conclude that young massive stars are largely responsible for powering the FIR luminosity of this galaxy.

The FIR and CO (1 – 0) distributions differ from the extinction morphology as seen in optical images and in the Brγ/Hα ratio. The starlight and the ionized gas are most highly reddened at the prominent dust lane 15″ to the west of the nucleus, while the CO and FIR emission peak near the nucleus. This result can be explained by either a high proportion of cold dust and gas at the dust lane, or a geometry in which the dust lane lies in front of the main body of the galaxy.

1. Introduction

NGC 2146 is a morphologically peculiar Sb galaxy, with a 'hand-shaped' dust lane silhouetted across the bulge (Pease 1920) and a disturbed outer disk (Benvenuti et al. 1975). Maps of NGC 2146 in the 21 cm HI line show a long tidal tail extending 150 kpc from the galaxy (Glendenning & Kronberg 1986), while Hα observations reveal the presence of a long arc of HII regions in the outer disk (Young et al. 1988a). These HII regions have discrepant velocities relative to the disk, implying non-planar orbits or high radial motions (Young et al. 1988a). This galaxy is likely the remnant of the merger between two galaxies (Hutchings et al. 1990).

NGC 2146 is currently undergoing a strong starburst, with an HII region-like optical spectrum (Keel 1984), and high Hα (Young et al. 1988b), Brγ (Hutchings et al. 1990), and radio continuum (Kronberg & Biermann 1981) luminosities. NGC 2146 also has a moderately high FIR luminosity of 4.1 $\times$ 10^{10} L$\odot$ (H_o = 75 km s^{-1} Mpc^{-1}).

We have used the Kuiper Airborne Observatory to make high spatial resolution 50 and 100 μm observations of this galaxy. A more detailed account of this investigation is presented in Smith, Harvey, and Lester (1994).

2. Observations

NGC 2146 was observed with the KAO at 50 and 100 μm on 1990 August 30, using the University of Texas 2 $\times$ 10 channel bolometer array. At 100 μm, the separation between the 2 banks of detectors is 28″ and the separation between the detectors in a bank is 13″.8. At 50 μm, the bank separation is 18″ and the detector spacing in a bank is 7″.0. The 100 and 50 μm beamsizes are 31″ $\times$ 41″ and 18″ $\times$ 25″, respectively, with higher resolution along the longer array axis.

For the NGC 2146 observations, the array was aligned along the major axis of the galaxy. For calibration, the point source objects Hygeia and IRC +10420 were also observed on this flight.

3. Data

Figures 1 and 2 show our 50 and 100 μm results, respectively, for NGC 2146 compared to the point source objects. Figures 1a and 2a show the data for the northern bank of detectors, which crosses the galaxy very close to the nucleus. These data demonstrate that NGC 2146 is resolved at both wavelengths along the major axis. At 50 μm, the observed FWHM of NGC 2146 is 26″ $\pm$ 2″, compared to 18″ $\pm$ 3″ for the point source objects. At 100 μm, the measured FWHM of NGC 2146 is 40″ $\pm$ 5″, compared to 31″ $\pm$ 5″ for Hygeia and IRC +10420. Gaussian deconvolutions give an intrinsic FWHM of 19″ $\pm$ 4″ (1.3 $\pm$ 0.3 kpc) at 50 μm for NGC 2146, and 25″ $\pm$ 7″ (1.7 $\pm$ 0.5 kpc) at 100 μm. In Figure 2a, the 50 μm data, smoothed to the resolution of the 100 μm data, are also displayed. These comparisons show that the 50 and 100 μm distributions agree within our uncertainties.

There is no evidence for extension along the minor axis of the galaxy; the flux observed in the second bank of detectors (Figures 1b and 2b) relative to the peak brightness is the same for the galaxy and the two point source objects at both wavelengths. Assuming symmetry along the minor axis, the FWHM of the 50 μm source in this direction is $\leq$16″ (1.1 kpc). Therefore the FIR emission from NGC 2146 is elongated along the major axis.

The KAO 50 and 100 μm flux densities for NGC 2146 are 123 Jy and 180 Jy, respectively, in agreement with those found by IRAS (Young et al. 1989). Therefore most of the total FIR luminosity of NGC 2146 is arising within the area we have observed.

4. Comparison with Other Wavelength Data

The 50 and 100 μm maxima are coincident, within our positional uncertainty ($\sim$10″), with those in the radio continuum (Condon et al. 1982), CO (1 - 0) (Young et al. 1988a; Jackson & Ho 1988), Hα (Young et al. 1988b), and the optical continuum (Young et al. 1988a), which lie within 5″ of each other. Smoothing the CO (1 $-$ 0) data (Jackson & Ho 1988), the Hα image (Young et al. 1988a,b), and the 20 cm radio continuum map (Glendenning 1994; private communication) to the 50 μm resolution, we find that the 50 μm distribution is similar to that in the CO and the radio continuum, while the observed Hα distribution is slightly more extended (Smith et al. 1994). The difference between

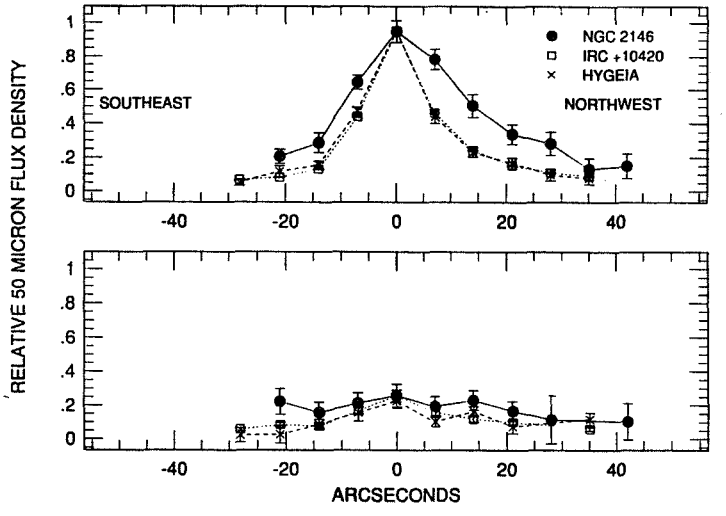

Figure 1. The 50 μm data. The top panel (1a) shows the data for the northern bank of detectors, while the lower panel (1b) displays the data for the second bank. For NGC 2146, the peak flux density is 76 Jy beam^{-1}. Along the x-axis, the offset from the Hα maximum is given.

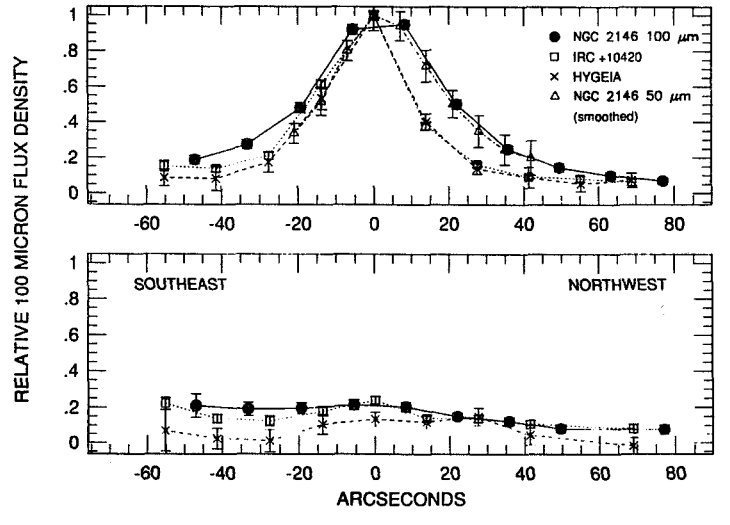

Figure 2. The 100 μm data. The top panel (2a) shows the data for the northern bank of detectors, while the lower panel (2b) displays the data for the second bank. For NGC 2146, the peak flux density is 105 Jy beam^{-1}. The 50 μm data points, smoothed to the 100 μm resolution, are also displayed in Figure 2a.

the FIR and the Hα distributions is consistent with the observed extinction (see Section 6). Thus we conclude that the FIR emission traces the star formation morphology in this galaxy.

5. What Powers the Far-Infrared Luminosity?

Do OB stars power the FIR luminosity of NGC 2146? L(FIR)/L(Hα) is 1,400, which after correction for extinction yields a ratio of $40 - 90$, consistent with that expected for young stars (Devereux & Young 1990). The extinction ($A_V = 4 - 5$) was obtained by several methods: the Hα/Hβ and Brγ/Hα ratios, the optical colors, the thermal radio continuum/Hα ratio, CO $(1 - 0)$ measurements, and the FIR data. All of these methods have reasonably large uncertainties (see Smith et al. 1994), however, the good agreement makes us confident that we are not significantly overestimating the number of young stars. Therefore, there *are* sufficient OB stars in NGC 2146 to account for the FIR luminosity.

Are non-ionizing stars also important in powering the FIR luminosity? From the V magnitude and stellar population synthesis models of galaxian bulges (Pritchet 1977), we find that $L_{BOL}^{old} \sim L_{BOL}^{young}$, so the amount of energy available from lower mass stars is the same as from hot young stars. However, OB stars are more efficient in dust heating because they are bluer (heating efficiency $\propto \lambda^{-1}$), and also, they tend to be in closer proximity to molecular clouds. Therefore, we conclude that OB stars dominate dust heating in this galaxy.

Another possible dust heating source, an AGN, is ruled out by the large extent of the FIR emission and the lack of an AGN signature in the optical and near-infrared spectra (Keel 1984; Hutchings et al. 1990).

6. The Dust Morphology

The FIR distribution in NGC 2146 is similar to that seen in CO $(1 - 0)$ (Section 4), however, it differs from the reddening morphology. The FIR and CO peak near the nucleus, which lies near the eastern edge of the dust lane (Young et al. 1988a). In contrast, the reddening seen in optical broadband images (Benvenuti et al. 1975; Hutchings et al. 1990) and Brγ/Hα is highest at the center of the dust lane, $\sim 15''$ to the west of the FIR peak.

One possible explanation for this effect is that the CO and FIR data may not trace the distribution of dust, if a higher proportion of the dust and gas at the lane is cold compared to near the nucleus. A second possibility is that the dust in the 'hand' lies in front of the star forming regions, while in the rest of the galaxy, the stars, dust, and ionized gas are more mixed. To test these possibilities, high spatial resolution submillimeter and millimeter continuum and line studies would be useful.

References

Benvenuti, P., Capaccioli, M., & D'Odorico, S. 1975, A&A. 180, 27
Devereux, N. A., & Young, J. S. 1990, ApJ, 350, L25
Glendenning, B. E., & Kronberg, P. P. 1986, BAAS, 18, 1006
Hutchings, J., Neff, S., Stanford, S., Lo, E., and Unger, S. 1990, AJ, 100, 60
Jackson, J. M., & Ho, P. T. P. 1988, ApJ, 324, L5
Keel, W. C. 1984, ApJ, 282, 75
Kronberg, P. P., & Bierman, P. 1981, ApJ, 243, 89
Pease, F. G. 1920, ApJ, 51, 276
Pritchet, C. 1977, ApJS, 35, 397
Smith, B. J., Harvey, P. M., and Lester, D. F. 1994, ApJ, submitted
Young, J. S. et al. 1988a, ApJ, 331, L81
Young, J. S., Kleinmann, S., & Allen, L. 1988b, ApJ, 334, L63
Young, J. S., Xie, S., Kenney, J. D. P., & Rice, W. L. 1989, ApJS, 70, 699

Allan Meyer

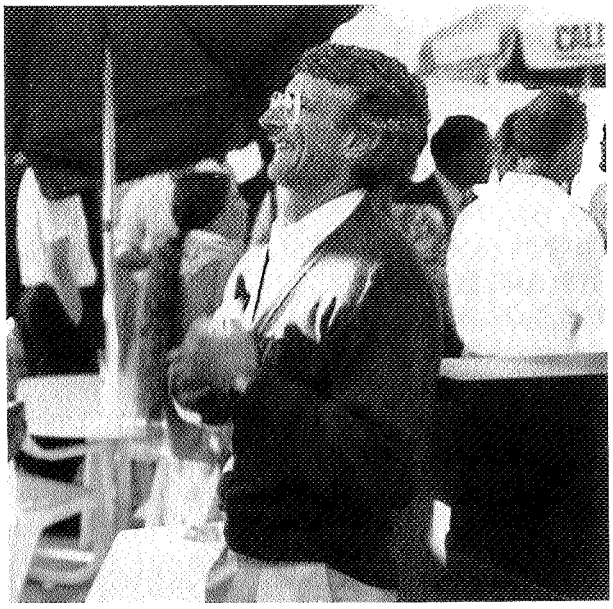

Neal Evans

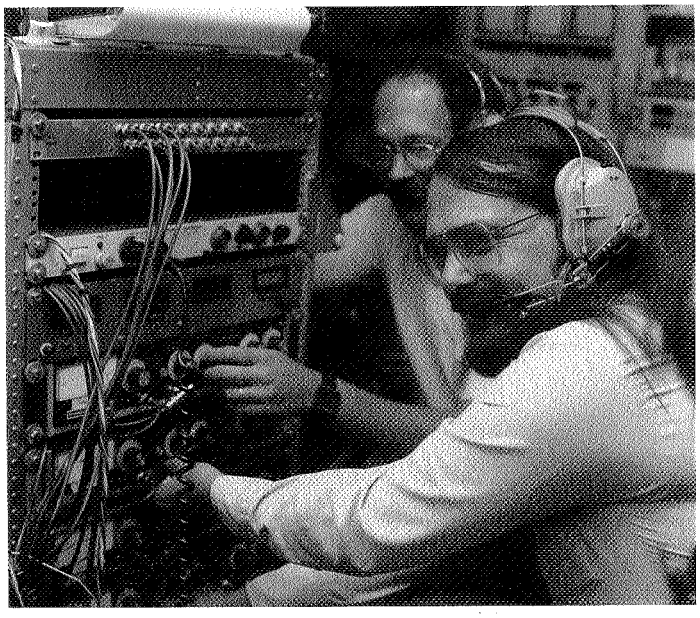

Paul Harvey, Marshall Joy (1986)

Airborne Astronomy Symposium on the Galactic Ecosystem
ASP Conference Series, Vol. 73, 1995
M.R. Haas, J.A. Davidson, and E.F. Erickson (eds.)

An Infrared Imaging Study of Galaxies in the Local Universe

Albert D. Grauer
University of Arkansas at Little Rock and Steward Observatory, University of Arizona

Marcia J. Rieke and Kim K. McLeod
Steward Observatory, University of Arizona

Abstract. This poster was a preliminary report on a survey of galaxies in the local universe at J and K using a NICMOS3 256 × 256 infrared photometric camera attached to the 61 inch telescope on Mt. Bigelow. Deep images are being obtained for a representative sample of galaxies in the Uppsala General Catalogue. Structural and color parameters are determined for a wide variety of galactic types. These data should prove to be valuable in characterizing stellar populations within disks and bulges, determining if IR-active galaxies have unusual global as well as nuclear properties, and understanding the effects of evolution and redshift dimming in distant galaxies.

This work was supported by:

Arkansas Space Grant Consortium
Research Corporation (Award C-3683)
National Science Foundation (AST-9116442)

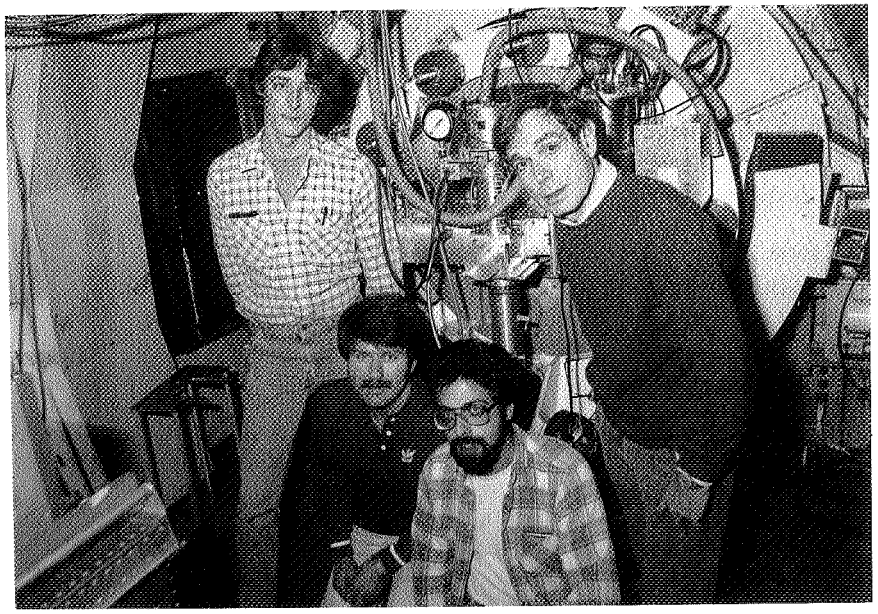

Chuck Fuller, Gordon Stacey, Paul Viscuso, Martin Harwit (1984)

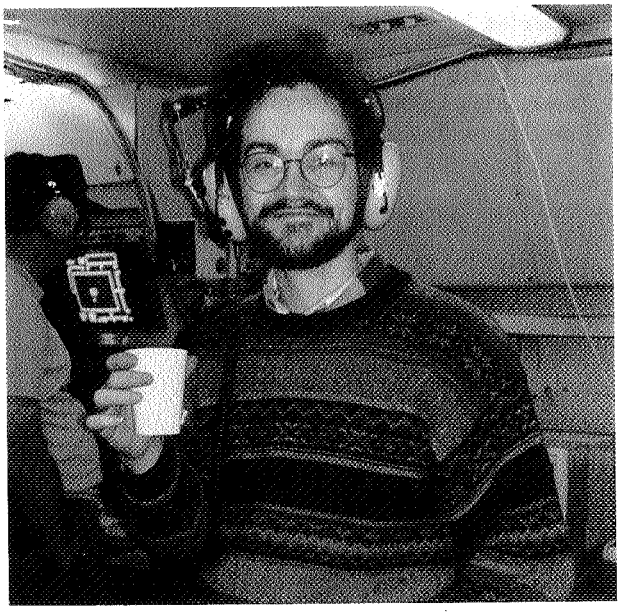

Chris Skinner

Airborne Astronomy Symposium on the Galactic Ecosystem
ASP Conference Series, Vol. 73, 1995
M.R. Haas, J.A. Davidson, and E.F. Erickson (eds.)

The Application of Infrared Speckle Interferometry to the Imaging of Remote Galaxies and AGN

Robert O. Olivares
Henri Poincaré Institute, Laboratory of Cosmology, CNRS, Paris, France

Abstract. A 1.5 meter reflector, used for both infrared and optical astronomy, is also being used for infrared speckle interferometry and CCD imaging. The application of these imaging techniques to remote galaxies and active galactic nuclei are discussed. A simple model for the origin of speckle in coherent imaging systems is presented. Very careful photometry of the continuum of the galaxy M31 is underway using CCD images. It involves extremely intensive data reduction because the object itself is very large and has low surface brightness.

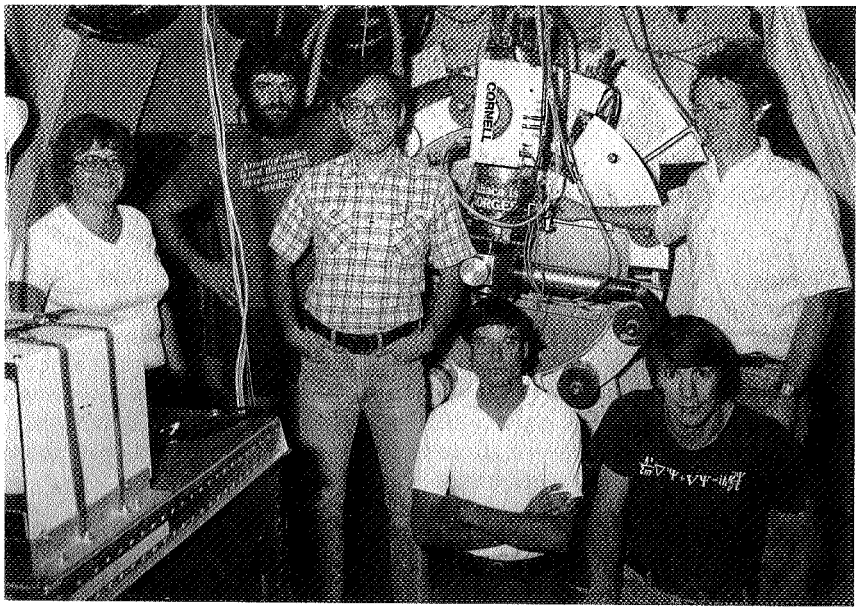

Judy Pipher, George Gull, Dan Briotta,
Mark Shure, Terry Herter, Jim Houck (1981)

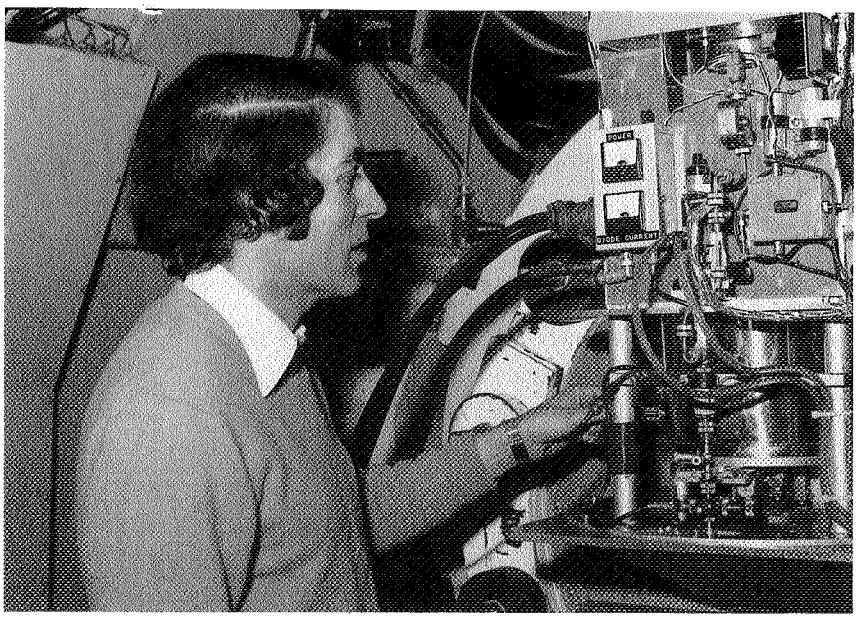

Tom Phillips (1979)

Airborne Astronomy Symposium on the Galactic Ecosystem
ASP Conference Series, Vol. 73, 1995
M.R. Haas, J.A. Davidson, and E.F. Erickson (eds.)

KAO 60-Micron Imaging Observations of Galaxies with Active Star Formation

Zhong Wang

MS-66, Smithsonian Astrophysical Observatory, Cambridge, MA 02138

George Helou and Nanyao Lu

100-22 IPAC, California Institute of Technology, Pasadena, CA 91125

David Cole

Dept. of Astron. & Astrophys., Univ. of Chicago, Chicago, IL 60637

Abstract. We have carried out 60 μm imaging observations of a sample of nearby, far-infrared bright galaxies, using the Yerkes infrared camera aboard the KAO. A total of eleven galaxies have been observed, most of which are actively star-forming, barred spirals. In this contribution we present our first set of observations on four galaxies: NGC 4102, NGC 4536, NGC 5962, and NGC 6181.

1. Introduction

Among the tens of thousands of galaxies that appear in the IRAS Sky Survey, those selected as the brightest ones in the far-infrared (FIR) are predominantly active, star-forming galaxies (Soifer *et al.* 1987). Since the FIR energy output is a significant, and sometimes dominant contributor to the bolometric luminosity, it is of considerable interest to investigate the origin and distribution of the bulk FIR emission in galaxies.

A closely related issue is the connection between the FIR and radio emissions and their spatial distributions. Having a clearly non-thermal origin, the radio continuum of a galaxy bears no apparent relationship to its FIR radiation which is mostly thermal. Yet FIR and radio flux densities are two of the best correlated global quantities in various galaxy samples (e.g., Helou *et al.* 1985; Condon *et al.* 1991). Is this correlation a mere coincidence having to do with the scale size of galaxies, or do these two quantities simply measure different aspects of the same phenomenon?

If the radio and FIR emitting regions are co-extensive, then a straightforward size measurement from radio continuum maps can be used to gauge the number of FIR photons produced per unit disk area. This so-called *equivalent FIR surface brightness* would serve as an indicator of the intensity at which stars are formed in the disk. Obviously, a better understanding of the origin of the emissions would hinge on our being able to map the galaxies in the FIR. However, except for a few cases, direct FIR imaging of galaxies has not been

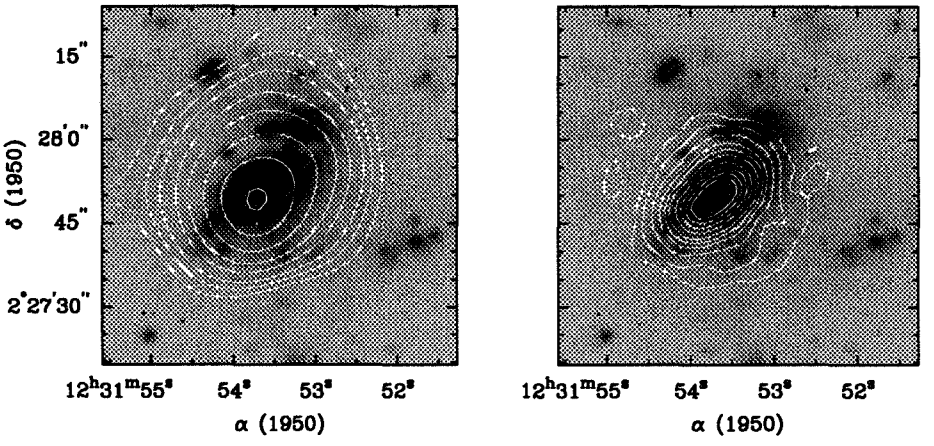

Figure 1a – Comparing the FIR (60 μm) contour map (left) with the radio continuum (VLA B-array at 1.49 GHz) map (right) for the central region of the barred spiral galaxy NGC 4536. The KAO data was obtained with the 60-element IRcam array, and has been smoothed to a 23″ beam. The greyscale image (same for both left and right maps) shows the continuum-subtracted Hα emission of the galaxy.

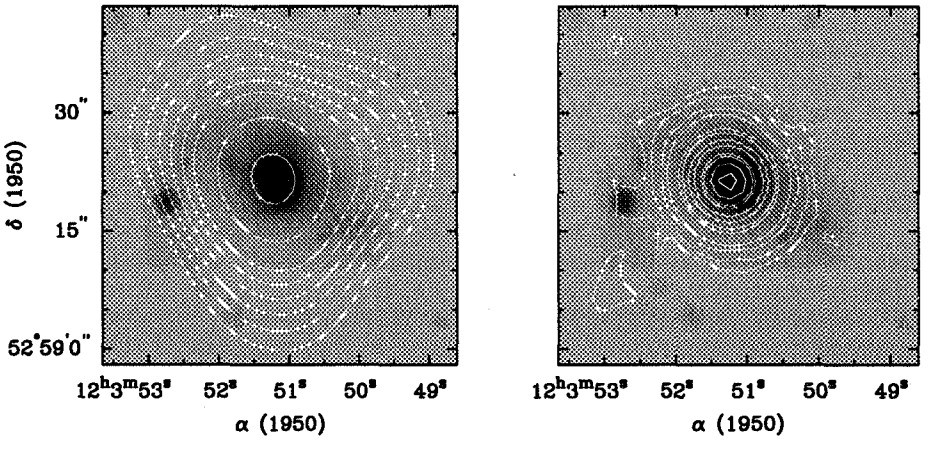

Figure 1b – Same as above, but for NGC 4102. KAO 60 μm contours are on the left, while the VLA radio continuum contours are on the right. This galaxy is only marginally resolved at 60 μm.

done. The present KAO observations are an attempt to provide answers to some of the questions above.

2. Target Selection and Observation

All of the galaxies selected are from the IRAS Bright Galaxy Sample (Soifer *et al.* 1987), and have: (a) a high *effective* FIR surface brightness, as measured by L_{FIR}/A_{eff}, where L_{FIR} is the far-infrared luminosity, while A_{eff} is the emitting area derived from radio continuum (VLA) maps made at 1.49 GHz (Condon *et al.* 1990); and (b) a radio continuum angular size of less than 2′, to fit in the limited field of view of the Yerkes Camera. All galaxies observed are unresolved sources in the coadded IRAS Sky Survey maps.

NGC 5962 and NGC 6181 were observed in 1991 with a 32-element camera at an effective resolution of 45″. NGC 4102 and NGC 4536 were observed in 1992 with the newer 60-element camera at a much improved $\sim$ 15″ resolution. Results for the latter two are shown in Figure 1. (7 more galaxies were observed in our 1994 run with the new camera and the data will be presented elsewhere).

To achieve better spatial sampling and reduce map noise, a standard "eight-point mapping" scheme was used, and the result is a map smoothed to approximately the beam resolution after noise rejection. The typical integration time is 25 minutes per map, and two or more maps were made for each galaxy. Flux calibration was determined by observing standard sources Vesta and Callisto. Detector-to-detector gain variations were measured by scanning a bright, extended source in two perpendicular directions over all array elements.

3. Summary of Results

All four galaxies are clearly detected at 60 μm. We find that most of the emission appears to be well concentrated within the galactic center region (see Fig. 1), despite the non-axisymmetry created by the presence of stellar bars. The relative flux density measurements are consistent with the values determined by IRAS. A typical radial scale for the FIR regions is only 1–2 kpc (FWHM).

The FIR emission contours of the galaxies show remarkable similarity to their radio counterparts (e.g., VLA B-array continuum maps at 1.49 GHz), although they are less well resolved due to the relatively large beam. However, careful deconvolution and fitting of the profiles show that the FIR emitting regions are of similar sizes or slightly smaller than the angular scales of the radio emitting regions.

Some slight asymmetry in the distribution of FIR emission appears to trace the extension of the stellar bar. However, the actual elongation of FIR contours is less extended than that of the bar itself, which can be seen, for example, in the corresponding H_α images.

A good example is the bar galaxy NGC 4536, as shown in Figure 1a. At 60 μm (white contours in map on the left), this galaxy is clearly resolved along its major axis (P.A. = 137°), and the FIR is morphologically similar to the radio continuum emission (map on the right). However, the VLA B-array data shown here probably underestimate the radio size because of the "missing fluxes" at high resolution: deconvolved radio size along the major axis is 24″ in the D-array

map which has a 60″ beam, but only 11″ in the B-array map with a 5″ beam. The deconvolved 60 μm size of 22″ from our KAO data is very similar to the radio size measured with the VLA at lower resolution.

4. Discussion

Since FIR emission is considered the product of past and on-going star formation (Helou *et al.* 1985; Wang & Helou 1992), its apparent concentration towards the galactic center suggests intensive nuclear star-forming regions. This is consistent with the greatly enhanced central emission seen in narrow-band H_α images (e.g., that of NGC 4536). The active star formation is also likely to be related to a heavy nuclear concentration of molecular gas and dust. The presence of a stellar bar in almost all cases is likely to help transfer gas radially inwards and perhaps also to trigger star formation.

The relative sizes of the FIR and radio continuum regions are in agreement with model predictions by Helou & Bicay (1993; see also Bicay & Helou 1990). The model assumes that the radio emission results from propagation of cosmic ray particles in the galactic magnetic field, while the FIR emission comes from photons produced in star formation and downgraded in energy while heating and re-radiating from interstellar dust. These two quantities are thus intrinsically related to each other through the formation of massive stars, because that is also a source of cosmic ray particles.

Despite their brightness in the radio continuum, all of the observed galaxies have relatively extended radio emissions that are very different from the highly compact AGN sources, or "monsters". The good match between FIR and radio morphological features supports the notion that both are produced in the galactic center and in extensive star forming regions, but not in AGNs.

Theoretical models further predict a correlation between the FIR/radio size ratio and the bolometric luminosity of galaxies (Helou & Bicay 1993). With our enlarged sample of 11 galaxies, almost all of which were observed at 15″ resolution, we expect to be able to better address these systematic trends in the FIR-radio correlation of FIR bright galaxies.

Acknowledgments We would like to thank the Yerkes IR Camera Group, especially Drs. D. A. Harper, J. F. Lees, and R. F. Loewenstein for their help in this study. We also thank Drs. J. J. Condon and L. Armus for allowing us to use their observational data for comparison.

References

Bicay, M. C., & Helou, G. 1990, ApJ, 362, 59

Condon, J. J., Anderson, M. L., & Helou, G. 1991, ApJ, 376, 95

Condon, J. J. *et al.* 1990, ApJS, 73, 359

Helou, G., & Bicay, M. C. 1993, ApJ, 415, 93

Helou, G., Soifer, B. T., & Rowan-Robinson, M. 1985, ApJ, 298, L7

Soifer, B. T. *et al.* 1987, ApJ, 320, 238

Wang, Z., & Helou, G. 1992, ApJ, 398, L33

omit

Session Three

Star and Planetary System Formation

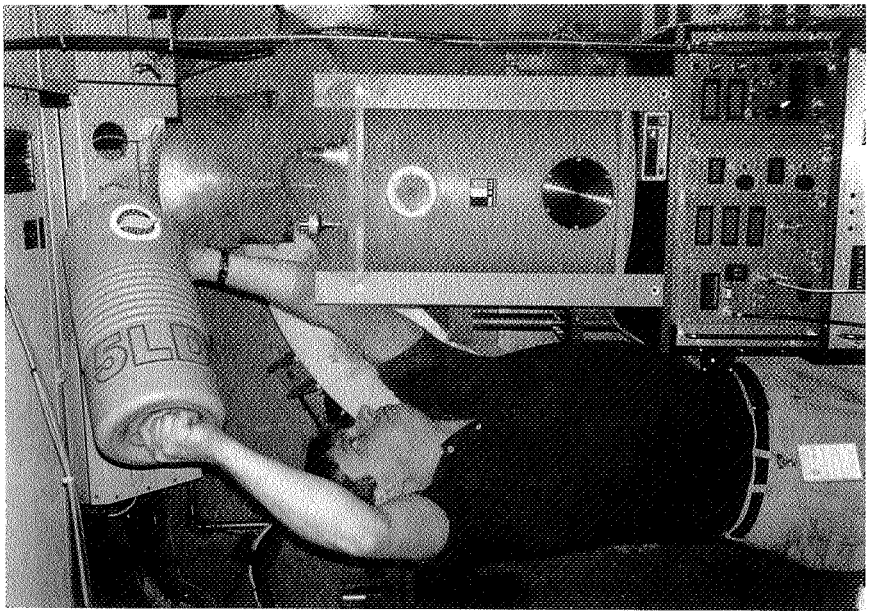

Jonas Zmuidzinas

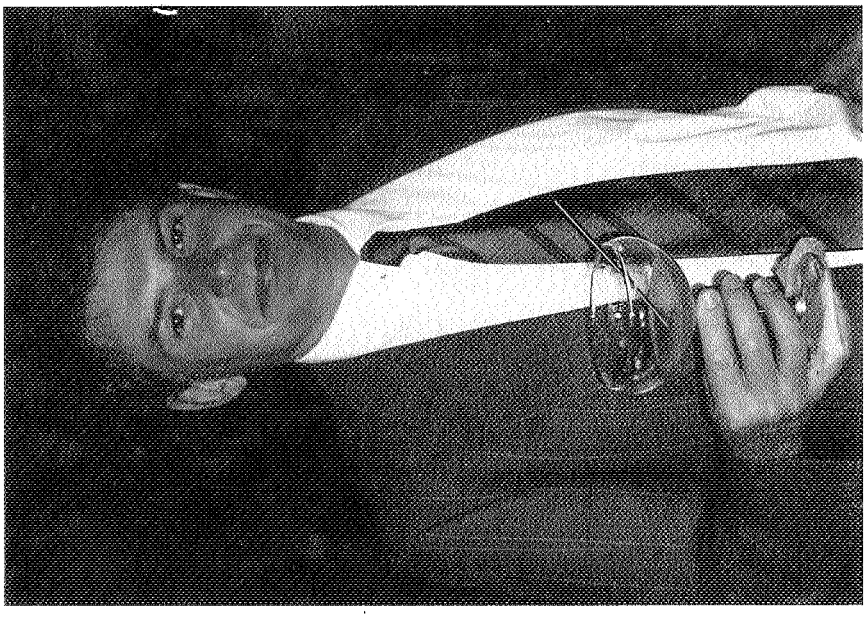

Hans Peter Röser

Airborne Astronomy Symposium on the Galactic Ecosystem
ASP Conference Series, Vol. 73, 1995
M.R. Haas, J.A. Davidson, and E.F. Erickson (eds.)

THE EARLY EVOLUTION OF STARS

Stephen E. Strom

Five College Astronomy Department, University of Massachusetts

Abstract. This review outlines the observational properties of young stellar objects as they evolve from their birth within dense rotating molecular cores to fully-formed pre-main sequence stars. Current work suggests that most of the mass which ultimately comprises a fully-formed star is transferred from a flattened infalling envelope (of size $\sim$ several thousand AU) through a circumstellar accretion disk to the stellar surface. We summarize current estimates for the duration of the envelope infall and disk accretion phases and discuss the implication of these timescales for the formation of stars of different mass and of planetary systems.

1. INTRODUCTION

Our current paradigm for stellar birth assumes that:

- stars are formed in "cores" of dense, rotating molecular gas and dust.
- the low angular momentum material in the core collapses to form a central protostellar "seed", while the high angular momentum core material forms a flattened, infalling envelope of gas and dust which begins to build and feed an accretion disk which surrounds the central object (see Shu, Adams, & Lizano 1987).
- a star is assembled as material is transferred from the infalling envelope, to the accretion disk and finally to the surface of the central protostellar "seed".
- a star is fully formed when the infall/accretion phase is terminated, either via (1) accretion (or dispersal) of all envelope and disk material; and/or (2) assembly of disk material into a planetary system.

This review will summarize the observational evidence which supports this picture, along with current estimates of the duration of the envelope infall and disk accretion phases for stars of different mass. These estimates provide both insight into the conditions which control the formation of high and low mass stars, and a constraint on the timescales available for assembling disk material into planetesimals.

2. EARLY STELLAR EVOLUTION: AN EMPIRICAL SEQUENCE

Over the past decade, surveys of star-forming complexes using emission lines arising from density-sensitive molecular species, along with IRAS and ground-based infrared surveys in combination provide the empirical basis for understanding

and modeling the early phases of stellar evolution. Beichman et al. (1986) and Myers et al. (1987) show that:

- optically-invisible infrared sources are located near the centers of dense, rotating (Goodman et al. 1993) molecular cores traced by NH_3 and CS.
- optically-visible stars with infrared excesses are often found within cores, but are typically located well away from the center. Quantitatively, an infrared spectral index defined as

$$s = log\,[25\,F(25\,\mu\mathrm{m})\,/\,2.2\,F(2.2\,\mu\mathrm{m})]$$

is largest ($s \sim 2$) for stars located near the geometrical center of the core and decreases to $s \sim -1$ for stars located further from the core center.
- young stars located near to, but outside the boundaries of molecular clouds rarely exhibit measurable infrared excesses (e.g., Walter et al. 1988).

Optically-obscured infrared sources located near the center of molecular cores are presumed to represent objects just forming from collapsing molecular material. Their steep ($s > 0$) spectral indices suggest that they are surrounded by optically-opaque infalling envelopes and circumstellar accretion disks (see section 3). Optically-visible stars with infrared spectral indices $s \sim -1$ appear to be older stars whose peculiar motions have carried them away from their birthplaces. While still surrounded by accretion disks, the mass contained in their infalling envelopes (and thus the envelope optical depth) has diminished significantly (see section 4.1). Young, optically-visible stars which lie outside molecular cloud boundaries and which no longer show evidence of infrared excesses indicative of either infall or accretion, are presumably fully-formed stars. The general character of these evolution-driven changes in the IR spectral properties of YSOs were anticipated in a prescient paper published by E. E. Mendoza v more than 25 years ago (Mendoza 1966, 1968).

3. OPTICALLY-OBSCURED YSOs

3.1. Observations and Recent Modeling

Modern theoretical models of collapsing, rotating molecular cores (e.g., Tereby, Shu, & Cassen 1984; Adams & Shu 1986; Shu, Adams, & Lizano 1987) all predict the formation of a star-accretion disk system surrounded by an optically-opaque, flattened envelope of infalling gas and dust. The spectral energy distributions of star-disk-envelope systems during their early evolutionary phases are determined by transfer of radiation from the central star-disk "source" through the much larger, optically-opaque infalling envelope. Adams & Shu (1986) and Adams, Lada, & Shu (1987) were the first to model the spectral energy distributions expected for such objects, and were quite successful in accounting for the general character of the flat or rising infrared spectra characteristic of optically-invisible infrared sources embedded within their parent cores. More recently, Kenyon et al. (1993a) have predicted spectral energy distributions for star-disk-envelope models which (1) have envelope density distributions of the form predicted from the rotationally-flattened infall solutions computed by Tereby, Shu & Cassen (1984), and (2) in which the infall rate (which controls the envelope

optical depth and thus the wavelength of maximum emission) is varied over 2 orders of magnitude. Kenyon et al. (1993a) compare their predicted spectral energy distributions with those observed for 21 optically-obscured YSOs in Taurus-Auriga having source luminosities $0.1 < L/L_\odot < 10$, and thus masses, $0.1 < M/M_\odot < 1.5$. Within a factor of 3, $\dot{M}_{infall} \sim 4 \times 10^{-6}$ $M_\odot$ yr^{-1} for this sample. The envelope infall rates derived by Kenyon et al. (1993a) are in remarkably good agreement with theoretical estimates for thermally supported molecular cores with $T \sim 10$ K (Shu 1977), typical of the molecular core temperatures derived by Myers & Benson (1983) in Taurus-Auriga. Hence it appears as if solar-mass stars may form from thermally-supported cores having relatively low kinetic temperatures. Unfortunately, the Kenyon et al. (1993a) study did not include sources of higher luminosity and thus possibly higher mass, and therefore cannot provide the basis for comparing envelope infall rates for high and low mass stars. However, high mass stars exhibit detectable infrared excesses for times much shorter (at least 10 times shorter for stars of masses $M > 5$ $M_\odot$) than those typical of solar-type stars. This result implies that the envelope infall rates during the time that high mass stars are assembled may be as much as 10 times higher. If so, then the effective temperatures of the cores may also be higher (see Myers & Fuller 1993).

Dusty infalling envelopes produce not only strong mid- and far-infrared emission arising from grains embedded within the envelope and heated by the central star-disk source, but near-infrared reflection nebulae, produced as star-disk light is *scattered* by envelope grains as well. An example is provided by the well-known source, L1551 IRS 5, which at a wavelength of 2.2 μm has the appearance of a diffuse, flattened reflection nebula of dimension $\sim$ 1000 AU. The illuminating source is obscured by dust most likely located in the equatorial plane of an infalling, protostellar envelope surrounding the source (Strom et al. 1985; Campbell et al. 1988; Hodapp et al. 1988; Butner et al. 1991). Kenyon et al. (1993b) have used a Monte Carlo radiative transfer code to predict the scattered-light patterns and near-infrared colors expected for star-disk systems surrounded by infalling envelopes characterized by the geometries and density distributions predicted by Tereby et al. (1984), and a variety of assumed envelope infall rates and source inclinations. Comparison of the Kenyon et al. (1993b) simulations with scattered-light patterns and surface brightness distributions observed for optically-obscured solar-type YSOs in Taurus-Auriga again lead to "best-fit" infall rates 2×10^{-6} $M_\odot$ $yr^{-1} < \dot{M}_{infall} < 10 \times 10^{-6}$ $M_\odot$ yr^{-1}.

According to Kenyon et al. (1993b), matching the range of near-infrared colors (J−H and H−K) observed for embedded YSOs in Taurus-Auriga requires not only the flattened envelope geometries predicted by Tereby et al. (1984), but in addition, an evacuated cone centered on the rotational axis of the infalling envelope. Such "polar holes" might be produced naturally by a collimated, bipolar mass outflow which emerges along the rotational axis of the star-disk-envelope system, and sweeps out the envelope material along its path. Indeed, molecular line observations of the environs of optically-obscured YSOs whose spectral energy distributions suggest the presence of infalling envelopes, invariably show a velocity pattern indicative of ambient material accelerated and swept up by bipolar winds. These winds are believed to be driven by processes related to accretion of material through a circumstellar disk and characterize all YSOs

from the time just after birth when they are visible only at far-infrared and submillimeter wavelengths, until the end of the disk accretion phase (e.g., Edwards, Ray, & Mundt 1993).

Recently, Hartmann, Calvet, & Boss (private communication) have suggested that the evacuated cones may instead arise as a natural outcome of collapse from initially highly flattened molecular clouds rather than from energetic wind/core interactions. High angular resolution surface photometry aimed at quantifying envelope properties, combined with deep monochromatic images aimed at diagnosing shocks at the wind/core interface, will be required in order to choose between these alternative explanations.

3.2. Evolutionary Timescales

As the star-disk-envelope system evolves, the material in the envelope is (1) depleted via infall onto the star-disk system, and (2) removed along the envelope rotational axis by collimated energetic winds powered by the disk accretion process. As a result, the envelope optical depth decreases (most rapidly along the poles; less rapidly in the equatorial plane) until the star-disk system is revealed first at near-infrared, and later at optical wavelengths. During this phase, the excess mid- and far-infrared emission which originates in the infalling envelope decreases in proportion to the envelope optical depth.

The length of time that a forming star spends obscured by an optically-opaque infalling envelope can be estimated from (1) the relative number of optically-invisible and optically-visible YSOs observed in an infrared-selected sample of stars which exhibit excess infrared emission; and (2) the average age of an optically-visible star which exhibits an infrared excess as derived from its location in the HR diagram (see Myers et al. 1987; Kenyon et al. 1990). In Taurus-Auriga, the number of optically-invisible YSOs is approximately 10 – 20 % of the number of optically-visible T Tauri stars (approximate age, t $\sim$ 1 Myr), thus leading to $t_{infall} \sim 0.1 - 0.2$ Myr for the envelope infall phase for stars in the mass range $0.1 < M/M_{\odot} < 1.5$. The duration of the envelope infall phase for more massive stars has not been well established, both because such stars are relatively rare, and because the infall/disk accretion phase may be considerably shorter for such stars (see section 4.2).

4. OPTICALLY-VISIBLE PRE-MAIN SEQUENCE STARS

4.1. Observations and Recent Modeling

YSOs which lie on the earthward side of their parent molecular clouds and cores, and which can be viewed along the polar axes of their infalling envelopes, will be the first to become visible optically. HL Tau appears to be an example of such a favorably-oriented, and thus optically-visible YSO which is located well away from its parent molecular core, and is just emerging from its optically-opaque infalling envelope. It exhibits (1) significant near-infrared ($\lambda < 3$ μm) excess emission and an infrared spectral energy distribution which rises steeply from $\sim$ 3 μm toward longer wavelengths. These observations suggest the presence of heated dust located both (a) within a circumstellar accretion disk (which dominates the near-IR emission from the system), and (b) in a flattened in-

falling envelope (which dominates the mid- and far-IR emission); (2) an *optical* scattered-light and polarization pattern suggestive of a star-disk-flattened envelope structure with a polar cavity (Grasdalen et al. 1984; Beckwith et al. 1984; Kenyon et al. 1993) and viewed within 20° to 30° of the polar axis; (3) a stellar jet indicative of a highly collimated outflow emerging along the polar axis of the star-disk-envelope system (Mundt & Fried 1983); (4) kinematic evidence of envelope infall provided by redshifted molecular absorption lines viewed against the stellar photosphere; the inferred mass infall rate is $\dot{M}_{infall} \sim 10^{-6}$ $M_\odot$ yr^{-1} (Grasdalen et al. 1989); (5) optical evidence of energy released as material accreted through the circumstellar accretion disk is channeled toward the stellar surface along magnetospheric loops and arrives on the photosphere at free-fall velocity; the accretion rate deduced from the excess optical luminosity produced by this "boundary layer" emission is $\dot{M}_{acc} \sim 0.5 \times 10^{-6}$ $M_\odot$ yr^{-1}. The favorable location and orientation of HL Tau thus provides us with a nearby "case study" of a YSO in transition between the optically-obscured infall phase, and the phase when disk accretion rather than envelope infall dominates the observed infrared spectral energy distribution. Further detailed study of HL Tau and its analogs offers the promise of deeper understanding of the major physical processes which dominate the optically-obscured infall phase: (1) envelope infall; (2) rapid disk accretion and associated strong boundary layer emission; and (3) highly-collimated, energetic mass outflow.

As the mass of material in the infalling envelope surrounding the YSO decreases further still, all star-disk systems are eventually revealed optically. At the same time, the excess infrared emission from the envelope (which dominates emission at long wavelengths) decreases as well. The observed spectral index, s, for optically-visible stars, is thus expected to approach the value characteristic of an optically thick, geometrically-thin accretion disk: $s = -4/3$. Observations of optically-visible T Tauri stars (solar-type PMS stars) and Herbig Ae/Be stars suggests that the progression to a pure disk system is gradual: most optically visible YSOs show infrared spectral energy distributions with $-4/3 < s < 0$, with only a modest fraction showing the $s = -4/3$ spectrum characteristic of an optically thick, geometrically flat accretion disk. This suggests that infall from a circumstellar envelope "feeds" the disk for a significant fraction of the time over which a star is fully assembled (Kenyon & Hartmann, private communication). By the time the IR spectrum of a YSO becomes disk – as opposed to envelope – dominated, the YSO is typically located at a distance of several core radii from the center of its parent molecular core.

High spectral resolution observations of optically-revealed YSOs enable reliable estimates of accretion luminosity (and thus disk accretion rates). Such spectra can diagnose and accurately measure excess optical continuum emission produced in a "boundary layer" (or more accurately in multiple "boundary spots") as material passing through the accretion disk lands at highly supersonic speeds on the stellar surface, releases its kinetic energy and locally heats the photosphere. The featureless continuum radiation produced in the hot boundary layer, when added to the photospheric spectrum, acts to decrease the residual intensity of individual photospheric absorption features, producing a spectrum which appears washed-out or "veiled" (Joy 1945; Hartigan et al. 1990, 1991; Bertout, Basri, & Bouvier 1988; Bertout 1989). Quantitative measurements of "spectral veiling" provide far less ambiguous estimates of accretion luminosity

than do measurements of excess infrared emission, which can include contributions not only from grains heated viscously in an accretion disk, but from grains located both in and above the disk and heated radiatively by the central star. Hartigan et al. (1991) derive spectral energy distributions for the excess optical emission for T Tauri stars by dividing high resolution echelle spectrograms of these stars by those of standard stars of identical spectral type; the ratio provides a measure of the excess optical emission required to account for the decreased residual intensity of photospheric absorption features. In turn, estimates of excess optical emission as a function of wavelength enable determination of both the temperature and thus the bolometric luminosity of the excess optical continuum radiation. These measurements thus yield an estimate of the accretion luminosity, L_{acc}, which in turn is related directly to the accretion rate: $L_{acc} = 1/2\ G\ M_\odot\ \dot{M}_{acc}\ /R_*$.

Bertout et al. (1988), Hartmann & Kenyon (1990) and Hartigan et al. (1991) use this procedure to derive disk accretion rates for solar type ($0.1 < M/M_\odot < 1.5$) pre-main sequence stars: $10^{-8}\ M_\odot\ yr^{-1} < \dot{M}_{acc} < 10^{-6}\ M_\odot\ yr^{-1}$. A "typical" steady-state value is $10^{-7}\ M_\odot\ yr^{-1}$. Over the range of disk lifetimes characteristic of solar-type pre-main sequence stars, $t_{disk} \sim 1 - 5$ Myr, between 0.1 and 0.5 $M_\odot$ can thus be added to the central star via steady-state accretion of material through the disk. A comparable amount of material may in fact be added during transient ($t \sim 100$ yr) phases of elevated accretion (FU Orionis events during which disk accretion rates, $\dot{M}_{acc}$ can reach values as large as $10^{-4}\ M_\odot\ yr^{-1}$; Hartmann & Kenyon 1987; Kenyon, Hartmann, & Hewitt 1988; Hartmann et al. 1989). Solar-type PMS stars may experience 10 to 20 such events during their disk-envelope evolutionary phases, and thus may accrete an additional 0.1 to 0.2 $M_\odot$ during FU Ori outbursts. *Hence, most of the material comprising a solar-type star must pass through a circumstellar accretion disk.* Indeed, the steady-state disk accretion rates estimated for solar-type stars suggest that even optically-visible PMS stars are still gaining significant mass from material passing through an accretion disk. Since "instantaneous" disk masses derived from mm-continuum measurements of both embedded and optically-visible solar-type YSOs are typically $M_{disk} \sim 0.1\ M_\odot$ (Beckwith et al. 1990), until the final phases of disk accretion (when the "last" $\sim 0.1\ M_\odot$ is accreted or assembled into larger bodies), the accretion disk must be fed continuously by material stored in a larger and more massive, flattened infalling envelope (see above).

For stars with masses $M > 1.5\ M_\odot$, disk accretion rates cannot be estimated directly from measurement of boundary layer emission. Indeed, such objects appear to lack measurable excess emission at optical or near ultraviolet wavelengths (Hartmann, Kenyon & Calvet 1993). The infrared excesses derived for more massive stars imply accretion rates which could be 10 to 100 times higher than those characterizing their lower mass analogs (Hillenbrand et al. 1992). However, infrared excesses in young massive stars reflect not only contributions from viscously heated grains contained within the disk, but from (1) heated micron-size disk and envelope grains in radiative equilibrium with the stellar radiation field, and (2) transiently heated smaller particles and molecular complexes which are excited by the copious ultraviolet radiation emitted by these stars (Natta 1993; Hartmann, Kenyon, & Calvet 1993). Consequently,

estimates of accretion luminosities (and thus mass accretion rates) based on infrared excesses are problematical at present. However, if high mass stars are also built largely from material which passes through disks, and if their disk lifetimes are as short as 0.1 Myr (see section 4.2), time-averaged disk accretion rates must be large ($\dot{M}_{acc} \sim 1\ M_\odot\ /\ 0.1\ Myr \sim 10^{-5}\ M_\odot\ yr^{-1}$).

4.2. Evolutionary Timescales

The duration of the disk accretion phase (and thus the timescale to fully assemble a star) is estimated by determining the fraction of young stars surrounded by accretion disks as a function of stellar age. Establishing the presence of an accretion disk *definitively* requires spectroscopic and photometric measurements of several indicators of disk accretion: optical excess emission arising from boundary layer emission; forbidden line emission arising in accretion-driven winds; hydrogen line emission arising in accretion columns; infrared excess emission (Edwards et al. 1993). However, careful study of a selection of nearby solar-type YSOs suggests that solar-type stars which show significant excess infrared emission above photospheric levels typically exhibit all other accretion signatures. Hence, the presence or absence of a circumstellar accretion disk can be inferred with considerable confidence by determining whether a star shows an infrared excess or normal photospheric colors.

Over the past five years, infrared and optical surveys of solar-type pre-main sequence stars in nearby star-forming regions have provided accurate measurements of infrared excess emission at $\lambda < 3.5\ \mu m$ for several hundred stars. For young (ages $t < 3$ Myr) optically-visible stars in the mass range $0.2 < M/M_\odot < 1.5$, approximately 50% show evidence of significant near-infrared excesses. Among this sample, some stars which show no evidence of excess emission appear to be as young as 0.3 Myr. For older stars (ages $3 < t < 10$ Myr), only 10% show evidence of excess infrared emission (Strom et al. 1989). No stars older than 10 Myr in this mass range exhibit infrared excesses (Strom, Edwards, & Skrutskie 1993; Dutkevitch et al. 1994). These results suggest that for solar-type stars, disk accretion can persist for as long as 10 Myr or be terminated at ages 0.3 Myr or less.

Surveys aimed at diagnosing infrared excess emission among young, higher mass optically visible stars suggest that for stars with $M > 3\ M_\odot$, accretion disks survive for much shorter times, $t << 1$ Myr. From their study of the young cluster NGC 6611, Hillenbrand et al. (1993) argue that among a sample of optically-visible pre-main sequence stars with masses $3 - 5\ M_\odot$ and ages $t \sim 0.1 - 0.2$ Myr, only 10% show evidence of significant excess infrared emission. This result suggests that the disk accretion (and the envelope infall) phase lasts no more than 0.1 Myr for a typical high mass star. If so, the envelope infall and disk accretion rates must be large ($\dot{M}_{acc}$, $\dot{M}_{infall} > 10^{-5}\ M_\odot\ yr^{-1}$).

5. IMPLICATIONS FOR PLANET BUILDING

The timescales for accretion disk survival summarized in section 4.2 provide an important astronomical constraint on the time available for planet building. During the time that young stars show evidence of measurable near-infrared excesses, mm-continuum measurements suggest that their disks appear to contain

material in quantity at least *sufficient* to build a solar system ($M_{disk} > 0.01\ M_\odot$; Beckwith et al. 1990; Hillenbrand et al. 1992; Weintraub, Sandell, & Duncan 1989). When near-infrared excesses are no longer measurable, the observed mm-continuum fluxes suggest the absence of heated micron-sized dust at a level $M_{disk} << 0.01\ M_\odot$.

Near-infrared surveys of both solar-type and high mass young stars are sufficiently sensitive to detect as little as $\sim 10^{20}$ gm (the mass of an asteroid!) of micron-size circumstellar dust provided that such dust is distributed throughout the inner region ($r < 0.1$ AU) of a circumstellar disk where it can be heated to temperatures $T \sim 1000$ K. The absence of significant excess infrared emission at ages $t > 0.1$ Myr for stars with $M > 3\ M_\odot$, and at ages $t > 10$ Myr for lower mass stars argues that either (1) on these timescales, micron-size grains have been thoroughly "cleaned" from circumstellar disks which originally contained $M_{disk} > 0.01\ M_\odot$; or (2) that such grains have been assembled into larger bodies, thus reducing the effective radiating area of solid material and consequently the excess infrared radiation.

Evidence that larger bodies may in fact have been built in disks is provided by observations of β Pictoris and a large number of analogous intermediate mass stars. This A-type main sequence star has an estimated age $t \sim 100$ Myr, and yet shows evidence of both (1) a measurable infrared excess, consistent with an asteroid mass of micron-size dust distributed over a disk of dimension 1000 AU, and (2) a disk-like structure manifest in scattered visible light (e.g., Backman & Gillett 1988). The presence of a disk surrounding a star of this age requires that the micron-size dust be replenished. Lacking a source of such dust, micron-size grains will spiral inward through the disk in response to the Poynting-Robertson effect, and reach the surface of the star on a timescale $t << 10^5$ yr. The most likely mechanism for replenishing the population of micron-size grains is collisions between larger bodies, analogous to the collisions which are believed to have occurred during the period of "maximum bombardment" responsible for the cratering manifest on the Lunar surface and on other bodies throughout the solar system.

The mass of β Pic is $\sim 2\ M_\odot$. From the statistics summarized in section 4.2, its circumstellar accretion disk could not have survived for much more than 1 Myr. Hence, agglomeration of micron-size grains to form entities of size much larger than 1 micron must have taken place on a timescale $t < 1$ Myr. Hence, the chain of events that ultimately leads to formation of larger grains and possibly planetesimals, must have been initiated no more than 1 Myr from the time that β Pic began to collapse within its natal core. The fact that intermediate mass stars such as β Pic can apparently assemble micron-size grains into larger bodies on relatively short timescales suggests that in stars like the sun, where the pace of disk evolution is more modest, formation of large bodies should not have been a challenge to nature.

6. ACKNOWLEDGEMENTS

The author would like to thank Suzan Edwards and Karen Strom for their assistance in preparing this text and for their contributions to the work summarized herein. This research was supported by grants from the NASA Planetary

Program, the NASA Origins of Solar Systems Program, the NASA Astrophysics Data Program and the National Science Foundation. Some of the results quoted here were based on observations made at the Kitt Peak National Observatory, supported through a contract from the National Science Foundation to the Associated Universities for Research in Astronomy, and at the Infrared Telescope Facility, operated by the University of Hawaii for the National Aeronautics and Space Administration.

References

Adams, F. C., and Shu, F. H. 1986, ApJ, 308, 836

Adams, F. C., Lada, C., and Shu, F. H. 1987, ApJ, 312, 788

Backman, D. E., and Gillett, F. C. 1988, Cool Stars, Stellar Systems and the Sun, eds. J. Linksky and R. Stencel, Springer-Verlag: Berlin

Beckwith, S., Zuckerman, B., Skrutskie, M. F., and Dyck, H. M. 1984, ApJ, 287, 801

Beckwith, S., Sargent, A., Chini, R., and Güsten, R. 1990, AJ, 99, 924

Beichman, C. A. et al. 1986, ApJ, 307, 337

Bertout, C. 1989, ARAA, 27, 351

Bertout, C., Basri, G., and Bouvier, J. 1988, ApJ, 330, 350

Butner, H. M., Evans, N. J. II, Lester, D. F., Levreault, R. M., and Strom, S. E. 1991, ApJ, 376, 636

Campbell, B., Persson, S. E., Strom, S. E., and Grasdalen, G. L. 1988, AJ, 95, 1173

Dutkevitch, D., Skrutskie, M. F., Backman, D., and Strom, S. E. 1994, ApJ (in preparation)

Edwards, S., Ray, T., and Mundt, R. 1993, Protostars and Planets III, eds. E. Levy and M. Matthews, University of AZ Press

Edwards, S., Strom, S., Hartigan, P., Strom, K., Hillenbrand, L., Herbst, W. Attridge, J., Merrill, M., Probst, R., and Gatley, I. 1993, AJ, 106, 372

Goodman, A., Benson, P., Fuller, G., and Meyers, P. 1993, ApJ, 406, 528

Grasdalen, G. L., Strom, S. E., Strom, K. M., Capps, R. W., Thompson, D., and Castelaz, M. 1984, ApJ, 283, L57

Grasdalen, G. L., Sloan, G., Stout, N., Strom, S. E., and Welty, A. D. 1989, ApJ, 339, L37

Hartigan, P., Hartmann, L. W., Kenyon, S. J., Strom, S. E., and Skrutskie, M. F. 1990, ApJ, 354, L25

Hartigan, P. et al. 1991, ApJ, 382, 617

Hartmann, L. W., and Kenyon, S. J. 1987, ApJ, 312, 243

Hartmann, L., et al. 1989, ApJ, 338, 1001

Hartmann, L., and Kenyon, S. 1990, ApJ, 349, 190

Hartmann, L., Kenyon, S. J., and Calvet, N. 1993, ApJ, 407, 219

Hillenbrand, L. A., Strom, S. E., Vrba, F. J., and Keene, J. 1992, ApJ, 397, 613

Hillenbrand, L. A., Massey, P., Strom, S. E., and Merrill, K. M. 1993, AJ, 106, 1906

Hodapp, K.-W., Capps, R. W., Strom, S. E., Salas, L., and Grasdalen, G. L. 1988, ApJ, 335, 814

Joy, A. H. 1945, ApJ, 102, 168

Kenyon, S. J., Hartmann, L. W., and Hewett, R. 1988, ApJ, 325, 231

Kenyon, S. J., Hartmann, L. W., Strom, K. M., and Strom, S. E. 1990, AJ, 99, 869

Kenyon, S. J., Calvet, N., and Hartmann, L. W. 1993a, ApJ, 414, 676

Kenyon, S. J., Whitney, B. A., Gomez, M., and Hartmann, L. 1993b, ApJ, 414, 773

Mendoza, E. E. v 1966, ApJ, 143, 1010

Mendoza, E. E. v 1968, ApJ, 151, 977

Mundt, R., and Fried, J. W. 1983, ApJ, 274, L83

Myers, P. C., and Benson, P. J. 1983, ApJ, 266, 309

Myers, P. C. et al. 1987, ApJ, 319, 340

Myers, P. C., and Fuller, G. A. 1993, ApJ, 402, 635

Natta, A. 1993 (in preparation)

Shu, F. 1977, ApJ, 214, 488

Shu, F. H., Adams, F. C., and Lizano, S. 1987, ARAA, 25, 23

Strom, S. E., Strom, K. M., Grasdalen, G. L., Capps, R. W., and Thompson, D. 1985, AJ, 90, 2575

Strom, K. M., Strom, S. E., Edwards, S., Cabrit, S., and Skrutskie, M. F. 1989, AJ, 97, 1451

Strom, S., Edwards, S., and Skrutskie, M. 1993, Protostars and Planets III, eds. E. Levy and M. Matthews, University of AZ Press

Tereby, S., Shu, F. H., and Cassen, P. 1984, ApJ, 286, 529

Walter, F. M., Brown, A., Mathieu, R. D., Myers, P. C., and Vrba, F. J. 1988, AJ, 96, 297

Weintraub, D., Sandell, D., and Duncan, W. D. 1989, ApJ, 340, L69

Airborne Astronomy Symposium on the Galactic Ecosystem
ASP Conference Series, Vol. 73, 1995
M.R. Haas, J.A. Davidson, and E.F. Erickson (eds.)

KWIC IMAGING OF THE ORION NEBULA

G.J. STACEY, G.E. GULL, T.L. HAYWARD, H. LATVAKOSKI and L. PENG
Department of Astronomy, Cornell University, Ithaca, NY 14853

ABSTRACT We present the first results obtained with our new imaging Fabry-Perot spectrometer, KWIC. We obtained a fully sampled 9.8" spatial resolution image of the inner 8' × 12' region of the Orion Nebula in the 37 μm continuum and a somewhat smaller scale image in the [SiII] 35 μm line. The continuum image traces out the structure of the interface region between the molecular cloud and the Orion A HII region, as well picking out embedded sources such as the BN-KL star cluster. The continuum directly yields the luminosity of the sources and is used to deduce dust mass and grain parameters. Our [SiII] image both reveals the clumpy structure of the interface region and signals the presence of a dissociative J-shock in the high velocity outflow from IRc2.

I. INTRODUCTION

The Kuiper Widefield Infrared Camera (KWIC) is an entirely new instrument we have constructed for use between 18 and 44 μm on the KAO. KWIC is well described in Stacey et al. (1993), and Latvakoski et al. (1994), so we provide only a short summary here. KWIC centers on a new SIRTF funded Rockwell International 128 × 128 pixel Si:Sb BIB detector array. The plate scale (2.73" per pixel) was chosen to oversample the diffraction lobe (8" at 35 μm) of the KAO telescope. Even with this oversampling, KWIC has a very large field of view: 5.8' × 5.8'. The resolution achieving devices are a pair of cryogenically cooled, fully tunable, scanning Fabry-Perot interferometers (FPI). One FPI is required for low resolution mode (R ~ 35 to 200), and the second is inserted into the beam for the high resolution mode (R ~ 2,000 to 10,000).

In low resolution mode, KWIC is sensitive to the continuum emission from warm (T ~ 80 K) dust in thermal equilibrium with stellar radiation fields. Since the peak of the spectral energy distribution for dust near star formation regions lies near 40 μm, the observed flux is relatively insensitive to grain temperature and may be used as a direct estimate of luminosity. For example, at the distance to Orion, 1 Jy at 40 μm corresponds to 1.2 ± 0.5 $L_\odot$ for dust temperatures between 50 and 200 K. KWIC offers good leverage to discern grain color temperatures: if the dust temperature increases by a factor of 3 (from 30 to 100 K), the 30 to 44 μm intensity ratio grows by a factor of 30. Comparing the observed emission with that of a blackbody, yields the dust optical depth, hence column density, assuming grain parameters. On the other hand, if we observe T_{dust} and know the local interstellar radiation field, we can

deduce grain properties such as the albedo and far-IR emissivity. Finally, since KWIC spectrally scans in low resolution mode, dust features such as those due to PAHs are observable. In low resolution mode, KWIC can detect (2 hours, 5σ = 0.7 Jy, BLIP) a 0.05 $L_\odot$, 80 K blackbody at the distance to the Taurus molecular cloud. The concomitant dust mass is about 0.02 $M_\oplus$ (earth masses).

A variety of fine-structure lines are available to KWIC in the high resolution mode (see Table 1, Latvakoski et al. (1994), this volume). These lines are bright, collisionally excited, and have low optical depth so that they are excellent extinction free probes of the dusty regions associated with star formation and galactic nuclei. The KWIC spectral regime includes lines which probe densities, mass and abundances in shocks and neutral gas regions (e.g. [SI] (25 μm), [SiII] (35 μm), and [FeII] (26 μm)), lines which probe gas densities, abundances and hardness of the ambient radiation field (hence stellar type) in HII regions excited by main sequence stars (e.g. [SIII] (18 & 33 μm), [ArIII] (22 μm) and [NeIII] (36 μm)), and lines from very high ionization states (e.g. [OIV] (26 μm) and [NeV] (24 μm)) which trace the very hard UV photons associated with AGNs and planetary nebula.

Funding for the development of KWIC was entirely through the KAO grants program and began in November 1992. Our first flights with KWIC were in February of 1994, just 15 months later.

II. KWIC OBSERVATIONS OF ORION.

The Orion molecular cloud is the nearest (D ~ 480 pc) site of massive star formation. As such, it is one of the most heavily studied interstellar clouds in the Galaxy. The visible Orion Nebula is excited by a young cluster of OB stars (predominantly the O6 star θ^1 Ori C). This cluster, born in the adjacent molecular cloud, has photoionized an HII region visible as a blister on the near side of the molecular cloud. The HII region has a "bowl" shaped morphology: the rims of the bowl point towards the observer, and the base of the bowl is roughly behind θ^1 Ori C along our line of sight.

At the interface between the fully ionized gas and the molecular cloud, far-UV photons ($6 < h\nu < 13.6$ eV) from the HII region penetrate the molecular cloud, ionizing atoms and dissociating molecules with binding energies less than 13.6 eV, thereby forming a "photodissociation region" (PDR) on the molecular cloud surface. Most of the UV energy goes into heating the dust in the PDR, which cools via its far-IR continuum radiation. The gas in the PDR is predominantly heated via photoelectric ejection of energetic electrons from grains and cooled via far-IR fine structure line radiation (e.g. [CII], [OI], [SiII], Tielens and Hollenbach 1985). A few tenths of a parsec behind the PDR lies a string of several dense cloud cores running in roughly a N-S direction (the Orion molecular ridge). The core nearest θ^1 Ori C has spawned the next generation of OB stars, the BN-KL cluster. This cluster is totally unobservable in the visible, but very prominent in the infrared.

A. Continuum Observations

We observed the Orion Nebula in the 37 μm continuum on 1994 February 24, using KWIC with a spectral resolution of 70. The map we obtained (Figure 1) consists of 4 separate pointings (> 55,000 pixels) with the array. The spatial

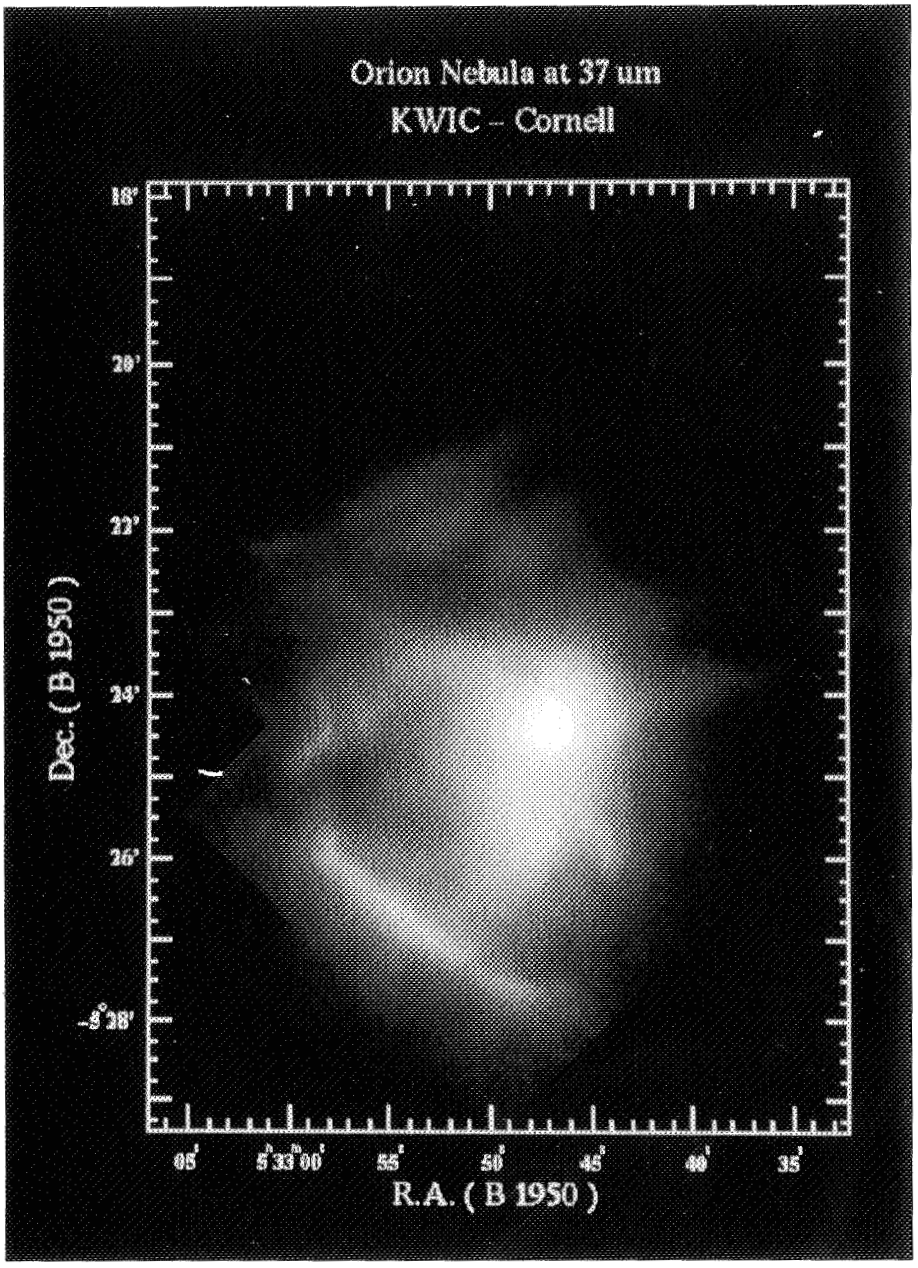

Figure 1. 37 μm continuum image of the Orion Nebula.

resolution of the KWIC/KAO system was 9.8" at 37 μm as determined via inflight observations of α Ori. Data reduction involved interpolating across bad pixels ($\sim$ 1% of the array), flat-fielding via division with an image of our internal blackbody calibrator, and registration of our 4 images. No additional operations (e.g. smoothing, sub-pixelation) were performed. The image has a 10,000:1 dynamic range per beam, so it is presented on a logarithmic scale.

There are many features of interest in our image. The bright circular source in the center of the image is the dense clump of gas and dust heated by the embedded BN-KL star cluster. The total luminosity of the cluster within a 15" radius is about 5×10^4 $L_\odot$, or 22% of that in the entire image. In the region we imaged at 37 μm, Batrla et al. (1983) find four NH_3 clumps which are part of the Orion molecular ridge. Two of these clumps (S4 and S5 (BN-KL)) are prominent in our 37 μm image. Therefore, like BN-KL, S4 probably contains embedded sources. S3 and the massive southern condensation (S6 - 100" south of BN-KL) are not apparent at 37 μm, indicating cold dust in these regions.

The bulk of the observed emission arises from warm dust in the PDR at the interface between the Orion A HII region and the parent molecular cloud. The bright ridge of emission running about 2' south from BN-KL is the surface of the Orion molecular ridge exposed to the UV radiation from the Trapezium cluster. The "finger" of emission which appears to curve around S6 is associated with a density clump visible in the free-free radio continuum, so that the clump is likely adjacent to the PDR. The 3' (0.4 pc) long thin structure running NE-SW across the bottom left of the image lies just outside the HII region and the optical "bar". This is the rim of the bowl, i.e. the PDR viewed edge-on. The 37μm continuum arises from the warm dust within $A_V \sim 3$ to 5 of the HII region. The dust emission is optically thin, so that the edge-on morphology limb-brightens the structure. There are several other features near the HII region - molecular cloud interface including the "gull" features (RA = $5^h32^m58^s$, Dec. = -5° 24'30") and the 3' long stripes running SE-NW near the northern edge of the HII region (Felli et al. (1993), Dec. = -5° 22'). A particularly interesting structure is the "western finger" of emission extending from near BN-KL westerly to the edge of the image. The apparent origin of this finger at BN-KL is likely a coincidence. The dust in the finger is probably the same dust associated with the optical reflection nebula.

Figure 2 zooms in to the brightest portions of the Orion molecular ridge, now using linear contouring and taking a slice between flux levels of 565 and 675 Jy per beam (5% of the BN-KL peak). This linear scaling brings out many features not obvious on the logarithmic plot. There is an extension of warm dust curving SE away from BN-KL, a deep "hole" in the emission near the center of the image and two small clumps of emission just resolved by our beam. Most of the heating for the "ridge" dust likely arises from the Trapezium cluster. The hole in the emission could then be an actual depression in the dust distribution, shielded by the ridge to the east from the UV flux. The clumps on the ridge have a luminosity of about 4 $L_\odot$ each. Assuming a dust temperature near 60 K (see below) and standard dust parameters, only about 1 $M_\odot$ of dust (5×10^{-4} $M_\odot$ of gas) is involved in this emission. There are several other small clumps in the interface map, including at least two prominent clumps of similar mass near the bar.

The bar appears as a very linear, narrow structure in our continuum image. There is 4 times as much flux at the peak of the bar as at the base of the

bowl in the center of the HII region. We estimate the bar has an intrinsic width at 37 μm of about 10" (7×10^{16} cm). From [OI] and [CII] studies, Stacey et al. (1993) estimate gas densities of about 4×10^5 cm^{-3} at the bar. If we assume the 37 μm continuum radiation arises solely from dust in the PDR, then the observed width of the bar means that UV radiation from the ionization source (θ^1 Ori C) is penetrating to $N_H \sim 3 \times 10^{22}$ cm^{-2}, or a visual extinction of 15 magnitudes. This is about 2 to 4 times the expected column in the PDR based on observed [CII] column densities and theoretical models. Therefore, the dust (and gas) in the PDR must be clumped by a factor of 2 to 4. Also notice that since the 37 μm continuum radiation is optically thin, the ratio of flux densities at the bar to that near the center of the nebula gives us a handle on the geometry of the interface region. Assuming similar grain temperatures, the column density of dust along the line of sight at the bar is 4 times higher than at the base of the bowl near θ^1 Ori C. The average densities in the PDR are roughly the same for both regions, which means that the bar interface must be about 4 times as deep (along the line of sight) as it is wide.

B. Physical Properties of the Dust

Harper et al. (1994) recently obtained a high quality 20" resolution map of Orion at 60 μm. We have convolved our 37 μm image to 20" resolution for direct comparison with the 60 μm image. The ratio of the continuum flux at these two wavelengths yields the color temperature of the dust. Assuming greybody ($\epsilon(\lambda) \propto 1/\lambda$) emission, we find 7 local peaks in the color temperature

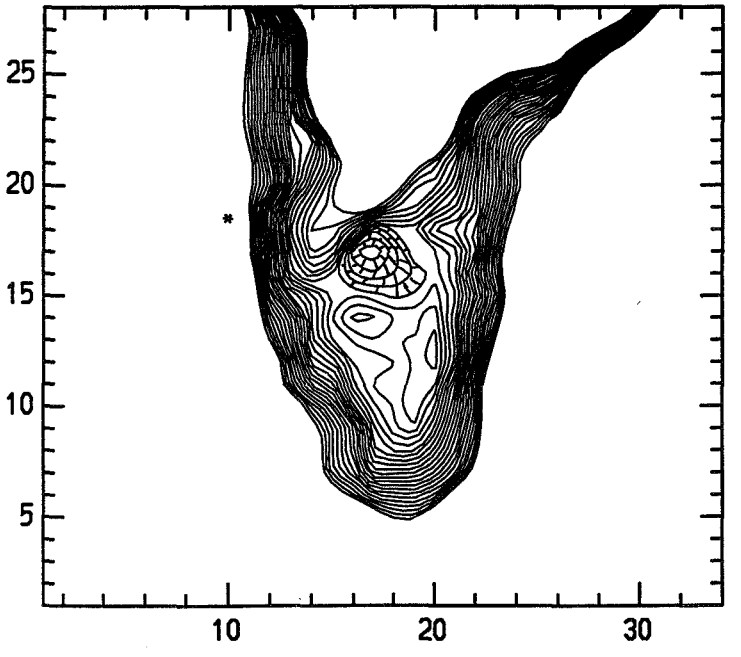

Figure 2. Linear contours of 37 μm emission on the Orion molecular ridge. Contour interval (3σ) is 2.1 Jy/beam. The position of θ^1 Ori C is indicated with a star. The units on the axes are pixels (2.73"), so that 5 units = 13.7".

map. The highest values (70 to 75 K) are reached in the region of the interface directly behind θ^1 Ori C and at BN-KL. Since the embedded cluster is 4 to 5 times less luminous than the Trapezium cluster and the dust temperature is about the same, the dust must be closer to the energy source in the embedded BN-KL cluster. The other five color temperature peaks are closely associated with the edge-on PDRs surrounding the bowl-shaped HII region: the bar (2 peaks), the gull feature, the westerly finger, and the northern edge of the HII region. Since they appear to be edge-on, we assume that these color peaks are at the projected distance from the heating source, θ^1 Ori C. Equating heating to cooling, we can derive the ratio of the grain albedo, A_{gr}, to the far-IR emissivity, ϵ_{IR}, of the grains. The color temperatures for the five regions range from 50 to 70 K. The derived grain properties are remarkably uniform: $\epsilon_{IR}/A_{gr} \sim 2.2 \pm 0.3 \times 10^{-2}$. This ratio is consistent with grain radii of 0.2 and 0.4 μm for silicate and graphite grains, respectively (Drain and Lee, 1984). Assuming these grain parameters, the observed color temperature at θ^1 Ori C implies that the star is 0.2 pc from the molecular cloud. In summary, central heating by θ^1 Ori C is consistent with uniform dust properties in the PDR.

Comparing the observed 37 μm flux to that expected from a blackbody at T_{color} yields the 37 μm optical depth. Our 37 μm optical depth map has several interesting properties. The embedded sources (e.g. BN-KL and the NH_3 clumps S3, S4, and S6) immediately appear as regions of high opacity at 37 μm with a peak opacity of 0.9 at S6. If we assume "outer cloud" dust, then this corresponds to a visual extinction of 225 magnitudes (Mathis 1990), or a gas column density of $\sim 4.5 \times 10^{23} cm^{-2}$. Within a 10" radius, the gas mass is $\sim$ 3 $M_\odot$, or 5% of the total gas mass of S6. The condensation at BN-KL has a larger linear extent, so even though the 37 μm optical depth here is only $\sim$ 0.5, the mass traced at 37 μm is $\sim$ 12 $M_\odot$ - 25% of that observed in the submm thermal continuum (50 $M_\odot$, Keene, Hildebrand and Whitcomb 1982).

Near the center of the HII region, where the PDR is viewed nearly face-on, the observed optical depth is $\sim$ 0.03, which corresponds to a column density of $\sim 1.5 \times 10^{22} cm^{-2}$. Based on [OI] to [CII] line intensity ratios, the column density of the gas in the PDR is identical. This remarkable circumstance reinforces our conclusion that the 37 μm continuum traces the PDR. Notice that the two estimates of column density in the PDR are totally independent. On face value, then, the coincidence of the values indicates the conversion between 37 μm optical depth and hydrogen column density and the assumed C^+ and O° gas phase abundances are roughly correct.

C. [SiII] Observations

Much about the structure of PDRs has been deduced via far-IR observations of their primary gas cooling lines, [CII] and [OI]. Physical parameters of the gas (density, temperature, and mass) are well constrained, and together with the far-IR continuum and PDR models, much can be learned about gas filling factors, ambient UV field strengths and grain parameters. One of the most interesting results from these studies is that the gas in PDRs must be clumped, with typical clump sizes between 0.01 and 0.1 pc, and volume filling factors between 1 and 50%. The large scale distribution of [CII] radiation from the Orion molecular cloud by itself indicates a clumpy structure (Stacey et al. 1993). Far-UV radiation is required to create and excite [CII] emission - the likely source of this radiation is "leakage" of far-UV flux from the Trapezium

through a clumpy PDR. The inferred clump sizes are similar to the beam sizes at [CII] (158 μm, 55" $\Leftrightarrow$ 0.13 pc) and [OI] (63 μm, 22" $\Leftrightarrow$ 0.05 pc). Yet, strong *direct* evidence for clumps in the [CII] and [OI] maps is lacking. This is easy to explain. The [CII] line is easy to excite ($n_{crit} \sim 3 \times 10^3$ cm^{-3}), so that density enhancements in the high density PDR do not result in stronger [CII] emission. The [OI] line has a higher critical density ($n_{crit} \sim 5 \times 10^5$ cm^{-3}), but is optically thick ($\tau \sim 3$, Stacey et al. 1993) so that clumpy structures are washed out.

However, the [SiII] line is also a primary gas coolant for high density PDRs, and this line both has a high critical density and low optical depth. Furthermore, at the transition wavelength (34.8 μm), the KAO beam size is ~ 9" ($\Leftrightarrow$ 0.02 pc). The [SiII] line is, therefore, much better suited to studies of the clumpy structure of PDRs.

On our second flight, we obtained a 5.8' square diffraction limited image of the Orion interface region in the [SiII] line. Due to difficulties with data reduction, the image we present here (Figure 3) is not fully reduced. It consists of only about half our data, and must be regarded as very preliminary. None the less, some very interesting features appear. The bar is very bright in [SiII] as are regions associated with other edge-on PDRs (e.g. the gull feature). There is enhanced emission along the Orion molecular ridge, and an interesting cross-shaped structure at the BN-KL cluster. As expected, clumpy structure is ubiquitous in this map: the mean density in the region is below the

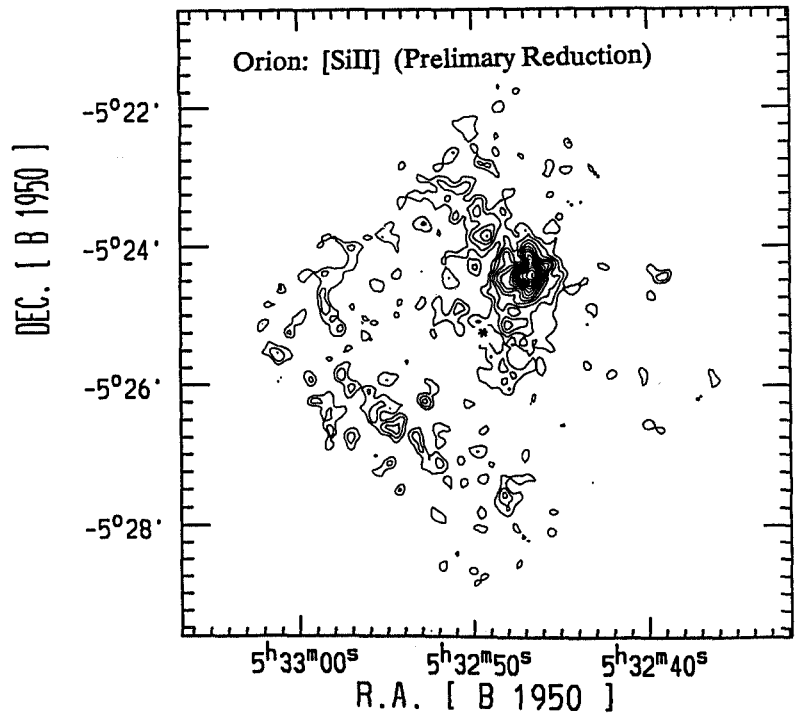

Figure 3. Preliminary [SiII] image of Orion. The contours floor is 6.7 × 10^{-19} Wcm^{-2} per beam (10 σ), and the interval is 2.2 × 10^{-19} W cm^{-2} per 9.2" beam (3σ). The star marks the position of θ^1 Ori C.

critical density and the line is optically thin. Typical clump size is $r_{clump} \sim$ 0.01 pc with enclosed masses of about 10^{-3} $M_\odot$. The [SiII] map tells us about the structure of the bar. The peak to minimum [SiII] intensity ratio is 3:1 there. Since our continuum measurements indicate that the column density along the bar is fairly uniform, this ratio directly reflects gas density enhancements. Hence, our [SiII] image *directly* reveals clumps in the bar with a clump to interclump density ratio of about 3. The density contrast is similar to that inferred by our continuum measurements above, and the prior large scale [CII] mapping.

Particularly interesting is the morphology of the [SiII] emission near BN-KL. In addition to tracing dense PDRs, [SiII] emission is enhanced by dissociating shocks - which destroy grains - releasing additional gas phase silicon. Haas et al. (1991) detected enhanced [SiII] emission from BN-KL, which they interpret as strong evidence for a J-shock in the high velocity outflow. Our measurements have nearly 4 times higher spatial resolution, so that we can spatially separate the [SiII] emission from the outflow and the foreground PDR. There is enhanced emission running N-S following the high density gas of the ridge (the PDR), and a SE-NW elongation along the position angle of the high velocity outflow from IRc2, as traced in its SiO emission (Wright et al. 1983). Clearly strong [SiII] emission arises in the outflow, signaling the presence of a fast, dissociative J-shock in the region where the high velocity outflow impacts the ambient gas.

III. ACKNOWLEDGEMENTS.

We thank Al Harper and his colleagues for communication of their 60 μm map prior to publication. This work was supported by NASA grant NAG2-800, and an NSF graduate fellowship.

IV. REFERENCES

Batrla, W., Wilson, T.L., Bastien, P., & Ruf, K. 1983, A&A, 128, 279.
Draine, B.T., & Lee, H.M. 1984, ApJ, 285, 89.
Felli, M., Churchwell, E., Wilson, T.L., & Taylor, G.B. 1993, A&ASS 98, 137.
Haas, M.R., Hollenbach, D., & Erickson, E.F. 1991, ApJ, 374, 555.
Harper, D.A., et al. 1994, in Proc of the Airborne Astronomy Symp on the Galactic Ecosystem: From Gas to Stars to Dust, ed. M.R. Haas, J.A. Davidson, & E.F. Erickson, (San Francisco: ASP), paper 301.
Keene, J., Hildebrand, R.H., & Whitcomb, S.E. 1982, ApJ, 252, L11.
Mathis, J.S. 1990, ARA&A 28, 37.
Stacey, G.J., Hayward, T.L, Latvakoski, H., & Gull, G.E. 1993, SPIE Proceedings, 1946, 238.
Latvakoski, H., Stacey, G.J., Hayward, T.L., Gull, G.E., & Peng, L. 1994 in Proc of the Airborne Astronomy Symp on the Galactic Ecosystem: From Gas to Stars to Dust, ed. M.R. Haas, J.A. Davidson, & E.F. Erickson, (San Francisco: ASP), paper 706.
Stacey, G.J., Jaffe, D.T., Geis, N., Genzel, R., Harris, A.I., Poglitsch, A., Stutzki, J., & Townes, C.H. 1993, ApJ, 404, 219.
Tielens, A.G.G.M., & Hollenbach, D.J., 1985, ApJ, 291, 722.
Wright, M.C.H., Plambeck, R.L., Vogel, S.N., Ho, P.T.P., & Welch, W.J. 1983, ApJ, 267, L41.

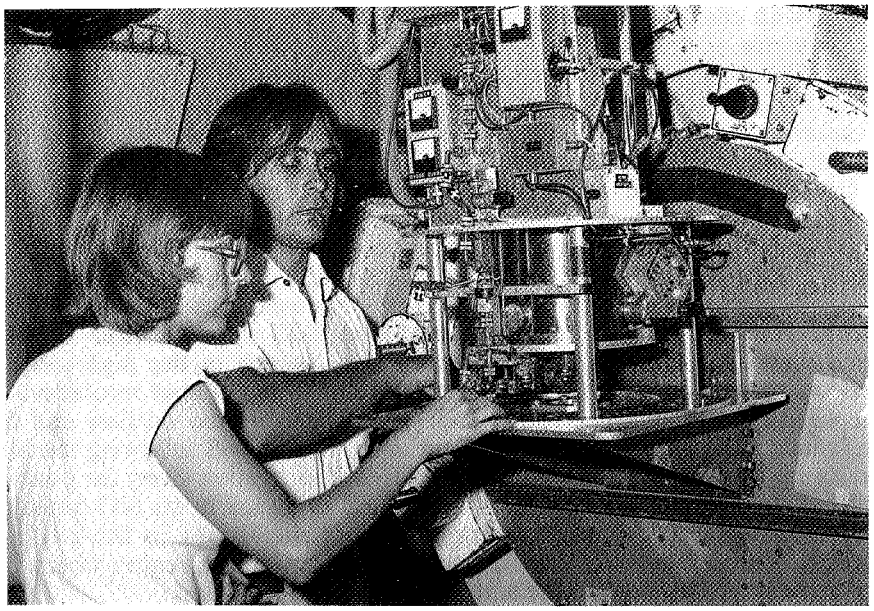

Jocelyn Keene, Chas Beichman (1981)

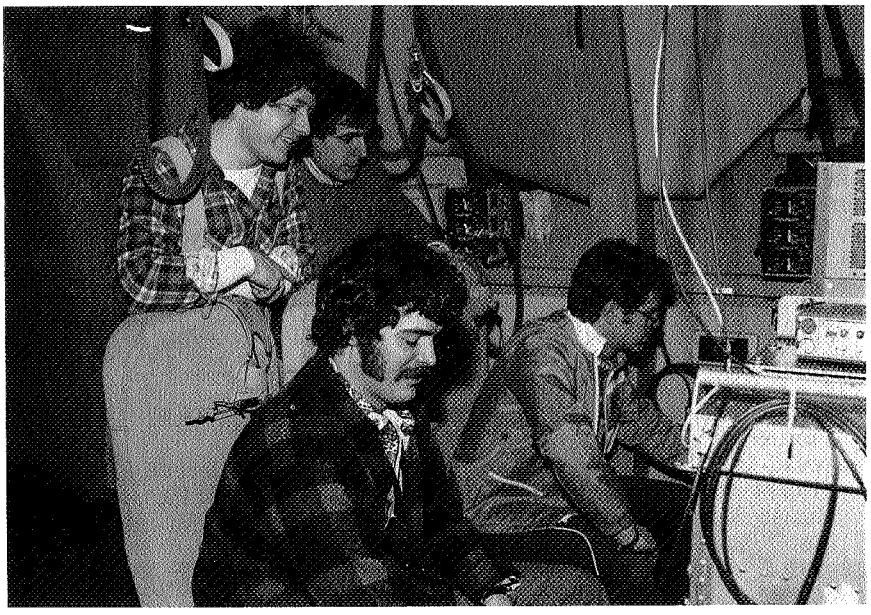

Gary Melnick, Martin Harwit, George Gull, Ray Russell (1978)

Airborne Astronomy Symposium on the Galactic Ecosystem
ASP Conference Series, Vol. 73, 1995
M.R. Haas, J.A. Davidson, and E.F. Erickson (eds.)

The Magnetic Field Structure in High-Mass Star Formation Regions

J. A. Davidson
SETI Institute; NASA Ames Research Center, MS 245-6, Moffett Field, CA 94035-1000

D. Schleuning, J. L. Dotson, C. D. Dowell, and R. H. Hildebrand
Department of Astronomy and Astrophysics, Yerkes Observatory, and Enrico Fermi Institute, The University of Chicago, Chicago, IL 60637

ABSTRACT. We present a preliminary analysis of far-IR polarimetric observations, which were made to study the magnetic field structure in the high-mass star formation regions of M42, NGC2024, and W3. These observations were made from the Kuiper Airborne Observatory (KAO), using the University of Chicago far-IR polarimeter, Stokes.

1. Introduction

It has long been thought that magnetic fields are important to the process of star formation. Magnetic fields probably influence the macroscopic formation of molecular clouds (e.g., Parker 1966). Magnetic pressure and tension may also regulate the efficiency of star formation in molecular clouds by halting cloud collapse until ambipolar-diffusion occurs (Mouschovias 1976). Once cloud cores have formed, magnetic fields may be the agents that help transfer angular momentum of the material in the cores to material in the outer envelopes, enabling further collapse to form protostars (Mouschovias & Paleologov 1980). Not only are magnetic fields invoked to make accretion possible, but to end it. Pudritz & Norman (1983) suggested that the observed molecular outflows from Young Stellar Objects (YSOs) could be magnetically driven. The force of these outflows could halt further accretion. More recently, Shu, Adams, & Lizano (1987) have suggested that the ratio of magnetic to gravitational energy in a molecular cloud could be one factor determining whether a particular cloud will form high-mass stars, since the accretion rate for a given protostar is proportional to the cube of the virial speed of the medium being accreted, and the virial speed can be enhanced by a high magnetic flux to mass ratio; the increase in accretion rates leads to more massive stars, since more massive protostars are formed before outflows can terminate the process.

In this paper we discuss the properties of the magnetic fields in three star formation regions as inferred from recent results of far-IR polarimetry. We will assume that polarized far-IR fluxes are due to the emission from

rotating, dust grains, which have their rotation axes aligned with the local magnetic field. It then follows that far-IR polarization measurements map the structure of magnetic field lines in the plane-of-the-sky; the field lines are perpendicular to the E-vector of the polarized emission.

2. Observations and Results

The far-IR polarimetry reported here was carried out on the KAO over a three year period from 1991 to late 1993. We used the far-IR polarimeter of the University of Chicago, Stokes. This instrument is described in Platt et al. (1994). Measurements were made at 100 μm with a spatial resolution of 35". Stokes has an array of 32 beams in a 6 x 6 configuration (with the corner beams omitted), covering an area of 3.'7 x 3.'7 on the sky. A list of the star forming regions studied by us during this period and an overview of our results are given by Hildebrand et al. (1994). Here we will discuss three regions of high-mass star formation, NGC 2024, M42, and W3.

2.1 NGC 2024 and M42

NGC 2024 and M42 are two regions in the Orion Cloud Complex, which lies in the Cygnus Arm of our galaxy only 500 pc from our sun. This complex of dark clouds, H II regions, supernova remnants, and both high-mass and low-mass star formation sites, buckles out of the plane of the Galaxy in a horseshoe shape extending vertically below the plane about 20 degrees or 180 pc (see the CO maps of Maddalena et al. 1986). NGC 2024 and M42 are small regions within the giant molecular clouds, Orion B and Orion A respectively, where high-mass stars have recently formed and are still forming; hence, these regions contain both H II regions and bright far-IR sources. The large scale magnetic field structure in the diffuse regions of the Orion Complex is predominantly perpendicular to the Galactic plane as determined by the optical polarization measurements of stars located in the Orion Complex region reported in Mathewson and Ford (1970).

Figure 1 shows continuum maps of NGC 2024 at 40 and 100 μm (Thronson et al. 1984), and at 350 μm (Mezger et al. 1988). Superimposed on the 100 μm map are vectors, showing our measurements of the direction and degree of polarization at 100 μm. The three maps in Figure 1 show how the short wavelengths highlight the warm, HII region in NGC 2024 (a region with an E-W morphology), while the long wavelengths highlight the cold, dark, dust lane (a region with a N-S morphology). The 100 μm emission lies between these two extremes. Polarimetry based on this emission will be complicated by the superposition of two distinct regions in the same line-of-sight. Our 100 μm polarimetry results show that in the outer regions of NGC 2024 the magnetic field seems orderly and approximately perpendicular to the plane of the Galaxy, but near and in the dust lane (in projection) they are distorted. However, this could be the effect of two uniform fields in projection, one in the warm gas and the other in the cold gas. Complementary observations at about 60 μm and 400 μm, for example, can help to disentangle these projection effects.

M42 is a compact, blister, H II region (diameter of ~0.5 pc) in front of and eating into the dense molecular cloud, OMC-1. The HII region is excited

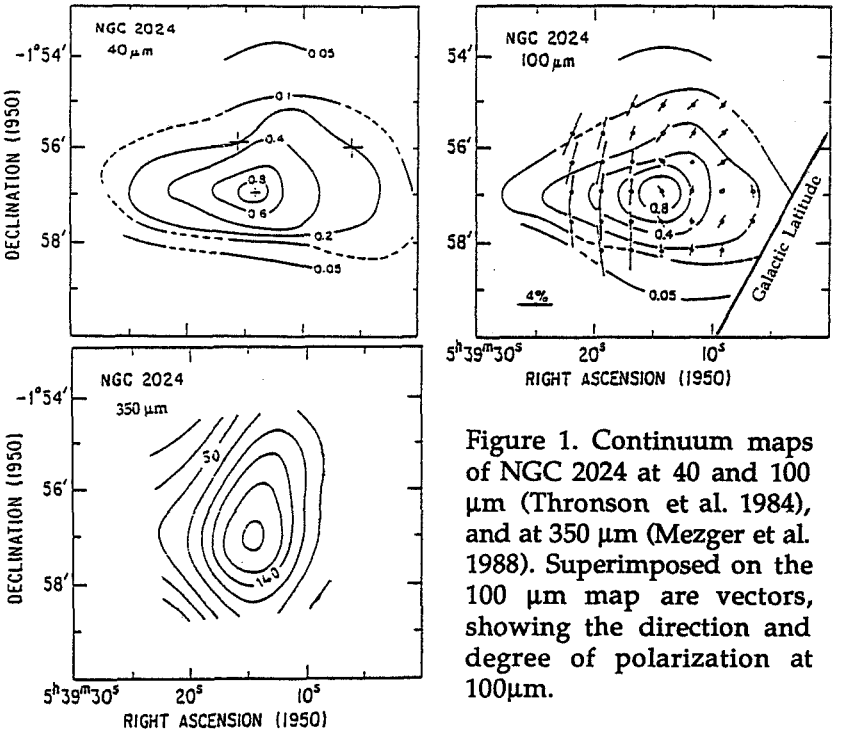

Figure 1. Continuum maps of NGC 2024 at 40 and 100 μm (Thronson et al. 1984), and at 350 μm (Mezger et al. 1988). Superimposed on the 100 μm map are vectors, showing the direction and degree of polarization at 100μm.

by OB stars in the Trapezium Cluster which lie in front of OMC-1. Within OMC-1, but presumably near its surface, lie four mass concentrations along a ridge (based on the CS measurements of Mundy et al. 1988), each about 0.04pc in diameter and 50 $M_\odot$ in mass. One is a bright IR source, BN-KL, which contains two massive YSOs, BN and IRc-2, of about 20 $M_\odot$ each; IRc-2 exhibits a powerful bipolar outflow. (Also forming within OMC-1 are a large number of low-mass stars, which are more evenly distributed.) Figure 2 shows our far-IR flux and polarization map of the M42/OMC-1 region. Indicated in this figure is the region called the molecular bar, which is thought to be part of the OMC-1 cloud that envelops the bottom of the HII region; it protrudes towards the observer (see Thronson et al. 1986). Our polarization measurements in Figure 2 were all made in November 1993 using Stokes. Previous 100 μm polarimetry observations of this region by Gonatas et al. (1990), made with the single-beam, University of Chicago polarimeter on the KAO, measured only ten positions in this region. The Gonatas et al. results agree with those presented here.

The polarization measurements in Figure 2 imply that: (i) the overall direction of the field in the OMC-1 ridge region is similar to the direction measured for the field on a larger scale using optical polarimetry (see Figure 12 in Hildebrand et al. 1994); (ii) the magnetic field in the OMC-1 ridge is perpendicular to the ridge; and (iii) the magnetic field in the molecular bar

region is distorted from the overall field. This picture of the magnetic field structure is consistent with the uniform magnetic field in the OMC-1 cloud being a simple compression of the external large scale field, where the contraction of the OMC-1 cloud has been predominantly in the direction of the magnetic field lines. The distortion in the molecular bar could be due to pressure on the cloud by the foreground HII region. The HII region compresses the field into the OMC-1 cloud; from our perspective, this compression maintains the uniformity of the field behind the HII region, but distorts the field in the OMC-1 cloud to the south of the HII region where the cloud is being compressed perpendicularly to our line-of-sight. In Section 3, we will look at this picture more quantitatively.

Figure 3 shows an outline of the OMC-1 cloud with the polarization vectors of Figure 2 rotated by 90 degrees to represent the mean direction of the magnetic field on the plane-of-the-sky. In the north region of the map, magnetic field lines have been sketched to give a probable field configuration. Here it can be seen that the magnetic field lines have been bent towards the dense BN-KL region in a way predicted by Mouschovias (1976) for a cloud which is initially spherical and contracting in the presence of a uniform

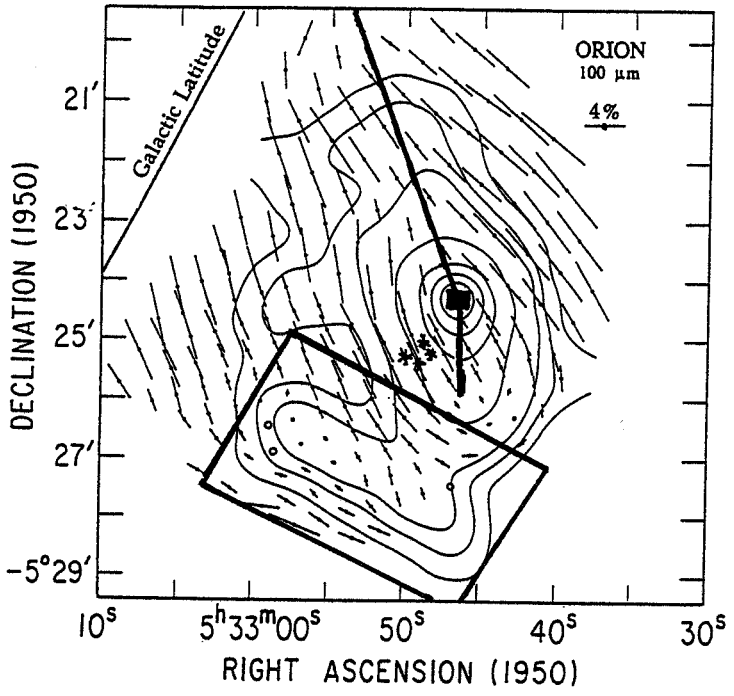

Figure 2. Our far-IR flux and polarization map of the M42/OMC-1 region. Vectors show the direction and degree of polarization. Also shown are the locations of the OMC-1 ridge (solid line), the BN-KL high-mass star formation region (solid square), the Trapezium Cluster (four stars), and "the molecular bar" (rectangle).

C-4.

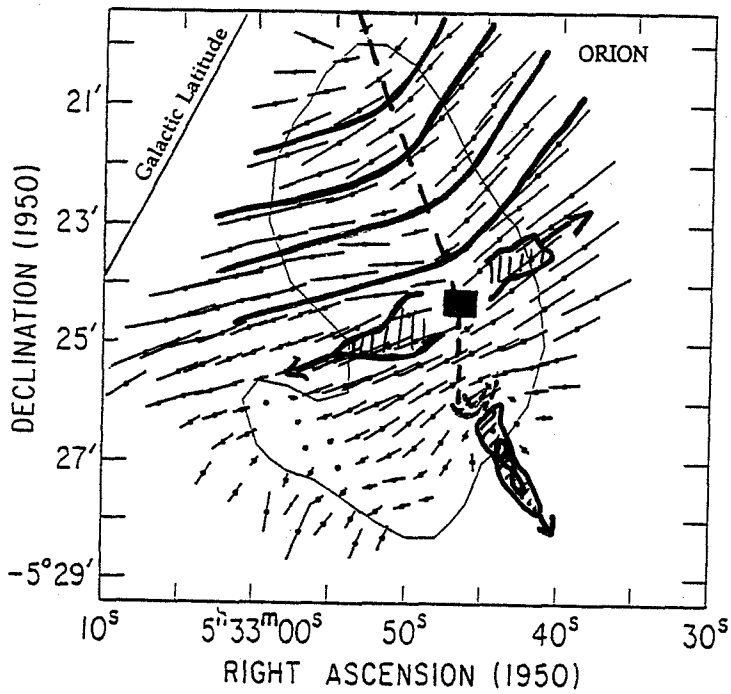

Figure 3. An outline of the OMC-1 cloud with the polarization vectors of Figure 2 rotated by 90 degrees to represent the mean direction of the magnetic field on the plane-of-the-sky. Probable magnetic field lines are sketched in the north. Also sketched are two observed outflows.

magnetic field until field gradients and distortion halts further contraction in the outer regions. Also shown in Figure 3 are the outflows observed in the OMC-1 region.

2.2 W3

W3, W4, and W5 form a chain (~ 240 pc long) of HII regions and clouds in the Perseus Arm of the Galaxy about 2.4 Kpc from our sun. This chain lies in the plane of the Galaxy. Optical polarization measurements imply that the magnetic field in this region of the Galaxy, on scales greater than 5 degrees, is aligned with the projection of the Galactic plane. Based on the molecular line work of Lada et al. (1975), it would seem that the well-developed, large H II region of W4 has expanded into the molecular cloud of W3, causing sequential high-mass star formation at the interface. Figure 4 shows our 100 μm photometry and polarimetry of a section of this interface, commonly designated W3, where the HII region of W4 lies to the east and the undisturbed cloud of the W3 region lies to the west of the region shown. Based on the vectors in Figure 4, one observes that: (i) the magnetic field lines

in this region are, on average, highly inclined to the plane of the Galaxy and, therefore, to the large scale magnetic field in the region; and (ii) the magnetic field within the region shown in Figure 4 is highly distorted. A possible explanation for the large inclination to the Galactic plane is that the H II region of W4 has pushed the ambient magnetic field into the overall configuration seen in Figure 4, a situation similar to the molecular bar in OMC-1. The distortion may be caused by gravitational or rotational effects, by expansion of internal H II regions, or by random turbulence generated by outflows. All of these potential causes of distortion are present in this part of W3, where at least 5 high-mass star formation sites are located. It should be noted that at the distance of W3, the M42/OMC-1 region shown in Figure 2 would occupy only a 1'x1' area. It is too early in our analysis to say which cause of distortion is dominant.

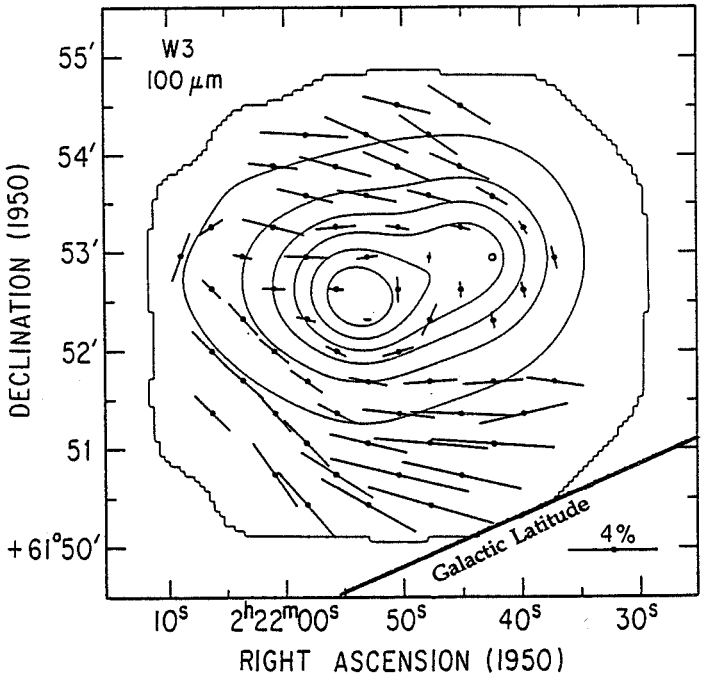

Figure 4. Our far-IR flux and polarization map of W3. Vectors show the direction and degree of polarization. Also shown is the direction of constant Galactic latitude.

3. Discussion

To quantify the qualitative scenario presented for M42 in Section 2.1, we must first estimate the magnetic field strength. There is no theory which can relate the degree of polarization to field strength; too many competing effects are involved (see Hildebrand 1988). However, an estimate of the strength of the field can be obtained by comparing the level of distortion in the direction of polarization to the forces known to be present. Distortion can be random

or systematic. Systematic distortions are caused by large scale forces such as gravity or H II shock fronts; random distortions are forces on the small scale such as turbulence. Chandrasekhar & Fermi (1953) were among the first to analyze field distortions to provide information about magnetic field strengths. Their analysis assumed that if the magnetic field is frozen into the medium and if signals travel along the field lines at the Alfvén speed $V_A = B/(4\pi\rho)^{1/2}$, then a small velocity perturbation, ∂V, perpendicular to the field lines will distort the field lines so as to produce a small transverse magnetic component, ∂B, satisfying : $\partial B/B = \partial V/V_A$. Here $\partial B/B$ can be obtained from the angular deviation, $\partial\phi$, of the magnetic field, or of the direction of polarization. If ∂V is random, as in turbulence, the above relation can be averaged over a number of data points and an estimate of the magnetic field given by

$$B = (<\partial V^2> / <\partial\phi^2>)^{1/2}(4\pi\rho)^{1/2} ,$$

where B is the strength of the total magnetic field, not just the field in the plane-of-the-sky. Before one can use this estimate, one must subtract the systematic distortions from the random. We have not yet done this in a sophisticated way, but the magnetic field lines sketched in Figure 3 crudely trace a likely systematic distortion in the magnetic field lines in the north. If we assume that along the ridge the field lines should be perpendicular to that ridge (as drawn), then deviations from this could be attributed to random forces such as turbulence. We selected the data points along the ridge, north of BN-KL, and found $(<\partial\phi^2>)^{1/2} \leq 5^o$ rms. Substituting this value into the above relation, and using

$$\Delta V_{FWHM}/(8\ln 2)^{1/2} \approx \sigma_{turb} = (<\partial V^2>)^{1/2} = 1.1 \text{km s}^{-1}$$

and $n \approx 10^5$ cm^{-3} (values from Mundy et al. 1988 for the northern OMC-1 ridge), we calculate an estimate for the magnetic field strength of approximately 3 mG. There is a caveat to this estimate, however: Zweibel (1990) argued that if a cloud is clumpy, where the clumps are dense and small so that ambipolar-diffusion has occurred leaving them untied to the cloud's magnetic field lines, but the motions of the unresolved clumps contribute significantly to the velocity dispersion measured for the cloud, then the estimate given above could be a gross overestimate.

Is 3 mG consistent with available Zeeman measurements? Troland, Heiles, & Gross (1989) have measured the Zeeman Effect in the 21 cm absorption line of H I towards M42. Their measurements covered the area shown in Figure 2 and were made with comparable beam sizes. Based on their measurements, they determined the strength of the magnetic field along the line-of-sight in the 400 cm^{-3}, H I gas, which lies just in front of the H II region of the Trapezium stars, to be about 70 μG. The value of the field strength for this foreground gas in the plane-of-the-sky is unknown, but if we assume it to be similar to that along the line-of-sight, then the total magnetic field strength is about 100 μG. If we assume a scaling law between gas density and magnetic field strength, $B/B_o = (n/n_o)^\alpha$, and substitute the

measured magnetic field strengths with their corresponding gas densities for the OMC-1 and the HI regions, we find $\alpha = 0.6$. This value is just outside the range calculated by Mouschovias (1976) for cloud contraction with field lines frozen-in (i.e., 0.3 - 0.5). This could be the result of our estimate being too high or of forced contraction of OMC-1 in the direction perpendicular to its magnetic field lines by the expansion of the HII region in the foreground.

We can use the Virial Equation to see if the HII region in front of OMC-1 is capable of distorting the magnetic fields in the region:

$$(0.5)(d^2I/dt^2) = 2K + 2T + M + W + \text{Surface Terms},$$

where I is the generalized moment of inertia; K, T, M, and W are the kinetic, thermal, magnetic, and gravitational energies of the OMC-1 ridge region; and the surface terms are due to thermal, kinetic, and magnetic forces acting on the surface of OMC-1 from the HII region. Here we have approximated: $2K \approx 3M_r\sigma_{turb}^2$; $2T \approx 3M_r c_s^2$; $2M \approx M_r V_A^2$; $W \approx -G M_r^2/R_r$; and Surface Terms $\approx -[P_{HII} + B_{HII}^2/24\pi]\,(4\pi R_r^3)$. In these expressions M_r and R_r are the mass of the OMC-1 ridge and its radius, and P_{HII} and B_{HII} are the gas pressure and magnetic field in the H II region. Using probable parameter values for the HII and OMC-1 regions as summarized in Genzel and Stutzki (1989) and Mundy et al. (1988), and our own estimates of the magnetic field strength and scaling law, we find that : (i) Within the OMC-1 ridge, the kinetic plus thermal terms are approximately equal and opposite the gravitational term and, therefore, cancel; and (ii) the magnetic term in the OMC-1 region is an order of magnitude greater than any other term except for the surface term, which within an uncertainty of three can be considered equal. These two results imply that magnetic fields are dynamically important, and that they have severely decreased the star formation rate in OMC-1, both by preventing gravitational collapse and by preventing the HII region from more severely compressing the molecular cloud.

4. Summary

The analysis of the far-IR polarimetry results presented here is only of first order. A more thorough analysis will improve the accuracy of the strength estimated for the magnetic field in OMC-1 (as well as in other clouds summarized in Hildebrand et al. 1994) by: (i) better separating random from systematic field distortions (e.g. Myers & Goodman 1991); and (ii) better determining which velocities are associated with the random motion of the gas tied to the magnetic field lines (as argued in Zweibel 1990). In addition, our maps of the magnetic field structure can be used to model probable magnetic field configurations, and thus better estimates of the dynamical importance of the magnetic fields in these clouds can be obtained using the magnetic tension term as well as the pressure term in the force equation of the gas in the clouds.

If one accepts our first order analysis at face value, however, then in summary: (i) the magnetic field - density law in M42/OMC-1 seems to be somewhat steeper than predicted by Mouschovias (1976), possibly because of the compression due to the HII region in the foreground of OMC-1; (ii) the

deformation of magnetic field lines by HII regions could also explain the large and small scale magnetic field configurations in W3, where the field lines in the HII region/W3 cloud interface are highly inclined to those of the large scale field in that region of the Galaxy, and the fields within W3 are distorted where there are embedded HII regions around YSOs; and (iii) the magnetic fields in M42/OMC-1 may well be dynamically important, being a major regulator of star formation, in that clumps within OMC-1 must wait for ambipolar-diffusion before further collapse can occur.

The measurement of magnetic fields in the dense ISM is a young study where measurements on large as well as small scales are still required. In the future, observations must include complementary far-IR and sub-mm polarimetry measurements, so that warm and cold regions along a common line-of-sight can be disentangled (recall the situation in NGC2024). In addition, future Zeeman measurements must use molecules which trace the more dense ISM than heretofore, in order to determine the structure and strength of the field in the line-of-sight of dense star formation regions, studies which will complement far-IR and sub-mm polarimetry of these same regions. And finally we look forward to more sensitive telescopes, which will enable the above studies to be extended to low-mass star formation regions.

References

Genzel, R., & Stutzki, J. 1989, Ann. Rev. Astr. Ap., 27, 41
Gonatas, D. P., et al. 1990, ApJ, 357, 132
Hildebrand, R. H. 1988, Q.J.R.Astr.Soc. 29, 327
Hildebrand, R. H., Dotson, J. L., Dowell, C. D., Platt, S. R., Schleuning, D., Davidson, J. A., Novak, G. 1994 in Proc. of the Airborne Astronomy Symposium on the Galactic Ecosystem: From Gas to Stars to Dust, eds. M. Haas, J. A. Davidson, and E. F. Erickson, (A.S.P. Conf. Series), paper 111
Lada, C. J., Elmegreen, B. G., Cong, H. I., & Thaddeus, P. 1975, ApJ, 226, L39
Maddalena, R. J., Morris, M., Moscowitz, J., Thaddeus, P. 1986, ApJ, 303, 375
Mathewson, D. S., & Ford, V. L. 1970, Mem. R. Astr. Soc., 74, 139
Mezger, P. G., Chini, R., Kreysa, E., Wink, J. E., & Salter, C. J. 1988, A&A, 191, 44
Mouschovias, T. C. 1976, ApJ, 207, 141
Mouschovias, T.C., & Paleologov, E. V. 1980, ApJ, 237, 877
Mundy, L. G., Cornwell, T. J, Masson, Scoville, N. Z., C.R., Baath, L. B., & Johansson, L. E. B. 1988, ApJ, 325, 382
Myers, P. C., & Goodman, A. A. 1991, ApJ, 373, 509
Parker, E. N. 1966, ApJ, 145, 811
Platt, S. R., Dotson, J. L., Dowell, C. D., Hildebrand, R. H., Novak, G., & Schleuning, D., 1994 in Proc. of the Airborne Astronomy Symposium on the Galactic Ecosystem: From Gas to Stars to Dust, eds. M. Haas, J. A. Davidson, and E. F. Erickson, (A.S.P. Conf. Series), paper 707
Pudritz, R. E., & Norman, C.A. 1983, ApJ, 274, 677
Shu, F. H., Adams, F. C., & Lizano, S. 1987, Ann. Rev. Astr. Ap., 25, 23

Thronson, H. A., Lada, C. J., Schwartz, P.R., Smith, H. A., Smith, J., Glaccum, W., Harper, D. A., & Loewinstein, R. F. 1984, ApJ, 280, 154
Thronson, H. A., et al. 1986, A.J., 91, 1350
Troland, T. H., Heiles, C., & Gross, W. M. 1989, ApJ, 337, 342
Zweibel, E. G. 1990, ApJ, 362, 545

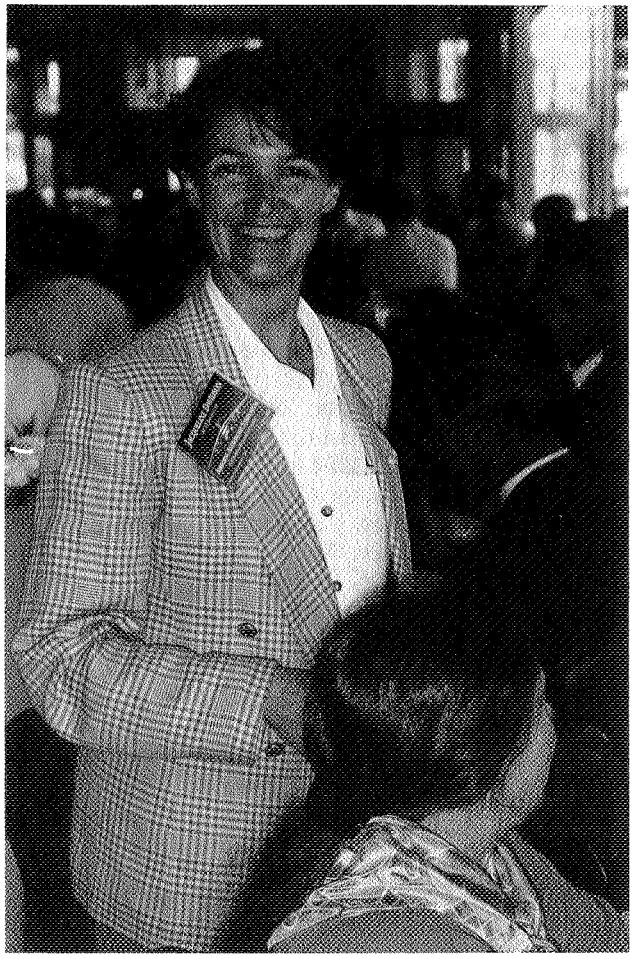

Jackie Davidson, Harriet Dinerstein

Airborne Astronomy Symposium on the Galactic Ecosystem
ASP Conference Series, Vol. 73, 1995
M.R. Haas, J.A. Davidson, and E.F. Erickson (eds.)

The Envelopes Around Young Stellar Objects: What Can Far-Infrared Observations Tell Us?

H. M. Butner

Dept. of Terrestrial Magnetism, Carnegie Institution of Washington, 5241 Broad Branch Road, N. W., Washington, D.C. 20015

G. H. Moriarty-Schieven

Dominion Radio Astrophysical Observatory, P. O. Box 248, Penticton, BC V2A 6K3, Canada

M. E. Ressler and M. W. Werner

Jet Propulsion Laboratory, California Institute of Technology, 4800 Oak Grove Drive, Pasadena, CA 91109

Abstract. High resolution, far-infrared spatial observations offer a way to probe the density structure of the envelopes around young stellar objects, and thus provide a test of star formation theories. As part of a long term program, we are using the Kuiper Airborne Observatory with the Yerkes Far-Infrared Camera system to study the far-infrared emission (60, 100, 160, and 200 μm) from a number of low mass embedded objects in Taurus. By comparing the observations with the results of radiative transfer models, we are able to estimate the envelope density distribution around these systems. We present our initial results for 4 embedded objects (L1551-IRS 5, L1489-IR, L1551-NE, and L1527-IR).

1. Introduction

In the mid-1980s, our understanding of star formation was revolutionized by two converging lines of research. First, there was the classification of young stellar objects (YSOs) by their spectral energy distribution (Lada 1987). Three classes were devised based on the slope of the infrared flux between 2-25 μm. A source where the flux rose as the wavelength increased was classified as Class I. A source that had a substantial infrared excess in the near- and mid-infrared but where overall the flux fell between 2 and 25 μm was designated Class II. A star with a nearly stellar spectral energy distribution fell into Class III. The three classes naturally suggest an evolutionary sequence from Class I (embedded objects, still shrouded in dust) through Class III (visible objects, little nearby dust). Thus, the observable spectral energy distribution (SED) could serve to identify the source's evolutionary state.

At the same time, the mid-1980's also saw tremendous advances in theoretical models for young stellar objects. Terebey, Shu, and Cassen (1984, henceforth TSC) developed the idea of a slowly rotating sphere undergoing inside-out col-

lapse. In this scenario, the initial condition is an isothermal sphere with an envelope radial density gradient $n(r) \propto r^{-2}$. Collapse begins at the center of the core, hence "inside-out" collapse. Once collapse has started, the infalling zone develops a density gradient of $r^{-1.5}$. Since material encounters a centrifugal barrier as it falls in towards the center due the slow rotation of the cloud, a disk forms. The TSC model makes definitive predictions for the expected envelope density gradient, density, central source luminosity, and overall size scales of a YSO throughout its formation.

Adams, Lada, and Shu (1987) combined the inside-out collapse model with a radiative transport model to predict what the SEDs of a protostar might look like. Dust in the infalling envelope reprocesses much of the central source luminosity, shifting the flux to longer wavelengths, and produces SEDs that are very similar in shape to those of Class I sources. Adams, Lada, and Shu modeled the SED of 6 Class I YSOs in detail and found excellent matches between their TSC-type models and the observations. These sources included the well known source L1551-IRS 5, a 30 $L_\odot$ YSO in Taurus. These models provided the first real test for the TSC picture and helped establish that theory as one of the dominant theories to explain low mass star formation.

2. The Need for Spatial Observations

More recent work, however, has revealed that the SED is not necessarily unique to a particular source model. For example, Zhou et al. (1990) found that the SED of B335, a deeply embedded YSO, could be modeled equally as well either as arising from an envelope with a very flat density gradient or as arising from the infalling envelope predicted by TSC. With an envelope dust optical depth equivalent to several hundred A_V, the envelope reprocesses the central source's radiation completely. The large value of extinction makes the individual radiative transport models insensitive to the assumed density gradient. Butner et al. (1991) found changing the dust opacity law assumed can also alter the predicted SED of deeply embedded sources, particularly in the mid-infrared. More recently, Kenyon et al. (1993) modeled Class I sources in Taurus with modified forms of the TSC model. They found several models that could match the observed SED. Hence, the SED alone does not provide a unique test of the TSC star formation scenario.

One way to further constrain source models and thereby test our understanding of star formation models is through far-infrared spatial observations. The basic idea is simple; if the envelope has a steep density gradient, it will have a narrower spatial extent than a flat density gradient envelope model (Figure 1) for the same total source luminosity and envelope optical depth. The University of Texas's 20 channel Si-bolometer system on board the Kuiper Airborne Observatory (KAO) can map sources at either 50 or 100 μm with near diffraction-limited resolution. With high signal to noise, observations can distinguish between the predictions of the various models. This technique has been used successfully on a number of sources such as L1551 (Butner et al. 1991, Butner, Natta, & Evans 1994) and NGC 2071 (Butner et al. 1990). For these sources, we found the density gradient $\alpha = 1.5$ ($n(r) \propto r^{-\alpha}$), with $\tau_{100\mu m} = 0.2$ to 0.4 (equivalent to A_V from 100 to 200). The far-infrared spatial observations

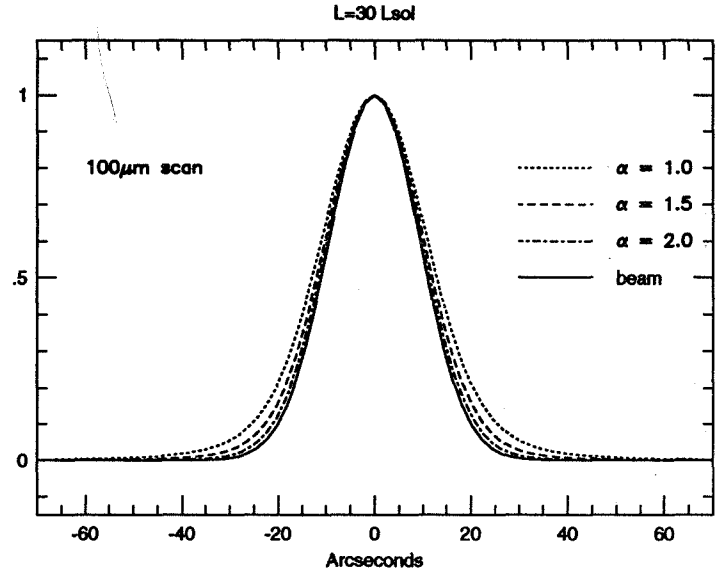

Figure 1. Comparison of the predicted 100 μm flux from 3 different density gradients ($\alpha = 1.0, 1.5, 2.0$) with the KAO beam profile. Each model first has been convolved with the KAO beam (24 arcseconds) and then normalized. The models are based on L1551-IRS 5 ($L=30L_{\odot}$) models (Butner et al. 1991)

of L1551-IRS 5 provide some of the strongest support for the TSC inside-out collapse model.

More recent studies of Herbig Ae/Be objects have revealed that the envelope density gradients around many of these sources are considerably flatter than what the TSC scenario would predict. Herbig Ae/Be stars are intermediate mass pre-main sequence stars (M_* between 2 and 8 $M_{\odot}$). Hillenbrand et al. (1992) classified the Herbig Ae/Be's in a manner similar to the Class I, II, III scheme of low mass YSOs. Natta et al. (1992, 1993) found density gradients $\alpha \leq 1.0$ for a number of "Class I" Herbig Ae/Be stars (the Group II sources of Hillenbrand et al.). The "Class II" Herbig Ae/Be stars (Group I sources of Hillenbrand et al.) also reveal very extended far-infrared emission (Di Francesco et al. 1994a,b), inconsistent with a disk alone or an envelope which has a steep density gradient. These results pose a potential problem for the TSC picture. However, Herbig Ae/Be stars are more massive than the typical source envisioned by TSC. In addition, they are visible stars, and probably have almost exhausted their envelope material, near the end of the infall stage modeled by TSC. To really test the TSC model requires studying solar mass stars which are still deeply embedded in their placental envelopes and are surrounded by either an isothermal shell ($\alpha = 2.0$) or an infalling envelope ($\alpha = 1.5$).

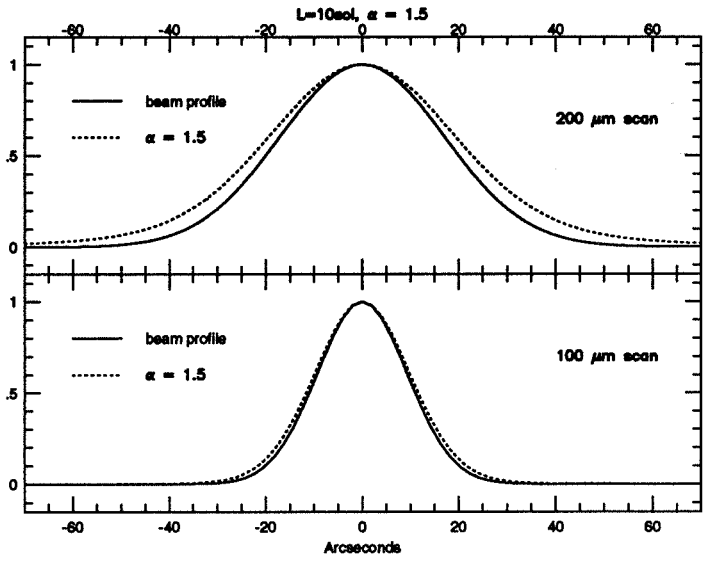

Figure 2. Comparison of the predicted 100 and 200 μm flux from the TSC infall envelope (density gradient $\alpha = 1.5$) for a 10 $L_\odot$ central source with the KAO beam profile. Each model has been convolved with the KAO beam (24 arcseconds at 100 μm, 52 arcseconds at 200 μm), and then normalized.

3. Observations

Tamura et al. (1991) did a 2 μm survey of low luminosity cold IRAS sources in Taurus. These sources were either Class I or Class II sources, all with luminosities less than 30 $L_\odot$ (implying $M_{YSO} \leq 1\ M_\odot$). The sources included L1551-IRS 5, one of the original Adams, Lada, and Shu (1987) sources, as well as many less well known sources. Moriarty-Schieven et al. (1992, 1994) have conducted searches for the presence of both CO outflows and millimeter emission. Many new CO outflows were identified, and a number have associated millimeter emission. These sources appear to be ideal for a large scale test of the TSC model.

Unfortunately, repeating the L1551-IRS 5 studies of Butner et al. (1991) and Butner, Natta &Evans (1994) is harder for a 10 $L_\odot$ source at the distance of Taurus. The reason is that a lower luminosity source does not light up as large a region as the 30 $L_\odot$ L1551-IRS 5. Thus, the 100 μm extent of the 10 $L_\odot$ YSO will be less for the same density gradient than we observed for L1551-IRS 5. In the case of L1551-IRS 5, Butner et al. (1991) barely resolved the emission. Thus, unless the density gradient is very flat, we would expect not to resolve any of the lower luminosity embedded sources from the Tamura sample at 100 μm. Fortunately, it is possible to get around this problem by going to longer wavelengths. If we were to observe at 200 μm instead of 100 μm, then we would expect to resolve the far-infrared emission from a $n(r) \propto r^{-1.5}$ envelope. Figure 2 illustrates how shifting to longer wavelength allows us to resolve easily

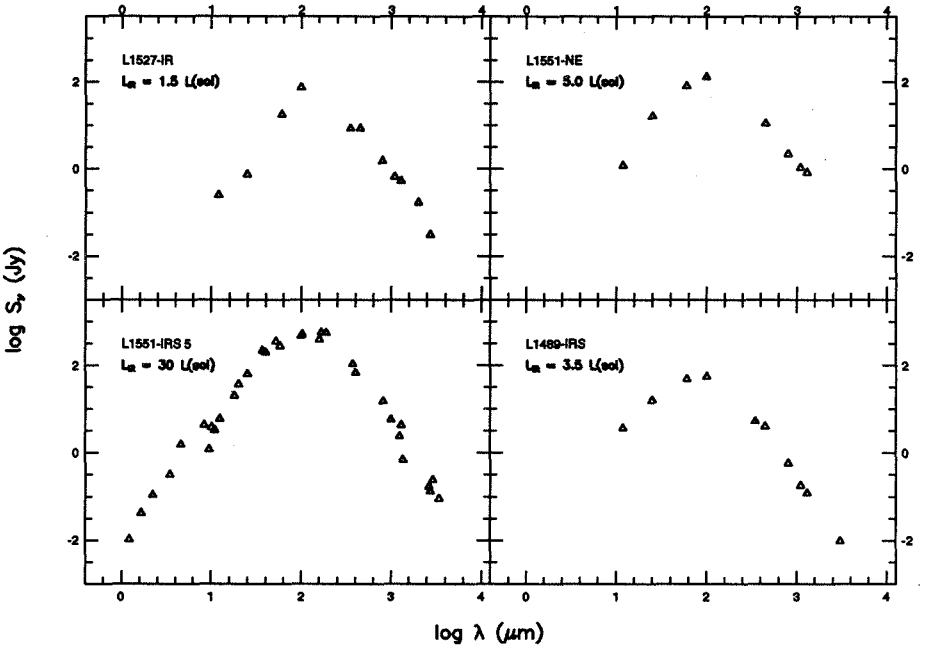

Figure 3. Log S_ν (Jy) vs Log λ (μm) : The observed spectral energy distributions for L1551-NE, L1527-IR, L1551-IRS 5, and L1489. Butner, Moriarty-Schieven, and Wannier (1994)

at 200 μm what is barely resolvable at 100 μm. We used the Yerkes Observatory 60-channel Far-Infrared Camera on board the KAO, which images at 60, 100, 160, and 200 μm at near the diffraction limit. See Harper et al. (1994) for details on the instrument.

In 1993 September, we observed four embedded sources from the Tamura list: L1551-IRS 5, L1489-IR, L1527-IR, and L1551-NE. They were all Class I sources (Figure 3), indicating that they are deeply embedded protostars. In fact, L1551-NE was barely detectable by IRAS at 12 μm, and L1527-IR is not seen at all by IRAS at 12 μm. L1527-IR is an example of a Class 0 source, which has been suggested as a candidate for the earliest stage of the star formation process (c.f. Andre, Ward-Thompson, and Barsony 1992). Each source was mapped by taking a snapshot, moving the camera position slightly, and taking another snapshot. By taking a number of such snapshots, we built up an oversampled image of each source. To measure the point spread function, we observed known point sources, such as Ceres or Pallas, in the same way. The data is co-added and smoothed to eliminate spikes. The initial smoothing function limited our resolution to 70 arcseconds at 200 μm. However, with a more refined smoothing algorithm, we will achieve the diffraction limit of 52 arcseconds at 200 μm for the KAO. We also have not removed the background extended emission from the images below.

Figure 4. L1489-IRS 100 and 200 μm images from the Yerkes Camera. The upper plot is 100 μm, the lower is 200 μm. The source is on the left-hand side and the point source profile is on the right-hand side. The size scale is 5 arcminutes to a side. The rotation of field is uncorrected.

We find that our sources split into two groups. Both L1551-IRS 5 and L1489-IRS are only slightly broader at the full width-half maximum point than the beam profile (as measured using Ceres) at both 100 and 200 μm (Figure 4). This implies a steep density gradient, around $\alpha = 1.5$ based on the models of Butner et al. (1991) and Butner, Natta & Evans (1994). In contrast, both L1551-NE and L1527-IR are only slightly broader than the point source at 100 μm but very extended at 200 μm relative to the beam profile's full width-half maximum (Figure 5). The large 200 μm spatial extent argues for a fairly flat density distribution. Initial models would suggest that the density gradient would have to be shallower than $\alpha = 1.0$. The dust optical depth at 100 μm is at least 0.1 ($A_V \geq 40$). In addition, both L1527-IR and L1551-NE show some structure at 200 μm. They are both somewhat flattened, suggesting that their geometry is not completely spherical. It is interesting to note that it is the "Class 0" sources, L1527-IR and L1551-NE, that are extended. Such behavior may reflect a different starting condition for the collapse or a different collapse pathway than envisioned by TSC. The TSC model does produce non-spherical structures, but typically on size scales of hundreds of AU, not the 10000 AU size scales we see for L1527-IR and L1551-NE at 200 μm. In addition, one would expect the non-spherical region of the TSC model to achieve large size scales only late in the YSO formation, when the envelope should be relatively thin. These preliminary results suggest that we have examples of sources that fit the TSC picture and sources that may require a different source model.

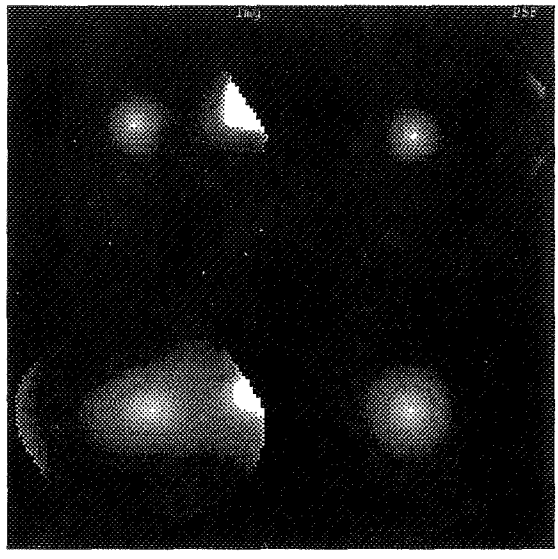

Figure 5. L1551-NE 100 and 200 μm images from the Yerkes Camera. The upper plot is the 100 μm image, the lower is 200 μm. The source is on the left-hand side and the point source profile is on the right-hand side. The size scale is 5 arcminutes to a side. The bright source off to the right of L1551-NE is the edge of L1551-IR. The rotation of field is uncorrected.

One such model is proposed by Hartmann et al. (1994). In this scenario, the collapse takes place not in a sphere but in an isothermal self-gravitating sheet. This geometry produces a flattened or toroidal distribution as the collapse proceeds.

4. Summary

Far-infrared observations at several different wavelengths have resolved a number of Class I YSOs at 100 and 200 μm. Some of the sources are compact (L1551-IRS 5, L1489-IRS) in agreement with TSC model predictions. Thus, some support for the TSC model is provided by our far-infrared spatial studies. However, other sources are more extended and are clearly non-spherical (L1527-IR, L1551-NE), in contrast to the simple TSC picture. An alternate collapse model based on a slab geometry for the initial conditions may provide a viable explanation for the observed far-infrared properties of L1527-IR and L1551-NE. Within Taurus, there exists a range of density gradients and geometries among the low mass YSOs.

Acknowledgments. This work was supported in part by grants from the NASA Origins of the Solar System Program (NAGW-4097) and from the Kuiper Airborne Astronomy Program.

References

Adams, F. C., Lada, C. J., & Shu, F. A. 1987, ApJ, 312, 788

Andre, P., Ward-Thompson, D., & Barsony, M. 1993, ApJ, 406, 122

Butner, H. M., Evans, N. J. II, Harvey, P. M., Mundy, L. G., Natta, A., & Randich, M. S. 1990, ApJ, 364, 164

Butner, H. M., Evans, N. J. II, Lester, D. F., Levreault, R. M., & Strom, S. E. 1991, ApJ, 396, 636

Butner, H. M., Moriarty-Schieven, G. H., & Wannier, P. G. 1994, ApJ, in preparation.

Butner, H. M., Natta, A., & Evans, N. J. II 1994, ApJ, 420, 674

Di Francesco, J., Evans, N. J. II, Harvey, P. M., Mundy, L. G., & Butner, H. M. 1994a, ApJ, 432, 710

Di Francesco, J., Evans, N. J. II, Harvey, P. M., Mundy, L. G., & Butner, H. M. 1994b, in Proc of the Airborne Astronomy Symp on the Galactic Ecosystem: From Gas to Stars to Dust, ed. M. R. Haas, J. A. Davidson, & E. F. Erickson, San Francisco: ASP), paper 304.

Harper, D. A., Cole, D. M., Loewenstein, F., McMahon, T., Pernic, R. J., & Wirth, C. 1994, in Proc of the Airborne Astronomy Symp on the Galactic Ecosystem: From Gas to Stars to Dust, ed. M. R. Haas, J. A. Davidson, & E. F. Erickson, (San Francisco: ASP), paper 704.

Hartmann, L., Boss, A., Calvet, N., & Whitney, B. 1994, ApJ, 430, L49.

Hillenbrand, L. A., Strom, S. E., Vrba, F. J., & Keene, J. 1992, ApJ, 397, 613

Kenyon, S. J., Calvet, N. & Hartmann, L. 1993, ApJ, 414, 676

Lada, C. J. 1987, in Star Forming Regions: Proc. IAU Symp. 115, ed. M. Peimburt & J. Jugaku, (Dordrecht: D. Reidel), 1

Moriarty-Schieven, G. H., Wannier, P. G., Tamura, M., & Keene, J. 1992 ApJ, 400, 260

Moriarty-Schieven, G. H., Wannier, P. G., Keene, J., & Tamura, M. 1994, ApJ, in press

Natta, A., Palla, F., Butner, H. M., Evans, N. J. II, & Harvey, P. M. 1992 ApJ, 391, 805

Natta, A., Palla, F., Butner, H. M., Evans, N. J. II, & Harvey, P. M. 1993 ApJ, 406, 374

Tamura, M., Gatley, I., Waller, W., & Werner, M. W. 1991, ApJ, 374, L25

Terebey, S., Shu, F. H., & Cassen, P. 1984, ApJ, 286, 529

Zhou, S., Evans, N. J. II, Butner, H. M., Kutner, M. L., Leung, C. M., & Mundy, L. G. 1990, ApJ, 363, 168

Airborne Astronomy Symposium on the Galactic Ecosystem
ASP Conference Series, Vol. 73, 1995
M.R. Haas, J.A. Davidson, and E.F. Erickson (eds.)

Infrared Spectra of Protostellar Collapse

David Hollenbach
NASA/Ames Research Center, MS 245-3, Moffett Field, CA 94035-1000

Cecilia Ceccarelli
IFSI-CNR, CP27, Frascati (Rome), Italy and Observatoire de Grenoble, UJF-B.P.53X - 38401 Grenoble Cedex, France

David A. Neufeld
Johns Hopkins University, Department of Physics and Astronomy, Homewood Campus, Baltimore, MD 21218

Alexander G. G. M. Tielens
NASA/Ames Research Center, MS 245-3, Moffett Field, CA 94035-1000

Abstract. Theoretical models of the formation of low mass stars by cloud collapse predict that OI(63μm) and IR rotational lines of CO and H_2O dominate the cooling in the freefalling region 10-1000 AU from the protostar. The freefalling gas supersonically hits the protoplanetary disk orbiting the protostar, forming an accretion shock with strong IR emission in rotational lines of H_2O and OH, and OI(63μm). The accretion shock spectra and line profiles depend on the mass flux through the shock and the typical distance $\bar{r}$ at which the freefalling gas strikes the disk. The line widths are of order the Keplerian speed, or $\sim 10(\bar{r}/10\mathrm{AU})^{-0.5}$ km s^{-1}, for the accretion shock lines, and less for the lines from the infalling gas. Measurement of the IR line fluxes and profiles from the freefalling gas and the accretion shock diagnoses how a protostar and disk are formed and requires high sensitivity and high spectral and spatial resolving power. SOFIA will be the optimum observatory for many of these lines, although ISO will contribute and the KAO may make a few pioneering detections.

1. Introduction

In its 20 year history the Kuiper Airborne Observatory (KAO) has made many observations of the *effects* of star formation on the surrounding ambient clouds of gas and dust. These observations include those of the dust heated by the stellar radiation, the gas heated by ultraviolet photons in HII regions or photodissociation regions, and the gas heated by the shocks driven by protostellar winds. However, a combination of theoretical predictions and technological advances now make possible the observation of the *actual collapse* of a cloud to form a star/disk system. To date, solid observational evidence for collapse is scant (see Zhou et al. 1993 for a rather convincing observation of collapse in B335 using millimeter line profiles). The KAO is likely to make

pioneering observations of collapsing cloud cores, but the sensitivity and high resolving power of its successor, the Stratospheric Observatory for Infrared Astronomy (SOFIA), are required to unambiguously identify the collapsing region in the infrared (IR) and to probe its physical characteristics.

We discuss below two regions in the collapsing cores amenable to IR airborne observation: the freefalling gas and the gas passing through the accretion shock. The accretion shock is generated by the supersonically infalling material striking the Keplerian disk orbiting the protostar. The freefalling gas and dust is decelerated and heated within the accretion shock which stands at the disk surface and through which all material must pass in entering the protostellar nebula.

2. The Freefalling Collapse

Ceccarelli, Hollenbach & Tielens (1995, hereafter CHT) have modeled the spectrum of the freefalling gas self-consistently including the dynamics, thermal balance and chemistry. The dynamics is based on the Shu (1977) spherical collapse solution, with an inner cutoff radius r_c which represents the radius at which spherical symmetry breaks down due to rotation. Inside r_c the freefalling material crashes through the accretion shock and merges with the disk. Terebey, Shu & Cassen (1984) included rotation in the collapse solution, and showed that this "centrifugal radius", $r_c \sim 10^{14} - 10^{15}$ cm, is determined by the angular momentum of the initial core. Galli & Shu (1993a,b) have shown that the presence of an ordered magnetic field through the molecular core can alter the spherical infall at distances $r \lesssim 10^{16}$ cm, due to the interaction of the infalling neutral gas with the trace amounts of charged particles tied to the magnetic field. The bulk of the infall is thereby channeled to a thick "pseudo-disk" whose plane is perpendicular to the average field direction. The disk is "pseudo" in the sense that it is not rotationally supported; the pseudo-disk material falls radially toward the central star until it hits the Keplerian disk at r_c. The CHT model does not strictly apply to such an infall, but may provide a first approximation even in this case.

The Shu (1977) collapse begins from an initial isothermal equilibrium state where the gas density $n \propto r^{-2}$. The collapse starts at the center and moves outwards at the sound speed, the so-called "inside-out" collapse. The hydrogen gas density of the infall scales as $r^{-3/2}$. The mass accretion rate $\dot{M}$ is constant in time, and is proportional to the cube of the sound speed; typically, $\dot{M} \sim 10^{-5}$ $M_\odot$ yr^{-1}. If this mass accretes steadily through the disk onto the star, the protostellar mass increases linearly with time $M_*(t) = \dot{M}t$. Therefore, 10^5 years is the characteristic time to be observing a protostar. At this time the density of the freefalling gas is about 10^7 cm^{-3} at 100 AU.

The thermal balance computation involves an interplay of gas and dust. The dust is radiatively heated by the luminosity L_* originating from the protostar and cooled by its own thermal (continuum) radiation. The dust modifies the continuum spectrum as a function of r as it absorbs and reradiates continuum photons. Typically, the dust extinction from r_c to the observer is of order $A_v \sim 10 - 1000$.

The luminosity of a steadily accreting protostar varies with time as

$$L_* = \frac{GM_*(t)\dot{M}}{R_*(t)}, \quad (1)$$

where R_* is the stellar radius. For a 1 $M_\odot$ star accreting at 10^{-5} $M_\odot$ yr^{-1}, the steady accretion luminosity is $L_* \sim 65$ $L_\odot$. The relative paucity of such luminous protostars, coupled with the existence of FU Orionis outbursts, has led Bell & Lin (1994) to argue that the disk does not steadily accrete at a rate $\dot{M}$ onto the star, but rather builds up mass and then sporadically dumps it onto the protostar, producing (long) low luminosity intervals interspersed with (short) FU Orionis outbursts. CHT therefore used the Shu (1977) dynamics of the freefalling gas and dust, but kept L_* as a constrained free parameter. For reasonable values of L_*, the dust temperature is $T_{gr} \sim 100(r/100\ \mathrm{AU})^{-2/5}$ K.

The freefalling gas is mainly heated by collisions with warmer dust (in the outer regions), by compressional heating, and by absorption of IR photons by H_2O and CO followed by collisional deexcitation (in the inner regions). The gas cools by IR emission of OI(63μm) and by rotational transitions of CO (in the outer regions) and H_2O (in the inner regions). CHT found that the thermal coupling of the gas to the grains is quite efficient, and that typically $T_{gas} \sim T_{gr}$.

The chemistry is inherently time dependent, since the freefall time is short compared to the chemical equilibration time. However, the chemistry of the dominant coolants is relatively simple. The hydrogen and carbon begin the collapse primarily as H_2 and CO and remain so through the freefall collapse. The gas phase oxygen begins the collapse as O and O_2, with trace amounts of H_2O. However, as much as $\sim$ 10% of the oxygen may exist as ice mantles on grain surfaces. Once the infalling dust is heated to $\sim$ 100 K ($r \lesssim 10^{15}$ cm), this H_2O is sublimated into the gas. In addition, once the gas is heated to $\gtrsim 200-300$ K ($r \lesssim 3\times10^{14}$ cm), gas phase chemical reactions convert the O and O_2 into H_2O. Therefore, inside of 100 AU, the abundance of H_2O in the freefalling gas rapidly rises to $\sim 10^{-5} - 10^{-4}$ relative to hydrogen, and H_2O plays a dominant role in the thermal balance of the gas.

Figure 1 shows the 40-200 μm spectrum of the freefalling gas and dust for the case $M_* = 1$ $M_\odot$, $\dot{M} = 10^{-5}$ $M_\odot$ yr^{-1}, $r_c = 3\times10^{14}$ cm, and $L_* = 65$ $L_\odot$. The spectrum assumes a spectral resolving power of $R = \lambda/\Delta\lambda = 10^4$ (or 30 km s^{-1}), and the fluxes are given for a source in Taurus. For comparison, fluxes required for a S/N=5 in 15 minutes by various IR instruments are roughly: 3×10^{-12} erg cm^{-2} s^{-1} for the KAO, 3×10^{-13} erg cm^{-2} s^{-1} for the ISO LWS Fabry Perot (30 km s^{-1} resolution), and 1×10^{-13} erg cm^{-2} s^{-1} for a 3 km s^{-1} resolution instrument aboard SOFIA. The high sensitivity and resolving power of SOFIA are needed to detect the weak CO lines above the continuum. The line widths will be of order 2-20 km s^{-1}, so that, of the planned IR missions, only SOFIA will be capable of measuring line profiles.

Although CHT is in progress, we can make several comments about determining physical parameters by comparing observations to our model spectra. The most definitive observation that gas is collapsing would be an observation of the line profiles of the high J CO emission lines. The higher J CO transitions are generated in the warmer gas which is closer to the protostar and therefore falling faster. We predict, therefore, a correlation of the linewidth Δv with J such that Δv(J=13-12)$\sim 5(M_*/M_\odot)^{1/2}$ km s^{-1}, whereas, for example,

Δv(J=22-21) $\sim 16(M_*/M_\odot)^{1/2}$ km s^{-1}. The mass of the protostar M_* can be derived from the CO linewidths. The mass accretion rate $\dot{M}$ is related to the spectrum in a rather complicated fashion and a careful comparison of spectra to models is required. However, a crude estimate may be obtained from the OI(63μm) flux F_{OI} which very roughly scales with $\dot{M}$. At a distance of Taurus, $F_{OI} \sim 2 \times 10^{-13}(\dot{M}/10^{-6}$ M$_\odot$ yr$^{-1})$ erg cm^{-2} s^{-1}, with an accuracy of perhaps a factor of 2-3. The temperature and density profiles $T(r)$ and $n(r)$ in the freefalling gas can be obtained by measuring the fluxes of optically thick and optically thin lines of H_2O and CO. The inner cutoff radius, r_c, which is a measure of the size of the disk or the accretion shock, can be derived by observations of high J transitions of H_2O, which are primarily excited at r_c.

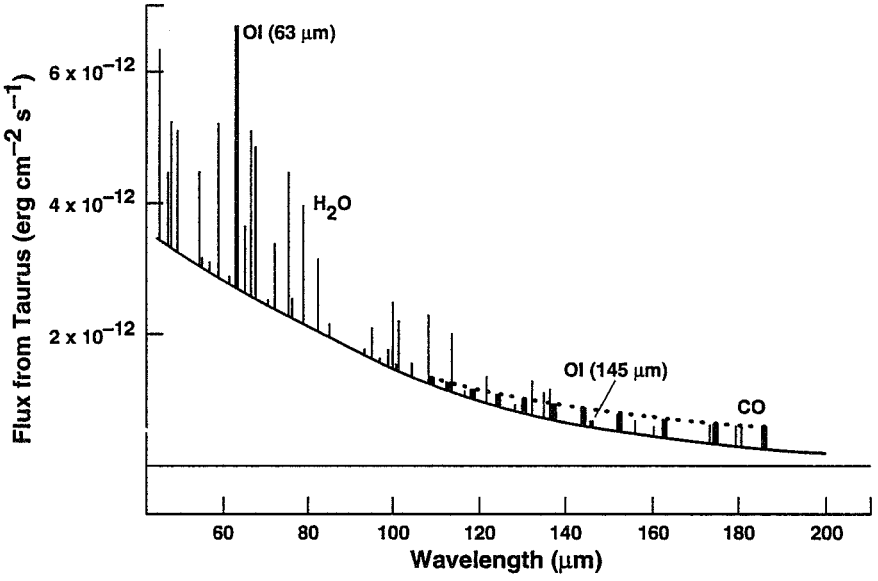

Figure 1. Freefall spectrum of 1 M$_\odot$ protostar in Taurus (see text).

3. The Accretion Shock

Neufeld & Hollenbach (1994, hereafter NH) discuss the physics of accretion shocks and model their spectrum. We review here briefly the results relevant for airborne astronomy. Figure 2 shows a schematic diagram of an accretion shock surrounding a protostar/disk system.

The disk size $r_d \sim r_c$ is set by the angular momentum of the material which has accreted onto the disk. In the Cassen and Moosman (1981) solution for the collapse of a uniformly rotating molecular cloud core, $r_d(t) \propto t^3$, where t is the elapsed time. Cassen and Moosman envisioned $r_d \sim 30-100$ AU at the end of the accretion phase when $M(t) \sim 1$ M$_\odot$. Because of the t^3 dependence of r_d, much of the accretion takes place when $r_d << 100$ AU. The freefalling material strikes the disk at all radii $r < r_d(t)$, and the preshock density and shock velocity vary with position in the accretion disk (see Figure 2). The median shock velocity,

$\bar{v}_s$, may be defined such that one-half the mass accretion rate occurs at radii for which the normal component of the infall velocity $v_n \geq \bar{v}_s$. The Cassen and Moosman solution then yields

$$\bar{v}_s = \left(\frac{GM}{3r_d}\right)^{1/2} = 17.2 \left(\frac{M_*(t)}{M_\odot}\right)^{1/2} \left(\frac{r_d(t)}{\mathrm{AU}}\right)^{-1/2} \mathrm{km\ s^{-1}}, \tag{2}$$

where $M_*(t)$ is the mass of the central protostar. The accompanying preshock density is

$$\bar{n}_0 = \frac{\dot{M}_s}{3\pi r_d^2 \mu \bar{v}_s} = 7.5 \times 10^{10} \dot{M}_{s-5} \left(\frac{M(t)}{M_\odot}\right)^{1/2} \left(\frac{r_d(t)}{\mathrm{AU}}\right)^{-3/2} \mathrm{cm^{-3}}, \tag{3}$$

where $\dot{M}_s = 10^{-5} \dot{M}_{s-5}\, M_\odot\ \mathrm{yr^{-1}}$ is the total mass accretion rate through the accretion shock and μ is the mass per H nucleus. The "median infall radius", $\bar{r}$, may be analogously defined such that one-half the infall occurs within $\bar{r}$. The median infall radius is found to be $\bar{r} = \frac{3}{4} r_d$.

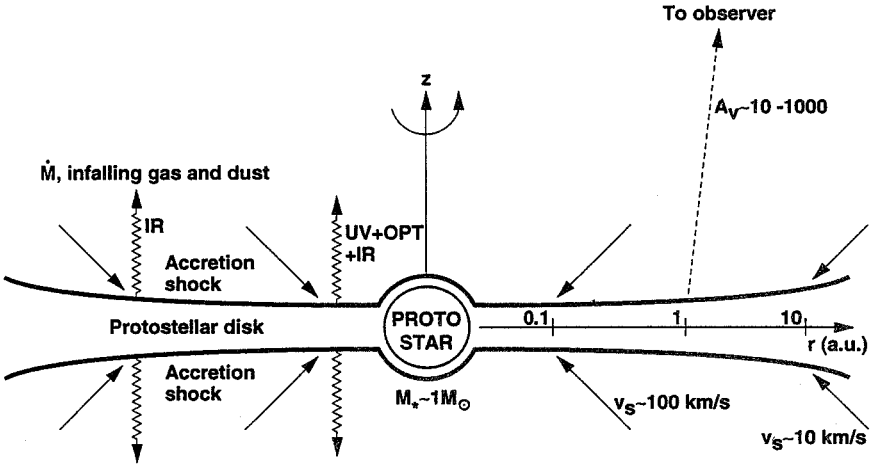

Figure 2. Schematic of accretion shock around 1 $M_\odot$ protostar/disk system.

In the Galli & Shu (1993a,b) magnetically-dominated collapse, the accretion shock occurs at the "edge" of the disk, instead of the face of the disk as in the Cassen and Moosman model. The normal component of the accretion shock velocity will be comparable to Eq.(2), but the preshock density for a given $\dot{M}_s$ will likely be somewhat higher than Eq.(3), because of the smaller surface area of the shock.

NH discuss whether the slower ($v_s \lesssim 30$ km s^{-1}) shocks in the outer regions ($r \gtrsim 0.25$ AU) of the disk are likely to be "J shocks" or "C shocks" (Draine 1980). In J shocks the ions and neutrals have a common bulk velocity and the

shock front can be treated as a thin, adiabatic region where the fluid variables *jump* suddenly as kinetic energy of bulk motion is converted to random thermal energy. In C shocks magnetic pressures on the ions cause the ions and neutrals to flow at different speeds, and the fluid variables must be treated *continuously* as the neutral particles are slowly heated and accelerated by the drag of the ions or charged grains. NH tentatively conclude that the small magnetic fields and/or low fractional ionizations in the preshock gas may allow J shocks to persist to $v_s << 30$ km s^{-1}, and they present J shock results for $v_s = 5 - 100$ km s^{-1} and $n_0 = 10^{7.5} - 10^{12}$ cm^{-3}. Kaufman, Hollenbach, & Neufeld (1995, in preparation) have begun analysis of C-type accretion shocks.

The dust opacity ($A_v \sim 10 - 1000$) in the overlying freefalling material obscures the optical and ultraviolet lines produced in fast, $v_s \gtrsim 30$ km s^{-1}, accretion shocks. IR observations are optimal because these wavelengths penetrate the infalling envelope and because these transitions are much more luminous than other penetrating radiation such as radio waves or X rays. NH show that accretion shocks produce strong CO vibrational emission, and airborne observations of the luminous v=1-0 lines will be extremely interesting diagnostics for sources with moderate A_v. However, we focus here on the far infrared emission. NH show that for the range of n_0 and v_s likely in accretion shocks, the individual H_2O or OH line fluxes F_l from a source in Taurus range from $10^{-12} - 10^{-14}\dot{M}_{s-5}$ erg cm^{-2} s^{-1}. The OI(63μm) flux is generally $< 10^{-13}\dot{M}_{s-5}$ erg cm^{-2} s^{-1}. These relatively weak lines are superimposed on a relatively strong continuum source. Assuming an instrument with spectral resolving power $R = \lambda/\Delta\lambda$, the line to continuum ratio L/C is given by

$$L/C \sim 10^{-2}\left(\frac{R}{10^4}\right)\left(\frac{F_l/\dot{M}_{s-5}}{10^{-13}\text{ erg cm}^{-2}\text{ s}^{-1}}\right), \tag{4}$$

so that $R \gtrsim 10^4$ is needed to distinguish the line from the continuum. ISO may observe some of the stronger H_2O lines with its Fabry-Perot instruments, and SOFIA should be able to resolve line profiles of OH and OI(63μm). The superior spatial resolution of SOFIA will also increase the line to continuum ratio in sources whose continuum is extended. The KAO may make pioneering observations of the strongest OH lines (e.g, 119 μm) in the brightest sources.

Comparison of observed spectra with the models of NH enables a diagnosis of the physical conditions in the accretion shock. Strong OH rotational emission is a signature of an accretion shock (as opposed to the freefalling material, for example), since the shock can dissociate molecules like H_2O and O_2 and produce radicals like OH. The mass accretion rate $\dot{M}_s$ through the shock, which should be roughly equal to the mass infall rate $\dot{M}$, scales monotonically with the magnitude of the fluxes of the strong coolants H_2O, OH, and OI(63μm). The average shock velocity $\bar{v}_s$ and average preshock density $\bar{n}_0$ can be deduced from the relative strengths of these fluxes. For example, for fixed $\dot{M}_s$, OI(63μm) is relatively bright for low $\bar{n}_0$ and high $\bar{v}_s$, because of its low critical density and the dissociation of molecules producing atomic oxygen at high $\bar{v}_s$. OH increases with $\bar{v}_s$ for the same reason. H_2O decreases with $\bar{n}_0$ because of the increasing importance of vibrational cooling by CO and gas cooling by collisions with dust. The average shock velocity $\bar{v}_s$ can also be determined by measuring individual line profiles since $\bar{v}_s \sim \Delta v$. The average shock velocity gives an estimate of the disk size r_d and the average location $\bar{r}$ of the shock (see Eq. 2). Knowledge of $\bar{n}_0$, $\bar{v}_s$, and $\dot{M}_s$

allow an estimate of the shock area, $A = \dot{M}_s/(m_H \bar{n}_0 v_s)$, where m_H is the mass of hydrogen. Finally, the determination of A, r_d, $\bar{n}_0$, and $\dot{M}_s$ may diagnose the possible presence of a pseudo-disk, since pseudo-disks have high $\bar{n}_0$ and low A for a given $\dot{M}_s$ and r_d.

4. Summary and Conclusions

In the future the KAO may be able to make pioneering observations of the OI(63μm) emission from freefalling gas and the OH rotational emission from accretion shocks in the brightest, nearby protostars. However, only with the increased sensitivity of ISO and SOFIA, and the increased spectral and spatial resolving power of SOFIA, will a thorough study of nearby regions of star formation be possible. In this paper we have shown how the IR line spectrum, which dominates the gas cooling, characterizes the nature of the collapse to form a star/disk system. Line profiles, requiring spectral resolving powers of $\sim 10^5$, will prove the existence of the collapse and probe the dynamics. The existence of an accretion shock is characterized by strong OH emission. The line fluxes and line profiles of OI(63μm), OH and H_2O enable a determination of the freefalling mass influx $\dot{M}$, the mass flux through the accretion shocks $\dot{M}_s$, the mass of the central protostar M_*, the morphology of the collapse [$n(r)$, $T(r)$, r_c, and the existence of a pseudo-disk], and the location of the accretion shock.

In this paper we have focused on the contribution airborne astronomy will make in understanding *the collapse* to form a star/disk system. More generally, airborne astronomy will be a vital component in the array of measurements that will lead to an understanding of the complete process of star and planet formation. Strelnitski et al (1994, this volume) describe how airborne instruments may measure hydrogen infrared lasers from disks irradiated by young, central, massive stars. Airborne observations will also probe the massive winds generated by young stars and the debris disks around older stars. This Symposium marks two decades of KAO science. The coming decade promises great advances in understanding star and planet formation through observations from the KAO and SOFIA.

5. Acknowledgments

We would like to acknowledge the support of the NASA Astrophysical Theory Program which funds the Center for Star Formation Studies, a consortium of researchers from NASA Ames, the University of California at Santa Cruz, and the University of California at Berkeley.

6. References

Bell, K. R., & Lin, D. N. C. 1994, ApJ, 427, 987

Cassen, P., & Moosman, A. 1981, Icarus, 48, 353

Ceccarelli, C., Hollenbach, D., & Tielens, A. G. G. M. 1995, in preparation (CHT)

Draine, B. T. 1980, ApJ, 241, 1021

Galli, D., & Shu, F. H. 1993a, ApJ, 417, 220

Galli, D., & Shu, F. H. 1993b, ApJ, 417, 243

Kaufman, M., Hollenbach, D., & Neufeld, D. 1995, in preparation

Neufeld, D. A., & Hollenbach, D. J. 1994, ApJ, 428, 170 (NH)

Shu, F. H. 1977, ApJ, 214, 488

Strelnitski, V. S. *et al.* 1994, in Proc of the Airborne Astronomy Symp on the Galactic Ecosystem: From Gas to Stars to Dust, ed. M. R. Haas, J. A. Davidson, & E. F. Erickson (San Francisco: ASP), paper 305

Terebey, S., Shu, F. H., & Cassen, P. 1984, ApJ, 286, 529

Zhou, S., Evans, N. J., Kompe, C., & Walmsley, C. M. 1993, ApJ, 404, 232

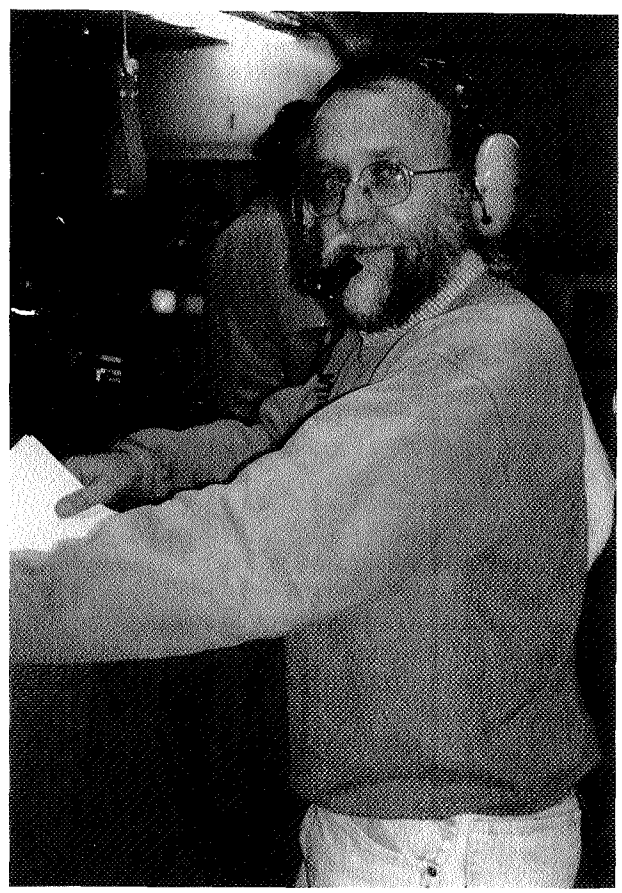

Xander Tielens

Airborne Astronomy Symposium on the Galactic Ecosystem
ASP Conference Series, Vol. 73, 1995
M.R. Haas, J.A. Davidson, and E.F. Erickson (eds.)

FAR-INFRARED OBSERVATIONS OF MAIN SEQUENCE STARS SURROUNDED BY DUST SHELLS

P. M. HARVEY, B. SMITH, J. DI FRANCESCO
Astronomy Department, University of Texas, Austin, TX 78712

ABSTRACT We have used a 20-channel bolometer array on NASA's Kuiper Airborne Observatory to obtain photometry and size information for several main sequence stars surrounded by dust shells. The observations were made at 50 and/or 100 μm on flights based in Christchurch, New Zealand, in 1992, 1993. The stars include the "Vega-like" star, Beta Pic, as well as two stars, HD 135344 and HD 139614, suggested by subsequent studies to belong possibly to the same class. The results of our observations are best interpreted as upper limits to the far-infrared sizes of the dust clouds around these stars. In addition to the basic size and flux measurements, we have fit simple, optically thin models to the Beta Pic data to explore the range of shell parameters consistent with our limits and with previous observations.

INTRODUCTION

One of the most exciting phenomena discovered by the IRAS sky survey was the presence of dust surrounding several nearby main-sequence stars (e.g. Gillett 1986). These dust clouds appear to be composed of grains, substantially larger than typical interstellar grains, in orbit around the central star, and almost certainly replenished because of their short lifetime due to a variety of effects (e.g. Backman and Paresce 1993). The KAO was instrumental in confirming the excess around Vega and extending the studies to higher angular resolution and longer wavelengths (Harvey, Wilking, and Joy 1984; Harper, Loewenstein, and Davidson 1984). In this paper we present preliminary results from a program of high angular resolution far-infrared observations of several of these objects. The angular resolution of the KAO is critical to determine accurately the sizes of the shells which place the strongest limits on the grain properties and spatial distribution of the circumstellar material.

FAR-INFRARED OBSERVATIONS

Our observations were made on several deployments of the KAO to the southern

hemisphere in 1992 and 1993. We used the University of Texas, 20-channel, bolometer array, described briefly by Smith et al. (1994) operating at 50 and 100μm with diffraction limited beam sizes of 15" × 25" and 25" × 35", respectively, for each pixel. In 1992, a number of spatial observations of Beta Pictoris were obtained and averaged at 50μm, and single pixel photometry was performed at 100μm. In 1993, photometry at 50μm was obtained of two stars suggested by Walker and Wolstencroft (1988) to belong possibly to the same class, HD 135344 and HD 139614. Preliminary photometry of Fomalhaut was also obtained at this time, but those results are deferred to a subsequent paper to be combined with data from a 1994 deployment of the KAO.

RESULTS

Our results are shown in Table I and Figures 1 and 2. Table 1 shows the photometry in the KAO beam obtained for the three stars; also indicated is the IRAS measured flux density in its much larger beam. Figure 1 shows the results of the spatial measurements of Beta Pic relative to the peak flux measured at the central position, as well as the point source profile, and the results of a model fit described below. Figure 2 shows the photometric data on Beta Pic taken from Backman, Gillett, and Witteborn (1992; BGW) and our study with the results of the model calculation described below. The simplest conclusion from these results is that the dust clouds around these three stars are quite compact, since the KAO photometry gives fluxes close to but less than the IRAS results. In the case of Beta Pic the discrepancy between the KAO and IRAS fluxes is definitely large enough that the circumstellar disk appears to be resolved.

TABLE I - Small Beam Photometric Results

STAR	KAO F_ν (Jy)	± stat. ± total	@ λ	IRAS F_ν (Jy) @ λ
β Pic	12.9	± 1.0 ± 1.6	@ 50μm	18.8 ± 0.9 @ 60 μm
	8.5	± 0.6 ± 1.0	@ 100μm	11.2 ± 1.0 @ 100 μm
HD 135344	24.3	± 1.8 ± 3.5	@ 50μm	26.3 ± 1.5 @ 60 μm
HD 139614	14.0	± 1.3 ± 2.5	@ 50μm	18.3 ± 1.2 @ 60 μm

MODELLING OF BETA PIC

In order to determine the constraints our data place on the dust distribution and properties around Beta Pic, we have calculated the emission from models

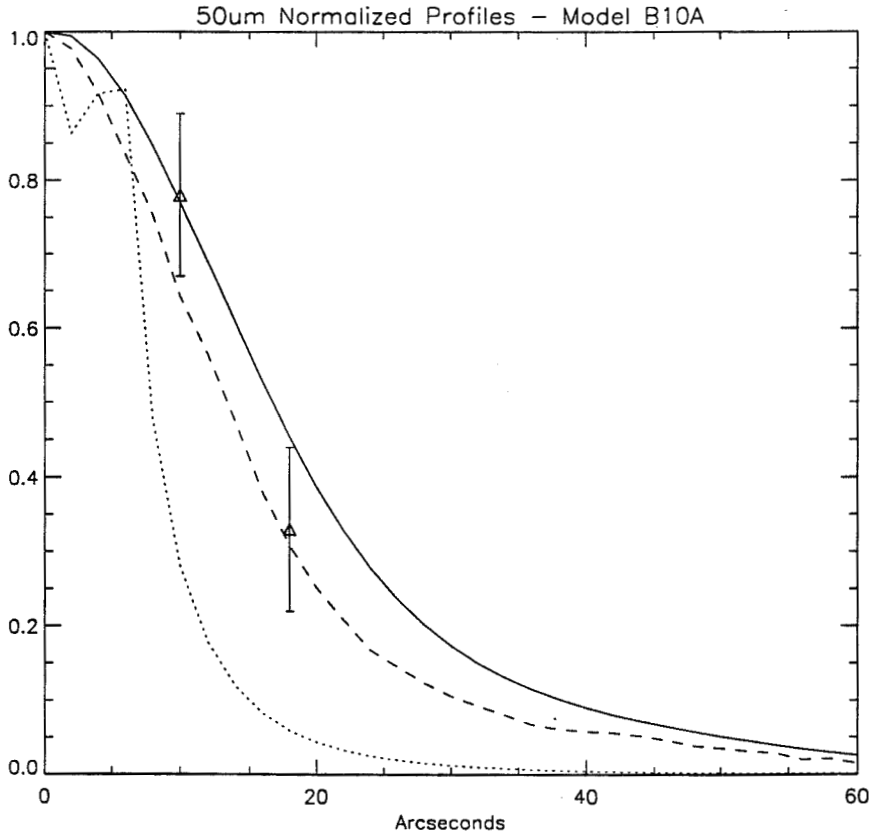

Figure 1 - Spatial measurements of the 50μm flux from Beta Pic relative to the point source profile (PSP) and to that from a model of the dust distribution. The data are shown as triangles with error bars attached; the PSP is dashed; the model flux distribution is dotted; and the model convolved with the PSP (for comparison with the data) is solid. The model consists of two thin disk components with parameters essentially identical to model 10 of Backman, Gillett, and Witteborn (1992).

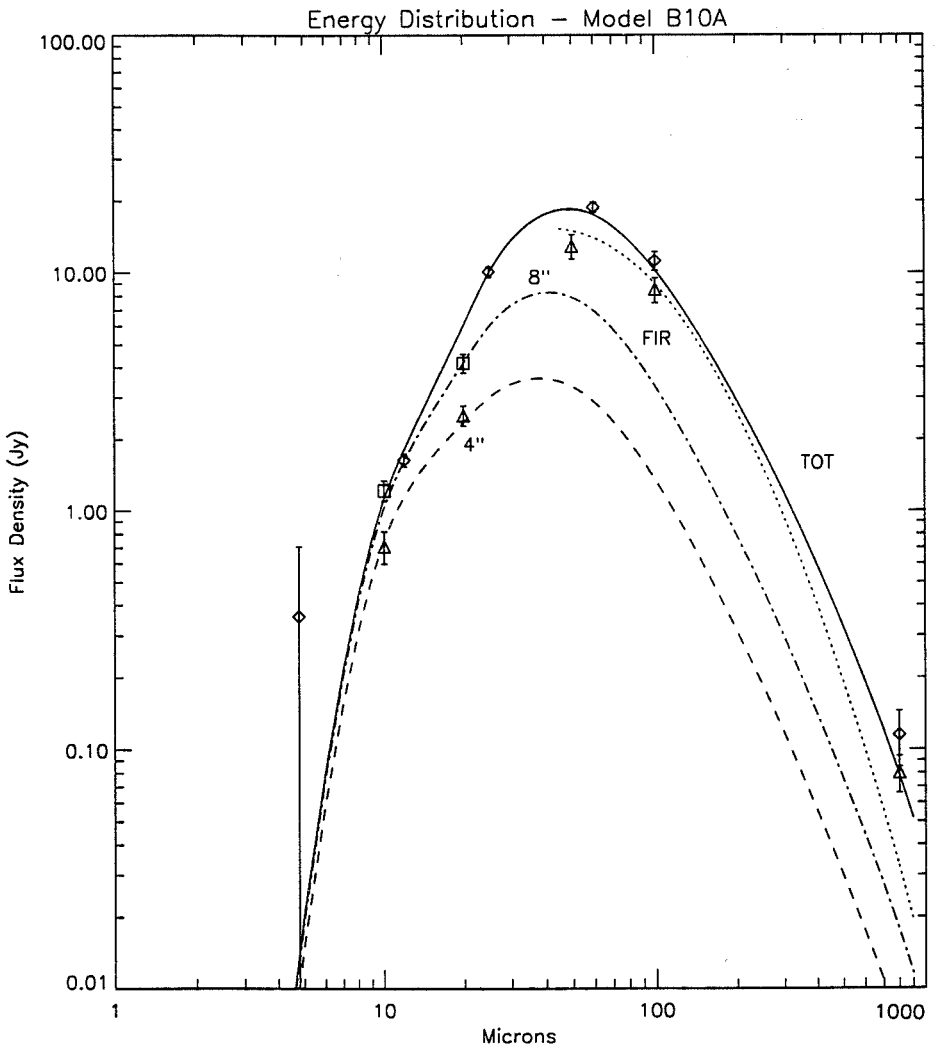

Figure 2 - Observed and model energy distributions for different aperture sizes. The data, taken from this paper and Backman, Gillett, and Witteborn (1992) are shown as various symbols with error bars. The solid line indicates the total flux from the model over all radii; the dashed line is the flux intercepted by a 4" aperture for comparison with the 10 and 20μm IRTF data; the dot-dash line is likewise for an 8" aperture; the dotted line shows the flux intercepted by the diffraction limited KAO apertures used in this paper as well as that of the 800μm observations of Zuckerman and Becklin (1993).

like those described by BGW. Figures 1 and 2 show the spatial and spectral results from a model essentially identical to BGW's number 10. Clearly this model does an excellent job of reproducing the spatial and spectral data; a similar quality of fit was found for a model close to their number 11, another of the best fits which they had found. The important features of these models are: a much lower grain density inside a radius of order 100 a.u. than outside this radius, a small inner radius and/or small grain size for the inner grains in order to reproduce the shorter wavelength infrared emission from the hottest grains, and an $r^{-1.7}$ surface density gradient in the outer disk to be consistent with optical surface brightness measurements.

CONCLUSIONS

The basic conclusions of this study are that the high spatial resolution KAO data for Beta Pic are consistent with existing models for the dust emission from this star which require a two-component disk with a strong dust "depletion" in the inner disk. For the two stars from the list of Walker and Wolstencroft (1988) we find that the far infrared emission is barely resolved, if at all, based on the ratio of KAO to IRAS measured flux density. Because of the much greater distance of these stars, this does not place strong constraints on the grain sizes, but it does call into question the conclusion that these stars' dust shells were resolved by IRAS.

We thank the staff of the KAO for their superb support during these deployments to the southern hemisphere which made possible these observations. This research was supported by NASA grant NAG 2-67 to the University of Texas.

REFERENCES

Backman, D.E., Gillett, F.C., & Witteborn, F.C. 1992, ApJ, 385, 670.

Backman, D.E. & Paresce, F. 1993, in Protostars and Planets III, ed. E.H.Levy & J.I. Lunine, University of Arizona Press, Tucson, p. 1253.

Gillett, F.C. 1986, in Light on Dark Matter, ed. F.P. Israel, D. Reidel, p. 61.

Harper, D.A., Loewenstein, R.F., & Davidson, J.A. 1984, ApJ, 285, 808.

Harvey, P.M., Wilking, B.A., & Joy, M. 1984, Nat., 307, 441.

Smith, B.J., Harvey, P.M., Colome; C., Zhang, C.Y., & Di Francesco, J. 1994, ApJ, 425, 91.

Walker, H.J. & Wolstencroft, R.D. 1988, PASP, 100, 1509.

Zuckerman, B. & Becklin, E.E. 1993, ApJ, 414, 793.

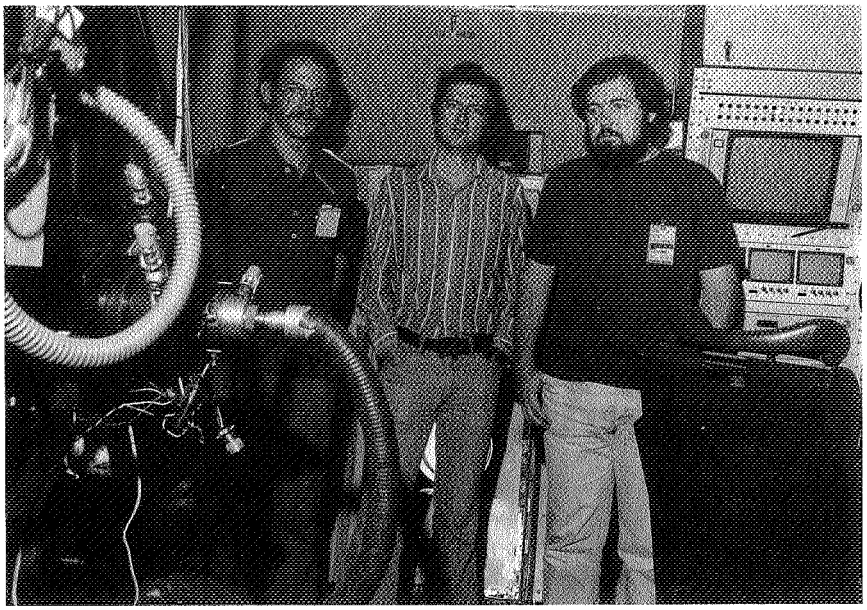

Paul Harvey, Harley Thronson, Ian Gatley (1977)

Bob Cameron, Milo Reisner

Airborne Astronomy Symposium on the Galactic Ecosystem
ASP Conference Series, Vol. 73, 1995
M.R. Haas, J.A. Davidson, and E.F. Erickson (eds.)

New Far Infrared Images of Bright, Nearby, Star-Forming Regions

D. A. Harper, D. M. Cole, C. D. Dowell, J. F. Lees, and R. F. Loewenstein
University of Chicago, Yerkes Observatory, Williams Bay, WI 53191

Abstract. Broadband imaging in the far infrared is a vital tool for understanding how young stars form, evolve, and interact with their environment. As the sensitivity and size of detector arrays has increased, a richer and more detailed picture has emerged of the nearest and brightest regions of active star formation. We present data on M 17, M 42, and S 106 taken recently on the Kuiper Airborne Observatory with the Yerkes Observatory 60-channel far infrared camera, which has pixel sizes of 17″ at 60 μm, 27″ at 100 μm, and 45″ at 160 and 200 μm. In addition to providing a clearer view of the complex central cores of the regions, the images reveal new details of the structure and heating of ionization fronts and photodissociation zones where radiation from luminous stars interacts with adjacent molecular clouds.

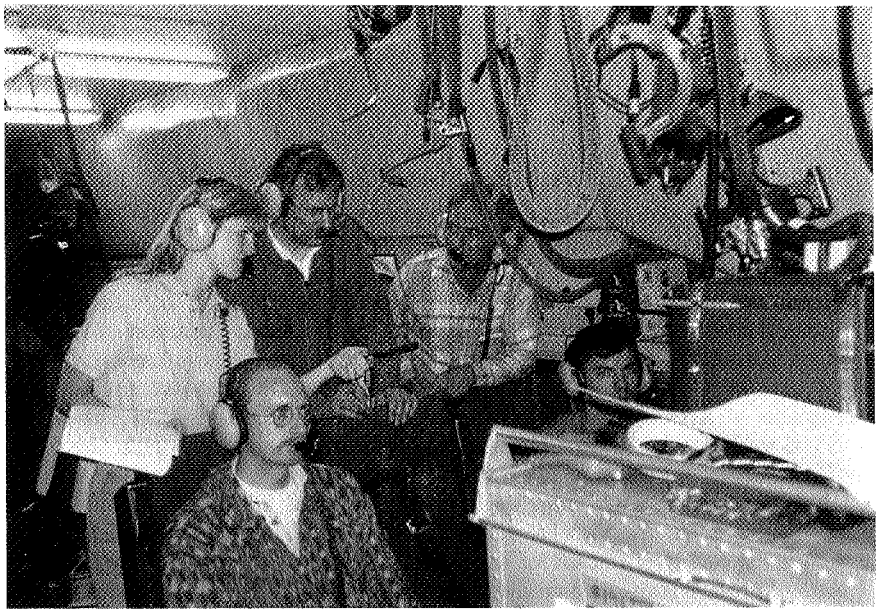

Joanna Lees, David Hughes, Al Harper, Steve Most, Darren Dowell

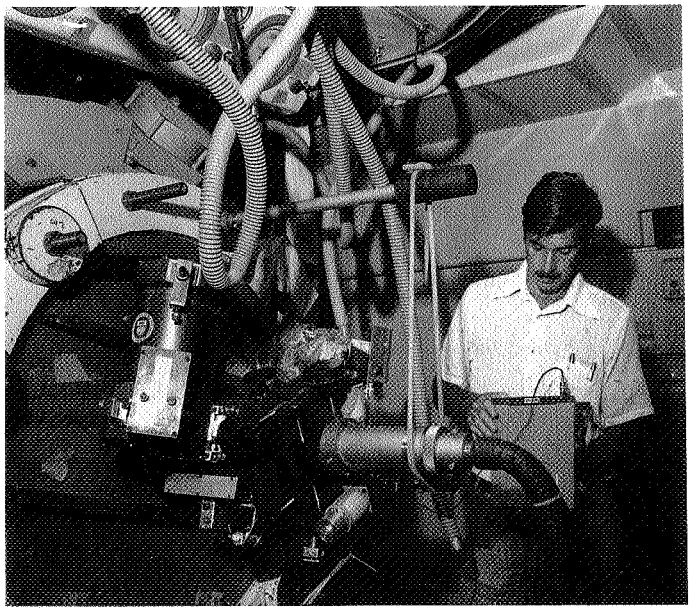

Bob Loewenstein (1980)

Airborne Astronomy Symposium on the Galactic Ecosystem
ASP Conference Series, Vol. 73, 1995
M.R. Haas, J.A. Davidson, and E.F. Erickson (eds.)

MODELS OF FAR-IR SOURCES AT W3-IRS4 & W3-IRS5

M. F. CAMPBELL AND M. B. CAMPBELL
Colby College, Waterville ME 04901

H. M. BUTNER
Carnegie Institution of Washington, Washington, DC 20015

D. F. LESTER, P. M. HARVEY AND N. J. EVANS, II
University of Texas at Austin, Austin, TX 78712

ABSTRACT Far-IR continuum maps made with the KAO of W3 at 47 and 95μm show peaks identified with the mid-IR sources IRS4 and IRS5 and extended emission identified with the radio source W3A. We have taken the steepest radial scan profiles from the peaks at IRS4 and IRS5 to represent the objects as spherical clouds. Spherically symmetric models were created in an attempt to match the observed profiles. Radiative transfer dust cloud models heated by central protostars or stars do not match extended emission in the 47μm scan profile for any assumed density distribution for either source. However, both sources can be approximately fit by power law density profiles and ad hoc temperature profiles which are much less steep than those by the single source radiative transfer models. One possible physical explanation for the shallow temperature gradients suggested by the data is heating by a distribution of luminosity sources.

INTRODUCTION

W3 is a region of compact HII regions, mid-IR sources, masers and submillimeter sources previously mapped in the far-IR with the KAO by Werner et al. (1980). We made maps of W3 with the KAO in 1987 in 47 and 95μm continuum emission to take advantage of the improved sensitivity of the Texas linear array of 8 ^{3}He-cooled bolometers. We confirm the conclusion of Werner et al. that the two peaks are associated with the mid-IR sources IRS4 and 5, and that the extended emission in the east is associated with W3A. Our observed peak flux densities are also

consistent with those of Werner et al. However, our new maps indicate that IRS4 and 5 are each much closer to spherical geometry than do the maps of Werner et al. Consequently, we have modeled the far-IR emission as arising from spherical dust clouds.

SCAN DATA AND INTERPRETATION

The detector array was scanned across the sources to produce the new maps. We have selected the steepest half-scans of IRS4 and 5 to represent each source's radial emission profile. The IRS4 half-scan position angles are ~20° west of north from the peak and the IRS5 angles are ~25° east of south. Scans were done with beams of 24" x 20" (47μm) and 36" x 23" (95μm), scanning in the direction of the detectors' long axes. A second 95μm map was made in 1989. The 1989 scans, while somewhat narrower, confirm the shapes of the 1987 scans for IRS4 and 5.

The source scans have widths which are 25-75% larger than the beams, and have very high S/N. The underlying density and temperature profiles cannot be well determined directly from the data, but we can derive them indirectly from source models whose emission is consistent with the observed scans. We compare calculational scans from physical source models convolved with the point source profiles (PSPs) to the data scans. For each wavelength, the model and data are compared in two ways: 1. Total flux density integrated along the scan; 2. Specific shape of the scan profile. The analysis is limited by relatively poorly determined PSPs from IRC+10420 and Callisto.

RADIATIVE TRANSFER MODELS

The code of Egan, Leung and Spagna (1988) was used to calculate the emission at 47 and 95μm. For each source, we assumed a spherical dust cloud with a power law density distribution. A central heating star was specified by luminosity and temperature; the temperature is not a critical parameter. The star is located in a dust-free cavity. Dust properties are as given in Mathis, Mezger and Panagia (1983). Specific assumptions and the quality of fit to the data for each source model are given below. In each case the model flux density integrated along the scan agrees to that of the 1987 data to within 10%.

We found for the best W3-IRS5 model: the star's luminosity is 500,000$L_\odot$; the cloud outer radius r_o and cavity radius r_c are 1.0 and 0.08pc; and the density radial function goes as $(r/r_c)^{-1}$ with an optical depth τ(95μm, r_c to r_o) of 0.30. We can characterize the fits of the model scans (convolved with PSP) to the data by comparing the model FWHM and full width at ten percent of maximum, FWTM, to data values calculated

from the half-scans. At 95μm, the model FWHM and data FWHM agree well, 46" vs 44", and the FWTMs are identical at 97". At 47μm the model and data FWHMs are 30" vs 34", but there is a major discrepancy in model and data FWTMs of 58" vs 79". We were unable to find any density distribution for a centrally heated cloud which will fit both core and extended emission for both the 47 and 95μm scans. Only the core of the scans of IRS5, out to the FWHM approximately, can be fit by centrally heated spherical models.

We found for the best W3-IRS4 model: the central star's luminosity is 300,000L_o; the radii r_o and r_c are 1.0 and 0.06pc; and the density is uniform with τ(95mm, r_c to r_o) of 0.30. At 95μm, the model and data FWHMs are 57" vs 53" and the FWTMs are 124" vs 132". At 47μm, the model and data FWHMs are 30" vs 36", and model and data FWTMs are 68" vs 97" The model does not fit the 47μm scan profile except in the inner core at flux levels above 80%. Again, we were unable to find any density distribution for a centrally heated cloud which will fit both core and extended emission for both the 47 and 95μm scans.

FIXED TEMPERATURE GRADIENT MODELS

The code by Campbell et al. (1989), which was used to model the emission from W3(OH), was used to calculate the emission for W3-IRS4 and 5. Instead of calculating temperature due to heating by a central star, the code uses a specified radial power law temperature distribution. The code has the advantage of quickly calculating emission profiles for situations which cannot be readily calculated by a radiative transfer code. In each case, the model flux density integrated along the scan agrees with that of the 1987 data to within 10%.

We found for the best W3-IRS5 model: the cloud outer radius r_o and cavity radius r_c are 1.0 and 0.06pc.; the density goes as $(r/r_c)^{-2}$ with τ(95μm, r_c to r_o) of 0.32; and the temperature radial function is $68K(r/r_c)^{-0.25}$. At 95μm, the model and data FWHMs agree well, 43" vs 44", and the FWTMs are 102" vs 97". At 47μm the model and data FWHMs are both 34", and model and data FWTMs are 70" vs 79"-- a much better agreement than for the radiative transfer model.

We found for the best W3-IRS4 model: r_o and r_c are also 1.0 and 0.06pc; the density goes as $(r/r_c)^{-1.5}$ with τ(95μm, r_c to r_o) of 0.11; and the temperature function is $65K(r/r_c)^{-0.20}$. At 95mm, the model and data FWHMs also agree well, 55" vs 53", and the FWTMs are 126" vs 132". At 47μm the model and data FWHMs are 37" vs 36", and model and data FWTMs are both 97"--again a much better agreement than for the radiative transfer model.

DISCUSSION

Many attempts were made to match the data with radiative transfer models of various density structures for the clouds, including core-halo structures and Gaussian profiles. Thin shell models can be ruled out by maximum entropy deconvolutions of the scan data which show both sources to have rather sharp emission cores. A radiative transfer model for IRS5 with a steeper density gradient which includes external heating fits the scans well enough that it cannot be ruled out. The external heating is 5000 times the local interstellar radiation field, and the central source luminosity is $450{,}000L_{\odot}$. Unlike IRS5, no model which includes external heating comes close to fitting both of the data scans for IRS4.

Our fixed temperature gradient models have much flatter gradients than the central source radiative transfer models would predict. Shallow temperature gradients can be explained by heating from a cluster of stars distributed throughout the cloud. A likely scenario would be that the central core of each cloud is heated by a single star or compact group of luminous stars with the outer portion heated by lower luminosity stars distributed throughout it. Separation of the two emission components would be difficult. Nevertheless, the luminosity determined for the central star in each radiative transfer model is a reasonable estimate for the total luminosity of the source. In the case of IRS5, $500{,}000L_{\odot}$ is required in the central star or stars to give a far-IR luminosity in a 30" beam of only $140{,}000L_{\odot}$ (Werner et al.).

ACKNOWLEDGEMENTS

This work was partly supported by NASA Grants NAG 2-67 and NAG 2-546.

REFERENCES

Campbell, M. F., Lester, D. F., Harvey, P. M., and Joy. M. 1989, ApJ, 345, 298

Egan, M. P., Leung, C. M., and Spagna, G. F. 1988, Comp. Phys. Comm., 48, 271

Mathis, J. S., Mezger, P. G., and Panagia, N. 1983, A&A, 128, 212

Werner, M. W., Becklin, E. E., Gatley, I., Neugebauer, G., Sellgren, K., Thronson, H. A., Harper, D. A., Loewenstein, R., and Moseley, S. H. 1980, ApJ, 242, 601

Airborne Astronomy Symposium on the Galactic Ecosystem
ASP Conference Series, Vol. 73, 1995
M.R. Haas, J.A. Davidson, and E.F. Erickson (eds.)

The Distribution of Warm Dust in the Star Forming Region Cepheus A: Infrared Constraints

Cecilia Colomé and Paul M. Harvey

Department of Astronomy, C1400. The University of Texas at Austin, Austin, TX 78712

Abstract. We have obtained new, high angular resolution far-infrared (FIR) maps (at 50 and 100 μm) of the star forming region Cepheus A and polarimetric images (1.65 and 2.2 μm) of the reflection nebulosity, IRS6, associated with this young stellar object. Our results are consistent with current star formation theories: a young stellar object surrounded by an infalling envelope with a characteristic density distribution of $n_d(r) \propto r^{-1.5}$, a circumstellar disk, and a cavity ($R_i \sim 0.07$ pc) in which n_d is constant, created by the dispersal of the initial dust cloud by a strong stellar wind.

1. Introduction

Cepheus A is a site of massive star formation situated in the large Cepheus OB3 association at a distance of 730 pc (Blaauw, Hiltgen & Johnson, 1959). There is a quadrupolar molecular outflow centered on Cepheus A (Bally & Lane, 1991). The fastest components of this outflow are bipolar and oriented East-West. All the infrared (12-400 μm) peaks of emission of Cepheus A roughly coincide with a continuum source known as HW2 (Hughes & Wouterloot, 1984). The polarization patterns previously observed in the reflection nebula, IRS6, associated with Cepheus A are centrosymmetric around HW2 (Lenzen, Hodapp & Solf, 1984; Joyce & Simon, 1986) and identify the possible position for the illuminating source as IRS6c, which is only detectable at $\lambda \geq 3.8\mu$m. The implied upper limit for the Lyman continuum flux, together with the total integrated luminosity of Cepheus A, indicates a spectral type of a ZAMS B0.5, assuming that the stellar activity is caused by a single young object.

Using the dust as a probe in this star forming region, we derive the density gradient in the cloud from which a young B0.5 (or earlier type) star has formed.

2. Observations

We observed Cepheus A at 50 and 100 μm with the Kuiper Airborne Observatory. We used The University of Texas 20 channel ^{3}He-cooled silicon bolometer array. The FWHM of the FIR beam is $18'' \times 25''$ (50μm) and $30'' \times 40''$ (100 μm). Callisto was observed in the same fashion and used as the point source profile and as a flux calibrator.

The NIR polarization observations (at 1.65 and 2.2 μm) were done with the 2.7 m telescope at McDonald Observatory, using the infrared camera (IRC2) of The University of Texas. The camera employs a 256×256 HgCdTe NICMOSIII array and its associated optics provide a plate scale of 0.4″/pixel. The FWHM of point sources was $\sim$ 1.2″ at both wavelengths. Several unpolarized stars were observed in the same manner in order to determine the instrumental polarization and also used as flux calibrators. The data reduction procedure will be presented elsewhere (Colomé & Harvey, 1994).

3. The NIR Polarization.

3.1. The Density Distribution of the Scattering Dust.

The NIR polarization increases with increasing radial distance, reaching a maximum of 80 % in the North-West portion of IRS6.

The overall nebular colors (H-K) are uniform, indicating that there is relatively small internal extinction between the central source and the scattering region (Joyce & Simon, 1986; Lenzen, Hodapp & Solf, 1984; Hodapp, 1990; this work), except for a small region located in the southwestern edge of the reflection nebula, where there seems to be a steep increase in the reddening.

If we assume that the geometry of the reflection nebula of Cepheus A can be approximated by a section of a sphere and that the dust distribution can be represented by a power law of the form: $n_s(r) = no_s(r/ro_s)^{-c}$, with the dust grains scattering isotropically, we can then use the relationship between the intensity of polarized radiation and the projected distance "b" from the central source (see Weintraub et al., 1992, and references therein) to deduce the exponent of the dust density law: "c". Applying this method to the observed polarized intensity of Cepheus A at the K band, we find that the range for the values of "c" is: (0.0, 0.2), up to angular displacement of b=40″, i.e., a very flat density distribution of the scattering dust.

4. The FIR Emission.

4.1. The Plane-Parallel Slab Model

Cepheus A is resolved at 50 and 100 μm and the observed FWHMs are 50″ and 60″ respectively. Applying a simple Gaussian deconvolution, the estimated FWHMs are 41″ (50 μm) and 44″ (100 μm). The dust optical depth and temperature are determined from the relationship between brightness and color temperature.

The dust temperature gradient, although not steep (from 30 to 55 K), is very symmetric, with elliptical isocontours around the FIR peak. The major axis of these concentric ellipses is oriented East-West, parallel to the main outflow in Cepheus A. The axial symmetry seen in the dust temperature map favors the interpretation that the stellar activity in Cepheus A is due to a single young star, or to an extremely compact, multiple stellar system ($\leq$ 40″). The 100 μm optical depth map indicates that there is a lower density region oriented preferentially East-West (parallel to the outflow).

4.2. A Dust Envelope Model for Cepheus A.

A radiative transfer code (Egan, Leung & Spagna, 1988; Butner et al., 1990) was used to model the available photometry (12 μm $\leq \lambda \leq$ 1300μm) of Cepheus A. A spherical dust cloud with a central young B0.5 type star was assumed, and the input parameters in this model were varied in order to reproduce: (a) the spectral energy distribution, taking into account beam size effects, and (b) the high angular resolution profile of the source at 50 and 100 μm.

Table 1. Input Parameters Common to All Radiative Transfer Models.

Parameter	Value
Distance	730 pc
T_{eff}	$2.6 \times 10^4 K$
L_*	$2.5 \times 10^4 L_\odot$
R_*	10 $R_\odot$
Geometry of cloud	Spherical
Density gradient	A power law of the form: $n_d(r) = n_o(r/r_o)^{-\alpha}$
Dust Opacity Law	that provided by Mathis, Mezger and Panagia (1983)

The models for which there is agreement in both the observed scan shape and the energy distribution define a narrow range for the exponent in the density distribution: $1.0 \leq \alpha \leq 1.5$, with the best fit to the observations for $\alpha \simeq 1.5$. The input parameters for the radiative transfer model which best fits the observations are: R_{outer}=0.5 pc, R_{inner}=0.07 pc, $\tau_{100\mu m}$=0.15, α=1.5, where R_{outer}, R_{inner}, $\tau_{100\mu m}$ and α are the outer radius of the dust cloud, the inner radius, the dust optical depth at 100 μm, and the exponent in the density distribution, respectively.

5. Summary and Conclusions.

From the variation of the polarized intensity at the K band with angular distance along the main axis of the reflection nebulosity in Cepheus A, we conclude that the density of the scattering dust remains constant or increases only slightly with distance from the illuminating source. Our two-dimensional maps of the dust temperature and optical depth at 100 μm favor the interpretation that the stellar activity is due to a single young stellar object, or to an extremely compact multiple stellar system. From our radiative transfer modelling, we conclude that the spectral energy distribution and the FIR profile shape of Cepheus A can be described by the re-processing of the radiation of a B0.5 star by a dust envelope with a density profile of the form: $n_d(r) = n_o(r/r_o)^{-1.5}$. In order to reproduce both the observed 100 μm profile and the spectral energy distribution of Cepheus A, a large inner radius ($R_{inner} \simeq$ 0.07 pc) of the dust cloud is required. The presence of this inner region of much lower dust optical depth is indicated in all three models in a consistent way. The elongation of this inner cavity is roughly

perpendicular to the circumstellar molecular gas structure detected by Torrelles et al. (1993); this structure as been interpreted by Torrelles et al. (1993) as an inner disk ($\sim$ 2400 AU) around HW2 (the center of the stellar activity). Our observations are in good agreement with current star formation theories (such as the one proposed by Shu, Adams & Lizano, 1987), namely the presence of an infalling envelope with a characteristic density distribution of $n_d(r) \propto r^{-1.5}$, a circumstellar disk (Torrelles et al., 1993), and the dispersal of the initial dust cloud by a strong stellar wind creating a cavity in which $n_d(r) \sim$ constant.

Acknowledgments. We thank the Kuiper Airborne Observatory staff for their excellent support in obtaining the FIR observations. This work was supported by NASA grant NAG 2-67 to The University of Texas at Austin.

References

Bally, J., & Lane, A.P. 1991, in Astrophysics with Infrared Arrays, ed. R. Elston (ASP Conf. Ser. V. 14), 273

Blauuw, A., Hiltner, W.A., & Johnson, H.L. 1959, ApJ, 130, 69

Butner, H.M., Evans, N.J. II, Harvey, P.M., Mundy, L.G., Natta, A., & Randich, M.S. 1990, ApJ, 364, 164

Colomé, C., & Harvey, P.M. 1994, in preparation

Egan, M.P., Leung, C.N., & Spagna, G.F., Jr. 1988, Comp. Physics Comm., 48, 271

Hodapp, K.-W. 1990, ApJ, 352, 184

Hughes, V.A., & Wouterloot, J.G.A. 1984, ApJ, 276, 204

Joyce, R.R., & Simon, T. 1986 AJ, 91 113

Lenzen, R., Hodapp, K.-W., & Solf, J. 1984, A&A, 137, 202

Mathis, J.S., Mezger, P.G., & Panagia, N. 1983, A&A, 137, 202

Shu, F.H., Adams, F.C., & Lizano, S. 1987, ARAA, 25 23

Torrelles, J.M., Verdes-Montenegro, L., Ho, P.T.P., Rodríguez, L.F., & Cantó, J. 1993, ApJ, 410, 202

Weintraub, D.A., Kastner, J.L., Zuckerman, B, & Gatley, I., 1992, ApJ, 391, 785

Airborne Astronomy Symposium on the Galactic Ecosystem
ASP Conference Series, Vol. 73, 1995
M.R. Haas, J.A. Davidson, and E.F. Erickson (eds.)

Far-Infrared Maps of Intermediate-Mass Young Stellar Objects

J. Di Francesco, N. J. Evans II, and P. M. Harvey

Dept. of Astronomy, The University of Texas at Austin, Austin, TX 78712-1083

L. G. Mundy

Astronomy Program, University of Maryland, College Park, MD 20742

H. M. Butner

Dept. of Terrestrial Magnetism, Carnegie Institution of Washington, Washington, DC 20015

Abstract. We have observed 8 Herbig Ae/Be stars and 9 embedded cold IRAS point sources of similar luminosity using the KAO. Most of these objects are resolved with respect to the KAO beam at 100 μm. These observations suggest an increased role of dust envelopes in future models.

1. Introduction

Circumstellar dust re-radiates absorbed ultraviolet and optical radiation from a central star at longer wavelengths, producing an infrared excess to that star's spectral energy distribution. Disk models that reproduce the observed infrared excess of young stellar objects (YSOs) have been used to argue for the presence of disks (Adams, Lada, & Shu 1988; Beckwith et al. 1990). Although compelling, these models are rarely constrained by the spatial distribution of infrared radiation around the YSOs. For example, the photometry which disk models reproduce include low-resolution data at crucial wavelengths that obscure details at circumstellar scales (i.e., from IRAS). We have observed two classes of YSO from the Kuiper Airborne Observatory (KAO) which provides better angular resolution at 100 μm than IRAS. These data will allow more accurate characterizations of the circumstellar environments of these YSOs.

2. Observations

The following two classes of YSO were observed with the University of Texas's 20-channel Si-bolometer system. In scanning mode, the twin columns of 10 detectors each can map 50 or 100 μm emission from objects in one or two dimensions at near diffraction-limited resolution (i.e., 22″ at 50 μm and 30″ at 100 μm).

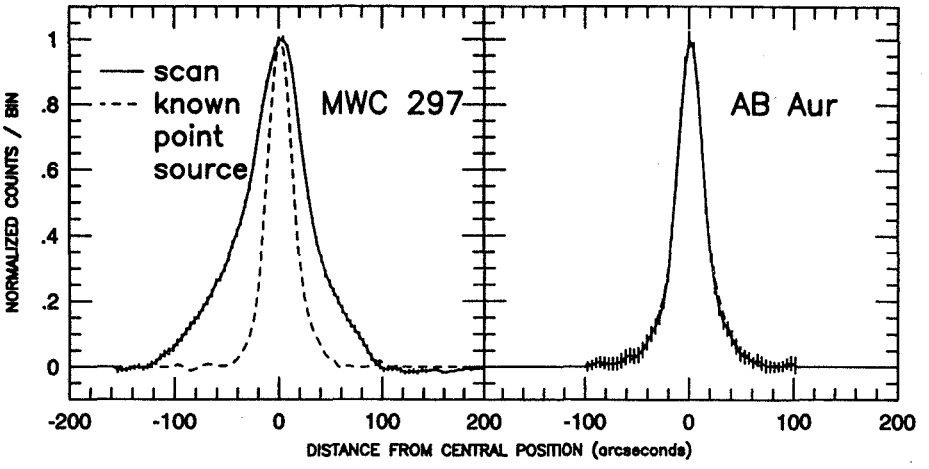

Figure 1. Normalized 100 μm scans of 2 Herbig Ae/Be stars.

1. **Herbig Ae/Be stars (HAEBEs)** (8 observed)

   HAEBEs are optically visible pre-main-sequence objects with significant infrared excesses and masses in the range 2–10 M$\odot$. Hillenbrand et al. (1992) reproduced the dereddened infrared excess at $\lambda < 20$ μm of 30 HAEBEs with models of optically-thick accretion disks only. Observations from IRAS were not reproduced because other infrared sources may have been possibly included in the IRAS beams. Hartmann, Kenyon, & Calvet (1993), however, reasoned that aspherical circumstellar envelopes alone could easily reproduce all the infrared excess of these stars instead, eliminating the need for massive disks.

2. **Cold IRAS sources** (9 observed)

   These sources were selected from the list of Wilking et al. (1989), who searched the IRAS Point Source Catalog for strong far-infrared emitters with $S_\nu(60\ \mu m) > 100$ Jy, $S_\nu(100\ \mu m) > S_\nu(60\ \mu m)$, IRAS color temperatures less than 50 K, and no optical counterpart. Their flux criteria limited their list to intermediate-luminosity objects (10^{3-4} L$\odot$) that may be evolutionary progenitors to the HAEBEs.

3. Discussion

3.1. Herbig Ae/Be stars

In Figure 1, we compare one-dimensional normalized 100 μm maps of 2 Herbig Ae/Be stars, MWC 297 and AB Aur, with the point sources, Ceres and IRC+10216 respectively. All observed HAEBEs were resolved at 100 μm except AB Aur. To determine if only a disk could reproduce such extended 100 μm emission, Di Francesco et al. (1994) modeled each source with a large, optically-thick disk using parameters directly from Hillenbrand et al. The expected far-infrared emission was then convolved with a Gaussian representing the 100 μm

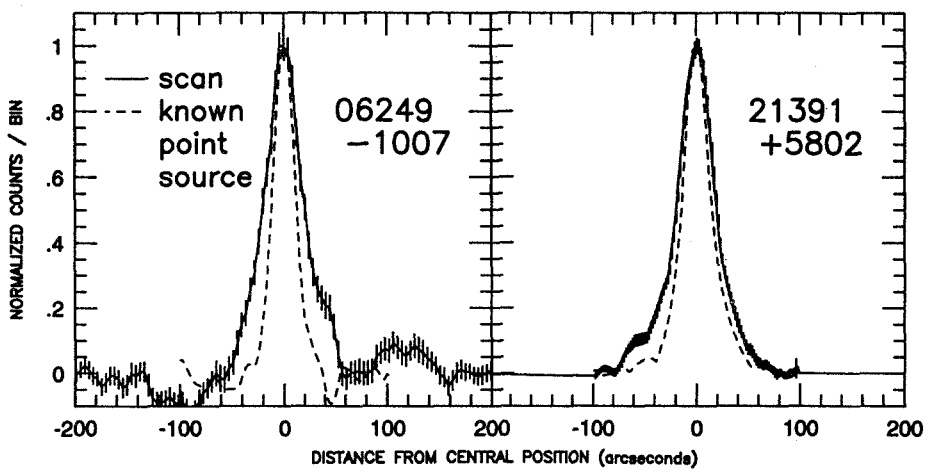

Figure 2. Normalized 100 μm maps of 2 cold IRAS sources.

KAO beam. Of these models, none were resolved even after the outer diameters of the disk models were enlarged to twice the deconvolved sizes of the sources. Only some disk models with artificially flattened temperature distributions (i.e., $q = 0.50$, if $T(r) \propto r^{-q}$) could be made extended. These profiles, however, were still far narrower than the observed profiles, suggesting that standard accretion disks alone cannot produce far-infrared emission on the scales observed. In turn, other structures like envelopes must be present. Such envelopes can re-radiate emission onto the disk, providing an additional source of heating that flattens the disk's temperature distribution (Natta 1993). Thus, failing to account for envelopes may lead to erroneous conclusions about disk properties derived from mid- and near-infrared observations.

3.2. Cold IRAS sources

In Figure 2, we compare one-dimensional normalized 100 μm maps of 2 cold IRAS sources, 06249-1007 and 21391+5802, with the point source, IRC+10420. All observed IRAS sources were resolved except 05380-0728. The Gaussian-deconvolved linear sizes for each observed source in each group at 50 and 100 μm are presented in Figures 3a and 3b. Sizes marked "Y" or "X" are derived from one- or two-dimensional scans respectively. A 3σ upper limit to the deconvolved size was determined for each unresolved source. Errors on the deconvolved sizes are estimated to be at the 20% level. The mean deconvolved linear size of the members of each class at 100 μm does not differ significantly at 100 μm (30 000 AU $\pm$ 25 000 AU (cold IRAS sources) vs. 38 000 AU $\pm$ 22 000 AU (HAEBEs)). In future models, we will explore the relationship between these two classes, especially to determine if their differences are a matter of evolution or viewing angle.

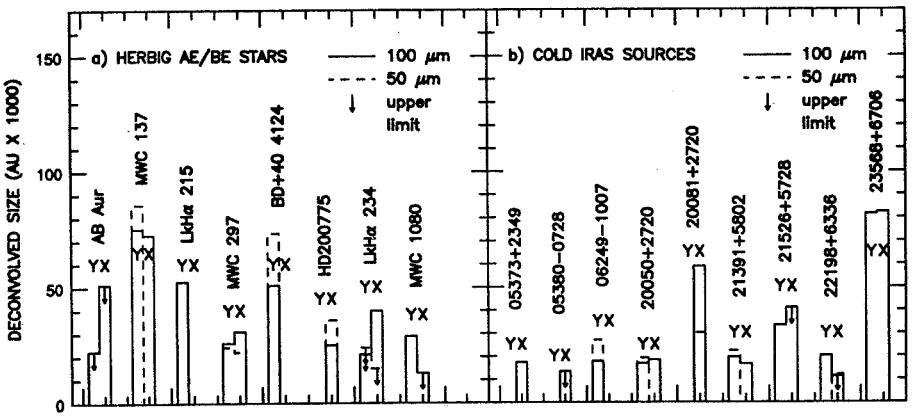

Figure 3. Deconvolved Linear Sizes of Observed YSOs.

4. Role of Observations in Models

We have shown that high-resolution KAO observations of the spatial distribution of far-infrared emission from YSOs can distinguish between the circumstellar components that can explain their observed photometery. These observations will also constrain envelope models effectively. Other high-resolution observations (e.g., millimeter interferometry), more sensitive to disks and less to envelopes, however, are required to constrain disk properties better. In addition, the combined thermal effects that disks and envelopes have on each other and the possibility of non-spherical envelope distributions will be considered in future models.

Acknowledgments. This work was supported in part by NASA grants NAG2-240, NAG2-67, and NAGW-2323.

References

Adams, F.C., Lada, C.J., & Shu, F.H 1988, ApJ, 312, 788

Beckwith, S.V.W., Sargent, A.I., Chini, R.S., & Güsten, R. 1990, AJ, 99, 924

Di Francesco, J., Evans, N.J., II, Harvey, P.M., Mundy, L.G., & Butner, H.M. 1994, in press

Hartmann, L., Kenyon, S.J., & Calvet, N. 1993, ApJ, 407, 219

Hillenbrand, L.A., Strom, S.E., Vrba, F.J., & Keene, J. 1992, ApJ, 397, 613

Natta, A., 1993, ApJ, 412, 761

Shu, F.H., Adams, F.C., & Lizano, S. 1987, ARAA, 25, 23

Wilking, B.A., Mundy, L.G., Blackwell, J.H., & Howe, J.E. 1989, ApJ, 345, 257

Airborne Astronomy Symposium on the Galactic Ecosystem
ASP Conference Series, Vol. 73, 1995
M.R. Haas, J.A. Davidson, and E.F. Erickson (eds.)

A Search for Hydrogen Lasers in MWC 349 from the KAO

Vladimir S. Strelnitski[1], Howard A. Smith[1], Michael R. Haas[2], Sean W. J. Colgan[2,3], Edwin F. Erickson[2], Norbert Geis[4], David J. Hollenbach[5], and Charles H. Townes[4]

[1] *Laboratory for Astrophysics, National Air and Space Museum, Smithsonian Institution, Washington, DC 20560*
[2] *MS 245-6, NASA-Ames Research Center, Moffett Field, CA 94035-1000*
[3] *SETI Institute, 2035 Landings Drive, Mountain View, CA 94043*
[4] *Physics Department, 557 Birge Hall, University of California at Berkeley, Berkeley, CA 94720*
[5] *MS 245-3, NASA-Ames Research Center, Moffett Field, CA 94035-1000*

Abstract. We report the first observations of H15α (169.4114 μm) and H10α (52.5349 μm) in MWC 349 from the KAO. We obtain a 3σ upper limit of 2×10^{-19} W/cm^2 for H15α and a flux of $3.6 \pm 1.3 \times 10^{-19}$ W/cm^2 for H10α. These fluxes are consistent with an appreciable excess due to laser amplification down to quantum numbers $n \approx 10$.

1. Introduction

Martin-Pintado *et al.* (1989) discovered, in the emission line star MWC 349, the first high gain masers in hydrogen recombination lines. Strong, double-peaked, masing components have now been detected in this star from H39α (2.8 mm) down to H21α (0.45 mm; Thum *et al.* 1994a), and it was argued (Gordon 1992; Planesas *et al.* 1992; Thum *et al.* 1992) that they come from the partly ionized, circumstellar disk of MWC 349. Since the integrated intensity of these lines increases with frequency, showing no sign of weaker masing at shorter wavelengths, and since the optical and near-IR hydrogen recombination α-lines observed to date (H2α – H7α) do not require a laser hypothesis for their interpretation, we conclude that strong masing (lasing) should extend into the IR and then vanish at some transition between H21α and H7α. Thus arises the possibility of detecting the first natural lasers in the IR domain. We discuss the potential for detecting hydrogen IR recombination lines in MWC 349 from the KAO and we report our first observations of H15α and H10α.

2. Why the KAO?

The KAO is presently the only suitable observatory, as the hydrogen recombination lines shortward of H21α (452.6 μm) and longward of H7α (19.1 μm) are not accessible from the ground. The α-lines from H7α through H16α (204.4 μm) are within the wavelength range of the Cryogenic Grating Spectrometer (CGS; Erickson *et al.* 1994) and those from H10α (52.5 μm) through H16α are observable with the Far-infrared Imaging Fabry-Perot Interferometer (FIFI; Geis

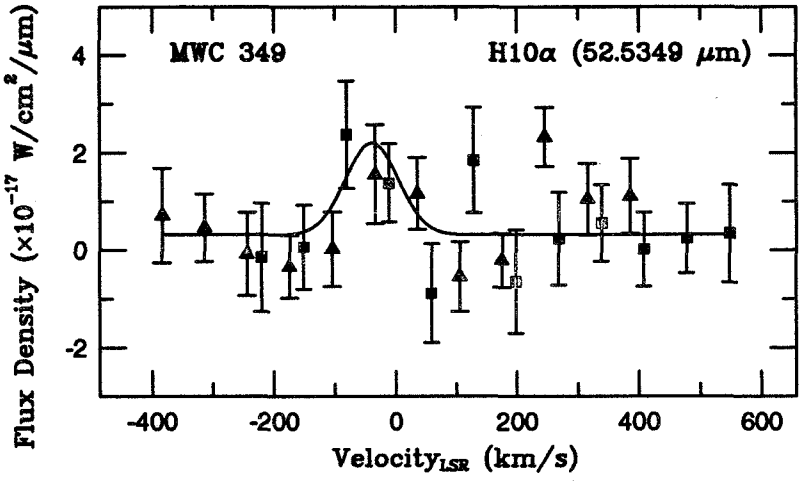

Figure 1. Two superimposed spectra of the H10α line (52.5349 μm) in MWC 349 observed with the CGS. The fitted curve assumes the intrinsic line shape is Gaussian.

et al. 1994). Excluding H13α, H14α, and H16α, which have bad atmospheric transmittance at 41,000 ft, and H7α, which has been observed from the ground (Smith *et al.* 1995), the candidates for observation with the CGS are H8α (27.8 μm), H9α (38.9 μm), H10α (52.5 μm), H11α (69.1 μm), H12α (88.8 μm), and H15α (169.4 μm). The last four of these lines are also accessible to FIFI. Finally, H18α at 288.2 μm, which has excellent atmospheric transmittance, could be observed with the Betz heterodyne spectrometer (Betz & Boreiko 1994).

Three β-lines with good atmospheric transmittances are also observable with the CGS: H9β (22.3 μm), H11β (38.8 μm), and H20β (210.1 μm). H11β is close enough in wavelength to H9α that it is automatically included in the same bandpass. α,β-pairs can provide a powerful extra handle on the lasing/non-lasing alternatives (Thum *et al.* 1994b).

3. Observations and Results

We chose two lines for our first observations: H15α for FIFI and H10α for the CGS. The H15α line was observed on June 7, 1994. The pixel spacing for the 5×5 array was 40″, each pixel subtended a 60″ FWHM beam. The integration time was 2170 s; the flux calibration was done using Jupiter. To maximize sensitivity, the spectrometer was used in "line-photometry" mode at $V_{LSR} = +17$ km/s with a FWHM bandwidth of 120 km/s. Our 5 × 5 map indicates extended emission of $\sim 30 \pm 15$ Jy over the southwest half of the array. The large spatial extent suggests that this is not H15α emission associated with MWC 349, but it is impossible to distinguish line and continuum emission in this mode. Assuming only line emission at the position of the star, the 3σ upper limit is 2×10^{-19} W/cm^2.

The H10α line was observed on June 15, 1994. The aperture size was 31″ FWHM; the flux calibration was done using Saturn. Data were taken using two

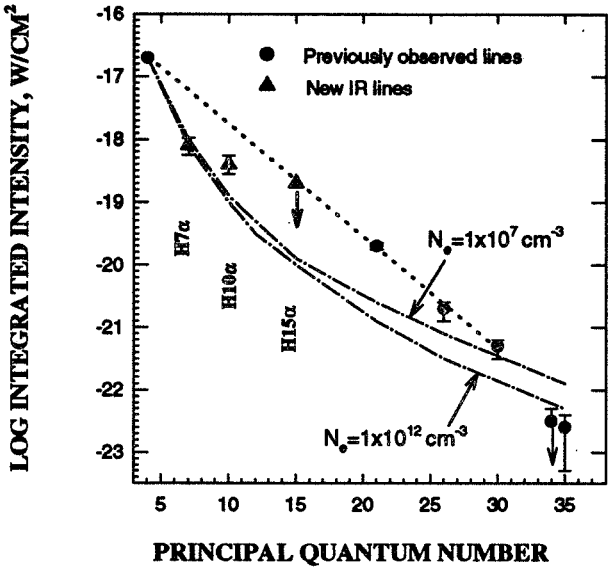

Figure 2. Predicted flux limits and first observational results for the IR hydrogen recombination α-lines in MWC 349.

grating settings which were separated by two detector resolution elements. The resulting spectra are shown in Figure 1 with the abscissa converted to V_{LSR}. The triangles show the first set of integrations (total time 3040 s) and the squares show the second set (total time 2160 s). In both cases, there is a broad feature (two channels or $\sim 100-150$ km/s wide) at $V_{LSR} \sim -35$ km/s. Considering our radial velocity uncertainty of about ± 0.6 channel (± 40 km/s), this is consistent with the MWC 349 systemic velocity of +8 km/s (Thum *et al.* 1994b). Averaging both data sets, we find a line flux of $(3.6 \pm 1.3) \times 10^{-19}$ W/cm^2 and a continuum consistent with $\sim$ 10 Jy, as measured by Harvey *et al.* (1980). Since each of the other two data points above the average continuum level occupy only one channel, we do not consider them statistically significant.

4. Discussion and Conclusions

In Figure 2, adapted from Strelnitski *et al.* (1994), the filled circles show the observed intensities in the masing double-peaked mm and submm lines (H35α – H21α) and in the supposedly non-masing Brα (H4α) line. The dotted line is a log-linear interpolation between the submm and Brα observations and provides a crude upper limit to the anticipated fluxes for the IR lines in question, should they lase. The dash-dotted lines show the predicted fluxes for two density extremes if the lines are generated by optically thin, spontaneous emission from the volume producing Brα and if reddening is negligible. These predictions are fairly insensitive to density and represent a reasonable lower limit to the anticipated fluxes. Our observations, together with the result of Smith *et al.* (1995) for H7α, are the triangles plotted in Figure 2. The flux in H7α is very close to the optically thin spontaneous emission case, while our flux for H10α

is a factor of about 4 ± 2 stronger than predicted. Our upper limit for H15α doesn't significantly constrain the model.

We conclude that an appreciable excess due to laser amplification may well be present in the MWC 349 spectrum down to quantum numbers $n \approx 10$. If lasing in H10α is confirmed, as opposed to non-lasing in H7α, this provides an important clue to the structure of the ionized part of the circumstellar disk. There are observational indications, for example, that the higher frequency masing lines ($n < 30$) are all emitted by the same region of the disk, whereas the lower frequency lines seem to originate at increasingly larger distances (Thum *et al.* 1994a). This suggests that the ionized component of the disk has an inner radius beyond which the density no longer increases. The density in this region is modeled to be a few $10^7\,\mathrm{cm}^{-3}$ (*e.g.*, Martin-Pintado *et al.* 1989) and the gain length can not surpass $\sim 1 \times 10^{15}$ cm (e.g., Ponomarev *et al.* 1994). According to calculations by Strelnitski *et al.* (1994), the resulting emission measure, EM $\sim 10^{30}$ to $10^{31}\,\mathrm{cm}^{-5}$, can be enough to produce maser gain $\gtrsim 1$ in the IR lines down to H10α, but is insufficient to make H7α optically thick, in accord with our observations. Further observations of these IR recombination lines in MWC 349, particularly with higher spectral resolution, are critical to our understanding of the inner parts of its ionized circumstellar disk.

5. References

Betz, A. L., & Boreiko, R. T. 1994, in Proc of the Airborne Astronomy Symp on the Galactic Ecosystem: From Gas to Stars to Dust, ed. M. R. Haas, J. A. Davidson, & E. F. Erickson (San Francisco: ASP), paper 717

Erickson, E. F., Haas, M. R., Colgan, S. W. J., Simpson, J. P., & Rubin, R. H. 1994, in Proc of the Airborne Astronomy Symp on the Galactic Ecosystem: From Gas to Stars to Dust, ed. M. R. Haas, J. A. Davidson, & E. F. Erickson (San Francisco: ASP), paper 702

Harvey, P. M., Thronson Jr., H. A., & Gatley, I. 1980, ApJ, 231, 115

Geis, N., *et al.* 1994, in Proc of the Airborne Astronomy Symp on the Galactic Ecosystem: From Gas to Stars to Dust, ed. M. R. Haas, J. A. Davidson, & E. F. Erickson (San Francisco: ASP), paper 708

Gordon, M. A. 1992, ApJ, 387, 701

Martin-Pintado, J., Bachiller, R., Thum, C., & Walmsley, C. M. 1989, A&A, 215, L13

Planesas, P., Martin-Pintado, J., & Serabyn, E. 1992, ApJ, 386, L23

Ponomarev, V. O., Smith, H. A., & Strelnitski, V. S. 1994, ApJ, 424, 976

Smith, H. A., Strelnitski, V. S., Kelly, D., Lacy, J., & Miles, J. 1995, in preparation

Strelnitski, V. S., Smith, H. A., & Ponomarev, V. O. 1994, in preparation

Thum, C., Martin-Pintado, J., & Bachiller, R. 1992, A&A, 256, 507

Thum, C., Matthews, H. E., Harris, A. I., Tacconi, L. J., Schuster, K. F., & Martin-Pintado, J. 1994a, preprint IRAM #322

Thum, C., Strelnitski, V. S., Martin-Pintado, J., Matthews, H. E., & Smith, H. A. 1994b, in preparation

Airborne Astronomy Symposium on the Galactic Ecosystem
ASP Conference Series, Vol. 73, 1995
M.R. Haas, J.A. Davidson, and E.F. Erickson (eds.)

Pixon Deconvolution of Far-Infrared Images from the UT Multichannel Photometer

Chris D. Koresko, Paul M. Harvey, Dian Curran

McDonald Observatory, The University of Texas at Austin, Austin, TX. 78712, USA

Rick Puetter

Center for Astrophysics and Space Sciences, University of California at San Diego, San La Jolla, CA. 92093-0111 USA

Abstract. Experiments with Pixon-based image deconvolution demonstrate that this technique can significantly enhance the spatial resolution of two-dimensional images acquired by the UT multichannel far-infrared photometer. A deconvolved 100μm image of the giant HII region NGC 3603 reveals a bright, asymmetrical central peak some 40 $\times$ 55 arcsec in size, possibly surrounded by several secondary peaks. The results using the pixon technique are compared with those obtained using the standard Maximum Entropy and Richardson-Lucy methods.

1. Introduction

The UT multichannel photometer, which is described in detail in an accompanying paper (Harvey *et al.* 1994), consists of a set of 20 ^{3}He-cooled bolometers arranged in two rows of ten. The detector spacing is chosen to be compatible with the diffraction limit of the KAO telescope in the 50μm and 100μm bands. Two-dimensional images are made by scanning the detectors across the source.

The combination of a stable, well-measured point-spread function (PSF) and a good signal-to-noise ratio should make it possible to use deconvolution techniques to achieve significant improvements in the resolution of images of bright sources taken with this instrument. This contribution describes a series of experiments with the promising new Pixon deconvolution technique and the older Richardson-Lucy (RL) and Maximum Entropy (MEM) methods.

2. Input Data Set

The data set chosen for these tests is an image of the bright HII region NGC 3603 taken in the 100μm bandpass on 10 April 1991. The data consist of three sweeps across the source in the direction perpendicular to the length of the detector array. The image was constructed by forming the weighted average of the detector responses, using the **kaoin** task in **MIRIAD** (Wright and Sault, 1993). The PSF was measured by observing the asteroid Ceres in the same way. The Ceres image was then rotated (using IRAF's **rotate** function) to make its

mean sweep direction equal to that in the NGC 3603 image. The results are presented in Figure 1a-c.

Comparison of the NGC 3603 image with the PSF shows that the HII region is clearly resolved, and a good candidate for deconvolution. The fact that the valid data in these images are of different sizes and do not fill out the entire image arrays represents a challenge to any deconvolution algorithm. This is especially true since the emission from the NGC 3603 region extends beyond the area measured by the scans, which produces the potential for strong edge effects. The Pixon and RL codes used for this work allow the valid regions of the data array to be specified in order to ameliorate these effects; the MEM code does not.

The uncertainty in the input image is not measured independently of the image itself. Instead, it is chosen to be uniform across the image and large enough to produce a reasonable-looking result in the first goodness-of-fit (GOF) run of the Pixon procedure.

3. Deconvolution Results

3.1. Pixon Method

The Pixon deconvolution method (Pina and Puetter, 1993) is a Bayesian approach based on the concept of the Pixon, defined as the fundamental unit of picture information. Pixons, rather than pixels, represent the degrees of freedom in the image. One seeks the most probable image and model given the data. The deconvolution is carried out by alternating between a simple GOF calculation to find the most probable image given a fixed model, and calculating an improved model while holding the image fixed. The implementation used here is by Pina and Puetter (1993). It permits both the image weights and a mask for the pixels outside the image to be specified. The result from the first iteration is presented in Figure 2a.

3.2. Richardson - Lucy Method

The Richardson - Lucy method is a widely-used iterative approach derived from Bayes' Theorem (Lucy 1974). Unlike the Pixon method, RL requires one to decide how many iterations to perform; the apparent resolution of the deconvolved image increases with the number of iterations as the goal of maximum likelihood of the image is approached, and it is quite possible to overfit the data and produce spurious features. The result is presented in Figure 2b. The implementation used here is from the STSDAS package in IRAF. The edge effects are reduced by allowing the algorithm to extend the area covered by the deconvolved image beyond the region for which there is data.

3.3. Maximum - Entropy Method

Maximum Entropy methods seek to maximize an "entropy" function of the image within the constraints of the data. The entropy is generally defined in terms of an image prior which can incorporate *a priori* information into the deconvolved image. The MEM package used here is from the STSDAS package in IRAF. The number of iterations in these runs is limited to about 110; at this point the

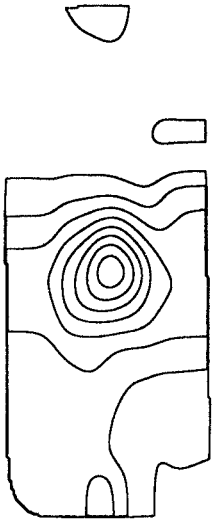

Figure 1a
Input Image

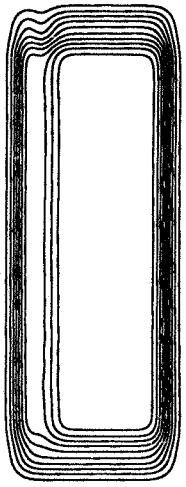

Figure 1b
Image Weights

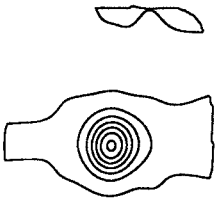

Figure 1c
Ceres PSF

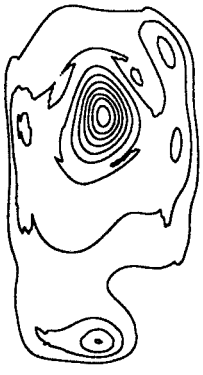

Figure 2a
Pixon

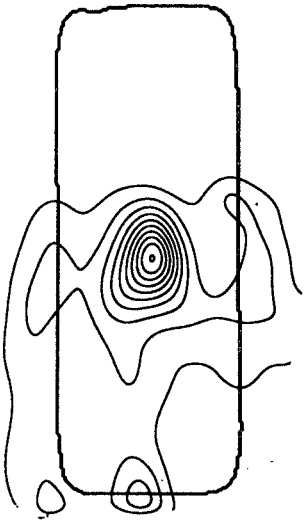

Figure 2b
Richardson-Lucy

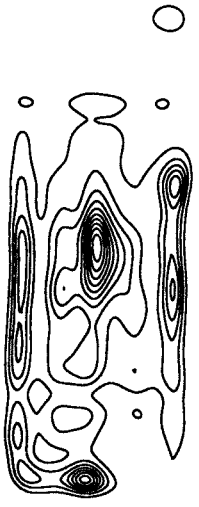

Figure 2c
Maximum Entropy

χ^2 value approached, but did not reach, its expected value. This may be an indication that the noise level has been somewhat underestimated.

The deconvolved image, presented in Figure 2c, is strongly affected by edge effects which are manifested as spurious emission which roughly traces out the edges of the valid data. The overfitting of the data is reduced somewhat as the size of the Intrinsic Correlation Function (ICF) is increased, but a really satisfactory deconvolution is never achieved.

4. Conclusions

It is clear from the numerical tests presented here that the resolution of the input image can be usefully increased by deconvolution. The three deconvolution techniques produce results which appear basically consistent with each other. In all three cases the deconvolved image consists of a bright asymmetrical central peak roughly 20×35 pixels in size and roughly triangular in shape. This result seems consistent with what is expected from a simple visual comparison of the input image with the PSF.

For the present data set, which is typical of many images constructed from data acquired with the UT multichannel far-infrared photometer, the most important determinant of the success of a technique appears to be the inclusion of some mechanism for specifying the range of pixels over which the data are valid. When this is not done, strong edge effects result which influence the shape of the central peak in the reconstructed image.

The Pixon and Richardson-Lucy methods do best, probably by virtue of their implementations' inclusion of image weights. The best RL reconstructions appear nearly free of edge effects within the region of the image which corresponds to the original measurements. It has the further advantage of requiring much less computer time to run (minutes *vs.* hours). These properties make it the most suitable technique of the three for the present data set. The more sophisticated handling of image noise by the Pixon method may give it an advantage when working with data of lower quality.

References

P. M. Harvey, B. Smith, C. Colome, J. Di Francesco, D. F. Lester, and D. Sill, 1994, in Proc of the Airborne Astronomy Symp on the Galactic Ecosystem: From Gas to Stars to Dust, ed. M. R. Haas, J. A. Davidson, & E. F. Erickson, (San Francisco: ASP), paper 705

Pina, R. K. and Puetter, R. C., 1993 P.A.S.P., 105, 630

Lucy, 1974 A.J. 79, 745

Wright, M. C. H. and Sault, R. J., 1993 ApJ. 402, 546

Session Four

Our Planetary System: The Solar System

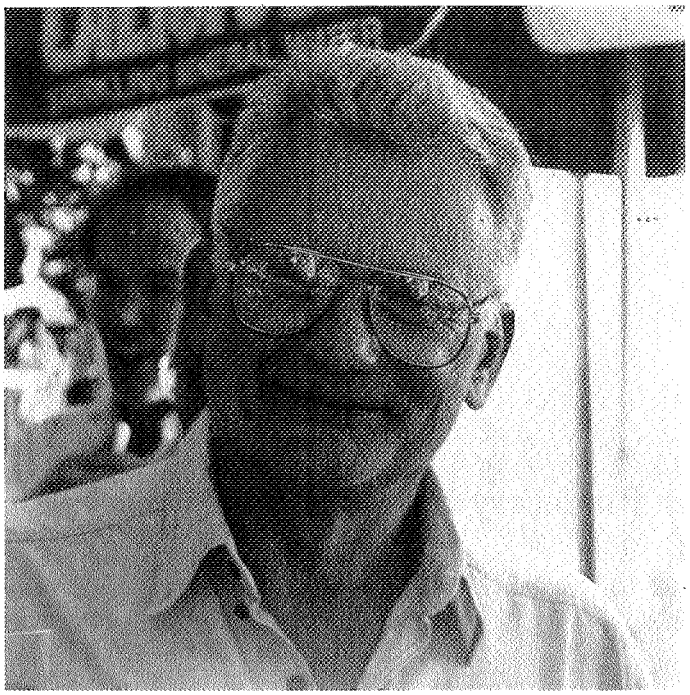

Bob Pernic

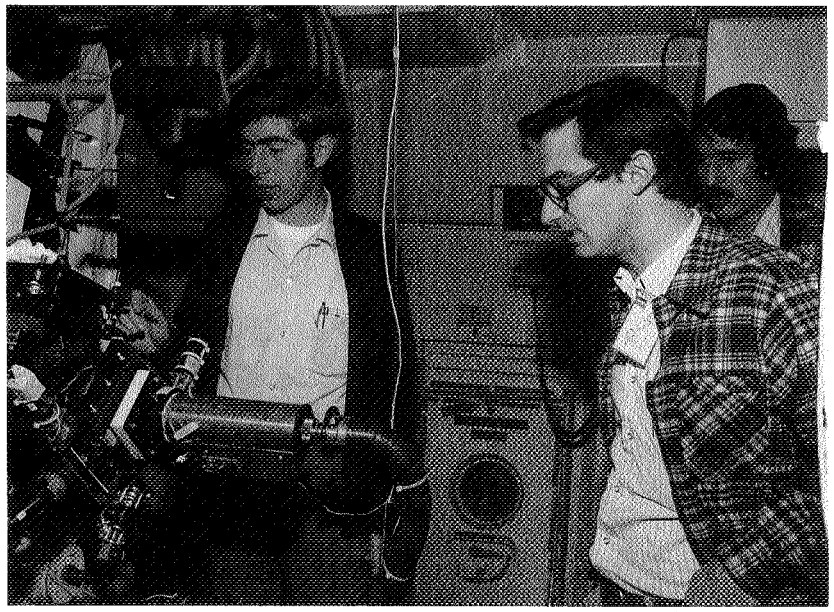

Steve Willner, Tom Soifer, Bob Walker (1979)

OUR PLANETARY SYSTEM: THE SOLAR SYSTEM

DONALD M. HUNTEN
Lunar and Planetary Laboratory, University of Arizona, Tucson, AZ 85721

ABSTRACT A survey is given of the accomplishments of airborne astronomy in solar-system science. They include identification of sulfuric acid in the clouds of Venus, establishment of Jupiter's internal heat source, discovery of water vapor and almost a dozen other molecules in Jupiter's atmosphere, important measurements of occultations of stars by Mars, Pluto, and Chiron, discovery of the rings of Uranus, and diagnosis of mineral composition on planetary surfaces.

INTRODUCTION

Measurements from the KAO have made important and unique contributions to our knowledge of the solar system. The important attributes of an airborne platform are well known, but still bear repeating:

1) Atmospheric absorption, especially by water vapor, is greatly reduced;
2) Observations are not (usually) hampered by clouds;
3) The aircraft can go almost anywhere on Earth.

Pioneering observations of Jupiter, Mars, Venus, and Halley's Comet have been made that take advantage of reduced water vapor. However, many of them have been largely superseded by observations from planetary spacecraft and probes. The truly unique legacy of airborne solar-system astronomy will be occultation results, especially those that were obtained from remote locations. Probably the most striking was the discovery of the rings of Uranus, but there has been important work on Mars, Pluto, and Chiron. For observations of occultations and of comets, both the mobility and the freedom from clouds have been important. A beginning has been made on diagnosing surface composition of rocky planets like Mars and Mercury, a field that shows promise for the future.

INFRARED SPECTROSCOPY

The first major achievement (actually from the Learjet Observatory, the predecessor of the KAO) was identification of the material of the Venus clouds by Pollack *et al.* (1975). Sulfuric acid has a highly diagnostic absorption from 2.7 to 4 μm; other candidates such as water ice or liquid, hydrochloric acid, or ferric chloride, simply did not fit the observed spectrum. As it happens, the nature of the clouds was simultaneously and independently identified by Sill and

by A.T. Young from the refractive index, deduced by Hansen from polarimetry. However, the IR data are substantially more diagnostic. Direct sampling by Pioneer Venus later confirmed all the results of remote sensing.

That Jupiter radiates almost twice as much energy as it absorbs from the Sun had been surmised for several years, but ground-based measurements left serious gaps in the thermal spectrum. The result was firmly demonstrated by Learjet measurements (see the convenient summary by Low, 1976).

One of the first major discoveries by the KAO (Larson *et al.*, 1975) was of water vapor on Jupiter. The absorptions are strong and obvious; all that was necessary was to fly an instrument of sufficient sensitivity and resolution above most of the Earth's water vapor. However, it is fortunate that these strong lines occur in the 5 μm region, where other gaseous absorptions are so weak that in cloud-free areas energy reaches space from levels as deep as 5 bars. The H_2O mixing ratio appeared to be remarkably small, in comparison with the $\sim$1 part per thousand (by volume) expected for a solar abundance of oxygen. The cloud-free regions from which the 5 μm emission is observed are presumably drier than normal, but would not be expected to be as dry as the observations implied. About a dozen other molecular species are also observed, most of them in this same region; a summary is given by Treffers *et al.* (1978). A thorough analysis, making use of developments in the theory of scattering in a cloudy atmosphere, was first provided by Bjoraker *et al.* (1986). The remarkably small mixing ratio of H_2O was supported by this analysis.

The IRIS (IR Interference Spectrometer) instruments on Voyagers 1 and 2 returned their Jupiter data in 1979. These spectra have about one-third the spectral resolution of the KAO data, but much higher spatial resolution and a complete absence of telluric absorption. A comprehensive re-analysis, recently published by Carlson *et al.* (1983), includes a greatly improved treatment of cloud scattering and absorption, and resolves the H_2O discrepancy mentioned above.

It has been almost a matter of faith since the work of Whipple in 1950, that a major component of cometary nuclei is water ice. Although there were indirect confirmations in the interim, the first direct determination of water vapor was made from the KAO by Mumma *et al.* (1986). This group also determined the ortho/para ratio (Mumma *et al.*, 1987).

OCCULTATIONS

Although planets and their atmospheres have been occulting stars for ages, the first useful observation (of a Jupiter event) was not obtained until 1952, and the technique did not gain broad application for another 20 years (Elliot, 1979). Elliot and his group have made excellent use of the KAO to fill in the gaps between ground-based observatories and to exploit its ability to fly above most clouds. The mobility of the KAO has been crucial in a number of cases, for a number of related reasons. The shadow of a planet is essentially the same size as the planet itself, and crosses only one side of the Earth; this side (often the Pacific Ocean) may not contain any substantial ground-based observatory. The position of the star relative to the planet is usually uncertain by as much as tenths of an arcsecond, corresponding to a displacement of the occultation track by as much as 1000 km; this uncertainty is not substantially reduced until

both objects can be photographed together, typically about a week before the event. The staff and crews of the KAO have several times responded to such a challenge by making last-minute modifications to the flight plan. Such response was essential for obtaining the Mars central flash (Elliot *et al.*, 1977b), the Pluto event (Elliot *et al.*, 1989), and the recent observation of Chiron. Perhaps the best-known result of this program was the discovery of the rings of Uranus (Elliot *et al.*, 1977a). This system is so large that last-minute mobility was not required, but the clear skies above the KAO were crucial, because all the surface stations that attempted the observation were hampered or wiped out by clouds.

PLANETARY SURFACES

IR spectroscopy of surfaces is a field just beginning to come into its own. Some of the most significant wavelength regions are much better observed from KAO altitudes than from even the highest mountain. A study of Mars in the 5.4 – 10.5 μm region by Pollack *et al.* (1990) yielded evidence for bound water in the surface (at 6.1 μm, a region absorbed by telluric H_2O). Sulfate and carbonate were inferred to be present in airborne dust, in volume proportions of 10 – 15% and 1 – 3% respectively.

Very recently Sprague *et al.* (1994) have reported a study of Mercury in the 7.3 - 13.5 μm region. This work, carried out at the IRTF on Mauna Kea, convincingly illustrates the need for the KAO. Spectra were obtained with FOGS and HIFOGS, the same instruments also used on the aircraft. IRTF results strongly suggest plagioclase feldspar is a major mineral near 120° mercurian longitude and the Christiansen frequency indicates it to be only slightly Ca-rich. A more detailed identification awaits further study from above Earth's absorbing H_2O, CH_4, and N_2O (below 8 μm) and diminished water-ice and CO_2 (between 12 and 14 μm). More generally, the 4 - 8 μm region is highly diagnostic, as illustrated in Fig. 2 of Nash *et al.* (1993).

DISCUSSION

Airborne astronomy has played an important role in the enormous progress of solar-system science over the last two decades. Although this work has had to compete with the results of planetary spacecraft, airborne observations have almost no competition in the area of stellar occultations. The new field of IR studies of surfaces has great potential for bodies that are too numerous or too distant to be visited by spacecraft.

REFERENCES

Bjoraker, G.L., Larson, H.P. & Kunde, V.G., 1986. Icarus, 66, 579.

Carlson, B.E., Lacis, A.A. & Rossow, W.B., 1983. J. Geophys. Res., 98, 5251.

Elliot, J.L., 1979. Ann. Rev. Astron. Ap. 17, 445.

Elliot, J.L., Dunham, E. & Mink, D., 1977a. Nature, 267, 328.

Elliot, J.L., French, R.G., Dunham, E., Gierasch, P.J., Veverka, J., Church, C.,

& Sagan, C, 1977b. ApJ, 217, 661.

Elliot, J.L., Dunham, E.W., Bosh, A.S., Slivan, S.M., Young, L.A., Wasserman, L.H., & Millis, R.L., 1989. Icarus 77, 148.

Hansen, J.E. and Arking, A., 1971. Science, 171, 669.

Hansen, J.E. and Hovenier, J.W., 1974. J. Atmos. Sci., 31, 1137.

Larson, H.P., Fink, U., Treffers, R.R., & Gautier, T.N., 1975. ApJL, 197, L137.

Low, F., 1976. in Jupiter, ed. T. Gehrels (Tucson: Univ. Arizona Press), 203.

Mumma, M.J., Weaver, H.A., Larson, H.P., Davis, D.S. & Williams, M., 1986. Science 232, 1523.

Mumma, M.J., Weaver,H.A. & Larson, H.P., 1987. A&A, 187, 419.

Nash, D.B., Salisbury, J.W., Conel, J.E., Lucey, P.G., & Christensen, P.R., 1993. J. Geophys. Res., 98, 23535.

Pollack, J.B., Erickson, E.F., Goorvitch, D., Baldwin, B.J., Strecker, D.W., Witteborn, F.C., & Augason, G.C. 1975, J. Atmos. Sci., 32, 1140.

Pollack, J.B., Roush, T., Witteborn, F., Bregman, J., Wooden, D., Stoker, C., Toon, O.B., Rank, D., Dalton, B. & Freedman, R., 1990. J. Geophys. Res. 95, 14,595.

Sill, G.T., 1972. Comm. Lunar Planetary Lab., No. 171, 191.

Sprague, A.L., Kozlowski, R.W.H., Witteborn, F.C., Cruikshank, D.P. & Wooden, D.H., 1994. Icarus, 109, 156.

Treffers, R.R., Larson, H.P., Fink, U. & Gautier, T.N., 1978. Icarus 34, 331.

Whipple, F.L., 1950. ApJ, 111, 375.

Young, A.T., 1973. Icarus, 18, 564.

Airborne Astronomy Symposium on the Galactic Ecosystem
ASP Conference Series, Vol. 73, 1995
M.R. Haas, J.A. Davidson, and E.F. Erickson (eds.)

Exploring Small Bodies in the Outer Solar System with Stellar Occultations

J. L. Elliot

Department of Earth, Atmospheric, and Planetary Sciences and Department of Physics, Massachusetts Institute of Technology, 77 Massachusetts Avenue, Cambridge, MA 02139 and Lowell Observatory, 1400 West Mars Hill Road, Flagstaff, AZ 86001

E. W. Dunham

Space Science Division, NASA Ames Research Center, Mail Stop 245-6, Moffett Field, CA 94035-1000

C. B. Olkin

Department of Earth, Atmospheric, and Planetary Sciences , Massachusetts Institute of Technology, 77 Massachusetts Avenue, Cambridge, MA 02139 and Lowell Observatory, 1400 West Mars Hill Road, Flagstaff, AZ 86001

Abstract. Stellar occultation observations probe the atmospheric structure and extinction of outer solar system bodies with a spatial resolution of a few kilometers, and an airborne platform allows the observation of occultations by small bodies that are not visible from fixed telescopes. Results from occultations by Triton, Pluto, and Chiron observed with the KAO are discussed, and future directions for this program are presented.

1. Introduction

From the perspective of an observer, a stellar occultation occurs when an intervening body blocks the reception of starlight. The starlight dims through differential refraction in the atmosphere of the occulting body, or through absorption by material associated with the body. As the apparent motion of the body takes it completely across the star, we record a single chord (or "line scan"), and with multiple occultation chords (obtained from several observing stations or from closely spaced stars observed from a single station), we build up a more complete picture of the body.

Since we are recording the intensity of light that has been transmitted and refracted, we can learn about the atmospheric structure of a body and the optical depth of associated material (Elliot 1979). An important aspect of occultation measurements is their extremely high spatial resolution, compared with other methods for Earth-based observations. Fresnel diffraction sets the fundamental

limit to the spatial resolution at about $\sqrt{\lambda D}$, where λ is the wavelength of observation and D is the distance between the observer and the occulting body. This is about 1 km for optical observations of objects at 10 AU. Other factors place more stringent limits on the spatial resolution in certain cases. These are the angular diameter of the occulted star and the signal-to-noise (S/N) of the data.

Airborne observations of occultations offer several advantages over ground-based observations. The most important of these for small bodies is the ability to locate the telescope within the occultation shadow. An airborne platform can be deployed virtually worldwide, and compared with the mobility of ground-based observers with portable telescopes, large adjustments to the planned location can be made much later with an airborne platform. Also, airborne observations avoid clouds and scintillation. Some of these advantages are shared with the HST, but the location of the HST cannot be adjusted, and the region of sky that can be observed at a given time is greatly reduced by sun, moon, and Earth avoidance requirements (Elliot et al. 1993). The stellar occultation work described here has similarities to the KAO observations of solar eclipses (Lindsey et al. 1986).

In the first decade of the KAO, we used a high-speed aperture photometer that employed photomultiplier tubes for detectors (Elliot, Veverka, & Goguen 1975). Our time standard was a temperature stabilized quartz crystal (synchronized with time signals from WWV), and the inertial navigation systems on the KAO determined observer coordinates. Our program began with the occultation of ε Geminorum by Mars, in which we made the first observations of the "central flash" (Elliot et al. 1977a) and discovered inertia-gravity waves in the Martian atmosphere (Elliot et al. 1977b). This was followed by our discovery of the Uranian rings (Elliot, Dunham, & Mink 1977; Elliot, Dunham, & Millis 1977) and an occultation probe of the Uranian atmosphere (Dunham, Elliot, & Gierasch 1980). Other work included securing upper limits on the optical depth of the Jovian rings (Dunham et al. 1982), probing Neptune's atmosphere (French et al. 1985), defining a limit on continuous rings around Neptune (Elliot et al. 1985), and observing the first occultation by an asteroid (Wasserman et al. 1979).

Although there were compelling scientific reasons to do so, observations of stellar occultations by small, distant bodies were rarely attempted because of the difficulty in predicting where the occultations would be visible—since they subtend such small angles as seen from Earth. This difficulty has been largely overcome in recent years (Olkin & Elliot 1994), opening up occultation investigations of bodies such as Triton, Pluto, Charon, and Chiron. To carry out these more recent observations, we have upgraded our instrumentation to employ visible and IR arrays (Dunham et al. 1985; Buie et al. 1993), as well as a Global Positioning System (GPS) receiver for more accurate determination of time and location. This second-decade program is the subject of this article.

2. Formation of an Occultation Light Curve

Figure 1 illustrates a stellar occultation where differential refraction by the atmosphere spreads out the parallel rays of starlight that enter the diagram from the left. A ray passing a closest approach distance r from the center of the body is received by the observer in the occultation shadow at a distance ρ from an axis defined by the star and the center of the body. If D is the observer-body

distance, r' a variable of integration, x the coordinate along the path of the ray, and $\nu(r')$ the refractivity of the atmosphere, then the atmospheric refraction angle $\theta(r)$ is given by (Elliot & Young 1992):

$$\theta(r) = \frac{\rho - r}{D} = \frac{d}{dr} \int_{-\infty}^{\infty} \nu[r'(x,r)]dx \tag{1}$$

In Fig. 1, $\phi(\rho)$, the flux received by the observer is schematically illustrated at the right of the diagram.

If we also define the optical depth traversed by a ray of closest approach r as $\tau(r)$, then we can write the observed stellar flux as the product of three terms (Elliot & Young 1992): one describing the effect of extinction, another, the effect of differential refraction, and a third, the effect of focusing of the stellar flux by the curvature of the planetary limb. For a spherically symmetric body, the equation for $\phi(\rho)$ is:

$$\phi(\rho) = \frac{\overbrace{e^{-\tau(r)}}^{\text{extinction}}}{\underbrace{\left[1 + D\frac{\theta(r)}{r}\right]}_{\text{focusing}} \underbrace{\left[1 + D\frac{d\theta(r)}{dr}\right]}_{\text{refraction}}} \tag{2}$$

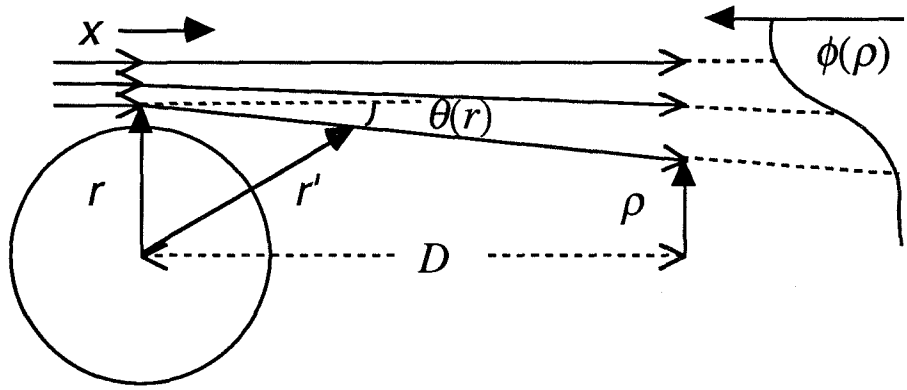

Figure 1. Stellar occultation by an atmosphere. Starlight, incident from the left is refracted by the atmosphere through an angle $\theta(r)$, whose magnitude increases exponentially as r decreases, due to the exponential decrease of density with distance from the center r. The flux, $\phi(\rho)$, received by the observer decreases, deeper into the shadow. From this flux and the known mean molecular weight, one can recover the density structure of the atmosphere, under the assumption of hydrostatic equilibrium.

By inspection of Eqs. (1) and (2), we see that $\phi(\rho)$ is a function of only the refractivity of the atmosphere and any optical depth encountered by the ray. If

the structure of atmosphere can be assumed to be in hydrostatic equilibrium, then temperature, pressure, and number density profiles can by recovered through the inversion technique (French, Elliot, & Gierasch 1978), or one can recover information about the atmosphere by fitting models (Elliot & Young 1992).

3. Some Small, Icy Bodies

Small, icy bodies in the outer solar system are of interest because some of them likely formed in the solar nebula (rather than a pre-planetary nebula), and from those we may learn much about early conditions in the outer solar system. Also, the low temperatures of the outer solar syste n, the reduced solar radiation, and the low masses of these bodies present new and interesting regimes of chemistry and physics to challenge our understanding. Important issues here are the escape of atmospheres from weak gravity fields and the interactions between atmospheres and surface ices through vapor-pressure equilibrium.

Table 1. Small Bodies that Likely Formed in the Solar Nebula

Body	Type	Orbit (au)	Radius (km)	Density ($g\ cm^{-3}$)	Detected Constituents
Triton	satellite	30	1350 ± 5	2.0	N_2, CH_4, CO, CO_2
Pluto	planet	30-49	1175 ± 25	1.8–2.9	N_2, CH_4, CO
Charon	satellite	30-49	600 ± 25	< 2.2	H_2O
Chiron	comet	8-19	110 ± 30	1 ?	CN

References for Table 1: Triton: Cruikshank et al. (1993); Tyler et al. (1989). Pluto: Millis et al. (1993); Owen et al. (1993). Charon: Elliot & Young (1991); Tholen & Buie (1990); Marcialis, Rieke, & Lebofsky (1987); Walker (1980); Young (1992). Chiron: Buie (1993); Bus et al. (1991); Elliot et al. (1994); Jewitt & Luu (1992).

Four bodies most amenable to study (because they are the largest) are listed in Table 1. Although generically these bodies belong to the category of "planet", "satellite", and "comet", they may well be closely related to each other in terms of their initial composition and where they were formed. Indeed, in a discussion on the KAO about why Chiron is classified as a "comet", rather than an "asteroid", our tracker operator, Ben Burress, suggested that it be called an "iceteroid"—reflecting the similarities between icy, outer solar system objects and the more familiar rocky, inner solar system objects.

Triton and Pluto are remarkably similar in size and density, and each suffered an early catastrophic event: Triton's retrograde orbit indicates that it was captured by Neptune in the early history of the solar system (Goldreich et al. 1989), while Pluto's binding with Charon also required a large dissipation of energy (McKinnon 1989). The low probability of such events for two isolated bodies implies that Triton, Pluto, and Charon are representatives of a large number of such bodies that existed in the past—perhaps remnants of building blocks for the larger planets. We do not know where Chiron formed, due to its chaotic orbit (Scholl 1979), but during most of its past, it must have been much further from the sun (Stern 1989).

Recent work on small-body occultations has been enabled by substantial improvements in methods used to predict where these occultations will be visible (Dunham, McDonald, & Elliot 1991; McDonald & Elliot 1992), and the three of these observed with the KAO are listed in Table 2.

Table 2. Icy-Body Occultations Observed with the KAO

Body	Occultation date	Deployment	Main results
Pluto	1988 June 9	Samoa	atmosphere (mostly N_2) discovered
Triton	1993 July 10	Chile	nearly central chord observed
Chiron	1994 March 9	Brazil	jet-like structures found

References for Table 2: Pluto: Elliot et al. (1989); Elliot & Young (1992); Millis et al. (1993). Triton: Elliot, Dunham, & Olkin (1993); Olkin et al. (1993). Chiron: Elliot et al. (1994).

3.1. Triton

The tenuous atmospheres of Triton and Pluto are similar in that the major constituent of each is N_2, although Pluto's atmosphere has considerably more CH_4 than does Triton's (Spencer, Buie, & Bjoraker 1990). Since these atmospheres are in vapor pressure equilibrium with surface ices, large seasonal changes in surface pressure have been predicted for each (Trafton 1990; Hansen & Paige 1992; Spencer & Moore 1992). Triton's atmosphere has been probed by several instruments aboard the Voyager 2 spacecraft: (i) the Imaging Science Subsystem, (ii) the Ultraviolet Spectrometer (UVS) and (iii) the Radio Science Subsystem (RSS). Each of these instruments investigated a different region of the atmosphere and was sensitive to different properties. The radio science team modeled Triton's atmosphere (Tyler et al. 1989) based on their observations. However, because the surface pressure of Triton is only about 16 μbar, the phase shift of the radio signal never reaches 2 radians, and these results are not considered as reliable as what has been obtained from RSS occultations at millibar pressures. The Strobel and Summers (1994) model is based mainly on the UVS data. These two models differ, in that the Strobel and Summers (1994) model incorporates the troposphere of Yelle et al. (1991), while the RSS model (Tyler et al. 1989) has a strong thermal inversion near the surface. Hence the two models predict temperature differences greater than 10K in the lower 20 km.

In an attempt to distinguish between these two competing models for Triton's atmosphere, we observed the occultation of Tr60 by Triton from the KAO (Elliot et al. 1993; Olkin et al. 1993). Unfortunately, we have the only occultation chord recorded for this event, and the error in the placement of our chord relative to the center of Triton's disk ("impact parameter") is 150 km. We are still working on improving the post-event astrometry to reduce the uncertainty in the impact parameter and therefore the uncertainty in the temperature at a given height. We have learned that previous astrometric methods are not sufficient for determining the impact parameter accurately enough for atmospheric modeling, so multiple chord observations will be desirable for future small-body occultations. The KAO results are closer to the Strobel and Summers (1994) model than the RSS model (Tyler et al. 1989), but additional improvement in the impact parameter is needed before our final results will become available.

3.2. Pluto

Four principal unknowns affecting the structure of Pluto's atmosphere are: (1) composition of the atmosphere, (2) haze or thermal gradient below 1215 km, (3) surface temperature, and (4) surface radius. First order information on the composition has come from two spectroscopic observations, which showed that the primary constituent must be N_2 (Owen et al. 1993) and the gaseous CH_4 component is about 1.2 cm-A (Young 1994). The following discussion describes how we might be able to resolve the haze issue through stellar occultations observed simultaneously in the visible and infrared. Resolution of this issue would also give us knowledge of the surface radius, and possibly the surface temperature by extending the measured atmospheric structure to the surface.

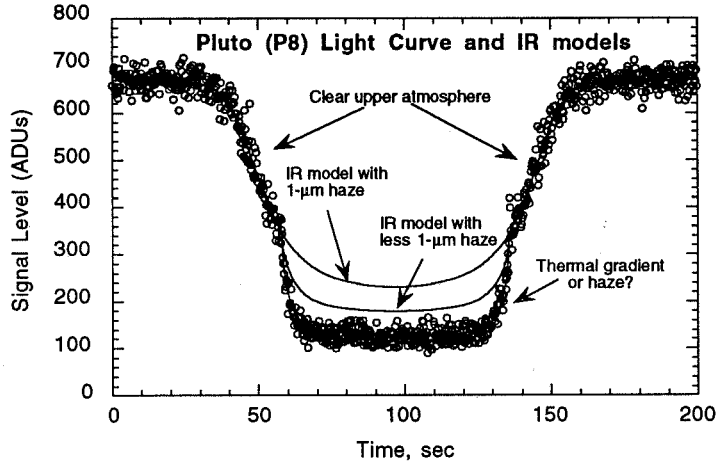

Figure 2. Pluto occultation light curve obtained with the KAO (in the optical) and IR light curve models. The sharp drop in the light curve may be caused either by haze or a sharp thermal gradient. A light curve in the IR would look the same if a thermal gradient is present, but it would be shallower if the sharp drop is caused by extinction from micron-sized haze particles [adapted from (Elliot et al. 1989)].

Most of what we know about the present state of Pluto's atmosphere comes from the stellar occultation observed from the KAO (Elliot et al. 1989) and other sites in 1988 (Millis et al. 1993). The KAO observations were carried out with our high-speed CCD imaging photometer, the SNAPSHOT (Dunham et al. 1985), and their purpose was to determine whether Pluto had an atmosphere. The results of that observation, described by Elliot et al. (1989) and Elliot and Young (1992) are summarized here. The observed light curve was unlike any we have encountered elsewhere in the solar system. As may be seen in Figure 2, the light

curve begins to drop in a manner consistent with differential refraction by a clear, isothermal atmosphere. Just below the half-light level, however, a sharp kink occurs, followed by a rapid decline to a level indistinguishable from the light from Pluto-Charon alone.

Although differential refraction by the planet's atmosphere is the usual mechanism that dims a star occulted by a distant body, it is possible for absorption to exceed differential refraction and become the dominant factor. Hence, the KAO light curve was interpreted by Elliot et al. (1989) in terms of differential refraction in a clear, isothermal atmosphere that lies above a layer of haze. This haze absorbs light at levels of the atmosphere corresponding to points on the light curve below the kink. This model fits the data very well (Elliot et al. 1989; Elliot & Young 1992; Millis et al. 1993).

The physical background to the haze model has been explored by Stansberry et al. (1989). They conclude that the photochemical mechanisms thought to be active on Neptune, Uranus and Titan are not able to produce a haze of sufficient opacity. Alternative mechanisms involving condensation near the surface of Pluto have not been explored. For example, CH_4 ice crystals could be causing the extinction. An alternative explanation of the lower part of Pluto's occultation light curve has been presented by Eshleman (1989) and Hubbard et al. (1990), who suggested that a large positive temperature gradient in Pluto's atmosphere (~10 K km^{-1}) would cause the light curve to drop steeply, as observed. We have fit the data with a model atmosphere consisting of smoothly joined layers with constant temperature gradients (Slivan & Dunham 1989) and achieved a somewhat inferior fit.

In summary, Pluto's occultation light curve can be well matched by two entirely different atmospheric models: one involving absorption by haze and the other involving a steep positive temperature gradient. We cannot decide which model is correct with the data in hand. However, because of the high sedimentation rates that occur with particles larger than 0.1 μm or so (Stansberry et al. 1989), any aerosols present must be very small. The extinction efficiency has a wavelength dependence that is stronger than $1/\lambda$ for Mie scattering particles of this size when observed at optical and near-infrared wavelengths. Hence, we can distinguish between the haze and thermal-gradient models by observing another occultation simultaneously at optical and near-infrared wavelengths. If the haze model is correct, we expect to see the optical light curve drop to the level of Pluto alone as we observed before, but the infrared light curve should drop more gently and might bottom out at a higher flux level (see Fig. 2). Conversely, if the thermal gradient model is correct, both light curves should show the same structure (except for a negligible difference due to the difference in the refractivity of Pluto's atmosphere at the two wavelengths).

3.3. Charon

Little is known about Charon. From the mutual occultations and eclipses of Pluto and Charon (Tholen & Buie 1990) we learned that its spectrum shows a band of H_2O ice (Marcialis et al. 1987), and we have a measurement of its radius—but with a significant error (see Table 2). Recent determination of its mass has shown a bulk density near that of Pluto (Young et al. 1994), although other work would favor a substantially lower bulk density (Null, Owen, & Synnott 1993). A single

chord from a stellar occultation observed by Walker (1980) yielded a lower limit on its radius and a possible detection of an atmosphere (Elliot & Young 1991). Further stellar occultation observations are needed to accurately determine its radius and to resolve the question of its possible atmosphere. Reducing the error in the radius is needed for an accurate density, since the radius enters the expression for the density as the third power.

3.4. Chiron

At the time of its discovery (Kowal 1979), 2060 Chiron was thought to be the most distant known asteroid from the sun. Subsequent photometric outbursts (Tholen, Hartmann, & Cruikshank 1988), followed by the detection of a coma (Luu & Jewitt 1990; Meech & Belton 1990; West 1991) and CN emission (Bus et al. 1991), however, have revealed its cometary nature. Considered as a comet, Chiron is unusual in two respects: (i) it exhibits outbursts at great distances from the sun (nearly up to its aphelion distance of 18.9 AU) (Bus et al. 1989), and (ii) its nucleus is much larger than that of any other known comet (Sykes & Walker 1991; Jewitt & Luu 1992). To probe its nuclear region, a stellar occultation by Chiron was recently observed (Buie 1993), but the light curve signatures proved puzzling because the apparent nuclear occultation was not complete (Buie 1993). With the more recent occultation of a brighter star observed with the KAO (Elliot et al. 1994), recorded simultaneously at visible and infrared wavelengths, we obtained much better S/N, These data have a spatial resolution better than 10 km at Chiron, and our chord passed close to the nucleus, but did not include it.

Our conclusions about Chiron from this work (Elliot et al. 1994) and the previous stellar occultation (Buie 1993) are: (i) the jet-like features observed provide evidence that the coma material originates from just a few, small active areas, rather than uniform sublimation, (ii) a bound coma has possibly been detected, (iii) the particle radii in at least one of the jet-like features are larger than 0.65 μm, (iv) material in Chiron's orbit plane has likely been detected, and (v) the radius of Chiron's nucleus lies between 83 and 146 km. Multiple-chord observations of future occultations (Bus, Wasserman, & Elliot 1994) should enable us to characterize further the near-nuclear structure of Chiron—the largest object known to exhibit cometary activity, far from the sun.

4. Future of the Occultation Program

4.1. Predictions

Clearly the most critical technical need is for accurate predictions of occultations by small bodies, far in advance of the event, so that plans can be made for deployments and supporting ground-based work. Even for the larger bodies, such as Triton and Pluto, we can probe the deepest into their atmospheres with central chords, and this requires predictions accurate to much better than 0.01 arcsec. HIPPARCOS should be a tremendous help in this regard, reaching accuracies of 0.002 arcsec for 9th magnitude stars (Lindegren, Kovalesky, & Perryman 1994).

4.2. Instrumentation

We plan to improve the speed at which we can read out our array detectors, while maintaining or reducing the read noise. Also, we need to adopt a more integrated approach to our simultaneous visible and IR observations in order to achieve greater throughput and optical flexibility in both channels.

4.3. SOFIA

Hopefully SOFIA will become available within a few years. Its larger collecting aperture would increase the S/N for all events. This would enhance what we can learn from occultations involving stars bright enough to observe with the KAO already and allow us to observe occultations of stars too faint to be useful for KAO observations. The 3-5 arcsec seeing on the KAO limits the quality of our data for most events, so any improvement on SOFIA would further increase its value for occultation work. Another benefit of SOFIA is its planned altitude limit of only 20° above the horizon, substantially less than the 35° limit for the KAO, which would make more occultations accessible for observation.

4.4. Scientific Opportunities

Several scientific opportunities would be enabled by these technical improvements. One example is that we could then characterize Pluto's predicted atmospheric collapse as it recedes from the sun. Now the frequency of observable events is not great enough (no occultation has been observed since our discovery of its atmosphere in 1988). Similarly, an increased frequency of observable events would enable us to decide which (if any) of the proposed models for seasonal surface-pressure variations is correct for Triton. We could investigate the putative double-object structure of the Trojan asteroid 624 Hektor. Also, we could improve our sparse knowledge of the optical depth, as a function of wavelength, for the dust-jets and other structures near the nucleus of Chiron and other comets. Finally, the larger collecting area of SOFIA (combined with improved methods for predicting occultations) would put the Kuiper belt objects within our grasp, allowing us to determine their albedos (from learning their radii) and probe for near-nuclear material in these recently discovered objects.

5. Acknowledgments

The complex deployments for occultation observations have continually presented new and varied challenges to KAO management and crews. They have invariably risen to meet these challenges so we could achieve the prime objective: to "get the data". Thanks to all!

6. References

Buie, M. W. 1993, IAU Circ. 5898

Buie, M. W. et al. 1993, BAAS 25, 1115

Bus, S. J., A'Hearn, M. F., Schleicher, D. G., & Bowell, E. 1991, Science 251, 774

Bus, S. J., Bowell, E., Harris, A. W., & Hewitt, A. V. 1989, Icarus 77, 223

Bus, S. J., Wasserman, L. H., & Elliot, J. L. 1994, AJ 107, 1814

Cruikshank, D. P. et al. 1993, Science 261, 742

Dunham, E., Elliot, J. L., & Gierasch, P. J. 1980, ApJ 235, 274

Dunham, E., Elliot, J. L., Mink, D. J., & Klemola, A. R. 1982, AJ 87, 1423

Dunham, E. W., Baron, R. L., Elliot, J. L., Vallerga, J. V., Doty, J. P., & Ricker, G. R. 1985, PASP 97, 1196

Dunham, E. W., McDonald, S. W., & Elliot, J. L. 1991, AJ 102, 1464

Elliot, J. L. 1979, ARA&A 17, 445

Elliot, J. L. et al. 1985, AJ 90, 2615

Elliot, J. L. et al. 1993, AJ 106, 2544

Elliot, J. L., Dunham, E., & Mink, D. 1977, Nature 267, 328

Elliot, J. L., Dunham, E. W., Bosh, A. S., Slivan, S. M., Young, L. A., Wasserman, L. H., & Millis, R. L. 1989, Icarus 77, 148

Elliot, J. L., Dunham, E. W., & Millis, R. L. 1977, S&T 53, 412

Elliot, J. L., Dunham, E. W., & Olkin, C. B. 1993, BAAS 25, 1106

Elliot, J. L., French, R. G., Dunham, E., Gierasch, P. J., Veverka, J., Church, C., & Sagan, C. 1977a, ApJ 217, 661

Elliot, J. L., French, R. G., Dunham, E., Gierasch, P. J., Veverka, J., Church, C., & Sagan, C. 1977b, Science 195, 485

Elliot, J. L. et al. 1994, Nature (submitted)

Elliot, J. L., Veverka, J., & Goguen, J. 1975, Icarus 26, 387

Elliot, J. L. & Young, L. A. 1991, Icarus 89, 244

Elliot, J. L. & Young, L. A. 1992, AJ 103, 991

Eshleman, V. R. 1989, Icarus 80, 439

French, R. G., Elliot, J. L., & Gierasch, P. J. 1978, Icarus 33, 186

French, R. G. et al. 1985, AJ 90, 2624

Goldreich, P., Murray, N., Longaretti, P. Y., & Banfield, D. 1989, Science 245, 500

Hansen, C. J. & Paige, D. A. 1992, Icarus 99, 273

Hubbard, W. B., Yelle, R. V., & Lunine, J. I. 1990, Icarus 84, 1

Jewitt, D. & Luu, J. 1992, AJ 104, 398

Kowal, C. T. 1979, Chiron. In Asteroids (ed. T. Gehrels), p. 436. Univ. of Arizona Press, Tucson

Lindegren, L., Kovalesky, J., & Perryman, M. A. C. 1994, HIPPARCOS proper motions and parallaxes. In Galactic and Solar System Optical Astrometry (ed. L. V. Morrison & G. F. Gilmore), p. 66. Cambridge University Press, Cambridge

Lindsey, C., Becklin, E. E., Orrall, F. Q., Werner, N. W., Jefferies, J. T., & Gatley, I. 1986, ApJ 308, 448

Luu, J. X. & Jewitt, D. C. 1990, AJ 100, 913

Marcialis, R. L., Rieke, G. H., & Lebofsky, L. A. 1987, Science 237, 1349

McDonald, S. W. & Elliot, J. L. 1992, AJ 104, 862

McKinnon, W. B. 1989, ApJL 344, L41

Meech, K. J. & Belton, M. J. S. 1990, AJ 100, 1323

Millis, R. L. et al. 1993, Icarus 105, 282

Null, G. W., Owen, W. M., & Synnott, S. P. 1993, AJ 105, 2319

Olkin, C. B. & Elliot, J. L. 1994, Occultation astrometry: Predictions and post-event results. In Galactic and Solar System Optical Astrometry (ed. L. V. Morrison & G. F. Gilmore), p. 286. Cambridge University Press, Cambridge

Olkin, C. B., Elliot, J. L., Dunham, E. W., Millis, R. L., Wasserman, L. H., & Bus, S. J. 1993, BAAS 25, 1106

Owen, T. C. et al. 1993, Science 261, 745

Scholl, H. 1979, Icarus 40, 345

Slivan, S. M. & Dunham, E. W. 1989, BAAS 21, 986

Spencer, J. R., Buie, M. W., & Bjoraker, G. L. 1990, Icarus 88, 491

Spencer, J. R. & Moore, J. M. 1992, Icarus 99, 261

Stansberry, J. A., Lunine, J. I., & Tomasko, M. G. 1989, Geophys. Res. Lett. 16, 1221

Stern, S. A. 1989, PASP 101, 126

Strobel, D. F. & Summers, M. E. 1994, Triton's upper atmosphere and ionosphere. In Neptune and Triton (ed. M. S. Matthews), p. in press. University of Arizona Press, Tucson

Sykes, M. V. & Walker, R. G. 1991, Science 251, 777

Tholen, D. J. & Buie, M. W. 1990, BAAS 22, 1129

Tholen, D. J., Hartmann, W. K., & Cruikshank, D. P. 1988, IAU Circ. 4554

Trafton, L. 1990, ApJ 359, 512

Tyler, G. L. et al. 1989, Science 246, 1466

Walker, A. R. 1980, MNRAS 192, 47

Wasserman, L. H. et al. 1979, AJ 84, 259

West, R. M. 1991, A&A 241, 635

Yelle, R. V., Lunine, J. I., & Hunten, D. M. 1991, Icarus 89, 347

Young, E. F. 1992. An albedo map and frost model of Pluto. Ph. D. Thesis, Massachusetts Institute of Technology

Young, L. A. 1994. Bulk properties and atmospheric structure of Pluto and Charon. Ph. D. Thesis, Massachusetts Institute of Technology

Young, L. A., Olkin, C. B., Elliot, J. L., Tholen, D. J., & Buie, M. W. 1994, Icarus 108, 186

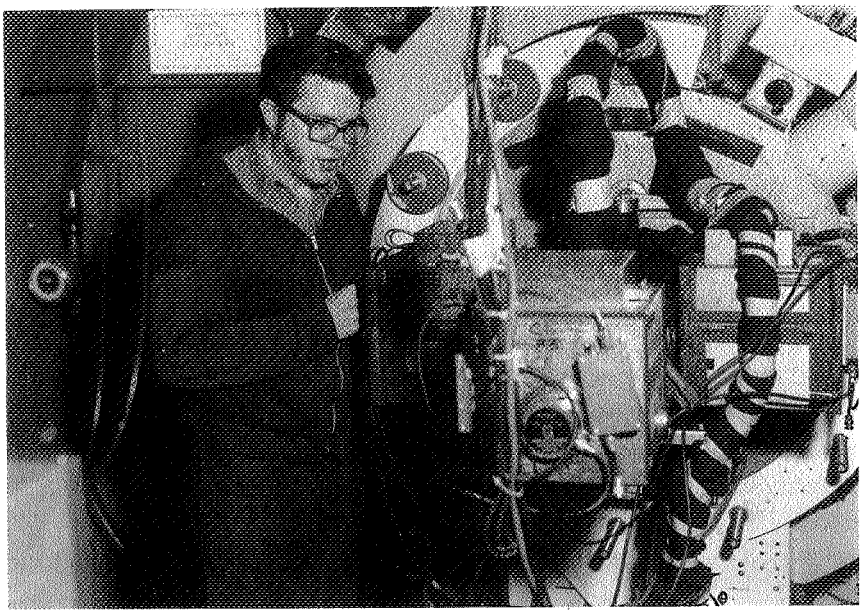

Jim Elliot (1976)

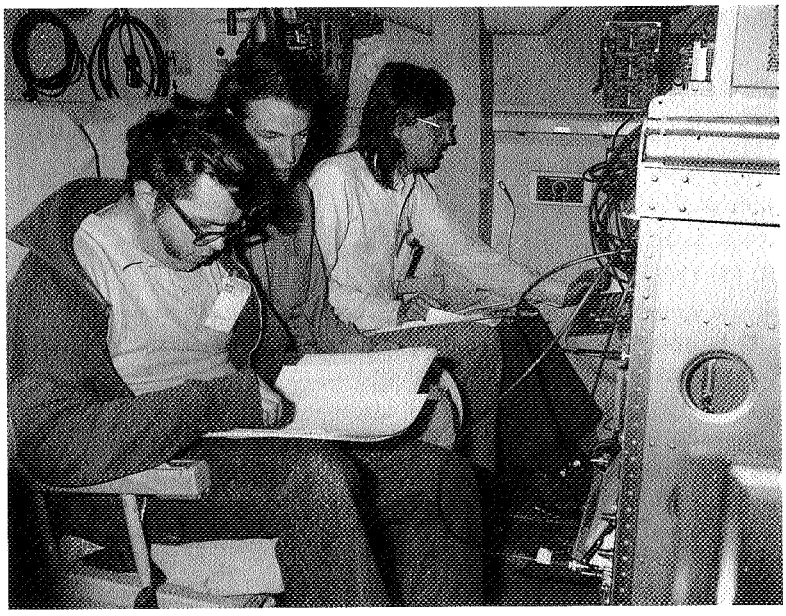

Jim Elliot, Ted Dunham, Doug Mink (1977)

Airborne Astronomy Symposium on the Galactic Ecosystem
ASP Conference Series, Vol. 73, 1995
M.R. Haas, J.A. Davidson, and E.F. Erickson (eds.)

Comets and the KAO

David K. Lynch

The Aerospace Corporation, M2/266, P.O. Box 92957, Los Angeles, CA 90009

Harold P. Larson

Lunar and Planetary Laboratory, University of Arizona, Tucson, AZ 85721

Abstract. Seven comets have been observed from the Kuiper Airborne Observatory (KAO) in its twenty year history. Of these, comets p/Halley (1986 III) and Comet Wilson (1987 VII) produced significant scientific results. Comet Halley was a bright and highly predictable comet that allowed a well-planned and coordinated observing program. Comet Wilson, on the other hand, was a dynamically new comet discovered only a few months before perihelion. In this paper we review the scientific discoveries made by the airborne program and the KAO on these comets, including the discovery of water, new structure in the silicate emission band , and a number of as yet unexplained spectral features.

1. Introduction

Comets are fascinating astronomical objects both because of their spectacular visual appearances and the potential links they offer to studies of the interstellar medium, circumstellar shells, asteroids, the formation of the solar system, and interstellar chemistry. The underlying reason for these connections is that samples of matter originally present in the primordial solar nebula may have been preserved in comet nuclei with little modification over the age of the Solar System. Observations of the gas and dust released from cometary nuclei, when warmed by the Sun, may provide clues to the composition of the comet formation region in the solar nebula and even to preexisting interstellar material. This type of connection was recently illustrated by Knacke et al. (1993), who noted that the thermal IR spectrum of ß Pictoris was very similar to spectra of comets Halley and Levy 1990.

The continuum spectrum of comet dust is observed in reflected sunlight at visible wavelengths and by its thermal emission at IR wavelengths. The neutral volatiles escaping from the nucleus become detectable through their interactions with solar radiation, particularly fluorescence excitation. Much of this diagnostic potential has been developed at ultraviolet and visible wavelengths, thanks to observations

from ground-based facilities and Earth-orbiting satellites and to advances in detector technology. However, progress has been much slower over the nearly three decades of wavelength between 1.0 and 1000 μm. Many comets have been successfully observed in the J, H, K, L, and M photometric windows at ground-based telescopes, but some of the most promising diagnostic regions of the IR spectrum remained inaccessible to astronomers until NASA's airborne astronomy program began in the mid-1960s. The reason is that many parent molecules thought to be present in cometary matter, particularly H_2O, CH_4, and CO, are also present in Earth's atmosphere with sufficient abundances that their absorption lines obscure weak cometary spectral features. Another impediment to using IR observations to study cometary matter was inadequate theoretical understanding of spectral line formation in cometary comae. The net result of these and other limitations to observing comets is that they remain one of the least understood classes of objects in the Solar System.

In Table I we list the eleven comets that have been studied from NASA airborne observatories (the twelfth entry is for comet Shoemaker-Levy, which was indirectly observed when its pieces struck Jupiter in July 1994). Pioneering airborne comet observers include Haughney, Bader and Innes (1967), Kleinman et al. (1971), Blamont and Festou (1974), Harvey (1974) and Roche et al. (1975). Planetary astronomers were ready to conduct still other observations of comets from the KAO (e.g., comet Kohoutek in 1975 and comet Austin in 1990), but their scheduled flights were canceled at the last minute. These efforts cover the entire 3-decade history of airborne astronomy. The entries in Table I demonstrate that the scientific return from these airborne observations was highest for comet Halley. There are a number of reasons for this success. First, this apparition of comet Halley allowed optimized Earth-based observations on either side of perihelion and there was plenty of advance time to plan observing programs. NASA scheduled a total of 22 KAO flights pre- and postperihelion that were divided among 11 investigator teams. The postperihelion flights required a deployment to New Zealand. No other comet listed in Table I received such large amounts of observing time. Second, comet Halley was sufficiently bright during this apparition that many different types of scientific investigations were feasible. Those selected for the Halley program exploited the broad range of focal plane instruments already operational on the KAO. Nine instruments ranging from photometers to high resolution spectrometers were used. Their spectral coverage as a group spanned a factor of 100 in wavelength, thus providing cometary data in regions of the IR spectrum where none previously existed. This complement of IR instruments could not have been assembled at any other telescope, whether ground-based or spaceborne. Third, there was very broad scientific participation in all phases of the airborne observations of comet Halley. Fifty-two authors and coauthors at 18 institutions have produced 33 papers and one Ph.D thesis (Larson 1992). As a result of these factors, published airborne studies of Solar System objects became dominated by comets (see Figure 1) and comet Halley became one of the most frequently observed objects in the history of the airborne program (see Table II).

TABLE I Airborne Observations of Comets

Comet	Year	Facility	Number of Literature Citations*
1. Ikeya-Seki	1965	CV990	1
2. Bennett	1969	LJO	1
3. Tago-Sato-Kosaka	1969	LJO	1
4. Kohoutek	1975	CV990	5
5. Chernykh	1977	KAO	0
6. Kohler	1977	KAO	0
7. Bradfield	1980	KAO	0
8. IRAS-Araki-Alcock	1983	KAO	0
9. Halley	1985-1986	KAO	33
		LJO	1
10. Wilson	1987	KAO	3
11. Brorsen-Metcalf	1989	KAO	0
12. Shoemaker-Levy	1994	KAO	--

TABLE II Most Frequently Observed Objects in the NASA Airborne Astronomy Program

Object	Number of Publications*
1. Orion Nebula	115
2. Galactic Center	61
3. Jupiter	38
4. Sun	33
5. Comet P/Halley	33
6. M17	29
7. W51	26
8. W3	26
9. NGC 7027	24
10. Saturn	22
11. Venus	19
12. NGC 1068	19
13. M82	19
14. Uranus	15
15. Mars	14
16. NGC 2024	13

* Current as of 1990 (Larson 1992)

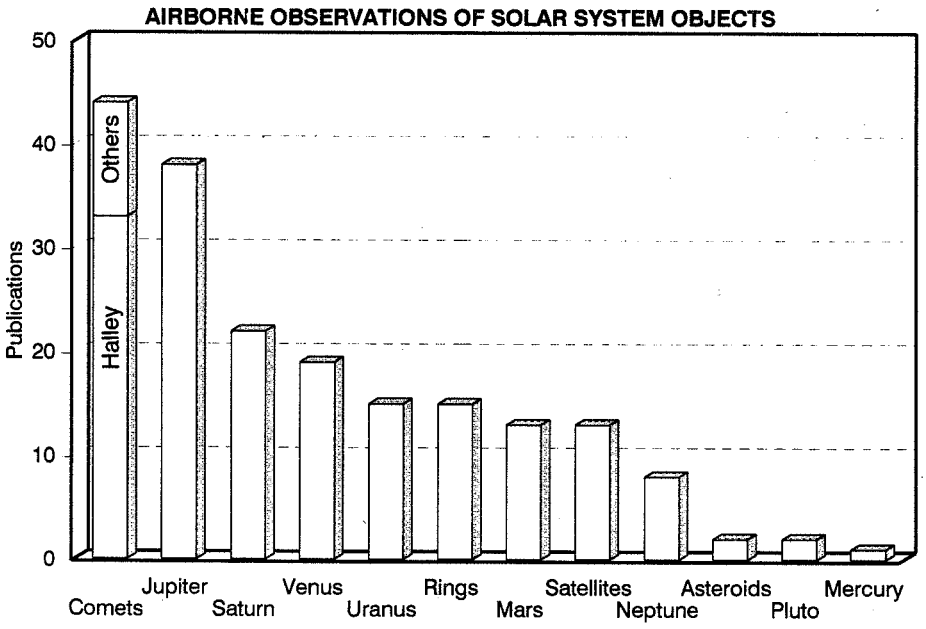

Figure 1. Published studies of Solar System objects observed from NASA's airborne telescopes between 1967-1990. Figure adapted from Larson (1992).

Even as the Halley data were still being reduced, a bright, new comet (Wilson) unexpectedly appeared on Aug 4, 1986. This event provided a perfect chance to compare the IR properties of Halley, a periodic or "old" comet, to those of a dynamically "new" comet making its first passage through the Solar System. The KAO schedule was reorganized to give two experiment teams (Larson/Mumma and Lynch/Russell/Witteborn) two flights each to observe comet Wilson as a target-of-opportunity. These groups used the same instruments that had just been used to observe Halley, thus ensuring that results obtained for these complementary types of comets could be objectively compared. Another deployment to New Zealand was required, but by now the KAO staff made these complex preparations look almost routine. As these plans were being made, another unexpected event occurred: on February 24, 1987, supernova 1987A was discovered in the Large Magellanic Cloud. It quickly brightened to about 4th magnitude, making it the brightest supernova in nearly 400 years. NASA quickly responded to this rare event by adding four flights to the comet Wilson expedition to observe SN1987A. Thus, what started out as a relatively simple southern hemisphere deployment for cometary science turned into a major operation driven by two non-recurring astronomical phenomena being in the sky at the same time. Southern hemisphere deployments subsequently became an annual part of the airborne program. It is probably fair to say that the expeditions originally approved for comets Halley and Wilson paved the way for this significant extension in program emphasis and capability.

In this paper we review NASA's airborne observations of comets with special emphasis on the KAO's contributions to cometary science. As a preview of what is to follow, Table III lists the IR features discovered from the KAO in the spectra of comets Halley and Wilson.

TABLE III - Spectral Features in Comets Discovered by the KAO

Feature	Reference	Identification
Halley		
2.65 μm lines	Mumma et al. 1986a	First detection of H_2O in a comet - ν_3 lines
6.8 μm feature	Bregman et al. 1987	carbonates or C-H
8 - 13 μm feature	Bregman et al. 1987	silicate emission
23.8 μm feature	Herter et al. 1987	
26.7 μm feature	Herter et al. 1987	
28.4 μm feature	Herter et al. 1987	
20-65 μm black body	Glaccum et al. 1987	
119 μm lines	Stacey et al. 1987	OH
FIR non-black body	Campins et al. 1987	submicron particles
Wilson		
2.65 μm ν_3 H_2O lines	Larson et al. 1989	Second detection of H_2O in a comet - ν_3 lines
8-13 μm feature	Lynch et al. 1989	silicate emission
12.2 μm feature	Lynch et al. 1989	ethane?

2. Dust (nonvolatiles)

Most of the "dirt" in Whipple's "dirty snowball" model of comets (Whipple 1950) is nonvolatile grains of dust that presumably were part of the solar nebula during the formation of the solar system. Since the dust consists of heavy elements, it must have originally come from novae or supernovae and then undergone some sort of evolution. It might have leisurely orbited the center of the galaxy in cold dark space under a heavy rain of cosmic rays or spent its days nestled in a giant molecular cloud, where it was shielded from cosmic rays, but experienced significant surface chemistry owing to the high gas densities. This dust was what we would today call interstellar dust. Yet there are some clear spectroscopic differences between interstellar dust and dust seen in comets. These differences may be due to their

isolation inside comet nuclei or to their physical history prior to becoming part of the solar nebula.

Detecting dust in the thermal infrared does not require high spectral resolution because solid-phase emission features generally lack narrow spectral features and thus broader bands may be used. Observers are aided by not facing competition with identical molecules in the atmosphere as are those people trying to measure, for example, water vapor. One difficulty in studying solid phase minerals in space is that their spectral signatures can vary significantly with precise elemental composition, temperature, crystallinity and particle size. Thus identification based on spectral structure alone can be misleading. Another problem is that their signatures span most of the infrared spectrum between 1 and 1000 microns, a range that is mostly unavailable from the ground. With the KAO, however, the latter problem is largely solved.

2.1 Thermal IR spectra of comets Halley and Wilson

Figure 2 shows the spectrum of comet Halley measured by Herter, Campins and Gull (1987) between 0.5 and 30 μm. Figures 3 and 4 from Glaccum et al. (1987) and Campins et al. (1987), respectively, extend the coverage to 160 μm. These spectra show that the gross spectrum of comet Halley, as with all comets, was dominated by emission characteristic of solid grains emitting like black or gray bodies (Campins et al. 1987: Glaccum et al. 1987). Slight departures from a true black body shape are indicative of particles whose emissivity Q_{abs} is wavelength dependent and usually suggests that the particles are small, one micron or less (Campins et al. 1987).

Embedded in this Planck-like emission were a number of features that were time-variable and specific to each comet. These features emitted a small fraction of the energy of the underlying grey body continuum but contained information about dust composition and particle size. Figure 5 shows the spectrum between 5 and 13 μm taken by Bregman et al. (1987). It clearly shows a significant departure from black body emission in the form of a structured silicate emission feature with two peaks, one at 9.2 μm and the other near 11.2 μm. Bregman et al.'s spectrum shows one of the few and certainly the best example of structure that can be used to identify the crystalline mineral species in an astronomical environment. The now characteristic "double peak" shape was first identified as being from small olivine particles (Bregman et al. 1987; Campins and Ryan 1989, Hanner, Lynch and Russell 1994). The feature is also remarkably similar to the one observed in the circumstellar disk of ß Pictoris (Knacke et al. 1993). Also shown in Figure 5 is a weak emission feature near 6.8 μm which might be due to the asymmetric stretch of the carbonate molecule CO_3 or the C-H deformation (bending) mode.

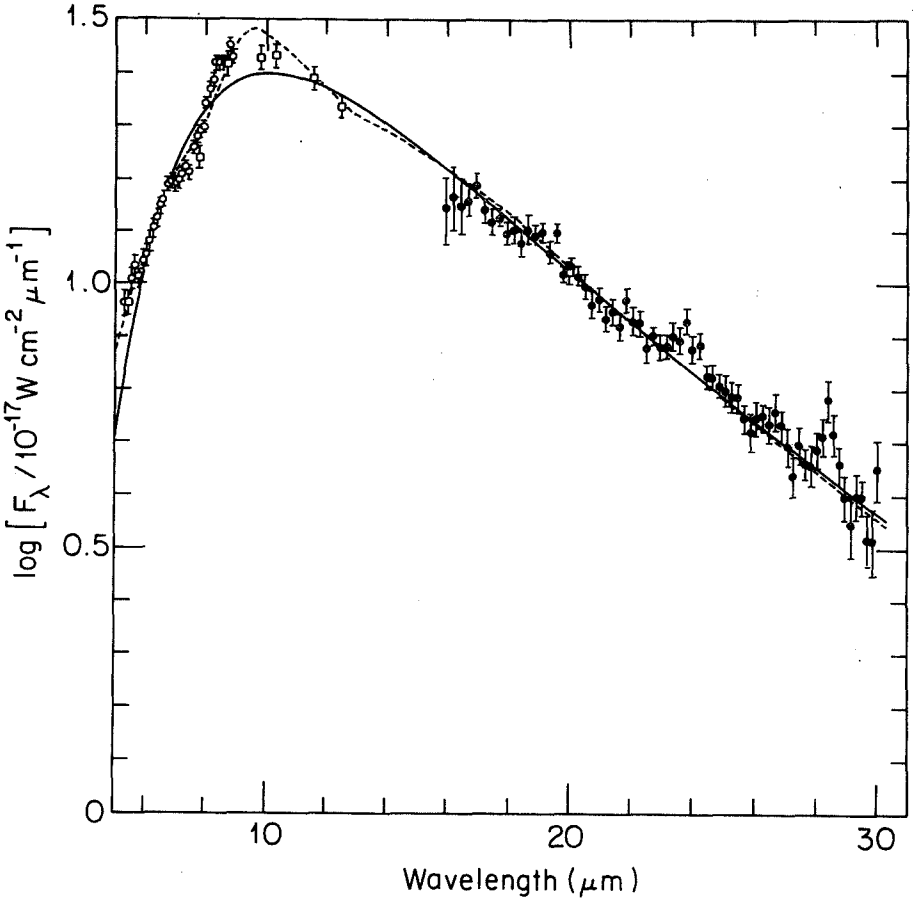

Figure 2. Composite spectrum of Comet Halley from Herter, Campins and Gull (1987). The sold line is Planck function and the dashed line is a silicate model fitt. Note that the majority of the thermal emission is Planck-like.

Comet Wilson's spectrum is shown in Figure 7 (Lynch et al. 1989). It shows a broad, almost structureless silicate emission as well as a definite emission peak at 12.2 μm. The 12.2 μm feature was present on both flights separated by two days. The combination of a smooth silicate feature with a peak at 12.2 μm is not matched by any known silicate complex. This suggests that the two features have separate origins.

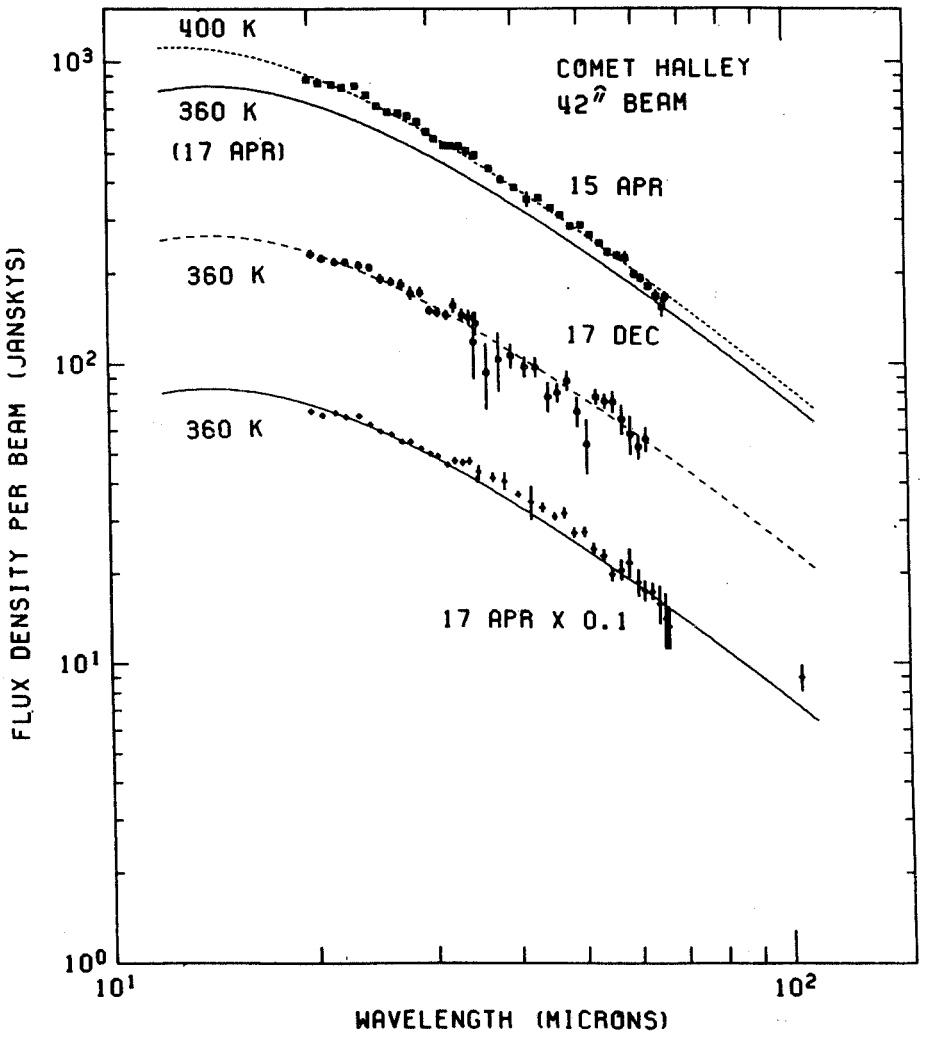

Figure 3. Spectra of comet Halley by Glaccum et al. (1987)

The only thermal IR spectral features that occur in comets with any regularity are the so-called silicate emission features near 10 and 20 μm (Hanner, Lynch and Russell 1994). The feature near 10 μm was first observed in comets by Maas et al. (1970) who identified it in Bennett 1970 II as being due to the fundamental asymmetric stretch vibration of the Si - O - Si silicate structure. The 20 μm feature, first seen in comet Kohoutek 1973 XII by Ney (1974a, 1974b), is due to O - Si - O deformation (bending) mode. The optical properties of silicates have been well-studied in the laboratory and as a result it is known that the imaginary part of the index of refraction k is of order unity (highly absorbing) in the depths of the silicate band. This leads to the conclusion that when the silicate feature is present, the

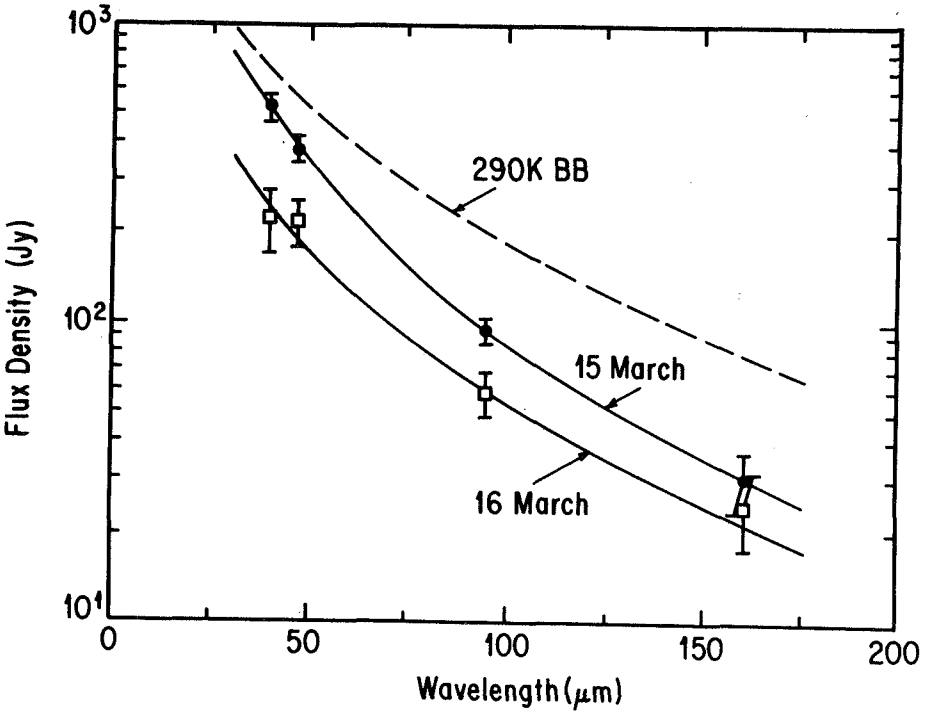

Figure 4. Far IR photometry of comet Halley by Campins et al. (1987)

particles are, on average, small enough that Q_{abs} varies significantly with wavelength. In the past, such structure was associated with particles that were near 1 μm in radius, but detailed calculations show that in some cases structure can persist even when the particles are significantly larger than 1 μm (See Figure 8 below). This is especially true when the particles are fluffy or fractal-like.

The features from comet Halley at 6.8, 23.8, 26.7 and 28.4 μm (Figure 6) are probably due to lattice emission by solids. Certainly silicates are the best candidates. It is interesting to note, however, that several of the most common terrestrial carbonates having strong bands at 6.8 μm (asymmetric stretch vibration) also have significant structure near 28 μm (libration). These include dolomite $CaMg(CO_3)_2$, magnesite $MgCO_3$ and siderite $FeCO_3$. Impurities and chemical substitutions in the lattice can make the features much more complex, as can a combination of several compounds (e.g. $MgCO_3$ and $FeCO_3$ together in a single grain).

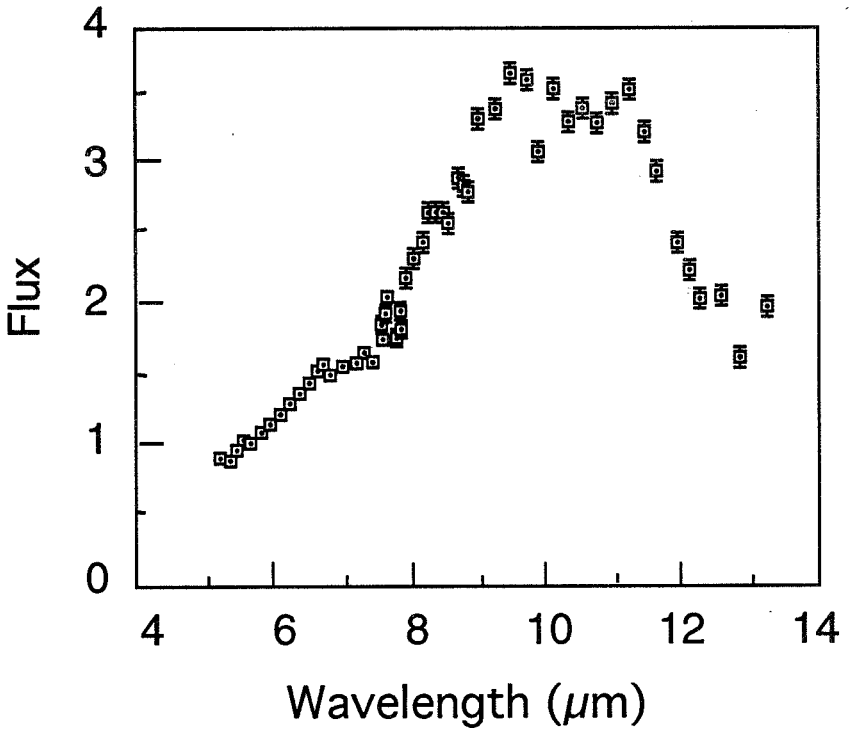

Figure 5. Spectrum of comet Halley (after Bregman et al. 1987) showing the structured silicate emission feature indicative of crystalline olivine. Also note the weak emission feature at 6.8 μm. Flux units are 10^{-16} W cm^{-2} μm^{-1}

In addition to spectral shape, brightness and changes in brightness were observed in both comets Halley and Wilson by many observers. Comet Halley showed dramatic outbursts, often increasing in brightness by a factor of 2 or more on time scales ranging from hours to days. Such changes were reported at all wavelengths and apertures, including the large apertures used by Russell et al. (1986) on the Learjet, where a mass estimate for an outburst was derived.

2.2 Thermal Emission from Dust

The IR spectra of comets originate as thermal-like emission from dust expelled from their surface. The total emission from a single dust grain is given by

$$E_\lambda = B_\lambda(T)\, Q_{abs}(\lambda)\, 4\pi\, a^2, \quad (1)$$

where $B_\lambda(T)$ is the Planck function, $Q_{abs}(\lambda)$ is the absorption efficiency ("emissivity") and $4\pi\ a^2$ is the area of the grain. This simple expression contains many complex notions. Dust grains do not have a single size (a), shape (spherical as "$4\pi\ a^2$" implies), or composition (Q_{abs}). Furthermore, the temperature T is dependent on size (a), composition (Q_{abs}), the spectrum of the incident radiation field, and, for the large particles, how they are rotating. Finally, and perhaps most importantly for the discussion that follows, Q_{abs} is a function of wavelength for small particles. For large particles, Q_{abs} is nearly constant with wavelength and, therefore, the emission is Planckian.

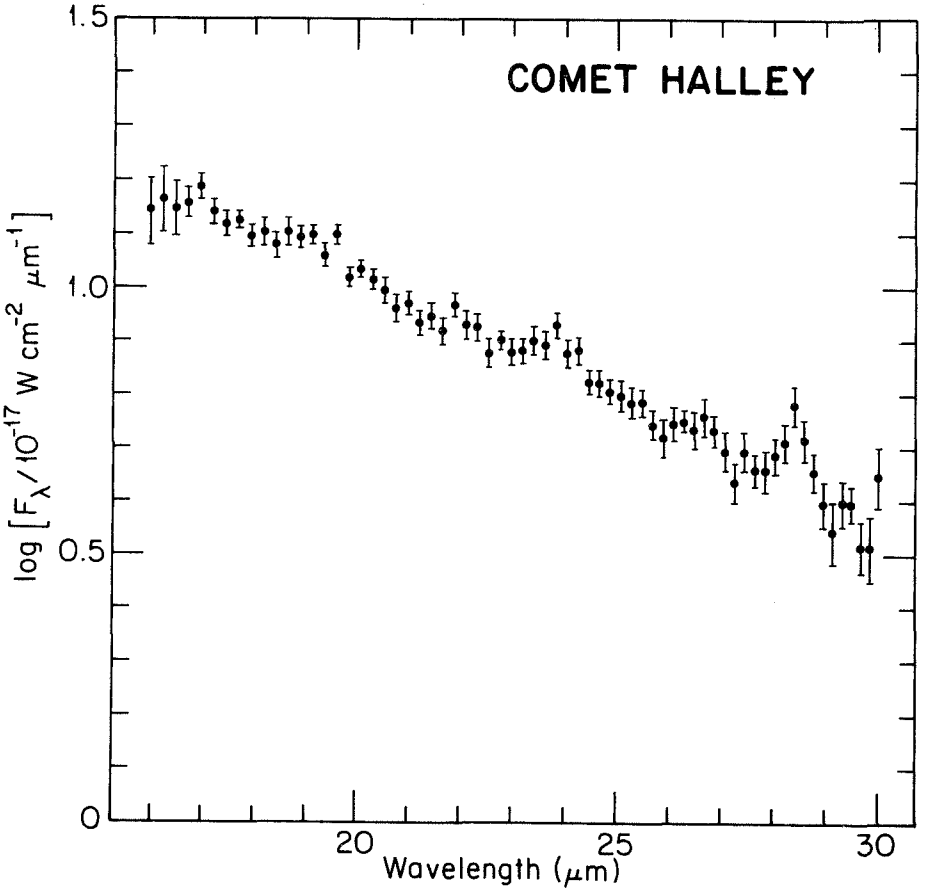

Figure 6 shows the spectrum of comet Halley by Herter, Campins and Gull between 15 and 30 μm. Three features are evident at 23.8 μm, 26.7 μm and 28.4 μm. At the present time these features are unidentified although, as we will discuss shortly, they may very well be due to silicates, perhaps even olivine.

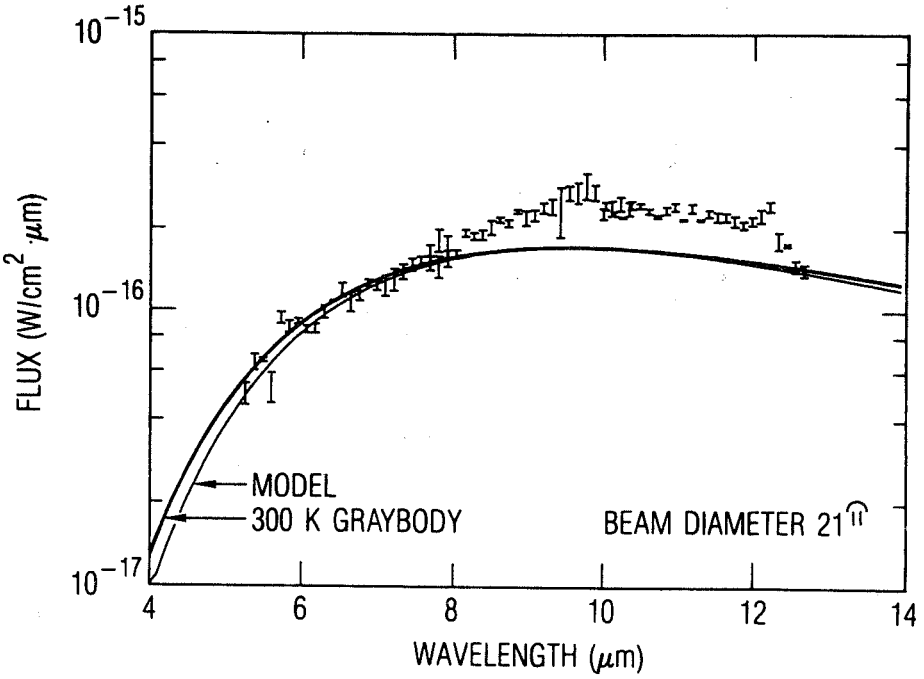

Figure 7. Spectrum of Comet Wilson from Lynch et al. (1989). Note the smooth silicate emission feature and the narrow feature at 12.2 μm.

Q_{abs} is strongly influenced by k, the imaginary part of the index of refraction. In the thermal IR, k is determined by the amount of absorption of three processes, all vibrational: (1) vibration and stretches of atoms relative to each other, (2) vibration of atoms relative to molecules, (3) lattice vibrations. These are classified as stretching, bending and libration modes. Additionally, the shape of the particle has a significant effect on Q_{abs}.

Figure 8 shows the thermal emission spectrum $E_\lambda / 4\pi\ a^2 = B_\lambda(T)\, Q_{abs}$ for glassy silicate particle parameterized by size. Q_{abs} was calculated from spherical particle codes ("Mie theory") using complex indices of refraction. Note that when the particle radius exceeds 20-30 μm, its spectral features are weak. Depending on the type of silicate, no spectral features other than a black body spectrum may be present.

It is important to understand that the wavelengths of the spectral peaks vary with particle size, as do the relative strengths of the peaks !

A cloud of particles will radiate in a complicated manner determined by its absorption and scattering characteristics. The spectrum emitted by an optically thin cloud of optically thick particles will appear like a dilute black body, while that from an optically thin cloud of optically thin particles will show spectral structure.

Comet dust fills only a fraction of the field and, in this sense, the comae of all comets are optically thin. This is shown by their emission optical depths, i.e. the ratio of their brightness to the brightness of a black body at the same temperature observed through the same aperture. For example, comet Wilson's 10 μm emission optical depth was about 5×10^{-13}. But this is not to say that the individual grains are optically thin because, as noted above, a very sparse cloud consisting of large silicate particles will emit like a dilute black body. This occurs when Q_{abs} is very nearly constant with wavelength.

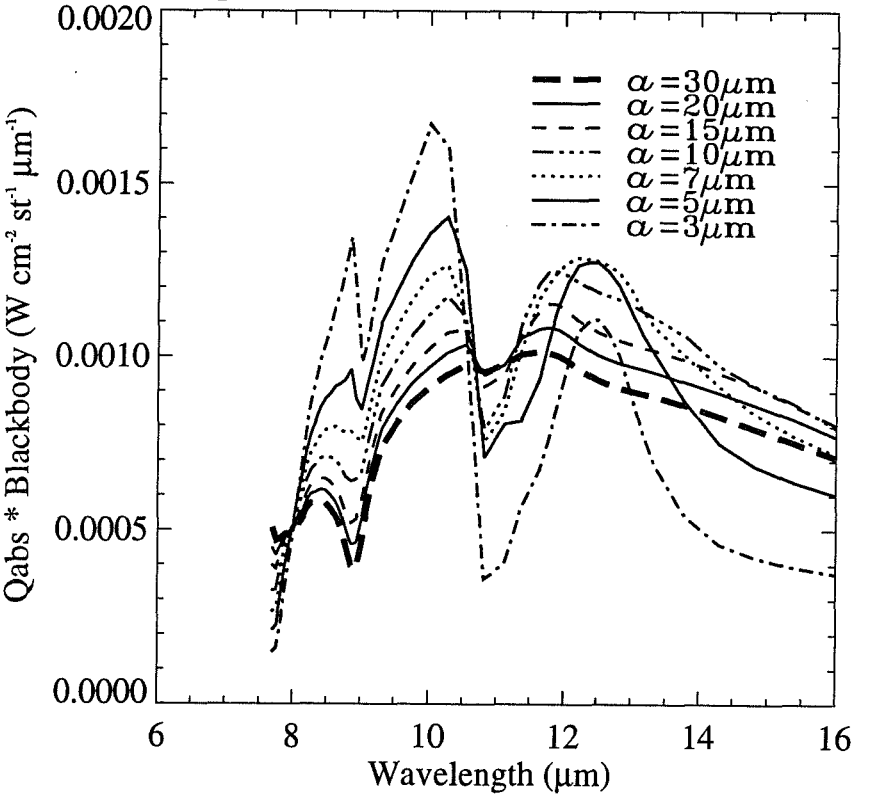

Figure 8. Emission spectrum $B_\lambda(T)\, Q_{abs}(\lambda)$ vs λ of a glassy silicate sample based on spherical particle calculations. As the particle becomes larger, the spectral structure decreases in contrast and the spectrum approaches that of a black body. Note that even relatively large particles can show significant spectral structure and that the wavelengths of the peaks vary with particle size.

The very existence of discrete spectral features in both Halley and Wilson tells us a good deal about the grains straight away. The particles must be optically thin at the wavelength of the feature (or at least not optically thick), otherwise no such feature could be present. Although an exact size cannot be deduced, we can be certain that the presence of spectral structure rules out a preponderance of large particles in the distribution. For siliceous material this means few if any particles larger than 50 - 100 μm.

The small particles deduced from the spectra of comet Halley explain another commonly observed phenomenon in comets: their IR color temperatures are almost always higher than their black body radiative equilibrium temperatures. This happens because small, dark comet particles are reasonably efficient absorbers of the abundant visible solar radiation. Energy balance leads to a grain temperature of t about $T = 278/R^{1/2}$, where R is the distance from the sun in A.U. For R = 1 A.U. the temperature is 278 K, and a black body at this temperature would reach a peak emittance at 10.4 μm. At this wavelength, however, the small grains do not emit efficiently. To balance their emission in the IR with their absorption in the visible, they heat up to temperatures higher than the black body equilibrium temperature. For a fixed composition, the smaller the grain, the hotter it is.

The degree of crystallinity is marked by the sharpness of spectral features. Purely crystalline materials, especially silicates, have many features about 0.1 μm wide in the infrared. A partially disordered crystal, i.e. one with some, but not all bonds, broken or distorted, displays features that are smoother and weaker. A completely amorphous substance should have little or no spectral structure. A smooth silicate feature like the one produced by comet Wilson suggests that the particles were largely amorphous, except for the Si-O-Si bond which is present, but smoothed and broadened by the reduction of atomic order.

The exact character of the spectral structure is indicative of the chemical composition and to some extent the thermal history of the crystalline grains (Ferraro 1982; Salisbury et al. 1991). The two peaks displayed by Halley (9.6 and 11.0 μm) are so similar to those produced by olivine (both from bulk terrestrial samples and from interplanetary dust particles) that a significant fraction of the dust is almost certainly due to small olivine or olivine-like particles (Bregman et al. 1987; Campins and Ryan 1989).

As a class of minerals, silicates have certain spectral signatures that are well understood (Hunt 1978; 1981). Between about 6.5 μm and 8.0 μm they emit very poorly as a result of the Christiansen effect, resulting from a region of high transmission. From 8.5 μm to about 11.0 μm, there is usually a region of strong emission due to the O-Si-O symmetric stretch. Features between 12 - 15 μm are normally only seen in more complex silicates and they indicate vibrational modes between the (Si,Al) - O - (Si,Al) structure. Only feldspars show structure between 15 and 20 μm. Between 20 and 40 μm most of the structure is due to various lattice vibrations and the symmetric Si-O-Si stretch.

Regarding olivine and certain other minerals, it is important to realize that they are a mixture of several distinct minerals. "Olivine" is not a unique chemical compositional, but rather a solid solution of at least two distinct minerals, in this case forsterite (Mg_2SiO_4), fayalite (Fe_2SiO_4) and possibly more. When found together in any composition ratio this mixture is termed "olivine".

In summary, remotely probing the dust in comets has benefitted greatly from KAO work, primarily because of the broad wavelength coverage and the ability to observe in regions inaccessible from the ground. At the same time, we face a number of difficult problems in determining the properties of dust grains. This is because identification is a sequential process that can be interrupted at almost any point. A grey body spectrum tells us virtually nothing about the grains, the presence of an elevated temperature notwithstanding. A structured spectrum indicates that the dust particles are not optically thick and possess some degree of crystallinity. Limits to the size of the particles can only be estimated, and then, only when we are reasonably certain of the composition. The determination of composition, of course, requires spectral structure. Matching comet spectra with laboratory spectra is difficult because crystallinity, particle size and composition all influence spectral shape. Particle shape, filling factor (solid vs porous) and orientation are beyond the ability of present observational techniques.

3. Gas (Volatiles)

Knowledge of the parent molecular composition of cometary nuclei is central to theories of their origin and evolution, but prior to Halley's last apparition there was very little hard evidence concerning the bulk composition of comets. The volatile fraction was thought to be dominated by H_2O with up to several dozen trace constituents at or below the few percent abundance level relative to H_2O. High resolution spectroscopy is required to detect these species and measure their elemental and isotopic abundance ratios, but some species do not fluoresce strongly at visible and ultraviolet wavelengths (e.g., H_2O, NH_3, CH_4, etc), and others lack electric dipole transitions at radio wavelengths (e.g., CH_4). Experimenters contemplating parent molecule searches might not be sure what transitions to observe or even what part of the electromagnetic spectrum would optimize chances for detection. When such insight did exist, the relevant spectral region was likely to be inaccessible to ground-based observations or instrumental sensitivities were inadequate. To compound matters further, most parent molecules are photochemically destroyed soon after release into the coma. Many decomposition products have been detected via remote observations, but most cannot be assigned uniquely to precursor parent molecules. Thus, at the time of Halley's last apparition in 1985, only two candidate parent molecules had been detected (CO and S_2), and even these could have had secondary origins. As for H_2O being the dominant volatile constituent of cometary matter, the detections of H, O, OH, and H_2O^+ provided compelling circumstantial evidence for it, but direct evidence for neutral H_2O in either its solid or gas phase did not exist. Water ice absorption features near 3 μm had been reported in several comets, but the detections were marginal and the interpretations controversial. Rotational lines of H_2O vapor were reported at radio wavelengths in two comets, but the excitation mechanism could not be identified and these transitions were not observed in radio

spectra of other comets. As a consequence of this long, frustrating history to clarify the role of H_2O in comets, the search for neutral gaseous H_2O became a primary objective for many of the ground-based, airborne, and spaceborne experiments planned for comet Halley. The first definitive detection was achieved in NASA's airborne astronomy program.

3.1 Detection of H_2O in Comets

The first direct detection of neutral gaseous H_2O in any comet was made during preperihelion observations of comet Halley from the KAO on 22 December 1985 (Mumma et al. 1986a) using the University of Arizona Fourier transform spectrometer (FTS) (Davis et al. 1980). Participants in this flight were the first to see the spectral evidence for H_2O when multiple emission lines in the 2.7-μm region appeared on the computer terminal during real-time processing of the first Halley interferogram. Photographs of the averaged spectrum produced later during this flight are contained in Figure 9. Even in this crude format, these data demonstrated beyond all doubt that H_2O was present in the coma of comet Halley. This was not a serendipitous discovery. It depended on a special combination of resources assembled for this specific observation: (1) the KAO, because the 2.7-μm region is totally obscured by terrestrial H_2O in ground-based observations, (2) the Arizona FTS, because of its high resolving power, broad spectral bandwidth, and large field-of-view, and (3) recently developed non-LTE excitation models (Weaver and Mumma 1984, Crovisier 1984) that were used to predict the IR spectra of candidate parent molecules and to select optimized strategies for their observation. The calculations indicated that the IR spectral region had high potential for detecting parent molecules through solar-pumped fluorescence, but even the most abundant volatiles could probably be detected only in their fundamental vibration-rotation bands which usually occur at wavelengths >2.5 μm. In the ν_3 band of H_2O near 2.7 μm, for example, the models predicted that Halley's spectrum should be dominated by only five emission lines under conditions of fluorescence equilibrium (i.e., no collisions). One fortuitous consequence of this non-LTE condition is that the intensities of these few transitions would be greatly enhanced, thus increasing the sensitivity for detection. Based on these predictions, the Arizona FTS was provided with an interference filter covering just the limited spectra bandwidth (<0.1 μm) containing these predicted lines near 2.7 μm to optimize the signal-to-noise ratio for detecting H_2O in comet Halley. The rapid emergence of a few, very intense cometary H_2O lines in the first real-time spectrum immediately validated the model and confirmed the presence of H_2O in cometary matter. This initial success was soon followed by high resolution near-IR airborne observations of H_2O in comet Halley postperihelion (Weaver et al. 1986) and comet Wilson (Larson et al. 1989) (see Figure 10).

Gulkis et al. (1989) attempted to detect H_2O in comet Halley in a sub-millimeter rotational transition (4_{14}-3_{21}) at 380.2 GHz. Measurements of the rotational level populations in the coma would complement the near-IR results, which were sensitive to vibrational level populations. Their model calculations predicted a limited number of intense rotational lines, but not that at 380.2 GHz. Their observed upper limit to H_2O was consistent with these predictions, but they still might have made a positive detection if observing circumtances had been better.

THE FIRST SPECTRUM OF H_2O IN COMET HALLEY

KAO, 22 December 1985

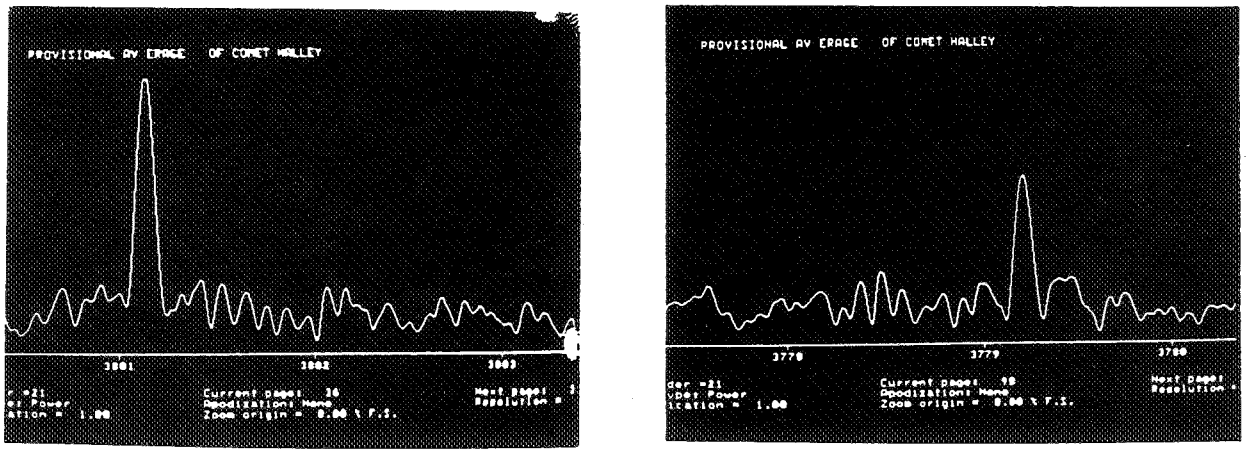

Ortho-H_2O (2_{02}-1_{01}) Para-H_2O (1_{01}-0_{00})

Figure 9. In-flight discovery photographs of H_2O in comet Halley. These sections of the first provisional average of Halley's airborne spectrum show two of the nine widely spaced emission lines that were present in this spectrum (see Mumma et al. 1986a for the final average)

C-5.

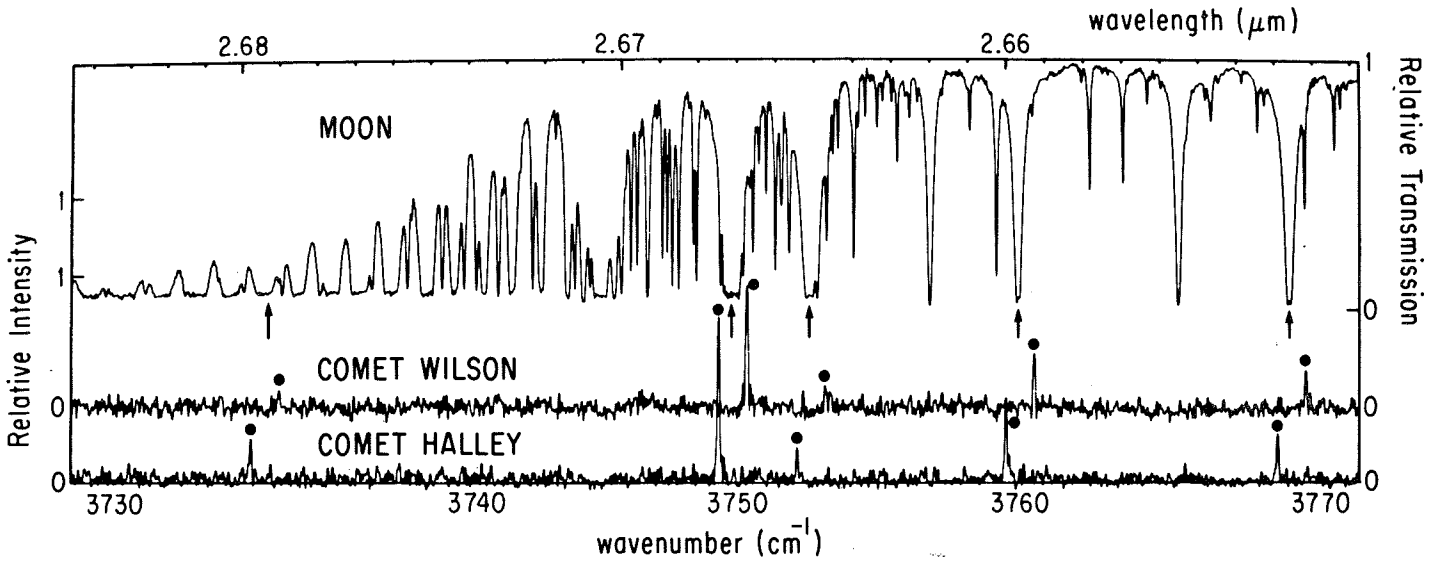

Figure 10A. Airborne IR spectra of H_2O in comets Halley (postperihelion) and Wilson: 3730 - 3770 cm^{-1}. Solid symbols mark cometary H_2O lines. Arrows in the lunar comparison spectrum identify the corresponding transitions in absorption in Earth's atmosphere. The cometary and telluric spectra of H_2O are so different that it is not obvious that they are even due to the same molecule. The lunar spectrum exhibits many H_2O absorption lines from levels with J as high as 8 (J ≡ total angular momentum quantum number), consistent with an H_2O rotational distribution in LTE maintained by collisions at an effective excitation temperature of ≈ 220 K. The small number of cometary H_2O lines indicates relaxed H_2O rotational level populations pumped by solar IR fluorescence. No cometary H_2O transition arises from levels higher than J = 2; all of the strongest observed lines originate from levels with J = 0 or 1. The wide separation of cometary H_2O lines is due to their large geocentric velocities (-47.4 km s^{-1} for Wilson, +35.1 km s^{-1} for Halley). Figure from Larson et al. (1989).

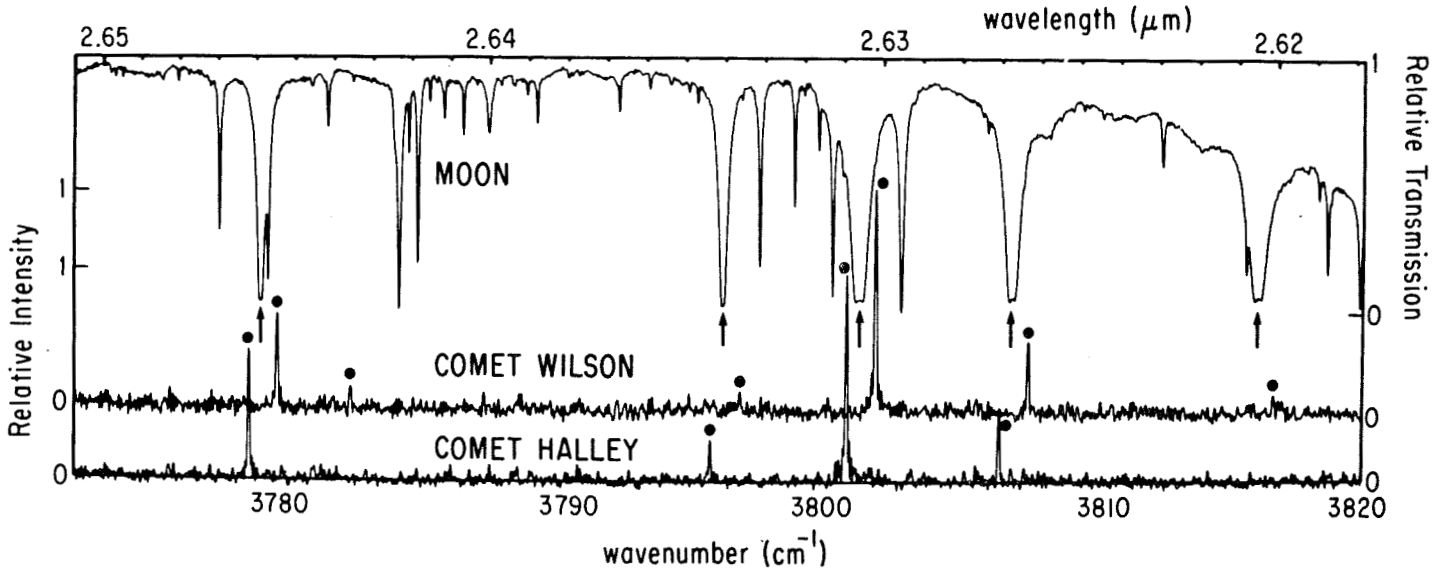

Figure 10B. Airborne IR spectra of H_2O in comets Halley (postperihelion) and Wilson: 3785 - 3820 cm^{-1}. Figure from Larson et al. (1989).

3.2 Using H_2O to Probe the Coma

The resolving power achieved in the airborne spectra in Figure 10 ($\lambda/\Delta\lambda$ up to 3 x 10^5) is much higher than that required just to identify the H_2O molecule. Values as low as $\lambda/\Delta\lambda \approx 10^3$ would have sufficed (see Figure 3 in Larson et al. 1986) to separate most H_2O transitions, and a strong signature of H_2O remained even when all lines were superimposed at $\lambda/\Delta\lambda \approx 40$ in the Vega IKS spectrum (Combes et al. 1986). However, the high information content of the KAO spectra made them suitable for numerous other types of analyses. In the sections below we review how these remote observations of H_2O molecules were used to reveal physical conditions in the coma.

3.3 Excitation Conditions in the Coma

The small number of cometary H_2O emission lines in Figure 10, compared with the larger number of telluric H_2O absorption lines in the same spectral interval, demonstrated that the H_2O rotational level populations were relaxed. The implied "cold" rotational distribution is characteristic of fluorescence excitation pumped by solar IR radiation. For pure fluorescence equilibrium only the lines at 3732, 3780, and 3801 cm^{-1} in Figure 10 should have appeared with measurable intensities. The presence of additional, relatively weak lines is probably due to optical depth effects and collisions in the coma, but the departure from fluorescence equilibrium is not severe because only the lowest rotational levels were populated by these processes. These additional lines were actually very useful for establishing a more realistic physical description of the relative roles of collisional and radiative processes in the coma. Bockelée-Morvan (1987) successfully fit a comprehensive excitation model the postperihelion KAO spectrum of comet Halley in Figure 10 (Bockelée-Morvan and Crovisier 1987). This model included uniform radial outflow, collisions, radiative trapping, and IR fluorescence. Weaver et al. (1987) used low resolution spatial maps of H_2O emission to deduce the state of H_2O excitation in different regions of the coma (see Figure 11). The observed strong sunward-tailward brightness asymmetry indicated that H_2O sublimation was most active on the sunlit side of the nucleus, but there was some H_2O outflow in the tailward direction, apparently due to the thermal inertia of cometary matter. The H_2O scale length was 3.2×10^4 km, consistent with that expected for a parent molecule, and the H_2O lifetime was $\approx 3 \times 10^4$ sec for a nominal outflow velocity of 1 km s^{-1}. The H_2O spectrum was rotationally relaxed to a greater degree in spectra off the nucleus, as evidenced by the persistence of the few fluorescence equilibrium transitions, such as the ortho-H_2O line at 3802 cm^{-1} in Figure 11. This behavior is consistent with the transition to pure fluorescence equilibrium in the less dense regions of the outer coma.

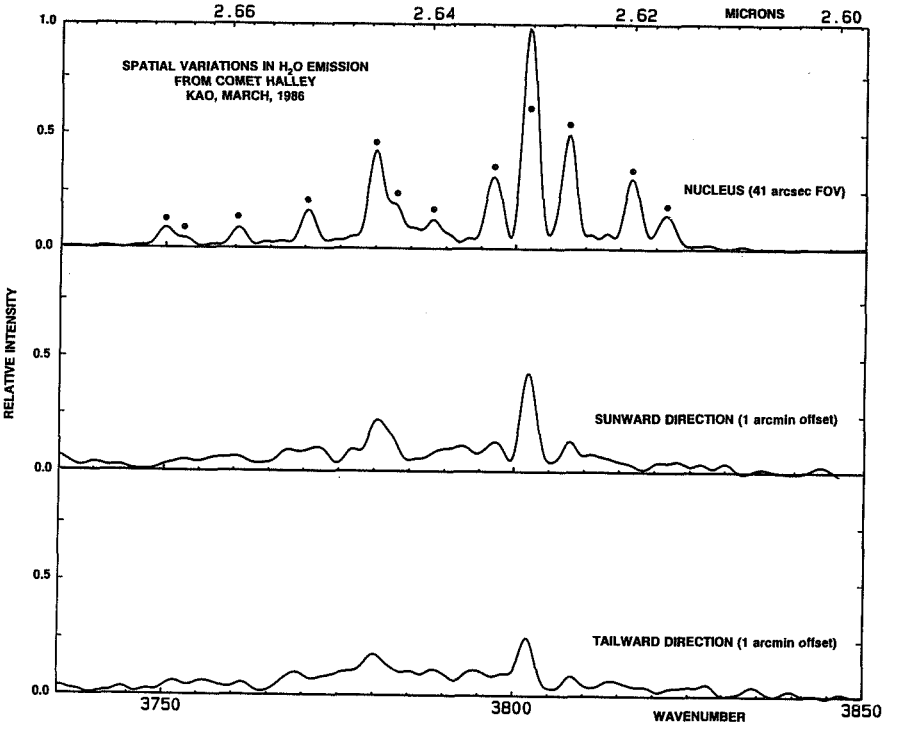

Figure 11. Comparison of moderate resolution ($\lambda/\Delta\ \lambda = 1300$) airborne spectra of comet Halley (postperihelion) at locations on and off the nucleus. The angular field-of-view (41" diameter) corresponds to 2×10^4 km at the comet. Most H_2O lines become relatively weaker in the offset spectra, compared to the persistent fluorescent equilibrium line at 3802 cm^{-1}, as collisional excitation becomes increasingly unimportant in the less dense regions of the coma.

3.4 Water Production Rates

The absolute H_2O line intensities in the KAO spectra of comets Halley and Wilson led to the first direct measurements of the water production rate Q, which is probably the best quantitative measure of mass loss from the nucleus. Representative values of Q derived from the KAO spectra are included in Table IV. The water production rates for comet Halley exhibited temporal variations as large as a factor of $\approx$3 in 48 hrs (Weaver et al. 1987). This activity was probably due to variable solar stimulation of the discrete areas that controlled the outflow from Halley's evolved surface. The

most rapid change observed occurred on UT 20 March 1986, when the comet's H_2O signal increased by a factor of ≈2 in 30 min. Larson et al. (1990) attributed this explosive event to some process in the nucleus, such as crystallization of amorphous ice, that dispersed $\approx 1.0 \times 10^{-3}$ km^3 of nuclear material into the coma as icy grains. The sudden exposure of this ejected material to solar photons caused the dramatic increase in H_2O production.

TABLE IV Water Production Rates, Q

Comet	Date (UT)	Q (10^{29} s^{-1})	R (AU)	Δ (AU)
Halley (preperihelion)	24 Dec 1985	0.2	1.13	1.00
Halley (postperihelion)	22 Mar 1986	1.0	1.00	0.75
Wilson (preperihelion)	15 Apr 1987	0.3	1.2	0.89

R - heliocentric distance, Δ - geocentric distance

Weaver et al. (1987) noted significant pre- and postperihelion asymmetry in Halley's water production rates. On average, postperihelion values of Q were about 8 times larger than preperihelion values for similar heliocentric distances R. This asymmetry was not observed in values of Q deduced from ultraviolet observations of OH, possibly because observations of OH were less sensitive to temporal variations in the gas outflow than were direct observations of H_2O. The water production rates observed in comet Wilson were reasonably constant which implied steady release of gas from a homogeneous surface (Larson et al. 1989).

3.5 Kinematic Processes in the Coma

The analyses described above depended upon the very high resolution of the KAO spectra of H_2O. The resolved widths of the H_2O line profiles were influenced by the radial outflow velocity, and the absolute line positions indicated the net outflow of H_2O molecules either toward or away from Earth after corrections for geocentric and topocentric velocity components. Hu et al. (1991) developed a coma outflow model to predict the positions and shapes of remotely observed spectral lines for realistic spatial distributions and velocity fields of the neutral gas in comets. Larson et al. (1991) applied this model to the airborne spectra of H_2O in comets Halley and Wilson. Some of their results are illustrated in Figure 12. Their first step was to prepare an averaged, deconvolved H_2O line profile for each observed spectrum; panel A in Figure 12 contains the velocity-resolved H_2O line profile (dashed curve)

extracted from the preperihelion spectrum of comet Halley. The outflow model was then used to calculate a synthetic line profile (solid curve in panel A) to fit the shape and position of the observed profile. The best fit was achieved by adjusting velocity and temperature distributions with hydrodynamic formulae and by constructing various types of anisotropic outflow patterns. Non-spectroscopic displays of parameters used in the best fit are included in Figure 12. The three-dimensional outflow distribution used to calculate the best-fit synthetic line profile was converted in panel B into a two-dimensional column density map to create a "spectroscopic" image of the outflow. The velocity distributions used in the best-fit calculations are plotted in Panel C; for comet Halley preperihelion, the curve was an unmodified hydrodynamic calculation. Finally, the H_2O density profile along a hypothetical spacecraft trajectory is illustrated in panel D for the best-fit profile to comet Halley postperihelion. The purpose of this display was to study the effects of anisotropic outflow on *in situ* measurements. These results demonstrated the extent to which detailed kinematic properties of the coma could be extracted from remote spectroscopic observations of a parent molecule.

3.6 Temperature of the Nuclear Ice

The KAO spectra in Figure 10 contain both ortho-H_2O and para-H_2O lines. Transitions between these configurations are strictly forbidden in radiative and collisional processes. The ortho/para ratio (OPR) is temperature dependent because the ground state levels in the two modifications of H_2O are different. Once H_2O is released into the coma, its OPR is invariant. Mumma et al. (1986a, 1987) explored the interesting possibility that the observed H_2O OPR and its associated nuclear spin temperature T_N gives the physical temperature of the nuclear ice in the sublimation zone. In effect, the IR spectrum of cometary H_2O becomes a remote spectroscopic thermometer of the physical temperature of cometary nuclei. Their revised OPR's for comet Halley pre- and post-perihelion were 2.3 ± 0.1 and 2.2 ± 0.1, respectively, which imply that $T_N \approx 25$ K (Mumma et al. 1988). Their OPR for comet Wilson was 3.2 ± 0.2 which is consistent with statistical equilibrium ($T_N > 50$ K). The results for both comets are consistent with interstellar origins, but their differences may reflect evolutionary factors. One possible interpretation is that Wilson's equilibrium value applies to its radiation-damaged outer layer, where the OPR would have been reset, while Halley's values represent its bulk composition because this outermost layer was lost long ago.

4. Far IR Detection of OH

Stacey et al. (1987) observed the far-IR rotational transitions $^2\Pi_{3/2}$ ($J = 5/2 \rightarrow 3/2$) in OH in comet Halley using a high resolution ($\lambda/\Delta\lambda = 3 \times 10^4$) Fabry-Perot spectrometer on the KAO. They detected the ($+ \rightarrow -$ parity) line at 119.44 μm and established an upper limit to the ($- \rightarrow +$ parity) line at 119.23 μm (Figure 13). They used the observed line flux ratios to demonstrate that radiative pumping, rather than collisional relaxation or photochemical pumping, determined the rotational level populations associated with the far-IR transitions.

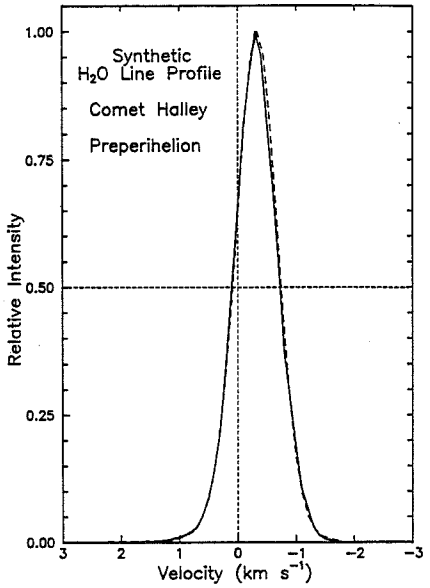

A. Velocity-resolved H_2O Line Profiles

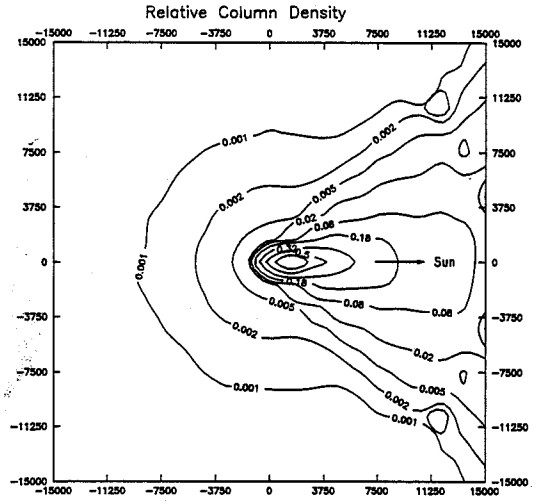

B. Retrieved 2-D H_2O Density Map

Figure 12 (parts A & B) Use of H_2O spectra to deduce kinematic properties of the coma. Panel A: observed (dashed line) and synthetic (solid line) H_2O line profiles for comet Halley preperihelion. The following panels contain non-spectroscopic representations of the best fit line profile in Panel A. Panel B: two-dimensional column density map of H_2O around comet Halley preperihelion.

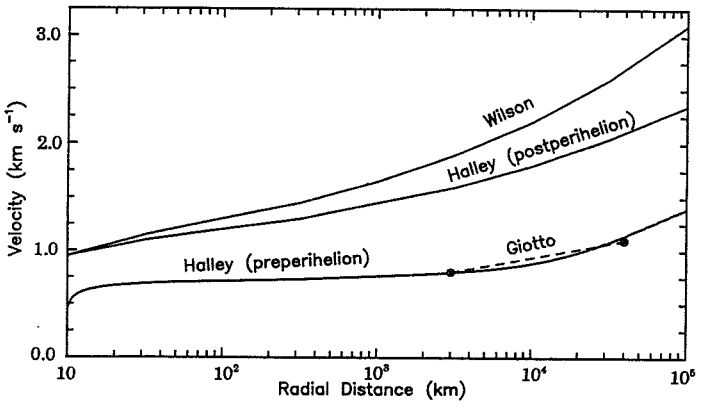

C. Retrieved H_2O Velocity Distributions

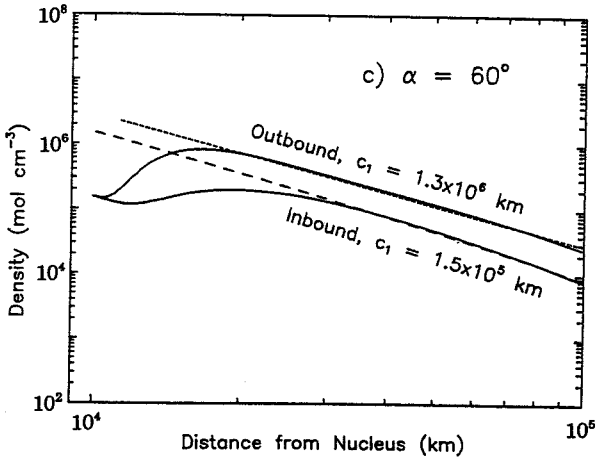

D. Retrieved H_2O Density Profiles

Figure 12 (Parts C & D) Use of H_2O spectra to deduce kinematic properties of the coma. Panel C: velocity distributions fit to the observed H_2O line profiles in comets Halley and Wilson. Panel D: calculated H_2O density profile along a hypothetical spacecraft trajectory through the coma of comet Halley postperihelion. Figure adapted from Larson et al. (1991).

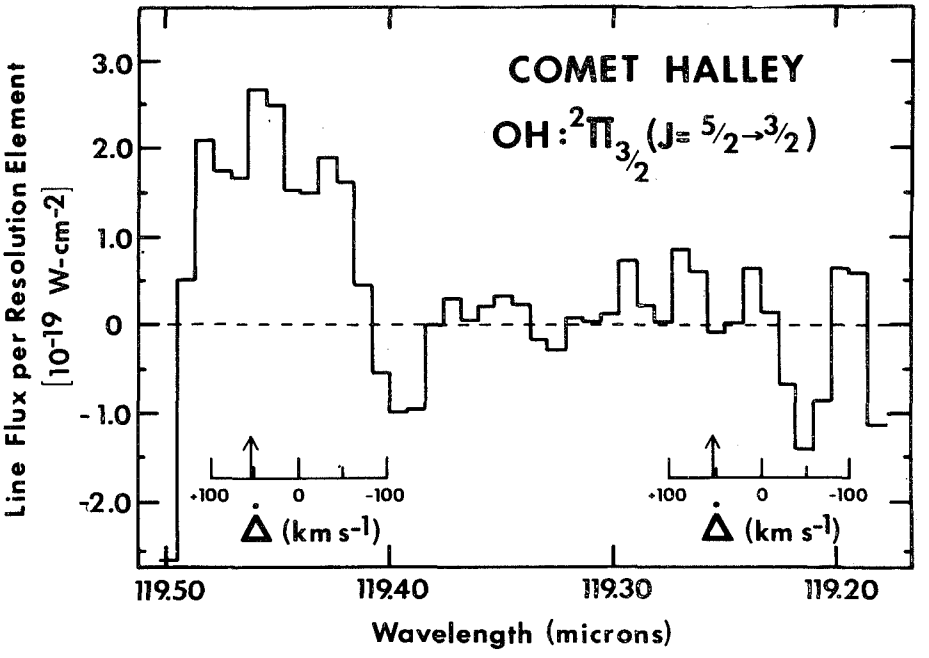

Figure 13. Spectrum of OH in comet Halley (Stacey et al. 1987) showing the rotational transition $^2\Pi_{3/2}$ (J = 5/2 → 3/2) at 119.44 μm.

5. Search for CH_4

Methane is expected to be the dominant carbon-bearing species in cometary matter. The first airborne search for cometary CH_4 was in comet Kohoutek from the CV990 by Roche et al. (1975), who used a tilting-filter spectrometer with $\lambda/\Delta\lambda = 9 \times 10^3$ to scan the positions of four P-lines in the ν_3 band of CH_4 at 3.3 μm. They did not detect any cometary signal, which implied an upper limit of $CH_4/H_2O < 5$ in comet Kohoutek. Drapatz et al. (1986, 1987) and Larson et al. (1989) searched high resolution KAO spectra ($\lambda/\Delta\lambda \approx 3.3 \times 10^4$) of comets Halley and Wilson for low-J R-lines of the ν_3 band of CH_4. No CH_4 signature was found in the Halley spectra, but their upper limit to the CH_4/H_2O abundance in comet Halley was 0.04, more than an order of magnitude more sensitive than the previous effort with Kohoutek. Larson et al. (1989) may have detected CH_4 lines at the 3σ confidence level in the spectrum of comet Wilson (see Figure 14). Their estimated CH_4 abundance was in the range $0.014 \leq CH_4 / H_2O \leq 0.045$, where the uncertainty was due primarily to the assumed effective excitation temperature of CH_4. These observed limits to CH_4 in comets Halley and Wilson are generally low compared to the predictions of equilibrium condensation models of the solar nebula ($CH_4/H_2O > 0.1$). If the clathrate hydrate compositional model is relevant to these comets, the IR measurements imply that guest molecules released into the coma are not predominantly CH_4.

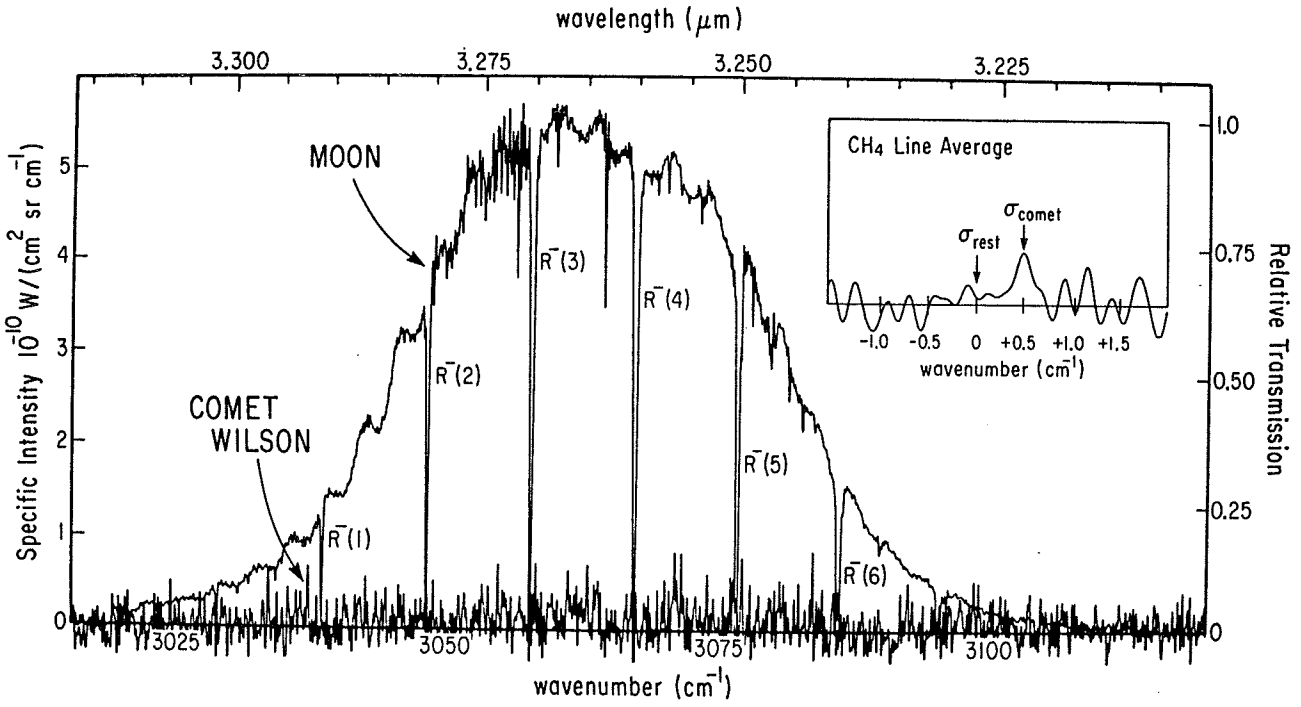

Figure 14. Possible detection of CH_4 in comet Wilson. The lunar spectrum defines atmospheric and instrumental transmission factors. The dominant absorptions are due to telluric CH_4. No individual cometary CH_4 emission line appeared above the noise. However, a marginal CH_4 signature appeared at the correct Doppler-shifted position (see inset) when six sections of the cometary spectrum, each centered on a CH_4 line, were averaged. If real, this feature constitutes a detection of cometary CH_4 with abundance $0.014 \leq CH_4/H_2O \leq 0.045$. Figure from Larson et al. (1989).

6. Ethane in Comets?

Is it possible that ethane (C_2H_6 or CH_3CH_3) was detected in both comet Halley and Wilson, but was not identified? The central wavelength and width of the 12.2 μm feature in comet Wilson's spectra (Lynch et al. 1989) closely match those of the ν_9 band of ethane (Figure 15). Although ethane has not been explicitly identified in a comet before, Crovisier and Encrenaz (1983) view it as a likely parent molecule. Encrenaz and Knacke (1991) also argue that the shape of the 3.4 μm band seen in many comets including comet Wilson (Tokunaga and Brooke 1990) can be plausibly explained by a superposition of several vibrational modes of the CH_3 molecule. Ethane also produces a band at 6.8 μm (Pouchert 1989) and, as noted in Table 2, Bregman et al. (1987) reported a 6.8 μm feature in the spectrum of comet Halley. It could have been due either to the asymmetric stretch vibration mode of the carbonate molecule or the C-H deformation (bending) mode in any number of organic molecules including ethane. In general, a 6.8 μm carbonate feature is wider than a 6.8 μm ethane band.

If ethane was responsible for the two bands, then two questions remain unanswered. (1) Why weren't both of them seen together in both comets? and (2) Why hasn't the 12.2 μm band been seen in other comets since this wavelength is accessible from the ground? We do not know, but we can suggest that the answer to the second question may be that Wilson was an ethane-rich comet resulting in an exceptionally strong ν_9 band. The answer to the first question may involve excitation and emission mechanisms of the ethane molecule that can enhance one band relative to the other.

We suggest that a ground-based search for ethane be carried with high resolution spectrographs in the 12.2 μ m region. This wavelength region is probably better suited than the 3.4 μm region, owing to the multiplicity of C-H related bands near 3.4 μm.

7. Summary and Conclusions

With data from two comets in a single sixteen month period, (Halley and Wilson), the KAO and its observing teams have added immeasurably to cometary science. This happened because airborne observatories offer special advantages for cometary science, including the ability to respond on short notice to targets-of-opportunity and the chance to reconfigure flight instruments quickly for optimized follow up to unexpected results. The direct detection of neutral gaseous H_2O in airborne spectra of comets Halley and Wilson demonstrated beyond any doubt that H_2O ice dominates cometary matter, thus confirming this key feature of the "dirty snowball" compositional model. The airborne spectra also confirmed theoretical predictions that IR fluorescence is the primary excitation mechanism for spectral lines of parent molecules in cometary comae. The possibility of detecting trace volatiles in cometary matter by their fluorescence spectra remains a compelling challenge for remote sensing methods. For CH_4, at least, IR spectroscopic methods were surprisingly competitive with direct sampling techniques (e.g., mass spectrometers on spacecraft).

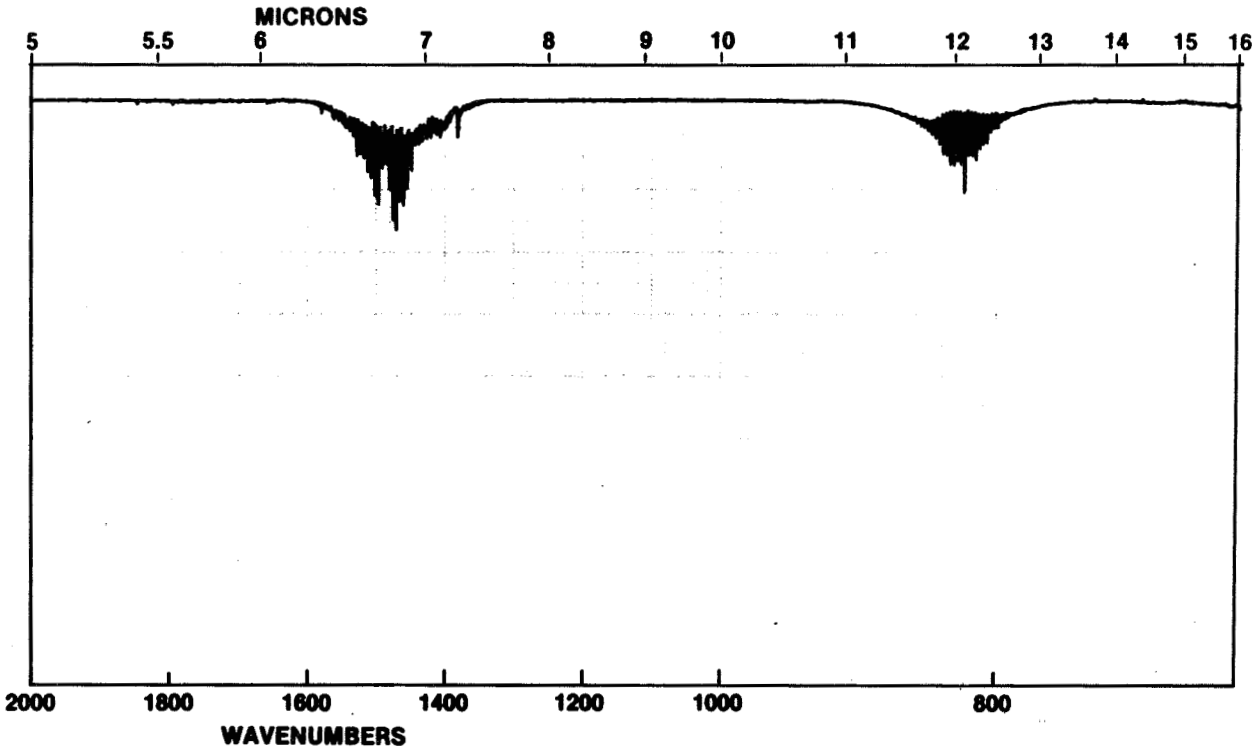

Figure 15. IR transmission spectra of ethane CH_3CH_3 from Pouchert (1989). Note the similarities between the 12.2 μm feature in Comet's Wilson's spectrum (Figure 7) and the 6.8 μm feature in comet Halley's spectrum (Figure 5).

The airborne spectra of H_2O also led to some unexpected insight concerning the nature of H_2O ice in the nucleus, including evidence for the possible role of amorphous ice in H_2O outbursts and the use of the H_2O OPR as a remote thermometer. The distinction between amorphous and crystalline H_2O ice is important because the low condensation temperature of amorphous H_2O ice ($T < 100$ °K) requires formation in an "interstellar" environment, rather than in the planetary region (15-30 AU) of the presolar nebula (cf. Lunine 1988). The H_2O OPR may be a cosmogonic invariant that preserves the temperature at which H_2O condensed on the grains that became incorporated into comets. If Halley's measured nuclear spin temperature (≈25 K, Mumma et al. 1988) is equal to the physical temperature at which H_2O last equilibrated, its H_2O ice condensed in a very low temperature environment, it was amorphous, and it was never reprocessed.

In the realm of nonvolatiles, a number of emission features characteristic of solid-phase, optically thin dust were discovered and most have yet to be identified. One of the features observed in comet Halley was almost certainly due to crystalline olivine. The others may very well be olivine or olivine-like silicates. The 12.2 μm feature may be indicative of ethane.

As a final note, we would like to point out how the KAO "one-upped" the ground based community. One of the requirements for acceptance of a KAO proposal is that the project can only be done from the airplane. This usually means working in a wavelength region inaccessible from the earth. Comet Wilson's silicate emission and 12.2 μ m feature discovered by the KAO are both in the atmospheric window between 8 - 13 μm. These features could have been observed from the ground but they were not. Why? Because no one bothered to look!

Acknowledgments. Over the years the KAO program has supported our research and we would like to thank NASA for its vision in creating the KAO as well as the opportunity to work with the fine people on staff. The airborne astronomy's flexibility in scheduling target-of-opportunity flights is a credit to their commitment to scientific excellence. We would also like to thank Drs. Ray Russell and Humberto Campins for helpful discussion for many years. Allan Meyer provided the KAO logs of comet observations and Ann Mazuk helped in preparing the figures. Preparation of this manuscript was supported by NASA grant NAG2-206 to the University of Arizona. This work was partially supported by the Aerospace sponsored research program.

References

Bockelée-Morvan, D. 1987, A&A, **181**, 169-181.
Bockelée-Morvan, D. & Crovisier, J., 1987, A&A, **187**, 425-430.
Bregman, J., Campins, H., Witteborn, F.C., Wooden, D.H., Rank, D.M., Allamandolla, L.J., Cohen, M. & Tielens, A.G.G.M., 1987, A&A, **187**, 616-620.
Blamont, J.E. & Festou, M. 1974, Icarus, **23**, 538-544.
Campins, H., Joy, M., Harvey, P.M., Lester, D.F. & Ellis, H.B., 1987, A&A, **187**, 632-634.

Campins, H. & Ryan, E. 1989, ApJ, **341**, 1059.
Combes, M., et al. 1986, Nature, **321**, 266-268.
Crovisier, J. & Encrenaz, T. 1983 A&A, **126**, 170-182
Crovisier, J. 1984, A&A, **130**, 361
Davis, D. S., Larson, H.P., Williams, M., Michel, G., & Connes, P., 1980, Appl. Optics, **19**, 4138-4155.
Drapatz, S., Larson, H. P., & Davis, D. S., 1986, In *Proc. 20th ESLAB Symposium on the Exploration of Halley's Comet*, ESA SP-250, 347-352.
Drapatz, S., Larson, H. P., & Davis, D. S., 1987, A&A, **187**, 497-501.
Encrenaz , T. & Knacke, R. 1991 "Carbonaceous Coumpounds in Comets: Infrared Observations", in Comets in the Post-Halley Era, R.L. Newburn, M. Neugebauer and J. Rahe, Eds., Kluwer, Boston, 107-137
Ferraro, F.R. (ed.) 1982. *The Sadtler Infrared Spectra Handbook of Minerals and Clays,* Sadtler Research Laboratores, Philadelphia, PA.
Glaccum, W., Moseley, S.H., Campins, H. & Loewenstein, R.F. 1987, A&A, **187**, 635-638.
Gulkis, S., et al. 1989, A&A, **213**, 465-468.
Hanner, M.S., Lynch, D.K. & Russell, R.W. , 1994, ApJ, **425**, 274-285.
Haughney, L.C., Bader, M. & Innes, R. , 1967, AJ, **72**, 1166-1169.
Harvey, G. 1974, PASP, **86**, 552-553.
Herter, T., Campins, H. & Gull, G.E., 1987 A&A, **187**, 629-631.
Hu, H-Y., Larson, H.P., & Hsieh, K. C. 1991, Icarus, **91**, 238-250.
Hunt, G.R., 1978, in *Remote Sensing in Geology*, Gillespie and Segal, eds..
Hunt, G.R. "Spectroscopic Properties of Rocks and Minerals", in *Handbook of Physical Properties of Rocks*, R.S. Carmichael, ed., CRC Press, Boca Raton (1981).
Knacke, R., Fajardo-Acosta, S., Telesco, C.M., Hackwell, J.A., Lynch, D.K. & Russell, R.W., 1993, ApJ, **418**, 440-450.
Kleinmann, D.E., Lee, T., Low, F.J. & O'Dell, C.R. 1971. Infrared Observations of Comets 1969g and 1969i, ApJ, **165**, 633-636.
Larson, H. P. 1992, PASP, **104**, 146-153.
Larson, H. P., Weaver, H. A. , Mumma, M. J. & Drapatz, S., 1989, ApJ, **338**, 1106-1114.
Larson, H. P., Hu, H.-Y., Mumma, M. J. & Weaver , H. A., 1990, Icarus, **86**, 129-151.
Larson, H. P., Hu, H.-Y., Hsieh, K. C., Weaver, H. A. & Mumma , M. J., 1991, Icarus, **91**, 251-269.
Lunine, J.I. 1989. Abundances of molecular species in Halley's comet: Their role in understanding the chemistry of cometary formation environments. In The Formation and Evolution of Planetary Systems (H.A. Weaver, F. Paresce, & L. Danly, Eds.), Cambridge University Press, pp. 213-242.
Lynch, D. K., Russell, R. W., Campins, H., Witteborn, F. C., Bregman, J. D., Rank, D. M. & Cohen, M. C., 1989, Icarus, **82**, 379-388.
Maas, R.W., Ney, E.P. & Wolff, N.F. 1970, ApJ, **160**, L101-L104.
Mumma, M. J., Weaver, H. A., Larson, H. P., Davis, D.S. , & Williams, M., 1986a, Science, **232**, 1523-1528.
Mumma, M. J., Weaver, H. A., Larson, H. P., 1986b. The ortho/para ratio of water vapor in comet Halley. In *Proc. 20th ESLAB Symposium on the Exploration of Halley's Comet*, ESA SP-250, 341-346.
Mumma, M. J., Weaver, H. A., Larson, H. P., 1987, A&A, **187**, 419-424.

Mumma, M. J., Blass, W. E, Weaver, H.A. & Larson, H. P., 1988. *Bull Amer. Astron. Soc.* **20**, 826.
Ney, E.P. 1974a, ApJ(L), **189**, L141-L144.
Ney, E.P. 1974b, Icarus, **23**, 551-560.
Pouchert, C.J. 1989 *The Aldritch Library of FT-IR Spectra, Vol. 3*, Aldritch Chemical Company, Milwaukee, 1.
Roche, A. E., Cosmovici, C. B., Drapatz, S., Michel, K. W. & Fields, W. C. 1975, Icarus, **24**, 120-127.
Russell, R. W., Lynch, D. K., Rudy, R. J., Rossano, G. S. , Hackwell, J. A. & H. C. Campins, C., 1986. Multiple Aperture Airborne Infrared Measurements of Comet Halley, *Proceedings of the 20th ESLAB Symposium on the Exploration of Halley's Comet,* European Space Agency, SP-250, **Vol. II**, 125-128, October
Salisbury, J.W., Walter, L.S., Vergo, N. & D'Aria, D.M. 1991. *Infrared (2.1 - 25 μm) Spectra of Minerals*, The Johns Hopkins University Press, Baltimore.
Stacey, G.J., Lugten, J.B. & Genzel, R., 1987, A&A, **187**, 451-454.
Weaver, H. A. & Mumma, M. J., 1984, ApJ, **276**, 782-796.
Weaver, H. A., Mumma, M. J., Larson, H. P. & Davis, D. S. 1986, Nature , **34**, 441-444.
Weaver, H. A., Mumma, M. J. & Larson, H. P. 1987, A&A, **187**, 411-418.
Whipple, F. 1950. ApJ, **111** , 375.

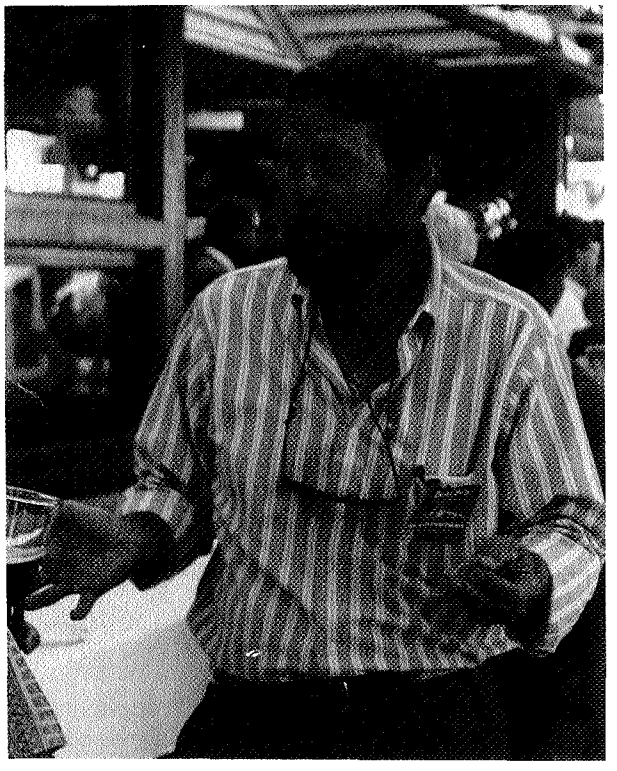

Dave Lynch

Airborne Astronomy Symposium on the Galactic Ecosystem
ASP Conference Series, Vol. 73, 1995
M.R. Haas, J.A. Davidson, and E.F. Erickson (eds.)

Submillimeter Solar Research with the KAO

E. E. Becklin
University of California, Los Angeles, CA 90024

C. Lindsey
National Solar Observatory, P. O. Box 26732, Tucson, AZ 85726-6732

Abstract. From 1981 to 1988 the KAO was used to measure the 30 to 670 μm continuum radiation from the Sun. The most significant result was the measurement of the limb brightness and extent during two total solar eclipses. The results clearly indicate a solar limb at 50 to 670 μm which is extended beyond that expected for an atmosphere in hydrostatic equilibrium. Unique measurements of far infrared solar oscillations and the brightness of active regions were also carried out. A complete set of references is included.

During the 1980s an extensive program of solar research was conducted on the Kuiper Airborne Observatory in the far infrared and submillimeter spectrum extending from approximately 30 μm out to nearly 1 mm. The program included two total eclipse observations over the Pacific that provided the first sub-arcsecond determinations of the extreme solar limb profile (Lindsey *et al.* 1983, Lindsey *et al.* 1986, Roellig *et al.* 1991). It also included sensitive LTE measurements of chromospheric temperature variations caused by compressional motion excited by solar p-modes, *i.e.*, the well-known five-minute oscillations. Submillimeter diagnostics are especially applicable to modeling of the solar medium, particularly the chromosphere in the region of the reversal of the temperature gradient, caused by mechanical heating of the chromospheric medium.

High-resolution limb brightness profiles provided by the KAO eclipse observations show a clear indication of sharp departures of the chromosphere from hydrostatic equilibrium simultaneous with the onset of strong chromospheric heating, very probably due to a connection between the physical processes responsible for both heating and acceleration of the media that form spicules, fibrils and other chromospheric inhomogeneities (see Figure 1; Hermans & Lindsey 1986; Braun & Lindsey 1987; Clark 1994; Jefferies 1994). Techniques developed for the KAO eclipse observations served as a model for later occultation observations made from the James Clark Maxwell Telescope and the Caltech Submillimeter Observatory during the total solar eclipse of 1991 July 11 over Mauna Kea (Lindsey *et al.* 1992), as well as for infrared occultation observations

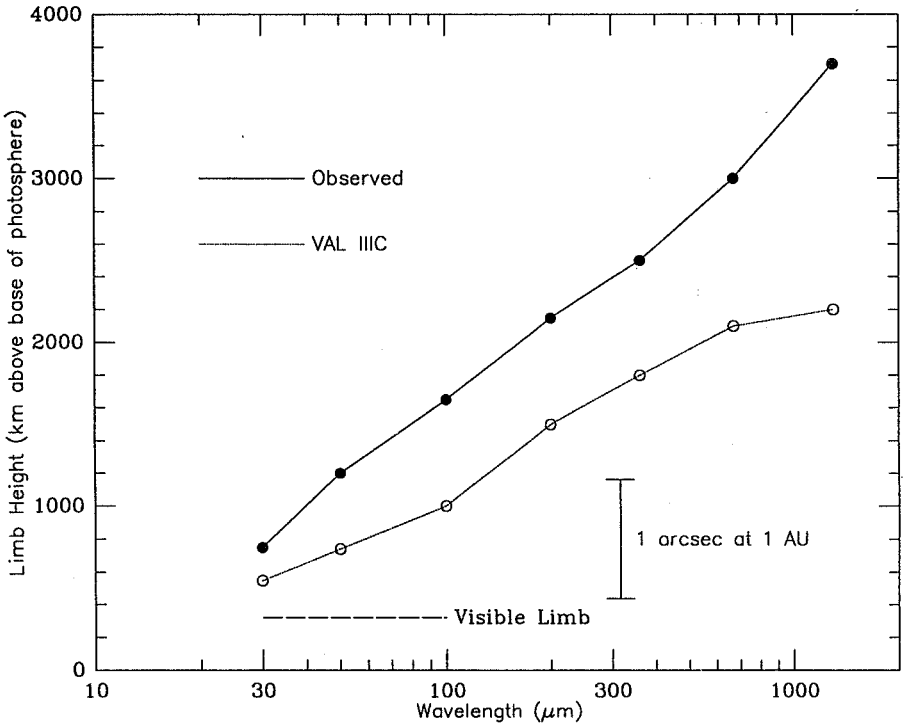

Figure 1. Limb heights determined by lunar occultation during a total solar eclipse are plotted (ordinate) against wavelength (abscissa). Solid points refer to observations; open circles refer to limb profile computations for Model C of Vernazza, Avrett & Loeser (1981). The horizontal dashed line at a height of 320 km indicates the height of the visible solar limb, used to reference the submillimeter observations. Observations from 30 to 200 μm were made from the KAO over the Pacific north-east of Japan in the total solar eclipse of 1981 July 31. Observations at 360 and 670 μm were made from the KAO over the Pacific north of Guam in the total solar eclipse of 1988 March 18. The observation at 1300 μm (1.3 mm) was made from the JCMT on Mauna Kea in the total solar eclipse of 1991 July 11.

of CO lines made from the McMath-Pierce Solar Telescope on Kitt Peak in the nearly-annular eclipse of 1994 May 11. The sub-arcsecond profiles of the sub-millimeter limb obtained by the KAO, the JCMT and the CSO are now making possible detailed statistical models of the chromosphere that specifically take account of fine-structure inhomogeneities. Other center-to-limb measurements were made from the KAO besides the eclipse experiments. These are described in Lindsey *et al.* (1984).

Careful observations of local chromospheric temperature variations made from the KAO simultaneously with ground-based Doppler observations from the Mees Solar Observatory in Hawaii and the Wilcox Solar Observatory at

Stanford clearly showed the thermal response of the chromosphere to five minute oscillations (Lindsey *et al.* 1990; Kopp 1990; Kopp *et al.* 1992). These observations provided the first clear, LTE indication that thermal relaxation of the low chromospheric medium was fast, with rates greater than 1 minute^{-1}. This rate rapidly decreases with height in the chromosphere. Earlier estimates of chromospheric relaxation rates, based on continuum emission, were more than an order of magnitude slower than those shown by the KAO observations.

In summary, submillimeter observations have given us a broad and powerful tool for diagnosing the solar atmosphere, and the KAO has played a clear pioneering role in making this research practical in the late 20th century.

Publications of KAO Solar Observations

Kopp, G., Lindsey, C., Roellig, T. L., Werner, M. W., Becklin, E. E., Orrall, F. Q., & Jefferies, J. T. 1992, ApJ, 388, 203

Kopp, G. 1990, "Chromospheric Dynamics Based on Infrared Solar Brightness Variations," PhD Thesis, Stanford University

Lindsey, C., Becklin, E. E., Jefferies, J. T., Orrall, F. Q., Werner, M. W., & Gatley, I. 1983, ApJ, 264, L25

Lindsey, C., Becklin, E. E., Jefferies, J. T., Orrall, F. Q., Werner, M. W., & Gatley, I. 1984, ApJ, 281, 862

Lindsey, C., Becklin, E. E., Jefferies, J. T., Orrall, F. Q., Werner, M. W., & Gatley, I. 1986, ApJ, 308, 448

Lindsey, C., Kopp, G., Becklin, E. E., Roellig, T., Werner, M. W., Jefferies, J. T., Orrall, F. Q., Braun, D., & Mickey, D. L. 1990, ApJ, 350, 475

Roellig, T. L., Becklin, E. E., Jefferies, J. T., Kopp, G. A., Lindsey, C., Orrall, F. Q., & Werner, M. W. 1991, ApJ, 381, 288

Related References

Braun, D., & Lindsey, C. 1987, ApJ, 320, 898

Clark, T. A. 1994, *Infrared Solar Physics, Proc. IAU Symp. 154*, eds. D. M. Rabin, J. T. Jefferies & C. Lindsey (Kluwer: Dordrecht), p 139

Hermans, L., & Lindsey, C. 1986, ApJ, 310, 907

Jefferies, J. T. 1994, *Infrared Solar Physics, Proc. IAU Symp. 154*, eds. D. M. Rabin, J. T. Jefferies & C. Lindsey (Kluwer: Dordrecht), p 1

Lindsey, C., Jefferies, J. T., Clark, T. A., Harrison, R. A., Carter, M., Watt, G., Becklin, E. E., Roellig, T. L., Braun, D. C., Naylor, D. A. & Tompkins, G. J. 1992, Nature, 358, 308

Vernazza, J. E., Avrett, E. H., & Loeser, R. 1981, ApJS, 45, 635

Eric Becklin, Mike Werner, Ian Gatley, Gerry Neugebauer (1976)

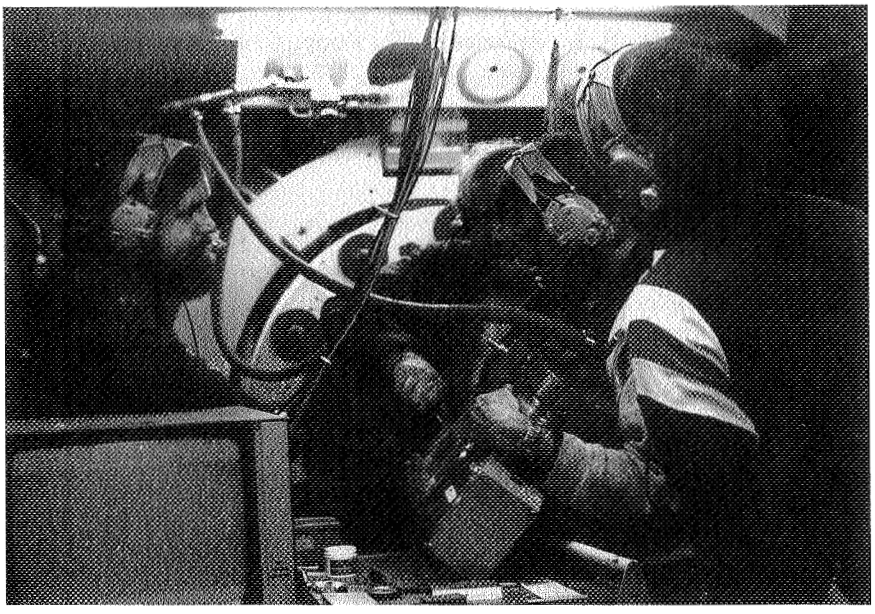

Ian Gatley, Eric Becklin, Gerry Neugebauer, and Gordon Forrester (1976)

Airborne Astronomy Symposium on the Galactic Ecosystem
ASP Conference Series, Vol. 73, 1995
M.R. Haas, J.A. Davidson, and E.F. Erickson (eds.)

On the Size of Particles Near the Nucleus of 2060 Chiron

C. B. Olkin

Department of Earth, Atmospheric, and Planetary Sciences, Massachusetts Institute of Technology, 77 Massachusetts Avenue, Cambridge, MA 02139 and Lowell Obs., 1400 West Mars Hill Road, Flagstaff, AZ 86001

J. L. Elliot

Department of Earth, Atmospheric, and Planetary Sciences and Department of Physics, Massachusetts Institute of Technology, 77 Massachusetts Avenue, Cambridge, MA 02139 and Lowell Obs., 1400 West Mars Hill Road, Flagstaff, AZ 86001

E. W. Dunham

Space Science Division, NASA Ames Research Center, Mail Stop 245-6, Moffett Field, CA 94035-1000

C. H. Ford

SETI Inst., 2035 Landings Drive, Mountain View, CA 94043

D. K. Gilmore, D. M. Rank, P. Temi

University of California, Lick Obs., Santa Cruz, CA 95064

Abstract. Simultaneous dual-wavelength observations by the KAO of a recent Chiron occultation provide a measure of the relative extinction efficiencies of particles near Chiron. This observation and Mie scattering theory allow us to constrain the size of grains causing the extinction of the starlight near Chiron.

1. Introduction

After it was given its asteroidal designation, 2060 Chiron exhibited cometary activity in the form of CN emission (Bus et al. 1991) and a coma (Luu & Jewitt 1990; Meech & Belton 1990; West 1991). Photometric outbursts have been seen far from the Sun–nearly up to its aphelion distance of 18.9 AU (Bus et al. 1989). However, the mechanism driving these outbursts is unknown. The particles investigated here may be a direct result of an outburst, since they have been tentatively identified as composing a jet emanating from Chiron's nucleus (Elliot et al. 1994).

Various methods have been used to determine particle-size distributions around comets and planets, including spacecraft measurements and ground-based observations. *In situ* techniques used by the Giotto and Vega spacecraft at Halley include penetration sensing, piezoelectric momentum sensing, capacitor discharge sensing and dielectric film depolarization (McDonnell, Lamy, & Pankiewicz

1991). Other *in situ* techniques include occultations of a spacecraft's radio signals, which has been used by Voyager to determine the particle size distribution of Saturn's and Uranus' rings (Marouf et al. 1983; Esposito et al. 1991). Remote observations typically involve observing the interaction of radiation with matter, such as spectra of the 10μm silicate feature which is sensitive to grain size (Hanner et al. 1987), and photometry to identify Rayleigh scattering (Luu & Jewitt 1990).

In this paper, we shall investigate the particle sizes near Chiron using the transmission of light at two wavelengths (0.68 μm and 2.2 μm), as observed by the KAO during the 1994 March 9 occultation of a 11.9 V mag star by Chiron. See Elliot et al. (1994) for a description of the observations and the interpretation of light curve features. From the relative extinction of the two wavelengths, we can place a lower limit on the size of the particles contributing to the extinction.

2. Analysis

Mie scattering theory (van de Hulst 1981) is a formal solution to Maxwell's equations that describes the scattering and absorption of light due to arbitrary-sized spherical particles as a function of the refractive index. Figure 1 shows the extinction efficiency given by Mie theory for two different materials as a function of radius, a, and the size parameter, $x=2\pi a/\lambda$. The size parameter is the ratio of the circumference of the sphere to the wavelength. This parameter and the refractive index are the independent variables in Mie theory.

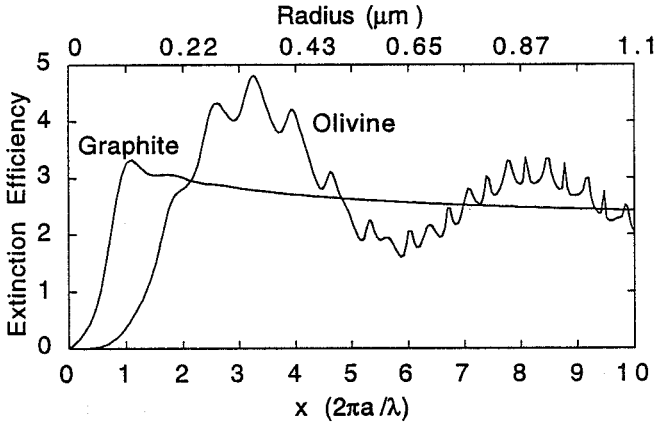

Figure 1. Extinction efficiency as a function of the parameter x. The upper abscissa is particle radius in μm for a wavelength of 0.68 μm (the effective wavelength of the optical data).

From the occultation observations, the depth of the light curve feature is similar in both wavelengths, yielding an extinction ratio (IR/optical) of 1.31 ± 0.65 (Elliot et al. 1994), giving an observed 1-σ low ratio of 0.66. The theoretical extinction ratio from Mie theory as a function of radius is shown in Figure 2 for olivine and graphite. These materials span the range of relevant refractive indices. The arrows indicate what particle sizes contribute to the extinction for the observed 1-σ low extinction ratio. For example, if the grains are graphite, then particles with a radius greater than 0.25 μm are contributing to the extinction by the jet.

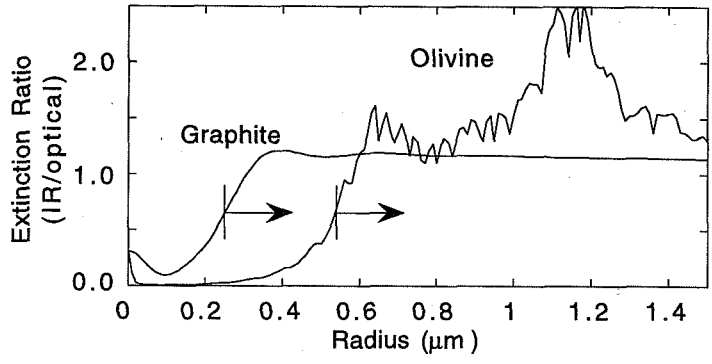

Figure 2. Extinction ratio (IR/optical) as a function of the radius for olivine and graphite. The vertical lines indicate the radius that corresponds to our observed 1-σ low extinction ratio. This sets a minimum radius for spherical particles of a given composition causing the extinction.

Table 1 shows the lower limit on the size of grains contributing to the extinction by this jet. These materials have refractive indices similar to those detected at Halley by mass spectrometric particle analyzers (Lamy, Grün, & Perrin 1987). Indications of olivine and chondrite have been seen in asteroid spectra (Gaffey, Bell, & Cruikshank 1989). Tholin is included, since organic materials are likely in comets; and the presence of silicate and graphite grains at Halley is supported by *in situ* measurements (Lamy et al. 1987). The lower limit ranges between 0.25 and 0.54 μm for the compositions shown. Most of the extinction we measure must be contributed by particles larger than this, and somewhat different limits would apply for non-spherical particles.

Table 1. Lower Limit of the Scattering Particle's Radius

Composition	Refractive Index*	Radius (μm)
Olivine	1.66 - 0.0001 *i*	0.54
Chondrite	1.90 - 0.0019 *i*	0.42
Tholin	1.70 - 0.02 *i*	0.52
Silicate	1.72 - 0.03 *i*	0.50
Magnetite	2.56 - 0.6 *i*	0.29
Graphite	2.70 - 1.4 *i*	0.25

*The index of refraction is from (Lamy et al. 1987) and pertains to a wavelength of 0.58 μm. We are assuming that this quantity is constant over the wavelength range of 0.58 to 2.2 μm.

3. Discussion and Conclusions

This result shows a particle population differing from that measured by the particle detectors on the Halley spacecraft, which found a significant population of particles with radii smaller than 0.25 μm (McDonnell et al. 1991). The

material probed here, however, is from a different object, much further from the Sun, and sampled much closer to the nucleus.

Previous attempts to estimate the particle sizes in Chiron's coma have involved looking for an excess blue component of the spectrum indicative of Rayleigh scattering. Luu and Jewitt (1990) report no Rayleigh scattering in near-UV narrow band photometry. From this, they infer no constraints on the size of grains except that the average radius is not $<< \lambda$. From observations taken one month later that show the coma to be blue, West (1991) concludes that there are sub-micron grains in Chiron's coma from photometric observations. The size distribution of grains probably changes with distance from the comet for Chiron, like it does for Halley (McDonnell et al. 1991). Therefore, one would not necessarily expect grain sizes in the coma to be the same as grain sizes near the nucleus (as in this observation).

On the other end of the size distribution, an upper limit to the dust grain sizes (Luu & Jewitt 1990) was set from the weight that can be lifted off the nucleus by escaping gas. This upper limit is 100 μm for CO and 10 μm for CO_2. In this work, we have shown that particles much smaller than one micron are not contributing substantially to the extinction due to this putative jet. This does not imply that particles much smaller than a micron are not present in the vicinity of Chiron, just that they are not significant in the extinction causing this one occultation light-curve feature.

4. References

Bus, S. J., A'Hearn, M. F., Schleicher, D. G., & Bowell, E. 1991, Science 251, 774

Bus, S. J., Bowell, E., Harris, A. W., & Hewitt, A. V. 1989, Icarus 77, 223

Elliot, J. L. et al. 1994, Nature (submitted)

Esposito, L. W., Brahic, A., Burns, J. A., & Marouf, E. A. 1991, in Uranus, ed. J. T. Bergstrahl, E. D. Miner, & M. S. Matthews (Tucson:University of Arizona), 410

Gaffey, M. J., Bell, J. F., & Cruikshank, D. P. 1989, in Asteroids II, ed. R. P. Binzel, T. Gehrels, & M. S. Matthews (Tucson:University of Arizona), 98

Hanner, M. S., Tokunaga, A. T., Golisch, W. F., Griep, D. M., & Kaminski, C. D. 1987, A&A 187, 653

Lamy, P. L., Grün, E., & Perrin, J. M. 1987, A&A 187, 767

Luu, J. X. & Jewitt, D. C. 1990, AJ 100, 913

Marouf, E. A., Tyler, G. L., Zebker, H. A., Simpson, R. A., & Eshleman, V. R. 1983, Icarus 54, 189

McDonnell, J. A. M., Lamy, P. L., & Pankiewicz, G. S. 1991, in Comets in the Post-Halley Era, ed. R. L. Newburn, M. Neugebauer, & J. Rahe (Dordrecht:Kluwer), 1043

Meech, K. J. & Belton, M. J. S. 1990, AJ 100, 1323

van de Hulst, H. C. 1981, Light Scattering by Small Particles. Dover, New York

West, R. M. 1991, A&A 241, 635

Airborne Astronomy Symposium on the Galactic Ecosystem
ASP Conference Series, Vol. 73, 1995
M.R. Haas, J.A. Davidson, and E.F. Erickson (eds.)

THE DETECTION OF A NEW STRONG BAND NEAR 3590 CM^{-1} (2.79 μm) IN THE SPECTRUM OF IO

F. SALAMA, L. J. ALLAMANDOLA, S. A. SANDFORD, J. D. BREGMAN, F. C. WITTEBORN, AND D. P. CRUIKSHANK
NASA-ARC, Mail Stop 245-6, Moffett Field, California 94035-1000

ABSTRACT A strong absorption band at 3590 ± 20 cm^{-1} (2.790 ± 0.015 μm) has been discovered in the spectrum of Io using the Kuiper Airborne Observatory (KAO). The $2\nu_1 + \nu_3$ combination mode of solid SO_2 falls at this position (Schmitt *et al.* 1994, Nash 1994). Since SO_2 is abundant on Io it must contribute to the new band. However, a band due to H_2O was also predicted near this frequency in Io's spectrum based on laboratory experiments of H_2O:SO_2 mixed Io ice analogs which were used to assign the two weak, variable features at 3370 and 3170 cm^{-1} (2.97 and 3.15 μm) to trace amounts of H_2O frozen in solid SO_2 on Io (Salama *et al.* 1990). The new band probably originates from both SO_2 and H_2O. Unfortunately, the spectral resolution of the data is insufficient to settle the issue of whether or not there are two resolvable components.

In this paper, we present the results of observations carried out on the Kuiper Airborne Observatory (KAO) to search for the predicted, strong solid H_2O-related feature near 3570 cm^{-1} (2.8 μm). The KAO was used because atmospheric H_2O makes this spectral region opaque to ground-based observatories. A more detailed discussion of this new finding and its potential implications for Io's surface composition can be found in Salama *et al* (1994).

The observations were performed on 8 May, 1992 using the Shortwave Infrared Array Spectrograph coupled to the KAO 0.9-m telescope. The spectra were measured in the 4000-2860 cm^{-1} (2.5-3.5 μm) range with a resolving power of 90 after Nyquist sampling. The two spectra of Io's leading hemisphere, shown in Figs. 1a & 1b, represent the ratio of the spectra of Io and the calibration star α Leo measured at comparable airmasses multiplied by the blackbody function of the standard star. The spectrum shown in Fig. 1c results from the overlapping of the two spectra in Figs. 1a & 1b after normalization at 3300 cm^{-1} (3.0 μm) and is Nyquist sampled at a resolving power of 90. This is equivalent to a resolution of about 40 cm^{-1} at the frequency of the new band. Finally, the relative reflectance spectrum shown in Fig. 2a was obtained by dividing the fluxed sum spectrum of Io (Fig. 1c) by the

solar spectrum and arbitrarily normalizing the reflectivity to 1.0 at 2857 cm^{-1} (3.50 μm).

The 4000-2860 cm^{-1} (2.5-3.5 μm) reflectance spectrum of Io (Figs. 1 & 2a), is dominated by a strong (25% deep) absorption feature peaking at 3590 ± 20 cm^{-1} (2.790 ± 0.015 μm) with a shoulder at about 3530 ± 20 cm^{-1} (2.833 ± 0.015 μm). This feature is barely resolved, with the strong band having a FWHM of about 60 cm^{-1} (0.04 μm). The apparent FWHM of the main band and shoulder combined is about 115 cm^{-1} (0.09 μm). The entire feature has a 210 cm^{-1} (0.16 μm) width at the continuum level and is the second strongest band measured in Io's spectrum.

Although the band falls very close to the position of a narrow (5 cm^{-1}), high order combination mode ($2\nu_1 + \nu_3$) of solid SO_2, it's intrinsic width and strength appear to be too large to be accounted for by SO_2 alone. The band also falls in the region of the spectrum characteristic of the stretching vibration of the hydroxyl group (OH). The position and width of the new band are characteristic of the stretching vibration of the OH group in low-order multimers of H_2O *isolated* in frozen SO_2. This is illustrated by the 4000-2800 cm^{-1} (2.5 - 3.8 μm) infrared transmission spectra of H_2O:H_2S:SO_2 ices formed by slow condensation at 9 K and subsequently warmed to higher temperatures (Figs 2b-d). Blending of the OH feature with the sharper SO_2 component would produce a band close to 3590 cm^{-1}. After comparing the data with laboratory spectra of SO_2-rich ices containing traces of H_2O (Fig. 2), *we tentatively assign the new feature to a combination of both the ($2\nu_1 + \nu_3$) combination band of SO_2, and the OH stretch in low-order multimers of H_2O complexed with SO_2* . Present best estimates indicate that the SO_2 band probably accounts for 30-50% of the feature in the spectrum of Io (Schmitt *et al* 1994). The position and strength of the newly detected Io band indicate that, if H_2O is responsible for the excess absorption, it is present in very low concentrations. While other OH-containing materials (minerals, NaOH, KOH, etc.) are conceivable carriers of the additional absorption, the good positional match between the astronomical and laboratory data leads us to favor H_2O in an SO_2 matrix.

The suggested presence of H_2O on Io has important implications for the composition of the surface material and its spectral properties. Furthermore, it raises the important question of the source of hydrogen, i.e. endogenic vs. exogenic. More observations of this new feature are needed to assess its temporal variability. Higher resolution measurements are also needed to obtain the precise shape and peak position of this band since the laboratory data indicate the profile and substructure will provide useful information about the thermal history of the ice and the relative concentrations of SO_2 and H_2O. Further progress can also be made in laboratory experiments utilizing isotopic substitutions, so that the bands due to SO_2 and contaminant H_2O can be more clearly delineated. The next generation of airborne observatory, SOFIA, with its higher sensitivity and spectral resolution, should provide the ideal platform for such measurements on Io and other bodies of the solar system.

REFERENCES

Nash, D. B. 1994, Icarus, **107**, 418.
Salama, F., L. J. Allamandola, F. C. Witteborn, D. P. Cruikshank, S. A. Sandford, and J. D. Bregman 1990, Icarus, **83**, 66.
Salama, F., L. J. Allamandola, S. A. Sandford, J. D. Bregman, F. C. Witteborn, and D. P. Cruikshank 1994, Icarus, **107**, 413.
Schmitt, B., C. De Bergh, E. Lellouch, J. P. Maillard, A. Barbe, and S. Doute 1994, Icarus, in press.

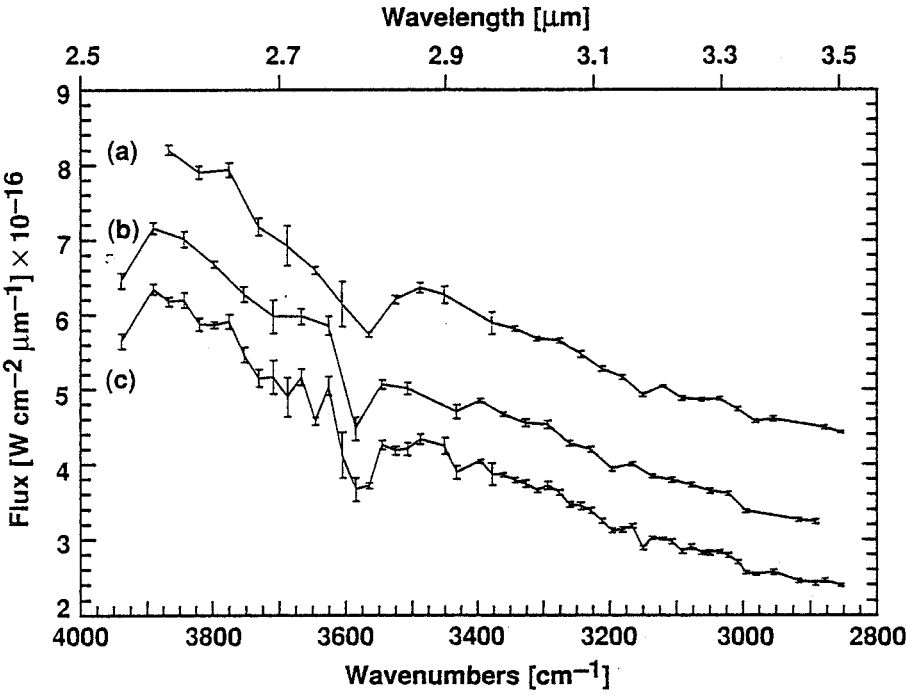

Figure 1: Measured reflectivity of Io in the ranges (a) 3868-2835 cm^{-1} (2.585-3.527 μm), and (b) 3940-2873 cm^{-1} (2.538-3.481 μm). (c) Sum spectrum derived from (a) and (b) normalized at 3.0 μm. [Note: For the clarity of the figure, the base lines of spectra (a) and (b) were shifted upwards by + 2.0 x 10^{-16} and + 1.0 x 10^{-16} flux units, respectively].

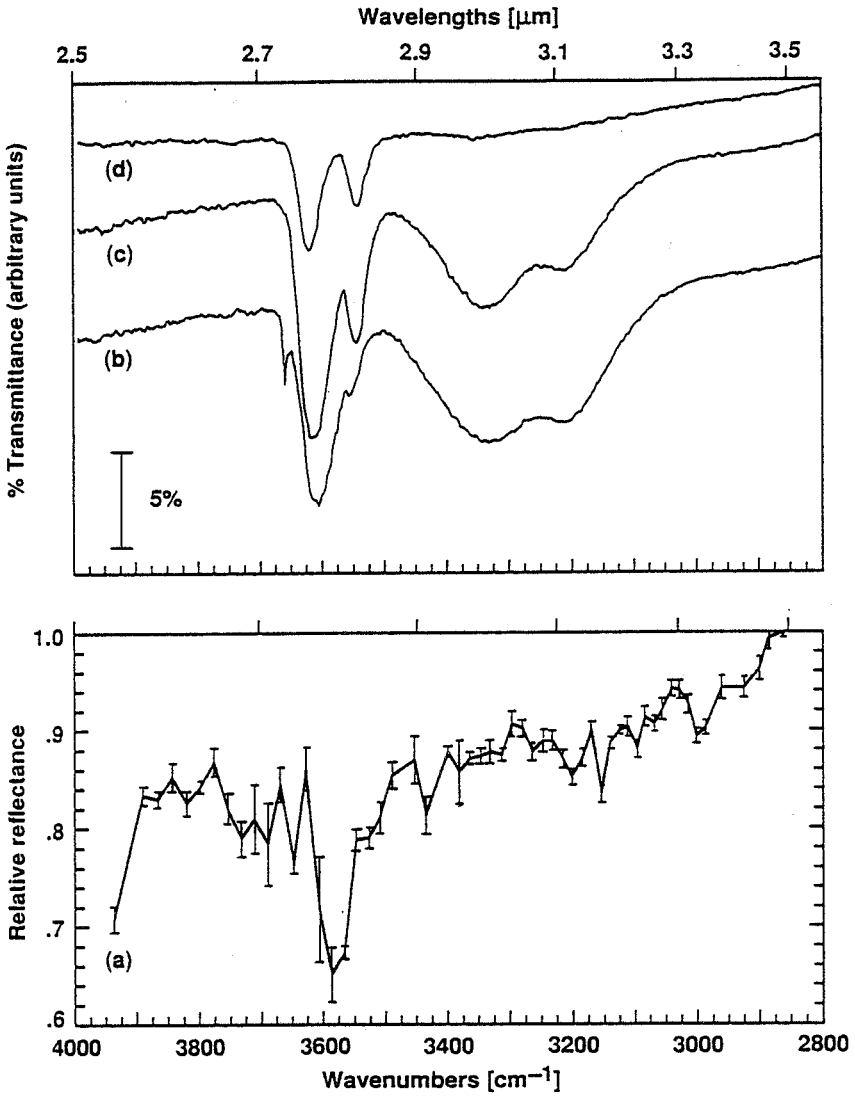

Figure 2: The relative reflectance spectrum of Io (a) is compared to the infrared absorption spectrum of a thick film (~ 0.5 mmole cm^{-2}) of an H_2O:H_2S:SO_2 (1:3:100) mixed molecular ice annealed from 9 K to 55 K (b), and 75 K (c) and to the infrared absorption spectrum of a thick film (~ 0.5 mmole cm^{-2}) of an H_2O:H_2S:SO_2 (1:100:3000) mixed molecular ice annealed from 9 K to 50 K (d).

Airborne Astronomy Symposium on the Galactic Ecosystem
ASP Conference Series, Vol. 73, 1995
M.R. Haas, J.A. Davidson, and E.F. Erickson (eds.)

MID-INFRARED (5.0-7.0 μm) IMAGING SPECTROSCOPY OF THE MOON FROM THE KAO

JAMES F. BELL III[1], JESSE D. BREGMAN[2], DAVID M. RANK[3], PASQUALE TEMI[3], TED L. ROUSH[1,4], B. RAY HAWKE[5], PAUL G. LUCEY[5], and JAMES B. POLLACK[1]

[1] *NASA Ames Research Center, Space Science Division, Theoretical Studies Branch, Mail Stop 245-3, Moffett Field, CA 94035-1000*

[2] *NASA Ames Research Center, Space Science Division, Astrophysics Branch, MS 245-6, Moffett Field, CA 94035-1000*

[3] *University of California-Santa Cruz, Santa Cruz,CA 95060*

[4] *Department of Geosciences, San Francisco State University*

[5] *Planetary Geosciences, Hawaii Institute of Geology and Planetology, University of Hawaii, Honolulu, HI 96822*

Abstract. A series of 71 mid-infrared images of a small region of the Moon were obtained from the KAO in October, 1993. These images have been assembled into a 5.0 to 7.0 μm image cube that has been calibrated relative to the average spectrum of this region of the Moon at these wavelengths. The data show that clear, detectable spectral differences exist on the Moon in the mid-IR. Some of the spectral differences are correlated with morphologic features such as craters. Specific spectral features near 5.6 and 6.7 μm may be related to the presence of plagioclase or pyroxene.

1. Introduction and Background

There is a limited range of rocks and minerals that can form and/or exist stably on the volatile-free, chemically-reducing lunar surface. As reviewed by Heiken et al. (1991) and Nash et al. (1993), previous visible to near-IR spectroscopic observations and detailed analyses of returned samples have revealed that the materials on the lunar surface can be classified into 2 main categories: (1) Soil/Regolith, composed of fine-grained rock and mineral fragments produced by the constant action of impacts on all size scales; and (2) Igneous Rocks/Breccias, composed of Mare rocks (basaltic lavas that contain pyroxene, plagioclase, olivine and opaque metallic oxides of varying composition, all of which may have widely varying Fe, Ti, and Al abundances) and Highlands rocks (dominated by plagioclase anorthosites, pyroxene, and olivine, and which have typically been pulverized and vitrified by impacts into unsorted, welded aggregates). Other, rarer lunar phases such as quartz and potassium feldspar have been detected in returned samples, but for the most part the mineralogy of the Moon is made up primarily of plagioclase, pyroxene, olivine, and ilmenite.

The detection of spectral features in the 4 to 8 μm "transition region" (the transition from volume to surface scattering (Nash et al. 1993; Salisbury and Walter, 1989; Salisbury and Wald, 1992)) was our main KAO observing goal. Nash et al. (1993) have presented a compilation of laboratory spectra for typical

lunar rock-forming mineral phases in the 4 to 8 μm region. Even at relatively coarse spectral resolution, plagioclase, pyroxene, olivine, and ilmenite have distinctive and diagnostic absorption and emission features and widely-varying spectral slopes. The average band depth of individual features is about 10%; the strongest bands have depths of 25%. Many mid-IR studies of returned lunar samples have also been performed (e.g., Nash, 1991; Nash et al., 1993). Like the pure mineral phases, the sample spectra show considerable variability in absorption/emission band position, band depth, and spectral slope.

The major questions in lunar science that can be addressed by mid-IR observations are: (1) What is the abundance and distribution of anorthite (the most common lunar mineral) and anorthositic rocks? (2) What is the chemical composition (Fe/Mg ratio) of lunar olivines? (3) What other iron-free minerals exist in detectable abundances on the Moon?

2. Observations and Data Reduction

Our observations were conducted during a 30-minute KAO observing leg in October 1993. The data were obtained by J.D. Bregman and D.M. Rank using a new KAO facility camera based on a 128×128 Si:Ga array and LHe dewar (Bregman et al. 1994). The images were obtained in a 30 degree longitude by 15 degree latitude region of the southwestern limb near the craters Schickard, Baade, and Inghirami (Figure 1). Images of this region in 71 wavelengths between 5.0 and 7.0 μm were obtained through a 1.5% CVF.

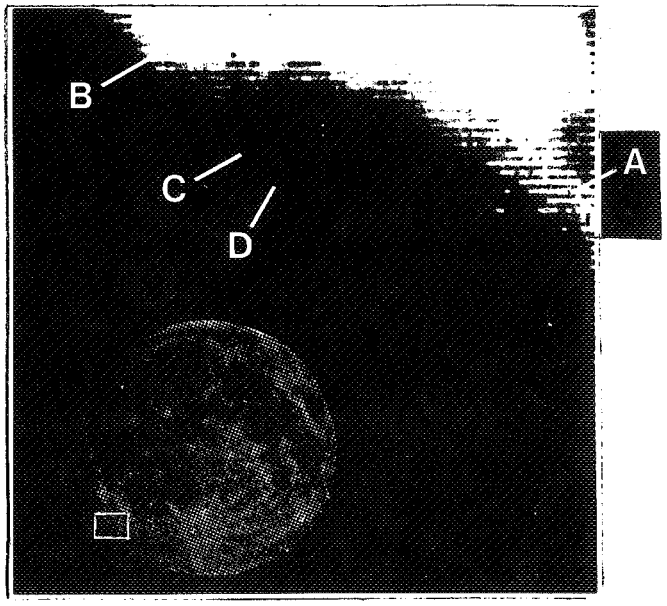

Figure 1. "Albedo" image at 7.01 μm of the region of the Moon imaged during our October 1993 KAO observing leg. North is up and the inset shows the location of this region relative to the full Moon. The image has had bootstrapped offset and flatfield corrections applied. Four types of surface regions were identified for spectroscopic analysis: (A) intercrater highlands, intermediate albedo; (B) intercrater highlands, high albedo; (C) dark crater floor; (D) bright crater floor/peak.

Because of the exploratory nature of these observations, it was not possible to obtain enough data for a complete and rigorous calibration of the images. However, we have devised a bootstrap relative calibration scheme that allows analysis of the compositional variability within the scene and that allows us to assess the general detectability of lunar rocks and minerals in the mid-IR. We

performed the "standard" data reduction steps using dark and flatfield images obtained in the lab shortly after the observing run. The images were then spatially co-registered by hand to within 0.5 pixel. The average spectrum of all the regions of the Moon imaged was determined, and then the final image cube (128×128×71) was generated by dividing this average spectrum from the original data. The resulting image cube cannot be directly compared to laboratory spectra, but it does allow relative spatial variations to be detected and the wavelengths of these variations can be directly associated with the wavelengths of features seen in laboratory rock and mineral spectra.

3. Results

Figure 2 shows the average spectrum of all regions in the raw image cube. For comparison, a model atmospheric transmission spectrum of the Earth's atmosphere above the KAO is also shown. The average spectrum shows evidence for features near 5.8-6.0 and 6.4-6.5 μm that are caused by telluric absorptions. Weaker features can also be seen at other wavelengths. These weaker features are amplified when the average spectral signature is removed from the data. Figure 3 shows relative flux spectra (raw spot DN / average Moon DN) for four regions labeled A to D in Figure 1. These four regions sample bright and dark plains, crater floor, and crater peak materials. Residual instrumental problems prevent the interpretation of features between 5.8 and 6.2 μm, but at other wavelengths, such as near 5.6 and 6.7 μm, relative spectral features are apparent. Laboratory spectra indicate that both plagioclase and pyroxene have absorption features near these wavelengths (e.g., Nash and Salisbury, 1991; Salisbury et al., 1991).

Figure 2: Average Raw Lunar Spectrum of all Regions in Figure 1

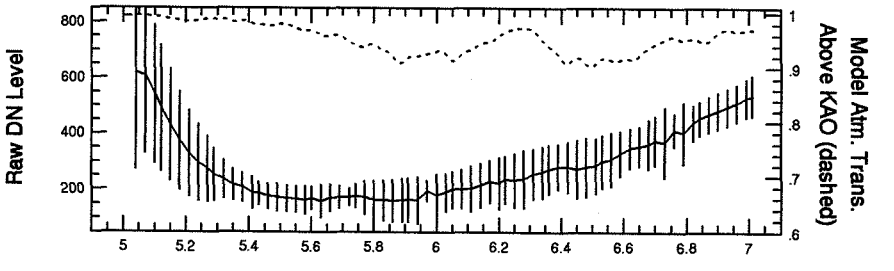

Figure 3: Spectra of Figure 1 spots / average spectrum

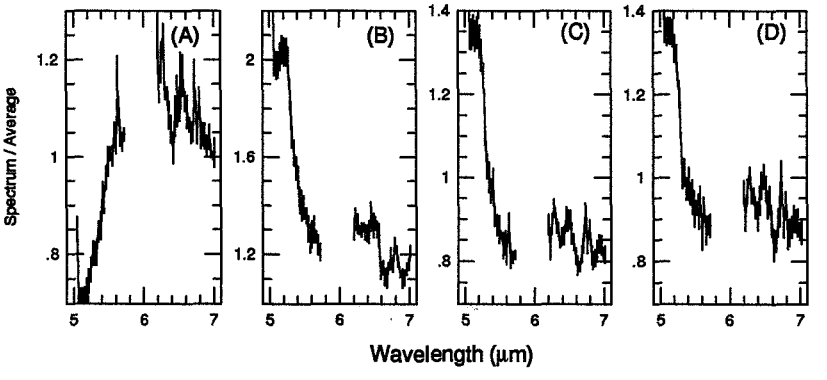

Figure 4a. Ratio image: 7.01 / 6.45 μm

Figure 4b. 6.7 μm band depth map

A more useful and appropriate way to view the spectral contrasts in this data set is by ratio images and relative band depth maps (e.g., Bell and Crisp, 1993). Two of the most illustrative examples are shown in Figure 4, which displays a map of the 7.01/6.45 μm ratio (Fig. 4a) and of the 6.7 μm band depth (Fig. 4b). Both of these images reveal spatially-coherent patterns of spectral behavior that correlate well with albedo and morphology in some places, such as near the crater labeled D, but poorly in other places, such as in the plains labeled A.

Our KAO mid-IR images and spectra have undergone only a preliminary analysis at this time. Clearly, there is a wealth of detail in the data shown above that needs to be examined. However, these exploratory observations show that the lunar surface is detectably heterogeneous at mid-IR wavelengths, which is encouraging for possible future, more detailed KAO and spacecraft mid-IR imaging observations.

Acknowledgments. This work was funded by grants to ARC, UH, and SFSU through the NASA Planetary Astronomy (NAGW-3427) and Planetary Geology (RTOP 151-01-60-01) programs. JFB acknowledges the additional support of the National Research Council, National Academy of Sciences.

4. References

Bell III, J.F. & D. Crisp 1993, Icarus, 104, 2

Bregman, J.D., D. Harker, D. Rank, & P. Temi 1994, in Proc of the Airborne Astronomy Symp on the Galactic Ecosystem: From Gas to Stars to Dust, ed. M.R. Haas, J.A. Davidson, & E.F. Erickson (San Francisco: ASP), paper 716

Heiken, G., D. Vaniman, & B. French 1991, Lunar Sourcebook (New York: Cambridge)

Nash, D.B. 1991, Geophys Res Lett, 18, 2145

Nash, D.B. & J.W. Salisbury 1991, Geophys Res Lett, 18, 1151

Nash, D.B., J.W. Salisbury, J.E. Conel, P.G. Lucey, & P.R. Christensen 1993, J Geophys Res, 98, 23535

Salisbury, J.W. & L.S. Walter 1989, J Geophys Res, 94, 9192

Salisbury, J.W. & A. Wald 1992, Icarus, 96, 121

Salisbury, J.W., L.S. Walter, N. Vergo, & D.M. D'Aria 1991, Infrared (2.1-25 μm) Spectra of Minerals (Baltimore: Johns Hopkins)

Airborne Astronomy Symposium on the Galactic Ecosystem
ASP Conference Series, Vol. 73, 1995
M.R. Haas, J.A. Davidson, and E.F. Erickson (eds.)

THERMAL INFRARED SPECTROSCOPIC OBSERVATIONS OF MARS FROM THE KUIPER AIRBORNE OBSERVATORY (KAO): CONSTRAINTS ON PAST CLIMATES AND WEATHERING PRODUCTS

TED ROUSH

Department of Geosciences, San Francisco State University, c/o NASA Ames Research Center, Space Sciences Division, Theoretical Studies Branch, MS 245-3, Moffett Field, CA 94035-1000

JAMES POLLACK

NASA Ames Research Center, Space Sciences Division, Theoretical Studies Branch, MS 245-3, Moffett Field, CA 94035-1000

FRED WITTEBORN and JESSE BREGMAN

NASA Ames Research Center, Space Sciences Division, Astrophysics Branch, MS 245-6, Moffett Field, CA 94035-1000

JAMES BELL, III

National Research Council, Resident Research Associate, c/o NASA Ames Research Center, Space Sciences Division, Theoretical Studies Branch, MS 245-3, Moffett Field, CA 94035-1000

BRADLEY SITTON

Synernet Corp., 3155 Kearney St., Suite 170, Fremont, CA 94538

Abstract. Spectral observations providing evidence for the presence of volatile-bearing minerals on the surface of Mars were obtained in 1988 and 1990 from the KAO. The 1988 data suggest the presence of 1-3 weight percent (wt%) of carbonate/bicarbonate and 10-15 wt% sulfate/bisulfate associated with martian atmospheric dust. Estimates of the optical depths are ~0.60 and ~0.35 in 1988 and 1990, respectively.

1. INTRODUCTION

There are ample geomorphic and theoretical reasons for suspecting the presence of several volatile-bearing minerals such as, carbonates, sulfates, and hydrates, to be present on the surface of Mars (e.g., Pollack et al. 1990, henceforth referred to as paper 1). Such minerals provide relatively permanent reservoirs for volatiles thought to have been outgassed during Mars' history and not present in the current martian atmosphere. Hence the identification of these materials can

provide information regarding both the surface and atmospheric history of Mars. Several previous studies, designed to identify spectral features associated with these minerals relied upon data which had: 1) low signal-to-noise (Mariner 9 IRIS); 2) incomplete calibration (Mariner 6 & 7); or 3) a wavelength region where only the much weaker combination and/or overtone bands occur (see Soderblom 1992 and Roush et al. 1993 for more details). In 1988 and 1990 we obtained spectral data, with high signal-to-noise, and accurate wavelength calibration, in the wavelength region where the fundamental vibrational modes of these minerals occur. This paper is a brief summary of these measurements; it relies heavily upon the detailed discussion and analysis presented in paper 1.

2. OBSERVATIONS

On 13 October 1988 (UT) and 28-29 November 1990 (UT) spectral observations of Mars were obtained at an altitude of 12.5 km from the KAO. Data were acquired simultaneously at each wavelength using a grating spectrometer that, in a given position (1988 = 2; 1990 = 4), disperses the incident energy across a linear detector array (Witteborn and Bregman 1984). Spectral resolution ($\lambda/\Delta\lambda$) and wavelength coverage in 1988 was ~60 over the 5.4-10.4 μm range and in 1990 $\lambda/\Delta\lambda$ was ~140 over the 5.5-9.2 μm range. Instantaneous and effective aperture sizes were 6.7″ and ~8.3″ in 1988, and 4.1″ and ~4.3″ in 1990; corresponding to roughly $\frac{1}{3}$ and $\frac{1}{4}$ the diameter of Mars in 1988 and 1990, respectively. In both years wavelength calibration was obtained by viewing a blackbody cavity through a sheet of polystyrene. Table I lists the centers of the field of view and the effective emission air masses for each spot. These data mostly sampled the equatorial and sub-equatorial regions of Mars with a few excursions to higher latitudes. Paper 1 discusses the detailed motivations behind our observing strategy. Briefly, differences of the ground temperatures and air masses among the various spots lead to spectral features having varying strengths, even if the absorbing materials are uniformly distributed. By ratioing spectra of pairs of spots, we obtained data that are unaffected by uncertainties in the spectral behavior of our standard star and telluric absorptions.

In both years, the elevation of α Tau was close to Mars and provided excellent first order removal of telluric absorptions. Over the spectral domain of our observations, the flux of α Tau is known (e.g., Hanner et al. 1984, Cohen et al. 1992). Figure 1 shows the derived brightness temperatures (BT, the temperature of the blackbody yielding the equivalent flux) for a center spot from both years. Several spectral features are readily apparent. Two broad maxima (A & B) are present in both spectra, and an additional maximum (C) occurs in the longer wavelength 1988 data. Several BT minima (1-7) are also present in these spectra.

Figure 1 also shows how weak features are enhanced by ratioing the spectral fluxes of pairs of spots. The center to NE ratios are best for defining weak features because the center spots had both a larger air mass and a larger thermal contrast between the ground and the atmosphere than the NE spots. The center/NE ratios obtained early and late during the 1988 flight are remarkably similar (Fig. 1), implying we can place a high level of confidence in the reality of the spectral features.

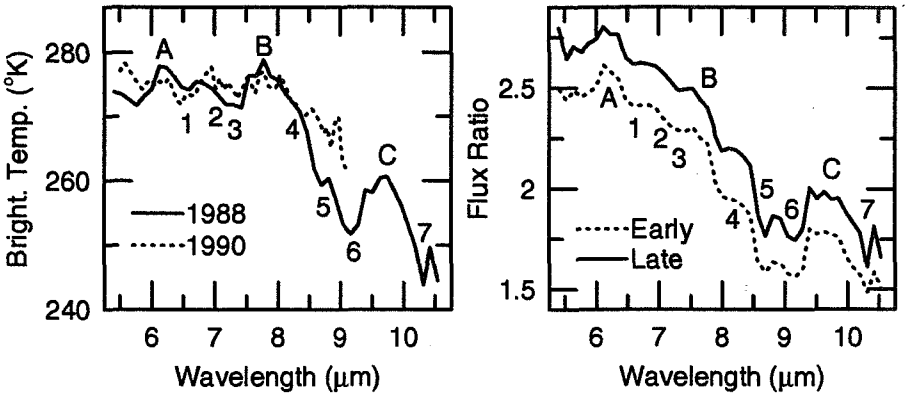

Figure 1. Derived brightness temperatures (left) for a center spot measured in 1988 and 1990 and flux ratio of the center spot to the northeast spot (right) measured in 1988. The maximum labeled A is attributed to surface hydrates, while maxima B and C are attributed to surface silicates. Minimum 1 and the shoulder labeled 2 are attributed to carbonates and/or bicarbonates, minima 3, 4, 6, and 7 are due to atmospheric CO_2, and the minimum labeled 5 is attributed to sulfates and/or bisulfates.

Table I Properties of Spots Observed on Mars

1988 Data			1990 Data		
Longitude (degrees, W)	Latitude (degrees)	Average Airmass	Longitude degrees, (W)	Latitude (degrees)	Average Airmass
132	-24	1.41	250	-9	1.01
174	-26	1.04	263	-44	1.24
off planet		2.92	235	-26	1.42
161	-48	1.30	off planet		$\gg 5$
172	-24	1.41	305	3	1.35
off planet		$\gg 5$	232	-18	1.34
214	-26	1.04	303	-9	1.01
off planet		2.92	319	-44	1.24
			293	-26	1.43
			off planet		$\gg 5$
			274	-22	1.21
			228	-9	1.02
			285	-9	1.02
			248	-7	1.36
			327	-8	1.37
			off planet		$\gg 5$

3. DISCUSSION

In paper 1 tentative identifications of the spectral features in the 1988 KAO data were made by considering both gaseous and solid materials as sources for these features. Assignments of features believed due to minerals have been based on the wavelength locations of the vibrational fundamentals of an ensemble of candidates and current knowledge about Mars (see paper 1). BT maxima features are attributed to spectral variations in the surface emissivity, and BT minima to gases and solids present in the martian atmosphere for reasons detailed in paper 1. The overall strong decline in BT from 8 to 9.5 μm is attributed to the effects of suspended dust particles in the martian atmosphere (paper 1). Based on modeling the BT decline observed in the 1988 data, an optical depth (τ_ν at 0.3 μm) of $\sim$0.60 was derived (see paper 1). Using the same assumptions as in paper 1, a τ_ν of $\sim$0.35 is derived for the 1990 data shown in Fig. 1. This decrease in τ_ν is consistent with other suggestions of reduced atmospheric dust loading during this time (Clancy et al. 1993).

Future observations involving imaging spectroscopy could provide valuable information regarding the spatial distribution of surface and atmospheric materials on Mars. The KAO provides a unique platform for obtaining such information. The identification of localized regions or deposits of volatile-bearing materials would be invaluable information for planning future robotic and manned missions to Mars.

Acknowledgments. This paper is dedicated to the lifelong scientific contributions of our friend and colleague James Pollack. Jim's dedication to advancing our knowledge of the solar system and the universe surrounding it will be sadly missed. This research is supported by NASA's Planetary Geology and Geophysics program via RTOP 151-01-60-01 and NASA's Airborne Astronomy program via RTOP 352-02-03-02.

References

Cohen, M., R. G. Walker, & F. C. Witteborn 1992, AJ, 104, 2030

Clancy, T., A. Grossman, and D. Muhleman 1993, BAAS, 25, 1060

Hanner, M. S., A. T. Tokunaga, G. S. Veeder, and M. F. O'Hearn 1984, AJ, 89, 162

Pollack, J. B., T. Roush, F. Witteborn, J. Bregman, D. Wooden, C. Stoker, O. B. Toon, D. Rank, B. Dalton, and R. Freedman 1990, JGR, 95, 14,595

Roush, T. L., D. L. Blaney, and R. B. Singer 1993, in Remote Geochemical Analysis: Elemental and Mineralogical Composition, eds. C. M. Pieters and P. A. J. Englert (Cambridge Univ. Press, New York) 367

Soderblom, L. A. 1992, in Mars, eds., H. H. Kieffer, B. M. Jakosky, C. W. Snyder, and M. S. Matthews (Univ. Arizona Press, Tucson) 557

Witteborn, F. C., and J. D. Bregman 1984, Proc. SPIE, 509, 123

Airborne Astronomy Symposium on the Galactic Ecosystem
ASP Conference Series, Vol. 73, 1995
M.R. Haas, J.A. Davidson, and E.F. Erickson (eds.)

MAGNETIC EXPANSION OF COSMIC PLASMAS

Wei-Hong Yang
Northwestern Polytechnic University, 105 Fourier Avenue, Fremont, CA 94539

ABSTRACT Plasma expansion is common in many astrophysical phenomena. The understanding of the driving mechanism has usually been focused on the gas pressure that implies conversion of thermal energy into flow kinetic energy. However, "*cool" expansions* have been indicated in stellar/solar winds and other expanding processes. Magnetic expansion may be the principal driving mechanism. Magnetic energy in the potential form can be converted into kinetic energy during global expansion of magnetized plasmas.

1. INTRODUCTION

A macroscopic expansion of a gas cloud requires an energy source. In astrophysical situations, the gas may be fully or partially ionized. The charged particles in the gas cloud may generate electromagnetic fields through their elementary charges and currents. The motions of these charged particles are influenced by the fields they generate and those externally imposed. It is recognized that magnetic fields play important roles in many astrophysical phenomena. In those situations, the ionized gas is a so-called magnetized plasma. A magnetized plasma contains energy in the magnetic form. This energy may be converted to thermal energy through Joule heating. This process would be extremely slow in a highly conducting plasma. The magnetic field dissipation may be enhanced in a current sheet where magnetic fields construct discontinuities and resistive tearing mode instability may set in. Magnetic field lines may reconnect while the system evolves toward lower magnetic energy states. Magnetic reconnection has been the main theory in interpretation of energy processes, e.g., geomagnetic activities, solar flares, and so on. Although great efforts have been made in understanding the physics of magnetic reconnection, some critical problems have not been resolved. The reconnection theory suggests that magnetic energy dissipation occurs in a small diffusion zone, e.g. on a X-type neutral point. This condition makes it difficult to connect the theory with the global phenomena of an energetic event.

2. MAGNETIC EXPANSION

An alternative process in regard to magnetic energy release is magnetic expansion. A magnetized system may evolve to consecutive lower energy states during expansion. Two different situations were studied for a low-ß plasma by Yang (1989). The parameter ß is the ratio of the plasma pressure to the magnetic pressure defined as

$$\beta = \frac{p}{B^2/8\pi}, \tag{1}$$

where p is the gas pressure, and B the magnetic field strength. A low-ß plasma means that the ß value is much smaller than unity, hence the magnetic field dominates the dynamic behavior of the plasma. The first case studied by Yang was a bipolar magnetic field anchored in a dense matter. The decrease of magnetic energy with expansion was calculated by a numerical method. The second case studied was on linear expansion of a magnetized plasmoid (meaning that the plasma is enclosed by its own magnetic surface). The magnetic energy of the linearly expanding plasmoid varies as

$$E_M(t) = \frac{1}{\xi} E_{M0} \tag{2}$$

where ξ is the expansion parameter defined as the ratio of the scale size of the plasmoid at time t with respect to an initial time t_0. The plasmoid releases half of its magnetic energy when it expands to twice its scale size. Contribution to expansion from magnetic field can be significant. Magnetospheric phenomena may be an applicable situation. We may take the magnetosphere of Earth as an example. Following individual field lines with rotation of Earth, we find that the magnetic energy is stored during the period of compression (by the solar wind). The stored magnetic energy then is released when field lines expand particularly in the magnetotail region. The magnetic energy release is an irreversible process. This implies that work has to be done continuously to pump energy into the magnetosphere and the energy is also continuously released. Similar processes may occur in other astrophysical situations.

3. THE STELLAR WINDS

Stars lose mass continuously through the winds (e.g., see Cassinelli & MacGregor 1986 for a review). The first dynamic model of the wind from the Sun was proposed by Parker (1958). According to his original theory, the solar wind is produced by the pressure imbalance between the inner solar corona and the interstellar medium. The driving force is the thermal pressure gradient and the retarding force results from the gravitational field of the Sun. However, the discovery of the high speed wind and the identification of its source to be

coronal holes have raised critical questions; the relatively low temperature of coronal holes would prohibit the possibility of a purely thermal expansion. To resolve this discrepancy, efforts have been aiming at possible mechanisms which may provide additional energy to coronal plasmas (e.g., hydromagnetic waves). There are excellent review articles in the literature of coronal heating and solar wind acceleration (Hundhausen 1972; Hollweg 1978; Leer, Holzer, & Flå 1982; Pneuman 1986; Barnes 1992).

In a magnetohydrodynamic (MHD) description, the equation of motion is

$$\rho \left(\frac{\partial}{\partial t}+\boldsymbol{v}\cdot\nabla\right)\boldsymbol{v} = -\nabla p+\frac{1}{4\pi}(\nabla\times\boldsymbol{B})\times\boldsymbol{B}-\rho\nabla\Phi \qquad (3)$$

where ρ is the mass density, v the flow velocity, and Φ the gravitational potential, respectively. In Parker's original theory, the magnetic force term was omitted because the magnetic field lines were considered to lie everywhere along the stream lines (Parker 1963). For a steady hydrodynamic flow, the Bernoulli equation is derived to be

$$\frac{1}{2}v^2 + \frac{\gamma}{\gamma-1}\frac{p}{\rho} - \frac{GM\odot}{r} = E_0. \qquad (4)$$

The three terms represent the kinetic energy (ϵ_k), the enthalpy (ϵ_{th}), and the gravitational energy (ϵ_g) per unit mass, respectively.

At 1AU, the speed of the solar wind v=700 kms^{-1} and the gas temperature T=1.5×10^{5}K, so ϵ_k=2.45×10^{15}erg, ϵ_{th}=6.2×10^{13}erg (for γ=5/3), and ϵ_g=-8.87×10^{12}erg. Hence the kinetic energy dominates the flow. At r=2$R\odot$, T=1.4×10^{6}K (a typical temperature of coronal holes), and v=65kms^{-1}, so ϵ_k=2.1×10^{13}erg, ϵ_{th}=5.8×10^{14}erg, and ϵ_g=-9.5×10^{14}erg, respectively. Although the local plasma contains significant thermal energy, the total energy is negative because of the strong gravitational potential. And at the coronal base where T=10^{5}K, v=0.5kms^{-1}, so ϵ_k=1.3×10^{9}erg, ϵ_{th}=4.1×10^{13}erg, and ϵ_g=-1.9×10^{15}erg. The plasma is overwhelmed by the gravitational potential. Based on these estimations, it would seem that the gas beneath the coronal base needs to gain *at least* an energy of 4.4×10^{15}erg per unit mass to form the wind. It is rather clear that a pure thermal model would not be able to explain how plasmas expand from the base, and the available thermal energy is insufficient to cause expansion of the upper corona.

If we consider the solar wind as magnetized plasmas, the energy deficiency may be eased. In such a model, the solar wind is composed of a large number of plasmoids which are produced in discrete small-scale energetic events. With some simplifications, we can derive a Bernoulli equation

$$\frac{1}{2}v^2 + \frac{\gamma}{\gamma-1}\frac{p}{\rho} + \frac{1}{4\pi}\frac{B^2}{\rho} - \frac{GM\odot}{r} = E \qquad (5)$$

for a magnetized plasma flow. If the plasmas have an average magnetic strength of $\sim$50G (a reasonable value for small-scale energetic events in the low solar atmosphere) and a density $n_p \sim 10^{10}\text{cm}^{-3}$ when being ejected from the transition zone, then the magnetic term in equation (5) is $\epsilon_m \sim 1.2\times10^{16}$erg per unit mass, which is about three times the energy carried in the high speed wind at infinity. For a qualitative estimate, we may apply linear expansion to approximate the variation of magnetic field (Yang 1989, 1990, 1992). The estimated field strength is $B \approx 3\times10^{-5}$G at 1AU which is well within the measured values of the interplanetary magnetic field. Thus magnetic fields may contribute significantly to the expansion. And the magnetic energy is also sufficient for heating coronal plasmas to the observed temperature under the above assumption of the field strength. Infrared observations of small-scale structures of the low solar atmosphere may provide important information on how cool gases are ejected, heated, and accelerated to form the wind.

The author would like to thank J.A.Davidson for her helpful suggestions which improved the manuscript of this paper.

REFERENCES:

Cassinelli,J.P., & MacGregor,K.B. 1986, in *Physics of the Sun*, vol III, ed. P.A.Sturrock, T.E.Holzer, D.M.Mihalas, & R.K.Ulrich (Dordrecht: Reidel).

Barnes,A. 1992, *Rev. Geophys.*, **30**, 43.

Hollweg,J.V. 1978, *Rev. Geophys. Space Phys.*, **16**, 689.

Hundhausen,A.J. 1972, *Coronal Expansion and the Solar Wind* (New York: Springer-Verlag).

Leer,E., Holzer,T.E., & Flå,T. 1982, *Space Sci. Rev.*, **30**, 161.

Parker,E.N. 1958, *ApJ*, **128**, 664.

Parker,E.N. 1963, *Interplanetary Dynamical Processes* (New York: Interscience).

Pneuman,G.W. 1986, *Space Sci. Rev.*, **43**, 105.

Yang,W.-H. 1989, *ApJ*, **344**, 966.

Yang,W.-H. 1990, *ApJ*, **348**, L73.

Yang,W.-H. 1992, *ApJ*, **392**, 465.

Airborne Astronomy Symposium on the Galactic Ecosystem
ASP Conference Series, Vol. 73, 1995
M.R. Haas, J.A. Davidson, and E.F. Erickson (eds.)

Radon Measurements Aboard the Kuiper Airborne Observatory

Mark A. Kritz and Stefan W. Rosner

Atmospheric Sciences Research Center, State University of New York, Albany, NY 12222

Abstract. We have carried out three (piggyback) radon-related projects aboard the KAO. The first, which was limited to upper tropospheric measurements while in level flight, revealed the systematic occurrence of unexpectedly high radon concentrations in this region of the atmosphere. The second project was an instrument development project, which led to the installation of an automatic radon measurement system aboard the NASA ER-2 High Altitude Research Aircraft. In the third, we installed a new system capable of collecting samples during the normal climb and descent of the KAO. The results obtained in these projects have resulted in significant contributions to our knowledge of atmospheric transport processes, and are currently playing a key role in the validation of global circulation and transport models.

1. Introduction

Radon (^{222}Rn) enters the atmosphere from the crust, where it is produced by the decay of trace quantities of its parent, ^{226}Ra. Radon is a noble gas and relatively insoluble in water, so that its removal from the atmosphere by precipitation scavenging is negligible and its only significant atmospheric sink is its own radioactive decay, which occurs with a half life of 3.8 days. For these reasons atmospheric radon measurements have been used as an indicator of vertical transport (e.g., Liu et al. 1984) as well as an indicator of the presence and transport of continental air over the oceans (e.g., Prospero and Carlson 1970).

More recently, with the emergence of advanced global circulation and global chemical transport models there has been a growing appreciation of the important role free tropospheric radionuclide measurements can play in the development and validation of these models, which are an important element in our attempts to understand and predict climatic change. To this end, many modelers have incorporated natural radionuclide tracers such as radon in their formulations, comparing predictions with observations to evaluate model performance (e.g., Jacob and Prather 1990; Feichter and Crutzen 1990). A recent manifestation of this activity was the 1993 World Climate Research Programme (WCRP) Workshop on the Parameterization of Sub-grid Tracer Transport, in which representatives of 21 models presented the global radon distributions (computed using a common source function) predicted by their models. However while the *intra*comparisons between models were a useful and valuable exercise, *inter*comparisons with data were limited by a lack of free tropospheric observations.

The three (piggyback) radon-related projects carried out aboard the Kuiper Airborne Observatory (KAO) over the last decade have addressed both of these applications. Our first project, in which the limitations of our equipment restricted our measurements to periods of level flight, revealed the systematic presence of unexpectedly high radon concentrations in the upper troposphere. Our second project focused on instrument development in support of an automatic radon measuring instrument which was eventually flown aboard a NASA ER-2 High Altitude Research Aircraft in NASA's Stratosphere-Troposphere Exchange Project (STEP), where it was used to follow the movement of radon-rich tropospheric air into the lower tropical stratosphere. The radon measurements in the third project were made for the specific purpose of global model development and validation, and utilized a new pumped whole air sampling system capable of collecting samples (for postflight laboratory analysis) during the normal ascent and descent of the KAO. These projects are outlined below.

2. Radon measurements in upper troposphere

In 1982, in cooperation with Jean-Claude Le Roulley of the French Centre des Faibles Radioactivitiés, our research group installed a radon measurement instrument aboard the KAO. The goal of this project was to look for small traces of radon in the lower mid-latitude stratosphere, which would have been evidence for a movement, in mid-latitudes, of tropospheric air into the stratosphere, as postulated by Danielsen (1968).

Measurements were made while the plane was in level flight, at altitudes of 37, 39, 41 and 45,000 feet. Samples were collected by passing ambient outside air through a filter for periods of 20 to 40 minutes, using an inlet specially designed and fabricated for this purpose. An on-board detector was used to monitor the alpha activity of the short-lived radon progeny present on the filter immediately after sampling. As these short-lived species are in equilibrium with radon in the free troposphere and stratosphere, their activity is indicative of the ambient radon concentration (Larson 1973; Polian 1984).

As it happened, we never observed a detectable quantity of radon while the plane was flying in the stratosphere. This might conceivably have been an artifact resulting from the long sampling time of our instrument, but in any case we were not able to provide support for Danielsen's (1968) hypothesis. Even so, we did make a totally unanticipated finding---the systematic occurrence of surprisingly high radon concentrations in the summertime upper mid-latitude troposphere. A frequency distribution plot of the 61 upper tropospheric observations made during the summers of 1983 and 1984 shows a distinct bimodal distribution, with approximately 40% of the observations falling close to 1 pCi/SCM---the "expected" value---and 60% clustering in a high concentration mode centered at ~11 pCi/SCM. Trajectory and synoptic analyses for two of the flights on which high radon concentrations were observed indicated that the radon-rich air originated in the Asian boundary layer, ascended in cumulus updrafts, and was carried eastward in the fast moving air on the anti-cyclonic side of the upper tropospheric jet. Transit times were on the order of 3 days, though in one instance transport from China to a point a few hundred kilometers west of San Francisco occurred in 48 hours (Kritz et al. 1990).

These findings, together with the frequency with which high radon concentrations were observed, suggested that the combination of rapid vertical transport from the surface

boundary layer to the upper troposphere, followed by rapid horizontal transport eastward could be an efficient mode of transport not only for radon, but for chemically reactive trace constituents as well, whose global distribution and chemical effects are an important factor in the evaluation of global pollution and global climatic change. Our radon measurements and the transport mechanism they elucidated led to a wider recognition of the inadequacy of the mathematically tractable but physically unrealistic diffusive vertical transport parameterizations used in many of the global chemical transport models of the time, and of the need to improve such parameterizations in these models; e.g., Brost and Chatfield (1989), Balkanski et al. (1992).

3. Systematic radon profiling to test and validate global transport models

The success of our upper tropospheric program led to a follow-on project, for which we built a fast sampling system capable of collecting whole air samples (for post-flight laboratory analysis) during the normal ascent and descent of the KAO. However unlike our first project, whose goal was to use radon as an indicator of individual troposphere-to-stratosphere exchange events, this second project was designed to obtain a statistically significant inventory of vertical profiles spanning the mid troposphere, to serve as a benchmark for testing the performance of global circulation and global chemical transport models (as was done in the WCRP workshop referred to earlier.)

The first phase of this project was carried out in the spring and summer of 1994. While these results have not yet been released, they have already attracted considerable interest from the modeling community. We hope to receive funding to continue and expand this work in 1995 and 1996, continuing our KAO profiles program for at least another year and flying aboard a second, dedicated aircraft to make a series of observations designed to test the transport parameterizations of a specific global chemical transport model.

4. Radon measurements in the lower tropical stratosphere

In late 1983 NASA organized the Stratosphere-Troposphere Exchange Project (STEP), a multi-agency effort to investigate the mechanisms and rates of irreversible transfer of mass, trace gases and aerosols from the troposphere into the stratosphere, and to explain the observed dryness of the stratosphere (Russell et al. 1993). The STEP Tropical Experiment, conducted in January-February 1987 from Darwin, Australia focused on the troposphere-to-stratosphere movement of air in the tropics, where the greater portion of such movement is believed to occur (Brewer 1949), with particular emphasis on exchange and dehydration associated with tropical cirrus and cumulo-nimbus clouds. Radon, because of its inertness, short (3.8 day) half-life, and immunity from removal by the processes thought to be responsible for the dehydration of air entering the stratosphere (Danielsen 1982), was a near-ideal tracer for air of recent tropospheric origin; in particular, the observation of stratospheric air with high radon and low total water contents would be unambiguous proof of the recent tropospheric provenance of this air, and of an effective dehydration process occurring during its movement into the stratosphere.

The Darwin experiments were flown aboard a NASA ER-2 high altitude research aircraft. Because of space and operational constraints we had to redesign our manually operated KAO system as an automatic instrument with both a faster response time and approximately one fifth the weight and volume. A key element in this task was reducing the size of the detector used to monitor the alpha activity of the exposed filters; on our KAO instrument this component was about the size of a five gallon can!

Our approach was to replace the ZnS scintillator/photomultiplier tube technology used in our KAO detector (where weight and size were not primary considerations) with a small solid-state, surface barrier detector. A key question here was whether the new detectors would work satisfactorily in the cosmic ray environment of the upper troposphere and lower stratosphere. As there was no assurance that they would, we would not have undertaken to build this new instrument had we not the possibility of testing the new detectors and their associated electronics aboard the KAO, side by side with our proved instrumentation. These flights aboard the KAO allowed us to optimize the performance of the new detectors and was an essential factor in the development of our instrument, and in the success of our measurements in the STEP Tropical Experiment---where we did in fact observe several instances of stratospheric air with high radon and low water contents (Danielsen 1993; Kritz et al. 1993).

5.0 Acknowledgments

While space limitations prevent us from recognizing all of the many people who made important, essential contributions to the success of our program, we would like to single out the contributions of Lou Haughney and Jim McClenahan, whose support and guidance at a point where our experience with airborne instrumentation was very limited made possible the original 1982 experiment which was the precursor to all that has followed.

6.0 References

Balkanski, Y., Jacob, D., Arimoto, R. and Kritz, M. 1992, J. Atmos. Chem., 14, 353

Brewer, A. 1949, Quart. J. Roy. Meteor. Soc., 75, 351

Brost, R. and Chatfield, R. 1989, J. Geophys. Res., 94, 5095

Danielsen, E. 1968, J. Atmos. Sci., 25, 502

Danielsen, E. 1982, Geophys. Res. Lett., 9, 605

Danielsen, E. 1993, J. Geophys. Res., 98, 8665

Feichter, J. and Crutzen, P. 1990, Tellus, 42B, 100

Jacob, D. and Prather, M., 1990, Tellus, 42B, 118

Kritz, M., Le Roulley, J.-C., and Danielsen, E. 1990, Tellus, 42B, 46

Kritz, M., Rosner, S., Kelly, K., and Chan, K. 1993, J. Geophys. Res., 98, 8725

Larson, R. E. 1973, Nucl. Instr. and Meth., 108, 467

Liu, S., McAfee, J., and Cicerone, R. 1984, J. Geophys. Res., 89, 7291

Polian, G. 1984, These de docteur de l'Universite Pierre et Marie Curie, Paris

Prospero, J. and Carlson, T. 1970, Science, 167, 974

Russell, P., Pfister, L. and Selkirk, H. 1993, J. Geophys. Res., 98, 8563

omit

Session Five

The Enrichment of the Interstellar Medium

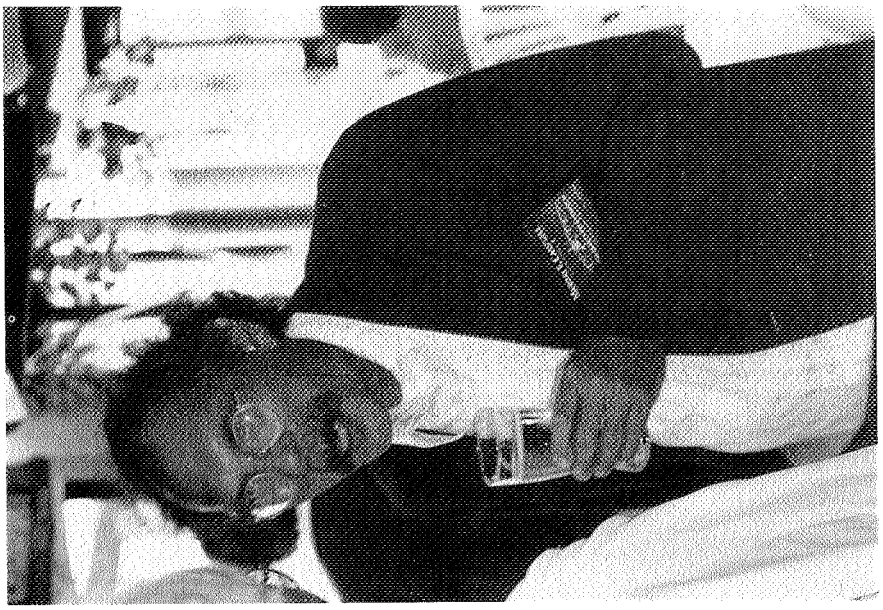

Murray Campbell

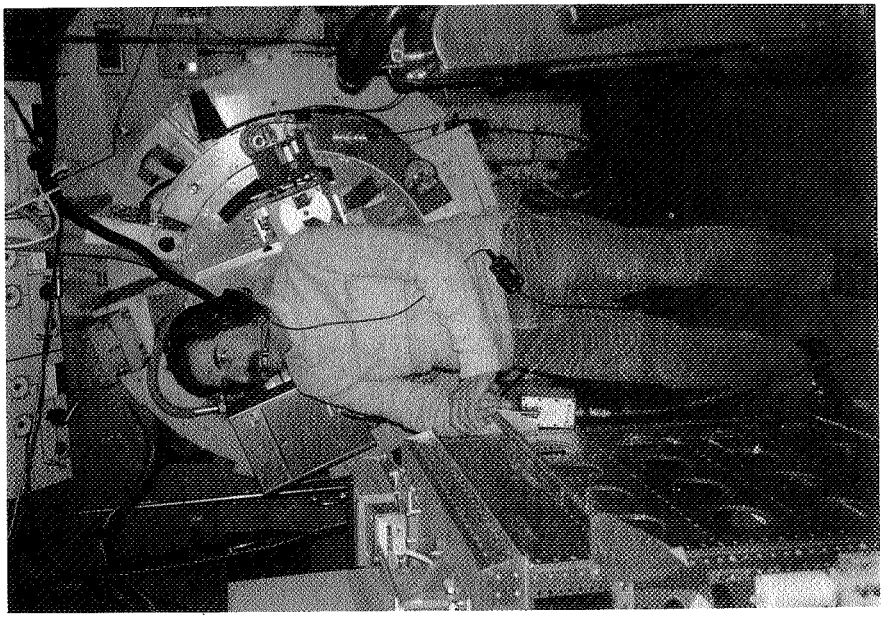

Martin Cohen

Airborne Astronomy Symposium on the Galactic Ecosystem
ASP Conference Series, Vol. 73, 1995
M.R. Haas, J.A. Davidson, and E.F. Erickson (eds.)

The Enrichment of the ISM: Evolved Stars and Meteorites

M. Jura
Department of Physics and Astronomy, UCLA, Los Angeles, CA 90024

Abstract. Small inclusions (diameters ranging from 0.001 μm to 10 μm) of isotopically anomalous material within meteorites were almost certainly produced in mass-losing stars. These solid particles preserved their individual identities as they passed through the interstellar medium and the pre-solar nebular. The relationship between studies of meteorites and mass-losing red giants is explored.

1. Introduction

One of the most fundamental results of modern astrophysics is that essentially all the elements heavier than helium have been synthesized within stars and returned to the interstellar medium. This is a topic that has received the attention of many different authors. Here, I focus on recent developments on how studies of meteorites can help us understand the return of matter to the interstellar medium by mass-losing red giants, a kind of star that can be very profitably studied in the infrared.

In the solar neighborhood, if all the main sequence stars between 1 and 5 $M_\odot$ ultimately evolve into white dwarfs of 0.7 $M_\odot$, then the mass return rate is about 8×10^{-4} $M_\odot$ kpc^{-2} yr^{-1} when projected onto the plane of the Milky Way. The mass-losing red giants on the Asymptotic Giant Branch are estimated to be losing between 3 and 6×10^{-4} $M_\odot$ kpc^{-2} yr^{-1}. About half of this mass loss is from oxygen-rich red giants and about half from carbon-rich red giants (Jura & Kleinmann 1989; Jura 1991). Within the uncertainties, we find about as many sources of interstellar matter as we expect.

Studies of meteorites may serve as very detailed and precise probes of the conditions in mass-losing red giants (Anders & Zinner 1993; Ott 1993). During the past few years, it has become possible to measure the isotopic abundances of small inclusions in meteorites, and it seems that many of these inclusions have survived essentially intact from their original stellar source.

2. Interstellar Grains in Meteorites

There are three kinds of isotopically anomalous inclusions in meteorites which appear to originate in carbon-rich stars: diamonds, SiC and "graphite". The diamonds are very small (~ 10 Å) and of unknown origin. About 95% of the mass of the SiC particles have diameters between 0.3 and 3 μm, while the "graphite" is found mainly to have diameters between 0.8 and 7 μm. Only parts per million

of the mass in primitive meteorites is found in these inclusions; most of the meteoritic material has been highly processed in the solar nebula. It seems likely that the largest particles are the hardiest, and the measured size distribution of these inclusions is not representative of the size distribution of their parent populations.

The SiC particles are thought largely to originate from mass-losing carbon stars because they mostly exhibit $^{12}C/^{13}C$ ratios near 40, which is characteristic of these stars and vastly different from the terrestrial value of 89. Solid SiC is thought to be a significant fraction (perhaps ~5% in the well-studied IRC+10216) of the dust mass produced in the outflows from carbon-rich stars (Martin & Rogers 1987; Griffin 1990; Lorenz-Martins & Lefévre 1993). Because the source of these SiC grains can be identified as mass-losing carbon stars, it is possible to make detailed comparisons between measurements and models for a wide variety of isotopic ratios including those of silicon, magnesium, titanium and nitrogen, as well as carbon (Gallino et al. 1994; Hoppe et al. 1994).

3. Passage Through the Interstellar Medium

For a number of years, the best model for the size distribution of interstellar grains was that of Mathis, Rumpl & Nordsieck (1977). They aimed to reproduce the interstellar extinction curve between 0.11 μm and 1.0 μm, and they derived a size distribution such that for the carbon-rich particles,

$$n(a)\ da = n_0\ a^{-3.5}\ da \tag{1}$$

with a maximum value for a of close to 1 μm. The upper limit to the size of the grains was not very well determined.

With advances in infrared instrumentation, it has been possible to measure the interstellar extinction curve to 10 μm. Consequently, it has been possible to make a more accurate estimate of the numbers of larger interstellar grains since the extinction properties scale as $2\pi a/\lambda$, where λ is the wavelength of light that is being used to study the grain. Kim, Martin & Hendry (1994) have argued that if a is the radius of a grain, then the size distribution of the carbon-rich grains in the interstellar medium can be represented by the expression:

$$n(a)\ da = n_0\ a^{-3.48}\ exp(-a/a_b)\ da \tag{2}$$

where $a_b = 0.28$ μm. With this representation, 94% of the mass of the carbon grains is found in particles with diameters smaller than 1 μm, while 0.1% of the carbon is found in particles with diameters larger than 3 μm. That is, there is a tail of large particles in the inferred size distribution of interstellar carbon grains.

4. Origin in Red Giants

It is still unsolved which types of carbon-rich red giants are responsible for the inclusions found in meteorites. IRC+10216 is the best studied mass-losing carbon star, and it can be evaluated as a possible source for grains larger than

1 μm in diameter, even though earlier models for the particle size distribution of the circumstellar material ejected by this star have predicted that the grains are smaller in diameter than 0.1 μm. For example, Martin & Rogers (1987) suggested that the data could be represented by a single size of the particles with a diameter of 0.10 μm. Griffin (1990) proposed that a size distribution similar to that of equation (1) above with the maximum diameter of the grains being 0.10 μm could explain the observational data.

Jura (1994) has reconsidered the data for IRC+10216. It was argued that the observed spatial distribution of the molecule rings found around IRC+10216 (such as HC_3N, Bieging & Tafalla 1993) can be explained if there are a large number of small grains. In this analysis, the best estimate of the total dust loss rate is derived from the infrared emission. Given the total amount of dust being lost by the star, then to produce the opacity required to protect the molecules from the diffuse interstellar ultraviolet radiation field, a large number of small grains ($a < 0.01$ μm) are required. However, not all the grains can be this small. Tamura et al. (1988) have detected a circumstellar reflection nebulosity around IRC+10216 by measuring spatially extended polarization at 2.2 μm. This polarization results from scattering by the circumstellar dust. The small grains that can account for the ultraviolet opacity are too small to produce measurable scattering at 2.2 μm. Therefore, some larger grains are required. Jura (1994) found that all the data for IRC+10216 can be reproduced if

$$n(a)\ da = n_0\ a^{-3.5}\ exp(-a/a_b)\ da \qquad (3)$$

where $a_b \approx 0.10$ μm. With this model, most of the grains are small, in agreement with previous studies, but this size distribution does allow for a tail of micron-sized carbon grains. However, even in this tail, there are predicted to be very few particles with diameters larger than 3 μm, although particles larger than this size are found in the meteorites. Furthermore, this model for the size distribution of the grains ejected from IRC+10216 has an average size that is smaller than the size of the carbon grains inferred to be present in the interstellar medium. Therefore, even though IRC+10216 seems to produce some grains as large as 3 μm in diameter, grains ejected from carbon stars besides IRC+10216 should be considered.

5. Future Studies

According to the models of Dominik et al. (1990), the mean value of the particles produced in the outflows from carbon-rich red giants tends to increase for stars with higher outflow velocities and luminosities. According to Barnbaum, Kastner & Zuckerman (1991), the luminosity and outflow velocity of a carbon star are correlated with each other. IRC+10216 is very well studied because it is so nearby (perhaps 130 pc). However, its outflow velocity of 15 km s^{-1} is not especially large and therefore the grains around this star may not be especially big. In view of the prediction by Dominik et al. (1990), it will be worthwhile to study the size distributions of particles ejected from carbon stars with outflow velocities near 30 km s^{-1}, about the maximum found for carbon stars. These studies will require improved instrumentation because the known stars with these higher velocity outflows, such as AFGL 2233, are $\sim$1 kpc from the Sun (Jura & Kleinmann 1989), much further away than IRC+10216.

The particles larger than 1 micron found in meteorites can be studied in astrophysical contexts by their scattering because the amount of scattered light is very sensitive to particle size if the diameter, d, is smaller than λ/π. Therefore, if we want to consider the number of grains with diameters of 5 or even 10 μm, we want to study, both by direct imaging and polarization, the extended reflection nebulosity around stars at wavelengths from 15 to 30 μm. Images at longer wavelengths are more sensitive to thermal emission than scattering (Harvey et al. 1991).

Another focus of future concern should be spectroscopy of the infrared emission from the grains. IRC+10216 displays an emission feature near 11.3 μm, and from the relative weakness of this feature, it has been argued that there is more amorphous carbon than SiC in the outflow (e.g., Lorenz-Martins & Lefévre 1993). Future spectroscopic studies will enable us to identify other substances in the outflows as well.

Spectroscopic mapping should also prove to be of great value in understanding the physics of these outflows. For example, in the Egg Nebula, in order to explain the morphology of the HC_7N molecular emission (Nguyen-Q-Rieu, Winnberg & Bujarrabal 1986), Jura & Kroto (1990) have proposed that there are significant numbers of grain-grain collisions concentrated in a hollow cone in the outflow from this star. Similarly, in the Red Rectangle, the emission feature at 5800 Å appears to form an "X-shaped" pattern centered on the observed star, HD 44179 (Schmidt & Witt 1991). This feature is probably produced by some carbon-rich species, and may, in fact, be a carrier of the mysterious Diffuse Interstellar Bands (Fossey 1990; Sarre 1991). While spherically symmetric models may represent well the data for many stars, there are objects (AFGL 618, Neri et al. 1992; AFGL 2688, Young et al. 1992; V Hya, Kahane, Maizels & Jura 1988) where the outflow velocity varies with position. The grains that are ejected in these outflows may similarly vary with position.

This work has been partly supported by NASA.

6. References

Anders, E. & Zinner, E. 1993, Meteoritics, 28, 490

Barnbaum, C., Kastner, J. H. & Zuckerman, B. 1991, AJ, 102, 289

Bieging, J. H. & Tafalla, M. 1993, AJ, 105, 576

Dominik, C., Gail, H.-P., Sedlmayr, E. & Winters, J. M. 1990, A&A, 240, 365

Fossey, S. F. 1990, Ph. D. thesis, University College London

Gallino, R., Raiteri, C. M., Busso, M. & Matteucci, F. 1994, ApJ, 430, 858

Griffin, I. P. 1990, MNRAS, 247, 591

Harvey, P. M., Lester, D. F., Brock, D. & Joy, M. 1991, ApJ, 368, 558

Hoppe, P., Amari, S., Zinner, E., Ireland, T. & Lewis, R. S. 1994, ApJ, 430, 870

Jura, M. 1991, A&AR, 2, 227

Jura, M. 1994, ApJ, in press

Jura, M. & Kleinmann, S. G. 1989, ApJ, 341, 359

Jura, M. & Kroto, H. 1990, ApJ, 351, 222

Kahane, C., Maizels, C. & Jura, M. 1988, ApJ, 328, L25

Kim, S.-H., Martin, P. G. & Hendry, P. D. 1994, ApJ, 422, 164

Lorenz-Martins, S. & Lefévre, J. 1993, A&A, 280, 567

Martin, P. G. & Rogers, C. 1987, ApJ, 322, 374

Mathis, J. S., Rumpl, W. & Nordsieck, K. H. 1977, ApJ, 217, 425

Neri, R., Garcia-Burillo, S., Guélin, M., Cernicharo, J., Guilloteau, S. & Lucas, R. 1992, A&A, 262, 544

Nguyen-Q-Rieu, Winnberg, A. & Bujarrabal, V. 1986, A&A, 165, 204

Ott, U. 1993, Nature, 364, 25

Sarre, P. J. 1991, Nature, 351, 356

Schmidt, G. D. & Witt, A. N. 1991, ApJ, 383, 698

Tamura, M., Hasegawa, T., Ukita, N., Gatley, I., McLean, I. S., Burton, M. G., Rayner, J. T. & McCaughrean, J. 1988, ApJ, 326, L17

Young, K., Serabyn, G., Phillips, T. G., Knapp, G. R., Gusten, R. & Schulz, A. 1992, ApJ, 385, 265

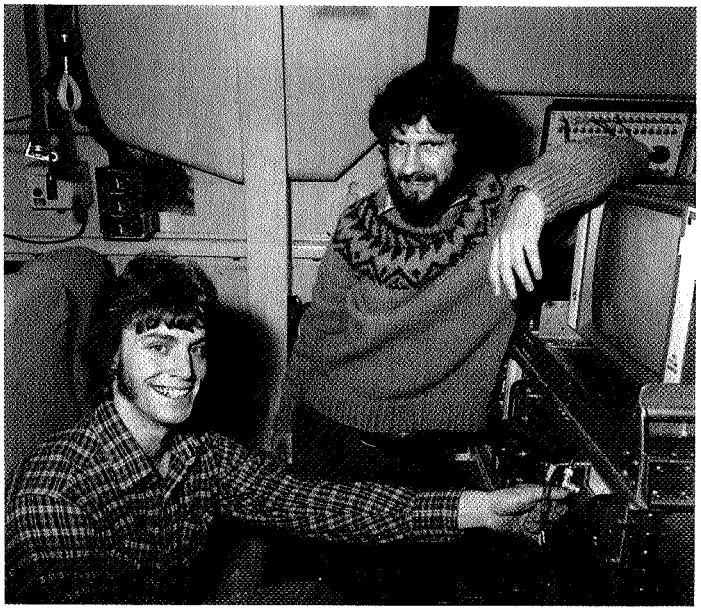

Dan Watson, John Storey (1981)

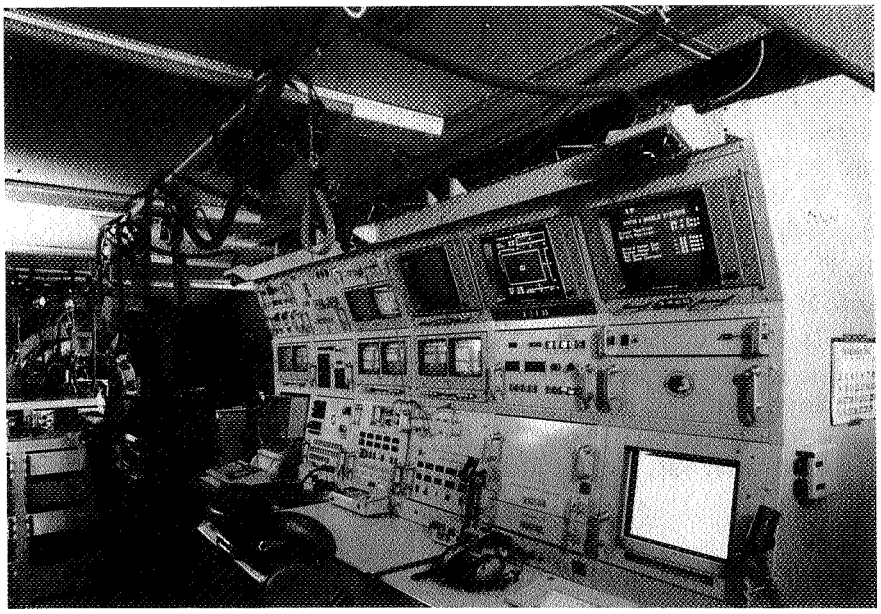

Main Console (1990)

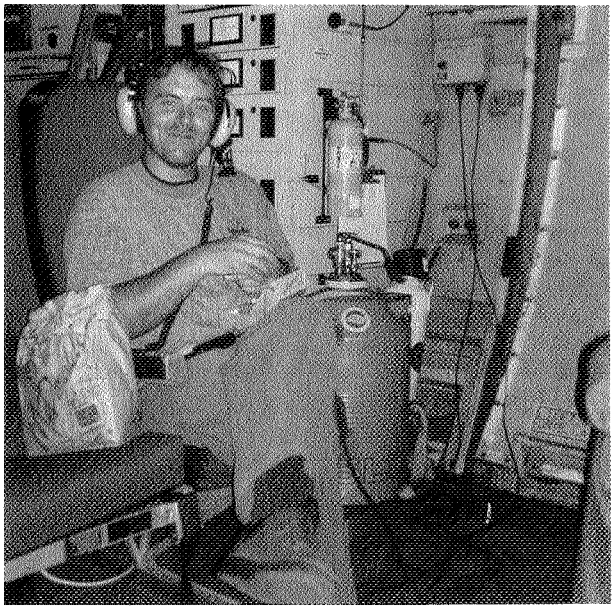

Tom McMahon

Airborne Astronomy Symposium on the Galactic Ecosystem
ASP Conference Series, Vol. 73, 1995
M.R. Haas, J.A. Davidson, and E.F. Erickson (eds.)

Supernovae, Supernova Remnants, and Superbubbles

J. Michael Shull[1]
Joint Institute for Laboratory Astrophysics, University of Colorado and National Institute of Standards and Technology, Boulder, CO 80309

Abstract. I review supernovae, supernova remmants, and superbubbles in the interstellar medium, with an emphasis on infrared studies of these phenomena. Superbubbles are likely to be relevant for understanding such Galactic and extragalactic issues as the photoionization of gas in the Galactic halo, "superwinds", and the contribution of "starbursts" to photoionization of the intergalactic medium.

1. Introduction

Supernovae (SN) provide a connection to a wide range of astrophysical processes in the context of the themes of this meeting. First and foremost, they provide the nucleosynthetic sources of many heavy elements (O, Fe, etc.). Second, Type II SN (from stars with initial masses $M \geq 8\ M_\odot$) are believed to be the progenitors of pulsars. Third, the supernova remnants (SNRs) of these explosions produce blast waves and large bubbles of hot gas which transport these heavy elements across large regions of the interstellar medium (ISM). These SNRs provide chemical transport and sources of hot halo gas for the "galactic fountain" (Shapiro & Field 1976; Bregman 1980). Fourth, the kinetic energy introduced at a rate of one SN (10^{51} ergs) every 30 yrs throughout the Galaxy (10^{42} ergs s^{-1}) is sufficient to power the fountain and generate the observed H I velocity dispersion (Lockman & Gehman 1991) and turbulence in the diffuse ISM (Slavin, Shull, & Begelman 1993). Fifth, because massive stars are produced in OB associations, the collective effects of their stellar winds and SN produce the much larger superbubbles, which are more disruptive of the ISM than individual SNRs.

It now appears likely that the largest superbubbles may break through the Galactic H I disk layer (Heiles 1990; Mac Low, McCray, & Norman 1989) and thereby provide conduits for the escape of hot gas and ionizing (LyC) radiation into the Galactic halo. Such processes produce the "galactic fountain" and are probably needed to explain a number of observations: the diffuse Hα emission (Reynolds 1989), the C IV emission and absorption lines (Martin & Bowyer 1990; Shull & Slavin 1994), the pulsar dispersion measure (Reynolds 1991), and the COBE observations of [N II] 205 and 122 μm emission (Wright et al. 1991).

---

[1] also at Center for Astrophysics and Space Astronomy, Department of Astrophysical, Planetary, and Atmospheric Sciences, University of Colorado, Boulder

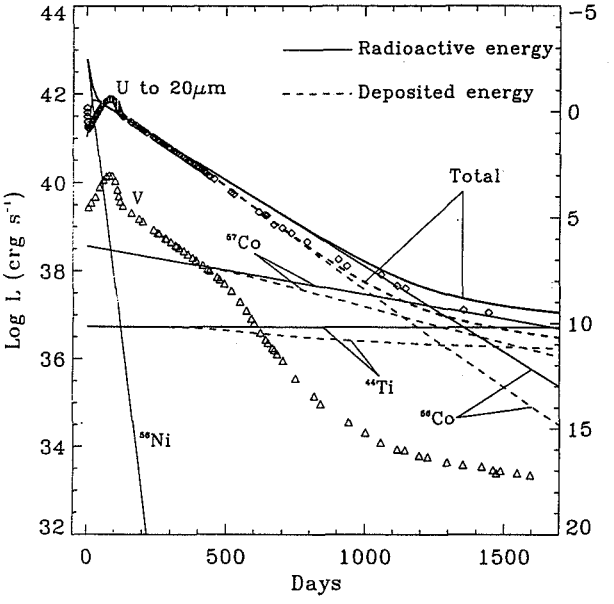

Figure 1. Luminosities and radioactive sources for SN 1987A (McCray 1993). Solid curve is total radioactive power, dashed curve shows power deposited in envelope, and thin lines show contributions from individual isotopes. Triangles show the V-magnitude.

This review will cover three topics, each related to the effects of SN explosions on the ISM of the Milky Way and external galaxies. The major emphasis will be on infrared studies of these phenomena. First, I will discuss the SN explosions themselves, particularly SN 1987A. Second, I will describe IR studies of SNRs. Third, I will discuss the collective effects of the stellar winds and SN from OB associations, and the resulting superbubbles. I conclude the review with some discussion of the relevance of superbubbles to such Galactic and extragalactic issues as the photoionization of gas in the Galactic halo, nuclear "superwinds", and the contribution of starburst galaxies to the ionization of the intergalactic medium.

2. Supernovae

The date of this conference presentation (July 8, 1994) marked "Day 2692" in the life of the celebrated SN 1987A in the Large Magellanic Cloud, from which we have learned so much. Because Diane Wooden will present a full-length review of the infrared/KAO science associated with this object, I will keep my

comments brief and more general in nature. Recent full-length reviews of this topic are given by McCray (1993) and Wooden et al. (1993).

This supernova galvanized the astronomical community at all wavelength bands, and it can truly be said that major contributions to our understanding were made by γ-ray, X-ray, optical, infrared, and radio observations. In the infrared, one of the major contributions came from the observation of emission lines of nickel, argon, and cobalt (Rank et al. 1988) and of [Fe I] and [Fe II] (Moseley et al. 1989; Haas et al. 1990; Colgan et al. 1994). The lines of radioactive [Co II] 10.52 μm and of stable [Ni II] 6.64 μm, [Fe II] 17.94 μm, and 25.99 μm are especially important for measuring the amounts of optically thin products of nucleosynthesis mixed into the clumps of ejecta. For example, Haas et al. (1990) found 0.026 $M_\odot$ of high-velocity ($V \leq 3000$ km s^{-1}) optically-thin Fe II, which is 40% of the total Fe deduced from the light curve power. Colgan et al. (1994) measured an abundance ratio, Ni/Fe $= 0.06 \pm 0.02$, near the solar value. The light curve for the first 1600 days is shown in Figure 1, and the time history of composite infrared spectra, compiled by McCray (1993), are shown in Figure 2. Several major scientific understandings were gleaned from this explosion and its aftermath:

1. The SN 1987A produced 0.07 ± 0.01 $M_\odot$ of radioactive (^{56}Ni) debris, whose γ-rays powered the light curve (Figure 1) for several years from decay to ^{56}Co (8.8 day lifetime) and ^{56}Fe (111.3 day lifetime). The late-time light curves are probably powered by the isotopes ^{57}Co (391 day lifetime) and ^{44}Ti (78 year lifetime). The possibility of residual energy deposition from a pulsar remains unsettled.

2. The interior structure of the remnant must have a "frothy" structure (Li, McCray, & Sunyaev 1993) consisting of "bubbles" of hot, low-density material generated by the heating of trapped Ni/Co radioactivity, occupying $\geq 30\%$ of the volume, and helping to define the filamentary ejecta.

3. Dust formation began somewhere between days 400 and 500 (Roche, Aitken, & Smith 1993; Wooden et al. 1993) with perceptible reprocessing of the optical radiation into mid-infrared continuum emission (Dwek et al. 1992) as shown in Figure 2. The total dust mass is of order 3×10^{-4} $M_\odot$ (Meikle et al. 1993; Wooden et al. 1993).

4. This Type II supernova produced 0.07 $M_\odot$ of ^{56}Fe, compared to a typical value of 0.5 $M_\odot$ from Type I. A sub-luminous SN resulted, owing to an explosion in a smaller blue supergiant. Thus, SN II contribute to Fe nucleosynthesis, but are poor "standard candles", in contrast to SN I.

5. Although the origin of a $0.03 - 0.05$ $M_\odot$ ring at 10^{18} cm (Fransson et al. 1989) around SN 1987A is a mystery, studies of its spectra and kinematics led to an accurate LMC distance of 51.2 ± 3.1 kpc (Panagia et al. 1991). Recent HST images of additional rings (Burrows 1994) and an hourglass-shaped nebula (Wampler et al. 1990) point to circumstellar matter compressed by pre-SN outflows. By coupling the SN ejecta dynamics to ring properties, Luo, McCray, & Slavin (1994) predict a spectacular display when the SN ejecta strike the ring in the year 2000 ± 3 A.D. It would be helpful if SOFIA were aloft to observe this event.

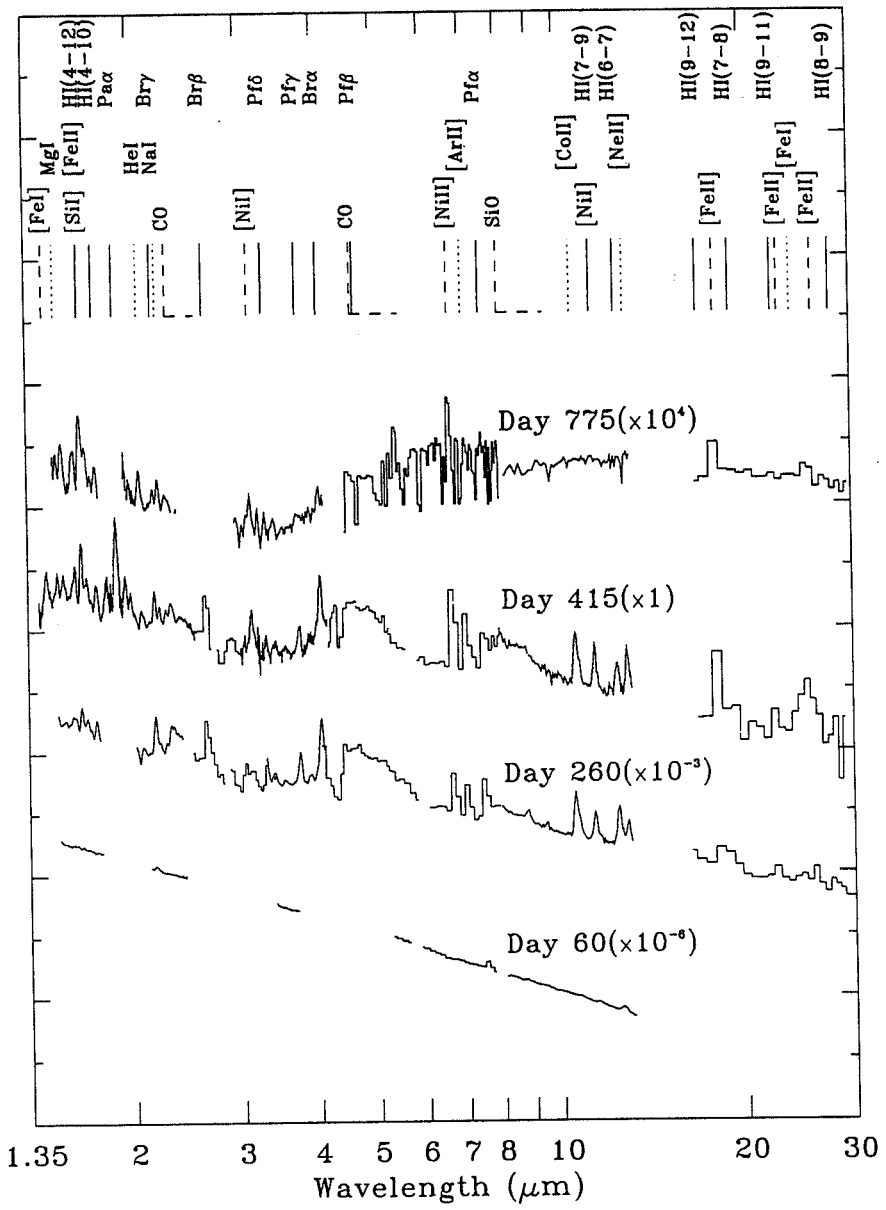

Figure 2. Composite spectra of SN 1987A (see McCray 1993 for original data sources). The flux in each spectrum, from day 60 to day 775, has been multiplied by the number in parenthesis.

While the explosion of a nearby SN in the LMC was a fortunate event, probably occurring once every 300 yrs on average, one might ask whether such infrared analyses could be performed on SN in more distant external galaxies. Van Buren & Norman (1989) estimated that infrared supernovae might be observable in "starburst galaxies" between 5 and 50 Mpc distant, through the [Co II] 10.52 μm line or through K-band imaging, for example in M 82 or NGC 253. In each technique, major technical challenges arise. The [Co II] line must be separated spectrally from the [S IV] 10.52 line, which is expected from H II regions around the hottest stars. In the K-band imaging, one must be able to discern the new source from a background of massive stars and nebulae in these galaxies.

3. Supernova Remnants

After the initial SN explosion, the luminosity fades over a period of months to years, and the "remnant phase" begins. Over the past decade, astronomers have realized the importance of circumstellar matter in shaping the emission and morphology of young remnants. Pre-SN mass loss from red supergiants (and blue supergiants, as was the case in SN 1987A) often sets the stage for the interactions of the blast wave with the surrounding medium. In SN 1987A, the rings located some $0.3 - 1$ pc away from the explosion will light up when the blast wave strikes them $\sim 10 - 15$ years after the explosion. A similar disk-like torus has been seen around the Crab Nebula (Fesen, Martin, & Shull 1992), which appears to have been shaped by a bipolar outflow from a period of pre-SN stellar mass loss. The interactions of the SN with circumstellar material are complex, and the interested reader is referred to reviews by Chevalier (1992a,b,c).

At later times, over the next 10^4 to 10^5 years, the SNR passes through an ejecta-dominated stage, an "adiabatic stage" (Sedov-Taylor), and eventually a "radiative stage" (snowplow solution). Examples of the ejecta stage can be found among young remnants such as Tycho, Kepler, Cas A, and SN 1006, which are quite bright in both X-rays and the infrared, as the dust radiates profusely in the hot interior before being destroyed by sputtering. Most of a SNRs lifetime, however, is spent in the latter two stages, during which time the shells expand to radii of $20 - 100$ pc, slow to velocities of $10 - 30$ km s^{-1}, and sweep up large masses ($\sim 10^{4-5}$ $M_\odot$) of the surrounding ISM. There is little wonder that SN are such powerful sources for stirring up the ISM; a single 8–100 $M_\odot$ OB star sweeps over a volume of space containing thousands of times more gaseous mass, providing chemical enrichment across some $50 - 100$ parsecs.

Virtually all Galactic supernova remnants (SNRs) are identified by their nonthermal radio emission. However, observations at other wavelengths are often better suited for determining some remnant properties, including the shock velocity, postshock density and temperature, swept-up mass, and sometimes even shell morphology. Until the last decade, the infrared was one of the least utilized bands for SNR studies, despite the fact that IR emission may be the dominant cooling mechanism for most SNRs throughout their lifetime (Draine 1981; Dwek et al. 1987).

The IR has several important advantages over other spectral regions for SNR studies. First, a substantial fraction of SNRs are expected to be strong IR

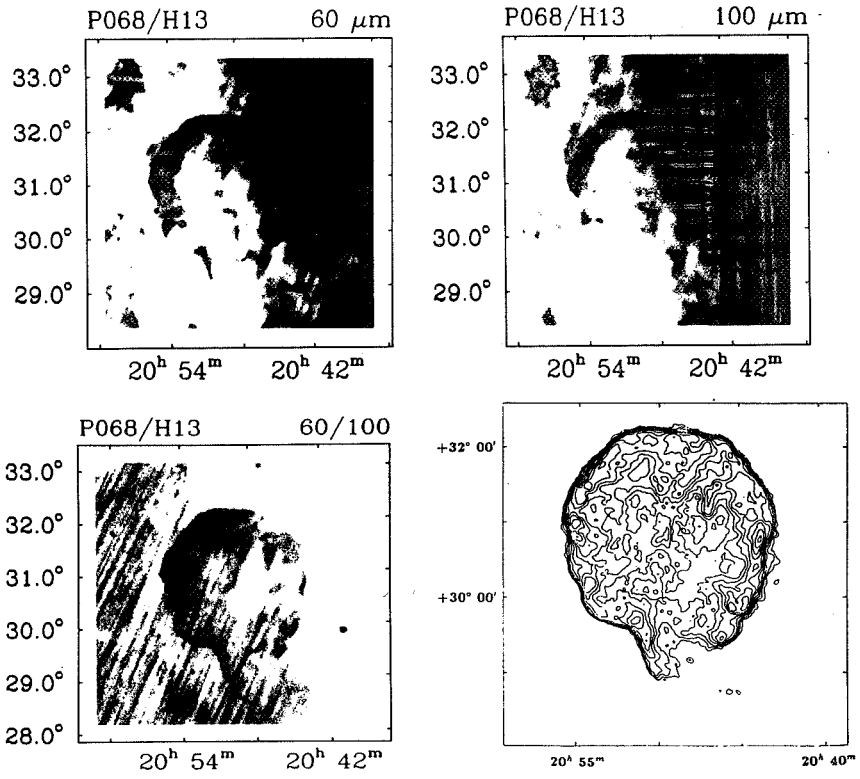

Figure 3. IRAS Skyflux images of the Cygnus Loop at 60 and 100 μm (Saken et al. 1992) together with the 60/100 μm ratio map and the *Einstein* IPC X-ray map from Seward (1990).

emitters from thermal dust and fine-structure lines. Second, interstellar absorption is less of a limiting factor in searches through the Galactic plane. Finally, IR observations can detect the shock-heated and radiatively-heated dust in the massive shells of older remnants, which are poorly studied or undetectable at other wavelengths. Such older remnants ($t \sim 10^5$ yr) often have weak radio, optical, UV, and X-ray emission due to low shock velocities, and yet can be relatively bright in the IR. Some of these old remnant shells have been rejuvenated in radio and optical emission owing to high-velocity pulsars catching up with their SNR shells (Shull, Fesen & Saken 1989; Frail & Kulkarni 1991).

Several individual SNRs have been studied in detail in the infrared. For the brightest remnants, these studies include the remnants of Tycho, Kepler, Cygnus Loop, Cas A, Pup A, and IC 443 (Braun 1987; Braun & Strom 1986a,b; Arendt, Dwek, & Petre 1991; Arendt, Dwek, & Leisawitz 1992) and CTB 80 (Fesen, Shull, & Saken 1988). Braun (1985) and Arendt (1989) used the IRAS Skyflux images to survey the global IR emission properties of resolved Galactic SNRs. The most complete IRAS surveys of Galactic SNRs are by Arendt (1989), who examined 157 SNRs and found IR emission from 51, and by Saken, Fesen,

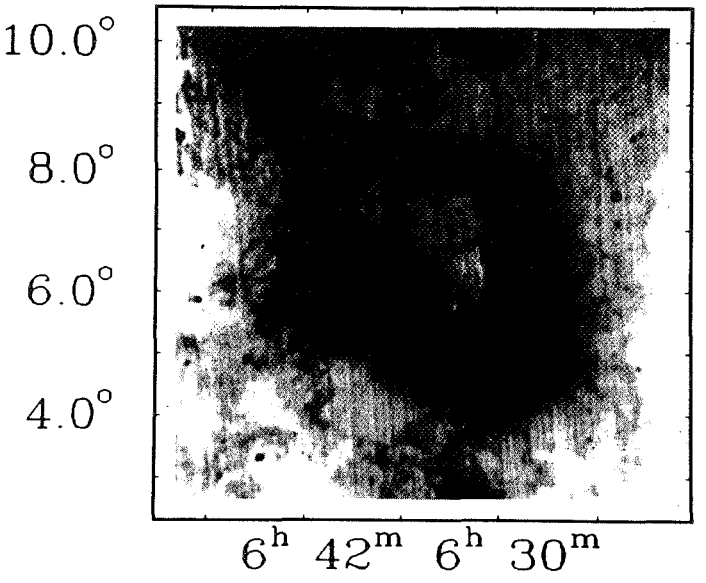

Figure 4. IRAS Skyflux 60/100 μm ratio image of the Monoceros Loop (Saken et al. 1992)

& Shull (1992), who examined 161 remnants and found IR emission from 44. Thus, about 25% of the known radio SNRs are detected by IRAS, a fraction comparable to the detection efficiency in the X-ray.

One of the biggest difficulties in infrared SNR detection is confusion with ambient dust emission and compact sources. This problem is especially acute in regions of star formation and H II regions. Figure 3 illustrates the IRAS Skyflux images of the Cygnus Loop at 60 and 100 μm, together with the "ratio map" of 60/100 μm emission (the infrared version of B-V color) which is particularly effective at distinguishing weak emission features from the background. Figure 4 shows the 60/100 ratio map of the Monoceros Loop. Evidently, the dust emission from SNR shells has a sufficiently different color temperature that it stands out against the background.

Spectroscopically, very little work has been done on SNRs in the infrared. In broad-band IRAS emission, most SNRs exhibit clear evidence for multiple temperature components (Figure 5). With only four bands, at 12, 25, 60, and 100 μm, the IRAS data allow only two-component fits, which generally fit a "cold dust" and "warm dust" component and assume a $\lambda^{-1.5\pm0.5}$ emissivity to derive dust masses. The resulting shell masses, within the validity of the model assumptions, are fairly inaccurate. In fact, the entire procedure is incredibly crude and model-dependent, since dust grains almost certainly exhibit a range of temperatures as a result of a wide size distribution and stochastic heating of the smallest grains (Draine & Anderson 1985; Dwek 1986). In addition, several of the IRAS bands are probably contaminated by fine-structure line emission from [O I] 63 μm and [O III] 52 and 88 μm. Burton et al. (1990) detected clear

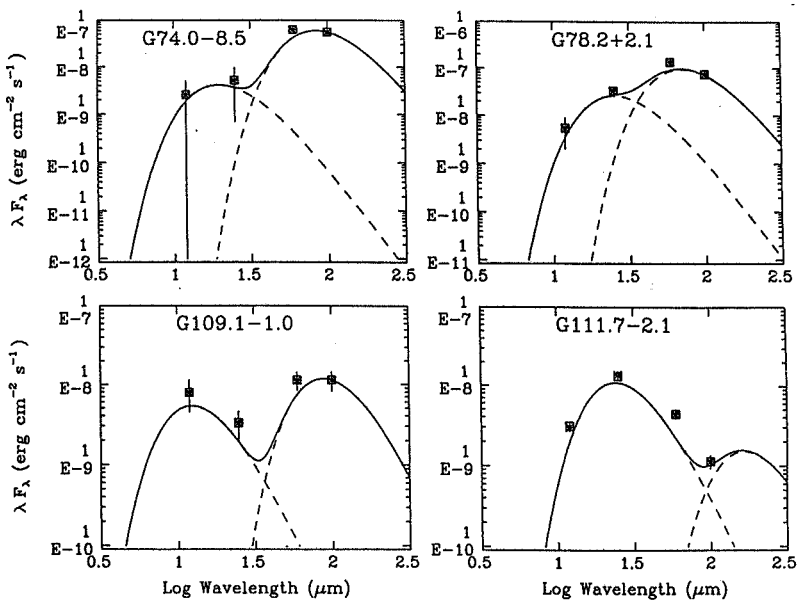

Figure 5. IRAS emission from four SNRs (Saken, Fesen, & Shull 1992) showing the spectral fits with two grain temperature components.

evidence of [O I] emission toward the remnant IC 443. Additional studies with ISO and future IR telescopes are sorely needed in order to obtain accurate SNR shell masses. Multiple wavelength channels will allow more sophisticated grain temperature modelling, while line subtraction will improve the accuracy of the 50 – 90 μm measurements.

I would like to conclude this section with an example of a new class of "pulsar-rejuvenated SNRs" discovered by IRAS (Shull, Fesen, & Saken 1989). Figure 6 shows one of best examples of this phenomenon. Among other suggested examples of this phenomenon, one in particular has been strikingly confirmed (Frail & Kulkarni 1991) in the remnant G5.4-1.2 ("The Duck"). In this remnant, the radio shell has just been penetrated by pulsar PSR 1757-24, which forms the "head of the duck". In these old remnants, the pulsar produced by the SN has a sufficiently high velocity, $V_p = (100 \text{ km s}^{-1})V_{100}$, that it can catch up with its decelerating SNR shell after a time

$$t_c = (6.5 \times 10^5 \text{ yr}) \left(\frac{E_{51}}{n_0}\right)^{1/3} V_{100}^{-5/3}, \quad (1)$$

where the shell radius is assumed to obey the Sedov-Taylor relation,

$$R_s = (31.5 \text{ pc}) \left(\frac{E_{51}}{n_0}\right)^{1/5} t_5^{2/5} \quad (2)$$

for a remnant of energy $(10^{51} \text{ ergs})E_{51}$ expanding into a homogeneous medium of ambient hydrogen density n_0 (cm^{-3}) for a time $t = (10^5 \text{ yr})t_5$. Note that

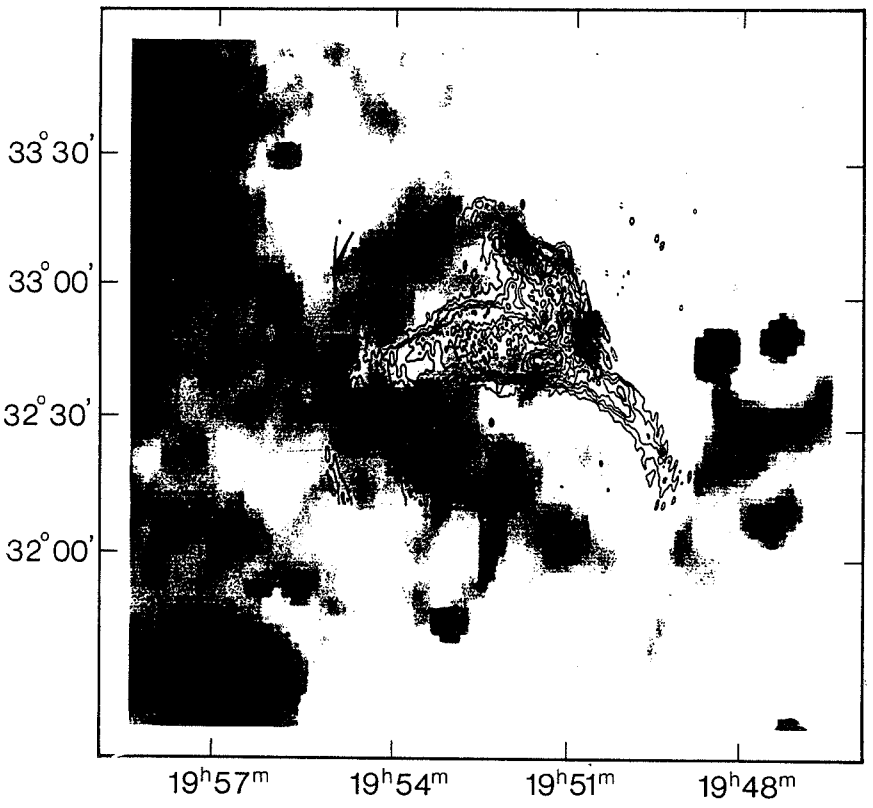

Figure 6. IRAS Skyflux 60/100 μm ratio image of the remnant CTB 80 (Fesen, Shull, & Saken 1988) which was rejuvenated when a fast (300 km s^{-1}) pulsar (Kulkarni et al. 1988) caught up with the remnant shell after $\sim 10^5$ yr.

actual SNRs evolve according to a $t^{0.30}$ power-law (Cioffi, McKee, & Bertschinger 1988) so that pulsars probably overtake their remnant shells somewhat sooner than indicated by equation (1). Also, the ambient medium is unlikely to be homogeneous as assumed. Pulsars are well known to have space velocities in excess of 100 km s^{-1} (Lyne, Anderson, & Salter 1982; Cordes 1986) with a recent survey suggesting a mean value as large as 450 ± 90 km s^{-1} (Lyne & Lorimer 1994). Thus, from equation (1), it would seem likely to find many cases in which pulsars have pierced remnants after periods of 50,000 – 100,000 yrs.

Many remnants appear to have lifetimes of order 10^5 yrs, and the infrared plays an important role in finding the SNR shells. Similarly, the distribution of ambient density in the ISM generally controls the rate of SNR expansion and the ultimate merger with the surrounding medium. Therefore, the distribution of SNR radio lifetimes (Frail, Goss, & Whiteoak 1994), coupled with the distri-

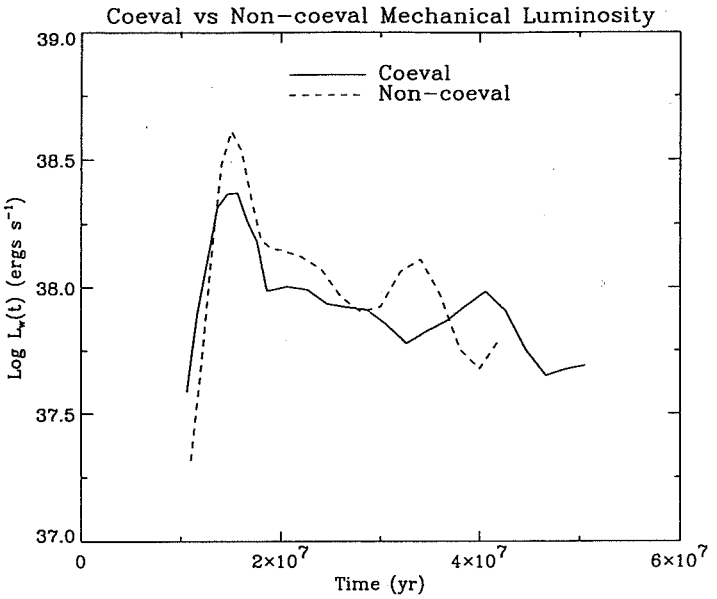

Figure 7. Energy deposition rate, $L_w(t)$, for a coeval and a non-coeval model (Shull & Saken 1995) of an OB association with 100 stars ranging in mass from 8 – 80 $M_\odot$ with an initial mass function $dN(>m)/dm \propto m^{-\Gamma}$ with $\langle\Gamma\rangle = 1.6 \pm 0.3$ (Garmany et al. 1982). Time axes of the two models have been aligned on peaks.

bution of pulsar velocities at birth, can be used to place strong constraints on the density and phase structure of the ISM (Shull et al. 1989).

4. Superbubbles

As discussed earlier, the kinetic energy input from supernovae dominates the gas dynamics and the production of hot gas in the ISM. The first theoretical models to study these effects (Cox & Smith 1974; McKee & Ostriker 1977) treated the SN as isolated, uncorrelated events, but it was soon realized (McCray & Snow 1979) that a more accurate description would consider the spatial and temporal correlations introduced by the fact that the majority, if not all, massive stars (and thus Type II SN) are formed in OB associations. The older, more dispersed Type I SN would still explode as a homogenous population.

Stellar winds and supernovae from OB associations are believed to be responsible for blowing much larger cavities in the ISM. The resulting "supershells" have been seen in H I (21-cm) emission (Heiles 1984) and modeled theoretically by many groups (Bruhweiler et al. 1980; McCray & Kafatos 1987; Tomisaka & Ikeuchi 1986; Tenorio-Tagle & Bodenheimer 1988) using the "constant energy input" assumption. However, by computing the energy deposition from upper main sequence evolutionary tracks, Shull & Saken (1995) showed (Figure 7) that

this is a poor approximation for the first 5–10 Myr in coeval bursts of star formation. In addition, they pointed out that there is strong evidence that the epoch of massive-star formation in OB associations is spread over intervals of 10 – 20 Myr as a result of sub-clustering, continuous or sequential star formation, or delayed collapse of the most massive stars. Thus, the growth of supershells is strongly influenced by this star formation history. In both coeval and non-coeval models, the energy deposition rises steeply as massive stars evolve off the main sequence, resulting in faster shell growth and a shell velocity evolution that differs from the constant-luminosity models. An excess of Wolf-Rayet stars is produced during short (coeval) bursts and in non-coeval models with changes in the initial mass function. This may have been observed in "Wolf-Rayet Galaxies" (Vacca & Conti 1992).

The standard model of wind-driven interstellar "bubbles" (Castor, McCray, & Weaver 1975; Weaver et al. 1977) considers a massive star with a constant deposition rate of mechanical luminosity, $L_w \approx 10^{36}$ ergs s^{-1}, appropriate for an O-type star with mass-loss rate $\dot{M}_2 \approx 10^{-6}\ M_\odot$ yr^{-1} and wind terminal velocity $V_w \approx 2000$ km s^{-1}. For models of supershells driven by tens to hundreds of hot-star winds and SN, the energy deposition has been treated as continuous (Mac Low & McCray 1988; Heiles 1987) at a rate $L_w(t) \approx (10^{38}$ ergs s$^{-1})L_{38}$. During the SN phase, for stars in the range 8 – 40 $M_\odot$, this energy input rate may be written as the product of the IMF, the mass-lifetime relation, and the supernova energy, $L_{SN}(t) = [dN(>m)/dm](dm/dt)E_{SN}$. Thus, we may parametrize $L_{SN}(t) \propto t^{(\Gamma/\alpha)-1}$, where the total stellar lifetime $t(m) \propto m^{-\alpha}$ and where the average IMF $dN(>m)/dm) \propto m^{-\Gamma}$. Because $\alpha \approx 1.2$ for stars between 9 and 40 $M_\odot$ (Maeder & Meynet 1989; Schaller et al. 1992; Schaerer et al. 1993) and $\Gamma \approx 1.6 \pm 0.3$ (Garmany, Conti, & Chiosi 1982), a constant energy source is a fair approximation for coeval associations at late times $t \geq 5$ Myr.

The energy input to the bubble interior, treated as an ideal gas with adiabatic index 5/3, produces a pressure $P_b = (E_b/2\pi R_s^3)$, where R_s is the radius of the outer shell and E_b is the total internal energy. If we assume that all swept-up mass resides in a thin shell, the equations of momentum and energy conservation for a spherical bubble of velocity $V_s = \dot{R}_s$, expanding into an external medium of mass density $\rho_0 = 1.4 m_H n_0$ and with ambient pressure $P_0 \ll P_b$, are,

$$\frac{d}{dt}\left[\frac{4\pi R_s^3}{3}\rho_0 \dot{R}_s\right] = 4\pi R_s^2 (P_b - P_0) \tag{3}$$

$$\frac{dE_b}{dt} = L_w(t) - 4\pi R_s^2 P_b \dot{R}_s - n_b^2 \frac{4\pi R_s^3}{3}\Lambda(T_b)\ . \tag{4}$$

Here, n_0 is the ambient H number density (cm^{-3}) and radiative cooling of the hot interior has been written in terms of a cooling function, $\Lambda(T_b)$, having units ergs cm^3 s^{-1} and appropriate for an isothermal interior at temperature $T_b = (P_b/2.3n_b)$ and hydrogen density n_b. If we neglect radiative cooling and ignore external pressure, equations (1) and (2) can be combined into a single third-order dynamical equation, which, for a constant energy input rate, $L_w(t) = L_0$, has a self-similar solution,

$$R_s \ = \ (125 L_0 t^3/154\pi\rho_0)^{1/5} = (65.9\ \mathrm{pc}) L_{38}^{1/5} n_0^{-1/5} t_6^{3/5} \tag{5}$$

$$V_s = (3R_s/5t) = (38.6 \text{ km s}^{-1}) L_{38}^{1/5} n_0^{-1/5} t_6^{-2/5} , \quad (6)$$

where t_6 is the superbubble age in units of 10^6 yr. In this approximation, the superbubble age can be derived from measurements of R_s and V_s; however, because $L_w(t)$ is usually not constant, this age is only approximate.

In the constant-wind case with no radiative cooling, the thermal energy content of the interior is 5/11 of the time-integrated mechanical luminosity, $E_b = (5L_0t/11)$, and the remaining 6/11 goes into $P\ dV$ work on the shell. The bubble pressure is then

$$\frac{P_b}{k} = \left(\frac{5L_0t}{22\pi R_s^3 k}\right) = (1.97 \times 10^5 \text{ cm}^{-3} \text{ K}) L_{38}^{2/5} n_0^{3/5} t_6^{-4/5} . \quad (7)$$

Because mass-loss rates and wind terminal velocities increase dramatically, as massive stars evolve off the ZAMS, the wind mechanical luminosity $L_w(t)$ is far from constant. Therefore, in all our models, we solve the time-dependent problem as a series of three first-order equations, in which the total rate of energy input due to stellar winds and SN is followed consistently with the rate of post-main-sequence evolution.

The interior pressure of the bubble (proportional to n_bT_b) is set by the integrated energy input from massive stars minus radiative and adiabatic losses. The characteristic density n_b and temperature T_b of the bubble interior are determined individually by the "mass loading" from evaporated gas off the shell, stellar mass loss, and other sources (photo-evaporation of surrounding clouds, entrainment, clouds that penetrate the shell). Mass loss from O stars injects around $10^{-6}\ M_\odot$ yr^{-1} per 10^{36} ergs s^{-1} of mechanical luminosity. Thus, for our fiducial superbubble, driven by a mechanical luminosity $L_w = (10^{38} \text{ ergs s}^{-1}) L_{38}$, we estimate that $\dot{M}_* \approx (10^{-4}\ M_\odot \text{ yr}^{-1}) L_{38}$. Supernovae inject mass at a rate a factor 3 – 10 less. Over 10^7 yr, these sources produce around $\sim 10^3\ M_\odot$ of interior mass.

Considerably more interior mass can be produced by conductive evaporation from the shell, with a classical, unsaturated mass loss rate of

$$\dot{M}_{\rm con} = \frac{16\pi\mu R_s (6 \times 10^{-7} T_b^{5/2}) \kappa_o}{25k} , \quad (8)$$

where $\mu = 0.609 m_H$ is the mean particle mass for fully-ionized gas with He/H = 0.1 by number. We have assumed the classical plasma conductivity (Spitzer 1962) in cgs units, multiplied by a dimensionless scaling factor $\kappa_o \leq 1$ to account for possible magnetic suppression. Because the conductive mass loss rate is quite sensitive to T_b, its value must be determined self-consistently with the bubble evolution, which leads to a "thermostating effect" (Castor, McCray, & Weaver 1975). For interior temperature and density profiles appropriate for spherically symmetric conductive flow,

$$T(r) = T_b[1 - (r/R_s)]^{2/5} \quad (9)$$

$$n(r) = n_b[1 - (r/R_s)]^{-2/5} , \quad (10)$$

one finds $M_b = (125\pi/39)(1.4 m_H n_b R_s^3)$ and $T_b = (P_b R_s^3/M_b)(\mu/k)(125\pi/39)$. By integrating $\dot{M}_b$ together with the previous expressions for $R_s(t)$, $P_b(t)$, and $T_b(t)$ one arrives at the expressions,

$$M_b(t) = (1590\ M_\odot) L_{38}^{27/35} n_0^{-2/35} t_6^{41/35} \kappa_o^{2/7} \quad (11)$$

$$T_b(t) = (5.3 \times 10^6\ K) L_{38}^{8/35} n_0^{2/35} t_6^{-6/35} \kappa_o^{-2/7} \quad (12)$$

$$n_b(t) = (1.6 \times 10^{-2}\ \mathrm{cm}^{-3}) L_{38}^{6/35} n_0^{19/35} t_6^{-22/35} \kappa_o^{2/7}\ , \quad (13)$$

where $n_b = (P_b/2.3kT_b)$. Substituting these values into eq. (8), we find that the conductive mass loss rate from an adiabatic bubble is,

$$\dot{M}_{\mathrm{con}} = (1.86 \times 10^{-3}\ M_\odot\ \mathrm{yr}^{-1}) L_{38}^{27/35} n_0^{-2/35} t_6^{6/35} \kappa_o^{2/7}\ . \quad (14)$$

Thus, the magnetic suppression of conductivity would need to be severe ($\kappa_o \ll 1$) to produce a large increase in the interior temperature.

Figure 8a shows an IRAS image of the Cygnus X region, encompassing the Cygnus Loop, the Cyg OB1 supershell (Saken et al. 1992), and many more regions disturbed by star formation. Figure 8b illustrates a close-up view of the large cavity around the Cyg OB1 association. In an IRAS survey of the Galactic plane, Saken, Shull, & Fesen (1995) have identified 13 other candidates for IRAS supershells around such objects as the Gum Nebula, Orion, and Cas OB6. The young bubbles in Cas OB6 are currently confined to individual subclusters in the OB association (Figure 9), but they will merge in the next several 10^5 yrs. A number of these superbubbles appear "capped" at their tops, suggesting that they have not yet broken through the Galactic H I layer. Thus, the dynamics of realistic superbubbles are likely to be quite complicated, since they depend on subclustering and inhomogeneous gas distributions.

5. Connections to Starburst Galaxies and Intergalactic Medium

As has been discussed, the formation rate and evolution of massive stars are intricately coupled to the large-scale structure of the interstellar medium (ISM) of galaxies. Multiple winds and supernovae (SN) from OB associations are responsible for blowing large cavities in the ISM (Heiles 1987; Shull 1993) and for producing the "superwinds" that emanate from the nuclei of many external "starburst galaxies" (Heckman, Lehnert, & Armus 1993). The excess of Wolf-Rayet stars observed in a subset of emission-line galaxies (Vacca & Conti 1992) is another result of large formation rates of massive stars.

The burst of energy deposition from OB supergiants and W-R stars provides a mechanism for driving "superwinds" in the nuclei of starburst galaxies. For star-forming regions in the nuclei of galaxies, $\sim$ 100 pc in size, a burst of massive star formation will naturally provide the needed high rate of injected mass and kinetic energy. However, the history of this star formation will be important in the resulting gas dynamics. Furthermore, if the starburst occurs in the vicinity of large complexes of molecular clouds, "poisoning" by photoevaporation and radiative losses may be an important process in limiting the

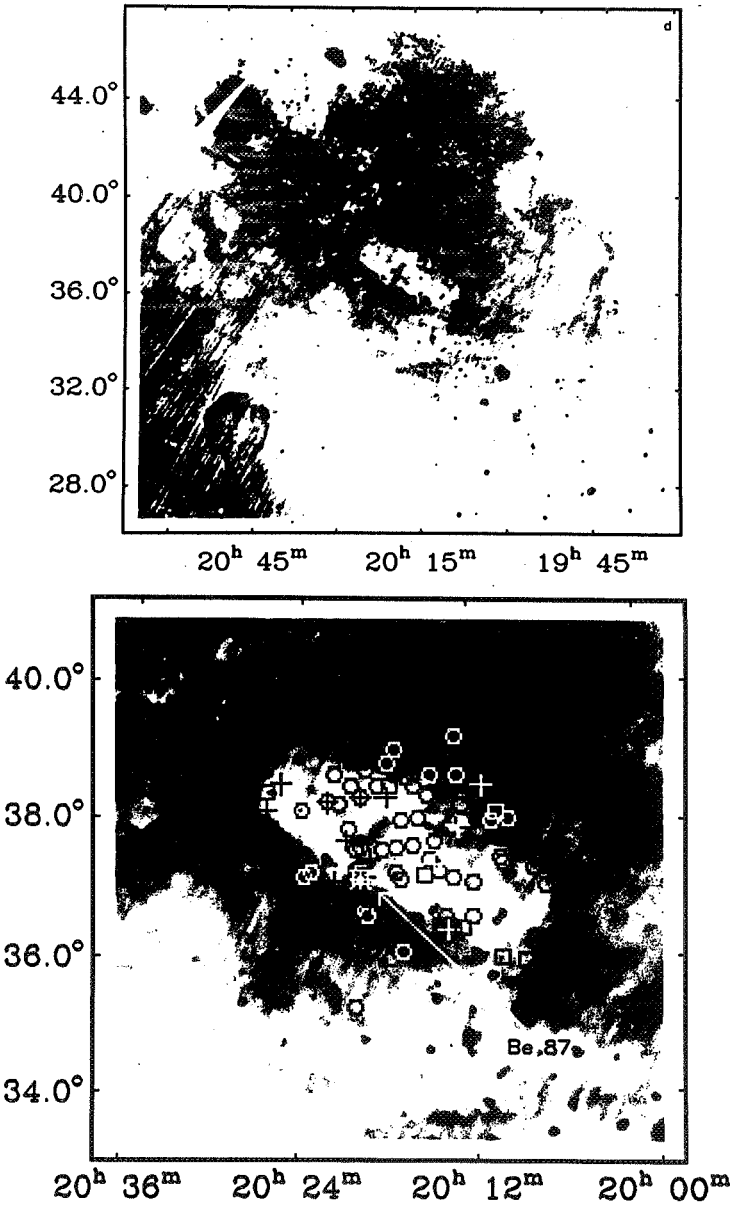

Figure 8. (a) IRAS Skyflux 60/100 μm ratio image of Cygnus X region (Saken et al. 1992) showing the Cygnus Loop (lower left) at 700 pc distance and a large 50 × 150 pc superbubble (center) surrounding the Cyg OB1 association at 1.5 kpc. (b) Cyg OB1 superbubble and locations of 77 member OB stars (Garmany & Stencel 1992) and 9 Wolf-Rayet stars (Conti & Vacca 1990). Post-main-sequence OB stars are plotted as crosses and Wolf-Rayet stars as squares.

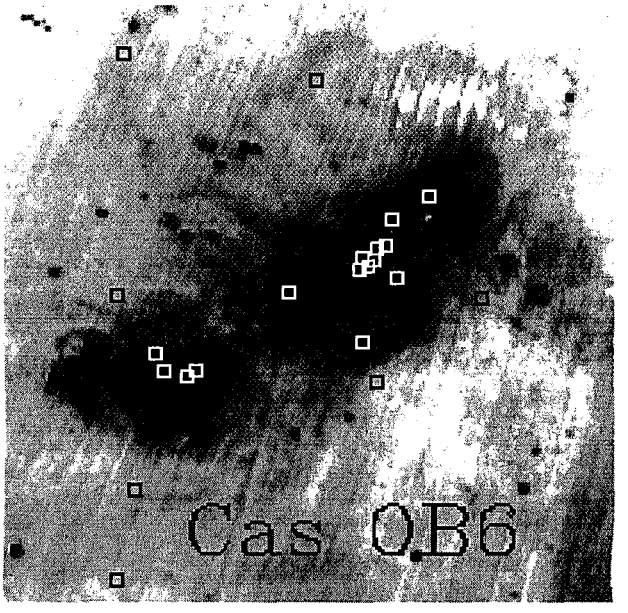

Figure 9. IRAS Skyflux 60/100 μm ratio image of the Cas OB6 association (Saken, Shull, & Fesen 1995) showing developing bubbles around two sub-clusters of OB stars.

outflow. It remains to be determined, observationally and theoretically, how much star-forming molecular material can be injected or entrained into these galactic winds. There is little doubt that the time history of massive star formation and the effects of radiative cooling must be included in accurate models of superbubbles, starbursts, and winds from the nuclei of galaxies.

The holes punched by superbubbles in the Galactic H I layer may also facilitate the escape of ionizing radiation into the halo. Reynolds (1984, 1991) has identified a layer of ionized hydrogen, with column density N(H II) $\approx 6 \times 10^{19}$ cm^{-2} and $\sim$ 1 kpc scale height, from diffuse Hα emission and pulsar dispersion. The diffuse [N II] 205 μm emission seen by COBE may arise from some of the same ionized gas. If this "Reynolds Layer" is photoionized and if the sources are located at the Galactic midplane, then the ionizing flux must be at least 2×10^6 photons cm^{-2} s^{-1} from each side of the disk (Reynolds 1984). The obvious source for much of this ionized gas is photoionization from O-stars, which have a Lyman Continuum (LyC) production rate per unit disk area, $\Psi_{\rm LyC} = S_T/(\pi D^2_{\rm max}) = 3.3 \times 10^7$ cm^{-2} s^{-1} based on a re-calculation of the LyC production rate from OB associations within a distance $D_{\rm max} = 2.5$ kpc (Dove & Shull 1994). The maximum LyC flux that can leak out each side of the disk is $\Psi_{\rm LyC}/2 = 1.65 \times 10^7$ cm^{-2}, which is about 8 times that required to ionize the H II layer. However, there has been some reluctance to accept O stars as the source for the Reynolds layer owing to the fact that the Galactic H I layer is thick enough that it may absorb the LyC radiation from O stars confined to the Galactic plane.

At this point, one appeals again to the collective effects of the ionizing sources. The O stars are grouped in OB associations, which will accentuate the effects of photoionization and mechanical energy deposition. The resulting superbubbles or "chimneys" (Norman & Ikeuchi 1989) will fracture the H I layer and provide a conduit for LyC to reach the halo. This process has been modeled by Norman (1991) and by Dove & Shull (1994). Figure 10 shows a Monte-Carlo simulation of a calculation by the latter authors, illustrating how the ionized zones above the most luminous OB associations begin to open up at $Z \geq 500$ pc and dominate the ionization of the lower halo. Dove & Shull (1994) conclude that ~14% of the O-star LyC produced at the midplane can escape the H I layers (7% from each side of the disk) in photoionized "H II chimnneys". The dynamic effects of superbubbles are now under investigation; they would be expected to increase the escaping flux above 14%. Therefore, there is some reason for believing that OB stars, concentrated in associations, are indeed the ionizing source for much of the Reynolds layer.

One can extend this discussion to galaxies other than the Milky Way, since OB star formation is common among disk galaxies. Over the region within 2.5 kpc of the Sun, the LyC production rate is around 6×10^{51} s^{-1} (Dove & Shull 1994). Scaling to the entire Milky Way disk, with effective radius 10 kpc, the total LyC production rate is $S(\mathrm{Gal}) \approx 10^{53}$ s^{-1}. If this production rate is typical of bright (L^*) galaxies, then we can estimate the ratio of LyC production from star-forming galaxies to that from bright active galactic nuclei (AGN), with $S(\mathrm{AGN}) \approx 10^{56}$ s^{-1} appropriate for L(AGN) $\approx 10^{46}$ ergs s^{-1},

$$\frac{I_o(\mathrm{Gal})}{I_o(\mathrm{AGN})} \approx \left(\frac{\phi(\mathrm{Gal})}{\phi(\mathrm{AGN})}\right)\left(\frac{S(\mathrm{Gal})}{S(\mathrm{AGN})}\right)\langle f_{\mathrm{esc}}\rangle \approx 10\,\langle f_{\mathrm{esc}}\rangle\,, \qquad (15)$$

where we have adopted comoving densities $\phi(\mathrm{Gal}) \approx \phi(L^*) \approx 0.01$ Mpc^{-3} and $\phi(AGN) \approx 10^{-6}$ Mpc^{-3} (at redshifts $z = 2 - 3$) and assumed that star-forming galaxies have a frequency comparable to that measured locally. Clearly, these two sources are comparable if the mean LyC escape fraction $\langle f_{\mathrm{esc}}\rangle \approx 0.1$. At low redshift, where AGN (Seyfert galaxies and BL Lac Objects) have much lower comoving densities, the contribution of star-forming galaxies could dominate the ionizing metagalactic background.

Some of these star-forming galaxies may produce their LyC distributed in OB associations across a 10 kpc disk. Others may produce nuclear starbursts, responsible for the "nuclear superwind" phenomenon. In either case, the production and propagation of ionizing radiation will likely be dominated by the collective effects of multiple OB stars and the dynamics of superbubbles. Figure 11 shows the composite spectrum of ionizing photons produced in a Gaussian burst of star formation (Sutherland & Shull 1995). The evolutionary tracks were taken from Schaller et al. (1992) at solar metallicity, and the model atmospheres are from Kurucz (1992). Note that the LyC radiation fades rapidly after the peak of the burst. These composite spectra are not well-fitted by any single stellar (T_{eff}) spectrum. The LyC radiation escaping the H I disks will be processed by absorption, recombination, and diffuse re-emission as it transfers out of the galaxy. Many of these effects need to be assessed theoretically, and the observations of such phenomena in the optical and infrared will provide a rich set of data to understand the physical processes at the "ISM–IGM Interface".

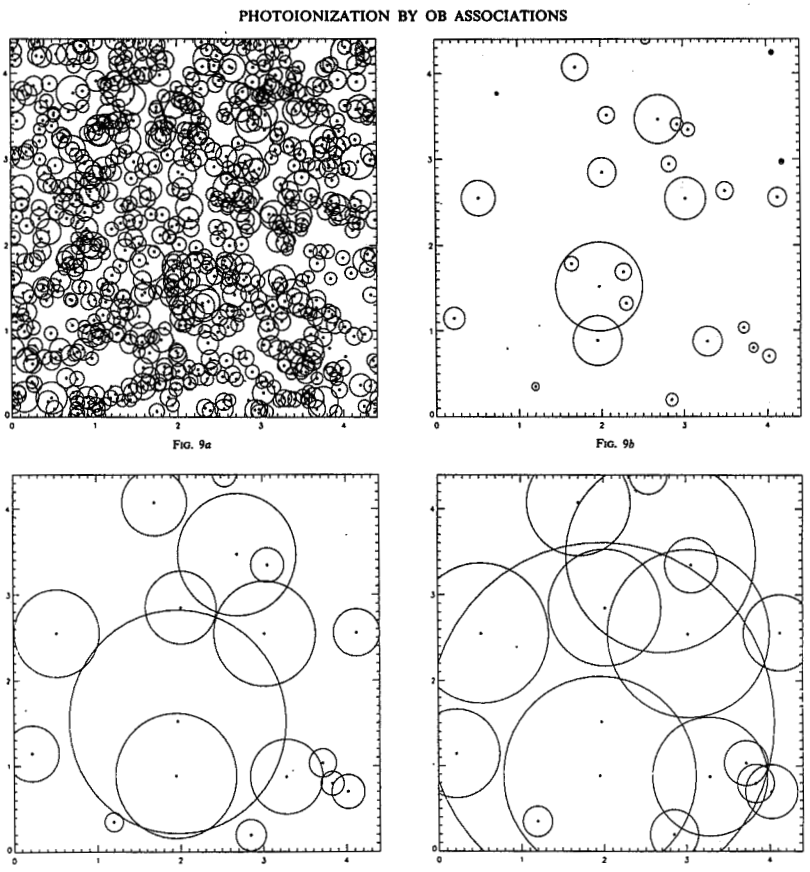

Figure 10. A Monte-Carlo simulation (Dove & Shull 1994) of the H II ionized zones ("H II chinneys") over a region 4.5 x 4.5 centered around the Sun and obeying the OB-association luminosity function of Kennicutt, Edgar, & Hodge (1989), $dN/dS \propto S^{-2}$, with a maximum LyC photon luminosity $S_{\rm max} = 10^{51}$ s^{-1}. Circles represent the cross section between the H II zones and planes located at heights Z = 0, 300, 500, and 800 pc.

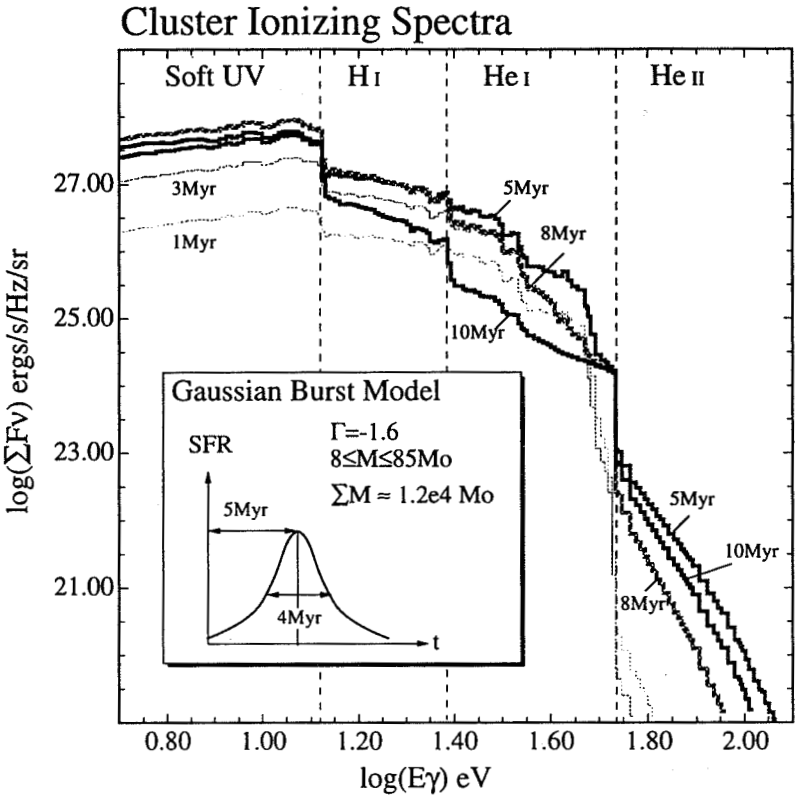

Figure 11. Composite photoionizing spectrum (Sutherland & Shull 1995) resulting from a Gaussian starburst in an evolving OB association whose IMF has a slope $\Gamma = 1.6$. Note the rapid evolution of the Lyman continuum flux above the ionization edges of H I (13.6 eV), He I (24.58 eV), and He II (54.4 eV) over time scales of 5–10 Myr.

Acknowledgments. Some of the research described in this review was supported by grants from the NASA Astrophysical Theory Program (NAG5-766) and NASA Astrophysical Data Program (NAG5-1224). I thank my colleagues Rob Fesen and Jon Saken for their many years of collaboration on studies of supernova remnants and superbubbles. Dick McCray and Hongwei Li provided figures and valuable discussions on SN 1987A.

References

Arendt, R. G. 1989, ApJS, 70, 181

Arendt, R. G., Dwek, E., & Petre, R. 1991, ApJ, 368, 474

Arendt, R. G., Dwek, E., & Leisawitz, D. 1992, ApJ, 400, 562

Braun, R. 1985, PhD Thesis, Leiden University

Braun, R. 1987, A&A, 171, 233

Braun, R., & Strom, R. 1986a, A&A, 164, 193

Braun, R., & Strom, R. 1986b, A&A, 164, 208

Bregman, J. N. 1980, ApJ, 236, 577

Bruhweiler, F. C., Gull, T. R., Kafatos, M., & Sofia, S. 1980, ApJ, 238, L27

Burrows, C. 1994, private communication

Burton, M., et al. 1990, ApJ, 355, 197

Castor, J., McCray, R., & Weaver, R. 1975, ApJ, 200, L107

Chevalier, R. A. 1992a, Nature, 355, 617

Chevalier, R. A. 1992b, Nature, 355, 691

Chevalier, R. A. 1992c, Nature, 394, 599

Cioffi, D. F., McKee, C. F., & Bertschinger, E. 1988, ApJ, 334, 252

Colgan, S. W. J., Haas, M. R., Erickson, E. F., Lord, S. D., & Hollenbach, D. J. 1994, ApJ, 427, 874

Conti, P. S., & Vacca, W. D. 1990, AJ, 100, 431

Cordes, J. M. 1986, ApJ, 311, 183

Cox, D. P., & Smith, B. W. 1974, ApJ, 189, L105

Dove, J. B., & Shull, J. M. 1994, ApJ, 430, 222

Draine, B. T. 1981, ApJ, 245, 880

Draine, B. T., & Anderson, N. 1985, ApJ, 292, 494

Dwek, E. 1986, ApJ, 302, 363

Dwek, E., Petre, R., Szymkowiak, A., & Rice, W. L. 1987, ApJ, 320, L27

Dwek, E., Moseley, S. H., Glaccum, W., Graham, J. R., Loewenstein, R. F., Silverberg, R. F., & Smith, R. K. 1992, ApJ, 389, L21

Fesen, R. A., Martin, C. L., & Shull, J. M. 1992, ApJ, 399, 599

Fesen, R. A., Shull, J. M., & Saken, J. M. 1988, Nature, 334, 229

Frail, D. A., Goss, W. M., & Whiteoak, J. B. Z. 1994, ApJ, in press (Dec. 1994)

Frail, D. A., & Kulkarni, S. R. 1991, Nature, 352, 785

Fransson, C. et al. 1989, ApJ, 336, 429

Garmany, C. D., & Stencel, R. D. 1992, A&AS, 94, 211

Garmany, C. D., Conti, P. S., & Chiosi, C. 1982, ApJ, 263, 777

Haas, M. R., Colgan, S. W. J., Erickson, E. F., Lord, S. L., Burton, M. G., & Hollenbach, D. J. 1990, ApJ, 360, 257

Heckman, T. M., Lehnert, M. D., & Armus, L. 1993, in The Environment and Evolution of Galaxies, ed. J. M. Shull & H. A. Thronson (Dordrecht: Kluwer), 453

Heiles, C. 1984, ApJS, 55, 585

Heiles, C. 1987, ApJ, 315, 55

Heiles, C. 1990, ApJ, 354, 483

Kennicutt, R. C., Edgar, B. K., & Hodge, P. W. 1989, ApJ, 337, 761

Kulkarni, S. R., Clifton, T. C., Backer, D. C., Foster, R. S., Fruchter, A. S., & Taylor, J. H. 1988, Nature, 331, 50

Kurucz, R. 1992, unpublished models (available on CD-ROM)

Li, H.-W., McCray, R., & Sunyaev, R. 1993, ApJ, 419, 824

Lockman, F. J., & Gehman, C. S. 1991, ApJ, 382, 182

Luo, D., McCray, R., & Slavin, J. 1994, ApJ, 430, 264

Lyne, A. G., Anderson, B., & Salter, C. J. 1982, MNRAS, 201, 503

Lyne, A. G., & Lorimer, D. R. 1994, Nature, 369, 127

Mac Low, M.-M., & McCray, R. 1988, ApJ, 324, 776

Mac Low, M.-M., McCray, R., & Norman, M. 1989, ApJ, 337, 141

Maeder, A., & Meynet, J. 1989, A&A, 210, 155

Martin, C., & Bowyer, S. 1990, ApJ, 350, 242

McCray, R. 1993, ARA&A, 31, 175

McCray, R., & Kafatos, M. 1987, ApJ, 317, 190

McCray, R., & Snow, T. P. 1979, ARA&A, 17, 213

McKee, C. F., & Ostriker, J. P. 1977, ApJ, 218, 148

Meikle, W. P. S., Spyromilio, J., Allen, D. A., Varani, G.-F., & Cumming, R. J. 1993, MNRAS, 261, 535

Moseley, S. H., Dwek, E., Glaccum, W., Graham, J. R., Loewenstein, R. F., & Silverberg, R. F. 1989, ApJ, 347, 1119

Norman, C. A. 1991, in The Interstellar Disk-Halo Connection in Galaxies, ed. H. Bloemen (Dordrecht: Kluwer), 337

Norman, C. A., & Ikeuchi, S. 1989, ApJ, 345, 372

Panagia, N., Gilmozzi, R., Macchetto, F., Adorf, H.-M., & Kirshner, R. P. 1991, ApJ, 380, L23 [erratum ApJ, 386, L31]

Rank, D. M., Pinto, P. A., Woosley, S. E., Bregman, J. D., Witteborn, F. C., Axelrod, T. S., & Cohen, M. 1988, Nature, 331, 505

Reynolds, R. J. 1984, ApJ, 282, 191

Reynolds, R. J. 1989, ApJ, 339, L29

Reynolds, R. J. 1991, ApJ, 372, L17

Roche, P. F., Aitken, D. K., & Smith, C. H. 1993, MNRAS, 261, 622

Saken, J. M., Fesen, R. A., & Shull, J. M. 1992, ApJS, 81, 715

Saken, J. M., Shull, J. M., & Fesen, R. A. 1995, ApJ, to be submitted

Saken, J. M., Shull, J. M., Garmany, C. D., Nichols-Bohlin, J., & Fesen, R. A. 1992, ApJ, 397, 537

Schaerer, D., Meynet, G., Maeder, A., & Schaller, G. 1993, A&AS, 98, 523

Schaller, G., Schaerer, D., Meynet, G., & Maeder, A. 1992, A&AS, 96, 269

Seward, F. 1990, in IAU Colloq. 101, Supernova Remnants and the Interstellar Medium, ed. R. Roger & T. Landecker (Cambridge Univ. Press), p. 115

Shapiro, P. R., & Field, G. B. 1976, ApJ, 205, 762

Shull, J. M. 1993, in Massive Stars: Their Lives in the Interstellar Medium, ed. J. P. Cassinelli & E. B. Churchwell (San Francisco: ASP), 327

Shull, J. M., Fesen, R. A., & Saken, J. M. 1989, ApJ, 346, 860

Shull, J. M., & Saken, J. M. 1995, ApJ, in press

Shull, J. M., & Slavin, J. D. 1994, ApJ, 427, 784

Slavin, J. D., Shull, J. M., & Begelman, M. C. 1993, ApJ, 407, 83

Spitzer, L., Jr. 1962, Physics of Fully Ionized Gases, (New York: Wiley - Interscience)

Sutherland, R., & Shull, J. M. 1995, in preparation

Tenorio-Tagle, G.. & Bodenheimer, P. 1988, ARAA, 26, 145

Tomisaka, K., & Ikeuchi, S. 1986, PASJ, 38, 697

Vacca, W. D., & Conti, P. S. 1992, ApJ, 401, 453

Van Buren, D., & Norman, C. 1989, ApJ, 336, L67

Wampler, E. J., et al. 1990, ApJ, 362, L13

Weaver, R., McCray, R., Castor, J., Shapiro, P., & Moore, R. 1977, ApJ, 218, 377 [errata ApJ, 220, 742]

Wooden, D., Rank, D. M., Bregman, J. D., Witteborn, F. C., Tielens, A. G. G. M., Cohen, M., Pinto, P. A., & Axelrod, T. S. 1993, ApJS, 88, 477

Wright, E. L., et al. 1991, ApJ, 381, 200

Back: Tom Kuiper; *Middle:* Herb Pickett, Peter Wannier, Patrik Dierich, Paul Batelaan, Mark Schaeffer; *Front:* Laurent Denis, Peg Frerking (1987)

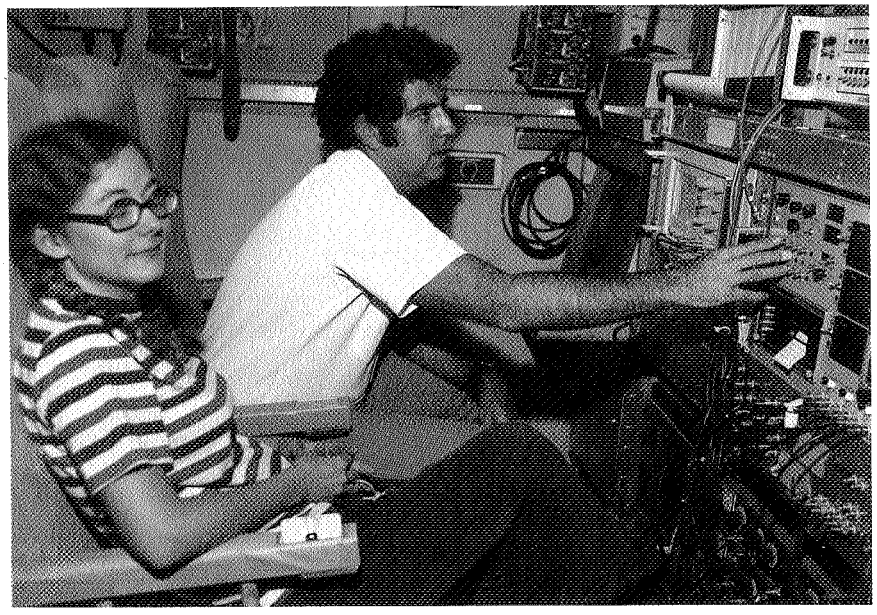

Kris Sellgren, Mike Werner (1977)

Airborne Astronomy Symposium on the Galactic Ecosystem
ASP Conference Series, Vol. 73, 1995
M.R. Haas, J.A. Davidson, and E.F. Erickson (eds.)

Far-Infrared Emission Lines from Planetary Nebulae

Harriet L. Dinerstein
Astronomy Department, University of Texas, Austin TX 78712

Michael R. Haas, Edwin F. Erickson
M/S 245-6, NASA Ames Research Center, Moffett Field CA 94035-1000

Michael W. Werner
M/S 233-304, Jet Propulsion Lab, Pasadena CA 91109

Abstract. The line trio [O III] 52, 88 μm, [N III] 57 μm has been measured in a number of planetary nebulae (PNe) and used to determine nebular properties such as density, temperature, and N/O abundance. The N/O ratios, which are elevated in many PNe due to nuclear processing in the progenitor star, agree well with optical determinations. The [O I] 63 μm line has been detected in about a dozen PNe, demonstrating the ubiquity of neutral envelopes. Measurements of [O I] 63, 146 μm and [C II] 158 μm, the primary cooling lines from the ionized/neutral interface zone or photodissociation region (PDR), have been made for six PNe. The line strengths indicate that the line-emitting regions are warm ($T \geq 500$ K), dense ($\log n \geq 4$), and contain of order 0.1 solar masses.

1. Introduction

The fine-structure transitions from the low-lying energy levels of many abundant ions in gaseous nebulae fall in the mid-infrared to far-infrared spectral region. As a result, they can only be observed from space, or from a stratospheric platform like the Kuiper Airborne Observatory (KAO). These emission lines possess a distinct set of characteristics which define both their advantages and limitations. The low excitation energies of the upper levels ensure that these levels have substantial populations as a result of collisional excitation and that the strengths of the emitted lines are insensitive to gas temperature in most situations. Because they have low transition probabilities but large collision strengths, these lines tend to have fairly low critical densities, the densities for which collisional de-excitations occur as frequently as radiative ones. For certain ground-state electronic configurations (p^1, p^5), the only transitions lie in the infrared, while for others (p^2, p^3, p^4), higher energy levels give rise to widely observed emission lines in the optical and ultraviolet. In the former case, the infrared lines are often the only way to detect particular ions, or gas that is too cool to emit the higher-energy optical lines; in the latter, the infrared lines offer probes of the gas that are complimentary to the more familiar optical indicators. The general physics of the infrared lines was explored in a pivotal paper by Simpson (1975); a recent review of observations in many kinds of nebulae was presented by Dinerstein (1995).

In this paper, we summarize results from a long-term program of far-infrared spectroscopy of emission lines from planetary nebulae (PNe). The observations were conducted with a moderate-resolution cooled grating spectrometer designed and built at NASA Ames Research Center as a facility instrument for the KAO (Erickson *et al.* 1984, 1985). One aspect of our program was to observe far-infrared emission lines from the ions O++ and N++, which in most PNe represent the majority ionic states for the important elements O and N, and provide unique diagnostics of conditions in the nebular gas. A second aspect was to search for evidence of neutral envelopes around PNe by observing the fine-structure lines of O0 and C+. These ions are the predominant states for their respective elements in the neutral material immediately adjacent to the ionized regions, and their far-infrared transitions are the main cooling lines for this warm, neutral, atomic gas.

2. Lines from Ionized Gas: [O III] and [N III]

The emission-line trio [O III] 52, 88 μm, [N III] 57 μm provides an exceptional tool for probing the physical conditions and elemental abundances in ionized nebulae. These lines were first observed in Galactic H II regions, many of which are so heavily obscured by interstellar dust that optical observations are not possible (i.e. Lester *et al.* 1983). The motivations for observing these lines in PNe are different than for H II regions, because PNe are easily observed at optical wavelengths. By obtaining beam-matched measurements of the optical and far-infrared [O III] lines, one can use the [O III] spectrum to constrain and determine the gas parameters in unprecedented ways (Dinerstein, Lester, & Werner 1985, hereafter DLW; Dinerstein 1986). The far-IR lines are also valuable for measuring N/O in high-excitation PNe, which tend to have the highest N enhancements, since the optically accessible ratio O+/N+ samples only a tiny fraction of the ionized gas. The major uncertainty for the infrared lines is flux calibration; the data discussed here have relatively high S/N (> 15 in most cases), and were generally calibrated from primary standards (Dinerstein *et al.* 1995).

a) Diagnostics

The ratio of the two far-infrared lines of [O III] is an excellent density indicator in the main bulk of the ionized gas, particularly in the range relevant to most planetary nebulae, 10^2 - 10^4 cm^{-3}. This can be compared to other density indicators, such as optical [O II] and [S II] lines. The ratio F(52 μm)/F(88 μm) varies by a factor of 18 between the low-density limit of 0.6 and the high-density asymptotic value of 10. In Table 1, we present densities derived from our observations of the infrared lines in nine PNe using atomic constants cited in DLW. We compare these with densities derived from the [O II] 3726, 29 Å lines, compiled from the literature by Stanghellini and Kaler (1989). The densities show reasonable agreement given the wide dispersion in published [O II] densities for an individual nebula (listed in parentheses in the Table). Note that, for several reasons, one does not *expect* the [O III] and [O II] values to be identical. First, these lines intrinsically arise from different physical regions. Second, the [O III] lines are integrated fluxes, encompassing the whole nebula, whereas the [O II] measurements are made at high-surface brightness positions which are likely to be regions of high density (such as nebular cores, bright knots, or swept-up shells). Finally, for an inhomogeneous nebula density indicators based on different line ratios can yield different values due to the density weighting of the respective line emissivities (DLW; Rubin 1989). In this case one expects that the [O III] lines would be biased toward lower values; we may see some evidence for this effect.

Table 1. Parameters Derived from the Ionized Lines

Nebula	log n_e ([O III)]	log n_e ([O II)][a]	N^{++}/O^{++}
IC 418	3.8 ± 0.20	3.3 (3.0-4.1)	.27 ± .07
NGC 2346	1.7 (0 → 2.1)[b]	2.5	.36 ± .22
NGC 2392	2.4 ± 0.15	3.2 (2.8-3.6)	.27 ± .08
NGC 2440	2.9 ± 0.15	3.2	1.2 ± .3
NGC 6210	3.1 ± 0.10	3.6	---
NGC 6302	3.2 ± 0.10	3.3 (3.0-3.6)	.74 ± .10
NGC 6543	3.3 ± 0.10	3.5 (3.0-4.2)	.30 ± .03
NGC 6572	3.8 ± 0.20	3.7	.16 ± .05
NGC 7009	3.4 ± 0.10	3.4 (3.2-3.6)	.16 ± .02

[a]Average n_e; range of cited values in parentheses (Stanghellini and Kaler 1989).
[b]Extreme values of n_e allowed by the uncertainties in the line fluxes.

In principle, the ratio of the infrared to optical line intensities in a multi-level ion gives a measurement of the electron temperature T_e. The first attempt to use the [O III] spectrum this way was by Dinerstein (1983), where the line ratios F(4363 Å)/F(5007 Å) and F(5007 Å)/F(88 μm) were used to simultaneously determine T_e and the electron density n_e for several PNe. This approach has the disadvantages that the latter ratio is sensitive to both T_e and n_e, and the two ratios are not always measured in the same beam. A better method was presented by DLW, who combined large-beam measurements of [O III] 5007 Å with infrared observations to obtain F(5007 Å)/F(52 μm) and F(52 μm)/F(88 μm). These ratios are more orthogonal in the variables n_e and T_e than the pair mentioned above (DLW, Fig. 4). Furthermore, real nebulae may not be isothermal. In a formalism first developed by Peimbert (1967), the internal nebular temperature distribution is represented by a mean value, T_0, and a second parameter, t^2, that measures the spread around this mean value. In DLW it is shown that T_e (5007 Å, 52 μm) ≈ T_0, while T_e (4363 Å, 5007 Å) ≈ T_0 $(1 + 3t^2)$. Therefore, by comparing these values, one can in principle determine both T_0 and t^2. Because both line ratios arise from the same ion, this is a cleaner test for small-scale temperature variations than comparison of line ratios from two non-coextensive ions, which provided the original evidence for non-isothermality (Peimbert and Costero 1969). The infrared/optical [O III] method does, however, require accurate and consistent flux calibrations for lines in widely different wavelength regions.

The presence and amplitude of internal variations in T_e are important because such variations have a major impact on the inferred O/H abundances of nebulae, a crucial parameter for understanding the composition of gas and stars as a function of time in our Galaxy. Correction for non-isothermality results in higher inferred O/H values (Peimbert and Costero 1969, Rubin 1969). For example, the current best value of t^2 for Orion, $t^2 \approx .04$, raises the inferred abundance by almost a factor of two (Peimbert 1993). Our earlier work (DLW) on PNe suggested t^2 values at least this large. However, our more recent and reliable line measurements show that temperature fluctuations, if present, are not as large as claimed in DLW. For example, we previously suggested that $t^2 \approx .13$ in NGC 6543; we now find T_e (5007 Å, 52 μm) ≈ 8500 ± 500 K, which is consistent within the errors with T_e (4363 Å, 5007 Å) ≈ 8000 ± 300 K.

b) N/O Abundances

The interpretation of the [N III] 57 μm line has long been problematical. Use of this line together with the far-infrared [O III] lines led to esimates of the elemental N/O ratio which were systematically larger by a factor of two to three than values derived from optical [N II] and [O II] lines for the same H II regions (i.e. Lester *et al.* 1983, 1987; Simpson *et al.* 1986). Possible causes of this so-called "zero-point" discrepancy (Dinerstein 1990) include: non-collisional excitation of the optical [O II] lines (Rubin 1986); ionization structure effects, such that the ionization volumes of O++ and N++ do not coincide, which mainly occur for cool ionizing stars (Rubin *et al.* 1988); or an error in the atomic parameters, particularly in the [N III] collision strength. Extensive efforts over the last decade failed to resolve the disagreement between N+/O+ and N++/O++ until the recent publication of an improved collision strength for the 57 μm transition by Blum and Pradhan (1992). Incorporation of this new, larger collision strength brings the infrared-derived N/O abundance for Orion into better agreement with recent optical determinations (Baldwin *et al.* 1991). Using the new collision strength, Dinerstein *et al.* (1993) derived N/O values for H II regions in the outer Galaxy that were lower than those in the solar neighborhood, thus extending the abundance "gradient," the trend of decreasing N/O with increasing Galactocentric distance, also seen in many external spiral galaxies (see Dinerstein 1990).

Our motivation for using the infrared [N III] and [O III] lines to derive N/O abundances for PNe was that the optical [N II]/[O II] line ratio samples only a tiny fraction of the gas in most of the nebulae suspected of having enhanced N abundances. These are nebulae in which nearly all of the N and O are ionized above the singly-ionized state, exactly the case where, as a result of ionization structure effects, one might have $N+/O+ \neq N/O$. This situation is not a coincidence: the highly N-rich or "Type I" PNe (Peimbert & Torres-Peimbert 1983) tend to have hot central stars and therefore be highly ionized. This is because both the more efficient dredge-up of N-rich material and the high central star temperatures appear to be evolutionary consequences of higher initial stellar mass (Iben & Renzini 1983). Our initial attempts to derive N/O from the infrared lines in PNe suffered somewhat from the zero-point problem discussed for H II regions above, although the error in the collision strength has less of an effect at the higher densities typical of the PNe (Dinerstein & Werner 1989). Nevertheless, the existence of an apparent systematic error called the values into question.

In Table 1, we present new values for N/O for the nebulae discussed above, using the new collision strength for [N III] 57 μm. We find that, averaging over the sample, there is no longer any evidence for a *systematic* difference between the N/O values derived from the infrared and optical methods (the measurement errors are large enough that one does not find exact agreement on a case-by-case basis). These planetary nebulae show a wide range in N/O values, as already known from optical work, ranging from about 0.17, which is essentially the same value as seen in H II regions, to a value of 1.2 for the extreme Type I PN NGC 2440. These enhanced abundances reflect nuclear processing and mixing in the progenitor star, offering constraints on stellar evolutionary models, and give a quantitative measure of one means for enriching the interstellar gas in nitrogen.

3. Lines from Neutral Gas: [O I] and [C II]

It had long been an unsolved problem whether planetary nebulae were "matter-bounded" structures, in which the edge of the ionized region coincided with the material boundary, or whether there was additional, neutral material outside the

ionized gas. Indications that the latter, "ionization-bounded" scenario was the usual case were mostly indirect (e.g. Pottasch 1980), until astronomers began to detect the molecules H_2 and CO in a number of PNe beginning in the late 1970's. However, even when molecules are absent it is possible for planetary nebulae to contain significant amounts of neutral matter in *atomic* form, where most of the hydrogen is in the form H I. When juxtaposed with ionized nebulae, such regions have recently come to be called "photodissociation regions" or PDR's (Tielens & Hollenbach 1985; hereafter TH). These regions cool primarily through the far-infrared fine-structure lines of [O I] and [C II]. In order to search for evidence of this component, we systematically surveyed PNe in the 63 μm line of [O I], which is the strongest line of the trio except at very low densities (*i.e.* TH, Fig. 10).

a) [O I] 63 μm Survey

The first planetary nebula in which the [O I] 63 μm line was detected was NGC 7027 (Melnick *et al.* 1981). Ellis & Werner (1984) remeasured this line, along with the [O I] 146 μm and [C II] 158 μm lines, and estimated a warm, neutral mass of 0.2 solar masses. Because its excitation energy E/kT is 227 K, the 63 μm line emission will be strongly peaked toward gas warmer than a few 100 K. Subsequent observations of five additional PNe yielded three detections and two upper limits, such that the [O I] 63 μm line strength was about 0.2% of the total far-infrared continuum flux from warm dust (Dinerstein *et al.* 1985). This correlation has held up, in general, for the approximately 20 PNe observed to date, although there appears to be intrinsic scatter of a factor of two or three in the ratio F([O I] 63 μm)/F(IR). A somewhat tighter correlation is found between the 63 μm line strength and the radio continuum flux from the ionized gas.

These correlations can be interpreted in terms of the basic physics of the situation in general, and photodissociation region models in particular. In the layers just beyond the boundary of the ionized region, the H-ionizing photons have been removed from the radiation field, but photons with energies less than 13.6 eV remain. These photons heat the dust, and eject photoelectrons from the grain surfaces, which heat the gas to temperatures of 100-1000 K. (The photons with energies above 11 eV also ionize carbon to C+ and pump H_2 molecules into vibrationally excited levels which give rise to "UV fluorescent" emission bands in the near-infrared.) The strength of the emitted [O I] line is therefore proportional to the dust emission, with some variation depending on the density and the grain charge, which is in turn depends on the strength of the UV radiation field (TH).

The exceptions to the correlation F([O I] 63 μm)/F(IR) = .002 ± .001 fall into two categories. The larger category consists of very dense, "young" PNe which contain a relatively small volume of ionized gas, or none at all. Some of these objects are usually categorized as "proto-PNe" rather than *bona fide* PNe; they include M 1-92, GL 618, Vy 2-2, and Hb 12. We detect weak [O I] lines at the 3-sigma level in the last three objects, but their strengths fall well below the standard ratio to the dust emission. This can be understood in terms of their extremely high densities (log n = 5-6). By balancing photoionization and recombination processes, one finds that the mass of gas that can be ionized by a given number of UV photons decreases with increasing density; a similar argument for dissociation suggests that the atomic mass will also be small in dense nebulae. Note that the *total* mass of the neutral/molecular envelope need not be small; indeed, all three objects are known to contain molecular material. In the case of M1-92, there is no evidence for any ionized gas; the central star of this nebula has not yet become hot enough to produce either an ionized region or a PDR.

There are also a few cases of evolved PNe in which we were unable to detect the 63 μm line despite high far-infrared and radio fluxes. These include NGC

6543 and Abell 30, both of which have ionized outer halos, leaving little room for residual neutral material unless the nebulae are highly asymmetrical, or the neutral material is located at large radii from the central star, which would be difficult for us to detect with our relatively small beams (30-45") and small chopper throws (2-3'). The main conclusion of our survey is that most PNe that have well-developed ionized cores show strong [O I] 63 μm emission, and therefore possess significant neutral circumnebular envelopes.

b) PDR Properties and Masses

The natural follow-up to detecting the 63 μm line as a ubiquitous, though not universal, feature of PNe is to measure the set of three lines [O I] 63, 146 μm, and [C II] 158 μm in several nebulae. Assuming that all three lines arise in the same physical region, their ratios can be used to determine the local gas temperature and density in a similar way to the [O III] diagnostic ratios discussed in section 2a (Watson 1985; Genzel *et al.* 1985). This approach makes few specific assumptions (e.g. about the heating mechanism), except that the cooling is controlled by collisional excitation by neutral species. Alternatively, line ratios calculated from PDR models can be compared with the data in order to infer parameters such as the UV field strength and gas density (*i.e.* Wolfire, Tielens, & Hollenbach 1990). This yields apparently reasonable inferred values but does not provide tight constraints on the physical conditions in the PN PDRs.

In either case, we face the problem that both the diagnostic ratios and the models are calculated assuming a typical, "interstellar" C/O abundance ratio of 0.5. Most PNe are carbon-rich, with C/O taking on a range of values. One approach is to "correct" the observed line ratio F([C II] 158 μm)/F([O I] 63 μm) to the C/O ratio measured from the ionized gas in the same nebula. Simple considerations suggest that, as long as the [C II] line itself does not dominate the cooling, its emitted strength should be directly proportional to the C abundance; however, the actual situation may be more complicated, since PNe also often have an unusually large amount of carbon-rich dust, which can affect the *heating* side of the thermal balance equation (Hollenbach, private communication).

The four nebulae with the most accurately measured line fluxes to date are NGC 6572, NGC 7027, BD+30° 3639, and IC 418. These objects cluster strongly in the line ratio plane, F(63 μm)/F(146 μm) vs. F(63 μm)/F(158 μm), with values of about 20 ± 5 and 8 ± 2, respectively. The former ratio immediately alerts us to the fact that these regions must be relatively warm and dense. In fact, they are in the regime where this ratio loses its sensitivity to temperature and becomes mainly sensitive to density (see Fig. 2 of TH). If we make no correction for the C/O abundance, then these ratios place the nebulae at the position in the diagnostic diagram where log n = 4.0, T = 500 K. Since the elevated carbon abundance is likely to artificially inflate the observed strength of [C II] 158 μm, presumably the "true" ratio is larger by a factor of 2-10, depending on the C/O ratio in the particular nebula. This drives the locus of points towards higher density and temperature, into a part of the diagnostic diagram where the line ratios are no longer orthogonal and we have lower limits: log n ≥ 4.3, T ≥ 1000 K. Comparison of the observed line ratios with the predictions of Wolfire *et al.* (1990) shows that the observed value, F(63 μm)/F(146 μm) = 20, is consistent with the nebular properties. This ratio is predicted for a wide range in the parameters G_0 (UV field strength) and n (gas density); the observed PNe fall well within this range. The F(63 μm)/F(158 μm) ratio is more problematical; it appears to require densities of log n ≥ 5, with or without the nominal correction for abundance. This is probably an indication that current models for O-rich PDRs do not adequately treat the physical processes in carbon-rich environments.

Given the strong indications of high temperature and density, we have a good handle on the emissivity of the [C II] 158 μm line, which is close to complete thermalization. Therefore, it yields an accurate measurement of the C+ mass, and, assuming published C/H values (from the ionized gas), an equivalent total neutral mass, M(H I). For the four PNe listed above, we find total masses of 0.05 - 0.1 solar masses. This number is, of course, dependent on the assumed distances, so perhaps more significant is the fact that the mass in this zone is comparable to the masses of ionized gas; the ratio M(H I)/ M(H II), a distance-independent quantity, is unity within 30%. (Details of this analysis will appear in Dinerstein *et al.* 1995).

To summarize, the PDRs around planetary nebulae contain of order a tenth of a solar mass of warm atomic material. Thus, the total masses of planetary nebulae, redefined as the total amount of circumstellar material rather than as the ionized gas alone, are at least a factor of two greater than the mass in H+. In fact, the total masses are probably substantially larger in many cases. As we pointed out above, the far-infrared lines have high enough excitation energies that they will only be emitted strongly from relatively warm gas. The outermost parts of the neutral envelopes may be too cool to emit substantially in the [O I] and [C II] lines. The material may also become molecular, so that O and C become locked up in CO; at that point, however, it becomes observable by other methods, such as millimeter-wave molecular transitions. An accurate global portrait of the environments of planetary nebulae will require input from a variety of observational techniques; airborne spectroscopy will be a crucial ingredient.

4. Summary and Future Prospects

We have shown how far-infrared spectroscopy of a variety of atoms and ions can be used to provide novel information about the composition and structure of PNe. The potential for studying the ionized gas was illustrated by an analysis of lines from O++ and N++. These lines provide opportunities to probe nebular internal conditions, including the presence of inhomogeneities. Observations of these lines in PNe, from which optical and UV lines can also be observed, provides checks on applying such methods to dust-obscured H II regions. Observations of lines characteristic of warm, neutral atomic gas, arising from O0 and C+, provide a unique way to detect, probe, and measure the mass in the inner portions of the neutral envelopes that are apparently present around most planetary nebulae. The discovery of this component overturns the traditional picture of planetary nebulae as mass-limited ionized shells around the central stars.

Looking to the future, significant observational progress in infrared emission-line spectroscopy of PNe will require a substantial advance in sensitivity. With the larger aperture of SOFIA it will be possible to measure additional lines from the PDRs, better constrain their temperatures, and determine the physical extent of these regions. It will also be possible to extend investigations of the ionized gas to other elements and to other, more diverse, populations of planetary nebulae.

Acknowledgments. This research was supported by NASA through Airborne Astronomy grant NAG 2-372; related ground-based work was supported by NSF grant AST 91-15101. We thank Jim Baltz, Sean Colgan, Bob Rubin, Jan Simpson, Jurgen Wolf, the rest of the CGS team, and the dedicated staff of the KAO for their invaluable assistance in obtaining the observations. Part of this work (MWW) was supported by the Jet Propulsion Laboratory, California Institute of Technology, under contract to NASA.

References

Baldwin, J. A., Ferland, G.J., Martin, P.G., Corbin, M. R., Cota, S. A., Peterson, B. M., & Slettebak, A. 1991, ApJ, 374, 580
Blum, R. D., & Pradhan, A. K. 1992, ApJS, 80, 425
Dinerstein, H. L. 1983, in Planetary Nebulae, IAU Symp. 103, ed. D. R. Flower, Dordrecht: Reidel, p. 79
Dinerstein, H. L. 1986, PASP, 86, 979
Dinerstein, H. L. 1990, in The Interstellar Medium of Galaxies, eds. H. A. Thronson, Jr. and J. M. Shull, Dordrecht: Kluwer, p. 257
Dinerstein, H. L. 1995, in The Analysis of Emission Lines, ed. M. Livio, Cambridge; U. Cambridge Press, in press
Dinerstein, H. L., Ellis, H.B., Haas, M R., & Werner, M. W. 1985, BAAS, 17, 908
Dinerstein, H. L., Haas, M. R., Erickson, E. F., & Werner, M. W. 1993, BAAS, 25, 850
Dinerstein, H. L., Haas, M. R., Erickson, E. F., & Werner, M. W. 1995, in preparation
Dinerstein, H. L., Lester, D. F., & Werner, M. W. 1985, ApJ, 291, 561 (DLW)
Dinerstein, H. L., & Werner, M. W. 1989, in Planetary Nebulae, IAU Symp. 131, ed. S. Torres-Peimbert, Dordrecht: Kluwer, p. 214
Ellis, H. B., & Werner, M. W. 1984, BAAS, 16, 463
Erickson, E F. *et al.* 1984, in Proc. Airborne Astronomy Symposium, eds. H. A. Thronson and E. F. Erickson, NASA Conference Publication 2353, p. 313
Erickson, E. F., Matthews, S., Augason, G. C., Houck, J. R., Rank, D. M., & Haas, M. R. 1985, Proc. Soc. Photo-Optical Instrumental Engineers, 509, 129
Genzel, R., Watson, D. M., Crawford, M. K., & Townes, C. H. 1985, ApJ, 297, 766
Iben, I., & Renzini, A. 1983, ARAA, 21, 271
Lester, D. F., Dinerstein, H. L., Werner, M. W., Watson, D. M., & Genzel, R. 1983, ApJ, 271, 618
Lester, D. F., Dinerstein, H. L., Werner, M. W., Watson, D. M., Genzel, R., & Storey, J. W. V. 1987, ApJ, 320, 573
Melnick, G., Russell, R. W., Gull, G. E., & Harwit, M. 1981, ApJ, 243, L35
Peimbert, M. 1967, ApJ, 150, 825
Peimbert, M. 1993, Revista Mex. de Astron. y Astrof., 27, 9
Peimbert, M., & Costero, R. 1969, Bol. Obs. Tonantzintla y Tacubaya, 5, 3
Peimbert, M. & Torres-Peimbert, S. 1983, in Planetary Nebulae, IAU Symp. 103, ed. D. R. Flower, Dordrecht: Reidel, p. 233
Pottasch, S. R. 1980, A&A, 89, 336
Rubin, R. H. 1969, ApJ, 155, 841
Rubin, R. H. 1986, ApJ, 309, 334
Rubin, R. H. 1989, ApJS, 69, 897
Rubin, R. H., Simpson, J. P., Erickson, E. F., & Haas, M. R. 1988, ApJ, 327, 377
Simpson, J. P. 1975, A&A, 38, 43
Simpson, J. P., Rubin, R. H., Erickson, E. F., & Haas, M. R. 1986, ApJ, 311, 895
Stanghellini, L., & Kaler, J. B. 1989, ApJ, 343, 811
Tielens, A. G. G. M., & Hollenbach, D. J. 1985, ApJ, 291, 722 (TH)
Watson, D. M. 1985, Physica Scripta, T11, 33
Wolfire, M. G., Tielens, A. G. G. M., & Hollenbach, D. 1990, ApJ, 344, 770

Airborne Astronomy Symposium on the Galactic Ecosystem
ASP Conference Series, Vol. 73, 1995
M.R. Haas, J.A. Davidson, and E.F. Erickson (eds.)

Infrared Dust Features of Late-Type Stars and Planetary Nebulae

W. Glaccum
Applied Research Corporation, 8201 Corporate Drive, Landover, MD 20785

Abstract. I present 16 – 65 μm spectra of late-type stars and PPN obtained with the Goddard 24-channel spectrophotometer from the Kuiper Airborne Observatory (KAO). The spectra of these objects contain most of the 9 – 13 known dust features – all discovered from the KAO – at wavelengths greater than 22 μm. I have modeled the 8 – 100 μm spectra of a few representative objects with simple grains selected from a wide range of candidate solids. Hot sapphire is the most likely source of the 13 μm feature found in some M and MS stars. Likely candidates for other features include ice, sulfides, and crystalline silicates. I also present a review of grain candidate materials for which optical properties in the far infrared have been measured, and a list of those for which measurements are needed.

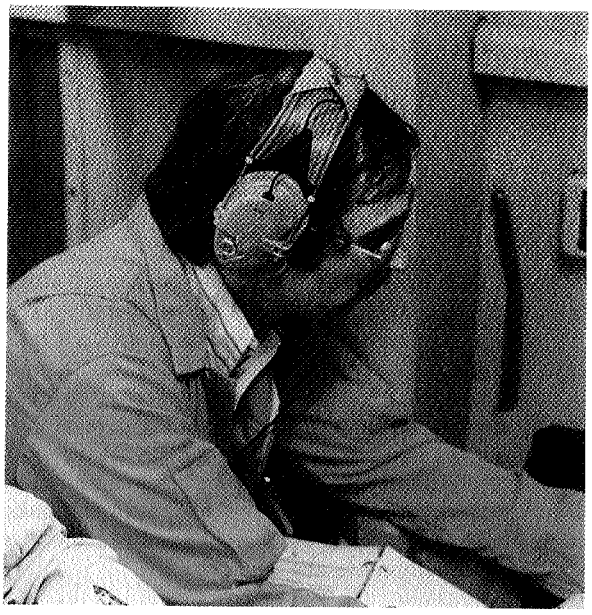

Mike Haas

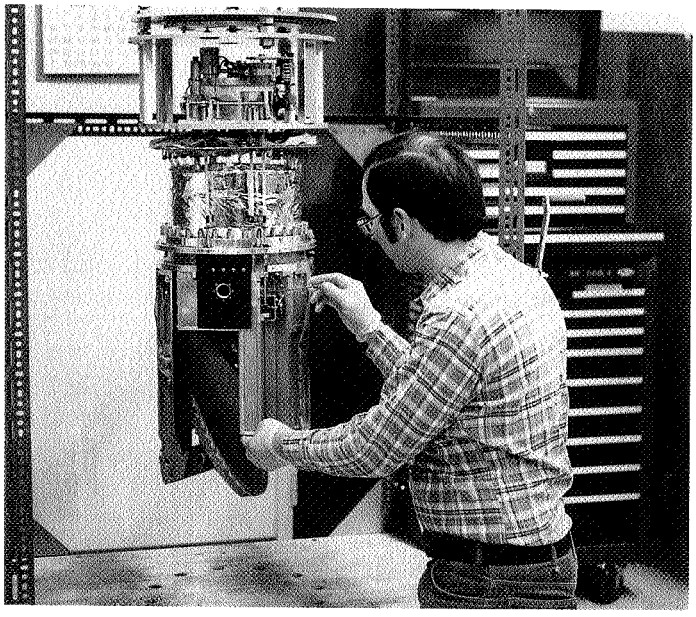

Mike Haas (1983)

Airborne Astronomy Symposium on the Galactic Ecosystem
ASP Conference Series, Vol. 73, 1995
M.R. Haas, J.A. Davidson, and E.F. Erickson (eds.)

Fine Structure Line Emission from Supergiants

Michael R. Haas
NASA/Ames Research Center, MS 245-6, Moffett Field, CA 94035-1000

Alfred E. Glassgold
Department of Physics, New York University, 2 Washington Place, New York, NY 10003

Alexander G. G. M. Tielens
NASA/Ames Research Center, MS 245-3, Moffett Field, CA 94035-1000

Abstract. We have detected [O I] 63 μm and [Si II] 35 μm emission from the oxygen-rich, M supergiants α Orionis (Betelgeuse), α Scorpii (Antares), and α Herculis (Rasalgethi). The measured fluxes indicate that the emission originates in dense, warm gas in the inner envelope or transition region where molecules and dust are expected to form and the acceleration of the wind occurs. Mass-loss rates are derived, evidence for time variability is presented, and results for other evolved stars are included.

1. Introduction

Though much has been learned about the circumstellar environments of red giants and supergiants, the connection between the surface and atmospheric phenomena, where the mass loss actually begins, remains poorly defined. A key problem is the state of the material between the top of the warm stellar photosphere and the base of the cold circumstellar envelope (CSE), the so-called "outer atmosphere" or "transition zone" which extends from a few stellar radii out to many stellar radii. The UV, visible, and near infrared lines primarily originate within a few stellar radii of the star and provide information about the physical conditions in the chromosphere. The thermal continuum and rotational transitions of molecules such as CO are useful diagnostics of the outer envelope. Our relatively poor understanding of the intervening transition zone stems, at least in part, from the lack of good observational probes.

Recent theoretical work by Rodgers & Glassgold (1991, hereafter RG) has shown that at least in the archetypal M supergiant, α Ori, the presence of a strong chromosphere causes the molecular content of its CSE to be extremely low and the [O I] 63 μm and [Si II] 35 μm fine structure lines become major coolants in the transition zone. Further out, carbon is ionized by the interstellar radiation field and some [C II] 158 μm emission is also produced. Our first attempt to use the Kuiper Airborne Observatory (KAO) to measure the [O I] and [Si II] lines in α Ori was successful (Haas & Glassgold 1993). Here we briefly review the RG theory, discuss our initial observations of α Ori, and describe some more recent observations of these lines in α Ori and other nearby giants and supergiants.

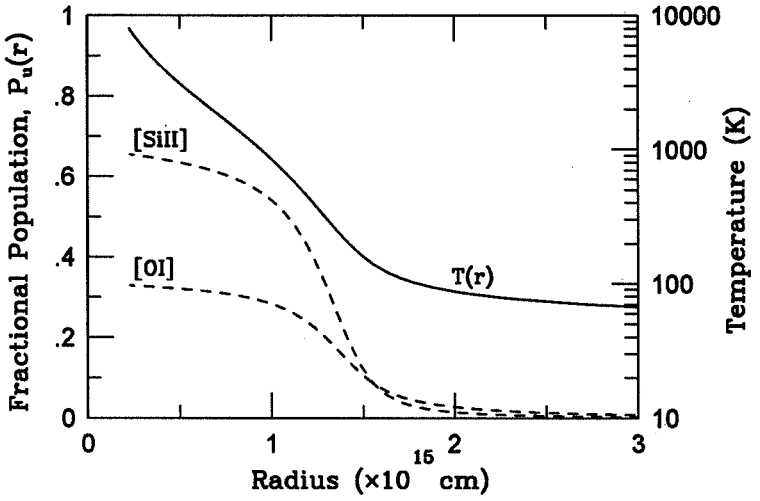

Figure 1. The RG "standard" temperature distribution for α Ori and the resulting populations of the upper levels for the [Si II] and [O I] transitions.

2. Theoretical Background

We discuss the case for α Ori, the supergiant modeled in detail by RG. α Ori's CSE is known to be principally atomic – only $\sim 10\%$ of its carbon is associated into CO (Huggins 1987), no SiO, H_2O, or OH masers have been detected (Benson *et al.* 1990), and 21 cm observations find that most of the hydrogen is H I (Bowers & Knapp 1987). Moreover, its gas-to-dust ratio is about 20 times smaller than typical for late-type stars (Skinner & Whitmore 1987). RG adopted the ionization model of Glassgold & Huggins (1986) for α Ori's CSE and computed its thermal structure. Their model assumed a spherically symmetric outflow with a density $n_{\rm H}(r) = C/r^2$, where $C = \dot{\rm M}_{\rm H}/4\pi m_{\rm H} u_{\rm w} = 7.5 \times 10^{36}\,{\rm cm}^{-1}$ if the mass-loss rate is $\dot{\rm M}_{\rm H} = 4 \times 10^{-6}\,{\rm M}_\odot\,{\rm yr}^{-1}$ and the terminal velocity is $u_{\rm w} = 16$ km s^{-1}. They assumed solar abundances, except for C and O, which had their photospheric values (Lambert *et al.* 1984).

RG considered a number of heating and cooling processes appropriate to the physical conditions in α Ori's CSE. They found fine structure emission in the [O I] and [Si II] lines to be the dominant coolant over a significant portion of the inner envelope, exceeding even adiabatic cooling between $\sim 10 - 40$ stellar radii (R_*). Figure 1 shows the temperature distribution, $T(r)$, for their "standard" model, wherein T drops from 8000 K at 3 R_* to $\sim$ 150 K at 20 R_*. The fine structure emission arises mainly from within this region where kT is greater than the level separation $h\nu$ ($h\nu/k = 228$ K for [O I] and 413 K for [Si II]), so that the upper levels are significantly populated. Since the optical depths are small ($\lesssim 1$ for [O I] and $<< 1$ for [Si II]), the luminosity for a transition $u \rightarrow \ell$ is simply

$$L_{u,\ell} = \mathcal{N}_u\, A_{u,\ell}\, E_{u,\ell}\,, \tag{1}$$

where $\mathcal{N}_u$ is the total number of atoms in the upper level and the other quantities are expressed in standard notation. Integrating over the assumed density

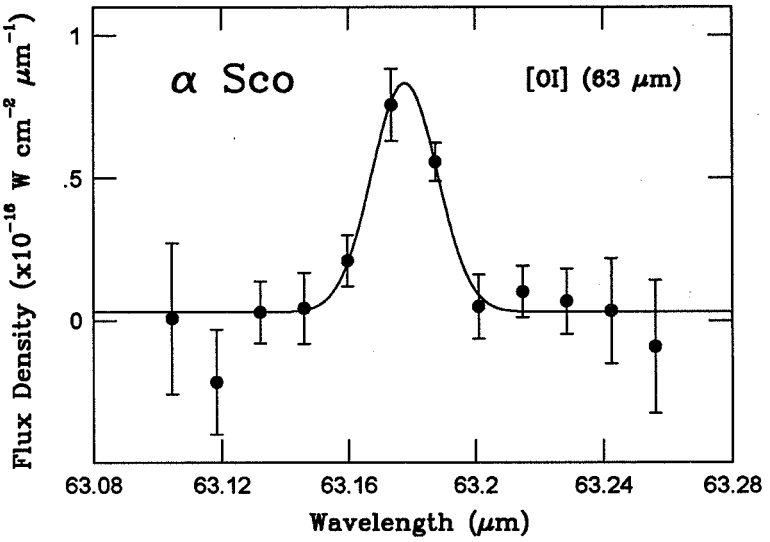

Figure 2. The [O I] 63 μm line in α Sco on 93 May 23.

distribution to obtain $\mathcal{N}_u$, equation (1) becomes

$$L_{u,\ell} = 4\pi C\, x_o\, A_{u,\ell}\, E_{u,\ell} \int_{3R_*}^{\infty} P_u(r)\, dr, \tag{2}$$

where x_o is the abundance with respect to hydrogen and $P_u(r)$ is the fractional population of the upper level (shown in Figure 1 for [O I] and [Si II]). Adopting the abundances and distance for α Ori from RG, we predict an [O I] flux of 1.4×10^{-18} W cm^{-2} and a [Si II] flux of 6.3×10^{-19} W cm^{-2}.

3. The Observations

The observations were carried out with the Cryogenic Grating Spectrometer (CGS; Erickson *et al.* 1994). We first observed α Ori in 1992 January and successfully detected both the [O I] 63 μm and [Si II] 35 μm lines (Haas & Glassgold 1993). We have subsequently expanded our investigation to include other nearby evolved stars, including the M supergiants α Sco, α Her, and μ Cep. The aperture size was $\sim 32''$ for all the [O I] 63 μm observations, but was $35''$ for [Si II] 35 μm in α Sco, $44''$ for [Si II] in α Ori, and $39''$ for [O I] 146 μm in α Ori. The [O I] 63 μm spectra were corrected for telluric absorption by a strong H_2O line centered just to the red of our bandpass. The absolute flux calibration was accomplished by observing Saturn at the same wavelengths or Orion/KL at nearby continuum wavelengths.

Figure 2 shows the final [O I] spectrum for α Sco and the best least-squares fit, assuming a flat continuum and a superimposed Gaussian line profile. The four free parameters are the continuum strength and the line strength, width, and wavelength. The 92 January spectra of α Ori, as well as additional details about our observational techniques and data reduction procedures, can be found

Table 1. Summary of CGS Observations of Evolved Stars

Source Name	Species and Wavelength	Line Flux ($\times 10^{-18}$ W/cm^2)	Date	Calibration Source	Spectral Type
α Ori	[O I] 63 μm	2.4 ± 0.2	1/92	Orion/KL	M1-M2Ia-Ibc
	[Si II] 35 μm	0.9 ± 0.4		Orion/KL	
	[O I] 63 μm	1.1 ± 0.2	11/93	Orion/KL	
35″ NE	[O I] 63 μm	< 0.6 (3σ)		Orion/KL	
35″ SW	[O I] 63 μm	0.7 ± 0.3		Orion/KL	
	[O I] 146 μm	0.11 ± 0.04		Orion/KL	
α Sco	[O I] 63 μm	2.0 ± 0.3	5/93	Saturn	M1.5Iab-Ib
	[Si II] 35 μm	3.4 ± 0.7		Saturn	
α Her	[O I] 63 μm	1.0 ± 0.2	6/94	Saturn	M5Ib-II
μ Cep	[O I] 63 μm	0.18 ± 0.08	6/92	Saturn	M2Ia
	[O I] 63 μm	< 0.7 (3σ)	6/94	Saturn	
o Cet	[O I] 63 μm	< 0.3 (3σ)	11/93	Orion/KL	M7III
R Leo	[O I] 63 μm	0.3 ± 0.1	11/93	Orion/KL	M6-M9.5IIIe
NML Cyg	[O I] 63 μm	< 0.6 (3σ)	6/92	Saturn	M6IIIe

in Haas & Glassgold (1993). The line fluxes for the stars observed to date are given in Table 1, along with their spectral types, observing epochs, and calibration sources. The errors quoted in Table 1 and plotted in Figure 2 are statistical and represent one standard deviation of the mean. They do not include the absolute calibration error, which is estimated to be $\pm 25\%$ (3σ).

4. Results and Discussion

The original observations of α Ori in 1992 January gave a minimum mass of $5.4 \times 10^{-7}\,M_\odot$ for [O I] in the $^3P_1$ level, assuming optically thin emission and a distance of 200 pc. For densities above the critical density, the levels are in thermal equilibrium and the corresponding minimum mass of warm neutral hydrogen is $1.6 \times 10^{-4}\,M_\odot$, using the photospheric oxygen abundance of 6.3×10^{-4} (Lambert *et al.* 1984). For a mass-loss rate of $4 \times 10^{-6}\,M_\odot$ yr^{-1}, this yields a dynamical time of 40 yr and a radius for the emitting region of 2×10^{15} cm, if the wind velocity is 16 km s^{-1}. Haas & Glassgold noted that their measured line fluxes were both $\sim 1.6\times$ as bright as predicted and included the term u_w/u in the expressions for density and line flux (equation (2)) to account for acceleration of the flow and argued that $u \sim 10$ km s^{-1}, the velocity of the S1 feature (Bernat *et al.* 1979; Goldberg *et al.* 1975), whereas $u_w \sim 16$ km s^{-1}. This brought the predicted fluxes into good agreement with those observed.

The Townes/Genzel group subsequently reobserved α Ori in 1993 March with the 5×5 array of FIFI (Geis *et al.* 1994) to examine the spatial extent of the [O I]. Surprisingly, they were unable to detect the line and set a 3σ upper limit of only $\sim 1/4$ our 92 January flux in their central pixel (Danchi *et al.* 1994). This apparent discrepancy is not easily attributable to differences in beam size, uncertainties in boresight, or other instrumental effects (Townes & Geis, private

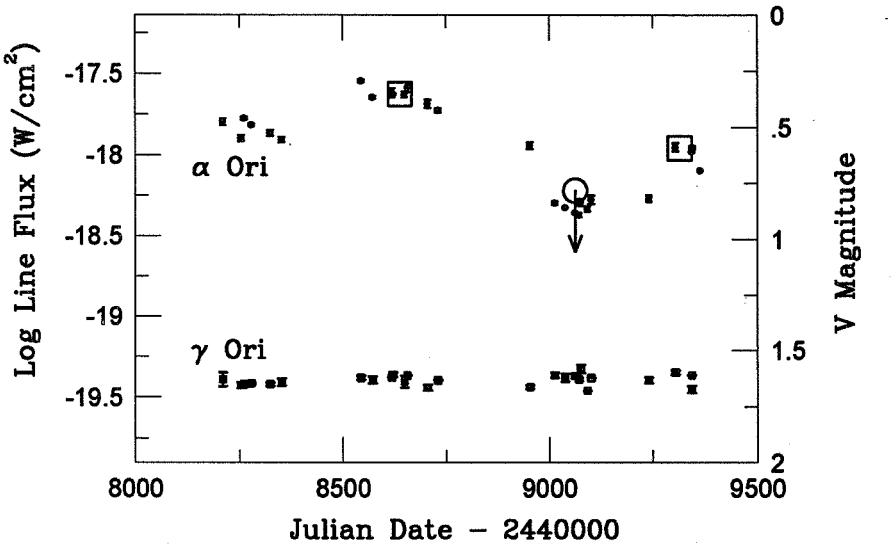

Figure 3. α Ori flux variations versus time ([O I] – the two large open squares are CGS points, the open circle is a FIFI upper limit); V magnitudes – the small closed circles are for α Ori, the small open squares are for γ Ori).

communication). Thus, to confirm our original detection, we reobserved α Ori in 1993 November and measured [O I] at about half its original intensity (*cf* Table 1). Both our 1992 January and 1993 November observations used the same aperture size and calibrated on Orion/KL. Our boresight was particularly well established on the latter flight (with the lower observed flux) because it was determined on the [O I] line in NGC 7027 and confirmed to $\pm 2''$ while offset guiding on the 63 μm continuum of Orion/KL.

These variations in α Ori's [O I] flux may be real. Figure 3 shows the three [O I] observations and the temporal variations observed at V by Krisciunas (1992, 1994). The comparison star for the optical photometry was ϕ-2 Ori and the check star (also shown in Figure 3) was γ Ori. The logarithmic scales are normalized to accentuate the correlation, which may result from luminosity-driven temperature variations similar to those discussed by Goldreich & Scoville (1976), but data at additional epochs is required for confirmation.

To further elucidate the nature of the observed fine structure emission, in 93 November we observed the [O I] 146 μm line centered on α Ori and the [O I] 63 μm line in two tangent beams, one 35″ to the NE and one 35″ to the SW of the star along a position angle of 30° (Table 1). IRAS shows that α Ori's 60 μm continuum emission is extended over several arcmin (Stencel *et al.* 1988), but the RG model predicts that the [O I] emission originates within a radius of $\sim 1.3 \times 10^{15}$ cm (0.″4). If the 2σ detection of [O I] 63 μm to the SW is confirmed, then at least some of the [O I] emission may not be associated with the star. If the 2σ detection of the 146 μm line is confirmed, then [O I] 63 μm/[O I] 146 μm $\sim$ 10, which can only obtain if [O I] 63 μm is optically thick (*cf* Tielens & Hollenbach 1985) or

$n_H \lesssim 100$ and $T >> h\nu/k$ (Watson 1985). Neither of these conditions is consistent with the RG model, in which the [O I]-emitting zone has $n_H > 10^6\,cm^{-3}$ and an optical depth in the Sobolev approximation of ~ 0.4. Note, however, that neither result is statistically significant and improved S/N is required before definitive conclusions can be drawn.

As shown in Table 1, we have also detected the [O I] 63 μm line in the M supergiants α Sco and α Her, which are similar to α Ori in many ways. All three stars possess warm chromospheres and have semi-regular pulsation periods with time scales from months to years. Their CSEs are O-rich, have no detectable H_2O, SiO, or OH maser emission, are relatively free of gas and dust, and are believed to be principally atomic. The fact that [O I] is seen in all three cases strongly suggests that the emission is physically associated with the stars.

In 1992 January, when both the [Si II] and [O I] lines were observed in α Ori, their ratio (0.40 ± 0.16) was very close to the predicted value (0.45), which assumed a photospheric abundance for oxygen (Lambert *et al.* 1984), a solar abundance for silicon, and that O^0 and Si^+ are the dominant ionization states. The flux ratio of [Si II] to [O I] in α Sco is 1.7 ± 0.4, considerably larger than for α Ori. However, using the circumstellar depletions of Si ($\delta = -0.12$) and O ($\delta = -0.79$) measured by UV absorption against α Sco's dwarf B companion (Snow *et al.* 1987) and assuming the temperature distribution of RG, equation (2) predicts a flux ratio of 1.5, again very close to the observed value. This excellent agreement tends to validate the RG picture that the lines originate in the high density, warm environment that extends into, if not throughout, the transition region between the chromosphere and the outer CSE and that the gas in this region is primarily atomic.

For α Sco, the inferred minimum mass of warm, atomic hydrogen in the [O I]-emitting zone is $5.2 \times 10^{-4}\,M_\odot$, assuming a distance of 180 pc (van der Hucht *et al.* 1980) and $O/H = 1.3 \times 10^{-4}$ (Snow *et al.* 1987). Similarly, for α Her, we obtain $M_H = 8.4 \times 10^{-6}\,M_\odot$, assuming a distance of 70 pc (Thiering & Reimers 1993) and $O/H = 6.3 \times 10^{-4}$ (same as α Ori). If α Her is at 150 pc (Danchi *et al.* 1994), M_H would be 4× larger. To obtain mass-loss rates for these stars, we assume an r^{-2} density distribution, so $dM/M = dr/r$ or $\dot{M} = Mu/R$, where R is the radius of the emitting region and u is the wind velocity at R. As illustrated in Figure 1, R is determined by the temperature distribution, which is relatively insensitive to the mass-loss rate (Rodgers 1990), and u is some fraction of the wind's terminal velocity, as discussed by Haas & Glassgold (1993). The inferred mass loss rates are $\sim 1.3 \times 10^{-5}\,M_\odot\,yr^{-1}$ for α Sco and $\sim 2.1 \times 10^{-7}\,M_\odot\,yr^{-1}$ for α Her, assuming the above M_H's and $u = 10\,km\,s^{-1}$.

Mass loss rates for these stars have been measured with a variety of tracers, including H I (Bowers & Knapp 1987), K I, Na I (Mauron & Caux 1992), Ca II (Hagen *et al.* 1983), [C I] (Huggins *et al.* 1994), and polarized dust (Mauron & Le Borgne 1986). They vary because of uncertainties in the abundances of the observed species relative to hydrogen and, more fundamentally, because these species sample the CSE over varying distances and, consequently, on different time scales (van der Veen & Olofsson 1990). In particular, the evidence for multiple dust shells (Danchi *et al.* 1994) and the rapid changes in α Ori's 10 μm silicate feature (Sloan *et al.* 1993) add to a growing body of evidence that the dust formation rate in these CSEs is highly variable. At the present time all three stars seem to have remarkably little dust close in ($\lesssim 1''$ or 3×10^{15} cm at 200 pc), where the RG temperature distribution (Figure 1)

shows a precipitous drop through the condensation temperature of the refractory elements ($\sim 1000-2000$ K). Either the strong chromospheric UV field is inhibiting dust formation at the present epoch or the mass-loss rate is variable and the density is currently too low for efficient nucleation (Tielens 1990). Periodic monitoring of the [O I] and [Si II] emission from these stars will help answer such questions.

Finally, we have searched for [O I] emission in several other nearby evolved stars, but have only obtained upper limits, except for a possible detection in R Leo. R Leo and *o* Cet are O-rich Miras with dust observed about as close in to their photospheres as it can fully condense (Danchi *et al.* 1994). NML Cyg is known to be extremely dusty and is believed to have a primarily molecular CSE. Only the supergiant μ Cep might be expected to possess an atomic CSE like α Ori, but its mass-loss rate is somewhat less than α Ori's (Hagen *et al.* 1983) and it is located $4-5\times$ further away, so our upper limit on [O I] is not particularly significant.

5. Summary

Our KAO observations show that [O I] and [Si II] are detectable in the free flowing winds of supergiants. The good agreement with theory supports the RG thermal model and indicates that the bulk of the fine structure emission originates in the transition zone at radii of ~ 3 to 20 R_*. In this region, the cooling from adiabatic expansion and fine-structure emission greatly exceeds the heating and the gas temperature decreases rapidly. This seems to provide an ideal environment for the formation of molecules and dust, but neither process appears to be particularly efficient in these supergiants – we require essentially all of the oxygen and silicon to be in O^0 and Si^+, respectively, to produce the observed fine structure emission in α Ori. The circumstellar depletions may be somewhat larger in α Sco (Snow *et al.* 1987), but are still small compared to interstellar depletions. The strong UV radiation field may inhibit dust formation in these CSE; episodic mass loss may also play a role.

The [O I] 63 μm and [Si II] 35 μm lines are ideal probes of the transition region because they have large critical densities and level separations. Other FIR transitions of interest are [O I] 146 μm, [Fe II] 26 μm, and [C II] 158 μm. Since [O I] 63 and 146 μm share a common level, their ratio is relatively insensitive to density and serves as an excellent temperature probe if the gas is optically thin (Tielens & Hollenbach 1985), as we expect. Observations of [Fe II] 26 μm would provide a direct measurement of the Fe abundance, but are difficult from the KAO because of the proximity of a strong, narrow telluric H_2O line. The [C II] 158 μm line originates in the outer envelope and is primarily a measure of the ambient UV field in the vicinity of the star. There is some evidence that the intensity of these lines varies by a factor of two or more on a time scale of a year – confirmation of this phenomena and its correlation with other observables will help elucidate the physics of the transition zone. Future high resolution spectroscopy ($\sim 10^5$) of these fine-structure lines will provide important information on the velocity field in the dust acceleration zone.

Acknowledgements. We thank J. Baltz, S. Colgan, E. Erickson, D. Lee, S. Lord, R. Rubin, A. Rudolph, and J. Simpson for assistance with the flight planning, observations, and data analysis. We acknowledge the continuing efforts of the

KAO staff and the support of NASA under UPN 352. The research of AEG is supported by a grant from NASA's program in infrared, sub-millimeter, and radio astronomy.

6. References

Benson, P. J. *et al.* 1990, ApJS, 74, 911
Bernat, A. P., Hall, D. N. B., Hinkle, K. H., & Ridgway, S. T. 1979, ApJ, 233, L135
Bowers, P. F., & Knapp, G. R. 1987, ApJ, 315, 305
Danchi, W. C., Bester, M., Degiacomi, C. G., Greenhill, L. J., & Townes, C. H. 1994, AJ, 107, 1469
Erickson, E. F., Haas, M. R., Colgan, S. W. J., Simpson, J. P., & Rubin, R. H. 1994, in Proc of the Airborne Astronomy Symp on the Galactic Ecosystem: From Gas to Stars to Dust, ed. M. R. Haas, J. A. Davidson, & E. F. Erickson (San Francisco: ASP), paper 702
Geis, N. *et al.* 1994, in Proc of the Airborne Astronomy Symp on the Galactic Ecosystem: From Gas to Stars to Dust, ed. M. R. Haas, J. A. Davidson, & E. F. Erickson (San Francisco: ASP), paper 708
Glassgold, A. E., & Huggins, P. J. 1986, ApJ, 306, 605
Goldberg, L., Ramsey, L., Testerman, L., & Carbon, D. 1975, ApJ, 199, 427
Goldreich, P., & Scoville, N. 1976, ApJ, 205, 144
Haas, M. R., & Glassgold, A. E. 1993, ApJ, 410, L111
Hagen, W., Stencel, R. E., & Dickerson, D. F. 1983, ApJ, 274, 286
Huggins, P. J. 1987, ApJ, 313, 400
Huggins, P. J., Bachiller, R., Cox, P., & Forveille, T. 1994, ApJ, 424, L127
Krisciunas, K. 1992, IAU Inform. Bull. on Variable Stars No. 3728.
Krisciunas, K. 1994, IAU Inform. Bull. on Variable Stars No. 4028.
Lambert, D. L., Brown, J. A., Hinkle, K. H., & Johnson, H. R. 1984, ApJ, 284, 233
Mauron, N. & Le Borgne, J. F., A&A, 1986, 168, 217
Mauron, N. & Caux, E. 1992, A&A, 265, 711
Rodgers, B. 1990, M.S. thesis, New York University
Rodgers, B., & Glassgold, A. E. 1991, ApJ, 382, 606 (RG)
Skinner, C. J., & Whitmore, B. 1987, MNRAS, 224, 335
Sloan, G. C., Tandy, P. C., Pirger, B. E., & Hodge, T. M. 1993, BAAS, 25, 876
Snow, T. P., Buss, R. H., Gilra, D. P., & Swings, J. P. 1987, ApJ, 321, 921
Stencel, R. E., Pesce, J. E., & Bauer, W. H. 1988, AJ, 95, 141
Thiering, I., & Reimers, D. 1993, A&A, 274, 838
Tielens, A. G. G. M. 1990, From Miras to Planetary Nebulae: Which Path for Stellar Evolution?, eds. M. O. Mennessier & A. Omont (Editions Frontieres), 186
Tielens, A. G. G. M., & Hollenbach, D. J. 1985, ApJ, 291, 722
van der Hucht, K. A., Bernat, A. P., & Kondo, Y. 1980, A&A, 82, 14
van der Veen, W., & Olofsson, H. 1990, From Miras to Planetary Nebulae: Which Path for Stellar Evolution?, eds. M. O. Mennessier & A. Omont (Editions Frontieres), 225
Watson, D. M. 1985, ESLAB Symposium XVI, Galactic & Extragalactic Infrared Spectroscopy, December, 1982, Toledo, Spain

Airborne Astronomy Symposium on the Galactic Ecosystem
ASP Conference Series, Vol. 73, 1995
M.R. Haas, J.A. Davidson, and E.F. Erickson (eds.)

KAO Observations of SN1987A

D.H. Wooden

NASA Ames Research Center, Moffett Field, CA 94035-1000

Abstract. Explosion calculations of SN1987A generate pictures of Rayleigh-Taylor fingers of radioactive ^{56}Ni (^{56}Ni $\longrightarrow$ ^{56}Co $\longrightarrow$ ^{56}Fe) which are boosted to velocities of several thousand km s^{-1}. From the KAO observations of the mid-IR iron lines, a picture of the iron in the ejecta emerges which is consistent with the 'frothy iron fingers' having expanded to fill about 50% of the metal-rich volume of the ejecta ($v_m \leq 2500$ km s^{-1}). The ratio of the nickel line intensities $I_{[Ni\ I]7.5\mu m}/I_{[Ni\ II]6.6\mu m}$ yields a high ionization fraction of $x_{Ni} \geq 0.9$ in the volume associated with the iron-group elements at day 415, before dust condenses in the ejecta.

From the KAO observations of the dust's thermal emission (2 μm – 100 μm), it is deduced that when the grains condense, their infrared radiation is trapped, their apparent opacity is gray, and they have a surface area filling factor of about 50%. The dust emission from SN1987A is featureless: no 9.7 μm silicate feature, nor PAH features, nor dust emission features of any kind are seen at any time. The total dust opacity increases with time even though the surface area filling factor and the dust/gas ratio remain constant. This suggests that the dust forms along coherent structures which can maintain their radial line-of-sight opacities, i.e., along fat fingers. The coincidence of the filling factor of the dust and the filling factor of the iron strongly suggests that the dust condenses within the iron, and therefore the dust is iron-rich. It only takes $\sim 10^{-4}$ $M_\odot$ of dust for the ejecta to be optically thick out to $\sim$100 μm; a lower limit of 4×10^{-4} $M_\odot$ of condensed grains exists in the metal-rich volume, but much more dust could be present.

The episode of dust formation started at about 530 days and proceeded rapidly, so that by 600 days 45% of the bolometric luminosity was being emitted in the IR; by 775 days, 86% of the bolometric luminosity was being reradiated by the dust. Measurements of the bolometric luminosity of SN1987A from 1000 – 2300 days are based on 10 μm and 20 μm photometry and rely on the suppositions that the IR emission is a graybody (proven to be true by the KAO observations at 615 and 775 days) and that the dust temperature drops to and remains at 150 K. The late-time bolometric luminosity is stronger than that expected from the radioactive decay of ^{56}Co, ^{57}Co, ^{44}Ti, and ^{22}Na and the the late-time dust temperatures are consistent with the presence of a compact object.

References to KAO observations of SN1987A include efforts by principal authors Colgan, Dwek, Erickson, Haas, Harvey, Moseley, Rank, Witteborn, & Wooden.

1. Iron in SN1987A

In the first week following the explosion of SN1987A, the rapid radioactive decay of ^{56}Ni $\longrightarrow$ ^{56}Co deposited about 40% of the total ^{56}Ni decay energy into the inner regions of the ejecta forming a hot low density 'nickel bubble' interior to denser overlying layers. This bubble and the denser overlying layers became Rayleigh-Taylor unstable, boosting fingers or bullets of ^{56}Co and iron-group elements to velocities of about 3000 km s^{-1}, penetrating the outer hydrogen envelope. Without the 'popping of the nickel bubble' the iron group elements are expected to have reached velocities of only about 1000 km s^{-1}. Models which include this mixing of ^{56}Co into the outer layers of the ejecta are required to account for the early appearance of x–rays and γ–rays, the observed γ–ray line ratios, and the bolometric light curve which is powered by the radioactive decay of ^{56}Co $\longrightarrow$ ^{56}Fe through 1000 days, and by the longer lived isotopes, ^{57}Co and ^{44}Ti, thereafter.

The mid-IR iron lines observed from the KAO show complex velocity structure and reveal the history of the Rayleigh-Taylor fingers. The mid-IR forbidden iron [Fe II] 26.0 μm , [Fe II] 17.9 μm , and [Fe II] 24.5 μm lines were observed on day 250 (Moseley et al. 1989; Erickson et al. 1988), day 410 (Haas et al. 1990), day 640 (Colgan et al. 1994), and day 1150 (Dwek et al. 1992). The similarity of the velocity-resolved line profiles of the low excitation [Fe II] 17.9 μm line ($T_{ex} \simeq 3500$ K) and the high excitation near-IR [Fe II] 1.26 μm line ($T_{ex} \simeq 11000$ K) (Figure 1) shows that the mid-IR lines and the near-IR lines arise from the same gas (Haas et al. 1990; Spyromilio, Meikle, & Allen 1990). The mass of iron deduced from the optically thin analysis of the mid-IR iron lines is, however, at most one-third of the iron deduced from both the near-IR iron lines and the bolometric light curve (Moseley et al. 1989; Haas et al. 1990; Dwek et al. 1992; Varani et al. 1990).

Only by combining the ground-state [Fe II] 26.0 μm, and the excited state [Fe II] 17.9 μm and [Fe II] 24.5 μm line strengths measured at day 250 (Moseley et al. 1989), does the picture emerge: under the assumption of LTE level populations ($n_e \geq 10^4$ cm^{-3}), the 17.9 μm/26.0 μm and 24.5 μm/26.0 μm line ratios yield a simultaneous solution of the electron temperature of $T_e = 3250 \pm 750$ K and the optical depth of the 26.0 μm line of $\bar{\tau}_{26\mu m} = 3 \pm 1$. The optical depth of the 26.0 μm ground-state line, in the Sobolev approximation, is proportional to the mean local number density of iron ions in the ejecta: $\bar{\tau}_{26\mu m} \simeq 3$ yields $\bar{n}_{Fe+} = 2.6^{+1.6}_{-1.2} \times 10^6$ cm^{-3}. Taking $x_{Fe} \simeq 0.6$, the ionization fraction determined from the optically thin near-IR [Fe II] 1.26 μm line (day 192, Oliva, Moorwood, & Danziger 1987; day 225, Meikle et al. 1989), the iron ions have a volume filling factor of $f = 0.5^{+0.4}_{-0.2}$ (Wooden 1994). For an ionization fraction of $x_{Fe} = 0.8$ and a higher electron temperature of $T_e \approx 4000$ K, the iron ions have a volume filling factor of $f \geq 0.4$, as shown by Li, McCray, & Sunyaev (1993) in their simultaneous fitting of many cobalt, iron, and nickel lines. Thus the 'frothy iron fingers' must fill about 50% of the metal-rich volume in order to produce the observed optical depth of the 26.0 μm line: the 0.075 $M_\odot$ of iron is seen as the leavening in the $\sim$1 $M_\odot$ metal rich volume. The spatially inhomogeneous distribution of iron-group elements arises first by the Rayleigh-Taylor instabilities in the early phases of the explosion, as demonstrated by hydrodynamic simula-

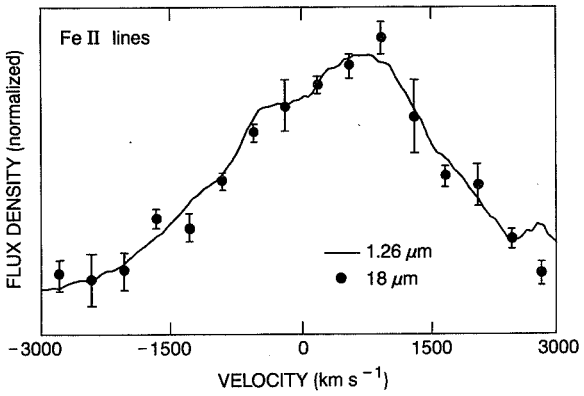

Figure 1. A comparison of the central portion of the 17.9 μm profile at day 407 (dots) with the normalized 1.26 μm profile at day 377 (line); Fig. 3 of Haas et al. (1990).

tions of Fryxell, Arnett, & Muller (1991), Herant, Benz, & Colgate (1992), and others. Secondly, the hot ^{56}Co clumps or fingers do work on the surrounding gas, compressing the non-iron group elements, while expanding to fill roughly half the metal-rich volume of the ejecta (Li et al. 1993).

As the ejecta expands with time, the drop in optical depth ($\tau \propto t^{-2}$) implies a corresponding increase in the 26.0 μm line strength with time. Between day 250 and day 410, an increase in the [Fe II] 26.0 μm line strength was observed by the Moseley group (Moseley et al. 1989; Dwek 1988), but not by the Erickson group (Erickson et al. 1988; Haas et al. 1990). Haas et al. (1990) argue that the lack of increase in the 26.0 μm line strength between day 250 and day 410 implies that the line emission arises from optically thin iron, and the hidden iron is very optically thick. This argues against the line intensity ratios providing a meaningful average optical depth $\bar{\tau}_{26\mu m}$, and argues in favor of regions with $\tau_{26\mu m} < 1$ and other regions with $\tau_{26\mu m} \gg 1$. The central portions of the optically thin near-IR line ($\tau_{1.26\mu m} \leq 0.01 \times \tau_{26\mu m}$) and the optically thick mid-IR line profiles are, however, the same. Also the detailed shapes of the near-IR forbidden line profiles remain essentially unchanged from day 250 through about day 600 (Spyromilio et al. 1990); for nearly a year there is no further 'revealing' of highly optically thick iron as the ejecta expands. Thus, there is little evidence from the near-IR forbidden lines for iron in the ejecta with $1 \ll \tau_{26\mu m} < 100$. While the evolution of the 26.0 μm line intensity provides a challenge, the velocity-resolved line profiles support the 'frothy iron finger' picture.

The velocity-resolved mid-IR [Fe II] 17.9 μm and [Ni II] 6.6 μm line profiles also show a high-velocity feature at $v \sim +3900$ km s^{-1} (day 415, Haas et al. 1990; day 640, Colgan et al. 1994). Colgan et al. (1994) deduce that the high velocity feature contains about 3% of the total iron in the ejecta. They suggest that the high velocity feature may provide evidence for an off-center explosion (Manchester et al. 1991; Frail & Kulkarni 1991); the momentum carried by the matter could balance the expulsion of a pulsar at high velocity.

2. Stable Nickel in the Ejecta

Stable nickel is created along with radioactive nickel in explosive silicon burning and thereby is a trace constituent of the iron-group fingers in the ejecta. By its relatively low abundance compared to iron, the mid-IR forbidden lines of stable nickel suffer less optical depth effects than the mid-IR iron lines. The nickel lines are therefore ideal for studying the degree of ionization in the inner regions of the ejecta. *All* forbidden lines from neutral, singly-, doubly-, and triply-ionized nickel *with* $T_{ex} \leq 5000\,\mathrm{K}$ occur in the $2\,\mu\mathrm{m} - 14.5\,\mu\mathrm{m}$ wavelength range. From the KAO, spectra of the [Ni I] and [Ni II] forbidden lines were obtained at 260, 415, 615, 775, and 1140 days (Wooden et al. 1993; Colgan et al. 1994; Witteborn et al. 1990). Lines from [Ni III] and [Ni IV] were not detected; in fact, only neutral and singly-ionized species were seen in the spectra of SN1987A (Wooden et al. 1993; McCray 1993).

The [Ni I] $7.5\,\mu\mathrm{m}$ and the [Ni II] $6.6\,\mu\mathrm{m}$ ground-state lines originate from upper levels with nearly identical excitation energies. The ratio of the [Ni I] $7.5\,\mu\mathrm{m}$ line to the [Ni II] $6.6\,\mu\mathrm{m}$ line is independent of the electron temperature for $T_e \geq 1000\,\mathrm{K}$, weakly dependent on the electron density n_e, and highly sensitive to the ionization fraction x_{Ni}. For a range of electron temperatures $T_e = 3000 - 4500\,\mathrm{K}$ (Haas et al. 1990; Li et al. 1993), the line intensity ratio $I_{[Ni\ I]\,7.5\mu\mathrm{m}}/I_{[Ni\ II]\,6.6\mu\mathrm{m}} = 0.05 \pm .01$ constrains the ionization fraction to be $x_{Ni} \geq 0.90$ at 415 days (Wooden et al. 1993). For an electron density of $n_e = 5 \times 10^6\ \mathrm{cm}^{-3}$ and the corresponding $x_{Ni} = 0.95 - 0.97$, a stable nickel mass of $M_{Ni} = 4.5 - 5.0 \times 10^{-3}\ M_\odot$ is derived (Wooden et al. 1993). This is close to the predicted nickel mass from Woosley, Pinto, & Weaver (1988)'s nucleosynthesis explosion models for an 18 $M_\odot$ and a 20 $M_\odot$ precursor, but about 4 times smaller than the nickel mass predicted by Hashimoto, Nomoto, & Shigeyama (1989)'s model for a 20 $M_\odot$ precursor.

The similarity of the shapes of the line profiles of the [Ni I]* $3.12\,\mu\mathrm{m}$, [Ni II] $6.6\,\mu\mathrm{m}$, [Fe II] $1.26\,\mu\mathrm{m}$, [Fe II] $17.9\,\mu\mathrm{m}$, and the [Fe II] $26.0\,\mu\mathrm{m}$ lines (Spyromilio et al. 1990; Haas et al. 1990; Colgan et al. 1994) indicates that the stable nickel and the iron occupy the same volume of the ejecta. The nickel has a relatively low abundance by number compared to the iron, so the iron provides the majority of electrons which collide with and excite the forbidden nickel lines.

3. The Thermal Dust Continuum Emission

A dramatic drop in the visual light output of the supernova commences around 530 days (Whitelock et al. 1989): the U to M light curve declines more rapidly than expected for the radioactive decay of ^{56}Co and the ejecta's decreasing opacity to γ–rays. This change in the light curve at 530 days signifies the rapid formation of grains in the ejecta. At 615 days, the thermalized ^{56}Co γ–ray luminosity (hereafter denoted $L_{56,\gamma}$) equals the sum of the UV, visual, and IR luminosities. The energy budget is balanced only when the drop in the visual light is compensated by the increase in the thermal IR continuum (Suntzeff & Bouchet 1990). After ~550 days optical line profiles of Mg I] 4571 Å, [O I] 6300 Å, [C I] 9844 Å(Lucy et al. 1989a, 1989b), and infrared profiles of [Si I], [Fe II], and [Ni II] become increasingly blue shifted with time (Spyromilio et al.

1990; Colgan et al. 1994). As dust condenses interior to the line-emitting volume, the emission from the far side of the ejecta suffers greater extinction compared to the near side and the line centroids become blue-shifted. At day 615, the dust reprocesses 45% of $L_{56,\gamma}$, and at day 775, 83% of $L_{56,\gamma}$. At even later times, the dust luminosity is ~90% of thermalized γ–ray luminosity (Bouchet et al. 1994).

From the KAO observations of the dust's thermal continuum spectrum at 615 and 775 days, the grains have a gray emissivity out to $30\,\mu$m – $100\,\mu$m (Wooden et al. 1993). At no time was there a $9.7\,\mu$m silicate emission feature, nor any identifiable dust feature, seen in the spectra of SN1987A. This is unlike other dusty astronomical objects in which grains have emissivities which fall as $\lambda^{-\beta}$ for $\beta = 1, 2$ compared to a blackbody (Hildebrand 1983). From the dust emission spectrum, either the grains in the ejecta of SN1987A are very large with radii $a > 6\,\mu$m or the optical depth of the IR emission is very high with $\tau_{dust}(30\,\mu\text{m}) > 1$. The small amount of visual light which does escape the dusty nebula suffers a λ^{-1} extinction law (Lucy et al. 1989a, 1989b). Therefore the grains are small with the bulk of the grains residing in optically thick regions (Lucy et al. 1989b; Wooden et al. 1993). An optical depth of $\tau_{dust}(30\,\mu\text{m}) \approx 1$ implies a minimum dust mass of $3.1 \times 10^{-4}\ M_\odot$ at 615 days, and a minimum dust mass of $5.0 \times 10^{-4}\ M_\odot$ at 775 days.

The *temporal evolution* of the dust temperatures is consistent with the grains being immersed in an optically thick medium with a gas-to-dust ratio which is constant in time (Wooden et al. 1993). It is convenient to think of the grains in optically thick 'clumps', although the dust optical depth arises from enhanced grain column depths along the observer's line-of-sight. If the dust is at an expansion velocity of $v_d = 1800$ km s^{-1}, then 400 K dust fills 55% of the surface area at day 615 and 266 K dust fills 56% of the surface area at day 775. The surface area filling factor stays constant, as the volume of the ejecta expands by a factor of 2 and the mass of gas participating in heating the dust more than doubles. Together these suggest that additional dust forms interior to and along the same radial-lines-of-sight as the first dust formed.

There is indirect evidence that the dust condenses within the iron-rich volume of the ejecta by consideration of the change in the iron-group element emission line profiles after about 575 days (Figure 2). While the He I $1.083\,\mu$m, Paschen β $1.282\,\mu$m, and Mg I $1.503\,\mu$m lines become blue-shifted with the same λ^{-1} dependence as the optical Mg I] and [O I] lines, the iron-group lines ([Fe II] $1.257\,\mu$m, [Fe II] $1.553\,\mu$m, [Fe II] $1.664\,\mu$m, and [Ni I] $3.119\,\mu$m) undergo a blueward shift about three times greater (Spyromilio et al. 1990). At 615 days and more so at 775 days the [Ni II] $6.634\,\mu$m line also becomes blue-shifted (Colgan et al. 1994; Wooden et al. 1993). The -440 ± 270 km s^{-1} blue-shift seen in the 615 day high resolution measurements of the [Ni II] $6.634\,\mu$m line is successfully modeled by placement of optically thick clumps of dust distributed proportional to the gas density interior to $v_d \simeq 1900$ km s^{-1} (Colgan et al. 1994). The line intensities of the near-IR [Fe II] $0.716\,\mu$m, $0.862\,\mu$m, and the $1.258\,\mu$m lines drop significantly between 575 and 735 days: the small mass of emitting iron at 735 days may be due to the iron being hidden in optically thick clumps of dust or the iron condensing into dust (Spyromilio & Graham 1992). The condensation of small iron-rich grains, i.e., Fe/Ni grains or FeS grains, in the ejecta of SN1987A explains the observed λ^{-1} extinction law, the absence of

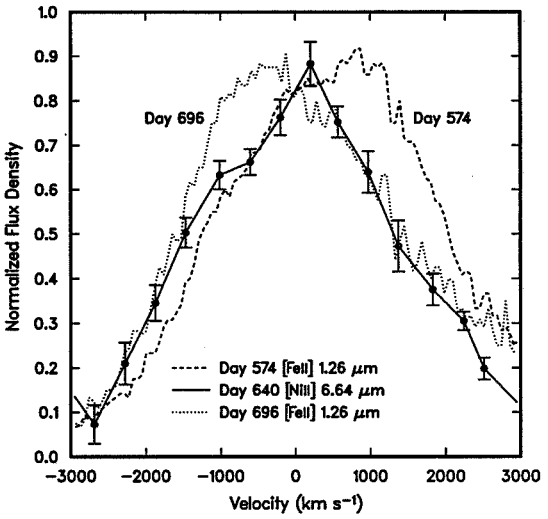

Figure 2. Comparison of the [Ni II] 6.6 μm profile at day 640 (dots) with the [Fe II] 1.26 μm profiles at day 574 (dashed) and day 696 (dotted); Fig. 3 of Colgan et al. (1994).

a 9.7 μm silicate emission feature, and may, in the case of FeS grains (Pollack et al. 1994), provide the observed gray emissivity through far-IR wavelengths. The dusty 'clumps' could very well be the 'dusty frothy iron fingers'!

4. Late Time Light Curve

Day 775 is the latest epoch for which the wavelength coverage and signal-to-noise of the KAO data is sufficient to constrain the dust temperature and grain emissivity: from the χ^2-fit of the continuum spectrum, the dust temperature is $T_{d,bb} = 422\,\mathrm{K}$ and the emission is a graybody (Wooden et al. 1993). At day 1316, nearly two years later, the dust temperature is determined from 10 μm and 20 μm photometry to be $T_{d,bb} = 155^{+0}_{-25}\,\mathrm{K}$, assuming the spectral shape is a blackbody (Bouchet, Danziger, & Lucy 1991). Then again, more than a year later, at day 1731 the blackbody dust temperature is unchanged, $T_{d,bb} \simeq 155\,\mathrm{K}$ (Bouchet et al. 1994). From ~2000 days, the *blackbody* dust temperature has been taken to be $T_{d,bb} \sim 155\,\mathrm{K}$ and the 10 μm photometry point (requiring 5 hours of integration to obtain a 3σ measurement) has been used to determine the late-time bolometric luminosity. The observed bolometric luminosity agrees with the models of radioactive decay (Frannson & Kozma 1993) plus a central compact object (Bouchet et al. 1994). The central compact object could be a $2 \times 10^{37}\mathrm{erg\ s^{-1}}$ accreting x-ray pulsator or a $5 \times 10^{37}\mathrm{erg\ s^{-1}}$ pulsar (Bouchet et al. 1994). At the time of the KAO observations, the dust temperature drops as the fourth-root of the bolometric luminosity, as expected for an optically thick medium. Figure 3 shows this law for the dust temperature, normalized at day 615 and extrapolated to day 2500. The solid line, which falls well below the

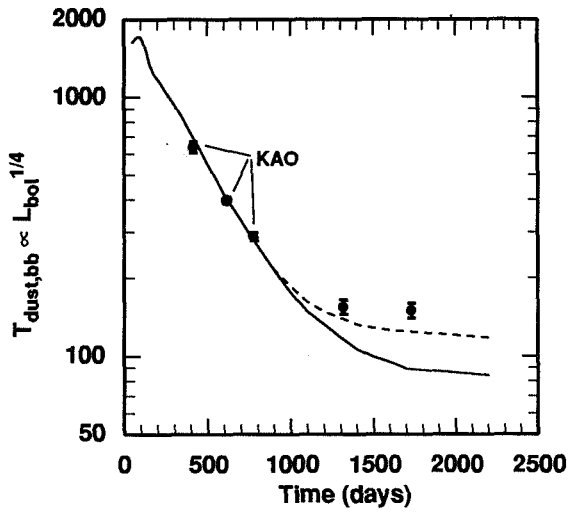

Figure 3. The graybody dust temperature computed as $L_{bol}^{1/4}$, normalized at day 615, compared to the observed late-time dust temperatures (dots). The three dust temperatures determined using the 2 μm - 100 μm airborne data are labeled "KAO" (Wooden et al. 1993). The solid line assumes L_{bol} has radioactive decay contributions from ^{57}Co, ^{44}Ti, and ^{22}Na; the dotted line assumes both radioactive decay contributions and an embedded compact object (Bouchet et al. 1994).

observed $\sim$ 155 K dust temperature, shows the dust temperatures expected for a light curve solely due to radioactive processes. The dotted line, which agrees with the observed dust temperatures, shows the dust temperatures expected for radioactive decay plus the central compact object. Thus, the value of the dust temperature $T_{d,bb} \sim 155$ K at late times is consistent with the presence of either an x-ray pulsator or a pulsar.

Acknowledgments. We acknowledge NASA's support of the Airborne Astronomy Program and the commitment of the staff and the crew of the Kuiper Airborne Observatory to the acquisition of this unique set of observations of SN1987A.

References

Bouchet, P., Danziger, I. J., & Lucy, L. B. 1991, AJ, 102, 1135

Bouchet, P., Danziger, I. J., Gouiffes, C., Della Valle, M., & Moneti, A. 1994, in IAU Coll. 145 on Supernovae and Supernovae Remnants. Xian, China, 24-29 May 1993. Cambridge University Press

Colgan, S. W. J., Haas, M. R., Erickson, E. F., Lord, S. D., & Hollenbach, D. J. 1994, ApJ, 427, 874

Dwek, E. 1988, Proc. ASA, 7, 468

Dwek, E., Moseley, S. H., Glaccum, W., Graham, J. R., Loewenstein, R. F., Silverberg, R. F., & Smith, R. K. 1992, ApJ, 389, L21

Erickson, E. F., Haas, M. R., Colgan, S. W. J., Lord, S. D., Burton, M. G., Wolf, J., Hollenbach, D. J., & Werner, M. 1988, ApJ, 330, L39

Frail, D. A., & Kulkarni, S. R. 1991, *Nature*, 352, 785

Fransson, C., & Kozma, C. 1993, ApJ, 408, L25

Fryxell, B., Miller, E., & Arnett, D. 1991, ApJ, 367, 619

Haas, M. R., Colgan, S. W. J., Erickson, E. F., Lord, S. D., Burton, M. G., & Hollenbach, D. J. 1990, ApJ, 360, 257

Hashimoto, M., Nomoto, K., & Shigeyama, T. 1989, A&A, 210, L5

Herant, M., Benz, W., & Colgate, S. 1992, ApJ, 395, 642

Hildebrand, R. H. 1983, QJRAS, 24, 267

Li, H., McCray, R., & Sunyaev, R. A. 1993, ApJ, 419, 824

Lucy, L. B., Danziger, I. J., Gouiffes, C., & Bouchet, P. 1989a, in Proc. IAU Coll. 120, Structure and Dynamics of the Interstellar Medium, ed. G. Tenorio-Tagle, M. Moles, & J. Melnick (Berlin: Lecture Notes in Physics, Springer-Verlag), 164

Lucy, L. B., Danziger, I. J., Gouiffes, C., & Bouchet, P. 1989b, in Supernovae: The Tenth Santa Cruz Workshop in Astronomy and Astrophysics, ed. S. E. Woosley (New York: Springer-Verlag), 82

Manchester, R. N., Kaspi, V. M., Johston, S., Lyne, A. G., & D'Amico, N. 1991, MNRAS, 253, 7P

McCray, R. 1993, ARA&A, 31, 175

Meikle, W. P. S., Allen, D. A., Spyromilio, J., & Varani, G.-F. 1989, MNRAS, 238, 193

Moseley, S. H., Dwek, E., Glaccum, W., Graham, J. R., Loewenstein, R. F., & Silverberg, R. F. 1989, ApJ, 347, 1119

Oliva, E., Moorwood, A. F. M., & Danziger, I. J. 1987, ESO Messenger, No. 50, 18

Pollack, J. B., Hollenbach, D., Simonelli, D. P., Beckwith, S., Roush, T., & Fong, W. 1993, ApJ, 421, 615

Spyromilio, J., Meikle, W. P. S., & Allen, D. A. 1990, MNRAS, 242, 669

Spyromilio, J. & Graham, J. R. 1992, MNRAS, 255, 671

Suntzeff, N. B. & Bouchet, P. 1990, AJ, 99, 650

Varani, G.-F., Meikle, W. P. S., Spyromilio, J., & Allen, D. A. 1990, MNRAS, 245, 570

Whitelock, P. A. et al. 1989, MNRAS, 240, 7P

Witteborn, F. C., Bregman, J. D., Wooden, D. H., Rank, D. M., & Cohen, M. 1990, BAAS, 22, 1147

Woosley, S. E., Pinto, P. A., & Weaver, T. A. 1988, Proc. ASA, 7, 355

Wooden, D. H., Rank, D. M., Bregman, J. D., Witteborn, F. C., Tielens, A. G. G. M., Cohen, M., Pinto, P. A., Axelrod, T. S. 1993, ApJS, 88, 477

Wooden, D. H. 1994, in IAU Coll. 145 on Supernovae and Supernovae Remnants. Xian, China, 24-29 May 1993. Cambridge University Press

Airborne Astronomy Symposium on the Galactic Ecosystem
ASP Conference Series, Vol. 73, 1995
M.R. Haas, J.A. Davidson, and E.F. Erickson (eds.)

Mid- and Far-Infrared Emission Bands in C-rich Proto-planetary Nebulae

A. Omont[1], P. Cox[2], S.H. Moseley[3], W. Glaccum[3], S. Casey[3], T. Forveille[4], R. Szczerba[5], Kin-Wing Chan[3]

[1] *I.A.P., CNRS, 98b bd. Arago, F-75014*

[2] *Observatoire de Marseille and MPIfR, Bonn*

[3] *Laboratory for Astronomy and Solar Physics, NASA/GSFC*

[4] *Observatoire de Grenoble*

[5] *Department of Physics and Astronomy, Calgary*

Abstract. The 16–48 μm spectra of five carbon-rich post-AGB objects known to have an unidentified 21 μm feature in their IRAS LRS spectra have been obtained using the *Kuiper Airborne Observatory*. A broad emission band extending from 24 to $\sim$ 45 μm is present in the spectra of these objects. The strength of this band is variable from source to source and is not correlated with the strength of the 21 μm band. The possible identifications for the emitting material of both the 21 and 30 μm emission bands is discussed.

1. Introduction

Circumstellar envelopes of stars in transition between the AGB red giants and planetary nebulae (often called proto-planetary nebulae, PPN) are particularly interesting because of their rapid variations in physical conditions. One intriguing class of C-rich PPN exhibits a strong unidentified band at 21 μm (Kwok, Volk & Hrivnak 1989). Although the properties of these sources are similar to those of the archetype PPN, AFGL 2688, it is not understood why their *IRAS* LRS spectra display such strong 21 μm bands, as well as equally strong $11 - 15\,\mu$m plateaus (Buss et al. 1990), while such structures are apparently absent in about half of the known C-rich PPN or very weak as in the case of AFGL 2688 (Buss et al. 1993).

In this paper we report the results of spectral observations in the range 16 to 48 μm on four sources displaying strong 21 μm features, IRAS 07134+1005, IRAS 20000+3239, IRAS 22272+5435 and IRAS 23304+6147; and, for AFGL 2688. The observations were obtained using the KAO during a series of flights in 1989 March and 1990 September with the GSFC 24-Channel Spectrophotometer, and in 1992 September with a new version of the instrument. A full description of the data and their analysis is presented elsewhere (Omont et al. 1994).

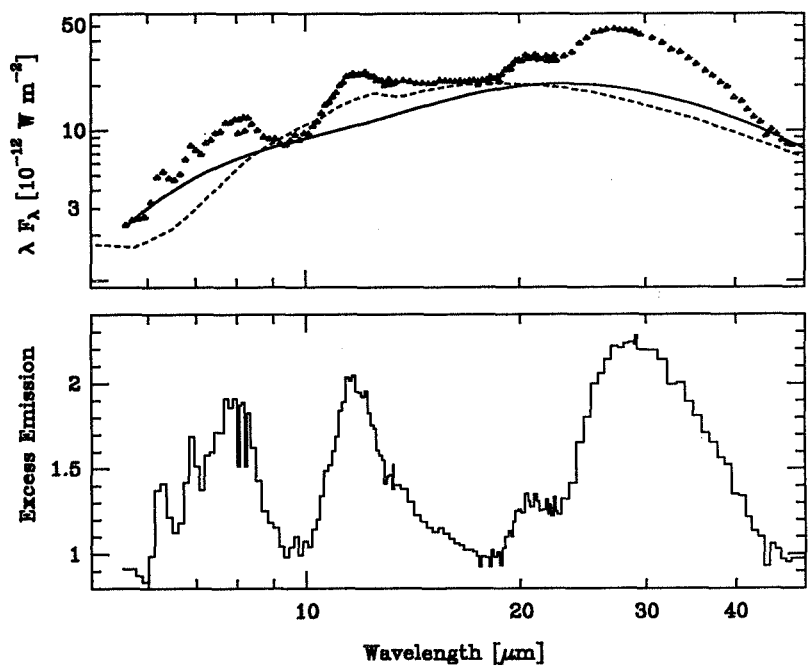

Figure 1. Spectra of the five carbon-rich proto-planetary nebulae. The filled squares show the first channel (16–29 μm, $\Delta\lambda = 0.6\,\mu$m), and the filled triangles the 30 to 48 μm channel with $\Delta\lambda = 1.2\,\mu$m. No scaling of the data has been applied.

2. Results

Figure 1 displays the 16 to 48 μm spectra obtained with the GSFC 24-Channel Spectrophotometer of the five sources. Three facts are clearly observed: i) the variety of strengths of the 21 μm bands, ii) the absence of further narrow features in the 23 – 48 μm range and iii) the rapid rise in emission from 24–25 μm to about 30 μm, which is particularly sharp in the case of IRAS 22272. The shape of the emission seen from 24 to $\sim$ 45 μm is clearly much narrower than expected from a distribution of dust temperatures, suggesting that a strong emission band is present.

Combining the present data with *IRAS* LRS spectra, PSC data, and published measurements in the 5 to 13 μm range, we show in Fig. 2a the composite spectrum of IRAS 22272. The continuum emission underlying the data has been approximated with a sum of two modified black-bodies $\nu^{\beta}\,B_{\nu}(T)$ at temperatures 280 and 120 K normalized at 10 and 43 μm, respectively. We adopted a dust emissivity index of $\beta = 1$. A more quantitative approach to the underlying continuum is based on a radiative model (shown as a dashed line in Fig. 2). Both models provide reasonable approximations for the underlying continuum, but clearly neither of them accounts for the excess emission observed at 30 μm, nor for the other emission bands.

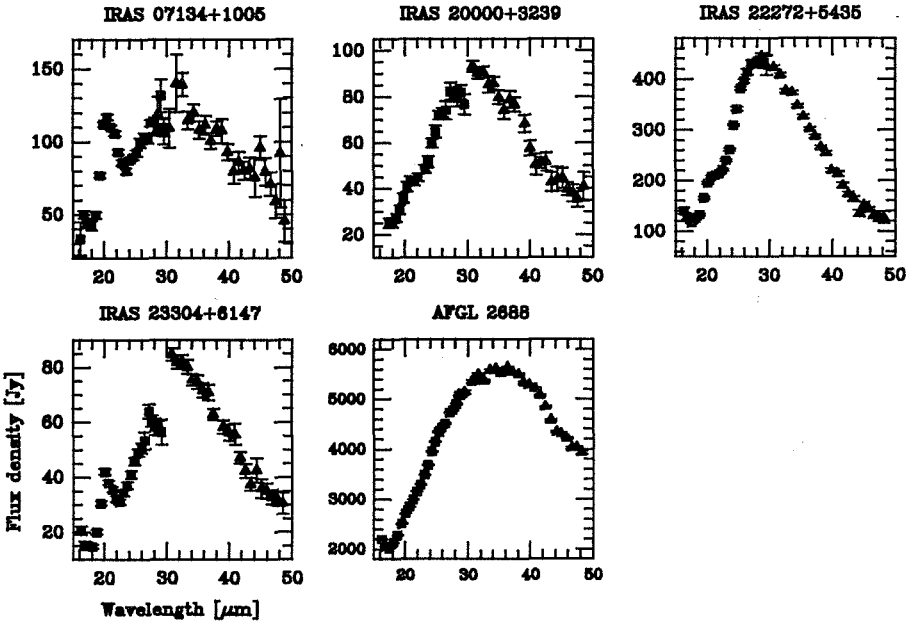

Figure 2. a) Composite infrared spectrum of IRAS 22272 combining the present KAO GSFC 24-Channel Spectrophotometer data with the *IRAS* LRS spectra, together with the KAO HIFOGS 5–8 μm spectra of Buss et al. (1990). Solid lines represent the emission expected from grains at temperatures [280, 120 K]. Dashed lines are the results of a transfer model. b) Infrared excess for IRAS 22272 (see text).

Fig. 2b presents, for IRAS 22272, the infrared excess emission defined as the ratio of the observed spectrum to the underlying continuum (adopting the two-temperature black-body approximation). A series of four major emission bands is seen at 6–9, 10–15, 19–22, and 24–45 μm. These features are also present in the four other PPN (Omont et al. 1994), although the relative intensities of these bands change from source to source. The 30 μm emission band is the strongest feature and accounts, in the case of IRAS 22272, for about 20% of its bolometric luminosity. This prominent emission band is detected in all the sources, including AFGL 2688. The relative strengths of the 30 and 21 μm emission bands vary strongly from source to source: in the spectra of IRAS 22272 and IRAS 20000, where the 21 μm feature is relatively weak, the 30 μm emission band is very strong; and the spectrum of IRAS 07134, which has a very strong 21 μm feature, displays a weak 30 μm band. Beside the 21 and 30 μm emission bands, there is a broad emission plateau peaking at 11 μm and extending out to 15 μm. This emission is particularly weak in the case of AFGL 2688. For IRAS 22272 and IRAS 07134, the measurements by Buss et al. (1990) show an emission plateau extending from 6 to 9 μm and a 6.2 μm emission feature attributed to circumstellar PAH molecules.

3. Discussion

3.1. The 21 μm emission band

The present observations have underscored the very broad range of strengths of the 21 μm emission feature. This feature is seen only in the short-lived PPN phase and never in AGB stars or PN. Its carrier is therefore likely to be a transient species related to the extreme conditions to which dust is exposed during the short lived PPN phase.

Many compounds have vibrational modes around 21 μm. However, they can be ruled out either because they display other infrared features not present in these sources or because they are unlikely in a carbon–rich environment. Although there is yet no definite candidate, the presence of 6–9 μm bands and of 11–15 μm plateaus, both likely related to HACs or clusters of PAHs (Buss et al. 1990), leads us to consider some kind of carbonaceous material as a possible carrier of the 21 μm feature.

3.2. The 30 μm emission band

The main result of our observations is the presence of a 30 μm emission band in all the 21 μm PPN observed so far. The strength of this excess emission is variable from source to source, reaching its highest value in IRAS 22272. There is only one other source where it is as spectacular, the PN IC 418 (Forrest et al. 1981; Moseley & Silverberg 1986). Unlike the 21 μm emission feature which has been only detected in PPN, the 30 μm band is also seen in sources both in the AGB and PN stage – Cox (1993) and references therein, implying that its carrier is not a transient form of dust. Given the strength of the 30 μm band, it also has to be an abundant dust component in C-rich circumstellar shells.

It was first suggested by Goebel & Moseley (1985), because of the good agreement between the observed spectra of IRC+10216 and AFGL 3068 and the laboratory measurements by Nuth et al. (1985), that the emitter is solid magnesium sulfide (MgS). Recent measurements of the MgS optical constants (Begemann et al. 1994) have further strengthened this conclusion, making solid MgS a likely candidate. However, the strength of the 30 μm emission in IC 418 and IRAS 22272 creates strong abundance constraints (Omont et al. 1994). One should also carefully consider the case for various carbonaceous materials which remain as viable alternatives since they are a major component of the dust population with a variety of possible structures and compositions.

References

Begemann, B., Dorschner, J., Henning, T., & Mutschke, H. 1994, ApJ, 423, L71

Buss Jr., R.H., Cohen, M., Tielens, A.G.G.M., Werner, M.W., Bregman, J.D., Witteborn, F.C., Rank, D., & Sandford, S.A. 1990, ApJ, 365, L23

Buss Jr., R.H. et al. 1993, ApJ, 415, 250

Cox, P. 1993, in *Astronomical Infrared Spectroscopy: Future Observational Directions*, ed. S. Kwok, ASP Conference Series, Vol. 47, p. 163

Forrest, W.J., Houck, J.R., & Mc Carthy, J.F. 1981, ApJ, 248, 195

Goebel J.H., & Moseley S.H. 1985 ApJ, 290, L35

Kwok, S., Volk, K.M., & Hrivnak, B.J. 1989, ApJ, 345, L51

Moseley, S.H., & Silverberg, R.F. 1986, in *Interrelations Among Circumstellar, Interstellar, and Interplanetary Dust*, eds. Nuth, J.E., III, & Stencel, R.E., NASA Conf. Pub. 2403, p. 233

Nuth, J.A., Moseley, S.H., Silverberg, R.F., Goebel, J.H., & Moore, W.J. 1985, ApJ, 290, L45.

Omont, A., Moseley, H.S., Cox, P., Glaccum, W., Casey, S., Forveille, T., Kin-Wing Chan, Loewenstein, R.F., Szczerba, R., Harvey, P.M., & Kwok, S. 1994, ApJ, submitted

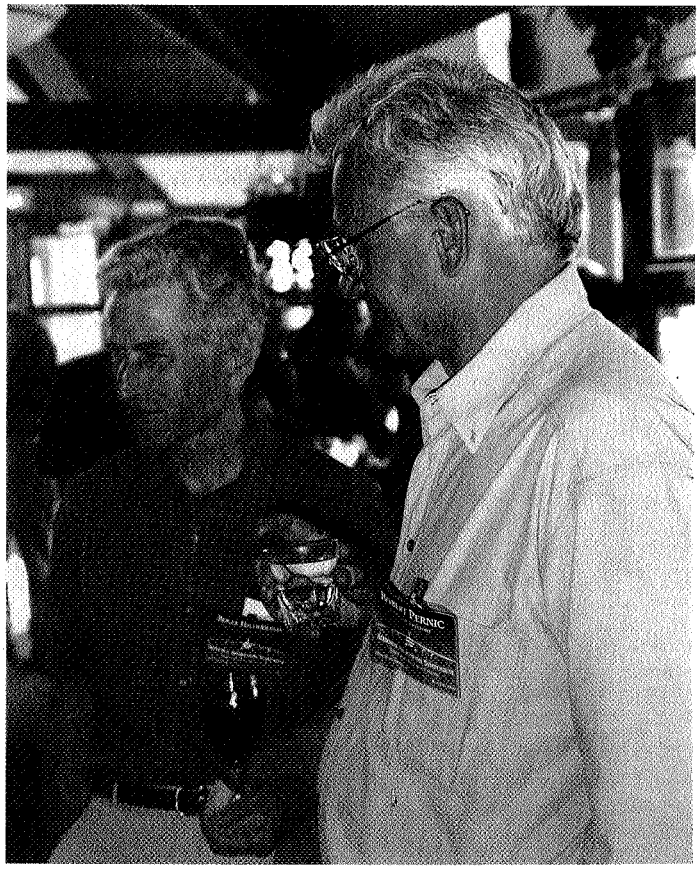

Roger Hildebrand, Bob Pernic

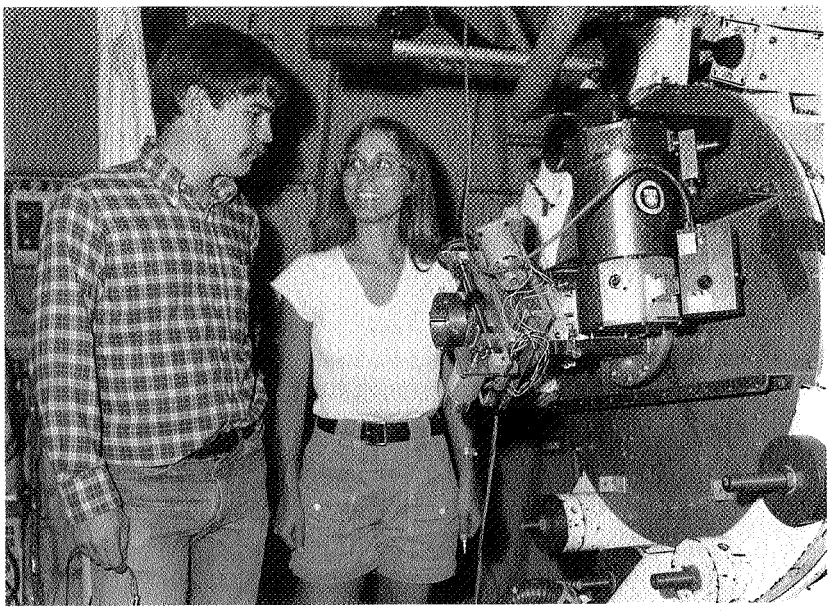

Harvey Moseley, Jocelyn Keene (1978)

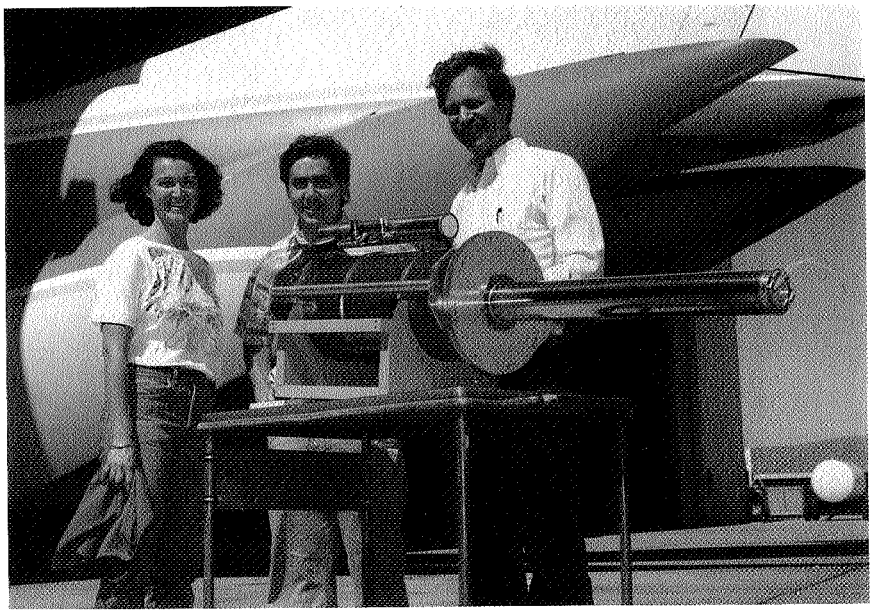

Jackie Davidson, Sean Casey, Al Harper (1985)

Airborne Astronomy Symposium on the Galactic Ecosystem
ASP Conference Series, Vol. 73, 1995
M.R. Haas, J.A. Davidson, and E.F. Erickson (eds.)

A 7 μm DUST EMISSION FEATURE IN OXYGEN-RICH CIRCUMSTELLAR SHELLS

J. H. GOEBEL
Technology Development Branch, Space Projects Division, NASA Ames Research Center, MS 244-10, Moffett Field, CA 94035-1000

J. D. BREGMAN and F. C. WITTEBORN
Astrophysics Branch, Space Science Division, NASA Ames Research Center, MS 245-6, Moffett Field, CA 94035-1000

ABSTRACT New 4 to 8 μm infrared spectroscopic observations of two oxygen-rich stars are presented and combined with IRAS LRS data to span the 4 to 24 μm wavelength range. In the 4 to 8 μm range, we observe a 7.15 μm (1400 cm^{-1}) emission feature. This new feature is not uniquely correlated with any of the sharply defined 10, 11, 13.1 and 19.7 μm emission features that are known to be present in this class of circumstellar shells, but it does appear to be correlated with the spectrally broad dust emission in the 10 to 20 μm spectral region. The feature has not been reported previously in any other astronomical environment. A reinterpretation of prior 4 to 8 μm spectroscopy of α Ori and R Cas reveals the presence of the 7.15 μm emission in α Ori and possibly in R Cas. The spectrally narrow 19.7 μm emission, that is distinctly different than the relatively broad silicate 18 μm emission feature in oxygen-rich dust shells, is also observed to be present in the LRS spectrum of SAO 197549. The implication of these observations is that a universal astronomical silicate does not exist in oxygen-rich circumstellar shells.

INTRODUCTION

With the advent of the IRAS LRS Atlas, it has become apparent that oxygen-rich stars display a wider variety of dust spectra than had been previously known (Little-Marenin and Price 1986; Goebel and Gerbault 1988; and Onaka *et al.* 1989a,b). Variations in the standard silicate feature range from subtle to profound. These were previously unrecognized due to the limited wavelength coverage available from mountain observatories. Gal *et al.* (1987), Little-Marenin (1986), Simpson (1991), Skinner and Whitmore (1988a and b), Vardya, de Jong, and Willems (1986), Noguchi (1990), and Willems and de Jong (1986) pioneered the study of these stars in the IRAS LRS database. They discussed the presence of spectral features at 10, 11, and 13.1 μm, and the variation of these features with spectral classification, variability, and

luminosity type. The traditional silicate is that which has been observed in emission in the Trapezium and in stars like α Ori and μ Cep. It is this silicate that has been considered widely as a reasonable approximation or average representation of the spectrum of silicates in astrophysical environments (*e.g.*, Draine and Lee 1984). It has formed the standard by which modeling of the circumstellar and interstellar media have been performed, and abundances of dust species determined.

Using the AutoClass II (AC II) method of automatic spectral classification on the LRS Atlas, Cheeseman *et al.* (1989) and Goebel *et al.* (1989) have found that the traditional silicate (Forrest, McCarthy, and Houck 1979; Gillett *et al.* 1975) forms only a minority in the oxygen-rich spectral population in the LRS Atlas. Also strong variations in galactic distribution were found to correlate with these spectral features. There appear to be galactic gradients in the forms of silicates that give rise to the spectral features; these gradients can be related to the evolution of these stellar populations. In light of current knowledge about the variety of silicates present in the IDPs and meteoritic samples (Sandford and Walker 1985), it is not surprising to find a greater variety among the silicates that form in circumstellar environments. The variety in the interstellar dust particle (IDP) silicates arises from a complex history of thermal processing, injection, and mixing from different sources (*cf.* Whittet 1992). While exactly the same mechanisms for the processing of circumstellar silicates and direct transfer of circumstellar particles to IDPs would not be expected, complex thermal processing and mixing mechanisms in the circumstellar environment should not be a surprising possibility (Tielens 1990). It is improbable, that the IDP's come fully processed from circumstellar environments without any further processing in the media through which they traverse (Tielens and Allamandolla 1987).

Observations of a new emission feature at 7.15 μm that appears to be correlated with dust in oxygen-rich circumstellar envelopes are presented here. The new 7.15 μm feature amplifies the varieties of silicate spectra present in oxygen-rich circumstellar shells, and increases the variety of species and grain generation processes which must be taken into account.

OBSERVATIONS

Spectra of the stars X Hya (IRAS 09331-1428, M6IIIe) and SAO 197549 (IRAS 07034-3551, M6IIIe) were obtained on two separate flights of the Kuiper Airborne Observatory (KAO), see Figure 1. These program stars and calibration standards were selected for convenience of flight planning purposes, rather than for the uniqueness of their spectra. They were considered to be representative of their classes. The KAO operated out of Christchurch, New Zealand, to observe X Hya on 14 April 1988 and SAO 197549 on 21 April 1987. For X Hya the secondary photometric and spectroscopic standard was α Boö, while for SAO 197549, it was α Hya. The calibration of the flux curve of α Hya is discussed by Wooden *et al.* (1993).

The KAO and LRS spectra are combined in Figures 1 and 2. Note that although the various segments were obtained at different epochs, the combined spectra join up very well. The recalibration of the LRS discussed by Volk and Cohen (1989) and performed by Cohen *et. al* (1992a), that takes SiO

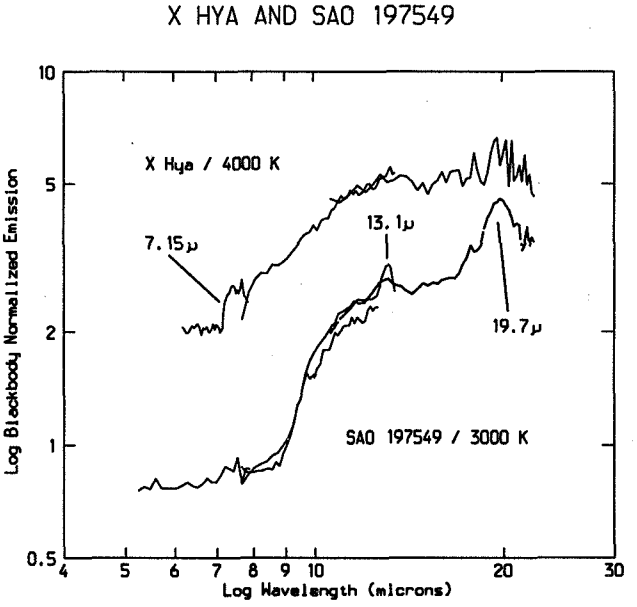

Figure 1. Blackbody normalized dust emission spectra of X Hya and SAO 197549 combining the KAO HiFOGS and LRS short and longwavelength spectra. Note that the 7.15 μm emission is not necessarily correlated with the narrow emissions at 13.1 and 19.7 μm. There have been no arbitrary shifts in the flux curves of either the KAO or IRAS LRS data sets, indicating that the spectral calibrations are independently consistent and reasonably similar.

absorption into account, does not greatly affect the continuum temperatures, T_C, that are quoted here for X Hya and SAO 197549. We have derived T_C from the KAO data, which is calibrated independently of the LRS. The combined spectra of X Hya do not have significant spectral overlap near 8 μm, while SAO 197549 was observed from 5 to 12.6 μm from the KAO, and with higher resolving power than the LRS. The higher resolution KAO spectrum confirms the overall shape of the LRS spectrum below 12.6 μm.

The 4 to 7 μm region of SAO 197549 is blackbody-like and free of strong spectral features. It appears that a weak feature may be present beyond 7.15 μm (1400 cm^{-1}). The 8 μm region forms the apparent continuum in the short wavelength LRS band data for SAO 197549. In contrast, X Hya displays a strong feature starting at 7.15 μm that continues out to the end of the KAO range. Due to the short wavelength cutoff at 8 μm of the LRS spectrometer, it is not possible to determine the presence of this new feature in the LRS spectra alone. Examination of the calibration standards (Cohen *et al.* 1992a,b and Wooden *et al.* 1993) reveals no significant absorption features starting at 7.15 μm that could cause an apparent emission in the star X Hya. The SiO absorption discussed by Cohen *et al.* 1992b occurs at the wrong wavelength.

In SAO 197549, the 13.1 μm emission is found in the short wavelength LRS channel and is corroborated in the long wavelength channel. In the

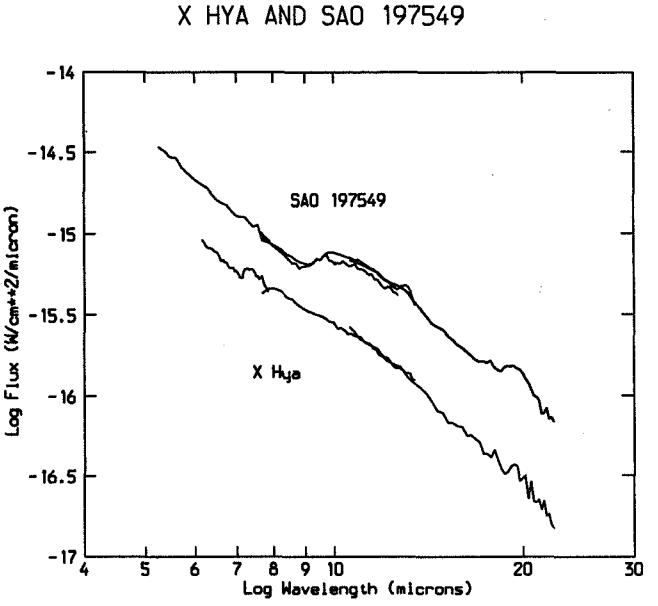

Figure 2. The flux spectra of SAO 197549 and X Hya. The observations from the KAO cover the wavelength ranges 5 to 8 and 7.8 to 12.5 μm in the case of SAO 197549 and are combined with the IRAS LRS short and long wavelength channels. Observations from the KAO of X Hya cover 6 to 8 μm and are combined with the long and short wavelength channels of the IRAS LRS. The 5 to 12 μm KAO data are independently calibrated and superimposed on the LRS data.

latter, the lower resolution has degraded the amplitude and width of the emission. Unfortunately, the KAO spectrometer's grating was incapable of coverage beyond 12.6 μm. The strong emission features in the 20 μm range peak at 19.7 μm and appear to display a blue shoulder at 17.7 μm. This 19.7 μm feature is distinctly characteristic of a large class of objects in the LRS (Little-Marenin and Price 1986; Cheeseman *et al.* 1989; Goebel *et al.* 1989); and it is not the same as the well known 18 μm silicate emission that has been attributed to silicates (Forrest, McCarthy, and Houck 1979). The 13.1 and 19.7 μm emissions have been mistaken for the 12.8 μm NeII emission line and the 18 μm silicate emission in the study of evolved objects by Jourdain de Muizon, Cox, and Lequeux (1990), who included SAO 197549 in the list of miscellaneous evolved objects.

REFERENCES

Cheeseman, P., Stutz, J., Self, M., Taylor, W., Goebel, J., Volk, K., and Walker, H. 1989, *NASA Ref. Publ. No.* 1217.

Cohen, M., Witteborn, F. C., Carbon, D. F., Augason, G., Wooden, D., Bregman, J. D., and Goorvitch, D. 1992a, *Astron. J.*, 104, 2045.

Cohen, M., Walker, R. G., and Witteborn, F. C. 1992, *Astron. J.*, **104**, 2030.
Draine, B. T. and Lee, H. M. 1984, *Ap. J.*, **285**, 89.
Forrest, W. J., McCarthy, J. F., and Houck, J. R. 1979, *Ap. J.*, **233**, 611.
Gal, O., de Muizon, M., Papoular, R., and Pégourié, B. 1987, *Astron. Astrophys.*, **183**, 29.
Gillett, F. C., Forrest, W. J., Merrill, K. M., Capps, R. W., and Soifer, B. T. 1975, *Ap. J.*, **200**, 609.
Goebel, J. H., and Gerbault, F. 1988, *Proc. Interstellar Dust: Contributed Papers, IAU Symp. No.* **135**, *NASA Conf. Publ.* No. **3036**, p. 519.
Goebel, J., Volk, K., Walker, H., Gerbault, F., Cheeseman, P., Self, M., Stutz, M., and Taylor, W. 1989, *Astron. Astrophys.*, **222**, L5.
Jourdain de Muizon, M., Cox, P., and Lequeux, J. 1990, *Astron. Astrophys. Suppl.*, **83**, 337.
Little-Marenin, I. R. and Price, S. D. 1986, *Summer School on Interstellar Processes*, July 2-8, 1986, ed. D. J. Hollenbach and H. A. Thronson, NASA TM-*B88342*, p. 137.
Little-Marenin, I. R. 1986, *Ap. J. (Letters)*, **307**, L15.
Noguchi, K. 1990 *P. A. S. J.*, **42**, 419.
Onaka, T., de Jong, T., and Willems, F. J. 1989, *Astron. Astrophys.*, **218**, 169.
Onaka, T., de Jong, T., and Willems, F. J. 1989, stron. Astrophys. Suppl., **81**, 261.
Sandford, S. A. and Walker, R. M. 1985, *Ap. J.*, **291**, 838.
Simpson, J. P. 1991, *Ap. J.*, **368**, 570.
Skinner, C. J., and Whitmore, B. 1988a, *Mon. Not. Roy Astron. Soc.*, **231**, 169.
Skinner, C. J., and Whitmore, B. 1988b, *Mon. Not. Roy Astron. Soc.*, **235**, 603.
Tielens, A. G. G. M. and Allamandolla, L. J. 1987, in *Physical Processes in Interstellar Clouds*, eds. G. E. Morfill and M. Scholer (Reidel, Dordrecht), p. 333.
Tielens, A. G. G. M. 1990, *From Miras to PN: Which Path for Stellar Evolution?*, ed. M. O. Mennessler and A. Omont (Editions Frontières), p. 186.
Vardya, M. S., de Jong, T., and Willems, F. J. 1986, *Ap. J. (Letters)*, **304**, L29.
Volk, K., and Cohen, M. 1989, *A. J.*, **98**, 1918.
Whittet, D. C. B. 1992, *Dust in the Galactic Environment*, Institute of Physics Publishing (Bristol).
Willems, F. J., and de Jong, T. 1986, *Ap. J. (Letters)*, **309**, L39.
Wooden, D. H., Rank, D. M., Bregman, J. D., Witteborn, F. C., Tielens, A. G. G. M., Cohen, M., Pinto, P. A., and Axelrod, T. S. 1993, *Ap. J. Suppl. Ser.*, **88**, 477.

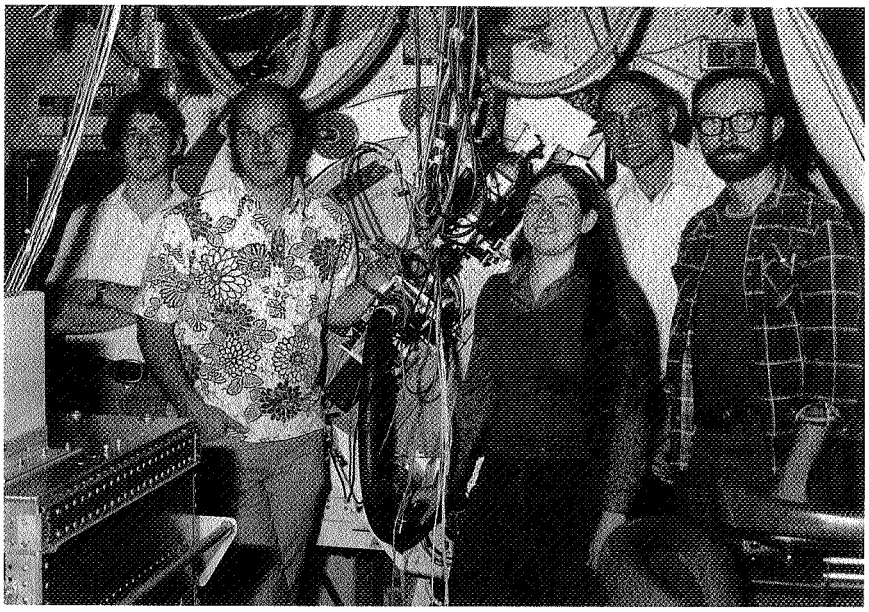

Dan Lester, Jesse Bregman, Harriet Dinerstein,
Fred Witteborn, Harold Crean (1980)

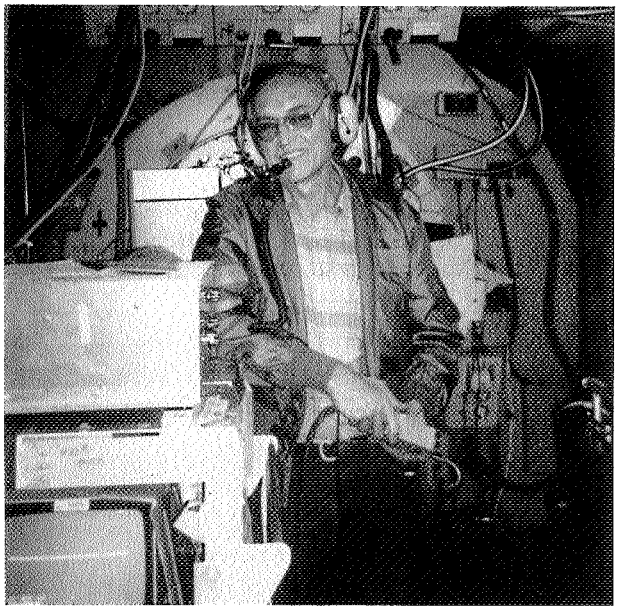

Fred Witteborn

Airborne Astronomy Symposium on the Galactic Ecosystem
ASP Conference Series, Vol. 73, 1995
M.R. Haas, J.A. Davidson, and E.F. Erickson (eds.)

SILICATE AND RELATED DUST EMISSION IN STARS ON THE ASYMPTOTIC GIANT BRANCH

G. C. SLOAN
NASA Ames Research Center, MS 245-6, Moffett Field, CA 94035-1000

S. D. PRICE
Phillips Laboratory, PL/GPOB, 29 Randolph Rd., Hanscom AFB, MA 01731-3010

I. R. LITTLE-MARENIN
University of Colorado, CASA, CB 389, Boulder, CO 80309-0389

P. D. LEVAN
Phillips Laboratory, PL/VTRP, 3550 Aberdeen SE, Kirtland AFB, NM 87117-5776

INTRODUCTION

The Low-Resolution Spectrometer (LRS) on the Infrared Astronomical Satellite (IRAS) produced a rich set of spectra from oxygen-rich circumstellar dust shells. Little-Marenin and Little (1988, 1990) found that in addition to the classic 10 μm emission feature due to silicate dust, many oxygen-rich shells also produce components at 11 and 13 μm. Some shells exhibit only a broad, low-contrast feature which peaks longward of 11 μm and has been attributed to alumina dust (Vardya, deJong and Willems 1986; Onaka, deJong and Willems 1989). We have modified the classification method of Little-Marenin and Little, applied it to a large sample of bright oxygen-rich variables on the asymptotic giant branch (AGB) (Sloan & Price 1994), and undertaken a study of the 13 μm emission feature and the sources which produce it (Sloan, LeVan, & Little-Marenin 1994). We present some of the results of these studies here.

CLASSIFICATION METHOD—THE SILICATE DUST SEQUENCE

We created our sample of AGB sources by cross referencing four classes of variables (Mira, SRa, SRb, and Lb) in the General Catalog of Variable

Stars (Kholopov et al. 1985-88) with stars brighter than 28 Jy in the IRAS Point Source Catalog (IPAC 1987). Of the 683 matches, 546 have optical spectral types indicating oxygen-rich photospheres: 241 Miras, 29 SRas, 157 SRbs, and 119 Lbs.

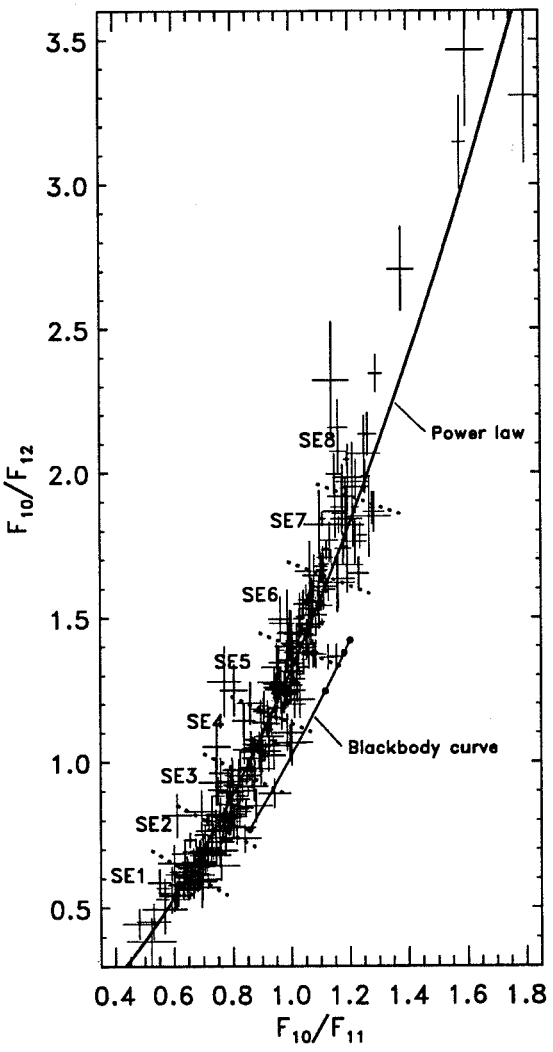

Figure 1. The silicate dust sequence for all sources with emission of S/N 10 or more. The points along the blackbody curve are for (top to bottom) 10^4 K, 3000 K, 1000 K, and 300 K.

For each of these, we obtained a spectrum from the LRS (IRAS Science Team 1986, Volk and Cohen 1989), corrected it as described by Cohen, Walker, and Witteborn (1992), and following Little-Marenin and

Little, removed the stellar contribution. We assumed that all of the stars could be approximated as M6 giants, and modeled them with a 3240 K Engelke function (Engelke 1992) with 15% SiO absorption at 8 μm. We defined the dust contrast to be the ratio of dust to stellar emission summed from 8 to 15 μm. Spectra with dust contrasts of 4% or less were classified as naked (N). Nearly all remaining spectra contained silicate or related dust emission (SE).

For emission spectra, we examined the dust emission at 10, 11, and 12 μm. We found that a plot of the flux ratios F_{10}/F_{12} versus F_{10}/F_{11} (Figure 1) produces a tight curve, which, for ease of reference, we refer to as the **silicate dust sequence**. This sequence can be modelled with a power law:

$$F_{10}/F_{12} = 1.32\ (F_{10}/F_{11})^{1.77}.$$

For each spectrum, we determine a SE index by finding the position on the power law closest to the position defined by the flux ratios F_{10}/F_{11} and F_{10}/F_{12}. Using the corrected flux ratios on the power law, we solve for the flux ratio F_{11}/F_{12}. The SE index is defined as:

$$n = 10\ F_{11}/F_{12} - 7.5.$$

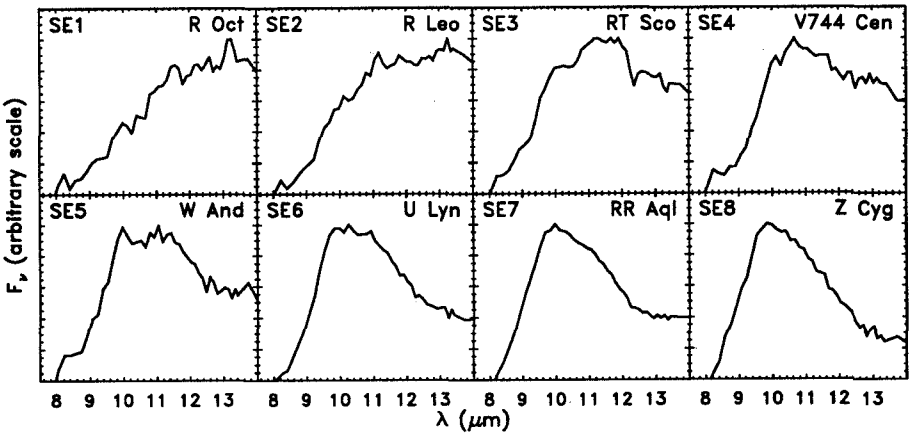

Figure 2. Sample spectra for each silicate emission index. The stellar contribution has already been removed.

RESULTS

● The silicate dust sequence shows convincingly that the emission due to oxygen-rich dust is constrained to a narrow range of possible spectra. All of the wide variety of observed emission features from oxygen-rich shells fall on this sequence.

● Broad emission features attributed to alumina dust fall on the lower portion of the silicate dust sequence. As the ratio of silicate to alumina dust increases, the emission feature grows narrower and moves progressively higher on the sequence.
● Broad features are always associated with low-contrast shells. Narrower emission features tend to occur in higher contrast shells, but the range of possible contrasts increases as the features grow narrower.
● The percentage of naked stars drops from over 40% of the irregulars to about one sixth of the semiregulars to less than 1% of the Miras.
● A comparison of the distribution of SE indices among the four variability classes reveals no systematic differences.

13 μm EMISSION

Glaccum (1994) has tentatively identified the carrier of the 13 μm emission feature as corundum (γ-Al_2O_3), a crystalline form of the alumina dust associated with the broad low-contrast feature (SE1-2). We find that 13 μm emission is far more common than previously thought. Of the brightest SRbs, *90% have spectra with 13 μm features.* Roughly half the bright Lbs and SRas also show 13 μm emission, but very few of the Miras do. The 13 μm feature occurs more frequently among broader emission classes, but can be found associated with all types of emission from oxygen-rich dust.

REFERENCES

Cohen, M., Walker, R.G., & Witteborn, F.C. 1992, *A.J.*, **104**, 2030.
Engelke, C.W. 1992, *A.J.*, **104**, 1248.
Glaccum, W. 1994, in *Proc. of the Airborne Astronomy Symp. on the Galactic Ecosystem: From Gas to Stars to Dust*, ed. M.R. Haas, J.A. Davidson, & E.F. Erickson (San Francisco: ASP), paper 5.2.
Image Processing and Analysis Center 1987, *IRAS Catalog of Point Sources, Version 2.0* (Washington: GPO).
IRAS Science Team 1986, *A&AS*, **65**, 607.
Kholopov, P.N., Samus, N.N., Frolov, M.S., Goranskij, V.P., Gorynya, N.A., Kireeva, N.N., Kukarkina, N.P., Kurochkin, N.E., Medvedeva, G.I., Perova, N.B., & Shugarov, S.Y. 1985-88, *General Catalogue of Variable Stars, 4th Ed.*, (Moscow: Nauka Publishing House).
Little-Marenin, I.R., & Little, S.J. 1988, *Ap.J.*, **333**, 305.
_____. 1990, *A.J.*, **99**, 1173.
Onaka, T., deJong, T., & Willems, F. 1989, *A&A*, **218**, 169.
Sloan, G.C., LeVan, P.D., & Little-Marenin, I.R. 1994, in preparation.
Sloan, G.C., Price S.D. 1994, *Ap.J.*, submitted.
Vardya, M., deJong, T., & Willems, F. 1986, *Ap.J.*, **304**, L29.
Volk, K., & Cohen, M. 1989, *A.J.*, **98**, 931.

Airborne Astronomy Symposium on the Galactic Ecosystem
ASP Conference Series, Vol. 73, 1995
M.R. Haas, J.A. Davidson, and E.F. Erickson (eds.)

High Rotational CO Lines in Post-AGB Stars and PNe

K. Justtanont, A. G. G. M. Tielens

NASA Ames Research Center, Mail Stop 245-3, Moffett Field, CA 94035-1000

C. J. Skinner

IGPP, L-413, Lawrence Livermore National Laboratory, PO Box 808, Livermore, CA 94551

Michael R. Haas

NASA Ames Research Center, Mail Stop 245-6, Moffett Field, CA 94035-1000

1. Introduction

A significant fraction of a star's initial mass is lost while it is on the Asymptotic Giant Branch (AGB). Mass loss rates range from 10^{-7} $M_\odot$/yr for early AGB stars to a few 10^{-4} $M_\odot$/yr for stars at the tip of the AGB. Dust grains condense from the outflow as the gas expands and form a dust shell around the central star. A superwind ($\sim 10^{-4} - 10^{-3}$ $M_\odot$/yr) is thought to terminate the AGB phase. In the post-AGB phase, the star evolves to a higher effective temperature, the mass loss decreases ($\sim 10^{-8}$ $M_\odot$/yr), but the wind velocity increases (~1000 km/s). During this evolution, dust and gas are exposed to an increasingly harsher radiation field and when T_{eff} reaches about 30,000 K, the nebula is ionized and becomes a planetary nebula (PN).

Photons from the central star can create a photodissociation region (PDR) in the expanding superwind. Gas can be heated through the photoelectric effect working on small grains and polycyclic aromatic hydrocarbons (PAHs) (e.g., Tielens & Hollenbach 1985; Bakes & Tielens 1994; Spaans et al. 1994). This gas can cool via the atomic fine structure lines of OI (63 μm and 145 μm) and CII (158 μm), as well as the rotational lines of CO. In the post-AGB phase, the fast wind from the central star will interact with the material ejected during the AGB phase. The shock caused by this interaction will dissociate and heat the gas. This warm gas will cool through atomic fine structure lines of OI and the rotational lines of (newly formed) CO.

2. Observations

We observed GL2688, GL618 and NGC7027 in November 1993 using the Ames Cryogenic Grating Spectrometer (CGS) on the KAO (Erickson et al. 1985). Three rotational lines of CO were observed: J=13-12 (201 μm), 17-16 (153 μm) and 22-21 (118 μm). The relative detector response was removed by dividing each spectrum by a calibration spectrum of Saturn at the same wavelength. The

Table 1. The observed line fluxes. The flux units are W/cm^2.

	F(J=13-12)	F(J=17-16)	F(J=22-21)
GL2688	5.0E-19	7.7E-19	7.4E-19
GL618	2.9E-19	6.0E-19	5.4E-19
NGC7027	–	2.2E-19	–

absolute flux calibration was done by multiplying the ratioed spectra by the flux of Saturn. The line flux was then determined by fitting the data points with a Gaussian profile and a flat continuum (see Table 1).

The three objects represent three different "snapshots" of the post-AGB evolution. The central star of GL2688 has a spectral type of F5Iae ($T_{eff} \sim$ 6,000 K), while GL618 has a B0 star ($T_{eff} \sim$ 30,000 K) and NGC7027 is a young PN ($T_{eff} \sim 10^5$ K).

3. Warm, Dense Molecular Gas in the Post-AGB Phase

For the two post-AGBs, GL2688 and GL618, the rotational emission peaks around J~20. Given the high excitation energies and densities of these levels, these observations imply the presence of copious amount of warm (~1000 K), dense ($\sim 3 \times 10^6$ cm^{-3}) molecular gas during this phase. This warm gas reflects heating of circumstellar gas either by stellar photons (i.e., a PDR) or by strong shock waves.

4. PDR Model

The penetrating visual and FUV photons from the star ionize, dissociate and heat the envelope ejected during the AGB phase. Models for PDRs are discussed elsewhere (e.g., Tielens & Hollenbach 1985), and here we concentrate on the flux in the high-J CO lines (Table 2). Figure 1a shows the results of a calculation for the expected CO intensity as a function of gas density. As the density increases, the peak of the CO line emission shifts to higher J, reflecting the increase in the critical density with increasing J. A peak in the line intensity around J=20 requires a density of $\sim 3 \times 10^6$ cm^{-3}.

FUV photons are more effective in dissociating CO and heating the gas than visual photons (Spaans et al. 1994). This is illustrated in Figure 1b, which shows the expected CO emission as a function of the effective temperature of the star. When the stellar temperature increases from 10,000 K to 30,000 K, the increasing UV flux pushes the C^+/C/CO transition deeper into the PDR where the gas is cooler and hence the emission in the high CO levels decreases. However, for even lower effective temperatures, this trend is more than offset by the decreased heating efficiency of visual photons.

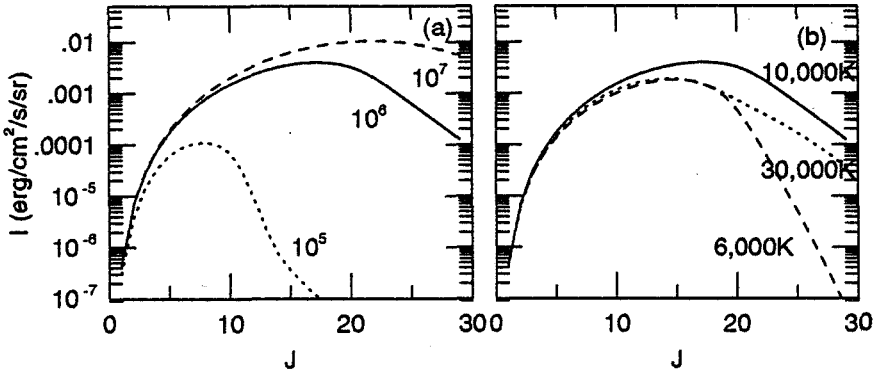

Figure 1. (a) CO line intensities as a function of rotational level J for a PDR illuminated by a 30,000 K star for three different density regimes. (b) For the same density (10^6 cm^{-3}), CO line intensities of higher J lines are larger for a star with a higher effective temperature.

5. Shock Model

There is direct observational evidence for the presence of fast winds in PPNe. Burton & Geballe (1986) report a line width for the v=1-0 S(1) molecular hydrogen line of 250 km/s for GL618, while Young et al. (1992) observe CO and HCN profiles from GL2688 to have a high velocity component of 100 km/s.

We have used the shock model of Hollenbach & Mckee (1989) to analyze the observed CO line intensities (Table 2). Not surprisingly, a peak intensity around J=20 requires preshock density of $\sim 3 \times 10^6$ cm^{-3}. This conclusion is not very sensitive to the assumed shock velocity.

6. Summary

The observed high fluxes in high-J CO lines imply the presence of warm (T$\sim$ 1000 K), dense ($\sim 3 \times 10^6$ cm^{-3}), molecular gas during the post-AGB phase. Our observations cannot determine whether this gas is the result of high incident stellar photon fluxes (a PDR) or from shocks. One possible way to distinguish between PDR and shock emission is to measure the atomic fine structure lines of CII and SI (Table 2). Both models predict peak CO line intensities of $\sim 10^{-2}$ erg cm^{-2} s^{-1} sr^{-1}. Hence, the observed fluxes imply a radiating surface of $\sim 2 \times 10^{-10}$ sr. Adopting a distance of 1 kpc and an (AGB) outflow velocity of 20 km/s, this source size and the derived gas density imply a mass loss rate of 3×10^{-3} $M_\odot$/yr. Thus, it seems that the AGB phase is terminated by a short lived ($< 10^3$ yr) phase of high mass loss.

For NGC 7027, there is no evidence of a fast wind and the observed image of the 3.3 μm dust feature (Graham et al. 1993) indicates that the nebula is strongly illuminated by FUV photons.

Table 2. Line intensities of CO and other species as calculated from PDR and shock models. The line intensities are in units of erg/cm^2/s/sr. The values in the square brackets are the observed values. Input parameters for each model are also listed.

	PDR			Shock
	GL2688	GL618	NGC7027	
CO J=13-12	3.7E-3 [3.5E-2]	4.4E-3 [2.5E-2]	1.8E-3	2.9E-3
CO J=17-16	7.0E-3 [3.6E-2]	8.1E-3 [2.8E-2]	1.5E-3 [1.5E-3]	6.4E-3
CO J=22-21	9.5E-3 [2.4E-2]	1.0E-2 [1.4E-2]	4.1E-4	1.1E-2
OI 63 μm	5.2E-2	2.2E-1	1.8E-1 [1.2E-1]	8.1E-2
OI 145 μm	2.1E-3	6.9E-3	6.0E-3 [5.0E-3]	4.5E-3
CII 158 μm	1.0E-4	2.8E-3	2.8E-3 [1.3E-2]	2.2E-4
SI 25 μm	3.1E-2	2.8E-4	-3.2E-4	1.9E-1
SiII 35 μm	1.3E-2	2.2E-2	1.5E-2	-
H_2 1-0	-	thermal	1.0E-3	5.3E-4
H_2 2-1	-	thermal	3.0E-5	2.6E-4
n (cm^{-3})	1.0E+7	1.0E+7	1.0E+6	1.0E+7
Ω (sr)	2.0E-10	2.0E-10	8.0E-10	1.5E-9
G (Habing)	1.0E+8	3.0E+7	2.0E+6	
T (K)	6000	30000	30000	
FIR (erg/cm^2/s)	2.5E-7	5.0E-7	2.0E-7	
v_s (km/s)				100

Acknowledgments. We would like to thank David Hollenbach for assisting us in calculating the effect of the dissociative shocks.

References

Bakes, E.L.O. & Tielens, A.G.G.M. 1994, ApJ, 427, 822

Burton, M.G. & Geballe, T.R. 1986, MNRAS, 223, 13p

Erickson, E.F., Houck, J.R., Harwit, M.O., Rank, D.M., Haas, M.R., Hollenbach, D.J., Simpson, J.P. & Augason, G.C. 1985, Infrared Physics, 25, 513

Graham, J.R., Serabyn, E., Herbst, T.M., Matthews, K., Neugebauer, G., Soifer, B.T., Wilson, T.D. & Beckwith, S. 1993, AJ, 105, 250

Hollenbach, D.J. & McKee, C.F., 1989 ApJ, 342, 306

Spaans, M., Tielens, A.G.G.M., van Dishoeck, E.F. & Bakes, E.L.O. 1994, ApJ, in press

Tielens, A.G.G.M. & Hollenbach, D.J. 1985, ApJ, 291, 722

Young, K., Serabyn, G., Phillips, T.G., Knapp, G.R., Gusten, R. & Schulz, A., 1992 ApJ, 385, 265

Airborne Astronomy Symposium on the Galactic Ecosystem
ASP Conference Series, Vol. 73, 1995
M.R. Haas, J.A. Davidson, and E.F. Erickson (eds.)

Physical Structure of the IRC+10216 Wind: Molecular Sidereoarcheology

C. J. Skinner
Institute of Geophysics & Planetary Physics, L-413, Lawrence Livermore National Laboratory, P. O. Box 808, Livermore, CA 94551

K. Justtanont and A. G. G. M. Tielens
NASA-Ames Research Center, MS245-3, Moffett Field, CA 94035

A. L. Betz and R. T. Boreiko
Center for Astrophysics and Space Astronomy, University of Colorado, Boulder, CO 80309

Abstract. We present KAO observations of the CO J=9-8 and 12-11 lines in the C-star IRC+10216; these are the highest rotational transitions so far observed in any AGB star. A model is developed for the CO emission by IRC+10216 in all the observed CO rotational transitions.

1. Introduction

AGB stars lose mass rapidly in the form of cool, high density winds. The most abundant gas-phase molecule in the winds of AGB stars, after H_2 which does not produce any spectral lines, is carbon monoxide (CO), and its rotational lines in the mm-, sub-mm and far-IR wavebands are often modelled in order to determine mass-loss rates. The C-star IRC+10216 is the prototype mass-losing AGB star, by virtue of having a moderately large mass-loss rate ($\sim 3 \times 10^{-5} M_\odot$/yr) and being very close to the Sun (~150–300pc). We present in this paper the first detections of an AGB star in the J=9-8 and J=12-11 rotational transitions of CO, the highest transitions in which any AGB star has yet been detected. In addition, we present a model of the CO emission in the J=1-0 to 12-11 lines of IRC+10216.

2. Observations

IRC+10216 was observed with the Colorado heterodyne spectrometer during a New Zealand deployment of the KAO in March 1994. We observed in both the J=9-8 and the J=12-11 lines, with integration times of about 40 minutes. Calibration observations of the Moon have been used to determine a radiation temperature T_r, and the results are displayed in Figure 1. The velocity of IRC+10216 in the local standard of rest is about –26km/sec, and we clearly detect the source in the 12-11 line, and just detect it at 9-8.

3. Models

We list in Table 1 some of the data we use to constrain our models, including some previously unpublished observations by us from SEST (the Swedish-ESO Submillimeter Telescope). We have modelled the CO line emission from IRC+10216 using a code described by Justtanont, Skinner & Tielens (1994). We consider excitation of CO molecules by radiation from the central star and by warm dust grains which coexist with the gas, allowing for attenuation of the central starlight by intervening dust, and by collisions between CO and H_2 molecules.

Table 1: CO observations of IRC+10216

Transition	1-0	1-0	2-1	2-1	3-2	6-5	7-6	9-8	12-11
Telescope	NRAO	SEST	NRAO	SEST	JCMT	JCMT	IRTF	KAO	KAO
Diameter [m]	12.0	15.0	12.0	15.0	15.0	15.0	3.2	1.0	1.0
Beam size ["]	50	45	31	23	16	7	45	73	55
T_{mb} (obs.) [K]	9.6	12.4	21.5	22.6	57.0	45	9	1.0	1.1
Reference	1	2	1	2	3	4	5	2	2
T_{mb} (A) [K]	11.1	15.4	26.5	30.2	42.4	57.8	5.7	0.5	0.4
T_{mb} (C) [K]	8.0	11.3	24.5	30.3	46.4	55.4	6.9	0.5	0.6

References:

1) Huggins, Olofsson, & Johansson, 1988; 2) this work; 3) Avery et al 1992; 4) Stutzki, 1990; 5) Wattenbach et al, 1988.

For IRC+10216 the dominant CO excitation mechanism is collisional, although radiation by both the central star and warm dust grains have some effect. We fix the distance and effective temperature of the star at 170pc and 2010K (Winters 1994), although changing the distance (and hence luminosity) of the star has only a small effect on the models. The turbulent velocity in the wind is set at 0.65km/sec (see Sahai, Wootten & Clegg 1984 and Schönberg 1989). We allow the gas kinetic temperature and density as a function of radius to vary arbitrarily, since neither can be determined a priori. The gas is thermalized, so the brightness of the lines is determined by the gas temperature, with the mass-loss rate having only a small effect. The line profiles are mainly determined by the mass-loss rate.

In the first set of models (model A, Table 1), the gas temperature is a simple power law function of radius, $T_{kin} \propto r^{-\epsilon}$. No model of this type can accurately reproduce the observations. Whilst it comes reasonably close to fitting the brightnesses of the J=2-1 and 6-5 lines, it underestimates the brightness of the 3-2 lines and overestimates the brightness of the 1-0 lines. It also fails to reproduce the extensive maps of IRC+10216 in the CO J=2-1 and 1-0 lines by Huggins, Olofsson & Johansson (1988), being very much too centrally peaked. We have previously published a treatment of the heating and cooling of the gas in an AGB star wind (Justtanont, Skinner & Tielens 1994), and have used this treatment to derive the gas temperature for IRC+10216 (model B). The gas temperature throughout the envelope is greatly overestimated by this treatment, suggesting that either the gas heating is greatly overestimated, or the gas cooling is greatly underestimated. Finally, we present a gas temperature distribution which can reasonably well reproduce the observed line strengths (model C). We

show in Figure 2 the three gas temperature distributions used in models A, B and C. Figure 3 shows the mass-loss rate as a function of time used in model C.

4. What Does It Mean?

The gas kinetic temperature distribution and mass-loss rate as a function of time are complicated. At the dust condensation point the gas temperature rises due to the streaming of grains through the gas. Beyond this the gas cools due to adiabatic expansion and molecular line cooling (CO and HCN). The gas temperature is higher in the region with lower mass-loss rate. This has been noted before (Sahai, 1987), and arises because grains heat the gas more efficiently in a less dense region, and molecular lines cool it less efficiently. Beyond this, where the envelope density rises due to the larger mass-loss rate, the cooling is more efficient and the gas temperature drops rapidly. In the outer part of the envelope the gas is heated by external UV radiation (Huggins et al. 1988).

Our model is not yet fully consistent with all observations. The 3-2 line is a particular problem: observations from the JCMT by Williams & White (1992) and by Avery et al. (1993) are not consistent with one another, nor with the CSO observations of Groesbeck et al. (1994). Our fit to the profile of the 7-6 line observed on the IRTF is also poor. In this and the 6-5 line, better S/N observations are desirable in order to better constrain our model. Finally we underestimate the flux in both the observed KAO lines. It is necessary to further adapt the temperature distribution and mass-loss history in the innermost region in order to improve our fits to the higher rotational lines. We obtain a good fit to the maps made by Huggins et al. (1988) in the 2-1 and 1-0 lines, and our predicted line width appears to drop with increasing offset just as their observations revealed.

5. Is It Unique?

This is actually two questions – first, is the model for IRC+10216 unique, and second is IRC+10216 unique in presenting evidence for such a complicated envelope structure.

The answer to the first question is 'yes'. The extended warm region at the outer edge is necessary to explain the unexpectedly bright CO emission from the extended envelope. The ring of very warm gas is necessary to explain the relative brightness of the higher rotational lines, particularly the 3-2 and 6-5 lines which have been seen to be extended. The mass-loss variations invoked in our model are absolutely necessary in order to obtain reasonable fits to the line profiles and to the maps of IRC+10216.

In other AGB stars we see a random assortment of line brightness ratios in our CO data covering the 1-0, 2-1, 3-2 and 4-3 lines. The C-star V Cyg is probably at a similar evolutionary stage to IRC+10216. While IRC+10216 has its brightest CO emission in the 3-2 and 4-3 lines, V Cyg has its brightest emission in the 2-1 line, with the 3-2, 4-3 and 6-5 lines steadily decreasing in brightness. V Cyg's spectral energy distribution, modelled as a spherical dust shell, suggests that whilst its mass-loss rate may have been higher many

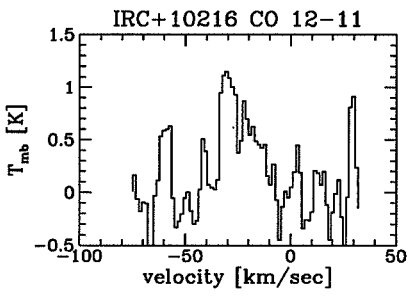

Figure 1(a)

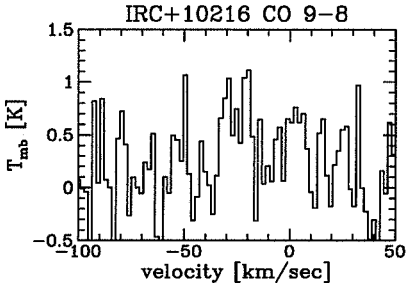

Figure 1(b)

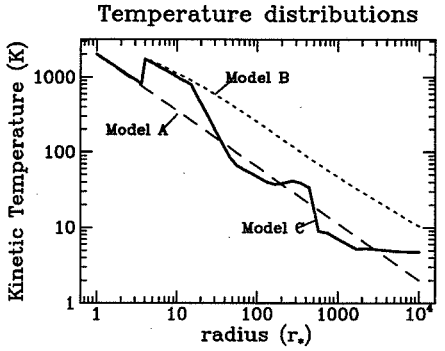

Figure 2

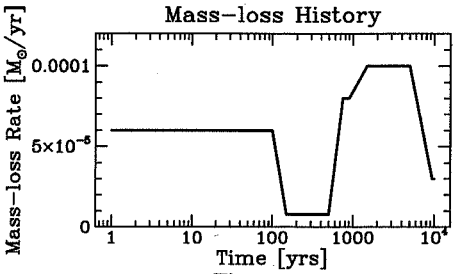

Figure 3

thousands of years ago, followed by a long period of more sedate behaviour, it is presently entering a period of more rapid mass-loss.

References

Avery, L. W., et al, 1993, ApJS, **83**, 363.

Groesbeck, T. D., Phillips, T. G., Blake, G. A., 1994, ApJS, In Press.

Huggins, P. J., Olofsson, H., Johansson, L. E. B., 1988, ApJ, **332**, 1009.

Justtanont, K., Skinner, C. J., Tielens, A. G. G. M., 1994, ApJ, In Press.

Sahai, R., Wootten, A., Clegg, R. E. S., 1984, ApJ, **284**, 144.

Sahai, R., 1987, ApJ, **318**, 809.

Schönberg, K., 1989, A&A, **208**, 219.

Stutzki, J., 1990, JCMT Newsletter, **9**, 9.

Wattenbach, R., Krügel, E., Röser, H. P., Nett, H., Schwaab, G., Densing, R., 1988, A&A, **202**, 133.

Williams, P. G., White, G. J., 1992, A&A, **266**, 365.

Winters, J. M., 1994, Ph.D. Dissertation, Technischen Universität Berlin.

Airborne Astronomy Symposium on the Galactic Ecosystem
ASP Conference Series, Vol. 73, 1995
M.R. Haas, J.A. Davidson, and E.F. Erickson (eds.)

Observations of Localized Ni II Emission in M 82: Evidence for Supernovae Activity in the Molecular Cloud East of the Nucleus

D. Rank and P. Temi

Astronomy Department, University of California, Santa Cruz, CA 95064

J. Bregman, E. Dunham, and D. Harker

NASA - Ames Research Center, Moffett Field, CA 94035

Abstract. Narrow band images of M82 at wavelength of 6.63 μm (NiII) and 6.8 μm (continuum) will be discussed in terms of new evidence for supernova activity in the nuclear region of the M82 starburst galaxy. Data were recorded using a 128x128 Si:Ga array in an infrared camera on the KAO Southern Expedition in April '94.

1. Introduction

Supernovae play a key role in the dynamics, structure, and chemical evolution of galaxies. The massive stars that end their lives as supernovae live for short enough times that many are still associated with dusty star formation regions when they explode, making them difficult to observe at visible wavelengths. In active star forming regions (galactic nuclei and starburst regions), dust extinction is especially severe. Thus, determining the supernova rate in active star forming regions of galaxies, where the supernova rate is expected to be one or two orders of magnitude higher than the average, has proven to be difficult. For normal galaxies, the supernova rate varies with type, but is in the range of 1-4 SNU where a SNU is the number of supernovae per 100 years per 10^{10} $L_{\odot}$ in blue luminosity. From observations of SN1987A we know that the [NiII] 6.63 μm emission line was the strongest line in the infrared spectrum for a period of a year and a half after the explosion. Since dust extinction is much less at 6.63 μm than at visible wavelengths ($A_{6.63}/A_V = 0.025$), the NiII line can be used as a sensitive probe for the detection of recent supernovae.

2. Observations

We present new multispectral images of M82 which were taken on the KAO using our 128x128 Si:Ga infrared camera. We used narrow band filters centered at the 6.63 μm NiII line and at 6.8 μm continuum wavelength. The reduction of the data includes all our images of M82 from the April 94 flight. The pointing of the telescope was independently derived by digitizing the KAO guider TV images. The average centroid position of the offset guide star was then used

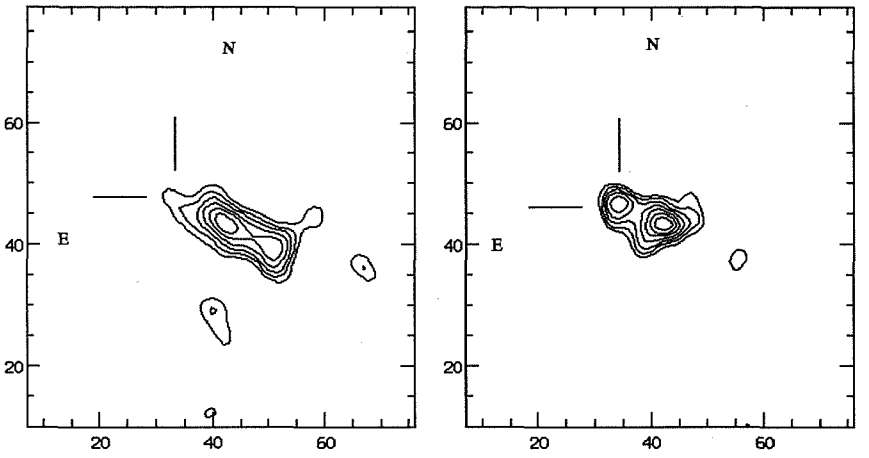

Figure 1. 6.8 μm (left) and 6.63 μm (right) images of M82. The eastern NiII source is indicated by the tick marks. Approximately 20 individual frames have been coadded with a 2.5 pixel (5 arcseconds) smoothing. Absolute positioning on the sky is within 2-3 pixels. $\delta\lambda/\lambda$ = 2.3%

to superimpose each LOS freeze frame image at a fixed rotation angle. From an analysis of the guide star errors and the IR images we have determined that the error in this procedure is about 2-3 pixels in the IR image. The images in Figures 1 and 2 are presented in a common reference frame as referred to the IR pixels on the chip.

Our new observations show clear evidence for NiII emission from the eastern side of the molecular cloud which surrounds the star burst region of the galactic core in M82 (see Figures 1 and 2). The 6.63 μm image shows an unresolved source, in the plane of the galaxy, 15-20 arcseconds to the east of the nucleus at the position of a dark dust lane in optical images. The NiII source shows up as an extension of the core emission in the images taken at the other wavelengths.

3. Discussion

Our observations would imply a large NiII line luminosity for the eastern source which is several million times the luminosity of the sun. Follow-up spectra of the eastern source taken a few weeks later with the KAO confirm our observations of NiII emission (Witteborn 1994). Thus we may have detected the infrared signature of a recent bright supernova in M82. If the observed source is a supernova, it is 100 times brighter than SN1987a in the NiII line, quite a surprise but not impossible. A second perhaps more common but also unexpected explanation for this observation is that the NiII emission arises in gas heated by supernova driven shocks or photo-dissociation regions which are concentrated near the center of the galaxy. These sources would likely be associated with the star burst activity of the nucleus.

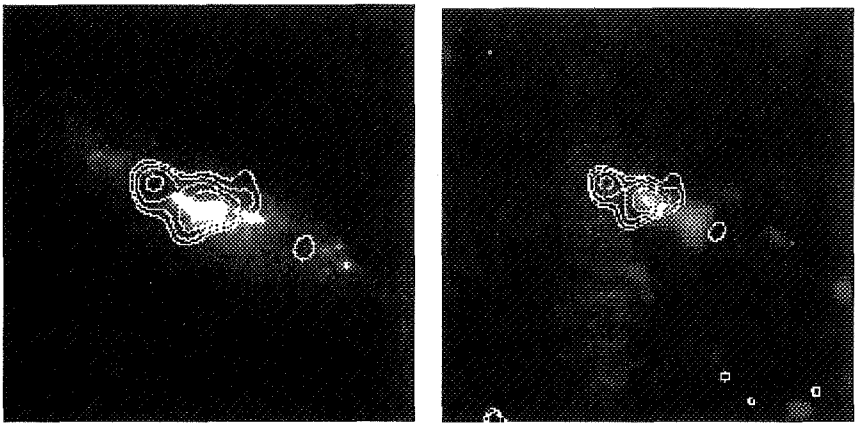

Figure 2. (left) 6.63 μm NiII image of M82 (contour) superimposed on a 1.6 μm FeII narrow band ground based image. It can be seen that the eastern NiII source coincides with a dark lane associated with a molecular cloud just outside the nuclear region of the galaxy. (right) 6.63 μm image superimposed on the 6.8 μm continuum image of Figure 1 showing the absolute registration of the galactic core.

If the NiII emission which we see in the eastern source of M82 is due to a supernova then a NiII/ArII line ratio of 1 or larger should be observed, based on our interpretation of previous IR spectroscopic data; Witteborn (1993) measured roughly equal line strengths for NiII and ArII in the ejecta of SN1987a. Such a large NiII/ArII line ratio is not observed in galactic HII regions where the Ni is depleted by the formation of solid dust grains. Lester et al. (1990), have observed strong FeII emission at 1.6 μm which is fairly uniformly distributed across the core of M82. The ratio of FeII/H lines is 100 times that seen in typical HII regions. These authors conclude that the FeII emission arises in gas heated by supernova driven shocks rather than in photo- dissociation regions which are concentrated at the center of the galaxy. Thus the FeII seen in their spectra is thought to be the result of sputtering of dust grains in the shocked gas. An integrated FeII luminosity of $5\text{x}10^5\ L_\odot$ for M82 is derived from their data. Our observations would imply an even larger NiII luminosity of $5\text{x}10^6\ L_\odot$ for the eastern source in M82. We see a marked difference between the eastern and western sources in the 6.6 μm NiII line luminosity. The two sources have nearly equal FeII luminosities in Lester's 1.6 μm data. Thus the eastern source may be intrinsically much brighter than the western source in these two metalic lines, but extinction surrounding M82's core substantially diminishes the flux at 1.6 μm.

References

D.F. Lester, J.S. Carr, M. Joy, and N. Gaffney, 1990, ApJ, 352,544
F. Witteborn, 1993, 1994 private communication

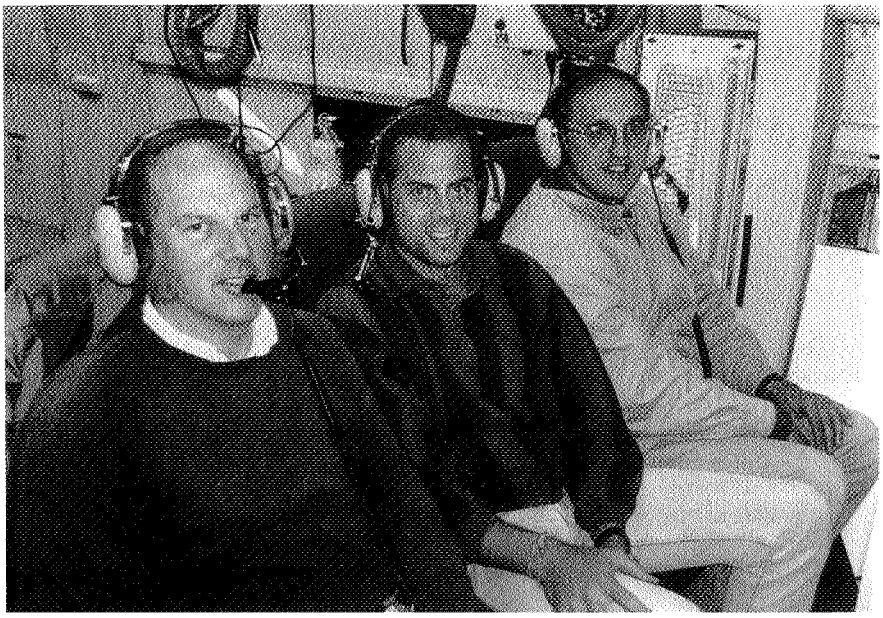

Jesse Bregman, David Harker, Zoran Ninkov

Scott Sandford, Amara Graps, Jesse Bregman

Airborne Astronomy Symposium on the Galactic Ecosystem
ASP Conference Series, Vol. 73, 1995
M.R. Haas, J.A. Davidson, and E.F. Erickson (eds.)

Type Ia Supernovae: Pulsating Delayed Detonation Models, IR Light Curves, and the Formation of Molecules

P. Höflich

CfA, Harvard University, 60 Garden Str.,Cambridge, MA 02138,USA

A. Khokhlov and C. Wheeler

University of Texas, Austin, TX 78712, USA

Abstract.

We computed optical and infrared light curves of the pulsating class of delayed detonation models for Type Ia supernovae (SNe Ia).

It is demonstrated that observations of the IR light curves can be used to identify subluminous SNe Ia by testing whether secondary maxima occur in the IR. Our pulsating delayed detonation models are in agreement with current observations both for subluminous and normal bright SN Ia, namely SN1991bg, SN1992bo, and SN1992bc.

Observations of molecular bands provide a test to distinguish whether strongly subluminous supernovae are a consequence of the pulsating mechanism occuring in a high-mass white dwarf (WD) or, alternatively, are formed by the helium detonation in a low-mass WD as was suggested by Woosley (1994). In the latter case, no carbon is left after the explosion of low-mass WDs whereas a lot of C/O-rich material is present in pulsating delayed detonation models.

1. Introduction

During the last two decades the observational data base for Type Ia supernovae has significantly increased. Despite their similarity both in their light curves (LC) and spectra, very recently, detailed observations of SNe Ia have proven that SNe Ia are not a perfectly homogeneous group, e.g. post-maximum declines of the LCs vary and many, but not all, SNe Ia show double peaks in the IR light curves (Sunzeff, 1994) and the discovery of SN 1991bg revealed a category of subluminous SNe Ia (Filippenko et al. 1992; Leibundgut et al. 1993).

Despite the uncertainties, Type Ia supernovae are thought to be thermonuclear explosions of carbon-oxygen WDs (Hoyle & Fowler 1960). The key question is how the flame propagates through the white dwarf, i.e. what is the speed of the burning front v_b compared to the speed of sound c_s? Several models of Type Ia supernovae have been proposed in the past, including detonation ($v_b \geq c_s$, Hansen & Wheeler 1969), deflagration ($v_b \leq c_s$) Nomoto, Sugimoto & Neo 1976) and delayed detonation model (Khokhlov 1991). In the delayed detonation model, the deflagration front turns into a detonation and more intermediate mass elements are produced. For the pulsating class of delayed detonation

models, the burning stops before sufficient energy is generated to disrupt the WD. The inner region collapses, burning is restarted and, eventually, results the disruption of the WD. For more details see Khokhlov et al. (1993) and Höflich et al. (1994).

Recently, light curves of different scenarios for normal bright SNe Ia including detonations, delayed detonations, pulsating delayed detonations and envelope models (Höflich et al. 1991; Müller et al. 1991; Khokhlov et al. 1991; Höflich et al. 1993; Khokhlov et al. 1993; Müller and Höflich 1994) have been investigated and compared with observations. Different models are needed to explain the observations but none of the previous models produced subluminous SNe Ia as required to account for SN1991bg. Recently, Woosley and Weaver (1994) suggested He-detonations in low-mass white dwarfs to explain subluminous SN Ia. This suggestion would call for two rather different classes of SNe Ia. Here, we propose the pulsating delayed detonation model as a possible mechanism. One intriguing feature of the PDD model is that the transition may happen at very low densities and the production of radioactive Ni in such an explosion can be very low. This raises the possibility of accounting for not only the standard, but also the subluminous SNe Ia within the same class of model (Khokhlov, Müller & Höflich 1993; Höflich, Khokhlov & Wheeler 1994). We compare the computed light curves with observations. Further, we propose molecule formation in the models of subluminous SNe Ia.

2. Hydrodynamic Models and Light Curves

The explosions are calculated using a one-dimensional Lagrangian code self-consistently with a nuclear reaction network (Khokhlov 1991). The hydrodynamical phase lasts about 10 seconds up to a minute. Thereafter, the envelope is freely expanding. The models investigated here are given in Table 1. They produce $\simeq 0.1 M_\odot$ up to $0.7 M_\odot$ of ^{56}Ni depending on the density at which the transition from a deflagration to a detonation occurs.

Subsequently, LCs are calculated using an elaborated treatment of the radiation transport, an LTE equation of state, expansion opacities including cooling by molecules and a Monte-Carlo γ-ray transport scheme (Höflich et al. 1992ab 1994). Note that a secondary maximum in the IR occurs if the photospheric radius reaches its maximum well after the bolometric maximum. Model light curves for subluminous SNe Ia show only one *late* IR-maximum (see Höflich et al., 1994).

3. Formation of Molecules in SNe Ia

Our pulsating delayed detonation models have outer layers of unburned C and O. In general, the formation of molecules requires rather low temperatures and is possible only in relatively cool, subluminous models (Fig. 1) No significant amount of CO will be formed in normal, bright SNe Ia.

In subluminous models, strong vibrational bands in the fundamental and first overtone of CO may be within the reach of ground based instruments 1 to 2 weeks past maximum (Table 2). In contrast, low-mass He-detonation models (e.g. Woosley & Weaver 1994) would not show CO or SiO vibrational bands

Table 1. Summary of theoretical SN Ia models. The quantities given in columns 2 to 11 are: mode of explosion: DD - delayed detonation, PDD - pulsating delayed detonation; ρ_c - central density of the white dwarf in $10^9 g/cm^3$; α - ratio of deflagration velocity and local sound speed; ρ_{tr} - transition density in $10^7 g/cm^3$ at which the deflagration is assumed to turn into a detonation; E_{kin} - final kinetic energy in 10^{51} ergs; M_{Ni} - mass of synthesized ^{56}Ni in solar masses; $< v >$ - average expansion velocity in 10^8 cm/sec; q_{CO} - mass fraction of the unburned CO envelope. Initial mass of the WD is $\simeq 1.4 M_\odot$ for all models.

Model	Mode	ρ_c	α	ρ_{tr}	E_{kin}	M_{Ni}	$< v >$	q_{CO}
N32	DD	3.5	0.03	2.6	1.52	0.56	9.0	≈ 0.01
PDD3	PDD	2.1	0.04	2.0	1.37	0.49	9.1	0.12
PDD535	PDD	2.7	0.035	0.45	0.34	0.15	4.5	0.21
PDD54	PDD	2.7	0.04	0.82	1.02	0.19	8.0	0.18
PDD5	PDD	2.7	0.03	0.76	1.23	0.12	8.4	0.06
PDD8	PDD	2.7	0.03	0.85	1.30	0.18	8.7	0.05
PDD7	PDD	2.7	0.03	1.1	1.40	0.36	9.1	0.04
PDD9	PDD	2.7	0.03	1.7	1.49	0.66	9.5	0.05
PDD6	PDD	2.7	0.03	2.2	1.49	0.56	9.1	0.04

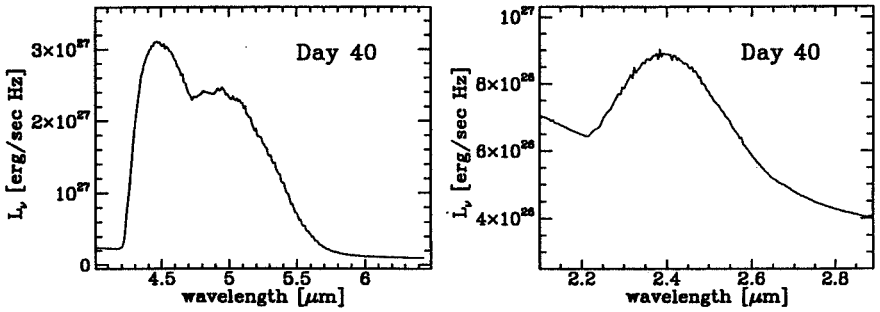

Figure 1. Luminosity of PDD54 at wavelengths corresponding to the fundamental and first overtone vibrational bands of CO at day 40 after the explosion, i.e. $\approx$ 2 and 3.5 weeks past maximum light.

even if subluminous because of the lack of unburned CO and strong radioactive heating, respectively. Therefore, IR-observations provide a sensitive tool to distinguish between different scenarios for subluminous SNe Ia.

4. Comparison with observations - Supernovae 1992bc, 1992bo, and 1991bg

To show that our models may have some resemblance to reality, our models PDD3, PDD8, and PDD5 are compared to the observed supernovae SN1992bc, SN1992bo, and SN1991bg (Höflich et al, 1994; see e.g. Figure 2). The first one is more or less normal, the second is $\simeq 0.8^m$ subluminous in V, and the third is the most subluminous supernova ($\approx 2.5^m$) known to date. There exists no observation in the wavelength range of the fundamental and first overtone band of CO, i.e. from 4-5 μm and 2.3-3 mum, respectively.

Table 2. Time since the explosion at which the mean temperature in the C/O-rich layers drops below a critical temperature T_{cr}. Typically, the models reach maximum light in V at about day 12 to 16.

Model	Type of explosion	5000 K	4500	4000
N32	DD	50	80	≥ 120
PDD535	PDD	-	25	35
PDD54	PDD	30	33	40
PDD5	PDD	20	26	38
PDD8	PDD	23	30	43
PDD7	PDD	38	45	62
PDD6	PDD	48	58	75
PDD9	PDD	70	90	≥ 150

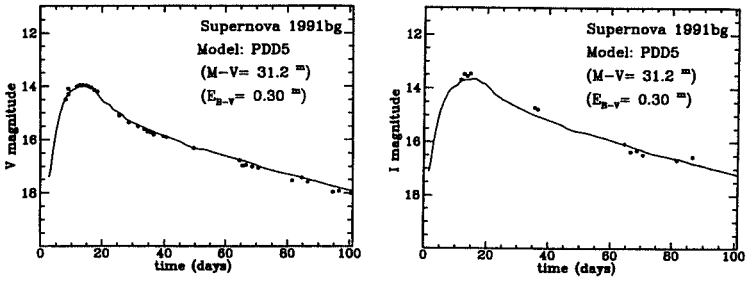

Figure 2. Comparison of observed and theoretical LCs for SN1991g.

References

Filippenko, A.V. et al., 1992, ApJ, 384, L15

Höflich, P., Khokhlov, A., Müller, E. 1991, A&A, 248, L7

Höflich, P., Khokhlov, A., Müller, E. 1992, A&A, 259, 549

Höflich, P., Müller, E,; Khokhlov, A. 1993, A&A, 268, 570

Höflich, P., Khokhlov, A., Wheeler, C. 1994, ApJ, submitted

Hoyle, P., Fowler 1960, ApJ, 132, 565

Khokhlov, A., Müller, E., Höflich, P. 1991, A&A, 253, L9

Khokhlov, A. 1991b, A&A, 245, 114

Khokhlov, A. 1991a, A&A, 245, L25

Khokhlov, A., Müller E., & Höflich, P. 1994, Workshop in Xian, ed. D. McCray, China

Leibundgut, B. et al. 1991, ApJ, 371, L23

Nomoto, K., Sugimoto, D., Neo, S. 1976 ApJ, 367, L19

Phillips, M. M. 1993, ApJ, 413, L108

Sunzeff, N.B. 1994, Workshop in Xian, ed. D. McCray, China,, in press

Woosley, S. E. and Weaver, T. A. 1994, preprint

Session Six

The Galactic Center: A Unique Region of the Galactic Ecosystem

Ted Dunham

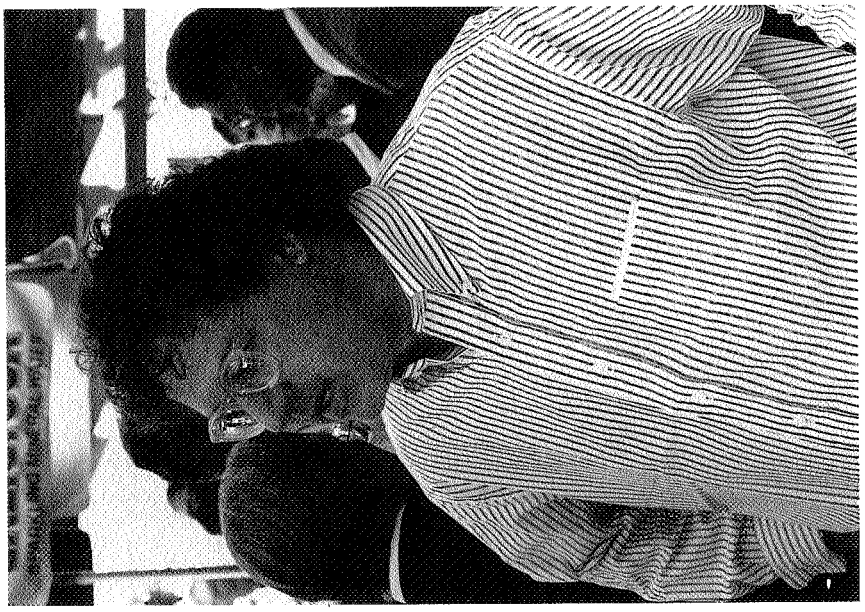

Gary Melnick

Airborne Astronomy Symposium on the Galactic Ecosystem
ASP Conference Series, Vol. 73, 1995
M.R. Haas, J.A. Davidson, and E.F. Erickson (eds.)

P-18

The Galactic Nucleus: A Unique Region in the Galactic Ecosystem

R. Genzel and A. Poglitsch

Max-Planck Institut für extraterrestrische Physik, Garching, Germany

Abstract. The nucleus is a unique region in the Galactic ecosystem. It is also a superb laboratory of modern astrophysics where astronomers can study, at unprecedented spatial resolution and across the entire electromagnetic spectrum, physical processes that may also happen at the cores of other galaxies. Infrared observations from the Kuiper Airborne Observatory have made important contributions to unraveling the mysteries of the Galactic nucleus and this review highlights some of these measurements, as well as recent results regarding the central parsec.

1. Introducing the Phenomena

Until about 20 years ago, investigations of the Galactic nucleus were severely impeded by the large amount of interstellar dust and gas situated in the Galactic plane between the sun and the nucleus, and preventing observations in the visible, ultraviolet and soft X-ray bands. In the past two decades, however, our knowledge about the Galactic nucleus has improved dramatically, as sensitive high resolution observations in the radio, infrared, hard X-ray and γ-ray bands have become available. In the following, a brief **summary of these phenomena** is given, followed by a more detailed account of two specific issues: the riddle of the **ionization of the so called "Radio Arc"** and the **exploration of the central few parsecs.** For more extensive discussions we refer to recent reviews (e.g., Genzel & Townes 1987; Blitz *et al.* 1993; Genzel, Hollenbach & Townes 1994).

The nuclear mass is dominated by stars, except perhaps in the innermost parsec. On a scale of 100 to 1000 pc, the stars appear to be distributed in a **rotating bar**. The gravitational torque of this bar drives **noncircular motions** in the interstellar gas clouds which leads to **gas infall** into the nucleus. The infall may be partially balanced by the evaporation of clouds into the 10^7 – 10^8 K intercloud, **coronal gas** that in turn escapes the Galactic disk as a **Galactic wind.** There is increasing evidence, discussed below, that **(massive) star formation** has occurred throughout the Galactic center region not longer than 10 million years ago so that the energy input responsible for this evaporation and hot gas may be **supernovae** exploding in the central bulge. Several variable, spectacular hard X-ray and γ-ray sources have been found and may represent **stellar black holes or neutron stars** accreting gas from a companion or from nearby dense gas clouds. A broad emission bump at ~500 keV and a twin radio

jet seen in one of these sources (the **"Great Annihilator"**) may signify the presence of an electron-positron jet in the environment of this compact source.

Throughout the central few hundred parsecs **giant molecular clouds** ($10^{5.5}$– 10^7 $M_\odot$) are found whose gas density and temperature are significantly greater than those of the clouds in the disk. The dust temperature of these clouds, on the other hand, is fairly low, indicating that most of them are presently not heated internally by active star formation. The dynamics of this central molecular cloud layer is characterized by large internal random motions and unusual streaming velocities that can be partially explained by the presence of the central bar potential. **Magnetic fields** as large as ~1mGauss appear to permeate the central 50 pc and are aligned approximately perpendicular to the Galactic plane. Where they interact with neutral gas clouds, spectacular filaments of nonthermal radio synchrotron emission are seen. The most spectacular such set of filaments, the **Radio Arc**, located about 13′ (34 pc) north of the dynamic center and the central radio source **SgrA***, also contains a set of more than 20 pc long filaments of thermal radio emission that are associated with ionized plasma of about 8000 K. The possible origin for the widespread ionization has been a great puzzle and will be discussed in more detail in §II. At 1.5 to 5 pc from the center there is a system of orbiting molecular filaments forming a molecular circum-nuclear ring or disk. The **circum-nuclear disk (CND)** is fed by gas infall from dense molecular clouds at $\geq$10 pc and appears to drop filaments or streamers into the central 1.5 pc which is comparatively devoid of interstellar matter (the **"central cavity"**). The ultraviolet (UV) radiation in this cavity is sufficiently high to ionize and heat to about 6000 K a significant fraction of these streamers. These central ionized streamers appear to be arranged in form of a **"mini-spiral"** and comprise the brightest part of the central radio source **SgrA (West)** . While the streamer velocities are largely dominated by the gravitational field, an **intense nuclear wind** (mostly from massive stars discussed below) also affects their motions.

The density of the nuclear star cluster increases with decreasing radius R approximately as R^{-2} outside of the "core" of less than a parsec in size. Inside that core radius, the stellar density is probably at least a few million times greater than in the solar neighborhood and direct collisions/mergers between stars and collisional destruction of stellar envelopes may play a role. Recent observations show individual **blue and red supergiants** in the core. These supergiants are very likely massive stars that have formed in the core within the last few million years. They appear to provide a significant and perhaps dominant fraction of the total luminosity of the central few parsecs. A discussion of the present state of our knowledge about this nuclear cluster, its distribution and evolution will be given in §III. Also inside that radius, the stellar and gas velocities are observed to increase, which may signal the presence of a black hole with mass ~$10^6 M_\odot$ at the dynamic center. A compact radio source, **SgrA***, lies approximately at that position and is close to, but not coincident with, a bright near-infrared source (**IRS16**) of blue color. **SgrA*** has stellar dimensions (size a few AU), but is presently not very conspicuous in any wavelength range other than the radio range. This is somewhat surprising if **SgrA*** is in fact a massive black hole surrounded by stars and gas clouds.

Clearly the modern multi-wavelength observations of the Galactic nucleus tell a fascinating story and show that a broad range of phenomena involving a

number of physical processes are at work. To help the reader find their way in the jargon of names Figure 1 gives a "road map" of the central 100 pc.

2. What Ionizes the Radio Arc?

Figure 2 shows a radio **VLA** map of the **Radio Arc** (adapted from Yusef-Zadeh, Morris & Chance 1984). One clearly recognizes basically straight filaments of **nonthermal** radio emission stretching from south-east to north-west, approximately perpendicular to the Galactic plane, as well as arched filaments of **thermal** radio continuum emission starting a few arcminutes north of **SgrA** and terminating near the nonthermal filaments. From the linearity of the nonthermal filaments despite the presence of dense interstellar gas clouds the magnetic field strength can be estimated to lie between 0.1 and a few mGauss (Morris 1990). The flat spectral index of the nonthermal filaments indicates that the relativistic electrons causing the synchrotron emission are accelerated locally, perhaps due to magnetic reconnection or fast shocks. There is no plausible external confinement mechanism for the hot and relativistic gas associated with the magnetic flux tubes. Therefore it appears most likely (Morris 1990) that a **poloidal** (i.e. perpendicular to the Galactic plane) magnetic field pervades the entire central ~50 parsecs and that the nonthermal filaments signify regions where electrons are injected and accelerated (Morris 1990).

The **thermal** arched filaments including the "**sickle**" feature (Figure 1) located approximately at the center of the nonthermal filaments, are associated with dense molecular clouds ($n(H_2) \approx$ a few 10^4 cm^{-3}), and the ionized gas probably forms the ionized surfaces of these clouds (Serabyn & Güsten 1987). Early measurements of the far-infrared continuum emission from the **KAO** already established that the arched filaments have a far-infrared luminosity of a few 10^7 $L_\odot$ (Gatley *et al.* 1978; see also Davidson *et al.* 1994); a recent 50 μm **KAO** map from Davidson *et al.* (1994) is shown in Figure 3. One fairly obvious interpretation, therefore, is that the ionization (and luminosity) of the arched filaments is caused by 10–10^2 **OB stars** that have formed there locally in the last 10^7 years. However, the characteristics of the arched filaments are highly unusual as far as classical HII regions are concerned; the ionization appears to be almost uniform over more than 20 pc while being spatially confined perpendicular to the filaments' long axis. The dust temperature does not show local peaks (Figure 3) characteristic of HII regions with embedded, newly formed massive stars. Furthermore, the arched filaments have negative radial velocities that cannot be explained by Galactic rotation. For these reasons and their obvious proximity to strong magnetic fields a number of "unconventional" models, involving fast shocks, plasma waves, ejection of gas/field tubes from the nucleus, and magnetohydrodynamic (MHD) effects have been proposed for the ionization of the filaments (e.g., Bally *et al.* 1988; Sofue & Fujimoto 1987; Heyvaerts, Norman, & Pudritz 1988; Morris & Yusef-Zadeh 1989). Perhaps the most intriguing one is due to Morris & Yusef-Zadeh (1989) who proposed that the ionization originates when a fast moving molecular cloud (the velocities of the arched filaments differ from normal Galactic rotation by at least 50 km/s) runs into a strong (and stiff) magnetic field. Kinetic energy can then be converted to ionization. The cascade ionization process that results when ions in the molecular gyrate in the field

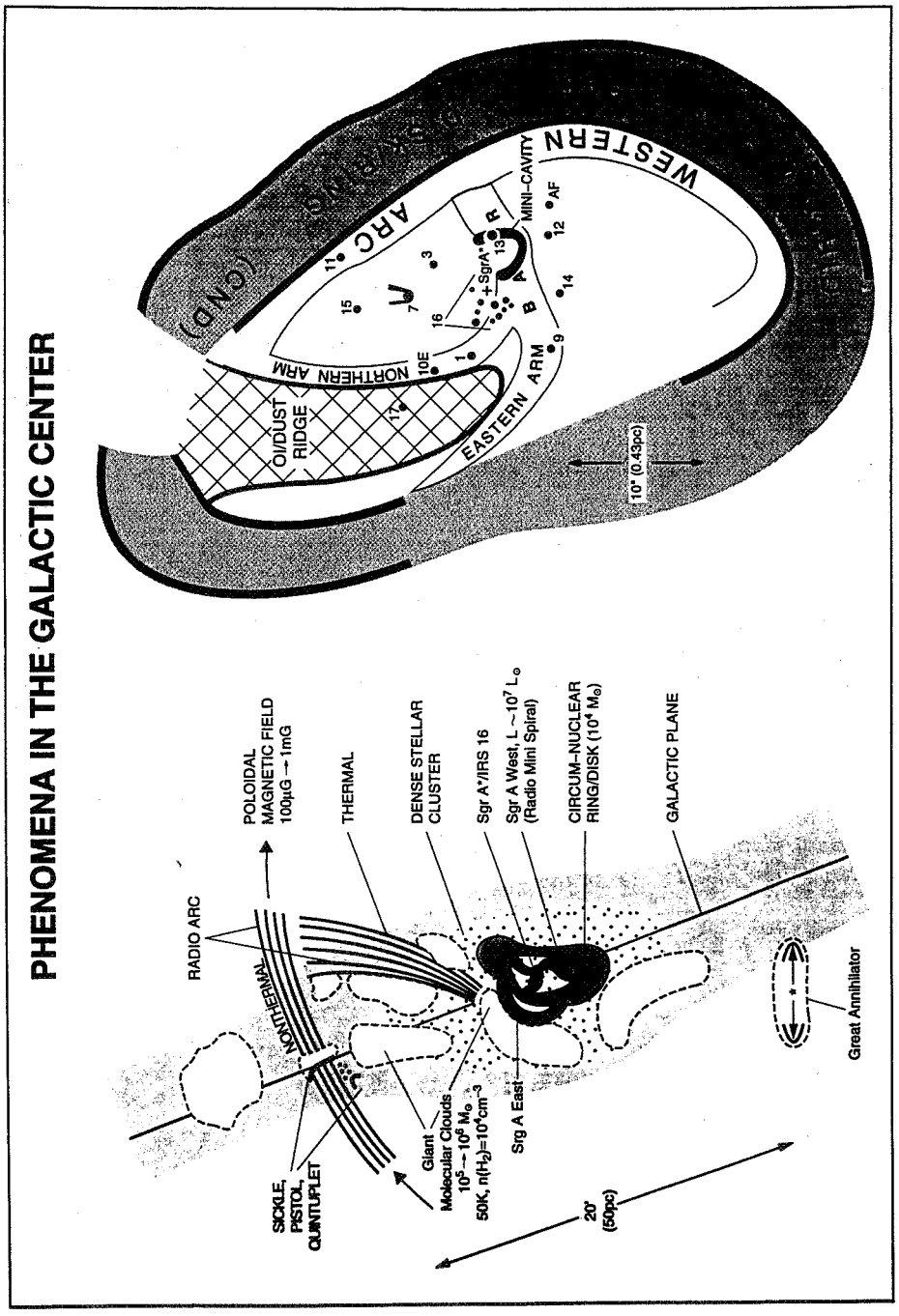

Fig. 1: Overview of the phenomena (and nomenclature) in the Galactic nucleus.

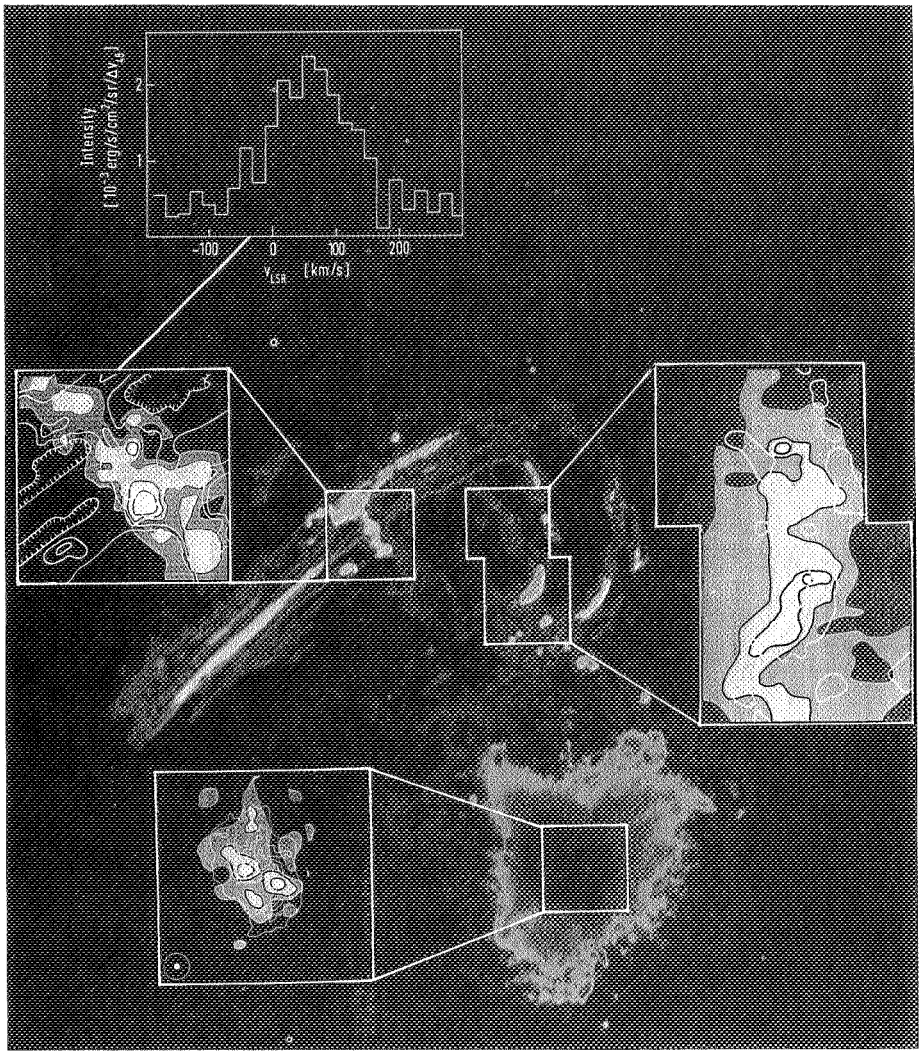

Figure 2: False color 20 cm VLA radio continuum map (adapted from Yusef-Zadeh, Morris and Chance (1984), and false color 88 μm [OIII] maps, taken with the MPE imaging Fabry-Perot FIFI on the KAO (insets). A 50 km/s resolution [OIII] spectrum of the sickle region (top inset) shows broad lines (from Timmermann *et al.* 1995).

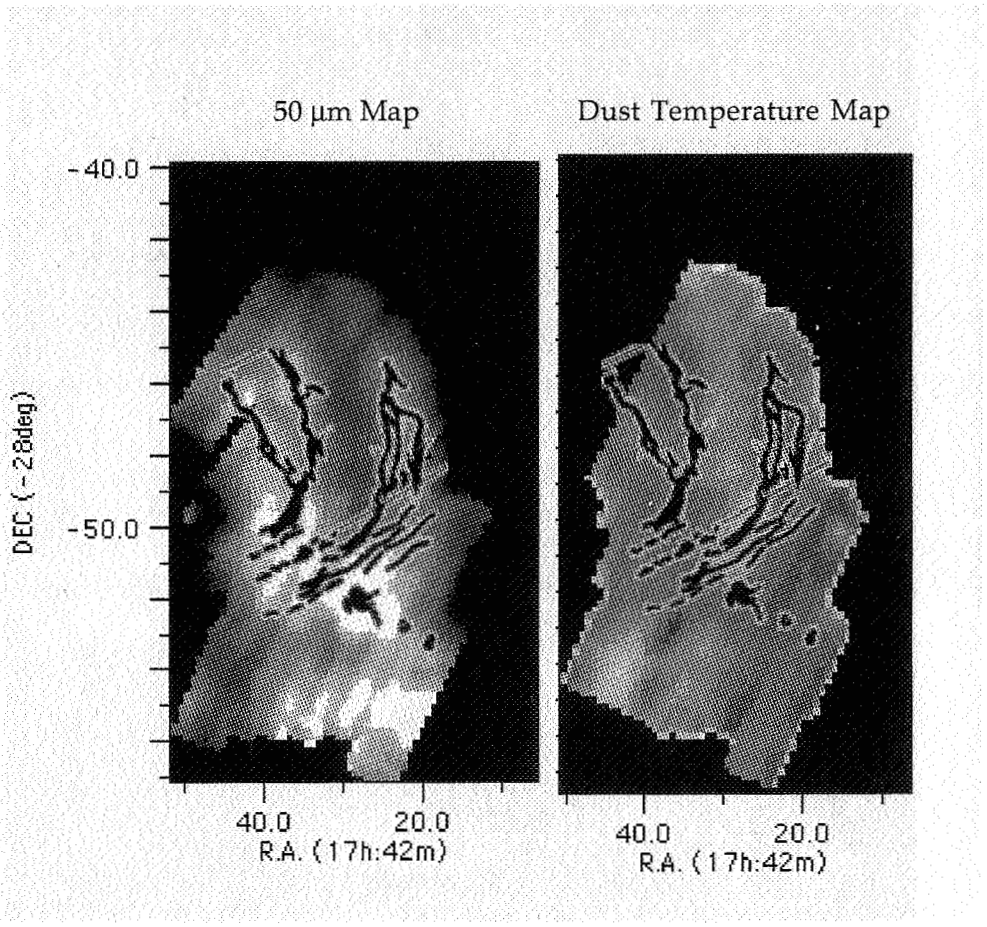

Figure 3: Grey color plot of 50 μm continuum map (left) and dust temperature map (right), superposed on a schematic of the arched thermal filaments (Davidson *et al.* 1994). The data were taken with the University of Texas **bolometer array** on the **KAO** .

and then collide with the neutrals is well known in plasma physics under the name **"critical ionization velocity" mechanism** . This mechanism is globally similar to a fast, ionizing shock and such fast shocks can in fact account for the observed emission measures of the radio continuum emission in the arched filaments ($\sim 10^6$ cm^{-6} pc) if the preshock gas is dense.

What is the solution of the riddle posed by the observations? Here photometry, polarimetry and spectroscopy with instruments onboard the **KAO** have contributed in the last few years key information that — together with near-infrared spectroscopy and imaging — **now favor the (conventional) OB star hypothesis**. The first finding is that far-infrared line and continuum emission from the arched filaments and the sickle does not match at all what is expected from fast shocks but resembles a classical HII region/photodissociation region (Genzel *et al.* 1990; Erickson *et al.* 1991). Strong 52/88 μm [OIII] (Figure 2, Timmermann *et al.* 1995), 33 μm [SIII] (Erickson *et al.* 1991) and 158 μm [CII] line emission (Poglitsch *et al.* 1991) track the thermal radio continuum distribution. The ratio of the two [OIII] lines shows unambiguously that the ionized gas has relatively low electron densities ($n_e \sim 10^{2.5}$ cm^{-3}). This in turn implies that the electron column densities ($\sim 10^{22}$ cm^{-2}) and likewise the O^{++} column densities (10^{17} cm^{-2}) are fairly large. For comparison, ionizing shocks predict $N_e \leq 10^{20}$ cm^{-2} and $N(O^{++}) \leq 10^{14.5}$ cm^{-2} (Hollenbach & McKee 1989; Shull & McKee 1979). Shocks also fail to explain the large C^+ column densities and the far-infrared luminosity by two orders of magnitude or more, whereas photoionized HII regions readily produce the observed columns and far-infrared luminosity (Genzel *et al.* 1990). A second piece of evidence against the "critical ionization velocity" model and other MHD models is the (**KAO**) observation of remarkably strong (5±1%) far-infrared continuum polarization aligned perpendicular to the arched filaments (Morris *et al.* 1992). The standard model of magnetically aligned dust grains thus implies that the B-field direction is along the filaments which is inconsistent with the prediction of a fast moving cloud running into a **stiff** poloidal field (Morris *et al.* 1992). The polarimetric observations also exclude models in which the magnetic field is generated by currents along the cloud surface (Benford 1988). Morris *et al.* (1992) conclude that the most probable hypothesis is that the field geometry follows from the shearing motion of a dense molecular cloud with a large noncircular motion.

Turning now to the conventional model with OB stars heating and ionizing thermal filaments the key questions are where and how many OB stars there are. From the large spatial extent and uniformity of the ionization the conclusion is inevitable that OB stars must be distributed over ~30 pc scale (Serabyn & Güsten 1987). Extrapolating from its observed radio continuum flux density (~20 Jy at 32 GHz) or its ionization characteristics ($N(OIII)/N(O) \sim 0.2$, $n_e \sim 500$ cm^{-3}) the **sickle** for instance, requires a Lyman continuum ionization rate of $1-3\times10^{50}$ photons s^{-1}, or the equivalent of about 20 to 60 O7 stars (Timmermann *et al.* 1995). Similar numbers apply to the other parts of the arched filaments. The OB star model has recently been boosted by the discovery of HeI/Bγ near-infrared emission line stars in several places in the vicinity of the filaments. There are 3 such stars associated with the **Quintuplet** cluster (Okuda *et al.* 1990) approximately located at the center of the **sickle** (Moneti *et al.* 1991; Cotera *et al.* 1992; Harris *et al.* 1994). A half a dozen Bγ stars have been discovered by Cotera *et al.* (1994) in a cluster located at the base of the easternmost arched

filament. Cotera *et al.* (1994) also found additional emission line stars in several locations east and north of the SgrA region. The near-infrared emission line stars have spectral characteristics quite similar to those found by Allen, Hyland & Hillier (1990) and Krabbe *et al.* (1991) in the central parsec of the Galaxy which will be discussed in more detail in the next section. They are most likely luminous (a few 10^5 $L_\odot$), mass losing blue supergiants. The discovery of such stars throughout the volume occupied by the thermal filaments thus is a qualitative proof of the concept for the OB star model. With the interpretation that the HeI/Bγ stars represent a relatively short-lived (10^5 to 10^6 years) phase in the (post-main sequence) evolution of massive stars (Allen *et al.* 1990; Krabbe *et al.* 1991) it is suggestive that the observed $\sim 10^1$ massive stars are just the tip of an iceberg; there may well be an additional hundred or more OB stars lurking in the same regions that could then fully account for the heating and ionization of the Radio Arc region. The probable post-main sequence state of (some of) the massive stars implies that OB stars have formed there already about 10^7 years ago. A possible explanation for the unusual, uniform ionization of the thermal filaments then may be that the OB stars have not formed in the filaments. The filaments may have just recently streamed into the volume occupied by the OB stars and are ionized on their surfaces by the pervasive stellar UV field. Given their unusual velocities, the arched filaments would move (with respect to material in normal rotation about the nucleus) about 3′ to 4′ within only about 10^5 years.

Although the thermal filaments may be photoionized by stars, the interaction of dense clouds with magnetic fields and injection of electrons as a result of that interaction are probably key elements for the understanding of the nonthermal filaments. Unusually wide ($\Delta v \sim 100$ km/s) [OIII] and radio recombination lines in the **sickle** (Figure 2) may be related to this interaction.

3. What Powers the Central Parsec?

KAO observations have also contributed in a major way to the exploration of the physical characteristics, dynamics and composition of the innermost core, associated with the peak of the stellar density and the radio source **SgrA**. A key result, for instance, was the finding that the innermost parsec contains little, but relatively hot dust and is surrounded by a double-lobed region of cooler dust with a much larger column density (Becklin, Gatley & Werner 1982). Becklin, Gatley and Werner's interpretation of this observation, confirmed by more recent, higher resolution **KAO** maps (Davidson *et al.* 1992) is that there is a ring or disk of dust (and gas) surrounding a $\sim$1 pc **central cavity** . The luminosity of the central parsec is about 10^7 $L_\odot$, most of which is intrinsically emitted in the visible and ultraviolet wavebands. This short-wavelength radiation is then absorbed by the dust disk and converted to far-infrared continuum radiation. The existence of this **circum-nuclear disk** (**CND**) plus central cavity has since been amply confirmed and its properties studied in detail by mapping of millimeter, submillimeter and far-infrared molecular lines (see Genzel 1989 for a review). A more recent development is the recognition from **KAO** 50 μm and 90 μm continuum maps (Davidson *et al.* 1992) and maps of 63 μm [OI] line emission (Jackson *et al.* 1993) that leading from the northern inside edge of the **CND**

to the center there is a ridge/tongue of neutral gas and dust (Figure 4). The ridge is probably associated with the northern **mini-spiral** streamer of ionized gas (Figure 4) and may represent gas that is currently falling into the central cavity (Jackson *et al.* 1993). Observations of far-infrared dust polarization in the **CND** and ridge, shown in Figure 5 (from Hildebrand & Davidson 1994), show a large and fairly uniform polarization in the central few arcminutes. Hildebrand *et al.* (1990, 1993) conclude that the average magnetic field as projected on the sky lies approximately north-south, along the major axis of the **CND**. Combining the molecular line maps and dynamics, dust polarization, and Zeeman measurements of the field strength in the disk (a few mGauss, Schwarz & Lasenby 1990; Killeen, Lo & Crutcher 1992), the following picture emerges. The **CND** consists of a set of **clumpy molecular streamers** orbiting in approximately the same plane. The streamer clumps lose angular momentum by clump-clump collisions and/or by "turbulent" friction mediated by the frozen-in magnetic fields. As a result the gas **accretes** toward the center at an average current rate of about 10^{-2} $M_\odot$ yr^{-1}. The **CND** is fed from large molecular clouds at 10 pc (Ho *et al.* 1991; Zylka, Mezger & Wink 1990). On its inner edge at ~1.5 pc the effect of the winds from the central parsec (see below) may on average prevent further accretion (Genzel, Hollenbach & Townes 1994; Ozernoy & Genzel 1994). From time to time, however, a cloud with large radial velocity (and low angular momentum) may penetrate into the inner cavity; the [OI]/dust ridge and the **mini-spiral** streamers may be such infalling clouds (Lo & Claussen 1983; Serabyn & Lacy 1985). Soon after an infalling cloud enters the central cavity its surface becomes ionized by the central ultraviolet radiation field. Alternatively, the ridge/northern arm may be a spiral density wave (Lacy, Achtermann & Serabyn 1991).

Figure 6 shows a composite spectral energy distribution of the central parsec (from Genzel, Hollenbach & Townes 1994). Again, many of the infrared observations entering this figure have been obtained on the **KAO** . The ionized gas spectroscopy demonstrates that **SgrA (West)** is a **low excitation HII region** with electron temperature ~6000 K and **a range of electron densities** (10^3 to 10^5 cm^{-3}, Lacy *et al.* 1980; Shields & Ferland 1994; Erickson *et al.* 1994). Combining the line ratios of the different fine structure lines, the flux density of the radio continuum, and the fluxes of the hydrogen and helium radio recombination lines in an excitation analysis, one derives a **relatively low effective temperature** (~35,000 K) for the ionizing radiation field (Lacy *et al.* 1980; Shields & Ferland 1994). Effective temperatures significantly in excess of 40,000 K are only possible if the strong 12.8 μm [NeII] line and most of the radio continuum come from very dense gas (10^6 to 10^7 cm^{-3}, Shields & Ferland 1994), a solution that is not entirely excluded but not favored by the data. More detailed spectroscopy of species with higher ionization potentials and of density sensitive line ratios, planned with the **ISO** spectrometers, should give a clearcut answer. The line ratios also suggest a **metal abundance of about twice solar** (Lacy *et al.* 1980; Lacy, Achtermann & Bruce 1989; Herter *et al.* 1984; Lester *et al.* 1987; Shields & Ferland 1994). What powers this low excitation HII region with a bolometric luminosity of $10^{7\pm0.3}$ $L_\odot$?

At this point we need to turn our attention to a number of recent high resolution **near-infrared** observations that pertain to the distribution and characteristics of the nuclear stellar cluster. These measurements have become possible

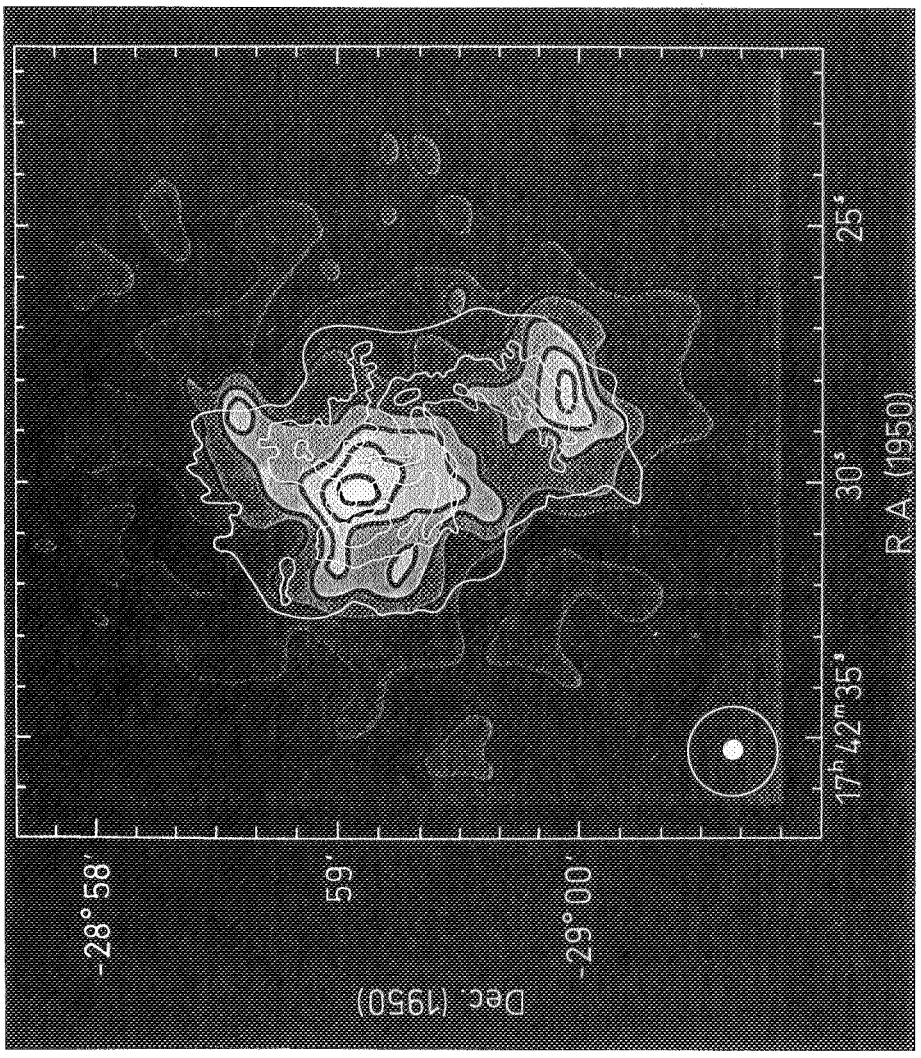

Figure 4: False color image of the 63 μm [OI] emission (**FIFI** on **KAO**), superposed on a schematic contour map of the 5 GHz radio continuum from the **mini-spiral** in the **SgrA (West)** HII region (from Jackson *et al.* 1993).

Figure 5. Left: 100 μm polarization vectors in SgrA (West), taken with the University of Chicago polarimeter **Stokes**, superposed on a 90 μm continuum map taken with the University of Texas **bolometer array**, both observed on the **KAO**. Right: Polarization vectors on a model of the polarization vectors for an accretion disk with an axisymmetric magnetic field (dashed) (adapted from Hildebrand & Davidson 1994).

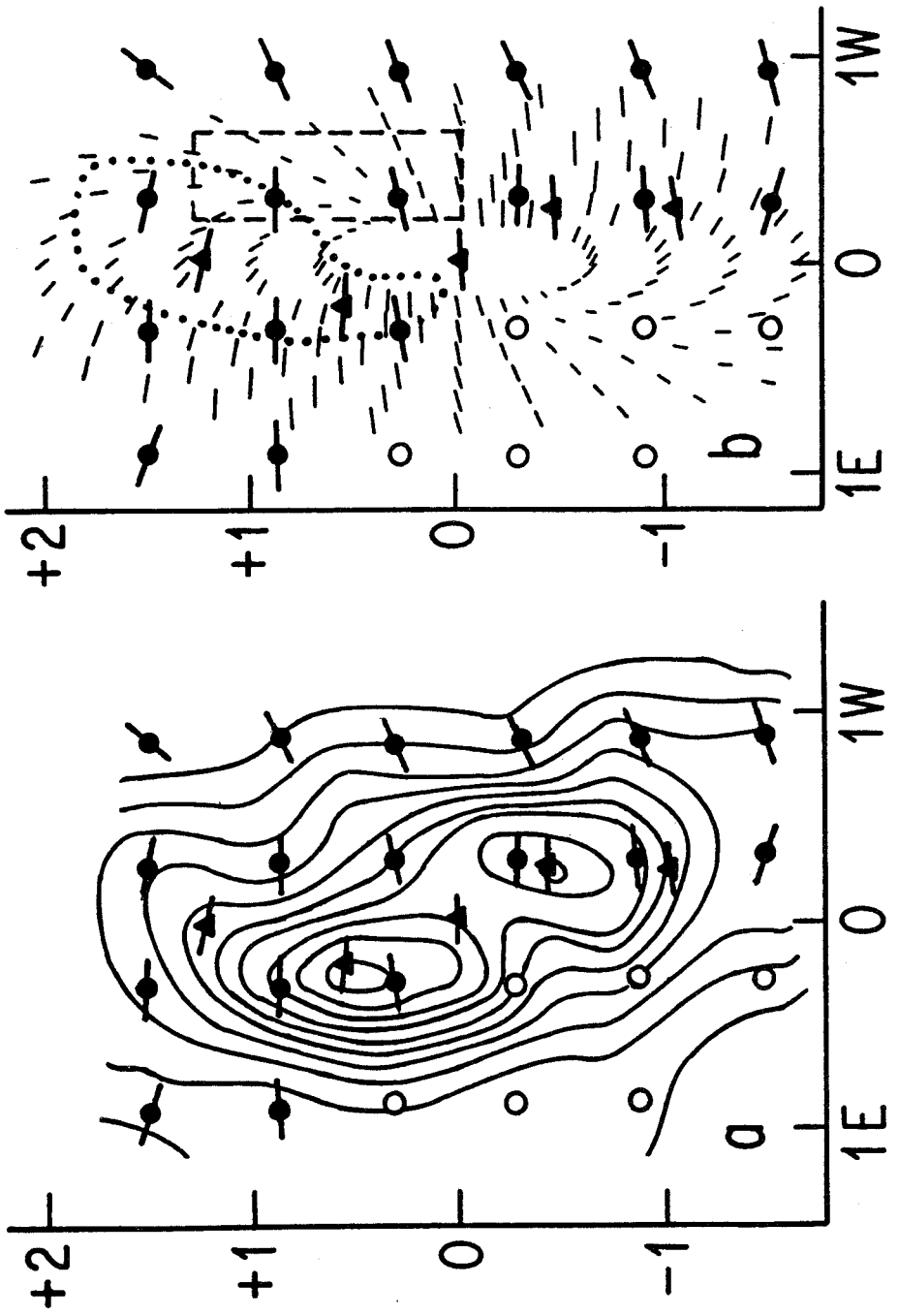
1W
0
1E
b
+2
+1
0
−1
1W
0
1E
a
+2
+1
0
−1

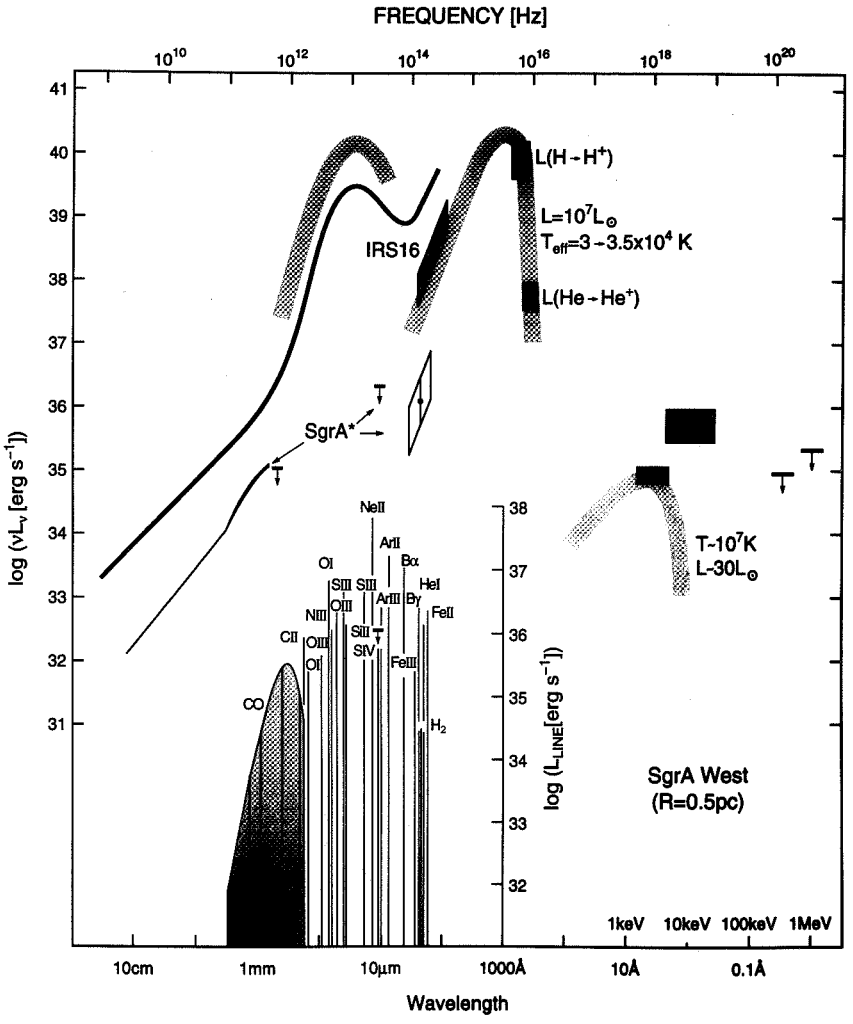

Figure 6: Schematic spectral energy distribution of the central few parsecs (heavy continuous), spectral line emission (bottom inset), X-ray fluxes and SgrA* spectrum. Observational constraints on the intrinsically emitted far-infrared spectrum, UV spectrum and X-ray emission are denoted by shaded curves and boxes (adapted from Genzel, Hollenbach & Townes). The far-infrared measurements were taken with the **Texas**, **Chicago**, and **Caltech** photometers, the **CGS** (NASA Ames), the **UCB Fabry-Perot** (UC Berkeley), the **Cornell grating spectrometer** (Cornell) and **FIFI** (MPE/UCB) on the KAO.

Figure 7: Seeing limited (left: 0.8″ MPE **FAST** on William Herschel Telescope) and diffraction limited (right: 0.15″ MPE **SHARP** on ESO **NTT**) 2 μm images of the central parsec of the Galaxy (cf. Eckart *et al.* 1993).

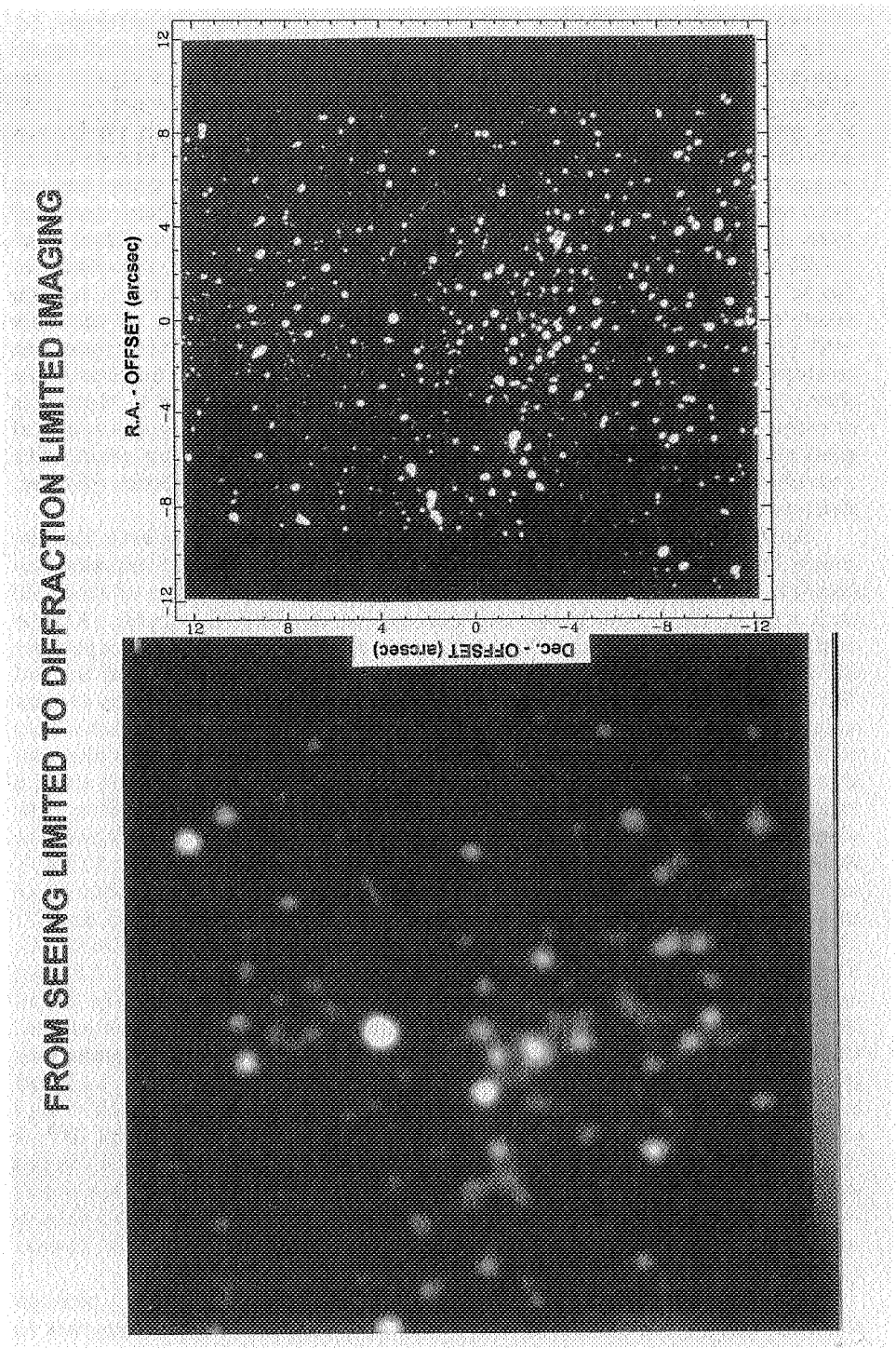
FROM SEEING LIMITED TO DIFFRACTION LIMITED IMAGING
R.A. - OFFSET (arcsec)
Dec. - OFFSET (arcsec)
12
8
4
0
−4
−8
−12

through the advent in the last half a dozen years of sensitive, large format detector arrays. In only a few years time it has become possible to first record high quality seeing limited images ($\sim 1''$, left side of Figure 7) and then further to improve the resolution to the diffraction limit of 4m class telescopes ($\sim 0.15''$ at 2 μm, right side of Figure 7, Eckart *et al.* 1993). These images resolve the near-infrared emission of the central parsec ($23''$) into about 350 stars with K-magnitudes $\leq$14. The central **IRS16** complex located within $1''$ of the compact radio source **SgrA*** consists of about two dozen single (or perhaps multiple) stars. From the number distribution of the near-infrared sources, Eckart *et al.* (1993) have concluded that the centroid of the stellar cluster is more likely on **SgrA*** than on the **IRS16** complex and that the core radius of the K$\leq$14, 2 μm stellar number density distribution is only about 0.15 to 0.2 pc. If the stars with K$\leq$14 are representative of the overall mass distribution of the cluster (an assumption that still needs to be proven by spectroscopic identification of the stars) such a small core radius would mean that the stellar density in the core is in excess of $10^{7.5}$ $M_\odot$ pc^{-3}. At these densities stellar mergers and disruption of giant star atmospheres by direct stellar collisions become very important, with a number of interesting consequences for stellar and cluster evolution (Genzel, Hollenbach & Townes 1994).

Another important ingredient of the near-infrared story has been the discovery by Allen *et al.* (1990) and Forrest *et al.* (1987) of a HeI/Bγ emission line star (the **AF-star**), followed by the discovery of an entire cluster of about 15 such stars in the central parsec and centered on the **IRS16** complex (Krabbe *et al.* 1991). In fact several of the brightest members of the **IRS16** complex are HeI-stars (Krabbe *et al.* 1991; Genzel, Hollenbach & Townes 1994) and the HeI "broad line region" (e.g., Geballe *et al.* 1987) is now identified as a group of mass losing, He-rich stars. A detailed non-LTE analysis of the emission characteristics of the **AF-star** by Najarro *et al.* (1994) confirms and quantifies the earlier conclusion of Allen *et al.* (1990) that the **AF-star** is similar to WN9/Ofpe stars, a rare class of evolved, luminous blue supergiants related to Luminous Blue Variables (LBVs, Krabbe *et al.* 1991). According to the Najarro *et al.* analysis, the **AF-star** has a luminosity of about $10^{5.5}L_\odot$, effective temperature near 20,000 K and ZAMS mass between 25 and 40 $M_\odot$. The **AF-star** has a He/H abundance ratio near unity and loses mass at a velocity of 700 km/s and rate of 6×10^{-5} $M_\odot$ yr^{-1}. A preliminary analysis of the brightest IRS16 stars (IRS16NE, C, SW) suggests that these stars may in most respects be similar to the AF-star, but about 5 to 10 times more luminous (Najarro, priv. comm.). The IRS16 HeI stars may also emit in excess of 10^{49} Lyman continuum photons per second. Combining the contributions from all its members, **the HeI-star cluster can plausibly account for most of the bolometric luminosity ($\sim10^7$ $L_\odot$) and a significant fraction of the Lyman-continuum luminosity ($\sim10^{6.2}$ $L_\odot$) of the central parsec** . The HeI-star cluster also provides in excess of 10^{38} /s in mechanical wind luminosity which may have a significant impact on the gas dynamics in the central parsec. In fact, the outward acceleration of the winds may explain why a possible central massive black hole is not likely to accrete very much interstellar gas at the present time (Genzel, Hollenbach & Townes 1994).

In agreement with an earlier proposal by Rieke & Lebofsky (1982), perhaps the most likely model for the recent evolution of the nuclear cluster appears to

be a small **star formation burst** $5-10\times10^6$ years ago in which a few hundred OB stars and perhaps a total of a few thousand stars were formed. This burst was perhaps triggered by a large influx of dense gas at that time. The HeI stars may be the most massive cluster members that in the mean time have evolved off the main sequence. In this scenario the central parsec is now in the late, **wind-dominated** (30 Doradus in LMC!) phase of the burst. The gas density in the central core is too low to form a substantial number of stars at the present time. This model accounts naturally for the low excitation of the **SgrA (West)** HII region. There are several difficulties, however. First, if the HeI stars are in fact closely related to LBVs, conventional wisdom would give an estimate of the duration of that phase of less than 10^5 years. Consequently, either there are $10^7/(\leq10^5)\times15\geq10^3$ additional OB stars lurking in the cluster (if star formation has been semi-continuous) that have not been identified yet. Such a large number of OB stars is probably inconsistent with the far-infrared luminosity constraint. Alternatively, the burst was very sharp in time and we happen to observe this last nuclear burst in the LBV phase (with an a priori probability of less than 1%). This explanation also cannot explain the simultaneous presence of stars in the HeI-phase that are different by a large factor in luminosity (**AF** and **IRS16 NE/C/SW**), and hence mass. A second problem is that there are only a few **red** supergiants (IRS7, IRS12N?) as compared to the ~15 blue supergiants, again inconsistent with normal stellar evolution and a spread of ages. A way out of the last two dilemmas may be a much longer duration of the HeI phase as compared to the traditional estimates of the LBV phase (metallicity?) and an additional destruction of red supergiants due to stellar collisions.

Eckart *et al.* (1993) have proposed **sequential merging** as an alternative to the starburst scenario, a possibility whose likelihood strongly depends on a very high density of the nuclear cluster (e.g., Genzel, Hollenbach & Townes 1994). Using a Focker-Planck formalism, Lee (1994) has recently modelled the evolution of dense stellar clusters including merger events. For the Galactic Center cluster he found, however, that a core of density $10^{7.5}$ $M_\odot$ pc^{-3} or greater cannot be maintained for a long enough time to produce enough 20 $M_\odot$ stars as required by the observed number of He-stars. Morris (1993) has suggested that the HeI stars are not classical blue supergiants at all but objects that have been created in **collisions between (~10 $M_\odot$) stellar black holes and red giants**. Both accounts of the HeI stars just cited are very specific to the high density environment of the central parsec. But a number of stars that look just like the SgrA HeI stars have now been found outside of the central, high density region, as reported above! In the case of the Morris (1993) scenario one would also probably expect a much larger X-ray emission as a result of the collisions than is observed (Lee, priv. comm.).

The last key issue that needs to be briefly commented on is the evidence for a central massive black hole. With the exception of the presence of the unusual radio point source SgrA* (see Backer 1994 and Zylka *et al.* 1994), the evidence for a central massive black hole is based entirely on observations of the gas and stellar dynamics. In fact if there is a massive black hole the observations imply that it is presently "accretion starved" and contributes little to the overall luminosity of the central parsec. Again observations from the **KAO** have played a significant role in determining gas velocities at a few parsec distance from the dynamic center. The presently available measurements, most recently reviewed

by Genzel, Hollenbach & Townes (1994), can be described as encouraging (for the existence of a $\sim 10^6$ $M_\odot$ black hole) but not yet sufficient as a proof. The key will be to determine the dynamic mass significantly inside the radius covered by the last present data points (at R$\sim$0.2 pc). An experiment is now well underway to determine the proper motions of the stars within $\leq 2''$ (0.08 pc) from **SgrA*** from repeated, high-resolution near-infrared imaging with the MPE **SHARP** camera on the ESO **NTT** (see Figure 7). First results of the first four epochs of the experiment (covering $\sim$2 years) are very encouraging and promise to confirm (or disprove) a 1 to 2×10^6 $M_\odot$ black hole in a measurement period of about 6 years.

References

Allen, D.A., Hyland, A.R., & Hillier, D.J. 1990, MNRAS, 244, 706

Backer, D.C. 1994, in Nuclei of Normal Galaxies: Lessons from the Galactic Center, eds. R. Genzel & A.I. Harris, (Dordrecht: Kluwer), in press

Bally, J., Stark, A.A., Wilson, R.W., & Henkel, C. 1988, ApJ, 324, 223

Becklin, E.E., Gatley, I., & Werner, M.W. 1982, ApJ, 258, 134

Benford, G. 1988, ApJ, 333, 735

Blitz, L., Binney, J., Lo, K.Y., Bally, J., & Ho, P.T.P. 1993, Nature, 361, 417

Cotera, A., Erickson, E.F., Simpson, J.P., Colgan, S.W.J., Allen, D.A., & Burton, M.W. 1992, BAAS, 24, 1262

Cotera, A., Erickson, E.F., Allen, D.A., Colgan, S.W., Simpson, J.P., & Burton, M.G. 1994, in Nuclei of Normal Galaxies: Lessons from the Galactic Center, eds. R. Genzel & A.I. Harris, (Dordrecht: Kluwer), in press

Davidson, J.A., Werner, M.W., Wu, X., Lester, D.F., Harvey, P.M., Joy, M., & Morris, M. 1992, ApJ, 387, 189

Davidson, J.A., Morris, M., Harvey, P.M., Lester, D.F., Smith, B., & Werner, M.W. 1994, in Nuclei of Normal Galaxies: Lessons from the Galactic Center, eds. R. Genzel & A.I. Harris, (Dordrecht: Kluwer), in press

Eckart, A., Genzel, R., Hofmann, R., Sams, B.J., & Tacconi-Garman, L.E. 1993, ApJ, 407, L77

Erickson, E.F., Colgan, S.W.J., Simpson, J.P., Rubin, R.H., Morris, M., & Haas, M.R. 1991, ApJ, 370, L69

Erickson, E.F., Colgan, S.W.J., Simpson, J.P., Rubin, R.H., & Haas, M.R. 1994, in Nuclei of Normal Galaxies: Lessons from the Galactic Center, eds. R. Genzel & A.I. Harris, (Dordrecht: Kluwer), in press

Forrest, W.J., Shure, M.A., Pipher, J.L., & Woodward, C.A. 1987, in The Galactic Center, ed. D.C. Backer, AIP Conference Proceedings, 155, 153

Gatley, I., Becklin, E.E., Werner, M.W., & Harper, D.A. 1978, ApJ, 220, 822

Geballe, T.R., Wade, R., Krisciunas, K., Gatley, I., & Bird, M.C. 1987, ApJ, 320, 562

Genzel, R., & Townes, C.H. 1987, ARA&A, 25, 377

Genzel, R. 1989, in The Center of the Galaxy, ed. M. Morris, (Dordrecht: Kluwer), 393

Genzel, R., Stacey, G.J., Harris, A.I., Townes, C.H., Geis, N., Graf, U.U., Poglitsch, A., & Stutzki, J. 1990, ApJ, 356, 160

Genzel, R., Hollenbach, D., & Townes, C.H. 1994, Rep.Progr.Phys., 57, 417

Harris, A.I., Krenz, T., Genzel, R., Krabbe, A., Lutz, D., Poglitsch, A., Townes, C.H., & Geballe, T.R. 1994, in Nuclei of Normal Galaxies: Lessons from the Galactic Center, eds. R. Genzel & A.I. Harris, (Dordrecht: Kluwer), in press

Herter, T., Houck, J.R., Shure, M., Gull, G.E., & Graf, P. 1984, ApJ, 287, L15

Heyvaerts, J., Norman, C., & Pudritz, R. 1988, ApJ, 330, 718

Hildebrand, R.H., Gonatas, D.P., Platt, S.R., Davidson, J.A., Werner, M.W., Novak, G., & Morris, M. 1990, ApJ, 417, 565

Hildebrand, R.H., Davidson, J.A., Dotson, J., Figer, D.F., Novak, G., Platt, S.R. & Tao, L. 1993, ApJ, 417, 565

Hildebrand, R.H., & Davidson, J.A. 1994, in Nuclei of Normal Galaxies: Lessons from the Galactic Center, eds. R. Genzel & A.I. Harris, (Dordrecht: Kluwer), in press

Ho, P.T.P., Ho, L., Szczepanski, J.C., Jackson, J.M., Armstrong, J.M., & Barrett, A.H. 1991, Nature, 350, 309

Hollenbach, D., & McKee, C.F. 1989, ApJ, 342, 306

Jackson, J.M., Geis, N., Genzel, R., Harris, A.I., Madden, S., Poglitsch, A., Stacey, G.J., & Townes, C.H. 1993, ApJ, 402, 173

Killeen, N.E.B., Lo, K.Y., & Crutcher, R. 1992, ApJ, 385, 585

Krabbe, A., Genzel, R., Drapatz, S., & Rotaciuc, V. 1991, ApJ, 382, L19

Lacy, J.H., Townes, C.H., Geballe, T.R., & Hollenbach, D. 1980, ApJ, 241, 132

Lacy, J.H., Achtermann, J.M., & Bruce, D.E. 1989, in The Center of the Galaxy, ed. M. Morris, (Dordrecht: Kluwer), 523

Lacy, J.H., Achtermann, J.M., & Serabyn, E. 1991, ApJ, 380, L71

Lee, H.M. 1994, in Nuclei of Normal Galaxies: Lessons from the Galactic Center, eds. R. Genzel & A.I. Harris, (Dordrecht: Kluwer), in press

Lester, D.F., Dinerstein, H.L., Werner, M.W., Watson, D.M., Genzel, R., & Storey, J.W.V. 1987, ApJ, 320, 573

Lo, K.Y., & Claussen, M.J. 1983, Nature, 306, 647

Moneti, A., Glass, I.S., & Moorwood, A.F.M. 1991, Mem.Soc.Astr.It. 62, 4, 755

Morris, M., & Yusef-Zadeh, F. 1989, ApJ, 343, 703

Morris, M. 1990, in Galactic and Extragalactic Magnetic Fields, eds. R. Beck, P. Kronberg & R. Wielebinski, (Dordrecht: Kluwer), 361

Morris, M., Davidson, J.A., Werner, M.W., Dotson, J., Figer, D.F., Hildebrand, R.H., Novak, G., & Platt, S. 1992, ApJ, 399, L63

Morris, M. 1993, ApJ, 408, 496

Najarro, F., Hillier, D.J., Kudritzki, R.P., Krabbe, A., Genzel, R., Lutz, D., Drapatz, S., & Geballe, T.R. 1994, A&A, 285, 573

Okuda, H. *et al.* 1990, ApJ, 351, 89

Ozernoy, L.M., & Genzel, R. 1994,.in prep

Poglitsch, A., Stacey, G.J., Geis, N., Haggerty, M., Jackson, J.M., Rumitz, M., Genzel, R., & Townes, C.H. 1991, ApJ, 374, L33

Rieke, G.H., & Lebofsky, M.J. 1982, in The Galactic Center, eds. G.R. Riegler & R.D. Blandford, AIP Conference Series 83 (New York), 194

Schwarz, U.J., & Lasenby, J. 1990, in Galactic and Extragalactic Magnetic Fields, eds. R. Beck, P. Kronberg, & R. Wielebinski, (Dordrecht: Kluwer), 383

Serabyn E., & Lacy, J.H. 1985, ApJ, 293, 445

Serabyn , E., & Güsten, R. 1987, A&A, 184, 133

Shields, J., & Ferland, G. 1994, ApJ, 430, 236

Shull, J.M., & McKee, C.F. 1979, ApJ, 227, 131

Sofue, Y., & Fujimoto, M. 1987, ApJ, 319, L73

Timmermann, R. *et al.* 1995, in prep.

Yusef-Zadeh, F., Morris, M., & Chance, D. 1984, Nature, 310, 557

Zylka, R., Mezger, P.G., & Wink, J.E. 1990, A&A, 234, 133

Zylka, R., Mezger, P.G., & Ward-Thompson, D. 1994, A&A, in press

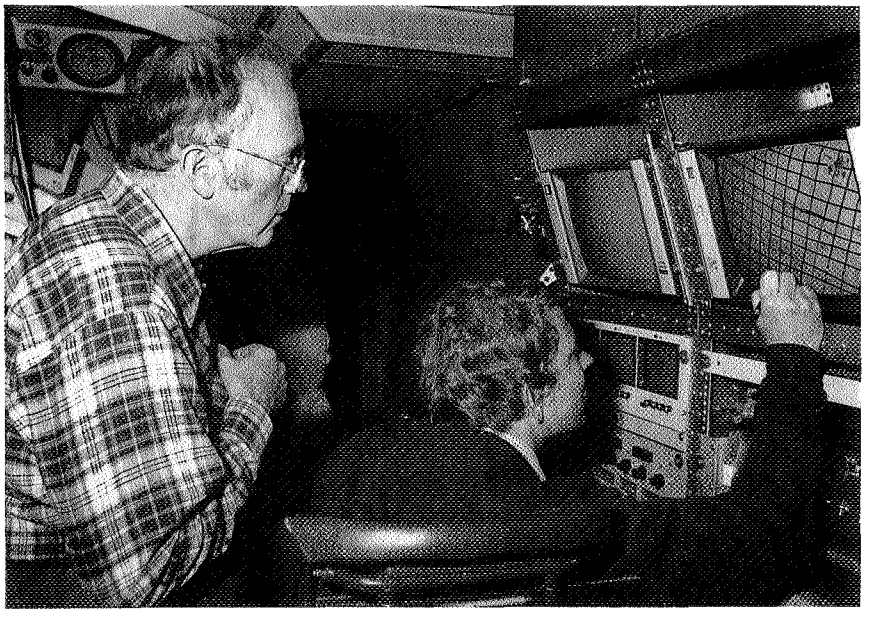

Charlie Townes, Reinhard Genzel (1981)

Airborne Astronomy Symposium on the Galactic Ecosystem
ASP Conference Series, Vol. 73, 1995
M.R. Haas, J.A. Davidson, and E.F. Erickson (eds.)

The Population One Core of the Galaxy

Michael Burton
School of Physics, University of New South Wales, Sydney, NSW 2052, Australia

David Allen
Anglo Australian Observatory, PO Box 296, Epping, NSW 2121, Australia

Abstract. Spectral imaging in the near-infrared of the central parsec of the Galaxy has revealed that a population of massive young stars resides in the core of our Galaxy. We suggest it has undergone a mild starburst.

1. Introduction

It is generally accepted that at least $10^6\,M_\odot$ of material resides within the central parsec of the Galaxy. Part of it comprises the core of the population II stellar component; old, cool stars at the center of the Bulge. In recent years evidence has steadily accumulated that there also exists a younger, more dynamic component to the galactic nucleus. This paper discusses new observations obtained with the 3.9-m Anglo Australian Telescope which suggest that indeed a cluster of massive population I stars resides at the very heart of the Bulge.

2. Observations

The infrared camera and spectrometer IRIS (Allen *et al.* 1993) was used to collect the data. Employing an echelle to disperse the light spectrally, the telescope was slowly drifted across the central 2 parsecs of the Galaxy, with the array read-out rate synchronized to the drift speed. In this way a data cube was constructed, comprising the spatial information at 0.8″ pixel scale and spectra at resolution 400 across both the H and (separately) K atmospheric windows.

The data from these observations have been presented, in part, in a series of papers (Burton & Allen 1992, 1993; Allen 1994; Allen & Burton 1994) and are not presented pictorially here. An in-depth analysis is currently in preparation. The data also both confirm and extend the results of Krabbe *et al.* (1991) who first identified the cluster of He I ($2.058\,\mu$m)-line stars in the galactic nucleus, following the initial discovery of a single bright He I star by Allen, Hyland & Hillier (1990).

Our data revealed a cluster of about a dozen stars emitting in the He I ($2.058\,\mu$m) line and located within 20″ (1 pc) of the center, and in many cases with He I/Brγ > 1. In our Galaxy such stars appear unique to its central regions, and from comparison with similar stars found in the LMC (McGregor,

Hillier & Hyland 1988), have been identified as massive ($> 20\,M_\odot$) stars at the top end of the main sequence. They are beginning to enter a Wolf-Rayet phase, and are somewhat akin to luminous blue variables. The cluster is surrounded by streamers of ionized gas called the 'mini-spiral,' first identified through its radio synchrotron emission (*e.g.,* Ekers *et al.* 1983) and also visible in the 2.166 μm hydrogen Br γ line. Surrounding and abutting the ionized gas is a clumpy ring of hot molecular hydrogen emitting in the 2.122 μm 1–0 S(1) line. Spectra of the H_2 suggest that UV–photons from the hot stars play a major role in fluorescently exciting the gas, but that both motions within and between the clumps, and stellar winds also result in considerable quantities of shocked gas. An image extracted in the line of [Fe II] (1.644 μm) shows a further collection of hot stars, as well as a region of diffuse line emission. The [Fe II] stars all lie within the ionized gas, suggesting $B_{[e]}$ stars, each around $10\,M_\odot$ with an extended envelope where the [Fe II] line is excited. They represent a continuation of the He I cluster to lower masses. The diffuse [Fe II] emission lies between the northern and eastern arms of the mini-spiral, roughly coincident with an infalling cloud emitting in the neutral [O I] (63 μm) line (Jackson *et al.* 1993). The [Fe III] (2.217 μm) line is also seen, arising from diffuse gas in the so-called 'mini-cavity' of cm-band radio continuum maps, 3.5″ SW of Sgr A*, as first identified by Lutz, Krabbe & Genzel (1994).

No He II (2.189 μm) emission is observed, restricting the population to late-type WR stars (*e.g.,* WN9), rather than early type. The CO overtone bandheads at 2.3 μm can, however, be used to extend our knowledge of the population to lower masses. 'Hot' and 'cool' stars can be distinguished by whether they have CO absorption features present, with a break-point at spectral type F. Extracting images from the cube based on this feature (as discussed by Allen, Hyland & Hillier 1990) neatly divides the stars into two populations, the 'cool' stars resembling the K band image outside the central 20″, and the 'hot' stars confined to the core.

3. Discussion

It is clear that a cluster of hot massive stars resides within the central parsec of the Galaxy. These stars must be young, less than 10 million years old, and their presence is unexpected. Together they can account for the far–IR luminosity, UV–flux and mass-loss rate from the central parsec of the Galaxy. Their luminosity peak, centered near IRS 16C, is 1″E of the radio source Sgr A* (Allen & Saunders 1986), presumed to be at the very center of the Galaxy.

There is, however, no suggestion that star formation was occurring at earlier epochs. Thus this is a recent and new event in the Galactic center. Several models have been invoked to explain the existence of this cluster without the need for star formation (*e.g.,* black hole 'atmospheres', Morris 1993; and mergers of old giants, Phinney 1989). However the presence of other similar (though smaller) clusters within the central 100 parsecs where massive star formation is clearly taking place (*e.g.,* Cotera *et al.* 1992), but where the conditions are less extreme, leads us to argue that star formation is occurring in the nucleus as well. Infalling molecular clouds are common within the region and we suggest the collision of two such clouds over the nucleus has initiated the recent burst.

It is of great interest to relate this cluster to the distribution of the population II core and its contribution to the central mass density. Eckart *et al.* (1993) recently showed from diffraction limited images (0.15″) that there are at least 340 sources within the central parsec with K < 14, and that their number distribution is consistent with an isothermal cluster of core radius 3.8″. Such a tight core would imply a high central density ($> 10^7\,M_\odot\,pc^{-3}$) and argue strongly for the existence of a massive central object. We have determined the flux distribution of the 'hot' and 'cool' populations, as indicated by the strength of the CO bandheads. We find that for the 'hot' stars the *flux* distribution is consistent with the *number* distribution found by Eckart *et al.* For the 'cool' stars, on the other hand, the flux distribution is similar to that expected for an isothermal cluster with larger core radius, around 20″. The central stellar density is then $\sim 10^6\,M_\odot\,pc^{-3}$.

Although we must caution against drawing too much inference from the loaded term 'core radius', and in particular to simple analytic fits which pertain to provide estimates of its value, it seems clear that the populations of 'hot' and 'cool' stars have different distributions. From the similarity of the number and 'hot' star flux distributions we infer they measure the same population. There must therefore be small numbers of 'cool' stars with K < 14, with most of the 'cool' star light emerging from fainter sources. Thus we infer that the majority of the 340 stars of Eckart *et al.* are 'hot' stars. This conclusion can, in principle, be tested by directly measuring the number distribution in the spectral tracers of the 'hot' stars, though in practice any such experiment will be hampered by the lower sensitivity levels that will be achieved. It is an important experiment to perform.

Assuming that the individual stars seen are indeed 'hot' stars, then equating the number and flux distributions implies an average K band magnitude of 12.8, which after correction for extinction makes an absolute magnitude $M_K \sim 5$. On the main sequence this would correspond to an O star, whereas a population of stars obeying the Salpeter IMF would contribute their maximum K light around spectral type F, with $M_K \sim +3$. While these estimates are necessarily crude, the 1000-fold difference in flux more than accounts for many subtle influences we may have neglected. We thus take this as further evidence that the young stellar population is heavily weighted towards higher masses. Out to a 20″ radius, therefore, the majority of the observed stars (K < 14) are 'hot' stars and contribute a total mass of around $10^4\,M_\odot$ to the core.

The bulk of the mass of the central parsec ($\sim 10^6\,M_\odot$) must thus comprise the unresolved old population II stars which contribute around 10% of the K-band flux. Such a scenario is consistent with the model of Bicknell, Saha & McGregor (1995), who fit the flux and velocity dispersion distributions with a simple mass model which has no central massive object. We stress, however, that this conclusion rests on the identification of the 'hot' star flux distribution with the number distribution of stars with K < 14 as observed by Eckart *et al.* (1993). It may require modification if a smaller 'core radius' than 20″ is appropriate. However, whatever the central mass, it seems clear that a young population of massive stars exists within the central parsec, the result of a mild starburst.

Acknowledgments. This work has been driven by the efforts of David Allen, who, sadly, is no longer with us to guide its further development.

References

Allen, D. A. 1994, in 'The Galactic Center', Reports on Progress in Physics (Ringsberg Conf.), in press

Allen, D. A., & Burton, M. G. 1994, Proc. Ast. Soc. Aust., 11, 191

Allen, D. A., Hyland, A. R., & Hillier, D. J. 1990, MNRAS, 244, 706

Allen, D. A., & Saunders, R. H. 1986, Nature, 319, 191

Allen, D. A. *et al.* 1993, Proc. Ast. Soc. Aust., 10, 298

Bicknell, G. V., Saha, P., & McGregor, P. 1995, in preparation

Burton, M. G., & Allen, D. A. 1992, Proc. Ast. Soc. Aust., 10, 55

Burton, M. G., & Allen, D. A. 1993, in 'Astronomical Infrared Spectroscopy: Future Observational Directions', ed. S. Kwok, ASP Conf. Series, 41, 289

Cotera, A. S., Erickson, E. F., Simpson, J. P., Colgan, S. W. J., Allen, D. A., & Burton, M. G. 1992, BAAS, 24, 1262

Eckart, A., Genzel, R., Hoffmann, B., Sams, B. J., & Tacconi-Garman, L. E. 1993, ApJ, 407, L77

Ekers, R. D., van Gorkom, J. H., Schwartz, U. J., & Goss, W. M. 1983, A&A, 122, 143

Jackson, J. M., Geis, N., Genzel, R., Harris, A. I., Madden, S., Poglitsch, A., Stacey, G. J., & Townes, C. H. 1993, ApJ, 402, 173

Krabbe, A., Genzel, R., Drapatz, S., & Rotaciuc, V. 1991, ApJ, 382, L19

Lutz, D., Krabbe, A., & Genzel, R. 1994, ApJ, in press

McGregor, P. J., Hillier, D. J., & Hyland, A. R. 1988, ApJ, 334, 639

Morris, M. 1993, ApJ, 408, 496

Phinney, E. S. 1989, IAU Symp. 136, 543

Airborne Astronomy Symposium on the Galactic Ecosystem
ASP Conference Series, Vol. 73, 1995
M.R. Haas, J.A. Davidson, and E.F. Erickson (eds.)

Dust Destruction and Kinematics in the Galactic Center

Susan R. Stolovy, Terry Herter, George E. Gull, Bruce Pirger, and Nicole P. Vogt

Astronomy Department, Cornell University, Ithaca, NY 14853

Abstract. We present observations of the 34.815μm [SiII] line and continuum emission from the inner few parsecs of the Galaxy obtained with the KAO Echelle Grating Spectrograph (KEGS) in June 1993. The SiII emission, which has been spectrally resolved at 64 km/s and spatially resolved at 10", is kinematically consistent with the motions of ionized and neutral gas interior to the circumnuclear disk (CND). In addition, the emission in the [SiII] line as well as the continuum extends northward along the "northern arm" past the inner edge of the CND. A peak in the [SiII] line/continuum ratio is observed at ~25" W and 75" N of Sgr A* with a large velocity dispersion. This may be an indication of dust destruction via cloud-cloud collisions.

1. Motivation

These measurements were undertaken in order to investigate the distribution and kinematics of the neutral gas in the inner few parsecs of the Galaxy. The collisionally excited 34.8μm [SiII] fine-structure line is found in photodissociation regions and also can be an indicator of strong J-shocks. These observations improve upon previous observations (Herter et al. 1989) by both spectrally resolving the SiII feature and by achieving diffraction limited spatial resolution.

2. SiII Observations and Data Reduction

We used KEGS on the KAO on June 15 and 17, 1993, using a 128×128 BIB Si:Sb detector array developed by Cornell in conjunction with Rockwell International. KEGS operates in high spectral resolution, low spectral resolution and camera modes. Each mode illuminates a different subsection of the array. A given mode is selected by rotating a grating carousel mechanism, which contains predisperser gratings for the echelle, a low resolution grating, and a flat mirror. The plate scale is 4"/pixel. The high spectral resolution Galactic Center observations presented here employed a 15"×80" entrance slit, with the 80" length in the cross-dispersion (spatial) direction. This configuration produced 20 simultaneous spectra for each pointed position on the sky, with 128 pixels per spectrum. The spectral dispersion was 1.8 x $10^{-3}\mu$m per pixel, yielding a resolving power of ~ 5000 when summing 4 pixels in the slit. Unfortunately, due to lack of time and to the fact that the sky rotation varied substantially over the observations, the spatial coverage was incomplete.

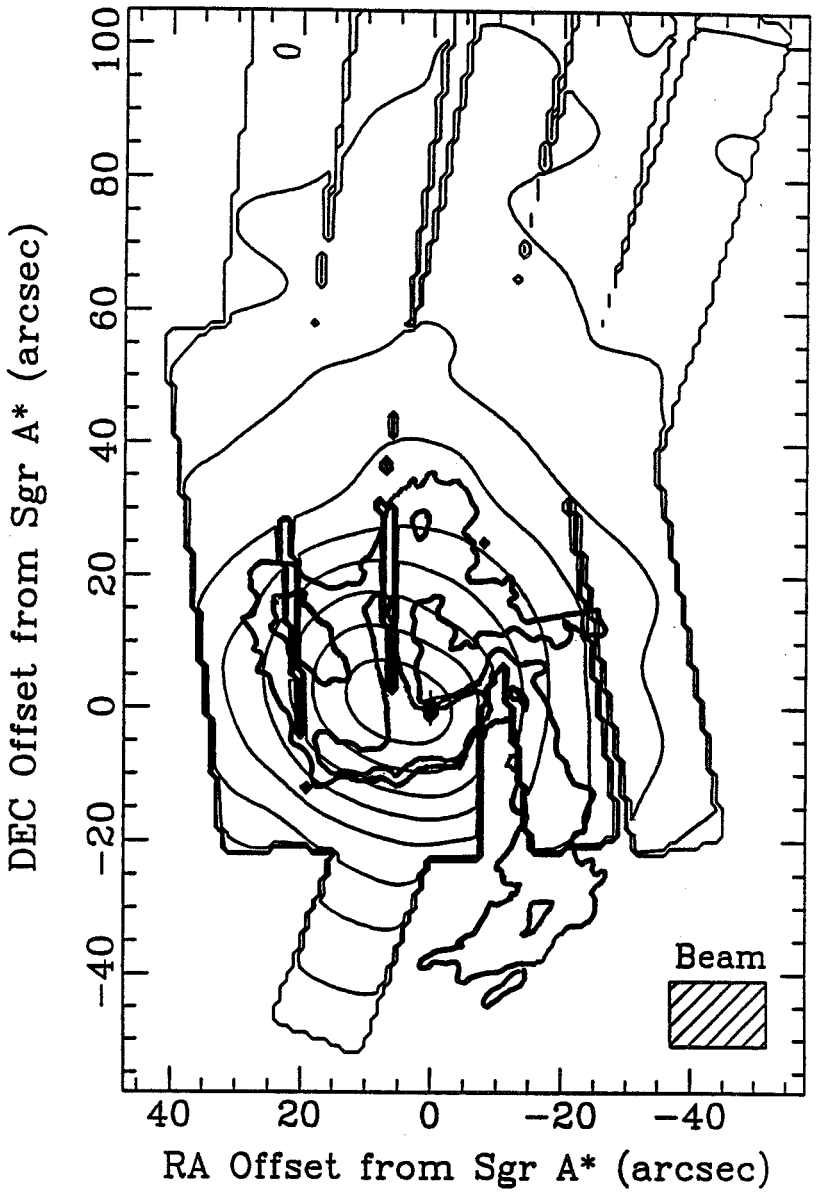

Figure 1. Superposition of smoothed continuum map at 34.8 μm, true spatial coverage, and 6 cm radio map (Lo and Claussen 1983). The unrotated beam size is shown in the lower right corner.

In order to track the kinematics and spatial distribution of the SiII emission, a series of velocity maps were constructed. At each pointed position, the line profiles were sampled in 32 km/s bins. By summing 2 spectral pixels for each velocity map, we have subsampled the actual spectral resolution of 64 km/s by a factor of 2. The images for each position were rotated to account for instrumental and sky rotation, spatially offset the appropriate amount, and mosaicked into a map extending roughly 2×3 arcminutes. Gaps in coverage were filled in by interpolation, and the maps were smoothed with a gaussian of FWHM roughly equal to our pixel size and further smoothed with a boxcar of our effective beam size (10"). A continuum map was formed in a similar way by averaging over a large part of the array (46 pixels = $\Delta\lambda \approx 0.1\mu$m) well separated in wavelength from the SiII emission. The continuum map has been scaled to represent the flux over the same wavelength range as the velocity maps (i.e. 32 km/s). This continuum map has been subtracted for each of the final silicon velocity maps to produce the images in panels 2-10 of Figure 2. Absolute wavelength calibration was determined by observing terrestrial water vapor lines in emission in DC (unchopped) images.

3. Discussion

3.1. SiII Observations

Figure 1 displays the 6-cm radio continuum map of the "mini-spiral" (adopted from Lo and Claussen 1983) superimposed on the smoothed continuum map restricted to the true spatial coverage. The 15"×10" beam (which rotates with the sky) is also indicated in Figure 1. The velocity channel maps presented in Figure 2 show a clear trend shifting from negative to positive velocity northward along the northern arm. This is consistent with OI, HCN, and NeII motions (Jackson et al. 1993; Lacy, Achterman, and Serabyn 1991). It appears that the region corresponding to the "east-west bar" has a large velocity dispersion, indicating that there may be overlapping of kinematically distinct material along the line of sight.

The continuum peak at 30 μm (bandwidth 5 μm) as observed by Telesco, Davidson, and Werner (1995, private communication) from the IRTF is located at IRS1, which is about 5" east and 1" north of Sgr A*. We have adopted this position as the peak of our continuum maps. The SiII distribution is quite clumpy when velocity resolved, and is not as smoothly concentrated as the continuum. The main SiII peak as shown in the average of the velocity maps (Figure 2, panel 11) is offset to the NE relative to the continuum peak by $\sim$ 9"E and 4"N. Accurate spatial registration of the continuum and velocity maps is insured because they were assembled in exactly the same way; hence, the relative offset is independent of pointing.

Evidence for Cloud-Cloud Collisions Maps of the line/continuum ratio reveal a localized peak at $\sim$ 25"W and 75"N of Sgr A*. This feature is most prominent in panel 6, weakly apparent in panel 7, and again quite prominent in panels 8 and 9 of Figure 2. The velocity range covered by these 4 channels is $\sim$ 55 to 180 km/s. This feature persists when the subsampled maps are binned 2 at a time to reproduce the true spectral resolution. The vector from Sgr A* to this

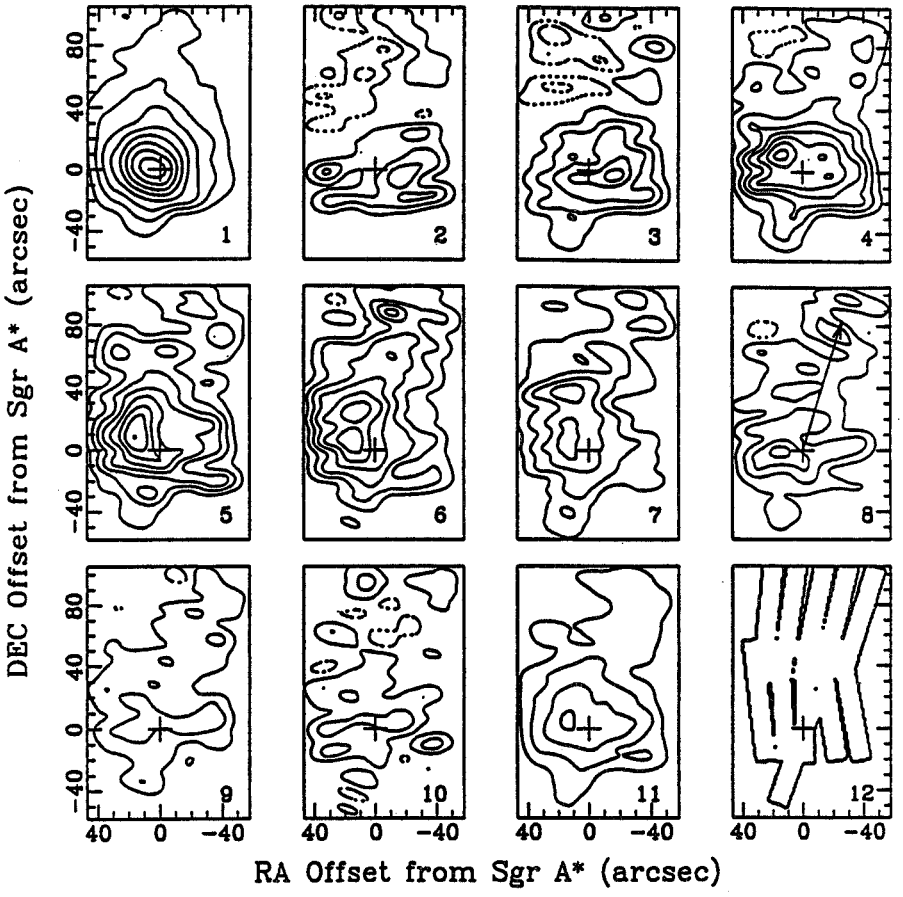

Figure 2. 1) Continuum, 2)-10) SiII velocity channel maps with central velocities ranging from -56 km/s to +200 km/s spaced by 32 km/s, 11) Integrated SiII map [average of 2)-10)], 12) True spatial coverage. A plus sign marks the position of Sgr A*. On map 8) a vector is drawn from Sgr A* to the location of the line/continuum peak. Contour levels are -18% to 90% of the peak in increments of 12% $=1\sigma$.

peak is indicated in panel 8 of Figure 2 and is plotted in Figure 3. It appears to be an extension of the northern arm of the ionized streamers. This peak also corresponds to the position of the secondary SiII peak detected by Herter et al. (1989) with a 28" beam.

The resolved SiII line exhibits a generally extended ridge in the direction of this region, but the line/continuum ratio is enhanced most prominently at this location. As a cautionary note, the line/continuum ratio is quite noisy where the continuum drops off, and the peak in the ratio may be due in part to a coincidental occurrence of adjacent low pixel values in the continuum. The scatter in the line/continuum ratio increases substantially just beyond this peak, so future better sensitivity measurements will be crucial in confirming these results. As a result of electronic readout and detector modifications as of July 1994, the sensitivity of KEGS is considerably better than it was for the observations presented here; therefore, we expect to improve over these preliminary results in future observations.

The peak observed in the line/continuum ratio of SiII supports the conjecture that silicate dust, the main source of the continuum radiation, is being destroyed, locally producing more atomic silicon and depressing the dust emission. The fact that the peak is such a broad feature in velocity also is consistent with the dust being destroyed via cloud-cloud collisions. If this material is shocked by counter-rotating clouds, the resulting loss of angular momentum may be sufficient to cause the gas and dust to flow inward.

Other supporting evidence for collisions and/or inflow include:

- Inflow of material through a gap in the northern part of the CND has been inferred (Jackson et al. 1993) from OI and HCN observations.
- C+ observations (Lugten et al. 1986) show a gas clump with negative velocity (-65 to -25 km/s) where the general ring rotation is $\sim$ 100 km/s. However, the 40-50" beam of these observations makes it difficult to compare their results with ours.
- Molecular hydrogen measurements (Ramsay, Mountain, and Geballe 1993) of redshifted (+60 km/s) gas adjacent to blueshifted gas (0 to -100 km/s) SW of Sgr A* imply the existence of clumpy, turbulent structure. This is in the SW lobe of the CND which was not included in our spatial coverage.

3.2. Camera Observations

We briefly observed the inner few parsecs with the camera mode of KEGS. For these observations, the camera mode utilized a narrow bandpass Fabry-Perot filter ($\Delta\lambda \approx 1\mu$m) centered at $\approx 38.4\mu$m and illuminated a 20×20 subsection of the array. The camera image has the advantage of better spatial resolution and continuous spatial coverage as compared to the continuum image culled from our long-slit spectra. The continuum image in Figure 4 has been smoothed to our 10" beam and represents only four minutes of data. The emission drops off sharply at the boundaries of the "mini-spiral", and the southwest lobe corresponding to the "western arc" is clearly evident. When registering the peak with IRS1, it is evident that the 38μm emission is concentrated closer in towards Sgr A* than the 50 and 90 μm peaks observed by Davidson et al. (1992). This supports the hypothesis that there is a dust temperature gradient in the central few parsecs.

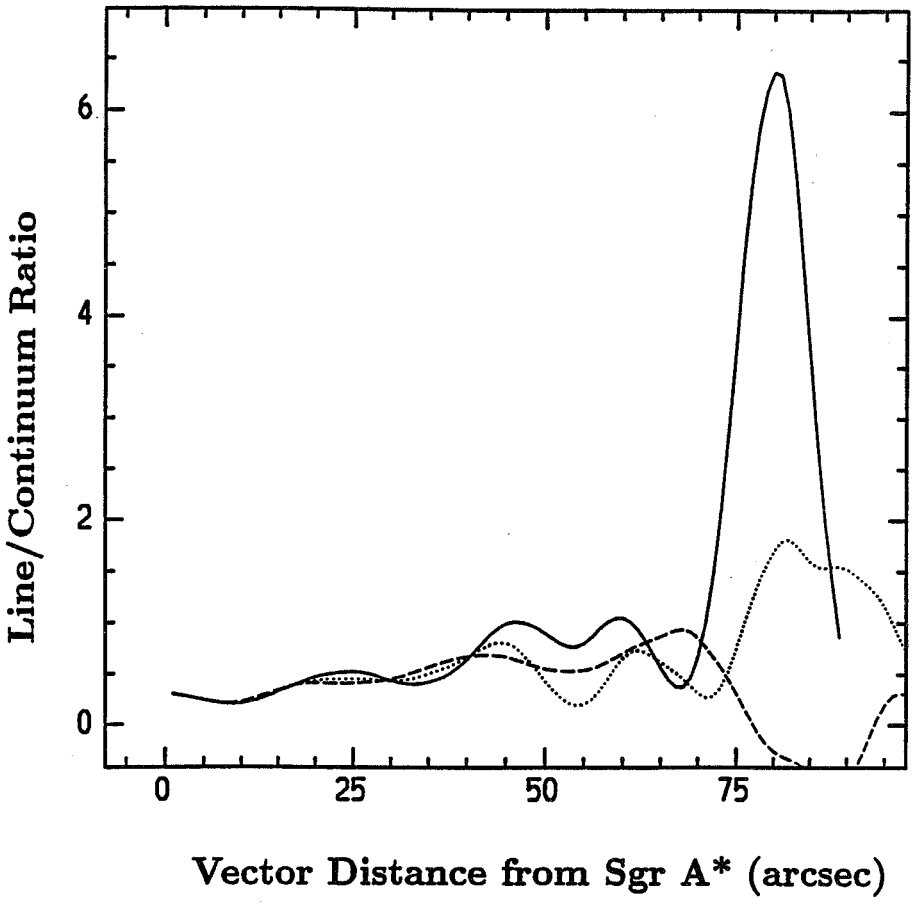

Figure 3. The SiII / dust continuum ratio at 34.8 μm along the vector shown in map 8 of Figure 2 from Sgr A* towards the NW (solid curve). The peak is at $\sim$ 25"W and 75"N of Sgr A*. Several other spatial cuts in other directions are shown for comparison.

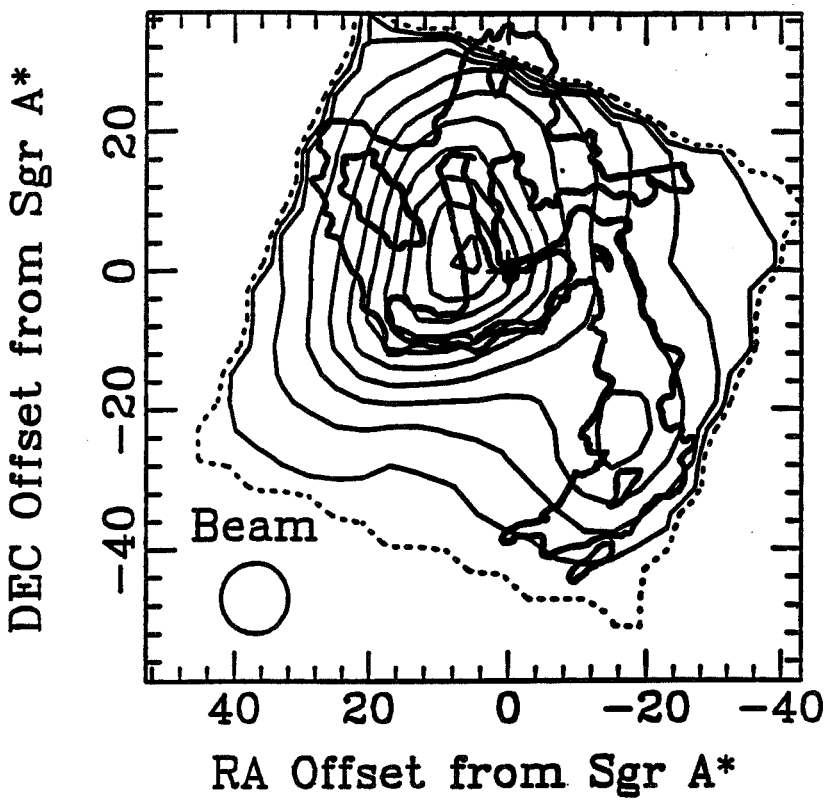

Figure 4. 38 μm continuum camera image superimposed on the 6 cm radio map (heavy contours). Infrared contour levels are: 10, 20, 30, 40, 50, 60, 70, 80, 90 and 98% of the peak. The dotted outline denotes the edges of the image. The position of Sgr A* is marked with a plus sign.

Acknowledgments. We would like to thank the KAO support staff for making these observations possible.

References

Davidson, J.A., Werner, M.W., Wu, X., Lester, D.F., Harvey, P.M., Joy, M., Morris, M. 1992, *ApJ* , 387, 189.

Herter, T., Gull, G.E., Megeath, S.T., Rowlands, N., and Houck, J.R. 1989, *ApJ* 343, 696.

Jackson, J. M., Geis, N. , Genzel, R., Harris, A.I., Madden, S.C., Poglitsch, A., Stacey, G.J., and Townes, C.H. 1993, *ApJ* 402, 173

Lacy, J. H., Achterman, J. M., and Serabyn, E. 1991, *ApJ* 380, L71.

Lo, K.Y, and Claussen, M.J. 1983, *Nature*, 306, 647.

Lugten, J.B., Genzel, R., Crawford, M.K., and Townes, C.H. 1986, *ApJ* 306, 691.

Ramsay, S., Mountain, M., and Geballe, T., ASP Conference Series, Vol. 41, 1993, p. 321-324.

Telesco, C. M., Davidson, J. A., and Werner, M.W., 1995, Ap.J. in preparation.

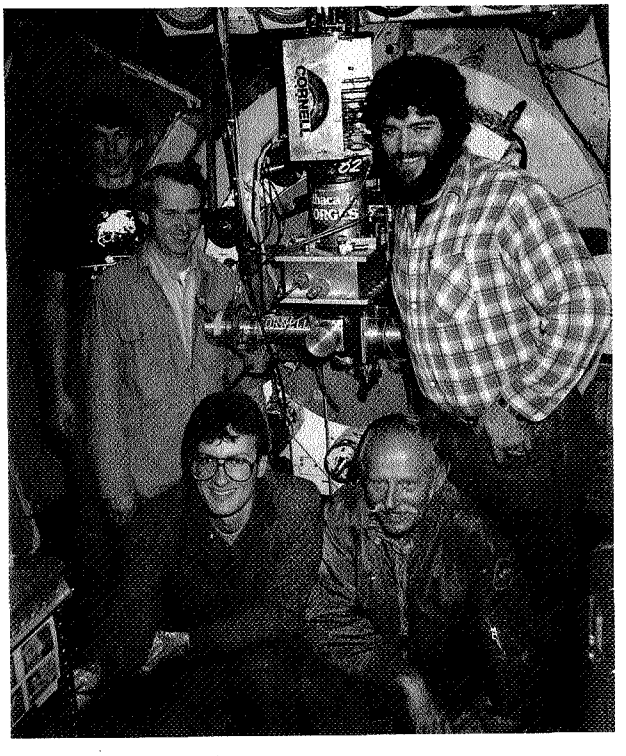

Terry Herter, Jim Houck, Paul Graf, Milo Reisner, George Gull (1985)

Airborne Astronomy Symposium on the Galactic Ecosystem
ASP Conference Series, Vol. 73, 1995
M.R. Haas, J.A. Davidson, and E.F. Erickson (eds.)

Far-Infrared Studies of the Galactic Center Arc Using the Kuiper Airborne Observatory

Mark Morris
Department of Physics & Astronomy, University of California, Los Angeles, CA 90024

J.A. Davidson
SETI Institute, c/o NASA Ames Research Center, MS 245-6, Moffett Field, CA 94035-1000

M.W. Werner
Jet Propulsion Laboratory, MS 169-327, Pasadena, CA 91109

Abstract. Two molecular clouds are clearly interacting with the Galactic Center Radio Arc. The HII regions located at both sites of interaction – the "Arched Filaments" and G0.18-0.04 – are powerful sources of far-infrared radiation, each having a total luminosity of $\sim 10^7$ $L_\odot$. Using the University of Texas far-IR Photometer at 50 and 90 μm, we found that the emission is substantially more extended than the filametary HII regions, and that, while the intensity peaks at the locations of the filaments, the dust temperature shows only weak variations, implying that the heating is relatively uniform. The Arched Filaments were also observed with the University of Chicago far-IR Array Polarimeter, STOKES, at 100 μm. The >100 independently sampled positions cover most of the 5′ x 7′ area of the Arched Filaments. The polarization is relatively strong (up to 9.4%) almost everywhere in this region. Also, the slow and smooth variations of the polarization angles across the region are consistent with the large magnetic field strengths and the highly-ordered geometry deduced from radio measurements. However, it appears that the magnetic field direction inferred from far-IR polarization (parallel to the Arched Filaments and following their curvature) is very different from that implied by the nonthermal radio filaments. The magnetic field, gas motions, and gravitational potential gradient in the arched filament region are all consistent with gravitational shearing of the molecular cloud underlying the Arched Filaments.

1. Introduction

The Radio Arc, a unique, large-scale, magnetically-organized structure lying near the Galactic center, is an unusually bright source of far-infrared radiation along portions of its overall structure. As such, it has been the

subject of study by the KAO for many years, and the data obtained have been extremely useful for formulating and testing hypotheses about its nature.

While it has thermal radio and infrared emission, the Arc is not an ordinary HII region. First, the morphology of the thermal radio emission is unusual — it is arranged into two sets of fleecy filamentary structures: the Arched Filaments and the Sickle (G0.18-0.04), the first of which stretches over a distance of ~25 pc (Figure 1). The Arched Filaments have no obvious center of activity, such as a group of compact HII regions, a pronounced central peak in radio intensity, or a ring structure which may reveal a central source of ionizing photons. Second, the thermal radio features are intimately

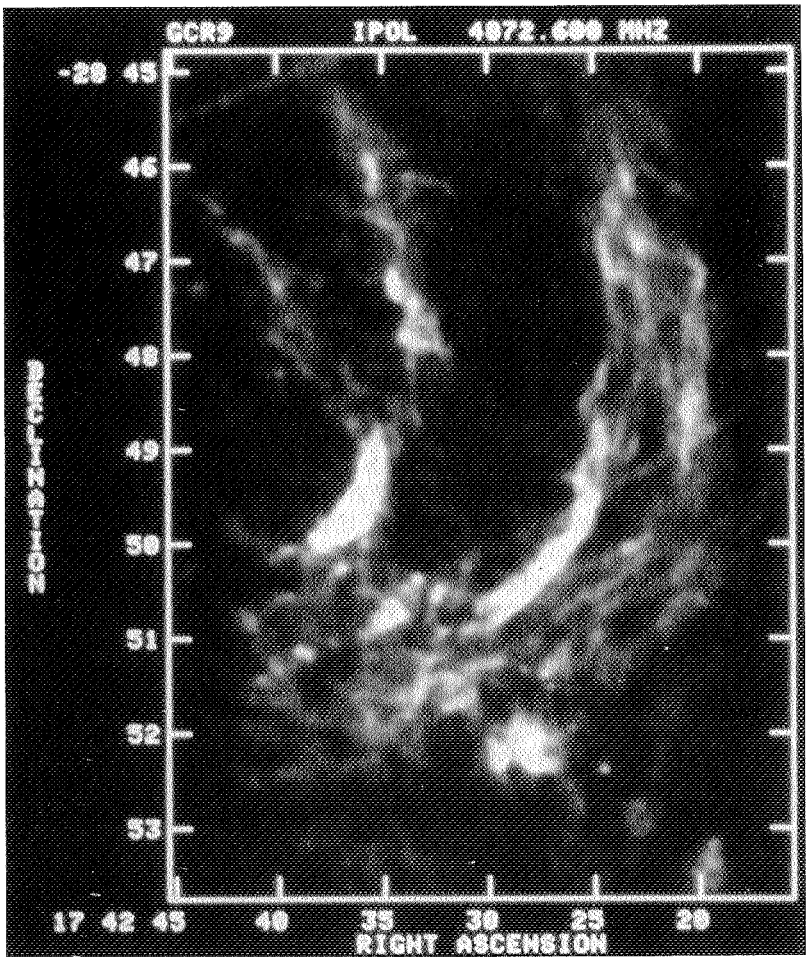

Figure 1: Radiograph at λ6-cm of the Arched Filaments of the Radio Arc.

linked to a set of discrete, parallel, linear, nonthermal radio filaments (Yusef-Zadeh and Morris 1987a,b; 1988). These strongly polarized, nonthermal filaments are oriented perpendicular to the Galactic plane; they, along with numerous isolated filaments having similar properties, are apparently magnetic flux tubes which have been "illuminated" by synchrotron emission from relativistic particles. They may be indicative of the presence of a large-scale poloidal magnetic field within the inner ~100 pc of the Galaxy (Morris 1990, 1994). The rigidity of the nonthermal filaments, inferred from their minimal distortion in the face of clear interactions with clouds, gives a minimum
magnetic field strength on the order of a milligauss. While the nonthermal filaments dominate the look of radio images of the Arc, they have not been detected so far at infrared wavelengths, consistent with our understanding that they are synchrotron-emitting structures.

The Arched Filaments are located within, or at the surface of, a large molecular cloud (Serabyn & Güsten 1987). Their radio recombination lines and far-infrared fine structure lines have velocities in agreement with the molecular cloud velocity (Yusef-Zadeh, Morris & van Gorkom 1987; Erickson *et al.* 1991). A large, north-south velocity gradient in the gas, from -80 to ~0 km s^{-1} across the cloud, indicates that the cloud is either rotating, or, more likely, shearing in the strong tidal field near the Galactic center. The Arched Filaments meet the linear, nonthermal filaments in a right angle at their northern extremity, coinciding with the northern extremity of the associated molecular cloud, and it is at this point where the two filamentary systems appear to be undergoing an interaction (Yusef-Zadeh & Morris 1988). However, the nature of this interaction remains to be elucidated.

The nonthermal filaments interact with another molecular cloud where they pass through the galactic plane and encounter the HII region, G0.18-0.04 (Yusef-Zadeh & Morris 1987b; Serabyn & Güsten 1991). It is plausible that the nearby "Quintuplet" cluster of luminous stars (Okuda *et al.* 1990; Nagata *et al.* 1990) is responsible for the ionization of G0.18-0.04, but this leaves open the question of why the nonthermal filaments appear to be linked to the HII region. In both G0.18-0.04 and the Arched Filaments, the magnetic field may play a substantial role in shaping the observed activity (Morris & Yusef-Zadeh 1989; Serabyn & Morris 1994).

2. Photometric Mapping

The Arched Filaments. In collaboration with Paul Harvey, Dan Lester, and Beverly Smith, we used the University of Texas far-infrared photometer array to study the Arched Filaments in 1988, when the array had a linear 8-channel configuration, and again in 1991, when it had its present 2x10-channel configuration.

A region roughly 8 by 16 arcminutes in extent was mapped at both 50 and 90 μm. The diffraction-limited aperture at 50 μm is 23 by 19 arcseconds, and at 90 μm, it is 35 by 24 arcseconds. In each case, the narrow dimension

is along the array. The separations of the beams along the array are only 7" and 12" at 50 and 90 μm, respectively. Because of that, and because data were recorded every 4" as the array was swept smoothly across the source with 6' sweeps in a direction perpendicular to the long axis of the array, the source was strongly oversampled. The images produced and used here are made from a data grid constructed by averaging all of the independent measurements lying near each grid point, weighting each measurement with a conical response function which drops to zero at a radius of 15".

A difficulty arises when mapping a source that is comparable in extent to the size of the chopper throw. Indeed, we used a chopper throw of only 4 arcminutes for the 8-channel observations, and 10 arcminutes for the 20-channel observations. Consequently, source emission was often present in the reference beam. To correct for this, we used a bootstrap technique to produce the final map. The edge of the map in the direction of the chop (roughly to the northwest) was made first, because we mapped well off the source in that direction and verifed that there is little emission above the smooth galactic background. Then, successive strips were added to the map in such a way that each data point could be corrected for emission at the chopper position (if any), using the growing map. One implication of this procedure is that we were unable to scan sufficiently off the source in both directions in every sweep to establish a baseline and thus to correct for instrumental drifts during the sweep. However, the fact that we scanned successively in both directions and subsequently averaged the results minimized this potential problem. Furthermore, scans of Uranus, which we used to calibrate the flux response, showed no significant baseline slopes.

The 50 and 100 μm images of the Arched Filaments are shown in Figure 2. The temperature map, constructed from the 50/90 μm flux ratio assuming an inverse, linear dependence of the grain emissivity upon wavelength, is reproduced in Genzel & Poglitsch (1994, this volume, their Figure 3).

Several things can be concluded from the maps, and from a map of the luminosity distribution derived from them (Davidson *et al.* 1994):
1) The luminosity follows the radio filaments; it is more specific to the radio continuum structures than it is to the broad ridge of CS emission defining the molecular cloud (Serabyn & Güsten 1987). We conclude that the heat deposition is associated with the ionization of the filaments.
2) The temperature is roughly uniform at values between 45 and 55 K along the radio filaments. That is, there is no preferred site along the filaments for the location of the heating source; it is either distributed uniformly or at a large distance (> 10 pc) from the entire system.
3) The temperature peaks weakly at the position of the filaments, although the radio filaments are somewhat narrower than the broad temperature peak, even when differences in spatial resolution are acounted for (see also Colgan *et al.* 1994, in this volume).
4) The overall luminosity across the region mapped is ~4 x 10^7 $L_\odot$, but most of this arises within the continuation of the forbidden-velocity molecular

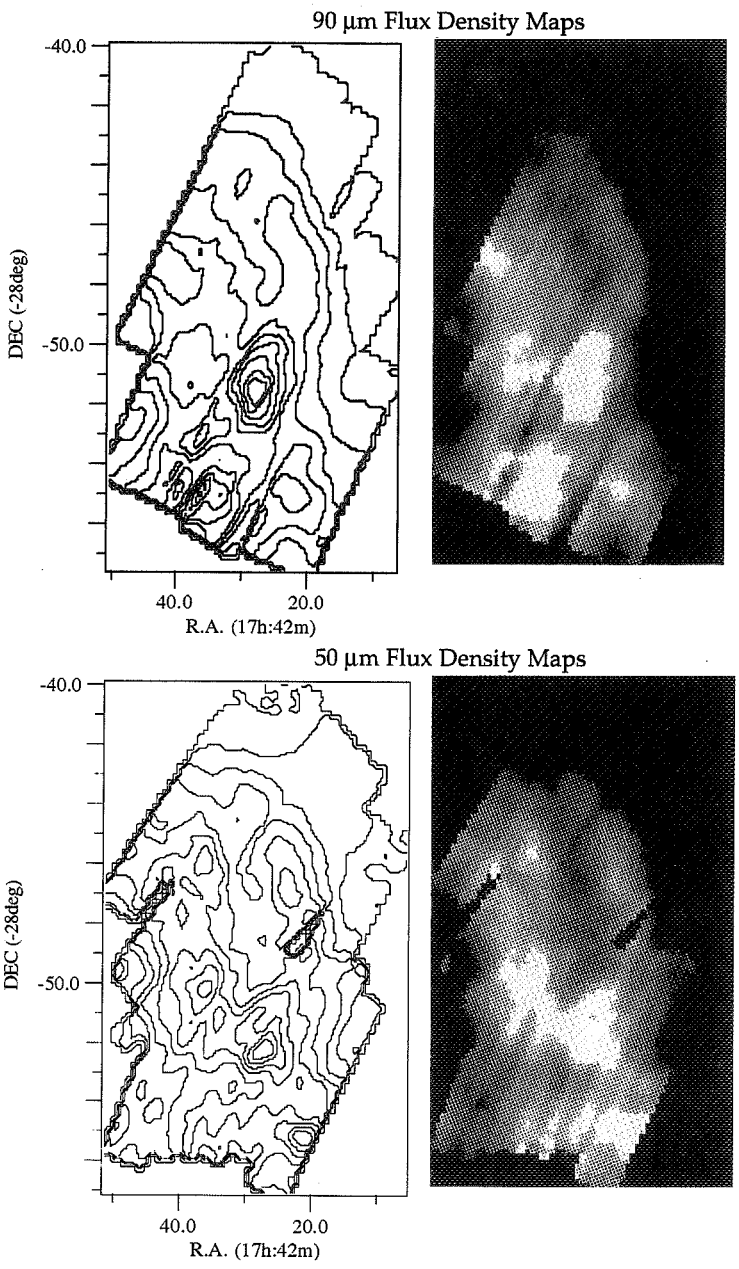

Figure 2: Images of the Arched Filaments at 50 and 90 μm. The effective spatial resolution, resulting from the convolution of the detector beams and the 15″ interpolation radius, is 26″ at 50 μm and 33″ at 90 μm. The contours begin at, and are spaced by, 190 Jy in the 50 μm map and 300 Jy in the 90 μm map.

cloud to the south of the Arched Filaments (Serabyn & Güsten 1987; Poglitsch *et al.* 1991), where a number of compact HII regions have been identified (sources H1 to H8 of Yusef-Zadeh & Morris 1987c). The total far-infrared luminosity of the Arched Filaments is about 1.0 x 10^7 $L_\odot$, which places a substantial requirement on the nature of the source of luminous energy in this direction, especially if it lies at some distance from the cloud, and therefore suffers from geometrical dilution.

As argued by Erickson *et al.* (1991, 1994), a stellar source of photoionization is most likely for the Arched Filaments. However, the uniformity of the ionic excitation along the filaments inferred from their data,coupled with the uniformity of the dust temperature found in our photometric study, presents a geometrical challenge. The centrally located cluster of emission line stars found by Cotera *et al.* (1994) is an interesting candidate for the source of energy and ionizing photons, but given the ~10 pc of physical separation needed between the cluster and the filaments in order to explain the observed uniformity of temperature and excitation, it is not yet

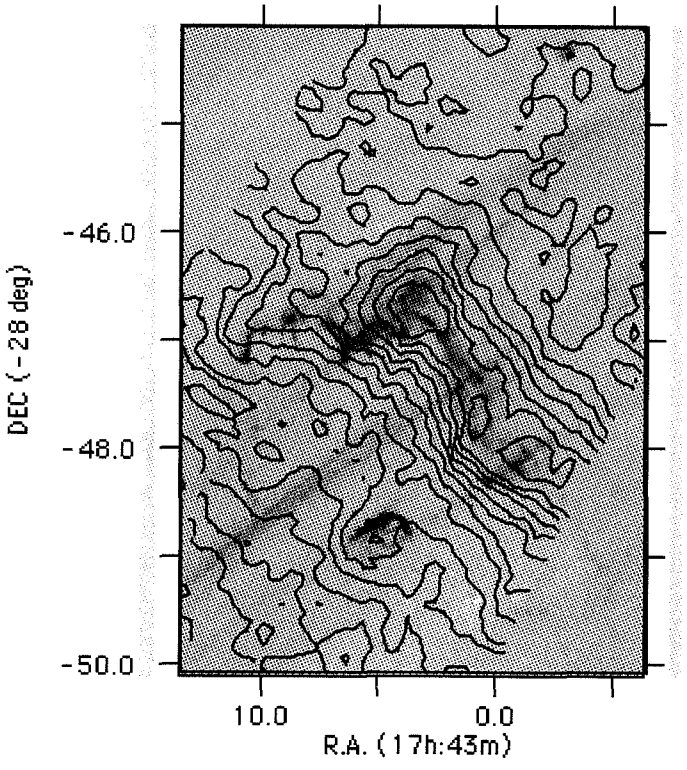

Figure 3: 50-μm image of G0.18-0.04, superimposed on a 6-cm radiograph from Yusef-Zadeh and Morris (1987b). The linear filaments crossing diagonally from northwest to southeast through the image are the nonthermal filaments, which are apparently interacting with the sickle-shaped HII region.

clear that this cluster can supply the required UV luminosity.

The HII Region G0.18-0.04 (the "Sickle"). We observed G0.18-0.04 during the 1991 flight series with the 20-channel photometer arrays. The 90 μm array was scanned twice across the source, while the 50 μm array was scanned four times in order to cover much of the same area. No correction was applied to the measured fluxes for emission in the reference beam, because there was insufficient time to thoroughly map along the scan direction to characterize the localized emission at the reference position. The resulting 50 μm image is shown in Figure 3.

The negative contours at the southern end of the region mapped are unlikely to be due to systematic instrumental drifts across the sweeps, as detailed above. Rather, they are ascribable to a slope in the large-scale background, in the sense that it increases to the northwest of the source.

There is a pronounced ridge of 50 μm emission in G0.18-0.04 which closely follows the thermal radio continuum ridge. The 90 μm image shows much more extended emission, and although the ridge is evident there as well, it is broader and less contrasted to the background. The temperature map

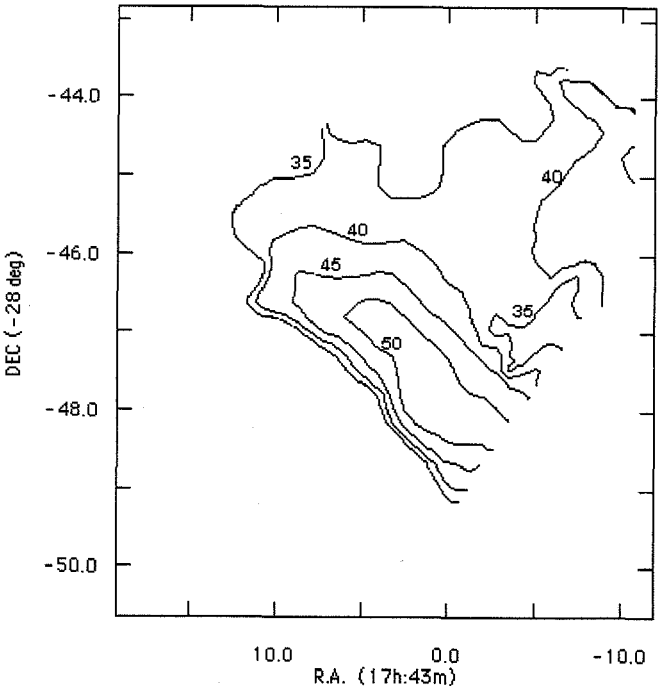

Figure 4: Map of the dust temperature in G0.18-0.04, derived using the ratio of surface brightness at 50 and 90 μm, and assuming a λ^{-1} dependence of the dust emissivity upon wavelength.

C-7

constructed from the 50/90 μm flux ratio, again assuming a λ^{-1} emissivity law, is shown in Figure 4. The ridge stands out as being particularly warm inthis image, on the order of 45 - 50 K. Also, within the resolution of the far-infrared measurements, it is coincident with the ionized gas mapped in the radio continuum. The contours in Figures 3 and 4 are somewhat steeper on the southern side of the ridge than on the northern side, consistent with the radio continuum image, which shows a sharp southern boundary to the HII region, and a weak, slowly declining plateau to the northwest. The sharp southern boundary is coincident with the edge of the molecular cloud, and suggests that G0.18-0.04 is being ionized from the southeast. As with the Arched Filaments, we do not lack a candidate source of heat and ionization; the prominent Quintuplet cluster (Okuda *et al.* 1990; Nagata *et al.* 1990) is located at roughly the center of curvature of the thermal HII filaments. According to Harris *et al.* (1994), who make various assumptions about the IMF in this cluster, the stars in the cluster can supply the number of ionizing photons needed to account for G0.18-0.04, if geometrical dilution and extinction effects are ignored.

The total luminosity of G0.18-0.04, gotten by using the inferred temperatures and integrating over the ridge, where the 50 μm emission is strong, is 9×10^6 $L_\odot$. This number would be corrected somewhat by a proper accounting for emission in the reference positions, although we do not expect this correction to be more than ~20%. The luminosity would also rise if the entire sickle cloud were included in our maps. The unmapped region to the northeast of the prominent ridge seen in Figure 3 may have a considerable fraction of the total luminosity of the sickle cloud.

Finally, we note that G0.15-0.05 (the "pistol") stands out in the 50-μm image (Figure 3) as a separate, warm source having a luminosity a few percent that of the ridge. The pistol is close in projection to the quintuplet cluster, so it may be partially ionized by that cluster, but it is also centered on a hot luminous star which may well be responsible for its ionization (Cotera *et al.* 1994). It is therefore possible that it is independent of, and unrelated to, G0.18-0.04 and the quintuplet. Indeed, its radial velocity, as determined by radio recombination lines, is quite different from that of G0.18-0.04 (Yusef-Zadeh, Morris & van Gorkom 1989), and the merger of the contours of G0.15-0.05 in Figures 3 and 4 with those of G0.18-0.04 may simply be owed to the finite resolution of the observation. Nonetheless, G0.15-0.05 and G0.18-0.04 are both interacting with the nonthermal filaments of the Arc (Yusef-Zadeh & Morris 1987b), so they both appear to be part of this large-scale structure, and thus indirectly related to each other in that manner.

3. Polarimetry of the Arched Filaments.

In collaboration with Roger Hildebrand, Jessie Dotson, Darren Dowell, and David Schleuning, we used the University of Chicago Array Polarimeter, STOKES (Platt *et al.* 1994), to study the 100-μm polarization of the arched

radio filaments. The initial measurements, made with a preliminary version of the array having 14 working detector pairs, showed that the 100 μm emission associated with the Arched Filaments exhibits high (up to 6.5%) and uniform linear polarization (Morris *et al.* 1992). Interpreted in terms of magnetic alignment of emitting grains, the position angles of the polarized E-vectors led to the conclusion that in the limited area originally mapped, the magnetic field lines are oriented parallel to the Arched Filaments. This result is particularly notable because it implies that the magnetic field lines within the emitting region — presumably the molecular cloud underlying the thermal radio filaments — are perpendicular to the magnetic field lines defining the nonthermal filaments, located external to this cloud, but apparently interacting with it in some way (Yusef-Zadeh and Morris 1988).

The question remained whether this orientation is respected throughout the curving, Arched Filaments. With the completed pair of 32-detector arrays, we reobserved this region much more completely in August 1993. Three separate pointings of the arrays were used, which, when combined with the initial measurements, cover almost all of the region of the Arched Filaments. The polarization, depicted in Figure 5, was found to be strong over this entire region. Polarization signals significant at least at the 3σ level were found at 60 positions, and when the data for several adjacent 35″-beams were averaged, three more positions in the northwest quadrant of the region studied attained a similar significance.

The position angles of the polarization vectors vary quite smoothly from one position to the next, vindicating our averaging procedure for the positions to the northwest. Assuming that the magnetic field lines are oriented perpendicular to the dominant E-vector of the polarized emission (Hildebrand 1988), we conclude that the magnetic field direction projected onto the plane of the sky is approximately uniform across the entire cloud, on scales from 1 to 16 pc, and is predominantly oriented north-south. The small local dispersion in polarization angle, coupled with information about the kinetic energy density within the molecular cloud, was interpreted by Morris *et al.* (1992) in terms of a large field strength, following the arguments of Chandrasekhar & Fermi (1953). Formally, one finds field strengths of 5 to 10 mG in the Arched Filaments, although there are various theoretical reasons for suspecting that this is an overestimate. In addition, OH Zeeman measures by Uchida & Güsten (1995) set an upper limit of several tenths of a milligauss on the line-of-sight field on scales of a few tens of parsecs, so it will take some work to fit these facts into a coherent model.

Departures from complete uniformity of the magnetic field occur primarily in the sense that the field lines follow the curving filaments. In the Eastern filaments, E1 and E2, the position angles vary from about 100° at declination -28° 46′ to ~80° at -28° 51′, whereas the radio filament, which can only be followed to about -28° 50′, has about twice that variation in curvature, though it is in the same sense. The Western filaments show the best correspondence between the orientations of the filaments and the implied magnetic field lines. Further south, the electric vectors flow smoothly back to

having approximately east-west orientations, like the northern part of the cloud and like Sgr A, located several arcminutes further to the south of the region mapped (Hildebrand *et al.* 1993). Thus, in the cloud underlying the Arched Filaments and extending to the south, the magnetic field lies along the long axis of the cloud, possibly as a result of shear within the cloud resulting

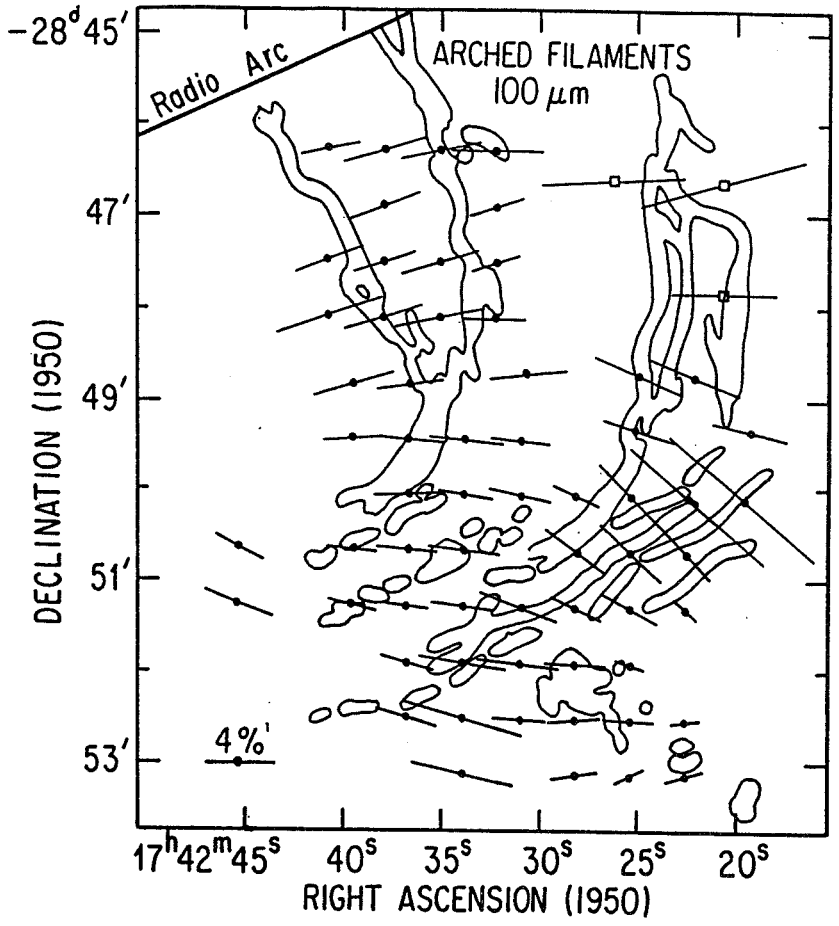

Figure 5: Polarization measurements across the Arched Filaments, superimposed on a schematic representation of the radio features. The orientations of the line segments represent the position angles of the electric vectors, while their length is proportional to the percent polarization. A vertical segment representing 4% polarization is shown at the side. The three points in the northwest quadrant, shown as open squares, represent the results of an average over four adjacent positions.

from the tidal forces that the cloud is subjected to this close to the Galactic center (Morris *et al.* 1992). Where the arched radio filaments are present, however, the magnetic field direction is locally influenced in the sense that it tends to follow the thermal filaments where they are prominent and identifiable.

4. Conclusions

Observations of far-infrared emission from the clouds associated with the Galactic center Arc have been essential for constraining models of this unique structure. The photometric mapping results have supported the conclusion that the luminosity being generated in the Arched Filaments and in G0.18-0.04 is too large to be ascribed to magnetohydrodynamic processes alone. An unusual stellar heating source is evidently called for: one which is either distributed uniformly along the filaments on parsec scales, or one which lies at a distance, but which must therefore be extremely luminous because of geometrical dilution (~10^8 $L_\odot$; Davidson *et al.* 1994). However, far-IR polarimetry of the arched filament cloud indicates that an ordered field, probably strong, is present within the cloud. Coupled with the radio continuum evidence that a strong and ordered field is present outside of dense clouds (albeit with a geometry approximately orthogonal to that in the clouds), the polarimetry suggests to us that the magnetic field may still account for much of the activity in and around the Arc, the nonthermal filamentary structures in particular. The magnetic field may also play a major part in the overall pressure balance of this region, but before this can be quantitatively assessed, techniques giving more precise estimates of the magnetic field strengths must be employed.

References

Chandrasekhar, S. & Fermi, E. 1953, ApJ, 118, 113.

Colgan, S.W.J., Erickson, E.F., Simpson, J.P., Haas, M.R., & Morris, M. 1994, in "Proc. of the Airborne Astronomy Symp. on the Galactic Ecosystem: From Gas to Stars to Dust", ed: M.R. Haas, J.A. Davidson, & E.F. Erickson (San Francisco:ASP), paper 604..

Cotera, A.S., Erickson, E.F., Simpson, J.P., Colgan, S.W.J., Allen, D.A. & Burton, M.G. 1994, in "Proc. of the Airborne Astronomy Symp. on the Galactic Ecosystem: From Gas to Stars to Dust", ed: M.R. Haas, J.A. Davidson, & E.F. Erickson (San Francisco:ASP), paper 605.

Davidson, J.A., Morris, M., Harvey, P.M., Lester, D.F., Smith, B. & Werner, M.W. 1994, in "Nuclei of Normal Galaxies: Lessons from the Galactic Center", eds: R. Genzel & A.I. Harris, Dordrecht: Kluwer, in press.

Erickson, E.F., Colgan, S.W.J., Simpson, J.P., Rubin, R.H., Morris, M. & Haas, M.R. 1991, ApJL, 370, L69.

Erickson, E.F., Colgan, S.W.J., Haas, M.R., Simpson, J.P., Rubin, R.H., Morris, M., Cotera, A.S., Allen, D.A. & Burton, M.G.

Genzel, R. & Poglitsch, A. 1994, in "Proc. of the Airborne Astronomy Symp. on the Galactic Ecosystem: From Gas to Stars to Dust", ed: M.R. Haas, J.A. Davidson, & E.F. Erickson (San Francisco:ASP), paper 6.0.

Harris, A.I., Krenz, T., Genzel, R., Krabbe, A., Lutz, D., Poglitsch, A., Townes, C.H. & Geballe, T.R. 1994, in "Nuclei of Normal Galaxies: Lessons from the Galactic Center", eds: R. Genzel & A.I. Harris, Dordrecht: Kluwer, in press.

Hildebrand, R.H. 1988, *QJRAS*, **29**, 327.

Hildebrand, R.H., Davidson, J.A., Dotson, J., Figer, D.F., Novak, G., Platt, S.R. & Tao, L. 1993, *ApJ*, **417**, 565.

Morris, M. 1990, in "Galactic and Intergalactic Magnetic Fields", eds: R. Beck, P.P. Kronberg, R. Wielebinski, Dordrecht: Kluwer, p 361.

Morris, M. 1994, in "IAU Symp. #169: Unsolved Problems in the Milky Way", ed: L. Blitz, Dordrecht: Kluwer, in press.

Morris, M., Davidson, J.A., Werner, M., Dotson, J., Figer, D.F., Hildebrand, R., Novak, G. & Platt, S. 1992, *ApJL*, **399**, L63.

Morris, M. & Yusef-Zadeh, F. 1989, *ApJ*, **343**, 703.

Nagata, T., Woodward, C.E., Shure, M., Pipher, J.L. & Okuda, H. 1990, *ApJ*, **315**, 83.

Okuda, H., Shibai, H., Nakagawa, T., Matsuhara, H., Kobayashi, Y., Kaifu, N., Nagata, T., Gatley, I. & Geballe, T.R. 1990, *ApJ*, **351**, 89.

Platt, S.R., Dotson, J.L., Dowell, C.D., Hildebrand, R.H., Novak, G. & Schleuning, D. 1994, in "Proc. of the Airborne Astronomy Symp. on the Galactic Ecosystem: From Gas to Stars to Dust", ed: M.R. Haas, J.A. Davidson, & E.F. Erickson (San Francisco:ASP), paper 707.

Poglitsch, A., Stacey, G.J., Geis, N., Haggerty, M., Jackson, J., Rumitz, M., Genzel, R. & Townes, C.H. 1991, *ApJL*, **374**, L33.

Serabyn, E. & Güsten, R. 1987, *A&A*, **184**, 133.

Serabyn, E. & Güsten, R. 1991, *A&A*, 242, 376.

Serabyn, E. & Morris, M. 1994, *ApJL*, **424**, L91.

Uchida, K. & Güsten, R. 1995, *A&A*, in press.

Yusef-Zadeh, F. & Morris, M. 1987a, *ApJ*, **322**, 721.

Yusef-Zadeh, F. & Morris, M. 1987b, *AJ*, **94**, 1178.

Yusef-Zadeh, F. & Morris, M. 1987c, *ApJ*, **320**, 545.

Yusef-Zadeh, F. & Morris, M. 1988, *ApJ*, **329**, 729.

Yusef-Zadeh, F., Morris, M. & van Gorkom, J.H. 1987, in AIP Conf. Proc. 155: The Galactic Center, ed: D.C. Backer, New York: AIP, p. 190.

Yusef-Zadeh, F., Morris, M. & van Gorkom, J.H. 1989, in IAU Symp. No. 136: "The Center of the Galaxy", ed: M. Morris, Dordrecht: Kluwer, p 275.

Airborne Astronomy Symposium on the Galactic Ecosystem
ASP Conference Series, Vol. 73, 1995
M.R. Haas, J.A. Davidson, and E.F. Erickson (eds.)

KAO and AAT Observations of the Galactic Center Filaments

E. F. Erickson[1], Sean W. J. Colgan[2,1], J. P. Simpson[3,1], R. H. Rubin[4,1], Michael R. Haas[1], M. Morris[5], A. S. Cotera[6], D. A. Allen[7], and M. G. Burton[8]

[1]*NASA/Ames Research Center, MS 245-6, Moffett Field, CA 94035-1000*
[2]*SETI Institute, Mountain View, CA 94035*
[3]*U.C. Berkeley, Berkeley, CA 94720*
[4]*Orion Enterprises, Mountain View, CA 94040-3874*
[5]*UCLA, Los Angeles, CA 90024*
[6]*Stanford University, Stanford CA 94305*
[7]*Anglo-Australian Observatory, Epping, NSW Australia*
[8]*University of New South Wales, Kensington, NSW Australia*

Abstract. We have used the Kuiper Airborne Observatory (KAO) and the Anglo-Australian Telescope (AAT) to investigate the nature of the filamentary radio emission from the Galactic center region. KAO observations of the FIR line and continuum emission from the radio peak G0.095+0.012 and the E2 thermal radio filament northeast of the Galactic center can be produced by numerous nearby stars with $T_{eff} \sim 35{,}000$ K; these can account for both the FIR luminosity and the excitation of the gas. Much of the FIR continuum and most of the strong [Si II] (34.8 μm) line emission are probably produced in the ionized gas of the filament. The FIR [O III] 52 & 88 μm lines imply an electron density of a few hundred; when compared with the radio emission measure, this implies the filament is roughly tubular or somewhat flattened in the plane of the sky. The [O III] and [S III] lines show higher excitation associated with the filament, and suggest that exciting stars may be located within the filaments and/or southeast of the E2 filament.

AAT observations in the near infrared (NIR) in fact reveal a nearby cluster of hot stars southeast of the E2 filament. Additional hot stars, not identifiable from their NIR spectra, are likely to be present. These stars and those in the cluster can plausibly produce the the observed radio and FIR emission in the region. The morphology of the filament is not explained by existing information however.

1. Introduction

The peculiar filamentary structures revealed by VLA maps of the Galactic center region are of uncertain origin and excitation. Figure 1 depicts the 20 cm VLA radiograph (Yusef-Zadeh & Morris 1987) overlaid with contours of CS emission (Serabyn & Gusten 1987, 1991). The straight filaments have a non-thermal radio

spectrum, while that of the arched filaments is thermal. The thermal filaments are relatively small details in the large scale radio emission distribution, which is suppressed in the VLA maps.

This paper summarizes and extends work described in three others: Erickson *et al.* (1991: ECSRMH), Colgan *et al.* (1994: Paper 604), and Cotera *et al.* (1994: Paper 605). The first two describe KAO observations of FIR fine structure lines and continuum made with the Cryogenic Grating Spectrometer (Erickson *et al.* 1984, 1994: Paper 702), and the third describes NIR observations done from the AAT with the imaging spectrometer, IRIS (Allen *et al.* 1993). Although we have observed a number of regions depicted in Figure 1, here we discuss only our work on the E2 thermal filament (Morris & Yusef-Zadeh 1989) and its immediate vicinity.

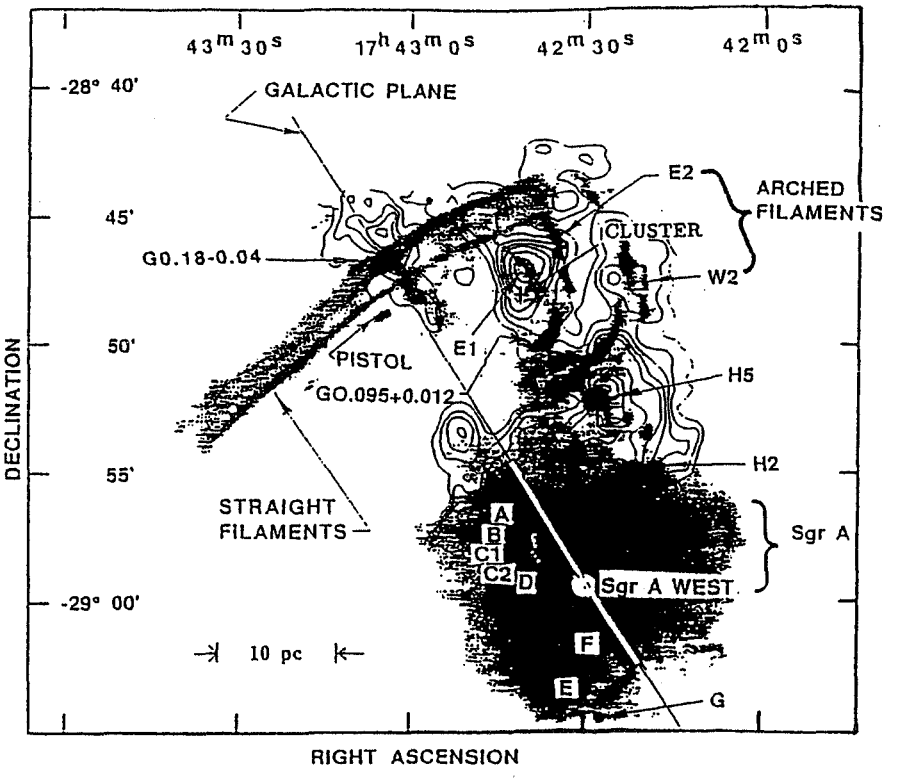

Figure 1. VLA radiograph with CS contours of the Galactic center region.

2. FIR Emission from the Radio Peak

The radio fluxes from the filaments suggest strong fine structure line emission in the FIR, which is confirmed by our KAO measurements (ECSRMH). The radio and 10 μm continuum emission in the filament region peaks at G0.095+0.012 (Figure 1), labelled position C in Figure 1 of Paper 604. At this location we measured thirteen line and continuum fluxes. Table 1 gives the measured fluxes

and the calculated extinction corrections. The data and their interpretation at point C are described here in some detail, to demonstrate the arguments used to interpret the FIR data on the filaments discussed below.

Table 1

Measurements of G0.095+0.012 (Position C)

Species	λ (μm)	Line Flux[a,b] (10^{-18} W cm^{-2})	Continuum Flux[b] (Jy)	Extinction[c] Correction
[S III]	18.7	21.3 ± 4.0	400 ± 100	3.27
[S I]	25.3	< 3.0[d]	1000 ± 100	1.98
[Fe II]	26.0	< 9.4[d]	1300 ± 200	1.91
[S III]	33.5	70.5 ± 1.1	1700 ± 100	1.48
[Si II]	34.8	31.5 ± 1.2	1500 ± 100	1.43
[Ne III]	36.0	< 0.7[d]	1600 ± 100	1.40
[O III]	51.8	12.8 ± 0.4	1900 ± 100	1.18
[N III]	57.3	13.0 ± 3.8	1580 ± 740	1.14
[O I]	63.2	5.2 ± 0.4[e]	2000 ± 100	1.11
[O III]	88.4	11.2 ± 0.3	1500 ± 50	1.06
[O I]	145.5	0.50 ± 0.05	500 ± 20	1.02
[C II]	157.7	8.2 ± 0.1	400 ± 40	1.02
[N II]	205.2	1.57 ± 0.05	540 ± 20	1.02

[a] $\overline{v}_{LSR} = -24 \pm 8$ km s^{-1} from doubly ionized lines.
[b] From Gaussian fit to spectrum uncorrected for extinction. Flux errors are 1σ deviations of the data about the fit.
[c] For $\tau_{9.7} = 3.0$
[d] Upper limits are 3σ.
[e] East and West chop position fluxes are < 0.6 and 0.9×10^{-18} Wcm^{-2} respectively.

The continuum measurements span the peak flux-density near 45 μm, and give an integrated FIR flux of 2.9×10^{-14} W cm^{-2}, or 6×10^5 L$_\odot$ at a distance of 8.5 kpc. The FIR continuum shape implies a temperature $T_{DUST} \sim 100$ K, but the size and optical depth of the emitting region are not independently constrained by our data. If the size of the emitting region in our beam is comparable to that at 6 cm, as is found for the 10 μm emission (Yusef-Zadeh, Telesco, & Decher 1989), then our flux and temperature imply a 60 μm optical depth $\tau_{60} \sim 0.008$, corresponding to a local $A_v \simeq 2$.

The [O III] and [S III] line pairs (Table 1) yield average electron densities of 240 ± 20 cm^{-3} and 220 ± 150 cm^{-3}, respectively, based on the density dependence of the volume emissivities of these species (Rubin 1989). The doubly ionized line fluxes are well fitted (within $\pm 50\%$) by a spherical photoionization model with stellar effective temperature $T_{eff} = 35{,}000$ K from the log $g = 4$ model atmospheres of Kurucz (1979, 1981), $N_{Lyc} \sim 10^{49}$ ionizing photons per second, a constant nebular density of 300 cm^{-3}, and a metallicity ~ 3 times that of Orion (Rubin *et al.* 1991), typical for regions close to the Galactic center. This stellar flux corresponds to about ten O7 ZAMS stars with a total luminosity of

4×10^5 $L_\odot$ (Schaller *et al.* 1992), close to the measured FIR continuum luminosity. The model also agrees with the 6 cm VLA recombination line observations of Yusef-Zadeh, Morris, & van Gorkom (1987), which give an electron temperature $T_e \sim 5300$ K in a $\sim 10''$ beam for position C; our model predicts $T_e = 5500$ K. The low T_{eff} of the model also explains the faintness of the [Ne III] 36 μm line and the lack of a measurable helium radio recombination line: in a 2.'6 beam overlapping about half of our beam at position C, Pauls & Mezger (1980) measured $He^+/H^+ \leq 0.03$. The success of this model in matching both our observed FIR line fluxes and the available radio data suggests that at point C we are observing emission generated by embedded hot stars. This conclusion is strengthened by the agreement between the luminosities of the photoionization model and the FIR continuum. The doubly ionized line emission from point C is typical of the Galactic H II regions we have observed (*e.g.* Colgan *et al.* 1991; Simpson *et al.* 1995), the only distinction being its somewhat lower N_e.

Molecular gas adjacent to typical H II regions is dissociated by non-ionizing UV flux from the embedded stars, producing a photodissociation region or PDR (Tielens & Hollenbach 1985: TH; Wolfire, Tielens & Hollenbach 1990: WTH). The measured line flux ratio ([Si II] 35 μm)/([O I] 63 μm) $\simeq 8$, is about ten times the value predicted by the PDR theory even if the Si/O gas-phase abundance ratio is increased to solar ($\simeq 0.05$). The solar abundance ratio is thought to exceed that for the diffuse interstellar medium by a factor ~ 45 due to the silicon content of grains. However, our limit on the [Fe II] 26 μm line strength argues against total grain destruction in the hypothesized PDR (TH).

Self-absorption of the [O I] 63 μm line could contribute to the large value of this ratio. However, if its width is comparable to that of the few km s^{-1}widths of the CS lines (Serabyn & Güsten 1987) the [O I] line is probably optically thin. The ratio of the 63/145 μm line fluxes implies a gas temperature ~1000K, and is consistent with either optically thin or thick emission (TH); if the emission is optically thin, this temperature is probably an overestimate of the value near the surface of the cloud. The FIR continuum flux suggests a value of the radiation field, G, of $\log(G/G_0) \simeq 4.7$ ($G_0 = 1.6 \times 10^{-10}$ W cm^{-2}); with this value both the [O I] line ratio *and* the ratio of ([O I]+[C II])/L_{FIR} imply $n_H \lesssim 10^4$ cm^{-3}. This density and temperature give a somewhat higher pressure than that of the H II region (above). However, thermal pressure equilibrium may not be required because the magnetic field pressure in the filaments is probably much higher (Morris *et al.* 1992). In summary, the FIR continuum and [O I] and [C II] line emission are compatible with production from a PDR, but the [Si II] emission is not.

It seems likely that most of the Si emission is produced in the ionized gas, where adequate gas phase Si^+ can exist without complete destruction of the grains. In fact, the A_v deduced from the radio emission measure is compatible with that estimated from the FIR continuum (within considerable uncertainties), so that it is possible that most of the FIR continuum is also produced in the ionized gas, which would alter considerably the PDR parameters deduced above.

The PDR theory predicts the [S I] 25 μm line to be much weaker than our upper limit (Table 1), since in the PDR most of the sulfur would be singly ionized. This limit is also consistent with the shock theory of Hollenbach & McKee (1989), so we conclude nothing from this non-detection. A shock mechanism would have difficulty producing the observed FIR continuum, however. We conclude that the combined H II region/PDR models provide

a good explanation of the observations of position C, although the PDR contributions to the observed emission are not well established because of possible continuum and singly-ionized line emission from the ionized gas.

3. FIR Emission Distribution Along the E2 Filament

We (ECSRMH) also used the KAO to probe the arched filament E2 (Morris & Yusef-Zadeh 1989) by measuring FIR line and continuum fluxes at eight positions separated by approximately 45″ along the filament. The emission from position C and that from the E2 filament discussed above are qualitatively similar. Instead of detailed modelling (as done for location C), we use semi-empirical methods (Rubin *et al.* 1994) to interpret the ionized line emission discussed below.

Figure 2 plots measured [S III] 33 μm and [O III] 88 μm line fluxes, the 88 μm continuum, and the 43 GHz continuum in a 38″ beam (Sofue *et al.* 1986) versus scan position. Figure 1 of Paper 604 shows the beam locations; larger numbered positions are further north; position numbers 6–9 also sample the non-thermal straight filament at the north end of the E2 filament.

The measured line velocities do not vary significantly along the filament, and the average velocity, $v_{LSR} = -11 \pm 6$ km s^{-1}, is in good agreement with the radio recombination and molecular lines. From the two [O III] line fluxes, we obtain N_e([O III]) $= 380 \pm 40$ cm^{-3}, 290 ± 50 cm^{-3}, 120 ± 50 cm^{-3}, and 220 ± 100 cm^{-3} at the even numbered positions from 2 to 8. These densities are much lower than the density $N_{H_2} \sim 10^4$ cm^{-3} found for the molecular regions adjacent to the filament (Serabyn & Güsten 1987, Genzel *et al.* 1990). Assuming that N_e([O III]) applies to the radio emitting volume, we used the radio emission measure computed from the 43 GHz measurements in a 38″ beam of Sofue *et al.* (1986) to calculate an average depth of the radio emission of 1.4 ± 0.3 pc. This corresponds to 34″ at a distance of 8.5 kpc, implying the E2 filament is roughly as deep as (or somewhat less deep than) it is wide.

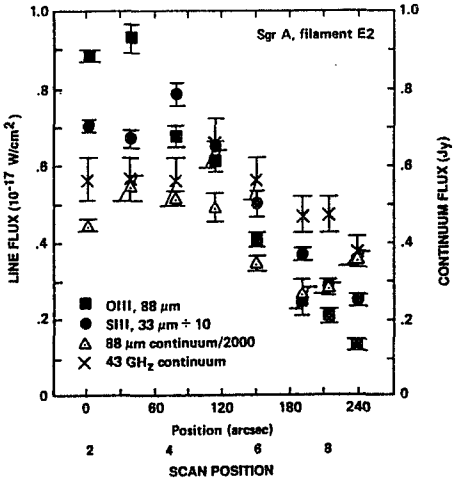

Figure 2. Scan data along E2.

The [S III] 33 μm and [O III] 88 μm line fluxes drop more rapidly than does the radio flux, suggesting decreasing excitation. We used the [S III] 33 μm and [O III] 52 μm line fluxes and their relative emissivities at the N_e([O III]) density to obtain the S^{++}/O^{++} ionic ratio, which increases from 0.35 to 0.75, or more than a factor of two, along the filament. This ratio is indicative of the excitation of the gas since S^{++} has a lower ionization potential (23.3 eV) than O^{++} (35.1 eV). Typical ratios in this filament correspond to photoionization by a star with $T_{eff} \sim 35{,}000$ K (as found at point C). The increase in the S^{++}/O^{++} ratio going

north along the filament corresponds to a decrease in T_{eff} of $\lesssim$1,000 K.

The 88 μm continuum shown in Figure 2 decreases by roughly a factor of two going north along the filament, corresponding to a drop in the continuum luminosity from $\sim 5 \times 10^5$ to 2×10^5 $L_\odot$ in each 45″ beam. However, the 33 μm/88 μm and 52 μm/88 μm continuum ratios are constant to within the errors, suggesting a constant dust temperature along the filament. If the emission fills the beam, it can be characterized by a dust temperature $\sim$ 50–70 K with $\tau_{60} \sim 0.01$, whereas if the emission is compact, $\tau_{60} \gtrsim 5$, and $T_{DUST} \lesssim 110$ K. The extent of the emission is probably comparable to that of the radio continuum, and so is closer to the optically thin case.

To summarize, the E2 filament is roughly tubular with a ~10:1 length to diameter ratio. Moving northward along the filament: (1) the radial velocity of the ionized gas is constant to ~10 km s^{-1}; (2) the electron density in the O^{++} emitting gas is ~250 cm^{-3}, much lower than the nearby molecular gas; (3) the excitation decreases slowly going north from ~35,000 K at the south end to ~34,000 K in the vicinity of the straight filament – to produce such uniform excitation, a single external photoionizing source would need to be ~10 pc distant; (4) the FIR continuum brightness decreases by a factor ~2, and (5) the grain temperature is roughly constant at ~70 K. As with location C, the continuum thermal emission is comparable to the photoionizing stellar luminosity required to excite the lines.

At its northern end, filament E2 appears to overlap the non-thermal linear radio filament crossing the Galactic plane; this is more apparent in contour maps than the radiograph of Figure 1. The data in Figure 2 show no effect at this intersection of the linear and straight filaments, suggesting either that they are independent (contrary to arguments of Morris & Yusef Zadeh 1989), or that their interaction has at most a minor effect on the ionization and luminosity of the E2 filament.

4. FIR Emission Distribution Across the E2 and W1 Filaments

We also scanned across the E2 and W1 filaments at position 4 of the scan along the E2 filament - see Figure 1 of Paper 604. These KAO data include lines of [S III] (33 μm), [O III] (52 & 88 μm), [Si II] (35 μm), [O I] (63 μm), and [C II] (158 μm). We registered the scan positions at different wavelengths to an estimated ±5″ using stellar offsets in our CCD focal plane guider.

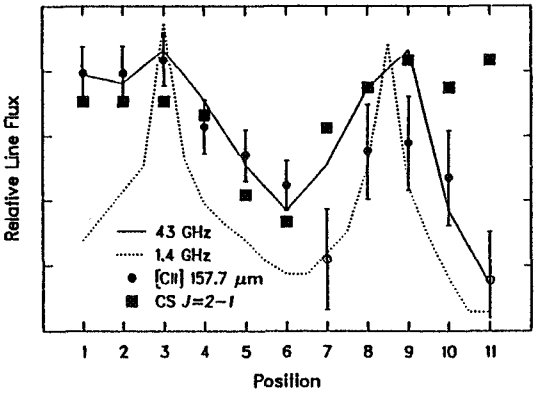

Figure 3. Profiles across E2 and W1 filaments.

Figure 3 compares relative profiles of the single dish 43 GHz radio continuum (Sofue *et al.* 1986), the VLA 1.4 GHz continuum (Morris & Ysef-Zadeh 1989), the CS (J=2–1) molecular emission

(Serabyn & Güsten 1987), and our [C II] 158 μm measurements. Position numbers increase from east to west; spacing is 30″. Beam sizes are comparable except for the VLA data, which effectively have arc-second resolution, and which actually have a small amplitude relative to the large scale 43 GHz emission distribution (as remarked in §I). The large scale ionized emission correlates well with the CS emission except at the west end of the scan, and our [C II] data also track the radio emission except in the vicinity of the W1 filament, where they are significantly lower. The [O I] line (data not shown) is weak and does not peak on the filaments.

Remarkably, however, our FIR luminosity and the [Si II] (35 μm) spatial distributions track the VLA distribution much more faithfully than the single beam 43 GHz distribution, from which we conclude that *both the dust (FIR continuum) emission and the Si^+ emission are produced predominantly in the filaments.* Tending to corroborate this conclusion are (a) the [Si II]/[O I] (35/63 μm) line ratio on the two filament ridges is $\gtrsim$15, the highest ever observed; and (b) the A_v estimated from the radio emission measure and the FIR continuum are compatible.

The distributions of the doubly ionized emission lines also peak near the filament ridges and with more contrast than the single dish radio distribution, suggesting that this emission is also produced predominantly in the filaments. These lines tend to peak slightly east of the VLA ridges, as does the FIR O^{++}/S^{++} line ratio (indicative of excitation), suggesting a source of excitation to the east of these filaments. However the peak/valley contrast in O^{++}/S^{++} corresponds to a difference in T_{eff} <1000 K.

The electron density distribution deduced from the [O III] line pair ratio peaks to the west of E2 and again to the east of W1 with a value $\sim$ 400 cm^{-3}, with a dip in between. The simplest interpretation is that the filaments are not density enhancements. Then the fact that the cross-scan distributions of the FIR continuum, the Si^+, and the doubly ionized lines trace the VLA filaments more closely than the large scale radio emission is most easily explained if the the excitation source(s) are in the filament.

5. NIR Images and Spectra

We obtained images and spectra of the E2 filament region in the J, H, and K′ bands (Paper 605). The images show no obvious correlation of the stellar distribution with the filament morphology, but do show a compact cluster of about 18 resolved stars roughly 2 pc (in projection) east of the south end of the E1 filament, at RA 17^h 42^m 40.0^s, Dec 28°48′ 19″. The NIR reddening of these stars (H−K$\simeq$2) implies they are indeed at the distance of the Galactic center. A dozen of the cluster stars seen show Brγ and HeI (2.11 μm) lines, and are tentatively identified as late WN stars by comparison with NIR spectra of classified stars (see Figure 1 of Paper 605).

These late WN stars are thought to have T_{eff} $\sim$ 30,000 K. This and the measured NIR continuum flux implies a luminosity $\sim$ 10^6 $L_\odot$ per star, somewhat larger than for the optically classified stars of this type, but within the range of late WN stellar models (Maeder 1990). This technique for luminsoity determination was verified on known WR stars. With this luminosity and T_{eff}, the identified cluster stars produce an ionizing photon flux N_{Lyc} $\sim$ 10^{50} s^{-1},

comparable to that required to ionize the filaments. Of course geometric dilution implies that only a fraction of the cluster stars' radiation can be effective in ionizing the filaments.

On the other hand, hotter OB stars typically do not have NIR line signatures which we would have detected. In OB associations, only about 15% of the hot stars are WR stars, which would suggest $\gtrsim 50$ unidentified hot stars associated with the cluster. Thus there could easily be numerous O stars in the region, in the filament, or in the cluster, which contribute to or dominate the ionization of the filaments. Finally, the T_{eff} of the cluster stars is nominally too low to produce the 35,000 K excitation we find from the FIR lines, implying that hotter stars must be present if the filament is photoionized.

6. Discussion

The agreement between the velocities of the doubly ionized FIR lines and the molecular gas along the E2 filament enforces the suggestion of Serabyn and Güsten (1987), that the filaments are ionized segments of the molecular cloud surface. However, although there is large-scale similarity in the morphology of the ionized and molecular gas, the morphology of the E2 filament and that of the molecular gas are quite different (see Figure 1).

The roughly tubular or somewhat flattened shape of the filament we deduce is consistent with the idea of containment of the gas by a magnetic flux tube. The KAO 100 μm polarization data (Morris *et al.* 1992) indeed are consistent with a magnetic field roughly parallel to the filament, but apparently not confined to the filament. Shorter wavelength FIR polarization measurements, around 50 μm where the continuum peaks, would help to identify such a flux tube if it exists; see also Hayvaerts, Norman, & Pruditz (1988). This explanation is plausible if the exciting sources are embedded in the filament, since we observe little or no density enhancement in the filament. Although our KAO line data *do* suggest that the gas excitation is higher to the southeast of the filament, which is in the (projected) direction of the stellar cluster revealed by our AAT observations, the evidence by no means rules out hot stars embedded in the filament. We conclude that the hot stars now known and others likely to exist in the region can readily account for the luminosity and excitation of the E2 filament, but explaining the geometry remains problematical.

To detect the presence of hot stars, one can look for ionization stratification produced in the surrounding gas, as characterized by the doubly ionized FIR fine structure lines discussed above. At the distance of the Galactic center, the ~pc size of an H II region corresponds to about 20″, too small to be resolved in the FIR from the KAO. With the Stratospheric Observatory for Infrared Astronomy – SOFIA – this will be a tractable problem, as will numerous others.

7. Acknowledgements

We are grateful to the staffs of the KAO and the AAT for their assistance with these observations, and to D. J. Hollenbach for helpful discussions. S.W.J.C. and J.P.S. acknowledge NASA/Ames Research Center Interchange Grants NCC 2-647 and NCC 2-548, respectively.

8. References

Allen, D.A., Barton, J.R., Burton, M.G., Davies, H., Farrell, T., Gillingham, P., Lankshear, A., Lindner, P., Mayfield, D., Meadows, V., Schafer, G., Shortridtge, K., Spyromilio, J., Straede, J., Waller, L., & Whittard, D. 1993, *Proc. ASA*, 10, 298

Bachiller, R., Cernicharo, J., Martin-Pintado, J., Tafalla, M., & Lazareff, B. 1990, A&A, 231, 174

Colgan, S.W.J., Erickson, E.F., Simpson, J.P., Haas, M.R., & Morris, M. 1994 Proc of the Airborne Astronomy Symp on the Galactic Ecosystem: From Gas to Stars to Dust, ed. M. R. Haas, J. A. Davidson, & E. F. Erickson (San Francisco: ASP), **Paper 604**

Colgan, S. W. J., Simpson, J. P., Rubin, R. H., Erickson, E. F., Haas, M. R., & Wolf, J. 1991, ApJ, 366, 172

Cotera, A.S., Erickson, E.F., Simpson, J.P., Colgan, S.W.J., Allen, D.A., & Burton, M.G. 1994 Proc of the Airborne Astronomy Symp on the Galactic Ecosystem: From Gas to Stars to Dust, ed. M. R. Haas, J. A. Davidson, & E. F. Erickson (San Francisco: ASP), **Paper 605**

Erickson, E.F., Colgan, S.W.J., Simpson, J.P., Rubin, R.H., Morris, M., & Haas, M.R. 1991 ApJL, 370, 69, **ECSRMH**

Erickson, E. F., Haas, M. R., Colgan, S. W. J., Simpson, J. P., & Rubin, R. H. 1994, Proc of the Airborne Astronomy Symp on the Galactic Ecosystem: From Gas to Stars to Dust, ed. M. R. Haas, J. A. Davidson, & E. F. Erickson (San Francisco: ASP), paper 702

Erickson, E. F., Houck, J. R., Harwit, M. O., Rank, D. M., Haas, M. R., Hollenbach, D. J., Simpson, J. P., Augason, G. C., & McKibbin, D. D. 1984, in Symp on Airborne Astronomy, NASA Conf Pub 2353, ed. H. Thronson & E. Erickson, 313

Genzel, R., Stacey, G.J., Harris, A.I., Townes, C.H., Geis, N., Graf, U.U., Poglitsch, A., & Stutzki, J. 1990, ApJ, 356, 160

Hayvaerts, J., Norman, C., & Pudritz 1988 ApJ, 330, 718

Hollenbach, D., & McKee, C.F. 1989 ApJ, 342, 306

Kurucz, R.L. 1979, ApJS, 40, 1

Kurucz, R.L. 1981, private communication

Maeder, A., 1990 STSI Synmposium series 5, "Massive Stars in Starbursts", eds. C Leitherer, N.R. Walborn, T.M. Heckman & C.A. Norman (Cambridge University Press: Cambridge), 97

Morris, M., Davidson, J.A., Werner, M., Dotson, J., Figer, D.F., Hildebrand, R., Novak, G., & Platt, S. 1992 ApJ, 399, L63

Morris, M. & Yusef-Zadeh, F. 1989, ApJ, 343, 703

Pottasch, S.R., Wesselius, P.R., & van Duinen, R.J. 1979 A&A, 77, 189

Rubin, R.H. 1989, ApJ, 69, 897

Rubin, R.H., Simpson, J.P., Erickson, E.F., & Haas, M.R. 1991, ApJ, 374, 564

Rubin, R.H., Simpson, J.P., Lord, S.D., Colgan, S.W.J., Erickson, E.F., and Haas, M.R. 1994, ApJ, 420, 772

Schaller, G., Schaerer, G., Meynet, G., & Maeder, A. 1992, A&AS, 96, 269

Serabyn, E., and Güsten, R. 1987, A&A, 184, 133

Sofue, Y., Inoue, M., Handa, T., Tsuboi, M., Hirabayashi, H., Morimoto, M., & Akabane, K. 1986, PASJ, 38, 475

Tielens, A.G.G.M., & Hollenbach, D.J. 1985, ApJ, 291, 722, TH

Wolfire, M.G., Tielens, A.G.G.M., & Hollenbach, D. 1990, ApJ, 291, 722, WTH

Yusef-Zadeh, F., Morris, M. 1987, ApJ, 322, 721

Yusef-Zadeh, F., Morris, M., & van Gorkom, J.H. 1987, AIP Conf. Proc. No. 155: The Galactic Center, ed. D.C. Backer, (New York: AIP), p. 190

Yusef-Zadeh, F., Telesco, C.M., & Decher, R. 1989, IAU Sym. 136: The Center of the Galaxy, ed. M. Morris, (Dordrecht:Kluwer), 287

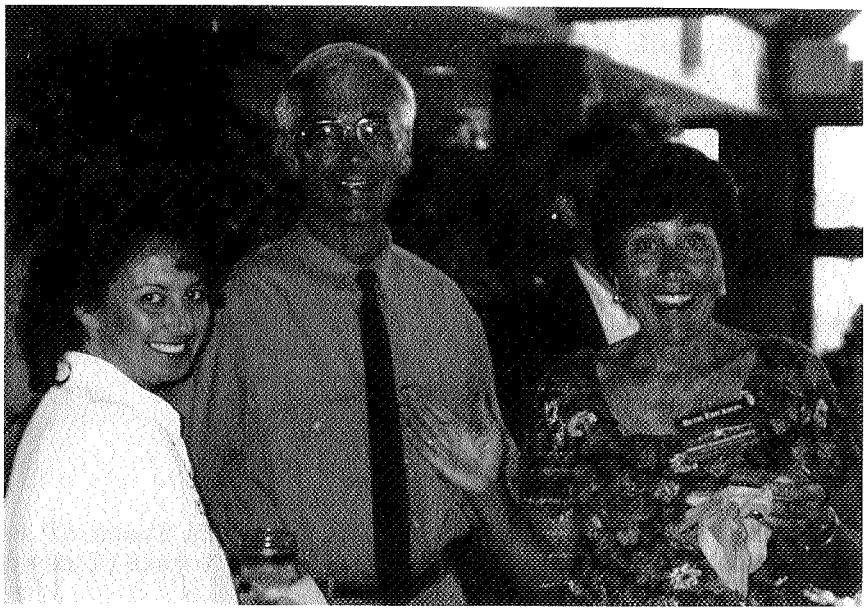

Yvonne Pendleton, Ed and Beth Erickson

Airborne Astronomy Symposium on the Galactic Ecosystem
ASP Conference Series, Vol. 73, 1995
M.R. Haas, J.A. Davidson, and E.F. Erickson (eds.)

Star Formation in Galactic Center GMC Cores: Sagittarius B2 and the Dust Ridge

D. C. Lis
Division of Physics Mathematics and Astronomy, California Institute of Technology, Pasadena, CA 91125

K. M. Menten
Harvard–Smithsonian Center for Astrophysics, Cambridge, MA 02138

1. Introduction

The total far–infrared luminosity and the ionizing flux inferred from radio continuum observations of the Galactic center region imply a rate of star formation per unit mass of molecular material comparable to that in the Galactic disk. However, H_2O and OH masers commonly found in sites of high–mass star formation are relatively rare in the nuclear disk. Far–infrared studies suggest that the formation rate of stars with masses greater than $\sim$20 $M_\odot$ is reduced in the central region compared to the Galactic disk. Star formation might be suppressed currently in the central region as a result of the different geometry and strength of the magnetic fields there, which arguably might tend to inhibit cloud collapse (Morris 1989). High gas pressures implied by observations of the diffuse X–ray emission suggest that giant molecular clouds (GMCs) in the nuclear disk may be held together by external pressure rather than self–gravity (Spergel & Blitz 1992). The gravitational collapse leading to the formation of high density cores may thus be suppressed in all but the most massive clouds.

2. Sagittarius B2

Sgr B2 is perhaps the most prominent and best studied star–forming region in the nuclear disk. High angular resolution far–infrared observations obtained with the *KAO* by Goldsmith et al. (1992) have been essential for understanding the energetics of this region. The H II/molecular core regions Sgr B2 (N), (M) and (S) were detected as separate sources for the first time in the far–infrared (Fig. 1). The far–infrared data confirm results of previous radiative transfer models (Lis & Goldsmith 1990), which indicated very large extinction in front of the northern source, prominent at submillimeter wavelengths. They also provide direct estimates of the luminosity of the embedded sources and establish Sgr B2(M) as the most energetic source in the region (L$\sim 10^7$ $L_\odot$). The far–infrared maps show evidence for the presence of an extended component coinciding with the low level radio free–free emission and with the portion of the Sgr B2 core having densities $\gtrsim 10^5$ cm^{-3}, as derived from molecular observations. One possible explanation is that the ionizing radiation from the massive stars in the compact sources is diffusing through a region with a beam–averaged visual extinction

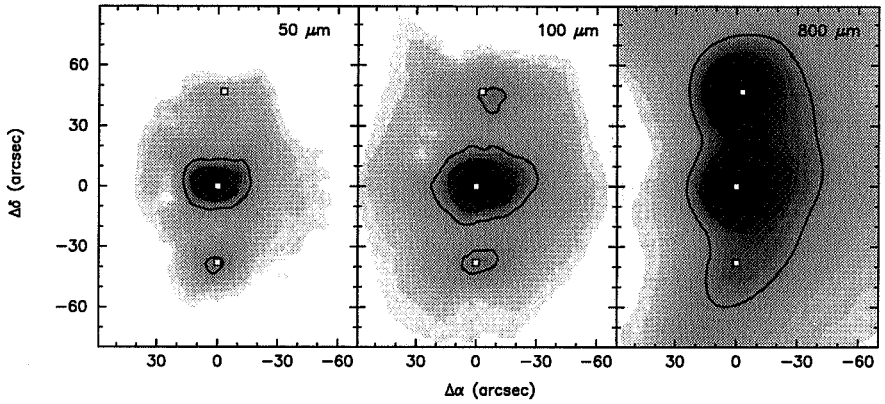

Figure 1. Gray–scale images of the far–infrared (50 and 100 μm; Goldsmith et al. 1992) and submillimeter (800 μm; Lis & Carlstrom 1994) continuum emission toward the Sgr B2 core. The far–infrared data have been restored using a one–dimensional maximum entropy algorithm. Sgr B2(N), the most prominent submillimeter peak, is barely visible at 50 μm, as a result of large foreground extinction. Sgr B2(M) is the most energetic source in the region ($L \sim 10^7$ $L_\odot$). Contour levels are 30, 50, 70, and 90% of the peak.

greater than or equal to a few hundred magnitudes. This would imply that the gas and dust distributions in the central portion of the cloud surrounding the compact sources are highly clumped. Alternatively, the dust in the extended component may be externally heated by the diffuse interstellar radiation field.

3. Dust Ridge

One of the most interesting results of a recent *CSO* survey of the 800 μm continuum emission from a $\sim 1\overset{\circ}{.}5 \times 0\overset{\circ}{.}2$ region toward the center of the Milky Way (Lis & Carlstrom 1994) was the detection of a narrow, clumpy ridge of dust emission apparently connected with the Galactic center arc (Fig. 2). The southernmost dust condensation in the dust ridge coincides with the ammonia peak M 0.25+0.01 (Lis et al. 1994). No compact radio continuum or far–infrared sources associated with the dust condensations in the ridge can be found in the existing surveys or the *IRAS* Point Source Catalogue. This prompted the speculation that the dust may be heated by the external radiation field rather than embedded young stars, in contrast to the well studied Galactic center GMC cores, such as Sgr B2 and Sgr C.

The detection of *massive and cold GMC cores* in the nuclear disk that are apparently *without ongoing high–mass star formation* would be of great importance and would provide new input for analysis of the magnitude of various dynamical effects invoked to explain the low rate of high–mass star formation

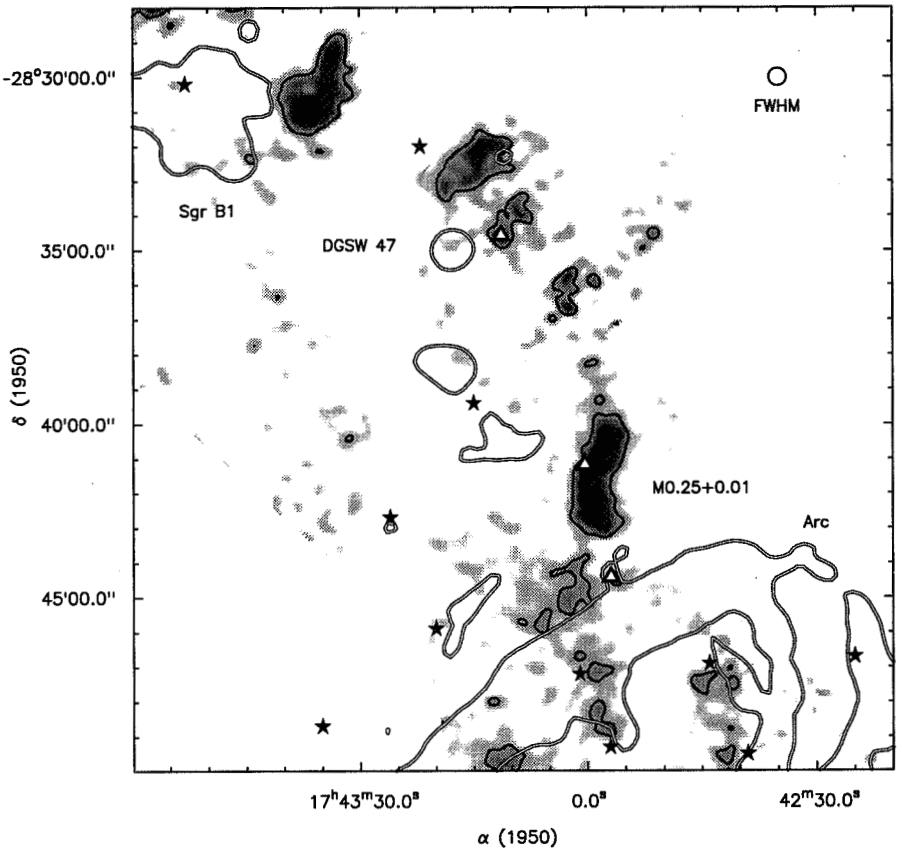

Figure 2. A gray–scale image of the 800 μm continuum emission toward the dust ridge (Lis & Carlstrom 1994). Limited CS J=5→4 data suggest a coherent structure which connects to the radio arc. Stars mark the positions of compact far–infrared sources (Odenwald & Fazio 1984). Double contours outline the regions of strong 20 cm emission (Yusef–Zadeh 1986). The radio arc, Sgr B1, and the radio continuum source 47 of Downes et al. (1978) are visible in this tracer. Notice the apparent lack of correlation between the distribution of the dust emission with that of the radio continuum emission and with compact far–infrared sources. The three H_2O masers detected in our *VLA* survey are marked as triangles. Their coordinates are: ($17^h43^m00\overset{s}{.}3$, $-28°41'10''$), ($17^h43^m11\overset{s}{.}3$, $-28°34'34''$), ($17^h42^m56\overset{s}{.}9$, $-28°44'25''$).

in the central region. We have, therefore, started a research program aimed at determining the physical conditions in the GMC cores in the dust ridge and identifying any star–formation sites that may be present there. H_2O masers are considered signposts of high–mass star formation. Ultracompact H II regions also mark the presence of recently formed high–mass stars in GMC cores. We have thus used the *VLA* for an optimized search for H_2O masers and ultracompact H II regions covering the whole dust ridge. Our search has revealed only three H_2O masers, two of which were known previously (Fig. 2). The presence of H_2O masers implies some ongoing low–mass star formation associated with the dust ridge. However, there is still no evidence for high–mass star formation within this molecular complex, in spite of its large mass ($\sim 5 \times 10^5$ $M_\odot$). Our VLA detection of emission in the H92α radio recombination line suggests that the radio continuum source 47 of Downes et al. (1978) is a shell–like H II region. This is so far the only evidence for past high–mass star formation in the vicinity of the dust ridge.

4. Need for Far–Infrared Observations

The most puzzling question emerging from past observations is *the apparent absence of luminous FIR sources embedded in the GMC cores in the ridge.* Our multi–wavelength submillimeter observations (350 – 800 μm) predict observable 100 μm emission from *extended* portions of the ridge for all plausible values of the dust temperature and grain emissivity. A sensitive search for young stellar objects embedded in these cores with the *KAO* or *ISO* would provide definitive information on the luminosity of any embedded sources and the current state of star formation in this region.

Acknowledgments. This research has been supported by NSF grant AST 93–13929 to the Caltech Submillimeter Observatory.

References

Goldsmith, P.F., Lis, D.C., Lester, D.F., & Harvey, P.M. 1992, ApJ, 389, 338

Downes, D., Goss, W.M., Schwartz, U.J., & Wouterloot, J.G.A. 1978, A&AS, 35, 1

Lis, D.C., & Carlstrom, J.E. 1994, ApJ, 424, 189

Lis, D.C., & Goldsmith, P.F. 1990, ApJ, 356, 195

Lis, D.C., Menten, K.M., Serabyn, E., & Zylka, R. 1994, ApJ, 423, L39

Morris, M. 1989, in *The Center of the Galaxy*, ed. M. Morris (Dordrecht: Kluwer), 171

Odenwald, S.F., & Fazio, G.G. 1984, ApJ, 283, 601

Spergel, D. N., and Blitz, L. 1992, Nature, 357, 665

Yusef–Zadeh, F. 1989, in *The Center of the Galaxy*, ed. M. Morris (Dordrecht: Kluwer), 243

Airborne Astronomy Symposium on the Galactic Ecosystem
ASP Conference Series, Vol. 73, 1995
M.R. Haas, J.A. Davidson, and E.F. Erickson (eds.)

High Angular Resolution 30 μm Observations of the Galactic Center

C. M. Telesco*
NASA/Marshall Space Flight Center, ES-63, Space Science Laboratory, Huntsville, AL 35812

J. A. Davidson*
SETI Institute; NASA/Ames Research Center, MS 245-6, Moffett Field, CA 94035-1000

M. W. Werner*
Jet Propulsion Laboratory, California Institute of Technology, Pasadena, CA 91109

Abstract. We have mapped the central 2′ (5 pc) of the Galaxy with 4″ resolution at 30 μm, using the MSFC bolometer array on the NASA Infrared Telescope Facility at Mauna Kea. Complementary maps at 10 and 20 μm covering the same region were obtained contemporaneously with the same instrumentation. The maps encompass both the central cavity at the very center of the Galaxy and the disk of gas and dust which surrounds it. Our data show thermal emission from dust particles within the cavity and – for the first time at this resolution – within the disk itself. The emission peaks at the position of IRS1 at all three wavelengths, and the 20/30 μm brightness ratio falls uniformly from this peak toward the outer regions of the source. The 30 μm emission correlates well with the HCN emission in the southwest portion of the circumnuclear disk and with the [O I] emission in the north. No feature is apparent at the position of SgrA* at any of the three wavelengths.

The circumnuclear disk was discovered from the KAO and has been extensively studied in both continuum and line emission in numerous subsequent flights. The poster will attempt to show how these latest ground-based observations intersect and build upon these airborne investigations.

*Guest Investigator at the IRTF, which is operated by the University of Hawaii under contract to NASA.

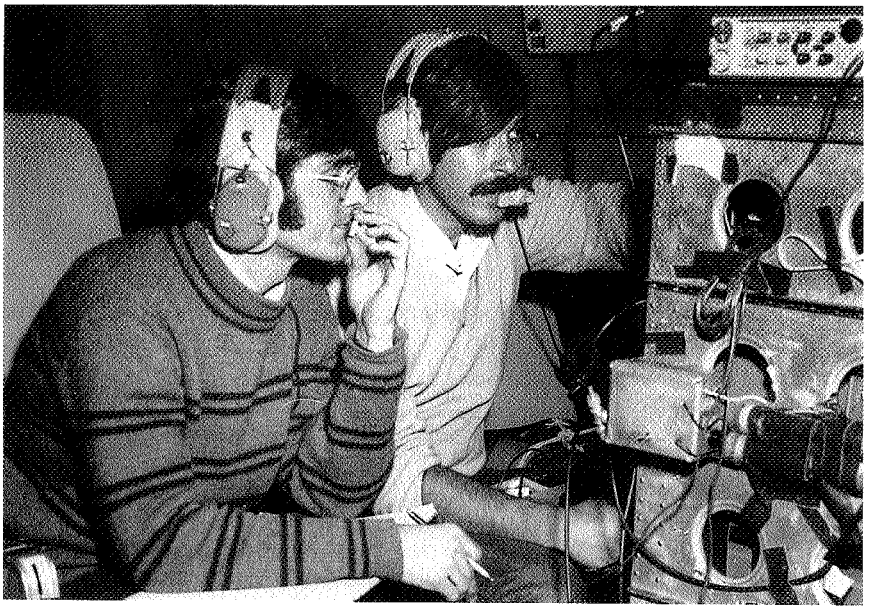

Charlie Telesco, Bob Loewenstein (1974)

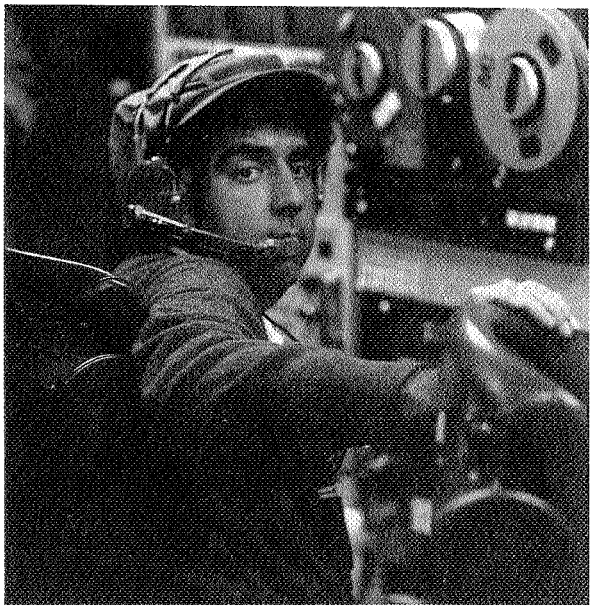

Mike Werner (1979)

Airborne Astronomy Symposium on the Galactic Ecosystem
ASP Conference Series, Vol. 73, 1995
M.R. Haas, J.A. Davidson, and E.F. Erickson (eds.)

The 16 - 45 μm Observations of the Galactic Center

Kin-Wing Chan
Department of Astronomy, University of Maryland, College Park, MD 20742

S. H. Moseley, S. Casey, E. Dwek
Lab. for Astronomy and Solar Physics, NASA GSFC , Greenbelt, MD 20771

R. Loewenstein
Yerkes Observatory, P.O. Box 258, Williams Bay, WI 53191

W. Glaccum
Applied Research Corp., 8201 Corporate Dr., Landover, MD 20781

Abstract. An outline of recent (May 1994) KAO 16 - 45 μm observations of the Galactic Center is given.

Introduction

Existing observations of the Galactic Center at infrared and radio wavelengths challenge our understanding of the detailed morphology and energy balance of the inner few parsec, including the Galactic Center and the infrared torus. The distribution and nature of the sources heating this region are still not well understood; existing determinations of dust temperature and ionization do not provide us with consistent pictures of the relative important of the central source and the embedded stars in this dusty region. From IR observations of the inner torus edge approximately 1 pc (26") from the central source, Davidson *et al.* (1992) infer an equilibrium dust temperature of about 55 K. They point out that a central luminosity of 10^7 $L_\odot$ (required to match their observed FIR emission) and the assumption of "normal" dust properties predict higher equilibrium grain temperature of 85 K. If the ionizing sources are distributed uniformly throughout the Galactic Center torus cavity, the minimum luminosity required to produce the observed ionization is 2×10^6 $L_\odot$ (Lacy *et al.* 1980, Serabyn & Lacy 1985). More recent observations suggest a central luminosity at a few times 10^6 $L_\odot$ in the UV (Jackson *et al.* 1993). This lower

central luminosity lessens but does not eliminate the anomalous dust temperature problem of the inner Galactic Center torus, since a dust temperature of 75 K would be expected for a $2x10^6$ $L_\odot$ ionizing source. The composite IR emission of the Galactic Center can be crudely divided into three categories: (1) hot dust heated directly by an incident UV field along the inner region of the Galactic Center torus; (2) warm dust heated by the non-ionizing radiation of the embedded stars and re-radiated NIR dust emission; (3) cooler absorbing dust located along the galactic line of sight. The apparent inconsistencies between the observations and theoretical expectations may stem from the interplay of various physical process and source-cloud geometries. Observations with increased spatial and spectral resolution are clearly needed to provide the information necessary to address the various problems. Therefore, we made 16 - 45 μm spectrophotometric observations of the inner 80" (3 pc) regions surrounding the Galactic Center with the 20" aperture of Goddard Cryogenic Grating Spectrometer #2 in May 1994 from the KAO. We measured nine points, including the 50 and 90 μm peaks of Davidson *et al.* and points between them and Sgr A*. The wavelength coverage of our instrument ensures sensitivity to the hot dust component, silicate emission and/or absorption features, and cooler dust at longer wavelengths. Our observations will be used to set limits on the luminosity of any central sources, or give an independent estimate of central luminosity, and to set limits on the range of acceptable dust parameters for this region.

References

Davidson, J. A., Werner, M. W., Wu, X., Lester, D. F., Harvey, P. M., Joy, M. & Morris, M. 1992, ApJ, 387, 189

Jackson, J. M., Geis, N., Genzel, R., Harris, A. I., Madden, S., Polglitsch, A., Stacey, G. J. & Townes, C. H. 1993, ApJ, 402, 173

Lacy, J. H., Townes, C. H., Geballe, T. R. & Hollenbach, D. J. 1980, ApJ, 241, 132

Serabyn, E. & Lacy, J. H. 1985, ApJ, 293, 445

Airborne Astronomy Symposium on the Galactic Ecosystem
ASP Conference Series, Vol. 73, 1995
M.R. Haas, J.A. Davidson, and E.F. Erickson (eds.)

EXCITATION OF THE "ARCHED" FILAMENTS NEAR THE GALACTIC CENTER

SEAN W. J. COLGAN
SETI Institute; NASA/Ames Research Center, MS 245-6, Moffett Field, CA 94035-1000

EDWIN F. ERICKSON
NASA/Ames Research Center, MS 245-6, Moffett Field, CA 94035-1000

JANET P. SIMPSON
University of California Berkeley; NASA/Ames Research Center, MS 245-6, Moffett Field, CA 94035-1000

MICHAEL R. HAAS
NASA/Ames Research Center, MS 245-6, Moffett Field, CA 94035-1000

MARK MORRIS
University of California Los Angeles, Dept. of Astronomy - 156205, 8979 Math-Sciences Bldg., Los Angeles, CA 90024

ABSTRACT We discuss measurements of the far-infrared (FIR) fine structure lines from [S III] (33 μm), [Si II] (35 μm), [O III] (51, 88 μm), [O I] (63 μm), [C II] (158 μm), and the adjacent continua in a strip crossing two of the thermal radio filaments in the Galactic Center "Arch". The near spatial coincidence of the line and continuum emission maxima with the radio filaments demonstrates that any excitation mechanism must account for both the line and continuum emission. The peak FIR luminosity and [O III] emission pose difficulties for collisional excitation models; photoionization of molecular cloud edges by a random distribution of stars is the most plausible mechanism proposed.

INTRODUCTION

The region immediately north of the Galactic Center contains long, remarkably thin, straight, nonthermal filaments perpendicular to the galactic plane which are connected to a system of arched, thermal filaments curving back toward the galactic plane (Yusef-Zadeh, Morris & Chance 1984, Yusef-Zadeh & Morris 1988, Morris & Yusef-Zadeh 1989). The excitation mechanism responsible for

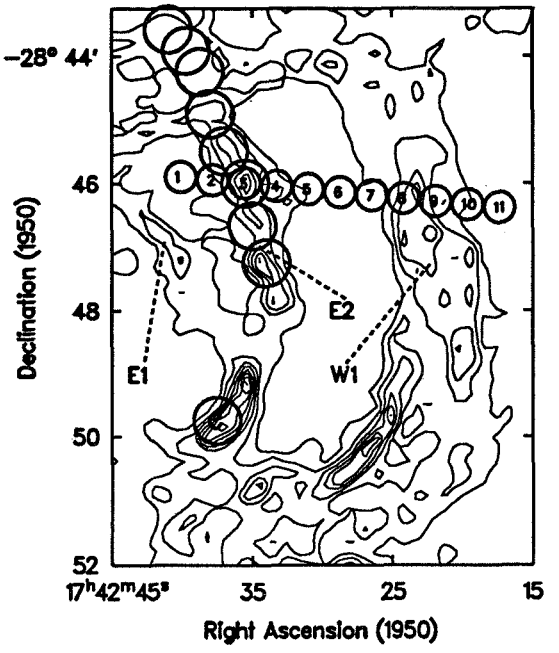

Figure 1: Positions of infrared observations overlaid on a VLA 6 cm continuum map from the data of Morris & Yusef-Zadeh (1989). The numbered beams are the measurements discussed in this paper. The observations in Erickson et al. (1991), including position C and the scan up the E2 filament, are included for reference. The circles indicate the beam sizes and the E1, E2, and W1 filaments are labeled.

the emission from both sets of filaments is controversial – we consider here the excitation of the arched filaments

A strip scan of 11 positions crossing the E2 and W1 arched radio filaments (nomenclature from Yusef-Zadeh 1986, Morris & Yusef-Zadeh 1989) with 30″ spacing was made. The observed positions, labeled 1–11, are shown overlaid on a 20 cm VLA continuum map (Morris & Yusef-Zadeh 1989) in Figure 1. The lines of [S III] (33 μm), [Si II] (35 μm), [O III] (52 μm), [O I] (63 μm), [O III] (88 μm), [C II] (158 μm), and the adjacent continua were measured with the Kuiper Airborne Observatory facility Cryogenic Grating Spectrometer (Erickson et al. 1985). The spectral resolution was 170 km/s at 158 μm and $\sim$ 70 km/s for the other transitions. The FWHM beamwidths were 41″ at 158 μm and 30 – 35″ for the other lines. The chopper throw was $\sim$ 10′.

RESULTS

The principal observational results are that most of the lines from ionized species (Si^+, S^{++}, O^{++}) and the continua at wavelengths $\lambda \lesssim 100$ μm show a significant enhancement at the radio continuum filaments. The distribution of [O III] (88.4

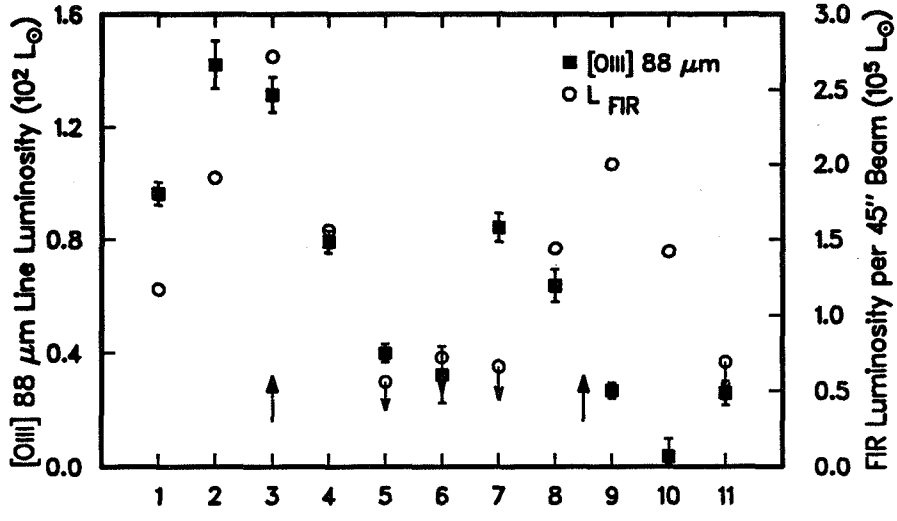

Figure 2: [O III] 88 μm line flux (filled squares) and L_{FIR} (open circles) as a function of position. Upper limits are denoted by down arrows. The solid up arrows show the location of the radio filaments.

μm) emission is shown in Figure 2. The location of the radio continuum ridges in the cross scan are shown by the up arrows.

The continuum spectrum at each position was fitted with both blackbody and λ^{-1} emissivity laws to estimate the total luminosity, L_{FIR}, also plotted in Figure 2. As confirmed by Morris, Davidson, & Werner (1994), L_{FIR} shows a strong enhancement at the location of the filaments. The peak luminosity is $L_{FIR} \sim 2.7 \times 10^5$ L$_\odot$ per beam.

The electron density N_e, deduced from the ratio of the 52 and 88 μm [O III] line fluxes (Rubin 1989), increases at the location of the filaments by a factor of two. The density enhancement is consistent with the filament emission being produced by a small fraction of the material ($\sim$ 5%) in higher density regions ($\sim$ 1000 cm^{-3}, from VLA measurements of Morris & Yusef-Zadeh 1989), with most of the ionized material along the line-of-sight having a lower ($\lesssim$ 150 cm^{-3}) electron density.

EXCITATION OF THE FILAMENTS

The enhancement of the FIR luminosity and the magnitude of the [O III] emission associated with the filaments (Figure 2) rule out proposed shock/collision models (see Colgan etal. 1994 for more details). The ionized line fluxes are well accounted for by excitation from a few ZAMS stars per beam with T_{eff} = 35,000 K. The [O I], [C II], FIR continuum, and some fraction of the [Si II] emission then originate from a photodissociated region adjacent to the ionized material. The distribution of the [Si II] emission is very similar to the [O III] and [S III] distributions, which strongly suggests that most of the

[Si II] emission originates in the ionized gas rather than in the photodissociated material.

The contrast between the filaments and the intervening regions is greatest for the doubly ionized line fluxes and the FIR continuum luminosity, but the contrast is small or even inverted for the singly ionized [C II] and neutral [O I] lines. This clearly associates the photoionized material and the heated dust with the radio filaments, but does not require the stars to be located in the filaments. The suggestion of Serabyn & Güsten (1987), that the ionized material is a density increase at the edge of the observed molecular cloud and the stars are outside of the cloud is plausible, otherwise the stars would have to be located in long lines to account for the morphology of the filaments. If stars external to the molecular clouds provide the excitation, the filamentary morphology is determined by whatever is responsible for the morphology of the molecular cloud edges, perhaps the magnetic fields (*e.g.* Sofue et al. 1987; Morris et al. 1992). The small shift between the maxima of the [O III] line emission and the FIR continuum (Figure 2) suggests an excitation source to the east of the filaments. The recently discovered cluster of hot stars near the E1 filament (Cotera et al. 1994) may provide some fraction of the ionization, but would need to be $\sim 5-10$ pc away from the E2 and W1 filaments in order to account for the uniformity of the excitation (cf. Erickson et al. 1991).

REFERENCES

Colgan, S. W. J., Erickson, E. F., Simpson, J. P., Haas, M. R., & Morris, M. 1994, ApJ, in preparation.

Cotera, A. S., Erickson, E. F., Simpson, J. P., Colgan, S. W. J., Allen, D. A., & Burton, M. G. 1994, in Proc of the Airborne Astronomy Symp on the Galactic Ecosystem: From Gas to Stars to Dust, ed. M. R. Haas, J. A. Davidson, & E. F. Erickson, (San Francisco: ASP), paper 605

Erickson, E. F., Colgan, S. W. J., Simpson, J. P., Rubin R. H., Morris, M., & Haas, M. R. 1991, ApJ, 370, L69

Erickson, E. F., et al. 1985, IRPhy, 25, 513

Morris, M., et al. 1992, ApJ, 399, L63

Morris, M., Davidson, J. A., & Werner, M. W. 1994, in Proc of the Airborne Astronomy Symp on the Galactic Ecosystem: From Gas to Stars to Dust, ed. M. R. Haas, J. A. Davidson, & E. F. Erickson, (San Francisco: ASP), paper 6.3

Morris, M., & Yusef-Zadeh, F. 1989, ApJ, 343, 703

Rubin, R. H. 1989, ApJS, 69, 897

Serabyn, E. & Güsten, R. 1987, A&A, 184, 133

Sofue, Y., Reich, W., Inoue, M., & Seiradakis, J. H. 1987, PASJ, 39, 95

Yusef-Zadeh, F., 1986, PhD thesis, Astronomy Department, Columbia University

Yusef-Zadeh, F., & Morris, M. 1988, ApJ, 329, 729

Yusef-Zadeh, F., Morris, M., & Chance, D. 1984, Nature, 310, 557

Airborne Astronomy Symposium on the Galactic Ecosystem
ASP Conference Series, Vol. 73, 1995
M.R. Haas, J.A. Davidson, and E.F. Erickson (eds.)

Stellar Ionization of the Thermal Radio Emission Regions of the Galactic Center

Angela S. Cotera[1], Edwin F. Erickson[2], David A. Allen[3], Sean W. J. Colgan[2,4], Janet P. Simpson[2,5], Michael G. Burton[6]

[1]*Stanford University,* [2]*NASA/Ames Research Center,* [3]*Anglo-Australian Observatory,* [4]*The SETI Institute,* [5]*Department of Astronomy, University of California, Berkeley,* [6]*University of New South Wales*

Abstract. We have used the Anglo-Australian Telescope imaging spectrometer IRIS to search for hot young stars which may ionize the thermal radio emission regions within the inner 40 pc of the Galaxy. Several hot stars were discovered based on their Brγ (2.165 μm) and He I (2.058 μm) emission, including a cluster of possible WN 8–9 stars. Comparison of the spectra of the new stars with optically classified stars suggests a spectral classification of B[e] and WN7-9. Based on the calculated luminosity of the new stars and comparisons with radio data, the emission stars could be largely responsible for the ionization of the thermal radio emission regions.

1. Introduction and Observations

It has been argued that the Arched Filaments near the Galatic Center (GC) are ionized as the result of an interaction between the magnetic field and a molecular cloud coincident with the filaments (Morris & Yusef-Zadeh 1989). However, KAO observations by Erickson et al. (1991) showed that the far infrared (FIR) line emission associated with the thermal radio emission is consistent with photoionization by hot stars. In addition, models based on that FIR emission were able to produce the observed FIR continuum luminosity, while the magnetohydrodynamic induced ionization models were not (Erickson et al. 1991).

During our investigation (Cotera et al. 1993, Cotera 1994), we have discovered $\gtrsim$20 emission lines stars lying adjacent to or coincident with the radio emission regions G0.15–0.04 (the 'Pistol'), the E1 and E2 Filaments, G0.10+0.02, and the Sgr A regions A-D, H5, H2 and H8 (nomenclature from Morris & Yusef-Zadeh 1989).

The observations were made on July 13-14, 1992 and June 13-15, 1993 with a 128×128 pixel HgCdTe array in the imaging spectrograph IRIS at the 3.9m Anglo-Australian Telescope. J, H and K′ photometry obtained at a scale of $\sim$0.6″/pixel, indicates the stars are located at the Galactic Center based on their H–K colors and the known extinction. Images of Brγ (2.156 μm) and He I (2.058 μm) emission revealed the existence and location of the emission line stars, whose spectra were subsequently obtained at a resolution of $\sim$350.

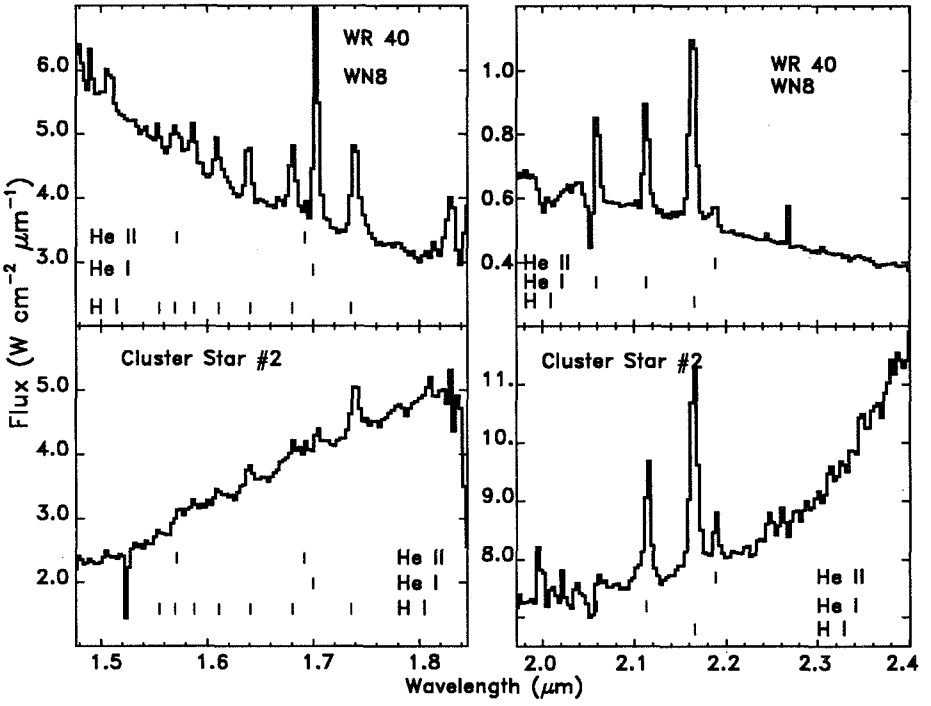

Figure 1. *Upper:* H and K band spectra of WR 40; a WN 8 star; flux density in units of 10^{-16}. *Lower:* H and K band spectra of the G0.12+0.02 cluster emission star #2; flux density in units of 10^{-18}.

2. Results

2.1. G0.12+0.02 Cluster Stars

Most remarkably, a compact cluster of $\gtrsim$20 stars was discovered near the E1 Filament at G0.121+0.017. Approximately 13 of the stars in the G0.12+0.02 cluster have emission lines in the H and K bands. From a comparison of H and K band emission lines in the G0.12+0.02 cluster stars and optically classified stars (Figure 1), a spectral identification of WN8-WN9 is plausible; although more data on optically classified stars at NIR wavelengths is needed. Assuming that the G0.12+0.02 stars are all WN 9 stars with $T_{eff} \sim 30,000K$ (Hamman et al. 1993), black body calculations using the 2.2 μm continuum imply that the total luminosity of the emission line stars is log $(L/L_{\odot})\sim$7.4. Using this luminosity, T_{eff} = 30,000 K, and the stellar atmosphere models of Kurucz (1979), the observed cluster emission line stars would produce log $N_{Lyc} \sim 50.3 \pm 0.4$ s^{-1} ionizing photons. Based on the Sofue et al. (1986) single-dish radio map, we estimate the region, including the E1 and E2 filaments, requires approximately the same number of ionizing photons. If our estimate is correct and all the ionizing photons produced by the cluster were absorbed in the E1 and E2 filaments,

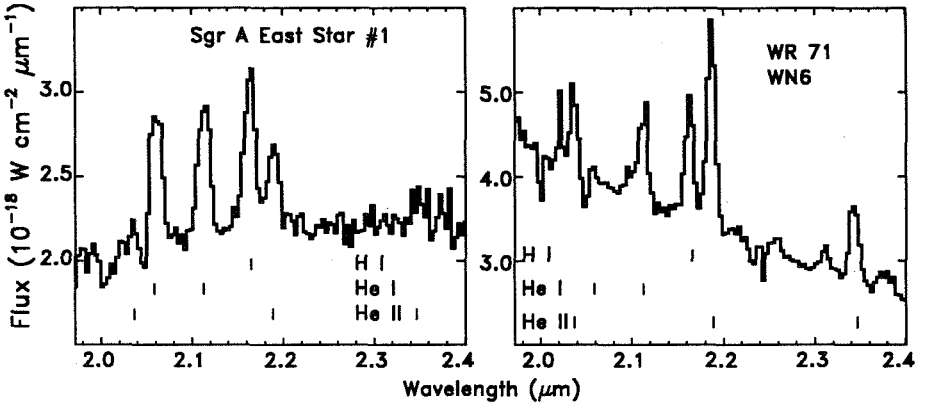

Figure 2. *Left:* K band spectra of a strong emission line star near the radio emission region A on the edge of Sgr A East. *Right:* K band spectra of the WN 6 star WR 71.

which neglects geometrical effects, they would be just sufficient to ionize the entire region under the given assumptions.

2.2. Stars near G0.15–0.05, the 'Pistol'

There are four emission line stars near the Pistol. The source directly below the Pistol, which we designate Source A, has a spectrum similar to the B[e] star He3-1191. Another new star (Pistol Source B) has a K′ band emission spectrum similar to the G0.12+0.02 cluster stars. The spectra of the two sources directly north of the Pistol (AFGL 2004 #8 and #10, Glass et al., 1990) differ from the G0.12+0.02 cluster stars in that they show a very weak He I 2.112/3 μm doublet line and a strong He I 2.058μm line. The spectra of these stars are similar to the better studied AF star located in the cluster of stars in the central parsec of the GC (Najarro et al. 1994, Allen et al. 1990, Forrest et al. 1987), which also has He I (2.058)/ Brγ (2.166) > 1.

Morphologically, it is plausible that Pistol Source A is responsible for the ionization of the Pistol. Its position corresponds with a small peak in the radio emission and its luminosity, based on our measured 2.2 μm continuum flux, is log $L/L_{\odot} \sim 7.0$, suggesting it dominates the energetics in that area. From numerical integration of the ionizing radiation, assuming a black body spectrum with $T_{\rm eff} = 20{,}000$ K, Source A could produce $N_{Lyc} \sim 2 \times 10^{50} s^{-1}$, which is sufficient to ionize the Pistol.

2.3. An Emission Line Star near Sgr A East

The most unusual new star, nearer to Sgr A West, lies to the west of the radio emission region Sgr A East A. Comparison of the emission lines in this star and optically classified stars (Figure 2) suggests a spectral identification of WN 7. For a WN 7 star $T_{\rm eff} \sim 30{,}000$ K. The calculated luminosity for this star would then be log $L/L_{\odot} \sim 6.4$. Using the stellar atmosphere models of Kurucz (1979), the star would produce $N_{Lyc} \sim 1 \times 10^{49}$ s^{-1}. Although this is not sufficient to

ionize all the nearby compact emission regions, the contribution to the required ionizing radiation is significant.

3. Conclusions

To our knowledge, our discovery of emission line stars near the GC, but outside central parsec, is the first direct evidence that stellar sources significantly contribute to the ionization of the radio filaments. Although these emission lines stars have been shown to contribute significant ionizing radiation to their respective radio emission regions, they do not produce enough photons to be the only sources. More detailed calculations require both an improved determination of spectral type and stellar models utilizing infrared emission lines.

The new stars are highly unusual objects. Like the cluster of stars within the central parsec of the Galaxy (Allen 1994; Krabbe et al. 1991), the newly discovered stars are extremely luminous and massive stars. If the G0.12+0.02 cluster emission line stars are type WN8-9, they are young stars, with lifetimes $\lesssim 10^7$years, supporting a hypothesis of recent star formation in the GC. Additionally, if the G0.12+0.02 cluster stars are in fact WN stars, they represent $\sim$14% of all known galactic WN stars (Hamann et al. 1993). Improving our understanding of their formation in the unique conditions of the Galactic Center should lead to a better grasp of the energetics in that region of the Galaxy and possibly the nature of WR stars.

References

Allen, D.A. 1994, in Nuclei of Normal Galaxies: Lesson from the Galactic Center. NATO Conference, in press.

Allen, D.A., Hyland, A.R. & Hillier, D.J. 1990, MNRAS, 244, 706.

Cotera, A.S. 1994, Ph.D. thesis, Applied Physics Department, Stanford University, in preparation.

Cotera, A.S., Erickson, E.F., Allen, D.A., Simpson, J.P., Colgan, S.W.J. & Burton, M.G. 1994, in Nuclei of Normal Galaxies: Lesson from the Galactic Center. NATO Conference, in press.

Erickson, E.F., Colgan, S.W.J., Simpson, J.P., Rubin, R.H., Morris, M. & Haas, M.R. 1991, ApJ., 370, L69.

Forrest, W., Shure, M.A., Pipher, J.L. & Woodward, C.E. 1987, in The Galactic Center, ed. D.C. Backer (New York:AIP), 153.

Glass, I., Moneti, A., & Moorwood, A. 1990, MNRAS, 242, 55p.

Hamann, W.R., Koesterke, L. & Weesolowski, U. 1993, A&A, 264, 397.

Krabbe, A., Genzel, R., Drapatz, S., & Rotaciuc, V. 1991, ApJ, 382, L19.

Kurucz, R.L. 1979, ApJS, 40, 1 and private communication.

Morris, M., & Yusef-Zadeh, F., 1989, ApJ, 343, 703.

Najarro, F. et al. 1994, A&A, in press.

Serabyn, E., & Güsten, R. 1991, A&A, 242, 376.

Sofue, Y. et al. 1986, Pub. Astro. Soc. Japan, 38, 475

Session Seven

Instrumentation for Airborne Astronomy

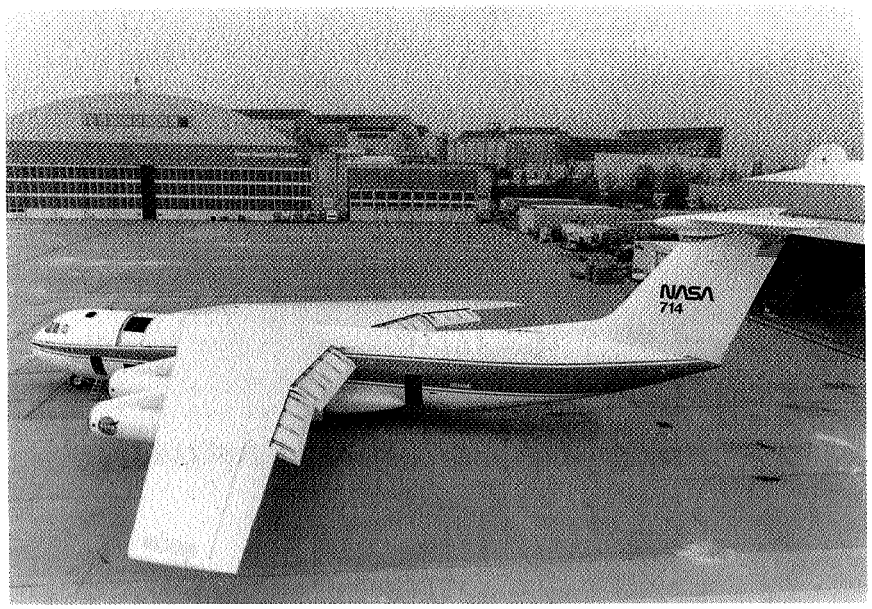

The Kuiper Airborne Observatory (1990)

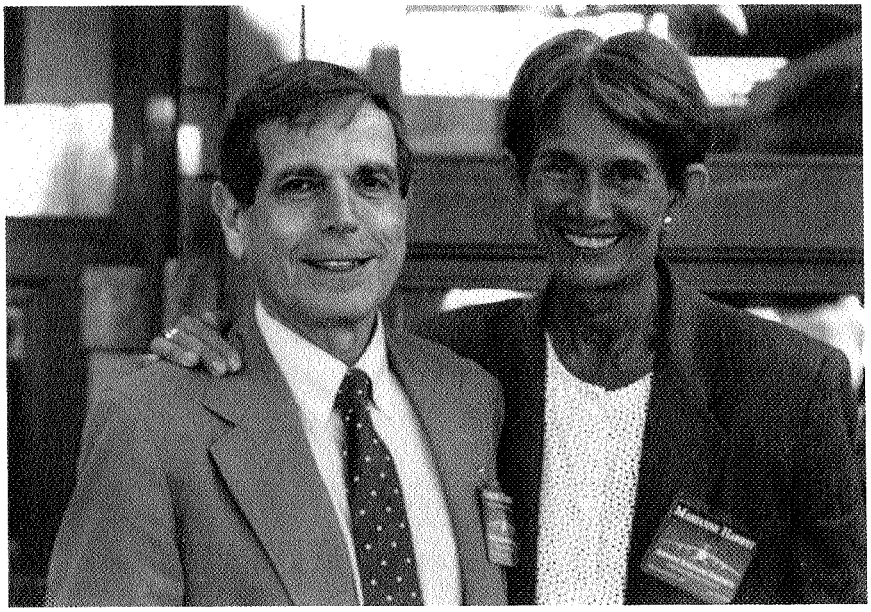

Martin and Marianne Harwit

Airborne Astronomy Symposium on the Galactic Ecosystem
ASP Conference Series, Vol. 73, 1995
M.R. Haas, J.A. Davidson, and E.F. Erickson (eds.)

OPTICAL INSTRUMENTATION FOR AIRBORNE ASTRONOMY

EDWARD W. DUNHAM
Space Science Division, NASA Ames Research Center, Mail Stop 245-6, Moffett Field, CA, 94035-1000

ABSTRACT Two flexible optical CCD camera systems are available for use on the KAO. One is optimized for occultation observations, the other for measurements of airborne image quality and motion.

INTRODUCTION

Optical observations during the KAO's second decade have focused on two general areas, occultation observations and image quality measurements. Both of these pursuits required high-speed imaging instrumentation, but differences in requirements resulted in development of two different high-speed CCD cameras.

SNAPSHOT CCD SYSTEM

The SNAPSHOT CCD camera system was developed and used for airborne image quality observations (Elliot et al. 1989a) and occultation observations (Elliot et al. 1989b). Like most KAO instruments, it has evolved over the years since it was first developed. The original camera (Dunham et al. 1985) was characterized by flexible clocking wave forms, high-speed operation, and precise timing. Early additions included automatic focusing capability, an evacuated pipe through the KAO air bearing, and an occultation mode of operation. Subsequently the SNAPSHOT was modified to its current network-oriented architecture to allow remote operation, and its functionality was split between two computers, as shown in Fig. 1. The system, including these modifications, is still in operation at MIT but no longer flies on the KAO. Further development has proceeded on a second system located at Ames which presently incorporates one 2K square CCD in place of the two smaller CCD's in the original system. The large format of the new detector required major modifications to the operating software, but the basic functionality of the system was unchanged. Some timing specifications also changed because of the detector size and clocking requirements, and are reflected in Table I.

The most recent upgrade was to the KAO, rather than the instrument. This was the installation of a time code generator incorporating a Global Positioning System (GPS) receiver. This unit provides very accurate time signals and position fixes (see Table I). This upgrade marks a major advance over the short-wave WWV time signal synchronization and inertial navigation used in the past.

The flexible optical system allows operation of the CCD camera with different filters, image scales, and ancillary optics. This instrument has carried out successful image quality observations with InSb cameras from the University of Texas and the University of California at Santa Cruz.

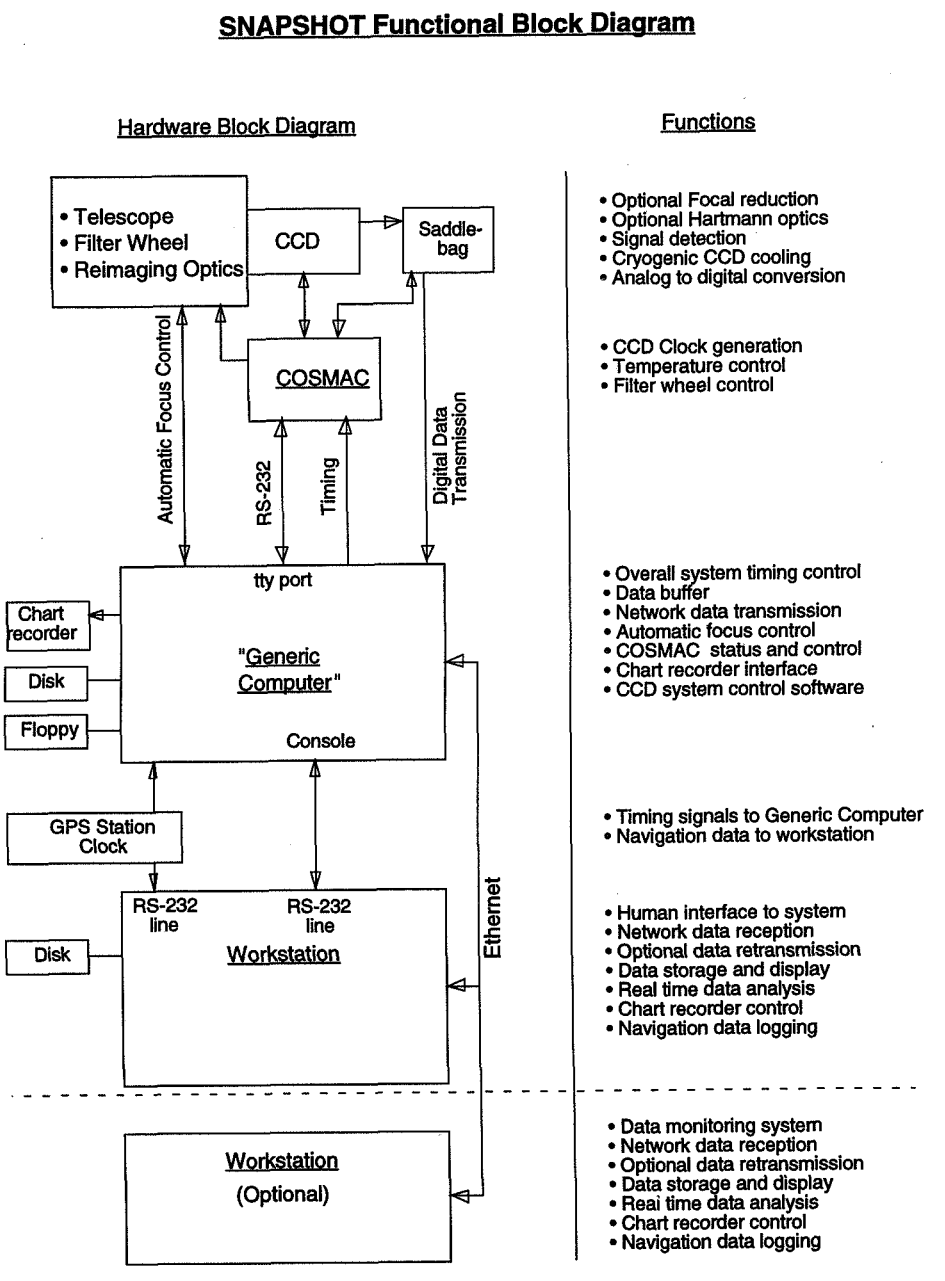

Fig. 1. Functional block diagram of the SNAPSHOT camera system.

TABLE I SNAPSHOT Specifications

- Detector
  CCD Type: Ford/Loral 3-phase frame transfer front illuminated
  Format: 2048x2048 15 μm square pixels with 100,000 e^- full well
  QE: 50% at 0.8 μm; ≥ 20% from 0.3 to 0.9 μm (UV coated)
  Dark Current: ≤ 0.004 electron/px/sec at -125 °C
  Read noise: 100 electrons

- Optics
  Filter Wheel: 6 positions, 2 inch square
  Shack-Hartmann optics and dichroic beamsplitters are available
  Image Scale: 0.22 "/px and 0.66 "/px with 3;1 reimaging optics
  Image Size: 3" FWHM typical

- Time and Position
  Data Rate: 50 KBytes/second, 2 bytes/pixel
  Time/Position: ± 200 nsec and ± 30 meters rms accuracy from GPS

- Operating Modes:
  Single Frames and Shuttered Full Frame Series
  - One or more exposures of a single rectangular subframe per data file
  - Dead time between exposures in a series is equal to the CCD read time
  - Full area of the CCD is available for imaging
  - Mechanical shuttering, minimum exposure time 10 msec

  Dots
  - Very high speed imaging mode
  - A small part of the CCD is available for imaging
  - Mainly used for high speed KAO image motion analysis
  - Time sequence:
    Integrate
    Shift charge down by a set number of rows
    Repeat the integration/shift cycle a set number of times
    Read out the CCD
  - Electronic shuttering, ≥800 μsec for a 20 row shift, 600 msec max.

  Strip Scanning
  - CCD continuously read out at a precise row rate, ≥ 80 msec per row
  - Used on ground based telescopes for occultation predictions
  - Produces an image that is very long in the E-W direction

  Occultation
  - Frame transfer operation to eliminate dead time
  - Half of the CCD is optically masked
  - Time sequence:
    Integrate
    Frame transfer image area to masked storage area
    Image area begins integrating; storage area read out
    After readout, image area completes integration
  - Electronic shuttering, ≥100 msec for 40x40 subframe, 60 sec max.

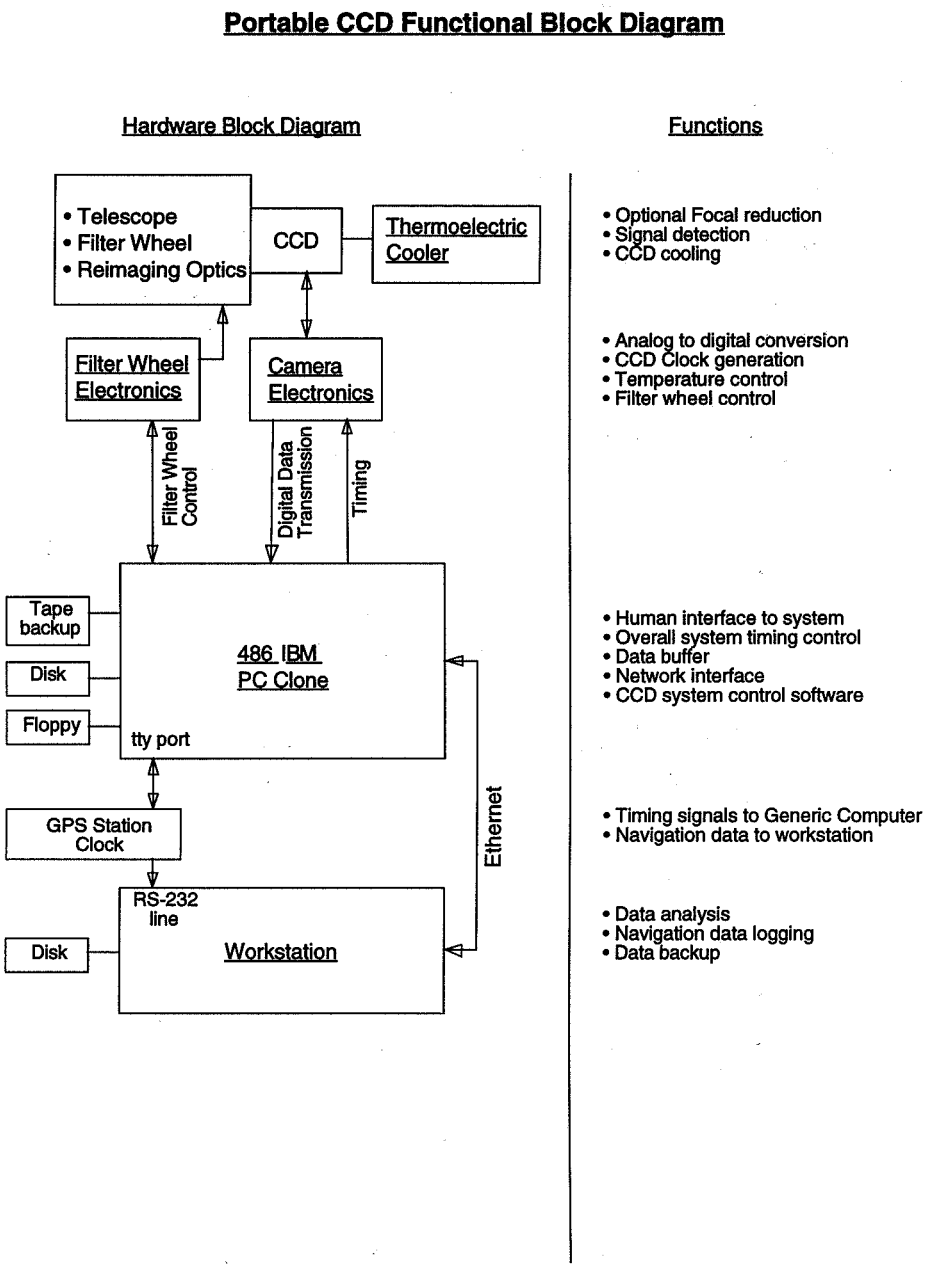

Fig. 2. Functional block diagram of the Portable CCD camera system.

TABLE II PCCD Specifications

- Detector
  CCD Type: Thomson 7883 3-phase frame transfer front illuminated
  Format: 384x576 23 μm square pixels with 160,000 e^- full well
  QE: 40% at 0.7 μm; ≥ 15% from 0.3 to 0.9 μm (UV coated)
  Dark Current: 7.4 electron/px/sec at -45 °C
  Read noise: 12 electrons

- Optics
  Filters: 10 position wheel, 1 inch circles
  Dichroic beamsplitters are available
  Image Scale: 0.33 "/px and 1.00 "/px with 3:1 reimaging optics
  Image Size: 3" FWHM typical

- Time and Position
  Data Rate: 80 KBytes/second, 2 bytes/pixel
  Time/Position: ± 200 nsec and ± 30 meters rms accuracy from GPS

- Operating Modes:
  Single Frames and Shuttered Full Frame Series
  - One or more exposures of 1-5 rectangular subframes per data file
  - Dead time between exposures in a series is equal to the CCD read time
  - Full area of the CCD is available for imaging
  - Mechanical shuttering, minimum exposure time 100 msec

  Strip Scanning
  - CCD continuously read out at a precise row rate, ≥ 30 msec per row
  - Used on ground based telescopes for occultation predictions
  - Produces an image that is very long in the E-W direction

  Occultation
  - Frame transfer operation to eliminate dead time
  - Half of the CCD is optically masked
  - Up to 5 subframes per integration may be observed
  - Time sequence:
    Integrate
    Frame transfer image area to masked storage area
    Image area begins integrating; storage area read out
    After readout, image area completes integration
  - Electronic shuttering, 100 msec minimum for 40x40 subframe

PORTABLE CCD SYSTEM

This instrument is one of four identical instruments developed by a collaboration of investigators at NASA Ames, Lowell Observatory, MIT, and the University of Arizona. The Portable CCD (PCCD) systems were developed to improve the instrumentation available for occultation observations using the KAO and ground based telescopes, both fixed and portable. The Ames system has been used on the KAO to observe a Triton occultation in 1993 (Elliot, et al., 1993) and a Chiron occultation in 1994 (Elliot, et al., 1994). The brief description of the PCCD given here is necessarily incomplete; a more thorough description is in preparation.

The PCCD systems largely utilize commercial components. The basic CCD camera is the Photometrics ATC200L system with 40 KHz, 16-bit digitization electronics, a liquid cooled thermoelectric cooler, and the AT-200 AT-bus controller card. (see Fig. 2 and Table II). The PC-based system was chosen for its flexible clock generation hardware, which allows the PCCD to read out multiple subframes per integration. This allows us to record a comparison star during an occultation, providing a point spread function (PSF) reference for PSF-fitting photometry (Elliot et al. 1994) and a field standard for differential photometry.

The operating software for the system was written by Eliot Young and myself at Ames and recently upgraded by Marc Buie of Lowell Observatory. It allows full PC control of the camera system, including control of operating mode, exposure, filter, readout configuration, selection of data storage method, and image stretch and color table selection. It also provides some on-line analysis functions and interfaces to a GPS time code generator (identical to the unit used on the KAO) to allow real-time PCCD clock synchronization and position determination. The PCCD does not support automatic focusing.

The fore optics modules were designed and built mainly by Marc Buie and Ralph Nye at Lowell Observatory. These modules provide a direct imaging option as well as 1:1 and 3:1 reimaging optics that provide an intermediate focal plane in which a mask may be inserted for frame transfer operation. When the PCCD is used on the KAO, the appropriate fore optics modules are mounted on the SNAPSHOT camera's interface hardware, thereby making the additional flexibility of that optical system available. For the recent Chiron occultation (Elliot et al. 1994) the Lick NICMOS camera was mounted with the PCCD to provide simultaneous optical and K-band observations of the occultation.

FUTURE DIRECTIONS

We will continue to improve and support these instruments for scientific and technical airborne work. Improvements will focus on lowering noise, increasing speed, and providing a more integrated approach for provision of simultaneous visible and infrared observations. We look forward to continued use of these instruments for the program of stellar occultation exploration of the outer solar system with both the KAO and SOFIA. SOFIA's larger aperture and superior image quality will revolutionize our occultation capability. Another fertile application of optical photometry on SOFIA will be in high precision photometry of stellar oscillations. The very low scintillation noise level present in airborne data (Dunham and Elliot, 1983) and low photon noise level achievable with SOFIA will enable observations of low amplitude P-mode oscillations in main sequence dwarf stars that are impossible using large ground-based telescopes.

REFERENCES

Dunham, E.W. and Elliot, J.L. 1983, PASP 95, 325.
Dunham, E.W., Baron, R.L., Elliot, J.L., Vallerga, J.V., Doty, J.P., and Ricker, G.R. 1985, PASP 97, 1196.
Elliot, J.L., Dunham, E.W., Baron, R.L., Watts, A.W., Kruse, S.E., Rose, W.C., and Gillespie, C.M. 1989a, PASP 101, 737.
Elliot, J.L., Dunham, E.W., Bosh, A.S., Slivan, S.M., Young, L.A., Wasserman, L.H., and Millis, R.L. 1989b, Icarus 77, 148.
Elliot, J.L., Dunham, E.W., and Olkin, C.B. 1993, BAAS 25, 1106.
Elliot, J.L., et al. 1994, Nature (submitted).

Airborne Astronomy Symposium on the Galactic Ecosystem
ASP Conference Series, Vol. 73, 1995
M.R. Haas, J.A. Davidson, and E.F. Erickson (eds.)

The Cryogenic Grating Spectrometer

Edwin F. Erickson, Michael R. Haas
NASA/Ames Research Center, MS 245-6, Moffett Field, CA 94035-1000

Sean W. J. Colgan
SETI Institute; NASA/Ames Research Center, MS 245-6, Moffett Field, CA 94035-1000

Janet P. Simpson
UC Berkeley; NASA/Ames Research Center, MS 245-6, Moffett Field, CA 94035-1000

Robert H. Rubin
Orion Enterprises; NASA/Ames Research Center, MS 245-6, Moffett Field, CA 94035-1000

Abstract. The Cryogenic Grating Spectrometer (CGS) first flew on the KAO in 1982 December and has been open to guest investigators since 1984 October. In the past 12 years it has completed over 100 research flights supporting 13 different principal investigators studying a variety of objects. We briefly describe the instrument, its capabilities and accomplishments, and acknowledge the people who have contributed to its development and operation.

1. Introduction

The 1980 proposal to build the Cryogenic Grating Spectrometer (CGS) recognized and recommended use of the then emerging far-infrared (FIR) photoconductor detector technology to achieve background-limited sensitivity for dispersive, high-resolution spectroscopy on the KAO. The instrument is described in Erickson *et al.* (1984a,b; 1985); the CGS design team included experts from a number of institutions. Since these publications, the CGS has evolved significantly to improve and extend its performance, as described below.

2. Configuration/Performance

The CGS utilizes an 18-inch echelle grating with a ruling spacing of 400 μm and a blaze angle of 63° to achieve a spectral resolving power ranging from $\sim$ 1500 at some long wavelengths (low orders) to $\sim$5000 at some short wavelengths (high orders), depending on the specific grating angle used for each wavelength. With

careful calibration, line velocities can be measured to $\sim 1/6^{th}$ of the spectral resolution.

In its "standard" configuration, the CGS focal plane contains thirteen Ge:Be, thirteen Ge:Sb, and six stressed Ge:Ga photoconductors (Table 1). For highest sensitivity at the shortest wavelengths, the Ge:Be detectors can be replaced with the Si:As IBC detectors (Table 1) with some loss in spectral coverage. The dewar is routinely operated at ~2 K and the two shorter wavelength arrays are actively heated to their optimum temperatures, so that all three arrays are simultaneously active in the focal plane. This provides good sensitivity over the entire 16 – 206 μm range on a single flight. As described in Table 1, sensitivities close to background limited performance have been achieved throughout this spectral range. The CGS can select any wavelength in its range in under a minute. Consequently, we routinely observe as many as 20 different wavelengths on a flight; calibration on a bright continuum source such as Saturn or the Kleinmann-Low Nebula typically takes ~2 min per line, including all telescope overheads and grating moves.

Table 1
Detector Configuration and Performance

Detector Type:	Si:As	Ge:Be	Ge:Sb	Ge:Ga
λ range (μm)	16-27	16-50	50-125	125-206
λ_T = typical λ (μm)	26	36	88	158
NEP measured at λ_T (10^{-14} W/$\sqrt{\text{Hz}}$)	1.2 ± 0.3	2.7 ± 0.5	0.5 ± 0.2	0.3 ± 0.1
Calculated BLIP NEP (10^{-14} W/$\sqrt{\text{Hz}}$)	1.1	1.7	0.4	0.3

For work on SN 1987A, the CGS was retrofitted with an array of 39 Si:As IBC detectors to permit operation at shorter wavelengths and with a lower resolution grating (ruling spacing of 36 μm and a blaze angle of 19°) to provide spectral coverage for the supernova's broad lines. This configuration permitted measurements of the ~3000 km/s wide lines from the supernova at wavelengths as short as the 6.6 μm Ni II line (Colgan *et al.* 1994).

3. Scientific Results

With its easy access to a broad range of wavelengths, the CGS has been used to study numerous lines between 6 and 206 μm. Table 2 lists the FIR fine-structure lines measured with the CGS. These lines sample a range of excitation and density (as indicated by their ionization potential, I.P., and critical density, N_{crit}, in the table) and so permit determination of a variety of conditions in the interstellar gas. This has led to the study of a wide assortment of objects, including H II regions, photodissociation regions (PDRs), interstellar shocks from supernovae and young stellar objects, planets, SN 1987A, evolved stars, planetary nebulae, reflection nebulae, the Galactic center region, and galactic nuclei.

As an example, we show a measurement of the previously undetected line of Fe^{++} at 22.9 μm (a ground state transition) in Figure 1. The CGS has been

Table 2

FIR Fine-Structure Lines Measured with the CGS

Species	λ (μm)	$\log N^{\dagger}_{crit}$ (cm^{-3})	I.P. Range (eV)
Ni II	6.6	7.0	7.6–18.2
Fe II	17.9	4.7	7.9–16.2
S III	18.7	4.1	23.4–35.0
• Fe III	22.9	4.8	16.2–30.6
Ne V	24.3	4.7	97.0–126.3
• S I	25.2	6.3	0.0–10.4
O IV	25.9	4.0	54.9–77.4
• Fe II	26.0	6.3	7.9–16.2
S III	33.5	3.3	23.4–35.0
• Si II	34.8	5.5	8.1–16.3
• Ne III	36.0	4.3	41.1–63.5
O III	51.8	3.5	35.1–54.9
N III	57.3	3.3	29.6–47.4
O I	63.2	5.7	0.0–13.6
O III	88.4	2.7	35.1–54.9
• N II	121.9	2.4	14.5–29.6
O I	145.5	5.0	0.0–13.6
C II	157.7	3.4	11.3–24.4
N II	205.3	1.6	14.5–29.6

• First detected with the CGS

† N_{crit} for collisions with e^- (I.P.> 13.6 eV) or H (I.P.< 13.6 eV).

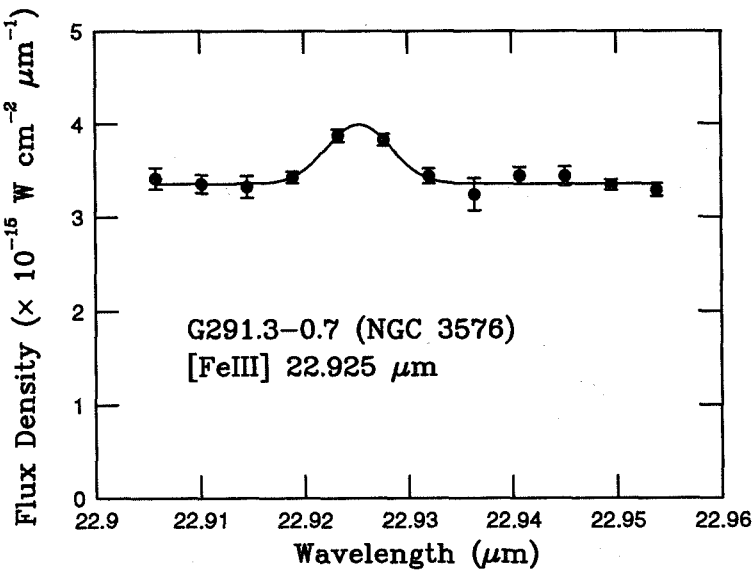

Figure 1. The [Fe III] 22.925 μm line in G291.3–0.7 (NGC 3576).

used to measure this line in six bright H II regions: G291.3–0.7 (NGC 3576), G291.6–0.5 (NGC 3603), G298.2–0.3, G333.6–0.2, W51, and the Orion nebula. The average of the Doppler-corrected wavelengths for these sources is 22.925 ± 0.002 μm, in good agreement with the calculated value. The low energy required to excite this transition and the abundant ionization state it characterizes suggest its importance for probing the iron abundance in H II regions. We use measurements of the density and excitation sensitive [O III] (52 and 88 μm) and [S III] (19 and 33 μm) lines made on the same flights to further characterize the nebulae, and have incorporated a 17-level iron atom in our nebular code, to compare with the measurements. Our analysis indicates that the gas-phase iron in these nebulae is considerably more abundant than in the diffuse interstellar medium, but is still significantly depleted. Most of the iron probably still resides in grains.

Molecular features and recombination lines measured with the CGS are listed in Table 3. As with the fine-structure lines, a number of these were measured for the first time with the CGS.

Table 3

Molecular and H-Recombination Lines Measured with the CGS

Species	λ (μm)	Dissociation Energy (eV)
H_2	17	4.5
H I	52.5*	–
OH	84.4*, 84.6*, 119	4.4
CH	149, 202*	3.5
CO	96, 118, 153, 200*	11.1
PH_3	103.2*	$\lesssim$4.3

* First detected with the CGS

The CGS has now successfully completed more than 100 research flights and has supported thirteen different principal investigators. The publications resulting from this work are given in §6 and some results in preparation are listed in §7.

4. Personnel

Participants in the development and operation of the CGS are recognized in Table 4. Many of those listed are students. In addition, the continued support of the entire KAO staff over the years has been essential to the success of the CGS. We are pleased to thank all for their contributions and apologize to anyone whose name has been inadvertently omitted.

5. The Future

Our experience with the CGS has demonstrated the power of this type of instrument. We are now considering the design of the next generation Airborne Infrared Echelle Spectrometer - AIRES - which will include the virtues of

the CGS (wide, contiguous wavelength coverage and the ability to acquire data without scanning) while increasing the spectral resolving power and incorporating the ability to image in the cross-dispersion direction. Preliminary work on the AIRES design is described by Haas *et al.* (1994).

Table 4

Participants in the CGS Development and Operations

George Anderson	- electronics engineer
Gordon C. Augason	- filters, science development team
James A. Baltz	- project engineer for operations
Dave Barewald	- drafting
Jeff W. Beeman	- detector fabrication
Eugene Bekstrom	- group technician
Glenn Boozer	- data acquisition software
Martin Burgdorf	- synchronous detection noise tests
Sean W. J. Colgan	- guiding, data analysis, filters
Hal Collard	- procurement, filter fabrication
Bruce DeBlois	- detector characterization
Phil B. Duffy	- prototype detector array
Edwin F. Erickson	- principal investigator, science development team
James Freel	- calibrator fabrication
George Gull	- prototype detector array
Michael R. Haas	- project scientist
Nancy M. Haegel	- detector fabrication
Eugene E. Haller	- detector fabrication
Bruce Hamilton	- data acquisition software
Martin O. Harwit	- spectrometer testing, science development team
Fred Haynes	- guiding software
Robert C. Hogan	- filters, data acquisition (software) menus
David J. Hollenbach	- stress analysis, science development team
James R. Houck	- prototype detectors, science development team
Nancy Jennerjohn	- specialized procurements
Robert Johnson	- structural analysis
Hank Kondracki	- cryostat design
David Lee	- data analysis software
Peter Lissol	- mechanical design
Erwin Loewen	- grating consulting and fabrication
Steven D. Lord	- atmospheric transmission computer program
Scott Matthews	- optical ray tracing
George McIntosh	- cryostat design
Darrell McKibbin	- data acquisition software
Allen Meyer	- data analysis
Rafael Miranda	- synchronous demodulation software
Michel Neviere	- grating efficiency calculations
Jim Pantaleo	- HP 1000 computer interface
David Parker	- baffle layout
Bruce Pittman	- project manager for development

Table 4, Cont.

CGS Design, Development, Fabrication, Assembly, Test, and Operations Team

Al Ragasa	- electronics technician
David M. Rank	- cryostat design, science development team
Ray Russell	- stressed detectors
Tom Schultz	- detector assembly mechanical design
David Scimeca	- thermal cycling
Janet P. Simpson	- flight planning, science development team
Robert Smithson	- cryostat fabrication
Gordon J. Stacey	- spectral line fitting routines
Rodger Thompson	- baffle design
Dustin Tranberg	- cabling, software
David Ungar	- hardware interface software
Paul J. Viscuso	- spectrometer testing
Michael W. Werner	- filter specification, science development team
Jürgen Wolf	- detector and preamplifier development
Robert Zeiger	- spectrometer fabrication

6. Refereed Publications Resulting from Work with the CGS

Burton, M. G., Hollenbach, D. J., Haas, M. R., & Erickson, E. F. 1990, ApJ, 355, 197. "Shocked [O I] 63 μm Line Emission from the SNR IC 443."

Carral, P., Hollenbach, D. J., Lord, S. D., Colgan, S. W. J., Haas, M. R., Rubin, R. H., & Erickson, E. F. 1994, ApJ, 423, 223. "The Interstellar Medium in the Starburst Regions of NGC 253 and NGC 3256."

Cohen, M., Hollenbach, D. J., Haas, M. R., & Erickson, E. F. 1988, ApJ, 329, 863. "Observations of the 63-micron [O I] Line in Herbig-Haro Objects."

Colgan, S. W. J., Haas, M. R., Erickson, E. F., Lord, S. D., & Hollenbach, D. J. 1994, ApJ, 427, 874. "Day 640 Infrared Line and Continuum Measurements: Dust Formation in SN 1987A."

Colgan, S. W. J., Haas, M. R., Erickson, E. F., Rubin, R. H., Simpson, J. P., & Russell, R. W. 1993, ApJ, 413, 237. "Detection of the [N II] 122 and 205 μm Lines: Densities in G333.6-0.2."

Colgan, S. W. J., Simpson, J. P., Rubin, R. H., Erickson, E. F., Haas, M. R., & Wolf, J. 1991, ApJ, 366, 172. "Far-Infrared Lines from G45.13+0.14A and K3-50 A: Density Fluctuations in Compact H II Regions"

Duffy, P. B., Erickson, E. F., Haas, M. R., & Houck, J. R. 1987, ApJ, 315, 68. "Far Infrared Spectroscopy of Star Formation Regions in M82."

Erickson, E. F., Colgan, S. W. J., Simpson, J. P., Rubin, R. H., Morris, M., & Haas, M. R. 1991, ApJ, 370, L69. "Far-Infrared Line and Continuum Observations of G0.095+0.012 and the E2 Thermal Radio Filament Near the Galactic Center."

Erickson, E. F., Haas, M. R., Colgan, S. W. J., Lord, S. D., Burton, M. G., Wolf, J., Hollenbach, D. J., & Werner, M. W. 1988, ApJ, 330, L39, "Observation of Fe II (26.0 Microns) in SN 1987A."

Haas, M. R., Colgan, S. W. J., Erickson, E. F., Lord, S. D., Burton, M. G., & Hollenbach, D. J. 1990, ApJ, 360, 257. "Velocity Resolved Far-Infrared

Spectra of [Fe II]: Evidence for Mixing and Clumping in SN 1987A."
Haas, M. R., Erickson, E. F., Goorvitch, D., McKibbin, D. D., & Rank, D. M. 1985, Icarus, 64, 549. "Observations of the J = 10 Manifold of the Pure Rotational Band of Phosphine on Saturn." Erratum published in 1986, Icarus, 67, 342.
Haas, M. R., & Glassgold, A. E. 1993, ApJ, 410, L111. "Detection of O I and Si II Far-Infrared Fine-Structure Emission from Alpha Orionis."
Haas, M. R., Hollenbach, D. J., & Erickson, E. F. 1986, ApJ, 301, L57. "Detection of [Si II] (34.8 Micron) Emission in Orion-KL: A Measurement of the Silicon Abundance in Dense Interstellar Gas."
Haas, M. R., Hollenbach, D. J., & Erickson, E. F. 1991, ApJ, 374, 555. "Observations of [Si II] (35 μm) and [S I] (25 μm) in Orion: Evidence for a Wind Shock near IRc2."
Lane, A. P., Haas, M. R., Hollenbach, D. J., & Erickson, E. F. 1990, ApJ, 361, 132. "Far-Infrared Spectroscopy of the DR 21 Star Formation Region."
Meixner, M. M., Haas, M. R., Tielens, A. G. G. M., Erickson, E. F., & Werner, M. W. 1992, ApJ, 390, 499. "Far-Infrared Observations of M17SW: The Clumpy Structure of the Photodissociation Region."
Petuchowski, S. J., Bennett, C. L., Haas, M. R., Erickson, E. F., Lord, S. D., Rubin, R. H., Colgan, S. W. J., & Hollenbach, D. J. 1994, ApJ, 427, L17. "The [N II] 205 Micron Line in M82: The Warm Ionized Medium."
Rubin, R.H. 1989, ApJS, 69, 897. "The Effect of Density Variations on Elemental Abundance Ratios in Gaseous Nebulae."
Rubin, R. H., Simpson, J. P., Erickson, E. F., & Haas, M. R. 1988, ApJ, 327, 377. "Determination of N/O from Far-Infrared Line Observations of Galactic H II Regions"
Rubin, R. H., Simpson, J. P., Haas, M. R., & Erickson, E. F. 1991, ApJ, 374, 564. "Axisymmetric Model of the Ionized Gas in the Orion Nebula."
Rubin, R. H., Simpson, J. P., Haas, M. R., & Erickson, E. F. 1991, PASP, 103, 834. "Modeling the Orion Nebula as an Axisymmetric Blister."
Rubin, R. H., Simpson, J. P., Lord, S. D., Colgan, S. W. J., Erickson, E. F., & Haas, M. R. 1994, ApJ, 420, 772. "Nebular Properties from Far-Infrared Spectroscopy."
Simpson, J. P., Colgan, S. W. J., Rubin, R. H., Erickson, E. F., & Haas, M. R. 1995, ApJ, in press. "Far Infrared Lines from H II Regions: Abundance Variations in the Galaxy."
Simpson, J. P., Rubin, R. H., Erickson, E. F., Haas, M. R. 1986, ApJ, 311, 895. "The Ionization Structure of the Orion Nebula: Infrared Line Observations and Models."
Viscuso, P. J., Stacey, G. J., Harwit, M., Haas, M. R., Erickson, E. F., & Duffy, P. B. 1985, ApJ, 296, 149. "Observation of Far-Infrared Transitions between Excited States of OH."

In addition, the papers in this Volume by Simpson (1.5), Afflerbach (113), Rubin (114), Lord (2.2), Strelnitski (305), Dinerstein (5.2), Haas (5.4), Justannont (504), Erickson (6.4), and Colgan (604) present and discuss CGS data and the papers by Wooden (5.5) and Genzel (6.0) also include some CGS results.

7. Publications in Preparation Describing CGS Observations

Colgan, S. W. J., Erickson, E. F., Simpson, J. P., Haas, M. R., & Morris, M. "Excitation of the 'Arched' Filaments near the Galactic Center."

Erickson, E. F., Colgan, S. W. J., Simpson, J. P., Rubin, R. H., & Haas, M. R. "Far-Infrared Line and Continuum Observations of Sgr A West."

Erickson, E. F., Rubin, R. H., Haas, M. R., Simpson, J. P., & Colgan, S. W. J. "[Fe III] (22.9 μm) Emission from H II Regions."

Lord, S. D., Hollenbach, D. J., Colgan, S. W. J., Haas, M. R., Rubin, R. H., Madden, S. C., Steiman-Cameron, T. Y., Carral, P., Maloney, P. R., Erickson, E. F. "Far-Infrared Spectroscopy of Bright IRAS Galaxies."

Lord, S. D., Hollenbach, D. J., Haas, M. R., Rubin, R. H., Colgan, S. W. J., Erickson, E. F. "Far Infrared Spectroscopy of the Nucleus of M82."

Petuchowski, S. J., Bennett, C. L., Colgan, S. W. J., Haas, M. R., & Erickson, E. F. "Detection of a 202.9 μm Line and Possible Attribution to Collisionally Excited CH."

Petuchowski, S. J., Bennett, C. L., Haas, M. R., Colgan, S. W. J., & Erickson, E. F. "The Height of Ionized Gas in the Inner Galaxy"

Steiman-Cameron, T.Y., Haas, M. R., & Tielens, A. G. G. M. "Infrared Observations and Physical Parameters of the Reflection Nebula NGC 2023."

8. References

Colgan, S. W. J., Haas, M. R., Erickson, E. F., Lord, S. D., & Hollenbach, D. J. 1994, ApJ, 427, 874. "Day 640 Infrared Line and Continuum Measurements: Dust Formation in SN 1987A."

Erickson, E. F., Houck, J. R., Harwit, M. O., Rank, D. M., Haas, M. R., Hollenbach, D. J., Simpson, J. P., & Augason, G. C. 1985, Infrared Physics, 25, 513. "A FIR Cooled Grating Spectrometer for the Kuiper Airborne Observatory."

Erickson, E. F., Houck, J. R., Harwit, M. O., Rank, D. M., Haas, M. R., Hollenbach, D. J., Simpson, J. P., Augason, G. C., & McKibbin, D. D. 1984a, Symposium on Airborne Astronomy, NASA Conference Publication 2353, eds. H. Thronson & E. Erickson, p. 313. "A Far Infrared Echelle Spectrometer for the Kuiper Airborne Observatory."

Erickson, E. F., Matthews, S., Augason, G. C., Houck, J. R., Harwit, M. O., Rank, D. M., & Haas, M. R. 1984b, Proc. SPIE, 509, 129. "All-aluminum Optical System for a Large Cryogenically Cooled Far Infrared Echelle Spectrometer."

Haas, M. R., Erickson, E. F., Colgan, S. W. J., Baltz, J. A., & Lynch, D. H. 1994, in Proc of the Airborne Astronomy Symp on the Galactic Ecosystem: From Gas to Stars to Dust, eds. M. R. Haas, J. A. Davidson, & E. F. Erickson (San Francisco: ASP), paper 703. "Design Considerations for a Large Airborne Infrared Echelle Spectrometer."

Airborne Astronomy Symposium on the Galactic Ecosystem
ASP Conference Series, Vol. 73, 1995
M.R. Haas, J.A. Davidson, and E.F. Erickson (eds.)

Design Considerations for a Large Airborne Infrared Echelle Spectrometer (AIRES)

Michael R. Haas, Edwin F. Erickson
NASA/Ames Research Center, MS 245-6, Moffett Field, CA 94035-1000

Sean W. J. Colgan, James A. Baltz
SETI Institute; NASA/Ames Research Center, MS 245-6, Moffett Field, CA 94035-1000

Dana H. Lynch
NASA/Ames Research Center, MS 213-2, Moffett Field, CA 94035-1000

Abstract. We propose a new facility instrument: the Airborne Infra-Red Echelle Spectrometer or '**AIRES**'. The scientific rationale, a preliminary optical and mechanical design, and the instrument's estimated performance are presented. Some of the major technical challenges are discussed.

Introduction

Twenty years of spectroscopy on the KAO, as well as large scale mapping by IRAS and COBE, have demonstrated the importance of the many far-infrared atomic and molecular transitions to the energy budget of the interstellar medium (ISM). Observations of these lines provide information on the temperatures, densities, excitation, abundances, and dynamics of the emitting gas. Our scientific and technical experience with the Cryogenic Grating Spectrometer (CGS; Erickson *et al.* 1994) has motivated us to propose a new, more capable KAO facility instrument: the Airborne Infra-Red Echelle Spectrometer (AIRES). Its major advantages over the CGS are its higher spectral resolution ($\sim 4-60$ km/s) and its ability to do diffraction-limited imaging of a $\sim 5'$ strip in the cross-dispersion direction. AIRES will nevertheless retain important CGS characteristics, including operation over a broad wavelength range ($16-210\ \mu$m), simultaneous measurement of lines and their adjacent continua, and the ability to change wavelengths rapidly.

The consideration of such an instrument is now possible because of the steady progress in grating technology and the ongoing advances in the development of two-dimensional infrared arrays. The imaging capability of AIRES will greatly improve mapping efficiency; the increased spectral resolution will provide greater sensitivity and additional dynamical information about the emitting gas. The increased sensitivity accrues from both reduced thermal backgrounds on the detectors (from sky and telescope) and larger line-to-continuum ratios for unresolved lines.

Optical Design

As discussed by Erickson *et al.* (1984a,b), our design goals for AIRES are best met by a grating spectrometer. Figure 1 shows a simplified optical diagram with mirrors depicted as lenses. The principal subsystems are the K-mirror (K1 – K3), which adjusts and maintains field rotation in the desired orientation, the predisperser (P1, P2, PS, PG), which sorts orders for the echelle (ES, E1 – E5, EG), and the detectors (D1 – D3). Oversized, off-axis reflecting optics eliminate chromatic aberrations and assure that diffraction effects are dominated by the telescope.

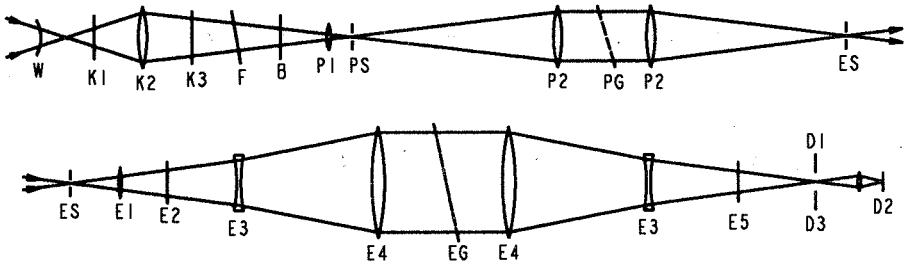

Figure 1. Simplified Optical Diagram for AIRES.

The telescope is focused between the cryostat window W and the flat K1. The off-axis ellipsoid K2 converts the $f/12$ telescope beam to $f/24$ and forms a pupil downstream of flat K3, where a Lyot stop is located near the selectable long-pass filter (F). The flat B directs the beam to the ellipsoid P1 near the predisperser entrance slit PS; P1, in conjunction with the paraboloidal collimator P2, reimages the pupil at the predisperser grating PG. The beam diffracted in the Littrow mode by PG returns to P2, which focuses it onto the echelle entrance slit ES. Thence E1 reimages the pupil through the echelle collimator (injection flat E2, hyperboloid E3, and paraboloid E4) at the center of the echelle grating EG, which also operates in Littrow mode. The collimator reimages the output beam via the flat E5 onto the detectors (D1 – D3).

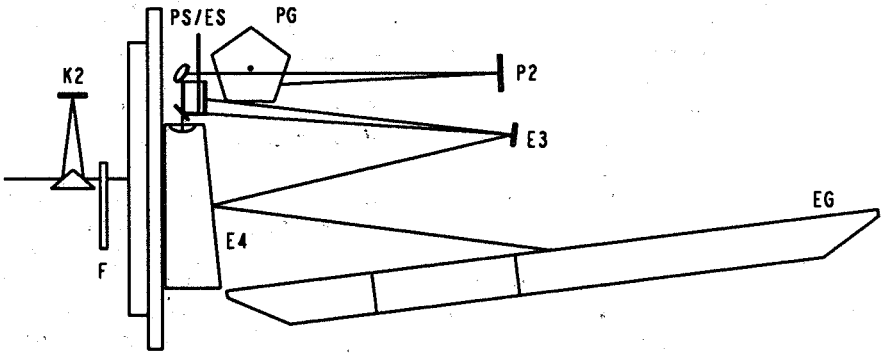

Figure 2. Side View of Optical Layout for AIRES.

Figure 2 shows a side view of the optical system with the central ray indicated by a solid line. The predisperser carousel (PG) contains five small gratings blazed at 19°, which are used in first order Littrow mode between 14.5 and 25° to maintain an optical efficiency $\gtrsim$75%. PG ruling spacings of 32, 53, 90, 150, and 250 μm give cut-on wavelengths of 16, 27, 45, 75, and 125 μm, respectively. The echelle operates between the angles of 56 – 77° in orders 6 – 80 to cover the entire 16 – 210 μm wavelength range. Its efficiency near the blaze angle typically exceeds 60%. The entire optical system operates in a liquid-helium cooled cryostat to minimize thermal emission on the detectors.

The Echelle Grating

Grating length is the limiting factor in achieving high resolution in a grating spectrometer. AIRES uses a 48 inch long, 12 inch wide, 76° blaze angle echelle with a 654 μm groove spacing (the corresponding CGS parameters are 18 inches, 6 inches, 63°, and 400 μm). Gratings blazed at 76° have become popular because they reduce the overall instrument size – compared to a 63.5° blaze angle grating with the same resolution, a 76° blaze angle grating is 8% shorter and requires a collimator with only half the diameter.

This grating is the most challenging aspect of the AIRES development. The 18-inch echelle in the CGS is still one of the largest monolithic gratings ever successfully ruled. Significantly larger gratings have been constructed from several segments arranged in a mosaic to provide increased light gathering power, but these have not been fully phased for increased resolution. However, at FIR wavelengths, the mechanical tolerances are 30× less stringent than for visible-light gratings and several manufacturers may possess the technical capability to rule such a large, coarse, monolithic grating.

We have established machining tolerances for the grating following Hutley (1982) and have identified several sources of cast aluminum alloys, such as A201, which are low in silicon and particularly well-suited for diamond machining. The grating blank could be fabricated in a light weight, near net shape, stress free configuration with a preferential layer optimized for optical turning. These alloys show excellent dimensional stability, low inclusion densities, low scatter, and high infrared reflectivity (Ogloza *et al.* 1988).

Mechanical Design

The AIRES cryostat is 28 inches in diameter and 70 inches in length, with a 24-inch diameter helium work surface. The vacuum enclosure has dished ends and circumferential stiffener rings to allow thin-walled construction for minimum weight. G-10 fiberglass tubes are used for thermally isolated structural support. The nitrogen reservoir is a toroid encircling the helium space at its midpoint and the helium reservoir is a dished, stay-reinforced cylinder at the rear of the cryostat. Both thermal enclosures are wrapped with multiple layers of super insulation and the reservoirs are sized for 30-hour hold times (unpumped). The spectrometer and its enclosure must operate below ~7 K to keep the background on the stressed detectors below that from the telescope as seen through the spectrometer.

To keep AIRES' center of mass close to the air bearing and minimize its peripheral hardware, the spectrometer is inserted into the KAO's Nasmyth instrument cavity with the optical bench at the window-end of the cryostat. The CCD offset guider is located at the Cassegrain focus using a dichroic tertiary to reduce weight, eliminate specialized foreoptics, simplify the mounting arrangement, and reduce the background on the detectors. To minimize gravity-induced deformation, the echelle is supported with the same mounting system and in nearly the same orientation as during the ruling process. The spectrometer can be removed from the cryostat without disturbing the cryogen reservoirs, super insulation, major heat shield enclosures, wire harnesses, or mechanical shafts.

Detector Arrays and Performance

Our design incorporates a Rockwell 128 x 128 Si:Sb impurity band conduction (IBC) array for $16 < \lambda < 42$ μm, a 12 x 16 array of discrete Ge:Sb photoconductors (PCs) for $42 < \lambda < 125$ μm, and a 6 x 8 array of stressed Ge:Ga PCs for $125 < \lambda < 210$ μm. The Ge:Sb array has a 2 mm pitch, so the $f/24$ beam gives 20″/pixel, comparable to the diffraction limit of the KAO telescope at ~ 70 μm; the stressed Ge:Ga array has a 4 mm pitch and is diffraction limited near 140 μm; the Si:Sb IBC array has a 75 μm pitch and receives the beam converted to $f/7.2$ by an antireflection-coated camera lens placed ahead of the array, resulting in a scale of 2.5″/pixel. All three arrays are simultaneously active in the focal plane with no moving parts.

Assuming background limited performance (BLIP), typical system noise equivalent powers (NEPs) are estimated to be 5, 20, and 8×10^{-16} W/$\sqrt{\text{Hz}}$ for resolutions of 35000, 20000, and 8000 at wavelengths of 35, 63, and 158 μm, corresponding to the transitions of [Si II], [O I], and [C II]. Going from long to short wavelengths, the theoretical NEPs for AIRES are 2 to 25× smaller than those for the CGS, whose performance is typically within 1.3 – 2×BLIP.

References

Erickson, E. F., Matthews, S., Augason, G. C., Houck, J. R., Rank, D. M., & Haas, M. R. 1984a, Proc. SPIE, 509, 129

Erickson, E. F., Houck, J. R., Harwit, M. O., Rank, D. M., Haas, M. R., Hollenbach, D. J., Simpson, J. P., Augason, G. C., & McKibbin, D. D. 1984b, Symp on Airborne Astronomy, NASA Conf Pub 2353, H. Thronson & E. Erickson, editors, p. 313

Erickson, E. F., Haas, M. R., Colgan, S. W. J., Simpson, J. P., & Rubin, R. H. 1994, Proc of the Airborne Astronomy Symp on the Galactic Ecosystem: From Gas to Stars to Dust, poster 702

Hutley, M. C. 1982, "Diffraction Gratings", Academic Press

Ogloza, A. A., Decker, D. L., Archibald, P. C., O'Connor, D. A., & Bueltmann, E. R. 1988, 32nd Annual Intl Tech Symp on Opt & Optoelectronic Appl Sci & Eng, San Diego

Airborne Astronomy Symposium on the Galactic Ecosystem
ASP Conference Series, Vol. 73, 1995
M.R. Haas, J.A. Davidson, and E.F. Erickson (eds.)

The Yerkes Observatory 60-Channel Far Infrared Camera for the Kuiper Airborne Observatory

D. A. Harper, D. M. Cole, R. F. Loewenstein, T. McMahon, R. J. Pernic, and C. Wirth

University of Chicago, Yerkes Observatory, Williams Bay, WI 53191

Abstract. The Yerkes Observatory Far Infrared Camera employs a two-dimensional, 60-detector array of ^{3}He-cooled silicon bolometers for broadband imaging in the spectral range of 40 – 240 μm. Four interchangeable filters have effective wavelengths of 60, 100, 160, and 200 μm. Three interchangeable lens sets give pixel sizes of 17″, 27″, and 45″. Signals are processed through nitrogen-temperature JFET source-follower amplifiers, warm preamplifiers, and digital signal processors, and the system is controlled through a graphical user interface on a Macintosh computer. The camera has been used to image a wide variety of galactic and extragalactic far infrared sources.

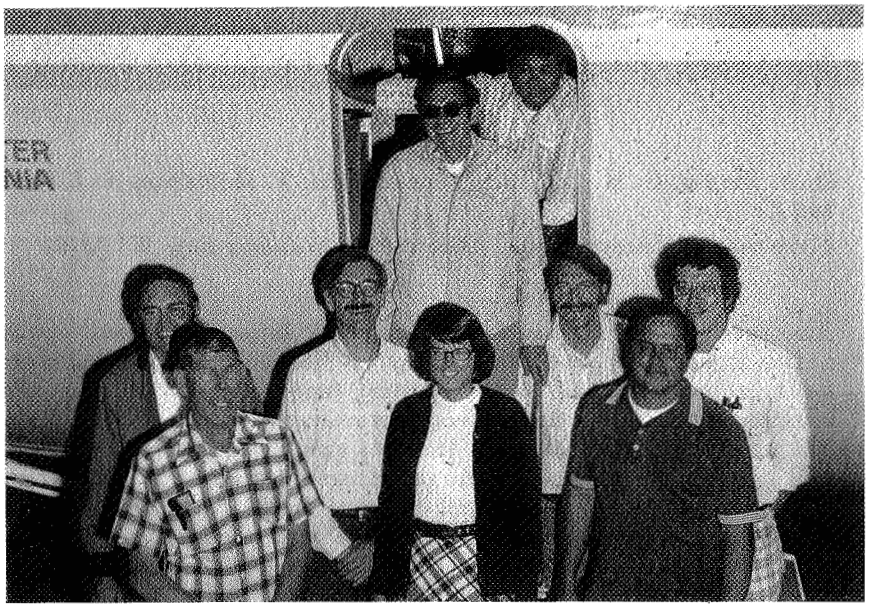

Doorway: Dave Goorvitch, Al Ragasa; *Front:* Fred Witteborn, John Gerdts, Ed Erickson, Jan Simpson, Larry Caroff, Gene Bekstrom, Don Strecker (1975)

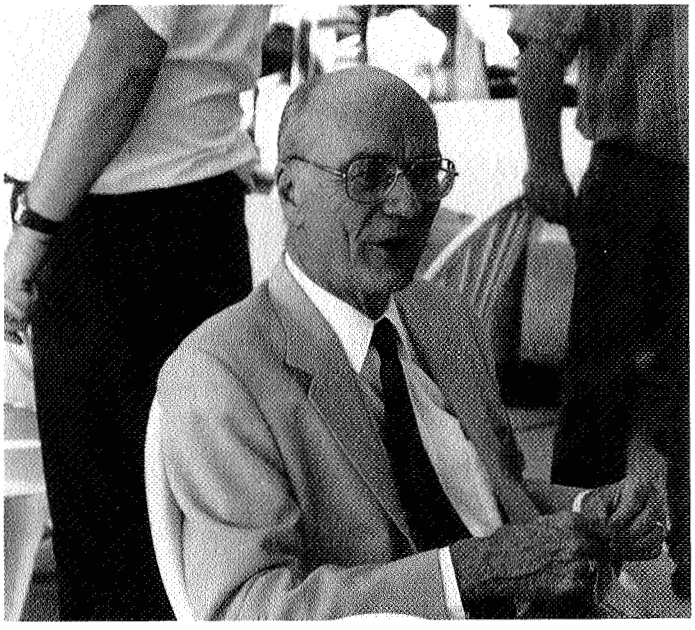

Don Osterbrock

Airborne Astronomy Symposium on the Galactic Ecosystem
ASP Conference Series, Vol. 73, 1995
M.R. Haas, J.A. Davidson, and E.F. Erickson (eds.)

A Diffraction-Limited Far-Infrared Imager for the KAO

P. M. Harvey, B. Smith, C. Colomé, J. Di Francesco, D. F Lester, and D. Sill
Astronomy Department, University of Texas, Austin, TX 78712

Abstract. We describe both our current instrument and a follow-on instrument expected to be operational at the start of the next flight year on the KAO. The current instrument uses a 20-channel bolometer array arranged in two columns of 10 detectors each. Broadband observations can be made at the true diffraction limit, $\lambda/2D$, at either 50 or 100 μm during a flight. Our forthcoming system will use two arrays of 3×10 detectors to enable simultaneous imaging at both 50 and 100 μm at the KAO diffraction limit for each wavelength. Observing modes and typical sensitivities will be discussed.

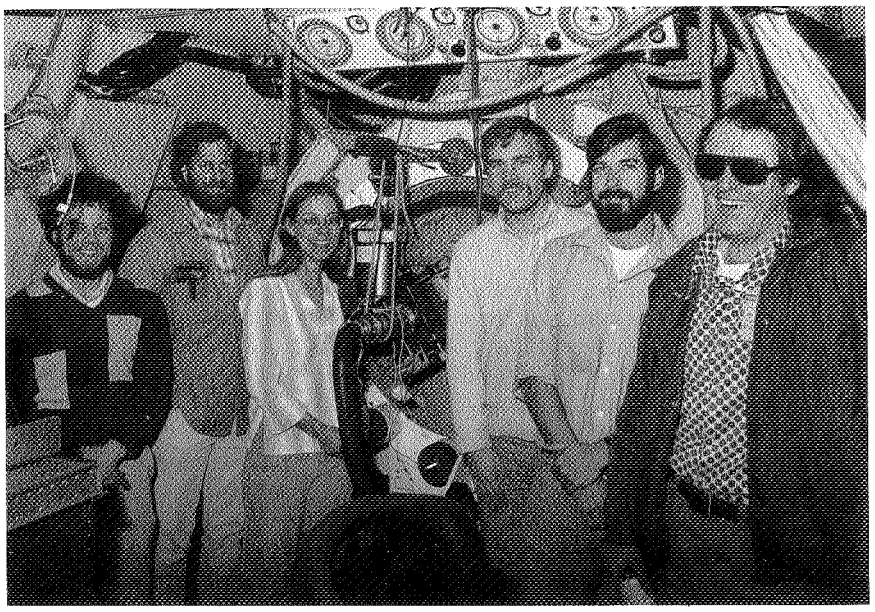

Ed Shaya, Al Harper, Jocelyn Keene,
Harvey Moseley, Bob Loewenstein, Jim Smith (1979)

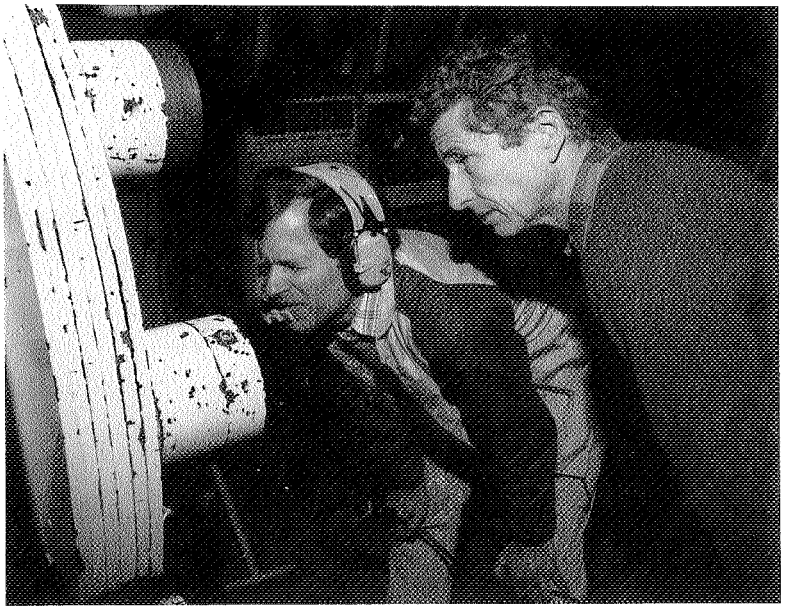

Al Harper, Roger Hildebrand (1980)

Airborne Astronomy Symposium on the Galactic Ecosystem
ASP Conference Series, Vol. 73, 1995
M.R. Haas, J.A. Davidson, and E.F. Erickson (eds.)

THE KUIPER WIDEFIELD INFRARED CAMERA (KWIC)

H. LATVAKOSKI, G. J. STACEY, T. L. HAYWARD, G. E. Gull
AND L. PENG
Cornell University, Ithaca New York, 14850

ABSTRACT KWIC is a wide-field (5.8'×5.8') imaging spectrometer for use on the KAO in the wavelength range of 18 to 44μm. Two resolution modes, R=35→200 and R=2000→10,000 are available. Diffraction limited and near background limited images were obtained on the first flights.

INTRODUCTION

KWIC (Kuiper Widefield Infrared Camera) is an imaging spectrometer and spectrophotometer designed for use between 18 and 44 μm on the Kuiper Airborne Observatory (KAO). KWIC's detector is a SIRTF funded Rockwell International 128×128 pixel Si:Sb Blocked Impurity Band (BIB) array. The pixel scale of 2.73"×2.73" over-samples the diffraction lobe from the KAO (8" at 35 μm) and still provides a 5.8'×5.8' field of view. Spectral resolution is attained by the use of two cryogenically cooled, fully tunable, scanning Fabry-Perot interferometers (FPI's) in series. A single low order FPI (LOFPI) is required for imaging spectrophotometer mode (R=35→200). A second high order FPI (HOFPI) is inserted into the beam for imaging spectrometer mode (R=2000→10,000). The HOFPI can be put into and taken out of the beam within 30 seconds to switch modes in flight. The entire field of view has uniform spectral and spatial properties.

KWIC addresses several important astrophysical problems. The fine-structure lines available to KWIC (see Table 1) are excellent probes of the density and ionization structure of interstellar gas clouds. The far-IR continuum arises from warm (T~85°K) dust heated by nearby starlight. Our primary scientific goals include exploration of molecular cloud structure and star formation activity on local and galactic scales, investigations of the complex structure of the gas clouds near the Galactic Center, and direct imaging of the dust disks thought to envelope young stellar objects and selected main sequence stars.

KWIC was very successful on its first flights. Through improvements in system parameters realized during the construction phase, KWIC met or exceeded the original design sensitivities in both spectral resolution modes. The images were diffraction limited at 37 μm (9.3" beam) over the entire field of view.

TABLE 1
FINE-STRUCTURE LINE PROBES AVAILABLE TO KWIC

Species	I.P.[1]	Transition	Wavelength	Critical Density	Astrophysical Regions
S^o	-	$^3P_1 \rightarrow {}^3P_2$	25.25 μm	1.9×10^6 cm^{-3}	Shocks
Si^+	8.15	$^2P_{3/2} \rightarrow {}^2P_{1/2}$	34.816	2.6×10^5	Shocks/PDRs
S^{++}	23.33	$^3P_2 \rightarrow {}^3P_1$	18.710	4.3×10^4	UV Hardness HII regions
		$^3P_1 \rightarrow {}^3P_0$	33.482	4.1×10^3	Density structure
Ar^{++}	27.63	$^3P_0 \rightarrow {}^3P_1$	21.84	4.0×10^4	Abundances
Ne^{++}	40.96	$^3P_0 \rightarrow {}^3P_1$	36.02	4.2×10^4	UV hardness HII regions
O^{+++}	54.93	$^2P_{3/2} \rightarrow {}^2P_{1/2}$	25.87	1.0×10^4	UV hardness: AGNs & PN
Ne^{4+}	97.11	$^3P_1 \rightarrow {}^3P_0$	24.28	1.1×10^4	UV hardness: AGNs & PN

[1]Photon energy required to form the species (eV).

INSTRUMENT DESCRIPTION

Our optical design is shown in Figure 1. The infrared beam from the KAO dichroic secondary is transmitted directly through the polyethylene window into the KWIC dewar. The seven diamond turned aluminum cryogenic mirrors in KWIC send a collimated beam through the HOFPI, and re-image it on the LOFPI and then on the array at the proper f-number. Near-IR and optical radiation are rejected by a scatter filter (80% transmission longward of 20 μm) near the entrance window. Just in front of the detector is an antireflection coated MgO reststrahlen crystal which reflects light from 12.5→27 μm, and transmits >75% longward of 30 μm. (Another salt would be used for observations involving wavelengths less than 27μm).

A fixed temperature chopped blackbody is used for flat fielding and to maintain flux calibration once an astronomical calibrator is observed. The beam from the blackbody is sent into KWIC via a flip mirror. A gas cell which lies between the blackbody and this flip mirror is used for spectral calibration through gas absorption lines.

The Fabry-Perot design is based on a thin steel flex-vane principle for translation (Poglitsch et al. 1991). The device is constructed of machined aluminum with magnetic stainless steel mesh rings. Coarse adjustments to the plate separation (20 to 66 μm) are made via a fine adjustment screw. Piezo-electric translators (PZTs) are used for both fine-adjustments and scanning. These PZTs expand ~24 μm at 4°K - more than a free spectral range at our longest wavelength (44 μm), thereby ensuring access to all wavelengths of interest. Parallelism is adjusted at room temperature via 3 fine adjustment screws and corrected at cryogenic temperatures with 3 short PZT stacks (2.5 μm displacement at 4 K). To minimize vibrations, the HOFPI is currently operated in a fixed order (70 to 200). The HOFPI is moved in and out of the beam during flight via a mechanical feed through to a translation stage. The FPI etalons are constructed of free standing metal mesh, with typical

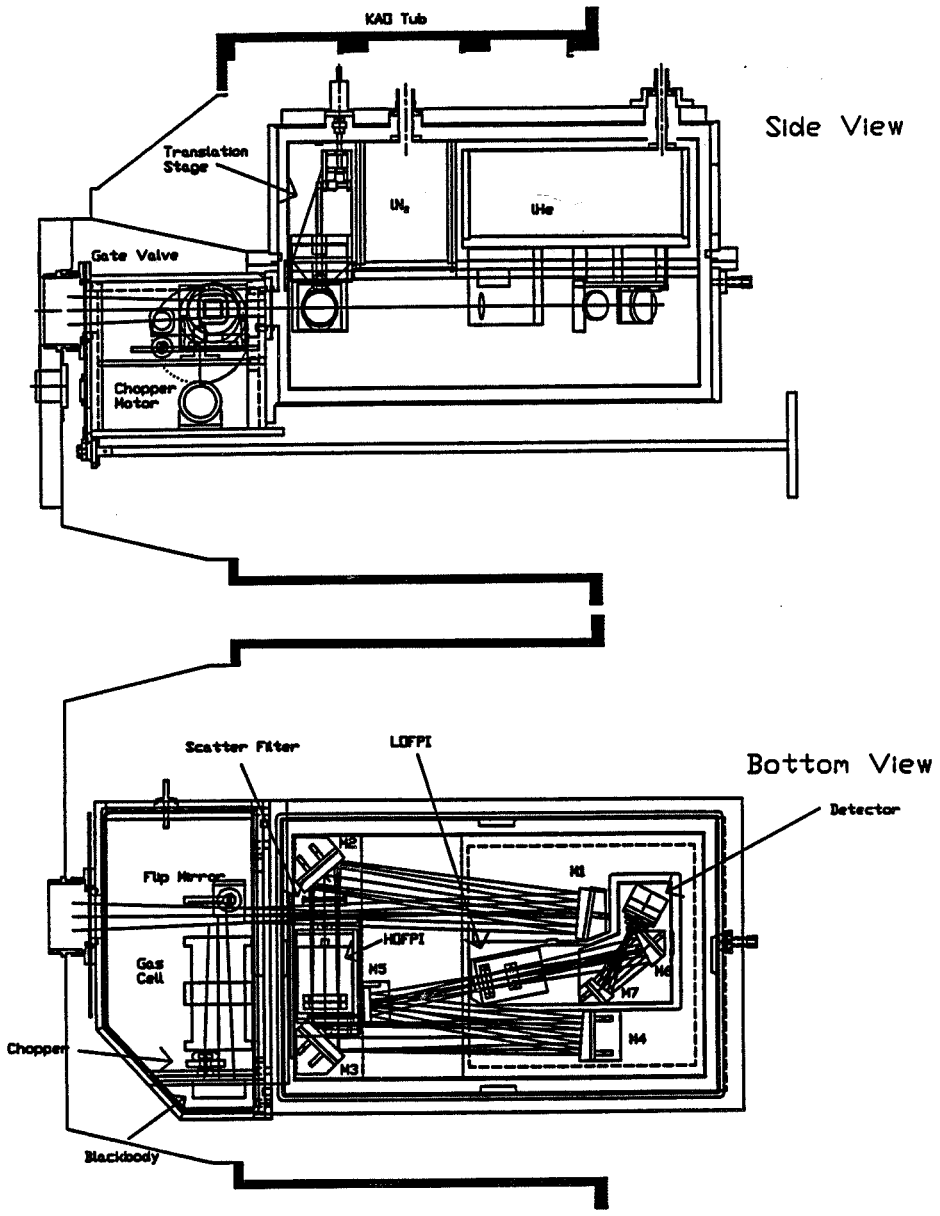

Figure 1. KWIC as installed in the bent Cassegrain focus of the KAO telescope. The inner outline of the KAO "tub" is superposed as a reference.

transmissions of 70% when operating with a finesse of 35. The FPI plate spacing is measured with a capacitance bridge circuit which compares the mesh-mesh capacitance to a reference capacitor and feeds back error signals to the high voltage supply. The FPI plates are electrically isolated from the LOFPI body with nylon plugs and held in place with magnets.

Rockwell International developed 128×128 Si:Sb BIB arrays for the SIRTF Infrared Spectrometer team (Huffman et al. 1992). Our current array has quantum efficiency ~30%, well depth ~6×10^6 e^- and a read noise of 500 e^- (Van Cleve et al. 1994). Dark current is 3×10^5 e/s per pixel - much smaller than the photo current (~$10^8\rightarrow10^9$ e^-/s) in the high KAO background. Table 2 lists the system sensitivities (including all loses) we hope to achieve when all sources of excess noise are tracked down. Also listed in bold are the sensitivities achieved on our first flights.

TABLE 2
OBSERVED AND CALCULATED SENSITIVITIES FOR KWIC[a]

λ	Beam	Solid	NEF ($W\ cm^{-2}Hz^{-1/2}$)		NEFD ($Jy\ Hz^{-1/2}$)	
(μm)	(arcsec)	Angle(sr)	R = 2000	R = 10,000	R = 70	R = 35
18	6.1	9.8×10^{-10}	9.5×10^{-19}	4.8×10^{-19}	11	8
25	7.2	1.3×10^{-9}	8.4×10^{-19}	4.2×10^{-19}	14	10
30	8.1	1.7×10^{-9}	7.6×10^{-19}	3.8×10^{-19}	15	11
35	9.1	2.2×10^{-9}	7.1×10^{-19}	3.6×10^{-19}	16	12
	Achieved in Flight:		**1.6×10^{-18}**	**Flight:**	**26**	
38	9.7	2.6×10^{-9}	6.7×10^{-19}	3.4×10^{-19}	17	12
				Achieved in Flight:	**21**	
44	10.9	3.2×10^{-9}	6.1×10^{-19}	3.1×10^{-19}	18	12

[a]Referred to single beam on the sky, including all telescope loses (chopping, nodding etc.). $R = \lambda/\Delta\lambda$.

ACKNOWLEDGEMENTS

This work was supported by NASA grant NAG2-800 and an NSF graduate fellowship.

REFERENCES

Huffman, J.E., Crouse, A.G., Halleck, B.L., Downes, T.V., & Herter, T.L. 1992, preprint.

Poglitsch, A., et al , 1991, *Internat. J. Infrared Millimeter Waves*, 12, 859.

Van Cleve, J.E., Herter, T., Pirger, B., Gull, G. Huffman, J., Seib, D. Hallec, B.L., and Reynolds, D.B. 1994, *Proceedings of IR Arrays: the Next Generation.*

Airborne Astronomy Symposium on the Galactic Ecosystem
ASP Conference Series, Vol. 73, 1995
M.R. Haas, J.A. Davidson, and E.F. Erickson (eds.)

STOKES, THE CHICAGO FAR-INFRARED POLARIMETER

S.R. PLATT, J.L. DOTSON, C.D. DOWELL, R.H. HILDEBRAND, and D. SCHLEUNING
Department of Astronomy and Astrophysics, Yerkes Observatory, and Enrico Fermi Institute, The University of Chicago, Chicago, IL 60637

G. NOVAK
Department of Physics and Astronomy, Northwestern University, Evanston, IL 60208-3112

ABSTRACT The far-infrared polarimeter, Stokes, has produced hundreds of measurements of the polarized emission from Galactic clouds. This paper gives examples of the results and describes the design and performance of the instrument.

INTRODUCTION

Observations with Mark I, the first far-infrared polarimeter flown on the Kuiper Airborne Observatory (Dragovan 1986; Novak et al. 1989), demonstrated the feasibility of mapping the magnetic fields in dense interstellar clouds by measuring the polarization of the thermal emission (e.g. Hildebrand, Dragovan, and Novak 1984; Gonatas et al. 1990). Mark I is now replaced by Stokes (Platt et al. 1991), an instrument with 32 beams. The gain in data rate is illustrated in Figure 1, a comparison of the best results of Mark I with the most recent results of Stokes for the same object (Orion).

DESCRIPTION OF THE INSTRUMENT

Stokes has been described by Platt et al. (1991). The plane of polarization of the incident radiation is rotated by a quartz half-wave plate. The two orthogonal components of polarization are then separated by a wire grid. The detectors are arranged in two 6×6 arrays (corners omitted), and are aligned to provide 32 independent beams on the sky. At 100 μm the beam diameter is 35 arc sec.

The polarization signal in each pixel has components from the source, the telescope, and the instrument. To remove the effects of the telescope and instrument we perform a series of rotations and translations as described by Platt et al. (1991). The result is a self-calibration that does not depend on *a priori* knowledge of the polarization from any celestial object.

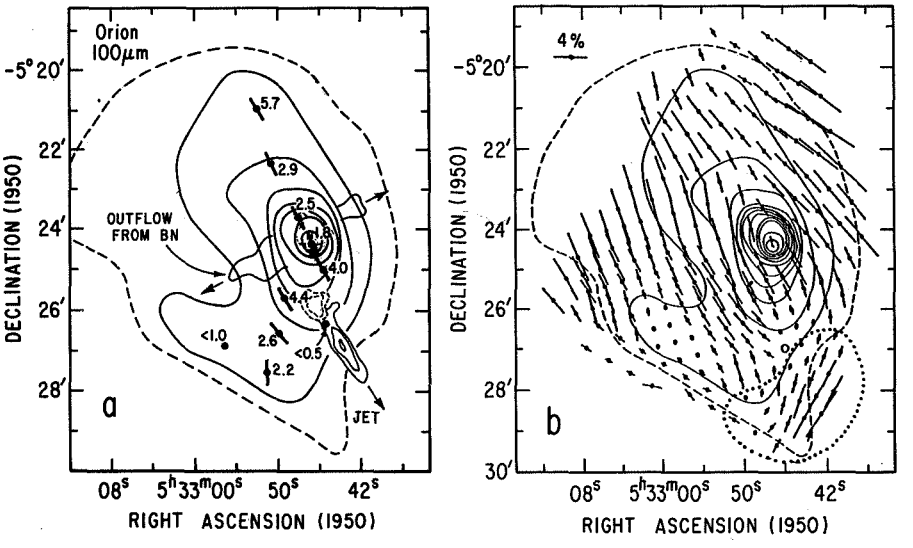

Fig. 1. Comparison of results for Orion as obtained a) with Mark I (Gonatas et al. 1990) and b) with Stokes (3 flights each). The inferred direction of the magnetic field is orthogonal to the polarization vectors. The flux density map is by Werner (1982). The points in the SW corner enclosed by the dotted line are likely to be spurious because of polarized flux in the NE reference beam.

PERFORMANCE

Ten polarization maps produced with Stokes are presented in an accompanying paper (Hildebrand et al. 1994).

The time, t, required to reach a given error, σ_p, in polarization on a source of mean flux density $\langle F \rangle$ is given by

$$t = 30 \text{ minutes} \left\{ \frac{1000 \text{ Jy} / 35'' \text{ beam}}{\langle F / 35'' \text{ beam} \rangle} \cdot \frac{1\%}{\langle \sigma_p \rangle} \right\}^2 \qquad (1)$$

where $\langle \sigma_p \rangle$ and $\langle F \rangle$ are averages taken over all points and t is measured from the beginning of the first integration to the end of the last integration on a particular source (including all overhead time).

The results of the observations are continuously revised and displayed in flight (Fig. 2). Photometric results are obtained simultaneously (Fig. 3).

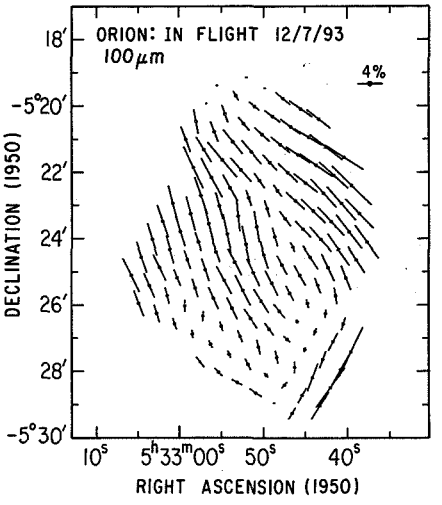

Fig. 2. Polarization vectors for Orion as displayed in flight. Compare Fig. 1b, the map drawn after a post-flight analysis.

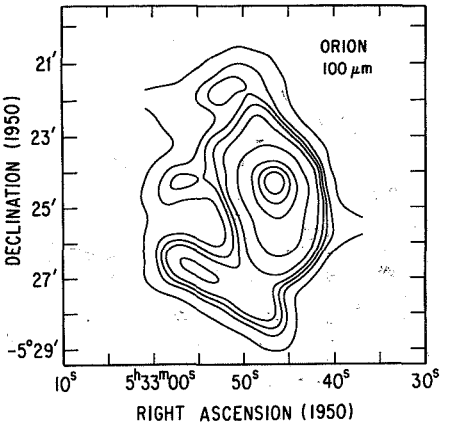

Fig. 3. A photometric map of Orion made by adding the signals for the two components of polarization. The contours are drawn at relative flux densities of 0.06, 0.08, 0.10, 0.12, 0.2, 0.4, 0.6, 0.8, and 1.0.

ACKNOWLEDGEMENTS

We are grateful to J. Jewell, T. McMahon, D. Pernic, R. Pernic, and J. Wirth for their assistance in the instrumentation and observations. We thank the crew of the Kuiper Airborne Observatory for their assistance during flights. The development and operation of Stokes has been supported by NASA grant NSG 2057. J.L.D. acknowledges support from NASA Graduate Student Researchers Grant NGT-50894.

REFERENCES

Dragovan, M. 1986, *ApJ*, **308**, 270

Gonatas, D. P., Engargiola, G. A., Hildebrand, R. H., Platt, S. R., Wu, X. D., Davidson, J. A., Novak, G., Aitken, D. K., & Smith, C. 1990, *ApJ*, **357**, 132

Hildebrand, R. H., Dragovan, M., & Novak, G. 1984, *ApJ*, **284**, L51

Hildebrand, R. H., Dotson, J. L., Dowell, C. D., Platt, S. R., Schleuning, D., Davidson, J. A., & Novak, G. 1994, in *Proc of the Airborne Astronomy Symp on the Galactic Ecosystem: From Gas to Stars to Dust*, ed. M. R. Haas, J. A. Davidson, & E. F. Erickson (San Francisco: ASP), paper 111

Novak, G., Gonatas, D. P., Hildebrand, R. H., & Platt, S. R. 1989, *PASP*, **101**, 215

Platt, S. R., Hildebrand, R. H., Pernic, R. J., Davidson, J. A., & Novak, G. 1991, *PASP*, **103**, 1193

Werner, M. W. 1982, in *Ann NY Acad. Sci.* No.395, ed. A. E. Glassgold, P. J. Hugsins, & E. L. Shurking (New York: N.Y.A.S.), p 79

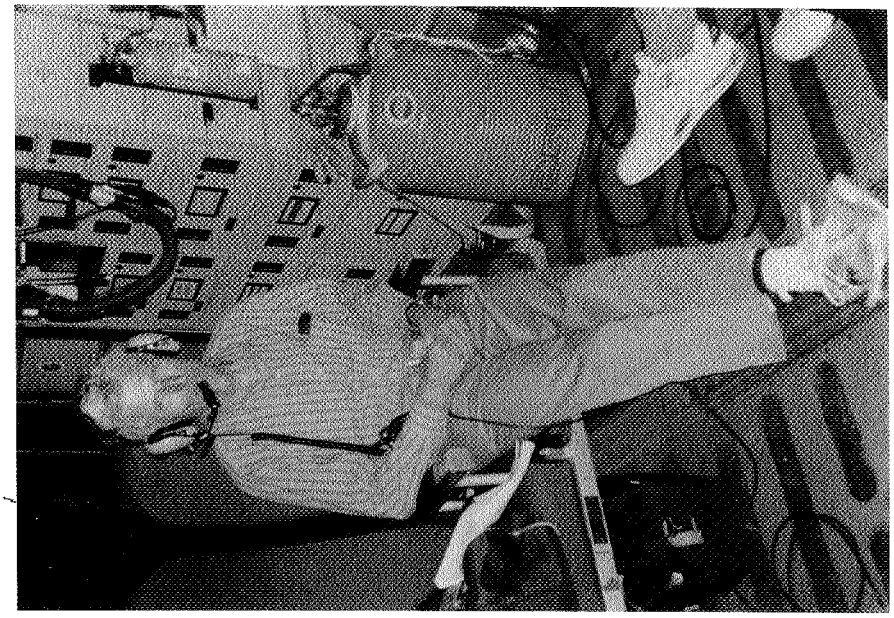

Roger Hildebrand

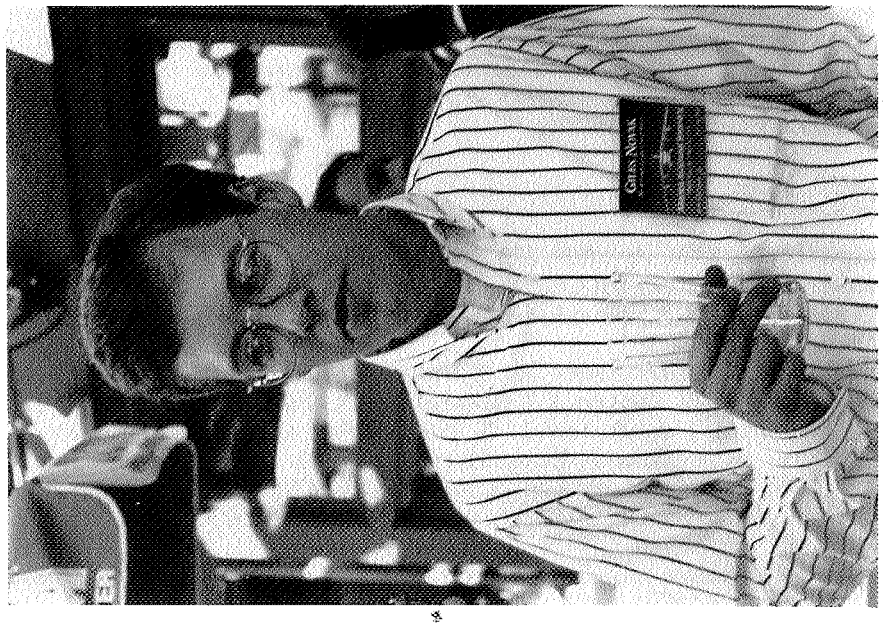

Giles Novak

Airborne Astronomy Symposium on the Galactic Ecosystem
ASP Conference Series, Vol. 73, 1995
M.R. Haas, J.A. Davidson, and E.F. Erickson (eds.)

FIFI - the MPE Garching / UC Berkeley Far-Infrared Imaging Fabry-Pérot Interferometer

N. Geis [1], R. Genzel [2], M. Haggerty [3], F. Herrmann [2], J. Jackson [4], S. C. Madden [5], T. Nikola [2], A. Poglitsch [2], M. Rumitz [4], G. J. Stacey [6], R. Timmermann [2], and C. H. Townes [1]

[1] *Physics Department, University of California, Berkeley, CA 94720*

[2] *Max-Planck-Institut f. extraterr. Physik, D-85740 Garching, Germany*

[3] *Kellogg Radiation Lab, California Institute of Technology, Pasadena, CA 91125*

[4] *Astronomy Department, Boston University, MA 02215*

[5] *NASA Ames Research Center, Moffet Field, CA 94035*

[6] *Astronomy Department, Cornell University, Ithaca, NY 14853*

Abstract. We describe the performance characteristics of the MPE-Garching/UC Berkeley Far-Infrared Imaging Fabry-Pérot Interferometer (FIFI) for the Kuiper Airborne Observatory (KAO). The spectrometer features 2 or 3 cryogenic tunable Fabry-Pérot filters in series giving spectral resolution R of up to 10^5 in the range 40 μm < λ < 200 μm, and an imaging 5×5 array of photoconductive detectors with variable focal plane plate scale. The instrument works at background limited sensitivity of up to 2×10^{-19} W cm^{-2} Hz$^{-1/2}$ per pixel per resolution element at $R = 10^5$ on the KAO.

1. Introduction

The sensitivity limit on the KAO for spectrometers with extrinsic photoconducting detectors is given by fluctuations in thermal background radiation emitted by the spectrometer, telescope optics, and the Earth's atmosphere. The goal in spectrometer design is therefore to maximize throughput and minimize emissivity of the apparatus, and to restrict the bandwidth to that required for observing a given astronomical line. Once such a system is optimized, the only avenue for improving observing efficiency (i.e., the amount of data per flight) is to observe several data channels at a time (multiplexing). This step has been made in recent years by implementing focal plane detector arrays. FIR arrays with discrete detector crystals are used on the KAO for both spatial (FIFI) and spectral multiplexing (CGS – Erickson et al. 1994). At the shorter FIR wavelengths, a monolithic array spectrometer (KWIC – Latvakoski et al. 1994, Stacey et al. 1994) has now been commissioned, yielding even higher data rates.

We describe the characteristics of the MPE-Garching/UC Berkeley Far-Infrared Imaging Fabry-Pérot Interferometer (FIFI). For lack of space we cannot show astronomical data in this contribution, but would like to refer the reader instead to papers 106, 107, 109, 2.1, 202 and 305 in these proceedings which feature recent FIFI data.

2. FIFI's Construction

The problems and constraints for feeding an image through Fabry-Pérot filters (FPIs) determine the overall optical layout and even the total size of FIFI, as described in detail elsewhere (Poglitsch et al. 1991, Geis 1991). Like its predecessor, the UCB MkII Tandem Fabry-Pérot spectrometer (Storey, Watson & Townes 1980, Lugten 1980), FIFI is divided into two parts – a dewar and a calibration unit.

2.1 The Dewar

The dewar contains all bandwidth limiting components with the associated beam shaping optics (off-axis conic section mirrors) and the detector array. The dewar can be removed from the telescope without disturbing the relative alignment between FIFI and the KAO. All optical elements except the High-Order Fabry-Pérot are cooled to 4K (or 2K). The cryogen tanks contain 10ℓ each of L-N_2 and L-He, the L-He hold time is $\sim$13 h.

The Fabry-Pérots. Since a single FPI transmits a comb of wavelengths with finesse $F \equiv$ free spectral range / spectral resolution $\sim$50, we need 3 FPIs in series to get a relative bandwidth $\sim 10^{-5}$.
Our FPIs use free-standing Nickel mesh – stretched over optically flat Nickel rings – as mirrors (Ulrich, Renk & Genzel 1963). Leaf-spring parallel translation stages perform the fine adjustment of plate spacing and keep the mesh plates aligned to 0.1 μm precision for motions up to 2 mm.

The High-Order Fabry-Pérot (HOFPI). The HOFPI is the only filter component in FIFI at L-N_2 temperature. For the wide range of plate spacing required (see 3.3), we split the mechanism into a coarse travel stage and a tilt/scanning section.

For coarse travel, a carriage carrying one of the two FPI mirrors is driven by a roller screw and stepper motor along precision rails.

The scanning motion is achieved with a piezoelectric transducer (PZT) with a throw of $\sim$60 μm at 80 K. We check parallelism of the plates by observing visible-light fringes from a HeNe laser shining on the mesh plates and adjust the tilt of one plate with two PZTs in a kinematic mount on the translation stage.

All moving parts in the HOFPI mechanism are spring-loaded (backlash free). Eddy-current dampers suppress resonances excited by aircraft noise. An HP laser position transducer monitors motions affecting the plate spacing in the HOFPI. During observation a feedback loop is closed and the HOFPI scans under control of the position transducer. The scanning system is fast and rigid enough to modulate the plate spacing with a 10 Hz square wave for frequency-switched operation.

The Mid-Order and Low-Order Fabry-Pérots (MOFPI, LOFPI). Both MOFPI and LOFPI are of very similar construction. All of the travel takes place via a parallel stage. Both FPIs were designed to warp only minimally ($\leq$ a few μm) during cool-down, so that plate parallelism can be adjusted by miniature PZTs of 5 μm travel at 4K. We adjust plate spacing by hand with a differential micrometer screw until within range of the feedback circuit. Then the plate spacing is measured and kept constant by a high-precision capacitance bridge using the mesh surfaces themselves as plate capacitors. Repeatability and stability of this method have proven to be excellent. While the LOFPI always stays in place, we can remove the MOFPI from the beam during flight to improve system transmission at low resolution.

Additional Filtering. A diamond dust and polyethylene scatter filter at L-He temperature eliminates visible, NIR, and MIR radiation from the beam. MIR and FIR radiation from unwanted transmission peaks of the LOFPI is suppressed by an appropriate combination of reststrahlen salt filters (alkali and alkaline halides) on two filter wheels, so that the LOFPI can often be used in 4th order.

The Detector Array and Electronics. The 5×5 detector array has an array of light cones in front of it which concentrates the light into the integrating detector cavities. Depending on the wavelength range, we use Ge:Ga, Ge:Sb, or stressed Ge:Ga photoconductive detectors of size ~ 1 mm^3. The focal plane is re-imaged onto the detector array with a plate scale of either 10″, 20″, or 40″ per pixel.

The first stage of the 25 TIA amplifiers with GaAs FET inputs operates at He temperature and is mounted piggyback on the array (see Stacey et al. 1992 for details). After analog amplification and A/D conversion the signals are lock-in detected and low-pass filtered in a VMEbus computer system that also controls all real-time tasks in the spectrometer. An HP 9000 UNIX workstation provides a graphical user interface to the instrument and stores the data.

2.2 The Calibration Unit

The calibration unit mounts between the telescope and our dewar, inside the instrument flange of the telescope. It contains

- an optical train for visible guiding: dichroic mirror, re-imaging optics and an integrating cooled CCD camera controlled by a PC,
- an image de-rotator (K-mirror assembly) in the FIR beam to compensate for image rotation due to the alt-azimuth mount of the KAO,
- a calibration source (gas absorption cell, mirror chopper wheel, and temperature controlled black-bodies in a pupil plane) which uniformly illuminates the detector array at the same f-ratio as the KAO,
- a 40 mm diameter collimator, producing the small angular divergence of the beam in the HOFPI required for high spectral resolution.

3. FIFI's Specifications

3.1 Spectral Range

The total wavelength range accessible to FIFI is $40\ \mu m < \lambda < 200\ \mu m$. On any one flight one of three configurations of the instrument is available. Based on the spectral response curves of the detector and FPI mesh installed, the spectral range available is λ = 45 μm...100 μm, 90 μm...145 μm, or 135 μm...205 μm, respectively. FIFI can be re-tuned to any wavelength and spectral resolution within a range in about 10 minutes, including all the necessary calibration measurements. A change-over between configurations takes 2 days, since it requires swapping of components inside the dewar and re-aligning the instrument.

3.2 Sensitivity

Stressed and unstressed Ge:Ga arrays have been thoroughly tested in flight and routinely yield the system sensitivities for the best pixels (incl. telescope and atmospheric losses) shown in Table 1. For at least 20 of the 25 pixels the NEFD is better than 1.3 times the quoted numbers. The sensitivity limit at 124 μm is an estimate based on values achieved with the UCB MkII Tandem Fabry-Pérot

spectrometer. With 3 FPIs in series, sensitivity improves with $\sqrt{R}$ up to the highest resolutions. For 2 FPIs, the bandwidth reaches its lower limit near $R \sim 10^4$ resulting in sensitivities at $\Delta V = 3$ km/s close to those given in the 30 km/s column.

Table 1. FIFI's Sensitivity.

Wavelength [μm]	Species and Transition	NEFD [a] [10^{-19} W cm^{-2}Hz$^{-1/2}$] at ΔV_{FWHM} = 3 km/s	30 km/s	100 km/s
187	CO (14→13)	2.3	7	9
158	[CII] $^2P_{3/2} \rightarrow ^2P_{1/2}$	1.8	5.5	7
145	[OI] $^3P_0 \rightarrow ^3P_1$	2.5	8	10
124	CO (21→20)	3	9	12
88	[OIII] $^3P_1 \rightarrow ^3P_0$	4	13	23
63	[OI] $^3P_1 \rightarrow ^3P_2$	14	43	70

[a] NEFD ≡ Flux density incident on the KAO yielding S/N = 1 in 1 sec. of integration time, in a single detector, and in 1 spectral resolution element ("line photometry mode"). For spectral scans of n resolution elements the observing time required would be n times as long to get the same S/N.

3.3 Spectral Resolution

FIFI's spectral resolution $R = \lambda/\Delta\lambda$ is determined by spacing and finesse F of the HOFPI. The spacing can be adjusted from ≈ 20 μm to 100 mm, leading to $50 \lesssim R \lesssim 10^5$. In practice, we use $10^3 < R < 10^5$ for astronomical observations.

Acknowledgements. This work has been supported by NASA grant NAG2-208.

References

Erickson, E. F., et al. 1994, in Proc. of the Airborne Astronomy Symp. on the Galactic Ecosystem: From Gas to Stars to Dust, ed. M. R. Haas, J. A. Davidson, & E. F. Erickson, (San Francisco: ASP), paper 702

Geis, N. 1991, Ph. D. Thesis, Ludwig-Maximilians-Universität, Munich, Germany

Lugten, J. B. 1980, Ph. D. Thesis, University of California at Berkeley

Latvakoski, H., et al. 1994, in Proc. of the Airborne Astronomy Symp. on the Galactic Ecosystem: From Gas to Stars to Dust, ed. M. R. Haas, J. A. Davidson, & E. F. Erickson, (San Francisco: ASP), paper 706

Poglitsch, A., et al. 1991, Internat. J. IR and MM Waves, 12, 859

Stacey, G. J., et al. 1992, Internat. J. IR and MM Waves, 13, 1689

Stacey, G. J., et al. 1994, in Proc. of the Airborne Astronomy Symp. on the Galactic Ecosystem: From Gas to Stars to Dust, ed. M. R. Haas, J. A. Davidson, & E. F. Erickson, (San Francisco: ASP), paper 3.1

Storey, J. W. V., Watson, D. M., & Townes, C. H. 1980, Internat. J. IR and MM Waves, 1, 15

Ulrich, R., Renk, K. F., & Genzel, L. 1963, IEEE Transactions on Microwave Theory and Techniques, 11, 364

Airborne Astronomy Symposium on the Galactic Ecosystem
ASP Conference Series, Vol. 73, 1995
M.R. Haas, J.A. Davidson, and E.F. Erickson (eds.)

Airborne Spectrograph for the Thermal IR: Broadband Array Spectrograph System

Ray W. Russell, John Hackwell, David Lynch, and Ann Mazuk

Space and Environment Technology Center, The Aerospace Corporation, M2-266, P.O. Box 92957, Los Angeles, CA 90009-2957

1. Introduction

Spectroscopic studies in the "fingerprint" region of the thermal IR from 3–14 μm of celestial dust components and the overall energy distribution of the sources are best served by moderate spectral resolution ($R = \lambda/\Delta\lambda \sim 30 - 200$), high sensitivity observations. Spectral purity and the reproducibility of the spectral shape are critical as well, when using the spectral shape to assign temperatures to dust grains or to gas clouds based on the wavelength and shape of molecular bands. These sensor attributes are also important to the use of wavelengths and ratios of solid state features to derive compositions of dust grains in celestial sources. The advent of high quality linear arrays of blocked impurity band (BIB) detectors of Si:As permitted the development of a state-of-the-art, patented, cooled prism spectrograph. Developed at The Aerospace Corporation largely on in-house funds, the Broadband Array Spectrograph System (BASS) has been used for a variety of remote sensing applications, but especially for IR astronomical studies on the Kuiper Airborne Observatory and at the NASA IRTF. The attributes of the spectrograph, specifically having the pupil imaged onto the 2 linear 58 element detector arrays so that the effects of guiding errors are minimized, being able to maximally exploit the limited observing time by acquiring all 116 spectral channels simultaneously, and having all spectral channels imaged through the same aperture so that spectral mapping is readily and reliably accomplished, afford the scientist with a unique opportunity to conduct both surveys of examples of many different types of sources as well as in-depth studies of a given class of object by thoroughly sampling the class members.

This duality was demonstrated with the BASS through a combination of KAO flights where spectral maps were obtained as part of in-depth studies of specific source regions (such as Orion and W3) and flights where up to 21 legs/flight were used to survey many different sources of different types. In W3, the intensity of the Unidentified InfraRed (UIR) bands were quantified as a function of the distance from the exciting source and relative to the morphological structure seen in the radio, where the ionized gas distribution is delineated. In Orion, the intensities of various spectral emission features as a function of position in the source were studied and presented in Grasdalen *et al.* (1992). CO emission, fine structure lines, molecular hydrogen emission, and UIR bands were shown to have different spatial extent and locations. The chopper

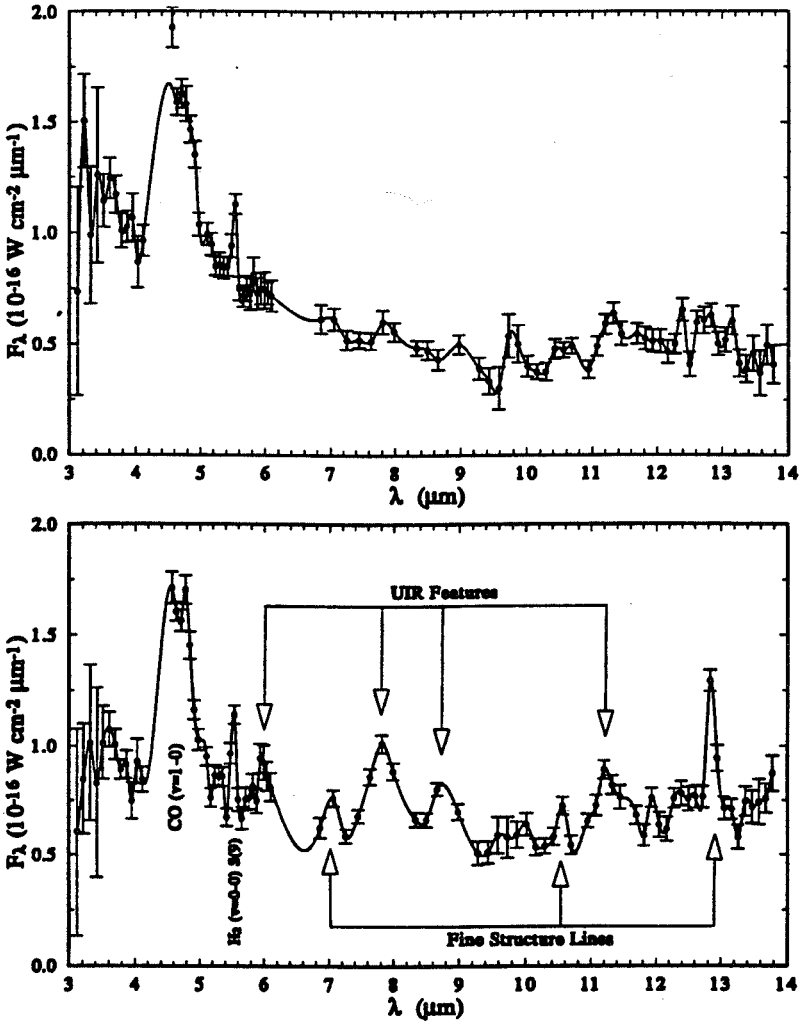

Figure 1. The upper panel contains the spectrum obtained on Pk 1 with a chopper throw of 115″. The spectrum obtained at Pk 1 with a chopper throw of 238″ is shown in the bottom panel. Useful observations near 4.4 μm could not be obtained because of the strong absorption by atmospheric CO_2. The gap in coverage around 6.5 μm results from an inefficient dichroic in the Aerospace spectrometer. The UIR features and the fine-structure lines grow dramatically with chopper throw and are therefore unlikely to be related to the molecular peak.

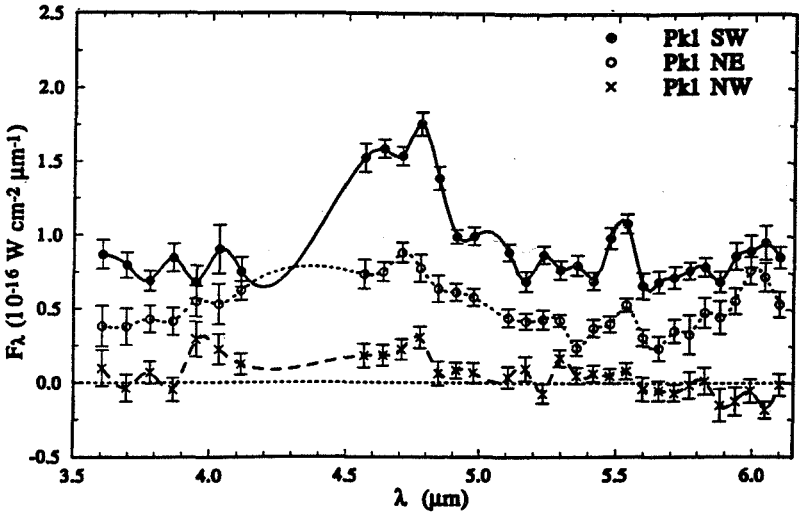

Figure 2. The 3 – 6 μm spectra at three positions around Pk 1. The two dominant spectral features are the H_2 S(9) (v = 0–0) line at 5.5 μm and the CO (v = 1–0) band around 4.6 μm. These spectra demonstrate that the features and the underlying continuum are highly correlated in their spatial distribution.

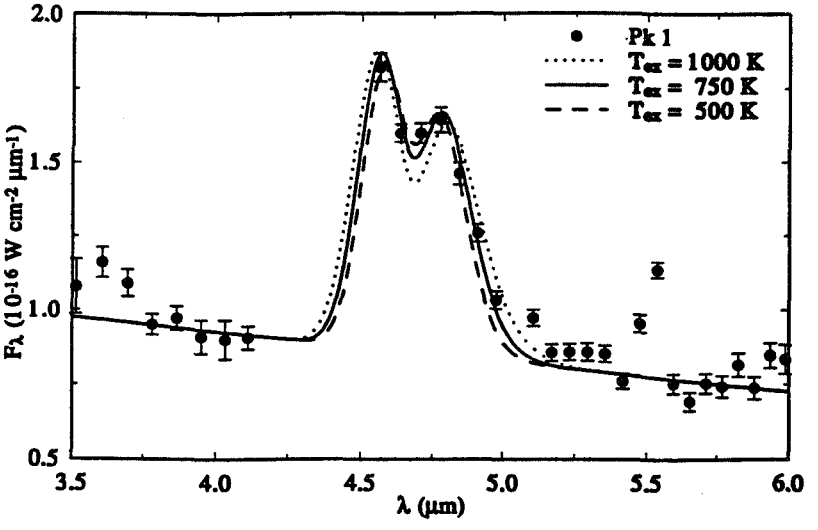

Figure 3. The mean spectrum near Pk 1 compared with predicted profiles for the CO (v = 1–0) band. The model predictions have been scaled and added to a linear continuum. The data are well represented by a model with T_{ex} = 750 K.

throw of 115″ or more insured that the reference locations were "off-source." The CO band and continuum emission were shown to be associated with shocked regions. The fine structure lines were strongest near the Trapezium where there is a large amount of ionizing radiation, and both the fine structure lines and the UIR bands were shown to increase in strength with a larger chopper throw, suggesting that they are not associated with the molecular hydrogen peak, but are more spatially extended. This is shown in Figures 1 through 3 (adapted from Grasdalen *et al.* 1992).

2. Sensor Design

The instrument design is presented in Hackwell *et al.* (1990). The concept is that a single aperture feeds the camera optics, which are cooled to liquid helium temperature. Two salt prisms, NaCl and CaF_2, are used to disperse the light separated by a cold beamsplitter into wavelengths longer and shorter than 6.5 μm. The prisms are curved and use a single spherical mirror to send the light back through the prisms to the arrays. This maximizes the optical throughput of the camera, and permits changing from $f/14$ to $f/24$ with the swap out of a single set of reimaging optics on a post. It also minimizes the scattering in the sensor by minimizing the number of optical elements.

The instrument characterization and calibration were extensively pursued as part of our standard star studies for the Midcourse Space Experiment, where sources must be known to 3% or better. The spectral purity was initially degraded by scattering in the front-illuminated arrays and the optics. The addition of optical baffles and a long pass filter to the short wavelength channel, and a switch to back-illuminated arrays without the back surface abraded resulted in less than 3% worst-case crosstalk in adjacent channels. The overall level of scattering is now less than 1% across the arrays. The linearity of responsivity was also extensively studied and shown to be better than 1%. This type of detector has been shown to exhibit high quantum efficiency (about 60%) and behavior typical of photovoltaic devices, rather than photoconductors.

The wavelength calibration and spectral resolution have also been measured and shown to meet theoretical predictions. Deliberate shifting of the source being studied to the edges of the aperture results in a worst-case spectral shift of 5%, while pupil maps show that all channels suffer the same signal loss from misalignments except at the wavelength of the crossover of the beamsplitter from reflection to transmission.

Guest investigators are encouraged to consider this flight-proven instrument for collaborative IR studies.

3. References

Grasdalen, G. L., Hackwell, J. A., Lynch, D. K., & Russell, R. W. 1993, ApJ, 397, L119; erratum 1993, ApJ, 405, L83

Hackwell, J. A., Warren, D. W., Chatelain, M., Dotan, Y., Li, P., Lynch, D. K., Mabry, D., Russell, R. W., & Young, R. 1990, in Proc SPIE Conference 1235 on Instruments in Astronomy VII, p. 171

Airborne Astronomy Symposium on the Galactic Ecosystem
ASP Conference Series, Vol. 73, 1995
M.R. Haas, J.A. Davidson, and E.F. Erickson (eds.)

THE CALTECH AIRBORNE SUBMILLIMETER SIS RECEIVER

J. ZMUIDZINAS, J. CARLSTROM, D. MILLER, N. G. UGRAS
Division of Physics, Mathematics, and Astronomy, California Institute of Technology, 320-47, Pasadena, CA 91125

ABSTRACT We have constructed a sensitive submillimeter receiver for the NASA Kuiper Airborne Observatory (KAO) which at present operates in the 500-750 GHz band. The DSB receiver noise temperature is about 5 $h\nu/k_B$ over the 500-700 GHz range. This receiver has been used to detect $H_2{}^{18}O$, HCl, and CH in interstellar molecular clouds, and also to search for C^+ emission from the highly redshifted galaxy ($z = 2.3$) IRAS 10214.

INTRODUCTION

The rotational transitions of many hydride molecules lie in the submillimeter band. These simple molecules play a fundamental role in interstellar chemistry, and may provide important cooling mechanisms for collapsing cloud cores. However, observations from the Kuiper Airborne Observatory (KAO) are often necessary. Over the past two years, we have detected CH at 532 and 536 GHz, HCl at 626 GHz, and $H_2{}^{18}O$ at 547 and 745 GHz, using our SIS receiver on the KAO; some of these observations are discussed in more detail elsewhere in this volume (Zmuidzinas *et al.* 1994b).

THE CALTECH SIS RECEIVER

Construction of our receiver was started in October, 1991, after our project was approved as a new instrument for the KAO. The first flights ocurred in September, 1992, and since then our instrument has flown four additional series. There has recently been a tremendous improvement in the sensitivity of submillimeter receivers which use superconducting (SIS) tunnel junctions. The progress is due to new materials and processes for fabricating robust tunnel junctions and superconducting circuits; novel circuit configurations to cancel the effects of the junction capacitance; and new techniques for coupling the radiation into the device. Figure 1 shows the receiver sensitivity we have obtained to date. Note that these noise temperatures are only a factor of several below those obtained with the pioneering InSb hot-electron bolometer receiver developed by

T. G. Phillips and which flew on the KAO during 1978-1986. However, the SIS receivers enjoy a large multiplex advantage since many frequency channels can be observed simultaneously, whereas the InSb system had a single 1 MHz channel.

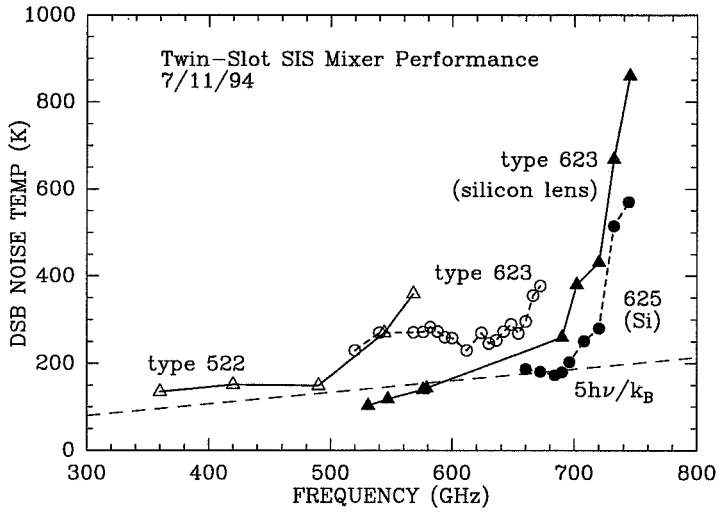

Figure 1. DSB noise temperature vs. frequency for our twin slot antenna mixers.

The local oscillator (LO) for this receiver is provided by a phase-locked Gunn oscillator followed by a waveguide frequency multiplier. Sources are available at present in the following bands: 500-580 GHz, 580-660 GHz, and 660-750 GHz. Switching between these bands requires the substitution of LO sources, but can be performed in flight in about 15-20 minutes.

The intermediate-frequency (IF) output of the receiver is analyzed by a radio-frequency spectrometer to provide a multichannel spectrum. We have constructed a digital autocorrelation spectrometer for our receiver, using the Caltech CSO320 CMOS correlator chip developed by B. von Herzen. Our KAO spectrometer provides a bandwidth of 350 MHz with 160 channels, and uses commercial silicon A/D converters running at a 350 MHz sample rate. To obtain the 350 MHz bandwidth with converters limited to a Nyquist bandwidth of 175 MHz, we use a quadrature mixer to convert the receiver 1.5 GHz IF output to baseband, and measure all four correlation products between the in-phase (I) and quadrature-phase (Q) baseband outputs. A 1 GHz bandwidth acousto-optic spectrometer (AOS) was also loaned to us by A. Betz and R. Boreiko, which allowed us to fly our receiver before the correlator was constructed. The wide bandwidth of the AOS was also necessary for the IRAS 10214 observations.

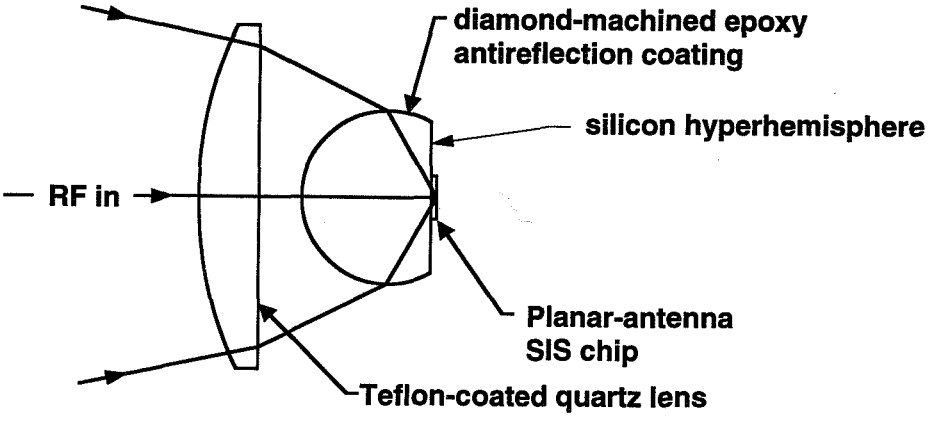

Figure 2. Optical layout of our twin-slot SIS mixer.

QUASIOPTICAL MIXERS

Figure 2 shows the optical layout of our mixer. The SIS chip is mounted on a silicon hyperhemispherical lens, which concentrates the radiation from the telescope onto an antenna fabricated lithographically on the SIS chip. Hyperhemispherical lenses with planar antennas were introduced by Rutledge and Muha (1982), and were first used with SIS mixers by Wengler *et al.* (1985). Another benefit of the hyperhemipherical lens is that the planar antenna radiates preferentially into dielectric material. The use of silicon ($\epsilon_r = 11.7$) as the dielectric results in a forward efficiency (for our antenna design) of 91%, compared to a 9% loss due to backward radiation into free space. To avoid the Fresnel reflection at the surface of the silicon lens, we have developed an anti-reflection coating. The coating material is epoxy loaded with alumina powder, which gives the proper combination of dielectric constant ($\epsilon_r \approx 4$), reasonably low loss ($< 2\%$), adhesion, and cryogenic recyclability. The coating is diamond machined to yield a very smooth coating with precisely the correct ($\lambda/4$) thickness.

Our mixer uses a twin-slot antenna (Figure 3) to receive the radiation. As discussed by Zmuidzinas *et al.* (1992), this antenna has a number of desirable properties, including linear polarization, a symmetric beam with low sidelobes, a low antenna impedance, and an octave bandwidth. The radiation received by the slot antennas is coupled into the SIS junctions with superconducting microstrip lines, and a novel two-junction circuit tunes out the SIS junction capacitance at the frequency of operation (Zmuidzinas *et al.* 1994a). The mixer chip fabrication is performed at the JPL Center for Space Microelectronics Technology, using Nb/Al-Oxide/Nb tunnel junctions.

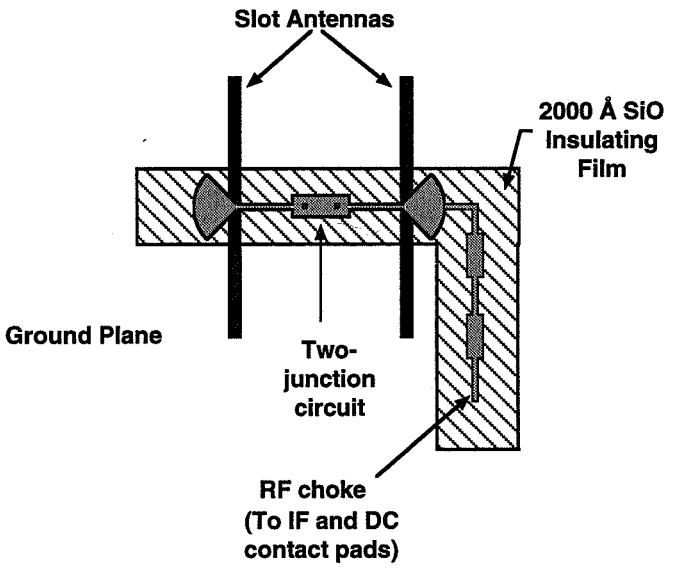

Figure 3. Our twin-slot SIS mixer chip.

ACKNOWLEDGEMENTS

We thank the staff of the Kuiper Airborne Observatory for their support. We are especially grateful to Rick LeDuc and Jeff Stern of the JPL superconducting devices group for their essential contributions. Special thanks go to A. Betz and R. Boreiko for the loan of their AOS. This work was supported by NASA grants NAG2-744 and NAGW-107, the NASA/JPL Center for Space Microelectronics Technology, and a NSF Presidential Young Investigator grant to J. Zmuidzinas.

REFERENCES

Rutledge, D. B., & Muha, M. S. 1982, IEEE Trans. Antennas Prop., 30, 535.

Wengler, M. J., Woody, D. P., Miller, R. E., & Phillips, T. G. 1985, Int. J. IR and MM Waves, 6, 697.

Zmuidzinas, J., & LeDuc, H. G. 1992, IEEE Trans. Microwave Theory Tech., 40, 1797.

Zmuidzinas, J., LeDuc, H. G., Stern, J. A., & Cypher, S. R. 1994, IEEE Trans. Microwave Theory Tech., 42, 698.

Zmuidzinas, J., Blake, G. A., Carlstrom, J., Keene, J., Miller, D., Schilke, P., & Ugras, N. G. 1994b, in Proc of the Airborne Astronomy Symp on the Galactic Ecosystem: From Gas to Stars to Dust, ed. M. R. Haas, J. A. Davidson, & E. F. Erickson (San Francisco: ASP), paper 1.2.

Airborne Astronomy Symposium on the Galactic Ecosystem
ASP Conference Series, Vol. 73, 1995
M.R. Haas, J.A. Davidson, and E.F. Erickson (eds.)

Site Testing Antarctica for Astronomy

Michael Burton
School of Physics, University of New South Wales, Sydney, NSW 2052, Australia.

Abstract.

The Antarctic Plateau provides the pre-eminent sites on the surface of the Earth for many types of astronomical observation. We have embarked on a site testing programme to quantify the ultimate sensitivity levels achievable. The programme is now in operation at the South Pole, where an infrared sky brightness monitor and micro-thermal temperature sensors have been deployed. We plan to extend these measurements, first at the Pole, and then to the highest parts of the Plateau, Domes Argus and Circe. The latter will involve adapting an 'Automated Geophysical Observatory', a mobile laboratory designed for autonomous operation on the Plateau, for astrophysical purposes.

1. Introduction

The Antarctic Plateau offers the promise of the best site conditions on the surface of the Earth for a wide range of astronomical observations. This is a result of the unique combination of cold, dry and tenuous air that is only found there. The Plateau reaches an elevation of nearly 4,300m, has average wintertime temperatures of -60°C , dropping below -90°C at times, and has columns of precipitable water vapour which can fall below 100 μm at times. Winds are generally light, with the katabatic wind, originating on the highest parts of the Plateau, not reaching its full fury till near the coast. Weather conditions are stable, with minimal diurnal temperature fluctuations. This environment provides superlative conditions for measurement of the photon fluxes incident on the Earth from space, particularly in the near-infrared and sub-millimetre regimes.

In the near–IR, at 2.4 μm, the background thermal flux from sky and telescope is reduced by a factor of 200 between Mauna Kea (0°C) and the South Pole (-60°C) (Harper 1989). From 2.27-2.45 μm there is no airglow emission and the zodiacal flux is near its minimum, at the transition from scattered sunlight to thermal emission. Thus a window exists through which unprecedently deep observations can be made, only limited by the natural background of the inner solar system.

The low water vapour content will open up the sub-millimetre windows, partly accessible from Mauna Kea, for virtually continuous viewing (Bally 1989). This cannot be achieved from any other ground based site. Existing atmospheric

windows will be cleaner, the mid–IR windows extended towards 50 μm, and a window at 200 μm opened for viewing at times.

The stable atmospheric conditions, tenuous air and absence of jet streams combine to produce conditions of superb clarity, or super-seeing (Gillingham 1993). The micro-thermal fluctuations in air temperature, which degrade spatial resolution from the diffraction limit, are minimised in this environment. Mitigating against these positive attributes, however, is the presence of a strong inversion layer which can occur during the most stable days of winter, where the air temperature can rise by 10 degrees in a few metres. It necessitates placing a telescope on a raised platform, whose height has to be determined.

Such are the conditions of the Antarctic Plateau. Their unique properties offer the potential of our making the most sensitive observations, with the greatest clarity, over a wide wavelength range, that are possible from the Earth. Ultimately, a telescope borne upon an aerostat above the tropopause might provide space-telescope image quality, with water columns similar to the KAO and negligible near–IR thermal background, all for a cost more akin to a large ground-based project than a space-based one. The scientific potential is immense (*e.g.* Burton *et al.*, 1994). It is, however, necessary to quantify these statements before they can form the basis of a drive to construct a major observatory on the high Plateau. A site testing programme is first necessary. In the remainder of this article we discuss the activity which is now underway towards this goal.

2. Current Programmes

The NSF has funded the Center for Astrophysical Research in Antarctica (CARA) to establish the first astronomical observatory at the South Pole. Building upon a series of isolated experiments, construction of the observatory is now well underway. Two experiments have been operating over the past Antarctic winter, an infrared camera (SPIREX, Hereld 1994) and a microwave background anisotropy experiment (Ruhl *et al.*, 1993). The first new scientific results have been recorded, for instance with the spectacular images of the comet Shoemaker-Levy 9 encounter with Jupiter, as recorded by SPIREX. Next year a sub-millimetre telescope will be installed (AST/RO, Stark 1989).

The University of New South Wales is conducting a site testing programme at the South Pole in collaboration with CARA. We are operating two experiments during this current winter, a near–IR sky brightness monitor and a set of micro-thermal turbulence sensors. The latter experiment also involves the Université de Nice. Both experiments have returned data, and we will report full results at a later date.

The IR sky brightness monitor uses the original IR photometer of the Anglo Australian Observatory, the 'Infrared Photometer Spectrometer' (IRPS), which has been modified for operation through the Antarctic winter. It operates in D.C. mode, measuring the incident sky flux on the detector through a 4° beam in the broad band J, H, K, L' and M filters, and through two 1% resolution CVF's (1.5-2.5 μm and 3-4 μm). The instrument is not attached to a telescope, but receives the sky radiation via a small mirror whose angle can be adjusted along a meridian from zenith to either horizon. While the experiment has been operated this year from the Pole, it is capable of being remotely controlled over

the internet through use of electronic mail. The IRPS is being used to measure not only the sky background level, but also sky fluctuation noise, from instabilities in the the background signal. Early results show the expected low thermal background levels at wavelengths longer than 2.3 μm, with the airglow dominating at shorter wavelengths. They also show cleaner atmospheric windows, with non-zero transmission between H and K.

The second experiment uses small resistive sensors to measure micro-thermal fluctuations in the air temperature at three heights, 7-m, 17-m and 27-m, up a mast above the ice level. Their resistance is responsive to small changes in temperature in less than 1 second, whose magnitude depends on the level of air turbulence. Readings from two pairs of sensors are taken at each level and compared to check for consistency. The results clearly show the increase in turbulence in the lowest layer during times when a strong inversion layer is present, and periods when all layers show similar, sustained levels of low turbulence when it is not.

3. Future Plans

These experiments will continue during the the 1995 Antarctic winter. The IRPS will undergo some small modifications to improve its performance, and obtain a second seasons data. The micro-thermal temperature measurements will be extended to balloon-borne sensors, enabling the contribution over the entire atmospheric column to be determined. A mid–IR monitor will be installed to measure sky emissivity and thus infer levels of winter time cloud cover.

In the long term, however, we do not believe the South Pole will provide the optimal site for astronomy. It is directly under the auroral circle, and thus suffers regularly from a bright optical background (albeit only in specific frequencies). It also experiences a steady katabatic wind of 5-10 m/s. Though low compared to many observatory sites it contributes to seeing degradation. The best observing sites are expected to lie at the high points of the Plateau, Domes Argus (82S, 80E) and Circe (73S, 127E). Dome Circe is close to the center of the auroral circle and the site of a planned French / Italian base. Dome Argus is the highest point on the Plateau. Communications would also be simplified as equatorial satellites can always be sighted.

It is essential to site test these uninhabited locations before a major observatory project can be initiated. It is desirable to do so without need for the prior construction of a new inland station. Fortunately the NSF sponsored 'Automated Geophysical Observatories' (AGOs), constructed by Lockheed, provide a means by which this programme can be achieved. The AGO is a mobile laboratory which can be deployed on the ice by an LC-130 aircraft, and left to run unattended in an autonomous manner for a year (Doolittle 1986). The interior provides a warm enclosure to control and power a series of attached experiments, and a data acquisition system to store the data. The AGO is deployed during the summer months and retrieved, with data, the following summer. It essentially provides a low cost means with which essential site data can be obtained rapidly and with minimal environmental impact. Australia is now committed to the purchase and equipping of an AGO, and with the USA have formed the 'Au-

tomated Astronomical Site Testing Observatory Working Group' (AASTOWG) to achieve this end.

Acknowledgments. The UNSW Antarctic astronomy programme owes a great debt to many people for allowing our work to get on 'The Ice', too many to mention here. I particularly which to thank my colleagues at UNSW for their unstinting efforts to get us where we are today; John Storey, Rodney Marks and Jamie Lloyd, and especially Michael Ashley. We owe a great debt to our colleagues at the Center for Astrophysical Research in Antarctica (CARA), particularly to John Briggs who has undertaken the winter time measurements at the Pole. We are also working closely with Jean Vernin and the Université de Nice.

References

Bally, J. 1989, in 'Astrophysics in Antarctica', Amer. Inst. Phys. conf. proc., 198, 100.

Burton, M.G. *et al.* 1994, Proc. Ast. Soc. Aust., 11, 127.

Doolittle, J.H. 1986, Lockheed Technical Report, LMSC-F171145.

Gillingham, P.R. 1993, in ANARE research notes, 88, 290. Publications of the Australian Antarctic Division.

Harper, D.A. 1989, in 'Astrophysics in Antarctica', Amer. Inst. Phys. conf. proc., 198, 123.

Hereld, M. 1994. in Infrared Astronomy with Arrays, 248: Kluwer.

Ruhl, J. *et al.* BAAS, 25, 927.

Stark, A.A. 1989, in 'Astrophysics in Antarctica', Amer. Inst. Phys. conf. proc., 198, 67.

Airborne Astronomy Symposium on the Galactic Ecosystem
ASP Conference Series, Vol. 73, 1995
M.R. Haas, J.A. Davidson, and E.F. Erickson (eds.)

p.4

POLARIMETRIC SUBMILLIMETER OBSERVATIONS FROM THE SOUTH POLE

GILES NOVAK
Department of Physics and Astronomy, Northwestern University, 2145 Sheridan Road, Evanston, IL 60208-3112

STEPHEN R. PLATT
Yerkes Observatory, University of Chicago, P.O. Box 258, Williams Bay, WI 53191

MARK DRAGOVAN
Department of Astronomy and Astrophysics, and Enrico Fermi Institute, University of Chicago, 5630 South Ellis Avenue, Chicago, IL 60637

ABSTRACT We discuss proposed observations of the polarization of submillimeter continuum emission from the extended Galactic Center region. The observations will be made from the South Pole, using the VIPER 2-meter telescope.

On the largest scales, magnetic fields in the disks of spiral galaxies have spiral configurations. This is true for both the hot, ionized regions and the cooler, predominantly neutral regions. However, for the nucleus of the Galaxy, observations of ionized regions show evidence for a large scale field that has a vertical orientation (i.e. the field is perpendicular to the Galactic Plane). Large quantities of neutral gas are also found in the Galactic nucleus: it contains about one tenth of the Galaxy's total supply, forming a layer roughly 40 pc thick and 450 pc across (Güsten 1989). The large scale configuration of the magnetic field within this neutral gas layer is unknown.

The last decade has witnessed the development of a new technique for observing magnetic fields in neutral regions: polarimetry of far-infrared/submillimeter thermal emission from magnetically aligned dust grains (Hildebrand 1988, Davidson et al. 1994). Polarimetry of 100 μm dust emission, obtained using the KAO, has provided magnetic field maps for several relatively small (~5–10 pc) regions within the Galactic nucleus, one of which is the circumnuclear ring in Sgr A (Werner et al. 1988, Hildebrand et al. 1993).

C-8

Due to recent advances in instrumentation and techniques for far-infrared/submillimeter polarimetry (Platt et al. 1994) it is now feasible to map the large scale magnetic field within the entire Galactic Center neutral gas layer, which stands out clearly at the center of the 240 μm DIRBE map of Fig. 1. It is highly advantageous, however, to use a telescope that permits chopper throws of about a degree, and to observe from a location that allows sensitive measurements over some portion of the far-infrared/submillimeter wavelength range. Such a telescope at such a location will be available when the VIPER telescope is installed at the South Pole in the Austral Summer of 1995-6. VIPER is a 2-meter submillimeter telescope that is being built by the Center for Astrophysical Research from Antarctica (CARA). We are building a 32-beam submillimeter polarimeter for operation on this telescope during the Antarctic winter, and will use it to map the large scale magnetic field in the neutral gas at the Galactic Center.

Our observations will consist of hundreds of individual polarization measurements (see Fig. 1), and we will use the resulting magnetic field map to answer the following questions:

(1) What is the Configuration of the Magnetic Field in the Material that Surrounds the Circumnuclear Ring?

The discovery of a magnetic field in the circumnuclear ring has stimulated investigators to model it using the theory of self-similar magnetic accretion disks — a theory that was originally developed by Blandford and Payne (1982) to account for extragalactic jets. One of the assumptions in this model is that the magnetic field far from the disk is axial (Wardle and Königl, 1990). Our observations will determine whether or not the field in the neutral gas that surrounds the ring has an axial configuration, thus providing an important test for the magnetic accretion disk model of the ring.

(2) Is There Evidence for a Large Scale Vertical Magnetic Field in the Neutral Gas?

The discovery of non-thermal radio filaments in the Galactic Center (Yusef-Zadeh, Morris, and Chance 1984) provided the first evidence for large-scale vertical magnetic fields in the hot, ionized regions of the Galactic Center. There is now evidence, from radio morphology and polarization, for organized vertical fields extending out to Galactocentric radii of several hundred pc (Haynes et al. 1992, Tsuboi et al. 1986). Various hypotheses for the origin of these fields have been proposed. For example, they could be generated by a dynamo mechanism, or they could be of primordial origin. A strong vertical field will influence cosmic ray confinement and transport (Blitz et al. 1985), star formation (Morris 1990), and gas dynamics and accretion.

Our observations will determine the extent to which these vertical fields extend into the neutral gas layer. Because most of the nuclear gas is in this layer, this information will have relevance for understanding the origin of the vertical fields and their role in the gas dynamics at the Galactic Center.

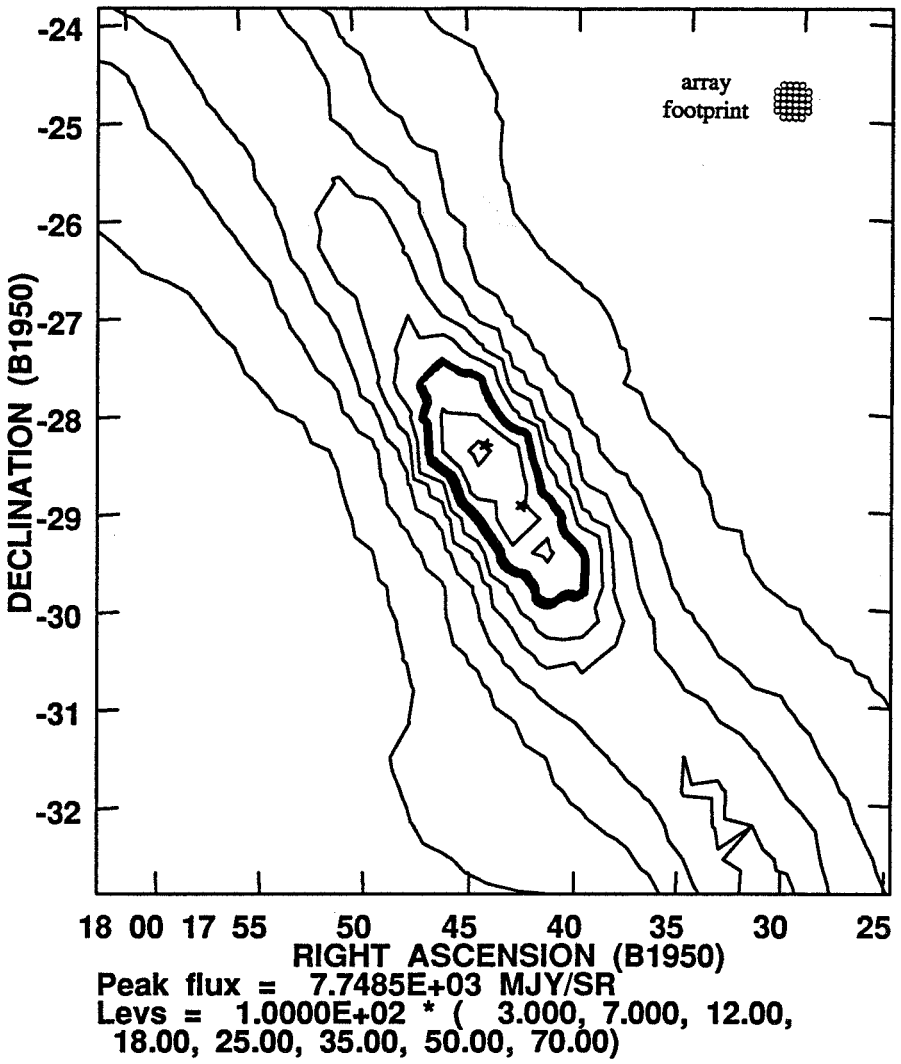

Fig. 1. 240 μm DIRBE map of the central 1.5 kpc of the Galaxy. The array polarimeter for VIPER will operate at 450 μm, and will have an angular resolution of four arcminutes. The brightness of the Galactic Center is sufficient for us to make a polarimetric map of the area within the heavy contour, to an accuracy of σ_P = 0.3%, during a few weeks of winter-over observations. The footprint of the array polarimeter is shown in the top right corner of the figure. The Northern and Southern symbols show the positions of Sgr B2 and Sgr A, respectively.

(3) What is the Configuration of the Magnetic Field in Regions where Massive Stars are Forming?

The formation of massive stars occurs in relatively high-mass molecular clouds, and the Sgr B2 molecular cloud represents an extreme case of this general behavior (Goldsmith et al. 1990). The mean density of Sgr B2 is comparable to that of high-density gas found in starburst nuclei. Polarimetry using VIPER represents the best method for obtaining complete maps of magnetic field configurations within Sgr B2 and other Galactic Center GMC's, and thus for determining the possible importance of magnetic fields for star formation in starburst galaxies.

(4) Can Dispersion in the Angle of Polarization be Used to Estimate Magnetic Field Strengths?

Our observations will provide an opportunity to estimate the *strength* of the Galactic Center magnetic field, using the method of Chandrasekhar and Fermi (1953).

REFERENCES

Blandford, R.D., and Payne, D.G. 1982, M.N.R.A.S. **199**, 883

Blitz, L., Bloemen, J.B.G.M., Hermsen, W., and Bania, T.M. 1985, Astron. Astrophys. **143**, 267

Chandrasekhar, S., and Fermi, E. 1953, Ap. J. **277**, 181

Davidson, J.A., Dowell, C.D., Schleuning, D., Dotson, J.L., and Hildebrand, R.H. 1994, paper 3.2 in this volume.

Goldsmith, P.F., Lis, D.C., Hills, R., and Lasenby, J. 1990, Ap. J. **350**, 186

Güsten, R. 1989, in *The Center of the Galaxy, I.A.U. Symp. No. 136*, ed. M. Morris (Boston:Kluwer), p. 89

Haynes, R.F., Stewart, R.T., Grey, A.D., Reich, W., Reich, P., and Mebold, U. 1992, Astron. Astrophys. **264**, 500

Hildebrand, R.H. 1988, Quart. J. R. A. S. **29**, 327

Hildebrand, R.H., Davidson, J.A., Figer, D.F., Novak, G., Platt, S.R., and Tao, L. 1993, Ap. J. **417**, 565

Morris, M. 1990, in *Galactic and Intergalactic Magnetic Fields, I.A.U. Symp. No. 140*, eds. R. Beck, P.P. Kronberg, and R. Wielebinski, (Boston:Kluwer), p. 361

Platt, S.R., Dotson, J.L., Dowell, C.D., Hildebrand, R.H., Novak, G., and Schleuning, D. 1994, paper 707 in this volume.

Tsuboi, M., Inoue, M., Handa, T., Tabara, H., Kato, T., Sofue, Y., and Kaifu, N. 1986, Astron. J. **94**, 818

Wardle, M., and Königl, A. 1990, Ap. J. **362**, 120

Werner, M.W., Davidson, J.A., Morris, M., Novak, G., Platt, S.R., and Hildebrand, R.H. 1988, Ap. J. **333**, 729

Yusef-Zadeh, F., Morris, M., and Chance, D. 1984, Nature **310**, 557

Airborne Astronomy Symposium on the Galactic Ecosystem
ASP Conference Series, Vol. 73, 1995
M.R. Haas, J.A. Davidson, and E.F. Erickson (eds.)

A CCD OFFSET GUIDER FOR THE KAO

SEAN W. J. COLGAN
SETI Institute; NASA/Ames Research Center, MS 245-6, Moffett Field, CA 94035-1000

EDWIN F. ERICKSON
NASA/Ames Research Center, MS 245-6, Moffett Field, CA 94035-1000

FREDRIC B. HAYNES
Nimbus Software, 8209 Villa Oak Drive, Citrus Heights, CA 95610

DAVID M. RANK
University of California Santa Cruz, 183 NS II, Santa Cruz, CA 95060

ABSTRACT We describe a focal plane guider for the Kuiper Airborne Observatory which consists of a CCD camera interfaced to an AMIGA personal computer. The camera is made by Photometrics Ltd. and utilizes a Thomson 576 × 384 pixel CCD chip operated in Frame Transfer mode. Custom optics produce a scale of 2.4″/pixel, yielding an ~ 12′ diameter field of view. Chopped images of stars with HST Guide Star Catalog magnitudes fainter than 14 have been used for guiding at readout rates $\gtrsim$ 0.5 Hz. The software includes automatic map generation, subframing and zooming, and correction for field rotation when two stars are in the field of view.

INTRODUCTION

A visible imaging system for the focal plane of the KAO has six major objectives:

1) High sensitivity for visually faint objects.
2) Visual monitoring of telescope stability for manual telescope pointing adjustments.
3) Display the sky image along with computer generated symbols, such as positions of known stars, the infrared boresight location, and auxiliary information, to facilitate guiding.
4) Offset pointing capability using a rotation angle to correct for motion of the guide star around the boresight.
5) Computer monitoring of telescope stability through the generation of error signals based on the difference between the measured and expected star positions.
6) Automatic guiding of the telescope using the error signals generated in (5) to correct for telescope pointing errors.

HARDWARE

The overriding requirement for this guiding system is sensitivity. A CCD camera offers the highest quantum efficiency and, hence, sensitivity for the ~ 1 Hz frame rates of interest. An intensifier followed by a CCD provides higher frame rates, but has additional complexity and lower quantum efficiency, which is crucial for guiding on faint stars. Frame transfer mode is essential, since it permits integration of the next picture while the current frame is being read out. In addition, frame transfer obviates the need for a mechanical shutter. Other important requirements for the system are at least a 1 Hz frame rate and a blemish-free CCD chip. To minimize development and maintenance costs, commercial products were used whenever possible. We selected the only commercial CCD camera with frame transfer available when we began the development, built by Photometrics.

The camera features a Thomson, front-illuminated, model 7882 CCD chip with a metal plate covering the storage half of the chip. The imaging area is 384 x 288 square pixels, each of width 22 μm. The peak quantum efficiency is ~ 40% and the read noise is 18 electrons. The gain is set to 10 electrons/Analog-Digital-Unit so that the digitization noise is much smaller than the read noise. Since the readout provides 12 bits (4096 levels), the effective full well is only ~40,000 electrons. Stars brighter than about 8th magnitude saturate the readout for a one second integration. For bright objects, neutral density filters can be manually inserted in the camera optics. The sky noise is typically $i_{sky} \sim 30$ electrons/pixel/second. The camera head includes a Thermo-Electric cooler. The dark current is reduced to $i_{dark} \sim 20$ electrons/pixel/second, a value $< i_{sky}$, by blowing cool cabin air past the fins of the camera head.

An illuminated reticle at the telescope focus is used to verify the computer generated boresight location. A reimaging lens changes the plate scale to a value appropriate for the ~ 6″ image size and the CCD pixel size. The system uses a 300 mm effective focal length (EFL), 82 mm diameter achromatic collimator lens and a 35 mm EFL f/2.0 SLR camera lens in front of the CCD to obtain a scale of 2.4″/pixel. The optics housing forms a periscope, shown in Figure 1, to keep the system compact.

The camera is controlled through ASCII commands sent over a standard RS–232 serial line. The controller supports arbitrary rectangular subframing and binning. The picture is output as an RS–170 video signal. The video is received, processed and the camera commanded with an AMIGA 2000 personal computer containing a LIVE! frame grabber, which can grab 4-bit black and white frames at 15 Hz. For the frame grabber to work properly, it was found necessary to use a video enhancer to condition the camera video signal. The frame rate is limited largely by the digital-to-analog conversion carried out in the camera. The maximum rate is 0.5 Hz for a full frame, binned-by-one image and a maximum of 1.4 Hz for a subframed image. The AMIGA parallel port is used to command telescope moves to correct pointing errors or to move to a new position in the field of view. Additional serial ports enable communication with KAO and experimenter computers.

Figure 2 shows a block diagram of the system, with interfaces to KAO and experimenter systems. The electronics mount on a plate installed under the experimenter's seat, and the system is operated from the tracker rack. The custom optical assembly (Figure 1) has no adjustments or moving parts, and is

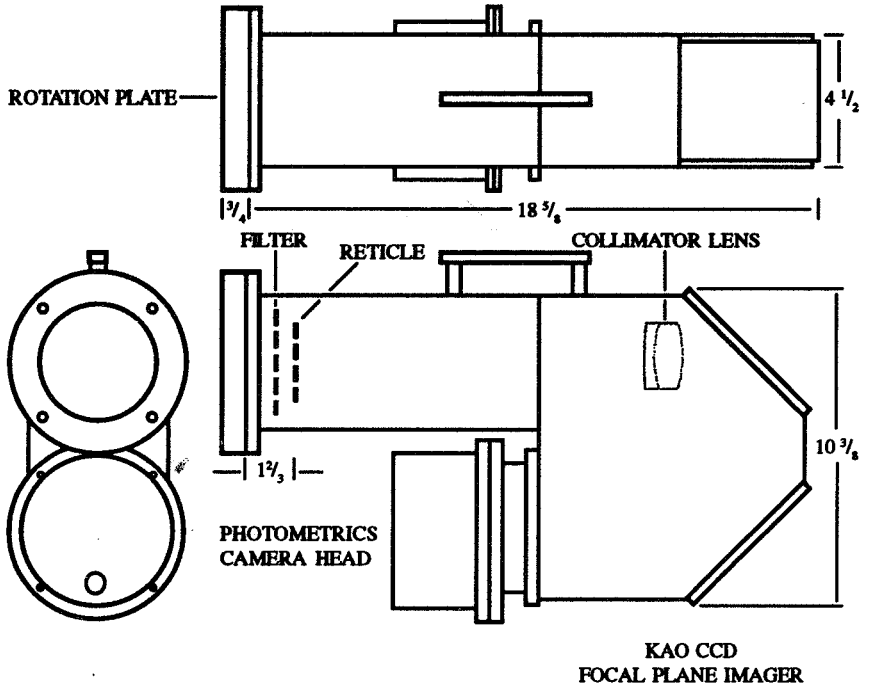

Figure 1: The periscope optics housing.

positioned, shimmed and bolted when mounting in order to achieve the proper focus and orientation.

SOFTWARE

The HST guide star catalog (Lasker et al. 1990, Russell et al. 1990) is used to calculate offsets from guide stars for each object location. The offsets are entered into a file before the flight. Offsets for a regular grid of points can be generated automatically. In-flight, points to be observed are selected on-line. For sources with only faint or distant guide stars, the telescope is nodded at intervals of 15 seconds or more to permit the guider camera to integrate up to several seconds.

The guiding software includes the following features:

- Auto-gain: camera gain is adjusted automatically to set the RS–170 output for maximum intensity on the brightest star.
- Auto-subframe and zoom: automatically implements an optimized format and zoom factor after star offsets are selected.
- Overlays on sky image: boxes and coordinates for guide stars, a diamond or slit for the location of the infrared boresight, experimenter run number, and current guiding errors.
- Correction for field rotation: using two stars of known orientation. With one star, the rotation angle can be received from the on-board computer system or entered manually from the flight plan.

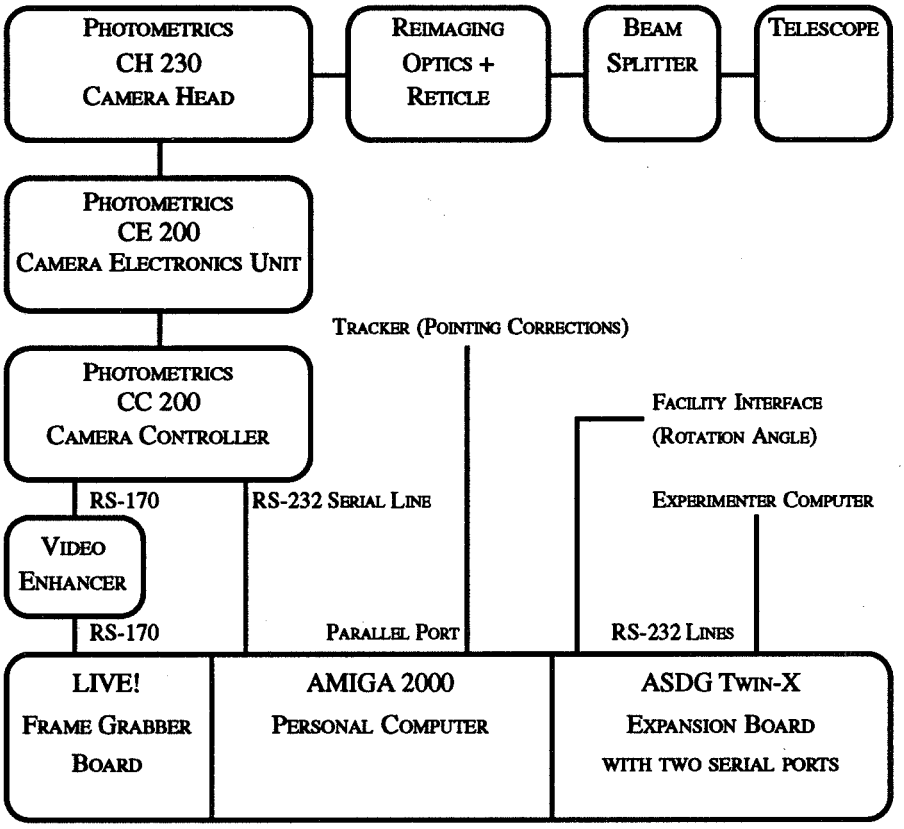

Figure 2: CCD Offset Guider Block Diagram.

- Autoguiding: automatically moving the telescope to correct pointing errors.
- Plate-scale measurement: using a star pair of known separation.
- Boresight verification: moves the telescope in a user defined cross pattern to verify the location of the IR detector on the sky.
- Data Recording: Guiding errors can be recorded with the infrared data and the guiding can be recorded with a VCR.
- User documentation: a 40 page User's manual is available.

PERFORMANCE AND PLANS

All the major system objectives listed in the introduction have been accomplished. The system has successfully guided on chopped images of stars with magnitudes of $\gtrsim 14.5$ in the Hubble Guide Star Catalog, for integration times $\lesssim 2$ seconds. The probability of finding a star with visual magnitude of 13 or less in the Field of View is over 90% at the Galactic poles, and over 99.9% averaged over the whole sky (Erickson and Meyer, 1988). The stability

of the video picture when changing CCD formats and zoom factors, due to the digital-to-analog conversion in the camera controller, is only $\lesssim 2.5''$. This can be improved somewhat by using the reticle as a reference each time the format or zoom factor is changed. The internal stability of the guider system for a fixed format and zoom factor is about 0.2 pixel (*e.g.* 0.5″ if binning by 1), better than typical KAO telescope pointing. Automatic guiding does require camera gain adjustment if the the guide star image is multiple or contaminated by a chopped image from the opposite beam. The system has been used on over 50 research flights and is very reliable.

With the installation of a faster CPU, a Direct-Memory-Access connection between the AMIGA and the CCD camera controller will soon be operational. This will obviate the need for the intermediate video signal, the video enhancer and the frame grabber. By eliminating the digital-to-analog conversion in the camera controller, the main speed bottleneck will be bypassed, and frame rates of 1 Hz (full frame) to 4 Hz (for $1' \times 1'$ subframes) are expected. This will also eliminate the $\sim 2.5''$ uncertainty in the boresight location due to instability of the video signal. The feasibility of operating the camera in the telescope cavity, at the straight Cassegrain focus, is being investigated. A motorized filter wheel has already been constructed for this option.

REFERENCES

Erickson, E.F., & Meyer, A.M., 1988, SOFIA Engineering Report: "Video Tracking System Performance Considerations for SOFIA"

Lasker, B.M., Sturch, C.R., McLean, B.J., Russell, J.L., Jenkner, H., & Shara, M.M., 1990, *A.J.*, **99**, 2019

Russell, J.L., Lasker, B.M., McLean, B.J., Sturch, C.R., & Jenkner, H., 1990, *A.J.*, **99**, 2059

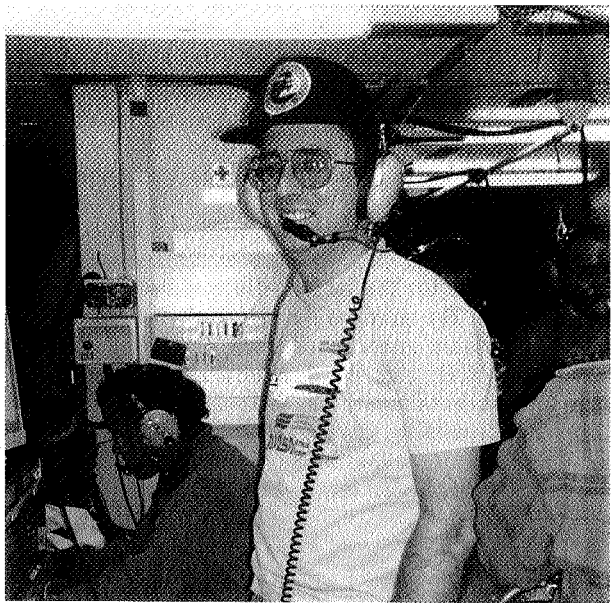

David Lee, Sean Colgan, Xander Tielens

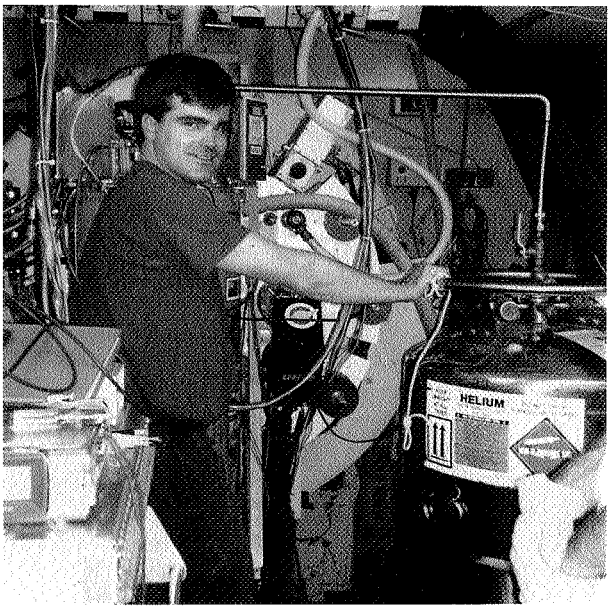

Jim Baltz

Airborne Astronomy Symposium on the Galactic Ecosystem
ASP Conference Series, Vol. 73, 1995
M.R. Haas, J.A. Davidson, and E.F. Erickson (eds.)

HIFOGS: ITS DESIGN, OPERATION AND CALIBRATION

FRED C. WITTEBORN
NASA Ames Research Center, MS:245-6 Moffett Field, CA 94035

MARTIN COHEN
Univ. of California, Radioastronomy Lab., 601 Campbell Hall, Berkeley, CA 94720

JESSE D. BREGMAN
NASA Ames Research Center, MS:245-6 Moffett Field, CA 94035

KAREN R. HEERE
Sterling Software, Ames Research Center, MS:245-6 Moffett Field, CA 94035

THOMAS P. GREENE
Institute for Astronomy, Univ. of Hawaii, 2680 Woodlawn Dr., Honolulu, HI 96822

DIANE H. WOODEN
NASA Ames Research Center, MS:245-6 Moffett Field, CA 94035

ABSTRACT The High-efficiency, Infrared Faint Object Grating Spectrometer (HIFOGS) provides spectral coverage of selectable portions of the 3 to 18 micron range at resolving powers from 100 to 1000 using 120 Si:Bi detectors. Additional coverage to 30 microns is provided by a bank of 32 Si:P detectors. Selectable apertures, gratings and band-pass filters provide flexibility to this system. Software for operation of HIFOGS and reduction of the data runs on a MacIntosh computer. HIFOGS has been used to establish celestial flux standards using 3 independent approaches: comparisons to star models, comparisons to asteroid models and comparisons to laboratory blackbodies. These standards are expected to have wide application in astronomical thermal-infrared spectroscopy.

INTRODUCTION

HIFOGS (the High-efficiency Infrared Faint Object Grating Spectrometer) was designed for studying solid state features and molecular bands at low to moderate resolution in the 3 to 30 micron spectral range. Its best performance is from 5 to 13 microns. Solid state features of interest include various ices surrounding protostellar sources (e.g. Tielens et al. 1984) such as water ice and methanol ice, dust in comets and stellar envelopes and mineral emission spectra from surfaces of asteroids and planets (e.g. Sprague et al. 1993). Molecular bands of interest include the polycyclic aromatic hydrocarbon emissions characteristic of many sources where interstellar or circumstellar clouds are illuminated by UV (e.g. Allamandola et al. 1989, Cohen et al. 1989, Sellgren et al. 1985). These topics require accurate measurements of the shapes of bands and relative intensities

across a wide spectral range. Mineral features such as the Christiansen maximum must be measured to a few percent to provide diagnostic information. The ice absorptions require accurate shape determinations at resolving powers from 200 to 1000. Such spectra require accurate flux calibrations and have stimulated a renewed examination of stellar standards (Cohen et al. 1992a,b,c) for which HIFOGS is well suited, provided that it is operated under conditions that assure similar responsivity when viewing different objects. Consequently this report describes not only the design of HIFOGS, but also its operation and calibration.

DESIGN

The optical system is shown schematically in Fig.1. Infrared light from the telescope passes through a vacuum, infrared window (e.g. KRS5) and is focussed at the LHe-cooled entrance aperture (bottom of figure). The aperture is externally selectable. Values range from 0.3 mm to 2.0 mm. Neutral density filters can be combined with some apertures. The diverging beam passes through an externally selectable cut-on or order sorting filter. Filters with cut-on wavelengths of 2.85, 4.5, 4.9, 7.5, 7.9, 13.7, and 14.7 microns are mounted for use with gratings in first order. Band-pass filters must be used for operation in higher orders. To achieve a focal length sufficiently long for resolving powers of 200 to 1000, the optical path is folded before reaching the parabolic collimator mirror. The mechanical layout and optical baffling in this first level of optics is shown in Fig.2. The transfer of the light path between levels is shown in Fig.3. The collimator mirror

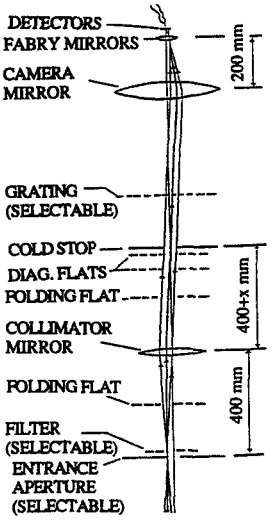

Fig. 1. Schematic of HIFOGS Optical Layout

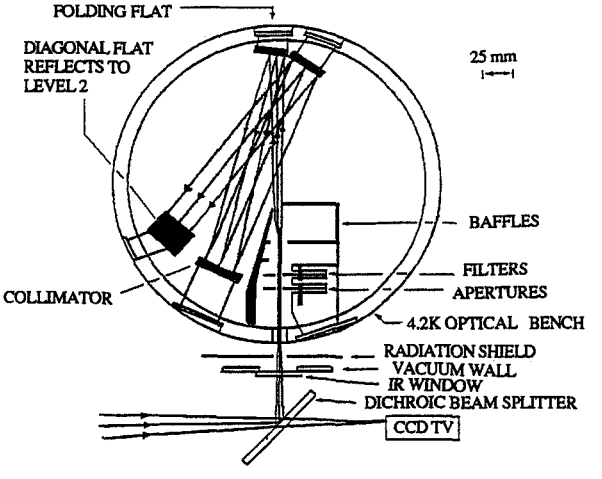

Fig. 2. 1st Optical Level: Mechanical Layout Mirrors are gold-surfaced, fused-silica glass. Filters and apertures are selected externally via gear trains and insulating shafts (not shown).

also serves to image the telescope's secondary mirror onto the cold stop (located in the second level between the diagonal flat and the grating). The cold stop is about 25 mm diameter for the KAO's f/17 focus. (It is replaced by a much smaller aperture located closer to the diagonal flat when used with the f/35, 3m diam. IRTF.) The collimated beam then reaches the grating. Two thin gratings are installed back-to-back to permit changing gratings in a few minutes. Grating

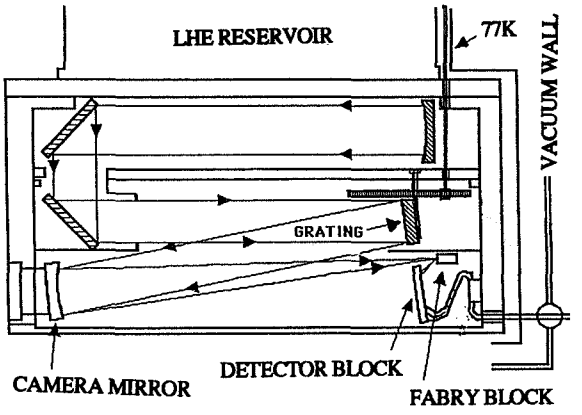

Fig.3. Side view: Schematic. The gratings are attached to a large spur gear driven by a worm gear through bevel gears and a long insulating shaft which is connected to the outside through a rotary-motion, high-vacuum feed-through (not shown).

angle adjustment is accomplished with a worm gear driven from outside the dewar through a rotary-motion, vacuum feedthrough. The grating disperses light across a large camera mirror in the third optical level. The camera mirror forms images of the entrance aperture (at each wavelength) on the Fabry bank which consists of 120 individual, off-axis ellipsoids. Each ellipsoid images the cold stop onto a corresponding detector in a small spectral range. The large size of the camera mirror and the length of the Fabry permit coverage of nearly an octave of the spectrum at resolving power 130-250.

OPERATION

HIFOGS is mounted at the Nasmyth focus of the KAO (f/17). Its optical axis is aligned with the secondary mirror by mechanical tilting of the dewar assembly. A thin gold beam splitter permits simultaneous viewing of visible light with a CCD camera (see Fig. 2) for accurate focal-plane guiding. The signal is modulated by moving the secondary mirror of the telescope to point alternately at an object and at empty sky at about 7 Hz so that the AC component is the signal from the object plus gradients in the foreground radiation. Gradients are removed by systematically alternating the relative positions of object and empty sky. The voltage output of each detector is connected to the gate of an adjacent, LHe-cooled, field-effect transistor (FET). Each FET is wired as a source follower (to provide low output impedance). The AC components of the outputs are then sampled (outside the dewar) by a multiplexed array of amplifiers (MUX). Commands to the MUX and storage of output are accomplished by a Macintosh IIx computer with National Instruments interface boards (including a 12 bit A/D converter). Software for storing data and analyzing them facilitate coaddition of spectra, statistical error analysis, wavelength assignments, flux determination and graphics display. Instruction manuals for the software (by A. Graps with an update by M. Whittemore) are available on request. Wavelength calibration is achieved by comparison with a carefully calibrated transmission spectrum of polystyrene. Flux calibration relative to a standard star is achieved by dividing by the spectrum of a standard star taken on the same night through similar (or correctable) air mass and then multiplying by the corresponding standard star flux at each wavelength interval. The determination of standard star fluxes is discussed in the next section.

Sensitivities achieved on the KAO using a 1.5 mm aperture (20 arcsecs on sky) are given below:

NEFD $W/cm^2/\mu m/Hz^{1/2}$	$Jy/Hz^{1/2}$	Wavelength μm	Resolving Power
1.6×10^{-16}	20	6	200
3.3×10^{-16}	110	10	200
2.2×10^{-16}	210	17	100

FLUX CALIBRATION STANDARDS

We have used three approaches to provide celestial flux standards for the 3 to 30 micron spectral range.

(1) Stellar model: So far, the most reliable approach is to measure ratios of bright A0-M0 star spectra to the spectrum of α CMa and multiply (at each wavelength) by the corresponding flux determined by Kurucz in his model for α CMa (see Cohen et al., 1992a). A spectrum of α Tau obtained by this approach using weighted averages of spectra from several instruments (including HIFOGS) is reported by Cohen et al., 1992b). The deep absorption caused by SiO (7.6-10 microns) and CO (4.2-5.8 microns and near 2.5 microns) illustrates why simple approximations such as Planck functions cannot be used for stellar spectra. Fig. 4 shows the increasing depth of the CO and SiO bands in stars of successively lower temperatures from F0 to G2 to K3. More HIFOGS spectra showing this effect from K0 to M0 appear in Cohen et al., 1992c.

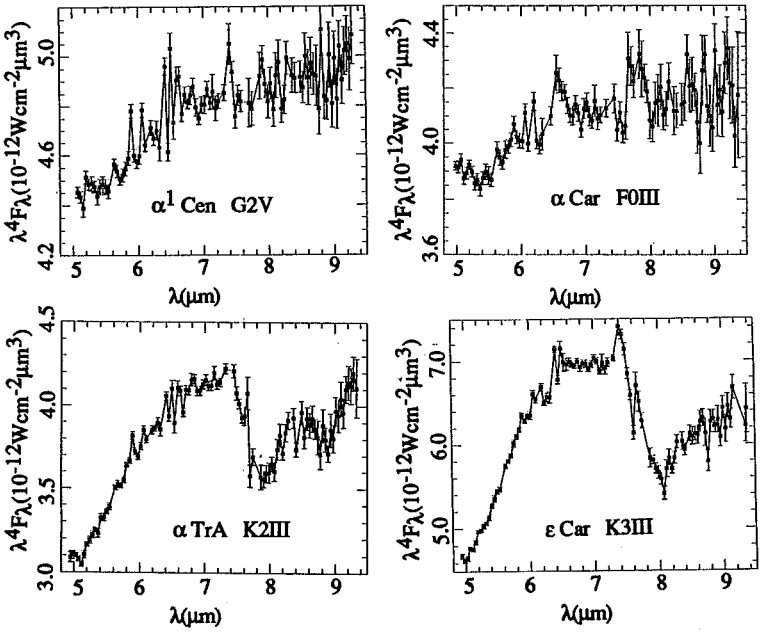

Fig. 4. Stellar spectra in the 5-9 micron spectral range: λ^4F_λ versus λ as determined from ratios of KAO/HIFOGS spectra of various stars to the α CMa spectrum, multiplied by the Kurucz model for α CMa.

(2) Asteroid model: The largest asteroids are much brighter than preferred standard stars at wavelengths longer than 15 microns. Good spectra of Vesta and Ceres have been obtained, but so far, models for asteroids have larger uncertainties than those for A0 stars (but see Fig. 7).

(3) Lab blackbody: The ultimate calibrator would seem to be a laboratory blackbody. Comparison of a star with a laboratory standard, however, requires careful correction for telescope transmission and atmospheric transmission. The laboratory blackbody spectrum must be measured at two temperatures to permit subtraction of the chopper blade emission, since this signal must also be modulated. Fig. 5 shows schematically how the blackbody spectrum and telescope transmission have been measured. The standard is the International Reference Blackbody (IRB) which has emissivity >0.999 throughout the 3-30 micron range and temperature stability of a few millikelvins.

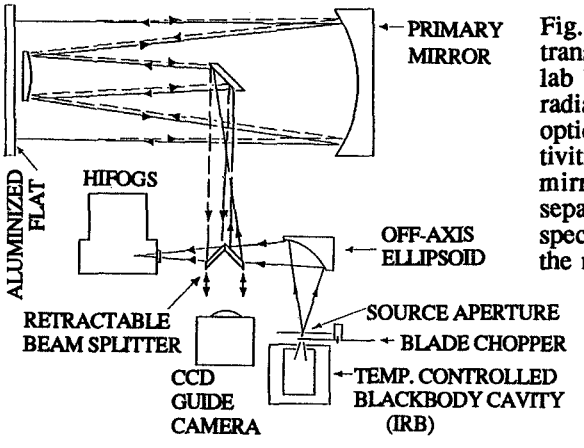

Fig. 5. Schematic for telescope transmission measurements and lab blackbody calibrations. The radiation traverses the telescope optical path twice. The reflectivities of the retractable mirrors are measured separately; the blackbody spectra are taken directly when the mirrors are retracted.

Our first attempts to calibrate detector responsivity against the IRB gave spurious results. We isolated the problem to a dependence of detector responsivity upon background emission. The responsivity increases with background + signal. Consequently the detector must see roughly the same background from the lab set-up as from the telescope at high altitude. This condition has, so far, been approximated by reducing the spectrometer entrance aperture in the lab IRB spectra. Plans for improved calibration with the IRB include (1) cooling the entrance path, optics and source aperture to values encountered in flight and (2) monitoring the DC levels of selected detectors so that these can be matched to flight values during lab IRB calibration. The need for matching of modulation frequency, f/cone and detector temperature was recognized earlier. Preliminary spectra based on roughly matched backgrounds are shown in Figures 6 and 7. As these spectra become more refined, they will provide increasingly accurate tests of the stellar and asteroidal models.

ACKNOWLEDGEMENTS

The Si:P detectors were provided by Drs. Alberto Salama and Leo Metcalfe of ESA/ESTEC. The operation and performance of these detectors will be discussed in a later paper. We are indebted to the flight and ground crews of the KAO for their successful efforts in obtaining the data presented here.

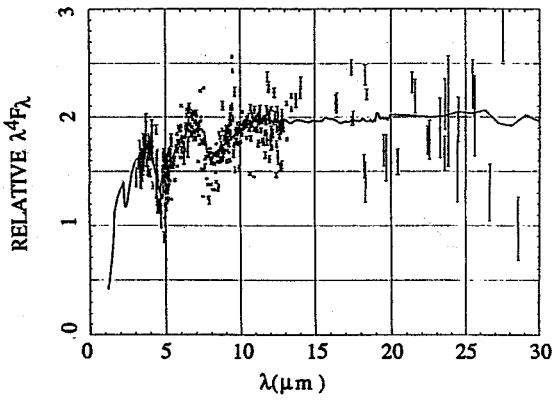

Fig. 6. The data points are spectral ratios of α Tau to the difference of two lab blackbodies times the difference of the corresponding Planck functions. The smooth line is based on measured ratios of α Tau to α CMa times the Kurucz model.

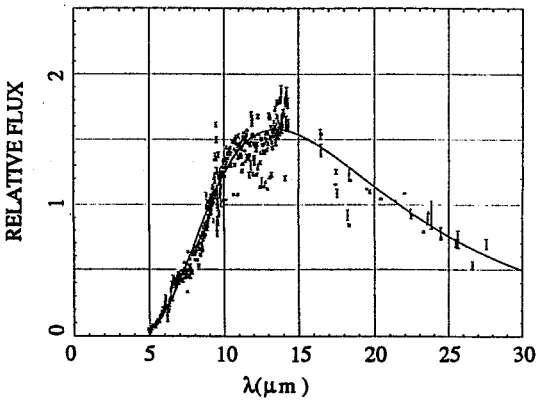

Fig. 7. The data points are spectral ratios of Ceres to the difference of two lab blackbodies times the difference of the corresponing Planck functions. The smooth line is just a 215K Planck function.

REFERENCES

Allamandola, L.J., Bregman, J.D., Sandford, S.A., Tielens, A.G.G.M., Witteborn, F.C. and Wooden, D.H., 1989, ApJ, 345, L59.

Cohen, M., Tielens, A.G.G.M., Bregman, J.D., Witteborn, F.C., Rank, D.M., Allamandola, L.J., Wooden, D.H., de Muizon, M., 1989, ApJ, 341, 246.

Cohen, M., Walker, R.G., Barlow, M.J., and Deacon, J.R., 1992a, AJ, 104, 1650.

Cohen, M., Walker, R.G. and Witteborn, F.C., 1992b, AJ, 104, 2030.

Cohen, M., Witteborn, F.C., Carbon, D., Augason, G., Wooden, D.H., Bregman, J.D., and Goorvitch, D., 1992c, AJ, 104, 2045.

Sellgren, K., Allamandola, L.J., Bregman, J.D., Werner, M.W. and Wooden, D.H., 1985, ApJ, 299, 416.

Sprague, A.L., Witteborn, F.C., Kozlowski, R.W., Cruikshank, D.P., Bartholomew, M.J. and Graps, A.L., 1993, Icarus , 100, 73.

Tielens, A.G.G.M., Witteborn, F., Goebel, J., Allamandola, L.J., d'Hendecourt, L.B., 1984, NASA CP 2353.

Airborne Astronomy Symposium on the Galactic Ecosystem
ASP Conference Series, Vol. 73, 1995
M.R. Haas, J.A. Davidson, and E.F. Erickson (eds.)

A SYNCHRONOUS MOTOR CHOPPER FOR LABORATORY TESTING OF DETECTOR SYSTEMS IN INFRARED ASTRONOMY

JAMES A. BALTZ
SETI Institute, NASA/Ames Research Center, MS 245-6, Moffett Field, CA 94035-1000

EDWIN F. ERICKSON
NASA/Ames Research Center, MS 245-6, Moffett Field, CA 94035-1000

ABSTRACT Airborne and ground-based IR telescopes have oscillating secondary mirrors to permit subtraction of background emission from the sky and telescope. These chopping mirrors are synchronized to a clock which may originate in the data acquisition system. For laboratory testing of detecting instruments with such data systems, externally synchronized chopped IR sources are required. We describe a laboratory chopper in which a synchronous motor is driven by 2-phase sinusoidal currents in sync with an external clock at frequencies from 5 to 50 Hz. This design is used with the KAO's facility sources, the Chopped Hotplate and the Portable Chopped Light Source (PCLS).

DESIGN OPTIONS

Before the development of this chopper, we used an unsynchronized system built around a DC motor with a tacho-generator for analog speed feedback. Light from a photodiode, chopped by the blade, drove a phototransistor to provide a reference square wave for a lock-in amplifier or an externally synchronized data acquisition chassis. When we developed a new data acquisition system that could not accept an external reference signal but generated its own instead, we required a synchronized chopper to go with it. Three alternative technologies were considered:

The simplest approach would use a solenoid to move a shutter-like chopper, with current switched by the external clock. This could work effectively in at least one of our applications, a chopped blackbody source inside a large vacuum tank. Here the chopper blade could be small and light, and the mass of the tank could easily absorb any vibration generated by reciprocating motion. However, in most of our other applications, involving larger blades and less steady mountings, a solenoid system would work poorly compared to a motor-based design.

We recognized that a DC motor system with digital feedback could do the job effectively. Good speed control would require a shaft encoder generating many pulses per revolution, with a phase-lock loop frequency multiplier making the reference signal from the incoming square wave. A position feedback loop would also be needed, to ensure lockup at the same phase every time. This solution could work well, but it involves considerable engineering complexity.

It also suffers from the disadvantage that performance would vary depending on chopper blade inertia; our blades range from 3.5 to 16 inches in diameter.

From our perspective, an easier solution was to use an AC synchronous motor, driven by synthetic waveforms generated in sync with the incoming square wave. Synchronous motors require two phase current, ideally sinusoidal with a 90° phase separation. The driving waveforms can be generated in several ways, the simplest of which uses active filters approximately tuned for the incoming square wave frequency. Beyond this, the only potential source of difficulty is that standard commercial synchronous motors run on line voltage and so must be driven by relatively high-voltage amplifier circuits. A synchronous motor system has the advantages that it requires little fine-tuning to achieve satisfactory operation, and it is fairly insensitive to changes in inertial load.

DESIGN OVERVIEW

The block diagram below shows the synchronous motor system as implemented for the KAO's Chopped Hotplate and Portable Chopped Light Source (PCLS). A logic level square wave signal comes from the outside, or from an internal clock providing frequencies from 1 to 99 Hz, adjustable by thumbwheel switches. It passes through a speed limiter circuit which, when enabled, cuts off the output whenever the frequency exceeds a set value. The next element is the sinewave generator, which produces two sinusoidal voltages 90° apart in phase, in sync with the incoming square wave. These signals go to identical class B amplifiers whose output currents are proportional to the input voltages, with output voltages varying with load impedance up to a limit of about 90 V RMS. A 4-pole polarized hysteresis motor turns a two-bladed chopper, providing stable chopping action at frequencies from 5 to 40 Hz.

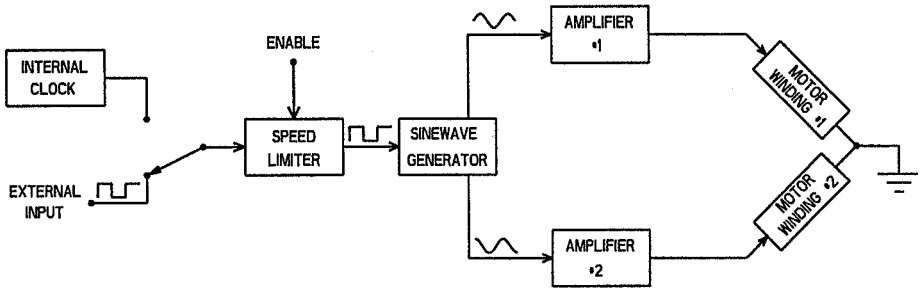

MOTOR SELECTION

Small AC synchronous motors come in two varieties, hysteresis and reluctance. Both types have two stator windings that are powered by sinusoidal currents 90° apart in phase, generating a rotating magnetic field. Hysteresis motors have cylindrical rotors that can lock in at any orientation relative to the driving field. This is highly undesirable for choppers. Hysteresis motors have the advantage that they can synchronize large inertia loads. Reluctance motors have salient

poles, so they lock in at discrete phases; a four pole motor used with a two-bladed chopper will have only two phase possibilities 180° apart. However, the reluctance motor has severe difficulty accelerating inertial loads.

Fortunately a better choice exists, the polarized hysteresis motor. It uses a small piece of permanent magnetic material in the rotor to force lock-in at a specific phase, while preserving most of the load handling ability of the hysteresis type. Most of our choppers, including that in the PCLS, use a polarized hysteresis motor made by Elinco of Norwalk, CT, designated type FSM-3748. It is rated at 1.6 oz.-in. of torque when run on 115 V at 60 Hz. This easily handles chopper blades of aluminum or fiberglass up to 8 in. diameter. We drive it with about 75 mA RMS per winding, at frequencies of 5 to 50 Hz. The voltage varies from about 30 to 90 V RMS over this frequency range.

This motor will not handle the Chopped Hotplate's large blade, a 16.5 in. diameter openwork aluminum frame covered by foil and/or paper. Experiment revealed that a regular unpolarized hysteresis motor of the same size can synchronize this load. The lack of phase reproducibility causes no hardship, because the Hotplate's signal phase varies with position across the large aperture, and so this source is usually not used with phased data systems.

ELECTRICAL DESIGN

To ensure smooth operation at low speeds, the synchronous motor should be driven by a clean sinusoidal waveform. Originally we used a concatenated pair of active low-pass filters to make a sinusoid from the square wave. Each filter had a Q of around 1, giving a gentle peak in amplitude response, so that the frequency could be varied over a range without much change in output level. Larger changes in frequency required retuning the filter by selecting a new set of resistors via a rotary switch. The phase delay for the second output was produced with a similar pair of filters, chosen so that each contributed about 45° phase lag. The system worked well, but we wished to eliminate the need to set a switch to match the incoming frequency.

To provide the same functionality without a switch, we replaced the filters with a circuit adapted from a function generator. Trig-Tek Inc., of Anaheim, CA, repackaged part of the circuitry in their Model 702 function generator on a 4.25 in. × 4.5 in. card, calling it the Model 702C. It uses a phase lock loop to generate a 100× multiple of the input frequency. This goes to a pair of special function ICs whose outputs change with every clock pulse to trace one cycle of sine and cosine in 100 clock ticks. The outputs go through an adjustable gain stage, giving sinusoids from 0 to 8 V RMS.

These signals go to a pair of class B amplifier circuits, built with bipolar transistors. Their outputs are current sources proportional to the input voltage. The motor windings receive essentially constant current over the entire frequency range, which ensures that I^2R heating will be independent of frequency. In order to provide an output voltage swing of 90 V RMS for the higher frequencies, the circuit uses ±120 V supply voltages. All transistors are rated for 300 V, and zeners across the output protect them against over-voltage caused by inductive flyback. We found it necessary to add capacitors across the outputs to suppress oscillations arising from an interaction with the cable and motor windings.

PERFORMANCE

Synchronous motors do not maintain perfectly smooth synchronization, even if the load remains steady and the driving waveform is clean. There is a tendency to 'hunt' about the synchronized position relative to the rotating magnetic field. We tested for stability at different frequencies by looking at the output of an optical sensor chopped by the blade. The FFT spectra obtained at frequencies of 5 and 16 Hz are shown here, plotted with the fundamental (indicated by the arrow) and odd harmonics off scale so that the jitter sidebands and even harmonics can be clearly seen. The sidebands are symmetrical at low frequencies, but become asymmetric at higher frequencies, probably because of 60 Hz ripple from the amplifiers' power supply.

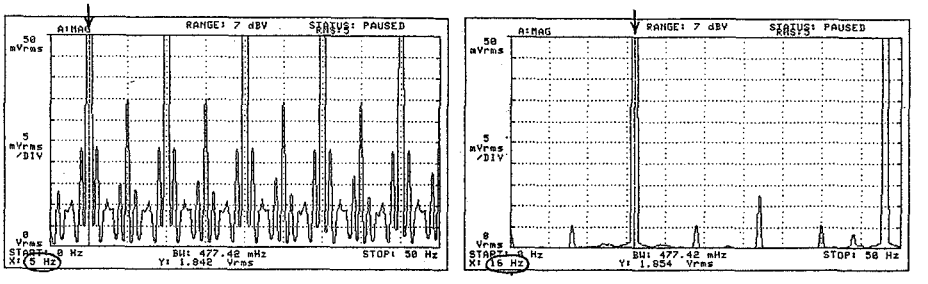

To make meaningful quantitative measurements of this jitter, we triggered a digital scope with the leading edge of the chopped output and recorded the peak-to-peak time variation in the trailing edge. The worst case was at the lowest frequency of 5 Hz, where the trailing edge varied by 3.1 % of the pulse width. This level of jitter can be tolerated because astronomical data systems integrate for comparatively long times, even in laboratory use. Synchronous demodulation of the 5 Hz waveform yielded a signal to noise of 640 in 8 seconds of integration. At higher frequencies we observed much better stability; for example, at 20 Hz the jitter was only 0.4 % of the pulse width.

The performance of this system has proved satisfactory for all of our applications, including the KAO's PCLS and Chopped Hotplate. It has been easy to implement and reliable over four years of operation. However, we should note that its stability cannot be improved by any means, since the motor's intrinsic characteristics dominate. If smoother operation were needed, only a DC motor system with digital feedback would suffice. We can suggest one modification that would be an improvement in some ways: Order customized motors wound for lower voltages, and reduce the amplifier supply voltages. This would simplify parts selection and facilitate higher-frequency operation.

Airborne Astronomy Symposium on the Galactic Ecosystem
ASP Conference Series, Vol. 73, 1995
M.R. Haas, J.A. Davidson, and E.F. Erickson (eds.)

MID-INFRARED ARRAY CAMERA ON THE KAO

Jesse Bregman and David Harker

NASA - Ames Research Center, Moffett Field, CA 94035

D. Rank and P. Temi

Astronomy Department, University of California, Santa Cruz, CA 95064

Abstract. The University of California at Santa Cruz and the NASA Ames Research Center have developed a mid-infrared Si:Ga 128x128 array camera. The camera has been used on several flights on the KAO to obtain data in the mid-infrared wavelength (4-8μm) range. At the f/17 bent Cassegrain focus, the pixel spacing is 1.6 arcsec, resulting in a FOV of 3.4 arcmin. The bandpass of the camera is determined by a set of 4 fixed filters and a 4-8μm CVF. Camera performance of 92mJy/square arcsec/minute has been achieved, but is far from optimal. Realistic improvements to the camera and pointing stability on the KAO in the near future should increase the camera's sensitivity on future flights by 5-10x.

1. Instrument Description

The introduction of large scale two dimensional infrared arrays is in the process of revolutionizing observational astronomy. We have extended this technology to mid-infrared wavelengths for spectroscopic imaging with the KAO. An Amber Engineering Inc. 128x128 Si:Ga detector is currently in operation in our mid-infrared camera. The camera is designed around a LHe dewar with an optical design shown in Figure 1. Anti-reflection coated lens, filter, and window assemblies, which are optimized for the bandpasses used, are modular in construction, allowing a change of array and optics in a few hours. The camera has a filter wheel with four fixed filters and a 2% CVF (4-8μm), a 38mm f/1.5 ZnSe reimaging lens operating at a focal reduction of 2, and Lyot stop baffles.

On the KAO, the camera is mounted at the bent Cassegrain focus (f/17), providing a pixel spacing of 1.6 arcsec and a FOV of 3.4 arcmin. This large FOV allows for chopping between two areas on the array when the sources are less extended than about an arcmin. The light path between the instrument and the air bearing is enclosed in a pipe which allows cold air to be drawn from the telescope cavity, past the beamsplitter, and vented overboard. This arrangement reduces the effective temperature gradient between telescope and camera, thereby improving the image quality and reducing the background as seen by the detector.

The array can be read in the stare and integrate mode or in phase with the chopper. The chopped data are coadded in two separate frame buffers. DC sky

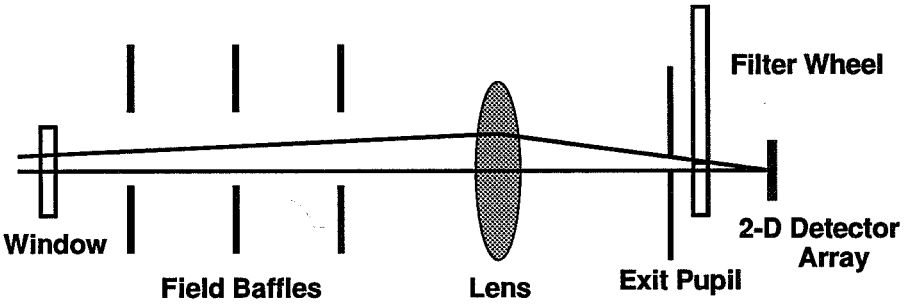

Figure 1. Optical layout of the spectrographics camera. The system is well baffled to assure low background and the exit pupil stop has a central blocking spot ($\approx$ 10% in area) which is matched to the telescope's central obscuration, thus eliminating direct thermal radiation from high emissivity surfaces.

and "flat" frames, which are used to calibrate the array, are stored separately at the beginning of data taking. We record the frame buffer data at intervals of 10 to 60 seconds as part of the data acquisition sequence, much as we do for our ground based observations. For on chip chopping, subtraction of the buffers produces a double image of the source minus the sky. This technique has the advantage of continuous measurement of the sky background and nearly 100% duty cycle for the focal plane light.

A block diagram of our portable data system is shown in Figure 2. Instrument control, data acquisition, and on-the-spot reduction are performed by a Macintosh IIx computer. A National Instruments I/O board provides the master clock timing signals to the array controller and computer interface electronics. Parallel 12 bit focal plane array data from the controller is captured by a second National Instruments digital I/O board and placed directly into memory for access by the Macintosh using both custom software and several commercial software packages. We also use an ethernet link to secondary computers so that IRAF can be used to process the data in near real time. The ethernet link is used with the Sun computers on the KAO for data reduction and backup storage.

To account for the rotation of the images, data are collected in the KAO's "freeze mode" in which many frames can be taken at one angle of rotation. The data are then later derotated in the reduction process. An example of the KAO stellar profile from the data at 6.2μm obtained on our April 1, 1994 flight is shown in Figure 3. The greyscale picture is of our standard, Alpha Ori, and the graph is a radial profile of the star.

2. Instrument Performance

Performance measurements were made of the Si:Ga camera at 6.6μm on the KAO during flights in March and April 1994. We have achieved a 50 pixel (12.8$''$ circle at 1.6$''$/pixel) sensitivity of $\approx 5 \times 10^{-19}$ W/cm^2 = 1 sigma rms in 330 sec or 92mJy/sq arcsec/min ($\Delta\lambda/\lambda = 40$).

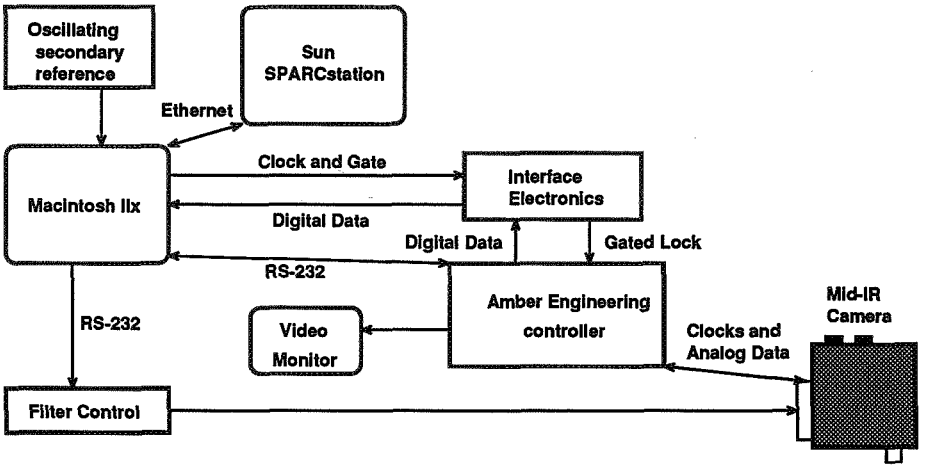

Figure 2. Block diagram of the present data taking system as it is installed on the KAO

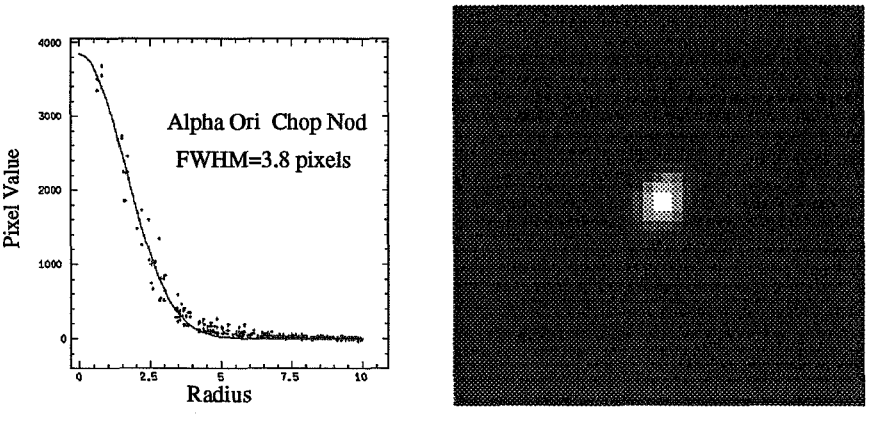

Figure 3. KAO stellar profiles of Alpha Ori. On the left is a profile taken on 4/1/94 at 6.2μm in a chop and nod sequence of four integrations, $+--+$ with the camera. On the right is a 64x64 section of the chip from which the profile is taken. The 6.2μm profile has a FWHM of 6.1 arcsec. This image size is mostly a measure of the tracker chop-nod stability of our flight.

This performance is more than an order of magnitude worse than for an optimized system (*i.e.* BLIP).We have identified two problems which degraded the camera sensitivity. First, the background power we measured was 14 times higher than for a 240K telescope with an emissivity of 10%. Secondly, the CVF we used had a transmission of only 20%. We can reduce the background substantially by changing the way we mount the camera, and we will improve the filter transmission by using fixed filters with peak transmission of 80%. In addition, the pointing stability of the telescope was poor, resulting in point source images spread over a diameter of 8 pixels (13 arcsec). We know from seeing experiments that the FWHM of a point source should be 3 arcsec. Image motion compensation (work now underway on the KAO) should additionally improve our total point source S/N by about 2x. Thus, we realistically expect a point source sensitivity improvement of 5-10 times that measured on our last flight, or 2×10^{-18} W/cm^2 = 5 sigma in 10 seconds.

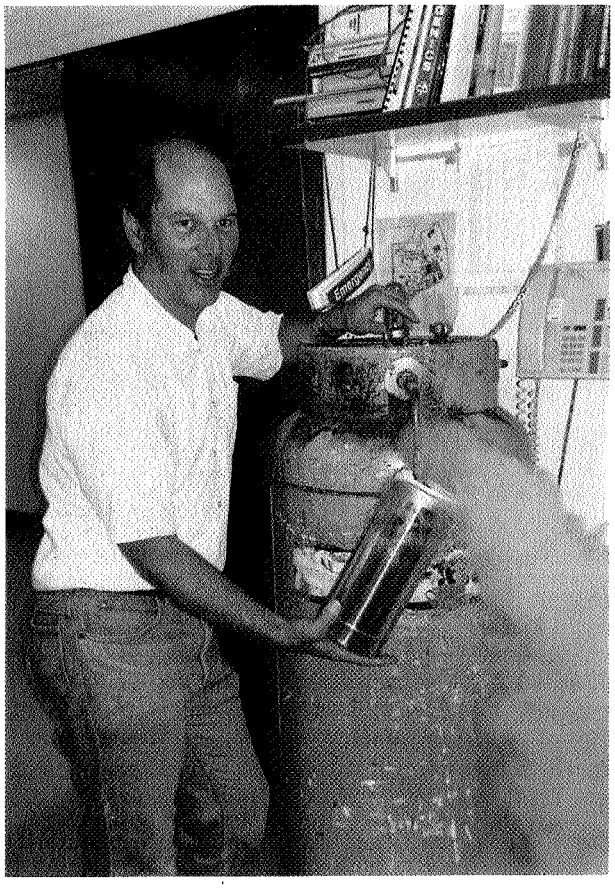

Jesse Bregman

Airborne Astronomy Symposium on the Galactic Ecosystem
ASP Conference Series, Vol. 73, 1995
M.R. Haas, J.A. Davidson, and E.F. Erickson (eds.)

Far-Infrared Heterodyne Spectrometer

R.T. Boreiko and A.L. Betz
Center for Astrophysics & Space Astronomy, University of Colorado, Boulder, CO 80309

1. Review

A far-infrared heterodyne spectrometer was designed and built by our group for observations of atomic and molecular lines from interstellar clouds. Linewidths as narrow as 1 km/s can be expected from such regions, and so the spectrometer is designed with sub-km/s resolution so that observed line profiles will be resolved. Since its debut on the Kuiper Airborne Observatory (KAO) in 1985, the instrument has been used in regular annual flight programs from both Moffett Field, CA and Christchurch, NZ. The basic plan of the spectrometer remains unchanged from the original design presented at the previous airborne science symposium (Betz and Zmuidzinas 1984). Numerous improvements and updates to the technical capability have of course been included over the many years of operational service (Betz and Boreiko 1990; Betz and Boreiko 1993).

2. Configuration

The infrared heterodyne spectrometer consists of the three basic components characteristic of all coherent receivers: a local oscillator, a mixer, and a spectral analyzer for the intermediate frequency (IF) signals. The local oscillator is a far infrared molecular gas laser that can be tuned to discrete transition frequencies of polar molecules. The mixer is a high speed GaAs Schottky diode in a special corner reflector type mount (Zmuidzinas, Betz, and Boreiko 1989). The mixer and the IF amplifier which follows are both cooled to 77 K. The LO signal is incident on the mixer together with the signal beam from the KAO telescope. IF signals from the mixer can be processed from near DC to frequencies as high as 24 GHz, but only a small part of this can be analyzed at one time. The spectral analyzer is an acousto-optic spectrometer (AOS) with 1000 channels covering 1000 MHz at a spectral resolution of 3.2 MHz. The size of the instrument mounted on the telescope is 2m x 0.5m x 0.5m and the mass is about 100 kg.

Spectral coverage is governed by the frequency range of the laser local oscillator and the capabilities of the Schottky mixer, and covers most of the 30-100 cm^{-1} band. The spectral resolution is ultimately limited by the frequency stability of the laser LO to about 1 MHz. Currently the practical limit is 3.2 MHz, which is the channel width of the AOS signal processor. The sensitivity of the instrument is best expressed in the parlance of radio astronomers, system noise temperature T_{sys}. Currently, T_{sys} = 5000 to 20000 K (SSB) over the signal frequency range of 900 to 2500 GHz, respectively. This sensitivity is roughly

equivalent to a net quantum efficiency of approximately 1%, so room for significant improvement remains.

This work was supported by NASA Grants NAG2-254 and NAG2-753.

References

Betz, A.L., and Zmuidzinas, J. 1984, NASA Conf. Publ. 2353, *Proceedings of the Airborne Astronomy Symposium,* 320

Betz, A.L., and Boreiko, R.T. 1990, in ESA SP-314, *Proc. 29th Liège International Astrophysical Colloquium: From Ground-Based to Space-Borne Sub-mm Astronomy,* 205

Betz, A.L., and Boreiko, R.T. 1993, in *Astronomical Infrared Spectroscopy,* ed. S. Kwok, Astron. Soc. of Pacific Conf. Series, **41,** 349

Zmuidzinas, J., Betz, A.L., and Boreiko, R.T. 1989, Infrared Physics, **29,** 119

Jonas Zmuidzinas, Rita Boreiko, Al Betz (1987)

Session Eight

KAO History and Education

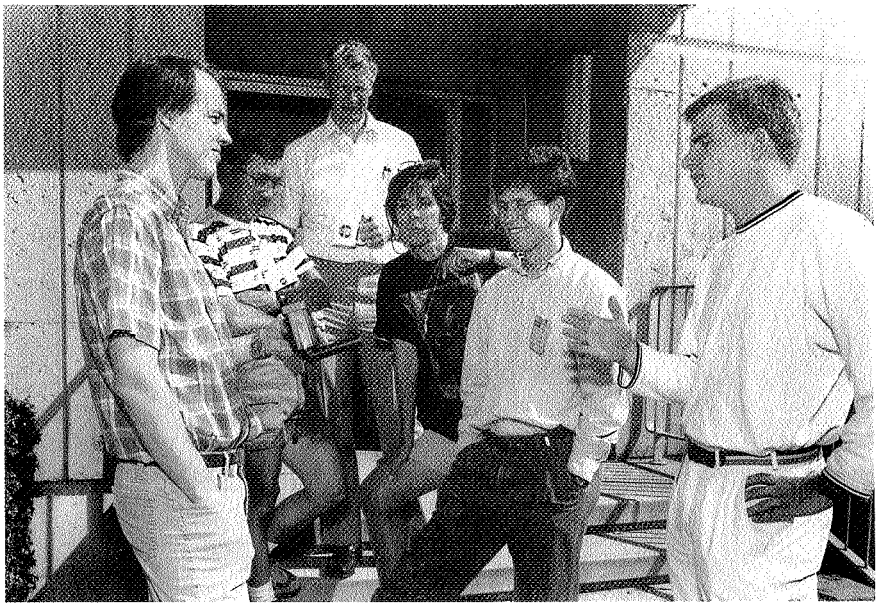

Ted Dunham, Glen Kimoto, Dave Koch,
Suzanne Williams, John Keller, Win Burleson

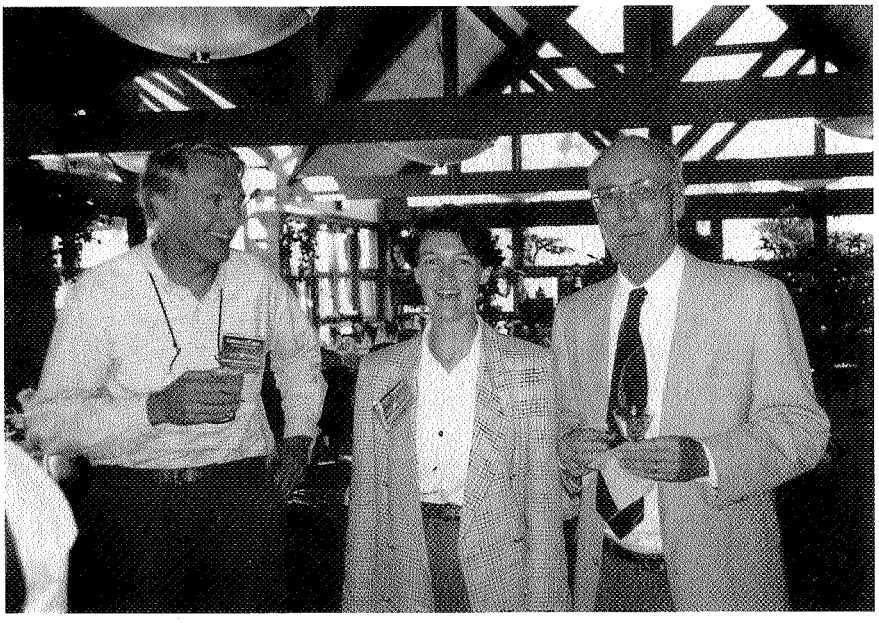

Larry Caroff, Jackie Davidson, Don Osterbrock

Airborne Astronomy Symposium on the Galactic Ecosystem
ASP Conference Series, Vol. 73, 1995
M.R. Haas, J.A. Davidson, and E.F. Erickson (eds.)

The NASA Airborne Astronomy Program: A Perspective on its Contributions to Science, Technology, and Education

Harold P. Larson
Department of Planetary Sciences, University of Arizona, Tucson, AZ 85721

Abstract. The scientific, educational, and instrumental contributions from NASA's airborne observatories are deduced from the program's publication record (789 citations, excluding abstracts, involving 580 authors at 128 institutions in the United States and abroad between 1967-1990).

This article has already appeared in print (Larson 1992), but is included here for completeness, as it was presented at the Symposium and provides an excellent summary of the Airborne Program.

1. Introduction

NASA-operated aircraft have been used for astronomical observations at stratospheric altitude (≥12 km) for more than 25 years (Bader & Wagoner 1970). The program has evolved from infrequently scheduled flights assigned to a few pioneering investigators to the current continuing program that is open to qualified observers nationally and abroad. The present facility is the Kuiper Airborne Observatory (KAO), a 0.9-m telescope in a modified Lockheed C-141 military transport (Cameron et al. 1971). The original motivation for conducting airborne observations was to open up regions of the infrared (IR) spectral region that were obscured by telluric H_2O at conventional mountain-top telescopes. Airborne observations are still dominated by IR techniques but significant applications have also been developed at visible and submillimeter wavelengths. The success of these diverse applications is not just due to operation at stratospheric altitude (12-15 km). Compared to other sub-orbital platforms (e.g., balloons and rockets), an airborne observatory also provides mobility, scheduling flexibility, rapid response to targets of opportunity, and a laboratory-like environment with few restrictions on the size, weight, and power requirements of focal plane instruments. In-flight access to instruments means that their alignment and performance can be optimized during a flight program, repairs and modifications may be made during or between flights, and new technology can be rapidly integrated into them for future flights. Frequent flight opportunities (currently ≈70 research flights per year, each of 7.5 hr duration) permit parallel evolution of science goals and instrument development on time scales consistent with Ph.D. dissertation projects and postdoctoral appointments, thus allowing young scientists to participate actively in all phases of an airborne project. These capabilities have created a special niche for airborne observatories that bridges the gap between opportunities at conventional ground-based telescopes and those on Earth-orbiting and deep space missions.

The purpose of this paper is to document how the NASA airborne astronomy program has contributed to science, education, and technology

development in IR astronomy for more than 2 decades. This information was originally compiled for the SOFIA project (Stratospheric Observatory For Infrared Astronomy), a proposed next-generation airborne observatory (a 2.5-m telescope in a modified Boeing 747SP aircraft). Many aspects of these results also relate to the more general considerations affecting the future growth of astronomy that were addressed in the recent National Research Council report (1991). The astronomy and astrophysics survey committee (the "Bahcall Committee") recommended that a balanced program of small, moderate, and large projects be implemented in the next decade. Their report emphasized the value of small and moderate projects because of their timely response to specific science objectives, their ability to assimilate new technology quickly, and their role in training young scientists. Since the NASA airborne astronomy program is a moderate-size, continuing program, it is used here as a case study to demonstrate why the survey committee believed that such endeavors are essential to the national research infrastructure. To make this study as objective as possible, the scientific, educational, and instrumental contributions from the airborne astronomy program since 1967 were deduced almost exclusively from publications cited in the *NASA Airborne Observatory Publication List.* This bibliography is compiled annually at the NASA Ames Research Center and is very complete thanks to the diligence of the Ames staff in screening the literature for new entries. The 1990 August edition was used, augmented by citations received through 1990 December. The following three criteria were adopted for selecting entries from this bibliography. (1) Only pointed observations conducted at airborne observatories were considered. Thus, airborne observations of the Sun were included, but airborne studies of Earth's atmosphere were not. (2) All refereed journal articles, books, and conference proceedings (refereed or not) were considered, but no abstracts or popular science articles were included. (3) Review articles, theoretical papers, and publications of ground-based observations and laboratory experiments were included only if they were explicitly related to airborne science objectives. A total of 789 papers met these criteria, each of which was screened for its authors, their institutions, the type of instrumentation used, the objects observed, which airborne facility was used, and where it was deployed. The status of all authors (e.g., student, postdoc, etc.) at the time of each publication and their subsequent career evolution were determined with help from members of the airborne astronomy community.

2. Airborne Science Publications

The information presented below demonstrates general aspects of the breadth and continuity of NASA's airborne astronomy program. A detailed review of its scientific accomplishments is beyond the intent of this paper, but a useful cross-section of airborne science results may be found in the proceedings of the *Airborne Astronomy Symposium* (1984).

(1) Publication history. The publication history of the airborne astronomy program is illustrated in Figure 1. The rapid increase in publications after 1975 is due to the KAO which provided more flight opportunities with a larger aperture telescope (90 cm). Prior to 1975 the airborne program was based on smaller telescopes (30 cm) in Convair 990 and Lear Jet aircraft. Some of the fluctuations in the KAO publication rate are due to conference proceedings where large numbers of airborne science results were presented (e.g., the *NASA Airborne Astronomy Symposium* in 1984 and the *ESLAB Symposium on the Exploration of Halley's Comet* in 1986). Except for these special situations, the relative

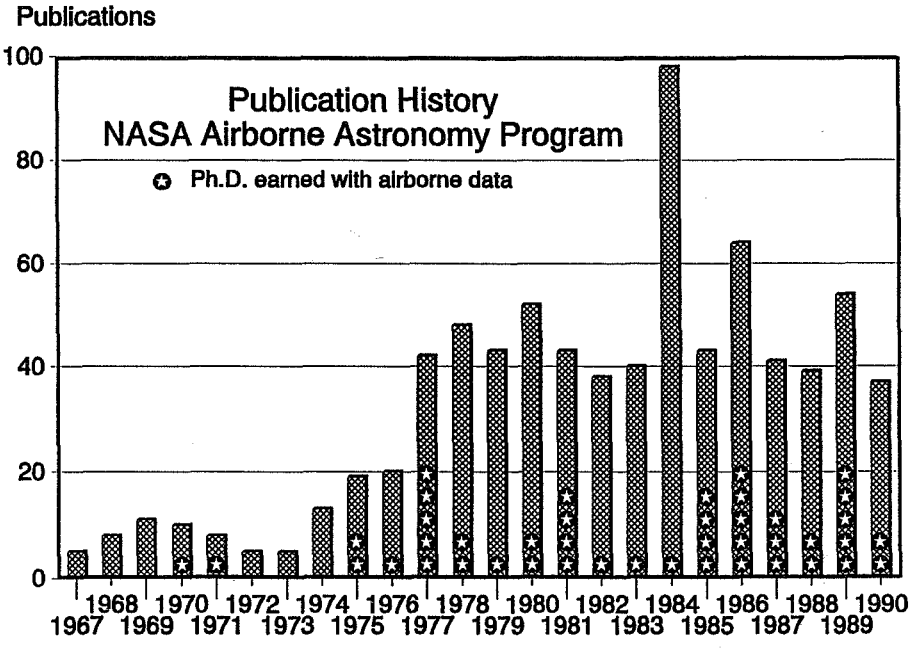

Figure 1. Publication history of the NASA airborne science program (excluding abstracts). The KAO started limited observatory operations in 1974 and was dedicated in 1975. The sharp rise in publications in 1977 indicates the rapid return from routine observatory operations that began in 1976. The increases in 1984 and 1986 are due to conference proceedings where airborne science results were concentrated.

constancy of the KAO publication record (≈50 papers per year using the selection criteria adopted in Sec. 1) is most likely due to available flight time. The KAO program was quickly ramped up to ≈80 flights per year in 1976 with further increases to 120 flights per year anticipated. The augmentation was never implemented, however, and even the nominal 80-flight program was only achieved once. The number of flights by itself does not present the whole picture since the observing time per flight is not necessarily constant. A research flight is nominally 7.5 hr in duration, but longer or shorter flights are possible for special situations (e.g., daytime observations, eclipses, occultations). Both the number of research flights actually flown and the total hours of flight time are summarized in Figure 2 for the KAO. The average over the past decade has been ≈500 flight hours divided into ≈70 research flights per year. The sharp drop in 1990 was due to an extended period of downtime for a major inspection of the aircraft.

Of special interest is the number of Ph.D. theses included in the publication record since they are a direct measure of graduate student participation in the airborne science program. A total of 42 doctoral theses (2-3 per year on average) have been completed with airborne data through the end of 1990.

(2) Discipline representation. The publications of airborne science were divided into four major categories: galactic astronomy (58%), planetary science (25%), extragalactic astronomy (9%), and instrumentation (8%). These analyses

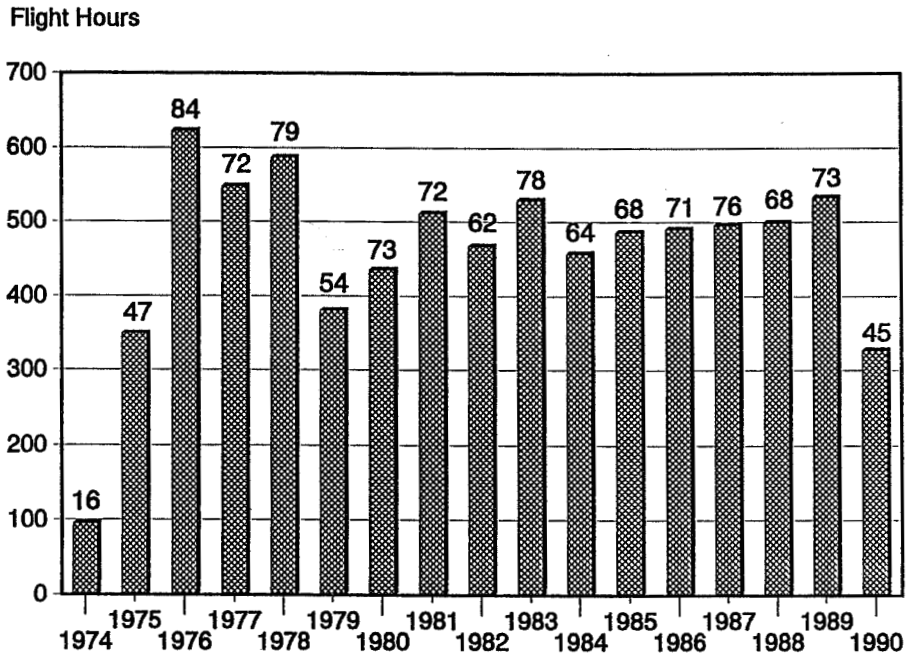

Figure 2. Hours of flight logged annually with the KAO. The figures above each bar indicate the actual number of research flights, each nominally 7.5 hours long.

TABLE 1
Most Frequently Observed Objects

Object	Number of Publications
Orion Nebula	115
Galactic Center	61
Jupiter	38
Sun	33
Comet P/Halley	33
M17	29
W51	26
W3	26
NGC 7027	24
Saturn	22
Venus	19
NGC 1068	19
M82	19
Uranus	15
Mars	14
NGC 2024	13

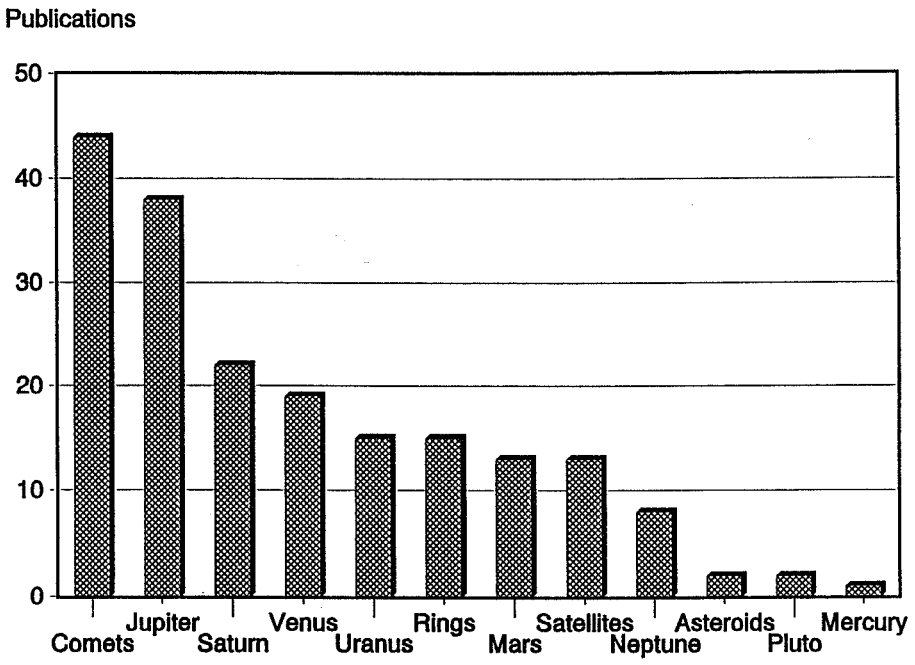

Figure 3. Publications of Solar System objects observed from NASA's airborne telescopes since 1967. Cometary studies are dominated (≈75%) by airborne observations of Comet Halley in 1985/86.

cover a large number (>472) of diverse astrophysical objects. The most frequently studied sources are listed in Table 1. Planetary objectives motivated the early development of airborne astronomy and Solar System observations remain an important component of the program. The coverage of Solar System objects is indicated in Figure 3. This record was compiled in parallel with NASA's Solar System exploration program using deep space probes. Although planetary airborne astronomy has not been treated programmatically by NASA as part of the Solar System exploration program, the results demonstrate the vital, complementary role of aircraft as vehicles for systematic exploration of certain properties of the Solar System over decades of time. In remote IR sensing studies, for example, airborne observations permit very high *spectral* resolution because there are few restrictions on the size and weight of instruments, while spacecraft allow high *spatial* resolution due to their proximity to the object.

(3) Literature citations. Airborne science publications are dispersed throughout the literature but there is a very obvious concentration (see Table 2) in *The Astrophysical Journal.* The interest with which airborne science results are received in the community is reflected in the large number of rapid publications, such as in *The Astrophysical Journal Letters* and in some of the many conference proceedings.

(4) "Quick-turnaround" science. One unique attribute of an airborne observatory is the ability to deploy it to optimum locations on short notice for unexpected or nonrecurring astronomical phenomena. Figure 4 illustrates the science return from KAO observations of Comet Halley and SN 1987A, both involving deployments to Christchurch, New Zealand. In each case there was

TABLE 2
Airborne Science Publications

Location	Number of Publications
Astrophysical Journal	259
Astrophysical Journal Letters	108
Icarus	54
Ph.D. Theses	42
Astronomical Journal	26
Applied Optics	25
Astronomy and Astrophysics	25
Publications Astronomical Society Pacific	21
Nature	19
Books	14
Other Refereed Journals	95
Conference Proceedings	101

rapid publication of initial results followed by more comprehensive analyses including Ph.D. dissertations. These expeditions were characterized by broad participation. The 22 KAO flights devoted to Comet Halley, for example, involved 11 Principal and Guest Investigator teams using nine instruments covering a factor of 100 in wavelength and a factor of 10^5 in spectral resolution. Such a package could not have been put together at any other Earth-based observatory. These experiments produced new types of spectral data relating to the gas and dust components of cometary comae that will retain long-term interpretive value. So far, these observations have produced 33 papers and one Ph.D. thesis by 52 authors and coauthors at 18 institutions.

3. Community Involvement

The visibility of the airborne astronomy program within the astronomy community has not always been high. Access to the aircraft at their home base at the NASA Ames Research Center is somewhat restricted and relatively few individuals can actually experience an airborne observatory in operation. In addition, the limited number of flights and the challenges associated with making complex focal plane instruments work in the hostile environment in an aircraft could have made the program accessible to only a few privileged astronomers. However, the following sections demonstrate that participation in the airborne astronomy program has always had a broad base in the scientific community.

(1) Number of participants. The human resources associated with airborne astronomy are its greatest asset. One measure of the size of this community is the number of individuals (580) who have authored publications of airborne science. A significant factor in this extent of community involvement is NASA's Guest Investigator Program that facilitates access to flight-qualified airborne instruments developed, maintained, and operated by the program's Principal Investigators.

(2) Institutional affiliation. The authors of airborne science publications represent 128 institutions in the United States and abroad. Universities dominate

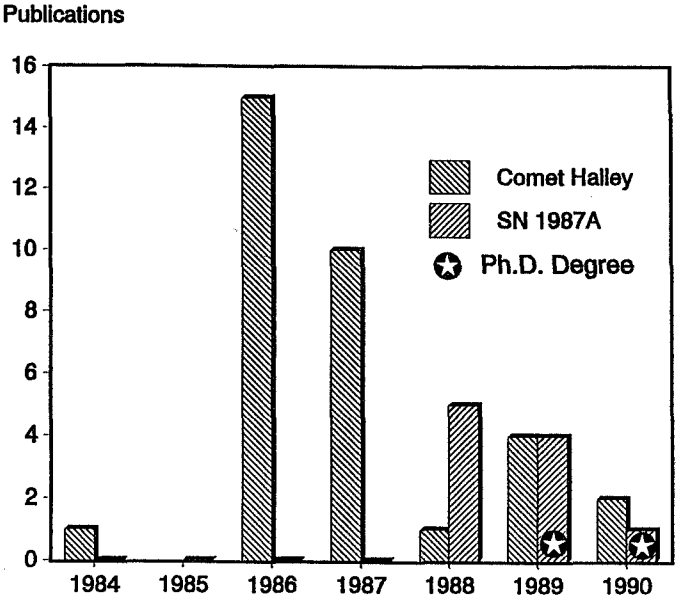

Figure 4. Quick turnaround science results for airborne observations of Comet Halley (1985/86) and SN 1987A (1987 and annually thereafter). The single comet paper in 1984 preceding airborne observations was a theoretical prediction of airborne capabilities that was subsequently realized.

the list (64%), followed by government laboratories (22%), foreign institutions (11%), and companies (3%). Unstructured and unmanaged, these institutions underwrite the strength of the airborne program by providing multiple, independent environments for data analysis, instrument development, and training young scientists.

(3) Geographic distribution. The geographic distribution of domestic institutions is indicated in Figure 5. Professional activity in the airborne astronomy program exists in 27 states and the District of Columbia. At least 18 institutions emerged from the survey as "centers of airborne astronomy" because of their sustained contributions of science, instruments, and people over one or more decades. In general, the airborne science community is strongly correlated with locations commonly associated with astrophysics and space science. The evidence in airborne science publications for professional collaborations between institutions and for combining data from different telescope facilities suggests that airborne astronomy is an important complement to other astrophysical programs.

(4) Accommodation of new participants. Figure 6 illustrates the number of new names showing up in the author lists of airborne science publications each year. Since 1975 when the KAO became operational, on average ≈30 new individuals participated in some aspect of the program each year. Many were collaborators contributing to the interpretation of airborne data (e.g., theoretical models, astronomical data acquired at other facilities, laboratory measurements) and some may never have actually flown on an airborne observatory. This rather fluid group is an important complement to the program's instrument teams because of its potential for broadening the intellectual base of the airborne

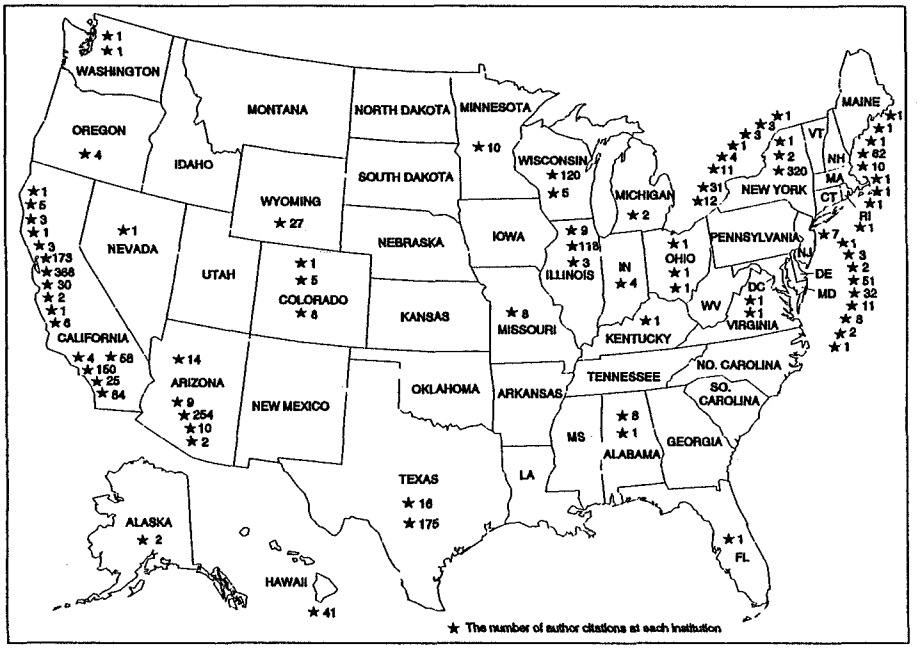

Figure 5. The geographic distribution of institutions associated with the NASA airborne science program. The figures are the number of author citations per institution. Numbers >100 indicate where "centers of airborne astronomy" have flourished.

science program. Some of the fluctuations in the number of new participants may be correlated with factors that should have restricted growth, such as the budget cuts and reduced flight rates around 1980 due to high fuel costs. The dip during 1986-1987 may be due instead to preoccupation with two major southern hemisphere expeditions: Comet Halley in 1986 and Comet Wilson and SN 1987A in 1987. In general, however, the intellectual life of the airborne program revealed in Figures 1 and 6 seems remarkably resilient to short-term perturbations in operations, but there has not been any obvious growth in the number of new participants over the history of the KAO program. The most likely explanation is that community participation was constrained by an initially low flight rate (≤80 per year) that became programmatically frozen at approximately two-thirds that considered appropriate for the facility (≈120 research flights per year). In effect, the KAO has been operated on a part-time basis. The price for such underutilization is lower science return, fewer opportunities for community participation, and reduced training of young scientists which may be the greatest loss when measured against national manpower needs.

4. Airborne Instrumentation

(1) Approach. No telescope is better than its complement of focal plane instruments. In contrast to the policy at most major telescope facilities, NASA

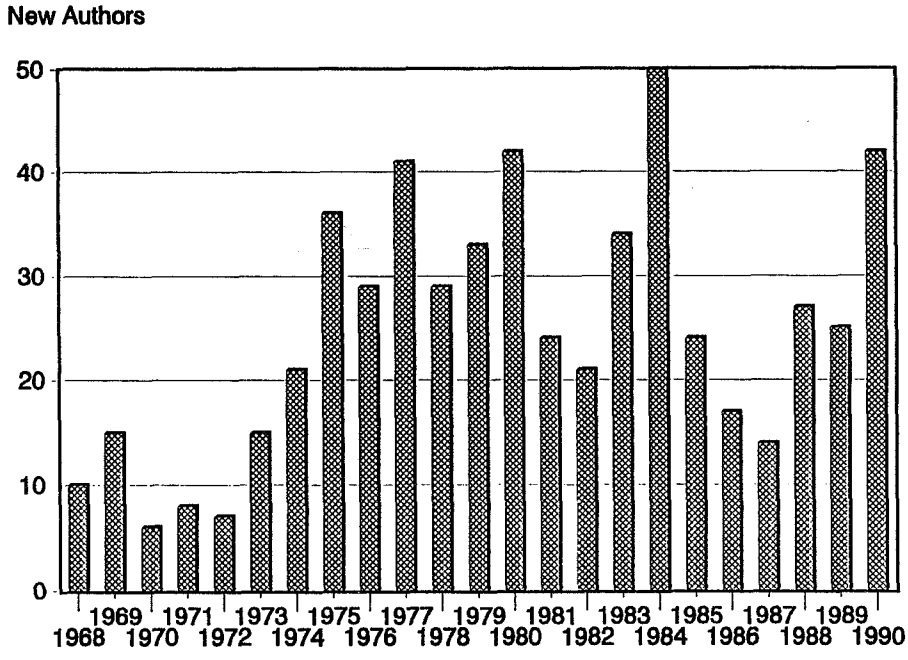

Figure 6. The number of new authors per year in publications of airborne science.

deliberately left all instrument development for its airborne observatories to initiative in the astronomy community. The result has been a suite of state-of-the-art PI-type instruments (≈14 in a typical year, see Table 3) refreshed periodically through peer review that no other major observatory would have been capable of developing and maintaining in-house as facility instruments. NASA supports these instruments and their associated teams of scientists, engineers, postdocs, students, and technicians at their home institutions. These instrument teams depend upon the success of their experiments not only for their own work but also for NASA-selected Guest Investigator flight programs. This approach to managing focal plane instrumentation has promoted flexible, creative responses to the challenges posed by new science objectives and the opportunities offered by rapidly evolving IR technology. Had the more conventional approach using facility instruments been adopted, airborne science objectives would have been constrained to fit technical characteristics that would have changed more slowly, if at all, to user requirements.

(2) Types of instruments. The classes of instruments responsible for the published record of airborne science are listed in Figure 7. Their resolving power and the spectral region in which they are operated are indicated in Figures 8 and 9, respectively. In general, the broad ranging capabilities of instruments developed for airborne astronomy have allowed maximum exploitation of the science potential of airborne observatories. These instruments do not necessarily represent unique types of apparatus, but their implementation involves features not normally found in more conventional experiments. For example, the hostile environment of an aircraft, particularly vibrations and electromagnetic

TABLE 3
Evolution of Airborne Instruments between 1982–1991

Principal Investigator/ Institution	Fiscal Year 1982			Fiscal Year 1991			
	Type of Instrument	Spectral Range (μm)	Spectral Resolution	Type of Instrument	Spectral Range (μm)	Number of Channels	Spectral Resolution
Beckwith/ Cornell	Grating Spectrometer	2–4, 4–8	$\approx$0.01 μm				
Betz/ UC/Berkeley				Heterodyne Spectrometer	150–500	1	$\Delta\nu \geq 1$ MHz
Bregman/ NASA/ARC				Grating Spectrometer	1.0–5.5	1$\times$32, 1$\times$31	$\lambda/\Delta\lambda \approx$ 100–700
Elliot/ MIT	Photometer	0.3–1.0	$\approx$0.005–0.1 μm	High-speed Photometer	0.4–1.1	256$\times$256	Determined by filters
Erickson/ NASA/ARC				Grating Spectrometer	20–180	32	$\lambda/\Delta\lambda \approx$ 1000–4000
Harper/ Yerkes	Photometer	20–300	$\approx$10–50 μm	Photometer/ Camera	30–500	8$\times$8	$\lambda/\Delta\lambda \approx 2$
Harvey/ Univ. Texas	Photometer	40–200	$\approx$20–100 μm	High Spatial Resolution Photometer	40–200	2$\times$10	$\approx$20–100 μm
Harwit/ Cornell	Grating Spectrometer	40–180	$\approx$0.3 μm				
	Polarizer	20					
Herter/ Cornell				Grating Spectrometer	5–30 30–50	10$\times$50 1$\times$5	$\approx$0.004 μm $\approx$0.009 μm

Hildebrand/ Univ. Chicago	Photometer	55–990	$\approx$30–730 μm	Photometer/ Polarimeter	100–300	6×6	$\lambda/\Delta\lambda\approx 2$
Houck/ Cornell	Grating Spectrometers	16–30 16–50	$\approx$0.2 μm $\approx$0.03–0.05 μm				
Jones/ UC/San Diego	Filter Wheel Spectrometer Grating Spectrometer	2–4, 4–8 4–8	$\approx$0.1,0.03 μm $\approx$0.03–0.08 μm				
Larson/ Univ. Arizona	Fourier Spectrometers	0.9–3.5 0.9–5.6	0.02 cm^{-1} 0.25 cm^{-1}	Fourier Spectrometer	0.9–5.6	1	0.02 cm^{-1}
Moseley/ NASA/GSFC	Grating Spectrometer	27–55	$\approx$3 μm	Grating Spectrometer	20–68	1×24, 1×48	$\lambda/\Delta\lambda\approx 25$
Phillips/ Caltech	Heterodyne Spectrometer	500–850	$\approx$0.3 km s^{-1}				
Roeser/ MPI Bonn				Heterodyne Spectrometer	300	1	$\lambda/\Delta\lambda\leqslant 2\times 10^6$
Russell/ Aerospace				Prism Spectrometer	2.9–13.5	2×(1×58)	$\lambda/\Delta\lambda\approx$25–120
Townes/ UC/Berkeley Genzel/ MPI Garching	Fabry–Perot Spectrometer	40–125	$\approx$0.03 μm	Imaging Fabry–Perot Spectrometer	40–200	5×5	$\lambda/\Delta\lambda\approx 10^3$–$3\times 10^5$
Witteborn/ NASA/ARC	Filter Wheel Spectrometer Grating Spectrometer	0.65–5.6 4–14	$\approx$0.01–0.08 μm $\approx$0.05 μm	Grating Spectrometer	5–14	1×30	$\lambda/\Delta\lambda\approx$50–200

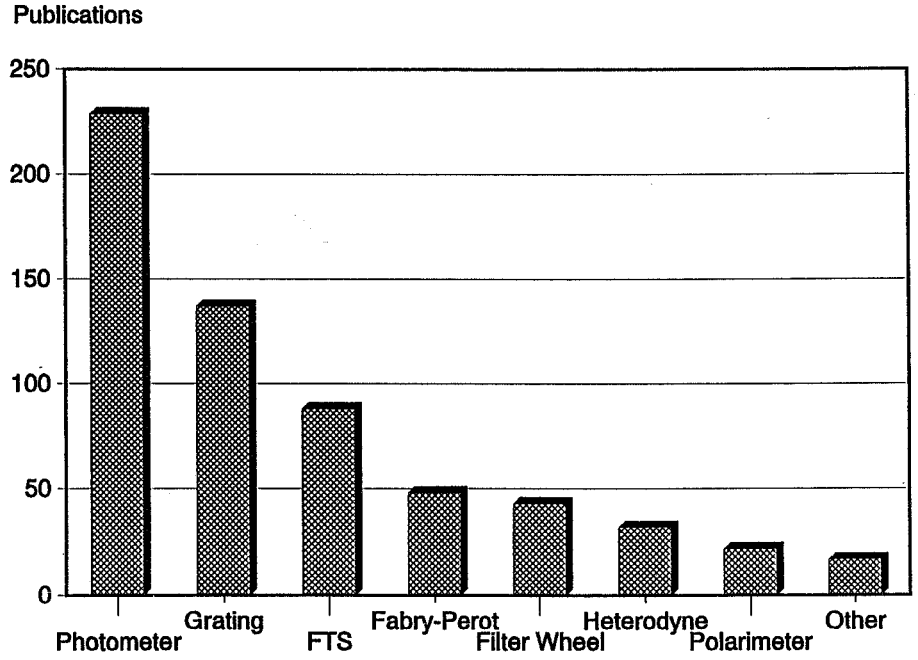

Figure 7. The types of focal plane instruments used in publications of airborne science. Array detectors used as cameras are included under photometers.

interference, creates serious problems for instrument builders that would not be encountered at conventional ground-based telescopes. Innovative engineering designs have therefore been developed for certain applications. Since airborne instruments operate in wavelength regions (e.g., 100 μm) that are inaccessible at ground-based facilities, they often represent innovative applications of detector technology to otherwise conventional instrument concepts. Testing these combinations at airborne observatories is important both for immediate science objectives and for developing a mature technological base for future applications at IR and submillimeter space observatories. Another special capability of some airborne experiments, compared with similar instruments at ground-based telescopes, is their ability to cover a very broad spectral bandwidth (factor of 5 and more in wavelength) unobscured by telluric absorptions. This perspective reveals types of spectral behavior that would not be possible in the more limited spectral bands accessible at conventional ground-based telescopes.

(3) Instrument development. Airborne instruments are constantly being modified, upgraded, or replaced. This attention to development is revealed in the number of publications devoted to instrumentation (≈8%) and in the long-term changes to the complement of focal plane instruments selected through peer review for each flight year. Table 3 indicates the evolution of flight-qualified instruments during the decade between 1982-1991. The entries for each year were taken from NASA's annual *Announcement of Opportunity* to participate in the airborne program. Considerable turnover in Principal Investigators is evident, but most striking are the changes in the instruments themselves: ≈80% of the

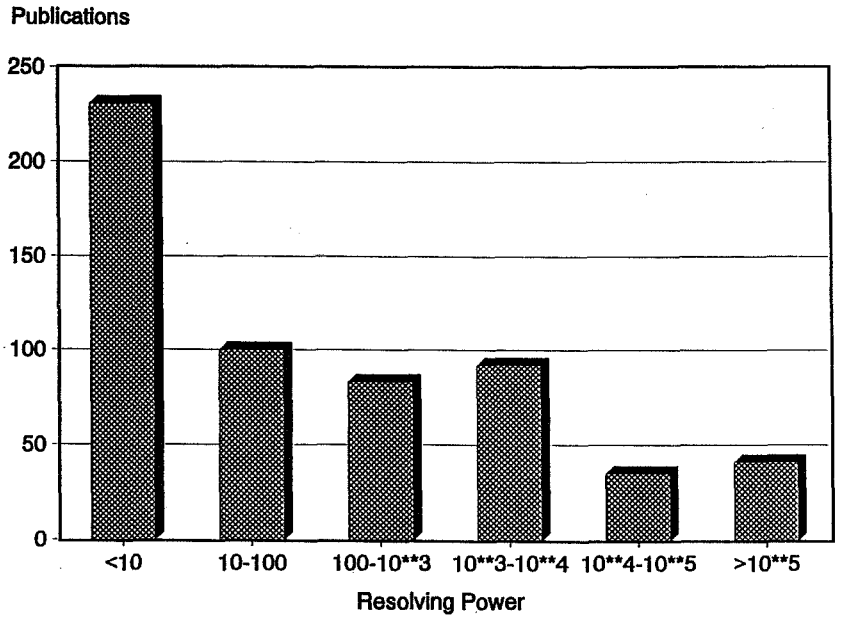

Figure 8. The resolving power achieved in publications of airborne observations.

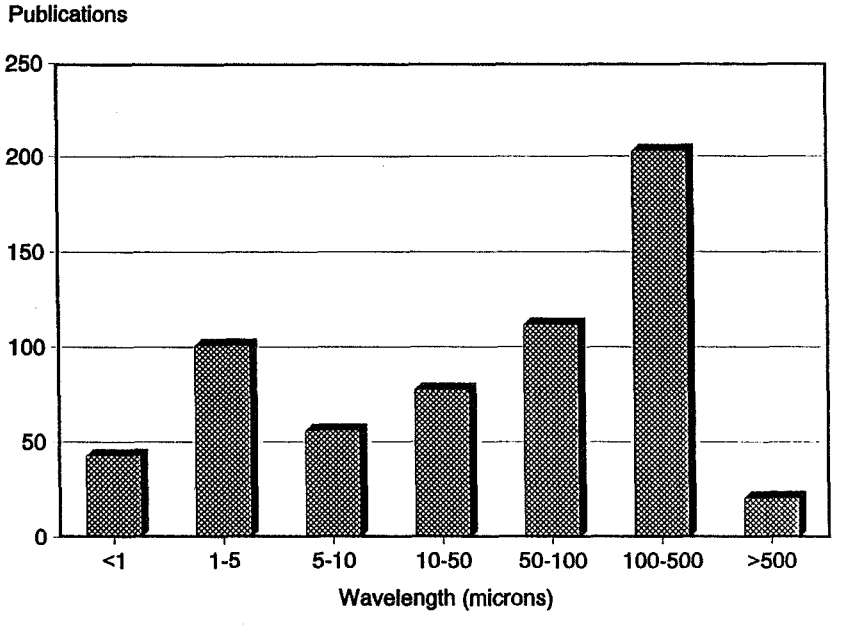

Figure 9. The spectral region in which focal plane instruments were used in publications of airborne science.

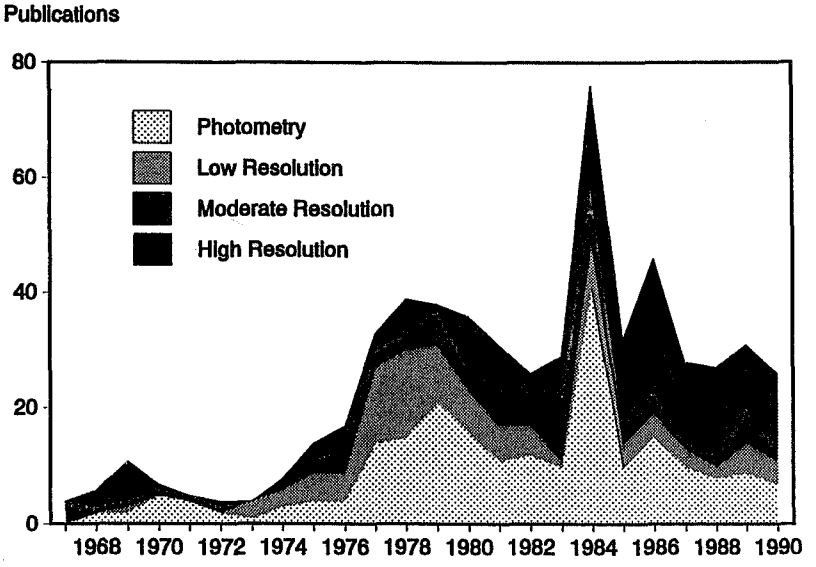

Figure 10. Instrumentation trends in publications of airborne science. There is a very clear shift to higher spectral resolution during the evolution of the airborne astronomy program. For this figure spectral resolution is defined as *low* ($5 \leq \lambda/\Delta\lambda \leq 10^2$), *moderate* ($10^2 < \lambda/\Delta\lambda < 10^3$), and *high* ($\lambda/\Delta\lambda \geq 10^3$). Photometric studies are characterized by $\lambda/\Delta\lambda < 5$. Currently, ≈50% of all airborne science publications are spectroscopic results with $\lambda/\Delta\lambda \geq 10^3$.

instruments available in 1991 represent new or substantially modified experiments compared to 1982. Focal plane instrument development is a continuous process because of the need for higher sensitivity, higher spectral resolution, and higher spatial resolution. The trend to higher spectral resolution is evident in the airborne science publications (see Figure 10) and accommodation of spatial resolution is apparent in the array detector systems used in most current instruments (see Table 3). Increased sensitivity is achieved by many means, including new detectors, cryogenic operation of the whole experiment, and modifications to the airborne telescope itself. The net effect of combining higher spatial and spectral resolution with higher sensitivity is continual increase in the information content of airborne data. As a consequence, the KAO is still capable of producing discoveries and definitive measurements nearly two decades into its operation.

5. Training of Young Scientists

(1) The potential of airborne astronomy. An important aspect of training at the graduate and postgraduate level is the transfer of expertise and experience from one generation to another in a research environment. This is a particularly compelling consideration in an era where astronomers are increasingly, often

deliberately, isolated from the design and operation of facility instruments at many conventional telescopes. The team-oriented nature of most airborne science investigations suggests that there should be many opportunities for hands-on, real-time participation by young scientists. The following insights drawn from the literature survey demonstrate how the airborne astronomy program has fulfilled its potential for training young scientists. For the purpose of this report a "young scientist" is an author of an airborne science publication who was *at that time* either a graduate student or in a postdoctoral position. Approximately 25% of the 580 authors of airborne science publications met this test.

(2) Doctoral degrees. The most obvious measure of the airborne program's contributions to education is the number of Ph.D. degrees earned with airborne data (42, see Figure 1). Frequent flight opportunities and extensive university participation were probably most influential in allowing this many dissertation projects to proceed from initial concept to data acquisition and analysis during the normal academic lifetime of a graduate student. Since a doctoral thesis must represent original research, this record also reflects the airborne program's ability to provide a rich variety of suitable topics that is continually being augmented with new instrumental capabilities.

(3) Professional activity of young scientists. Doctoral theses are only one manifestation of the role of young scientists in airborne astronomy. The conspicuous presence of graduate students and postdocs in author lists (63% of all publications) indicates broad participation in all phases of airborne astronomy (instrument development, flight programs, data analyses, etc.). The number of papers having graduate students as co-authors (43% of all publications) is especially interesting because it means that they either published their dissertation research very rapidly or they were extensively involved in collaborative projects as students. Either way, it indicates aggressive career development at an early stage.

Another measure of professional activity was obtained from examination of the participants in recent meetings of the American Astronomical Society (AAS) and its Division for Planetary Sciences (DPS). Approximately 40% of all young scientists who were or still are associated with airborne astronomy presented papers at the 1989 October DPS and the 1990 January AAS meetings. It appears from this "snapshot" of professional activity that these individuals remain productive representatives of their specialties, which are not necessarily still connected with airborne astronomy.

(4) Career tracking. The career evolution of the young scientists identified in this survey is summarized in Figure 11. A high percentage of them (68%) have retained careers in astronomy at universities, in government laboratories, and in private industry. The fraction (20%) remaining as students and postdocs represents a vital, renewable pool of candidates for participation in future projects. The importance of training adequate numbers of scientists with expertise in IR and submillimeter techniques cannot be underestimated given current directions in Earth-based and space astronomy. It is interesting in this context to note the extent to which former participants in the airborne science program subsequently became involved in even more ambitious endeavors in space. A strikingly high correlation is revealed by comparing the airborne science author list with the science/instrument teams of such IR/submillimeter projects as the *Cosmic Background Explorer (COBE)*, the *Infrared Astronomy Satellite (IRAS)*, the *Submillimeter Wavelength Astronomy Satellite (SWAS)*, and the Space Infrared Telescope Facility (SIRTF). Approximately 34% of the members of the *COBE* and *SWAS* teams, 70% of the SIRTF team, and 83% of the U.S. members of the *IRAS* team were authors of airborne science publications. A closer look was taken at one of these projects to determine the type and extent of its team's involvement with the airborne program. SIRTF was chosen because it

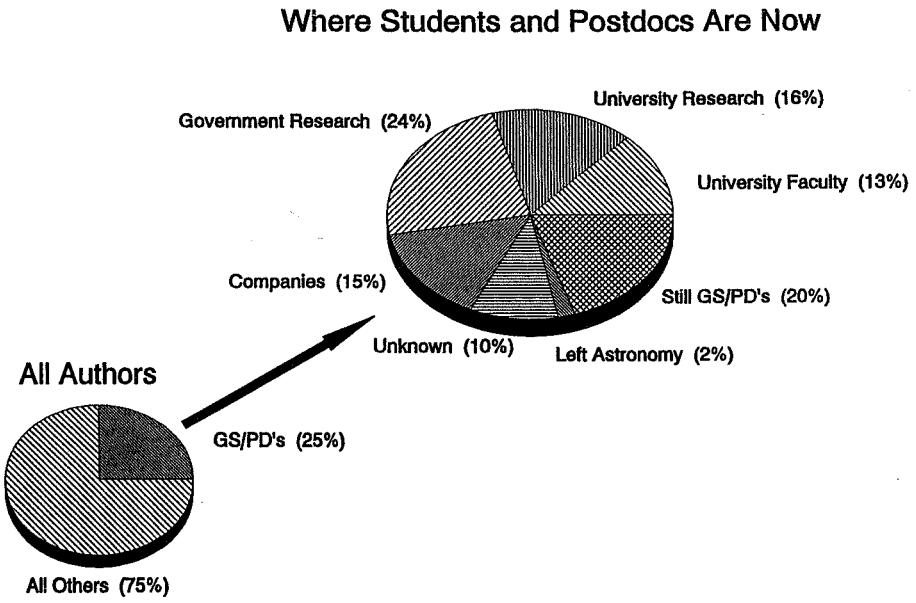

Figure 11. Career tracking of graduate students and postdocs (GS/PD's) associated with the NASA airborne astronomy program.

overlaps with the KAO in wavelength coverage and its instrumental requirements and scientific objectives are similar, but distinguished by the much higher photometric sensitivity possible in a cryogenic space environment. The four SIRTF instrument teams include 40 scientists, 28 of whom authored airborne science publications. Their activity was characterized as *major* (>15 papers), *substantial* (5-15 papers), or *minor* (<5 papers). In this group of 28 there were 10 major, 7 substantial, and 11 minor contributors to airborne science publications. In addition, 10 SIRTF team members were Principal Investigators of instrument teams in the airborne program. The SIRTF IR spectrometer (IRS) team has an especially strong association with airborne astronomy: 10 of its 11 members. These statistics imply that participation in the airborne astronomy program was for many scientists an important intermediate step in their careers that allowed them to compete successfully for follow-on roles in space astronomy.

6. Summary

This survey has demonstrated that NASA's airborne astronomy program has sustained high levels of scientific productivity over decades while providing hands-on opportunities for training young scientists and testing new instrumental techniques in a near-space environment. A similar role is anticipated for SOFIA in developing the new instruments and training the next generation of scientists that will be necessary to conduct future projects in space at IR and submillimeter wavelengths. The increased aperture and higher angular resolution of SOFIA will give an immediate boost to the discovery potential and information content of airborne data, and continued emphasis on PI-type instrument development with

extensive Guest Investigator participation should maximize long-term creative use of the facility.

This study would not have been possible without the *NASA Airborne Observatory Publication List* as its primary resource. Special thanks are extended to its editor, Carl M. Gillespie, Jr., for his enthusiastic help and useful suggestions. Comments and supplemental information contributed by members of the SOFIA Science Working Group are gratefully acknowledged. This report was prepared with partial support from NASA Grant No. NAG2-206.

References

Bader, M., and Wagoner, C. B. 1970. Appl. Opt., 9, 265
Cameron, R. W., Bader, M., and Mobley, R. E. 1971. Appl. Opt., 10, 2011
Larson, H. P. 1992, PASP, 104, 146
Proceedings: Airborne Astronomy Symposium 1984, ed. H. A. Thronson, and E. F. Erickson (NASA Conference Publication No. 2353)
Proceedings: International Symposium on the Exploration of Halley's Comet 1986, ed. B. Battrick, E. J. Rolfe, and R. Reinhard (ESA SP-250)
The Decade of Discovery in Astronomy and Astrophysics 1991 (Washington, DC, National Academy Press)

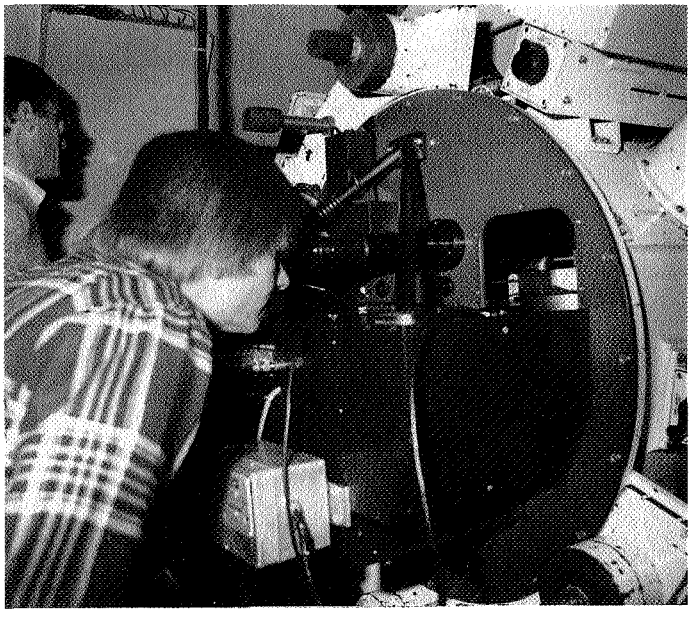

Guy Michel, Hal Larson (1979)

Larry Hintz, Marianne Gielow

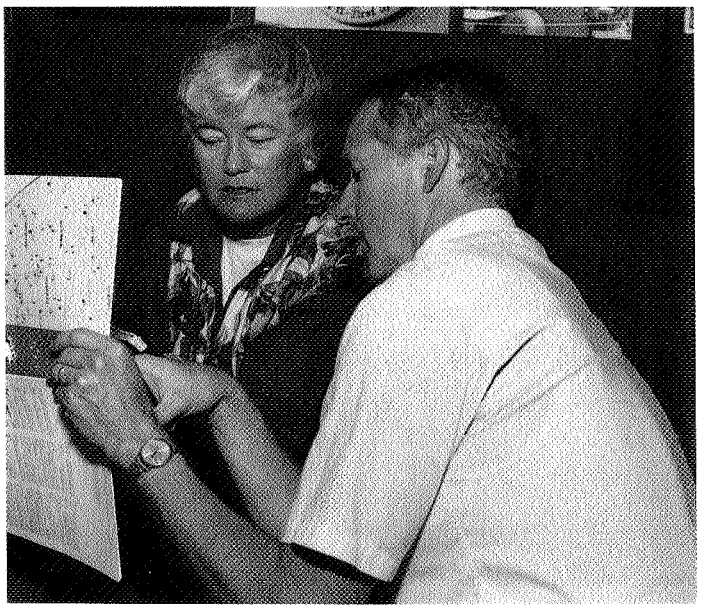

Penny Moore, Dave Koch

OMIT

Airborne Astronomy Symposium on the Galactic Ecosystem
ASP Conference Series, Vol. 73, 1995
M.R. Haas, J.A. Davidson, and E.F. Erickson (eds.)

From the KAO Archives: Photographs and Video from the First 20 Years

Wendy A. Whiting
NASA/Ames Research Center, MS 248-1, Moffett Field, CA 94035-1000

Elaine C. Mathias
NSI Technology Services; NASA/Ames Research Center, MS 248-2, Moffett Field, CA 94035-1000

Abstract. This poster was a display of photographs spanning twenty years of KAO operation, including photographs taken during the initial modification of the aircraft and the building of the telescope. Many of the photographs featured the people, both scientists and KAO staff, who have participated in the airborne astronomy program over the years. Also displayed was the collection of KAO patches that have been produced during the lifetime of the KAO, some of which commemorate various KAO foreign deployments.

In addition, a video display was set up for viewing *The Big Window*, a tape which was produced in the 1970's about the development of the KAO. *The Big Window* contains footage taken during the fabrication of the primary mirror, the construction of the KAO air bearing, the structural modification of the C-141, and the integration of the telescope system into the aircraft.

Some of the photographs from this poster are distributed throughout the volume.

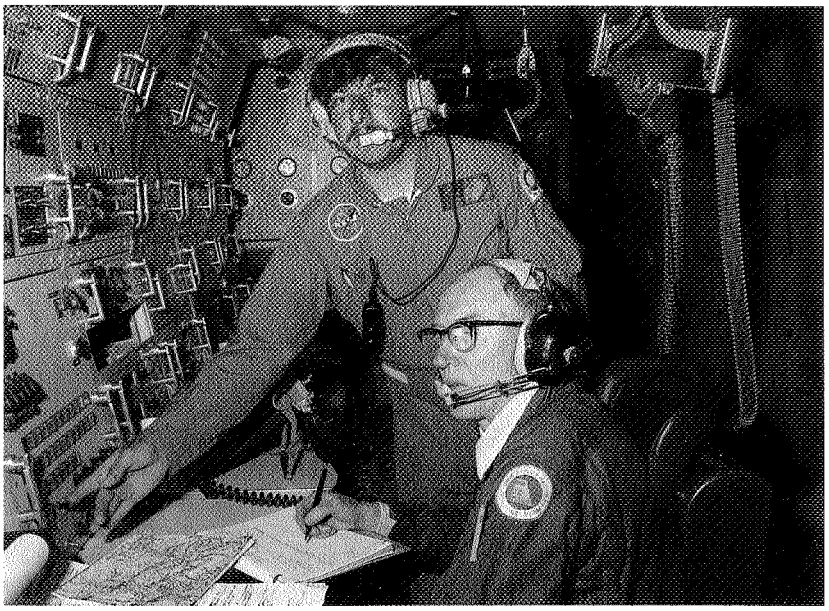

Jim McClenahan, Lou Haughney (1978)

Charlie Townes, Sara Beck, Tom Mathieson, Carl Gillespie (1978)

Airborne Astronomy Symposium on the Galactic Ecosystem
ASP Conference Series, Vol. 73, 1995
M.R. Haas, J.A. Davidson, and E.F. Erickson (eds.)

OMIT

20 Years of Airborne Astronomy Computing

John Graybeal
Sterling Software; NASA/Ames Research Center, MS 248-1, Moffett Field, CA 94035-1000

Abstract. A flowing data-dump on the experiences and achievements of the "Cave" computing staff on the KAO.

"*A lot of things have changed. When we first started this work, here's how requirements were defined: 'Hey Tom, here's a computer. Why don't you see if you can make it do something useful on the airplane?'* " —*Tom Mathieson (Informatics Inc.).* Not to say that the first computers on the KAO were an afterthought, but it's safe to say the KAO would have taken its first flights whether the computers worked or not. Early deliverables (1974) included a housekeeping program, a tracker, star plots, track maps, and experimenter programs doing such arcane tasks as data logging. Contrary to popular opinion, Space Wars[1] was **not** the first application to be developed for use on the KAO. Without exception, programs were developed iteratively; what we call prototypes today (well, among ourselves anyway) would have qualified as a well-tested flight release in the first few years.

The new model HP 21MX series, with its futuristic LEDs and rocker switches replacing individually lit push switches, proved a major improvement, if only because horizontal card slots made "right-side up" somewhat more, umm, user-friendly. An extensive study over the first 20 years of the contract confirmed three benefits with the newer CPUs: cards were installed wrong way around less often; cards blew up less often when they were installed wrong; and the computer itself almost never got fried by upside-down cards. We think.

"*I can't help but note with some dismay that although the old ADAMS Logs are here (at the Cave-In Party), no one brought the old ADDAS*[2] *logs. Obviously a major oversight. Symptomatic of the decline of proper management awareness in the Cave.*" —*John Peck (Informatics Inc.).* Computer support on a Convair 990 aircraft began almost simultaneously with support on the KAO. Through two more aircraft (one crashed, and a second Convair 990 burned on the

[1] Space Wars: An interactive strategy game programmed for HP 1000 computers, largely in HP Assembly language, in the early days of the Cave. Recent discovery of the original source code confirmed that much of the programming style of Cave Assembly language programmers was derived directly from Space Wars.

[2] ADDAS: Airborne Data Display and Acquisition System, the computer system supporting the two Convair 990 aircraft which have been supported on this contract. Replaced by DADS on the DC-8 aircraft.

runway, leading to acquisition of the current DC-8 Airborne Laboratory) regular exchanges of equipment, staff, and ideas kept the airborne science community at Ames computationally compatible. Bootstrap programming skills – in machine language, naturally – honed on CV-990 HP 2100 computers proved invaluable in impressing users of the KAO Tracker computer 10 years later.

Software guru and ADDAS/DADS lead Susan Cherniss (who might have been held responsible for the ADDAS logs oversight above, had anyone the nerve) proved an inspiration to machine language programmers everywhere. In addition to entering 64 words of bootstrapping code from the front panel in about 2 minutes during flights (8.5 bits/second, or baud as we say now), Susan could trace interrupt routines (from the front panel, using octal listings of the code) faster than the eye could follow. This trick was also attempted by several early KAO experimenters, with varying degrees of success. Rumors that Bob Loewenstein successfully wrote an entire data program in machine language after the KAO took off for that night's observations could not be confirmed.

"I would just like to say, looking at this ADAMS User's Manual, that it's really disgusting. We would never have put something out like this in the early days. Documentation was just not an acceptable way to spend our valuable time – we had programs to write." —Don Wilson (Informatics Inc.). Documentation was always a source of frustration, consternation, and debate on the computer support contract – either due to its absence, its presence, or its content. In deference to the great traditions of the early staff (and, to be fair, some NASA managers), documentation avoidance was practiced on a widespread basis through the early '90's.

Alas, with the advent of "modern" software engineering on systems such as the ADAMS Upgrade, an expectation of "standard software engineering practices" prevailed. Unfortunately, none of us who wanted documentation to follow standard practices could agree on what those were. Regular citation of the "NASA Software Management and Assurance Program" standards, quickly replaced by the "NASA Software Documentation Set" standards, apparently failed to consistently convey the proper air of authority. This was eventually resolved by documenting everything via flowcharts.

"Why on earth would you want a Macintosh?" —Lou Haughney, on several occasions pre-ADAMS Upgrade. "You won't believe what I just got – a Macintosh. It's really great!" —Lou Haughney, after his retirement in 1991. The advent of the Mac created a major change in the nature of documentation for the KAO. Gone were the days of custom and esoteric programs for text documentation and formatting; now they were replaced by intuitive, WYSIWYG – and massive – documents. A major update of the ADAMS User's Manual – before the Mac – took several months. The first major update of the most recent ADAMS User's Guide took 2 weeks. Despite fears that the time saved in instant WYSIWYG document production would be spent in document beautification, there can be no doubt that the Mac was, in fact, great. (Where we **did** spend all our time was trying to convert Mac files to PC files. For some odd reason, certain contractors resisted converting their PCs to Macs, clearly a more sensible solution.[3])

[3] Just kidding, you guys. Really.

On the down side, now we had to figure out how to maintain all that documentation and keep it consistent. We're, uh, working on that one.

"They're creepy and they're kooky, They're mysterious and spooky, They're altogether ooky, The ADDAMS family." —Preface to an ADAMS Log Book. ADAMS Logs have captured the essence of ADAMS support for the last 20 years. From entries in some early logs – "Good flight" – to the 10-page chapters from more recent flights, ADAMS personnel have spilled their secrets in the log. On one flight, a flyer wrote "There's really nothing I can do, but the Mission Director expects me to work on it busily anyway, so I'm going to write some Grateful Dead lyrics in the log."

There have been 41 logs in the 20 years of flight support. The first 5 logs or so were 50 pages each, never more than a page or two per flight. The last 5 logs or so run 130 pages of notes, with another 15 pages of records at the end, and each flight takes an average of 6 pages. (I love those statistics.) The first squawk was labeled with a star "because we had to make up some symbol to label it with, so we picked a star," said Tom Mathieson. Now there are stars (squawks), daggers (blames), exclamation points – 'bangs' to some of us (problems, but not **our** problems), pound/sharp/number signs (notes), arrows (action items), and – our personal favorite – Mr. Bill faces (reconfigurations – oh noooo!). Oh yes, and please put the UT before every comment, a line at the beginning and end of the flight, and follow the correct format in labeling each flight in the log book. Personally, I think electronic log books are long overdue. (And, with the new ADAMS Upgrade, they're finally possible!)

"Well, my worst experience was walking along the beach in Hawaii about an hour before the preflight, and seeing the only other ADAMS flyer walking toward me on the beach. 'Aren't you taking the flight?' I asked. 'I thought **you** *were taking it,' he answered. A mad drive through rush hour traffic got me to the airplane just as the doors were closing." —Jeff Terry (Informatics General Corporation).* Deployments always seemed to bring out the best, or worst, of flight support. From Japan, to Punta Arena (Chile), to Easter Island, the KAO has flown any number of interesting deployments. (As in, 'May you live in interesting times.') The smallest staff ever supporting ADAMS on a deployment was 1 – this was probably done several times, but most recently by Michael Pruznick in 1993 in Hawaii (with all those new complicated systems!). The most at one time was 6 – this year for the comet impact with Jupiter. With 4 of us sick, and the massive flight and Internet connectivity demands, another 3 or 4 people would have been more than welcome! Fortunately, yeoman flyer Chris Bero took six 9.5 hour flights in 9 days, a modern day record which will probably never be beat. There are any number of entertaining stories about KAO deployments, more than can ever be described here. From nearly overflying Russian air space, to landing on very short notice in Argentina, to relying on a Brazilian military representative to get final approval for an occultation flight plan 15 minutes before the takeoff, the KAO has provided an exciting international backdrop for its work. ADAMS can be proud that no one-time event has ever been compromised by an ADAMS failure. (Although that one time the data computer stopped 10 minutes **after** an occultation was a little disconcerting.)

MISSION 76-024 HARPER / McNUTT #2

ADAMS: FONG

TAKEOFF: 9 MARCH 1976 4:59 U.T.

DURATION: 5:39 HOURS

[redacted]

8 .U.T STILL ALIVE. [redacted] MISSION HAD. FOLLOWING PROBLEMS:

1. ENGINE FAILURE DELAYED TAKEOFF 2½ HOURS.

2. EARL GILLESPIE, BEFORE TAKEOFF, MADE ME GENERATE 3 DIFFERENT FLIGHT PLANS BASED ON DIFFERENT PROJECTED TAKEOFF TIMES. HE GAVE DIFFERENT PLANS TO DIFFERENT PEOPLE.

3. Mc NUT GROUP EXPECTED ME TO RUN THEIR PROGRAM.

4. Mc NUT GROUP SUDDENLY AND FRANTICALLY ASKED ME TO LOAD THEIR PROGRAM IN MIDDLE OF HARPER EXPERIMENT. HARP GROUP HARPS LOUDLY.

5. HARP GROUP RENEGES ON GIVING NUT GROUP TIME ON LEG BECAUSE DELAY CAUSED LEG TO BE SHORTENED.

Figure 1. ADAMS Log Book for Mission 76-024, 1976 March 10, or Classic, Unedited and Unrehearsed Stories of KAO ADAMS Support.

6. MISSION DIRECTOR CAN BE QUOTED TO SAY:
"I REALLY DON'T KNOW WHAT'S GOING ON,"
"I WANT TO HEAD FOR HOME."

7. IT WAS DISCOVERED THAT A BABYSITTER WAS NEEDED TO TAKE CARE OF SOME KINDERGARDEN KIDS ON BOARD.

AFTER FOLLOWING STEPS WERE TAKEN, THINGS WENT CALMLY:

A. NEW FLIGHT PLAN WAS GENERATED WHICH WAS ACCEPTABLE TO PILOTS & DIRECTOR.

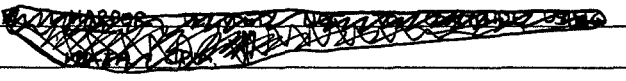

B. I RAN THE NUT's PROGRAM FOR THEM

C. HARP GROUP DECIDED THAT THEY HAD PRIDRITY OVER NUT GROUP.

NO ADAMS OPERATION [redacted] FAILURE OF A TECHNICAL MANNER. PROGRAMS & HARDWARE ALL FUNCTIONED AS EXPECTED.

Paul

P.S. - WE HAD DIFFICULTY FINDING MARS AND I WAS ASKED TO MAKE A NEW FLIGHT PLAN. "TARO" INDICATED THAT TELESCOPE WAS ONLY A FEW DEGREES OFF & A NEW PLAN WAS UNNECESSARY. MARS WAS EVENTUALLY SPOTTED.

Paul (10 MAR 76 U.T.)

My favorite personal experience from KAO travel occurred when we arrived at the 'primary objective' of the 1994 Brazilian occultation mission (just another planet-in-front-of-a-star episode, except it was an asteroid). In this case, the primary objective was Easter Island. On the ferry flight over, KAO participants watched a video tape showing various archaeologists discussing the mysteries of Easter Island. (Long gone are the days in which the on-board video tapes were more, shall we say, revealing. Yes indeed, the KAO world has definitely changed.) Upon arriving at Easter Island and walking over to the local statues that afternoon, whom should we encounter but one of the famed archaeologists herself. The next night, Juan Rivera and I got a memorable tour of island nightlife (no, not like that); hopefully Juan's forgiven me for giving out at 3 a.m. At least no one had to drag me out of bed after I didn't show up for a ferry flight, like **some** ADAMS Operations Managers I could name.

"Well, we might have seen something, but we're not sure." —Jim Elliot, 1994 Chiron occultation (they did see something, as it turned out).

Allan Meyer (Tracker Operator, NSI): "Yes, the star is fading out, I can see it!"
Jim Elliot: "Well, maybe it is – no, I don't think so. Maybe we . . ."
Allan Meyer: "Yes it is, it's gone!"
Jim Elliot: "No, I don't – oh yeah, there it is, we've got it!" —1989 Pluto occultation. (Allan was watching on video, while Jim was seeing delayed 1/2 second CCD frames. I guess you had to be there.)

"Huh, we're losing signal. No, here it is back again. Must be noise or something." —Jim Elliot, (before the) rings of Uranus discovery in 1977. Of course, one of the best parts of the KAO program has been doing real science, often in real time. Occultations, eclipses, comets, supernova, comet/planet collisions, and even space shuttles tend to eclipse (sorry) some of the more "mundane" experiments. But even on the 'bread-and-butter' flights, there is always the opportunity for excitement. Especially with certain experimenters – or certain ADAMS Operators. (See Figure 1 for an ADAMS Log entry on an early flight.)

> *"Supernova calibrator expialidocious*
> *Saw the target field but the cameras weren't in focus*
> *Found the cobalt line although the noise was quite atrocious*
> *Supernova calibrator expialidocious!" —Lyrics by Brian Wright.*
> *(Informatics Inc., Informatics General Corp., Sterling Software).*

For many of us, the knowledge that we are contributing to the science of the facility is what makes the job so terrific. Returning home after a flight in which we got the data – particularly when the computer staff contributed directly to that success – is an extremely rewarding experience. Being a trusted assistant to the science team, helping with technical support or simply advice, has always tied the computer operations staff particularly closely to this project. Entering the next 20 years of airborne astronomy support, now with the KAO and soon with SOFIA, we will see ever-closer linkage between the computer support and the successful operations of the facility as a whole. Those who work on the airborne science program will be the lucky ones who get to enjoy that increased interaction. Based on the last 20 years, it seems likely that they will indeed live

in interesting times.

"Oh, I suppose I could manage that. In my spare time. Sigh." —Jim Pantaleo (Informatics Inc., Informatics General Corporation, Sterling Software).

Disclaimer.

All quotes are without the permission of the speaker. In fact, most of the quotes are from memory, except for some that are second-hand. Apologies to those who are misquoted and/or misrepresented by these excerpts; I meant only the best.

Acknowledgements.

The author would like to gratefully acknowledge the contributions of all Cavers, past, present, and honorary, who have supported NASA's Airborne Science Program at Ames. It has been a wonderful time, and you have been great at work and play. (I wish I could list all 75 of you here, but we'll have to take a picture of the 'attic' instead.) This paper is dedicated to you. Thanks!

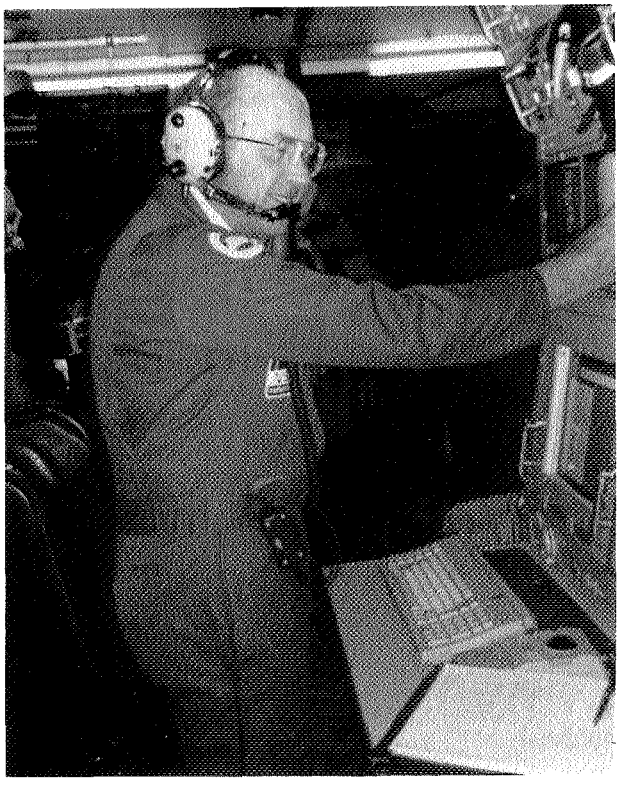

Curt Laughlin

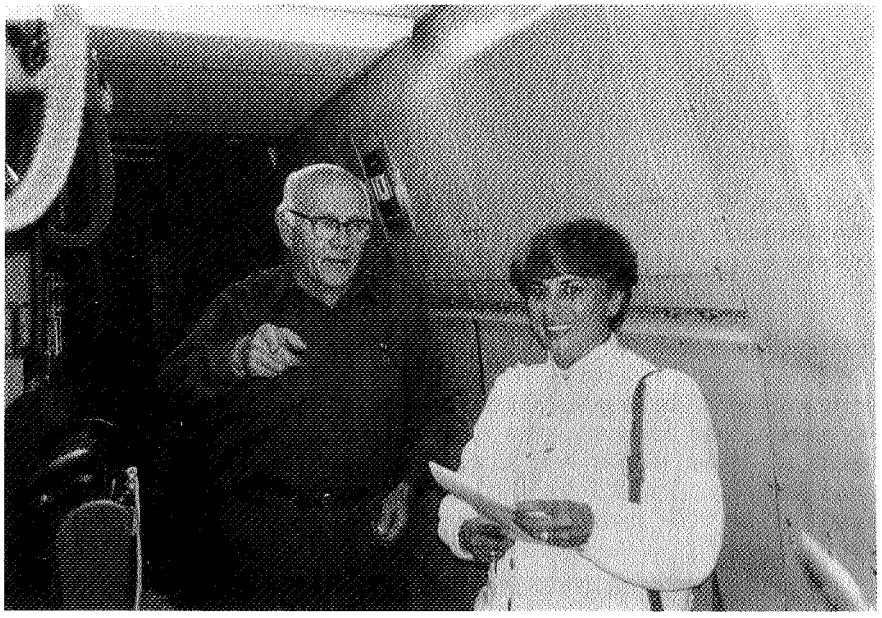

Carl Gillespie, MaryLou Zandona

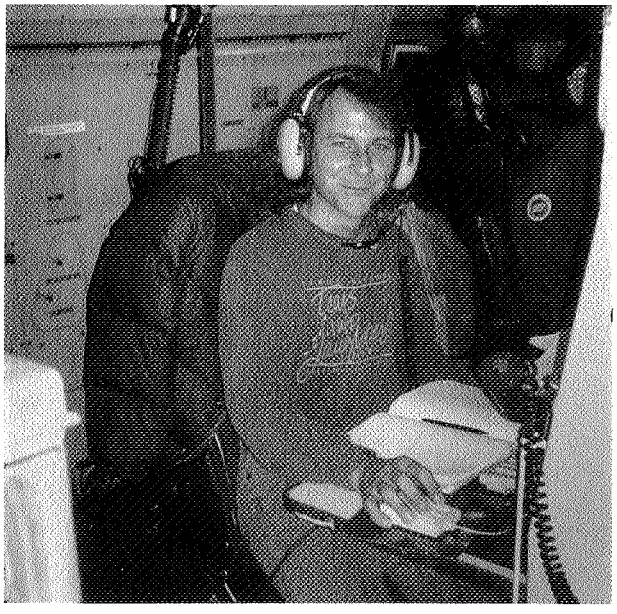

Alan Steiner

Airborne Astronomy Symposium on the Galactic Ecosystem
ASP Conference Series, Vol. 73, 1995
M.R. Haas, J.A. Davidson, and E.F. Erickson (eds.)

AN INFRARED ASTRONOMER'S EARLY VISION OF AIRBORNE ASTRONOMY: PAUL MERRILL 1920

DONALD E. OSTERBROCK
University of California Observatories/Lick Observatory,
University of California, Santa Cruz, CA 95064

ABSTRACT The first published paper by a professional, research astronomer which discussed airborne astronomy from airplanes was by Paul W. Merrill. In it he proposed some of the types of observations which might be made, looking up at astronomical objects in the sky. This paper describes Merrill's paper, his education, training and subsequent career, and a few other aspects of the early history of airborne astronomy.

INTRODUCTION

In a paper given at the Airborne Astronomy Symposium ten years ago, Craine (1984) explored the early history of airborne astronomy from powered, manned aircraft. He traced the idea of making such airborne observations back to a letter from Col. John Millis, of the U.S. Army Corps of Engineers, to the Chief of Engineers in Washington, dated January 5, 1918. Craine's main sources were surviving correspondence obtained from Army and Air Force archives, files and individuals. Some additional information on these early days is available in various astronomical archives and published papers, and forms the basis of the present paper.

COLONEL JOHN MILLIS

Millis, whose suggestion was to photograph shadow bands, looking downward from an airplane, as they swept across the surface of the earth at a total solar eclipse, was deeply interested in astronomy. As head of the Army Engineers' Office, first in Newport, Rhode Island, then in Savannah, Georgia, he had been in correspondence since 1915 with George Ellery Hale, W. W. Campbell, and Edwin B. Frost, the directors of Mount Wilson, Lick, and Yerkes Observatories, respectively, and with their staff members, secretaries, and photographic assistants. Millis wrote them all, seeking direct photographs of planetary nebulae and spiral "nebulae" (as galaxies were then almost universally known). He obtained quite a few such pictures, and demonstrated so much interest in them that Heber D. Curtis, the pioneer Lick Observatory nebular researcher, sent him reprints of some of his papers.

MERRILL'S PAPER

The first paper by an experienced, professional research astronomer which discussed the possibility of airborne astronomy was by Paul W. Merrill, of the Mount Wilson Observatory staff. In it he first stated in print some of the types of astronomical observations which might be made from an airplane, looking up at the sky (Merrill 1920). They included direct photography of the solar corona at an eclipse, photographic spectroscopy of the flash spectrum (of the chromosphere), also at an eclipse, polarization measurements of the daytime sky at high altitude, measurements of the absorption of solar ultraviolet radiation at these altitudes, and photography and spectroscopy of the corona, especially in the red and infrared, without an eclipse. In his paper Merrill emphasized the main advantages he saw in airborne astronomy: relatively clear skies, free of low or mid-level clouds and haze, and that "[t]o reach an altitude of 15,000 to 20,000 feet, it would be easier to ascend in a suitable airplane than to go on mule back up a mountain trail, and to reach much higher altitudes it would be the only way." He was referring to Campbell's expedition to the summit of Mount Whitney, little more than a decade earlier, to obtain spectrograms of Mars to search for water vapor in its atmosphere, from above as much of the contaminating effects of terrestrial water vapor as possible (Osterbrock 1989).

Merrill's paper, entitled "Progress in Photography Resulting from the War", was based on his experiences working at the National Bureau of Standards in Washington during World War I. There, along with other astronomers and physicists, he was working on a crash development program to improve the aerial photography capability of the nascent Army Air Service, then part of the Signal Corps. Most of his efforts were devoted to improving the techniques of hypersensitizing photographic plates for use in the red and infrared spectral regions. As part of this work, Merrill took part in numerous experimental aerial photography flights from Langley Field, Virginia, operating a camera from the rear, open cockpit of the two-seated De Haviland biplanes then in use by the Army. These planes had normal flight altitudes of 7,000 to 13,000 feet, maximum altitudes of 18,000 to 20,000 feet, and maximum flight times of 5 or 6 hours at normal altitudes (Luckiesh 1919). Merrill's specific suggestions for using airplanes for astronomy were clearly based on his own experience, although he probably had heard of Millis's previous idea.

Very soon after the Armistice effectively ended World War I in November 1918, Merrill hurried to California, where Hale had promised him a research position on the Mount Wilson Observatory staff. Its 60-inch reflector was the second largest telescope in the world, and its 100-inch, then completed but not yet in operation, was soon to become the largest. Merrill never returned to airborne astronomy, which indeed was not ripe for take-off at that time. Instead he had an outstanding research career with the Mount Wilson ground-based telescopes, specializing in spectroscopy of red stars, Hα in stellar spectra, long-period variable stars, and infrared spectroscopy. In his long lifetime, he published over 250 research papers and four books, summarizing his results (Joy 1962; Wilson 1964).

MERRILL'S EARLY LIFE

Merrill was born in Minneapolis, Minnesota in 1887, the son of a Congregational minister. Paul attended grade school there, and as his family moved west, in

Silverton, Colorado and in California. He took his first three years of high school at Oroville, California, and his last year at Santa Clara, graduating in 1904. His father then had a church in nearby Saratoga. Paul entered Stanford that fall, majoring in mathematics, and also taking physics, astronomy and other sciences, as well as German, Latin and Greek. He made his first recorded visit to Lick Observatory in the fall of his freshman year, and was already planning then to go on to graduate work in astronomy there and at Berkeley. Merrill applied for a summer job at Lick in 1906, with high recommendations from his physics and mathematics teachers, Fernando Sanford and John A. Miller (later the long-time professor of mathematics and astronomy at Swarthmore College). Both described Merrill as a hard worker, "thoughtful and studious", who was liked by his classmates and professors alike. Lick Director Campbell hired him as an electrician's assistant for the summer. Merrill worked so well that Campbell offered him the chance to come back the next summer, but instead the young student took a better paying job with a surveying party in Idaho. He had to earn enough money to stay in school.

When he graduated from Stanford in 1908, Merrill took a field job with the U. S. Geological Survey in California, but on Christmas Eve he received a letter from Campbell, offering him an assistantship at Lick Observatory. He accepted at once, and hurried to Mount Hamilton to begin work in January 1909, observing with the 36-inch refractor on the observatory's radial-velocity program, and measuring and reducing the spectrograms he and others had obtained. Merrill was learning to be an astronomer even before he entered the University of California as a graduate student a year and a half later, in the fall of 1910. By then he had a Lick Observatory Fellowship for support. He spent that fall on the mountain, observing, and then the second semester and the entire following academic year at Berkeley, taking courses, but returning to Mount Hamilton to observe during his Christmas and summer vacations. Then he returned to Lick for the 1912-13 academic year, to complete his Ph. D. thesis on B stars with Hα emission lines in their spectra (Merrill 1913). He received his degree at the University of California Fiftieth Anniversary Commencement, one of six astronomy Ph.D.'s that year, along with a total of only three other Ph.D.'s and one Sc.D. from the rest of the university (Osterbrock 1990).

Merrill hoped for a staff position at Lick, and Campbell wanted to keep him. But there was no opening, and instead Merrill found a job as an instructor in astronomy at the University of Michigan. He was not happy there. He wanted to do research, and there was a 36-inch reflector in Ann Arbor, but it was not nearly so well equipped as the Lick refractor. The observing weather was very poor compared with that at Mount Hamilton, and Merrill longed to be back in California. Beginning in 1914 he bombarded Hale, at Mount Wilson, and Campbell with letters seeking a job. By now Merrill was convinced that physics was more closely related to the kind of astronomy he wanted to do than the mathematics with which it was taught at Stanford and Berkeley. In 1916, fed up with Michigan observing, he left Ann Arbor to become a research physicist at the National Bureau of Standards. His friend Keivin Burns was already at the Bureau, working in its spectroscopy laboratory, and his former Berkeley room-mate, Carl C. Kiess, was to join them there in 1917. All three were astronomy Ph. D.'s who had been at Lick. Merrill fitted naturally into the work, particularly because of his interest and experience in hypersensitizing photographic plates for the red spectral region, learned as part of his thesis project. He liked experimental spectroscopy, but he longed to get back into astronomy. In 1917

Merrill seized the opportunity to get away for a week's observing at Harvard, obtaining stellar spectra in the red and near-infrared regions. When America entered World War I, his skills fitted perfectly into the aerial photography development program at the Bureau of Standards.

Hale spent much of the years 1917-18 in Washington, as chairman of the National Research Council, America's science establishment mobilized for warfare. Merrill was in contact with him there, and hoped to transfer from the Bureau of Standards to a wartime photographic-dye development project at Throop Polytechnic Institute (later Caltech) in Pasadena, to get his hand in at Mount Wilson. However, Samuel W. Stratton, the head of the Bureau, told him he was needed there, and Merrill loyally stayed. But in August 1918 Hale, with the 100-inch reflector nearly ready to go into operation, finally offered Merrill a Mount Wilson position, which he could take up as soon as the war ended. Merrill immediately accepted, expecting to go west the next spring, but in the event he got there even sooner, and began his long and fruitful career at Mount Wilson Observatory in January 1919.

MERRILL'S LATER CAREER

Merrill's later career at Mount Wilson Observatory is well documented in his memorial biographies (Joy 1962; Wilson 1964). As stated above, he was an extremely productive research worker, who continued to push the observational limits of photographic infrared stellar spectroscopy out to longer wavelengths until he retired in 1952. Although in his later years he suffered terribly from arthritis, which he fought with massive doses of aspirin, he continued very actively in research after his retirement, using plates he had obtained earlier or which his colleagues had obtained for him, measuring and reducing them himself.

ACKNOWLEDGEMENTS

This paper is based on the papers cited, and on correspondence in the Mary Lea Shane Archives of the Lick Observatory, the Mount Wilson Observatory Collection in the Henry E. Huntington Library, San Marino, California, and the George Ellery Hale Papers, Microfilm Edition. I am most grateful to Dorothy Schaumberg, curator of the Shane Archives, and to Ronald Brashear, history of science curator at the Huntington Library, for their friendly and efficient help.

REFERENCES

Craine, E. 1984, in Airborne Astronomy Symposium, ed. H. A. Thronson, Jr., & E. F. Erickson, NASA Conference Publication 2353, p. 9
Joy, A. H. 1962, PASP, 74, 41
Luckiesh, M. 1919, ApJ, 49, 108
Merrill, P. W. 1913, Lick Obs. Bull., 7, 162
———— 1920, PASP, 32, 16
Osterbrock, D. E. 1989, JHA, 20, 77
———— 1990, Astronomy Quarterly, 7, 115
Wilson, O. C. 1964, Bio. Mem. Nat. Acad. Sci., 37, 237

Airborne Astronomy Symposium on the Galactic Ecosystem
ASP Conference Series, Vol. 73, 1995
M.R. Haas, J.A. Davidson, and E.F. Erickson (eds.)

Time Flies Too: Random Photos, Articles, etc.

A. W. Meyer
NSI Technology Services; NASA/Ames Research Center, MS 248-2, Moffett Field, CA 94035-1000

Abstract. This poster displayed a selection of articles from popular magazines, newspapers and professional journals describing the activities of the Kuiper Airborne Observatory. Some of these were feature articles, while others were brief news items in astronomy-oriented popular magazines such as *Sky and Telescope* and *Astronomy*. The first of a half-dozen *Sky and Telescope* articles appeared in the August, 1974, issue and described far-infrared observations of the Egg Nebula (AFGL 2688). Articles have also appeared in such diverse publications as *Popular Mechanics*, and the journals *Nature* and *Science*. Many articles have appeared in local newspapers over the years; the news media in Australia and New Zealand have carried enthusiastic coverage of KAO southern hemisphere missions. Some of the events which have led to these articles include occultations by Mars, Uranus and Pluto, Galactic center expeditions, Comet Halley, Supernova 1987A, and the Comet Shoemaker-Levy/Jupiter collisions.

Some Popular Articles

E. P. Ney, Sky & Telescope, January, 1975; "The Mysterious Egg Nebula"
J. L. Elliot *et al.*, Sky & Telescope, July, 1976; "A Unique Airborne Observation"
J. L. Elliot *et al.*, Sky & Telescope, June, 1977; "Discovering the Rings of Uranus" (contains transcript of the intercom audio)
[anon], Sky & Telescope, December, 1980, p. 482; "What Powers M17?"
L. J. Robinson, Sky & Telescope, November, 1982; "Orion's Stellar Nursery"
R. Gore, National Geographic, June, 1983; "The Birth and Death of Stars"
H. Campins & D. Lynch, Astronomy, March, 1986; "The Airborne Assault on Comet Halley"
P. Stryker & M. Willis, Stardate, January/February, 1994; "Two Nights on a Flying Observatory"
S. Stephens, Astronomy, November, 1994; "Telescopes That Fly"

Allan Meyer, Yvonne Pendleton

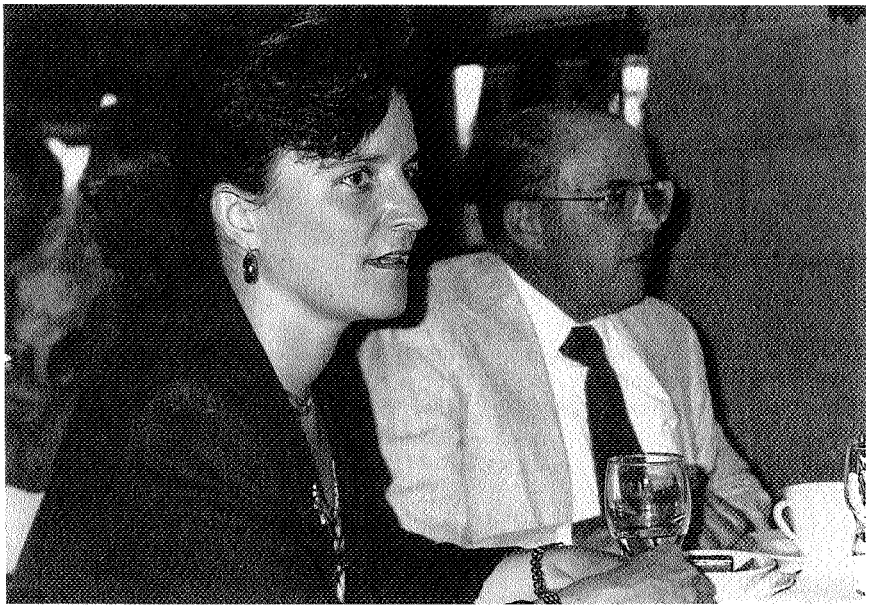

Wendy Whiting, Curt Laughlin

Airborne Astronomy Symposium on the Galactic Ecosystem
ASP Conference Series, Vol. 73, 1995
M.R. Haas, J.A. Davidson, and E.F. Erickson (eds.)

FLIGHT OPPORTUNITIES FOR SCIENCE TEACHER ENRICHMENT

EDNA DeVORE
SETI Institute, 2035 Landings Drive, Mountain View, CA 94043

CARLTON GILLESPIE, JR., Airborne Astronomy Missions Branch
GARTH HULL, Educational Programs Office
DAVID KOCH, Astrophysics Branch
NASA Ames Research Center, Moffett Field, CA 94035

ABSTRACT NASA Astrophysics Division supports a pre-college teacher program to provide Flight Opportunities for Science Teacher EnRichment (FOSTER). To date, forty-five teachers are participating, and the program will expand nation-wide to serve fifty teachers per year on board the Kuiper Airborne Observatory. In the future, the Stratospheric Observatory for Infrared Astronomy (SOFIA) will bring more than one-hundred teachers per year on board for astronomical research missions. FOSTER is supported by a grant to the SETI Institute from the NASA Astrophysics Division, NAGW 3291.

Introduction

NASA's Kuiper Airborne Observatory (KAO) is a unique high-flying observatory and science on board the KAO involves many disciplines and technologies: astronomy, optics, cryogenics, solid state physics, chemistry, mathematics, meteorology, mathematics, computer science, atmospheric science aeronautics, navigation, and engineering. Each research flight of the KAO is a microcosm of the scientific method. Flying teachers obtain first-hand, real-time experiences of the scientific process: its excitement, hardships, challenges, discoveries, teamwork, and educational value. Further, work on board the KAO involves cooperation, teamwork and problem solving—critical skills for students in the 21st century—in the process of doing cutting-edge scientific research. By involving precollege teachers in airborne astronomy, FOSTER enriches their experiences and understanding of the content of science, mathematics and technology, as well as enabling them to develop insights into the careers of all of the people involved in this scientific enterprise.

FOSTER and Science Literacy

The goals of the FOSTER project are to 1) enhance science education using the unique opportunities offered by NASA's Kuiper Airborne Observatory; 2) enrich teachers' experiences and understanding of science, mathematics, and technology; 3) increase scientific literacy of students and the public through teachers; and 4) encourage teacher teams to jointly develop supplementary curriculum materials. These goals align with national goals for science and mathematics education described in *America 2000*.[1] Simply, FOSTER offers a program to improve the scientific and technological literacy of the American public through teachers and schools. With FOSTER, NASA's unique facilities and workforce enrich precollege teachers, a prominent part of the educational goals in *NASA's Strategic Plan*.[2] FOSTER supports NASA's goals,[3] the FCCSET-CEHR's goals,[4] and the National Education Goals for educational excellence. Simply stated, "NASA's highest education priority is elementary and secondary teacher enhancement activities....."[5] In bringing research teams and teachers together for meaningful interaction and learning, both the scientific research and the education communities benefit. At this interface, research teams contribute directly and personally to the scientific and technological literacy of teachers and students. Teachers bring to the research community their students' excitement about and interest in the science, technology and the people who work in airborne astronomy, bridging the barriers between schools and research institutions. Such partnerships between the scientists and educators are critical for the improvement of science education. In the words of Bruce Albers, President of the National Academy of Sciences, "I now view effective partnerships between scientists and precollege science teachers...as the only hope for lasting systemic change in precollege science education and, therefore, as an important national priority of the United States."[6]

The FOSTER Experience

FOSTER teachers are recruited and selected in teams of two. Typically, the team represents a middle and high school that share students. In this way, FOSTER builds bonds between teachers, schools and students to enhance science, mathematics and technology education. The teacher teams meet at NASA Ames for a summer workshop on contemporary astrophysics and to learn lessons and activities which enrich their curriculum. The workshop experience also prepares them for a research mission on board the KAO. They learn about the KAO: the telescope, the investigators' instruments, the computer technology for data collection and navigation, and other systems. Teachers are provided with internet accounts and training through the K Through 12 Internet Project, and introduced to FOSTER On-Line, an electronic resource for educators. The workshop initiates the personal contact between teachers and NASA scientists, engineers, pilots and others, which continues to the research flight experience and beyond.

As a part of FOSTER, teachers host a NASA Aerospace Education Special-

ist for a visit to their school for assembly programs, classroom visits, and teacher workshops which helps to share NASA with many students and teachers. FOSTER teachers become teacher-leaders. In conjunction with the project, presentations have been made at scientific and educational conferences, conventions and workshops to over 1,100 other educators. Most of these presentations provided an overview of airborne astronomy and lessons for other educators to take back to the classroom.

Subsequently, teacher teams return to Moffett Field (NASA Ames Research Center) or to Hickam Field (Honolulu, HI), for a research mission on board the KAO. During the deployment for missions on the Comet Shoemaker-Levy 9 impacts into Jupiter, FOSTER '94 teacher, Michael Ahern, was supported by his school district to go to Australia for flights on the KAO. For teacher flights, the principal and guest investigators guide teachers through the science and instrumentation in pre-flight briefings and discussions. KAO staff review the operation of the telescope, and the object list for the flight. The flight plan is shared with the teachers, and, often, they fly in the cockpit as observers during take-off and landing. The flight crew provides on-the-spot lessons in the operations of jet aircraft. During the night, teachers are informed observers of science-in-action, and, with some research teams, they become science team members, guiding the telescope and monitoring data collection. Teacher teams record their flights on film and videotape to share with their students, and have recorded lessons inflight. Teacher flights are facilitated by a member of the FOSTER staff or an experienced FOSTER teacher.

Forty-five teachers have been selected to participate in FOSTER since its inception. They represent elementary, middle and high schools of wide socio-economic and ethnic diversity. The pilot group, FOSTER '92, was from the greater San Francisco Bay Area; they met for eight days throughout the first school year, 1992-93. They tested lessons and activities, and were the first FOSTER teachers to fly. Twelve teachers were chosen for the second group, FOSTER '93; they were the pilot group for geographic expansion of the program and for the first week-long summer workshop. FOSTER '94 included twenty-two teachers: six Bay Area teams, one team from Hawaii, and four teams affiliated with KAO principal or guest investigators from across the United States. The experiences of FOSTER teams affiliated with principal and guest investigators will help the project develop models for scientist-teacher partnerships. The FOSTER teachers are:

FOSTER Teachers, 1992

Jill Baumgartel	Woodside High School	Woodside, CA
Gail Chaid	Independence Planetarium	San Jose, CA
Robert Choate	O'Hara Park Middle School	Oakley, CA
Jackie Ervin	J. F. Kennedy High School	Richmond, CA
Vivian Huang	Skyline High School	Oakland, CA
George O'Neel	Burnett Middle Academy	San Jose, CA

Mark Piccillo	Oakland Senior High School	Oakland, CA
Jeff Ring	San Jose High Academy	San Jose, CA
Raymond Rogoway	Independence High School	San Jose, CA
Chelda Ruff	Golden West Middle School	Travis AFB, CA
Mary Lou Zandona	McNair Intermediate School	East Palo Alto, CA

FOSTER Teachers, 1993

Sandra Engel	Bret Harte Middle School	San Jose, CA
Kim Fanter	Baker Elementary School	San Jose, CA
Marianne Gielow	Piedmont Middle School	Piedmont, CA
Margaret Gwaltney	Leland High School	San Jose, CA
Pauline Higa	Mililani High School	Mililani, HI
John Keller	Los Altos High School	Los Altos, CA
Glen Kimoto	S. C. Rogers Middle School	San Jose, CA
Penny Moore	Piedmont High School	Piedmont, CA
Hurbert Pate	Yganico Valley High School	Concord, CA
JoAnne Payne	Pine Hollow Int. School	Concord, CA
Suzanne Williams	Graham Middle School	Mt. View, CA
Arlene Yoshimura	Mililani Mauka Elementary	Mililani, HI

FOSTER Teachers, 1994

Michael Ahern	Corte Madera Middle School	Portola Valley, CA
Arthur Altshiller	Van Nuys High School	Van Nuys, CA
Victoria Brady	Marin School	Albany, CA
Greg Camacho-Light	Jefferson School	Paicines, CA
Robert Coutts	Van Nuys High School	Van Nuys, CA
Karen Cowan	Mendenhall Middle School	Livermore, CA
Karen Hanson	Williams Bay Elementary	Williams Bay, WI
Deborah Havens	Bitterwater-Tully School	King City, CA
Lucille Holloway	Livermore High School	Livermore, CA
Judith Inouye	Kawananakoa Int. School	Honolulu, HI
Jane Kincaid	Silverado Middle School	Napa, CA
Randal Lau	Likelike Elementary School	Honolulu, HI
John Loftus	East Boston High School	East Boston, MA
Suzanne Maly	Safford Middle School	Tucson, AZ
Robin McClohn	Menlo School	Atherton, CA
Michael Meneghetti	Stanley Intermediate School	Lafayette, CA
Patricia Merha	Amphitheater High School	Tucson, AZ
Alexandra Montes	Trinity Middle School	Roxbury, MA
Wilfred Oswald	Napa High School	Napa, CA
Kara Shultis	Williams Bay High School	Williams Bay, WI
Kay Sorg	Albany Middle School	Albany, CA
Janet Thomas	Campolindo High School	Moraga, CA

FOSTER continues a long tradition of educational outreach to teachers and

schools by the staff and scientists who fly on board the KAO. Teachers have flown with KAO teams from several universities and institutions, meeting and working with leading scientists in infrared astronomy. The principal and guest investigators who have worked with FOSTER teachers during their research flights include: Drs. L.Allamandola, J. Davidson, M. Cohen, S. Colgan, E. Erickson, E. Dunham, M.Haas, D. Koch, A. Tielens, Y. Pendelton, J. Bregman, S. Madden, A. Rudolph, S. Sandford, F. Witteborn, and D. Wooden of NASA Ames Research Center; Drs. M. Werner, J. Zmuidzinas, J. Keene, and P. Wannier of Jet Propulsion Laboratories; Dr. G. Bjoraker of NASA Goddard Space Flight Center; Drs. N. Evans, D. Lester and P. Harvey of the University of Texas at Austin; Drs. D. Harper and R. Lowenstein of Yerkes Observatory; Dr. R. Hildebrand of University of Chicago; Dr. D. Hunten of University of Arizona; Dr. K. Noll of Space Telescope Science Institute; Dr. D. Rank of Lick Observatory; Dr. C. Skinner of Lawrence Livermore Laboratories; Dr. M. Morris of University of California at Los Angeles; Drs. C. Townes and N. Geis of University of California at Berkeley; Dr. R. Genzel of Max-Planck Institute; and Drs. A. Betz and R. Boreiko of University of Colorado at Boulder. Many other people have also contributed time and energy to the workshops, FOSTER On-Line, the videotape, "Kuiper:Window on the Universe," and in other ways to the development of the program for teachers and schools. The project is a team effort by people at the SETI Institute; the Airborne Astronomy Missions Branch, the Astrophysics Branch, the Educational Programs Branch, Sterling Software and NSI, Inc. at NASA Ames Research Center; Astrophysics Division, NASA Headquarters; and teachers and students from across the United States.

The FOSTER experience gives teachers pride and a sense of special achievement. Their accomplishments are admired by all—involvement in the high-tech flying of the KAO brings prestige and glamour to the teachers and schools. But, more importantly, these teachers bring the excitement and adventure of doing first-class science to their students and the public.

REFERENCES

[1]The National Education Goals from *America 2000* state as goal 4: "U. S. students will be first in the world in science and mathematics achievement." And goal 5 states: "Every adult American will be literate and will possess the knowledge and skills necessary to compete in a global economy and exercise the rights and responsibilities of citizenship."

[2]*NASA Strategic Plan, May 1994,* states "We will use NASA's inspiring mission, unique facilities, and specialized workforce to promote excellence in America's educational system. Specifically, we will work to enhance scientific and technical competence and literacy. We will do this by capturing the educational potential of each NASA program and by conducting and facilitating education programs at all educational levels. We will maximize the delivery and impact of our education programs by using state-of-the-art

educational technologies, and by developing partnerships with the education community. We seek to help the national education system to meet civilian aerospace needs and the broader scientific and technological needs of our Nation. Special emphasis will be placed on fostering historically underrepresented groups to pursue careers in science, mathematics and engineering." p. 19.

[3]*NASA's Strategic Plan for Education: A Strategy for Change: 1993-1998.* p. 14 and pp. 21-22.

[4]*Pathways to Excellence, A Federal Strategy for Science, Mathematics, Engineering, and Technology Education.* FCCSET CEHR FY 1994 - FY 1998, p. 15.

[5]*Investment in Our Future.* Report of the FCCSET Committee on Education and Human Resources, FY1994, Budget Summary, p. 27.

[6]Sussman, Art, ed. *Science Education Partnerships: Manual for Scientists and K-12 Teachers.* University of California, San Francisco. 1993, p. 2.

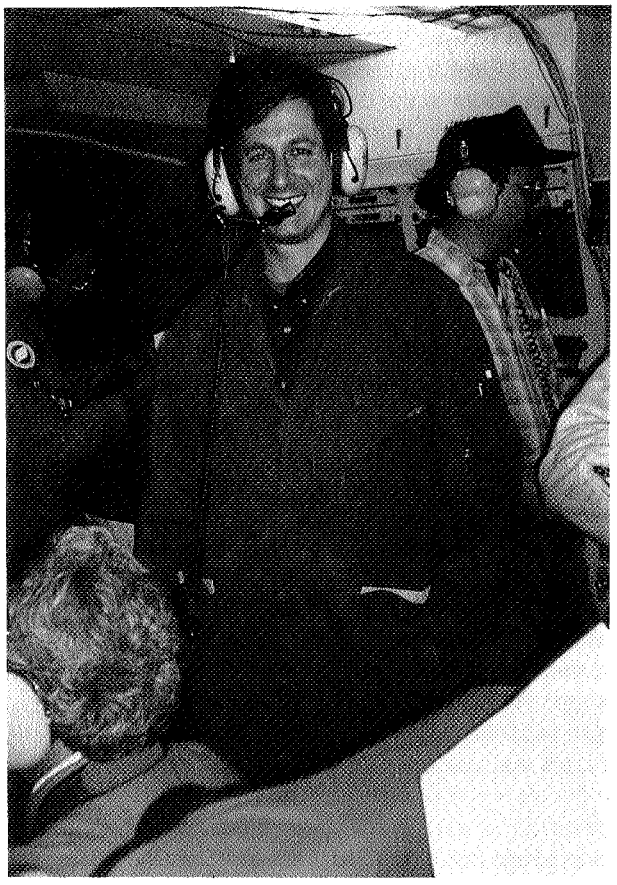

Allan Meyer, Marianne Gielow, Alex Rudolph, Sean Colgan

Airborne Astronomy Symposium on the Galactic Ecosystem
ASP Conference Series, Vol. 73, 1995
M.R. Haas, J.A. Davidson, and E.F. Erickson (eds.)

AIRBORNE ASTRONOMY OUTREACH THROUGH EDUCATION

EDNA DeVORE
Flight Opportunities for Science Teacher EnRichment, SETI Institute, 2035 Landings Drive, Mountain View, CA

DAN LESTER
Science in the Stratosphere, Department of Astronomy, University of Texas, Austin, TX

ABSTRACT NASA's Kuiper Airborne Observatory has a long history of educational outreach programs. Since June 1992, precollege teachers have participated in Flight Opportunities for Science Teacher EnRichment and Science in the Stratosphere, which have generated many articles in local, regional and national publications.

The Flight Opportunities for Science Teacher EnRichment (FOSTER) and the Science in the Stratosphere (SIS) projects bring scientists and teachers together on board NASA's Kuiper Airborne Observatory. These experiences are communicated through the media—newspapers, articles, and video—to the larger public. In this unique environment, exciting and memorable experiences occur. We see rich educational returns. The science goals of these missions are as exciting to teachers and students as they are to scientists. Airborne astronomy is one of the finest examples of real-world cooperative learning and problem solving. The need for cooperation is easily understood when the observatory is cruising at 41,000 feet, in the middle of the night, a thousand miles out over the Pacific Ocean. Even the youngest student understands that modern science depends on teamwork, and that these teams are composed of people with diverse careers: traditionally-trained scientists, computer specialists, engineers, pilots, aircraft ground crew and others who support the missions. Finally, these experience gives teachers pride and a sense of special achievement. FOSTER and SIS teachers bring the excitement and adventure of doing first-class science to their students and communities. Their accomplishments are admired by their students, colleagues, schools, and communities.

The media have carried the teachers' experiences to the public in newspaper and magazine articles, and radio and television interviews. Since the

initiation of the SIS and the FOSTER projects in 1991 and 1992, many articles have appeared in major newspapers such as the San Francisco Chronicle, San Jose Mercury News, Oakland Tribune, and San Antonio Express News, as well as several local community newspapers. These reports highlight the involvement of precollege teachers with airborne astronomy, and the impact of the teachers' experiences on students. In addition, up-close-and personal accounts of airborne astronomy research missions were written by teachers, scientists and reporters and published in the popular magazines, Star Date and Destination Discovery. These articles brought airborne astronomy to many people across the country. Finally, articles on the educational impact of astrophysics programs like FOSTER and SIS were published in professional journals. In addition to articles in the NASA Ames Research Center's Astrogram, the following articles appeared between June, 1992 and June, 1993.

REFERENCES

_____"Machacek to Participate in NASA and UT Science Project." The Shiner Gazette 17 June 1993.

_____"S. A. Teacher's Spirits Soar." San Antonio Express News 23 Aug. 1993.

_____"Teachers Fly in Observatory." Education Bulletin of Santa Clara County Office of Education Dec.-Jan., 1993-94, v. vii, no. 4, 1+.

Aratani, L. "NASA Takes Teachers to Stars." San Jose Mercury News 10 Nov. 1993, peninsula morning ed., sec. 2, 1B+.

Aratani, L. "Students Boldly Go Where U. S. Budget Might Not Reach." San Jose Mercury News 4 June 1994, final edition, 1+.

Aratani, L. "Two Teachers Get Space Lesson." San Jose Mercury News 9 Nov. 1993, peninsula morning ed., sec. 2: 1+.

Aratani, L. "Two Science Teachers Take Off for Space Lessons at 40,000 Feet." San Jose Mercury News 9 Nov. 1993, morning ed., sec. 2, 4B.

Bennett, J. and C. Morrow. "NASA's Initiative to Develop Education Through Astronomy (IDEA)," Astrophysics and Space Science. 214: 237-252, 1994.

Brower, K. "The View from Cloud 9," Destination Discovery. Oct., 1992, 42-48.

DeVore, E. "Teachers Learn Science in the Stratosphere." California Classroom Science Jan. 1994, v. 5, no. 3, 10+; 21.

Fernandez, L. "Starry-Eyed Teachers Take Flight," San Francisco Chronicle 10 Nov. 1993, peninsula ed., A1+.

Gilmore, W. "NASA Flight Gives Science Teacher Insight" Round Rock Leader July 1992.

Lester, D. "Already Soaring." Space News. 23-29 May 1994, 18+.

Lester, D. "Astronomy From the Stratosphere," Star Date. July-Aug., 1994, 4-9.

Lester, D. and D. Koch. "School Teachers Take to the Skies on the Kuiper Airborne Observatory." AAS Newsletter Oct. 1993, no. 67, 17+.
Mason, E. "Teachers Take Ride in NASA Observatory." Oakland Tribune 29 Nov. 1993, city ed: A-1+.
Mead, D. "Seeing Stars: Local Teacher Ride on Kuiper Airborne Observatory." The Sun 22 Dec. 1993, v. 1, no. 36, 1+.
Morrow, C. "Meaningful Experiences in Science Education: Engaging the Space Researcher in a Cultural Transformation to Greater Science Literacy," Journal of The British Interplanetary Society. 46: 449-454, 193.
Newton, J. "Science Teachers Take to the Skies in Kuiper Flight." The Voice of Mountain View Dec. 1993, v. 1, no. 11, 3.
Newton, J. "Teacher's Star-Studded Experience Brings Science Down to Earth." Los Altos Town Crier 17 Nov. 1993, v. 46, no. 46, 13.
Obregón, E. "Head in the Clouds, Teacher Flies in Astronomy Laboratory." Austin American-Statesman July 1992.
Stryker, P. and M. Willis. "Two Nights on a Flying Observatory—A KAO Journal." Star Date Jan.-Feb., 1994, 4-9.
Wakeland, J. "Science at 'The Edge of Space:' 8 Miles Up, Teachers Study Stars." Contra Costa Times 17 Nov. 1993, sec. 1+.
Whitten, C. "Teacher Gets Close-Up Look at Stars." The Navasota (Texas) Examiner and Grimes County Review 5 Aug. 1993, 4b.

Suzanne Williams, Kim Fanter, Garth Hull, Glen Kimoto, Geary Tiffany, Penny Moore, John Keller, Edna DeVore, Sandra Engel, and Marianne Gielow

Mark Piccillo, Norbert Geis, Sue Madden, Vivian Huang, Albrecht Poglitsch

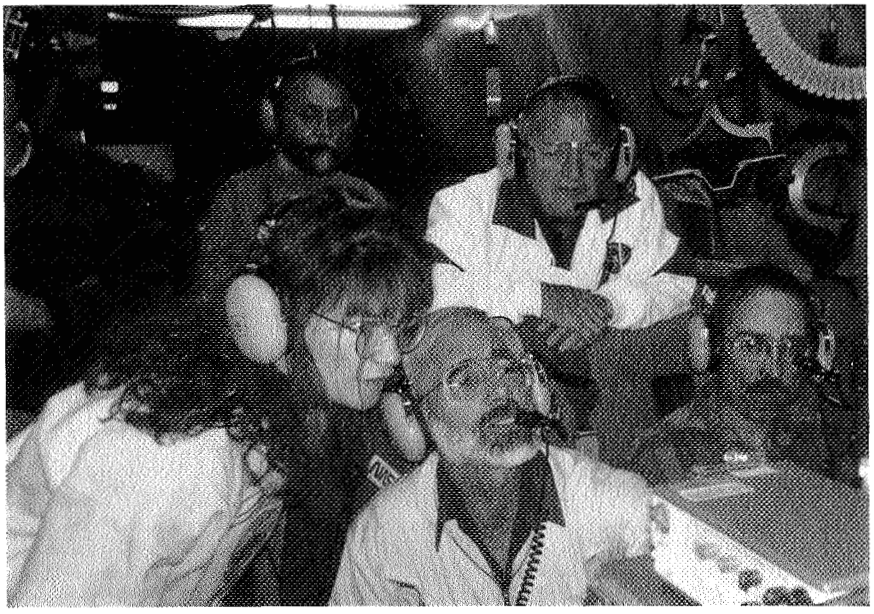

Cheri Morrow, Xander Tielens, Ed Erickson, Burt Pate, Mike Haas

Airborne Astronomy Symposium on the Galactic Ecosystem
ASP Conference Series, Vol. 73, 1995
M.R. Haas, J.A. Davidson, and E.F. Erickson (eds.)

BRINGING STUDENTS TOGETHER: THE IMPACT OF THE FOSTER PROGRAM FOR TEACHERS

JOHN KELLER
Los Altos High School, 201 Almond Avenue, Los Altos, CA

SUZANNE WILLIAMS
Graham Middle School, 1175 Castro Street, Mountain View, CA

ABSTRACT The following is a case study of how the Flight Opportunities for Teacher EnRichment (FOSTER) Project influenced the teaching, curriculum, and lives of two precollege teachers, John Keller and Suzanne Williams.

Summer Workshop at NASA Ames Research Center, June, 1993

The FOSTER week during the summer was an intense, concentrated period of learning astronomy, physics, and aeronautics. We were very impressed with the many guest presentations from astronomers, pilots, data analysts, telescope operators, and others. We were taken on marvelous tours of NASA's Kuiper Airborne Observatory (KAO), a high school planetarium, Lick Observatory on Mt. Hamilton, and more. We received many very valuable lesson plans for teaching our students, including actual classroom supplies for carrying out the activities. These lessons were presented by Edna DeVore and our fellow FOSTER teachers. We were all placed "on-line" with e-mail accounts through the California On-line Resources for Education system and trained by the NASA K-12 Internet Project team. The learning curve for that week was tremendous. Finally, we began forming a teaching bond that still continues today.

The Flight on NASA's Kuiper Airborne Observatory

Once the school year began, Project FOSTER played an essential role in the experiences we were able to provide our students. The most visible impact FOSTER played related to our actual flight aboard the KAO in November, 1993. We had both talked with our students about the KAO prior to our flight and had explained several lessons about infrared astronomy, meteorology, and aeronautics relating to the KAO. As the scheduled date of the flight approached, however, our students became more and more excited about the prospect of our actually flying. The morning after the flight, not only were

there newspaper articles to read about our trip, but we had also produced a home-video of the flight to share with our students. We spent the next two days going over the experience with our classes and using it as a teaching platform. Students were highly motivated and excited by our experience.

Lesson Planning

FOSTER's impact on our teaching stretched far beyond our flight through the stratosphere. First, the many lesson plans we had learned and discussed during the summer workshop were very useful in our classes. In particular, Project SPICA activities were very successful. We also used the diffraction grating experiments on light. It is rare to obtain so many immediately usable curricular items in a summer workshop.

Guest Speakers From NASA

FOSTER also provided actual teachers in our classrooms. Tom Gates, a NASA Aerospace Education Specialist, visited our schools and presented a large school group assembly, classroom presentations and after-school teacher workshops. Suzanne's assembly and workshop programs were given one week prior to the actual flight, where as John's assembly program was given the week after the flight. The assembly focused on NASA and its education value and career advantages, while the classroom lesson presentations were on light and extraterrestrial intelligence. The after-school workshop was to discuss with the teachers the advantages of using NASA materials that are up-to-date and available at the Teacher Resource Center at Ames Research Center. Students, as well as the teachers, especially at Graham MS, were very impressed and entertained by the "NASA Guy." His lessons, comments, and advice lent credence to the lessons we had been teaching since September. Tom was very inspiring for the students, as well as to the teachers. While it was difficult to coordinate a large assembly, we both were told by most all the teachers who attended that it was the best assembly they had seen. Tom Gates can captivate his audience and keep them wanting more.

The Los Altos High School-Graham Middle School Link

Most exciting of all is the link which FOSTER has catalyzed between us and our schools. Prior to FOSTER, John had taught Suzanne's daughter in a physics class. We had talked twice over the year and at different school functions about collaborating and integrating our curriculum and schools. However, we simply never seemed to have that extra time to just sit and plan. FOSTER provided this needed push.

Following the FOSTER workshop, we made plans for what we would develop over the rest of the summer. Suzanne modified her class syllabus to include an entirely new quarter in astronomy and John helped in creating this curriculum. The first real link between our students came out of one of these lessons, a session on Extra-Terrestrial (ET) intelligence. Suzanne's students encoded pictorial ET messages and e-mailed them to Los Altos High School.

John's students received these mysterious messages and had to decode them. The high school students became very enthusiastic and motivated to solve the codes once they learned they were from middle schoolers and not a teacher or another adult. They then exchanged messages. Now that we understand the logistics of the process ourselves, we plan to send more messages between Graham and Los Altos. The students still talk of these lessons. One middle school student commented that "This was fun, it really wasn't like real homework and you got to make friends with high schoolers."

A second link involved teaching. We switched classes for a day—John taught 7th and 8th grade science and Suzanne taught John's 9th-12th graders. This worked amazingly well for several reasons. 1) It was logistically very easy as we simply went to each others school for the day to teach, which meant there was no money needed for substitutes. 2) John followed lessons we had developed for the day together. He was able to observe how middle schoolers function and how they experience their school work and life. 3) Suzanne was able to observe how her work in middle school science relates to high school, how it is used, and what the students are expected to know in a typical lesson before they get to high school. 4) Students from both schools got the chance to talk with us about each other's school, advise us, and learn from a different adult who is an actual teacher.

The teacher exchange led to the exchange of students. Two opportunities arose during the year. First, high school physics students went to Graham on their own to help 7th graders with their science fair projects for the month of March. The high schoolers almost uniformly viewed the experience as exciting, challenging, and a rewarding opportunity. They also received extra credit points, as well as community work credit. The middle schoolers benefited from having another student dedicated solely to their project. This made their projects not only more professional, but more importantly to them, they had a chance to talk to high schoolers about science in high school which validated the learning behind the projects.

Things did not stop here, however. During two days in May, we switched classes again, only this time John took eight high school physics students with him to teach a lesson on light to the 8th graders during an extended science lab. The high schoolers were quite anxious at first, but once there, they did a great job. In addition, teaching increased their confidence in their own knowledge of physics, and gave them a taste of being a teacher. The 8th graders loved having the opportunity to work and talk with high school students. They not only talked about what they were learning but they seemed to sneak in a few questions and answers to "What is high school like? Do the upper classmen really tie freshman to water fountains? Mrs. Williams says that you really have a lot of homework. Is that true? Do you have to do it every night? What are the dances like? Are you going to college after high school?" Suzanne noted that her 8th graders were quite motivated to keep up with their homework and understanding of work assigned for the remainder of the school year. The 8th graders seem to become more aware of the

fact that their actions would have graver consequences and that the skills they were learning would really pay off in high school and beyond.

FOSTER On-Line

The FOSTER On-Line Project provided a direct link to scientists and research on the KAO. John's class did beta testing of the videotape, "Kuiper: Window on the Universe," for FOSTER. His students were impressed that they had been chosen to review a video by NASA before its release, and with how much the video changed when they saw the final version. Hopefully, the project can be repeated and we will make more use of it this coming year. There is definitely something intrinsically appealing to working on-line with researchers in remote parts of the world. It provides the seeds for a more solid global awareness to the students.

National Science Teachers Association (NSTA) National Convention

Another extension of the FOSTER Program was John's presentation at the NSTA National Convention in Anaheim, April, 1994. John presented an hour talk with Edna DeVore and Gail Chaid (FOSTER '92) on "Seeing the Light: Lessons in Astronomy." This was John's first NSTA conference and he was very impressed with the workshops and displays he found there. It was a very enriching experience for him.

Conclusion

All of these activities and collaborations were inspired by our time together during the FOSTER week. Without FOSTER or Edna DeVore, we would not have had as strong a motivation to explore the connections which we could make. We were very happy and pleased with the links made during the past year and look forward to working with each other from now on to really tie student learning between the two schools.

Finally, FOSTER has provided more relevance to both our teaching at the different grade levels, as well as a better understanding of astronomy and NASA. It has also allowed us to relate these experiences to our students in discussions regarding science, the nature of science, and pursuing science beyond high school. John's current (summer 1994) project at NASA, which is spearheaded by FOSTER, is making the NASA link even stronger and he looks forward to promoting and sharing it with other teachers beyond this summer.

FOSTER Teacher Team and School Information

John Keller teaches at Los Altos High School (LAHS) which draws students from Graham Middle School. Prior to becomming a FOSTER teacher, he had completed two years of teaching at LAHS in physics, astronomy, earth science, and biology. Following the FOSTER summer workshop, he taught physics, earth science, astronomy and marine biology. LAHS has a fairly heterogeneous mix of students. Suzanne Williams teaches 7th and 8th grade

science at Graham Middle School. Prior to FOSTER she taught at Graham for six years in the areas of science, math, English, and social studies. Graham Middle School is also heterogenous: Mexican/Latino (~40%), Vietnamese/ Asian (~25%), Caucasian (~20%), and Black (~10%) and Other(~5%). With so many primary language learners, hands-on science is very important in understanding basic science concepts. FOSTER's methods and activities teach all aspects and levels of astronomy, and have added a great deal to the curriculum.

Pam Stryker

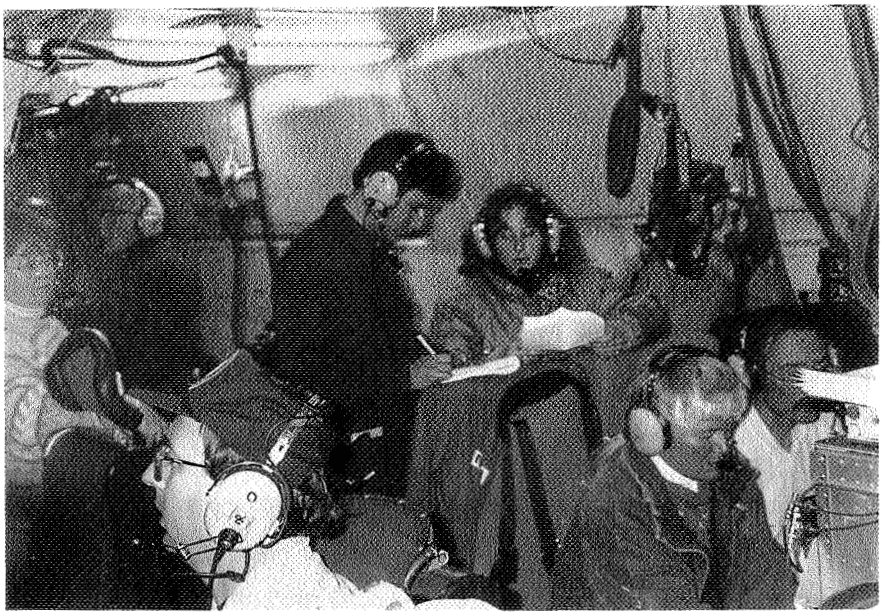

Edna DeVore, Carl Gillespie, Sean Colgan, Alex Rudolph,
Elizabeth Mason, Penny Moore, Mike Haas

Allan Meyer, Norbert Geis, Jill Baumgartel

Airborne Astronomy Symposium on the Galactic Ecosystem
ASP Conference Series, Vol. 73, 1995
M.R. Haas, J.A. Davidson, and E.F. Erickson (eds.)

omit

Gastrointestinal Anomalies aboard The Kuiper Airborne Observatory

Frederick L. Pants[1]
University of California at Palo Alto, Palo Alto, CA 94684

Louise Gorgonzola-Nitz[2]
DeVry Institute of Technology, Plano, TX 71012

Abstract. Over the years, scientists have eaten a lot of food on the KAO. We have observed scientists during one flight and noted certain discomforts they experienced during flight.

1. Introduction

Throughout history, Man has always been fascinated by food. Our particular interest has been the study of the nutrition amongst peoples who live at high altitude. In years past, our research has led to the proof of the connection between the consumption of yogurt by elderly men of the Carpathian Mts. and the extension of their virility until the age of 106 (Pants & Gorgonzola-Nitz 1956). In addition, we established the correlation between the consumption of cheese and purchases of leather suspenders by Peruvians living high in the Andes Mts. (Pants & Gorgonzola-Nitz 1963).

In this new era of "strategic research", we have become interested in a subject closer to home: the consumption habits of sleep-deprived North Americans flying for lengthy times at high altitude. This will provide the crucial calibration necessary for our ongoing efforts to develop a sponge cake that does not impair cognitive ability.

2. Observations

We flew on NASA's Kuiper Airborne Observatory (KAO) on 1993 April 1st to observe what the observers and crew ate. We did not use the Observatory's 0.91 m telescope. There were 4 observers during the flight as well as 4 crew members. Including ourselves, there were 15 guests onboard. Unfortunately, we were not allowed to observe the consumptive practices of the pilot, co-pilot, or navigator.

To ensure an uncontaminated observation, we posed as participants of the FOSTER program. We took many notes describing the foods, the frequency of

---

[1]In no way affiliated with the University of California System...yet.

[2]We're serious about success.

consumption, the caloric intake, and subsequent effects of the stomach size of the observers and crew. Unfortunately, we lost our notes the following night at St. James' Infirmary. However, we remember the night really, really clearly. Also, we stole the garbage to calibrate the data.

3. Results and Discussion

In Table 1, we present the type of food eaten during the flight, the number of servings per food type, its respective total caloric value, and the predominant class of food consumer (observers or crew). Our choices of food type was arbitrarily made to reflect the seven major foods consumed that night: caffeine, sugar, polycyclic aromatic hydrocarbons (PAHs), fruit, TV dinners, soup, and CornNuts^{TM}. Astonishingly, a whopping 10^{23} calories was consumed during the flight. We would convert this into joules but we can't find the conversion factor. Obviously, sugar was responsible for the bulk of this, skewing the totals by dwarfing the caloric values of all other consumed foods.

Table 1. Food Types Consumed In-flight and Caloric Total.

Type	Amounts	Caloric value	Consumer class
caffeine[1]	35 servings	30 cal	observers
sugar[2]	142 servings	10^{23} cal	both
polycyclic aromatic hydrocarbons (PAHs)[3]	3 servings	2 cal	observers
fruit	1 serving	59 cal	crew
horrible TV dinners	6 servings	-32 cal	crew
soup (packets)	3 servings	8000 cal	observers
CornNuts^{TM}	2 servings	54 cal	1 observer
	TOTAL CALORIES:	10^{23} cal	

1. Includes: coffee, tea, coke, jolt, battery acid.

2. Includes: soda pop, chocolate, stardust, jujubes, Good'n'Plenty's, Rolos, Caramilks, Fruit'n'Nuts, Milk duds, jelly beans, cookies, Jello, cookies, chocolate chip cookie dough, red hots, licorice, taffy, ice cream sundaes, York peppermint patties, Little Debbie cakes, Twinkies, cupcakes, pastries, lollipops, cotton candy, candied apples, hot fudge sauce, whipped cream, Hot Tamales, Raisinets, M & M's, tape gum, bubble gum, gum balls, Chiclets, popsicles, glazed doughnuts, marzipan, marshmallows, rockcandy, sugared pralines, pecan pie filling, Hershey's kisses, cotton candy, and several jars of corn syrup, etc.

3. not just for breakfast anymore!

To monitor the after-effects of this hideously aberrant discovery, we recorded the variation of the stomach sizes of members of both the observers and crew. Figure 1 shows the variation of stomach size with time averaged over consumer class (crew or observer) normalized to the stomach size of the Mission Director. Persistent snacking led to an overall increase in average stomach size with sharp jumps attached to the several meals consumed during flight. Reduction of stomach size was occasional and mostly attributable to periods of intense turbulence.

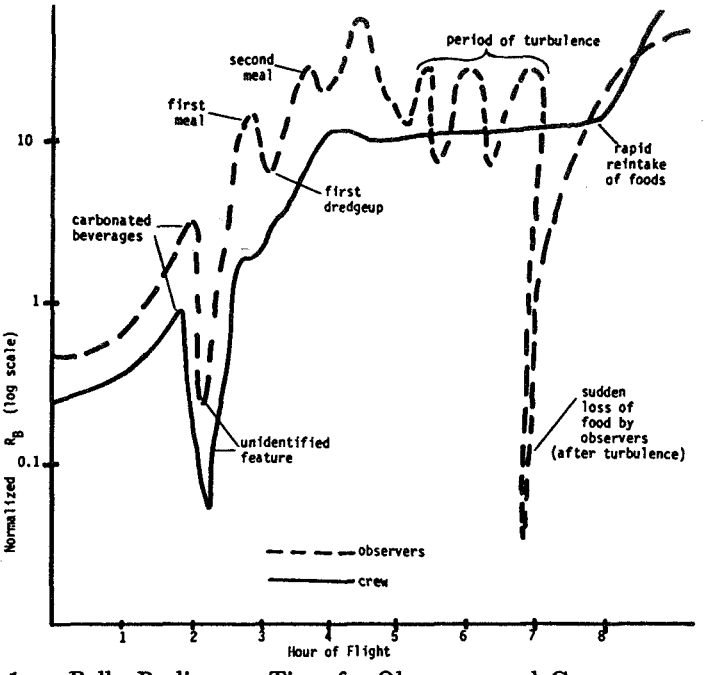

Figure 1. Belly Radius vs. Time for Observers and Crew

This explanation, however, does not account for all periods of belly contraction. For example, the anomalous "unidentified feature" noted in the Figure does not correlate with any periods of turbulence. Oh, just see the damn Figure.

4. Conclusions

1. Observers seem to take in stride the rapid variations of stomach size experienced during flight. After eight hours, many left the plane fat and bloated but relaxed. Unfortunately, one observer required assistance leaving the plane from the ground crew. His egress was happily accomplished with the application of liberal amounts of spare airplane grease to the door.

2. The crew, who fly more regularly than observers, seemed more experienced with flight snacking. They limited their caloric intake to well below that of the observers. Eerily, their final average stomach radius was larger than that of the observers! However, we should note crew stomach size measurements have higher uncertainties attached to them as a result of the disguising qualities of their ubiquitous blue jumpsuits.

3. More analysis is required before anomalies reported in Figure 1 can be verified. To facilitate this, we hope to fly again on a flight very soon!

Acknowledgments. We would like to thank the staff and crew of the Kuiper Airborne Observatory for their patience and sense of humor. L.G-N. would like to thank her cats. F.L.P. would like to acknowledge the continued financial support of his mother.

References

Actor in film "Delicatessen", private interview,
Anonymous Mission Director, private comunication.
Foot, B. in "Analyzing Stolen Garbage", ed. G. Schultz. (Dordrecht: Reidel), p. 892
Nubby, E. 1992, Gourmet & Country Living, 51, 692
Pants, F.L. & Gorgonzola-Nitz, L. 1956, in press
Pants, F.L. & Gorgonzola-Nitz, L. 1963, in preparation
Some booklet we picked up at the gas station
U.S. Food Guide

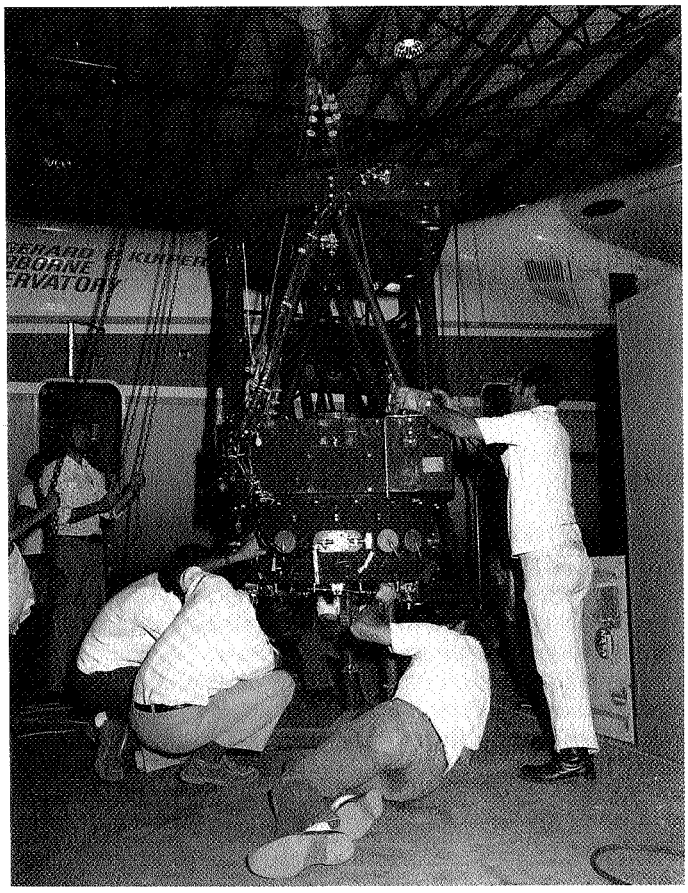

Far left: Louise Gorgonzola-Nitz, Lloyd Domeier; *Foreground:* Bob Walker, Don Oishi, Bruce Kelly, Ben Horita; *Behind telescope:* Fred Pants (1978)

Session Nine

Missions and the Future of Infrared Astronomy

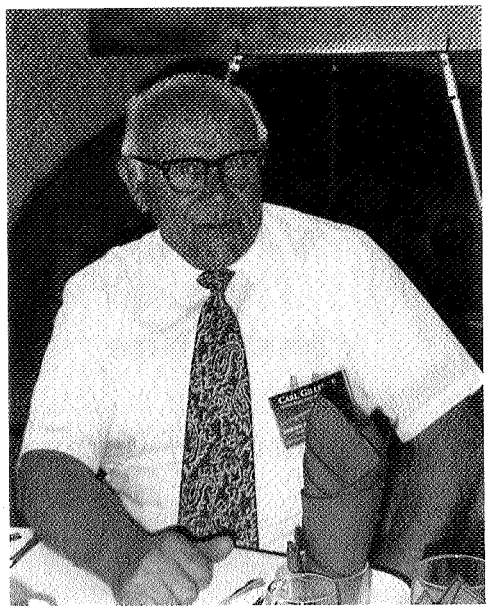

Carl Gillespie

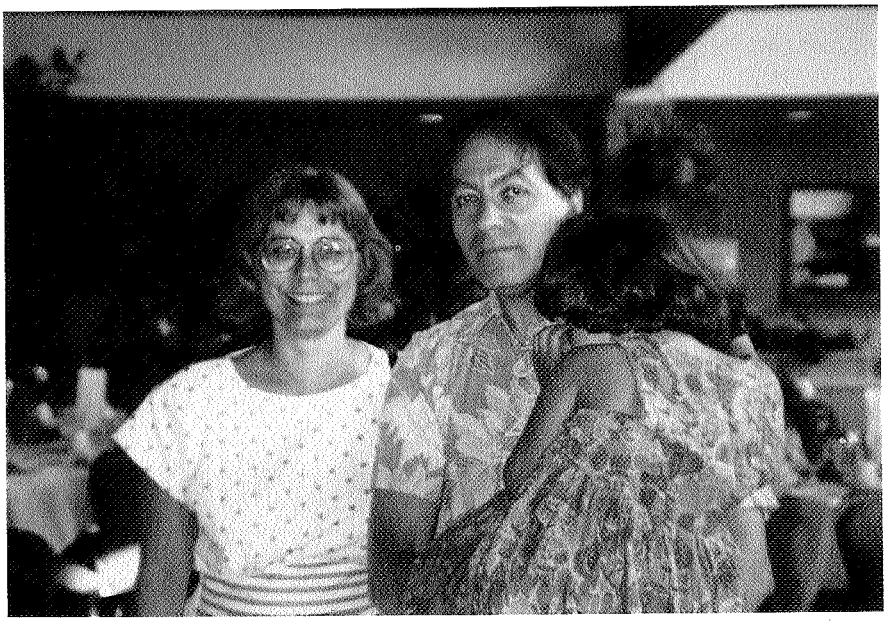

Jocelyn Keene, Tom Phillips, Elizabeth Phillips

Airborne Astronomy Symposium on the Galactic Ecosystem
ASP Conference Series, Vol. 73, 1995
M.R. Haas, J.A. Davidson, and E.F. Erickson (eds.)

PANEL DISCUSSION: THE FUTURE OF IR ASTRONOMY

LAWRENCE J. CAROFF
Astrophysics Division, NASA Headquarters, Washington, D.C., 20546

ABSTRACT A panel discussion was held on the future of IR astronomy. The chairman gave a brief introduction to current planned programs for NASA and other space agencies, followed by short contributions from the six panel members on a variety of special topics. After that, a short question and answer session was held.

INTRODUCTION

In 1991 the National Academy of Sciences produced its third decadal survey on astronomy entitled: *The Decade of Discovery in Astronomy and Astrophysics* (National Research Council 1991). That report emphasized that Infrared Astronomy is poised to make major discoveries in the next 10 to 20 years, and is likely to reshape the way we view the Universe. The purpose of this session was to explore the current status of approved and planned programs, particularly space missions in IR astronomy, to explore the scientific potential of these missions or facilities, and to examine some of the issues and concerns in the science community about the status of IR astronomy.

Panel members were: Eric E. Becklin (UCLA), Lawrence J. Caroff, Chair (NASA/HQ), James L. Elliot (MIT and Lowell Observatory), Gary J. Melnick (CfA), Anneila I. Sargent (Caltech), J. Michael Shull (Univ. CO), and Charles M. Telesco (NASA/MSFC).

CURRENT AND PLANNED MISSIONS IN IR ASTRONOMY

Figure 1a is an attempt to portray past, present, and currently planned space IR astronomy missions. Of course, several parameters are necessary to describe the nature of each mission adequately, but we have limited ourselves here to wavelength coverage vs. time, and have restricted the list of missions to include only those whose principal focus is IR astronomy. Hence, missions like the Air Force Geophysical Lab surveys and the upcoming Mid Course Surveillance Experiment (MSX) are not included. (Descriptions of each of the missions in Figure 1a plus a few others are included later in this Volume.)

The figure makes several interesting points. To begin with, most infrared space missions to date have had relatively short lives, limited by their cryogen lifetimes, and this will be true of the cryogenically cooled missions planned for the near future, as well. It is also evident that activity in space IR

astronomy is picking up and, if the plans of the various space agencies can be realized, several exciting missions will fly in the next 10 to 15 years. In addition, the growing importance of international cooperation is evident. The Infrared Telescope in Space (IRTS) and the Infrared Imaging Survey (IRIS) are Japanese-led missions with substantial US involvement underway or planned. The Infrared Space Observatory (ISO), Far Infrared Space Telescope (FIRST), and the Fifth Cornerstone are European Space Agency missions. In the case of ISO, US tracking stations will serve to extend the useful observing time, while for FIRST and any future missions, we hope to participate actively in the development of the instrument packages and,

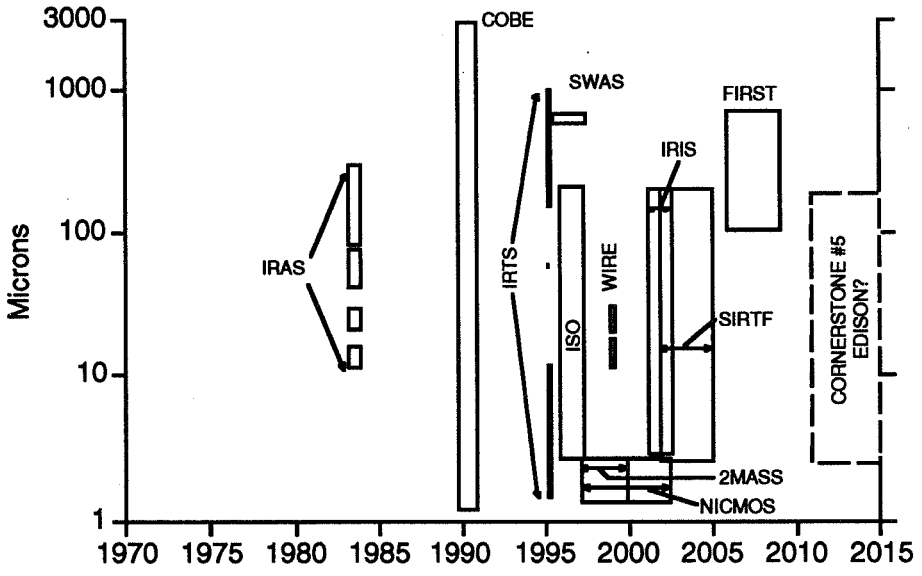

Figure 1a. Past, current, and future space missions for IR astronomy. (Note: 2MASS is included here because of its importance for future space missions.)

perhaps, the telescopes and spacecraft, as well. The Submillimeter Wave Astronomy Satellite (SWAS) and the Space Infrared Telescope Facility (SIRTF) are US-led missions with significant participation by other countries underway or under discussion. (So is SOFIA, of course.)

Because of the short lifetime of space IR missions, the relative infrequency of launches so far, and the necessarily limited capabilities and complement of instruments on these missions, the importance of airborne infrared astronomy is clear, particularly beyond 10 microns. The Lear Jet Observatory, the KAO, and, eventually, SOFIA, can be regarded as the "glue" that holds the space IR astronomy program together. This point is easily made graphically by including airborne astronomy missions in the above

figure (see Figure 1b). The broad wavelength coverage and continuous access to nearly the entire bandpass between 1 and 1000 microns, provided by airborne platforms, enable the continuous pursuit of many fundamental science questions, the development and perfecting of a wide variety of instrumental techniques and technologies, and the hands-on training of a community of scientists to lead the future US space IR effort.

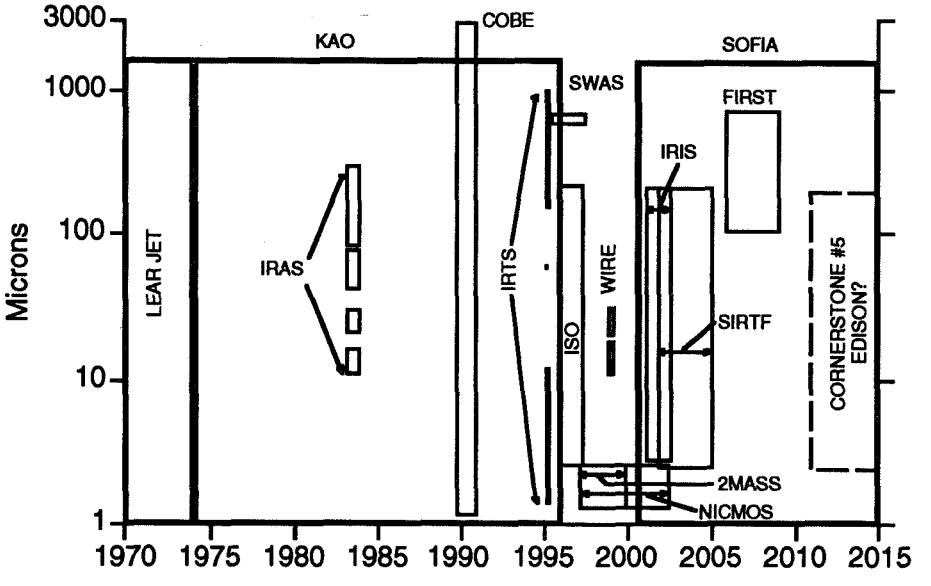

Figure 1b. Same as Figure1a, but with the airborne astronomy missions overlaid.

In light of the pivotal role played by airborne astronomy, the planned five year gap in airborne coverage between 1995 and the beginning of 2001 is striking. That hiatus is the consequence of two facts: first, that SOFIA represents the future of airborne astronomy, there is no technological substitute that matches the effect of SOFIA's increased aperture that would keep the KAO scientifically on the forefront into the next century; and second, NASA's budget is at best flat for the foreseeable future, so gaining approval to start any new mission is likely to require heroic sacrifice. In this case, not only is the substantial contribution to SOFIA planned by the German space agency, DARA, critical to getting the approval to proceed with SOFIA, funds made available by grounding the KAO are also required. Of course, those two elements alone are insufficient to fund SOFIA's development and that means that further belt tightening in NASA will be necessary in order for SOFIA to begin development in 1996.

C-9

So in the last half of this decade, one of the major challenges facing the IR astronomy community will be to maintain the interest and expertise base in airborne astronomy in the absence of an operating observatory. The study and development of an initial complement of instruments for SOFIA will help to keep the program viable, but considerable effort beyond that will be called for to ensure that SOFIA lives up to her full scientific potential right from the start.

PANEL CONTRIBUTIONS

Major Astronomical Problems for the Next 10 Years (J. Michael Shull, University of Colorado)

In my presentation, I was asked to put forward my thoughts on what the most important areas of astrophysical research might be in the coming decade, with some emphasis on how IR and submillimeter astronomy might contribute. In this written contribution, I have added further thoughts that arose from discussions at the meeting following our panel presentations. My subjective list includes some of the major astronomical problems expected to be explored in the 1990's and beyond. In unranked order, these are:

1. Nature and distribution of the sources of Gamma-Ray Bursts
2. Search for extra-solar planetary systems
3. Physical nature and large-scale distribution of dark matter
4. Physical mechanisms of star formation in galaxies
5. Production of heavy elements and evolution with redshift
6. Evolution of dense galactic nuclei (AGN, jets, nuclear winds, deshrouding)
7. Hubble expansion rate and cosmological closure parameter
8. Epoch, modes, and dynamics of galaxy and cluster formation
9. Late stages of stellar evolution, mass-loss, SNe, chemical processing
10. Gas dynamics (and MHD) of the ISM and molecular clouds

In contemplating the possible contributions that IR and submillimeter astronomy could make, it becomes obvious that their role is important in at least 7 and perhaps as many as 9 of these areas. Historically, measurements of the Hubble constant H_0 and closure parameter Ω_0 have been the domain of optical astronomy. However, more recently, the IR and submillimeter have made major contributions to cosmological issues such as 3 and 7 above, through infrared studies of Cepheids, unbiased surveys of galaxies (e.g., IRAS 2 Jansky survey), and COBE measurements of fluctuations in the cosmic microwave background. Even in the area of Gamma-Ray Bursts the IR band may ultimately play a role in source identification.

Among the other areas, the IR role is obvious. To address problem 2, search techniques for Extra-Solar Planetary Systems are optimized at the 10--40 micron wavelengths appropriate for the greybody peaks of the spectra from planets some 5--20 AU from solar-type stars. For problems 4, 5, 6, and 8, the longer wavelength bands are natural spectral regions, owing to the

cosmological redshifts of protogalaxies, high-redshift clusters, and AGN, which push the stellar energy distributions and many key spectroscopic features into the near- and mid-infrared. For studies of stars (Cepheids, buried O-stars and Wolf-Rayet stars, red giants, AGB stars) and gaseous star-forming regions in the Milky Way and low-redshift galaxies, the infrared and submillimeter fine-structure lines of [CI], [CII], [NII], [OI], [OIII], [SiII], [FeII], [NeII], [SIV], and many molecular lines of CO, H_2O, etc. provide key diagnostics of abundances and physical conditions.

If the coming decade does turn out to be the 'Decade of Infrared Astronomy', as prophesied by the National Academy of Science's decadal survey, it is likely that instruments such as SOFIA, SIRTF, ISO, SWAS, and WIRE will lead many of the advances. However, it is equally important for NASA to keep its 'space-borne eye' on the potential instruments for the 21st century. The European Space Agency's approved FIRST mission and the EDISON concept spring immediately to mind. Such missions or their descendants will build on the contributions from the first generation of telescopes launched with sensitive, space-qualified IR detectors.

Important Problems in Solar System Astronomy in the Next 10 Years (James L. Elliot, MIT and Lowell Observatory)

Infrared plays an essential role in solar system studies for two reasons: (i) at planetary temperatures, most of the thermal radiation is emitted within the infrared portion of the spectrum, and (ii) infrared spectra probe the vibration-rotation transitions of molecules, from which we learn the physical state of planets and other solar system bodies. Infrared spectrometers travel with all major planetary probe missions, and we have learned much from Earth-based infrared observations as well. So, IR is part of the fabric of solar system work, for now and the foreseeable future.

Deep space probes have been paramount in planetary exploration, having revealed many unanticipated wonders from the close-up vantage point of a flyby or orbiting spacecraft. Yet such missions are an extremely limited resource, and we certainly can't do all planetary science with missions, especially investigations that involve understanding seasonal and climatic changes. Right now, for example, we are anticipating the arrival of Galileo at Jupiter, which will put a probe into Jupiter's atmosphere and then observe the system for an extended time. After that, we plan to launch Cassini to Saturn, but it won't arrive until after the turn of the millennium. The Russians are planning a series of missions to Mars, with a launch every two years; ESA and the Japanese also have a limited solar system exploration program. We have our Discovery program, which, if it develops as NASA would like, might allow a launch every year or so. These would be missions constrained to cost no more than $150M, which limits where one can go and what one can do. Right now NEAR (Near-Earth Asteroid Rendezvous) is under development as a Discovery mission. Maybe we'll get a new start of the Pluto Fast Flyby soon, but that's about all that's on the books for the next ten years. So, most of the solar system will not be under the scrutiny of a probe, which means that Earth-bound observers using visible, IR, and radio

telescopes will have a lot to do. Especially as the sensitivity and power of telescopes and instruments improve, more and more can be done from Earth and Earth orbit. For the purpose of this panel, we'll concentrate then on the future of IR in remote observations of the solar system.

What will be the "hot topics" in this domain for the next ten years, and what role will IR likely have? To a great extent, the hot topics are generated by new observing capabilities. Right now, the IRTF and the KAO provide IR access for the community at large, with several private facilities that serve various sets of constituents. In the future, the community can anticipate using larger ground-based telescopes and, of the planned space and airborne IR observatories, ISO, SIRTF, and SOFIA should prove the greatest use to planetary scientists. Since solar system sources are extended, the use of array detectors will have a substantial impact on future solar system work in the IR.

A current hot topic is the search for planets around other stars that might be like our own (not the pulsar planets, which would be quite different), and the direct imaging approach is best carried out in the IR because a distant Jupiter, for example, would have a much greater contrast to its star in the IR than in the visible. This work will be pursued directly and interferometrically with Keck and Keck II. Such a direct detection of another planet or planets would have great philosophic as well as scientific impact.

A broad area of investigation that has been underway for awhile is the use of near IR spectra to identify ices on the surfaces of outer solar system bodies, such as Pluto, Triton, and Charon. Not much observing time has been devoted to this topic yet, since the IRTF does not have an appropriate spectrograph; only a limited number of nights have been available on UKIRT. This work has impact also in the broad area of star and planet formation, because we can test our theories in great detail in the outer parts of our solar system, where it is cold and less has changed since formation compared with the inner solar system. Theorists have been predicting that CO would be the major volatile constituent for Pluto and Triton, but--surprise!--N_2 has been found to be the major constituent on the surfaces and in the atmospheres of these two bodies. Extending this work to cometary nuclei and Kuiper belt objects should certainly help us to understand how our outer solar system formed and evolved. Investigating smaller bodies will take larger telescopes and will make good use of IR arrays.

Related to this is the use of near IR spectra to identify mineral bands on the surfaces of asteroids. With this approach, one can become more sophisticated in assigning asteroids to families (which formed from a single parent, due to a collision), which has been done until now almost entirely by dynamical relationships.

Atmospheres and their seasonal changes are likely to become much better understood with further IR observations. In the thermal IR, one can invert the spectra to reconstruct the thermal profile and see how the atmospheric structure varies with position on the planet and responds to changes in seasonal insolation. Echelle spectrographs in the IR have been available for several years now, and these are enabling us to separate the gaseous from the solid component for materials such as CH_4 on Pluto. Another approach to learning about atmospheres is through stellar

occultations, which give us the atmospheric structure at very high spatial resolution. With SOFIA, occultations will be observed with much greater signal-to-noise and more frequently, which will give us a chance to understand the seasonal variations of small-body atmospheres and their exchanges with surface ices through sublimation and condensation.

Since this symposium has highlighted the work of the KAO, we should make the distinction between the future of IR astronomy and the future of airborne astronomy to solar system work, noting that not all airborne solar-system observations have been in the IR, many have been made in the optical. Transient phenomena--especially those with limited zones of visibility such as stellar occultations and solar eclipses--really need the mobility of an airborne platform to be successful. One can compare the success in observing occultations of HST relative to the KAO; even though the HST has a great aperture advantage, it has never observed a small-body occultation because, in its fixed orbit it is highly improbable that it would intercept the very small and fast-moving shadow of the occulting body. On the other hand, since it can be moved to the desired position, the KAO has observed several occultations. However, in background limited situations, such as imaging Saturn's rings, the excellent image quality of HST gives it a distinct advantage over the KAO.

This brings me to my last point. I should emphasize the importance of spatial resolution for solar system observations. We can always learn so much more from data that have good spatial resolution (even forgetting about the increased signal-to-noise for background-limited observations made at wavelengths smaller than the diffraction limit of the telescope). As an example, Pluto and its satellite Charon reach a maximum separation of nearly an arcsecond for their present orbital position near perihelion. So, if SOFIA has an image quality of 3-5 arcseconds like the KAO, you can forget about making separate observations of these bodies. One will be stuck with untangling the spectra and radiometric measurements of the blend and deciding what came from Pluto and what came from Charon--very messy, if it can be done at all. So, the message here is: let's do all we can to keep the image quality of SOFIA better than one arc-second. At least for solar system work, the benefits would be great.

The Submillimeter and the Interstellar Medium and Star Formation Gary J. Melnick, CfA)

(*Note: This material is adapted from viewgraphs shown at the Symposium.*)

1. Scientific Attraction of the Submillimeter. Observations in the submillimeter part of the spectrum address the Where, What, and Whys of the ISM and star formation: Where is the material, i.e., what is the distribution of gas in clouds? Broad passband bolometer systems operating longward of 100 microns can detect the bulk of the material, including cool, deeply embedded sources missed at shorter wavelengths. Examples discussed by Steve Strom in this symposium (Strom 1994) include so-called Class 0 objects, which remain so deeply embedded within their parent cloud that the magnitude of

the dust extinction prevents their study at near- and mid-infrared wavelengths--only photons in and longward of the submillimeter can penetrate the cloud and reveal the presence of such objects. Also discussed by Strom was the determination of spectral indices for the dust emission surrounding young stellar objects. This emission peaks in the far-infrared and displays its greatest sensitivity to the dust emissivity spectral index in the submillimeter. Knowledge of the spectral index can then be used to constrain particle emissivities and sizes.

What is the composition of molecular clouds? Cooling of the gas--essential to its collapse--is primarily due to trace atoms and molecules (H, H_2, and He are very poor coolants at T<500K). Dave Hollenbach's talk (Hollenbach 1994) illustrated the cooling power of trace gases and Figure 2 shows that the most abundant oxygen- and carbon-bearing species have their lowest lying transitions in the submillimeter.

Why do some regions within clouds experience star formation while other regions do not? Polarization studies in the far IR and submillimeter may help in understanding the mechanisms that support clouds against collapse in regions where little or no star formation is going on. Recall that Alyssa Goodman warned in her talk (Goodman 1994) that optical and near-IR polarization measurements often yield misleading results since they sample only regions with small visual extinction (optical) or cloud surface polariz-

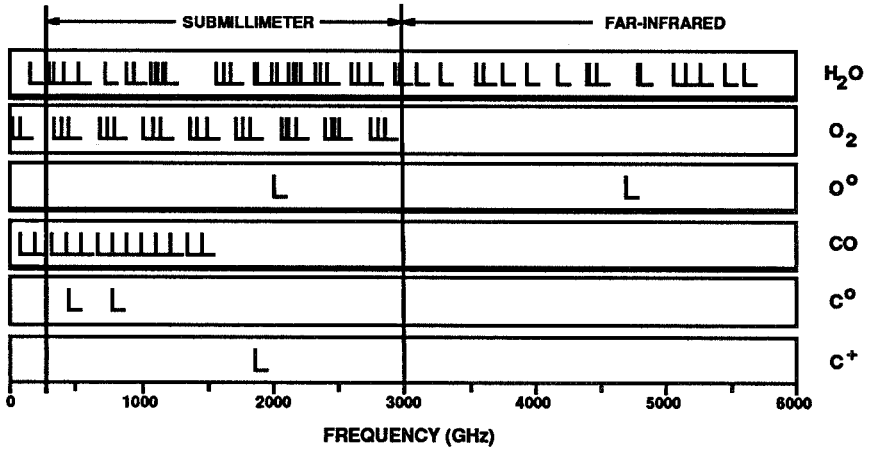

Figure 2. Line frequencies of the lowest lying transitions (T<500K) of the most abundant oxygen and carbon bearing species.

ation (near-IR). Polarization studies performed at far IR and submillimeter wavelengths have the decisive advantage of sampling the embedded gas believed to be more representative of the sites of future star formation.

2. State of Submillimeter Detector Technology. Remarkable progress has been made over the past 15 or 20 years in the sensitivity of discrete bolometers and in the number of elements in bolometers arrays. As can be seen from Figure 3, the per-pixel sensitivity of a modern 24 element Silicon-based monolithic array is at least three orders of magnitude better than what was possible with discrete Germanium bolometers in 1975.

Similarly, there has been rapid progress made in the development of sensitive heterodyne receivers in the submillimeter. Figure 4 shows that receivers at or below five times the quantum limit are now available up to 700 GHz (~ 430 microns) and there is every reason to be optimistic that this level of performance will soon be available in the Terahertz range.

3. Present and Future Facilities. Table 1 is a list of existing and planned submillimeter telescopes, including ground-based, airborne, and space facilities. As ground-based submillimeter telescopes in the 10--15 meter category become more commonplace, the need for SOFIA's increased spatial resolution becomes even more compelling.

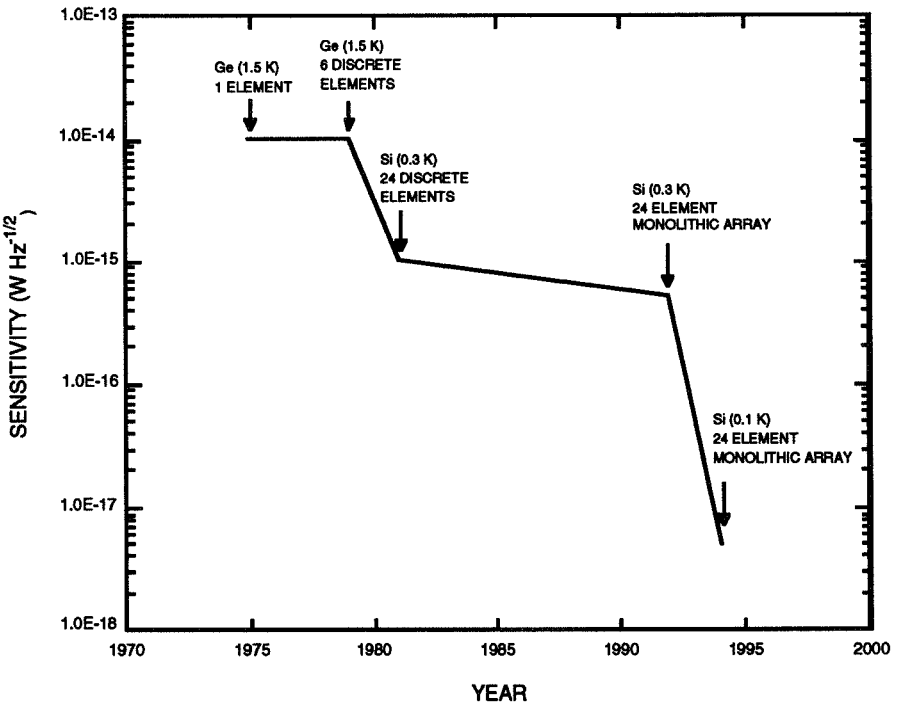

Figure 3. State of the technology for IR bolometers.

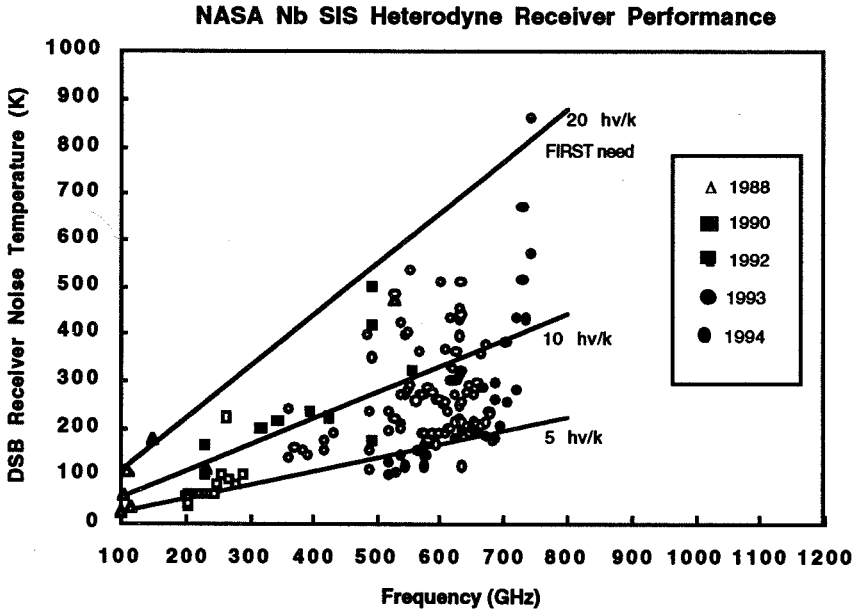

Figure 4. State of the technology for NASA-sponsored Nb SIS heterodyne receivers in the submillimeter.

TABLE I Present and Future Submillimeter Facilities

Category	Existing		Planned	
Ground-Based	CSO	(Hawaii--10 m)	SMT	(Arizona-10 m)
	JCMT	(Hawaii--15 m)	ASTRO	(Antarctica-1.6 m)
	SEST	(Chile--15 m)	SMA	(Hawaii-6x6 m)
Airborne	KAO	(Calif.-0.9 m)	SOFIA	(Calif.--2.5 m)
Space	(none)		SWAS	(0.6 m)
			FIRST	(3-4 m)

CSO: Caltech Submm Observatory; JCMT: James Clerk Maxwell Telescope; SEST: Swedish ESO Submm Telescope; SMT: Submm Telescope; ASTRO: Antarctic Submm Telescope/Remote Observatory

Search for and Study of Other Solar Systems (Anneila I. Sargent, Caltech)

One of the fundamental discoveries made at infrared wavelengths was the IRAS observation of dust around a significant fraction of main sequence stars such as Vega. These results, followed by ground-based coronagraph mea-

surements that showed a disk-like distribution of dust around Beta Pictoris, effectively caused a sea-change in community acceptance of the concept of extra-solar planetary systems. It now seems likely that there are numerous potential planetary systems like our own. IRAS observations also suggest that many pre-main sequence stars are surrounded by relatively massive disks that may represent planetary systems in formation. Thus, in principle, the evolution of extra-solar planetary systems can be studied through infrared and submillimeter observations of the environs of solar-type stars of various ages. Efforts to detect actual planets around other stars are also best carried out in the near- to mid-infrared wavelength regime, where the overwhelming effect of the radiation from the central star diminishes in relative importance.

The possibility that life exists beyond Earth has preoccupied mankind for centuries and we are now on the brink of enormous advances in this area. NASA's ASEPS (Astronomical Search for Extrasolar Planetary Systems) is a multi-phased project whose ultimate aim is to detect other Earths. In the first phase the Keck I and Keck II telescopes will be used as an infrared interferometer to search for indications of Jupiter-like bodies around nearby stars. In addition, a number of pending or expected infrared missions will contribute significantly to the effort to identify pre- and post-planetary disks. A large body of observations of possible planetary disks, and more sensitive searches for new candidates, are already scheduled for ISO. The KAO is providing information about the earliest stages of star/disk formation (Butner 1994), and the spectroscopic capabilities of SOFIA will be invaluable for evolutionary studies.

Future missions such as FIRST and SIRTF will make seminal contributions to our understanding of planetary disks. However, developing the technologies necessary to achieve the larger goal of detecting mature planets around other stars must be a prime endeavor of the next decade. At present, the optimum search and detection methods appear to require infrared interferometry in space or on the lunar surface. Ground-based tests of the likely techniques--with the Keck and outriggers, for example--and airborne platform trials of detector arrays, exploiting the advanced capabilities of SOFIA, are vital to this effort. Although planet detection may lie more than a decade away, the groundwork must begin as soon as possible.

Future Prospects for Ground-Based IR Astronomy (Eric Becklin, UCLA)

Dr. Becklin described the large aperture optical-IR telescopes that are or will be coming on line in the near future and also reviewed the progress in monolithic detector arrays for the near- and mid-IR bands. He discussed how the combination of these capabilities presents a tremendous opportunity for discovery in ground-based IR astronomy in the coming decade.

Issues and Concerns (Charles M. Telesco, NASA/MSFC)

Dr. Telesco raised several concerns currently present in the astronomical community: access by the general community to large ground-based telescopes, the planned hiatus

in airborne astronomy during the development of SOFIA, and community participation in planning for SIRTF. A brief discussion followed.

REFERENCES

National Research Council (NRC) 1991,*The Decade of Discovery in Astronomy and Astrophysics* (the 'Bahcall Report'). National Academy of Sciences, Washington, D.C.

Butner, H. M. 1994, in *Proc of the Airborne Astronomy Symp on the Galactic Ecosystem: From Gas to Stars to Dust*, eds. M. R. Haas, J. A. Davidson, & E. F. Erickson, (San Francisco: ASP), paper 3.3.

Goodman, A. A., ibid, paper 1.4.

Hollenbach, D. J., ibid, paper 3.4.

Strom, S. I., ibid, paper 3.0.

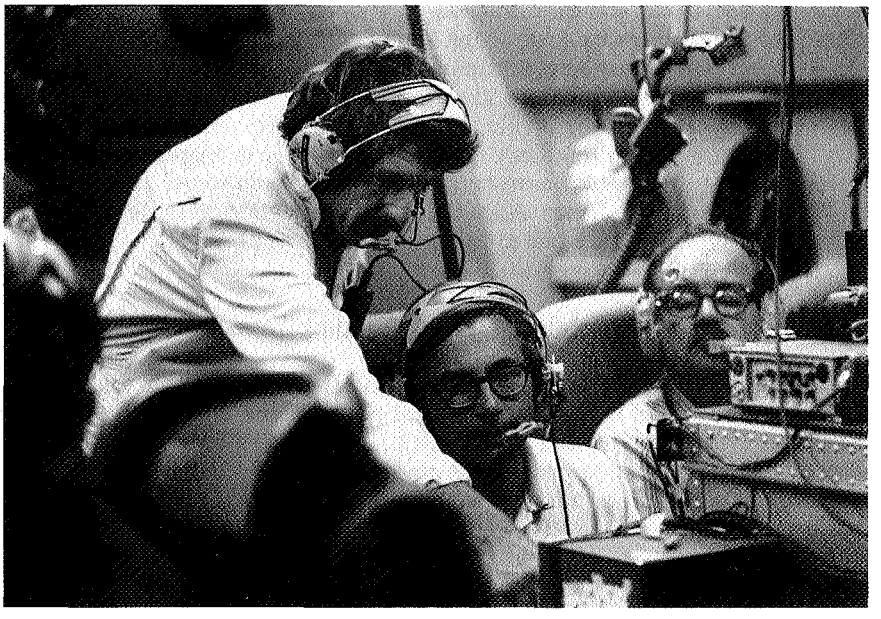

Larry Caroff, Ed Erickson, Darrell McKibbin (1979)

Airborne Astronomy Symposium on the Galactic Ecosystem
ASP Conference Series, Vol. 73, 1995
M.R. Haas, J.A. Davidson, and E.F. Erickson (eds.)

THE INFRARED SPACE OBSERVATORY (ISO)

GEORGE HELOU
IPAC, MS 100-22, California Institute of Technology, Pasadena, CA 91125

MARTIN F. KESSLER
ESA/ESTEC, Postbox 299, 2200 AG Noordwijk, Nederland

ABSTRACT ISO, scheduled to launch in 1995, will carry into orbit the most sophisticated infrared observatory of the decade. Overviews of the mission, instrument payload and scientific program are given, along with a comparison of the strengths of ISO and SOFIA.

INTRODUCTION

As the "Decade of the Infrared" approaches its mid-point, the banner of space-borne infrared astronomy seems destined to fly with ISO, a mission of the European Space Agency (ESA) with participation by NASA and Japan's Institute for Space and Astronautical Science (ISAS). ISO will perform spectroscopy, imaging, photometry and polarimetry at wavelengths between 2.5 and 240 μm, using a liquid-helium cooled telescope with a 60-cm primary. It is expected to launch on 19 September 1995 into a high-ellipticity 24-hour Earth orbit and to operate for at least 18 months.

PAYLOAD AND MISSION

The ISO focal plane holds four instruments, viewing the sky simultaneously (though active one at a time) and pointed with an accuracy of a few arcsec. Table 1 outlines the characteristics of each instrument and an indication of typical sensitivity is given in the last column. Because of complexities in instrument design, operation overheads, and detector properties, these sensitivity numbers cannot be simply scaled to characterize the performance in all observing modes. More information on the mission can be obtained from Helou (1994), from the Mission and Instrument Manuals published by the ISO project in conjunction with the Call for Proposals, and from the other references below.

The majority of ISO's observing time was made available to the astronomical communities in ESA member states, the USA and Japan, by means of a Call for Observing Proposals published in April 1994. The teams involved in building the instruments and in operating the mission have organized their

Table 1. Main Characteristics of the ISO Instruments

Instrument (Principal Investigator)	Wavelength Range and Main Function	Outline Description	Spectral Resolution	Spatial Resolution	Typical Signal (1) Detectable in 200 sec at SNR≥10
ISOCAM (C. Césarsky, CEA-Saclay, F)	2.5–17μm Camera and polarimeter	(i) 32 × 32 array for 2.5–5 μm (ii) 32 × 32 array for 4.5–17 μm	(i) 11 filters 2≤R≤20 circular var. filter R∼40 (ii) 10 filters 2≤R≤14 circular var. filter R∼40	Choice of 1.5, 3, 6 or 12″ per pixel	(i) 3mJy at 2.5–5 μm (ii) 1mJy at 5–15 μm
ISOPHOT (D. Lemke, MPI für Astronomie Heidelberg, D)	2.5–240μm Imaging photo-polarimeter	(i) Multi-aperture, multi-band photopolarimeter (3–110 μm) (ii) Far-infrared camera 30–100 μm: 3 × 3 pixels 100–200 μm: 2 × 2 pixels (iii) Spectrophotometer (2.5-12 μm)	(i) 14 filters 2≤R≤15 (ii) 6 filters 1≤R≤3 5 filters 2≤R≤3 (iii) grating, R∼90	(i) Choice of diffraction-limited to 3′ apertures (ii) 43″ per pixel 89″ per pixe (iii) 24 × 24″ aperture	(i) 30mJy at 10 μm (ii) 15mJy at 100 μm
ISO–SWS (Th.de Graauw, Lab. for Space Research, Groningen, NL)	2.5–45μm Short wavelength spectrometer	(i) Two gratings 2.5–45 μm (ii) Two Fabry-Pérot interferometers 15–30μm	(i) R∼1000 (ii) R∼3×10^4	(i) 14 × 20″ 14×27″, and 20 × 33″ (ii) 10 × 39″	Grating mode: (2) 6×10^{-16}Wm^{-2} at 12-30 μm
ISO–LWS (P. Clegg, Queen Mary and Westfield College, London, UK)	45–196μm Long wavelength spectrometer	(i) Grating (ii) Two Fabry-Pérot interferometers	(i) R∼200 (ii) R∼10^4	1′.65 diameter aperture	Grating mode: (2) 3×10^{-16}Wm^{-2} at 55 μm 10^{-16}Wm^{-2} at 100 μm 3×10^{-17}Wm^{-2} at 180 μm

(1) Adopted from corresponding Observer's Manual for each instrument.

(2) Total source flux (continuum plus line) detected in one resolution element.

Guaranteed Time into a Central Programme intended as a solid and coherent core to the ISO observing programme. Finally, some Discretionary Time has been set aside for observations that could not have been foreseen at the time of the proposal process.

SCIENTIFIC PROGRAM

Given the breadth of its spectral range, and the advances it offers in observational capabilities, ISO will make fundamental contributions in almost every area of astrophysics. Investigations will span objects and phenomena ranging from asteroids to the earliest bursts of star formation. A brief overview of the Central Programme follows, organized by research area.

Solar System: The main topics are the chemistry and structure of the giant planets and comets, and the properties of interplanetary dust, with less ambitious studies of Mars, Titan, the Galilean satellites, and the asteroids.

Interstellar Medium and Star Formation: The major areas addressed are spectroscopy and spectrophotometry of the cold, diffuse medium, and of the warm medium — ionized and photo-dissociated regions and supernova remnants; the chemistry of gas and dust; mapping of clouds to search for embedded sources and for dust property variations; Galactic Center and Galactic Structure; pre-main sequence and early stages of star formation for low-mass and high-mass stars, including outflows and dust formation.

Stars and Circumstellar Material: Most of the effort here goes into studying dusty stellar envelopes, the candidate material for the formation of planetary systems, and into understanding dust production in the outflows from cool evolved stars, asymptotic giant branch stars, and planetary nebulae. Also included are a search for OH and H_2O in those same envelopes, the study of ejecta from hot stars, a spectral survey of normal stars, and a search for brown dwarf companions to nearby main sequence stars.

Extragalactic Systems: Most projects here address the nature and evolution of various classes of objects from dwarf galaxies to quasars. Nearby spatially resolved galaxies will be mapped in the continuum from 5 to 240 μm, in PAH features, and in spectral lines such as C II (158 μm), O I (63 μm) and N II (122 μm). There are far-infrared photometric, mid-infrared imaging, and line surveys of many samples of "normal galaxies": optically selected, star-forming, dwarfs, ellipticals, and Virgo Cluster members. Similar surveys are planned for more active systems: blue compact dwarfs, starbursts, active galactic nuclei and quasars, radio galaxies and ultraluminous galaxies.

Cosmology: About 130 hours will be devoted to a deep ISOCAM survey at 7 and 15 μm searching for primordial galaxies in dark areas of the sky. Similar searches reaching down to the instrumental or natural (confusion) limits will look at 90 and 160 μm for primeval quasars beyond $z = 2$, for active galaxies at high redshift, for the "missing mass" as brown dwarf haloes of disk galaxies, and for the diffuse extragalactic background in the mid- and far-infrared.

COMPARISON TO SOME OTHER MISSIONS

ISO represents great advances over the capabilities of IRAS, the KAO and other current facilities. Its sensitivity will remain unparalleled until the advent of SIRTF, whose detectors will have benefited from many more years of development. ISO's most prominent advantages are in spectroscopy, imaging in the mid-infrared, and photometry and mapping in the far-infrared:

• Spectroscopy with IRAS was limited to the LRS, covering $7 - 23$ μm, with a spectral resolution R$\sim 20 - 60$. ISO SWS and LWS open up the whole range from 2.5 to almost 200 μm, and each offer a grating mode at R$\sim 200 - 1000$, and a Fabry-Pérot mode at R$\gtrsim 10^4$. SWS (grating) can measure in minutes the spectra of sources at a few hundred mJy, a factor of 10–50 improvement over IRAS. Atomic and ionic fine-structure lines, powerful diagnostics of the physical conditions in ionized and photo-dissociated media, have been studied by the KAO only in the brightest sources; ISO will measure them in sources up to a hundred times fainter, *e.g.*, molecular cloud haloes, normal galaxy disks, and distant luminous galaxies.

• ISO-PHOT provides a ten- to a hundred-fold improvement in photometric sensitivity over IRAS 60 and 100 μm, in $0.7' \times 0.7'$ pixels instead of $1.5' \times 4.5'$ and $3' \times 5'$; it offers a thousand-fold improvement over current KAO sensitivity at $\lambda > 100$ μm at a slight cost in spatial resolution. The far-infrared capabilities of ISO will bring into focus the cold dust in molecular clouds and galaxies, thereby greatly improving our estimates of the dust mass in these objects. They will also allow detection of redshifted dust emission from distant ultra-luminous galaxies.

• ISO-CAM will provide a hundred-fold or more improvement in sensitivity in the mid-infrared over IRAS, coupled with ten-fold improvement in linear angular resolution. CAM will excel in low surface brightness measurements, complementing ground-based mid-infrared cameras, which operate at sub-arcsecond resolution to mitigate against high backgrounds.

ISO and SOFIA are quite different missions in scope and design, but they overlap in some observational areas. These overlap areas, however, reveal mostly complementary capabilities, as the cursory comparison below indicates.

Because of the low backgrounds achieved by a cold telescope in space, ISO will excel in the study of low surface brightness sources (*e.g.*, galaxy disks, diffuse interstellar emission), cold sources (*e.g.*, molecular clouds, outer solar system objects). ISO will be about 100 times more sensitive than SOFIA in far-infrared photometry pixel for pixel; SOFIA will be better suited, however, to the study of compact bright sources (*e.g.*, star forming regions, galactic nuclei) with its ~ 4 times better spatial resolution, and its larger detector arrays.

From its vantage point above the atmosphere, ISO will excel at the study of spectral lines (redshifted or otherwise) at any wavelength within its instrumental range. Some H_2O and OH transitions, for instance, are inaccessible from any suborbital platform. However, at wavelengths where the atmosphere is relatively transparent, high-resolution spectroscopy will be better handled by SOFIA since performance is then dominated by collecting area and detectors. SOFIA will easily achieve ten times better spectral resolution than possible with

ISO, and will continue to benefit from improvements in focal plane technology, resulting in better instrumental transmission, better detector sensitivity, and the multiplexing advantage of detector arrays.

REFERENCES

Encrenaz, Th., & Kessler, M. F., editors, 1992, *Infrared Astronomy with ISO*, Proceedings of the Workshop held 13–27 June, 1991 in Les Houches, France (Nova Science Publishers: Commack, NY)

Helou, G. 1994, in Proc of the Airborne Astronomy Symp on the Galactic Ecosystem: From Gas to Stars to Dust, ed. M. R. Haas, J. A. Davidson, & E. F. Erickson (San Francisco: ASP), paper 911

Scholl, M. S., editor, 1993, *Infrared Spaceborne Remote Sensing*, Proceedings SPIE 2019, Conference held 14–16 July 1993, San Diego, California.

Anneila Sargent

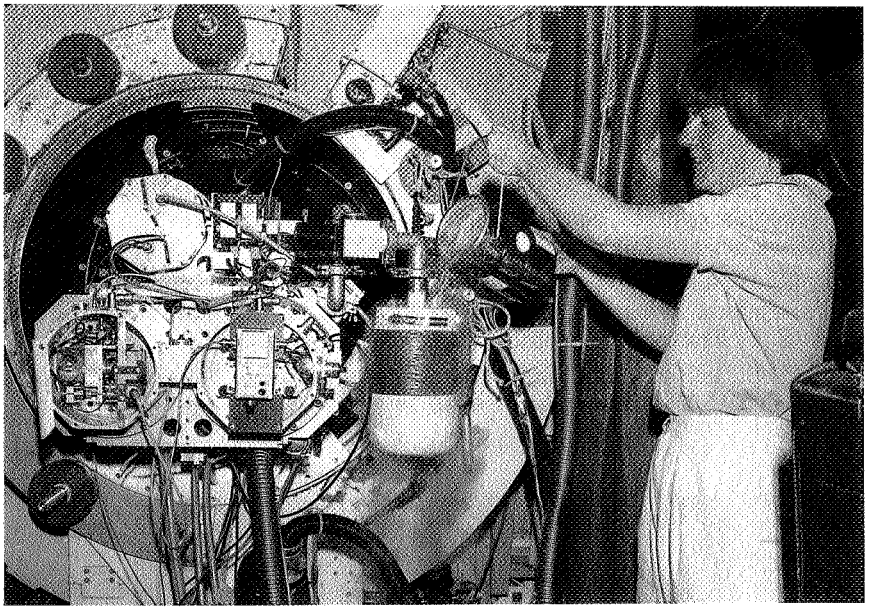

Ruth Titz (1988)

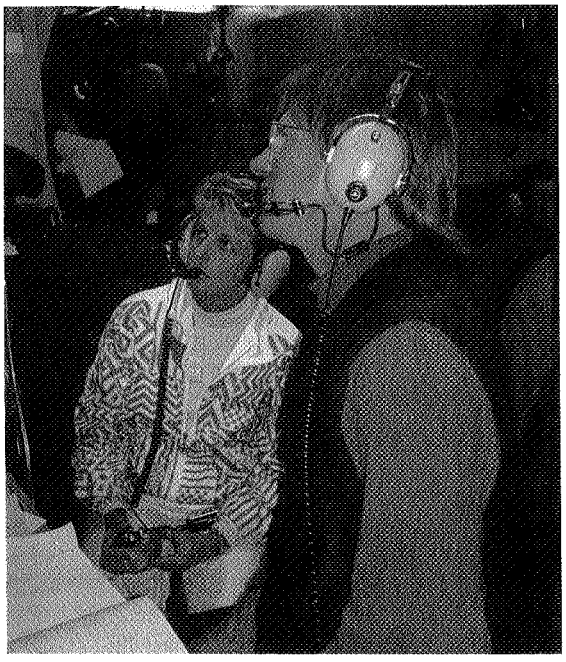

Sandra Engel, Ben Burress

Airborne Astronomy Symposium on the Galactic Ecosystem
ASP Conference Series, Vol. 73, 1995
M.R. Haas, J.A. Davidson, and E.F. Erickson (eds.)

The Infrared Telescope in Space (IRTS) Mission

Thomas L. Roellig

NASA-Ames Research Center, Moffett Field, CA 94035

Abstract. The Infrared Telescope in Space is a cryogenically-cooled NASA/ISAS space survey instrument scheduled for a February, 1995 launch. The telescope optical system is optimized for studies of extended low surface-brightness objects. Four focal-plane instruments cover wavelengths ranging from 1 to 800 microns.

1. Introduction

The Infrared Telescope in Space (IRTS) is a collaborative space project between NASA and the Institute for Space and Astronautical Science (ISAS) of Japan. The composition of the science team and their institutional affiliations are given in Table 1. The IRTS is scheduled as one of a complement of seven experiments to be launched on the first Space Flyer Unit mission (SFU-1) from Tanegashima Space Center in February, 1995 by a Japanese H-2 rocket and then subsequently retrieved by NASA's Space Transportation System. After separation from the launch booster, the SFU will be inserted into a nearly circular, 482 km altitude, 28.5° inclination orbit. After a nominal eight day checkout period, the IRTS aperture cover will be ejected and observations will begin from all four focal plane instruments. In the present mission plan, survey data will then be taken for 20.5 days. The IRTS will orbit the Earth with the telescope sweeping across the sky at a rate of 0.067° sec^{-1} in great circles that are defined by various Earth and Sun avoidance angle constraints. In the nominal orbit, the great circle scans will be offset from one another by approximately 4', or approximately one-half of the instruments' smallest beam size. This means that the IRTS will survey up to approximately 1.5 str or 12% of the sky during the anticipated 20.5 days of infrared data taking.

2. The IRTS Telescope

The IRTS telescope is a Cassegrain design with gold-coated aluminum optics. Table 2 gives a summary of the relevant telescope dimensions. The telescope is surrounded by a 100 liter-capacity liquid helium cryostat, which is pumped through a porous plug by the vacuum of space to a temperature of 1.8 K, dramatically reducing the infrared background seen by the instruments. Tests of the flight cryostat indicate that the superfluid helium hold time will be more than adequate to last through the extended observation period.

Table 1. The IRTS Science Team

ISAS	NASA - Ames
H. Okuda	T. Roellig
H. Murakami	
H. Shibai	
T. Nakagawa	UC Berkeley
	A. Lange
Nagoya University	M. Freund
T. Matsumoto	
S. Sato	University of Tokyo
H. Matsuhara	T. Onaka
T. Hirao	T. Tanabe

Further information on the IRTS mission can be found in Murakami et al. (1994).

Table 2. IRTS Telescope Specifications

Primary mirror size:	15 cm
Final focal ratio:	F/4
Focal plane temperature:	2.0 K
Cryogen coolant:	Superfluid liquid-helium
Estimated cryogen lifetime:	5 weeks

3. The IRTS Focal Plane Instruments

Four scientific instruments will share the IRTS focal plane together with a Ge visible/near-infrared star sensor that will be used for telescope pointing reconstruction. A brief synopsis of the instrument capabilities can be found in Table 3. As can be seen from the table, the four instruments will be capable of infrared measurements ranging from 1 to 800 μm. The instrumental sensitivity, as measured in the laboratory with the flight telescope under the expected space background conditions, is shown in Figure 1. In the case of the MIRS, the instrument sensitivity is limited by the Zodiacal background. For the other instruments, the sensitivity is limited by detector and amplifier noises. Figure 1 does not include confusion-limited sensitivities in crowded fields. As can be seen from Table 3, a wide variety of science goals are being attacked within the IRTS mission, ranging from observations of solar system objects to cosmological studies.

Data will be taken from all of the focal plane instruments in parallel and stored on the spacecraft's 80 M-bit onboard bubble memory data recorder. These data will then be subsequently played back during downlinks while the spacecraft passes over receiving stations in NASA's Deep Space Network and Japan's Kagoshima Space Center. After the receiving stations record and archive the data on-site, they will be transmitted to the IRTS Science Operations Center at ISAS in Japan for

Table 3. The IRTS Focal Plane Instruments

Near-Infrared Spectrometer (NIRS)	
Field of view:	8' x 8'
Wavelength range:	1.4 - 4.0 μm
Spectral resolution:	$\Delta\lambda \sim 0.12$ μm
Detectors:	24 InSb
Science goals:	•Near-infrared cosmic background radiation •3.3 μm line Galactic mapping •Zodiacal spectrum •Stars
Institution:	Nagoya University
Reference:	Noda et al. (1994)
Mid-Infrared Spectrometer (MIRS)	
Field of view:	8' x 8'
Wavelength range:	4.5 - 11.7 μm
Wavelength resolution:	$\Delta\lambda \sim 0.23$-0.36 μm
Detectors:	32 Si:Bi
Science goals:	•Spectrum of infrared cirrus •Zodiacal spectrum •Point-source objects
Institutions:	NASA/ARC, U. Tokyo
Reference:	Roellig et al. (1994)
Far-Infrared Line Mapper (FILM)	
Field of view:	8' x 13'
Wavelength range:	63.2 μm, 157.7 μm
Wavelength resolution:	$\lambda/\Delta\lambda \sim 400$ in OI, CII lines, ~ 150 in continuum
Detectors:	1 Ge:Ga, 3 stressed Ge:Ga
Science goal:	•Maps of galactic structure in OI and CII
Institution:	ISAS
Reference:	Shibai et al. (1994)
Far-Infrared Photometer (FIRP)	
Field of view:	30' dia.
Wavelength range:	100, 250, 400, 700 μm
Wavelength resolution:	$\lambda/\Delta\lambda \sim 3$
Detectors:	4 NTD bolometers operating at 0.3 K, He-3 refrigerator
Science goals:	•Extragalactic background •Interstellar dust emission •Sunyaev-Zel'dovich effect
Institutions:	U. C. Berkeley, Nagoya U.
Reference:	Lange et al. (1994)

processing. The IRTS Science Team will have a 30 month proprietary period to analyze the data, after which it will be archived by the Infrared Processing and Analysis Center (IPAC) for use by the general astronomical community.

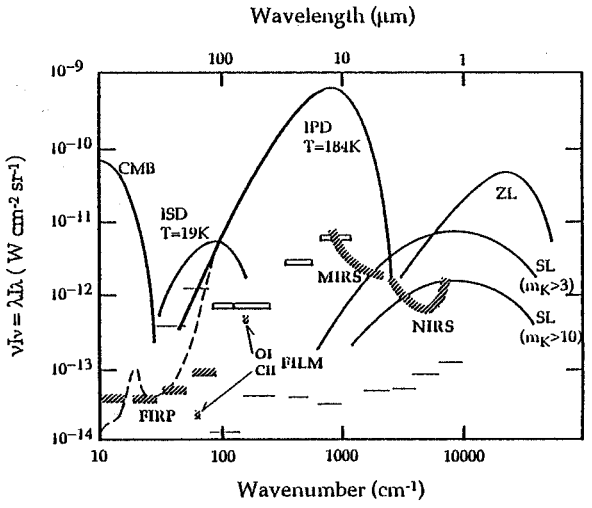

Figure 1. The sensitivities of the four focal-plane instruments in the IRTS, as measured in the laboratory under simulated background conditions of space, are shown as thick cross-hatched lines. The plotted sensitivities are one-sigma for one field-of-view. Diffuse extragalactic starlight (SL), the reflected zodiacal light (ZL), the warm interplanetary dust emission (IPD), the interstellar dust emission (ISD), and the cosmic microwave background radiation (CMB) are indicated with labeled heavy black lines. The one-sigma, one-year sensitivity of COBE's FIRAS and DIRBE experiments are shown as thin dashed and solid lines, respectively. The IRAS survey limits are shown as open rectangles. The IRTS Ge star sensor has a one-sigma sensitivity of +6 magnitude.

Acknowledgments

We would like to a acknowledge the support of the NASA grants program for the funding of the U.S. portion of this project.

References

Lange, A. E., Freund, M., Sato, S., Hirao, T., Matsumoto, T., & Watabe, T. 1994, ApJ, 428, 384.

Murakami, H., et al. 1994, ApJ, 428, 354.

Noda, M., Christov, V. V., Matsuhara, S., Noguchi, K., Sato, S., & Murakami, H. 1994, ApJ, 428, 363

Roellig, T. L., Onaka, T., McMahon, T. J., & Tanabe, T. 1994, ApJ, 428, 370

Shibai, H., Yui, M., Matsuhara, H., Hiromoto, N., Nakagawa, T., & Okuda, H. 1994, ApJ, 428, 377

Airborne Astronomy Symposium on the Galactic Ecosystem
ASP Conference Series, Vol. 73, 1995
M.R. Haas, J.A. Davidson, and E.F. Erickson (eds.)

THE CENTER FOR ASTROPHYSICAL RESEARCH IN ANTARCTICA

ROBERT J. PERNIC, D. A. HARPER, JR., and JUDITH A.BAUSCH
Yerkes Observatory, The University of Chicago, P.O. Box 258,
Williams Bay, WI 53191-0258

ABSTRACT The Center for Astrophysical Research in Antarctica is described.

1. INTRODUCTION

Nowhere on Earth are the infrared skies clearer, darker, or more stable than on the high Antarctic Plateau. At some wavelengths, Antarctic telescopes may be more than one to two orders of magnitude more efficient than at other sites. However, exploiting these advantages requires first addressing the formidable practical difficulties of working in the remote and frigid polar environment. This was the motivation for the Center for Astrophysical Research in Antarctica (CARA), one of twenty-five National Science Foundation Science and Technology Centers.

The Center was formed in February 1991. Its administrative headquarters are located at the University of Chicago's Yerkes Observatory. Key Center researchers work at AT&T Bell Laboratories, Boston University, Carnegie-Mellon University, the University of Colorado, the University of Chicago, the University of Illinois, Northwestern University, Princeton University, Rockwell International Science Center, and the Smithsonian Astrophysical Observatory. Additional institutions which are partners in the educational and outreach activities of the Center include the Adler Planetarium and George Williams College.

2. RESEARCH PROJECTS

At its inception, the Center organized its research into four projects. Three—AST/RO, COBRA, and SPIREX—address key problems in star formation, evolution of galaxies, and the distribution of matter in the early universe. They feature surveys which can be conducted effectively with moderate-size telescopes operated in a highly automated mode. They also explore the

potential of the Antarctic Plateau for a broad range of astrophysical research over a spectral range extending from the near-infrared to millimeter wavelengths. A fourth, ATP, was created to obtain quantitative data on the qualities of the South Pole site and to plan for future scientific projects. During the next five years, AST/RO, COBRA, and SPIREX will become operational, and the Center will begin to build a second generation of telescopes which can address a broader range of problems and accommodate a larger community of users.

During the first two and one-half years of the Center, a major concern has been establishing the infrastructure required to support the Center's research project. A site development plan has been created, one building (designed to support operation of the AST/RO telescope) has been completed, and construction of a larger laboratory building has begun. Steps have been taken to upgrade data communications to the Pole and to provide a year-round supply of liquid helium and liquid nitrogen. A major milestone occurred this year with the beginning of year-round Center operations at the Pole.

AST/RO (Antarctic Submillimeter Telescope and Remote Observatory) will use a 1.7 m diameter submillimeter telescope to survey the Galactic plane, the Galactic center, and the Magellanic Clouds in the emission from the fine-structure line from C I at 609 microns and the J=4–3 line of CO at 650 microns. The telescope is currently operational and has undergone testing in Boston. A building has been completed at the South Pole and will be readied for the telescope during the austral summer of 1993-1994. Installation at the Pole will begin in November, 1994, and year-round observing will begin in February 1995.

COBRA (Cosmic Background Radiation Anisotropy) will search for and map anisotropies in the 2.7 K cosmic background radiation on angular scales ranging from 15 arcminutes to 20 degrees. During the austral summer of 1992-1993, Center scientists conducted a successful series of observations at a wavelength of 3 mm, the spectral region least affected by interference from Galactic foreground radiation. A new 0.75 m telescope using a four-detector array with beam sizes of 45 arcminutes detected structure with an amplitude of $\Delta T/T = 3 \times 10^{-5}$. Another measurement with an older 1.2 m telescope set an upper limit of $\Delta T/T = 1 \times 10^{-5}$ using a beam size of 11 arcminutes. The 0.75 m telescope was returned to the Pole in its present form and was operated over the austral winter of 1994, a year earlier than originally planned. In future years, larger detector arrays capable of mapping large areas of the sky at wavelengths of 1, 2 3, and 9 mm and a 2 m telescope optimized for measurements of structure with scales down to 10 arcminutes will be used to establish whether the observed signals are, indeed, anisotropies in the cosmic microwave background radiation and to measure their spatial power spectrum.

SPIREX (South Pole Infrared Explorer) is initially using a 60 cm diameter near-infrared telescope to explore the potential of the South Pole as an infrared site and to make deep 2.4 micron surveys for primeval

galaxies and brown dwarf stars. In its second phase, the project will construct a 2.5 m telescope and a million-pixel infrared camera, enabling near-infrared imaging to unprecedented depths and sensitive surveys of much of the southern sky. A camera/spectrometer using a 128x128 pixel detector and a manually operated 60 cm telescope was deployed to the Pole for operation over the austral winter of 1994 on the AST/RO telescope pier. Next year, the automated 60 cm survey telescope will be installed at a site adjacent to the new laboratory building which will be constructed during the austral summers of 1993-1994 and 1994-1995.

In **ATP** (Advanced Telescope Project), Center researchers and a broadly based group of astronomers from other US and foreign institutions are collecting data on the qualities of the Antarctic Plateau as an astronomical site and developing plans for a more powerful infrared-submillimeter telescope which could be built during the last half of the 1990s.

The Center has focused on a broad range of educational outreach and knowledge transfer activities. A special focus has been an intensive, longitudinal program targeted at minority high school and grammar school students in Chicago. The program is designed to increase the students' interest and facility in the mathematical and physical sciences and to encourage a greater number of them to pursue careers in science and engineering. In the future, we will continue to develop this program by strengthening our ties with teachers in the schools from which the students are drawn. We are also working to establish linkages with other groups and individuals which will allow us to develop similar programs in communities near other Center institutions.

3. PROGRESS AND FUTURE PLANS

The birth of CARA has coincided with a number of other major activities affecting operations at the South Pole, including (1) a period of intensive planning for a major renovation of the Amundsen-Scott South Pole Station (in a sense, construction of CARA support facilities represents the initial phases of construction of the new Station), (2) a series of high-priority repairs and renovations to the South Pole base driven by safety, environmental, and health requirements, (3) the parallel development of another major scientific experiment (the AMANDA project) which will also put significant demands on resources at the Pole, and (4) institution of a new systems management approach to South Pole logistics and operations.

We feel that there has been considerable progress during the past two and one-half years, and that a solid foundation is being created for future work. Accomplishments include the following.

(1) Selection of a site for Center support facilities. The CARA site has been located in a newly created "dark sector" located grid west of the main base and skiway which will be reserved for experiments requiring isolation from sources of light and other forms of electromagnetic interference. The

CARA facilities will be approximately one kilometer from the geodesic dome at the main South Pole Base.

(2) A telescope pier and building have been constructed to support operations with the AST/RO telescope. The building will be ready for occupancy during the coming austral summer.

(3) Power and data communications cables have been run to the CARA site from the Dome.

(4) In January 1993, site was prepared for a laboratory building (Dark-Sector Lab #1). This lab will support both CARA and AMANDA during the next few years. Building materials have been shipped to the Pole, and construction began in November 1993. Partial occupancy (to support initial AMANDA tests) began in January 1994. Full occupancy will begin in the austral summer of 1994/1995. This winter, CARA is basing its operations in the AST/RO building.

(5) We have prepared a preliminary design for a telescope pier to be located adjacent to the Dark-Sector Lab #1. Our construction goal is to be ready for the SPIREX 60 cm survey telescope beginning in January 1995. The pier will be sized to accommodate the SPIREX 2.5 m telescope when it is ready for operation.

(6) We have selected a site for a second laboratory building (Dark-Sector Lab #2). Construction will begin in November 1995.

(7) Tests conducted in January 1993 demonstrated that data transmission rates of 56 Kbaud or greater could be achieved using a formerly geostationary satellite which has exhausted its station-keeping fuel and is now becoming visible at the Pole. Use of this satellite may begin this year. This should allow a direct Internet connection for approximately 2 hours per day (increasing in future years), a major step toward badly needed improvements in communications to the Pole.

(8) The NSF has authorized procurement of cryogenic storage systems capable of sustaining CARA experiments through the polar winter. These include an actively cooled liquid helium dewar and a nitrogen re-liquifier. They should be delivered to the Pole this coming austral summer.

ACKNOWLEDGMENTS

This research was supported in part by the National Science Foundation under a cooperative agreement with the Center for Astrophysical Research in Antarctica (CARA), grant number NSF DPP 89-20223. CARA is a National Science Foundation Science and Technology Center.

Airborne Astronomy Symposium on the Galactic Ecosystem
ASP Conference Series, Vol. 73, 1995
M.R. Haas, J.A. Davidson, and E.F. Erickson (eds.)

The Submillimeter Wave Astronomy Satellite

Gary J. Melnick

Harvard-Smithsonian Center for Astrophysics, 60 Garden Street, Cambridge, MA 02138

Abstract. The Submillimeter Wave Astronomy Satellite (SWAS) mission is dedicated to the study of star formation and interstellar chemistry. To carry out this mission, SWAS will survey dense ($n_{H_2} > 10^3$ cm^{-3}) molecular clouds within our galaxy in either the ground-state or a low-lying transition of five astrophysically important species: H_2O, $H_2^{18}O$, O_2, CI, and ^{13}CO. By observing these lines SWAS will: (1) test long-standing theories that predict that these species are the dominant coolants of molecular clouds during the early stages of their collapse to form stars and planets and (2) supply heretofore missing information about the abundance of key species central to the chemical models of dense interstellar gas. SWAS will employ two independent Schottky barrier diode mixers, passively cooled to ~ 150 K, coupled to a highly efficient 54×68-cm off-axis Cassegrain antenna. During its two-year mission, SWAS will observe giant and dark cloud cores with the goal of detecting or setting an upper limit on the water abundance of 3×10^{-6} and on the molecular oxygen abundance of 2×10^{-6}, both relative to H_2. In addition, advantage will be taken of SWAS's relatively large beamsize of 3.2×4.0 arcminutes at 551 GHz and 3.6×4.5 arcminutes at 492 GHz to obtain large-area ($\sim 1^\circ \times 1^\circ$) maps of giant and dark clouds in the ^{13}CO and CI lines. SWAS is scheduled for launch in mid–1995.

1. Introduction

The dominance of gravitational over thermal energy throughout the collapse phase of a molecular cloud is an immutable requirement for star formation. During the earliest stages of this collapse much of the gas cools through collisional excitation of low-lying energy states within abundant atoms and molecules which, following their eventual decay, produce photons that carry energy from the cloud. By far the most abundant collision partners in these clouds are H, H_2, and He. Unfortunately, none of these species possess excited states capable of being collisionally populated at the $10 - 30$ K temperatures typical of these clouds. The next most abundant elements are oxygen and carbon. In addition to their atomic form, oxygen and carbon are present within a variety of molecules: some of these atoms and molecules have energy levels that are easily excited between 10 and 30 K (e.g., CO, CI, H_2O, and O_2) while others do not (e.g., OI). In this way, the chemistry within a cloud can directly affect the cooling which, in turn, can affect the cloud dynamics. This paper will briefly

Table 1. Spectral Lines to be Observed by SWAS †

Species	Transition	Energy Above Ground State (E/k)	Frequency (GHz)	Critical Density (cm^{-3})
O_2	$(3,3-1,2)$	26 K	487.249	10^2
CI	$(^3P_1 - {}^3P_0)$	24 K	492.162	10^4
^{13}CO	$(J = 5-4)$	79 K	550.926	3×10^5
H_2O	$(1_{10} - 1_{01})$	27 K	556.936	10^9 ‡
$H_2^{18}O$	$(1_{10} - 1_{01})$	26 K	547.676	10^9 ‡

† SWAS will *simultaneously* observe the O_2, CI, ^{13}CO, and H_2O transitions.
‡ The critical density for H_2O will likely be less than this value by a factor of $10^3 - 10^4$ due to significant radiation trapping in this line. The critical density for $H_2^{18}O$ could be reduced by a factor of $1.5 - 50$ due to the same effect.

summarize: (i) the relevance of the SWAS-selected lines to these questions, (ii) the key elements of the SWAS instrument, and (iii), the observing strategy.

2. Science Objectives

The species selected for study by SWAS are important because:

(1) they are predicted to be major reservoirs of oxygen and carbon in dense interstellar clouds

(2) they should be valuable probes of the physical conditions in these regions

(3) they will provide important tests of chemical models in both well-shielded and photo-illuminated regions of molecular clouds

(4) they are predicted to play a major role in determining the temperature within interstellar clouds.

Oxygen and Carbon Reservoirs: Oxygen and carbon atoms and molecules, including their hydrated forms, are expected to be major constituents of molecular clouds – examples include OI, O_2, CI, CO, H_2O, OH, and CH. Radio observations have clearly demonstrated the significant presence of CO within molecular clouds; however estimates of the CO abundance in these clouds leave most of the oxygen and carbon unaccounted for. More recent observations of CI from both COBE and ground-based observatories and of C^+ from the Kuiper Airborne Observatory imply abundances of carbon in these forms which go a long way toward bridging the gap between the carbon abundance derived from CO

measurements and the solar abundance of carbon. The situation with oxygen remains quite different: the amount of oxygen locked up in CO is typically less than 10 percent of the solar abundance of oxygen, and other oxygen-bearing species measured to date, such as OI and OH, do not account for the difference. The low apparent oxygen abundance may be reconciled with its solar abundance in two ways. First, oxygen in the form of OI may be present in large amounts but, because its first excited state lies 228 K above the ground-state, OI emission is too weak to be detectable toward regions with $T \sim 10 - 30$ K. Second, a large fraction of the oxygen may be tied up in H_2O or O_2, neither of which has been detected (in non-masing transitions for H_2O) due to strong atmospheric absorption above current observing platforms. By observing both H_2O and O_2 SWAS will determine whether these species are significant reservoirs of interstellar oxygen. If SWAS does not detect H_2O or O_2, particularly toward warmer regions where H_2O– and O_2–ice is expected to evaporate from grain mantles, and sensitive searches with facilities such as ISO fail to detect OI toward the same lines of sight, then it may be concluded that the oxygen abundance is unusually high in the solar neighborhood.

Probes of Physical Conditions: The conditions required to excite each of the SWAS lines are sufficiently different so as to make these transitions useful diagnostics of the densities and temperatures within molecular clouds. One measure of the relative sensitivity of the SWAS lines to density is given in Table 1 in which the critical density for collisional de-excitation, n_{cr}, is given for temperatures characteristic of molecular clouds ($10 - 30$ K). As an example of their diagnostic potential, the line strengths of O_2 and CI are largely temperature insensitive at densities greater than 10^4 cm^{-3}, varying by only a factor of 2 between 10 K and 35 K, whereas H_2O and ^{13}CO display variations in line strength greater than a factor of 10 over this same temperature range. Thus, H_2O and ^{13}CO make very effective probes of warm, dense gas. Similarly, limited observations of both CI and ^{13}CO ($J = 6 \rightarrow 5$) have demonstrated that these lines are good tracers of UV-illuminated photodissociation regions.

Molecular Cloud Chemistry: The distribution of oxygen and carbon in atomic and molecular form in the gas phase and on the surfaces of grains is a critical unknown in understanding the chemistry, the ionization structure, and the thermal balance of interstellar clouds, and hence in predicting their evolutionary course. The abundances of the more complex carbon-containing interstellar molecules are directly responsive to the fraction of the carbon that is available as neutral atoms and, because of the different reactivities of O, O_2, and H_2O, the overall molecular composition is sensitive to the oxygen distribution. The cooling rate depends on composition because OH and H_2O are efficient radiators whereas O_2, by virtue of its not possessing a dipole moment, is not. In this way, cloud evolution, dynamics, fragmentation, collapse, and star formation can all be directly affected by the chemistry.

3. Instrument

The SWAS instrument consists of three major subsystems: (1) the telescope, (2) the submillimeter heterodyne receivers, and (3), the spectrometer. The

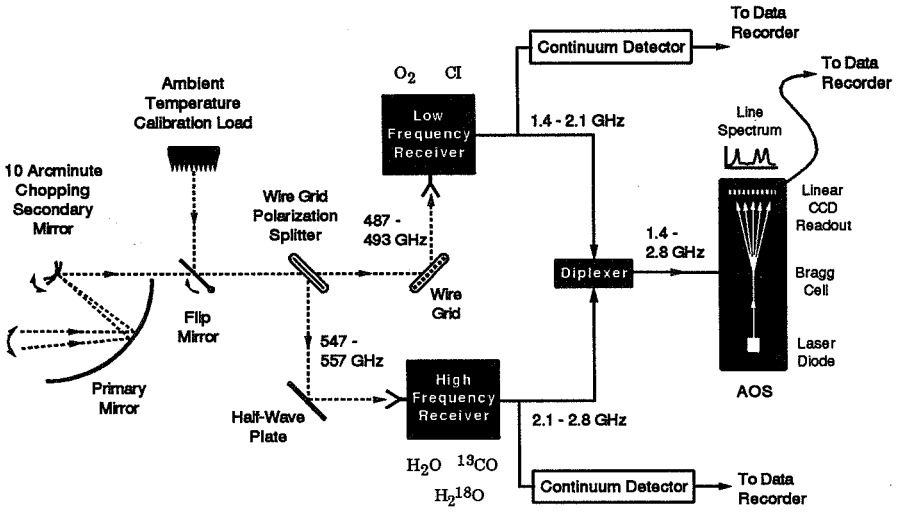

Figure 1. Block diagram of the SWAS signal detection system.

SWAS optical subsystem consists of a 54 × 68-cm diameter off-axis Cassegrain primary mirror, a secondary mirror, a secondary mirror chopping mechanism, a calibration load, and a calibration load flip mirror (see Figure 1). Both the primary and secondary mirrors are made of aluminum and have been polished to a combined rms surface accuracy of 6.5 μm. This mirror surface accuracy along with a receiver feedhorn Gaussian edge taper of 11 dB results in an overall aperture efficiency of about 80% and a main beam efficiency of almost 90%. For sources that appear point-like within the approximately 3.5 × 4.5-arcminute SWAS beam, a chopping secondary mirror mechanism is available for beam switching 10 arcminutes on the sky along a fixed axis. The chopping rate is selectable among three options: 2 Hz, 1/4 Hz, and off. The 2 Hz rate is used in conjunction with the total power continuum detectors associated with each receiver channel and is synchronized with their readout. The 1/4 Hz rate is used in conjunction with spectroscopic observations and is synchronized with the readout rate of the acousto-optical spectrometer (AOS). When the chopping mechanism is off, the incoming beam is on-axis. This mode will be employed when the spacecraft is used to nod the telescope over spatial distances greater than 10 arcminutes, as will be required for extended sources. An ~ 240 K blackbody radiator thermally connected to the instrument structure will be used in combination with blank sky measurements to periodically measure the system noise temperature. This calibration load is nominally out of the beam, but it can be viewed by engaging a flip mirror.

The detection system consists of two independent second harmonic Schottky diode mixers, operating in orthogonal linear polarizations, pumped by frequency-tripled InP Gunn oscillators. The lower frequency receiver is used to observe O_2 and CI at 487 GHz and 492 GHz respectively, while the higher frequency receiver is used to observe H_2O and ^{13}CO at 557 GHz and 551 GHz respectively.

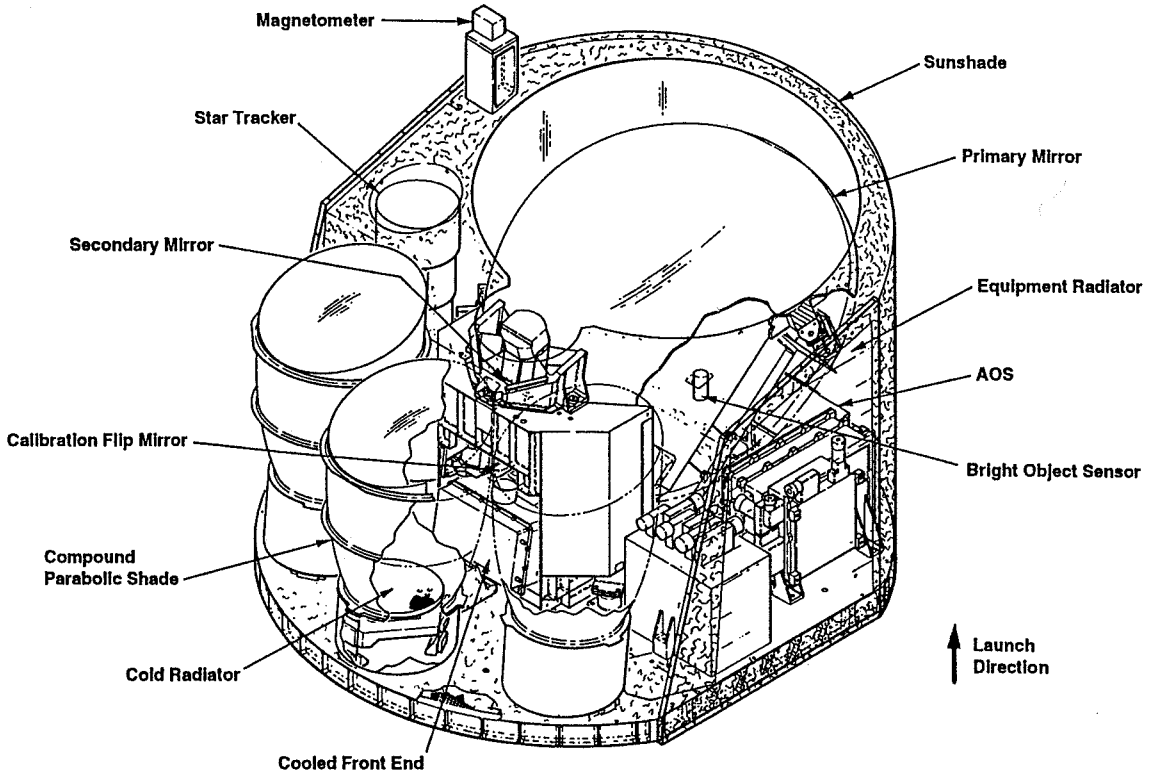

Figure 2. Cutaway view of the SWAS instrument. In the foreground are the three Winston cone shades, inside of which are the passively cooling radiators. These radiators cool the mixers and the first amplifier stages to ~150 K. The cooled frontend and the secondary mirror support structure are located behind the radiators. Most electronics boxes and AOS components are mounted onto the baseplate under the primary mirror. The baseplate mounts to the top of the spacecraft.

A fifth line, the ground state transition of ortho-$H_2^{18}O$ at 548 GHz, can be observed by tuning the higher frequency local oscillator slightly beyond its normal operating range resulting in about two times higher system noise temperature. (The $H_2^{18}O$ is deemed to be worth observing, in spite of the higher system noise temperature, since it can be used to obtain a better estimate of the water abundance than may be derived from the $H_2^{16}O$ line alone, which is likely to be highly optically thick.) To improve the sensitivity of the receivers, the first IF stage, consisting of input optics, a mixer, a tripler, and a HEMT amplifier for each of the two receiver channels, is passively cooled to $\sim$ 150 K. The measured noise temperature in each channel is approximately 1500–2000 K (DSB) at this operating temperature. The output of each receiver is down converted and diplexed with a resulting bandwidth per channel of 700 MHz and an input band to the AOS of 1.4 to 2.8 GHz.

The SWAS spectrometer is a single AOS with 1400 1-MHz channels (about 1700 kHz resolution bandwidth and about 2100 kHz equivalent noise bandwidth per channel). This yields a velocity channel spacing of approximately 0.6 km s^{-1} and a total bandwidth of 840 km s^{-1}, or about 200 km s^{-1} per line. A cutaway view of the SWAS instrument is shown in Figure 2.

4. Observing Strategy

The observing strategy for SWAS is twofold: (1) establish the presence of, or set a scientifically interesting abundance upper limit on, H_2O and O_2, and (2) map the large-scale distribution of CI and ^{13}CO. A measured upper bound on the H_2O and O_2 abundance (relative to H_2) of 3×10^{-6} and 2×10^{-6}, respectively, has been adopted for the SWAS mission for several reasons. For H_2O, a non-detection at an abundance of 3×10^{-6} implies that the ion-molecule chemistry within interstellar clouds does *not* favor the production of H_2O, but instead may favor the production of OH. Further, a non-detection of H_2O at this abundance toward warmer regions would eliminate the class of models which predicts that large amounts of water will be injected into the interstellar medium when water-ice evaporates from the mantles of dust grains. A non-detection of O_2 at an abundance of 2×10^{-6} would eliminate all models of molecular cloud chemistry which start from the assumption that oxygen is more abundant than carbon (as in the solar region). If the H_2O and O_2 abundances are low and SWAS must integrate for the time required to set the above limits, then SWAS will be able to observe approximately 50 giant and 50 dark cloud cores during the half of the mission dedicated to this part of the science objective. Clearly, if H_2O and O_2 are detected then more regions will be observed.

Since the presence of CI and high-J ^{13}CO emission has been established, approximately half of the mission will be dedicated to conducting large-scale CI and ^{13}CO mapping of giant and dark clouds. Based on a combination of measured and predicted line strengths, it is expected that about 15 giant and 15 dark clouds can be mapped over $\sim 1^\circ \times 1^\circ$ with half-beam spacing.

Acknowledgments. A. Dalgarno, N. R. Erickson, G. G. Fazio, P. F. Goldsmith, M. Harwit, D. J. Hollenbach, D. G. Koch, D. A. Neufeld, R. Schieder, R. L. Snell, J. R. Stauffer, P. Thaddeus, V. Tolls, and G. F. Winnewisser.

Airborne Astronomy Symposium on the Galactic Ecosystem
ASP Conference Series, Vol. 73, 1995
M.R. Haas, J.A. Davidson, and E.F. Erickson (eds.)

OMIT TO P. 707

KAO Mission Summary

Edward W. Dunham
MS 245-6, NASA Ames Research Center, Moffett Field, CA 94035-1000

Abstract. The **Kuiper Airborne Observatory** (KAO) is a Lockheed C-141 aircraft with an open port, 0.9 meter telescope. The KAO provides frequent airborne access to the spectral region between 0.3 and 1600 μm. Most of the KAO's work is done in infrared spectral regions that are obscured by water vapor as seen from ground-based observatories. It is a mobile observatory and may be positioned as necessary to observe transient phenomena.

Primary science goals:

Physics and chemistry of the interstellar medium in our galaxy and others
Formation and evolution of stars
Conditions in galactic nuclei
Novae and supernovae
Composition of planetary atmospheres and surfaces
Composition of comets

Launch (flight) year: 1974

Design lifetime: 25 years

Optics temperature: 240 K (after pre-cool)

Optics emissivity: 0.3

Vehicle: Lockheed C-141 Aircraft

Orbit: 41,000 ft

Wavelength range: 0.3 - 1600 μm

Primary mirror diameter: 0.91 m

Angular resolution:

For wavelengths greater than 20 microns, the KAO is diffraction limited. The resolution is 3" at 5 μm and 35" at 100 μm.

Pointing stability: 1 - 2 arcsec rms

Field of view: ~12 arcmin

Focal plane instruments:

Photometer Cameras (1.25 - 200 μm) with detector arrays
High Speed CCD Photometer (0.3 - 1.1 μm)
Heterodyne Spectrometers (100 - 600 μm)
Grating Spectrometers (5 - 150 μm) with detector arrays
Echelle Spectrometers (16 - 210 μm)
Fabry-Perot Imaging Spectrometers (18 - 200 μm) with detector arrays
Prism Spectrometer (3 - 13 μm)
Polarimeters (60 and 100 μm) with detector arrays

Minimum/maximum spectral resolving power: $\lambda/\Delta\lambda = 2$ to 10^6

Total anticipated observing time: 70 x 6.5 x 25 = 11,300 hours

Level of community participation:

35 investigator teams are chosen each year from peer review of submitted proposals.

Data format and availability to the community:

Data is reduced by instrument and guest investigator teams. Information is made available via publications or private collaborations.

Sponsoring agency: NASA

Rear: Carl Gillespie, Don Oishi, Milo Reisner, Don Olsen, Bob Cameron, Ben Horita; *Front:* Jim McClenahan, Bob Mason, Bruce Kelly, and Mike Maloney (1975)

Airborne Astronomy Symposium on the Galactic Ecosystem
ASP Conference Series, Vol. 73, 1995
M.R. Haas, J.A. Davidson, and E.F. Erickson (eds.)

IRAS Mission Summary

George Helou
IPAC, MS 100-22, California Institute of Technology, Pasadena, CA 91125

Abstract. The Infrared Astronomical Satellite (IRAS) operated between January and November 1983, conducting the first unbiased all-sky survey at 12, 25, 60 and 100 μm. In addition to that primary mission, IRAS carried a Low Resolution Spectrograph (LRS), which surveyed thousands of the brighter sources between 8 and 22 μm, and a Chopped Photometric Channel (CPC), which covered selected targets. The survey covered 96% of the sky in about two-thirds of the time, the rest of the mission being used for "Additional Observations" of individual targets. More information is available in the Explanatory Supplement to the IRAS Catalogs and Atlases (1988, eds. Beichman et al.)

Primary science goals:

The primary goal of IRAS was the all-sky unbiased survey. IRAS data touched just about every area of astrophysics, yielding major discoveries in several of them:

- Comets and asteroids (several thousand of the latter)
- Potential protoplanetary systems detected as infrared excesses
- Interstellar matter: PAHs, cirrus, structure of molecular clouds, etc.
- Star forming regions: protostars, cold cores, etc.
- Galaxies: normal, starbursts and active nuclei
- Infrared-luminous galaxies: the starburst to AGN connection
- Cosmology: source counts, individual objects with $0.5<z<2.3$

Launch year:	1983
Lifetime:	10 months
Optics temperature:	2 - 5 K
Optics emissivity:	<0.1
Launch vehicle:	Delta
Orbit:	900 km polar Sun-synchronous, 103 minutes
Wavelength range:	8 - 120 μm
Primary mirror diameter:	0.6 m

Angular resolution:

Detector mask apertures: 0.'76 x 4.'5 at 12 μm; 0.'76 x 4.'7 at 24 μm; 1.'51 x 4.'8 at 60 μm; and 3.'03 x 5.'1 at 100 μm.

Pointing stability:

Slew Mode; reconstructed survey pointing to 1 x 5 arcsec (in-scan x cross-scan)

Field of view: 63 arcmin

Focal plane instruments:

Survey Array: 62 staggered detectors in four rows per band; 16, 15, 16, and 15 detectors at 12, 25, 60 and 100 μm. All data taken while the detectors scanned the sky.

Low Resolution Spectrometer: 15" slit, 2 sub-modules, 7.7 - 13.4 μm and 11 - 23 μm resolution varies with wavelength, $\lambda/\Delta\lambda \sim 12$ - 60.

Minimum/maximum spectral resolving power: $\lambda/\Delta\lambda = 1.5$ and 60

Total observing time: 10 months of data collection

Level of community participation: Science Team

Data format and availability to the community:

Survey results published as soon as possible
Source lists circulated during mission
Catalogs and Atlases verified and published 1 year after mission
Reprocessing for greatest sensitivity continued for several more years

Products: Point Source Catalog, Faint Source Catalog, Small-Scale Structure Catalog, Atlas of Additional Observations, LRS Atlas, LRS Database, SkyFlux Maps, Low Resolution Maps, and IRAS Sky Survey Atlas.

Sponsoring agencies:

IRAS was initiated in 1975 as a joint program of the United States, the Netherlands, and the United Kingdom. Most of the data products were produced at the Infrared Processing and Analysis Center (IPAC), which is funded by NASA.

Airborne Astronomy Symposium on the Galactic Ecosystem
ASP Conference Series, Vol. 73, 1995
M.R. Haas, J.A. Davidson, and E.F. Erickson (eds.)

COBE Mission Summary

J. A. Davidson*
MS 245-6, NASA Ames Research Center, Moffett Field, CA 94035-1000

Abstract. The Cosmic Background Explorer (COBE) was a free-flying Explorer mission containing three instrument packages, DMR, FIRAS and DIRBE (see below), to survey the sky for diffuse emission in the wavelength range from 1 μm to 1 cm. A 600 liter helium cryostat was used to cool FIRAS and DIRBE and a sun shield was employed to protect the instruments from illumination by the Sun and Earth. FIRAS was used to determine the detailed spectrum of the cosmic background radiation, DMR mapped this background and DIRBE was used to search for radiation from the first galaxies.

Primary science goals:

Investigate the beginnings of organization of matter into galaxies, voids, and clusters of galaxies following the Big Bang.

Examine departures from perfect uniformity that must have occurred shortly after the Big Bang, appearing as spectral irregularities and anisotropy in the microwave and far-infrared cosmic background radiation.

Search for the accumulated light from the very first stars and galaxies.

Anticipated launch year:	1989
Design lifetime:	1 year
Optics temperature:	2 K (FIRAS & DIRBE)
Optics emissivity:	0.3
Launch vehicle:	Delta
Orbit:	Circular, polar, 900 km
Wavelength range:	1 - 10,000 μm
Primary mirror diameter:	N/A. Each instrument had its own optics.

---

* This summary is adapted from COBE Literature.

Angular resolution:

DMR and FIRAS both had a resolution of 7 degrees (420 arcmin). DIRBE had a resolution of 0.7 degrees (42 arcmin).

Pointing stability: Continuously scanning

Field of view: DIRBE: 42 arcmin; FIRAS and DMR: 420 arcmin

Focal plane instruments:

The Differential Microwave Radiometer (DMR) contained three receivers; each mapped the sky at one of three wavelengths: 3.3, 5.7, and 9.6 μm. Each receiver used two antenna horns separated by 60 degrees on the sky. The beam size of each antenna was 7 degrees.

The Far Infrared Absolute Spectrometer (FIRAS) was a Michelson interferometer with a Black Body reference source for calibration. FIRAS covered the wavelength range from 0.1 mm to 10 mm with a spectral resolution of 1 wavenumber. FIRAS used a trumpet-shaped cone to collect light with a beam size of 7 degrees.

The Diffuse Infrared Background Experiment (DIRBE) was an off-axis Gregorian telescope which covered simultaneously the wavelength range from 1 to 300 μm with 10 different broad-band, wavelength filter/detector packages. DIRBE also had 1 to 3 μm polarimetry capabilities. Its beam size was 42 arcmin.

Minimum/maximum spectral resolving power: $\lambda/\Delta\lambda = 2$ and 100

Total anticipated observing time: ~ 8,000 hours

Level of community participation: P.I. class experiment

Data format and availability to the community:

Data archived through the National Space Science Data Center (NSSDC) at NASA Goddard Space Flight Center (GSFC). The final data set will be released to the community in late 1994.

Sponsoring agency: NASA

Airborne Astronomy Symposium on the Galactic Ecosystem
ASP Conference Series, Vol. 73, 1995
M.R. Haas, J.A. Davidson, and E.F. Erickson (eds.)

MSX Mission Summary

S. D. Price
Phillips Laboratory, PL/GPOB, 29 Randolph Road, Hanscom AFB, MA 01731-3010

Fred C. Witteborn
MS 245-6, NASA Ames Research Center, Moffett Field, CA 94035-1000

Abstract. The Midcourse Space Experiment (MSX) is a Ballistic Missile Defense Organization (BMDO) satellite. The mission objective is to measure a wide range of man-made and natural space-based phenomena. Most of the data taken during the first two years will be on the natural backgrounds from the Earth's atmosphere and the celestial sphere. MSX will make a variety of astronomical observations in the form of imagery and spectroscopy in the 0.15 - 0.9 μm and 2.5 - 25 μm spectral regions.

Astronomical measurements will be obtained by two instrument suites: a cryogenic telescope with infrared focal planes covering the 2.5 to 25 μm spectral region and a set of 9 ultraviolet and visual imagers. Of the nine, there are a narrow and a wide field ultraviolet telescope, narrow and wide field visible instruments and 5 ultraviolet and visible imaging spectrographic cameras.

Primary Science Goals:

Mapping and spectroscopy of zodiacal emission 25 to 60 degrees from the sun and in the anti-solar direction: Explore regions not covered by IRAS and COBE and look for structure, time variability and compositional information.

Make radiometric and spectral maps of the Galactic plane to examine structure.

Examine latitude variations in UIR (PAH) features.

Numerous discrete and extended sources will be examined spectroscopically and photometrically.

Anticipated launch year:	1995
Design Lifetime:	1.5 years
Optics temperature:	10 K
Optics emissivity:	0.2
Launch vehicle:	Delta

Orbit: Polar

Wavelength range 2.5 - 28 μm

Primary mirror diameter: 0.34 m (0.21 m clear aperture for interferometer)

Angular resolution: 20" (photometry); 5.5' (spectroscopy)

Pointing stability: TBD arcsec rms

Field of view: 5 - 60 arcmin

Focal plane instruments:

Multiband radiometer (6 - 11 μm, 14 - 16 μm, 17 - 25 μm);
Interferometer/Spectrometer (2.5 - 28 μm)

Minimum/maximum spectral resolution: $\Delta\sigma = 20$ cm^{-1} and 2 cm^{-1}

Total anticipated observing time: 300 hours

Level of community participation: Only P.I. and Co-I's until validation of data.

Data format and availability to the community:

Currently IPAC is negotiating with NASA and the MSX Program Office to archive astronomical data after a proprietary period has passed. If an agreement is reached, there would be a catalog of point sources, images and spectra available to the community.

Sponsoring agency: Ballistic Missile Defense Organization (BMDO).

Lou Haughney, Jim McClenahan, Don Oishi, Bob Walker,
Milo Reisner, Ben Horita, and B. B. Grey (1985)

Airborne Astronomy Symposium on the Galactic Ecosystem
ASP Conference Series, Vol. 73, 1995
M.R. Haas, J.A. Davidson, and E.F. Erickson (eds.)

IRTS Mission Summary

Thomas L. Roellig
MS 245-6, NASA Ames Research Center, Moffett Field, CA 94035-1000

Abstract. The Infrared Telescope in Space (IRTS) is a collaborative space project between NASA and the Institute for Space and Astronautical Science of Japan. The telescope will be launched in February 1995 by a Japanese expendable launch vehicle and then subsequently retrieved by NASA's Space Transportation System. The telescope optics are cooled by superfluid liquid-helium to dramatically reduce the infrared background seen by the instruments. Four scientific instruments sharing a common focal plane will be used to survey approximately 12% of the sky with a variety of spectral resolutions at wavelengths ranging from 1 to 1000 μm.

Primary science goals:

Near-infrared cosmic background radiation
UIR line Galactic mapping
Zodiacal spectrum
Spectrum of infrared cirrus
Maps of galactic structure in OI and CII
Extragalactic background
Interstellar dust emission
Sunyaev-Zel'dovich effect

Anticipated launch year:	1995
Design lifetime:	3 weeks
Optics temperature:	4 K
Optics emissivity:	0.05
Launch vehicle:	Space Flyer Unit, H-2 launch
Orbit:	500 km circular
Wavelength range:	1 - 700 μm
Primary mirror diameter:	0.15 m
Angular resolution:	8' to 30' (see below)
Pointing stability:	survey mission

Field of view: (see below)

Focal plane instruments:

Near-Infrared Spectrometer (NIRS) 1.4 - 4.0 μm; $\Delta\lambda$ = 0.12 μm; 8' x 8' FOV.
Mid-Infrared Spectrometer (MIRS) 4.5 - 11.7 μm; $\Delta\lambda$ = 0.23 - 0.36 μm; 8' x 8' FOV.
Far-Infrared Line Mapper (FILM) 63, 158 μm; $\lambda/\Delta\lambda$ = 400; 8' x 13' FOV.
Far Infrared Photometer (FIRP) 100 - 700 μm; $\lambda/\Delta\lambda$ = 3; 30' dia. FOV.

Minimum/maximum spectral resolving power: (see above)

Total anticipated observing time: 3 weeks

Level of community participation: P.I. class mission

Data format and availability to the community:

After a 30 month proprietary data period, all the mission data will be released to the general community through IPAC.

Sponsoring agencies:

Institute for Space and Astronautical Science (ISAS), Japan and NASA.

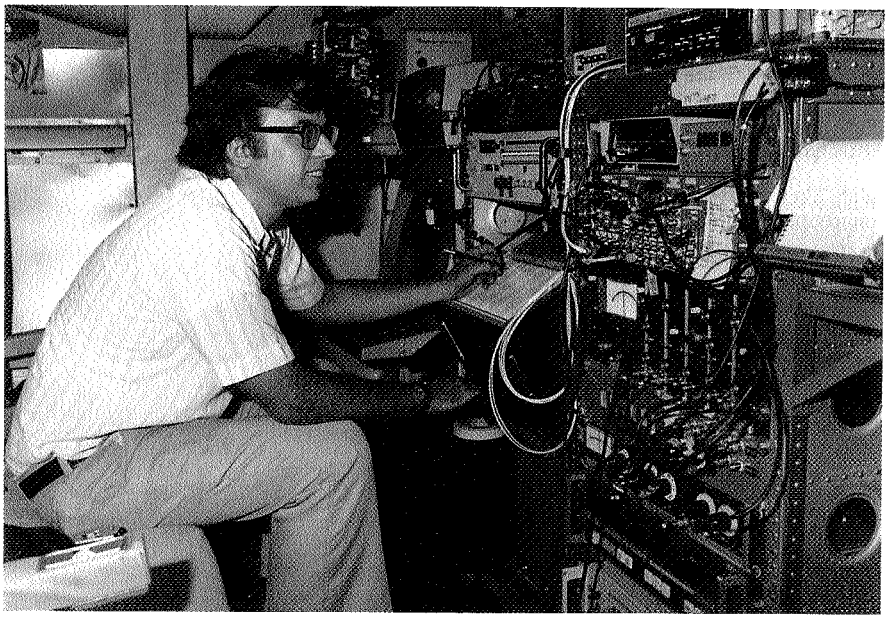

Roger Knacke (1977)

Airborne Astronomy Symposium on the Galactic Ecosystem
ASP Conference Series, Vol. 73, 1995
M.R. Haas, J.A. Davidson, and E.F. Erickson (eds.)

SWAS Mission Summary

Gary J. Melnick
Harvard-Smithsonian Center for Astrophysics, 60 Garden Street, Cambridge, MA 02138

Abstract. The Submillimeter Wave Astronomy Satellite (SWAS) is a self-contained radio telescope capable of carrying out pointed observations from orbit. SWAS is comprised of a highly efficient, off-axis Cassegrain antenna, two heterodyne receivers, an acousto-optical spectrometer, pointing system, solid-state memory capable of storing 24 hours of data, and a high bit-rate (~1 Mbit/sec) uplink/downlink receiver and transmitter. The two heterodyne receivers are tuned to observe either the ground state or a low-lying transition in five important atomic and molecular species that are either difficult or impossible to observe from the ground: O_2, CI, ^{13}CO, H_2O, and $H_2{}^{18}O$ at 615.276, 609.134, 544.161, 538.289, and 547.390 microns respectively.

SWAS can operate in two spectroscopic modes: one in which it can simultaneously observe the O_2, CI, ^{13}CO, and H_2O lines or one in which the O_2, CI, and $H_2{}^{18}O$ lines are observed simultaneously. From its 600-km altitude orbit, SWAS will typically observe between three and six sources during each 97-minute orbit. Longer integrations will be built up by averaging spectra from several orbits.

Primary science goals:

SWAS will primarily survey dense ($n(H_2) > 1000$ cm^{-3}) molecular clouds and cloud cores within our galaxy in order to:

(1) Test long-standing theories that predict that the above species are the dominant coolants of molecular clouds during the early stages of their collapse to form stars and planets.

(2) Supply heretofore missing information about the abundance of key species central to the chemical models of molecular clouds.

Anticipated launch year:	1995
Design lifetime:	3 years
Optics temperature:	273 - 283 K
Optics emissivity:	0.05
Launch vehicle:	Pegasus-XL

Orbit: 600 km circular/65 deg. inclination

Wavelength range: 538 - 615 μm

Primary mirror diameter: 0.54 x 0.68 m

Angular resolution: 3.3 x 4.3 arcmin

Pointing stability: 19 arcsec rms

Field of view: 3.3 x 4.3 arcmin

Focal plane instruments:

Two Heterodyne Receivers
609 - 615 μm (487 - 492 GHz) used to observe O_2 and CI
538 - 547 μm (547 - 557 GHz) used to observe H_2O, $H_2{}^{18}O$, and ^{13}CO

One Acousto-Optical Spectrometer with a total bandwidth of 1.4 GHz
(total bandpass of 840 km/s or 210 km/s/spectral line)

Minimum/maximum spectral resolving power: 1 km/s (fixed)

Total anticipated observing time: 2 years x 24 hours/day = 17,472 hours.

Level of community participation:

Co-Investigator participation includes: Smithsonian Astrophysical Observatory (SAO), Johns Hopkins University, Cornell University, National Air and Space Museum, NASA Ames Research Center, University of Massachusetts, and University of Cologne (Germany).

Data format and availability to the community:

Data will be reduced and archived at SAO and made available to the National Space Science Data Center (NSSDC) in FITS format.

Sponsoring agencies: NASA and DARA

Airborne Astronomy Symposium on the Galactic Ecosystem
ASP Conference Series, Vol. 73, 1995
M.R. Haas, J.A. Davidson, and E.F. Erickson (eds.)

ISO Mission Summary

George Helou
IPAC, MS 100-22, California Institute of Technology, Pasadena, CA 91125

Abstract. The **Infrared Space Observatory** (ISO) is a European mission with Japanese and US participation, which will orbit a He-cooled telescope and operate it in observatory mode, collecting data at wavelengths between 2.5 and 240 μm. ISO will be the premier infrared mission of the nineties, surpassing the IRAS capabilities by orders of magnitude in sensitivity and improved spatial and spectral coverage, and allowing follow-up studies of individual objects as well as small surveys. (More information is available in the Call for Open Time Proposals published by ESA in April, 1994.)

Primary science goals:

ISO will provide IR data relevant to most areas of astrophysics:

- Comets and asteroids
- Giant planets, Mars and Titan
- Protoplanetary systems
- Interstellar matter, properties of both gas and dust
- Stars: their birth, evolution, and death
- Galaxies: normal, starbursts and active nuclei
- Quasars and their energy sources
- Cosmology: deep surveys in selected areas

Anticipated launch year:	1995
Design lifetime:	1.5 years
Optics temperature:	3 - 4 K
Optics emissivity:	< 0.04
Launch vehicle:	Ariane-4
Orbit:	1,000 x 70,000 km, 24 hr
Wavelength range:	2.5 - 240 μm
Primary mirror diameter:	0.6 m
Angular resolution:	Diffraction-limited for $\lambda > 5$ μm; variety of apertures available

Pointing stability: Jitter: 2.7" over 30 sec; 2 sigma half-cone
Drift: 2.8" over 1 hour, 2 sigma, half-cone
Absolute pointing error: 12", 2-sigma, half-cone

Field of view: 3 arcmin per instrument; 20 arcmin total

Focal plane instruments:

ISO-CAM: Camera and Polarimeter, 2.5 - 17 μm, 32 x 32 pixels, at 1.5, 3, 6 or 12 arcsec/pixel.

ISO-PHOT: Imaging photo-polarimeter and spectrometer, 2.5 - 240 μm with 3 modules:

PHOT-P: Multi-band, multi-aperture photopolarimeter, 3 - 110 μm

PHOT-C: Far-IR camera, 3 x 3 pixels at 30 - 110 μm, 2 x 2 pixels at 100 - 240 μm

PHOT-S: Near-IR spectrophotometer, 2.5 - 12 μm, resolution ~90

ISO-SWS: Spectrometer, 2.5 - 45 μm, apertures range from 14 x 20 to 20 x 33 arcsec
Grating mode: 2.5 - 45 μm, resolution ~1000
Fabry-Perot mode: 15 - 30 μm, resolution ~30000

ISO-LWS: Spectrometer, 45 - 196 μm, 1.65 arcmin diameter aperture
Grating mode: resolution 200 - 300
Fabry-Perot mode: resolution about 10000

Minimum/maximum spectral resolving power: $\lambda/\Delta\lambda = 1.5$ and 30,000

Total anticipated observing time: 6,500 hours (science observing time)

Level of community participation: 55% of science time to Open-Time proposals

Data format and availability to the community:

FITS formatted reduced data from observations with 2 - 6 weeks lag.
Science archive made public after 1 yr proprietary period.

Sponsoring agencies: ESA, with participation by ISAS and NASA

Airborne Astronomy Symposium on the Galactic Ecosystem
ASP Conference Series, Vol. 73, 1995
M.R. Haas, J.A. Davidson, and E.F. Erickson (eds.)

NICMOS Mission Summary

Marcia J. Rieke
University of Arizona, Steward Observatory, Tucson, AZ 85721

Abstract. NICMOS (Near-Infrared Camera and Multi-Object Spectrometer) is a near-infrared instrument for the Hubble Space Telescope.

Primary science goals:

Diffraction limited imaging from 1 - 2 μm with science goals including:

[1] Study of the black hole candidate at the Galactic center,
[2] Search for substellar companions to stars,
[3] Search for very high redshift quasars,
[4] Studies of nuclear activity in galaxies,
[5] Use of M supergiants for extragalactic distance scale work, and
[6] Use of the surface brightness fluctuation technique for distance scale work as well as stellar population studies.

Anticipated launch year:	March, 1997
Design lifetime:	5 years
Optics temperature:	297 K
Optics emissivity:	20%
Launch vehicle:	Shuttle
Orbit:	Low-earth
Wavelength range:	1 - 2.5 μm
Primary mirror diameter :	2.4 m
Angular resolution:	0.045" to 0.2"
Pointing stability:	0.002 arcsec rms
Field of view:	1 arcmin

Focal plane instruments:

Three cameras with plate scales of 0.045"/pix, 0.075"/pix, and 0.2"/pix.

Array sizes: 256 x 256
Read noise: 20 electrons
Dark Current: <0.2 electrons/sec

NICMOS will have a sensitivity advantage over even the largest ground-based telescopes at wavelengths shorter than 2.0 μm due to the factor of 1000 reduction in background due to the lack of OH airglow. NICMOS should be able to routinely detect point sources at H(1.6 μm) = 22 to 24.

These cameras are equipped with a selection of filters for both broad band and line imaging. A slitless grism is available for low-resolution spectroscopy. For deep imaging near bright objects, a coronagraph is available. Polarimetry with wire grids will also be possible.

Minimum/maximum spectral resolving power: $\lambda/\Delta\lambda$ = 2 to 1000

Total anticipated observing time: 4,000 hrs (more if proposals are successful)

Level of community participation:

360 hrs for P.I. team, remainder for community

Data format and availability to the community:

Data will be delivered in standard HST manner, probably on Exabyte tapes, with all data in archive 1 year after an observation is complete.

Sponsoring agency: NASA

Airborne Astronomy Symposium on the Galactic Ecosystem
ASP Conference Series, Vol. 73, 1995
M.R. Haas, J.A. Davidson, and E.F. Erickson (eds.)

WIRE Mission Summary

Helene Schember
Jet Propulsion Laboratory, California Institute of Technology, Pasadena, CA 91109

Abstract. The Wide-field Infrared Explorer (WIRE) is a two-color imaging space telescope designed to study the evolution of starburst galaxies and to search for ultraluminous galaxies and protogalaxies. WIRE is a candidate mission in the NASA Small Explorer program. Perry Hacking (JPL) is the Principal Investigator.

Primary science goals:

To answer the following questions:

[1] What fraction of the luminosity of the Universe at a redshift of 0.5 and beyond is due to starburst galaxies?
[2] How fast and in what ways are starburst galaxies evolving?
[3] Are luminous protogalaxies common at redshifts less than 3?

Anticipated launch year:	1998
Design lifetime:	0.33 years
Optics temperature:	12 K
Optics emissivity:	<0.05
Launch vehicle:	Pegasus XL
Orbit:	500 km, circular, sun-synchronous, dawn-dusk
Wavelength range:	12, 25 μm (band centers)
Primary mirror diameter:	0.3 m
Angular resolution:	Diffraction limited in both bands
Pointing stability:	6 arcsec rms
Field of view:	32 arcmin

Focal plane instruments:

Single instrument mission: 30 cm Cassegrain telescope, f/3.5, no reimaging optics, imaging in 2 bands (9 - 15 μm, 21 - 27 μm) using Si:As 128 x 128 arrays cooled to below 7.5 K.

Minimum/maximum spectral resolving power: (see above)

Total anticipated observing time:

$6x10^6$ sec (in primary target zone) x ~0.5 observing efficiency ≈ 850 hrs of primary observations.

Level of community participation:

TBD. If WIRE is selected to proceed, a program may be developed in conjuction with NASA Headquarters for additional funding to permit the investigation of other science investigations using the WIRE dataset.

Data format and availability to the community:

Data will be reduced and archived by the Infrared Processing and Analysis Facility (IPAC) in Pasadena, CA. Information will be made available via publications and upon request to IPAC one year after the mission is concluded.

Sponsoring agency: NASA Small Explorer Program

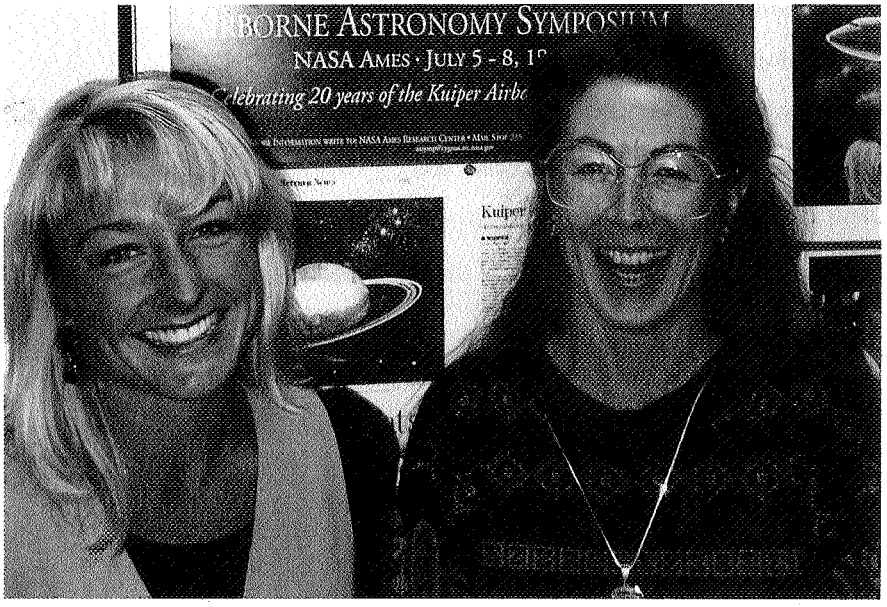

Juliet Wiersema and Sara Acevedo

Airborne Astronomy Symposium on the Galactic Ecosystem
ASP Conference Series, Vol. 73, 1995
M.R. Haas, J.A. Davidson, and E.F. Erickson (eds.)

SOFIA Mission Summary

Edwin F. Erickson
MS 245-6, NASA Ames Research Center, Moffett Field, CA 94035-1000

Abstract. The **Stratospheric Observatory for Infrared Astronomy** (SOFIA) will be a Boeing 747 with a 2.7 meter telescope mounted in an open port aft of the left wing. It permits observations of a broad range of infrared wavelengths not detectable from earth-bound telescopes. Its mobility enables all sky coverage and precise positioning for ephemeral events. A long lifetime and hands-on working environment assure SOFIA's role as a technological test bed and unique educational facility.

Primary science goals:

Physics and chemistry of the interstellar medium in our galaxy and others
Formation and evolution of stars
Conditions in galactic nuclei
Novae and supernovae
Structure and composition of planetary atmospheres, surfaces, and rings
Composition of comets

Anticipated launch (flight) year: 2000

Design lifetime:	20 years
Optics temperature:	240 K
Optics emissivity:	0.15
Vehicle:	Boeing 747 Aircraft
Orbit:	12 - 14 km
Wavelength range:	0.3 - 1600 μm
Primary mirror diameter:	2.7 m (2.5 m clear aperture for large chop angles)

Angular resolution:

Diffraction limited beyond 15 μm; 10" at 100 μm.
Seeing limited up to 5 μm; 3" at 3 μm.

Pointing stability:	0.2" rms
Field of view:	8 arcmin

Focal plane instruments:

Photometer Cameras (1.25 - 200 μm) with array detectors
High Speed CCD Photometer (0.3 - 1.1 μm)
Heterodyne Spectrometers (100 - 600 μm)
Grating Spectrometers (5 - 150 μm) with array detectors
Echelle Spectrometers (16 - 210 μm) with array detectors
Fabry-Perot Imaging Spectrometers (18 - 200 μm) with array detectors
Prism Spectrometer (3 - 13 μm) with array detectors
Polarimeters (60 and 100 μm) with array detectors

Minimum/maximum spectral resolving power: $\lambda/\Delta\lambda = 2$ to 10^7

Total anticipated observing time: 150 x 6.5 x 20 = 19,500 hours

Level of community participation:

60 investigator teams selected by annual peer review

Data format and availability to the community:

Data will be reduced by instrument and guest investigator teams.
Results will made available via publications or private collaborations.

Sponsoring agencies: NASA (80%) and DARA (20%).

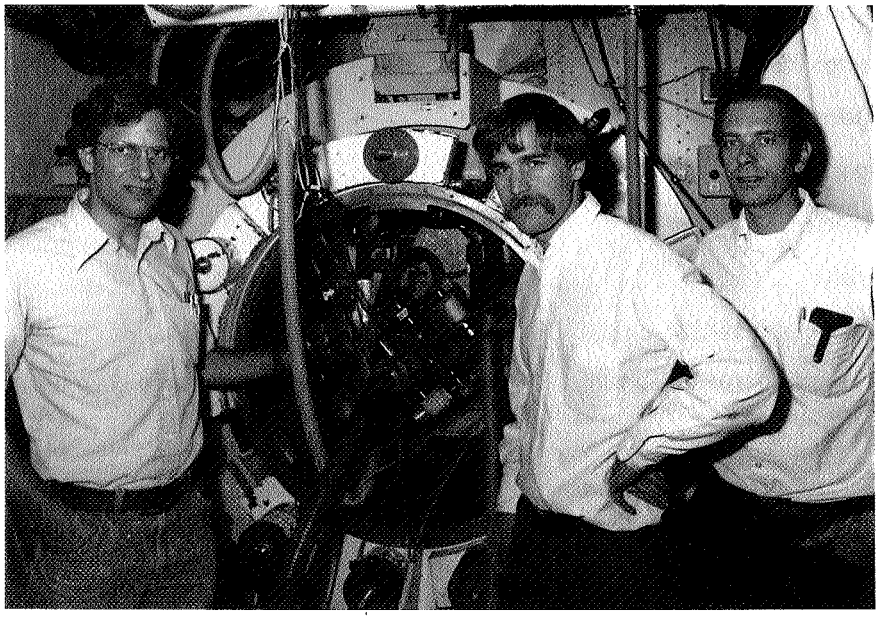

Al Harper, Harvey Moseley, and Bob Silverberg (1981)

Airborne Astronomy Symposium on the Galactic Ecosystem
ASP Conference Series, Vol. 73, 1995
M.R. Haas, J.A. Davidson, and E.F. Erickson (eds.)

IRIS Mission Summary

M. W. Werner*
MS 169-327, Jet Propulsion Laboratory,
California Institute of Technology, Pasadena, CA 91109

Abstract. IRIS -- the Infrared Imaging Surveyor -- is being developed within the Japanese infrared community as a contender for the next mission in the "Astro" series. It will a have 70-to-85 cm aperture and a lifetime of one to two years. The optics and instruments will be cooled by a combination of mechanical coolers and stored cryogens. The scientific program will include pointed surveys in the near infrared and scanning surveys in the far infrared.

Primary science goals: Birth and evolution of galaxies

Anticipated launch year:	2001 or 2003
Design lifetime:	1 - 2 years
Optics temperature:	<10 K
Optics emissivity:	TBD
Launch vehicle:	M-V
Orbit:	Polar, sun-synchronous [IRAS/COBE orbit]
Wavelength range:	3.5 - 180 μm
Primary mirror diameter:	70 - 85 cm
Angular resolution:	~2" in near-infrared; 30" at 90 μm
Pointing stability:	Goal is 0.25 arcsec rms
Field of view:	40 arcmin

Focal plane instruments:

Imaging bands at 2.2, 3.4, 5.0, 9, 18, 36 μm [one InSb + one Si:As array simultaneously view same 20 arcmin field of view]
Scanning bands at 50, 90, 150 μm [two linear arrays in each band]
Near infrared grism is an option

* This summary is based on recent information from Japan.

Minimum/maximum spectral resolving power: $\lambda/\Delta\lambda \sim 2$ and 100

Total anticipated observing time:

2500 hours for pointed observations
5000 hours for scanning observations [assumes 1.5 yr lifetime]

Level of community participation: TBD

Data format and availability to the community:

TBD. If NASA collaboration materializes, data will eventually be archived in the US.

Sponsoring agencies:

ISAS. (A collaboration between NASA and the Japanese Space Agency ISAS for joint implementation of SIRTF and IRIS as a complementary two-mission program is under active consideration at this time. The description given here is based on the latest information from ISAS, not on any NASA-ISAS discussions.)

Dora Willoughby

Airborne Astronomy Symposium on the Galactic Ecosystem
ASP Conference Series, Vol. 73, 1995
M.R. Haas, J.A. Davidson, and E.F. Erickson (eds.)

SIRTF Mission Summary

M. W. Werner
MS 169-327, Jet Propulsion Laboratory,
California Institute of Technology, Pasadena, CA 91109

Abstract. SIRTF -- the Space Infrared Telescope Facility -- is a 1-m class, radiatively- and cryogenically-cooled observatory for infrared astronomy from space. It will combine the intrinsic sensitivity of a cryogenic telescope in space with the great imaging and spectroscopic power of large-format, low-noise infrared arrays and reach sensitivity levels one to ten thousand times fainter than did IRAS. Scientific programs will be weighted towards large scale Key Projects to be defined and executed by the broad astronomical community. SIRTF has been rescoped as a Moderate Mission in the face of recent budgetary and programmatic pressures.

Primary science goals:

Protoplanetary and planetary debris disks
Brown dwarfs and superplanets
Ultraluminous galaxies and active galactic nuclei
The early Universe
Serendipitous exploration, both imaging and spectroscopic

Anticipated launch year: 2001

Design lifetime: 2.5 years

Optics temperature: < 5.5 K

Optics emissivity: ≤10% -- consistent with natural Background Limited Performance (BLIP) out to 180 μm

Launch vehicle: Delta 792 or 7925

Orbit: Solar

Wavelength range: 3.5 - 180 μm

Primary mirror diameter: 0.85 m

Angular resolution:

2" images at 3.5 μm. Use of super-resolution at 30 μm and longward will improve angular resolution by ~2x over Rayleigh limit [which is 8" at 30 μm].

Pointing stability: 0.25 arcsec rms

Field of view: 26 arcmin, imaging arrays have 5' x 5' fields of view

Focal plane instruments:

Imaging bands @ 3.5, 4.5, 6.5, 8, 30, 70, 180 μm, each with a separate array -- simultaneous operation possible

Spectroscopic modules:
4 - 5.3, 5 - 15, 15 - 40 μm [$\lambda/\Delta\lambda$~100] -- long slit imaging spectroscopy
12 - 24, 20 - 40 μm [$\lambda/\Delta\lambda$~600] -- echelle format spectroscopy
50 - 100 μm [$\lambda/\Delta\lambda$~20] -- for spectral energy distribution determination

Minimum/maximum spectral resolving power: $\lambda/\Delta\lambda$ ~ 2 and 600

Total anticipated observing time: 16,500 hours, assuming 75% efficiency

Level of community participation:

High level of community participation in defining and executing Key Projects and through Guest Observer program.

Data format and availability to the community:

Key Project data to be available electronically without proprietary period to facilitate follow-up during mission. Entire mission data set to be available for archival research according to usual NASA procedures.

Sponsoring agencies:

NASA. (A collaboration between NASA and the Japanese Space Agency ISAS for joint implementation of SIRTF and the Japanese IRIS missions as a complementary two-mission program is under active consideration at this time. For further information, contact the SIRTF Project Scientist, Michael Werner, at mww@ipac.caltech.edu.)

Airborne Astronomy Symposium on the Galactic Ecosystem
ASP Conference Series, Vol. 73, 1995
M.R. Haas, J.A. Davidson, and E.F. Erickson (eds.)

FIRST Mission Summary

Thomas G. Phillips
MS 320-47, Department of Physics, Caltech, Pasadena, CA 91125

Abstract. The Far-Infrared and Submillimeter Telescope (FIRST) is a large aperture, passively cooled telescope with a cooled focal plane for far-infrared and submillimeter wave astronomy. It is approved as the 4th Cornerstone of the ESA "Horizon 2000" plan.

Primary science goals:

Studies of important atomic and molecular cooling lines in the 85 to 900 μm range (OI, OIII, NII, CI, CII, CO and H_2O) at high spectral and spatial resolution in star-forming regions of the ISM and nearby galaxies. Searches for important rare species such as HD and HeH^+ are also planned.

Studies of atomic and molecular lines from distant galaxies in the early Universe, over a wide range of redshifts.

Studies of the redshifted dust continuum of protogalaxies at $z \geq 2$.

Anticipated launch year:	2006
Design lifetime:	6 years
Optics temperature:	160 K (possibly much less)
Optics emissivity:	<4%
Launch vehicle:	ARIANE 5 (shared, upper)
Orbit:	Eccentric (1,000 x 70,000 km) (possibly L2)
Wavelength range:	85 - 900 μm
Primary mirror diameter:	3 m (possibly 4.5 m)
Angular resolution:	7" at 100 μm (possibly 5")
Pointing stability:	< 3" rms
Field of view:	15' (radius)

Focal plane instruments:

Multifrequency heterodyne receiver 490 - 900 GHz, with extra high frequency channel at 1113 GHz.
Far-infrared photoconductor array for spectroscopy and photometry.
Far-infrared bolometer arrays (2) for spectroscopy and photometry.

Minimum/maximum spectral resolving power:

Heterodyne: $\lambda/\Delta\lambda = 3 \times 10^6$
FIR spectroscopy: $\lambda/\Delta\lambda = 10^5 - 10^3$
FIR continuum: $\lambda/\Delta\lambda = 3$

Total anticipated observing time: 37,000 hours (possibly 52,000 hours)

Level of community participation:

35% to P.I.s etc., remainder to general community (presumably of participating countries).

Data format and availability to the community:

ESA rules are that data is proprietary for one year, then available to community through the Science Data Center.

Sponsoring agencies: ESA (possibly also NASA).

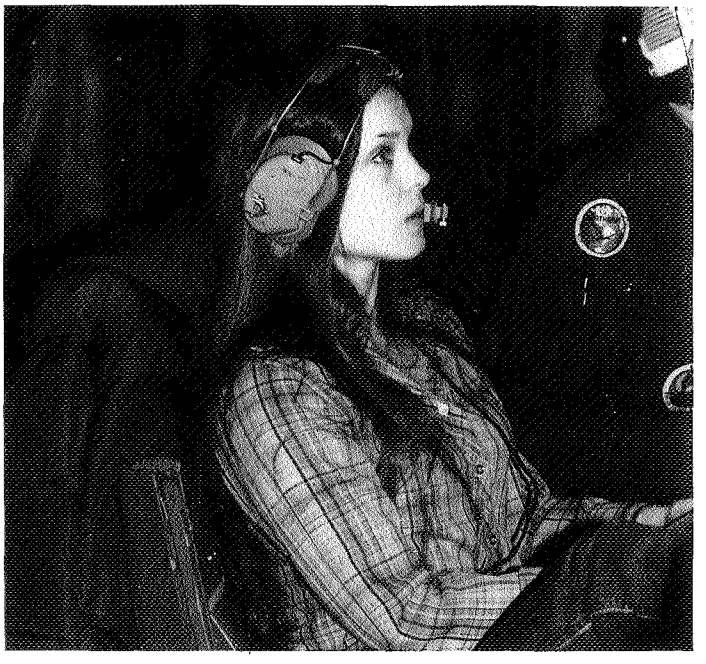

Tamara Jernigan (1986)

Airborne Astronomy Symposium on the Galactic Ecosystem
ASP Conference Series, Vol. 73, 1995
M.R. Haas, J.A. Davidson, and E.F. Erickson (eds.)

EDISON Mission Summary

Harley Thronson, Jr.
University of Wyoming, Wyoming Infrared Observatory, Box 3905, Laramie, WY 82071-3905

Abstract. EDISON is a large-aperture, long-lived space observatory optimized for operation in the 3 to 100+ micron band. It is presently under evaluation by ESA as a candidate for that agency's largest mission class ("Cornerstone").

Primary science goals:

EDISON is proposed to operate as an observatory for the international community. Some "key projects" have been identified, however, which take advantage of the observatory's high sensitivity and long life, including:

[1] Composition, evolution, mineralogy, and petrology of objects out to trans-Pluto distances in the solar system, as well as of planetary material around other stars.

[2] Composition, physical conditions, and evolution of the ejecta of individual dying stars at distances as great as the Virgo Cluster.

[3] Composition, physical conditions, and spatial distribution of the ISM throughout the local universe.

[4] Stellar populations and formation, as well as mass and velocity distribution in very young galaxies at $z > 3$.

Anticipated launch year:	2010+
Design lifetime:	10+ years
Optics temperature:	< 20 K (goal: < 5 K)
Optics emissivity:	TBD
Launch vehicle:	Ariane 5/Proton SL-12/Atlas IIAS
Orbit:	L2 "halo"
Wavelength range:	3 to 100+ μm
Primary mirror diameter:	1.7+ m

Angular resolution: Diffraction limited for > 5 μm

Pointing stability: 0.2 arcsec rms

Field of view: 5 arcmin

Focal plane instruments:

Following ESA guidelines, to be proposed by national groups (presumably a suite of imaging and spectroscopic devices to cover the proposed wavelength range of operation).

Minimum/maximum spectral resolving power: TBD

Total anticipated observing time: 44,000+ hours (@ 0.5 efficiency)

Level of community participation:

Extensive and international via formal collaboration on both spacecraft and instrumentation.

Data format and availability to the community: Following ESA guidelines.

Sponsoring agencies:

Currently under consideration by ESA; formal offer of collaboration by the Russian Space Research Institute (IKI).

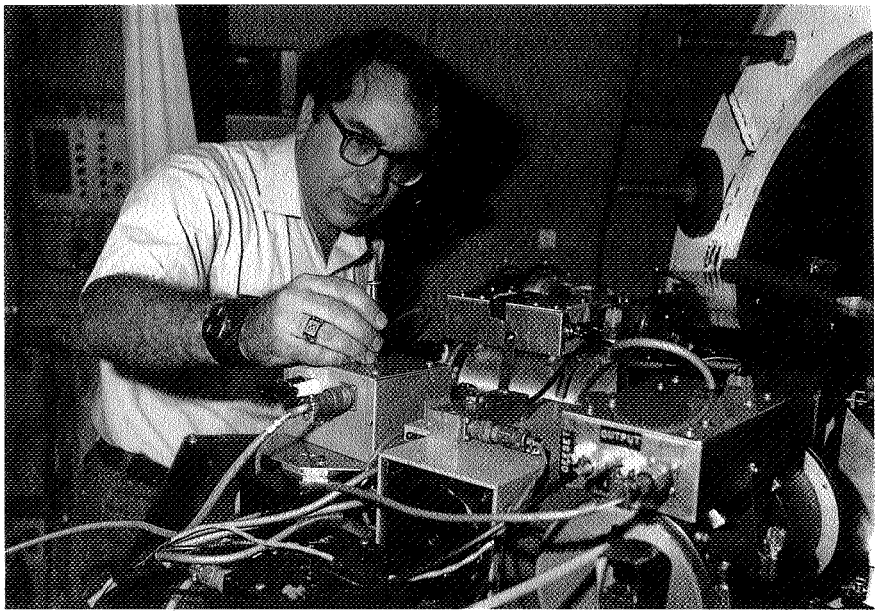

Ted Hilgeman (1978)

Airborne Astronomy Symposium on the Galactic Ecosystem
ASP Conference Series, Vol. 73, 1995
M.R. Haas, J.A. Davidson, and E.F. Erickson (eds.)

SOFIA: The Future of Airborne Astronomy

E. F. Erickson
NASA/Ames Research Center, MS 245-6, Moffett Field, CA 94035-1000

J. A. Davidson
SETI Institute; NASA/Ames Research Center, MS 245-6, Moffett Field, CA 94035-1000

Abstract. For the past 20 years, the 91 cm telescope in NASA's Kuiper Airborne Observatory (KAO) has enabled scientists to observe infrared sources which are obscured by the earth's atmosphere at ground-based sites, and to observe transient astronomical events from anywhere in the world. To augment this capability, the United States and German Space Agencies (NASA and DARA) are collaborating in plans to replace the KAO with a 2.5 meter telescope installed in a Boeing 747 aircraft: SOFIA – The Stratospheric Observatory for Infrared Astronomy. SOFIA's large aperture, wide wavelength coverage, mobility, accessibility, and sophisticated instruments will permit a broad range of scientific studies, some of which are described here. Its unique features complement the capabilities of other future space missions. In addition, SOFIA has important potential as a stimulus for development of new technology and as a national resource for education of K–12 teachers. If started in 1996, SOFIA will be flying in the year 2000.

1. Airborne Astronomy – the Legacy

For nearly three decades astronomers have been making infrared observations from aircraft based at NASA's Ames Research Center in California. In 1965 Gerard Kuiper used the NASA Convair 990 to show that the clouds of Venus were nearly devoid of water, demonstrating the advantages of airborne observations in the near infrared. In 1968 the Ames Learjet was used by Frank Low to measure far infrared luminosities of Jupiter and Galactic nebulae. In 1974 the Kuiper Airborne Observatory (KAO) started its now 20 year career as a national facility for astronomy. Its users have produced ~ 1000 refereed publications, and ~ 50 Ph.D. theses for students at U.S. and foreign universities; it also supports kindergarten through high school teacher outreach programs. A good review of the KAO program and its contributions to science, education, and technology is given by Larson (1994).

Most infrared radiation from astronomical objects which never reaches the ground is detectable from the lower stratosphere. This fact is the principal justification for an airborne telescope. Figure 1 plots computed atmospheric transmission (Traub & Stier 1976) as a function of wavelength for aircraft (14 km) and mountain-top (4 km) altitudes. The absorption is largely due

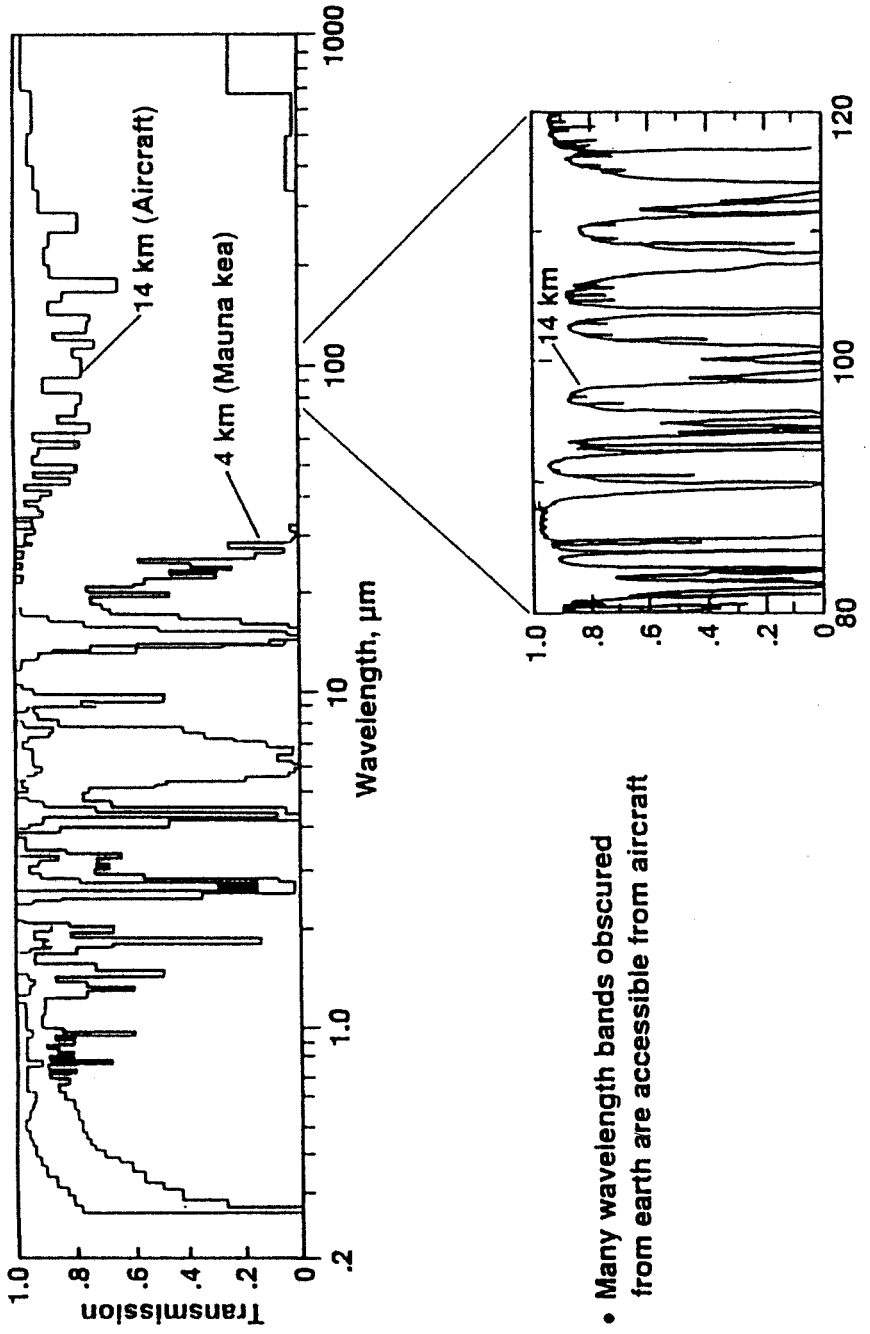

Figure 1. Atmospheric Transmission versus Wavelength

to water vapor, with significant contributions from carbon dioxide and ozone in some wavelength bands. The model assumes overhead water quantities of 2.3 μm for the aircraft and 1.2 millimeters for the ground-based telescope, and a zenith angle of 60 degrees. From 14 km, the broadband atmospheric transmission is adequate ($\gtrsim$70%) for photometric observations at most infrared wavelengths, but the emissivity limits detector sensitivity due to the fluctuations in the arrival rate of the photons from the sky. A number of the water lines in the far infrared are still saturated at aircraft altitudes, as shown in the lower panel. Between these lines the transmission can exceed 95%, the emissivity is correspondingly low, and so high resolution spectrometers can achieve sensitivity limited principally by the emission of the telescope.

Despite the numerous saturated atmospheric lines at aircraft altitudes, most important astronomical spectral features can be measured from an airborne observatory. To demonstrate this, we list in Table 1 the spectral features originating in the interstellar medium (ISM) which have been observed from the KAO. These features characterize important phases of material in the ISM: molecules, neutral and ionized atoms, and solids, as discussed in Section 3. A sample of the research done from the KAO is presented in this volume.

The extensive scientific and technical heritage of the airborne program, and particularly our experience with the KAO, provides a solid basis to project the performance and the design of the next generation airborne observatory – **SOFIA**.

2. Characteristics and Performance

SOFIA's characteristics are summarized in Table 2. The large aperture and wavelength range, routine accessibility to most infrared wavelengths, and mobility are unique features of the observatory (Caroff 1994). Relative to the KAO, SOFIA will be roughly ten times more sensitive for compact sources, enabling observations of fainter objects and measurements at higher spectral resolution. Also, it will have three times the angular resolving power for wavelengths greater than about 10 μm, permitting more detailed imaging throughout the far infrared.

The anticipated performance of SOFIA is indicated as a function of wavelength in Figures 2 through 5. Figure 2 shows the expected image quality, which is limited by seeing from the air flow over the telescope cavity at visible and near infrared wavelengths, and by diffraction at long wavelengths. The specified performance of the optical system limits the image quality in the $\sim 4-10$ micron range. Figure 3 shows the anticipated photometric sensitivity per pixel, which is simply scaled from the performance achieved on the KAO. Here "PSC" and "FSC" refer to the IRAS Point Source and Faint Source Catalogues, respectively. We see that SOFIA would be able to observe any of the compact infrared sources in these catalogues. High resolution spectrometers are expected to be available for most of the wavelength range of SOFIA, as indicated in Figure 4. Interstellar lines are typically broadened to a km/sec or more, whereas higher resolving power can be useful for study of solar system objects. Spectroscopic sensitivity, shown in Figure 5, corresponds to the spectral resolving power shown in Figure 4. Narrow lines emitting more than 0.1% of the total continuum emission from the IRAS sources should be detectable. The important cooling lines of neutral

Table 1

INTERSTELLAR SPECTRAL FEATURES DETECTED FROM THE KUIPER AIRBORNE OBSERVATORY

DUST GRAINS		ATOMS		MOLECULES	
λ (μm)	SPECIES	λ (μm)	SPECIES	λ (μm)	SPECIES
2.95?, 6.3, 7.1 a	NH_3 Ice	1.88, 2.62, 2.67, 2.76, 4.65,	H I	1.4, 1.8 a	C_2
5.2, 5.6, 6.2, 6.9, 7.6, 7.8	PAH	5.91, 6.6, 7.5, 52.5		2.0, 2.6, 7.5 a	C_2H_2
5.5 a	HCO in Ice	3.1, 7.5	Ni I	2.3, 4.6, 77, 84, 87, 97, 100, 103,	CO
6.0, 62, 45 a/e	H_2O Ice	4.5	Mg IV, Ar VI (?)	119, 124, 153, 163, 174,	
6.8 a	Hydrocarbon	5.6	Mg V	186, 200, 289, 302, 650	
19.0 a/e	silicate	6.6	Ni II	2.9 a	C_2H
24-30+	MgS (?)	6.98	Ar II	3.0, 3.5, 7.5 a	HCN
45, 62 a/e	H_2O	7.63	Ne VI	5.0 a	C_3
		8.99, 21.8	Ar III	8.5	Si O
		17.9, 26.0	Fe II	17.0	H_2
		18.7, 33.4	S III	53.4, 84.4, 84.6, 119.3,	OH
		22.9	Fe III	119.5, 149, 163.1, 164.4, 202 a/e	
		24.3	Ne V	154, 308	^{13}CO
		25.2	S I	120.0, 120.2 a/e	^{18}OH
		25.9	O IV	125, 166, 524	NH_3
		34.8	Si II	149.1, 149.4, 203	CH
		36.0	Ne III	479	HCl
		51.8, 88.4	O III	790, 1600	H_2O
		57.3	N III	805	H_2D^+
		63.2, 146	O I		
		121.9, 205	N II		
		158	C II		
		158	^{13}C II		
		370, 609	C I		

Almost all of these features were first detected from NASA's airborne observatories, and cannot be studied from ground-based sites. Features seen in absorption are indicated with "a", and seen in both emission and absorption with "a/e". Whereas the dust features typically originate in regions cooler than a few hundred degrees Kelvin, the various gaseous lines originate in regions ranging in temperature from ~10^5K down to ~10K. Thus these infrared spectral features characterize material in all phases of the interstellar medium: solid particles, molecules, neutral atoms, and ionized atoms.

Table 2
Summary of Basic SOFIA Characteristics

In-flight access to focal plane instruments – continuous
Vehicle – Boeing 747
Operating altitudes – 41,000 to 45,000 feet
Aircraft-limited duration at or above 41,000 feet $\gtrsim$ 5 hours
Nominal flight duration (crew-limited) – 7.5 hours
Research flights per year – $\sim$ 160
Number of PI teams flown per year – $\sim$ 60
Number of focal plane instruments flown per year – $\sim$ 15
Frequency of science proposal peer review – annual
Stabilized telescope system weight – $\sim$ 8,000 kg
Effective primary mirror diameter – $\sim$ 2.5 meters
Wavelength range – 0.3 to 1600 microns
Telescope configuration – Nasmyth
Design f/ ratio – $\sim$ 20
Design plate scale – 4 arcseconds/mm
Unvignetted field of view – 8 arcminutes
Telescope optical image quality $\lesssim$ 1 arcseconds
Shear layer seeing – $\sim$ 3 arcseconds (0.3 to $\sim$5 microns)
Diffraction-limited at wavelengths – $\gtrsim$ 10 microns
RMS pointing stability – $\lesssim$ 0.2 arcseconds
Telescope emissivity – $\lesssim$ 15%
Telescope elevation range – 20 to 60 degrees
Nominal operating optics temperature – $\sim$ 250K

oxygen at 63 μm and C^+ at 158 μm from photodissociation regions are typically this strong relative to the continuum. Shocked interstellar gas will produce a higher line to continuum ratio.

3. Science

The infrared spectral regime encompasses a multitude of rich and varied physical processes and is uniquely suited for the study of cosmic birth on all scales. SOFIA will be an essential tool in many of these studies. Among the primary goals of SOFIA scientists is a detailed and comprehensive study of the processes which lead from cold clouds in the Interstellar Medium (ISM), through the formation and evolution of stars and planetary systems, to the eventual return of processed material to the ISM. Astronomers will also use SOFIA's superior spatial and spectral resolution to examine the dust and gas in the vicinity of our Galactic Center, to search for the signature of a massive black hole which may be the central powerhouse of the Galaxy, and to examine the origin of the massive stars observed there. On still larger scales, SOFIA will provide new understanding of global star formation in galaxies and the origin of the extraordinary luminosities of some infrared-emitting galaxies discovered by IRAS. In addition, the unique mobility of an airborne observatory

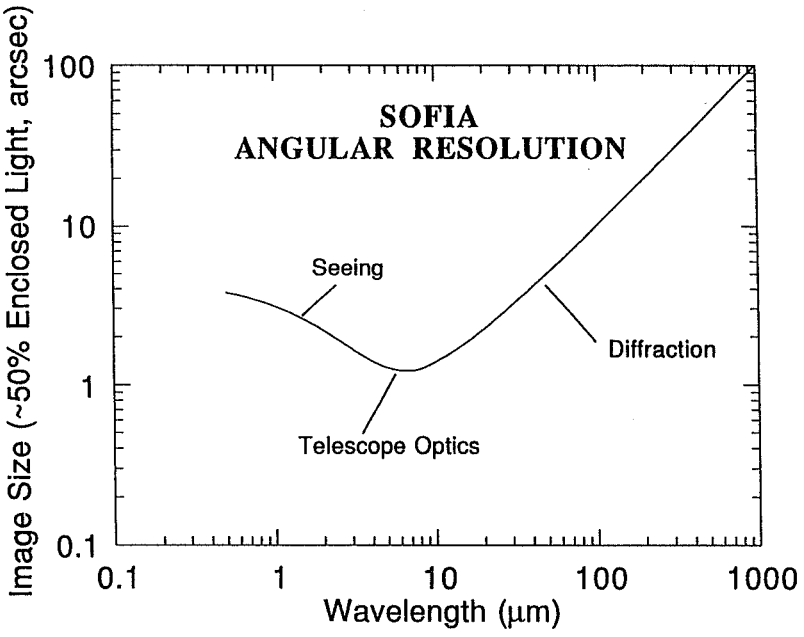

Figure 2. Anticipated image quality versus wavelength.

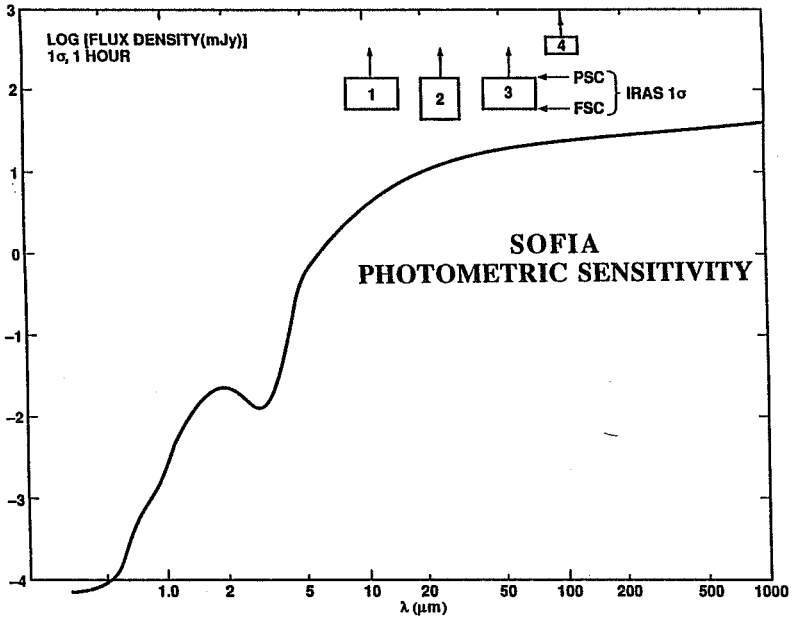

Figure 3. Anticipated photometric sensitivity versus wavelength.

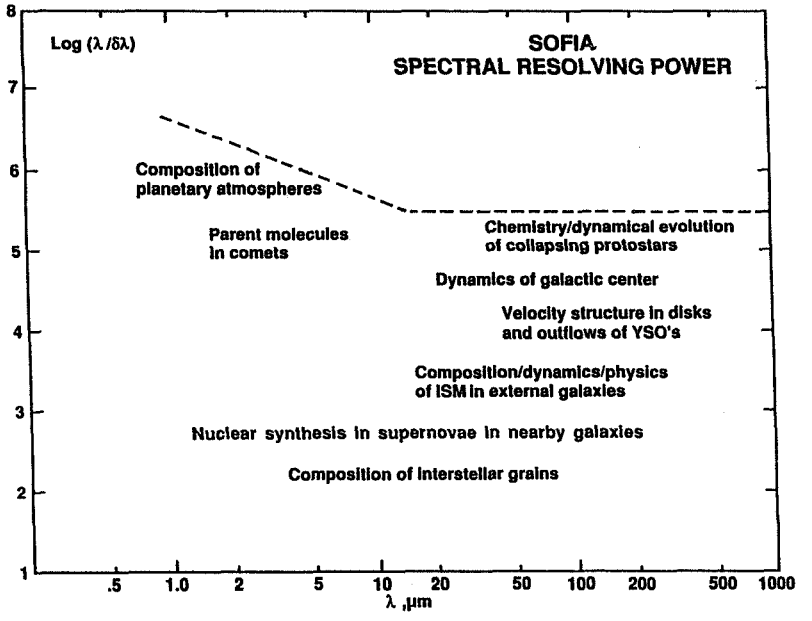

Figure 4. Anticipated spectral resolving power versus wavelength.

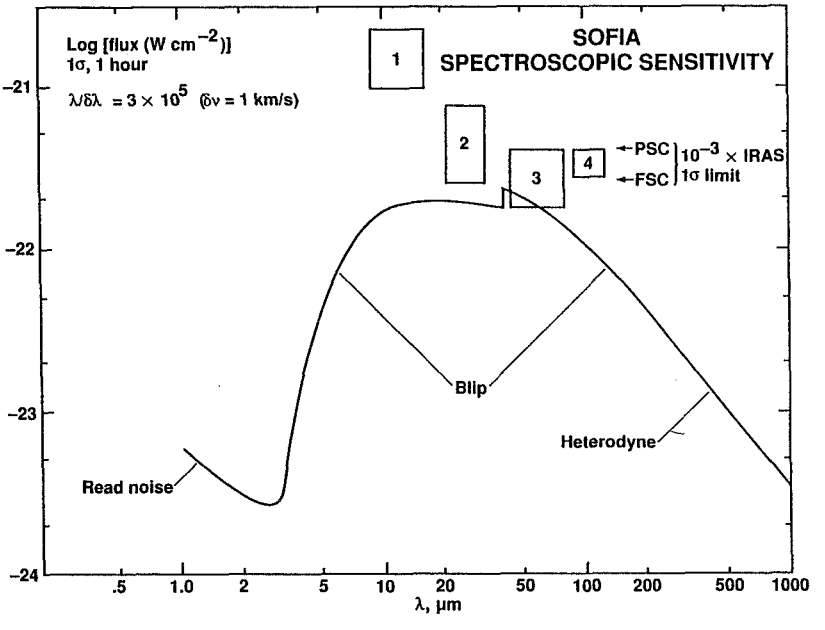

Figure 5. Anticipated spectroscopic sensitivity versus wavelength.

allows effective response to a number of highly localized and sometimes quite transient phenomena, such as solar eclipses, comets, novae, supernovae, and stellar occultations by solar system bodies. We discuss a number of specific examples below:

(i) The Interstellar Medium

All galaxies are permeated by an Interstellar Medium, but with properties which may vary greatly from galaxy to galaxy. Fundamental components of the ISM – solids, molecular gas, neutral atomic gas, and ionized gas – are characterized by infrared, far-infrared, or sub-millimeter emission and this emission generally dominates the cooling of the gas and dust. Observations of the ISM are critical to the study of the cycle of gestation, birth, evolution, and death of stars for the following reasons:

(a) The composition of the ISM determines the chemical makeup of the objects which form from it; (b) The structure, energy balance, and physical state of the ISM in a particular region determine the nature of subsequent evolution, for example in the formation of high mass versus low mass stars; (c) The structure and dynamics of the ISM, in turn, are strongly influenced by young stars which interact with the ISM via wind-driven shocks and ultraviolet radiation; and (d) Interesting phenomena are often embedded in dense, dusty regions of the ISM and can only be observed indirectly through the interaction of the source with the ISM. Therefore an understanding of the properties of the ISM is essential to interpret observations of the embedded sources correctly.

From SOFIA, astronomers would map the total and polarized thermal continuum from cool dust in molecular clouds with high spatial resolution, as well as the corresponding power radiated in atomic fine structure and rotational molecular lines. These measurements provide estimates of the density, luminosity, temperature, chemical and dust grain makeup, magnetic fields, dynamics, and detailed morphology of these regions.

Carbon chemistry is the basis of life as we know it, and has its beginnings in the ISM. Carbon emission lines also provide a large percentage of gas cooling in the ISM, thus altering the ISM environment and subsequent chemical evolution. Spectroscopy will yield particularly significant results on carbon chemistry in clouds, via

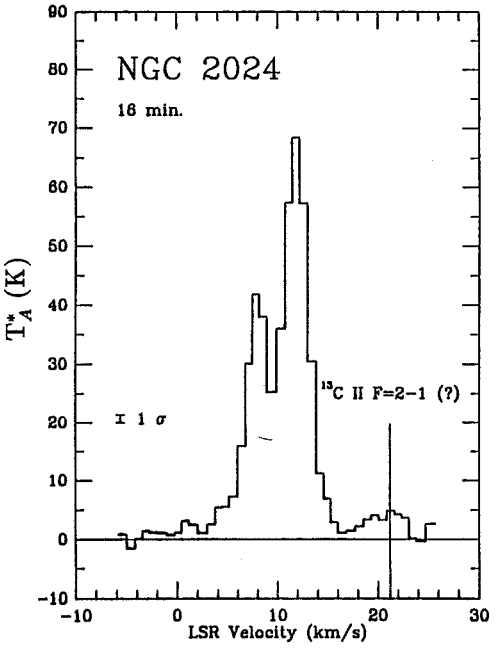

Figure 6. Velocity resolved spectrum of C^+ at 158 μm.

the 158 μm C^+ line, the 370 and 609 μm C lines, a host of FIR and submm rotational CO lines, and numerous near-infrared absorption lines of basic organic molecules such as CH_4, C_2H_2, and C_2H_4. As an example, Figure 6 shows a KAO measurement of the C^+ line from NGC 2024, a molecular cloud/ionized gas complex, obtained with a velocity resolution $\lesssim$1 km/s. Line observations at such high spectral resolution provide information on systematic and turbulent motions within a cloud.

(ii) Star Formation

The ubiquitous associations of young stars with dark clouds clearly tells us that star formation occurs in dense regions of the ISM. The star formation process is not well understood. For example, it is not known why or when a region of a cloud will start to collapse. In order to form a one solar mass star, the collapse must extend to a radius of about 10^{17} cm in a quasi-stable dense clump in an interstellar cloud. This distance would correspond to just under an arcminute on the sky if we were observing the collapse in the nearest star formation region, the Taurus cloud, which is 160 pc away. SOFIA's ten arcsecond resolution at 100 μm will readily resolve this infall region. The radiation from the star formation region in its early stages of evolution would be dominated by an accretion shock around the small protostar, and would peak in the far-infrared due to the large dust opacity in the surrounding cloud.

A number of IRAS point sources have been studied from the KAO and have been shown to be visibly obscured young stellar objects (YSO's). The improved spatial resolution of the KAO over IRAS has allowed determination of the mean densities and temperatures of the infall regions and star formation environments. SOFIA's ten times better sensitivity and three times higher spatial resolution will enable us to make detailed images of the infall regions and their envelopes. SOFIA will, for the first time, detect the dominant cooling transitions of the infalling gas and directly measure the mass infall rate and velocity structure by high spectral resolution observations of the far infrared CO and O I emission lines. High spatial resolution observations of the dust continuum will probe the density structure of the circumstellar gas down to scales of 100–1000 AU. The ambient molecular core is expected to have a density $\propto r^{-2}$, while the infall region theoretically has a density $\propto r^{-3/2}$. The infalling gas and dust generally have sufficient angular momentum to impact an opaque ($\sim$100 AU) accretion disk which orbits and feeds the growing star. SOFIA will measure infrared OH spectral lines generated in the accretion shock and thereby determine the mass accretion rate, the location on the disk where the infalling gas and dust mainly strike, and the angular momentum of the impacting material. In summary, SOFIA will revolutionize our understanding of the collapse phase of star formation.

In massive clouds, stars often form in clusters where we currently cannot separate the individual YSO's. Many of these could be isolated in the beam of SOFIA so that, for example, their individual luminosities, masses, and motions relative to one another could be determined. The shape and color of the continuum spectra reveal the evolutionary state of the system. These observations will greatly help us understand the process of fragmentation of large clouds to form star clusters.

(iii) Bipolar Outflows

Since the 1980's, observations have shown that many embedded YSO's are associated with powerful bipolar outflows. These outflows may collide with the circumstellar gas and cause accretion to cease. In this way, they may help determine the final mass of the star. Several theories have arisen to explain the origin of these protostellar winds; they share a common idea that magnetic fields rotating with the protostar or the disk fling trace ions from the inner part of the disk outwards and these ions drag neutral gas along. With SOFIA we can look for evidence of simultaneous inflow along the equatorial plane with outflow along the poles, determine the stage in the evolution of a star when the outflows "turn on", trace the shock interaction of the outflow with the circumstellar gas, and measure the mass-loss rates in the protostellar winds with good fidelity by observing the luminosities in shock-excited O, S, and Si II fine structure lines. FIR polarimetry from SOFIA of the infall regions will show, in the more luminous cases, the association between magnetic fields and outflows.

(iv) Circumstellar Disks

Circumstellar disks have been observed around T Tauri stars, which are thought to be very young stars with masses comparable to that of our Sun. These stars and their disks are formed in obscuring parent clouds. It is thought that the outflows mentioned above could eventually halt the disk accretion. The outflows could also dissipate the surrounding cloud, making the YSO's eventually visible as T Tauri stars. At a later evolutionary stage the disks will dissipate or form planets, and there will be considerable disk clearing. Theoretical models predict that OH emission produced by shock waves set up in the disks by accreting material should be detectable from SOFIA, and the OH line luminosities and profiles can be used to measure the mass accretion rate feeding the disk and the location on the disk where the infalling gas and dust mainly strike. Photometric submm and FIR observations help determine the mass of the disk, which is an essential quantity in understanding planet formation and how disk instabilities may cause the orbiting particles to spiral inwards and accrete onto the star. The disk mass and the accretion rate onto the disk determine the timescale for the formation of the disk; if this timescale is very short it may indicate that, on average, the disk feeds material onto the star as fast as infalling material feeds the disk. Observations of T Tauri stars have shown indirectly that circumstellar disks are generally not much more than 100 AU in diameter – comparable to the size of the solar system – or about 0.6 arcsec at 160 pc. However, HL Tau has been observed at millimeter wavelengths to have a dim 4000 AU (or 24 arcsecond) diameter disk, and FIR photometry from the KAO shows extended emission associated with several T Tauri stars, for example SVS 13. One theory posits that the extended disks are caused by ordered magnetic fields in the ambient cloud which channel the infalling material to an equatorial "pseudo-disk" that is not rotationally supported. The infalling gas then falls radially inward along the equator until it strikes the much smaller rotationally supported disks. Thus at an early stage of their evolution, these disks may be sufficiently extended and luminous to be imaged directly at FIR and submm wavelengths from SOFIA, which would be an exciting and extremely important input to theoretical understanding of low- and intermediate mass star formation.

At later stages of circumstellar disk evolution, when planets are forming or have formed, the disks are harder to see. However, there are $\sim$ 50 candidates for evolved stars with disks which are on the order of 20 times closer to Earth than the nearest T Tauri star, and at their distances 100 AU in the disk corresponds to 10 – 15 arcsec on the sky. The spatial resolving power and sensitivity of SOFIA will allow direct imaging of the structure of a number of these disks for the first time in the FIR. For example, Beta Pictoris ("β Pic") is a main-sequence star that is 17 pc away from Earth with an infrared-luminous disk discovered by IRAS. The infrared disk diameter is $\sim$ 2400 AU, or 140 arcseconds, with the bulk of the infrared flux coming from the central 30 arcseconds. The total IRAS 60 μm flux of the disk, when distributed into five arcsecond diameter pixels – the resolution of SOFIA at 60 μm – will require less than 30 minutes of integration on SOFIA for a signal to noise ratio of 10. It will be possible, therefore, to determine the disk temperature profile and morphology. Combining these results with the knowledge of the illuminating star, β Pic, will enable the properties of the dust in the disk to be studied, in particular the dust-grain size distribution. Figure 7 shows the visible β Pic system with the 5 arcsecond diameter, 60 μm SOFIA beam. The properties of the dust are important since it is probably from these particles that the cores of planets may eventually form, if not in the β Pic system, then in similar disks around other stars. SOFIA can map spectroscopic features in the disk as well, for example the water ice feature at 48 microns and the polycyclic aromatic hydrocarbon (PAH) features at 5.2, 6.2 and 7.7 microns. Such features help to ascertain the composition of the dust and hence the nature of planets which may be forming at particular locations in the disk.

Figure 7. Optical photograph of the β Pic disk, with 60 μm SOFIA beam size superposed. The stellar image has been blocked with an occulter.

(v) Our Solar System

The initial composition of our pre-solar nebula is of great interest because it contained the building blocks of the planets and of life. SOFIA's ability to explore an early pre-planetary system environment through observations of nearby circumstellar disks was discussed in §(iv). SOFIA will also image, spectroscopically as well as photometrically, dense clumps in nearby dark clouds, in order to determine the composition of future pre-solar nebulae. However, to better understand the origin of our Solar System, studies of comets, planets, and satellites are essential.

Comets

Comets are aggregates of ice, dust, and organic solids that accumulated in the region of the solar nebula where the outermost planets formed, and as such they are the most accessible repositories of chemical remnants of the original interstellar material that spawned the solar nebula. Observations of many comets show that they are an eclectic sampling of different regions of the solar nebula; some show abundant reduced carbon, some show no carbon at all, some exhibit silicate minerals, and others show hydrocarbons and minerals in various proportions.

Spectroscopic studies of comets in the near infrared ($2-8\ \mu$m) with SOFIA can address questions of the chemistry and processing of carbon in the solar nebula through analyses of the reduced carbon (CH_3OH = methanol, and other organics) and oxidized carbon (CO_2 = carbon dioxide). Carbon dioxide in comets cannot be observed from the ground, but with a favorable Doppler shift, high-resolution spectroscopy from SOFIA will permit observations of this key molecule in the volatile carbon budget. Even though the discovery of organic material in the nuclear dust of Comet Halley was achieved from the ground looking at the C–H stretch feature near 3 microns, in order to determine the nature of the molecules producing this feature we must observe these species between 5 and 8 μm where the C–O, C–C, and C–N stretch bands are found. Again these wavelengths cannot be observed from the ground, but are readily accessible to an airborne platform.

Similarly, water in comets cannot be detected from ground-based observatories, but as demonstrated by its discovery in Comet Halley from the KAO (Figure 8), water is readily measured at high spectral resolving power ($\sim 10^5$) from the lower stratosphere. The ortho-to-para ratio in the hydrogen in H_2O in comets (measurable at 2.75 μm), as well as the deuterium content of the water (HDO/H_2O), establishes the temperature of formation of the comets (~ 30 K for Halley), as well as the local chemistry of the solar nebula at the comet formation site(s). A basic question about the local chemistry is whether the processing of water and the organics was controlled by kinetics or by ion-molecule reactions. The relevant observations can only be made from SOFIA, whose large aperture, long lifetime, and sensitive two-dimensional array spectrometers will make available many more comets than can be observed from the KAO.

Finally, SOFIA will have the sensitivity to study solid state features (such as water ice and olivine) in short period comets. These comets have orbits that extend to about 7 AU from the Sun, and therefore may contain material that has undergone considerable processing by solar radiation. Comparison of these materials with those seen in long period comets, which sample a more pristine environment, will be extremely interesting.

Planets and Satellites

A related fundamental question concerns the initial compositions of the volatiles incorporated into the giant planets and their satellites during formation, since these would imply certain conditions in the regions of the solar nebula where they formed. Two extreme models are that the outer planets and their satellites consisted of (a) water, methane, and ammonia (in order of decreasing abundance) or (b) carbon monoxide, water, and molecular nitrogen. In the

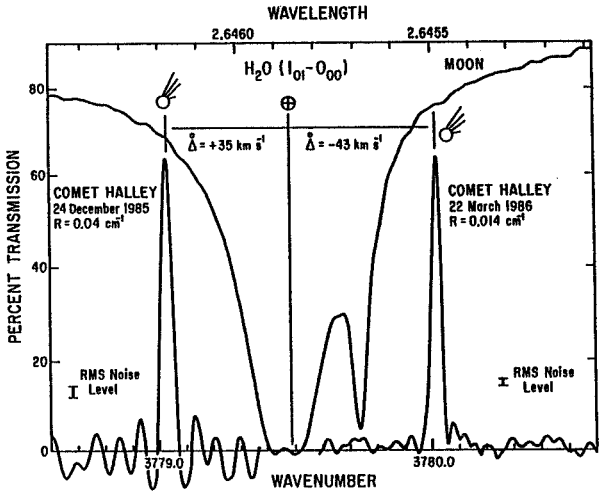

Figure 8. Spectra of water in Comet Halley and the moon taken from the KAO, which was scheduled to maximize the Doppler-shifted separation of the comet and telluric features. The spectral resolving power is $\sim 2 \times 10^5$.

currently accepted model, the giant planets consisted of composition (b), while in their satellites composition (a) dominated. Jupiter and Saturn might have converted the carbon monoxide to carbon dioxide and methane, and the nitrogen to ammonia, but Uranus and Neptune should have retained substantial amounts of their original composition. The satellites of the outer planets may retain surface spectral signatures of the primordial partitioning of these constituents. It is therefore important to determine the composition of the volatile-rich outer planet satellites and Pluto, the composition of their atmospheres (if any) and the nature of the surface-atmosphere interactions.

Better understanding of the atmospheres of the giant planets will further elucidate questions about the chemistry of the solar nebula. High resolution spectroscopy from near infrared to submillimeter wavelengths enabled by SOFIA will be especially suited to measurements of trace constituents in the atmospheres of the giant planets. Several trace gases on Jupiter (*e.g.*, GeH_4 and CO, present at the 10^{-8} levels of concentration with respect to H_2) have been found with the KAO in the $2-5$ μm spectral region. The determination of a larger inventory of these constituents in Jupiter and the other giant planets from sub-millimeter spectra, and the computation of the vertical distribution profiles, will yield fundamental information on the photochemistry in the atmospheres of these planets. Some of the same photochemical processes occur in the atmospheres of the Earth and other terrestrial planets, thus allowing comparative studies of direct relevance to our own planet.

SOFIA's angular resolution will permit zonal resolution on a number of Solar System bodies. Imaging spectroscopy will reveal spatial variations of atmospheric, comatic, or surface constituents with a resolution of about 2 arcsec in the near infrared, increasing to 10 arcsec at 100 microns. The spatial resolution also reduces line broadening. On Mars (diameter 4800 km), 2 arcsec

corresponds to ~ 400 km, and on Jupiter (diameter 14300 km) to ~ 700 km. Spatially resolved spectra of Mars with SOFIA will give important information on the exchange of volatiles (CO_2, and perhaps H_2O) between the polar caps and the temperate regions as the Martian seasons change, and will reveal the zonal and latitudinal distribution of the major and minor atmospheric constituents. SOFIA can resolve the Great Red Spot of Jupiter in the $2-8$ μm region where the chromophores, causing the still-unexplained color, may have their diagnostic spectral signatures.

In addition, much valuable research will be done from SOFIA on planetary bodies too small to be spatially resolved. For example, Pluto and Triton are two significant bodies in the outer Solar System, each composed of a mixture of rock and ice. Their tenuous atmospheres (of mostly nitrogen) appear to be in vapor pressure equilibrium with their surface ices. Both Triton and Pluto experience extreme seasonal cycles, and determining the interaction between their surfaces and atmospheres over these cycles is quite complex. Understanding this interaction requires simultaneous knowledge of several related parameters, such as the dimensions of the body, albedo distribution across the surface, temperature, surface composition, and atmospheric density. Significant variations in the parameters will occur during the lifetime of SOFIA. A unique contribution to this problem will be SOFIA's observations of stellar occultations by Pluto and Triton over the years, to determine the densities of their tenuous atmospheres at various points in their seasonal cycles. The same observations are vital in constraining the diameter of Pluto (Triton's diameter is already well known from spacecraft data). FIR photometric measurements from SOFIA can provide the color temperature and its variation with rotation and season for both bodies. In combination with optical photometry, these data will provide information on the albedo distribution and its time variation. Finally, low-resolution IR spectroscopy will provide new information on the composition of the surface ices.

Stellar occultations, which probe Solar System objects with a spatial resolution of only a few kilometers, are of course applicable to a variety of other problems. An airborne observatory is ideally suited to this powerful technique, since it permits the telescope to be optimally located and weather-free for a particular event. The value of deployment has been demonstrated by the KAO's history of occultation work, most dramatically by the discovery of the ring system around Uranus in 1977 (Figure 9).

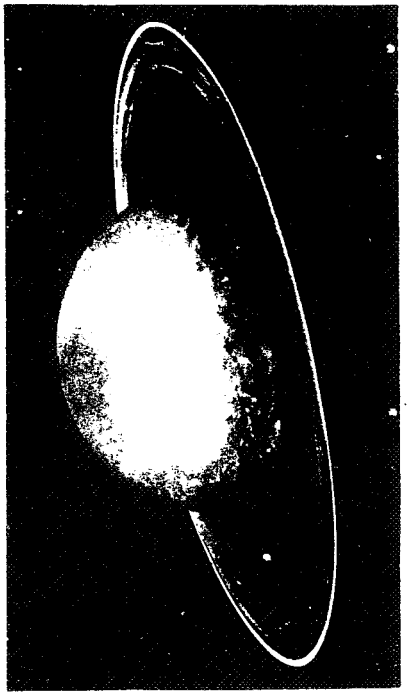

Figure 9. Artist's concept of the rings of Uranus discovered from the KAO.

SOFIA will be capable of observing many more occultations than the KAO, with greatly improved signal-to-noise, because of its increased aperture. Besides the studies of Triton and Pluto, SOFIA can obtain temperature, pressure, and number density profiles of the atmospheres of Uranus and Neptune, bodies for which no spacecraft entry probes are currently planned. SOFIA can also be used, in conjunction with ground-based information observations, to vastly improve our knowledge of Saturn's ring dynamics through observations of a series of ring occultations. From observations spanning several years, the orbits of the edges and narrow singlets in the ring system can be determined with much greater precision than has been possible with flyby spacecraft. Improved orbital information will lead to further understanding of the ages of the rings (whether they were formed with Saturn or more recently), the evolutionary processes in particle disks, and the internal structure of Saturn (from its gravitational harmonic coefficients).

As spacecraft are sent to Jupiter (Galileo), Saturn (Cassini), and to the small bodies of the Solar System (e.g., Clementine and NEAR), supporting observations from SOFIA will be of long-term importance. For example, the infrared spectrometer ($\sim$ 15 – 500 μm) planned for Cassini has a spectral resolution of only 1 cm^{-1}, sufficient for detection of molecular lines in the far-infrared, but insufficient for observations of the intrinsic line profiles. Complementary high-resolution spectroscopy from SOFIA will establish the intrinsic line shapes to reveal physical conditions, in the atmospheres of Saturn and Titan, for example. Similarly, results obtained from SOFIA may help to define future space missions, as the KAO occultation results on Pluto have done for the Pluto Fast Flyby mission.

(vi) The Sun

The star that influences Earth the most is our Sun, not only through its radiation but through its solar wind as well. The solar wind originates in the chromosphere and corona, although the energy transport mechanism which heats the corona and drives the wind is not well understood. Oscillation of the solar atmosphere probably plays a role in this process, and pioneering FIR observations on the KAO, combined with ground-based sub-millimeter observations, have detected the oscillations at different depths in the solar atmosphere. Wavelength-dependent phase differences show the vertical transport of energy at the oscillation frequency. Far-infrared beam sizes from SOFIA will be well matched to the size of the oscillation cells, and will provide improved information on the strength of the oscillations and on the correlation between adjacent cells. This will yield significant insight into the energy transport mechanisms in the solar atmosphere.

(vii) Stellar Structure

In the last fifteen years, studies of multi-mode pulsations in the Sun (helioseismology) have revealed a wealth of detail concerning the Sun's internal structure and dynamics. Observations of pulsations on other Sun-like stars would extend our understanding of stars in general, and in particular would permit more exhaustive tests of stellar evolution theories than previously possible. CCD ensemble photometry at visible wavelengths provides one of

the most promising techniques for measuring such pulsations, but the expected pulsation amplitudes for Sun-like stars are small (only about three micro-magnitudes), while the best ground-based observations (conducted with a network of 4 meter-class telescopes) produce detection limits about 5 times as large.

Ground-based photometry is limited in precision by scintillation noise, which arises mostly in the troposphere. Simple scaling of ground-based scintillation noise to SOFIA, ignoring the lower turbulence amplitude in the stratosphere, indicates that the signal-to-scintillation noise ratio will be at least a factor of 3 lower than for a 10 meter ground-based telescope. This noise level would permit detection of solar-like pulsations within about 3 hours of observing time from SOFIA on any of about 300 stars. Rough amplitude estimates alone would significantly probe the mechanisms that excite and damp oscillations in stars like the Sun. For suitable stars (G and K dwarfs brighter than roughly 6th magnitude), observing the same star for 2 hours at the beginning and end of a 7.5-hour flight would allow resolution of the so-called "large frequency separation" in the stellar frequency spectrum, which immediately yields a precise estimate of the mean stellar density. Observations of one star over several nights could provide accurate frequency estimates for up to a dozen pulsation modes. Thus SOFIA will enable a significant program of stellar seismology.

(viii) Reprocessing of the ISM

The bulk of the elements heavier than helium have been synthesized in dying stars. These stars have finished the hydrogen burning phase in their cores and have commenced burning helium to form heavier elements. The central material is then mixed to the surface and is observable in the infrared in the form of bands of molecules, such as CN and CO, in the stellar spectrum. As the star evolves, these surface elements can be ejected back into the ISM by stellar winds, as in the case of the red giants, or in some cases by the loss of the star's whole outer shell, either at a non-catastrophic rate, as in the case of a planetary nebula, or at an explosive rate, as in the case of a supernova. In supernovae considerable nucleosynthesis of heavy elements can occur in the blast; for example observations from the KAO detected lines from nickel, cobalt, and iron atoms produced by the explosion of Supernova 1987A. The KAO also detected the formation of dust in the ejecta about 600 days after the explosion. SOFIA's sensitivity and resolution would permit improved studies of bright supernovae in other galaxies. Also, SOFIA will be well suited to study the common mass-loss stars such as the red giants and planetary nebulae, with sufficient sensitivity to permit resolution of the spectral lines of many important atoms and molecules, permitting studies of both the dynamics and rates of mass-loss.

(ix) Other Galaxies

Observations from the KAO discovered that spiral galaxies typically emit as much energy at far-infrared wavelengths as they do throughout the visible and ultraviolet. The extensive IRAS observations of galaxies showed that many have infrared luminosities exceeding their visible luminosities by factors of ten or more. ISO and SIRTF are anticipated to make great contributions

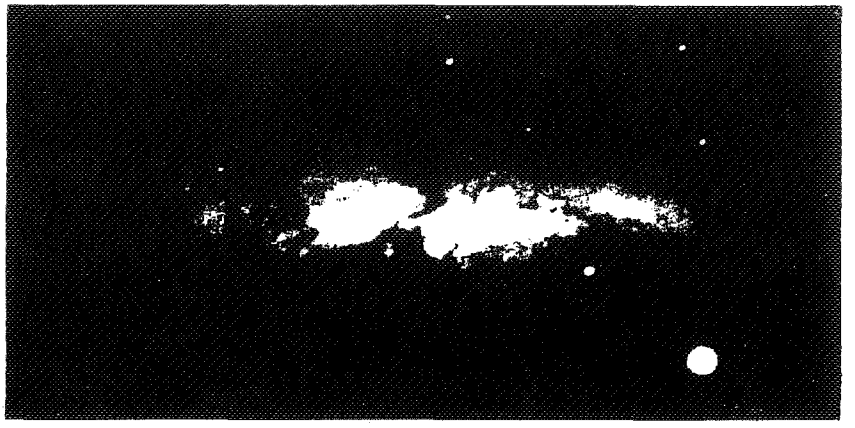

Figure 10. Optical photograph of M82.

to the understanding of other galaxies, but the high spatial resolution and the anticipated development of large far-infrared arrays enable SOFIA to make an important complementary contribution as well. SOFIA will observe nearby ($\sim$ 1 Mpc) spiral and irregular galaxies, nearby ($\sim$ 10 Mpc) starburst and Seyfert galaxies, and nearby ($\sim$ 100 Mpc) extremely luminous galaxies such as Arp 220 and Mrk 231. In the nearby spirals and irregulars, SOFIA's FIR arrays will investigate galactic structure and its influence on star formation at scales $\sim$ 10 pc, primarily by mapping dust continuum and fine structure lines from atomic and ionized gas. At these scales, the relative positions and velocities of the molecular gas, dense photodissociated gas and H II regions, diffuse HI gas, dust IR continuum and the optical images of star forming regions will probe the roles of bars and spiral density waves in controlling star formation. Pressures in the neutral and ionized gas can be determined and correlated with star formation. Elemental abundance gradients can be measured as functions of galactocentric radius to constrain the past history of star formation and nucleosynthesis.

In nearby starbursts and Seyferts, SOFIA's $\sim$ 100 pc resolution will map the star formation activity in the central kpc and may spatially separate the central interstellar medium affected by an AGN from the more extended region affected primarily by the ultraviolet radiation and shock waves induced by star formation and supernovae. NGC 1068 is an important example of a nearby Seyfert in which SOFIA will separate these two regions. M82 is a nearby starburst galaxy in which SOFIA will help unravel the nature of the central starburst. KAO measurements of O III (52 and 88 μm), N III (57 μm), O I (63 μm) and Si II (35 μm) line profiles from the obscured nucleus of M82 are consistently asymmetric and suggest strong variation in the emission from different components of the source. These components may be areas of intensive localized star formation, or recent supernova outbursts; supernovae are thought to occur in M82 every few years. Judging from radio maps, SOFIA could readily isolate some of the candidate components, but telescopes the size of the KAO and smaller ($\lesssim$90 cm) cannot. The disturbed visible appearance of M82 (Figure 10) gives only a hint of the recent formation and violent demise of massive stars there.

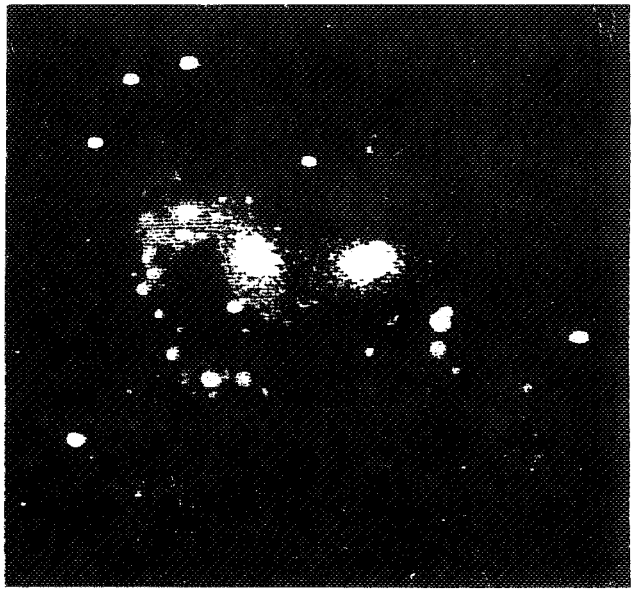

Figure 11. CCD image of the galaxy pair NGC 7318.

Many of the galaxies found to have large infrared excesses by IRAS have subsequently been identified as galaxies in collision. Study of these ultraluminous infrared mergers is seriously hindered at near-infrared, optical, and ultraviolet wavelengths because of the large obscuration by dust embedded in them. However, SOFIA will permit FIR, photometric, and spectroscopic imaging on a scale of $\sim$ 1 kpc, adequate to reveal brightness distributions of emitting dust and gas on a scale comparable to the visible structure seen in many of these systems, and ample to distinguish components such as the active nuclei, the young starburst (O and B stars), the older starburst (SNRs, red supergiants), the shocked clouds, and the old stellar population.

Figure 11 shows the interacting galaxy pair NGC 7318 in Stephan's Quintet. In this false color image, which is a superposition of two optical CCD images taken through different filters, one can distinguish the older generation of stars that make up the bulk of the galaxies from the distribution of ionized hydrogen gas, which traces sites of recent star formation activity within the galaxies. The nuclei of the two galaxies are separated by 20 arcseconds.

Images at different wavelengths, including those beyond 100 μm which IRAS did not sample, will yield temperature and optical depth profiles. Far-infrared and sub-millimeter spectroscopy will probe the excitation conditions, temperature, density, composition, and dynamics of the gas in these systems with similar spatial resolution. Far infrared rotational CO lines, and fine structure lines of O I, Si II, C II, O III, S III, and N III, will be important diagnostics.

(x) The Galactic Center

In many ways, the most exciting place in our own Galaxy is at its center where the stellar densities are very high, stellar collisions are probably frequent, and the existence of a central, massive black hole not unlikely. This region represents the closest galactic nucleus to us. Far-infrared observations have shown that the Galactic Center has an infrared luminosity of roughly 10^7 $L_\odot$, is enshrouded in a dense dust ring, is to some degree shaped by magnetic fields, and is obscured at visible wavelengths by the intervening dust in the galactic plane by a factor of roughly 10^{10}. The distribution of red stars can be studied (with large extinction corrections) in the near-infrared and the distribution of ionized gas can be studied at radio wavelengths. However, the neutral atomic gas, thermally emitting dust, and important characteristics of the ionized gas can best be studied at the wavelengths accessible from SOFIA.

The ring of dust emission about the galactic center, which was first discovered from the KAO, is about 3 arcminutes in diameter and the cavity it defines at the center is only 30 arcseconds in diameter. Current results show that material from the ring (or outside it) may be spiraling into the center, that high turbulent velocities are present, and that magnetic fields may be important in this region. The data are consistent with the existence of a massive central object, possibly a black hole, or a compact cluster of stars. The exact location and character of the dominant source of luminosity in the cavity is unknown; two possibilities are the emission from a black hole accretion disk or emission from a number of massive stars. Of all the candidates for a massive black hole, if it exists, the non-thermal point source SgrA* is the most probable. Further, there is indirect evidence for the existence of a wind or jet originating at SgrA* causing a mini-cavity to be formed in the gas and dust about 5 arcsec southeast of SgrA*.

SOFIA will clarify the picture within the cavity on three times finer spatial scales than possible with the KAO, by resolving regions of different velocities, ionization levels, magnetic field directions (i.e. polarizations), temperatures, and gas densities. For example, a more accurate estimate of the location, UV spectrum, and luminosity of the central powerhouse within the cavity would be obtained by SOFIA by mapping the distribution of dust, neutral atomic and ionized atomic emission within the cavity with a three-fold improvement in spatial resolution over that achievable on the KAO. SOFIA could also study the jet (or wind) originating from SgrA* by measuring the fine structure line emission from the mini-cavity which is 4 arcsec in diameter. Line dilution makes this study impossible from the KAO. In addition, SOFIA could address the puzzle of where the massive stars in the cavity originate, if they are the source of the luminosity. The main sequence lifetimes for such stars are too short for the stars to form farther out and then diffuse into the central cavity. There is no evidence for dense molecular gas in the cavity but SOFIA may show the existence of neutral atomic clumps, perhaps characterized by high velocities, that cannot be spatially resolved by the KAO.

SOFIA, with its superior FIR resolution, would reveal if the streamer of neutral atomic gas inside the cavity is spiraling into the center from the inner surface of the dust ring or from outside the ring, possibly from clouds tens of parsecs away. Using FIR polarimetry, SOFIA will also image the structure of the magnetic fields within the dust ring and the cavity at a resolution that

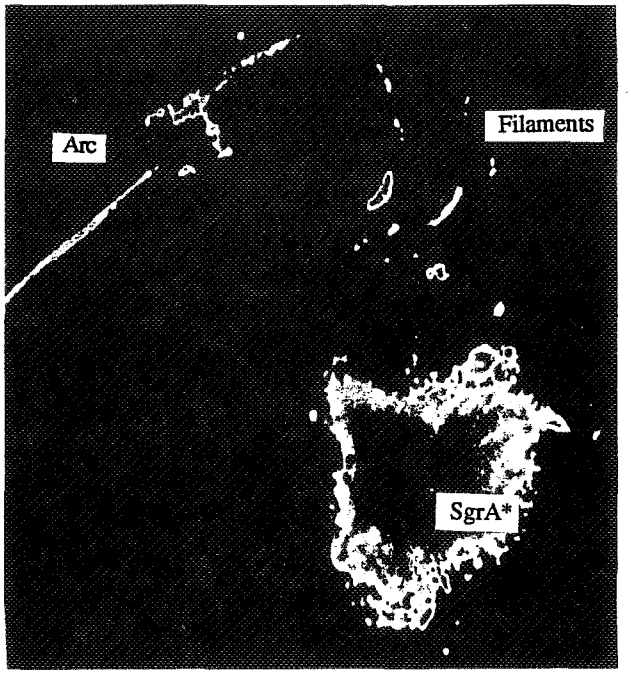

Figure 12. A grayscale radio (20 cm) image of the Galactic Center region. The figure is roughly 30 pc × 30 pc or ~ 15 × 15 arcmin in extent.

will be sufficient to test whether the dust ring is a magnetic accretion disk, removing its angular momentum centrifugally, or an assembly of unresolved magnetic streamers, or some other scenario.

Magnetic fields play an extensive role at larger scales in the vicinity of the Galactic Center as well. Ten arcminutes north of the dust ring, radio maps have shown the existence of peculiar large arcs of synchrotron emission, extending for about 20 pc perpendicular to the Galactic plane. The source of the electron excitation is unknown. These arcs seem, in projection, joined to the dust ring region of the Galactic Center via thermal arched filaments of ionized and neutral gas, and dust (see Figure 12). The KAO has shown that these filaments have luminosities $\sim 10^7$ $L_\odot$, and that the magnetic fields lie along the filaments, almost parallel to the Galactic plane. The source of ionization and heating of the arched filaments is also unknown, although undetected hot stars are the most likely candidate. However, the morphology of the filaments and the connection between the magnetic fields and such stars is a mystery. With the improved resolution of SOFIA we can use FIR fine-structure lines to examine ionization stratification in the arched filaments to seek the hypothetical embedded clumps of stars if they exist.

Obviously SOFIA will clarify our currently limited perception of phenomena in and around our own Galactic Center, which in turn will be a crucial step toward understanding similar phenomena seen on larger scales in many other galactic nuclei.

4. Comparison with Other Missions

Many important problems in modern astronomy require infrared observations with high sensitivity, high spectral resolution, and high angular resolution, or a combination of these capabilities. To fill these needs, the National Academy of Sciences Decade Survey (Bahcall) Committee has recommended *both* SOFIA and SIRTF (the Space Infrared Telescope Facility) as high priorities for development by NASA during the 1990's. A discussion and individual mission summaries of past and future infrared missions is contained in Session Nine of these proceedings, starting with the discussion summary by Caroff (1994).

Here we present a brief comparison of the principal missions SOFIA, SIRTF, ISO (the Infrared Space Observatory), KAO, and IRAS. Figure 13 and Table 3 depict the features of these missions which underlie the differences in their science goals. Table 3 compares launch/first flight dates, telescope diameters, design lifetimes, instrument complements, mobilities, and sponsors.

Table 3

KAO	IRAS	ISO	SOFIA	SIRTF
1974	1983	1995	2000	2002
0.91 meter	0.60 meter	0.60 meter	2.5 meter	0.85 meter
20+ years	1 year	$1\frac{1}{2}$ year	20 years	$2\frac{1}{2}$ years
12/Evolving	2/Fixed	4/Fixed	15/Evolving	3/Fixed
Deployable	Earth Orbit	Earth Orbit	Deployable	Solar Orbit
USA	USA+NED+UK	ESA+JPN+USA	USA+FRG	USA

Basically, the cryogenically cooled space missions achieve far higher sensitivity in broad wavelength bands, whereas the airborne facilities permit higher angular resolution and capacity to accommodate new instruments and science programs over a long lifetime. For example, the SOFIA science program will capitalize on its spatial and spectral resolution, for example in revealing how stars form, and on its mobility, which permits optimum observations of ephemeral events such as occultations. The SIRTF science goals exploit its excellent sensitivity and large detector arrays, for example to study galaxy formation at the edge of the visible Universe. SOFIA's targets will typically be galactic objects or nearby galaxies that may be studied in detail not possible with SIRTF, while many of SIRTF's targets will be faint or distant objects that would be undetectable with SOFIA. SIRTF's focal plane instruments are optimized for the highest priority scientific goals, but will be used for a range of scientific investigations. SOFIA's program is broad in scope because of its wide wavelength coverage, long lifetime, and annual opportunities to propose new science investigations and focal plane instruments.

As pointed out by Caroff (1994), in addition to its unique science potential, the airborne program provides unique continuity, training opportunities, and wavelength coverage to the infrared community.

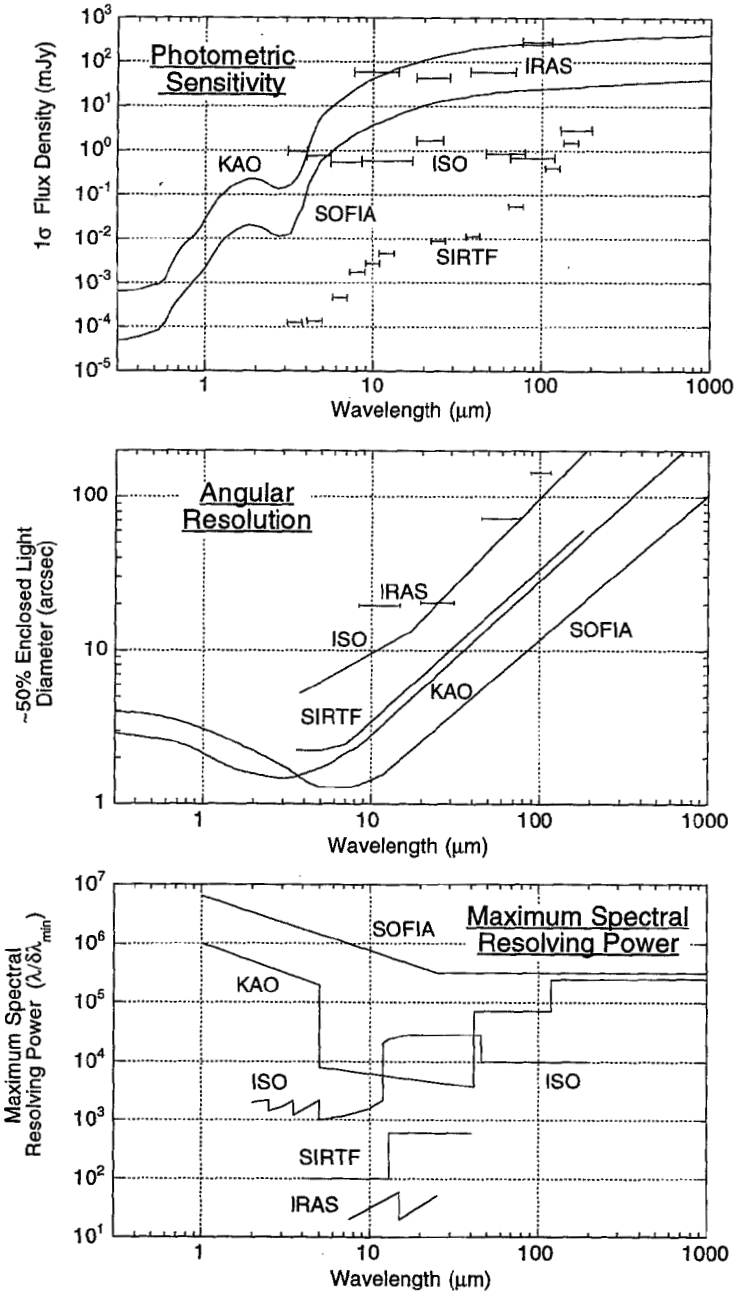

Figure 13. Photometric sensitivity, angular resolution, and spectroscopic resolving power for the KAO, IRAS, ISO, SOFIA, and SIRTF as a function of wavelength.

5. Education

Scientific and technical literacy are among the most critical needs of our nation. We benefit not only from brilliant researchers and creative inventors, but also from understanding of and respect for scientific endeavors by the taxpayers who must support them, and who themselves will be working in an increasingly scientifically and technologically advanced world. Thus, education in the fields of science, mathematics, and technology is not simply an investment in future scientists and engineers, but an investment in the appreciation of society for these endeavors. Through its unique scientific mission, SOFIA can increase this appreciation.

For scientists, SOFIA will provide a unique window to view the invisible infrared universe. However, for educators, it will be an exciting and accessible example of leading-edge high technology in the telescope, the scientific instrumentation, and the mission operations systems. For the public, SOFIA will serve as a high visibility, modern scientific facility, *epitomizing* the American ideals of innovation, exploration, and achievement.

The extensive participation in SOFIA observations by the science community, and the opportunities for teachers and the media to experience science in action on board, guarantee the potential of SOFIA for education. The rapid response of an airborne observatory to ephemeral astronomical events also helps to attract and focus public attention on science, as was the case for the KAO observations of Supernova 1987A, and for the impact of Comet Shumaker-Levy on Jupiter in 1994. These events frequently require remote deployments, which will expose this modern flagship of astronomy to the public world-wide, amplifying its effectiveness in expanding awareness of science.

The education program on SOFIA will offer to non-scientists a first-hand view of scientific research: its excitement, hardships, challenges, frustrations, teamwork, and discoveries. The intent of the SOFIA educational program is to bring these experiences to American students, teachers and the public routinely and on a significant scale. These outreach efforts will be built into the core program and evolve from the experiences with programs currently conducted with the KAO, such as the Flight Opportunities for Science Teacher EnRichment (FOSTER). SOFIA will be larger and fly more frequently than the KAO, and thus can support an expanded program.

Outreach activities are planned which will serve (1) pre-college students and teachers, (2) undergraduate and graduate students and faculty, and (3) the public and the media. SOFIA will promote excellence in science, mathematics and technology education through direct involvement of non-scientists with the SOFIA investigators, and via workshops, internships, and utilization of existing educational infrastructure such as museums and planetaria. In addition, many people will be able to experience SOFIA research remotely through the Internet and telepresence. Ongoing internal and external evaluation of the program will assure its effectiveness, much as the peer review process will do for the science program. Educational activities on SOFIA will touch the spirit and imagination of many American youth.

6. Technology

The unique observing potential, 20 year lifetime, and frequent opportunities for participation which SOFIA will offer the scientific community assure the development and prompt application of new technologies. Many of these will surely be valuable in future space and ground-based astronomy, as well as in other areas. The history of the airborne astronomy program is a guide to this process: the chopping secondary mirror, a feature of all modern infrared telescopes, was initially developed for the Learjet telescope. This facility also allowed the first "hands-on" testing of far-infrared bolometer detectors and a He^3 refrigerator in an astronomical application.

KAO investigators have extended this work by making significant contributions to bolometer array and newer refrigerator technologies, which are used on ground-based submillimeter telescopes, as well as on the KAO. Detectors anticipated for use on SIRTF and AXAF are currently being flown in KAO instruments. Experience with KAO focal plane instruments has been applied to the design of the space missions IRAS, COBE, ISO, SWAS, Cassini, AXAF, WIRE, and SIRTF. Germanium photoconductor detectors developed for use on the KAO were actually used on IRAS. We anticipate that nearly all future space IR missions (*e.g.,* FIRST and Edison) will reap major benefits from SOFIA-related technology.

Some of the technologies evolved in conjunction with SOFIA may have commercial applications. For example on the KAO, extensive research was done to develop infrared radiometers to measure the atmospheric water column depth overhead; this technique proved useful in detecting clear air turbulence, and the technology is now under review for suitability on commercial aircraft. In conjunction with wind tunnel testing of the SOFIA model, a pressure sensitive paint has been developed to provide very high spatial resolution of the pressure variations on airfoils; this technology has already been applied by major American aircraft companies in new wing designs. Future SOFIA technology could find application in aerodynamic noise reduction for aircraft, automated intelligent systems monitoring of real-time control systems, and mission operations and planning procedures for space flight.

7. Readiness

A configuration with the telescope cavity located behind the wing has been shown in predevelopment studies with aircraft modifiers to be much less expensive than putting the telescope ahead of the wing. Extensive analysis, including infrared observations of the exhaust plumes from NASA's Shuttle Carrier Aircraft (a Boeing 747), has shown that scattered emission from this source is not a concern for all but a very small class of possible science investigations. The aft configuration has been adopted as a cost cutting measure, although it may increase the seeing distortion of the images at near infrared wavelengths (Figure 2) due to the thicker boundary layer in the rear of the plane. Figure 14 depicts the design with the aft cavity installation of the telescope.

Wind tunnel tests of the airflow over the open-port telescope in an aft cavity have resulted in a quiet, low drag shear-layer control concept for SOFIA, and have demonstrated that the flow reattachment is stable and the control

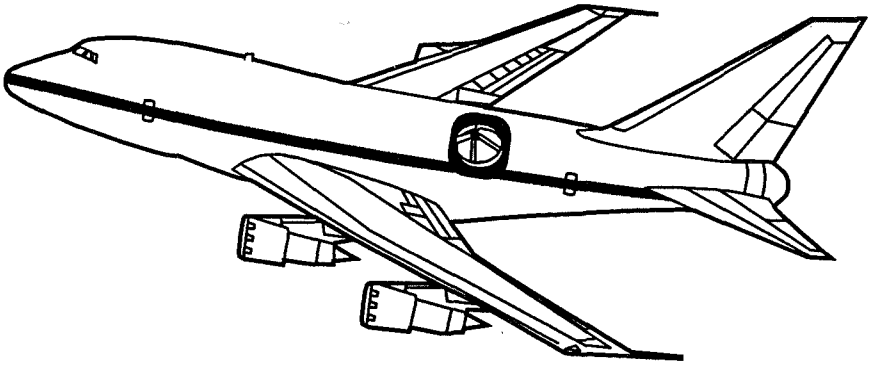

Figure 14. The baseline SOFIA design concept.

of the aircraft is not affected for expected flight conditions. These tests also provide good estimates of the wind loading on the telescope. Further wind tunnel tests are anticipated to select among the door design concepts currently being considered.

The telescope design (Figure 15) features an airbearing support and numerous other similarities to the KAO telescope, which has achieved sub-arcsecond pointing stability even in light turbulence. Structural and optical analyses indicate that either a metal or composite structure could be used, and that any of several (glass) primary mirror designs would work. The 2.5 m primary can be as slow as ~f/1.5 with the telescope in the aft location, so that figuring is not a problem; the chopped image quality is better for larger primary f-numbers.

SOFIA definition studies, sponsored jointly by NASA and the German Space Agency DARA, have been completed, and the project has been deemed ready for development by these agencies. If funding is available, NASA and DARA plan to begin the development of SOFIA in 1996, which would permit the first flights to occur in the year 2000.

8. Conclusion

The characteristics of SOFIA – its astronomical promise, moderate cost, maintainability, and opportunities for broad-based community participation – will extend the tradition of the airborne program for innovation, education, and exciting science. Its vision will penetrate dark reaches of our own and other galaxies, revealing objects and processes otherwise hidden from view with spatial resolution which will be unmatched until well into the next century. It will elucidate problems ranging from the spectacular death of massive stars to the inconspicuous incubation of low mass stars, from the composition of interstellar dust to the formation of prebiotic materials and protoplanetary

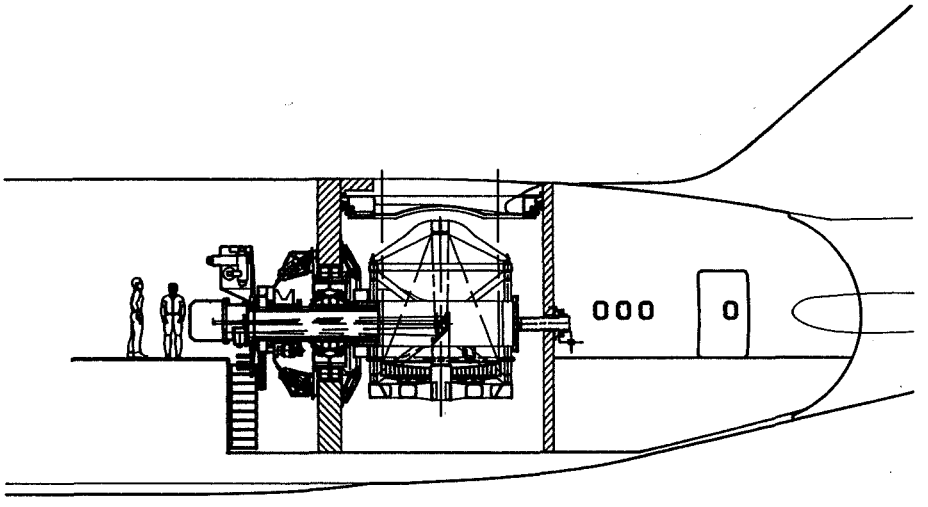

Figure 15. The SOFIA telescope installation in a Boeing 747-SP.

systems, and from the enigmatic character of our own Galactic Center to the nature of stupendous luminosity sources in colliding galaxies. SOFIA's image, performance, and accomplishments will be a credit to its heritage.

9. Acknowledgments

It is a pleasure to thank Al Betz, Harold Butner, Dale Cruikshank, Ted Dunham, David Hollenbach, and Dan Lester for contributions to the science section, Edna DeVore for contributions to the education section, and Mike Werner for assistance with the comparison of SOFIA to other missions. The photograph of M82 was provided by the Mount Wilson and Las Campanas Observatories, Carnegie Institution of Washington. The photograph of Beta Pictoris is credited to Bradford Smith (University of Arizona) and Richard Terrile (JPL). The picture of Uranus and its ring system was painted by Rick Sternbach. Howard Bushouse (Computer Sciences Corporation) provided the CCD image of NGC 7318. The drawings SOFIA and of the SOFIA telescope were produced by Dan Machak and Will Valloton (respectively) of NASA Ames.

10. References

Caroff, L. J. 1994, in Proc of the Airborne Astronomy Symp on the Galactic Ecosystem: From Gas to Stars to Dust, ed. M. R. Haas, J. A. Davidson, & E. F. Erickson (San Francisco: ASP), p 647

Larson, H. P. 1994, in Proc of the Airborne Astronomy Symp on the Galactic Ecosystem: From Gas to Stars to Dust, ed. M. R. Haas, J. A. Davidson, & E. F. Erickson (San Francisco: ASP), p 591

Traub, W. A., and Stier, M., 1976, Applied Optics, 15, 364

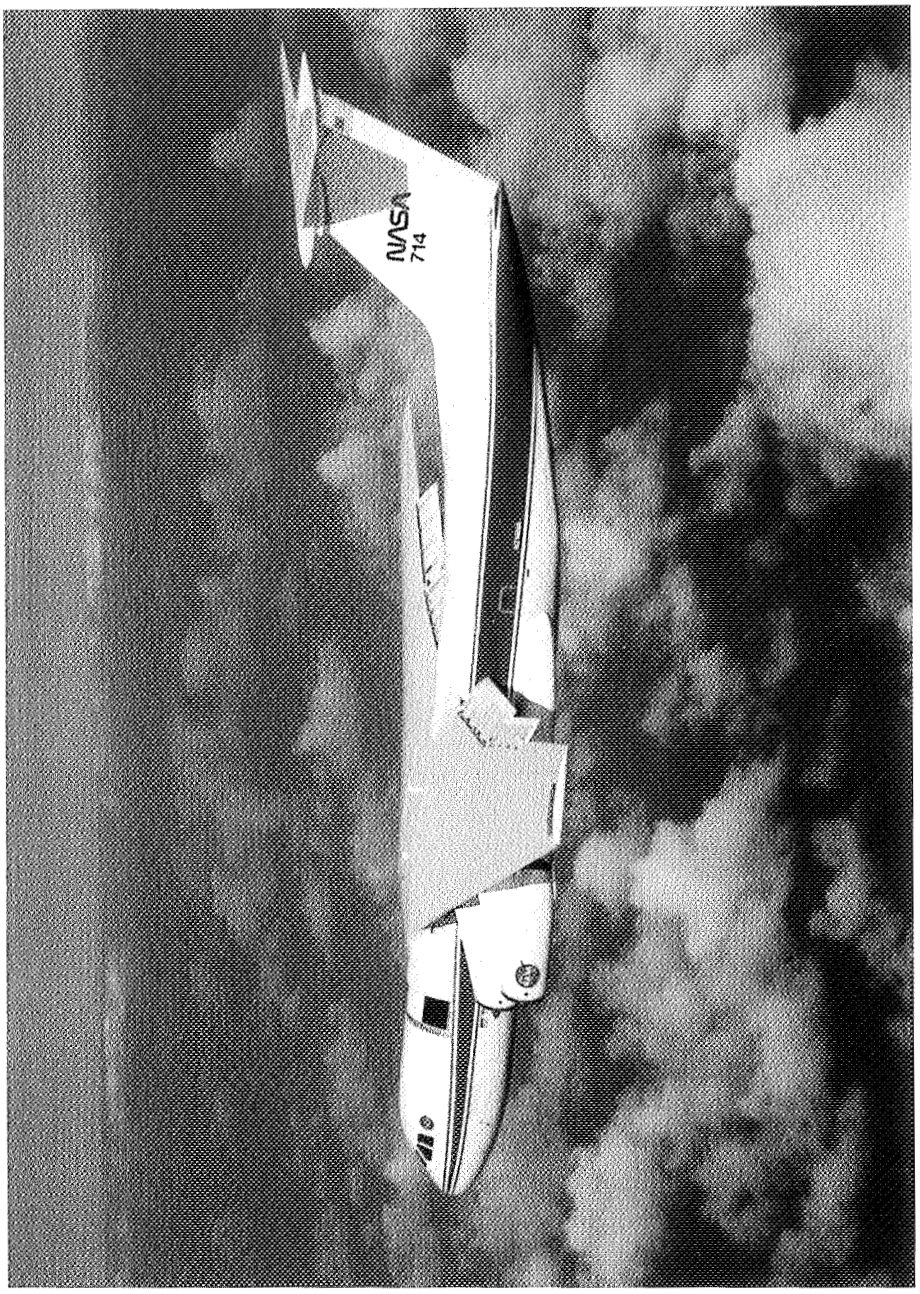

The Kuiper Airborne Observatory (1994)

Page intentionally left blank

Author Index